

M20

Temperature Dependence of Mode Coupling in low-NA Plastic Optical Fibers

Svetislav Savović, Milan S. Kovačević, Jovan S. Bajić, Dragan Z. Stupar, Alexandar Djordjevich, Miloš Živanov, Branko Drljača, Ana Simović, and Kyunghwan Oh

Abstract—Using the power flow equation and experimental measurements, investigated in this paper is the state of mode coupling in low NA (0.3) step-index (SI) plastic optical fibers under varied temperature. Numerical results obtained using the power flow equation agree well with experimental measurements. It is found that elevated temperatures of low-NA SI plastic optical fibers strengthened mode coupling. These properties remained after a year, with the fiber being subjected to environmental temperature variations of >35 K. These thermally induced changes of the fiber properties are attributed to the increased intrinsic perturbation effects in the PMMA material at higher temperatures. This results in an increase of the measured bandwidth with increasing fiber temperature as well as earlier the bandwidth switch from the functional dependence of $1/z$ to $1/z^{1/2}$ (slower bandwidth decrease).

Index Terms—Mode coupling, step index plastic optical fiber, thermal treatment.

I. INTRODUCTION

THE importance of plastic optical fibers (POFs) has grown tremendously over past decades. POFs are highly promising transmission media for short-range applications including in local area networks, multi-node bus networks, sensors, power delivery systems, and light guides (as in toys, entertainment and medical devices). The attractiveness of POFs is chiefly due to their low cost, flexibility and ease of handling and interconnecting. However, their relatively large attenuation and modal dispersion limit the link length and transmission rate. The main

types of POFs, their manufacturing and possible present and expected future applications have been reported [1]. Much effort has been made in recent decades to mitigate the effect of limited bandwidth of SI-POFs [1], [2]. Temperature variation as an avenue for additional improvements has been indicated by simulation [3] by showing that modal dispersion decreases as temperature is increased, leading to a bandwidth improvement. One should mention here that in reference [3] the simulations that concerned POFs were based on measurements for bulk PMMA and this is only a coarse approximation.

Ambient temperature can often affect structure of the POF material [4], [5]. Intrinsic perturbation effects may also change with temperature [3], [5] (these perturbations are by irregularities introduced predominantly during the fiber manufacturing process that resulted in microscopic bends, irregularity of the core-cladding boundary, and inconsistency of the refractive index). In spite of all fibers undergoing some degradation of optical transmission when exposed to heating, fiber-optic systems are nevertheless implemented in warm environments particularly as optical fiber sensors [5], [6] and the influence of temperature may be considerable. Changes optical fibers undergo with temperature fluctuation have been investigated [3], [5], [7], [8].

Transmission characteristics of multimode SI optical fibers depend heavily upon the differential mode attenuation and rate of mode coupling. The latter represents power transfer from lower to higher-order modes caused by the above-mentioned intrinsic perturbation effects. Mode coupling reduces modal dispersion, leading to a bandwidth improvement in local area networks [9]. On the other hand, it increases the amount of power radiated in fiber curves or bends [10]–[12], significantly changing the output-field properties and degrading the beam quality. These consequences are difficult to predict intuitively and have a particular importance for power delivery and sensory systems.

The far-field pattern of an optical fiber is determined by the optical power distribution that depends on the launch conditions, fiber properties and fiber length. Light launched at a specific angle $\theta_0 > 0$ with respect to the fiber axis will form a sharply defined ring radiation pattern at the output end of only short fibers. Because of mode coupling, the boundary (edges) of such a ring become fuzzy at the end of longer fibers. Up to a “coupling length” L_c from the input fiber end, the extent of this fuzziness increases further with fiber length and the ring-pattern evolves gradually into a disk extending across the entire fiber cross-section. An equilibrium mode distribution (EMD) exists beyond the coupling length L_c of the fiber. It is characterized by the absence of rings regardless of launch conditions, even though the resulting light distribution of the disk-pattern may

Manuscript received August 24, 2014; revised October 27, 2014 and November 21, 2014; accepted November 24, 2014. Date of publication December 4, 2014; date of current version December 16, 2014. This work was supported by the Strategic Research Grant of City University of Hong Kong through Project CityU 7004069 and by a grant from Serbian Ministry of Education, Science and Technological Development through Projects 171011 and III43008.

S. Savović is with the Faculty of Science, University of Kragujevac, 34000 Kragujevac, Serbia, and also with the City University of Hong Kong, Kowloon, Hong Kong (e-mail: savovic@kg.ac.rs).

M. S. Kovačević is with the Faculty of Science, University of Kragujevac, 34000 Kragujevac, Serbia, and also with Institute of Physics and Applied Physics, Department of Physics, Yonsei University, Seoul 120-749, Korea (e-mail: kovac@kg.ac.rs).

J. S. Bajić, D. Z. Stupar, and M. Živanov are with the Faculty of Technical Sciences, University of Novi Sad, 402920 Novi Sad, Serbia (e-mail: bajić@uns.ac.rs; drstupar@uns.ac.rs; zivanov@uns.ac.rs).

A. Djordjevich is with the City University of Hong Kong, Kowloon, Hong Kong (e-mail: mealex@cityu.edu.hk).

B. Drljača is with the Faculty of Science, University of Kosovska Mitrovica, 38220 Kosovska Mitrovica, Serbia (e-mail: brdljaca@gmail.com).

A. Simović is with the Faculty of Science, University of Kragujevac, 34000 Kragujevac, Serbia (e-mail: asimovic@kg.ac.rs).

K. Oh is with the Institute of Physics and Applied Physics, Department of Physics, Yonsei University, Seoul 120-749, Korea (e-mail: koh@yonsei.ac.kr).

Digital Object Identifier 10.1109/JLT.2014.2375515

vary with launch conditions. EMD indicates a substantially complete mode coupling. It is of critical importance when measuring characteristics of multimode optical fibers (linear attenuation, bandwidth, etc). Indeed, measurement of these characteristics would only be considered as meaningful if performed at the EMD condition when it is possible to assign to a fiber a unique value of loss per unit length [13].

In order to determine the fiber length L_c where the EMD is achieved, one can either perform pulse broadening measurements as a function of fiber length [9] or analyze the change of the output angular power distribution as a function of fiber length for different launch angles [14]. In the former case, L_c is the fiber length after which the bandwidth becomes proportional to $1/z^{1/2}$ instead of $1/z$ (z is the fiber length). In the latter case, L_c is the fiber length after which all output angular power distributions take the disk-form regardless of the incidence angle. The shorter the length L_c , the earlier the bandwidth would switch from the functional dependence of $1/z$ to $1/z^{1/2}$ (slower bandwidth decrease).

Output angular power distribution in the near and far fields of an optical fiber end has been studied extensively. Work has been reported using geometric optics (ray approximation) to investigate mode coupling and predict output-field patterns [15], [16]. By employing the power flow equation [14], [17]–[20] as well as the Fokker–Planck and Langevin equations [21], these patterns have been predicted as a function of the launch conditions and fiber length. A key prerequisite for achieving this is the knowledge of the rate of mode coupling expressed in the form of the coupling coefficient D [17]–[19], which has been shown to correctly predict coupling effects observed in practice (e.g. [14]).

In this work, we use the Savović–Djordjević method [22] for determining the mode coupling coefficient D in a low-NA POF at temperatures ranging from 293.15 to 353.15 K. This enabled us to solve the power flow equation numerically in order to examine the state of mode coupling in the fiber being analyzed at different temperatures. As a result, the coupling length L_c at which the EMD is achieved and the fiber length z_s required for achieving the steady-state mode distribution (SSD) are obtained for different fiber temperatures. These numerical results are verified experimentally.

II. POWER FLOW EQUATION

Gloge’s power flow equation is [17]:

$$\frac{\partial P(\theta, z)}{\partial z} = -\alpha(\theta)P(\theta, z) + \frac{D}{\theta} \frac{\partial}{\partial \theta} \left(\theta \frac{\partial P(\theta, z)}{\partial \theta} \right) \quad (1)$$

where $P(\theta, z)$ is the angular power distribution, z is distance from the input end of the fiber, θ is the propagation angle with respect to the core axis, D is the coupling coefficient assumed constant and $\alpha(\theta)$ is the modal attenuation. The simplifying assumption of constant coupling coefficient D (independent of the propagation angle) in SI POFs has been used by many authors [9], [12]–[14], [17]–[19], [22]–[24]. In our previous work [23] we have shown that modeling mode coupling in SI POFs assuming a constant coupling coefficient D can be used instead of

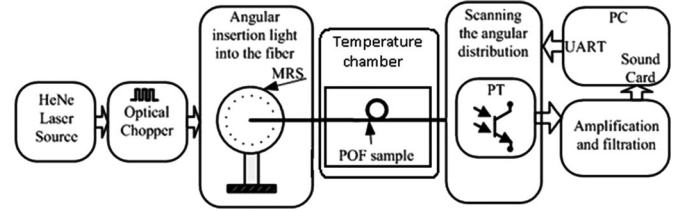


Fig. 1. Block diagram of the experimental setup for measuring the far-field intensity pattern (MRS—manual rotation stage, PT—phototransistor, PC—personal computer).

the more complicated approach with angle-dependent coupling coefficient. The boundary conditions are $P(\theta_c, z) = 0$, where θ_c is the critical angle of the fiber, and $D(\partial P/\partial \theta) = 0$ at $\theta = 0$. Condition $P(\theta_c, z) = 0$ implies that modes with infinitely high loss do not carry power. Condition $D(\partial P/\partial \theta) = 0$ at $\theta = 0$ indicates that the coupling is limited to the modes propagating with $\theta > 0$. Except near cutoff, the attenuation remains uniform $\alpha(\theta) = \alpha_0$ throughout the region of guided modes $0 \leq \theta \leq \theta_c$ [19], [20] (it appears in the solution as the multiplication factor $\exp(-\alpha_0 z)$ that also does not depend on θ). Therefore, $\alpha(\theta)$ need not be accounted for when solving (1) for mode coupling and this equation reduces to [14]:

$$\frac{\partial P(\theta, z)}{\partial z} = \frac{D}{\theta} \frac{\partial P(\theta, z)}{\partial \theta} + D \frac{\partial^2 P(\theta, z)}{\partial \theta^2}. \quad (2)$$

In order to obtain numerical solution of the power flow (2) we have used the explicit finite-difference method employed in our earlier works [12], [14].

III. EXPERIMENTAL METHOD

In this section, we present the experimental setup and methodology used to obtain the far-field intensity in the MH4001 ESKA Mitsubishi Rayon fiber (MH fiber). The fiber has a core diameter $d_{\text{core}} = 980 \mu\text{m}$ and clad diameter $d_{\text{clad}} = 1000 \mu\text{m}$, numerical aperture $\text{NA} = 0.3$, core refractive index $n = 1.49$ and critical angle $\theta_c = 11.7^\circ$ measured inside the fiber and $\theta_c = 17.6^\circ$ measured in air. The MH fiber has 0.15 dB/m of nominal attenuation. The number of modes in this step-index multimode POF, for $\lambda = 633 \text{ nm}$, is $N = 2\pi^2 a^2 (\text{NA})^2 / \lambda^2 \approx 1.06 \times 10^6$, where a is radius of the fiber core. This large number of modes may be represented by a continuum as required for application of (2). The ends of the sample fibers have been polished carefully for reduced imperfections and associated light diffraction.

Fig. 1 shows schematics of the experimental setup for measuring the far-field intensity profile at different temperatures. The light source was a helium neon laser (HRR005 by Thorlabs, Inc) with maximum power of 0.5 mW at 633 nm, modulated by a chopper at $f = 700 \text{ Hz}$. The input fiber end was mounted on a rotation stage (MRS-PRM1/M by Thorlabs, Inc) in order to achieve an angled launch. Using a phototransistor (BPW17, 520–950 nm range), the far-field output intensity from the other fiber-end was profiled in 3-D by a two-motor scanning setup.

For the temperature variation, a chamber with adjustable temperature has been used. The temperature has been also measured with an external high precision digital thermometer. The heating

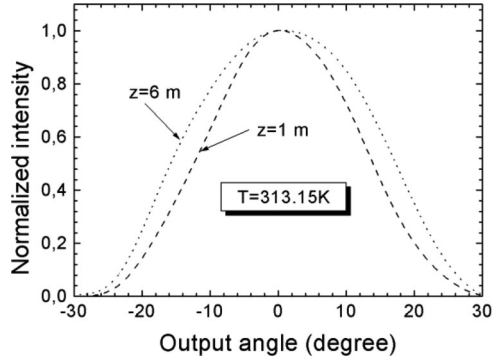


Fig. 2. Normalized experimental output power distribution at two different locations along the MH4001 POF for centrally launched ($\theta_0 = 0^\circ$) Gaussian beam, at $z = 1$ m (dashed line) and $z = 6$ m (dotted line) at temperature $T = 313.15$ K.

TABLE I
FIBER TEMPERATURE T , COUPLING COEFFICIENT D , COUPLING LENGTH L_c
FOR ACHIEVING THE EMD AND LENGTH z_s FOR ACHIEVING THE SSD

Temperature T (K)	D (rad ² /m)	L_c (m)	z_s (m)
293.15	1.62×10^{-3}	4.0	10.0
313.15	3.41×10^{-3}	3.0	7.5
333.15	4.53×10^{-3}	2.25	5.5
353.15	5.82×10^{-3}	1.5	4.0

process consisted of increasing the temperature of the chamber by 20 K every 30 min, from 293.15 to 353.15 K.

IV. RESULTS AND DISCUSSION

In our recently published work [24], coupling coefficient D for this fiber was calculated as $D = 1.62 \times 10^{-3}$ rad²/m at ambient temperature of $T = 293.15$ K. From $D = (\sigma_2^2 - \sigma_1^2) / 2(z_2 - z_1)$ [22], the coupling coefficient D was calculated as $D = 3.41 \times 10^{-3}$ rad²/m for $\sigma_1 = 12^\circ$ and $\sigma_2 = 16^\circ$ being the two standard deviations of the experimental output angular power distribution at fiber lengths $z_1 = 1$ m and $z_2 = 6$ m (see Fig. 2), at $t = 40^\circ\text{C}$. The values of the mode coupling coefficient D for the analyzed fiber at different temperatures are summarized in Table I, respectively, to facilitate easier comparisons.

Starting with the fiber length of 15 m, this length was shortened by 0.25 m in successive steps until the final length of just 0.75 m remained. In each step, the launch angle was swept in 5° increments from 0 to 15° and for each such sub-step the far-field output pattern was recorded (by the photo detector in the two-motor scanning setup). The fiber placed inside the temperature-controlled chamber was coiled on a reel with diameter in excess of 0.5 m to minimize the influence of curvature on mode coupling.

Fig. 3 shows experimental results for the normalized output power distribution for different fiber lengths at $T = 313.15$ K. We show results for four different input angles $\theta_0 = 0, 5, 10$ and 15° (measured in air). In Fig. 4, our numerical solution of the power flow equation is presented by Nero PhotoSnap Viewer.Ink

showing the evolution of the normalized output power distribution with fiber length at temperature $T = 313.15$ K. A good agreement between the numerical and experimental results can be observed. A good agreement between theory and experiment means that the position of the maximum of the output angular power distributions for different launch beam angles at particular fiber lengths obtained experimentally is the same as the position obtained by numerical calculations. Radiation patterns in the short fiber ($z = 1$ m) in Figs. 3(a) and 4(a) indicate that the coupling is stronger for the low-order modes: their distributions have shifted towards $\theta = 0^\circ$. Coupling of higher-order modes can be observed after longer fiber lengths [see Figs. 3(b) and 4(b)]. It is not until the fiber's coupling length L_c of 3 m that all the mode-distributions have shifted their mid-points to zero degrees (from the initial value of θ_0 at the input fiber end), producing the EMD in Figs. 3(c) and 4(c). The coupling continues further along the fiber beyond the L_c mark until all distributions' widths equalize and SSD is reached at length z_s in Figs. 3(d) and 4(d): $z_s = 7.5$ m. The maximum estimated relative error of determining the coupling coefficient $\Delta D/D$, coupling length $\Delta L_c/L_c$ and length at which a SSD is achieved $\Delta z_s/z_s$ is approximately 10%.

It can be seen from Table I that with increasing fiber temperature there is an increase of the coupling coefficient D , meaning that intrinsic perturbation effects in the fiber are stronger. With increasing fiber temperature the width of the output angular power distribution measured at a fixed fiber length increases too (see Fig. 5). Consequently, the lengths L_c and z_s (see Fig. 6) shorten.

It is shown through simulations [3] that if the temperature is increased, the modal dispersion decreases, due to the change of the fiber refractive index. As a result, the stronger mode coupling, the shorter the length L_c , and the earlier the bandwidth switches from the functional dependence of $1/z$ to $1/z^{1/2}$ (slower bandwidth decrease) (Fig. 7). Therefore, thermal control can serve to shorten the coupling length and slow bandwidth drop in POFs. One can also see from Fig. 7 that there is an increase of the measured bandwidth (for central launch ($\theta_0 = 0^\circ$)) with increasing the fiber temperature. This increase is more pronounced at short fiber lengths (up to 40 m). It has been observed previously that mode coupling can also be increased significantly by proper bending of POFs [11], [12] resulting in a similar change of transmission characteristics (in terms of the coupling length for achieving EMD, length for achieving SSD, and bandwidth).

We have obtained that with increasing temperature, there is a very small change of numerical aperture of the fiber (Fig. 8). Namely, measured numerical aperture of MH4001 fiber varies between $\text{NA} = 0.37$ and $= 0.38$, at temperatures between 293.15 and 353.15 K, respectively. Thus, the influence of the change of the numerical aperture on temperature dependence of the coupling constant D can be excluded. One should mention here that measured numerical aperture of $\text{NA} = 0.37$ at 293.15 K for MH4001 fiber differs from its theoretical numerical aperture of $\text{NA} = 0.3$, due to the fact that this fiber is a double cladding fiber and not typical SI POF [1].

We have also obtained that with increasing fiber temperature, there is a slight increase of mode dependent attenuation

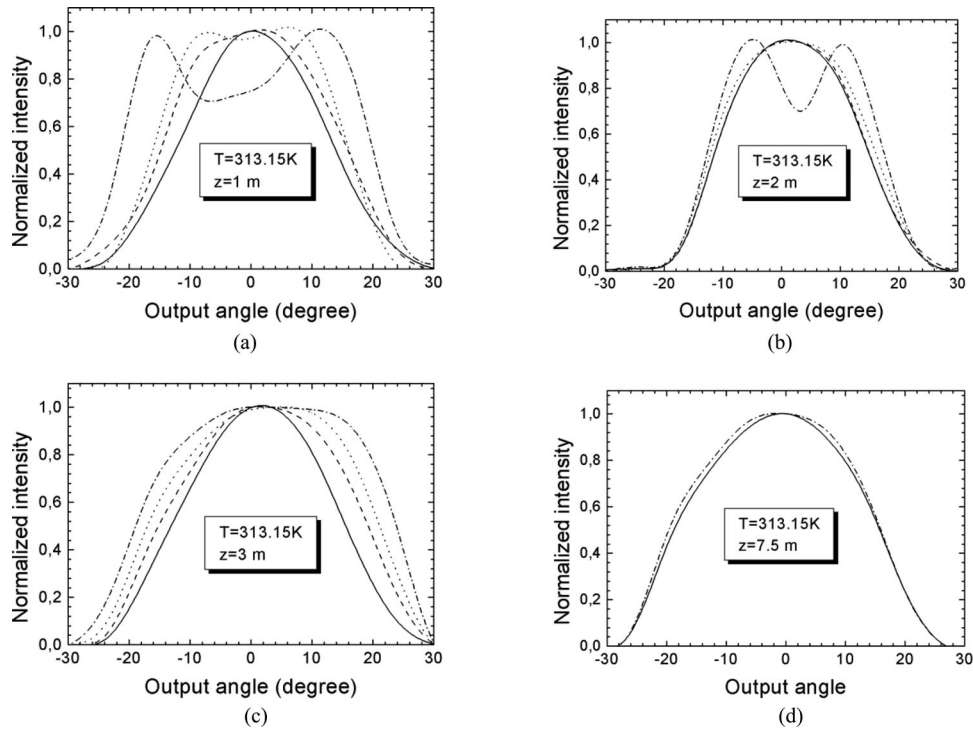


Fig. 3. Normalized experimental output angular power distribution at different locations along the MH4001 POF at $T = 313.15 \text{ K}$ for four Gaussian input angles $\theta_0 = 0^\circ$ (solid line), 5° (dashed line), 10° (dotted line) and 15° (dash-dotted line) at: (a) $z = 1 \text{ m}$ (solid line); (b) $z = 2 \text{ m}$ (dashed line); (c) $z = 3 \text{ m}$ (dotted line) and (d) $z = 7.5 \text{ m}$ (dash-dotted line).

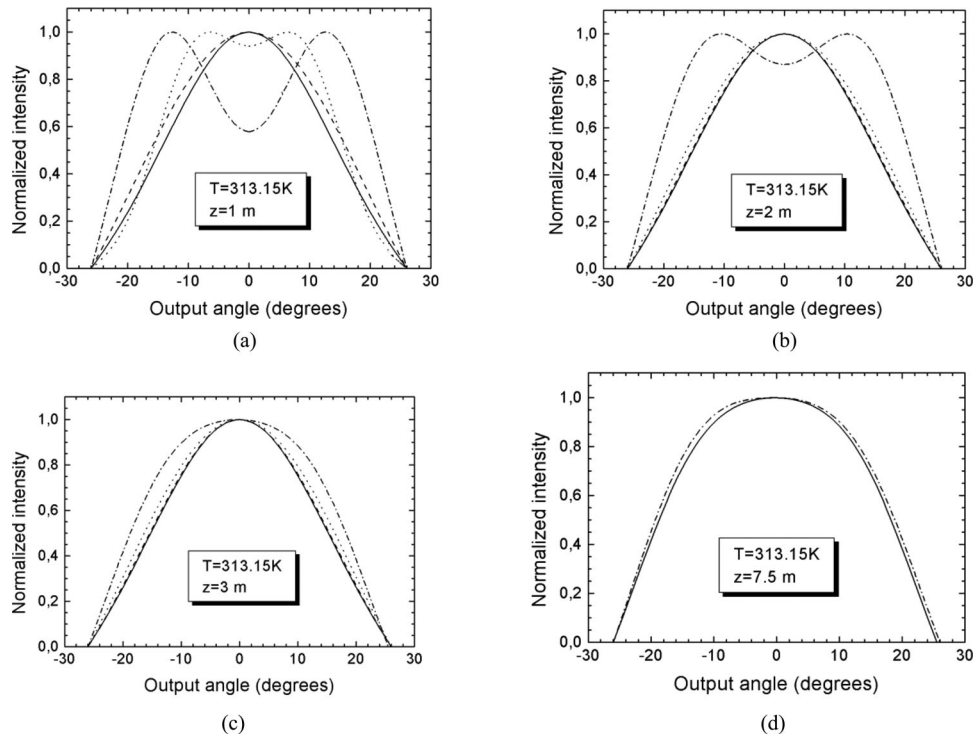


Fig. 4. Normalized output angular power distribution at different locations along the MH4001 POF at $T = 313.15 \text{ K}$ calculated for four Gaussian input angles $\theta_0 = 0^\circ$ (solid line), 5° (dashed line), 10° (dotted line) and 15° (dash-dotted line) for: (a) $z = 1 \text{ m}$ (solid line); (b) $z = 2 \text{ m}$ (dashed line); (c) $z = 3 \text{ m}$ (dotted line) and (d) $z = 7.5 \text{ m}$ (dash-dotted line).

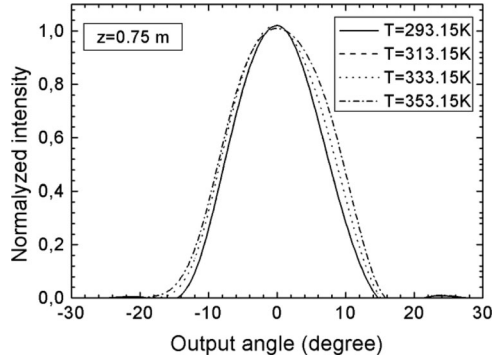


Fig. 5. Normalized experimental output angular power distribution along the MH4001 POF of length $z = 0.75$ m at different temperatures for centrally ($\theta_0 = 0^\circ$) launched Gaussian beam.

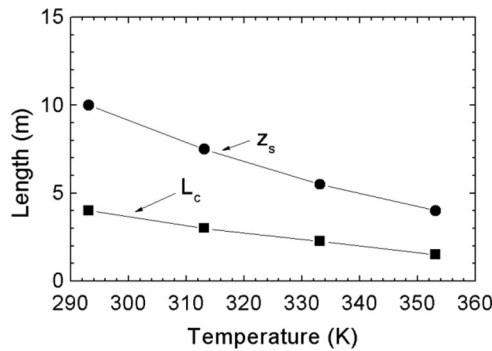


Fig. 6. Variation of the fiber's coupling length L_c for achieving the EMD and length z_s for achieving the SSD with temperature for MH4001 POF.

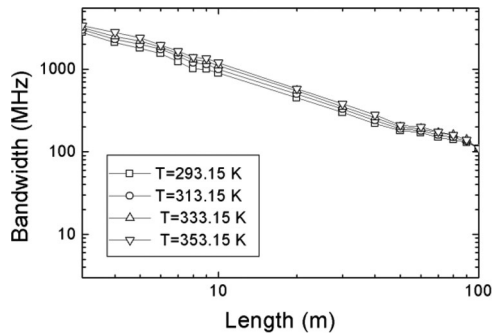


Fig. 7. Bandwidth of the MH4001 POF measured for central launch ($\theta_0 = 0^\circ$) at different temperatures.

coefficient (see Fig. 9). This is in contrast with results reported by Chen *et al.* [7] for the MH4001 POF with higher numerical aperture of $NA = 0.5$. They have obtained that there is a decrease of power loss with increasing fiber temperature.

One can see from Fig. 9 that the modal attenuation at a given temperature could be considered approximately constant with the propagation angle in the range $\theta = 0^\circ$ to $\approx 18^\circ$, which enabled us to numerically solve the power flow equation in its simpler form (2) instead of solving the power flow (1).

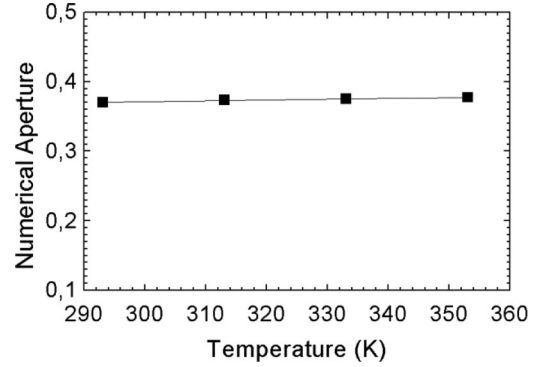


Fig. 8. Variation of the numerical aperture with temperature for MH4001 POF.

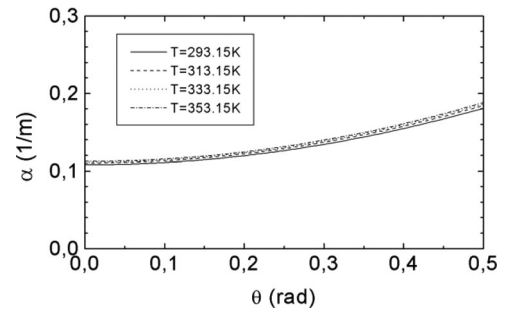


Fig. 9. Mode-dependent attenuation $\alpha(\theta)$ for MH4001 POF measured at different temperatures.

V. CONCLUSION

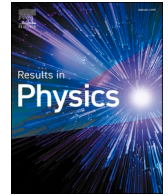
Using the power flow equation and experimental measurements, investigated in this article is the state of mode coupling in low-NA (0.3) step-index (SI) POFs under varied temperature. Results are verified experimentally. It is found that elevated temperatures of low NA SI POF strengthened mode coupling. These properties remained after a year, with the fiber being subjected to environmental temperature variations of >35 K. The thermally induced changes of the fiber properties are attributed to the increased intrinsic perturbation effects in the fiber material. This results in an increase of the measured bandwidth with increasing the fiber temperature. Stronger mode coupling shortens lengths L_c (for achieving the EMD) and z_s (for achieving the SSD) causing thus an earlier bandwidth switch from the functional dependence of $1/z$ to $1/z^{1/2}$ (slower bandwidth decrease). Therefore, bandwidth can be altered by controlling fiber temperature and the results presented in this paper can be used to predict such change.

REFERENCES

- [1] W. Daum, J. Krauser, P. E. Zamzow, and O. Ziemann, *POF-Polymer Optical Fibers for Data Communications*. Berlin, Germany: Springer, 2002.
- [2] N. Raptis, E. Grivas, E. Pikasis, and D. Syvridis, "Space-time block code based MIMO encoding for large core step index plastic optical fiber transmission systems," *Opt. Exp.*, vol. 19, pp. 10336–10350, 2011.

- [3] M. Kovačević and A. Djordjević, "Variation of modal dispersion and bandwidth with temperature in PMMA based step-index polymer optical fibers," *J. Optoelectron. Adv. Mater.*, vol. 11, pp. 1821–1825, 2010.
- [4] L. Hoffmann, M. S. Müller, S. Krämer, M. Giebel, G. Schwotzer, and T. Wieduwilt, "Applications of fibre optic temperature measurement," *Proc. Estonian Acad. Sci. Eng.*, vol. 13, pp. 363–378, 2007.
- [5] T. Reinsch and J. Henniges, "Temperature dependent characterization of optical fibres for distributed temperature sensing in hot geothermal wells," *arXiv:1206.1853v1 [physics.geo-ph]*, Jun. 8, 2012.
- [6] A. T. Moraleda, C. V. García, J. Zubia Zaballa, and J. Arrue, "A temperature sensor based on a polymer optical fiber macro-bend," *Sensors*, vol. 13, pp. 13076–13089, 2013.
- [7] L.-W. Chen, W.-H. Lu, and Y.-C. Chen, "An investigation into power attenuations in deformed polymer optical fibers under high temperature conditions," *Opt. Commun.*, vol. 282, pp. 1135–1140, 2009.
- [8] N. Raptis and D. Syvridis, "Bandwidth enhancement of step index plastic optical fibers through a thermal treatment," *IEEE Photon. Technol. Lett.*, vol. 25, no. 16, pp. 1642–1645, Aug. 2013.
- [9] A. F. Garito, J. Wang, and R. Gao, "Effects of random perturbations in plastic optical fibers," *Science*, vol. 281, pp. 962–967, 1998.
- [10] J. Arrúe, J. Zubía, G. Fuster, and D. Kalymnios, "Light power behaviour when bending plastic optical fibers," in *Proc. Inst. Elect. Eng. Optoelectron.*, 1998, vol. 145, pp. 313–318.
- [11] M. A. Losada, J. Mateo, I. Garcés, J. Zubía, J. A. Casao, and P. Pérez-Vela, "Analysis of strained plastic optical fibers," *IEEE Photon. Technol. Lett.*, vol. 16, no. 6, pp. 1513–1515, Jun. 2004.
- [12] S. Savović and A. Djordjević, "Mode coupling in strained and unstrained step-index plastic optical fibers," *Appl. Opt.*, vol. 45, pp. 6775–6780, 2006.
- [13] J. Dugas and G. Maurel, "Mode-coupling processes in polymethyl methacrylate-core optical fibers," *Appl. Opt.*, vol. 31, pp. 5069–5079, 1992.
- [14] A. Djordjević and S. Savović, "Investigation of mode coupling in step index plastic optical fibers using the power flow equation," *IEEE Photon. Technol. Lett.*, vol. 12, no. 11, pp. 1489–1491, Nov. 2000.
- [15] M. Eve and J. H. Hannay, "Ray theory and random mode coupling in an optical fibre waveguide. I," *Opt. Quantum Electron.*, vol. 8, pp. 503–508, 1976.
- [16] J. Arrue, G. Aldabaldetrekú, G. Durana, J. Zubía, I. Garcés, and F. Jiménez, "Design of mode scramblers for step-index and graded-index plastic optical fibers," *J. Lightw. Technol.*, vol. 23, no. 3, pp. 1253–1260, Mar. 2005.
- [17] D. Gloge, "Optical power flow in multimode fibers," *Bell Syst. Tech. J.*, vol. 51, pp. 1767–1783, 1972.
- [18] W. A. Gambling, D. N. Payne, and H. Matsumura, "Mode conversion coefficients in optical fibers," *Appl. Opt.*, vol. 14, pp. 1538–1542, 1975.
- [19] M. Rousseau and L. Jeunhomme, "Numerical solution of the coupled-power equation in step index optical fibers," *IEEE Trans. Microw. Theory Tech.*, vol. MTT-25, no. 7, pp. 577–585, Jul. 1977.
- [20] L. Jeunhomme, M. Fraise, and J. P. Pocholle, "Propagation model for long step-index optical fibers," *Appl. Opt.*, vol. 15, pp. 3040–3046, 1976.
- [21] S. Savović and A. Djordjević, "Solution of mode coupling in step-index optical fibers by the Fokker-Planck equation and the Langevin equation," *Appl. Opt.*, vol. 41, pp. 2826–2830, 2002.
- [22] S. Savović and A. Djordjević, "Method for calculating the coupling coefficient in step index optical fibers," *Appl. Opt.*, vol. 46, pp. 1477–1481, 2007.
- [23] S. Savović and A. Djordjević, "Influence of the angle-dependence of mode coupling on optical power distribution in step-index plastic optical fibers," *Opt. Laser Technol.*, vol. 44, pp. 180–184, 2012.
- [24] S. Savović, M. S. Kovačević, A. Djordjević, J. S. Bajić, D. Z. Stupar, and G. Stepniak, "Mode coupling in low NA plastic optical fibers," *Opt. Laser Technol.*, vol. 60, pp. 85–89, 2014.

Authors' biographies not available at the time of publication.



High bandwidth performance of multimode graded-index microstructured polymer optical fibers

Svetislav Savović^{a,b}, Ana Simović^a, Branko Drljača^c, Milan S. Kovačević^a,
Ljubica Kuzmanović^a, Miloš Ivanović^a, Alexander Djordjevich^b, Konstantions Aidinis^{d,e},
Daniele Tosi^f, Rui Min^{g,*}

^a Faculty of Science, University of Kragujevac, R. Domanovića 12, 34000 Kragujevac, Serbia

^b Department of Mechanical Engineering, City University of Hong Kong, 83 Tat Chee Avenue, Hong Kong, China

^c Faculty of Sciences, University of Pristina in Kosovska Mitrovica, Lole Ribara 29, 38220 Kosovska Mitrovica, Serbia

^d Department of Electrical Engineering, Ajman University, P.O. Box 346, Ajman, United Arab Emirates

^e Center of Medical and Bio-allied Health Sciences Research, Ajman University, Ajman P.O. Box 346, United Arab Emirates

^f School of Engineering, Nazarbayev University, Astana, Kazakhstan

^g Center for Cognition and Neuroergonomics, State Key Laboratory of Cognitive Neuroscience and Learning, Beijing Normal University at Zhuhai, Zhuhai 519087, China

ABSTRACT

The investigation of the bandwidth in multimode graded-index microstructured polymer optical fiber (GI mPOF) with a solid core is proposed using a modal diffusion approach. For a variety of launch radial offsets of multimode GI mPOF, bandwidth is reported by numerically solving the time-dependent power flow equation (TD PFE) using the explicit finite difference method (EFDM) and physics-informed neural networks (PINN). The decline in bandwidth with fiber length becomes slower at fiber lengths close to the coupling length L_c at which an equilibrium mode distribution (EMD) is attained, showing that mode coupling enhances bandwidth at longer fiber lengths. As fiber length is increased, bandwidth approaches complete independence from radial offset, suggesting the steady-state distribution (SSD) has been reached. We compare multimode GI mPOF performance in terms of bandwidth with that of traditional multimode GI POFs made of the same material. Higher bandwidth performance and quicker bandwidth improvement are displayed by the GI mPOF. To enhance fiber performance in GI mPOF links, such a fiber characterization can be used.

Introduction

High-speed short-range signal transmission via POF has drawn a lot more attention in recent years [1–2]. POF's benefits of a large core, a simple connection, and a diversity of materials [3–16] may offer a cost-effective option for the in-home network. Up until now, POF has most typically been produced using Polymethyl-methacrylate (PMMA) [17]. POF can generally be divided into three types: single-mode [18], few-mode [12], and multimode [19] fibers. The two refractive index (RI) distributions that are most frequently used to create POFs are step-index (SI) [20] and GI [21] distributions. The RI distribution of GI multimode POF continually lowers from the core axis to the cladding. Using this RI distribution, intermodal dispersion can be reduced, the POF's bandwidth can be improved, and transmission distance may be raised. However, in order to manufacture GI POF, advanced doping techniques are required.

The versatility in designing the optical fiber is greatly increased by the microstructure of microstructured optical fiber (MOFs). Many

excellent MOF properties [22], including birefringence [23], light dispersion [24], supercontinuum light [25], and wavelength conversion [26], have been investigated by modifying the microstructure. The fabrication of multimode mPOF was first reported by Eijkelenborg et al. in 2001 [27], and afterwards, mPOF garnered research interest for its various uses [28–29]. An optical fiber called a multimode mPOF is made to simultaneously guide numerous light modes. It has a core region surrounded by cladding, and the core and/or cladding region's periodic arrays of air holes give it its distinctive structure. Thus, an mPOF can have its core and/or cladding layer modified by changing the placement and/or size (d) of air holes (Fig. 1). In Fig. 1, a mPOF that mimics a GI optical fiber features a core with different-sized air-holes. Instead of requiring complex doping methods, GI mPOF has the advantage of being more adjustable when it comes to altering the air-hole diameters d and pitch Λ . Additionally, research has shown that GI mPOF has a wider bandwidth than conventional multimode GI POF [30,31]. Numerous industries, including telecommunications, sensing, and imaging in medicine, use multimode GI and SI mPOFs. They are appropriate for

* Corresponding author.

E-mail address: rumi@alumni.upv.es (R. Min).

<https://doi.org/10.1016/j.rinp.2023.106548>

Received 23 March 2023; Received in revised form 7 May 2023; Accepted 11 May 2023

Available online 22 May 2023

2211-3797/© 2023 The Author(s). Published by Elsevier B.V. This is an open access article under the CC BY-NC-ND license (<http://creativecommons.org/licenses/by-nc-nd/4.0/>).

high-power applications due to their large mode areas and ability to transmit high-power lasers. Due to their high sensitivity to variations in the refractive index of the surrounding medium, they are also beneficial for sensing applications.

The PFE is used to characterize transmission performance of different types of conventional multimode optical fibers [31–35] and is thus the most promising tool for modeling multimode MOFs. Since other two alternative approaches, wave optics or geometrical optics, are not able to offer an efficient and accurate modeling tool for transmission characteristics of multimode optical fibers (including MOFs), the importance of the approach used in this work is obvious. A very good efficiency and accuracy of the method used in this work has already been demonstrated in modeling bandwidth of conventional multimode GI POF [35]. Following this route, the bandwidth in GI mPOF for a various launch radial offsets is determined in this paper, to the best of our knowledge for the first time, by numerically solving the TD PFE. These theoretically obtained results for multimode GI mPOF bandwidth are contrasted with previously reported bandwidth for conventional multimode GI POFs [35]. The results reported in this study can be useful for various MOFs applications [36–39].

GI mPOF design

Fig. 1 shows a GI mPOF that was considered in this investigation. Six air-hole rings, numbered rings 1, 2, ..., 6, make up the GI mPOF. The fiber material is a PMMA, and the air holes are held in place by a triangular lattice with a pitch of Λ . The air-hole diameter in rings 5 and 6 is the same as the air-hole diameter in ring 4 ($d_4 = d_5 = d_6$). The TD PFE was used to simulate this system.

TD PFE for GI optical fibers

The RI profile of GI optical fiber may be expressed as:

$$n(r, \lambda) = \begin{cases} n_{co}(\lambda) \left[1 - 2\Delta(\lambda) \left(\frac{r}{a} \right)^g \right]^{1/2} & (0 \leq r \leq a) \\ n_{cl}(\lambda) [1 - 2\Delta(\lambda)]^{1/2} = n_{cl}(\lambda) & (r > a) \end{cases} \quad (1)$$

where $n_{co}(\lambda)$ is the maximum RI of the core (measured at the fiber axis), $n_{cl}(\lambda)$ is the RI of the cladding, $\Delta(\lambda) = (n_{co}(\lambda) - n_{cl}(\lambda)) / n_{co}(\lambda)$ is the relative RI difference, g is the core index exponent and a is the core radius (Fig. 1). The wavelength λ of the source determines the optimum value of the core RI exponent g to get the maximum bandwidth.

For multimode GI optical fibers, the TD PFE is:

$$\begin{aligned} \frac{\partial P(m, \lambda, z, \omega)}{\partial z} + j\omega\tau(m, \lambda)P(m, \lambda, z, \omega) &= -\alpha(m, \lambda)P(m, \lambda, z, \omega) + \\ + \frac{\partial P(m, \lambda, z, \omega)}{\partial m} \frac{\partial d(m, \lambda)}{\partial m} + d(m, \lambda) \frac{1}{m} \frac{\partial P(m, \lambda, z, \omega)}{\partial m} &+ d(m, \lambda) \frac{\partial P^2(m, \lambda, z, \omega)}{\partial m^2} \end{aligned} \quad (2)$$

where $P(m, \lambda, z, \omega)$ is the power in the m -th principal mode (modal group) [32], z is position along the fiber axis from the input fiber end, $\alpha(m, \lambda)$ is the attenuation coefficient, $d(m, \lambda) \equiv D$ is the coupling

coefficient, $\omega = 2\pi f$ is the baseband angular frequency, $\tau(m, \lambda)$ is delay time per unit length, which can be determined as:

$$\begin{aligned} \tau(m, \lambda) \cong \frac{n_1(\lambda)}{c} \left[1 + \frac{g-2}{g+2} \Delta(\lambda) \left(\frac{m}{M(\lambda)} \right)^{2g/(g+2)} \right. \\ \left. + \frac{1}{2} \frac{3g-2}{g+2} \Delta(\lambda)^2 \left(\frac{m}{M(\lambda)} \right)^{4g/(g+2)} \right] \end{aligned} \quad (3)$$

where c is the free-space velocity of light and:

$$P(m, \lambda, z, \omega) = \int_{-\infty}^{+\infty} P(m, \lambda, z, t) \exp(-j\omega t) dt \quad (4)$$

The maximum principal mode number is [32]:

$$M(\lambda) = \sqrt{\frac{g\Delta(\lambda)}{g+2}} a k n_1(\lambda) \quad (5)$$

where $k = 2\pi/\lambda$. Gaussian launch-beam distribution $P_0(\theta, \lambda, z=0)$ can be transformed into $P_0(m, \lambda, z=0)$ (one needs $P_0(m, \lambda, z=0)$ to numerically solve the TD PFE (2)), using the following relationship [32–34]:

$$\frac{m}{M} = \left[\left(\frac{\Delta r}{a} \right)^g + \frac{\theta^2}{2\Delta} \right]^{(g+2)/2g} \quad (6)$$

where Δr represents the radial separation (radial offset) between the launch beam point and the core center and θ represents the tilt angle measured in relation to the fiber axis. One should note that the condition of validity of the model proposed in this work is that guiding modes can be treated as a modal continuum. This is the case with all types of multimode optical fibers, such as a GI mPOF investigated in this work. Details regarding numerical solving the TD PFE (2) using EFDM and calculating bandwidth, can be found in our earlier work [35]. In this work, in order to further validate our proposed method for calculating bandwidth in a multimode GI mPOF, in our best knowledge for the first time, the TD PFE (2) is also solved using PINN. Methodology regarding numerical solving the partial differential equations (PDEs), such as TD PFE (2), using PINN are given in the Appendix A of this work.

We investigated the bandwidth in a multimode GI mPOF, which consists of different SI distributed layers (Fig. 1(b)), for which the effective V parameter is given as:

$$V = \frac{2\pi}{\lambda} a_{eff} \sqrt{n_{co}^2 - n_{fsm}^2} \quad (7)$$

where $a_{eff} = \Lambda/\sqrt{3}$ [40], and n_{fsm} is effective RI of different core and cladding layers, which can be obtained from equation (7), with the effective V parameter [40]:

$$V \left(\frac{\lambda}{\Lambda}, \frac{d}{\Lambda} \right) = A_1 + \frac{A_2}{1 + A_3 \exp(A_4 \lambda / \Lambda)} \quad (8)$$

with the fitting parameters A_i ($i = 1$ to 4) given as:

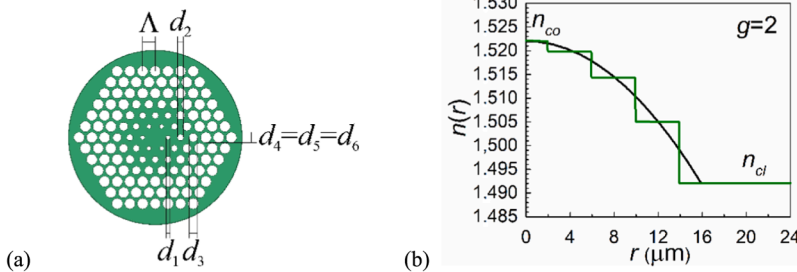


Fig. 1. (a) The cross-section of the multimode GI mPOF (PMMA is the fiber material, shown in green color). A triangular lattice's air holes are positioned using pitch Λ . The air-hole sizes of the four inner air-hole rings in the core are d_1 , d_2 , d_3 , and d_4 . The cladding's air holes in rings 5 and 6 have the same diameter as those in air-hole ring 4 ($d_4 = d_5 = d_6$). (b) The referent multimode GI mPOF's RI performance (green solid line). The parabolic distribution of the RI in the core has $g = 2$ (black solid line). (For interpretation of the references to color in this figure legend, the reader is referred to the web version of this article.)

$$A_i = a_{i0} + a_{i1} \left(\frac{d}{\Lambda}\right)^{b_{i1}} + a_{i2} \left(\frac{d}{\Lambda}\right)^{b_{i2}} + a_{i3} \left(\frac{d}{\Lambda}\right)^{b_{i3}} \quad (9)$$

where the coefficients a_{i0} to a_{i3} and b_{i1} to b_{i3} ($i = 1$ to 4) are given in Table 1.

We applied our method to the multimode GI mPOF which has a core radius $a = 4\Lambda = 16 \mu\text{m}$, where $\Lambda = 4 \mu\text{m}$, and fiber diameter $b = 1 \text{ mm}$. The GI mPOF material is PMMA, the same material as used for the GI POF (OM Giga, Fiber Fin™), which we previously investigated experimentally [35]. The RI of the core measured at the fiber axis is $n_{co} = 1.5220$ while the RI of the cladding is $n_{cl} = 1.4920$ [33,35,41]. For the GI mPOF under examination, the maximum principal mode number is $M = 24$ (the maximum mode number is $N = 580$) at $\lambda = 633 \text{ nm}$, for $g = 2.0$ and $\Delta = (n_1 - n_2)/n_1 = 0.019711$. The modal attenuation is $\alpha(m, \lambda) \equiv \alpha_c = 0.0122 \text{ m}^{-1}$ and coupling coefficient is $D = 1482 \text{ m}^{-1}$ [35] (typical values of α_c and D for conventional multimode GI POFs and multimode GI mPOFs). The similar presumption was used to model a silica MOF [42]. For $\Lambda = 4 \mu\text{m}$ and air-hole diameters of the four air-hole rings in the core $d_1 = 0.6 \mu\text{m}$, $d_2 = 0.7 \mu\text{m}$, $d_3 = 1.3 \mu\text{m}$ and $d_4 = 3.1 \mu\text{m}$, the RI $n_1 = 1.5201$, $n_2 = 1.5145$, $n_3 = 1.5050$ and $n_4 = 1.4920$, respectively, are calculated by means of equations (7) and (8). Thus, a parabolic RI distribution in the core with $g = 2.0$ is achieved (Fig. 1). The diameter of the cladding's air-holes in the rings 5 and 6 is $d_4 = d_5 = d_6 = 3.1 \mu\text{m}$, which corresponds to the cladding RI $n_4 = n_5 = n_6 = n_{cl} = 1.4920$.

A Gaussian beam is assumed to be launched with $\langle \theta \rangle = 0^\circ$ in the numerical calculations. Fig. 2 shows the numerically estimated bandwidth using EFDM and PINN for four radial offsets $\Delta r = 0, 4, 8$ and $12 \mu\text{m}$ for varied fiber lengths. A good agreement between solutions obtained using EFDM and PINN solutions can be seen. According to Fig. 2, bandwidth decreases as radial offset increases as a result of increased modal dispersion brought on by the excitation of higher guided modes. A more pronounced decline is seen with shorter fiber lengths. When the fiber length is $z \approx 20 \text{ m}$, which is close to the theoretically determined coupling length $L_c = 18 \text{ m}$ [37] at which an EMD is established, strong mode coupling results in bandwidth improvement (slower bandwidth drop) in multimode GI mPOFs. An SSD is established as fiber length increases (in our earlier work [41], we found that an SSD is established at $z = 60 \text{ m}$). As fiber length further increases, bandwidth becomes essentially radially offset-independent. Consequently, assuming a radial offset of $\Delta r = 0 \mu\text{m}$ for the examined GI mPOF, we obtain a bandwidth of around 28 GHz at a distance of 100 m, which results in a bandwidth-length product of 2.8 GHz·km. This bandwidth-length product is substantially higher than those for standard GI POFs studied in our earlier work [35] (Fig. 3) and Chun-Yu Lin et al.'s work [43], which were 0.46 GHz·km and 0.156 GHz·km, respectively. Because the GI mPOF investigated in this work has a smaller core radius and fewer propagating modes than a conventional GI POF, the EMD is obtained in GI mPOF at a shorter length. Namely, the coupling length of $L_c = 31 \text{ m}$ is reported for conventional GI POF [33]. When there are fewer propagating modes, the mode coupling process requires a shorter length to complete, accelerating the transition to the slower bandwidth drop phase. The mode coupling process requires a shorter length to complete the mode coupling process when there are fewer propagating

Table 1

The fitting coefficients in equation (9).

	$i = 1$	$i = 2$	$i = 3$	$i = 4$
a_{i0}	0.54808	0.71041	0.16904	-1.52736
a_{i1}	5.00401	9.73491	1.85765	1.06745
a_{i2}	-10.43248	47.41496	18.96849	1.93229
a_{i3}	8.22992	-437.50962	-42.4318	3.89
b_{i1}	5	1.8	1.7	-0.84
b_{i2}	7	7.32	10	1.02
b_{i3}	9	22.8	14	13.4

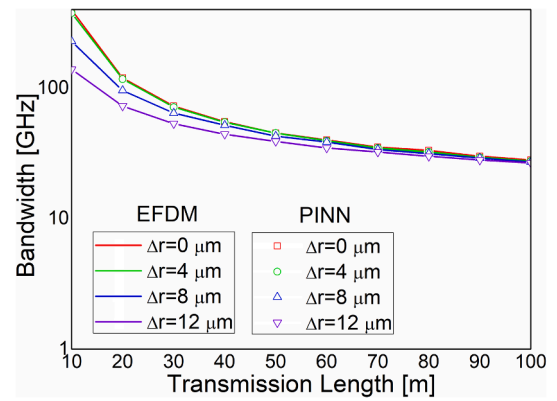


Fig. 2. Numerically calculated bandwidth using EFDM (lines) and PINN (open symbols) as a function of transmission length of GI mPOF for various radial offsets.

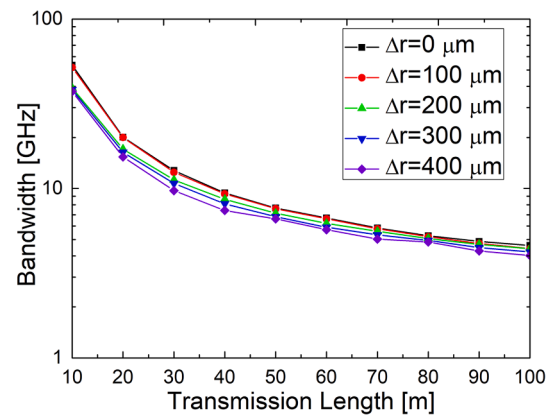


Fig. 3. Measured bandwidth (solid symbols) as a function of transmission length of conventional multimode GI POF for various radial offsets (lines are drawn to guide the eye) [35].

modes, which accelerates the transition to the slower bandwidth decline regime.

Improved fiber performance on GI mPOF lines, especially in in-home networks, can be attained by using such a fiber characterization. This optimization can be carried out by comparing the performance characteristics and numerical simulation results of different GI mPOFs with different RI distribution (different g), coupling coefficient D , and attenuation α_c . Finally, since in contrast to GI POF, fabrication of GI mPOF does not require an advanced doping techniques and, as shown in this work, and it can achieve a much higher bandwidth, it deserves recommendation as a good choice for various high bandwidth fiber optic systems. A range of different fabrication methods is available for mPOF preform fabrication, including extrusion, drilling, casting or injection molding [7,44].

Conclusion

By numerically solving the TD PFE using the EFDM and PINN, we were able to determine the bandwidth for various multimode GI mPOF launch conditions (radial offsets). We discovered that when radial offset increases, bandwidth decreases. There is a more noticeable bandwidth decrease at short fiber lengths. The fact that this decline slows down as coupling length L_c gets closer to the point at which an EMD is reached, shows how strongly mode coupling affects the bandwidth in GI mPOFs. The length at which EMD is reached is shorter, the quicker the bandwidth would change from a steep to a moderate bandwidth decrease. The formation of an SSD is indicated by the bandwidth becoming almost

entirely independent of radial offset as fiber length is extended. Consequently, for the GI mPOF that was the subject of this work, with radial offset of $\Delta r = 0 \mu m$, we obtain a bandwidth-length product of 2.8 GHz·km. This bandwidth-length product is substantially higher than those for typical GI POFs studied in our previous work [35] and Chun-Yu Lin et al.'s work [43], which were 0.46 GHz·km and 0.156 GHz·km, respectively. We have demonstrated that GI mPOF has a wider bandwidth compared to its conventional counterpart due to carefully tuned structure of the GI mPOF, which allowed reduction of modal dispersion-induced pulse spreading. Furthermore, mPOFs with a relatively large core diameter can support multiple modes, which can be used for mode-division multiplexing to increase the bandwidth.

Funding

This research was funded by the National Natural Science Foundation of China (62111530238, 62003046); the Strategic Research Grant of City University of Hong Kong (Project No. CityU 7004600); The grants from Serbian Ministry of Science, Technological Development and

Innovations (Agreement No. 451–03-68/2022–14/200122 and 451–03-47/2023–01/200123); The grant from Science Fund of the Republic of Serbia (Agreement No. CTPCF-6379382); Guangdong Basic and Applied Basic Research Foundation (2021A1515011997); Special project in key field of Guangdong Provincial Department of Education (2021ZDZX1050); The Innovation Team Project of Guangdong Provincial Department of Education (2021KCXTD014); Department of Science and Technology of Guangdong Province (2021A1313030055).

Declaration of Competing Interest

The authors declare that they have no known competing financial interests or personal relationships that could have appeared to influence the work reported in this paper.

Data availability

Data will be made available on request.

Appendix A. : PINN for solving PDEs

The PINN is a machine-learning technique that can be used to approximate the solution of PDEs. PDEs with corresponding initial and boundary conditions can be expressed in a general form as [45]:

$$\begin{aligned} \frac{\partial u(x,t)}{\partial t} + N[u(x,t)] &= 0, \quad x \in \Omega, \quad t \in [0, T] \\ u(x, t = 0) &= h(x), \quad x \in \Omega \\ u(x, t) &= g(x, t), \quad x \in \Omega_g, \quad t \in [0, T] \end{aligned} \quad (A1)$$

Here, N is a differential operator, $x \in \Omega \subseteq R^d$ and $t \in R$ represent spatial and temporal dimensions respectively, $\Omega \subseteq R^d$ is a computational domain, $\Omega_g \subseteq \Omega$ is a computational domain of the exposed boundary conditions, $u(x, t)$ is the solution of the PDEs with initial condition $h(x)$ and boundary conditions $g(x, t)$.

PINN consists of two subnets: an approximator network and a residual network. The approximator network receives input $u(x, t)$ undergoes the training process, and provides an approximate solution $\hat{u}(x, t)$ as an output. The approximator network trains on a grid of points, called collocation points, sampled randomly or regularly from the simulation domain. The weights and biases of the approximator network make up a set of trainable parameters, trained by minimizing a composite loss function of the following form:

$$L = L_r + L_0 + L_b \quad (A2)$$

where:

$$\begin{aligned} L_r &= \frac{1}{N_r} \sum_{i=1}^{N_r} |u(x^i, t^i) + N[u(x^i, t^i)]|^2 \\ L_0 &= \frac{1}{N_0} \sum_{i=1}^{N_0} |u(x^i, t^i) - h^i|^2 \\ L_b &= \frac{1}{N_b} \sum_{i=1}^{N_b} |u(x^i, t^i) - g^i|^2 \end{aligned} \quad (A3)$$



Here, L_r , L_0 , and L_b represent residuals of governing equations, initial and boundary conditions, respectively. N_r , N_0 , and N_b are the numbers of mentioned collocation points of the computational domain, initial and boundary conditions, respectively. These residuals are computed by a non-trainable part of the PINN model called the residual network. The approximator network is used to approximate the solution $u(x, t)$ which then goes to the residual network to calculate the residual loss L_r , boundary condition loss L_b , and initial condition loss L_0 . The weights and biases of the approximator network are trained using a composite loss function consisting of residuals L_r , L_0 , and L_b through gradient-descent technique based on the back-propagation [45]. To calculate the residual L_r , PINN requires derivatives of the outputs with respect to the inputs x and t . Such calculation is done through automated differentiation, which relies on the fact that combining derivatives of the constituent operations by the chain rule produces the derivative of the entire composition.

References

- [1] Barbio C, Mekonnen KA, Huijskens F, Koonen T, Tangdongga E. Bidirectional gigabits per second spatial diversity link using POF for passive optical front-ends. *J Light Technol* 2022;40(20):6753–61.
- [2] Huang O, Shi J, Chi N. Performance and complexity study of a neural network post-equalizer in a 638-nm laser transmission system through over 100-m plastic optical fiber. *Opt Eng* 2022;61(12):126108.
- [3] Ye Y, Zhao C, Wang Z, Teng C, Marques C, Min R. Portable multi-hole plastic optical fiber sensor for liquid level and refractive index monitoring. *IEEE Sens J* 2023;23(3):2161–8.

- [4] Teng C, Wang Y, Min R, Deng S, Deng H, Li Y, et al. Plastic optical fiber based SPR sensor for simultaneous measurement of refractive index and liquid level. *IEEE Sens J* 2022;22(7):6677–84.
- [5] Leal-Junior A, Guo J, Min R, Fernandes AJ, Frizzera A, Marques C. Photonic smart bandage for wound healing assessment. *Photonics Res* 2021;9(3):272–80.
- [6] Guo J, Niu M, Yang C. Highly flexible and stretchable optical strain sensing for human motion detection. *Optica* 2017;4(10):1285–8.
- [7] Fasano A, Woyessa G, Stajanca P, Markos C, Stefani A, Nielsen K, et al. Fabrication and characterization of polycarbonate microstructured polymer optical fibers for high-temperature-resistant fiber Bragg grating strain sensors. *Opt Mater Express* 2016;6(2):649–59.
- [8] Zubeil MG, Fasano A, Woyessa GT, Min R, Leal AG, Theodosiou A, et al. Bragg gratings inscribed in solid-core microstructured single-mode polymer optical fiber drawn from a 3D-printed polycarbonate preform. *IEEE Sens J* 2020;20(21):12744–57.
- [9] Akimoto Y, Asai M, Koike K, Makino K, Koike Y. Poly(styrene)-based graded-index plastic optical fiber for home networks. *Opt Lett* 2012;37(11):1853–5.
- [10] Makino K, Akimoto Y, Koike K, Kondo A, Inoue A, Koike Y. Low loss and high bandwidth polystyrene-based graded index polymer optical fiber. *J Light Technol* 2013;31(14):2407–12.
- [11] Leal-Junior AG, Theodosiou A, Min R, Casas J, Díaz CR, Dos Santos WM, et al. Quasi-distributed torque and displacement sensing on a series elastic actuator's spring using FBG arrays inscribed in CYTOP fibers. *IEEE Sens J* 2019;19(11):4054–61.
- [12] Chapalo I, Chah K, Gusarov A, Ioannou A, Pospori A, Nan Y-G, et al. Gamma-radiation enhancement of sensing properties of FBGs in a few-mode polymer CYTOP fiber. *Opt Lett* 2023;23(1):39.
- [13] Woyessa G, Rasmussen HK, Bang O. Zeonex – a route towards low loss humidity insensitive single-mode step-index polymer optical fibre. *Opt Fiber Technol* 2020;57:1–6.
- [14] Dash JN, Cheng X, Tam H. Low gas pressure sensor based on a polymer optical fiber grating. *Opt Lett* 2021;46(5):933–6.
- [15] Markos C, Stefani A, Nielsen K, Rasmussen HK, Yuan W, Bang O. High-Tg TOPAS microstructured polymer optical fiber for fiber Bragg grating strain sensing at 110 degrees. *Opt Express* 2013;21(4):4758–65.
- [16] Woyessa G, Fasano A, Stefani A, Markos C, Nielsen K, Rasmussen HK, et al. Single mode step-index polymer optical fiber for humidity insensitive high temperature fiber Bragg grating sensors. *Opt Express* 2016;24(2):1253–60.
- [17] Broadway C, Min R, Leal-Junior AG, Marques C, Caucheteur C. Toward commercial polymer fiber Bragg grating sensors: Review and applications. *J Light Technol* 2019;37(11):2605–15.
- [18] Cheng X, Gunawardena DS, Pun CJ, Bonefacino J, Tam H. Single nanosecond-pulse production of polymeric fiber Bragg gratings for biomedical applications. *Opt Express* 2020;28(22):33573–83.
- [19] Kuang R, Ye Y, Chen Z, He R, Savović I, Djordjević A, et al. Min Low-cost plastic optical fiber integrated with smartphone for human physiological monitoring. *Opt Fiber Technol* 2022;71:102947.
- [20] X. Hu, Z. Chen, X. Cheng, Min, H. Qu, C. Caucheteur, and H.-Y. Tam, Femtosecond laser point-by-point Bragg grating inscription in BDk-doped step-index PMMA optical fibers, *Opt. Lett.* 47(2), 249-252 (2022).
- [21] Theodosiou A, Min R, Leal-Junior AG, Ioannou A, Frizzera A, Pontes MJ, et al. Long period grating in a multimode cyclic transparent optical polymer fiber inscribed using a femtosecond laser. *Opt Lett* 2019;44(21):5346–9.
- [22] Knight JC, Birks TA, St P, Russell J, Atkin DM. All-silica single-mode optical fiber with photonic crystal cladding. *Opt Lett* 1996;21(19).
- [23] K. Stefanska, S. Majchrowska, K. Gemza, G. Soboń, J. Sotor, P. Mergo, K. Tarnowski, and T. Martynkien, Soliton trapping and orthogonal Raman scattering in a birefringent photonic crystal fiber, *Opt. Lett.* 47(16), 4183-4186 (2022).
- [24] Zhao S, Guo R, Zeng Y. Effects of frequency-dependent Kerr nonlinearity on higher-order soliton evolution in a photonic crystal fiber with one zero-dispersion wavelength. *Phys Rev A* 2022;106(3):033516.
- [25] Wang C, Lin K, Cao S, Feng G, Wang J, Abdalla AN. Polarized supercontinuum generation in CS 2-core all-normal dispersion photonic crystal fiber. *IEEE Photon J* 2022;14(6):1–7.
- [26] Heydarian K, Nosratpour A, Razaghi M. Computational study of wavelength conversion based on XGM by photonic crystal semiconductor optical amplifier. *Opt Laser Technol* 2022;156(1):108531.
- [27] Eijkelenborg MA, Large MCJ, Argyros A, Zagari J, Manos S, Issa NA, et al. Microstructured polymer optical fibre. *Opt Express* 2001;9(7):319–27.
- [28] Woyessa G, Pedersen JKM, Fasano A, Nielsen K, Markos C, Rasmussen HK, et al. Zeonex-PMMA microstructured polymer optical FBGs for simultaneous humidity and temperature sensing. *Opt Lett* 2017;42(6):1161–4.
- [29] Min R, Pereira L, Paixao T, Woyessa G, Hu X, Antunes P, et al. Chirped POF Bragg grating production utilizing UV cure adhesive coating for multiparameter sensing. *Opt Fiber Technol* 2021;65:102593.
- [30] Lwin R, Barton G, Harvey L, Harvey J, Hirst D, Manos S, et al. Beyond the bandwidth-length product: Graded index microstructured polymer optical fiber. *Appl Phys Lett* 2007;91(19):191119.
- [31] Garito AF, Wang J, Gao R. Effects of random perturbations in plastic optical fibers. *Science* 1998;281:962–7.
- [32] Olshansky R. Mode coupling effects in graded-index optical fibers. *Appl Opt* 1975;14:935–45.
- [33] Savović S, Simović A, Drljača B, Djordjević A, Stepniak G, Bunge CA, et al. Power flow in graded index plastic optical fibers. *J Lightwave Technol* 2019;37:4985–90.
- [34] Nagano K, Kawakami S. Measurements of mode conversion coefficients in graded-index fibers. *Appl Opt* 1980;19:2426–34.
- [35] A. Simović, A. Djordjević, B. Drljača, S. Savović, and R. Min, Investigation of bandwidth in multimode graded index plastic optical fibers, *Opt. Express* 29, 29587-29594 (2021).
- [36] Dadabayev R, Malka D. A visible light RGB wavelength demultiplexer based on polycarbonate multicore polymer optical fiber. *Opt Laser Technol* 2019;116:239–45.
- [37] Gelkop B, Aichnboim L, Malka D. RGB wavelength multiplexer based on polycarbonate multicore polymer optical fiber. *Opt Fiber Technol* 2021;61:102441.
- [38] Malka D, Peled A. Power splitting of 1×16 in multicore photonic crystal fibers. *Appl Surface Sci* 2017;417:34–9.
- [39] Malka D, Cohen E, Zalevsky Z. Design of 4×1 power beam combiner based on multicore photonic crystal fiber. *Appl Sci* 2017;7:695.
- [40] Saitoh K, Koshiba M. Empirical relations for simple design of photonic crystal fibers. *Opt Express* 2005;13(1):267–74.
- [41] S. Savović, A. Simović, B. Drljača, M. S. Kovačević, Lj. Kuzmanović, A. Djordjević, K. Aidinis, and R. Min, Power flow in multimode graded-index microstructured polymer optical fibers, *Polymers* 15, 1474 (2023).
- [42] Savović S, Kovačević MS, Simović A, Kuzmanović L, Drljača B, Djordjević A. Method for investigation of mode coupling in multimode step-index silica photonic crystal fibers. *Optik* 2021;246:167728.
- [43] Lin C-Y, Li C-Y, Lu H-H, Chang C-H, Peng P-C, Lin C-R, Chen J-H. A hybrid CATV/16-QAM-OFDM in-house network over SMF and GI-POF/VLC transport. *IEEE Phot Technol Lett* 2015;27:526–9.
- [44] van Eijkelenborg MA, Large MCJ, Argyros A, Zagari J, Manos S, Issa NA, et al. Microstructured polymer optical fibre. *Opt Express* 2001;9:319–27.
- [45] Raissi M, Perdikaris P, Karniadakis GE. Physics-informed neural networks: A deep learning framework for solving forward and inverse problems involving nonlinear partial differential equations. *J Computat Phys* 2019;378:686–707.

Power Flow in Multimode Graded-Index Microstructured Polymer Optical Fibers

Svetislav Savović^{1,2}, Ana Simović¹, Branko Drljača³ , Milan S. Kovačević¹, Ljubica Kuzmanović¹,
Aleksandar Djordjevich², Konstantinos Aidinis^{4,5} and Rui Min^{6,*} 

¹ Faculty of Science, University of Kragujevac, R. Domanovića 12, 34000 Kragujevac, Serbia

² Department of Mechanical Engineering, City University of Hong Kong, 83 Tat Chee Avenue, Hong Kong, China

³ Faculty of Sciences, University of Priština in Kosovska Mitrovica, Lole Ribara 29, 38220 Kosovska Mitrovica, Serbia

⁴ Department of Electrical Engineering, Ajman University, Ajman P.O. Box 346, United Arab Emirates

⁵ Center of Medical and Bio-Allied Health Sciences Research, Ajman University, Ajman P.O. Box 346, United Arab Emirates

⁶ Center for Cognition and Neuroergonomics, State Key Laboratory of Cognitive Neuroscience and Learning, Beijing Normal University at Zhuhai, Zhuhai 519087, China

* Correspondence: rumi@alumni.upv.es

Abstract: We investigate mode coupling in a multimode graded-index microstructured polymer optical fiber (GI mPOF) with a solid core by solving the time-independent power flow equation (TI PFE). Using launch beams with various radial offsets, it is possible to calculate for such an optical fiber the transients of the modal power distribution, the length L_c at which an equilibrium mode distribution (EMD) is reached, and the length z_s for establishing a steady-state distribution (SSD). In contrast to the conventional GI POF, the GI mPOF explored in this study achieves the EMD at a shorter length L_c . The earlier shift to the phase of slower bandwidth decrease would result from the shorter L_c . These results are helpful for the implementation of multimode GI mPOFs as a part of communications and optical fiber sensory systems.

Keywords: polymer optical fiber; graded-index optical fiber; microstructured optical fiber; power flow equation



Citation: Savović, S.; Simović, A.; Drljača, B.; Kovačević, M.S.; Kuzmanović, L.; Djordjevich, A.; Aidinis, K.; Min, R. Power Flow in Multimode Graded-Index Microstructured Polymer Optical Fibers. *Polymers* **2023**, *15*, 1474. <https://doi.org/10.3390/polym15061474>

Academic Editors: Igor Ayesta and Maria Asunción Illarramendi

Received: 27 February 2023

Revised: 12 March 2023

Accepted: 13 March 2023

Published: 16 March 2023



Copyright: © 2023 by the authors. Licensee MDPI, Basel, Switzerland. This article is an open access article distributed under the terms and conditions of the Creative Commons Attribution (CC BY) license (<https://creativecommons.org/licenses/by/4.0/>).

1. Introduction

High-speed, short-range signal transmission over POF has attracted much research interest in recent years [1,2]. POF has the benefit of an easy connection and a large core, which could be an economic solution for the in-home network. Different kinds of materials are implemented for POF fabrication, such as polymethyl methacrylate (PMMA) [3,4], polydimethylsiloxane (PDMS) [5,6], polycarbonate (PC) [7,8], polystyrene (PS) [9,10], perfluorinated polymer (commercially known as CYTOP[®] (AGC, Inc., Tokyo, Japan) [11,12], cycloolefin polymer (commercially known as ZEONEX[®] *ZEON (Corporation, Tokyo, Japan) [13,14], and cycloolefin copolymer (commercially known as TOPAS[®]) (TOPAS Advanced Polymers, Farmington Hills, MI, USA) [15,16]. The flexibility of POF material allows for the production of POFs with varying specifications or materials to meet the needs of various applications. Until now, PMMA has been the most commonly used material for the production of POF [17]. POF can normally be classified as singlemode [18] or multimode [19] based on the number of propagation modes, the step-index (SI) [20], or the GI [21] based on the refractive index (RI) distribution. The GI multimode POF is a type of POF where its RI distribution decreases continuously from the core axis to the cladding. This RI distribution can minimize intermodal dispersion, improve the POF's bandwidth, and increase the transmission distance. However, GI POF needs sophisticated doping processes for its fabrication.

Microstructured optical fiber (MOF), which is referred to as photonic crystal fiber, was successfully proposed in the 1990s [22]. The microstructure of MOFs significantly improves the optical fiber's flexibility. By adjusting the microstructure, various excellent MOF features have been explored, such as birefringence [23], light dispersion [24], supercontinuum light [25], and wavelength conversion [26]. Argyros developed the first PMMA mPOF in 2001 [27], and then mPOF attracted research interests for its different applications [28,29]. The core and/or cladding layer of a typical mPOF design, as depicted in Figure 1, can be changed by altering the arrangement and/or size (d) of air holes within a concentric ring-like region. Figure 1 depicts an mPOF that mimics a GI optical fiber by having a core with varying sizes of air-holes. Greater flexibility in modifying the air-hole diameters and pitches, as opposed to the necessity for sophisticated doping processes with typical GI POF, is the advantage of GI mPOF over conventional GI POF. Additionally, GI mPOF has been found to have a higher bandwidth and a lower loss than conventional GI POF [30].

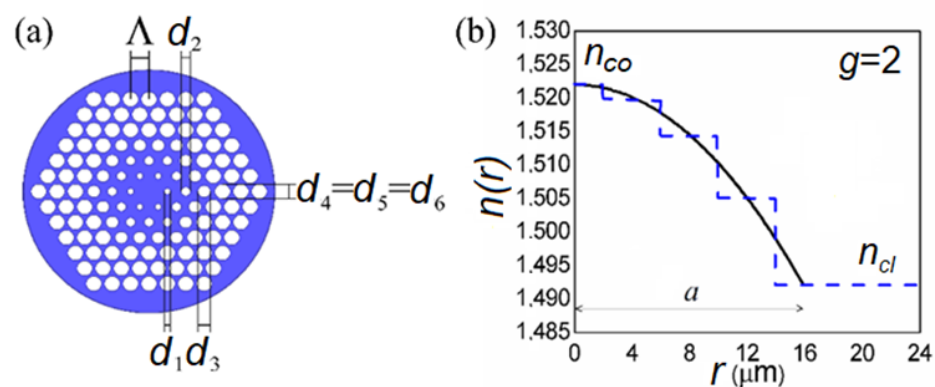


Figure 1. (a) The multimode GI MOF's cross-section. Pitch Λ is used to position the air holes in a triangular lattice. The four inner air-hole rings in the core have the following air-hole diameters: d_1 , d_2 , d_3 , and d_4 . The diameter of the air holes in the cladding in rings 5 and 6 is the same as that in air-hole ring 4 ($d_4 = d_5 = d_6$). (b) The RI performance of the referent multimode GI MOF (blue dashed line). The RI in the core has a parabolic distribution (1) with $g = 2$ (black solid line).

The performance of GI mPOF is substantially impacted by mode coupling. Light scattering, which happens when random anomalies in multimode optical fibers transfer power from one mode to another, is the main cause of mode coupling. Power distribution changes as fiber length increases until an EMD is created at "coupling length" L_c . The coupling length L_c at which EMD is achieved marks the fiber length at which the highest-order guiding mode shifted its distribution to $m = 0$. Beyond L_c , the light is equally distributed, and the coupling process is essentially complete. With the creation of the SSD, every distribution that is launched has a unique disc far-field pattern. In other words, length z_s designates the fiber length at which the distribution of the output angular power is entirely independent of the launch beam. Transmission bandwidth is increased, and modal dispersion is decreased via mode coupling [30]. It is also interesting to note that until the SSD has been entirely obtained, the fundamental optical characteristics of an optical fiber, such as attenuation and bandwidth, cannot be precisely characterized due to mode coupling. So, knowledge of the fiber length at which an SSD is established is essential.

Up until recently, there were no commercial simulation tools available for studying the transmission characteristics of multimode MOFs. To overcome this problem, this research numerically solves the TI PFE to characterize light transmission in GI mPOF. We determined lengths for accomplishing the EMD and SSD for multimode GI mPOF with a solid core utilizing launch beam distributions with various radial offsets. We assumed that the core's and cladding's air holes are arranged in a series of triangles with a regular pitch Λ (see Figure 1). According to our best knowledge, this research is the first to investigate how mode coupling affects the power flow in mPOF with a GI refractive index distribution.

2. GI mPOF Design

Figure 1 depicts a GI mPOF considered in this study. The GI mPOF has six air-hole rings, which are designated as rings from 1 to 6.

A polymer is taken into consideration as the fiber material, and a triangular lattice with a pitch Λ is used to hold the air holes. The four inner air-hole rings in the core provide a parabolic RI distribution due to the selected air-hole diameter distribution. The air-hole diameter in rings 5 and 6 is the same as the air-hole diameter in ring 4 ($d_4 = d_5 = d_6$). This system was simulated using the TI PFE.

3. Time-Independent Power Flow Equation

The refractive index profile of GI optical fibers is given as:

$$n(r, \lambda) = \begin{cases} n_{co}(\lambda) \left[1 - 2\Delta(\lambda) \left(\frac{r}{a}\right)^g\right]^{1/2} & (0 \leq r \leq a) \\ n_{cl}(\lambda) & (r > a) \end{cases} \quad (1)$$

where g is the core index exponent, a is the core radius, $n_{co}(\lambda)$ is the core's highest index (measured at the fiber axis), $n_{cl}(\lambda)$ is the cladding's index, and $\Delta = [n_{co}(\lambda) - n_{cl}(\lambda)]/n_{co}(\lambda)$ is the relative index difference.

The TI PFE for a GI optical fiber is [31]:

$$\frac{\partial P(m, \lambda, z)}{\partial z} = \frac{D}{m} \frac{\partial P(m, \lambda, z)}{\partial m} + D \frac{\partial P^2(m, \lambda, z)}{\partial m^2} \quad (2)$$

where $P(m, \lambda, z)$ is the power in the m -th principal mode (modal group), z is the coordinate along the fiber axis, and D is a constant mode coupling coefficient. The maximum principal mode number $M(\lambda)$ can be obtained as [31]:

$$M(\lambda) = \sqrt{\frac{g\Delta(\lambda)}{g+2}} a k n_{co}(\lambda) \quad (3)$$

where $k = 2\pi/\lambda$.

Using the explicit finite difference method, the discretization of Equation (2) leads to [31]:

$$P_{i,j+1} = \left(\frac{D\Delta z}{(\Delta m)^2} - \frac{D\Delta z}{2m_i\Delta m}\right) P_{i-1,j} + \left(1 - \frac{2D\Delta z}{(\Delta m)^2}\right) P_{i,j} + \left(\frac{D\Delta z}{2m_i\Delta m} + \frac{D\Delta z}{(\Delta m)^2}\right) P_{i+1,j} \quad (4)$$

where i and j refer to the discretization step lengths Δm and Δz for the mode m and length z , respectively. This work reports, to the best of the authors' knowledge, the first solution of Equation (4) of the TI PFE Equation (2) for an investigation of mode coupling along a GI mPOF in terms of mode variable (m).

The principal mode m excited at the input fiber end is [31]:

$$\frac{m}{M} = \left[\left(\frac{\Delta r}{a}\right)^g + \frac{\theta^2}{2\Delta}\right]^{(g+2)/2g} \quad (5)$$

where θr is the launch beam radial offset and θ is the launch beam angle.

4. Numerical Simulation Results

The light transmission in a multimode GI mPOF with a solid core (Figure 1) was investigated. For such a fiber, the effective V parameter is given as:

$$V = \frac{2\pi}{\lambda} a_{eff} \sqrt{n_0^2 - n_{fsm}^2} \quad (6)$$

where $a_{eff} = \Lambda/\sqrt{3}$ [32], and n_{fsm} is the effective RI of different core and cladding layers, which are obtained from Equation (6), with the effective V parameter [33]:

$$V\left(\frac{\lambda}{\Lambda}, \frac{d}{\Lambda}\right) = A_1 + \frac{A_2}{1 + A_3 \exp(A_4 \lambda / \Lambda)} \tag{7}$$

with the fitting parameters A_i ($i = 1$ to 4) as below:

$$A_i = a_{i0} + a_{i1} \left(\frac{d}{\Lambda}\right)^{b_{i1}} + a_{i2} \left(\frac{d}{\Lambda}\right)^{b_{i2}} + a_{i3} \left(\frac{d}{\Lambda}\right)^{b_{i3}} \tag{8}$$

where the coefficients from a_{i0} to a_{i3} and from b_{i1} to b_{i3} ($i =$ from 1 to 4) are given in Table 1.

Table 1. The fitting coefficients in Equation (8).

	$i = 1$	$i = 2$	$i = 3$	$i = 4$
a_{i0}	0.54808	0.71041	0.16904	−1.52736
a_{i1}	5.00401	9.73491	1.85765	1.06745
a_{i2}	−10.43248	47.41496	18.96849	1.93229
a_{i3}	8.22992	−437.50962	−42.4318	3.89
b_{i1}	5	1.8	1.7	−0.84
b_{i2}	7	7.32	10	1.02
b_{i3}	9	22.8	14	13.4

We applied our method to the GI mPOF, which has a core radius of $a = 4\Lambda = 16 \mu\text{m}$, where $\Lambda = 4 \mu\text{m}$, and a fiber diameter of $b = 1 \text{ mm}$. Measured along the fiber axis, the core’s refractive index is $n_{co} = 1.5220$ and the refractive index of the cladding is $n_{cl} = 1.4920$ [29]. The maximum principal mode number for the GI mPOF under study is $M = 580$ at $\lambda = 633 \text{ nm}$, for $g = 2.0$, and $\Delta = (n_{co} - n_{cl})/n_{co} = 0.019711$. The coupling coefficient is $D = 1482 \text{ 1/m}$ [29] (the typical value of D for GI mPOFs and conventional GI POFs). Because the strength of mode coupling in both conventional GI POFs and GI mPOFs is correlated with the polymer core material, it is significant to highlight that while modeling the GI mPOF, the typical values of D that describe a conventional GI POF can be utilized. In modeling a silica MOF, the same assumption was made [31]. For $\Lambda = 4 \mu\text{m}$ and the air-hole diameters of the four air-hole rings in the core, $d_1 = 0.6 \mu\text{m}$, $d_2 = 0.7 \mu\text{m}$, $d_3 = 1.3 \mu\text{m}$, and $d_4 = 3.1 \mu\text{m}$, the refractive indexes $n_1 = 1.5201$, $n_2 = 1.5145$, $n_3 = 1.5050$, and $n_4 = 1.4920$, respectively, are calculated utilizing Equations (6) and (7). Thus, a parabolic RI distribution in the core with $g = 2.0$ is achieved (Figure 1). The diameter of the cladding’s air-holes in rings 5 and 6 is $d_4 = d_5 = d_6 = 3.1 \mu\text{m}$, which corresponds to the cladding refractive index $n_4 = n_5 = n_6 = n_{cl} = 1.4920$.

Figure 2 depicts the evolution of the fiber length-dependent normalized output modal power distribution $P(m, \lambda, z)$. The numerical calculations assume a Gaussian beam $P(\theta, z)$ launched with $\langle \theta \rangle = 0^\circ$ (Equation (5)). The results are shown for four different radial offsets, $\Delta r = 0, 4, 8,$ and $12 \mu\text{m}$. Low-order modes’ coupling is stronger in short fibers (their modal distributions have already shifted towards $m = 0$). Due to the transfer of optical power during transmission from lower- to higher-order modes, higher-order modes can only be coupled with longer fiber lengths. The midpoints of all modes’ power distributions have been moved to zero ($m = 0$) at the coupling length of $L_c = 18 \text{ m}$, resulting in the EMD, Figure 2d. SSD is established at $z \equiv z_s = 60 \text{ m}$. It should be noted that a coupling length of $L_c = 31 \text{ m}$ is reported for a conventional GI POF, which had the same coupling coefficient $D = 1482 \text{ 1/m}$ and was investigated in our previous work [31]. The smaller core radius and consequently fewer propagating modes in the GI mPOF than in a conventional GI POF (the maximum principal mode number for a conventional GI POF was $M = 656$) result in a shorter coupling length in the former. To put it another way, fewer propagating modes need to couple together for a shorter length. Silica MOFs have significantly less mode coupling than the GI mPOF that was the subject of this study and, therefore, much longer

lengths L_c from $\simeq 1.45$ to 1.65 km at which an EMD is achieved and length z_s from $\simeq 3.30$ to 3.80 km at which an SSD is established [33]. One should note that in modeling optical fibers with a GI distribution, it is commonly assumed that D is constant, i.e., it is independent of m [31]. The same assumption of mode-independent D is also used in modeling step-index microstructured polymer optical fibers [33,34].

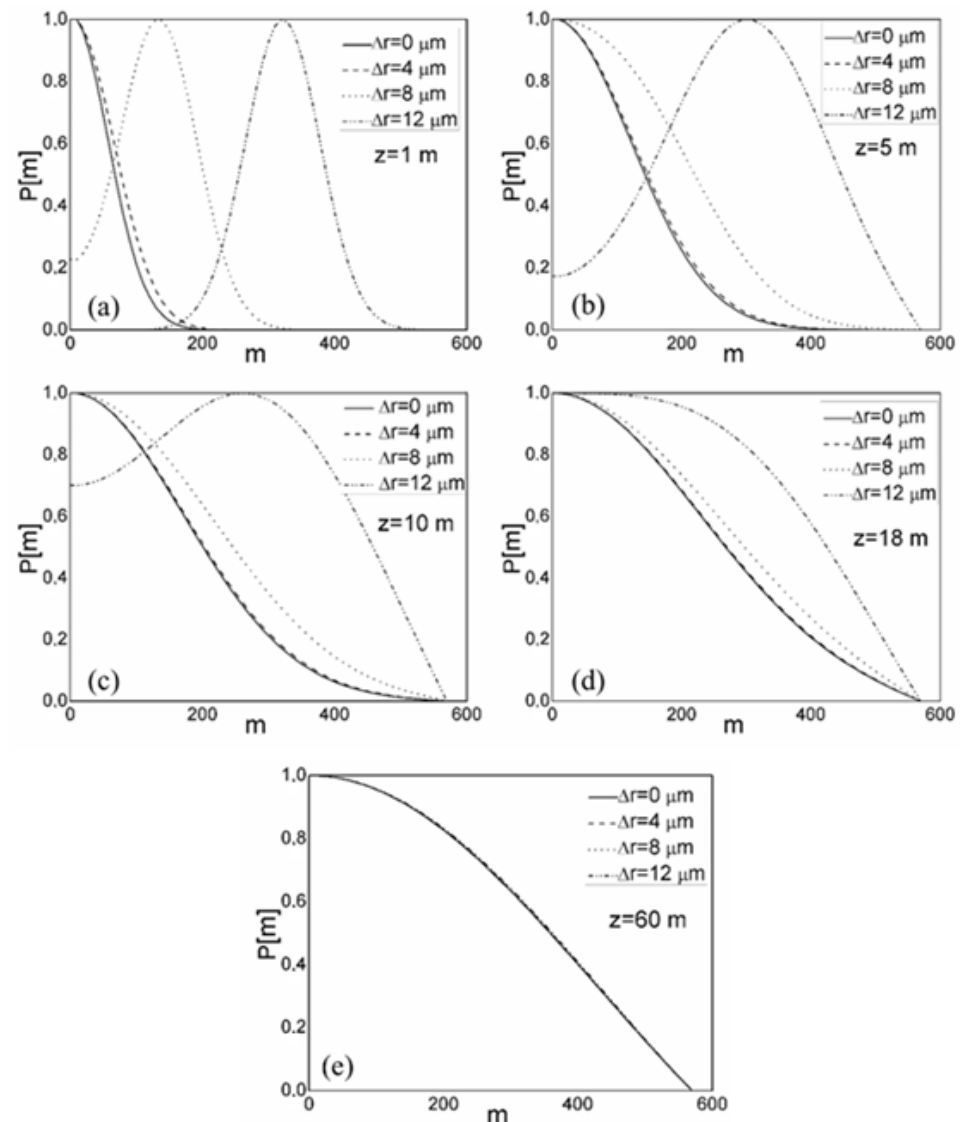


Figure 2. Normalized output modal power distribution $P(m, \lambda, z)$ over a range of radial offsets Δr obtained by numerically solving the TI PFE (2) at different fiber lengths: (a) $z = 1$ m, (b) $z = 5$ m, (c) $z = 10$ m, (d) $z = 18$ m, and (e) $z = 60$ m.

It is significant to note that the length dependence of the GI MOF bandwidth is determined by mode coupling behavior. A length below the coupling length L_c has an inverse linear effect on the bandwidth. However, it has a $z^{-1/2}$ dependence beyond this equilibrium length L_c . The faster shift to the phase of slower bandwidth decrease would therefore result from the shorter L_c [29,34]. A quicker bandwidth enhancement in the examined mPOF is expected compared to conventional GI POFs, demonstrating that GI mPOFs are a superior option for short-range telecommunication lines since the lengths needed to establish an EMD and SSD in GI mPOFs are less than in conventional GI POFs [31].

It is obvious that forcing a mode coupling process results in faster bandwidth improvement. In practice, mode coupling can be increased using an appropriate scrambler,

which can be installed near the input fiber end. This would lead to a significant decrease in coupling length L_c and, therefore, a faster bandwidth improvement (a slower bandwidth decrease).

The findings obtained in this research can be used in a variety of communication and sensory systems that utilize multimode GI mPOFs. The ability to identify the modal distribution of the GI mPOF used as a component of the optical fiber sensory system at a specific length is also crucial. The theoretical approach of modal diffusion in MOFs utilized in this study can be used to calculate the bandwidth of a fiber; however, one must solve the time-dependent power flow equation [35] rather than the TI PFE (2) that was used in this work.

5. Conclusions

The TI PFE used to investigate the state of mode coupling along a GI mPOF has a numerical solution reported in this work. As a result of a strong mode coupling process, which is common for polymer optical fibers, the results demonstrate that the coupling lengths for obtaining the EMD and the lengths for establishing SSD are short in this fiber. Due to the significant intrinsic perturbation effects in the GI mPOF, such strong mode coupling is explained. In comparison to a conventional GI POF, the EMD in the GI mPOF examined in this study is attained at an even shorter length, L_c , i.e., the coupling length L_c is reduced by a factor of 1.7 ($L_c = 18$ m in GI mPOFs as compared to $L_c = 31$ m in conventional GI POFs). This is because the GI mPOF has a smaller core radius and, thus, a smaller number of propagating modes. Namely, a smaller number of propagating modes necessitates a shorter length to complete the mode coupling process. As a result, the shorter L_c leads to a faster transition to the slower bandwidth regime. For their employment in data transmission, power supply, sensing, and other systems that could be impacted by variations in power quality, the fiber characterization given in this work is essential.

Author Contributions: Conceptualization, S.S., A.S. and M.S.K.; methodology, software, S.S., A.S., M.S.K., L.K. and B.D.; writing—original draft preparation, S.S., A.D., K.A. and R.M.; writing—review and editing, S.S., A.D. and R.M.; supervision, S.S.; project administration, funding acquisition, R.M. All authors have read and agreed to the published version of the manuscript.

Funding: This research was funded by the National Natural Science Foundation of China (62111530238, 62003046); the Strategic Research Grant of City University of Hong Kong (Project No. CityU 7004600), and grants from Serbian Ministry of Science, Technological Development and Innovations (Agreement No. 451-03-68/2022-14/200122 and 451-03-47/2023-01/200123); by grant from Science Fund of the Republic of Serbia (Agreement No. CTPCF-6379382); Guangdong Basic and Applied Basic Research Foundation (2021A1515011997); Special project in key field of Guangdong Provincial Department of Education (2021ZDZX1050); The Innovation Team Project of Guangdong Provincial Department of Education (2021KCXTD014).

Institutional Review Board Statement: Not applicable.

Informed Consent Statement: Not applicable.

Data Availability Statement: The data presented in this study are available on request from the corresponding author.

Conflicts of Interest: The authors declare no conflict of interest.

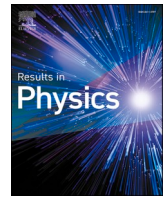
References

1. Barbio, C.; Mekonnen, K.A.; Huijskens, F.; Koonen, A.; Tangdiongga, E. Bidirectional Gigabits per Second Spatial Diversity Link Using POF for Passive Optical Front-Ends. *J. Light. Technol.* **2022**, *40*, 6753–6761. [[CrossRef](#)]
2. Huang, O.; Shi, J.; Chi, N. Performance and complexity study of a neural network post-equalizer in a 638-nm laser transmission system through over 100-m plastic optical fiber. *Opt. Eng.* **2022**, *61*, 126108. [[CrossRef](#)]
3. Ye, Y.; Zhao, C.; Wang, Z.; Teng, C.; Marques, C.; Min, R. Portable Multi-hole Plastic Optical Fiber Sensor for Liquid Level and Refractive Index Monitoring. *IEEE Sens. J.* **2023**, *23*, 2161–2168. [[CrossRef](#)]
4. Teng, C.; Wang, Y.; Min, R.; Deng, S.; Deng, H.; Li, Y.; Yuan, L. Plastic Optical Fiber Based SPR Sensor for Simultaneous Measurement of Refractive Index and Liquid Level. *IEEE Sens. J.* **2022**, *22*, 6677–6684. [[CrossRef](#)]

5. Leal-Junior, A.; Guo, J.; Min, R.; Fernandes, A.J.; Frizzera-Neto, A.; Marques, C. Photonic smart bandage for wound healing assessment. *Photonics Res.* **2021**, *9*, 272. [[CrossRef](#)]
6. Guo, J.; Niu, M.; Yang, C. Highly flexible and stretchable optical strain sensing for human motion detection. *Optica* **2017**, *4*, 1285–1288. [[CrossRef](#)]
7. Fasano, A.; Woyessa, G.; Stajanca, P.; Markos, C.; Stefani, A.; Nielsen, K.; Rasmussen, H.K.; Krebber, K.; Bang, O. Fabrication and characterization of polycarbonate microstructured polymer optical fibers for high-temperature-resistant fiber Bragg grating strain sensors. *Opt. Mater. Express* **2016**, *6*, 649–659. [[CrossRef](#)]
8. Zubel, M.G.; Fasano, A.; Woyessa, G.T.; Min, R.; Leal-Junior, A.G.; Theodosiou, A.; Marques, C.A.F.; Rasmussen, H.K.; Bang, O.; Ortega, B.; et al. Bragg Gratings Inscribed in Solid-Core Microstructured Single-Mode Polymer Optical Fiber Drawn from a 3D-Printed Polycarbonate Preform. *IEEE Sens. J.* **2020**, *20*, 12744–12757. [[CrossRef](#)]
9. Akimoto, Y.; Asai, M.; Koike, K.; Makino, K.; Koike, Y. Poly(styrene)-based graded-index plastic optical fiber for home networks. *Opt. Lett.* **2012**, *37*, 1853–1855. [[CrossRef](#)]
10. Makino, K.; Akimoto, Y.; Koike, K.; Kondo, A.; Inoue, A.; Koike, Y. Low Loss and High Bandwidth Polystyrene-Based Graded Index Polymer Optical Fiber. *J. Light. Technol.* **2013**, *31*, 2407–2412. [[CrossRef](#)]
11. Leal-Junior, A.G.; Theodosiou, A.; Min, R.; Casas, J.; Diaz, C.R.; Dos Santos, W.M.; Pontes, M.J.; Siqueira, A.A.; Marques, C.; Kalli, K.; et al. Quasi-Distributed Torque and Displacement Sensing on a Series Elastic Actuator's Spring Using FBG Arrays Inscribed in CYTOP Fibers. *IEEE Sens. J.* **2019**, *19*, 4054–4061. [[CrossRef](#)]
12. Chapalo, I.; Chah, K.; Gusarov, A.; Ioannou, A.; Pospori, A.; Nan, Y.-G.; Kalli, K.; Mégret, P. Gamma-radiation enhancement of sensing properties of FBGs in a few-mode polymer CYTOP fiber. *Opt. Lett.* **2023**, *23*, 39. [[CrossRef](#)]
13. Woyessa, G.; Rasmussen, H.K.; Bang, O. Zeonex—A route towards low loss humidity insensitive single-mode step-index polymer optical fibre. *Opt. Fiber Technol.* **2020**, *57*, 102231. [[CrossRef](#)]
14. Dash, J.N.; Cheng, X.; Tam, H.-Y. Low gas pressure sensor based on a polymer optical fiber grating. *Opt. Lett.* **2021**, *46*, 933–936. [[CrossRef](#)] [[PubMed](#)]
15. Markos, C.; Stefani, A.; Nielsen, K.; Rasmussen, H.; Yuan, W.; Bang, O. High-Tg TOPAS microstructured polymer optical fiber for fiber Bragg grating strain sensing at 110 degrees. *Opt. Express* **2013**, *21*, 4758–4765. [[CrossRef](#)]
16. Woyessa, G.; Fasano, A.; Stefani, A.; Markos, C.; Nielsen, K.; Rasmussen, H.K.; Bang, O. Single mode step-index polymer optical fiber for humidity insensitive high temperature fiber Bragg grating sensors. *Opt. Express* **2016**, *24*, 1253–1260. [[CrossRef](#)] [[PubMed](#)]
17. Broadway, C.; Min, R.; Leal-Junior, A.G.; Marques, C.; Caucheteur, C. Toward commercial polymer fiber Bragg grating sensors: Review and applications. *J. Light. Technol.* **2019**, *37*, 2605–2615. [[CrossRef](#)]
18. Cheng, X.; Gunawardena, D.S.; Pun, C.-F.J.; Bonefacino, J.; Tam, H.-Y. Single nanosecond-pulse production of polymeric fiber Bragg gratings for biomedical applications. *Opt. Express* **2020**, *28*, 33573–33583. [[CrossRef](#)] [[PubMed](#)]
19. Kuang, R.; Ye, Y.; Chen, Z.; He, R.; Savović, I.; Djordjevich, A.; Savović, S.; Ortega, B.; Marques, C.; Li, X.; et al. Low-cost plastic optical fiber integrated with smartphone for human physiological monitoring. *Opt. Fiber Technol.* **2022**, *71*, 102947. [[CrossRef](#)]
20. Hu, X.; Chen, Z.; Cheng, X.; Min, R.; Qu, H.; Caucheteur, C.; Tam, H.-Y. Femtosecond laser point-by-point Bragg grating inscription in BDk-doped step-index PMMA optical fibers. *Opt. Lett.* **2022**, *47*, 249–252. [[CrossRef](#)]
21. Theodosiou, A.; Min, R.; Leal-Junior, A.G.; Ioannou, A.; Frizzera, A.; Pontes, M.J.; Marques, C.; Kalli, K. Long period grating in a multimode cyclic transparent optical polymer fiber inscribed using a femtosecond laser. *Opt. Lett.* **2019**, *44*, 5346–5349. [[CrossRef](#)]
22. Knight, J.C.; Birks, T.A.; Russell, P.S.J.; Atkin, D.M. All-silica single-mode optical fiber with photonic crystal cladding. *Opt. Lett.* **1996**, *21*, 1547–1549. [[CrossRef](#)] [[PubMed](#)]
23. Stefańska, K.; Majchrowska, S.; Gemza, K.; Soboń, G.; Sotor, J.; Mergo, P.; Tarnowski, K.; Martynkien, T. Soliton trapping and orthogonal Raman scattering in a birefringent photonic crystal fiber. *Opt. Lett.* **2022**, *47*, 4183–4186. [[CrossRef](#)]
24. Zhao, S.; Guo, R.; Zeng, Y. Effects of frequency-dependent Kerr nonlinearity on higher-order soliton evolution in a photonic crystal fiber with one zero-dispersion wavelength. *Phys. Rev. A* **2022**, *106*, 033516. [[CrossRef](#)]
25. Wang, C.; Lin, K.; Cao, S.; Feng, G.; Wang, J.; Abdalla, A.N. Polarized Supercontinuum Generation in C 2-Core All-Normal Dispersion Photonic Crystal Fiber. *IEEE Photonics J.* **2022**, *14*, 3061607. [[CrossRef](#)]
26. Heydarian, K.; Nosratpour, A.; Razaghi, M. Computational study of wavelength conversion based on XGM by photonic crystal semiconductor optical amplifier. *Opt. Laser Technol.* **2022**, *156*, 108531. [[CrossRef](#)]
27. Van Eijkelenborg, M.A.; Large, M.C.J.; Argyros, A.; Zagari, J.; Manos, S.; Issa, N.A.; Bassett, I.; Fleming, S.; McPhedran, R.C.; De Sterke, C.M.; et al. Microstructured polymer optical fibre. *Opt. Express* **2001**, *9*, 319–327. [[CrossRef](#)] [[PubMed](#)]
28. Woyessa, G.; Pedersen, J.K.M.; Fasano, A.; Nielsen, K.; Markos, C.; Rasmussen, H.K.; Bang, O. Zeonex-PMMA microstructured polymer optical FBGs for simultaneous humidity and temperature sensing. *Opt. Lett.* **2017**, *42*, 1161–1164. [[CrossRef](#)]
29. Min, R.; Pereira, L.; Paixao, T.; Woyessa, G.; Hu, X.; Antunes, P.; Andre, P.; Bang, O.; Pinto, J.; Ortega, B.; et al. Chirped POF Bragg grating production utilizing UV cure adhesive coating for multiparameter sensing. *Opt. Fiber Technol.* **2021**, *65*, 102593. [[CrossRef](#)]
30. Lwin, R.; Barton, G.; Harvey, L.; Harvey, J.; Hirst, D.; Manos, S.; Large, M.C.J.; Poladian, L.; Bachmann, A.; Poisel, H.; et al. Beyond the bandwidth-length product: Graded index microstructured polymer optical fiber. *Appl. Phys. Lett.* **2007**, *91*, 191119. [[CrossRef](#)]
31. Savovic, S.; Simovic, A.; Drljaca, B.; Djordjevich, A.; Stepniak, G.; Bunge, C.A.; Bajic, J. Power Flow in Graded-Index Plastic Optical Fibers. *J. Light. Technol.* **2019**, *37*, 4985–4990. [[CrossRef](#)]

32. Saitoh, K.; Koshiba, M. Empirical relations for simple design of photonic crystal fibers. *Opt. Express* **2005**, *13*, 267–274. [[CrossRef](#)] [[PubMed](#)]
33. Savović, S.; Kovačević, M.S.; Simović, A.; Kuzmanović, L.; Drljača, B.; Djordjevich, A. Method for investigation of mode coupling in multimode step-index silica photonic crystal fibers. *Optik* **2021**, *246*, 167728. [[CrossRef](#)]
34. Drljača, B.; Savović, S.; Kovačević, M.S.; Simović, A.; Kuzmanović, L.; Djordjevich, A.; Min, R. Theoretical Investigation of Bandwidth in Multimode Step-Index Silica Photonic Crystal Fibers. *Photonics* **2022**, *9*, 214. [[CrossRef](#)]
35. Simović, A.; Drljača, B.; Savović, S.; Djordjevich, A.; Min, R. Investigation of bandwidth in multimode graded-index plastic optical fibers. *Opt. Express* **2021**, *29*, 29587–29594. [[CrossRef](#)]

Disclaimer/Publisher's Note: The statements, opinions and data contained in all publications are solely those of the individual author(s) and contributor(s) and not of MDPI and/or the editor(s). MDPI and/or the editor(s) disclaim responsibility for any injury to people or property resulting from any ideas, methods, instructions or products referred to in the content.



Wavelength dependent equilibrium mode distribution and steady-state distribution in double-clad W-type microstructured polymer optical fibers

Branko Drljača^a, Svetislav Savović^{b,c}, Milan S. Kovačević^b, Ana Simović^b,
Ljubica Kuzmanović^b, Alexandar Djordjević^c, Konstantinos Aidinis^{d,e}, Rui Min^{f,*}

^a University of Priština in Kosovska Mitrovica, Faculty of Sciences and Mathematics, L. Ribara 29, 38220 Kosovska Mitrovica, Serbia

^b University of Kragujevac, Faculty of Science, R. Domanovića 12, 34000 Kragujevac, Serbia

^c City University of Hong Kong, Department of Mechanical Engineering, Hong Kong, China

^d Department of Electrical Engineering, Ajman University, P.O. Box 346, Ajman, UAE

^e Center of Medical and Bio-allied Health Sciences Research, Ajman University, Ajman P.O. Box 346, UAE

^f Center for Cognition and Neuroergonomics, State Key Laboratory of Cognitive Neuroscience and Learning, Beijing Normal University, Zhuhai 519087, China

ARTICLE INFO

Keywords:

Equilibrium mode distribution
Polymer optical fiber
Mode coupling
Microstructured optical fiber
Steady-state distribution

ABSTRACT

This paper investigates wavelength dependence of equilibrium mode distribution and steady-state distribution in W-type (double-clad) microstructured polymer optical fibers (mPOFs) with a solid core for parametrically varied refractive index and width of the intermediate layer (IL) (inner cladding) by solving the time-independent power flow equation (TI PFE). In the case of wider IL, independent of wavelength, the lengths for establishing the equilibrium mode distribution and steady-state distribution are larger. We have demonstrated that the wavelength has no effect on these lengths for IL's width that is larger. These lengths drop in a wavelength-dependent manner as the IL's width decreases. Equilibrium mode distribution and steady-state distribution occur at shorter optical fiber lengths as the depth of the IL diminishes, which is due to the similarly declining number of leaky modes. The smaller the depth of the IL, the shorter the fiber length is required for completion of the coupling process. These programmable characteristics allow double-clad W-type mPOFs to be easier customized for a particular use in optical fiber sensors and communications at various wavelengths.

Introduction

Multimode POF technology is suitable for short-range communication lines, due of their ductility, light weight, and wide core diameters (up to 1 mm), POFs are easy to treat. Large-core POFs are simple to combine with VCSELs, LEDs, and lasers to produce inexpensive and effective communication systems. In their applications, they have also utilized lighting, sensing, and data processing. Due to the optical fiber's microstructured patterning's flexibility to influence the sectional profile [1–7], mPOFs have showed capability unmatched by traditional optical fibers. We are aware of the realization of an “endlessly single-mode” mPOF that functions across a broad range of wavelengths [2]. The definition of the hollow core mPOF is also made possible by photonic bandgap guiding [8–13]. Light dispersion [14–16], birefringence [17], supercontinuum light production [18–20], light wavelength conversion [21–22], optical fluids [23–24], and sensing [24] are a few applications where mPOFs have been exploited. The typical numerical aperture (NA)

of the mPOF is $NA \approx 0.5$ [25–27]. It has been shown that bandwidth of graded-index mPOF is larger if compared to bandwidth of conventional graded-index POF [26]. It has been possible to accomplish lensless focusing with great resolution by utilizing high NA mPOFs [28].

In the recent few decades, there has been a lot of interest in the design of the refractive index profile of multimode mPOFs with an aim to improving their transmission characteristics. As a result, a variety of step-index, graded-index, and W-type mPOF designs have been proposed [3–5,26,28,29]. The IL of W-type fibers bonds the guided modes to the core more firmly, resulting in a broader bandwidth as compared to a matching single-clad (SC) fiber. As a result, modal dispersion is smaller in W-type optical fibers than it is in SC fibers. An air-hole pattern and/or diameter change within a concentric ring-like region can alter the cladding layer in a conventional mPOF design, as shown in Fig. 1. Fig. 1 depicts a mPOF that mimics a W-type optical fiber by having a changing pattern in the cladding. W-type mPOF has a better degree of adaptability when it comes to changing the geometric characteristics, including the

* Corresponding author.

E-mail address: rumi@doctor.upv.es (R. Min).

<https://doi.org/10.1016/j.rinp.2022.106124>

Received 29 August 2022; Received in revised form 17 October 2022; Accepted 21 November 2022

Available online 23 November 2022

2211-3797/© 2022 The Authors. Published by Elsevier B.V. This is an open access article under the CC BY license (<http://creativecommons.org/licenses/by/4.0/>).

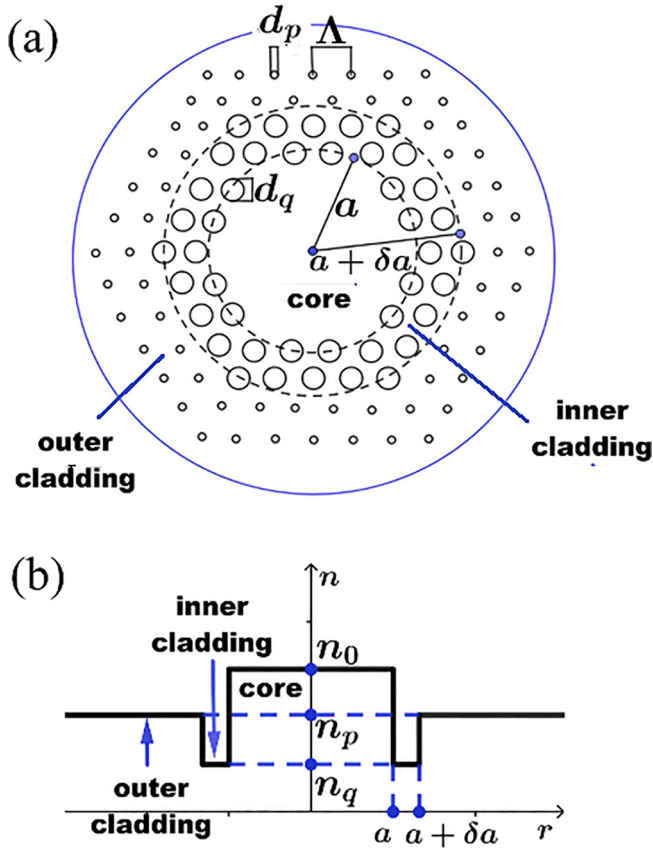


Fig. 1. (a) The cross section of the multimode W-type microstructured optical fiber. Λ is the pitch, d_q and d_p are the diameters of inner and outer cladding air-holes, respectively. (b) The refractive index performance of the referent multimode W-type microstructured optical fiber.

air-hole diameters d_q , d_p , and pitch Λ . Mode coupling, modal attenuation, and modal dispersion all affect how well multimode optical fibers propagate light. Mode coupling is primarily caused by light scattering in multimode optical fibers, which results from the inherent perturbations. Numerous imperfections, including as vacancies, cracks, tiny bends, and density differences, can result in light dispersion. Light launched at a specific angle $\theta_0 > 0$ with respect to the fiber axis will only form a ring radiation pattern when it is transmitted through short fibers. Due to mode coupling, the boundaries of such a ring become hazy near the ends of longer fibers. An equilibrium mode distribution (EMD) is established at length L_c , where the ring pattern which represents the highest-order modes transforms into a disk. The unique angular power distribution will become fixed and centered (independently on the launch beam angle θ_0) when the optical fiber is lengthened beyond the value known as z_{ss} , denoting that a steady-state distribution (SSD) is established.

Commercial simulation software packages were not created until recently to investigate the transmission properties of multimode mPOFs. In order to resolve this shortcoming, the TI PFE for double-clad W-type mPOF is numerically solved using the explicit-finite difference method in this study [37]. This gave us the opportunity to examine the multimode W-type mPOF's transmission capabilities at various wavelengths. We determined characteristic lengths for this optical fiber for accomplishing the EMD and SSD for launch beams of various wavelengths, for parametrically varying inner cladding width, and for varying the diameter of the inner cladding's air-holes. We presumed that the triangle pattern formed by the cladding air-holes has a constant pitch Λ (see Fig. 1). We study the transmission capabilities of mPOF with W-type refractive index distribution at various wavelengths for the first time to our knowledge, in this paper.

W-type mPOF design

Conventional mPOFs' cladding air-holes normally form a regular triangular lattice. Changing the geometric parameters d_q , d_p and Λ , will alter the effective refractive index profile for the chosen optical fiber layer, as shown in Fig. 1-a. Smaller air-holes can be found in the outer cladding than the inner cladding (d_p vs d_q in Fig. 1-a). The core has a greater refractive index than the two claddings (Fig. 1-b). The lowest effective refractive index n_q (the largest diameter d_q of the air-holes) is found in the inner cladding, and the outer cladding's effective refractive index is n_p ($n_q < n_p < n_0$). The TI PFE was used to simulate such a system.

Time-independent power-flow equation

The following Gloge's TI PFE can treat light transmission in a multimode optical fiber [30]:

$$\frac{\partial P(\theta, z)}{\partial z} = -\alpha(\theta)P(\theta, z) + \frac{D}{\theta} \frac{\partial}{\partial \theta} \left(\theta \frac{\partial P(\theta, z)}{\partial \theta} \right) \quad (1)$$

where (θ, z) is the angular power distribution at distance z from the input of the optical fiber, D is the coupling coefficient assumed constant [30,31], θ is the emission angle with respect to the fiber core axis, $\alpha(\theta) = \alpha_0 + \alpha_d(\theta)$ is the modal attenuation – α_0 represents standard mode losses, which is ignored because it only serves as a multiplier $\exp(-\alpha_0 z)$ in the solution of equation (1).

W-type optical fiber introduced in Part 2 (Fig. 1-b) can be considered as a system of a SC_q optical fiber and cladding [32], in which the angle $\theta_q \cong (2\Delta_q)^{1/2}$ is the critical angle for the guided modes – where $\Delta_q = (n_0 - n_q)/n_0$. Similarly, the angle $\theta_p \cong (2\Delta_p)^{1/2}$ is the critical angle for the guided modes of a SC_p optical fiber, where $\Delta_p = (n_0 - n_p)/n_0$. In the case of entirely investigated W-type fiber, the guided mode is when the propagation angle of the mode is less than θ_p , and the leaky mode is when the propagation angle of the mode is between θ_p and θ_q :

$$\alpha_d(\theta) = \begin{cases} 0 & \theta \leq \theta_p \\ \alpha_L & \theta_p < \theta < \theta_q \\ \infty & \theta \geq \theta_q \end{cases} \quad (2)$$

where the attenuation of leaky modes is given as [33]:

$$\alpha_L(\theta) = \frac{4(\theta^2 - \theta_p^2)^{1/2}}{a(1 - \theta^2)^{1/2}} \frac{\theta^2(\theta_q^2 - \theta^2)}{\theta_q^2(\theta_q^2 - \theta_p^2)} \exp\left(2\delta a n_0 k_0 (\theta_q^2 - \theta^2)^{1/2}\right) \quad (3)$$

and where $k_0 = 2\pi/\lambda$, and λ is the wavelength of light.

Numerical results

We looked into the light transmission in a multimode W-type mPOF, shown in Fig. 1. The effective V parameter for such fiber is given as:

$$V = \frac{2\pi}{\lambda} \sqrt{a_{eff} n_0^2 - n_{fsm}^2} \quad (4)$$

where $a_{eff} = \Lambda/\sqrt{3}$ [34], and n_{fsm} is cladding's effective refractive index, which is obtained from equation (4), using the following equation [34]:

$$V\left(\frac{\lambda}{\Lambda}, \frac{d}{\Lambda}\right) = A_1 + \frac{A_2}{1 + A_3 \exp(A_4 \lambda / \Lambda)} \quad (5)$$

with the parameters A_i ($i = 1$ to 4), which are given in the following form:

$$A_i = a_{i0} + a_{i1} \left(\frac{d}{\Lambda}\right)^{b_{i1}} + a_{i2} \left(\frac{d}{\Lambda}\right)^{b_{i2}} + a_{i3} \left(\frac{d}{\Lambda}\right)^{b_{i3}} \quad (6)$$

where the coefficients a_{i0} to a_{i3} and b_{i1} to b_{i3} ($i = 1$ to 4) are given in

Table 1
The coefficients a_{ij} and b_{ij} in equation (6).

	a_{ij}				b_{ij}		
	$j = 0$	$j = 1$	$j = 2$	$j = 3$	$j = 1$	$j = 2$	$j = 3$
$i = 1$	0.54808	5.00401	-10.43248	8.22992	5	7	9
$i = 2$	0.71041	9.73491	47.41496	-437.50962	1.8	7.32	22.8
$i = 3$	0.16904	1.85765	18.96849	-42.4318	1.7	10	14
$i = 4$	-1.52736	1.06745	1.93229	3.89	-0.84	1.02	13.4

Table 1.

Significant values of the effective refractive index of the inner cladding n_q , relative refractive index difference Δ_q , critical angles θ_q , are shown in Table 2, for two inner cladding air-holes diameters d_q and four wavelengths, where $\Lambda = 3 \mu\text{m}$. The effective refractive index of the outer cladding n_p , relative refractive index difference Δ_p , and critical angle θ_p , are given in Table 3, for outer cladding air-holes diameter $d_p = 1 \mu\text{m}$ and four wavelengths, where $\Lambda = 3 \mu\text{m}$.

The W-type mPOF investigated in this work has core diameter $2a = 600 \mu\text{m}$, diameter $d = 1 \text{ mm}$ and coupling coefficient $D = 1.649 \times 10^{-4} \text{ rad}^2/\text{m}$ (typical value of D for conventional POFs and mPOFs) [35,36]. It is worth noting that when modeling the W-type mPOF, the typical values of D that characterize a conventional POF can be used, because the strength of mode coupling both in conventional POFs and mPOFs is related to the polymer core material. In modeling a silica W-type microstructured optical fiber, a similar assumption was made [37]. Refractive index of the W-type mPOF's core is $n_0 = 1.492$ at $\lambda = 645 \text{ nm}$, $n_0 = 1.493$ at $\lambda = 568 \text{ nm}$, $n_0 = 1.496$ at $\lambda = 522 \text{ nm}$ and $n_0 = 1.499$ at $\lambda = 476 \text{ nm}$ [38].

The cases with $d_q = 1.5$ and $2 \mu\text{m}$ were simulated, for a fixed diameter of the outer cladding air-holes $d_p = 1 \mu\text{m}$, for two widths of the inner cladding $\delta a = 2.4 \mu\text{m}$ ($\delta = 0.008$) and $\delta a = 7.2 \mu\text{m}$ ($\delta = 0.024$) in order to study the effect of the inner cladding air-holes diameter d_q and the width of the inner-cladding δa on the angular power distribution along the W-type mPOF at different wavelengths. As illustration, Fig. 2 shows the output angular power distribution at different optical fiber lengths, in the case of $d_p = 1 \mu\text{m}$, $d_q = 2 \mu\text{m}$, and $\delta = 0.008$, calculated for Gaussian launch beam distributions with input angles $\theta_0 = 0^\circ, 6^\circ$, and 12° , with $(\text{FWHM})_{z=0} = 5^\circ$ at wavelength $\lambda = 476 \text{ nm}$. Fig. 2 demonstrates that when Gaussian launch beam distribution at the input fiber

Table 2

For two air-hole diameters d_q in the inner cladding, the data show the effective refractive index n_q , relative refractive index difference Δ_q and critical angle θ_q all for the inner cladding and at four different wavelengths λ .

$\lambda = 476 \text{ nm}$	$d_q (\mu\text{m})$	1.5	2.0
	n_q	1.4826	1.4580
	$\Delta_q = (n_0 - n_q)/n_0$	0.01094	0.02735
	$\theta_q (\text{deg})$	8.5	13.4
$\lambda = 522 \text{ nm}$	$d_q (\mu\text{m})$	1.5	2.0
	n_q	1.4808	1.4541
	$\Delta_q = (n_0 - n_q)/n_0$	0.01016	0.02801
	$\theta_q (\text{deg})$	8.2	13.6
$\lambda = 568 \text{ nm}$	$d_q (\mu\text{m})$	1.5	2.0
	n_q	1.4790	1.4501
	$\Delta_q = (n_0 - n_q)/n_0$	0.00938	0.02873
	$\theta_q (\text{deg})$	7.8	13.8
$\lambda = 645 \text{ nm}$	$d_q (\mu\text{m})$	1.5	2.0
	n_q	1.4757	1.4458
	$\Delta_q = (n_0 - n_q)/n_0$	0.01092	0.03097
	$\theta_q (\text{deg})$	8.5	14.3

Table 3

For one air-hole diameter d_p in the outer cladding, the data show the effective refractive index n_p , relative refractive index difference Δ_p and critical angle θ_p all for the outer cladding and at four different wavelengths λ .

$\lambda = 476 \text{ nm}$	$d_p (\mu\text{m})$	1
	n_p	1.4877
	$\Delta_p = (n_0 - n_p)/n_0$	0.00754
	$\theta_p (\text{deg})$	7.0
$\lambda = 522 \text{ nm}$	$d_p (\mu\text{m})$	1
	n_p	1.4868
	$\Delta_p = (n_0 - n_p)/n_0$	0.00615
	$\theta_p (\text{deg})$	6.4
$\lambda = 568 \text{ nm}$	$d_p (\mu\text{m})$	1
	n_p	1.4860
	$\Delta_p = (n_0 - n_p)/n_0$	0.00469
	$\theta_p (\text{deg})$	5.5
$\lambda = 645 \text{ nm}$	$d_p (\mu\text{m})$	1
	n_p	1.4844
	$\Delta_p = (n_0 - n_p)/n_0$	0.00509
	$\theta_p (\text{deg})$	5.8

end is centered at $\theta_0 = 0^\circ$, with increasing the optical fiber length, its width increases as a result of mode coupling. Low-order modes coupling rises with optical fiber length, and the distributions move more strongly towards $\theta = 0^\circ$. Higher-order modes significantly couple only after longer optical fiber lengths. At the optical fiber's coupling length $z=L_c = 36.1 \text{ m}$, the EMD is established. The optical fiber length $z=z_s = 93 \text{ m}$ denotes the point at which the mode-distribution transforms into an SSD and becomes entirely independent of the launch beam distribution.

One can observe in Figs. 3 and 4 that independently on wavelength, the lengths L_c and z_s are larger in the case of wider IL ($\delta = 0.024$). Because leaky mode losses are lower in fibers with wider IL, power remains in leaky modes for a longer fiber length, postponing the onset of EMD and SSD. Figs. 3 and 4 also show that there is almost no effect of wavelength on lengths L_c and z_s for the wider IL, since almost the equal number of leaky modes remain guided at nearly the equal fiber lengths at different wavelengths. L_c and z_s lengths drop in a wavelength-dependent manner as the IL's width decreases. Since the number of leaky modes has already been reduced at short fiber length in the case of $\delta = 0.008$, consequently, it takes a shorter fiber lengths for establishing the EMD and SSD – compared to the case with $\delta = 0.024$. As depth of the IL (Δ_q) decreases, EMD and SSD occur at shorter fiber lengths – which is result of decreasing number of leaky modes (the shorter fiber length is required for completion of the coupling process (Table 4)) [29]. It is also important to note that the shorter the length L_c , the earlier the bandwidth will switch from the functional dependence of $1/z$ to $1/z^{1/2}$ (slower bandwidth decrease) [39,40]. Compared with the mPOF investigated in this work, silica microstructured optical fibers show much weaker mode coupling ($D \approx 10^{-6} \text{ rad}^2/\text{m}$) and therefore shorter lengths at which SSD is achieved ($z_s \approx 1$ to 10 km) [37].

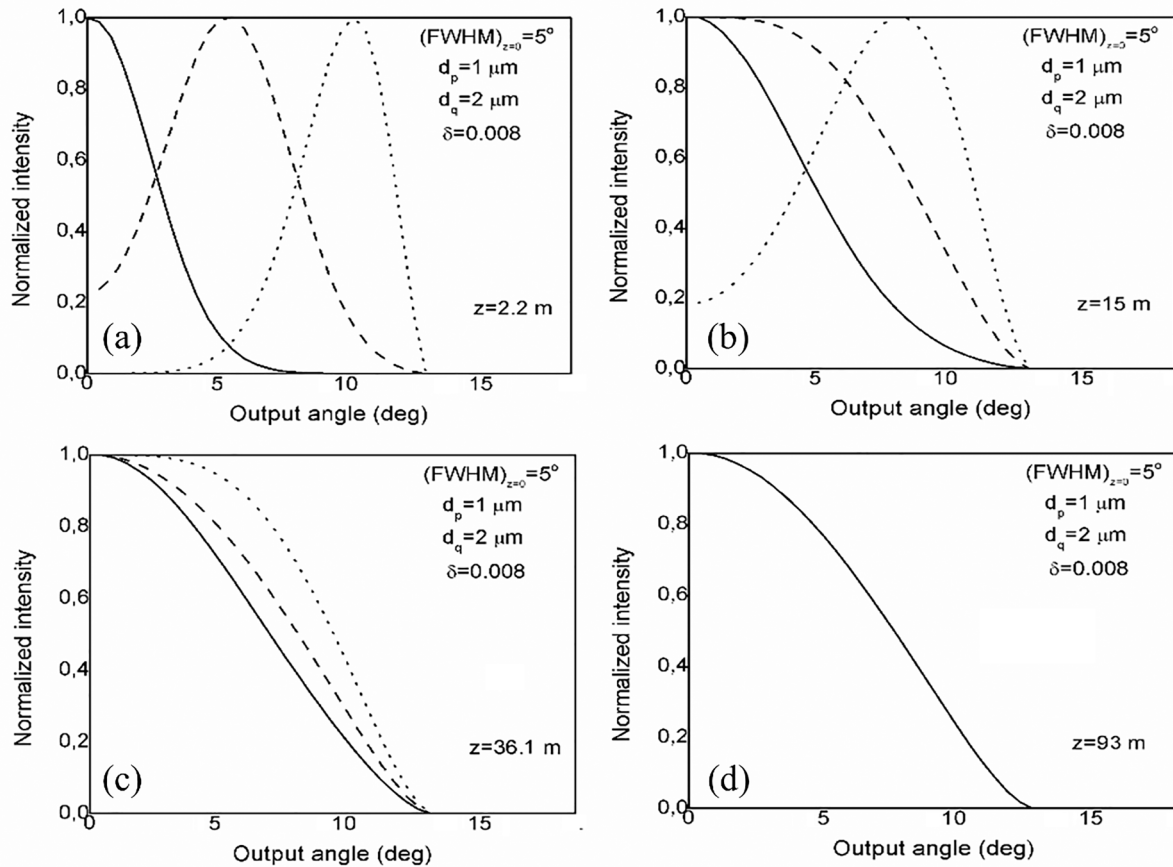


Fig. 2. Normalized output angular power distribution at different fiber lengths for the case with $d_p = 1 \mu\text{m}$, $d_q = 2 \mu\text{m}$ and $\delta = 0.008$, calculated for Gaussian launch distribution with input angles $\theta_0 = 0^\circ$ (—), 6° (---), and 12° (···) with $(\text{FWHM})_{z=0} = 5^\circ$ for: (a) $z = 2.2 \text{ m}$; (b) $z = 15 \text{ m}$; (c) $z = L_c = 36.1 \text{ m}$ and (d) $z = z_s = 93 \text{ m}$, for launch beam wavelength $\lambda = 476 \text{ nm}$.

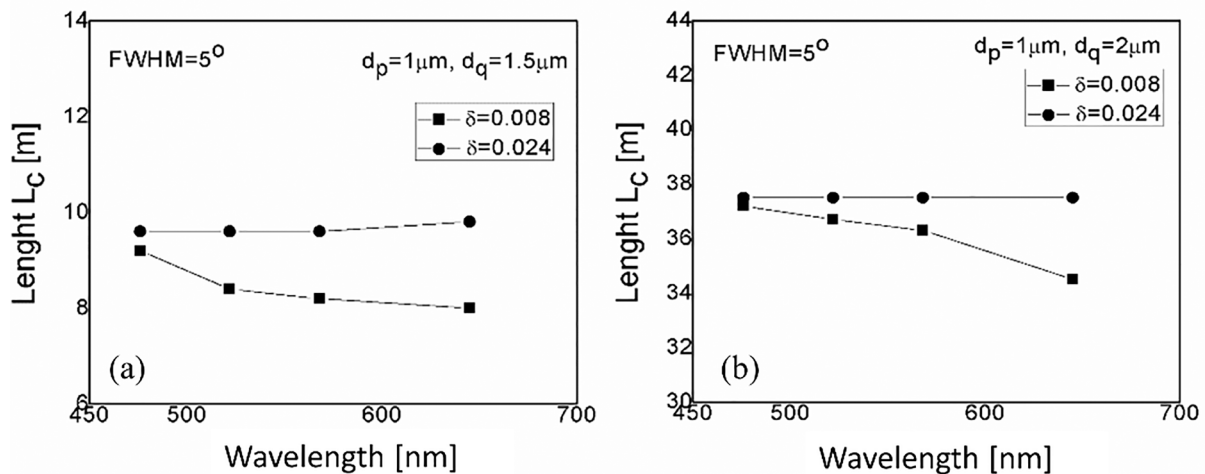


Fig. 3. Length L_c (for EMD) as a function of the launch beam's wavelength, for $(\text{FWHM})_{z=0} = 5^\circ$, $d_p = 1 \mu\text{m}$, (a) $d_q = 1.5 \mu\text{m}$ and (b) $d_q = 2 \mu\text{m}$, where $\delta = 0.008$ and 0.024 .

Conclusion

We examined how the wavelength of the launch beam, the width of the inner cladding, and the diameter of the air holes in the inner cladding affect the transmission of multimode W-type mPOFs. Independent of wavelength, the lengths for achieving the EMD and SSD are longer

when the ILs are wider (larger δ). Because leaky mode losses are lower in fibers with wider IL, power remains in leaky modes for a longer fiber length [29]. For smaller width of the IL, with increasing wavelength, the lengths at which EMD and SSD are attained, decrease. This is due to the fact that, in the case of a narrower IL, leaky mode losses increase with increasing wavelength, meaning that fewer leaky modes are guided in

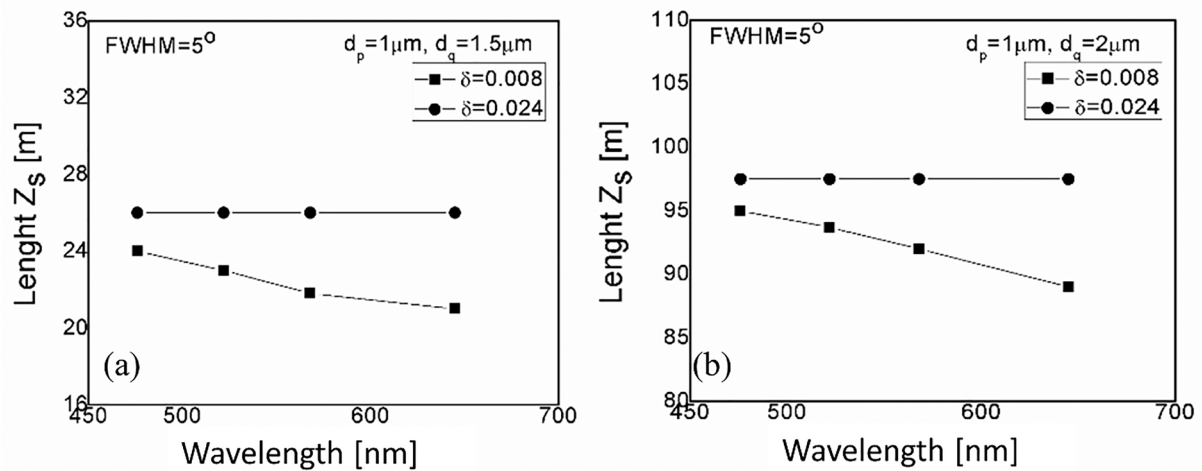


Fig. 4. Length z_s (for SSD) as a function of the launch beam's wavelength, for $(FWHM)_{z=0} = 5^\circ$, $d_p = 1 \mu\text{m}$, (a) $d_q = 1.5 \mu\text{m}$ and (b) $d_q = 2 \mu\text{m}$, where $\delta = 0.008$ and 0.024 .

Table 4

Length L_c (for EMD) and length z_s (for SSD) in mPOF with $d_p = 1 \mu\text{m}$, $\Lambda = 3 \mu\text{m}$, for two different δ and d_q , and four different λ of the incident Gaussian launch beam distribution.

		$\lambda = 476 \text{ nm}$		$\lambda = 522 \text{ nm}$		$\lambda = 568 \text{ nm}$		$\lambda = 645 \text{ nm}$	
		$L_c \text{ [m]}$	$z_s \text{ [m]}$	$L_c \text{ [m]}$	$z_s \text{ [m]}$	$L_c \text{ [m]}$	$z_s \text{ [m]}$	$L_c \text{ [m]}$	$z_s \text{ [m]}$
$\delta = 0.008$	$d_q = 1.5 \mu\text{m}$	9.2	23.8	8.4	22.2	8.2	21.1	8.0	21.0
	$d_q = 2 \mu\text{m}$	36.1	93.0	35.2	91.0	34.9	89.5	34.5	89.0
$\delta = 0.024$	$d_q = 1.5 \mu\text{m}$	9.6	25.4	9.6	25.4	9.6	25.4	9.8	26.0
	$d_q = 2 \mu\text{m}$	37.2	97.1	37.2	97.1	37.2	97.1	37.5	97.5

longer fibers at higher wavelengths. It requires a shorter fiber lengths for the commencement of EMD and SSD compared to the case with a broader IL, because the number of leaky modes is minimized at short fiber length in the case of a thinner IL. EMD and SSD occur at shorter fiber lengths as the depth of the IL (Δ_q) diminishes, which is due to the similarly declining number of leaky modes (the shorter the fiber length is required for completion of the coupling process). These programmable characteristics allow W-type mPOFs to be developed with better adaptability for use at various wavelengths.

Funding

National Natural Science Foundation of China (62003046, 6211101138); Strategic Research Grant of City University of Hong Kong (CityU 7004600); Serbian Ministry of Education, Science and Technological Development grant (451-03-68/2022-14/200122); Science Fund of the Republic Serbia (CTPCF-6379382); Guangdong Basic and Applied Basic Research Foundation (2021A1515011997); Special project in key field of Guangdong Provincial Department of Education (2021ZDZX1050); The Innovation Team Project of Guangdong Provincial Department of Education (2021KCXTD014).

CRedit authorship contribution statement

Branko Drljača: Conceptualization, Methodology. **Svetislav Savović:** Conceptualization, Methodology, Project administration, Funding acquisition. **Milan S. Kovačević:** Conceptualization, Methodology. **Ana Simović:** Conceptualization, Methodology. **Ljubica Kuzmanović:** Writing – original draft, Writing – review & editing. **Alexandar Djordjevich:** Writing – original draft. **Konstantinos Aidinis:** Writing – review & editing. **Rui Min:** Project administration,

Funding acquisition.

Declaration of Competing Interest

The authors declare that they have no known competing financial interests or personal relationships that could have appeared to influence the work reported in this paper.

Data availability

Data will be made available on request.



References

- [1] Knight JC, Birks TA, St P, Russell J, Atkin DM. All-silica single-mode optical fiber with photonic crystal cladding. *Opt Lett* 1996;21:1547–9.
- [2] Birks TA, Knight JC, St P, Russell J. Endlessly single-mode photonic crystal fiber. *Opt Lett* 1997;22:961–3.
- [3] St P, Russell J. Photonic crystal fibers. *Science* 2003;299:358–62.
- [4] Knight JC. Photonic crystal fiber. *Nature* 2003;424(14):847–51.
- [5] St P, Russell J. Photonic-crystal fibers. *J Lightwave Technol* 2006;24:4729–49.
- [6] Knight JC, Broeng J, Birks TA, Russell PSJ. Photonic band gap guidance in optical fibers. *Science* 1998;282:1476–8.
- [7] Knight JC, Russell PSJ. Photonic crystal fibers: new way to guide light. *Science* 2002;296:276–7.
- [8] Cregan RF, Mangan BJ, Knight JC, Birks TA, Russell PSJ, Roberts PJ, et al. Single-mode photonic band gap guidance of light in air. *Science* 1999;285:1537–9.
- [9] Amezcua-Correa R, Gerome F, Leon-Saval SG, Broderick NGR, Birks TA, Knight JC. Control of surface modes in low loss hollow core photonic bandgap fibers. *Opt Express* 2008;16:1142–9.
- [10] Bouwmans G, Bigot L, Quiquempois Y, Lopez F, Provino L, Douay M. Fabrication and characterization of an all-solid 2d photonic bandgap fiber with a low-loss region (<20 db/km) around 1550 nm. *Opt Express* 2005;13:8452–9.
- [11] Luan F, George AK, Hedley TD, Pearce GJ, Bird DM, Knight JC, et al. All-solid photonic bandgap fiber. *Opt Lett* 2004;29:2369–71.
- [12] Benabid F, Knight JC, Antonopoulos G, St P, Russell J. Stimulated Raman scattering in hydrogen-filled hollow-core photonic crystal fiber. *Science* 2002;298:399–402.

- [13] Light PS, Benabid F, Couy F, Maric M, Luiten AN. Electromagnetically induced transparency in Rb-filled coated hollow-core photonic crystal fiber. *Opt Lett* 2007;32:1323–5.
- [14] Mogilevsev D, Birks TA, St P, Russell J. Group-velocity dispersion in photonic crystal fibers. *Opt Lett* 1998;23:1662–4.
- [15] Saitoh K, Koshiba M, Hasegawa T, Sasaoka E. Chromatic dispersion control in photonic crystal fibers: application to ultra-flattened dispersion. *Opt Express* 2003;11:843–52.
- [16] Lee S, Ha W, Park J, Kim S, Oh K. A new design of low-loss and ultra-flat zero dispersion photonic crystal fiber using hollow ring defect. *Opt Commun* 2012;285(20):4082–7.
- [17] Chen D, Tse MLV, Tam HY. Optical properties of photonic crystal fibers with a fiber core of arrays of sub-wavelength circular air holes: birefringence and dispersion. *Prog Electromagn Res* 2010;105:193–212.
- [18] Ranka JK, Windeler RS, Stentz AJ. Visible continuum generation in air silica microstructured optical fibers with anomalous dispersion at 800 nm. *Opt Lett* 2000;25:25–7.
- [19] Hilligsøe KM, Andersen TV, Paulsen HN, Nielsen CK, Mølmer K, Keiding S, et al. Supercontinuum generation in a photonic crystal fiber with two zero dispersion wavelengths. *Opt Express* 2004;12:1045–54.
- [20] Wadsworth WJ, Joly N, Knight JC, Birks TA, Biancalana F, St P, et al. Supercontinuum and four-wave mixing with Q-switched pulses in endlessly single-mode photonic crystal fibres. *Opt Express* 2004;12:299–309.
- [21] Lee JH, Belardi W, Furusawa K, Petropoulos P, Yusoff Z, Monro TM, et al. Four-wave mixing based 10-Gb/s tunable wavelength conversion using a holey fiber with a high SBS threshold. *IEEE Photon Technol Lett* 2003;15:440–2.
- [22] Andersen TV, Hilligsøe KM, Nielsen CK, Thøgersen J, Hansen KP, Keiding SR, et al. Continuous-wave wavelength conversion in a photonic crystal fiber with two zero-dispersion wavelengths. *Opt Express* 2004;12:4113–22.
- [23] Park J, Kang DE, Paulson B, Nazari T, Oh K. Liquid core photonic crystal fiber with low-refractive-index liquids for optofluidic applications. *Opt Express* 2014;22(14):17320–30.
- [24] Kassani SH, Khazaeinezhad R, Jung Y, Kobelke J, Oh K. Suspended ring-core photonic crystal fiber gas sensor with high sensitivity and fast response. *IEEE Photon J* 2015;7:2700409.
- [25] Wadsworth W, Percival R, Bouwmans G, Knight J, Birks T, Hedley T, et al. Very high numerical aperture fibers. *IEEE Photon Technol Lett* 2004;16:843–5.
- [26] Lwin R, Barton G, Harvey L, Harvey J, Hirst D, Manos S, et al. Beyond the bandwidth-length product: Graded index microstructured polymer optical fiber. *Appl Phys Lett* 2007;91:191119.
- [27] Hansen KP, Olausson CB, Broeng J, Noordegraaf D, Maack MD, Alkeskjold TT, et al. Airclad fiber laser technology. *Opt Eng* 2011;50:111609.
- [28] Amitonova LV, Descloux A, Petschulat J, Frosz MH, Ahmed G, Babic F, et al. High-resolution wavefront shaping with a photonic crystal fiber for multimode fiber imaging. *Opt Lett* 2016;41:497–500.
- [29] Drljača B, Savović S, Kovačević MS, Simović A, Kuzmanović LJ, Djordjević A, Min R. Transmission performance of multimode W-type plastic photonic crystal fibers. *Opt Express* 2022;29:29589.
- [30] Gloge D. Optical power flow in multimode fibers. *Bell Syst Tech J* 1972;51:1767–83.
- [31] Rousseau M, Jeunhomme L. Numerical solution of the coupled-power equation in step index optical fibers. *IEEE Trans Microw Theory Tech* 1977;25(7):577–85.
- [32] Tanaka TP, Yamada S. Steady-state characteristics of multimode W-type fibers. *Appl Opt* 1979;18:3261–4.
- [33] Kawakami S, Nishida S. Perturbation theory of doubly clad optical fiber with a low index inner cladding. *IEEE J Quant Electron* 1975;QE-11:130–8.
- [34] Saitoh K, Koshiba M. Empirical relations for simple design of photonic crystal fibers. *Opt Express* 2005;13:267–74.
- [35] Mateo J, Losada MA, Garcés I, Zubia J. Global characterization of optical power propagation in step-index plastic optical fibers. *Opt Express* 2006;14:928–35.
- [36] Savović S, Kovačević MS, Drljača B, Simović A, Kuzmanović L, Djordjević A. Power flow in multimode step-index plastic photonic crystal fibers. *Optik* 2021;247:167868.
- [37] Kovačević MS, Kuzmanović LJ, Simović A, Savović S, Djordjević A. Transients of modal power distribution in multimode solid core W-type photonic crystal fibers. *J Lightwave Technol* 2017;35:4352–7.
- [38] Ishigure T, Nihei E, Koike Y. Optimum refractive-index profile of the graded-index polymer optical fiber, toward gigabit data links. *Appl Opt* 1996;35:2048–53.
- [39] Savović S, Drljača B, Djordjević A. Influence of launch beam distribution on bandwidth in step index plastic optical fibers. *Appl Opt* 2013;52:1117–21.
- [40] Drljača B, Savović S, Kovačević MS, Simović A, Kuzmanović LJ, Djordjević A, Min R. Theoretical investigation of bandwidth of multimode step-index silica photonic crystal fibers. *Photonics* 2022;9:214.



Transmission performance of multimode W-type microstructured polymer optical fibers

BRANKO DRLJAČA,¹  SVETISLAV SAVOVIĆ,^{2,3}  MILAN S. KOVAČEVIĆ,² ANA SIMOVIĆ,² LJUBICA KUZMANOVIĆ,² ALEXANDAR DJORDJEVIĆ,³ AND RUI MIN^{4,*}

¹Faculty of Sciences and Mathematics, University of Priština in Kosovska Mitrovica, L. Ribara 29, Kosovska Mitrovica, 38220, Serbia

²Faculty of Science, University of Kragujevac, R. Domanovića 12, 34000 Kragujevac, Serbia

³Department of Mechanical Engineering, City University of Hong Kong, Hong Kong, China

⁴Center for Cognition and Neuroergonomics, State Key Laboratory of Cognitive Neuroscience and Learning, Beijing Normal University, Zhuhai 519087, China

*rumi@doctor.upv.es

Abstract: By solving the time-independent power flow equation (TI PFE), we study mode coupling in a multimode W-type microstructured polymer optical fiber (mPOF) with a solid-core. The multimode W-type mPOF is created by modifying the cladding layer and reducing the core of a multimode singly clad (SC) mPOF. For such optical fiber, the angular power distributions, the length L_c at which an equilibrium mode distribution (EMD) is achieved, and the length z_s for establishing a steady state distribution (SSD) are determined for various arrangements of the inner cladding's air-holes and different launch excitations. This information is useful for the implement of multimode W-type mPOFs in telecommunications and optical fiber sensors.

© 2022 Optica Publishing Group under the terms of the [Optica Open Access Publishing Agreement](#)

1. Introduction

Multimode POFs are frequently used for short-range communication links. POFs are simple to treat due to their ductility, light weight and large core diameters (up to 1 mm). POFs with a large core diameter can be easily combined with VCSELs, LEDs and lasers, to create low-cost and efficient communication systems. They have also used illumination, sensing, and data processing in their applications. Microstructured optical fibers (MOFs) have demonstrated performance unrivaled by conventional optical fibers because the optical fiber's micro-structured patterning provides flexibility to affect the sectional profile at the design stage [1–7]. As we know, “endlessly single-mode” MOF that operates over a wide range of wavelengths has been realized [2]. Also, because of photonic bandgap guidance, the hollow core MOF is defined [8–13]. MOFs have been used in light dispersion [14–16], birefringence [17], supercontinuum light generation [18–20], light wavelength conversion [21,22], optical fluids [23], and sensing [24]. The typical numerical aperture (NA) of the MOF is $NA \approx 0.5-0.6$ [25–27]. High NA MOFs [28] have been used to achieve lensless focusing with excellent resolution. In a typical MOF design, as shown in Fig. 1, the cladding-layer can be effected by changing the pattern and/or size (d) of air-holes within a concentric ring-like region. A MOF with a varying pattern in the cladding imitating a doubly clad W-type optical fiber is shown in Fig. 1. The advantage of W-type MOF over conventional W-type optical fiber is greater flexibility in adjusting the geometric parameters: air-hole diameters d_q , d_p and pitch Λ .

The propagation characteristics of a multimode optical fibers are influenced by mode coupling, modal attenuation, and modal dispersion. Light scattering in multimode optical fibers, which is due to fiber's intrinsic perturbations, is the primary cause of mode coupling. Light scattering can be caused by a variety of irregularities, including voids, cracks, microscopic bends, and density variations. Only short fibers will produce a highly defined ring radiation pattern when light is

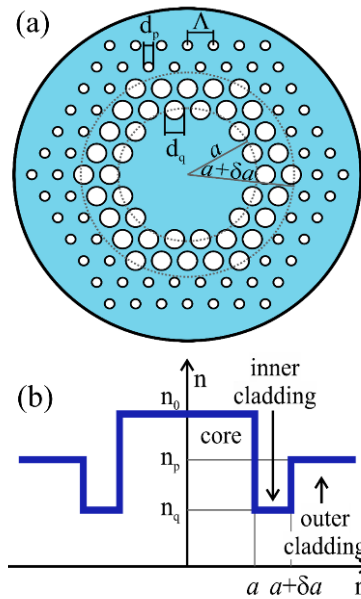


Fig. 1. (a) The cross section of the multimode doubly clad W-type MOF. Λ is the pitch, d_q and d_p are the diameters of inner outer cladding air-holes, respectively. (b) The RI performance of the referent multimode W-type MOF.

launched at a given angle $\theta_0 > 0$ with respect to the fiber axis. The boundaries of such a ring grow fuzzy at the end of longer fibers due to mode coupling. At length L_c , where the highest-order mode ring-pattern evolves into a disk, an EMD is established.

Until recently, commercial simulation software packages were not designed for investigation of transmission characteristics of multimode microstructured optical fibers. This deficiency is addressed in this paper by numerically solving the time-independent power flow equation in the case of W-type mPOF. This enabled us to investigate the transmission performance of the multimode W-type mPOF, which is affected by the width of the inner cladding, spacing and size of air-holes, and the type of launch condition. For multimode W-type mPOF with a solid-core, we calculated characteristic lengths for achieving the EMD and SSD for launch beam distribution with different widths, for two different diameters of air-holes in the inner cladding. We assumed that cladding air-holes form a triangular pattern with a constant pitch Λ (see Fig. 1). In our best knowledge for the first time in this paper we investigate the transmission performance of mPOF with W-type refractive index distribution.

2. W-type mPOF design

Cladding air-holes of conventional mPOFs are typically arranged as a regular triangular lattice. The effective refractive index (RI) profile for a selected optical fiber layer can be adjusted by changing the geometric parameters d_q , d_p and Λ , as Fig. 1-(a) shows. The air-holes in the outer cladding are smaller than those in the inner cladding (d_p vs d_q in Fig. 1-(a)). The RI of the core n_0 (central part) is higher than those in two claddings. The lowest effective RI n_q is found in the inner cladding, and the outer cladding's effective RI is n_p ($n_q < n_p < n_0$). We used the TI PFE to simulate such a system.

3. Time-independent power-flow equation

The light transmission in a multimode optical fiber can be treated by Gloge's TI PFE [29]:

$$\frac{\partial P(\theta, z)}{\partial z} = -\alpha(\theta)P(\theta, z) + \frac{D}{\theta} \frac{\partial}{\partial \theta} \left(\theta \frac{\partial P(\theta, z)}{\partial \theta} \right) \quad (1)$$

where $P(\theta, z)$ is the angular power distribution at distance z from the input of the optical fiber, D is the coupling coefficient assumed constant [29,30], θ is the propagation angle with respect to the core axis, $\alpha(\theta) = \alpha_0 + \alpha_d(\theta)$ is the modal attenuation – where α_0 represents conventional losses (scattering and absorption), which is ignored because it only serves as a multiplier $\exp(-\alpha_0 z)$ in the solution of Eq. (1).

The W-type optical fiber with the index profile depicted in Fig. 1-(b) can be thought as a system of a SCq optical fiber and cladding [31], in which the angle $\theta_q \cong (2\Delta_q)^{1/2}$ is the critical angle for the guided modes – where $\Delta_q = (n_0 - n_q)/n_0$. Likewise, the angle $\theta_p \cong (2\Delta_p)^{1/2}$ is the critical angle of a singly clad SCp optical fiber. For the complete analyzed W-type fiber, the modes are guided if they propagate with angles $\theta \leq \theta_p$, while modes with angles between θ_p and θ_q are lossy leaky modes:

$$\alpha_d(\theta) = \begin{cases} 0 & \theta \leq \theta_p \\ \alpha_L & \theta_p < \theta < \theta_q \\ \infty & \theta \geq \theta_q \end{cases} \quad (2)$$

where the attenuation of leaky modes is given as [32]:

$$\alpha_L(\theta) = \frac{4(\theta^2 - \theta_p^2)^{1/2} \theta^2(\theta_q^2 - \theta^2)}{a(1 - \theta^2)^{1/2} \theta_q^2(\theta_q^2 - \theta_p^2)} \exp(2\delta a n_0 k_0 (\theta_q^2 - \theta^2)^{1/2}) \quad (3)$$

and where $k_0 = 2\pi/\lambda$, and λ is the wavelength of light.

4. Numerical results

We investigated a light transmission in a multimode W-type mPOF with a solid-core (Fig. 1). The effective V parameter for such fiber is given as:

$$V = \frac{2\pi}{\lambda} a_{eff} \sqrt{n_0^2 - n_{fsm}^2} \quad (4)$$

where $a_{eff} = \Lambda/\sqrt{3}$ [33], and n_{fsm} is cladding's effective RI, which can be obtained from Eq. (4), with the effective V parameter [33]:

$$V \left(\frac{\lambda}{\Lambda}, \frac{d}{\Lambda} \right) = A_1 + \frac{A_2}{1 + A_3 \exp(A_4 \lambda / \Lambda)} \quad (5)$$

with the fitting parameters A_i ($i = 1$ to 4) given in the following form:

$$A_i = a_{i0} + a_{i1} \left(\frac{d}{\Lambda} \right)^{b_{i1}} + a_{i2} \left(\frac{d}{\Lambda} \right)^{b_{i2}} + a_{i3} \left(\frac{d}{\Lambda} \right)^{b_{i3}} \quad (6)$$

where the coefficients a_{i0} to a_{i3} and b_{i1} to b_{i3} ($i = 1$ to 4) are given in Table 1.

Significant values of the effective RI of the inner cladding n_q , relative RI difference Δ_q , critical angles θ_p , and inner cladding air-holes diameters d_q are shown in Table 2, for $\lambda=645$ nm and $\Lambda = 3\mu\text{m}$. The critical angle θ_p for $d_p = 1\mu\text{m}$ is $\theta_p = 5.79^\circ$, and the effective RI of the outer cladding is $n_p = 1.4844$ (Table 2).

Table 1. The fitting coefficients in Eq. (6).

	$i = 1$	$i = 2$	$i = 3$	$i = 4$
a_{i0}	0.54808	0.71041	0.16904	-1.52736
a_{i1}	5.00401	9.73491	1.85765	1.06745
a_{i2}	-10.43248	47.41496	18.96849	1.93229
a_{i3}	8.22992	-437.50962	-42.4318	3.89
b_{i1}	5	1.8	1.7	-0.84
b_{i2}	7	7.32	10	1.02
b_{i3}	9	22.8	14	13.4

Table 2. For two air-hole diameters d_q in the inner cladding, the data show the effective refractive index n_q , relative refractive index difference Δ_q and the corresponding critical angle θ_q - all for the inner cladding and at $\lambda=645$ nm.

d_q (μm)	1.5	2.0
n_q	1.4757	1.4458
$\Delta_q = (n_0 - n_q)/n_0$	0.677645	0.691611
θ_q (deg)	8.48	14.28

The explicit finite differences method was used to solve the TI PFE (1) for the multimode W-type mPOF with a solid-core [29,34], for a Gaussian launch-beam distribution of the form:

$$P(\theta, z) = \frac{1}{\sigma\sqrt{2\pi}} \exp\left[-\frac{(\theta - \theta_0)^2}{2\sigma^2}\right] \quad (7)$$

where θ_0 is the mean value of the launch angular distribution, σ is the standard deviation, and $\text{FWHM} = 2\sigma\sqrt{2\ln 2} = 2.355\sigma$.

The W-type mPOF was designed from the SC mPOF, which we theoretically investigated in our recently published work [35]. The characteristics of the SC mPOF were: $n_0 = 1.492$, optical fiber diameter $b = 1$ mm, and coupling coefficient $D = 1.649 \times 10^{-4}$ rad²/m (typical value of D for conventional POFs and mPOFs) [34,35]. It is worth noting that when modeling the W-type mPOF, the typical values of D that characterize a conventional POF can be used, because the strength of mode coupling both in conventional POFs and mPOFs is related to the polymer core material. In modeling a silica W-type MOF, a similar assumption was made [36].

To examine the effect of air-holes diameter in the inner cladding on the angular power distribution, the cases with $d_q = 1.5$ and $2 \mu\text{m}$ were simulated, for a fixed diameter of the outer cladding air-holes $d_p = 1 \mu\text{m}$, for two widths of the inner cladding $\delta a = 2.4 \mu\text{m}$ ($\delta = 0.008$) and $\delta a = 7.2 \mu\text{m}$ ($\delta = 0.024$), where core diameter $2a = 600 \mu\text{m}$ of W-type mPOF is assumed in the calculations. We examined cases of launch beam distributions with $(\text{FWHM})_{z=0} = 1^\circ, 5^\circ$ and 10° . Figure 2 shows the output angular power distribution at different optical fiber lengths, in the case of $d_p = 1 \mu\text{m}$, $d_q = 2 \mu\text{m}$, and $\delta = 0.008$, calculated for Gaussian launch beam distributions with input angles $\theta_0 = 0^\circ, 6^\circ$, and 12° with $(\text{FWHM})_{z=0} = 5^\circ$. Figure 2 shows that when the Gaussian launch beam distribution at the input fiber end is centered at $\theta_0 = 0^\circ$, with increasing the optical fiber length, its width increases as a result of mode coupling. As the optical fiber length increases, low-order modes coupling becomes stronger: the distributions shift more towards $\theta = 0^\circ$. Higher-order modes significantly couple only after longer optical fiber lengths. At the optical fiber's coupling length $z = L_c = 34.5$ m, the EMD is established. The optical fiber length

$z_s \equiv z_s = 89$ m denotes the point at which the mode-distribution becomes completely independent of the launch beam distribution, i.e. it becomes a SSD.

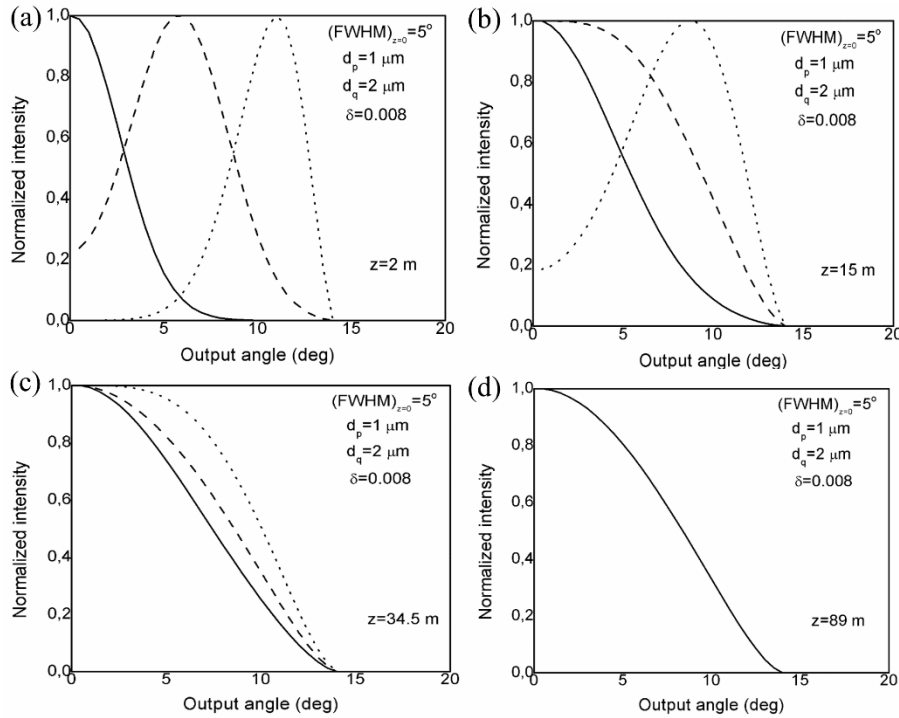


Fig. 2. The evolution of the normalized output angular power distribution with fiber length for the case with $d_p = 1 \mu\text{m}$ ($n_p = 1.4844$), $d_q = 2 \mu\text{m}$ ($n_q = 1.4458$), $\delta = 0.008$, calculated for Gaussian launch distribution with input angles $\theta_0 = 0^\circ$ (solid line), 6° (dashed line), and 12° (dotted line) with $(\text{FWHM})_{z=0} = 5^\circ$ for: (a) $z = 2$ m; (b) $z = 15$ m; (c) $z \equiv L_c = 34.5$ m and (d) $z \equiv z_s = 89$ m.

We also solved the TI PFE (1) for different excitations to determine the optical fiber lengths L_c and z_s . The resulting graphs in Figs. 3 and 4 show the lengths L_c and z_s as a function of the $(\text{FWHM})_{z=0}$ of the launch beam, for two inner cladding's air-holes sizes d_q (Fig. 3(a)) and two widths δa of the inner cladding (Fig. 3(b)). Figures 3 and 4 show that the wider the launch beam distribution results in the earlier onset of the EMD and SSD, respectively. This is a consequence of more uniform energy distribution among guided modes, so the EMD and SSD are established at shorter distances. The effect of launch excitation on lengths L_c and z_s is also affected by fiber structural parameters (Table 3). With large leaky mode losses, the influence of launch excitation is less pronounced for smaller inner cladding's air-holes diameter d_q . Leaky mode losses decrease with increasing d_q , that leads to a more pronounced influence of the launch excitation.

Figures 3(a) and 4(a) show that the lengths L_c and z_s increase with the size of the inner cladding's air-holes (diameter d_q). This is due to a decrease in leaky mode losses for larger air-holes; power then remains in higher-order leaky modes over longer transmission lengths, postponing the onset of the EMD and SSD (longer L_c and z_s).

The lengths L_c and z_s are shorter for the optical fiber with a narrower inner cladding (Figs. 3(b) and 4(b)). Because leaky mode losses are lower in optical fibers with wider inner cladding, power remains in leaky modes for a longer light transmission length. The lengths L_c and z_s for W-type mPOF (Figs. 3 and 4) are shorter if compared to these lengths for two SC mPOFs, shown in Fig. 5: SC_{q(1)} fiber with $n_0 = 1.492$ and $n_q = 1.4757$, and SC_{q(2)} fiber with $n_0 = 1.492$

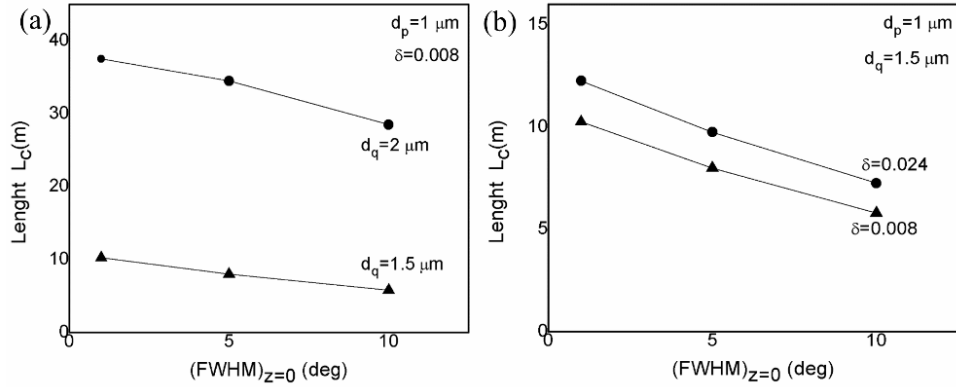


Fig. 3. Length L_c as a function of the launch beam's angular distribution that is Gaussian with $(FWHM)_{z=0} = 1^\circ, 5^\circ$ and 10° , for $d_p = 1 \mu\text{m}$ ($n_p = 1.4844$) and (a) $d_q = 1.5 \mu\text{m}$ ($n_q = 1.4757$) and $2 \mu\text{m}$ ($n_q = 1.4458$), where $\delta = 0.008$, and (b) $\delta = 0.008$ and 0.024 , where $d_q = 1.5 \mu\text{m}$ ($n_q = 1.4757$).

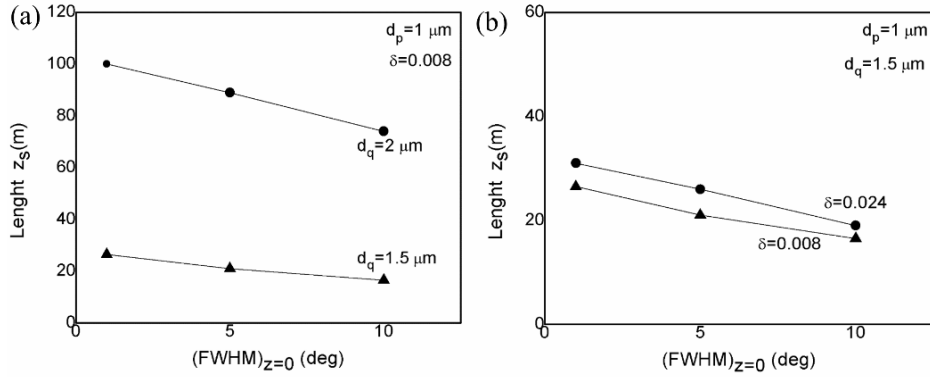


Fig. 4. Length z_s as a function of the launch beam's angular distribution that is Gaussian with $(FWHM)_{z=0} = 1^\circ, 5^\circ$ and 10° , for $d_p = 1 \mu\text{m}$ ($n_p = 1.4844$) and (a) $d_q = 1.5 \mu\text{m}$ ($n_q = 1.4757$) and $2 \mu\text{m}$ ($n_q = 1.4458$), where $\delta = 0.008$, and (b) $\delta = 0.008$ and 0.024 , where $d_q = 1.5 \mu\text{m}$ ($n_q = 1.4757$).

Table 3. Coupling length L_c (for EMD) and length z_s (for SSD) in mPOF with $d_p = 1 \mu\text{m}$, $\Lambda = 3 \mu\text{m}$, for different δ , d_q , and $(FWHM)_{z=0}$ of the incident Gaussian launch beam distribution.

		$(FWHM)_{z=0} = 1^\circ$		$(FWHM)_{z=0} = 5^\circ$		$(FWHM)_{z=0} = 10^\circ$	
		L_c [m]	z_s [m]	L_c [m]	z_s [m]	L_c [m]	z_s [m]
$\delta = 0.008$	$d_q = 1.5 \mu\text{m}$	10.3	26.5	8	21	5.8	16.5
	$d_q = 2 \mu\text{m}$	37.5	100	34.5	89	28.5	74
$\delta = 0.024$	$d_q = 1.5 \mu\text{m}$	12.3	31	9.8	26	7.3	19
	$d_q = 2 \mu\text{m}$	41	106	37.5	97.5	31.3	85

and $n_q = 1.4458$. In particular, a portion of the guiding modes in W-type mPOFs become leaky modes, reducing the number of actually guided modes and, as a result, the lengths required to establish an EMD and SSD are shorter compared to the SC mPOFs.

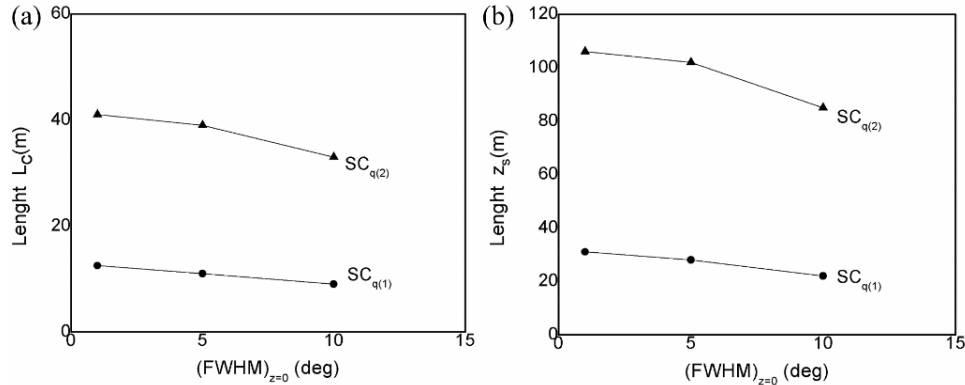


Fig. 5. (a) Length L_c as a function of the launch beam's angular distribution that is Gaussian with $(FWHM)_{z=0} = 1^\circ, 5^\circ$ and 10° , for $SC_{q(1)}$ fiber with $n_0 = 1.492$ and $n_q = 1.4757$ ($d_q = 1.5 \mu\text{m}$) and $SC_{q(2)}$ fiber with $n_0 = 1.492$ and $n_q = 1.4458$ ($d_q = 2 \mu\text{m}$); (b) Length z_s as a function of the launch beam's angular distribution that is Gaussian with $(FWHM)_{z=0} = 1^\circ, 5^\circ$ and 10° , for $SC_{q(1)}$ fiber with $n_0 = 1.492$ and $n_q = 1.4757$ ($d_q = 1.5 \mu\text{m}$) and $SC_{q(2)}$ fiber with $n_0 = 1.492$ and $n_q = 1.4458$ ($d_q = 2 \mu\text{m}$).

Compared with mPOF investigated in this work, silica microstructured optical fibers show much weaker mode coupling ($D \approx 10^{-6} \text{ rad}^2/\text{m}$) and therefore much longer lengths at which SSD is achieved ($z_s \approx 1$ to 10 km) [36].

It is worth noting that the length dependence of the bandwidth of W-type MOF is determined by mode coupling behavior. The bandwidth is inverse linear function of length below the coupling length L_c . However, it has a $z^{-1/2}$ dependence beyond this equilibrium length. Thus, the shorter L_c leads to the faster transition to the regime of slower bandwidth decrease [37,38]. Since the lengths required to establish an EMD and SSD in W-type mPOFs are shorter compared to the SC mPOFs (Figs. 3 and 5(a)), a faster bandwidth improvement in mPOFs is expected than in SC mPOFs, which prove that W-type mPOFs are better choice for short-range telecommunication links. It is also important to be able to determine a modal distribution at a certain length of the W-type mPOF employed as a part of optical fiber sensory system.

Finally, it is interesting to note that the theoretical approach of modal diffusion in microstructured optical fibers employed in this work can be used for calculation of fiber's bandwidth, but instead of time-independent power flow Eq. (1) which is solved in this work, one has to solve the time-dependent power flow equation [38].

5. Conclusion

We investigated how the transmission of the multimode W-type mPOFs is affected by the width of the inner cladding, the size and spacing of inner cladding's air-holes, and the type of launch excitation. We demonstrated that the greater the width of the launch beam distribution, the shorter the lengths at which an EMD and SSD are established. Due to large leaky mode losses, the influence of launch excitation is less pronounced for smaller air-holes diameters of the inner cladding. The lengths required to achieve the EMD and SSD are shorter for the fiber with a narrower inner cladding. Because leaky mode losses are lower in fibers with wider inner cladding, power remains in leaky modes for a longer fiber length. Finally, because of these adjustable parameters, W-type mPOFs can be designed with greater versatility.

Funding. National Natural Science Foundation of China (62003046, 6211101138); Ministry of Education, Science and Technological Development (451-03-68/2020-14/200122); Science Fund of the Republic of Serbia (CTPCF-6379382); Basic and Applied Basic Research Foundation of Guangdong Province (2021A1515011997); City University of Hong Kong (CityU 7004600); The Innovation Team Project of Guangdong Provincial Department of Education (2021KCXTD014); Special project in key field of Guangdong Provincial Department of Education (2021ZDZX1050).

Disclosures. The authors declare no conflicts of interest.

Data availability. Data underlying the results presented in this paper are not publicly available at this time but may be obtained from the authors upon reasonable request.

References

1. J. C. Knight, T. A. Birks, P. S. J. Russell, and D. M. Atkin, "All-silica single-mode optical fiber with photonic crystal cladding," *Opt. Lett.* **21**(19), 1547–1549 (1996).
2. T. A. Birks, J. C. Knight, and P. S. J. Russell, "Endlessly single-mode photonic crystal fiber," *Opt. Lett.* **22**(13), 961–963 (1997).
3. P. S. J. Russell, "Photonic crystal fibers," *Science* **299**(5605), 358–362 (2003).
4. J. C. Knight, "Photonic crystal fiber," *Nature* **424**(6950), 847–851 (2003).
5. P. S. J. Russell, "Photonic-crystal fibers," *J. Lightwave Technol.* **24**(12), 4729–4749 (2006).
6. J. C. Knight, J. Broeng, T. A. Birks, and P. S. J. Russell, "Photonic band gap guidance in optical fibers," *Science* **282**(5393), 1476–1478 (1998).
7. J. C. Knight and P. S. J. Russell, "Photonic crystal fibers: New way to guide light," *Science* **296**(5566), 276–277 (2002).
8. R. F. Cregan, B. J. Mangan, J. C. Knight, T. A. Birks, P. S. J. Russell, P. J. Roberts, and D. C. Allan, "Single-mode photonic band gap guidance of light in air," *Science* **285**(5433), 1537–1539 (1999).
9. R. Amezcua-Correa, F. Gerome, S. G. Leon-Saval, N. G. R. Broderick, T. A. Birks, and J. C. Knight, "Control of surface modes in low loss hollow core photonic bandgap fibers," *Opt. Express* **16**(2), 1142–1149 (2008).
10. G. Bouwmans, L. Bigot, Y. Quiquempois, F. Lopez, L. Provino, and M. Douay, "Fabrication and characterization of an all-solid 2d photonic bandgap fiber with a low-loss region (<20 db/km) around 1550 nm," *Opt. Express* **13**(21), 8452–8459 (2005).
11. F. Luan, A. K. George, T. D. Hedley, G. J. Pearce, D. M. Bird, J. C. Knight, and P. S. J. Russell, "All-solid photonic bandgap fiber," *Opt. Lett.* **29**(20), 2369–2371 (2004).
12. F. Benabid, J. C. Knight, G. Antonopoulos, and P. S. J. Russell, "Stimulated Raman scattering in hydrogen-filled hollow-core photonic crystal fiber," *Science* **298**(5592), 399–402 (2002).
13. P. S. Light, F. Benabid, F. Couny, M. Maric, and A. N. Luiten, "Electromagnetically induced transparency in Rb-filled coated hollow-core photonic crystal fiber," *Opt. Lett.* **32**(10), 1323–1325 (2007).
14. D. Mogilevtsev, T. A. Birks, and P. S. J. Russell, "Group-velocity dispersion in photonic crystal fibers," *Opt. Lett.* **23**(21), 1662–1664 (1998).
15. K. Saitoh, M. Koshiba, T. Hasegawa, and E. Sasaoka, "Chromatic dispersion control in photonic crystal fibers: application to ultra-flattened dispersion," *Opt. Express* **11**(8), 843–852 (2003).
16. S. Lee, W. Ha, J. Park, S. Kim, and K. Oh, "A new design of low-loss and ultra-flat zero dispersion photonic crystal fiber using hollow ring defect," *Opt. Commun.* **285**(20), 4082–4087 (2012).
17. D. Chen, M. L. V. Tse, and H. Y. Tam, "Optical properties of photonic crystal fibers with a fiber core of arrays of sub-wavelength circular air holes: birefringence and dispersion," *Prog. Electromagn. Res.* **105**, 193–212 (2010).
18. J. K. Ranka, R. S. Windeler, and A. J. Stentz, "Visible continuum generation in air silica microstructured optical fibers with anomalous dispersion at 800 nm," *Opt. Lett.* **25**(1), 25–27 (2000).
19. K. M. Hilligsøe, T. V. Andersen, H. N. Paulsen, C. K. Nielsen, K. Mølmer, S. Keiding, R. Kristiansen, K. P. Hansen, and J. J. Larsen, "Supercontinuum generation in a photonic crystal fiber with two zero dispersion wavelengths," *Opt. Express* **12**(6), 1045–1054 (2004).
20. W. J. Wadsworth, N. Joly, J. C. Knight, T. A. Birks, F. Biancalana, and P. S. J. Russell, "Supercontinuum and four-wave mixing with Q-switched pulses in endlessly single-mode photonic crystal fibres," *Opt. Express* **12**(2), 299–309 (2004).
21. J. H. Lee, W. Belardi, K. Furusawa, P. Petropoulos, Z. Yusoff, T. M. Monro, and D. J. Richardson, "Four-wave mixing based 10-Gb/s tunable wavelength conversion using a holey fiber with a high SBS threshold," *IEEE Photonics Technol. Lett.* **15**(3), 440–442 (2003).
22. T. V. Andersen, K. M. Hilligsøe, C. K. Nielsen, J. Thøgersen, K. P. Hansen, S. R. Keiding, and J. J. Larsen, "Continuous-wave wavelength conversion in a photonic crystal fiber with two zero-dispersion wavelengths," *Opt. Express* **12**(17), 4113–4122 (2004).
23. J. Park, D. E. Kang, B. Paulson, T. Nazari, and K. Oh, "Liquid core photonic crystal fiber with low-refractive-index liquids for optofluidic applications," *Opt. Express* **22**(14), 17320–17330 (2014).
24. S. H. Kassani, R. Khazaiezhad, Y. Jung, J. Kobelke, and K. Oh, "Suspended ring-core photonic crystal fiber gas sensor with high sensitivity and fast response," *IEEE Photonics J.* **7**(1), 1–9 (2015).
25. W. Wadsworth, R. Percival, G. Bouwmans, J. Knight, T. Birks, T. Hedley, and P. S. J. Russell, "Very High Numerical Aperture Fibers," *IEEE Photonics Technol. Lett.* **16**(3), 843–845 (2004).

26. R. Lwin, G. Barton, L. Harvey, J. Harvey, D. Hirst, S. Manos, M. C. J. Large, L. Poladian, A. Bachmann, H. Poisel, and K.-F. Klein, "Beyond the bandwidth-length product: Graded index microstructured polymer optical fiber," *Appl. Phys. Lett.* **91**(19), 191119 (2007).
27. K. P. Hansen, C. B. Olausson, J. Broeng, D. Noordegraaf, M. D. Maack, T. T. Alkeskjold, M. Laurila, T. Nikolajsen, P. M. W. Skovgaard, M. H. Sorensen, M. Denninger, C. Jakobsen, and H. R. Simonsen, "Airclad fiber laser technology," *Opt. Eng.* **50**(11), 111609 (2011).
28. L. V. Amitonova, A. Descloux, J. Petschulat, M. H. Frosz, G. Ahmed, F. Babic, X. Jiang, A. P. Mosk, P. S. J. Russell, and P. W. H. Pinkse, "High-resolution wavefront shaping with a photonic crystal fiber for multimode fiber imaging," *Opt. Lett.* **41**(3), 497–500 (2016).
29. D. Gloge, "Optical power flow in multimode fibers," *Bell Syst. Tech. J.* **51**(8), 1767–1783 (1972).
30. M. Rousseau and L. Jeunhomme, "Numerical solution of the coupled-power equation in step index optical fibers," *IEEE Trans. Microw. Theory Tech.* **25**(7), 577–585 (1977).
31. T. P. Tanaka and S. Yamada, "Steady-state characteristics of multimode W-type fibers," *Appl. Opt.* **18**(19), 3261–3264 (1979).
32. S. Kawakami and S. Nishida, "Perturbation theory of doubly clad optical fiber with a low index inner cladding," *IEEE J. Quantum Electron.* **11**(4), 130–138 (1975).
33. K. Saitoh and M. Koshiba, "Empirical relations for simple design of photonic crystal fibers," *Opt. Express* **13**(1), 267–274 (2005).
34. J. Mateo, M. A. Losada, I. Garcés, and J. Zubia, "Global characterization of optical power propagation in step-index plastic optical fibers," *Opt. Express* **14**(20), 9028 (2006).
35. S. Savović, M. S. Kovačević, B. Drljača, A. Simović, L. Kuzmanović, and A. Djordjević, "Power flow in multimode step-index plastic photonic crystal fibers," *Optik* **247**, 167868 (2021).
36. M. S. Kovačević, L. Kuzmanović, A. Simović, S. Savović, and A. Djordjević, "Transients of modal power distribution in multimode solid core W-type photonic crystal fibers," *J. Lightwave Technol.* **35**(20), 4352–4357 (2017).
37. S. Savović, B. Drljača, and A. Djordjević, "Influence of launch beam distribution on bandwidth in step index plastic optical fibers," *Appl. Opt.* **52**(6), 1117–1121 (2013).
38. B. Drljača, S. Savović, M. S. Kovačević, A. Simović, L. Kuzmanović, A. Djordjević, and R. Min, "Theoretical investigation of bandwidth of multimode step-index silica photonic crystal fibers," *Photonics* **9**(4), 214 (2022).



Calculation of the Coupling Coefficient in Step-Index Multimode Polymer Optical Fibers Based on the Far-Field Measurements

Svetislav Savović^{1,2}, Alexandar Djordjevich³, Branko Drljača⁴, Ana Simović² and Rui Min^{1*}

¹Center for Cognition and Neuroergonomics, State Key Laboratory of Cognitive Neuroscience and Learning, Beijing Normal University, Zhuhai, China, ²Faculty of Science, University of Kragujevac, Kragujevac, Serbia, ³Department of Mechanical Engineering, City University of Hong Kong, Kowloon, China, ⁴Faculty of Sciences, University of Priština in Kosovska Mitrovica, Kosovska Mitrovica, Serbia

OPEN ACCESS

Edited by:

Sushank Chaudhary,
Quanzhou Institute of Equipment
Manufacturing (CAS), China

Reviewed by:

Lei Liu,
Harbin Engineering University, China
Yuyang Peng,
Macau University of Science and
Technology, Macao SAR, China

*Correspondence:

Rui Min
ruimin@bnu.edu.cn

Specialty section:

This article was submitted to
Optics and Photonics,
a section of the journal
Frontiers in Physics

Received: 25 April 2022

Accepted: 09 May 2022

Published: 25 May 2022

Citation:

Savović S, Djordjevich A, Drljača B, Simović A and Min R (2022) Calculation of the Coupling Coefficient in Step-Index Multimode Polymer Optical Fibers Based on the Far-Field Measurements. *Front. Phys.* 10:927907. doi: 10.3389/fphy.2022.927907

Using the power flow equation (PFE), this article investigates mode coupling in step-index (SI) multimode (MM) polymer optical fiber (POF). This equation's coupling coefficient was initially fine-tuned so that it could appropriately reconstruct previously recorded far-field (FF) power distributions. The equilibrium mode distribution (EMD) and steady-state distribution (SSD) in the SI MM POF were found to be obtained at lengths $L_c = 15$ m and $z_s = 41$ m, respectively. These lengths are substantially shorter than their glass optical fiber counterparts. Such characterization of the investigated POF can be used in its employment as a part of the communication or sensory system. Namely, the POF's bandwidth is inverse linear function of fiber length (z^{-1}) below the coupling length L_c . However, it has a $z^{-1/2}$ dependence beyond this equilibrium length. Thus, the shorter the coupling length L_c , the sooner transition to the regime of slower bandwidth decrease occurs. It is also important to be able to determine a modal distribution at a certain length of the POF employed as a part of optical fiber sensory system.

Keywords: polymer optical fiber, modal distribution, coupling length, bandwidth, distance dependence, sensory system

INTRODUCTION

Silica optical fiber has a lot of advantages such as a low loss, lightweight, and high bandwidth [1–4]. Although silica optical fiber has a lot of advantages, is not appropriate for short-distance applications such as automotive [5], local area networks [6], and visible light communication (VLC) applications [7]. On the other hand, POFs are made of poly (methylmethacrylate) (PMMA) [8, 9], polycarbonate (PC) [10, 11], ZEONEX[®] [12, 13], TOPAS[®] [14, 15], poly dimethyl siloxane (PDMS) [16, 17] or hydrogel [18, 19].

Apart from optical fiber material, optical fibers usually have step-index or graded-index refractive index distribution, and can operate in a single-mode or multimode regime. There are several typical commercial POFs, such as Mitsubishi Rayon's Eska Extra EH 4001 SI MM POF [20] and CYTOP[®] graded index (GI) POF [21], both of them could transmit a large number of modes, and have been used for short-range communications and sensing area in fiber optic sensory systems [22]. Additionally, micro-structured polymer optical fiber which was first produced by Argyros' group, is one very specific type of POF [23]. However, due to the transmission loss and but-coupling with commercial silica optical fiber, only one Start-up Company supplied the commercial

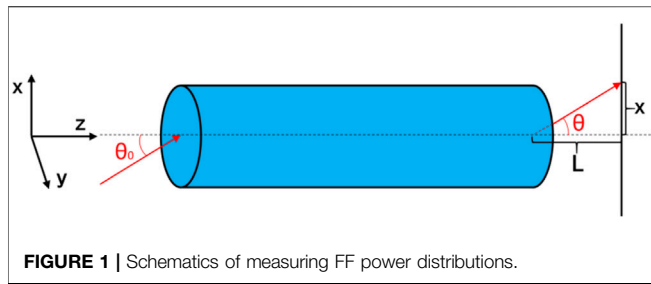


FIGURE 1 | Schematics of measuring FF power distributions.

product [24]. PMMA SI MM POF is still the most common one with lots of commercial products on the market.

Mode coupling has a significant impact on the transmission performance of PMMA SI MM POF. The transfer of power between nearby modes is represented by such coupling. It causes the launched light's angular power distribution to be disrupted [25, 26]. It is caused by the optical fiber's intrinsic perturbation effects (for example, variations of the refractive index distribution and microscopic bends). The angular power distribution is predicted to be influenced by the launch conditions and mode coupling characteristics. Thus, a Gaussian beam launched at an angle θ_0 in respect to the optical fiber axis, at the output end of a short piece of optical fiber, is seen as a sharp ring pattern (the ring diameter depends on θ_0). Mode coupling, on the other hand, causes such a ring pattern to be distorted in longer fibers and finally transformed into disk. The coupling length L_c marks the fiber length at which the ring pattern of the highest order guiding mode evolved into disk, indicating that an EMD is established. Coupling can fully complete at optical fiber length z_s ($z_s > L_c$), which is referred to as an SSD.

The light transmission performance of PMMA SI MM POF is investigated in this work. The modal power diffusion model is used to obtain the coupling coefficient D . In this way, we computed the L_c required to accomplish the EMD and the length z_s to achieve the SSD. By such a characterization of mode coupling process in an optical fiber one can predict at which length $z = L_c$ one can expect that bandwidth decrease with length would start to decelerate, as explained in more details in Results and Discussion. It is also important to know the state of mode coupling in an optical fiber employed as a

part of optical fiber sensory system, especially in terms of the modal distribution at certain fiber length.

POWER FLOW EQUATION

The Gloge's PFE has the following form [27]:

$$\frac{\partial P(\theta, z)}{\partial z} = -\alpha(\theta)P(\theta, z) + \frac{D}{\theta} \frac{\partial}{\partial \theta} \left(\theta \frac{\partial P(\theta, z)}{\partial \theta} \right) \quad (1)$$

where $P(\theta, z)$ is the angular power distribution, θ is the angle of propagation, z is the distance of the propagation, D is the coupling coefficient (assumed constant [27, 28]) and $\alpha(\theta)$ is the modal attenuation. Eq. 1 can be reduced to [29]:

$$\frac{\partial P(\theta, z)}{\partial z} = \frac{D}{\theta} \frac{\partial P(\theta, z)}{\partial \theta} + D \frac{\partial^2 P(\theta, z)}{\partial \theta^2} \quad (2)$$

Steady-state solution of Eq. 2 is given as [28]:

$$P(\theta, z) = J_0 \left(2.405 \frac{\theta}{\theta_c} \right) \exp(-\gamma_0 z) \quad (3)$$

where J_0 is the Bessel function of the first and zero-order, γ_0 [m^{-1}] = $2.405^2 D / \theta_c^2$ is the attenuation coefficient. In this work, solved Eq. 2 using the explicit finite difference method [29].

In our earlier published work, we proposed a method which enables that the coupling coefficient D can be obtained from just two output angular power distributions $P(\theta, z)$ in the case of centrally launched beam [30]. As an alternative, in this work we propose a method for calculating the coupling coefficient D on the basis of the measured FFPs $p(x, z)$, illustrated in Figure 1.

RESULTS AND DISCUSSION

We used the PFE (2) to calculate the lengths L_c and z_s for the POF that Ribeiro et al. [31] studied experimentally. This POF (Mitsubishi Rayon's Eska Extra EH 4001) had NA = 0.47, the inner critical angle $\theta_c = 18^\circ$ ($\theta_c = 27.4^\circ$ measured in air), core

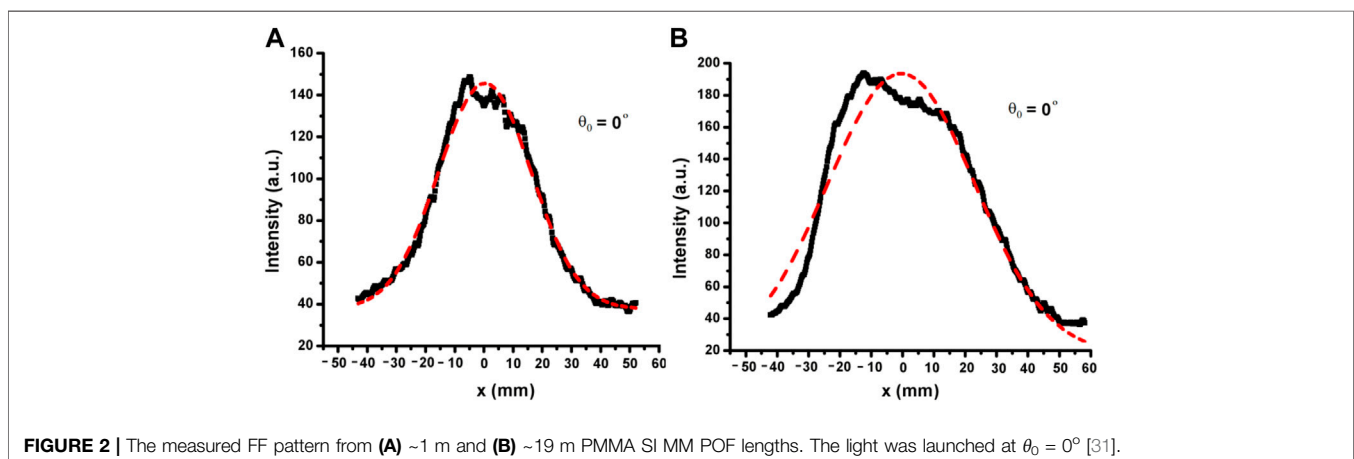


FIGURE 2 | The measured FF pattern from (A) ~1 m and (B) ~19 m PMMA SI MM POF lengths. The light was launched at $\theta_0 = 0^\circ$ [31].

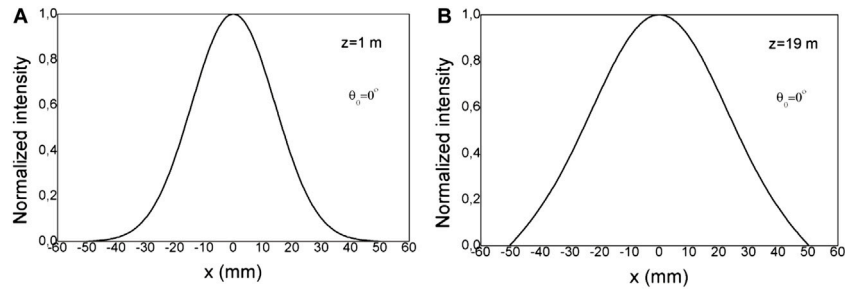


FIGURE 3 | Normalized output power distribution $P(x, z = 1$ and 19 m, $L = 110$ mm) at the end of (A) 1 m and (B) 19 m long PMMA SI MM POF, obtained by solving the PFE for Gaussian launch distribution with input angle $\theta_0 = 0^\circ$, obtained from the $P(x, z = 1$ and 19 m, $L = 110$ mm), for $x = L \cdot \tan \theta$, where L is the receiving distance.

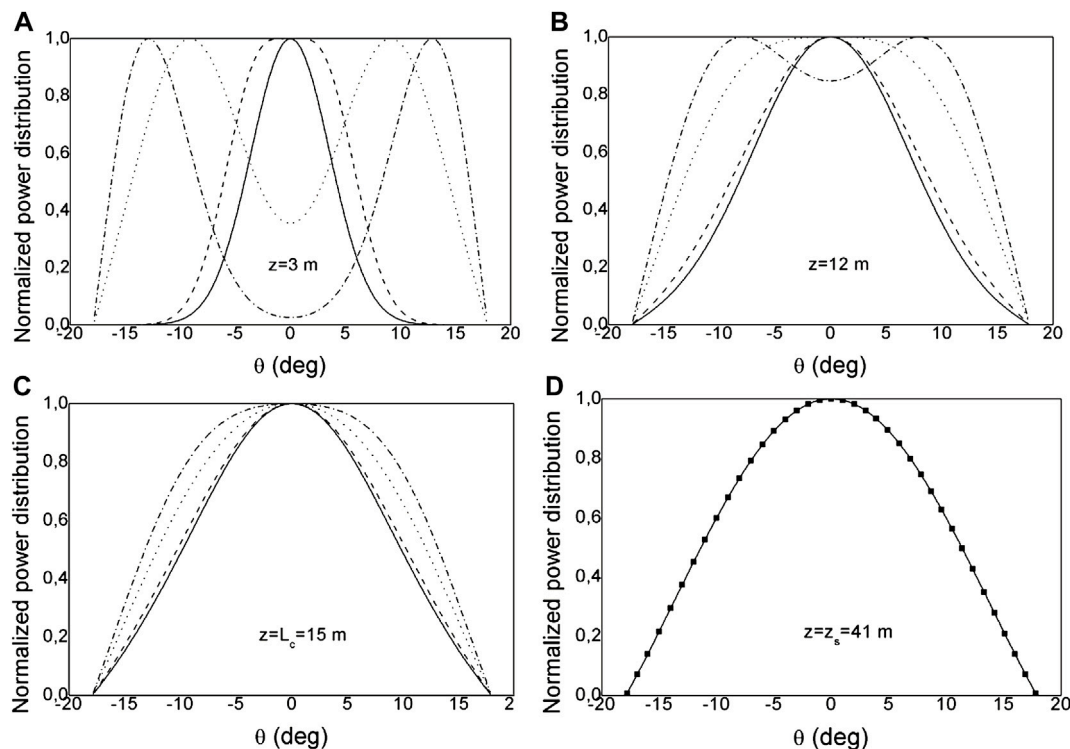


FIGURE 4 | The normalized angular power distribution at the end of PMMA SI MM POF, obtained by solving the PFE for four Gaussian launch distributions with input angles $\theta_0 = 0^\circ$ (—), $\theta_0 = 5^\circ$ (---), $\theta_0 = 10^\circ$ (●●●) and $\theta_0 = 15^\circ$ (—●—), with $(FWHM)_{z=0} = 7^\circ$ (g represent the analytical SSD).

refractive index $n_{core} = 1.4897$, numerical aperture $NA = 0.46$ and fiber diameter $d = 1$ mm. Ribeiro et al. focused a He-Ne laser beam at 633 nm onto the input end of the fiber in their experiment (Figure 1). They used a CCD to detect the FF patterns of the fiber output.

The coupling coefficient D is obtained by its fine-tuning in the PFE, thus recreating the Ribeiro et al.'s measured FF patterns in this fiber for lengths of $z = 1$ m and $z = 19$ m (Figure 2). This necessitated numerically calculating the PFE for various values of D . The value of $D = 9.2 \times 10^{-4} \text{ rad}^2/\text{m}$ enabled the best fit between the calculated and measured output power distributions.

A Gaussian launch beam with $(FWHM)_{z=0} = 7^\circ$ is used in the computations. Figure 3 shows the output power distribution for a $z = 1$ and 19 m length POF with an input angle of $\theta_0 = 0^\circ$ obtained as numerical solution of Eq. 2. The distributions $P(x, z = 1$ and 19 m, $L = 110$ mm) are generated from the distributions $P(\theta, z = 1$ and 19 m, $L = 110$ mm), where $x = L \cdot \tan \theta$ and L is the receiving distance.

In Figure 4, our numerical results for the normalized output angular power distribution for input angles $\theta_0 = 0, 5, 10,$ and 15° are shown. At short fiber lengths, a significant mode coupling is observed for low order modes, as can be seen in Figure 4A. The EMD is achieved at length $z = L_c = 15$ m (Figure 4C), while the SSD is established at $z_s = 41$ m in Figure 4D.

The coupling coefficient D for the PMMA SI MM POF evaluated in this work is similar to those which we obtained for other investigated POFs ($\sim 10^{-4}$ rad²/m), so the characteristic lengths for coupling, L_c and z_s , are similar (L_c is between ≈ 15 – 35 m and z_s is between ≈ 40 and 100 m [25, 29, 30]). We have previously reported that glass optical fibers show the weakest strength of mode coupling ($D \sim 10^{-7}$ to 10^{-6} rad²/m), so their SSD lengths z_s are between ≈ 1 – 10 km [32].

It is worth noting that the length dependence of the bandwidth of POF is determined by mode coupling behavior. The bandwidth is inverse linear function of fiber length (z^{-1}) below the coupling length L_c . However, it has a $z^{-1/2}$ dependence beyond this equilibrium length. Thus, the shorter the coupling length L_c , the sooner transition to the regime of slower bandwidth decrease occurs [26]. It is obvious that mode coupling has a beneficial influence on bandwidth. Therefore, it is of great interest to characterize mode coupling in an optical fiber in order to predict its transmission characteristics, especially to determine at which coupling length L_c one can expect that bandwidth would start to improve. It is also important to know the state of mode coupling in an optical fiber employed as a part of optical fiber sensory system, especially in terms of the modal distribution at certain fiber length.

CONCLUSION

We investigate a mode coupling along a PMMA SI MM POF previously investigated experimentally by Ribeiro et al. [31]. To appropriately recreate the measured FF patterns reported before, the coupling coefficient D in the PFE is tweaked. As a result, the lengths L_c and z_s that characterize the coupling process are obtained. Such characterization of the investigated PMMA SI MM POF can be used in its employment as a part of communication or sensory system. In practice, by characterization of mode coupling in an optical fiber one can predict its transmission characteristics, especially to determine length-dependent bandwidth behavior. Since POF's bandwidth is inverse linear function of fiber length (z^{-1}) below the coupling

length L_c , while it has a $z^{-1/2}$ dependence beyond this equilibrium length, it is obvious that the shorter the coupling length L_c leads to the sooner transition to the regime of slower bandwidth decrease. It is also important to be able to determine a modal distribution at a certain length of the fiber employed as a part of optical fiber sensory system.

DATA AVAILABILITY STATEMENT

The original contributions presented in the study are included in the article/supplementary material, further inquiries can be directed to the corresponding author.

AUTHOR CONTRIBUTIONS

SS: methodology, conceptualization, formal analysis, validation, writing—original draft. RM: conceptualization, formal analysis, funding acquisition, writing—review and editing. AD: formal analysis, validation, writing—review and editing. BD: validation, writing—review and editing. AS: validation, writing—review and editing.

FUNDING

This research was funded by the National Natural Science Foundation of China (62003046, 6211101138); the Strategic Research Grant of City University of Hong Kong (Project No. CityU 7004600); Serbian Ministry of Education, Science and Technological Development (Agreement No. 451-03-68/2020-14/200122); Science Fund of the Republic Serbia (Agreement No. CTPCF-6379382); Guangdong Basic and Applied Basic Research Foundation (2021A1515011997); The Innovation Team Project of Guangdong Provincial Department of Education (2021KCXTD014); Special project in the key field of Guangdong Provincial Department of Education (2021ZDZX1050).

REFERENCES

- Min R, Liu Z, Pereira L, Yang C, Sui Q, Marques C. Optical Fiber Sensing for marine Environment and marine Structural Health Monitoring: A Review. *Opt Laser Techn* (2021) 140:107082. doi:10.1016/j.optlastec.2021.107082
- Xiang M, Fu S, Xu O, Li J, Peng D, Gao Z, et al. Advanced DSP Enabled C-Band 112 Gbit/s/λ PAM-4 Transmissions with Severe Bandwidth-Constraint. *J Lightwave Technol* (2022) 40(4):987–96. doi:10.1109/jlt.2021.3125336
- Maeda H, Saito K, Sasai T, Hamaoka F, Kawahara H, Seki T, et al. Real-time 400 Gbps/carrier WDM Transmission over 2,000 Km of Field-Installed G654E Fiber. *Opt Express* (2020) 28(2):1640–6. doi:10.1364/oe.383471
- Li Y, Fan H, Zhang L, Wang K, Wu G, Liu Z. A bend-tolerant BOTDR Distributed Fiber Sensor. *Opt Commun* (2022) 514:128110. doi:10.1016/j.optcom.2022.128110
- POF automotive application. Automotive (2022). Available at: <https://www.kdpof.com/automotive/> (Access on 04 02, 2022).
- Forni F, Shi Y, Tran N-C, Van Den Boom H, Tangdionga E, Koonen T. Multi-Format Wired and Wireless Signals over Large-Core Plastic Fibers for in-home Network. *J Lightwave Technol* (2018) 36:1. doi:10.1109/JLT.2018.2839029
- Apolo JA, Ortega B, Almenar V, Almenar V. Hybrid POF/VLC Links Based on a Single LED for Indoor Communications. *Photonics* (2021) 8(7):254. doi:10.3390/photonics8070254
- Liu L, Zheng J, Deng S, Yuan L, Teng C. Parallel Polished Plastic Optical Fiber-Based SPR Sensor for Simultaneous Measurement of RI and Temperature. *IEEE Trans Instrum Meas* (2021) 70:1–8. doi:10.1109/TIM.2021.3072136
- Hu X, Woyessa G, Kinet D, Janting J, Nielsen K, Bang O, et al. BDK-doped Core Microstructured PMMA Optical Fiber for Effective Bragg Grating Photo-Inscription. *Opt Lett* (2017) 42(11):2209–12. doi:10.1364/ol.42.002209
- Zubel MG, Fasano A, Woyessa GT, Min R, Leal-Junior AG, Theodosiou A, et al. Bragg Gratings Inscribed in Solid-Core Microstructured Single-Mode Polymer Optical Fiber Drawn from a 3D-Printed Polycarbonate Preform. *IEEE Sensors J* (2020) 20(21):12744–57. doi:10.1109/JSEN.2020.3003469
- Moslan MS, Othman MHD, Samavati A, Salim MAM, Rahman MA, Ismail AF, et al. Fabrication of Polycarbonate Polymer Optical Fibre Core via Extrusion Method: The Role of Temperature Gradient and Collector Speed


- on its Characteristics. *Opt Fiber Techn* (2020) 55:102162. doi:10.1016/j.yofte.2020.102162
12. Woyessa G, Rasmussen HK, Bang O. Zeonex - a Route towards Low Loss Humidity Insensitive Single-Mode Step-index Polymer Optical Fibre. *Opt Fiber Techn* (2020) 57:102231. doi:10.1016/j.yofte.2020.102231
 13. Dash JN, Cheng X, Gunawardena DS, Tam H-Y. Rectangular Single-Mode Polymer Optical Fiber for Femtosecond Laser Inscription of FBGs. *Photon Res* (2021) 9(10):1931–8. doi:10.1364/prj.434252
 14. Marques CAF, Min R, Junior AL, Antunes P, Fasano A, Woyessa G, et al. Fast and Stable Gratings Inscription in POFs Made of Different Materials with Pulsed 248 Nm KrF Laser. *Opt Express* (2018) 26(2):2013–22. doi:10.1364/oe.26.002013
 15. Markos C, Stefani A, Nielsen K, Rasmussen HK, Yuan W, Bang O. High-T_g TOPAS Microstructured Polymer Optical Fiber for Fiber Bragg Grating Strain Sensing at 110 Degrees. *Opt Express* (2013) 21(4):4758–65. doi:10.1364/oe.21.004758
 16. Leal-Junior A, Guo J, Min R, Fernandes AJ, Frizzera A, Marques C. Photonic Smart Bandage for Wound Healing Assessment. *Photon Res* (2021) 9(3):272–80. doi:10.1364/prj.410168
 17. Shentu Z, Kang J, Zhu Z, Wang L, Guo Y, Xu T, et al. No-core PDMS Fiber for Large-Scale Strain and Concentration Measurement. *Opt Fiber Techn* (2021) 63:102531. doi:10.1016/j.yofte.2021.102531
 18. Elsherif M, Hassan MU, Yetisen AK, Butt H. Hydrogel Optical Fibers for Continuous Glucose Monitoring. *Biosens Bioelectron* (2019) 137(15):25–32. doi:10.1016/j.bios.2019.05.002
 19. Guo J, Liu X, Jiang N, Yetisen AK, Yuk H, Yang C, et al. Highly Stretchable, Strain Sensing Hydrogel Optical Fibers. *Adv Mater* (2016) 28(46):10244–9. doi:10.1002/adma.201603160
 20. Mitsubishi POF SH4001. Ibsstore (2022). Available at: <https://www.ibselectronics.com/ibsstore/sh4001-mitsubishi-rayon-eska-plastic-optical-fiber-cable.html> (Access on 04 02, 2022).
 21. Woyessa G, Theodosiou A, Markos C, Kalli K, Bang O. Single Peak Fiber Bragg Grating Sensors in Tapered Multimode Polymer Optical Fibers. *J Lightwave Technol* (2021) 39(21):6934–41. doi:10.1109/JLT.2021.3103284
 22. He R, Teng C, Kumar S, Marques C, Min R. Polymer Optical Fiber Liquid Level Sensor: A Review. *IEEE Sensors J* (2022) 22(2):1081–91. doi:10.1109/jsen.2021.3132098
 23. van Eijkelenborg M, Large M, Argyros A, Zagari J, Manos S, Issa N, et al. Microstructured Polymer Optical Fibre. *Opt Express* (2001) 9(7):319–27. doi:10.1364/oe.9.000319
 24. Shute Company. Shute (2022). Available at: <https://shute.dk/> (Access on 04 02, 2022).
 25. Savović S, Djordjevich A. Mode Coupling in Strained and Unstrained Step-index Plastic Optical Fibers. *Appl Opt* (2006) 45:6775–80. doi:10.1364/AO.45.006775
 26. Mateo J, Losada MA, Zubia J. Frequency Response in Step index Plastic Optical Fibers Obtained from the Generalized Power Flow Equation. *Opt Express* (2009) 17:2850–60. doi:10.1364/oe.17.002850
 27. Gambling WA, Payne DN, Matsumura H. Mode Conversion Coefficients in Optical Fibers. *Appl Opt* (1975) 14:1538–42. doi:10.1364/ao.14.001538
 28. Rousseau M, Jeunhomme L. Numerical Solution of the Coupled-Power Equation in Step-Index Optical Fibers. *IEEE Trans Microwave Theor Techn.* (1977) 25:577–85. doi:10.1109/TMTT.1977.1129162
 29. Djordjevich A, Savović S. Investigation of Mode Coupling in Step index Plastic Optical Fibers Using the Power Flow Equation. *IEEE Photon Technol Lett* (2000) 12:1489–91. doi:10.1109/68.887704
 30. Savović S, Djordjevich A. Method for Calculating the Coupling Coefficient in Step-index Optical Fibers. *Appl Opt* (2007) 46:1477–81. doi:10.1364/AO.46.001477
 31. Ribeiro R, Silva V, Balod Y, Barbero AP, Germano S, Santos Pd. *Profile Scanning Measurements of Far-Field from Plastic Optical Fibre (POF) Passive Devices for Bandwidth Characterization in Datacom Networks*. Rio de Janeiro: XXVI Simposio Brasileiro de Telecomunicacoes-BrT' (2008). p. 08. doi:10.14209/sbrt.2008.42632
 32. Djordjevich A, Savović S, Tse PW, Drljača B, Simović A. Mode Coupling in Strained and Unstrained Step-index Glass Optical Fibers. *Appl Opt* (2010) 49:5076–80. doi:10.1364/AO.49.005076

Conflict of Interest: The authors declare that the research was conducted in the absence of any commercial or financial relationships that could be construed as a potential conflict of interest.

Publisher's Note: All claims expressed in this article are solely those of the authors and do not necessarily represent those of their affiliated organizations, or those of the publisher, the editors and the reviewers. Any product that may be evaluated in this article, or claim that may be made by its manufacturer, is not guaranteed or endorsed by the publisher.

Copyright © 2022 Savović, Djordjevich, Drljača, Simović and Min. This is an open-access article distributed under the terms of the Creative Commons Attribution License (CC BY). The use, distribution or reproduction in other forums is permitted, provided the original author(s) and the copyright owner(s) are credited and that the original publication in this journal is cited, in accordance with accepted academic practice. No use, distribution or reproduction is permitted which does not comply with these terms.

Calculation of Bandwidth of Multimode Step-Index Polymer Photonic Crystal Fibers

Branko Drljača ¹, Svetislav Savović ^{2,3}, Milan S. Kovačević ², Ana Simović ², Ljubica Kuzmanović ²,
Aleksandar Djordjevich ³ and Rui Min ^{4,*}

¹ Faculty of Sciences and Mathematics, University of Priština in Kosovska Mitrovica, L. Ribara 29, 38220 Kosovska Mitrovica, Serbia; branko.drljaca@pr.ac.rs

² Faculty of Science, University of Kragujevac, R. Domanovića 12, 34000 Kragujevac, Serbia; savovic@kg.ac.rs (S.S.); kovac@kg.ac.rs (M.S.K.); asimovic@kg.ac.rs (A.S.); ljubica.kuzmanovic@pmf.kg.ac.rs (L.K.)

³ Department of Mechanical Engineering, City University of Hong Kong, 83 Tat Chee Avenue, Hong Kong, China; mealex@cityu.edu.hk

⁴ Center for Cognition and Neuroergonomics, State Key Laboratory of Cognitive Neuroscience and Learning, Beijing Normal University at Zhuhai, Zhuhai 519087, China

* Correspondence: rumi@alumni.upv.es

Abstract: By solving the time-dependent power flow equation, we present a novel approach for evaluating the bandwidth in a multimode step-index polymer photonic crystal fiber (SI PPCF) with a solid core. The bandwidth of such fiber is determined for various layouts of air holes and widths of Gaussian launch beam distribution. We found that the lower the NA of SI PPCF, the larger the bandwidth. The smaller launch beam leads to a higher bandwidth for short fibers. The influence of the width of the launch beam distribution on bandwidth lessens as the fiber length increases. The bandwidth tends to its launch independent value at a particular fiber length. This length denotes the onset of the steady state distribution (SSD). This information is useful for multimode SI PPCF applications in telecommunications and optical fiber sensing applications.

Keywords: photonic crystal fiber; PMMA fiber; step-index fiber; power flow equation; bandwidth



Citation: Drljača, B.; Savović, S.; Kovačević, M.S.; Simović, A.; Kuzmanović, L.; Djordjevich, A.; Min, R. Calculation of Bandwidth of Multimode Step-Index Polymer Photonic Crystal Fibers. *Polymers* **2021**, *13*, 4218. <https://doi.org/10.3390/polym13234218>

Academic Editors: Igor Ayesta and Maria Asunción Illarramendi

Received: 17 November 2021

Accepted: 29 November 2021

Published: 1 December 2021

Publisher's Note: MDPI stays neutral with regard to jurisdictional claims in published maps and institutional affiliations.



Copyright: © 2021 by the authors. Licensee MDPI, Basel, Switzerland. This article is an open access article distributed under the terms and conditions of the Creative Commons Attribution (CC BY) license (<https://creativecommons.org/licenses/by/4.0/>).

1. Introduction

Selective stacking and chemical doping of materials have historically been employed for fabrication of optical fibers with different refractive-index (RI) distributions. Another method is to use a micro-structured pattern of very small holes that runs the length of the “holey” or PCFs. A PCF can have a solid core part and a holey cladding part, as shown in Figure 1. The hole pattern lowers the effective RI of the cladding, allowing the fiber to direct light. By selecting the hole pattern in the cladding throughout the design phase, the RI profile of the fiber can be modified. A variety of different micro-structured patterns of the PCF allows a broad versatility to modify its profile at the design stage [1–7]. A single-mode PCF has been produced for operation in a wide wavelength range [2]. The hollow core of a PCF, on the other hand, is also possible [8–13]. PCFs have been used in a variety of applications, including dispersion [14–16], supercontinuum production [17–19], birefringence [20], optofluidics [21], wavelength conversion [22,23] and sensing [24,25]. A typical numerical aperture of PCFs is $NA = 0.5–0.6$ [26–30]. With high NA PCFs, lensless beam focusing with the outstanding resolution has been recorded [31].

PCF propagation characteristics are influenced by differential mode attenuation, mode coupling, and modal dispersion. Light scattering in multimode optical fibers transfers power from one mode to another due to intrinsic perturbations, which causes mode coupling. Until recently, commercial simulation software packages were not designed for multimode PCFs. This deficiency is addressed in this paper for the first time, to our knowledge, by numerically solving the time-dependent power flow equation. The mode

coupling properties of SI PPCF, and hence bandwidth, are affected by the parametric variance of the width of the launch beam distribution and the size of air holes. For three distinct widths of the launch beam distribution and sizes of air holes in the cladding, we estimated bandwidth in multimode SI PPCF (Poly(methyl methacrylate) or PMMA optical fibers) with solid core. The holes in the cladding are arranged in a triangular pattern with a uniform pitch (see Figure 1).

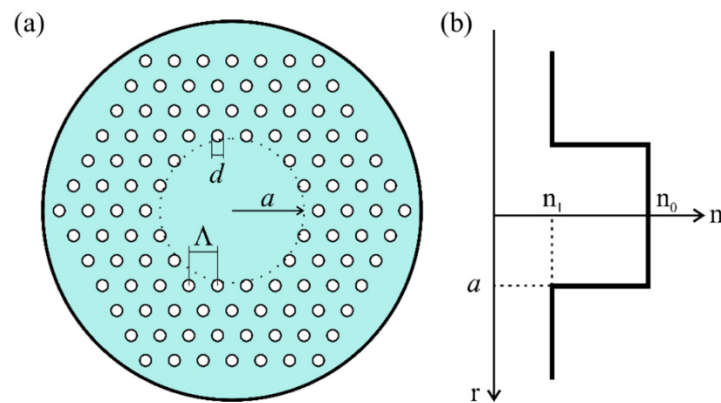


Figure 1. (a) Cross section of a multimode SI PPCF (Λ is the pitch, d is the diameter of air holes in the cladding); (b) RI profile of the proposed SI PPCF.

2. Design of SI PPCF

The SI PPCF is designed with air holes of uniform diameter in the cladding, which become a regular triangular lattice. The desirable effective RI is achieved by choosing the size (d) and pitch (Λ) of the cladding layer (Figure 1). The solid core region has the highest RI n_0 .

3. Time-dependent Power Flow Equation

The following time-dependent power flow equation [32] describes the time-dependent power flow for multimode optical fibers:

$$\frac{\partial p(\theta, z, t)}{\partial z} + \tau(\theta) \frac{\partial p(\theta, z, t)}{\partial t} = -\alpha(\theta)P(\theta, z, t) + \frac{1}{\theta} \frac{\partial}{\partial \theta} \left[D(\theta) \frac{\partial p(\theta, z, t)}{\partial \theta} \right] \quad (1)$$

where t is time; $p(\theta, z, t)$ is the distribution of power over angle, space, and time; $\tau(\theta)$ is mode delay per unit length; $D(\theta)$ is the mode-dependent coupling coefficient (usually assumed constant [32,33]); and $\alpha(\theta) = \alpha_0 + \alpha_d(\theta)$ is the modal attenuation, where α_0 represents conventional losses due to absorption and scattering. Except near cutoff, the attenuation is uniform $\alpha(\theta) = \alpha_0$ ($0 \leq \theta \leq \theta_m$) [33] (it appears in the solution as the multiplication factor $\exp(-\alpha_0 z)$ which also does not depend on θ). Therefore, $\alpha(\theta)$ need not be accounted for when solving (1). In this paper for the first time, to our knowledge, by numerically solving the time-dependent power flow equation (1) we obtain bandwidth of the multimode SI PPCF.

4. Numerical Results and Discussion

For multimode solid-core SI PPCF, the bandwidth was examined for varying widths of launch beam distribution. For PCFs with air holes in a triangular lattice, the effective parameter V is given as:

$$V = \frac{2\pi}{\lambda} a_{eff} \sqrt{n_0^2 - n_{fsm}^2} \quad (2)$$

where n_0 is the RI of the core. The effective RI of the cladding part n_{fsm} is the effective RI of fundamental space-filling mode in the triangular hole lattice, and $a_{eff} = \Lambda/\sqrt{3}$ [34].

The effective RI of the cladding $n_1 = n_{fsm}$ can be obtained from equation (2), using the following equation [35]:

$$V\left(\frac{\lambda}{\Lambda}, \frac{d}{\Lambda}\right) = A_1 + \frac{A_2}{1 + A_3 \exp(A_4 \lambda / \Lambda)} \tag{3}$$

with the fitting parameters A_i ($i = 1$ to 4):

$$A_i = a_{i0} + a_{i1} \left(\frac{d}{\Lambda}\right)^{b_{i1}} + a_{i2} \left(\frac{d}{\Lambda}\right)^{b_{i2}} + a_{i3} \left(\frac{d}{\Lambda}\right)^{b_{i3}} \tag{4}$$

where the coefficients a_{i0} to a_{i3} and b_{i1} to b_{i3} ($i = 1$ to 4) are shown in Table 1.

Table 1. Fitting coefficients in Equation (4).

	$i = 1$	$i = 2$	$i = 3$	$i = 4$
a_{i1}	0.54808	0.71041	0.16904	−1.52736
a_{i2}	5.00401	9.73491	1.85765	1.06745
a_{i3}	−10.43248	47.41496	18.96849	1.93229
a_{i4}	8.22992	−437.50962	−42.4318	3.89
b_{i1}	5	1.8	1.7	−0.84
b_{i2}	7	7.32	10	1.02
b_{i3}	9	22.8	14	13.4

Figure 2 depicts the cladding’s effective RI $n_1 \equiv n_{fsm}$ as a function of λ/Λ , for $\Lambda = 3 \mu\text{m}$ and for three values of d . Relevant values of the structural parameters of the analyzed multimode SI PPCF are summarized in Table 2, for $\lambda = 645 \text{ nm}$.

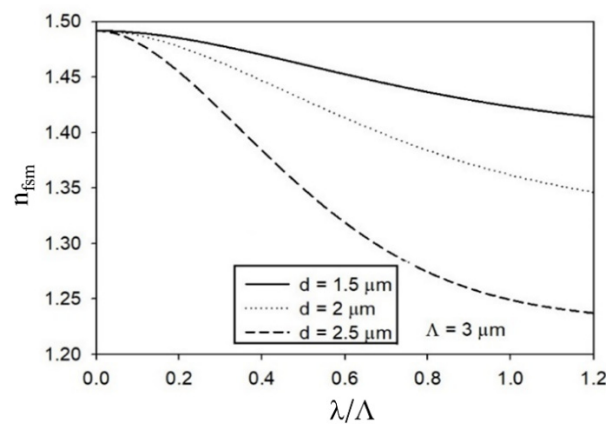


Figure 2. Effective RI of the inner cladding n_{fsm} as a function of λ/Λ .

Table 2. Effective RI of the cladding n_1 , relative RI difference $\Delta = (n_0 - n_1)/n_0$, where $n_1 = 1.492$, and the critical angle θ_m for varied d (air hole diameter) at 645 nm wavelength.

d (μm)	1.0	1.5	2.0
n_1	1.4844	1.4757	1.4458
$\Delta = (n_0 - n_1)/n_0$	0.673673	0.677645	0.691611
θ_m (deg)	5.79	8.48	14.28

For the multimode SI PPCF with RI of the core $n_0 = 1.492$, core diameter $2a = 0.980 \text{ mm}$, and optical fiber diameter $b = 1 \text{ mm}$, we solved the time-dependent power flow Equation (1) using a finite-difference method, assuming $D = 1.649 \times 10^{-4} \text{ rad}^2/\text{m}$ and $\alpha_0 = 0.22 \text{ dB/m}$ [35,36]. We looked at impact of the diameters of air holes in the

cladding of $d = 1, 1.5,$ and $2 \mu\text{m}$ (i.e., the influence of NA of the fiber) and width of the launch beam distribution with $(\text{FWHM})_{z=0} = 1^\circ, 5^\circ,$ and 10° on the bandwidth. A detailed explanation of the numerical solution of the time-dependent power flow equation (1) is given in our previous work [37]. As illustration, Figure 3 shows the evolution of the bandwidth with fiber length calculated for three Gaussian launch beam distributions with $(\text{FWHM})_{z=0} = 1^\circ, 5^\circ,$ and 10° for the case with $d = 1 \mu\text{m}$ ($n_1 = 1.4844$) (Figure 3a), $d = 1.5 \mu\text{m}$ ($n_1 = 1.4757$) (Figure 3b) and $d = 2 \mu\text{m}$ ($n_1 = 1.4458$) (Figure 3c). Figure 3 shows that the lower NA (larger n_1 , smaller d), the higher bandwidth is obtained. In the case of the narrowest Gaussian launch beam, the highest bandwidth is observed at short optical fiber lengths. This is due to the guiding modes' modal dispersion being reduced due to the narrower launch beam. The influence of the width of the launch beam distribution on bandwidth lessens as fiber length increases. Because mode coupling causes energy redistribution between guiding modes, the initial modal excitation (the FWHM of the launched beam) has a reduced impact on bandwidth for longer fibers. Figure 3 shows how bandwidth drops linearly for short lengths before switching to a $1/z^{1/2}$ functional dependence. This switch, and equilibrium mode distribution, occur at shorter optical fiber lengths for the wider Gaussian launch beam and lower NA. For $(\text{FWHM})_{z=0} = 1^\circ$ this length is $L_c \simeq 5 \text{ m}$ for $n_1 = 1.4844$, $L_c \simeq 12.5 \text{ m}$ for $n_1 = 1.4757$ and $L_c \simeq 41 \text{ m}$ for $n_1 = 1.4458$. For $(\text{FWHM})_{z=0} = 5^\circ$ this length is $L_c \simeq 4.5 \text{ m}$ for $n_1 = 1.4844$, $L_c \simeq 11 \text{ m}$ for $n_1 = 1.4757$ and $L_c \simeq 39 \text{ m}$ for $n_1 = 1.4458$. For $(\text{FWHM})_{z=0} = 10^\circ$ this length is $L_c \simeq 2.5 \text{ m}$ for $n_1 = 1.4844$, $L_c \simeq 9 \text{ m}$ for $n_1 = 1.4757$ and $L_c \simeq 33 \text{ m}$ for $n_1 = 1.4458$ [36]. One can see that the shorter the length L_c results in the faster bandwidth improvement. The bandwidth tends to its launch independent value at a particular fiber length. This length denotes the onset of the SSD. It is worth noting that the proposed method for calculation of bandwidth in multimode SI PPCF can also be employed for multimode step-index silica PCFs.

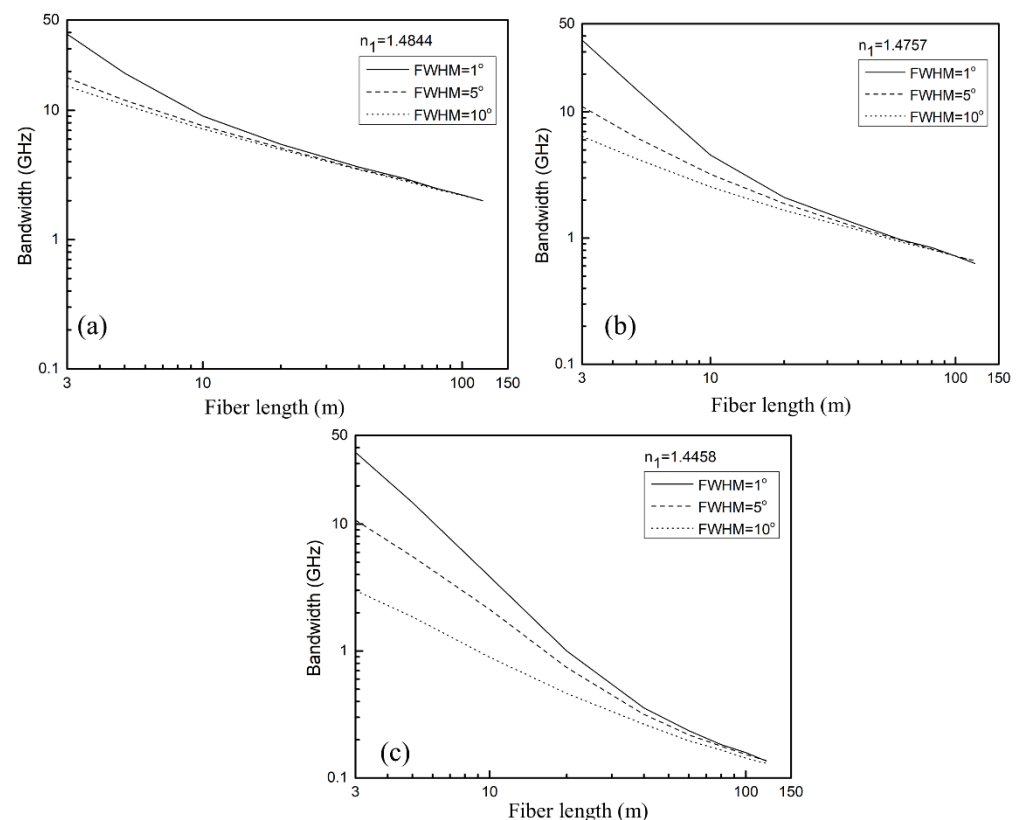


Figure 3. Bandwidth versus fiber length for multimode SI PPCF for three Gaussian launch beam widths with $(\text{FWHM})_{z=0} = 1^\circ, 5^\circ,$ and 10° for (a) $d = 1 \mu\text{m}$ ($n_1 = 1.4844$), (b) $d = 1.5 \mu\text{m}$ ($n_1 = 1.4757$) and (c) $d = 2 \mu\text{m}$ ($n_1 = 1.4458$).

5. Conclusions

By numerically solving the time-dependent power flow equation, we proposed a novel approach for evaluating the bandwidth in a multimode SI PPCF with a solid core and triangular air-hole lattice in the cladding. We showed that the lower the NA, the higher the bandwidth. The narrower Gaussian launch beam leads in increased bandwidth for short optical fibers. The influence of the width of the launch beam distribution on bandwidth lessens as fiber length increases. The bandwidth tends to its launch-independent value at a particular fiber length. This length denotes the onset of the steady state distribution. These customizable parameters allow for additional variety in the construction of multimode photonic crystal fibers. By changing the interplay between the material and geometrical dispersions, such design freedom in adjusting structural elements of the optical fiber for dispersion management.

Author Contributions: Conceptualization, B.D.; methodology, software, B.D., M.S.K., L.K. and A.S.; writing—original draft preparation, B.D. and S.S.; writing—review and editing, A.D. and R.M.; supervision, S.S.; project administration, funding acquisition, R.M. All authors have read and agreed to the published version of the manuscript.

Funding: This research was funded by the National Natural Science Foundation of China (62003046, 6211101138); the Strategic Research Grant of City University of Hong Kong (Project No. CityU 7004600) and by a grant from Serbian Ministry of Education, Science and Technological Development (Agreement No. 451-03-68/2020-14/200122) and by grant from Science Fund of Republic Serbia (Agreement No. CTPCF-6379382); Guangdong Basic and Applied Basic Research Foundation (2021A1515011997); Special project in key field of Guangdong Provincial Department of Education (2021ZDZX1050); The Innovation Team Project of Guangdong Provincial Department of Education (2021KCXTD014).

Institutional Review Board Statement: Not applicable.

Informed Consent Statement: Not applicable.

Data Availability Statement: The data presented in this study are available on request from corresponding author.

Conflicts of Interest: The authors declare no conflict of interest.



References

1. Knight, J.C.; Birks, T.A.; Russell, P.S.J.; Atkin, D.M. All-silica single-mode optical fiber with photonic crystal cladding. *Opt. Lett.* **1996**, *21*, 1547–1549. [[CrossRef](#)]
2. Birks, T.A.; Knight, J.C.; Russell, P.S.J. Endlessly single-mode photonic crystal fiber. *Opt. Lett.* **1997**, *22*, 961–963. [[CrossRef](#)] [[PubMed](#)]
3. Russell, P.S.J. Photonic crystal fibers. *Science* **2003**, *299*, 358–362. [[CrossRef](#)]
4. Knight, J.C. Photonic crystal fiber. *Nature* **2003**, *424*, 847–851. [[CrossRef](#)]
5. Russell, P.S.J. Photonic-crystal fibers. *J. Lightwave Technol.* **2006**, *24*, 4729–4749. [[CrossRef](#)]
6. Knight, J.C.; Broeng, J.; Birks, T.A.; Russell, P.S.J. Photonic band gap guidance in optical fibers. *Science* **1998**, *282*, 1476–1478. [[CrossRef](#)]
7. Knight, J.C.; Russell, P.S.J. Photonic crystal fibers: New way to guide light. *Science* **2002**, *296*, 276–277. [[CrossRef](#)] [[PubMed](#)]
8. Cregan, R.F.; Mangan, B.J.; Knight, J.C.; Birks, T.A.; Russell, P.S.J.; Roberts, P.J.; Allan, D.C. Single-mode photonic band gap guidance of light in air. *Science* **1999**, *285*, 1537–1539. [[CrossRef](#)]
9. Amezcua-Correa, R.; Gerome, F.; Leon-Saval, S.G.; Broderick, N.G.R.; Birks, T.A.; Knight, J.C. Control of surface modes in low loss hollow core photonic bandgap fibers. *Opt. Express* **2008**, *16*, 1142–1149. [[CrossRef](#)] [[PubMed](#)]
10. Cheng, L.; Wu, J.; Hu, X.; Peng, J.; Yang, L.; Dai, N.; Li, J. Ultrahigh Temperature Sensitivity Using Photonic Bandgap Effect in Liquid-Filled Photonic Crystal Fibers. *IEEE Photon. J.* **2017**, *9*, 6802907. [[CrossRef](#)]
11. Gao, F.; Song, N.; Xu, X.; Wang, X. Low-loss hollow-core photonic bandgap fiber with isolated anti-resonance layer. *Opt. Commun.* **2019**, *441*, 208–211. [[CrossRef](#)]
12. Benabid, F.; Knight, J.C.; Antonopoulos, G.; Russell, P.S.J. Stimulated Raman scattering in hydrogen-filled hollow-core photonic crystal fiber. *Science* **2002**, *298*, 399–402. [[CrossRef](#)]
13. Light, P.S.; Benabid, F.; Couny, F.; Maric, M.; Luiten, A.N. Electromagnetically induced transparency in Rb-filled coated hollow-core photonic crystal fiber. *Opt. Lett.* **2007**, *32*, 1323–1325. [[CrossRef](#)]

14. Wang, Y.; Yu, F.; Hu, L. Inverse design of equivalent-graded-index Photonic-Crystal Fiber based on empirical dispersion formula. *J. Lightwave Technol.* **2021**, *39*, 5598–5603. [[CrossRef](#)]
15. Xu, H.; Kong, Q.; Zhou, C. Crossings in photonic crystal fiber with hybrid core and de-sign of broadband dispersion compensating photonic crystal fiber. *Opt. Fiber. Tech.* **2021**, *63*, 102485. [[CrossRef](#)]
16. Lee, S.; Ha, W.; Park, J.; Kim, S.; Oh, K. A new design of low-loss and ultra-flat zero dispersion photonic crystal fiber using hollow ring defect. *Opt. Commun.* **2012**, *285*, 4082–4087. [[CrossRef](#)]
17. Vengelis, J.; Kuliesaitė, M.; Jukna, V.; Jarutis, V.; Sirutkaitis, V. Investigation of super-continuum generation in photonic crystal fiber using bursts of femtosecond pulses. *Opt. Commun.* **2021**, *496*, 127132. [[CrossRef](#)]
18. Suresh, M.; Hammer, J.; Joly, N.Y.; Russel, P.; Tani, F. Deep-UV-enhanced super-continuum generated in a tapered gas-filled photonic crystal fiber. *Opt. Lett.* **2021**, *46*, 4526–4529. [[CrossRef](#)] [[PubMed](#)]
19. Saleh, M.F.; Biancalana, F. Ultra-broadband supercontinuum generation in gas-filled photonic-crystal fibers: The epsilon-near-zero regime. *Opt. Lett.* **2021**, *46*, 1959–1962. [[CrossRef](#)]
20. Zhou, X.; Wang, E.; Han, Q.; Yuan, H.; Li, J. A large birefringence and high nonlinearity liquid crystal photonic crystal fiber with low confinement loss. *Opt. Fiber. Tech.* **2021**, *65*, 102610. [[CrossRef](#)]
21. Zhang, N.; Li, K.; Cui, Y.; Wu, Z.; Shum, P.; Auguste, J.L.; Dinh, X.Q.; Humbert, G.; Wei, L. Ultra-sensitive chemical and biological analysis via specialty fibers with built-in micro-structured optofluidic channels. *Lab. Chip.* **2018**, *18*, 655–661. [[CrossRef](#)] [[PubMed](#)]
22. Liaugminas, G.; Zeludevicius, J.; Regelskis, K. Fiber source of femtosecond pulses at 910–940 nm based on a Mamyshev pulse oscillator and wavelength conversion in a photonic crystal fiber. *J. Opt. Soc. Am. B* **2021**, *38*, 2920–2925. [[CrossRef](#)]
23. Cui, Y.; Huang, W.; Li, Z.; Zhou, Z.; Wang, Z. High-efficiency laser wavelength conversion in deuterium-filled hollow-core photonic crystal fiber by rotational stimulated Raman scattering. *Opt. Express* **2019**, *27*, 30396–30404. [[CrossRef](#)]
24. Kassani, S.H.; Khazaeinezhad, R.; Jung, Y.; Kobelke, J.; Oh, K. Suspended ring-core photonic crystal fiber gas sensor with high sensitivity and fast response. *IEEE Photon. J.* **2015**, *7*, 2700409. [[CrossRef](#)]
25. Chaudhary, V.S.; Kumar, D.; Kumar, S. Gold-immobilized photonic crystal fiber-based SPR biosensor for detection of malaria disease in human body. *IEEE Sens. J.* **2021**, *21*, 17800–17807. [[CrossRef](#)]
26. Wadsworth, W.; Percival, R.; Bouwmans, G.; Knight, J.; Birks, T.; Hedley, T.; Russell, P.S.J. Very high numerical aperture fibers. *IEEE Photon. Technol. Lett.* **2004**, *16*, 843–845. [[CrossRef](#)]
27. Hansen, K.P. High-power photonic crystal fibers. *Proc. SPIE* **2006**, *6102*, 61020B-11.
28. Hansen, K.P.; Olausson, C.B.; Broeng, J.; Noordegraaf, D.; Maack, M.D.; Alkeskjold, T.T.; Laurila, M.; Nikolajsen, T.; Skovgaard, P.M.W.; Sorensen, M.H.; et al. Airclad fiber laser technology. *Opt. Eng.* **2011**, *50*, 111609.
29. Stepien, R.; Siwicki, B.; Pysz, D.; Stepniewski, G. Characterization of a large core photonic crystal fiber made of lead–bismuth–gallium oxide glass for broadband infrared transmission. *Opt. Quant. Electron.* **2014**, *46*, 553–561. [[CrossRef](#)]
30. Tefelska, M.M.; Ertman, S.; Wolinski, T.R.; Mergo, P.; Dabrowski, R. Large area multimode photonic band-gap propagation in photonic liquid-crystal fiber. *IEEE Photon. Technol. Lett.* **2012**, *24*, 631–633. [[CrossRef](#)]
31. Amitonova, L.V.; Descloux, A.; Petschulat, J.; Frosz, M.H.; Ahmed, G.; Babic, F.; Jiang, X.; Mosk, A.P.; Russell, P.S.J.; Pinkse, P.W.H. High-resolution wavefront shaping with a photonic crystal fiber for multimode fiber imaging. *Opt. Lett.* **2016**, *41*, 497–500. [[CrossRef](#)] [[PubMed](#)]
32. Gloge, D. Optical power flow in multimode fibers. *Bell Syst. Tech. J.* **1972**, *51*, 1767–1783. [[CrossRef](#)]
33. Rousseau, M.; Jeunhomme, L. Numerical solution of the coupled-power equation in step index optical fibers. *IEEE Trans. Microw. Theory Tech.* **1977**, *25*, 577–585. [[CrossRef](#)]
34. Saitoh, K.; Koshiba, M. Empirical relations for simple design of photonic crystal fibers. *Opt. Express* **2005**, *13*, 267–274. [[CrossRef](#)] [[PubMed](#)]
35. Mateo, J.; Losada, M.A.; Garcés, I.; Zubia, J. Global characterization of optical power propagation in step-index plastic optical fibers. *Opt. Express* **2006**, *14*, 928–935. [[CrossRef](#)]
36. Savović, S.; Kovačević, M.S.; Drljača, B.; Simović, A.; Kuzmanović, L.; Djordjevich, A. Power flow in multimode step-index plastic photonic crystal fibers. *Optik* **2021**, *247*, 167868. [[CrossRef](#)]
37. Savović, S.; Drljača, B.; Djordjevich, A. Influence of launch beam distribution on bandwidth in step index plastic optical fibers. *Appl. Opt.* **2013**, *52*, 1117–1121. [[CrossRef](#)]

Communication

Theoretical Investigation of the Influence of Wavelength on the Bandwidth in Multimode W-Type Plastic Optical Fibers with Graded-Index Core Distribution

Ana Simović¹, Svetislav Savović^{1,2}, Branko Drljača³ , Alexandar Djordjevich² and Rui Min^{4,*} 

¹ Faculty of Science, University of Kragujevac, R. Domanovića 12, 34000 Kragujevac, Serbia; asimovic@kg.ac.rs (A.S.); savovic@kg.ac.rs (S.S.)

² Department of Mechanical Engineering, City University of Hong Kong, 83 Tat Chee Avenue, Hong Kong 7903, China; mealex@cityu.edu.hk

³ Faculty of Sciences, University of Priština in Kosovska Mitrovica, Lole Ribara 29, 38220 Kosovska Mitrovica, Serbia; branko.drljaca@pr.ac.rs

⁴ Center for Cognition and Neuroergonomics, State Key Laboratory of Cognitive Neuroscience and Learning, Beijing Normal University at Zhuhai, Zhuhai 519087, China

* Correspondence: rumi@alumni.upv.es

Abstract: The bandwidth of multimode W-type plastic optical fibers (POFs) with graded-index (GI) core distribution is investigated by solving the time-dependent power flow equation. The multimode W-type GI POF is designed from a multimode single-clad (SC) GI POF fiber upon modification of the cladding layer of the latter. Results show how the bandwidth in W-type GI POFs can be enhanced by increasing the wavelength for different widths of the intermediate layer and refractive indices of the outer cladding. These fibers are characterized according to their apparent efficiency to reduce modal dispersion and increase bandwidth.

Keywords: Poly(methyl methacrylate) optical fiber; W-type plastic optical fiber; graded-index optical fiber; power flow equation; bandwidth



Citation: Simović, A.; Savović, S.; Drljača, B.; Djordjevich, A.; Min, R. Theoretical Investigation of the Influence of Wavelength on the Bandwidth in Multimode W-Type Plastic Optical Fibers with Graded-Index Core Distribution. *Polymers* **2021**, *13*, 3973. <https://doi.org/10.3390/polym13223973>

Academic Editors: Igor Ayesta and Maria Asunción Illarramendi

Received: 3 November 2021

Accepted: 15 November 2021

Published: 17 November 2021

Publisher's Note: MDPI stays neutral with regard to jurisdictional claims in published maps and institutional affiliations.



Copyright: © 2021 by the authors. Licensee MDPI, Basel, Switzerland. This article is an open access article distributed under the terms and conditions of the Creative Commons Attribution (CC BY) license (<https://creativecommons.org/licenses/by/4.0/>).

1. Introduction

In the last three decades, data traffic demand has increased exponentially for access and backbone networks. The growth was accelerated by streaming transmissions and cloud computing. This concept also becomes a strong approach for use in optical networking strategies for automotive communications systems, given the advances in both intelligent driving systems and multimedia services. These systems usually use multimode POFs (Poly(methyl methacrylate), or PMMA, optical fibers) thanks to their easy connection and strength in tight curves.

Transmission characteristics of multimode POFs strongly depend upon the differential mode-attenuation and mode coupling [1]. The latter represents power transfer between neighboring modes caused by fiber impurities and inhomogeneities introduced during the fiber manufacturing process (such as microscopic bends, irregularity of the core-cladding boundary and refractive index distribution fluctuations) [2]. Mode coupling increases fiber bandwidth in data networks by reducing modal dispersion [3]. In practice, when installing a POF-based link, the cable has to be repeatedly bent, thus increasing the strength of mode coupling and radiation losses [4]. It has been shown that organic glass-clad PMMA fibers show a similar strength of mode coupling compared to standard POFs but stronger mode coupling than do the plastic-clad silica fibers [5].

Studies have been reported using geometric optics (ray approximation) to investigate transmission in optical fibers [6,7]. By employing the time-independent power flow equation [2,8] as well as the Fokker–Planck and Langevin equations [9], far-field patterns in SI POFs have been predicted as a function of the launch conditions and fiber length.

By employing the time-dependent power flow equation, the bandwidth of GI POF has been obtained for different radial launch conditions [10].

In terms of the number of functional cover layers, multimode optical fibers are usually SC fibers. Special detection [11], modulation [12], equalization [13] and compensation for modal-dispersion [14] can improve the bandwidth and attenuation properties of SC fiber. Since the structure of fiber can influence its features significantly, different POFs (double-clad fibers) of the step-index (SI), GI and W types were proposed [15–17]. Due to their progressively decreased core refractive index with a radial distance from the fiber axis, GI POFs have a much lower modal dispersion than SI POFs [18]. Since the dispersion of the W-type fiber is smaller than that of SC fiber [19], W-type fiber has a larger bandwidth and lower bending losses compared to a corresponding fiber of SC. The glass optical fiber's bandwidth-distance product is approximately 30 MHz·km for SC and approximately 50 MHz·km for W-type fiber. The POFs have a bandwidth-distance product of approximately 15 MHz·km for the SC and approximately 200 MHz·km for the W-type fibers [15,17,20].

The intermediate layer of a W-type fiber (inner cladding) decreases the dispersion and enlarges the bandwidth, thereby lowering the number of guided modes that are held closer to the core [20,21]. Optical power is transferred between modes because of the mode coupling [2]. Methods are needed for calculating modal attenuation and coupling to loss modes of W-type fiber's intermediate layer, and for optimizing the fiber's refractive index profile in order to minimize the group delay difference between modes in the output field [20,22]. In this study, we examined how the wavelength influences the bandwidth for various W-type GI POF configurations. It should be noted that our calculations include modal attenuation, mode coupling and modal dispersion.

2. Time-Dependent Power Flow Equation

Consider a W-type GI fiber with refractive index profile, as shown in Figure 1b. The refractive index profile of W-type optical fibers with GI distribution of the core may be expressed as [8,23]:

$$n(r, \lambda) = \begin{cases} n_0(\lambda) \left[1 - \Delta_q(\lambda) \left(\frac{r}{a} \right)^g \right]^{1/2} & (0 \leq r \leq a) \\ n_q & (a < r \leq a + \delta a) \\ n_p & (a + \delta a < r \leq \frac{b}{2}) \end{cases} \quad (1)$$

where g is the core index exponent, a is the core radius, δa is the intermediate layer width, b is the fiber diameter, $n_0(\lambda)$ is the maximum index of the core (measured at the fiber axis), n_q and n_p are refractive indices of the intermediate layer and cladding respectively, and $\Delta_q = (n_0 - n_q)/n_0$ is the relative index difference between the core and intermediate layer.

The time-dependent power flow equation for multimode optical fibers with GI core distribution is:

$$\frac{\partial P(m, \lambda, z, \omega)}{\partial z} + j\omega\tau(m, \lambda)P(m, \lambda, z, \omega) = -\alpha(m, \lambda)P(m, \lambda, z, \omega) + \frac{\partial P(m, \lambda, z, \omega)}{\partial m} \frac{\partial d(m, \lambda)}{\partial m} + d(m, \lambda) \frac{1}{m} \frac{\partial P(m, \lambda, z, \omega)}{\partial m} + d(m, \lambda) \frac{\partial P^2(m, \lambda, z, \omega)}{\partial m^2} \quad (2)$$

where $P(m, \lambda, z, \omega)$ is the power in the m —the principal mode (modal group), z is the coordinate along the fiber axis from the input fiber end, $\alpha(m, \lambda) = \alpha_0 + \alpha_d(m, \lambda)$ is the attenuation of the mode m , where α_0 represents conventional losses due to absorption and scattering (the term α_0 leads only to a multiplier $\exp(-\alpha_0 z)$ in the solution and is thus neglected, the term $\alpha_d(m, \lambda)$ in the expansion of $\alpha(m)$ is dominant for higher-order modes),

$d(m, \lambda)$ is the coupling coefficient of the mode m , $\omega = 2\pi f$ is the baseband angular frequency and $\tau(m, \lambda)$ is delay time per unit length of mode m , which can be determined as:

$$\tau(m, \lambda) \cong \frac{n_0(\lambda)}{c} \left[1 + \frac{g-2}{g+2} \Delta_q(\lambda) \left(\frac{m}{M(\lambda)} \right)^{2g/(g+2)} + \frac{1}{2} \frac{3g-2}{g+2} \Delta_q(\lambda)^2 \left(\frac{m}{M(\lambda)} \right)^{4g/(g+2)} \right] \quad (3)$$

where c is the free-space velocity of light and:

$$P(m, \lambda, z, \omega) = \int_{-\infty}^{+\infty} P(m, \lambda, z, t) \exp(-j\omega t) dt \quad (4)$$

The maximum principal mode number, $M(\lambda)$, can be obtained as [24]:

$$M(\lambda) = \sqrt{\frac{g\Delta_q(\lambda)}{g+2}} a k n_0(\lambda) \quad (5)$$

where $k = 2\pi/\lambda$ is the free-space wave number. Gaussian launch-beam distribution, $P_0(\theta, \lambda, z = 0)$, can be converted to $P_0(m, \lambda, z = 0)$ (one needs $P_0(m, \lambda, z = 0)$ to solve the power flow equation numerically (2)), using the following relationship [25]:

$$\frac{m}{M(\lambda)} = \left[\left(\frac{r_0}{a} \right)^g + \frac{\theta^2}{2\Delta_q(\lambda)} \right]^{(g+2)/2g} \quad (6)$$

where r_0 is radial distance (radial offset) between the launch beam position and the core center and θ is the propagation angle with respect to the core axis.

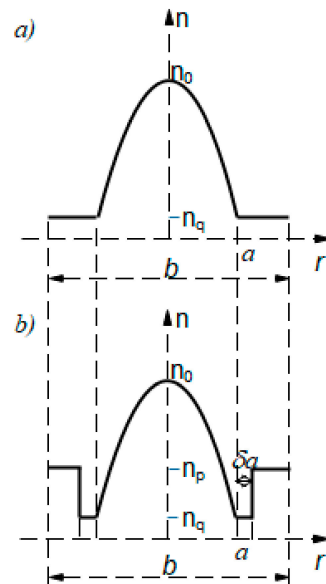


Figure 1. Refractive index profile of (a) SC GI POF and (b) W-type GI POF.

The relative refractive index difference, $\Delta_q = (n_0 - n_q)/n_0$, between the core and intermediate layer is larger than the difference $\Delta_p = (n_0 - n_p)/n_0$ between the core and cladding. Modes propagating along with subcritical angles $m < m_q$ are guided. The same is true for those propagating through the complete W-fiber, with m below the critical value m_p . On the other hand, modes with angles between m_p and $m_q \equiv M$ are transformed into leaky modes [10]. The leaky mode attenuation constants are provided as:

$$\alpha_L(m, \lambda) = \frac{4\sqrt{2\Delta_q} \left(\left(\frac{m}{m_q} \right)^{\frac{2g}{g+2}} - \left(\frac{m_p}{m_q} \right)^{\frac{2g}{g+2}} \right)^{1/2} \left(\frac{m}{m_q} \right)^{\frac{2g}{g+2} \left(1 - \left(\frac{m}{m_q} \right)^{\frac{2g}{g+2}} \right)} }{a \left(1 - 2\Delta_q \left(\frac{m}{m_q} \right)^{\frac{2g}{g+2}} \right)^{1/2} \left(1 - \frac{\Delta_p}{\Delta_q} \left(\frac{m_p}{m_q} \right)^{\frac{2g}{g+2}} \right)} \exp \left[-2\delta a n_0 k \left(2\Delta_q \left(1 - \left(\frac{m}{m_q} \right)^{\frac{2g}{g+2}} \right) \right)^{1/2} \right] \quad (7)$$

One can see from Equation (7) that for thick intermediate layer widths, δ , the lower leaky modes are substantially guided because of the low leaky modes' losses. Experiments in a SC GI fiber reveal that attenuation remains constant throughout the guided-mode region ($m \leq m_p$) and rises quite steeply in the radiation-mode region [26]. As a result, in a W-type GI POF, the modal attenuation can be expressed as:

$$\alpha_d(m, \lambda) = \begin{cases} 0 & m \leq m_p \\ \alpha_L(m, \lambda) & m_p < m < m_q \\ \infty & m \geq m_q \end{cases} \quad (8)$$

A W-type fiber can be thought of as a combination of SCq fiber with cladding. In the SCq fiber, modes $m < m_q$ can be guided. When the SCq fiber is coupled with surrounding medium of index n_p , the lower-order modes $m < m_p$ remain guided, while the higher-order modes m ($m_p < m < m_q$) are transformed into leaky modes. Due to the strong dependence of $\alpha_L(m)$ on the intermediate layer width δa (Equation (7)), it is expected that characteristics of a W-type GI fiber also depend on δa and coincide with those of SCp and SCq GI fibers in the limits of $\delta \rightarrow 0$ and $\delta \rightarrow \infty$, respectively [20,27].

It is obvious that $P(m, \lambda, z, \omega)$ is complex. By separating P into the real part P^r and imaginary part P^i , Equation (2) can be rewritten as the following simultaneous partial differential equations:

$$\frac{\partial P^r}{\partial z} = -\alpha P^r + \frac{\partial d}{\partial m} \frac{\partial P^r}{\partial m} + \frac{d}{m} \frac{\partial P^r}{\partial m} + d \frac{\partial^2 P^r}{\partial m^2} + \omega \tau P^i \quad (9)$$

$$\frac{\partial P^i}{\partial z} = -\alpha P^i + \frac{\partial d}{\partial m} \frac{\partial P^i}{\partial m} + \frac{d}{m} \frac{\partial P^i}{\partial m} + d \frac{\partial^2 P^i}{\partial m^2} - \omega \tau P^r \quad (10)$$

where $P = P^r + jP^i$. Assuming a constant coupling coefficient $d \equiv D$, Equations (9) and (10) can be written as:

$$\frac{\partial P^r}{\partial z} = -\alpha P^r + \frac{D}{m} \frac{\partial P^r}{\partial m} + D \frac{\partial^2 P^r}{\partial m^2} + \omega \tau P^i \quad (11)$$

$$\frac{\partial P^i}{\partial z} = -\alpha P^i + \frac{D}{m} \frac{\partial P^i}{\partial m} + D \frac{\partial^2 P^i}{\partial m^2} - \omega \tau P^r \quad (12)$$

Using the EFDM, discretization of Equations (11) and (12) leads to:

$$P_{k,l+1}^r = \left(\frac{\Delta z D}{\Delta m^2} - \frac{\Delta z D}{2m_k \Delta m} \right) P_{k-1,l}^r + \left(1 - \frac{2\Delta z D}{\Delta m^2} - \alpha_k \Delta z \right) P_{k,l}^r + \left(\frac{\Delta z D}{2m_k \Delta m} - \frac{\Delta z D}{\Delta m^2} \right) P_{k+1,l}^r + \frac{\omega n_0 \Delta z}{2c} m_k^2 P_{k,l}^i \quad (13)$$

$$P_{k,l+1}^i = \left(\frac{\Delta z D}{\Delta m^2} - \frac{\Delta z D}{2m_k \Delta m} \right) P_{k-1,l}^i + \left(1 - \frac{2\Delta z D}{\Delta m^2} - \alpha_k \Delta z \right) P_{k,l}^i + \left(\frac{\Delta z D}{2m_k \Delta m} - \frac{\Delta z D}{\Delta m^2} \right) P_{k+1,l}^i - \frac{\omega n_0 \Delta z}{2c} m_k^2 P_{k,l}^r \quad (14)$$

where k and l refer to the discretization step lengths Δm and Δz for the mode m and length z respectively, i.e., $P_{k,l}^r \equiv P^r(m_k, z_l, \omega)$ and $P_{k,l}^i \equiv P^i(m_k, z_l, \omega)$.

If P^r and P^i are obtained by solving Equations (13) and (14), the transmission characteristics can be calculated. Thus, the frequency response of fiber at length z is:

$$H(\lambda, z, \omega) = \frac{\int_1^M 2m[P_r(m, \lambda, z, \omega) + jP_i(m, \lambda, z, \omega)]dm}{\int_1^M 2m[P_r(m, \lambda, z, 0) + jP_i(m, \lambda, z, 0)]dm} \quad (15)$$

where the factor $2m$ denotes degeneracy of modal group m . The frequency responses for a specific fiber can be determined over a wide range of lengths, revealing the bandwidth dependence with distance. The modal power distribution, $P_F(m, \lambda, z, \omega)$, and the spatial transient of power, $P_L(\lambda, z, \omega)$, can be obtained by:

$$P_F(m, \lambda, z, \omega) = [P^r(m, \lambda, z, \omega)^2 + P^i(m, \lambda, z, \omega)^2]^{1/2} \quad (16)$$

$$P_L(\lambda, z, \omega) = 2\pi \int_0^M mP_F(m, \lambda, z, \omega)dm \quad (17)$$

One should note here that the numerical solution of the time-dependent power flow equation as well as the calculation of the frequency response and bandwidth in the analyzed W-type GI POF have been obtained by employing our FORTRAN90 code. This enabled us to determine the relationship between the transmission length and bandwidth in the W-type GI POF.

3. Numerical Results and Discussion

In this research, we investigated the bandwidth at various wavelengths in a differently constructed W-type GI POF designed from the SC GI POF (Figure 1a), which we experimentally investigated in our previously published works [8,10]. For the structure shown in Figure 1b, a W-shape refractive index model is adopted. SC GI POF (OM Giga, Fiber FinTM) had the following characteristics: The fiber's core diameter was $2a = 0.9$ mm (fiber diameter was $b = 1$ mm), the core's refractive index measured along the fiber axis was $n_0 = 1.522$ and the intermediate layer (inner cladding) cladding's refractive index was $n_q = 1.492$. The maximum principal mode number for the examined SC GI POF was $M = 656$ at wavelength $\lambda = 633$ nm, $g = 1.80101$ and $\Delta_q = (n_0 - n_q)/n_0 = 0.019711$. The W-type GI POF with GI distribution of the core is designed from this SC GI POF in such a way that the W-type GI POF's inner cladding retains the distribution of the SC GI POF's cladding, while the W-type GI POF's outer cladding has a refractive index, n_p , that is higher than the inner cladding's refractive index, n_q (Figure 1b). In the modeling, three values of the outer cladding refractive index, n_p , were used: $n_p = 1.51366$ ($m_p = 346$), $n_p = 1.51065$ ($m_p = 404$) and $n_p = 1.50718$ ($m_p = 461$). The normalized intermediate layer widths of $\delta = 0.001$, $\delta = 0.002$ and $\delta = 0.003$ (actual width is $\delta \cdot a$ mm) were used. In the calculations, the constant coupling coefficient $d(m, \lambda) \equiv D = 1482$ 1/m was employed [8]. At $\lambda = 476, 522, 568$ and 633 nm, the maximum principal mode number in such proposed W-type GI POFs is $M = 872, 795, 731$ and 656 , respectively. In the numerical calculations, a Gaussian beam, $P(\theta, z)$, is assumed to be launched with $\langle \theta \rangle = 0^\circ$ and standard deviation $\sigma_\theta = 1.3^\circ$ (FWHM = 3.06°). The width of the launched beam measured at the end of a single-mode optical fiber, which is butt-coupled to the SC GI POF examined in our earlier experimental work [8], is described by this standard deviation. The numerical calculations have been performed for radial offset $\Delta r = 0$ μ m.

Figure 2 shows our numerical solution to the time-dependent power flow equation. It depicts the evolution of the W-type GI POF's bandwidth at 30 m with wavelength for varied widths of intermediate layer, δ , in three inserts corresponding to three outer cladding refractive indices: $n_p = 1.51366$ ($m_p = 346$), $n_p = 1.51065$ ($m_p = 404$) and $n_p = 1.50718$ ($m_p = 461$). Figure 2 shows that the influence of wavelength on bandwidth is less noticeable for the smallest width of the intermediate layer ($\delta = 0.001$). This is due to large leaky mode losses (Figure 3), and as these modes are practically not guided along the fiber, modal

dispersion (bandwidth) changes very little. There is a wavelength-dependent drop in bandwidth as the width of the intermediate layer increases. At short wavelengths, this decrease is more pronounced because leaky mode losses are reduced (Figure 3), resulting in a rise in modal dispersion and a fall in fiber bandwidth.

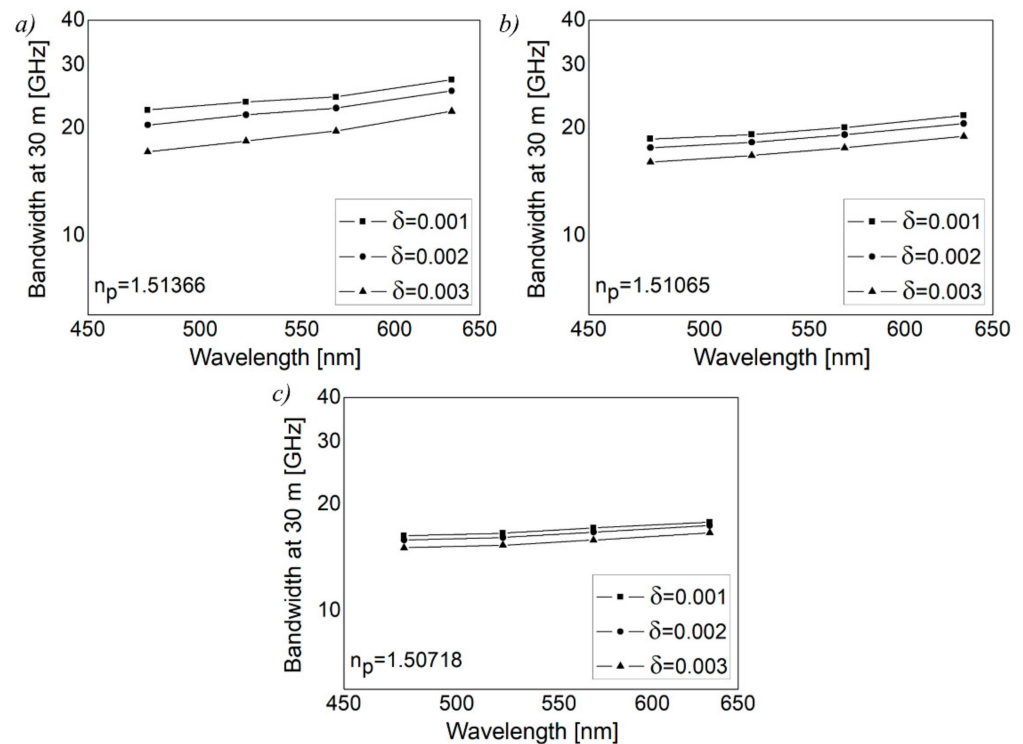


Figure 2. Numerical results for bandwidth for W-type GI POF at 30 m as a function of wavelength for (a) $n_p = 1.51366$, (b) $n_p = 1.51065$ and (c) $n_p = 1.50718$, where $(FWHM)_{z=0} = 3.06^\circ$, $\delta = 0.001$, 0.002 and 0.003 and $D = 1482$ 1/m.

When the refractive index of the outer cladding, n_p , is increased, leaky mode losses increase, resulting in the maximum bandwidth values in the case of $\delta = 0.001$. The improvement in the bandwidth of W-type GI POFs is more noticeable at longer fiber lengths, as seen in Figure 2. Since a narrow launch beam distribution is assumed in the calculations, only guided modes are excited at the input fiber length. As a result, for short fiber lengths, leaky modes play a less important role. More leaky modes are filtered out with longer fiber lengths due to mode coupling, resulting in the significant improvement of the bandwidth of the W-type GI POF [28].

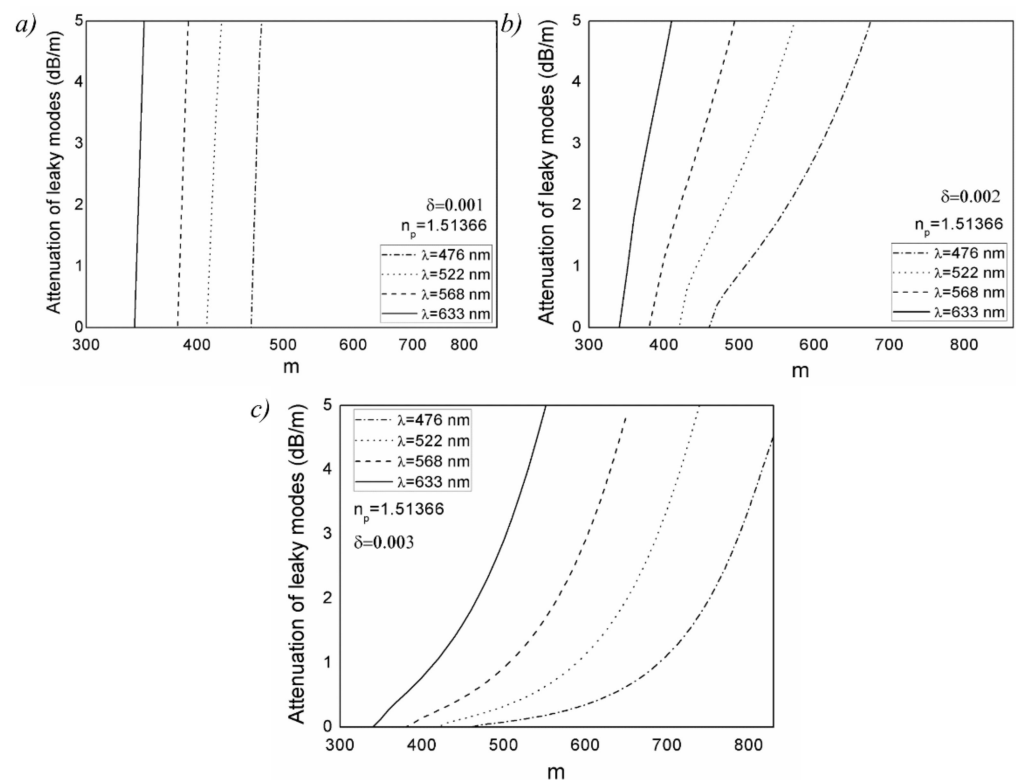


Figure 3. Leaky mode losses for W-type GI POF as a function of wavelength, for (a) $\delta = 0.001$, (b) $\delta = 0.002$ and (c) $\delta = 0.003$, and $n_p = 1.51366$.

4. Conclusions

For W-type GI POFs with a variable width of the intermediate layer and refractive index of the outer cladding, bandwidth was determined using the time-dependent power flow equation over a variety of light wavelengths. The bandwidth of W-fibers broadened with larger wavelengths for all intermediate layer widths, as shown in this study. Higher leaky mode losses and the resulting decline in modal dispersion caused this broadening of the bandwidth. Since leaky mode losses grow as the outer cladding's refractive index rises, the bandwidth rises as well. These findings can be used to design and implement a W-type GI POF at various operating wavelengths.

Author Contributions: Conceptualization, A.S.; methodology, software, A.S. and B.D.; writing—original draft preparation, A.S. and S.S.; writing—review and editing, A.D. and R.M.; supervision, S.S.; project administration, funding acquisition, R.M. All authors have read and agreed to the published version of the manuscript.

Funding: This research was funded by the National Natural Science Foundation of China (62003046, 6211101138), the Strategic Research Grant of City University of Hong Kong (Project No. CityU 7004600), a grant from the Serbian Ministry of Education, Science and Technological Development (Agreement No. 451-03-68/2020-14/200122), a grant from the Science Fund of the Republic of Serbia (Agreement No. CTPCF-6379382), the Guangdong Basic and Applied Basic Research Foundation (2021A1515011997), a special project in key field of Guangdong Provincial Department of Education (2021ZDZX1050) and The Innovation Team Project of Guangdong Provincial Department of Education (2021KCXTD014).

Institutional Review Board Statement: Not applicable.

Informed Consent Statement: Not applicable.

Data Availability Statement: The data presented in this study are available on request from the corresponding author.

Conflicts of Interest: The authors declare no conflict of interest.

References

1. Ziemann, O.; Krauser, J.; Zamzow, P.E.; Daum, W. Optical Short Range Transmission Systems. In *POF Handbook*; Springer: Berlin/Heidelberg, Germany, 2008; ISBN 978-3-540-76629-2.
2. Gloge, D. Optical power flow in multimode fibers. *Bell Syst. Tech. J.* **1972**, *51*, 1767–1783. [[CrossRef](#)]
3. Gloge, D. Impulse response of clad optical multimode fibers. *Bell Syst. Tech. J.* **1973**, *52*, 801–816. [[CrossRef](#)]
4. Savović, S.; Djordjevich, A. Mode coupling in strained and unstrained step-index plastic optical fibers. *Appl. Opt.* **2006**, *45*, 6775–6780. [[CrossRef](#)]
5. Savović, S.; Djordjevich, A. Mode Coupling in Plastic-Clad Silica Fibers and Organic Glass-Clad PMMA Fibers. *J. Lightwave Technol.* **2014**, *32*, 1290–1294. [[CrossRef](#)]
6. Eve, M.; Hannay, J.H. Ray theory and random mode coupling in an optical fibre waveguide, I. *Opt. Quantum Electron.* **1976**, *8*, 503–508. [[CrossRef](#)]
7. Borecki, M. Light behaviour in polymer optical fibre bend—a new analysis method. *Opt. Appl.* **2003**, *33*, 191–204.
8. Savović, S.; Simović, A.; Drljača, B.; Djordjevich, A.; Stepniak, G.; Bunge, C.A.; Bajić, J. Power flow in graded index plastic optical fibers. *J. Lightwave Technol.* **2019**, *37*, 4985–4990. [[CrossRef](#)]
9. Savović, S.; Djordjevich, A. Solution of mode coupling in step-index optical fibers by the Fokker-Planck equation and the Langevin equation. *Appl. Opt.* **2002**, *41*, 2826–2830. [[CrossRef](#)]
10. Simović, A.; Djordjevich, A.; Drljača, B.; Savović, S.; Min, R. Investigation of bandwidth in multimode graded index plastic optical fibers. *Opt. Express* **2021**, *29*, 29587–29594. [[CrossRef](#)] [[PubMed](#)]
11. Patel, K.M.; Ralph, S.E. Enhanced multimode fiber link performance using a spatially resolved receiver. *IEEE Photon. Technol. Lett.* **2002**, *14*, 393–395. [[CrossRef](#)]
12. Tyler, E.J.; Webster, M.; Penty, R.V.; White, I.H.; Yu, S.; Rorison, J. Subcarrier modulated transmission of 2.5 Gb/s over 300 m of 62.5- μm -core diameter multimode fiber. *IEEE Photon. Technol. Lett.* **2002**, *14*, 1743–1745. [[CrossRef](#)]
13. Zhao, X.; Choa, F.S. Demonstration of 10 Gb/s transmission over 1.5-km-long multimode fiber using equalization techniques. *IEEE Photon. Technol. Lett.* **2002**, *14*, 1187–1189. [[CrossRef](#)]
14. Abbott, J.S.; Smith, G.E.; Truesdale, C.M. Multimode Fiber Link Dispersion Compensator. U.S. Patent 6,363,195, 26 March 2002.
15. Yamashita, T.; Kagami, M. Fabrication of light-induced self-written waveguides with a W-shaped refractive index profile. *J. Lightwave Technol.* **2005**, *23*, 2542–2548. [[CrossRef](#)]
16. Asai, M.; Inuzuka, Y.; Koike, K.; Takahashi, S.; Koike, Y. High-bandwidth graded-index plastic optical fiber with low-attenuation, high-bending ability, and high-thermal stability for home-networks. *J. Lightwave Technol.* **2011**, *29*, 1620–1626. [[CrossRef](#)]
17. Mikoshiba, K.; Kajioaka, H. Transmission characteristics of multimode W-type optical fiber: Experimental study of the effect of the intermediate layer. *Appl. Opt.* **1978**, *17*, 2836–2841. [[CrossRef](#)] [[PubMed](#)]
18. Koike, Y.; Koike, K. Progress in low-loss and high-bandwidth plastic optical fibers. *J. Polym. Sci. B* **2011**, *49*, 2–17. [[CrossRef](#)]
19. Takahashi, K.; Ishigure, T.; Koike, Y. Index profile design for high-bandwidth W-shaped plastic optical fiber. *J. Lightwave Technol.* **2006**, *24*, 2867–2876. [[CrossRef](#)]
20. Tanaka, T.; Yamada, S.; Sumi, M.; Mikoshiba, K. Microbending losses of doubly clad (W-type) optical fibers. *Appl. Opt.* **1977**, *18*, 2391–2394. [[CrossRef](#)]
21. Simović, A.; Savović, S.; Drljača, B.; Djordjevich, A. Influence of the fiber design and launch beam on transmission characteristics of W-type optical fibers. *Opt. Laser Technol.* **2015**, *68*, 151–159. [[CrossRef](#)]
22. Savović, S.; Simović, A.; Djordjevich, A. Explicit finite difference solution of the power flow equation in W-type optical fibers. *Opt. Laser Technol.* **2012**, *44*, 1786–1790. [[CrossRef](#)]
23. Kitayama, K.; Seikai, S.; Uchida, N. Impulse response prediction based on experimental mode coupling coefficient in a 10-km long graded-index fiber. *IEEE J. Quant. Electron.* **1980**, *16*, 356–362. [[CrossRef](#)]
24. Olshansky, R. Mode coupling effects in graded-index optical fibers. *Appl. Opt.* **1975**, *14*, 935–945. [[CrossRef](#)] [[PubMed](#)]
25. Nagano, K.; Kawakami, S. Measurements of mode conversion coefficients in graded-index fibers. *Appl. Opt.* **1980**, *19*, 2426–2434. [[CrossRef](#)]
26. Yabre, G. Comprehensive theory of dispersion in graded-index optical fibers. *J. Lightwave Technol.* **2000**, *18*, 166–177. [[CrossRef](#)]
27. Ishigure, T.; Endo, H.; Ohdoko, K.; Takahashi, K.; Koike, Y. Modal bandwidth enhancement in a plastic optical fiber by W-refractive index profile. *J. Lightwave Technol.* **2005**, *23*, 1754–1762. [[CrossRef](#)]
28. Simović, A.; Djordjevich, A.; Drljača, B.; Savović, S. Power flow in W-type plastic optical fibers with graded index core distribution. *Opt. Laser Technol.* **2021**, *143*, 107295. [[CrossRef](#)]

Investigation of bandwidth in multimode graded-index plastic optical fibers

ANA SIMOVIĆ,¹ BRANKO DRLJAČA,² SVETISLAV SAVOVIĆ,^{1,3} ALEXANDAR DJORDJEVICH,³ AND RUI MIN^{4,*}

¹University of Kragujevac, Faculty of Science, R. Domanovića 12, Kragujevac, Serbia

²University of Priština in Kosovska Mitrovica, Faculty of Sciences and Mathematics, Kosovska Mitrovica, Serbia

³City University of Hong Kong, 83 Tat Chee Avenue, Kowloon, Hong Kong, China

⁴Center for Cognition and Neuroergonomics, State Key Laboratory of Cognitive Neuroscience and Learning, Beijing Normal University at Zhuhai, Zhuhai 519087, China

*rumi@doctor.upv.es

Abstract: A new method is proposed for investigating the bandwidth in multimode graded-index plastic optical fibers (GI POFs). By numerically solving the time-dependent power flow equation, bandwidth is reported for a varied launch conditions (radial offsets) of multimode GI POF. Our theoretical results are supported by the experimental results which show that bandwidth decreases with increasing radial offset. This decrease is more pronounced at short fiber lengths. At fiber length close to the coupling length L_c at which an equilibrium mode distribution (EMD) is achieved, this decrease becomes slower, indicating that mode coupling improves bandwidth at larger fiber lengths. With further increase of fiber length, bandwidth becomes nearly independent of the radial offset, indicating that a steady-state distribution (SSD) is achieved. Such a fiber characterization can be applied to optimize fiber performance in POF links.

© 2021 Optical Society of America under the terms of the [OSA Open Access Publishing Agreement](#)

1. Introduction

Multimode POFs are often used in local area networks, sensors, power delivery systems, and automobile communication systems. Multimode POFs have large numerical aperture which simplifies employment of various light sources (laser, LED and VCSEL). POFs offer a low-cost installation with low-precision plastic components without precision couplers. Their flexibility is especially useful when installing them in tight spaces such as in homes, offices or vehicles. GI POFs exhibit far less modal dispersion than step-index (SI) POFs. This is due to their gradual decreasing of the refractive index of core with radial distance from the fiber axis. A bandwidth-length product of SI POF of ~ 50 MHz·100 m has been reported [1], while a bandwidth of around 5.2 GHz at a distance of 30 m, which leads to a bandwidth-length product of 0.156 GHz·km for GI POF has been reported [2].

Propagation characteristics of GI POFs are influenced by differential mode attenuation, mode coupling and modal dispersion [3–10]. Modal attenuation originates from conventional loss mechanisms, such as absorption, Rayleigh scattering and loss on reflection at the core-cladding interface. Mode coupling is mainly caused by scattering of light that transfers power from one mode to another due to intrinsic perturbations in multimode optical fibers. These effects can be attributed to various irregularities such as microscopic bends, voids and cracks, diameter variation, and density and refractive index fluctuations. Mode coupling effects results in the length-dependence variations of pulse dispersion and bandwidth [5]. It has been shown that the shorter the fiber length at which equilibrium mode distribution is achieved, the faster bandwidth improvement (slower bandwidth decrease) occurs [9]. Since GI POFs are primarily used within short distances (few tens of meters up to 100 m), it is important to characterize transmission in GI POFs as a function of fiber length for various launch conditions (radial offset and tilt angle).

Until recently, commercial simulation software packages were either designed specifically for single mode optical fibers or individual guided modes in few mode optical fibers. This is not adequate for multimode optical fibers with thousands or even millions of propagation modes and strong mode coupling. There is a clear need for a new and effective simulation tool for modeling of transmission in multimode optical fibers. The most effective way to describe mode coupling, modal attenuation and modal delay is provided by the time-dependent power flow equation to describe light transmission in multimode fibers. Since for this equation an analytical solution has been reported only for the steady state in GI optical fiber [11], in a more general cases this equation has to be solved by applying an appropriate numerical method. Along the way, one has to overcome many challenges to ensure the accuracy of the numerical model as well as a stability of the proposed numerical schemes. The model proposed in this work provides the space-time evolution of the modal power distribution when it is transmitted along the GI optical fiber. Following this path, in this article, in our best knowledge for the first time, by numerical solving the time-dependent power flow equation using explicit finite difference method (EFDM), the bandwidth in GI POF for various launch conditions (radial offsets) is obtained. Such obtained theoretical results for bandwidth are compared to our experimental findings.

2. Time-dependent power flow equation for GI optical fibers

The index profile of GI optical fibers may be expressed as:

$$n(r, \lambda) = \begin{cases} n_1(\lambda) \left[1 - 2\Delta(\lambda)\left(\frac{r}{a}\right)^g\right]^{1/2} & (0 \leq r \leq a) \\ n_1(\lambda)(1 - 2\Delta(\lambda))^{1/2} = n_2(\lambda) & (r > a) \end{cases} \quad (1)$$

where g is the core index exponent, a is the core radius, $n_1(\lambda)$ is the maximum index of the core (measured at the fiber axis), $n_2(\lambda)$ is the index of the cladding and $\Delta = [n_1(\lambda) - n_2(\lambda)]/n_1(\lambda)$ is the relative index difference (Fig. 1). The optimum value of the core index exponent g to obtain maximum bandwidth depends on the wavelength λ (in free-space) of the source.

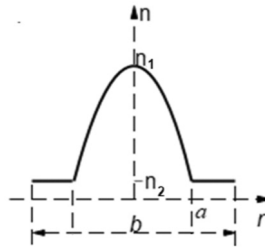


Fig. 1. Refractive index distribution of graded-index optical fiber, where a is core radius and b is fiber diameter.

Time-dependent power flow equation for multimode GI optical fibers is:

$$\frac{\partial P(m, \lambda, z, \omega)}{\partial z} + j\omega\tau(m, \lambda)P(m, \lambda, z, \omega) = -\alpha(m, \lambda)P(m, \lambda, z, \omega) + \frac{\partial P(m, \lambda, z, \omega)}{\partial m} \frac{\partial d(m, \lambda)}{\partial m} + d(m, \lambda) \frac{1}{m} \frac{\partial P(m, \lambda, z, \omega)}{\partial m} + d(m, \lambda) \frac{\partial P^2(m, \lambda, z, \omega)}{\partial m^2} \quad (2)$$

where $P(m, \lambda, z, \omega)$ is the power in the m -th principal mode (modal group) (the principal mode number m is treated as a continuous variable [11]), z is coordinate along the fiber axis from the input fiber end, $\alpha(m, \lambda)$ is the attenuation of the mode m , $d(m, \lambda)$ is the coupling coefficient of

the mode m , $\omega=2\pi f$ is the baseband angular frequency, is delay time per unit length of mode m , which can be determined as:

$$\tau(m, \lambda) \cong \frac{n_1(\lambda)}{c} \left[1 + \frac{g-2}{g+2} \Delta(\lambda) \left(\frac{m}{M(\lambda)} \right)^{2g/(g+2)} + \frac{1}{2} \frac{3g-2}{g+2} \Delta(\lambda)^2 \left(\frac{m}{M(\lambda)} \right)^{4g/(g+2)} \right] \quad (3)$$

where c is the free-space velocity of light and:

$$P(m, \lambda, z, \omega) = \int_{-\infty}^{+\infty} P(m, \lambda, z, t) \exp(-j\omega t) dt \quad (4)$$

The first and second term on the left-hand side of Eq. (2) describe the space and time evolution of the modal power distribution along the fiber, respectively. The first term on the right-hand side of Eq. (2) describes modal attenuation, the second and third term describe drift of the power distribution towards $m=0$, and the fourth term describes diffusion (broadening) of the modal power distribution. The maximum principal mode number is [10]:

$$M(\lambda) = \sqrt{\frac{g\Delta(\lambda)}{g+2}} a k n_1(\lambda) \quad (5)$$

Where $k = 2\pi/\lambda$. Gaussian launch-beam distribution $P_0(\theta, \lambda, z=0)$ can be transformed into $P_0(m, \lambda, z=0)$ (one needs $P_0(m, \lambda, z=0)$ to numerically solve the time-dependent power flow Eq. (2)), using the following relationship [12]:

$$\frac{m}{M(\lambda)} = \left[\left(\frac{r_0}{a} \right)^g + \frac{\theta^2}{2\Delta(\lambda)} \right]^{(g+2)/2g} \quad (6)$$

where r_0 is radial distance (radial offset) between the launch beam position and the core center and θ is tilt angle measured in respect to the fiber axis.

It is apparent that $P(m, \lambda, z, \omega)$ is complex. By separating P into the real part P^r and imaginary part P^i , Eq. (2) can be rewritten as the following simultaneous partial differential equations:

$$\frac{\partial P^r}{\partial z} = -\alpha P^r + \frac{\partial d}{\partial m} \frac{\partial P^r}{\partial m} + \frac{d}{m} \frac{\partial P^r}{\partial m} + d \frac{\partial^2 P^r}{\partial m^2} + \omega \tau P^i \quad (7)$$

$$\frac{\partial P^i}{\partial z} = -\alpha P^i + \frac{\partial d}{\partial m} \frac{\partial P^i}{\partial m} + \frac{d}{m} \frac{\partial P^i}{\partial m} + d \frac{\partial^2 P^i}{\partial m^2} - \omega \tau P^r \quad (8)$$

where $P = P^r + jP^i$. Assuming a constant coupling coefficient $d \equiv D$ [10], Eqs. (7) and (8) can be written as:

$$\frac{\partial P^r}{\partial z} = -\alpha P^r + \frac{D}{m} \frac{\partial P^r}{\partial m} + D \frac{\partial^2 P^r}{\partial m^2} + \omega \tau P^i \quad (9)$$

$$\frac{\partial P^i}{\partial z} = -\alpha P^i + \frac{D}{m} \frac{\partial P^i}{\partial m} + D \frac{\partial^2 P^i}{\partial m^2} - \omega \tau P^r \quad (10)$$

Using the EFDM, discretization of Eqs. (9) and (10) leads to:

$$\begin{aligned} P_{k,l+1}^r &= \left(\frac{\Delta z D}{\Delta m^2} - \frac{\Delta z D}{2m_k \Delta m} \right) P_{k-1,l}^r + \left(1 - \frac{2\Delta z D}{\Delta m^2} - \alpha_k \Delta z \right) P_{k,l}^r + \\ &+ \left(\frac{\Delta z D}{2m_k \Delta m} - \frac{\Delta z D}{\Delta m^2} \right) P_{k+1,l}^r + \frac{\omega n_0 \Delta z}{2c} m_k^2 P_{k,l}^i \end{aligned} \quad (11)$$

$$\begin{aligned}
P_{k,l+1}^i = & \left(\frac{\Delta z D}{\Delta m^2} - \frac{\Delta z D}{2m_k \Delta m} \right) P_{k-1,l}^i + \left(1 - \frac{2\Delta z D}{\Delta m^2} - \alpha_k \Delta z \right) P_{k,l}^i + \\
& + \left(\frac{\Delta z D}{2m_k \Delta m} - \frac{\Delta z D}{\Delta m^2} \right) P_{k+1,l}^i - \frac{\omega n_0 \Delta z}{2c} m_k^2 P_{k,l}^r
\end{aligned} \quad (12)$$

where k and l refer to the discretization step lengths Δm and Δz for the mode m and length z , respectively, i.e. $P_{k,l}^r \equiv P^r(m_k, z_l, \omega)$ and $P_{k,l}^i \equiv P^i(m_k, z_l, \omega)$.

If P^r and P^i are obtained by solving Eqs. (11) and (12), the transmission characteristics can be calculated. Thus, the frequency response of fiber at length z is:

$$H(\lambda, z, \omega) = \frac{\int_1^M 2m [P_r(m, \lambda, z, \omega) + jP_i(m, \lambda, z, \omega)] dm}{\int_1^M 2m [P_r(m, \lambda, z, 0) + jP_i(m, \lambda, z, 0)] dm} \quad (13)$$

where the factor $2m$ denotes degeneracy of modal group m . The frequency responses for a given fiber can be obtained at a range of lengths providing information on the bandwidth dependence with distance. The modal power distribution $P(m, \lambda, z, \omega)$ and the spatial transient of power $P_L(\lambda, z, \omega)$ can be obtained by:

$$P(m, \lambda, z, \omega) = [P^r(m, \lambda, z, \omega)^2 + P^i(m, \lambda, z, \omega)^2]^{1/2} \quad (14)$$

$$P_L(\lambda, z, \omega) = 2\pi \int_0^M m P(m, \lambda, z, \omega) dm \quad (15)$$

This enable us to determine the relationship between the transmission length and bandwidth in GI POF for various launch conditions.

3. Results and discussion

We applied our method to the GI POF (OM Giga, Fiber FinTM), which we previously investigated experimentally [10]. The core diameter of the fiber was $2a=0.9$ mm (fiber diameter was $b=1$ mm). The refractive index of the core measured at the fiber axis was $n_1=1.522$ and the refractive index of the cladding was $n_2=1.492$ (measured at $\lambda=633$ nm). For the GI POF under investigation, the maximum principal mode number is $M=656$ (for $\lambda=633$ nm), $g=1.80101$ and $\Delta=(n_1-n_2)/n_1=0.019711$. The constant coupling coefficient for the investigated GI POF is $D=1482$ 1/m [10], which we adopted in this work. One should note that assumption of constant coupling coefficient for this GI POF led to the correct prediction of the output angular power distribution [10] (constant coupling coefficient is commonly used in modeling GI POF, e.g. in Ref. [13]). One can observe from Fig. 2, that except near $m \approx M$, measured mode-dependent attenuation can be assumed constant $\alpha(m, \lambda) \equiv \alpha_c = 0.0122$ 1/m. In the numerical calculations, a Gaussian beam $P(\theta, z)$ is assumed to be launched with $\langle \theta \rangle = 0^\circ$ and standard deviation $\sigma_\theta = 1.3^\circ$ (FWHM = 3.06°) [10]. The bandwidth of the GI POF was evaluated by the time domain measurement method in which the bandwidth was estimated by measuring the output pulse waveform. The optical signal was injected through a single-mode fiber which was butt-coupled to the GI POF being tested and aligned parallel to the fiber axis with controlled lateral displacement to the axis [10]. The output pulse from the fiber was measured by a sampling optical oscilloscope (Hamamatsu Photonics Co. C8188-03).

Figures 3 and 4 show the numerically calculated and measured bandwidth, respectively, for five radial offsets $\Delta r = 0, 100, 200, 300$ and 400 μm at different fiber lengths. One can see that our theoretical and experimental results for bandwidth are in good agreement. One can see from

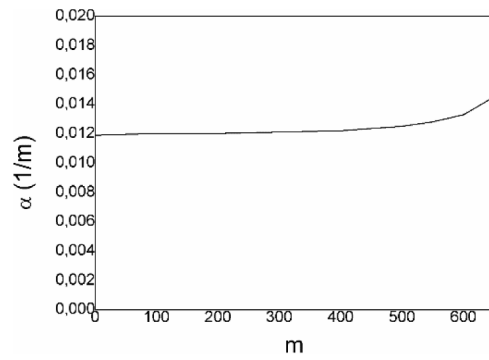


Fig. 2. Measured mode-dependent attenuation $\alpha(m)$ for GI POF.

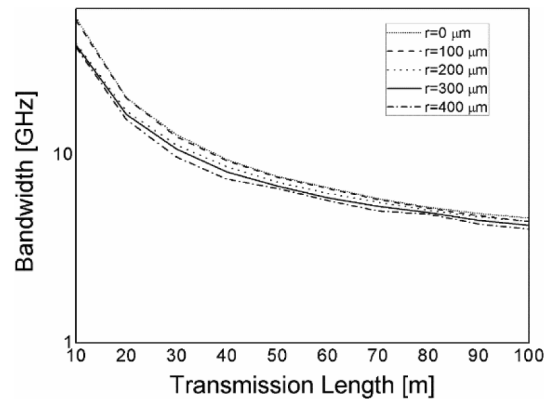


Fig. 3. Numerically calculated bandwidth as a function of transmission length of GI POF for a various radial offsets.

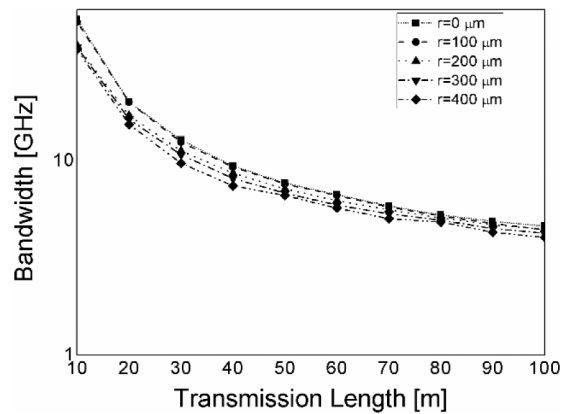


Fig. 4. Measured bandwidth as a function of transmission length of GI POF for a various radial offset (lines are drawn to guide the eye).

Figs. 3 and 4 that bandwidth decreases with increasing radial offset, which is a consequence of larger modal dispersion in case of excitation of higher guided modes.

This decrease is more pronounced at short fiber lengths. At fiber length $z \approx 30$ m, which is close to the experimentally obtained coupling length $L_c = 31$ m (Fig. 5) [10] at which an EMD is achieved, this decrease becomes slower, indicating that strong mode coupling causes bandwidth improvement in GI POFs. Thus, we obtain a bandwidth of around 4.6 GHz at a distance of 100 m, which leads to a bandwidth-length product of 0.46 GHz·km for radial offset of $\Delta r = 0$ μm for the investigated GI POF. This bandwidth-length product is greater than a bandwidth-length product of 0.156 GHz·km for GI POF investigated by Chun-Yu Lin et al. [2].

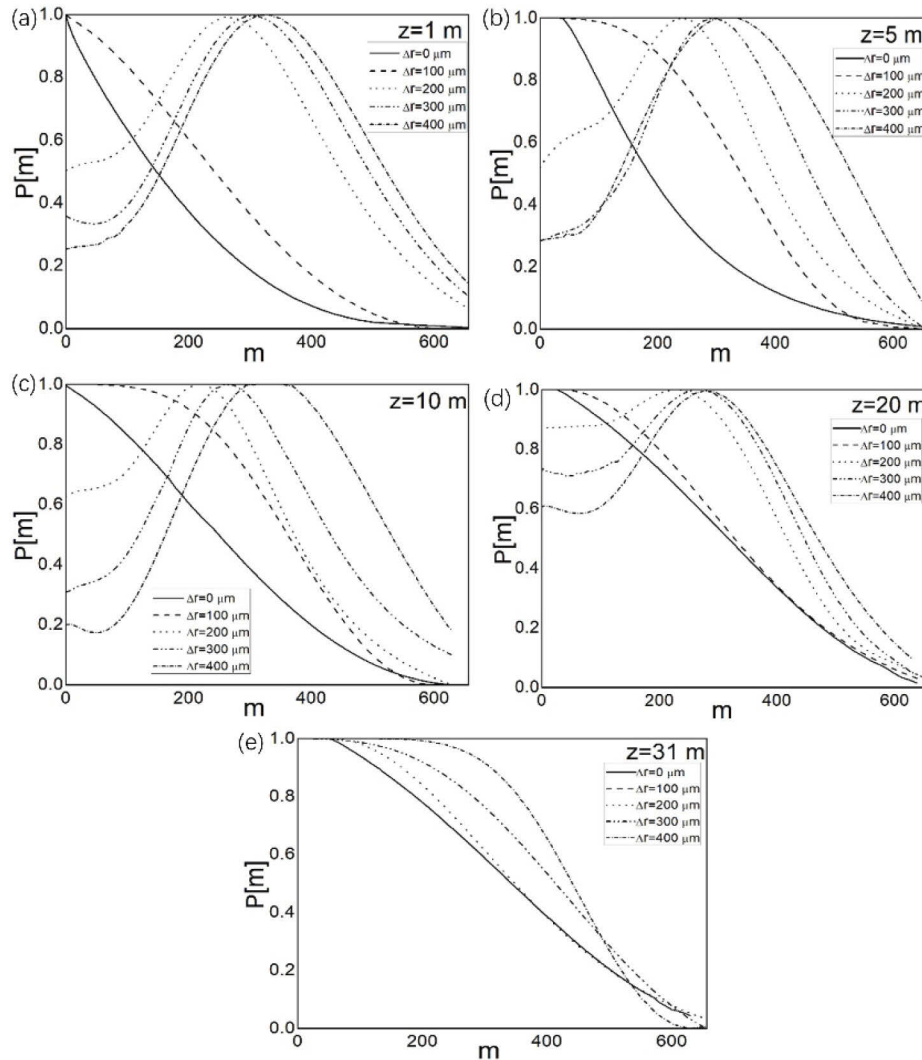


Fig. 5. Normalized output modal power distribution $P(m)$ in SC GI POF over a range of radial offsets Δr , obtained from the measured angular power distributions $P(\theta)$, at different fiber lengths (a) $z=1$ m, (b) $z=5$ m, (c) $z=10$ m, (d) $z=20$ m and (e) $z=31$ m [10].

One should note that L_c marks the length at which the distribution of the highest guiding mode (excited by largest radial offset launch) becomes centrally located (Fig. 5(e)). The shorter the length at which EMD is achieved, the earlier the bandwidth would switch from steep to slower

bandwidth decrease. With further increase of fiber length, bandwidth becomes nearly independent of the radial offset, indicating that a SSD is established. Finally, such a fiber characterization can be applied to optimize fiber performance in POF links, particularly in in-home networks [14]. This optimization can be performed by comparing a performance properties and numerical simulation results of various GI POFs with different refractive index distributions (different g), coupling coefficient D and attenuation α_c . One should note that the proposed method for investigating the bandwidth in multimode GI POF can be employed for any multimode optical fiber with GI core distribution, such as silica optical fibers and plastic clad silica fibers.

4. Conclusion

By numerically solving the time-dependent power flow equation we calculated bandwidth for various launch conditions (radial offsets) of multimode GI POF. We found that our theoretical and experimental results are in good agreement, showing that bandwidth decreases with increasing radial offset. This decrease is more pronounced at short fiber lengths. At coupling length L_c at which an EMD is achieved, this decrease becomes slower, indicating a strong influence of mode coupling on transmission in GI POFs. The shorter the length at which EMD is achieved, the earlier the bandwidth would switch from steep to slower bandwidth decrease. With further increase of fiber length, bandwidth becomes nearly independent of the radial offset, indicating that a SSD is established. Thus, we obtain a bandwidth of around 4.6 GHz at a distance of 100 m for radial offset of $\Delta r=0 \mu\text{m}$ for the investigated GI POF.

Funding. National Natural Science Foundation of China (62003046); Guangdong Basic and Applied Basic Research Foundation (2021A1515011997); Science Fund of Republic Serbia (CTPCF-6379382); Serbian Ministry of Education, Science and Technological Development (451-03-68/2020-14/200122); The Strategic Research Grant of City University of Hong Kong (CityU 7004600).

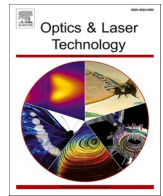
Disclosures. The authors declare no conflicts of interest.

Data availability. Data underlying the results presented in this paper are not publicly available at this time but may be obtained from the authors upon reasonable request.

References

1. C. Gimeno, E. Guerrero, C. Sánchez-Azqueta, J. Aguirre, C. Aldea, and S. Celma, "Multi-rate adaptive equalizer for transmission over up to 50-m SI-POF," *IEEE Photonics Technol. Lett.* **29**(7), 587–590 (2017).
2. C. Lin, C. Li, H. Lu, C. Chang, P. Peng, C. Lin, and J. Chen, "A Hybrid CATV/16-QAM-OFDM In-House Network Over SMF and GI-POF/VLC Transport," *IEEE Phot. Technol. Lett.* **27**(5), 526–529 (2015).
3. M. J. Yadlowsky and A. R. Mickelson, "Distributed loss and mode coupling and their effect on time-dependent propagation in multimode fibers," *Appl. Opt.* **32**(33), 6664–6677 (1993).
4. T. Ishigure, M. Kano, and Y. Koike, "Which is more serious factor to the bandwidth of GI POF: differential mode attenuation or mode coupling?" *J. Lightwave Technol.* **18**(7), 959–965 (2000).
5. K. Kitayama, S. Seikai, and N. Uchida, "Impulse response prediction based on experimental mode coupling coefficient in a 10-km long graded-index fiber," *IEEE J. Quantum Electron* **16**(3), 356–362 (1980).
6. S. Louvros, A. C. Iossifides, G. Economou, G. K. Karagiannidis, S. A. Kotsopoulos, and D. Zevgolis, "Time domain modeling and characterization of polymer optical fibers," *IEEE Photon. Technol. Lett.* **16**(2), 455–457 (2004).
7. S. Golowich, W. White, W. Reed, and E. Knudsen, "Quantitative estimates of mode coupling and differential modal attenuation in perfluorinated graded-index plastic optical fiber," *J. Lightwave Technol.* **21**(1), 111–121 (2003).
8. H. Hajjar, D. Montero, P. Lallana, C. Vázquez, and B. Fracasso, "Spectral and spatial characterization of perfluorinated graded-index polymer optical fibers for the distribution of optical wireless communication cells," *Appl. Opt.* **54**(5), 1138–1145 (2015).
9. A. Garito, J. Wang, and R. Gao, "Effects of random perturbations in plastic optical fibers," *Science* **281**(5379), 962–967 (1998).
10. S. Savović, A. Simović, B. Drljača, A. Djordjevich, G. Stepniak, C. A. Bunge, and J. Bajić, "Power flow in graded index plastic optical fibers," *J. Lightwave Technol.* **37**(19), 4985–4990 (2019).
11. R. Olshansky, "Mode coupling effects in graded-index optical fibers," *Appl. Opt.* **14**(4), 935–945 (1975).
12. K. Nagano and S. Kawakami, "Measurements of mode conversion coefficients in graded-index fibers," *Appl. Opt.* **19**(14), 2426–2434 (1980).
13. A. Polley and S. E. Ralph, "Mode Coupling in Plastic Optical Fiber Enables 40-Gb/s Performance," *IEEE Photonics Technol. Lett.* **19**(16), 1254–1256 (2007).

14. F. Forni, Y. Shi, N. C. Tran, H. P. A. van den Boom, E. Tangdionga, and A. M. J. Koonen, "Multiformat wired and wireless signals over large-core plastic fibers for in-home network," *J. Lightwave Technol.* **36**, 3444–3452 (2018).



Full length article

Power flow in multimode W-type plastic optical fibers with graded index core distribution

Ana Simović^a, Alexandar Djordjevich^b, Branko Drljača^c, Svetislav Savović^{a,b,*}

^a University of Kragujevac, Faculty of Science, R. Domanovića 12, 34000 Kragujevac, Serbia

^b City University of Hong Kong, 83 Tat Chee Avenue, Hong Kong, China

^c Faculty of Science, University of Kosovska Mitrovica, Lole Ribara 29, Kosovska Mitrovica, Serbia

ARTICLE INFO

Keywords:

W-type plastic optical fiber
Graded-index optical fiber
Power flow equation
Equilibrium mode distribution

ABSTRACT

A method is proposed for investigation of transmission along a multimode W-type (doubly clad) plastic optical fiber (POF) with graded index (GI) distribution of the core. The multimode W-type GI POF is designed from a multimode singly clad (SC) GI POF fiber upon modification of the cladding layer of the latter. The transmission characteristics of such proposed W-type GI POF are determined from the numerical solution of the power flow equation. We have shown that coupling length L_c at which an equilibrium mode distribution (EMD) is achieved in W-type GI POF is shorter than this length experimentally determined for the original SC GI POF. This is a consequence of leaky mode losses which reduce the number of higher guided modes involved in the coupling process, thus reducing the length L_c . We have shown that the shorter the length L_c , the earlier the bandwidth switches from the functional dependence of $1/z$ to $1/z^{1/2}$. We found that bandwidth improves with thinner and shallower intermediate layers. Finally, the bandwidth of the W-type GI POF analyzed in this work is greater if compared to the bandwidth of the original SC GI POF.

1. Introduction

Data traffic demand in access and backbone networks has been increasing exponentially in the last three decades. Streaming transmissions and cloud computing have accelerated this growth. Furthermore, in view of the advances in both intelligent driving systems and multimedia services, this concept becomes a powerful approach for use in optical networking strategies for automobile communication systems. These systems are usually implemented using multimode POFs due to their ease of connection and robustness for tight bends.

Transmission characteristics of POF are affected by mode coupling. Mode coupling occurs as a consequence of light scattering due to random anomalies in multimode optical fibers (various irregularities such as microscopic bends and refractive index fluctuations). They cause the change of the power distribution until an “equilibrium mode distribution” (EMD) is achieved at a distance called “coupling length” L_c down the fiber. The L_c marks the length at which the distribution of the highest guiding mode becomes centrally located.

Multimode optical fibers are usually SC in terms of the number of functional cladding layers. A bandwidth and attenuation properties of SC fibers can be improved by special detection [1], modulation [2],

equalization [3], and compensation of modal-dispersion [4]. Since a fiber design can significantly influence its transmission characteristics, a various step-index (SI), GI and W-type POFs (doubly clad fibers) have been proposed [5–7]. GI POFs exhibit far less modal dispersion than SI POFs due to their gradual decreasing of the refractive index of core with radial distance from the fiber axis [8]. Since waveguide dispersion is smaller in the W-type fiber than it is in the SC fiber [9], W-type fiber has a wider bandwidth and lower bending losses compared to a corresponding SC fiber. The bandwidth-distance product of glass optical fibers is ≈ 30 MHz·km for the SC variety and ≈ 50 MHz·km for the W-type. For POFs, these figures are ≈ 15 MHz·km for the SC and ≈ 200 MHz·km for the W-type fibers [5,7,10].

A W-type fiber's intermediate layer (inner cladding) layer lowers dispersion, widens bandwidth and reduces the number of guided modes which are thus held tighter to the core [11,12]. Due to mode coupling optical power is transferred between modes [13], which reduces modal dispersion and improves fiber bandwidth [14]. Methods are needed for calculating modal attenuation and coupling to lossy modes of W-type fiber's intermediate layer, and for optimizing the fiber's refractive index profile in order to minimize the group delay difference between modes in the output field [10,15].

* Corresponding author at: University of Kragujevac, Faculty of Science, R. Domanovića 12, 34000 Kragujevac, Serbia.
E-mail address: savovic@kg.ac.rs (S. Savović).

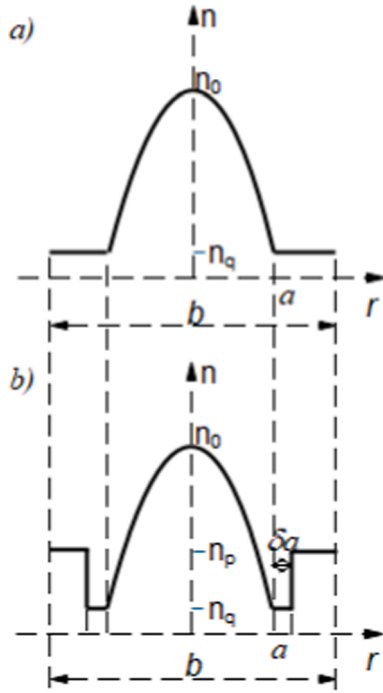


Fig. 1. Refractive index profile of a) SC GI POF and b) W-type GI POF.

In this work, we investigated how the length at which an EMD is achieved changes for various configurations of W-type POFs with GI

where g is the core index exponent, a is the core radius, δa is the intermediate layer width, b is the fiber diameter, $n_0(\lambda)$ is the maximum index of the core (measured at the fiber axis), n_q and n_p are refractive indices of the intermediate layer and cladding, respectively, $\Delta_q = (n_0 - n_q)/n_0$ is the relative index difference between core and intermediate layer. The maximum principal mode number $M(\lambda)$ can be obtained as [18]:

$$M(\lambda) = \sqrt{\frac{g\Delta_q(\lambda)}{g+2}} akn_0(\lambda) \quad (3)$$

where $k = 2\pi/\lambda$ is the free-space wave number. Gaussian launch-beam distribution $P_0(\theta, \lambda, z=0)$ can be transformed into $P_0(m, \lambda, z=0)$ (one needs $P_0(m, \lambda, z=0)$ to numerically solve the power flow equation (1)), using the following relationship [19]:

$$\frac{m}{M(\lambda)} = \left[\left(\frac{r_0}{a} \right)^g + \frac{\theta^2}{2\Delta_q(\lambda)} \right]^{(g+2)/2g} \quad (4)$$

where r_0 is radial distance (radial offset) between the launch beam position and the core center and θ is the propagation angle with respect to the core axis.

The relative refractive index difference $\Delta_q = (n_0 - n_q)/n_0$ between the core and intermediate layer is larger than the difference $\Delta_p = (n_0 - n_p)/n_0$ between core and cladding. Modes propagating along with subcritical angles $m < m_q$ are guided. The same is true for those propagating through the complete W-fiber with m below the critical value m_p . However, modes with angles between m_p and $m_q \equiv M$ are transformed into leaky modes [10]. Attenuation constants of leaky modes are given as:

$$\alpha_L(m, \lambda) = \frac{4\sqrt{2\Delta_q} \left(\left(\frac{m}{m_q} \right)^{\frac{2g}{g+2}} - \left(\frac{m_p}{m_q} \right)^{\frac{2g}{g+2}} \right)^{1/2} \left(\frac{m}{m_q} \right)^{\frac{2g}{g+2}} \left(1 - \left(\frac{m}{m_q} \right)^{\frac{2g}{g+2}} \right)}{a \left(1 - 2\Delta_q \left(\frac{m}{m_q} \right)^{\frac{2g}{g+2}} \right)^{1/2} \left(1 - \frac{\Delta_p}{\Delta_q} \left(\frac{m_p}{m_q} \right)^{\frac{2g}{g+2}} \right)} \exp \left[-2\delta a n_0 k \left(2\Delta_q \left(1 - \left(\frac{m}{m_q} \right)^{\frac{2g}{g+2}} \right) \right)^{1/2} \right] \quad (5)$$

distribution of the core. Results are compared to our experimental measurements for SC GI POF.

2. Time-independent power flow equation

The time-independent power flow for multimode GI fibers (Fig. 1a) is described by the following coupled-power equation [16]:

$$\frac{\partial P(m, \lambda, z)}{\partial z} = -\alpha(m, \lambda)P(m, \lambda, z) + \frac{1}{m} \frac{\partial}{\partial m} \left(md(m, \lambda) \frac{\partial P(m, \lambda, z)}{\partial m} \right) \quad (1)$$

where $P(m, \lambda, z)$ is power in the m -th principal mode (modal group), z is the coordinate along the fiber axis from the input fiber end, $d(m, \lambda)$ mode coupling coefficient which can be assumed constant D [17], $\alpha(m, \lambda) = \alpha_0(\lambda) + \alpha_d(m, \lambda)$ is the modal attenuation, where α_0 represents conventional losses (absorption and scattering). The term α_0 leads only to a multiplier $\exp(-\alpha_0 z)$ in the solution and can be neglected.

Consider a W-type GI fiber with index profile shown in Fig. 1b. The index profile of W-type optical fibers with GI distribution of the core may be expressed as:

$$n(r, \lambda) = \begin{cases} n_0(\lambda) \left[1 - \Delta_q(\lambda) \left(\frac{r}{a} \right)^g \right]^{1/2} & (0 \leq r \leq a) \\ n_q(a < r \leq a + \delta a) \\ n_p(a + \delta a < r \leq \frac{b}{2}) \end{cases} \quad (2)$$

One can see from Equation (5) that for thick intermediate layer widths δ , the lower leaky modes are substantially guided because of the low leaky modes losses. In a SC GI fiber, experimental results show that attenuation remains constant throughout the guided-mode region ($m \leq m_p$) and rises quite steeply in the radiation-mode region [20]. Consequently, the modal attenuation in a W-type GI POF can be expressed as:

$$\alpha_d(m, \lambda) = \begin{cases} 0 & m \leq m_p \\ \alpha_L(m, \lambda) & m_p < m < m_q \\ \infty & m \geq m_q \end{cases} \quad (6)$$

A W-type fiber can be regarded as a system consisting of SC_q fiber and cladding. In the SC_q fiber, modes $m < m_q$ can be guided. When the SC_q fiber is coupled with surrounding medium of index n_p , the lower order modes $m < m_p$ remain guided, while the higher order modes m ($m_p < m < m_q$) are transformed into leaky modes. Because of the strong dependence of $\alpha_L(m)$ on the intermediate layer width δa (Eq. (5)), it is expected that characteristics of a W-type GI fiber also depend on δa and coincide with those of SC_p and SC_q GI fibers in the limits of $\delta \rightarrow 0$ and $\delta \rightarrow \infty$, respectively [10,21].

Using the explicit finite difference method (EFDM), discretization of equation (1) leads to:

$$P_{i,j+1} = \left(\frac{d(m_i, \lambda) \Delta z}{(\Delta m)^2} - \frac{d(m_i, \lambda) \Delta z}{2m_i \Delta m} - \frac{\partial d(m_i, \lambda)}{\partial m} \frac{\Delta z}{2 \Delta m} \right) P_{i-1,j} + \left(1 - \frac{2d(m_i, \lambda) \Delta z}{(\Delta m)^2} - \alpha_d(m_i, \lambda) \Delta z \right) P_{i,j} + \left(\frac{\partial d(m_i, \lambda)}{\partial m} \frac{\Delta z}{2 \Delta m} + \frac{d(m_i, \lambda) \Delta z}{2m_i \Delta m} + \frac{d(m_i, \lambda) \Delta z}{(\Delta m)^2} \right) P_{i+1,j} \quad (7)$$

where i and j refer to the discretization step lengths Δm and Δz for the mode m and length z , respectively. This is a simple formula for $P_{i,j+1}$ at the $(i, j + 1)$ th mesh point in terms of the known values along the j th distance row. As first in the authors' best knowledge, numerical solution (7) of the time-independent power flow equation (1) is reported in this work for investigation of the state of mode coupling along a W-type GI POF in terms of mode variable (m).

3. Time-dependent power flow equation

$$P_{k,l+1}^r = \left(\frac{\Delta z D}{\Delta m^2} - \frac{\Delta z D}{2m_k \Delta m} \right) P_{k-1,l}^r + \left(1 - \frac{2\Delta z D}{\Delta m^2} - \alpha_k \Delta z \right) P_{k,l}^r + \left(\frac{\Delta z D}{2m_k \Delta m} - \frac{\Delta z D}{\Delta m^2} \right) P_{k+1,l}^r + \frac{\omega n_0 \Delta z}{2c} n_k^2 P_{k,l}^i \quad (15)$$

$$P_{k,l+1}^i = \left(\frac{\Delta z D}{\Delta m^2} - \frac{\Delta z D}{2m_k \Delta m} \right) P_{k-1,l}^i + \left(1 - \frac{2\Delta z D}{\Delta m^2} - \alpha_k \Delta z \right) P_{k,l}^i + \left(\frac{\Delta z D}{2m_k \Delta m} - \frac{\Delta z D}{\Delta m^2} \right) P_{k+1,l}^i - \frac{\omega n_0 \Delta z}{2c} n_k^2 P_{k,l}^r \quad (16)$$

Time-dependent power flow equation for multimode optical fibers with GI core distribution is:

$$\begin{aligned} \frac{\partial P(m, \lambda, z, \omega)}{\partial z} + j\omega\tau(m, \lambda)P(m, \lambda, z, \omega) = & -\alpha(m, \lambda)P(m, \lambda, z, \omega) \\ + \frac{\partial P(m, \lambda, z, \omega)}{\partial m} \frac{\partial d(m, \lambda)}{\partial m} + d(m, \lambda) \frac{1}{m} \frac{\partial P(m, \lambda, z, \omega)}{\partial m} + & d(m, \lambda) \frac{\partial P^2(m, \lambda, z, \omega)}{\partial m^2} \end{aligned} \quad (8)$$

where $P(m, \lambda, z, \omega)$ is the power in the m -the principal mode (modal group), z is coordinate along the fiber axis from the input fiber end, $\alpha(m, \lambda)$ is the attenuation of the mode m (Eq. (6)), $d(m, \lambda)$ is the coupling coefficient of the mode m , $\omega = 2\pi f$ is the baseband angular frequency, $\tau(m, \lambda)$ is delay time per unit length of mode m , which can be determined as:

$$\tau(m, \lambda) \cong \frac{n_1(\lambda)}{c} \left[1 + \frac{g-2}{g+2} \Delta_q(\lambda) \left(\frac{m}{M(\lambda)} \right)^{2g/(g+2)} + \frac{1}{2} \frac{3g-2}{g+2} \Delta_q(\lambda)^2 \left(\frac{m}{M(\lambda)} \right)^{4g/(g+2)} \right] \quad (9)$$

where c is the free-space velocity of light and:

$$P(m, \lambda, z, \omega) = \int_{-\infty}^{+\infty} P(m, \lambda, z, t) \exp(-j\omega t) dt \quad (10)$$

It is apparent that $P(m, \lambda, z, \omega)$ is complex. By separating P into the real part P^r and imaginary part P^i , equation (8) can be rewritten as the following simultaneous partial differential equations:

$$\frac{\partial P^r}{\partial z} = -\alpha P^r + \frac{\partial d}{\partial m} \frac{\partial P^r}{\partial m} + \frac{d}{m} \frac{\partial P^r}{\partial m} + d \frac{\partial^2 P^r}{\partial m^2} + \omega\tau P^i \quad (11)$$

$$\frac{\partial P^i}{\partial z} = -\alpha P^i + \frac{\partial d}{\partial m} \frac{\partial P^i}{\partial m} + \frac{d}{m} \frac{\partial P^i}{\partial m} + d \frac{\partial^2 P^i}{\partial m^2} - \omega\tau P^r \quad (12)$$

where $P = P^r + jP^i$. Assuming a constant coupling coefficient $d \equiv D$,

equations (11) and (12) can be written as:

$$\frac{\partial P^r}{\partial z} = -\alpha P^r + \frac{D}{m} \frac{\partial P^r}{\partial m} + D \frac{\partial^2 P^r}{\partial m^2} + \omega\tau P^i \quad (13)$$

$$\frac{\partial P^i}{\partial z} = -\alpha P^i + \frac{D}{m} \frac{\partial P^i}{\partial m} + D \frac{\partial^2 P^i}{\partial m^2} - \omega\tau P^r \quad (14)$$

Using the EFDM, discretization of equations (13) and (14) leads to:

where k and l refer to the discretization step lengths Δm and Δz for the

mode m and length z , respectively, i.e. $P_{k,l}^r \equiv P^r(m_k, z_l, \omega)$ and $P_{k,l}^i \equiv P^i(m_k, z_l, \omega)$.

If P^r and P^i are obtained by solving Eqs. (15) and (16), the transmission characteristics can be calculated. Thus, the frequency response of fiber at length z is:

$$H(\lambda, z, \omega) = \frac{\int_0^M 2m [P_r(m, \lambda, z, \omega) + jP_i(m, \lambda, z, \omega)] dm}{\int_0^M 2m [P_r(m, \lambda, z, 0) + jP_i(m, \lambda, z, 0)] dm} \quad (17)$$

where the factor $2m$ denotes degeneracy of modal group m . The fre-

quency responses for a given fiber can be obtained at a range of lengths providing information on the bandwidth dependence with distance. The modal power distribution $P_F(m, \lambda, z, \omega)$ and the spatial transient of power $P_L(\lambda, z, \omega)$ can be obtained by:

$$P_F(m, \lambda, z, \omega) = [P^r(m, \lambda, z, \omega)^2 + P^i(m, \lambda, z, \omega)^2]^{1/2} \quad (18)$$

$$P_L(\lambda, z, \omega) = 2\pi \int_0^M m P_F(m, \lambda, z, \omega) dm \quad (19)$$

This enable us to determine the relationship between the transmission length and bandwidth in W-type GI POF.

4. Numerical results and discussion

In this paper we investigate the transmission characteristics of W-

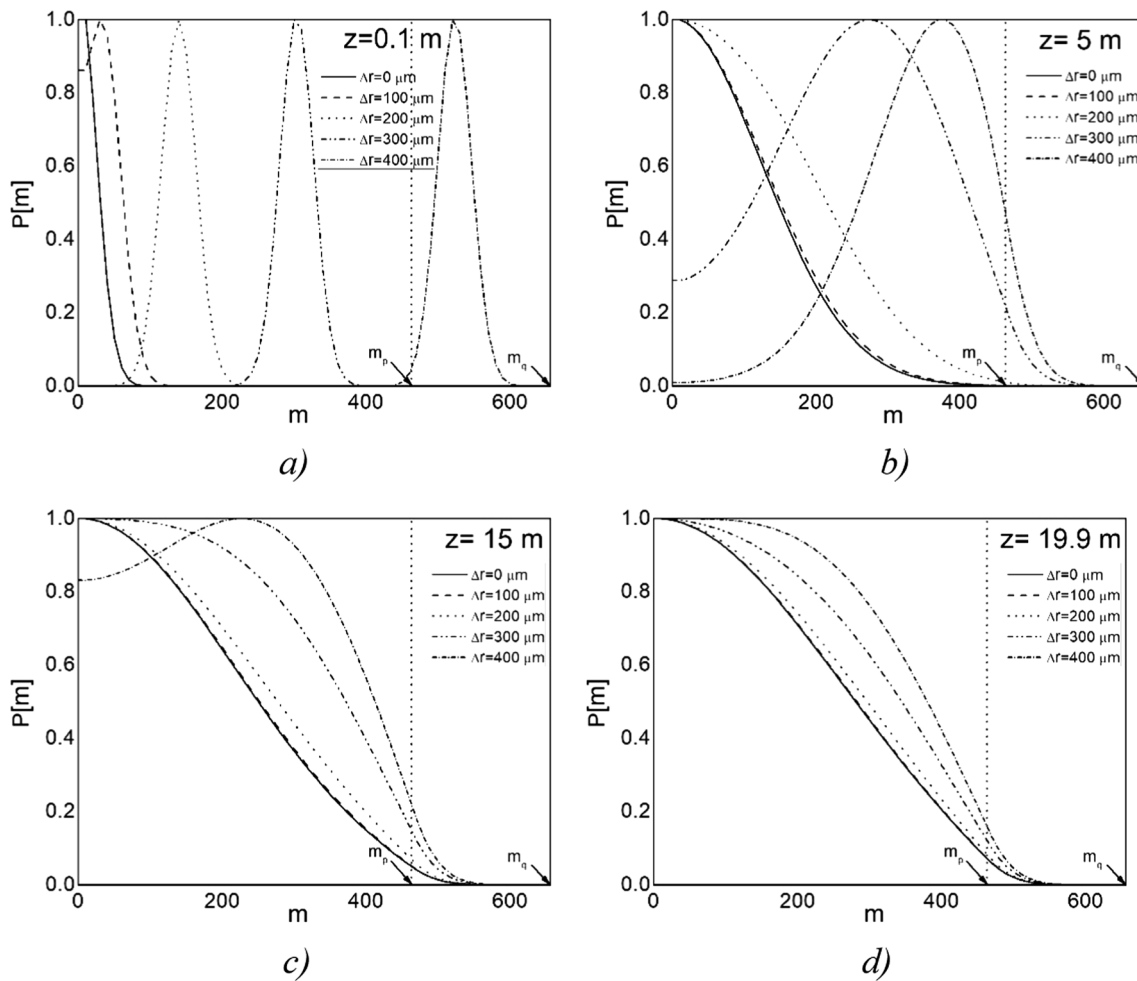


Fig. 2. Calculated output modal power distribution $P(m)$ in W-type GI POF with $\delta = 0.003$, $n_p = 1.50718$, over a range of radial offsets Δr , at fiber lengths a) $z = 0.1$ m, b) $z = 5$ m, c) $z = 15$ m and d) $z = 19.9$ m. for Gaussian launch beam distribution with $\langle \theta \rangle = 0^\circ$ and $(\text{FWHM})_{z=0} = 3.06^\circ$.

type GI POF designed from the SC GI POF (Fig. 1a), which we experimentally investigated in our recently reported work [17]. A W-shape refractive index model is used for the structure shown in Fig. 1b. The characteristics of SC GI POF (OM Giga, Fiber Fin™) were: The core diameter of the fiber was $2a = 0.9$ mm (fiber diameter was $b = 1$ mm), the refractive index of the core measured at the fiber axis was $n_0 = 1.522$ and the refractive index of the intermediate layer (inner cladding) cladding was $n_q = 1.492$. For the investigated SC GI POF, the maximum principal mode number is $M = 656$, $g = 1.80101$ and $\Delta_q = (n_0 - n_q)/n_0 = 0.019711$. The W-type POF with GI distribution of the core is designed from this SC GI POF in such a way that the W-type GI POF's inner cladding retains the distribution of the SC GI POF's cladding while an outer cladding of the W-type POF with GI distribution of the core has a refractive index n_p which is higher than refractive index n_q of the inner cladding (Fig. 1b). The three values of the refractive index of the outer cladding n_p were used in the modeling: $n_p = 1.51366$ ($m_p = 346$), $n_p = 1.51065$ ($m_p = 404$) and $n_p = 1.50718$ ($m_p = 461$). The normalized intermediate layer widths $\delta = 0.001$, $\delta = 0.002$ and $\delta = 0.003$ were employed (actual width is $\delta \cdot a$ mm). The maximum principal mode number in such designed W-type GI POFs is the same as in the investigated SC GI POF ($M \equiv m_q = 656$). The constant coupling coefficient $d(m, \lambda) \equiv D = 1482$ 1/m and wavelength $\lambda = 633$ nm were used in the calculations [17].

Using the time-independent power flow equation, we calculated the length L_c , at which the EMD is achieved in W-type GI POF. As illustration, Fig. 2 shows the output angular power distribution in W-type GI POF with the width of the intermediate layer $\delta = 0.003$ and

$n_p = 1.50718$, obtained by numerical solving the time-independent power flow equation (1). In the numerical calculations, a Gaussian beam $P(\theta, z)$ is assumed to be launched with $\langle \theta \rangle = 0^\circ$ and standard deviation $\sigma_\theta = 1.3^\circ$ ($(\text{FWHM})_{z=0} = 3.06^\circ$). This standard deviation describes the width of the launched beam measured at the end of a single-mode optical fiber which was butt-coupled to the SC GI POF investigated in our previous experimental work [17]. Results are shown for five different radial offsets $\Delta r = 0, 100, 200, 300$ and 400 μm . Fig. 3 shows the normalized experimental output modal power distributions $P(m, \lambda, z)$ obtained in SC GI POF [17]. One can see from Fig. 2 that with increasing the fiber length, the EMD is first achieved in W-type GI POF for $\delta = 0.001$ at fiber length $L_c = 17.7$ m, then for $\delta = 0.002$ at fiber length $L_c = 18.5$ m, and finally for $\delta = 0.003$ at fiber length $L_c = 19.9$ m (Table 1). For comparison, the EMD in SC GI POF was achieved at $L_c = 31$ m (Fig. 3). In the case of W-type GI POF fibers the number of higher guided modes involved in the coupling process is reduced, thus reducing the length L_c . With increasing the width of the inner cladding, leaky mode losses decrease (number of guided modes increases), which results in the longest length L_c in the case $\delta = 0.003$. With decreasing the refractive index n_p , the length L_c increases for three different widths of the inner cladding (Table 1). The influence of the width of the intermediate layer δ on leaky mode losses is more pronounced than the influence of n_p , which leads to a stronger influence of δ on the length L_c .

One can see from Fig. 4 that bandwidth decreases linearly for short lengths and switches later to the $1/z^{1/2}$ functional dependence, thus the shorter the length L_c , a slower bandwidth decrease occurs. This switch, and therefore EMD, occurs at shorter fiber lengths for the thinner

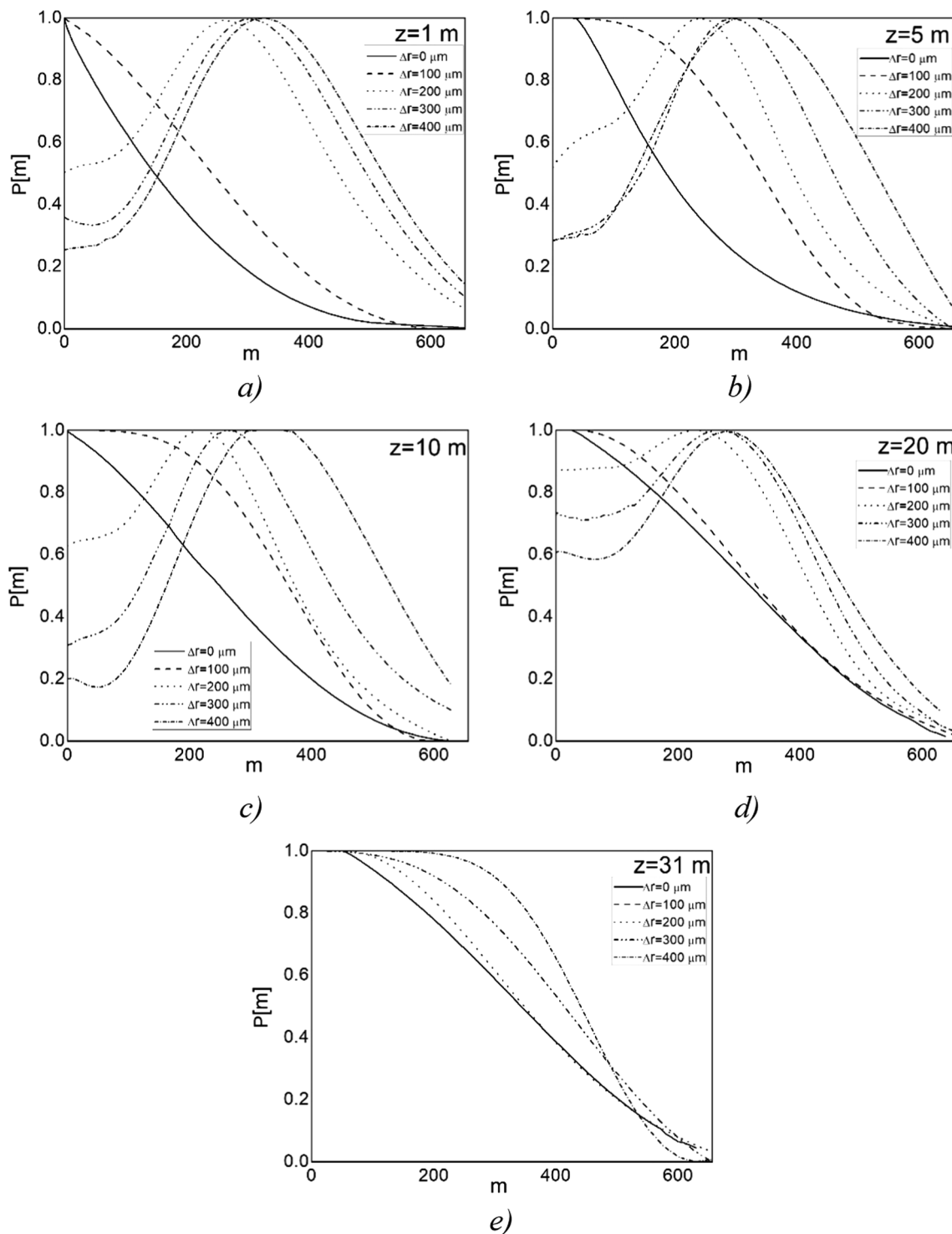


Fig. 3. Normalized output modal power distribution $P(m)$ in SC GI POF over a range of radial offsets Δr , obtained from the measured angular power distributions $P(\theta)$, at different fiber lengths (a) $z = 1$ m, (b) $z = 5$ m, (c) $z = 10$ m, (d) $z = 20$ m and (e) $z = 31$ m [17].

intermediate-layers. Bandwidth improves as the depth of the intermediate layer is reduced because fewer leaky modes then persist along the fiber and dispersion lessens. The smaller the depth of the intermediate layer, the shorter the fiber length for complete coupling. This decrease is more pronounced for thinner intermediate layers (smaller δ) due to their higher leaky mode loss that shortens the coupling length further (Table 1). In conclusion, the bandwidth of the W-type GI POF analyzed in this work is greater if compared to the bandwidth of the original SC GI POF [22].

Table 1
Coupling length L_c at which the EMD is achieved in W-type GI POF with different widths of the intermediate layer δ and refractive index of the cladding n_p .

	L_c [m]		
	$n_p = 1.51366$	$n_p = 1.51065$	$n_p = 1.50718$
$\delta = 0.001$	10.4	13.8	17.7
$\delta = 0.002$	11.8	14.9	18.5
$\delta = 0.003$	14.4	16.9	19.9

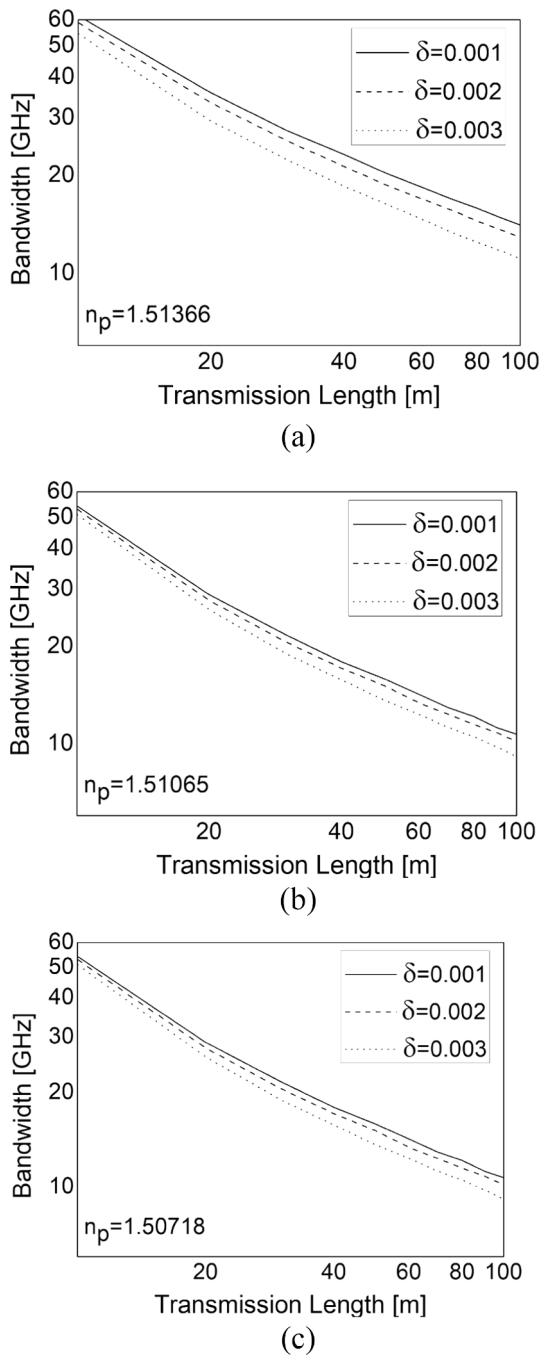


Fig. 4. Bandwidth versus transmission length for (a) $n_p = 1.51366$, (b) $n_p = 1.51065$ and (c) $n_p = 1.50718$, where $(FWHM)_{z=0} = 3.06^\circ$, $\delta = 0.001, 0.002, 0.003$, and $D = 1482$ 1/m.

5. Conclusion

We proposed a method for investigation of transmission along a multimode W-type GI POF which is designed from a multimode SC GI POF upon modification of its cladding layer. We have shown that the coupling length L_c of the W-type GI POF is shorter than L_c experimentally determined for the original SC GI POF. This is a consequence of leaky mode losses which reduce the number of higher guided modes involved in the coupling process, thus reducing the length L_c . We have shown that the shorter the length L_c , the earlier the bandwidth switches from the

functional dependence of $1/z$ to $1/z^{1/2}$. We found that bandwidth improves with thinner and shallower intermediate layers. Finally, the bandwidth of the W-type GI POF analyzed in this work is greater if compared to the bandwidth of the original SC GI POF [22].

Declaration of Competing Interest

The authors declare that they have no known competing financial interests or personal relationships that could have appeared to influence the work reported in this paper.


Acknowledgements

The work described in this paper was supported by the Strategic Research Grant of City University of Hong Kong (Project No. CityU 7004600) and by a grant from Serbian Ministry of Education, Science and Technological Development (Agreement No. 451-03-68/2020-14/200122).

References

- [1] K.M. Patel, S.E. Ralph, Enhanced multimode fiber link performance using a spatially resolved receiver, *IEEE Photon. Technol. Lett.* 14 (2002) 393–395.
- [2] E.J. Tyler, M. Webster, R.V. Pentyl, I.H. White, S. Yu, J. Rorison, Subcarrier modulated transmission of 2.5 Gb/s over 300 m of 62.5- μ m-core diameter multimode fiber, *IEEE Photon. Technol. Lett.* 14 (2002) 1743–1745.
- [3] X. Zhao, F.S. Choa, Demonstration of 10 Gb/s transmission over 1.5-km-long multimode fiber using equalization techniques, *IEEE Photon. Technol. Lett.* 14 (2002) 1187–1189.
- [4] J.S. Abbott, G.E. Smith, C.M. Truesdale, Multimode fiber link dispersion compensator, U.S. Patent 6 363 195, 2002.
- [5] T. Yamashita, M. Kagami, Fabrication of light-induced self-written waveguides with a W-shaped refractive index profile, *J. Lightwave Technol.* 23 (2005) 2542–2548.
- [6] M. Asai, Y. Inuzuka, K. Koike, S. Takahashi, Y. Koike, High-bandwidth graded-index plastic optical fiber with low-attenuation, high-bending ability, and high-thermal stability for home-networks, *J. Lightwave Technol.* 29 (2011) 1620–1626.
- [7] K. Mikoshiba, H. Kajioaka, Transmission characteristics of multimode W-type optical fiber: experimental study of the effect of the intermediate layer, *Appl. Opt.* 17 (1978) 2836–2841.
- [8] Y. Koike, K. Koike, Progress in low-loss and high-bandwidth plastic optical fibers, *J. Polym. Sci. B* 49 (2011) 2–17.
- [9] K. Takahashi, T. Ishigure, Y. Koike, Index profile design for high-bandwidth W-shaped plastic optical fiber, *J. Lightwave Technol.* 24 (2006) 2867–2876.
- [10] T. Tanaka, S. Yamada, M. Sumi, K. Mikoshiba, Microbending losses of doubly clad (W-type) optical fibers, *Appl. Opt.* 18 (1977) 2391–2394.
- [11] V. Rastogi Babita, A. Kumar, Design of large-mode-area three layered fiber structure for femtosecond laser pulse delivery, *Opt. Commun.* 293 (2013) 108–112.
- [12] A. Simović, S. Savović, B. Drljača, A. Djordjević, Influence of the fiber design and launch beam on transmission characteristics of W-type optical fibers, *Opt. Laser Technol.* 68 (2015) 151–159.
- [13] D. Gloge, Optical power flow in multimode fibers, *Bell Syst. Tech. J.* 51 (1972) 1767–1783.
- [14] D. Gloge, Impulse response of clad optical multimode fibers, *Bell Syst. Tech. J.* 52 (1973) 801–816.
- [15] S. Savović, A. Simović, A. Djordjević, Explicit finite difference solution of the power flow equation in W-type optical fibers, *Opt. Laser Technol.* 44 (2012) 1786–1790.
- [16] K. Kitayama, S. Seikai, N. Uchida, Impulse response prediction based on experimental mode coupling coefficient in a 10-km long graded-index fiber, *IEEE J. Quant. Electronics* 16 (1980) 356–362.
- [17] S. Savović, A. Simović, B. Drljača, A. Djordjević, G. Stepniak, C.A. Bunge, J. Bajić, Power flow in graded index plastic optical fibers, *J. Lightwave Technol.* 37 (2019) 4985–4990.
- [18] R. Olshansky, Mode coupling effects in graded-index optical fibers, *Appl. Opt.* 14 (1975) 935–945.
- [19] K. Nagano, S. Kawakami, Measurements of mode conversion coefficients in graded-index fibers, *Appl. Opt.* 19 (1980) 2426–2434.
- [20] G. Yabre, Comprehensive theory of dispersion in graded-index optical fibers, *J. Lightwave Technol.* 18 (2000) 166–177.
- [21] T. Ishigure, H. Endo, K. Ohdoko, K. Takahashi, Y. Koike, Modal bandwidth enhancement in a plastic optical fiber by W-refractive index profile, *J. Lightwave Technol.* 23 (2005) 1754–1762.
- [22] A. Simović, A. Djordjević, B. Drljača, S. Savović, Theoretical investigation of bandwidth in multimode graded index plastic optical fibers (submitted for publication).

Power Flow in Graded-Index Plastic Optical Fibers

Svetislav Savović , Ana Simović, Branko Drljača, Alexandar Djordjevich, Grzegorz Stepniak ,
Christian Alexander Bunge, and Jovan Bajić

Abstract—A method is proposed for predicting the evolution of the power distribution along graded-index plastic optical fibers. This method is verified against our recently reported measurements. The strong influence of mode coupling on the power distribution is demonstrated on a specific graded-index plastic fiber to illustrate the influence of mode coupling in applications, such as data transmission, power delivery, and sensing systems.

Index Terms—Equilibrium mode distribution, graded-index optical fiber, mode coupling, power flow equation.

I. INTRODUCTION

PLASTIC optical fibers (POFs) are often used in local area networks (LANs), sensors, power delivery systems, and light-transmission guides (such as endoscopes or entertainment applications). Multimode POFs have large numerical aperture which simplifies coupling of light. Compared to their glass counterparts, POFs offer a low-cost installation alternative with low-precision plastic components without precision couplers; POFs also tend to cost less to produce and are easier to handle. Their flexibility is especially useful when installing them in tight spaces such as in homes, offices or vehicles. Step-index (SI) POFs have large modal dispersion and low bandwidth-length product. Graded index (GI) POFs exhibit far less modal dispersion than SI POFs. This is due to their gradual, usually parabolic, decreasing of the refractive index of core with radial distance from the fiber axis. Thus, a bandwidth of 40 Gbps for a 100-m GI POF has been reported [1].

Manuscript received April 25, 2019; revised June 4, 2019, June 20, 2019, and July 1, 2019; accepted July 1, 2019. Date of publication July 3, 2019; date of current version September 24, 2019. This work was supported in part by the City University of Hong Kong under Project CityU7004851 and in part by the Serbian Ministry of Education, Science and Technological Development under Project 171011. (Corresponding authors: Svetislav Savović and Alexandar Djordjevich.)

S. Savović is with the Faculty of Science, University of Kragujevac, 34000 Kragujevac, Serbia, and also with the City University of Hong Kong, Kowloon, Hong Kong (e-mail: savovic@kg.ac.rs).

A. Simović is with the Faculty of Science, University of Kragujevac, 34000 Kragujevac, Serbia (e-mail: asimovic@kg.ac.rs).

B. Drljača is with the Faculty of Sciences, University of Priština, 38220 Kosovska Mitrovica, Serbia (e-mail: brdljaca@gmail.com).

A. Djordjevich is with the City University of Hong Kong, Kowloon, Hong Kong (e-mail: mealex@cityu.edu.hk).

G. Stepniak is with the Institute of Telecommunications, Warsaw University of Technology, 00-665 Warsaw, Poland (e-mail: stepniak@tele.pw.edu.pl).

C. A. Bunge is with the Institute for Communications Technology, University of Applied Sciences Leipzig, 04277 Leipzig, Germany (e-mail: bunge@hft-leipzig.de).

J. Bajić is with the Faculty of Technical Sciences, University of Novi Sad, 21000 Novi Sad, Serbia (e-mail: bajic@uns.ac.rs).

Digital Object Identifier 10.1109/JLT.2019.2926700

Propagation characteristics of GI POFs are influenced by differential mode attenuation, mode coupling and modal dispersion [2]–[7]. Inoue *et al.* [8] have investigated the influence of mode coupling on bandwidth of GI POFs, both experimentally and numerically by solving the coupled power equation. Noda and Koike have enhanced bandwidth of GI POFs by controlling differential mode attenuation [9]. Sato *et al.* [10] investigated the influence of temperature of GI POFs on refractive index distribution, modal attenuation and bandwidth. Tsekrekos *et al.* [11] have investigated selective excitation of GI POFs for mode group diversity multiplexing. Tsekrekos *et al.* [12] also investigated near-field intensity patterns at the output of silica-based graded-index multimode fibers under selective excitation with a single-mode fiber and mode-selective spatial filtering for increased robustness in a mode group diversity multiplexing link [13]. The temporal stability of transparent mode group diversity multiplexing links employing GI silica optical fibers is experimentally investigated [14]. S. Schöllmann *et al.* [15] realized the transmission of 10.7 Gb/s over 300 m GI-MMF using a 2×2 MIMO system based on mode group diversity multiplexing. C. Schöllmann *et al.* [16] also experimentally investigated the mode group diversity multiplexing on multimode fiber. J. Siuzdak *et al.* [17] investigated a 2 and 3 channel mode group diversity multiplexing transmission over graded and step index multimode fibers.

GI POF performance is strongly affected by mode coupling. Mode coupling is mainly caused by scattering of light that transfers power from one mode to another due to random anomalies in multimode optical fibers. These effects can be attributed to various irregularities such as microscopic bends, voids and cracks, diameter variation, and density and refractive index fluctuations. They cause the power distribution to evolve with distance from the input fiber-end until an “equilibrium mode distribution” (EMD) results some distance called “coupling length” L_c down the fiber. Beyond L_c , the distribution of light is centrally located and the coupling process is substantially complete for practical purposes.

Since GI POFs are primarily used within short distances (few tens of meters) and only rarely at distances longer than 100 m, it is important to characterize mode coupling in GI POFs as a function of fiber length for various launching conditions (radial offset and tilt angle). It is thus of interest to propose an effective method for predicting the evolution of the power distribution with fiber length and determining that particular length at which the EMD is achieved. In this article, we investigate mode coupling in GI POF by the time-independent power flow equation. Results are compared to our experimental measurements [18]. In

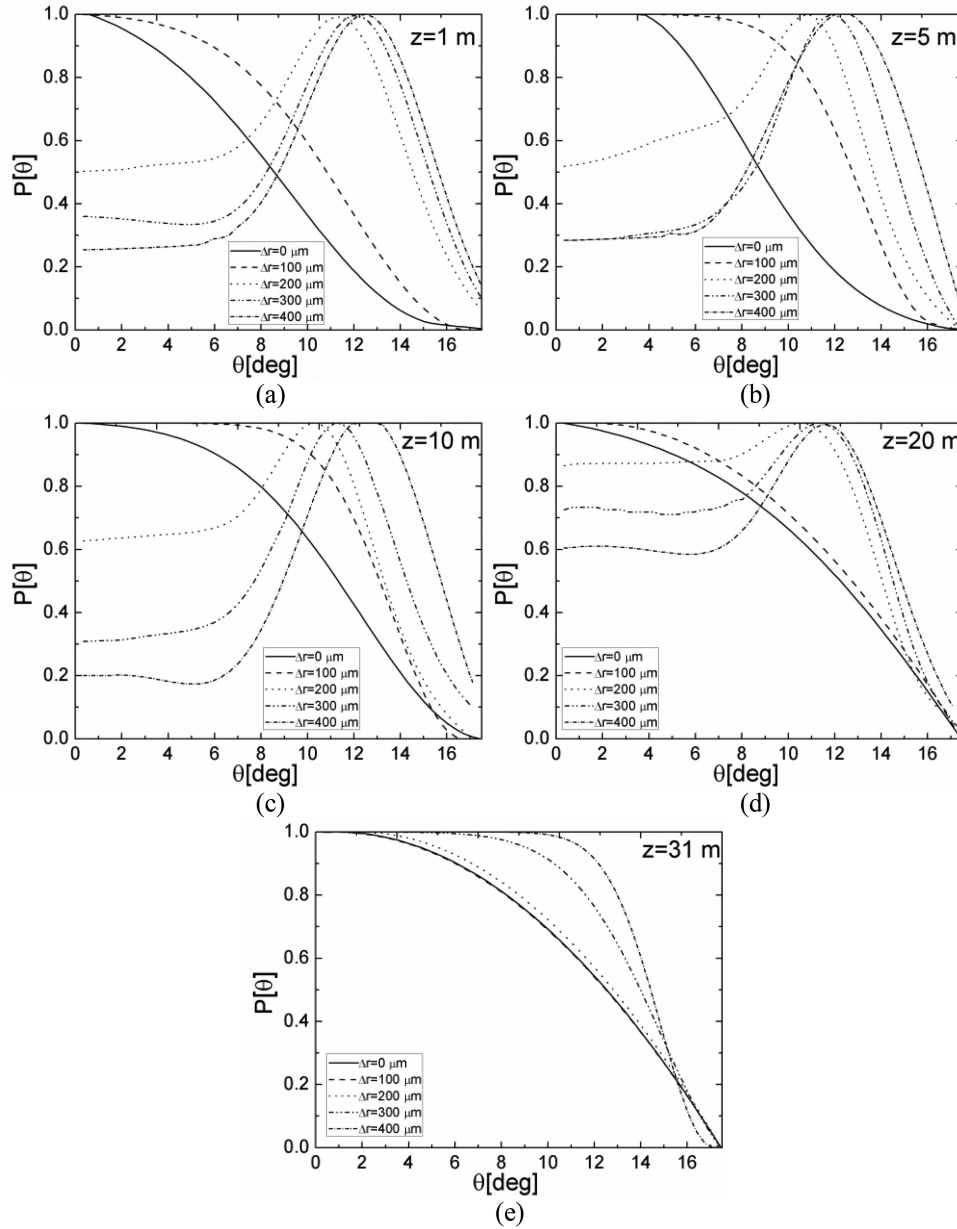


Fig. 1. Normalized output angular power distribution $P(\theta, z)$ over a range of radial offsets Δr measured at different fiber lengths: (a) $z = 1$ m, (b) $z = 5$ m, (c) $z = 10$ m, (d) $z = 20$ m, and (e) $z = 31$ m [18].

fact, the simulated far field patterns are compared to measured far field patterns, which discriminates this approach from the approaches that have been reported in the literature.

II. TIME-INDEPENDENT POWER FLOW EQUATION FOR GI OPTICAL FIBER

The index profile of GI optical fibers may be expressed as:

$$n(r, \lambda) = \begin{cases} n_1(\lambda) \left[1 - 2\Delta(\lambda) \left(\frac{r}{a} \right)^g \right]^{1/2} & (0 \leq r \leq a) \\ n_1(\lambda) (1 - 2\Delta(\lambda))^{1/2} = n_2(\lambda) & (r > a) \end{cases} \quad (1)$$

where g is the core index exponent, a is the core radius, $n_1(\lambda)$ is the maximum index of the core (measured at the fiber axis), $n_2(\lambda)$ is the index of the cladding and $\Delta = [n_1(\lambda) - n_2(\lambda)]/n_1(\lambda)$ is the relative index difference. The optimum value of the core index exponent g to obtain maximum bandwidth depends on the wavelength λ (in free-space) of the source [19].

Time-independent power flow equation for GI optical fiber is [20]–[22]:

$$\frac{\partial P(m, \lambda, z)}{\partial z} = \frac{D}{m} \frac{\partial P(m, \lambda, z)}{\partial m} + D \frac{\partial P^2(m, \lambda, z)}{\partial m^2} \quad (2)$$

where $P(m, \lambda, z)$ is power in the m -th principal mode (modal group), z is the coordinate along the fiber axis from the input fiber end, D is a constant mode coupling coefficient [22]. The

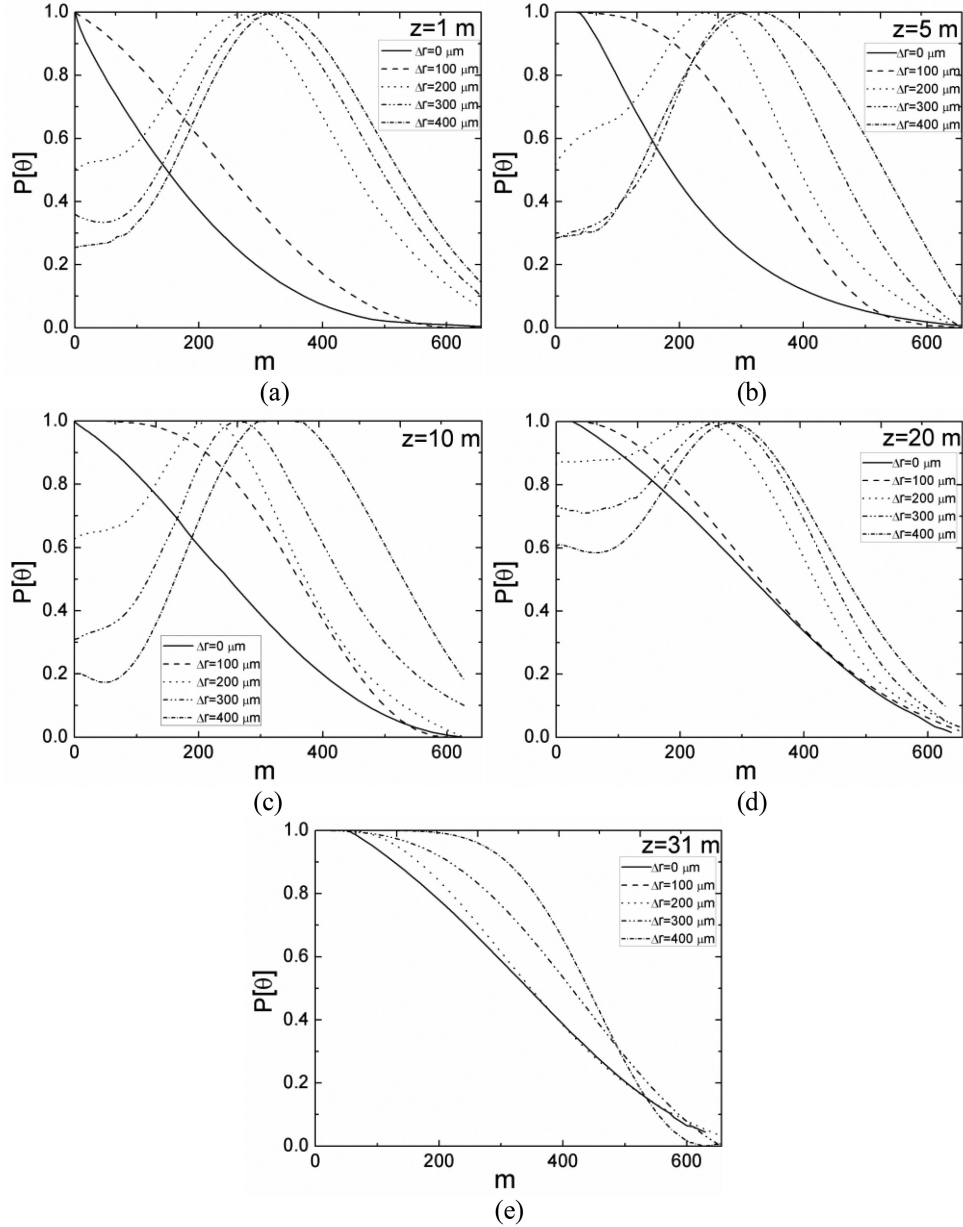


Fig. 2. Normalized output modal power distribution $P(m, \lambda, z)$ over a range of radial offsets Δr , obtained from the measured angular power distributions $P(\theta, z)$ (Fig. 1) using equation (6), at different fiber lengths: (a) $z = 1$ m, (b) $z = 5$ m, (c) $z = 10$ m, (d) $z = 20$ m, and (e) $z = 31$ m.

maximum principal mode number $M(\lambda)$ can be obtained as [20], [21]:

$$M(\lambda) = \sqrt{\frac{g\Delta(\lambda)}{g+2}} akn_1(\lambda) \quad (3)$$

where $k = 2\pi/\lambda$.

Using the explicit finite difference method (EFDM), discretization of equation (2) leads to [23]:

$$P_{i,j+1} = \left(\frac{D\Delta z}{(\Delta m)^2} - \frac{D\Delta z}{2m_i\Delta m} \right) P_{i-1,j} + \left(1 - \frac{2D\Delta z}{(\Delta m)^2} \right) P_{i,j} + \left(\frac{D\Delta z}{2m_i\Delta m} + \frac{D\Delta z}{(\Delta m)^2} \right) P_{i+1,j} \quad (4)$$

where i and j refer to the discretization step lengths Δm and Δz for the mode m and length z , respectively. This is a simple formula for $P_{i,j+1}$ at the $(i, j + 1)^{\text{th}}$ mesh point in terms of the known values along the j^{th} distance row. As first in the authors' best knowledge, numerical solution (4) of the time-independent power flow equation (2) is reported in this work for investigation of the state of mode coupling along a graded-index plastic optical fiber in terms of mode variable (m).

III. RESULTS

We applied our method to the GI POF (OM Giga, Fiber Fin), which we previously investigated experimentally [18]. The core diameter of the fiber was 0.9 mm (fiber diameter was 1 mm). The

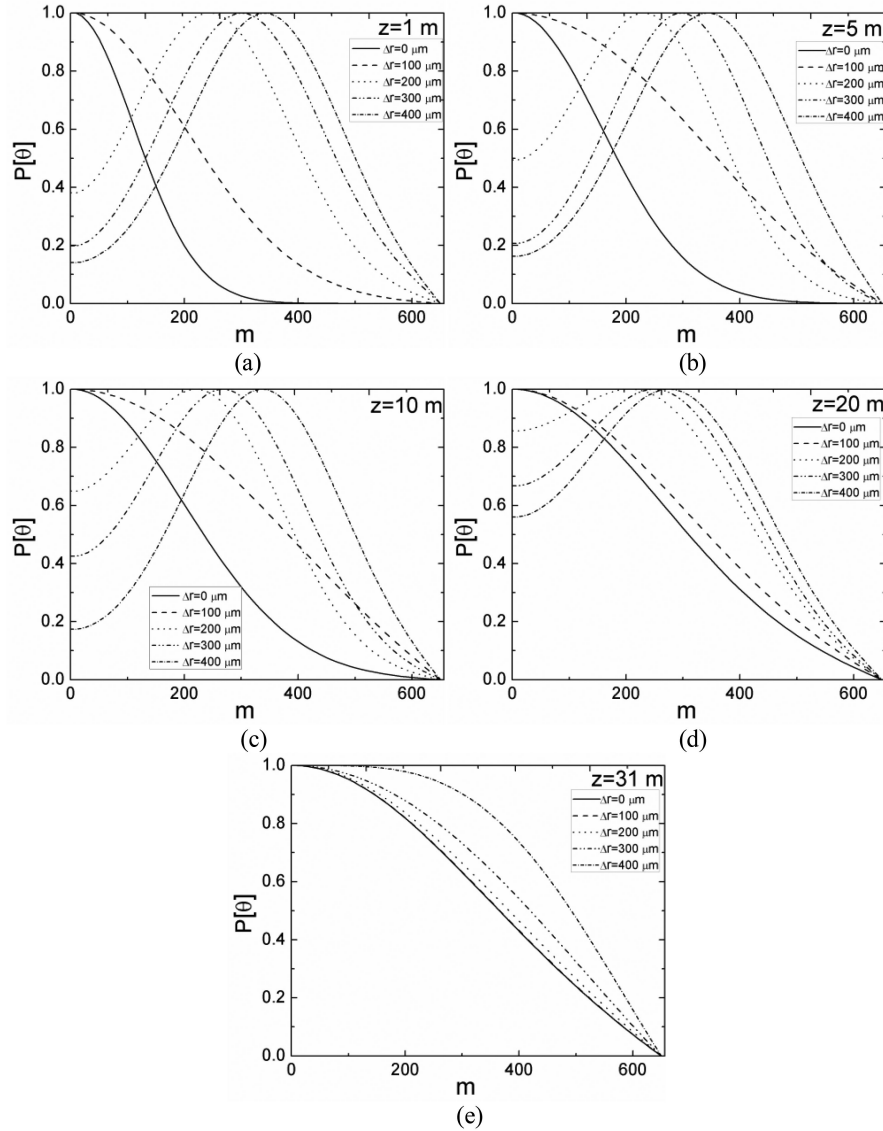


Fig. 3. Normalized output modal power distribution $P(m, \lambda, z)$ over a range of radial offsets Δr obtained by solving numerically the time-independent power flow equation (2) at different fiber lengths (a) $z = 1$ m, (b) $z = 5$ m, (c) $z = 10$ m, (d) $z = 20$ m and (e) $z = 31$ m.

refractive index of the core measured at the fiber axis was $n_1 = 1.522$ and the refractive index of the cladding was $n_2 = 1.492$. A single-mode fiber was butt-coupled to the GI POF being tested and aligned parallel to the fiber axis with controlled lateral displacement to the axis. A HeNe laser operating at 633 nm with output power of 10 mW was used as the light source. The resulting spot size of the excitation was about $8 \mu\text{m}$ in diameter. With increasing radial offset Δr , higher-order mode groups were excited. The relation between the radial offset Δr and the principal mode m excited at the input fiber end is [24]:

$$\frac{m}{M} = \left[\left(\frac{\Delta r}{a} \right)^g + \frac{\theta^2}{2\Delta} \right]^{(g+2)/2g} \quad (5)$$

For the GI POF under investigation, the maximum principal mode number is $M = 656$, $g = 1.80101$ and $\Delta =$

$(n_1 - n_2)/n_1 = 0.019711$. The output modal power distribution $P(m, \lambda, z)$ is obtained from the modified far-field measurements ($P(\theta, z)$) that were based on spatial filtering with a pin hole according to [24]. However, whereas the near field in [24] was projected on the pinhole using a confocal double-lens setup, we used a pinhole of appropriate size directly on the fiber end facet. The pin hole with radius $R_{\text{ph}} = 50 \mu\text{m}$ was placed around the fiber axis as close as possible to the end face of the GI POF. The output modal power distribution $P(m, \lambda, z)$ is obtained from the output angular power distribution $P(\theta, z)$ using the following relation [21], [24]:

$$\frac{m}{M} \approx \left[\frac{\theta^2}{2\Delta} \right]^{(g+2)/2g} \quad (6)$$

Fig. 1 shows the normalized experimental output angular power distributions $P(\theta, z)$ for five radial offsets $\Delta r = 0, 100,$

200, 300 and 400 μm at different fiber lengths [18]. Fig. 2 shows the normalized output modal power distributions $P(m, \lambda, z)$ obtained from the measured output angular power distributions $P(\theta, z)$ using equation (6).

In order to apply numerical solution (4) of the time-independent power flow equation (2), the coupling coefficient D for the fiber has to be known. It is obtained using the following relation [22]:

$$D = \frac{\sigma_{z_2}^2 - \sigma_{z_1}^2}{2(z_2 - z_1)} \quad (7)$$

where $\sigma_{z_1}^2$ and $\sigma_{z_2}^2$ are variances of the modal power distribution $P(m, \lambda, z_1)$ and $P(m, \lambda, z_2)$ measured at the fiber lengths $z_1 > 0$ and $z_2 > 0$, respectively ($z_2 > z_1$), for launch beam without radial offset ($\Delta r = 0$). We used the two standard deviations of $\sigma_{z_2} = 111$ and $\sigma_{z_1} = 262$ which characterize the modal power distributions at fiber lengths $z = 1$ m and $z = 20$ m, respectively (Fig. 2). Introducing these values into equation (7), we have obtained the coupling coefficient of $D = 1482$ 1/m. It is worth noting that the coupling coefficient D obtained using equation (7) takes into account all random anomalies in the optical fiber (such as microscopic bends, voids and cracks, diameter variation, and density and refractive index fluctuations). This is in contrast to the method for determining the coupling coefficient D used by Inoue *et al.* [8], which takes into account only microbending-induced coupling.

We used the step lengths of $\Delta m = 1$ and $\Delta z = 0.00001$ m in order to achieve the stability of our finite-difference scheme (4) for GI POF. The smaller step length $\Delta z = 0.00001$ m for GI POF if compared to $\Delta z = 0.0001$ m (where $\Delta\theta = 0.05^\circ$ is used) for SI POF [23], is due to much larger coupling coefficient for the analyzed GI POF ($D = 1482$ 1/m) if compared to the SI POFs ($D \approx 10^{-4}$ rad²/m) [23], [25]. This leads to the finer mesh and therefore to a larger CPU time for numerical calculations in the case of GI POFs.

Fig. 3 shows the evolution of the normalized output modal power distribution $P(m, \lambda, z)$ with fiber length. In the numerical calculations, a Gaussian beam $P(\theta, z)$ is assumed to be launched with $\langle\theta\rangle = 0^\circ$ and standard deviation $\sigma_\theta = 1.3^\circ$ in equation (5). This standard deviation describes the width of the launched beam measured at the end of a single-mode optical fiber which was butt-coupled to the GI POF being tested. Results are shown for five different radial offsets $\Delta r = 0, 100, 200, 300$ and 400 μm . A good agreement is apparent between the results in Fig. 3 and measurements shown in Fig. 2. Modal power distributions in short fibers indicate that the coupling is stronger for low-order modes (their modal distributions have already shifted towards $m = 0$). As a result of redistribution of the optical power from lower to higher order modes during propagation, the coupling of higher-order modes can be observed only after longer fiber lengths. Power distributions of all modes have shifted their mid-points to zero ($m = 0$) at the coupling length of $L_c = 31$ m (from their initial values at the input fiber end), resulting in the EMD, Fig. 3(d). It is worth noting that coupling length of ≈ 100 m is reported for GI POF investigated by Inoue *et al.* [8]. The coupling length in SI POFs is typically between 14 and 34 m [25]. One can conclude that strong mode coupling characterizes

both SI and GI POFs, which is attributed to their strong intrinsic perturbation effects. In contrast, silica optical fibers have much weaker intrinsic perturbation effects and their coupling lengths could be a few kilometers long [26].

Finally, the method proposed for predicting the evolution of the power distribution along GI POFs can also be employed in GI fibers where the number of modes is not excessive, e.g., GI glass optical fibers with small core size ($2a = 51$ μm) [20] and Perfluorinated GI POFs with smaller core size ($2a = 50$ μm , 62.5 μm , 120 μm).

IV. CONCLUSION

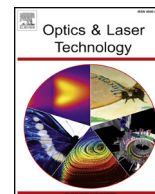
A numerical solution is reported of the time-independent power flow equation employed to investigate the state of mode coupling along a plastic optical fiber with graded refractive index profile in the core. Numerical results have been compared with our previously reported measurements [18]. These results confirm the experimental observation that the coupling length for achieving the equilibrium mode distribution is short in these fibers due to a strong mode coupling process. Such strong coupling is attributed to the strong intrinsic perturbation effects in the fiber.

The experimental verification has demonstrated that the numerical solution of the time-independent power flow equation predicts accurately the evolution of the optical power along the graded-index fiber. Since these fibers are often used for short distances (up to a few tens of meters), such a fiber characterization is important for its employment in data transmission, power delivery, sensing and other systems that may be affected by change in the input power quality.

REFERENCES

- [1] Y. Koike and K. Koike, "Progress in low-loss and high-bandwidth plastic optical fibers," *J. Polym. Sci. B*, vol. 49, pp. 2–17, 2011.
- [2] M. J. Yadlowsky and A. R. Mickelson, "Distributed loss and mode coupling and their effect on time-dependent propagation in multimode fibers," *Appl. Opt.*, vol. 32, pp. 6664–6677, 1993.
- [3] T. Ishigure, M. Kano, and Y. Koike, "Which is more serious factor to the bandwidth of GI POF: Differential mode attenuation or mode coupling?," *J. Lightw. Technol.*, vol. 18, no. 7, pp. 959–965, Jul. 2000.
- [4] A. F. Garito, J. Wang, and R. Gao, "Effects of random perturbations in plastic optical fibers," *Science*, vol. 281, pp. 962–967, 1998.
- [5] S. Louvros, A. C. Iossifides, G. Economou, G. K. Karagiannidis, S. A. Kotsopoulos, and D. Zevgolis, "Time domain modeling and characterization of polymer optical fibers," *IEEE Photon. Technol. Lett.*, vol. 16, no. 2, pp. 455–457, Feb. 2004.
- [6] S. E. Golowich, W. White, W. A. Reed, and E. Knudsen, "Quantitative estimates of mode coupling and differential modal attenuation in perfluorinated graded-index plastic optical fiber," *J. Lightw. Technol.*, vol. 21, no. 1, pp. 111–121, Jan. 2003.
- [7] H. A. Hajjar, D. S. Montero, P. C. Lallana, C. Vázquez, and B. Fracasso, "Spectral and spatial characterization of perfluorinated graded-index polymer optical fibers for the distribution of optical wireless communication cells," *Appl. Opt.*, vol. 54, pp. 1138–1145, 2015.
- [8] A. Inoue, T. Sassa, R. Furukawa, K. Makino, A. Kondo, and Y. Koike, "Efficient group delay averaging in graded-index plastic optical fiber with microscopic heterogeneous core," *Opt. Express*, vol. 21, pp. 17379–17385, 2013.
- [9] T. Noda and Y. Koike, "Bandwidth enhancement of graded index plastic optical fiber by control of differential mode attenuation," *Opt. Express*, vol. 18, pp. 3128–3136, 2010.
- [10] M. Sato, T. Ishigure, and Y. Koike, "Thermally stable high-bandwidth graded index polymer optical fibers," *J. Lightw. Technol.*, vol. 18, no. 7, pp. 952–958, Jul. 2000.

- [11] C. P. Tsekrekos, A. M. J. Koonen, and H. P. A. van den Boom, "Selective excitation of graded-index multimode fibres resulting in annular near field patterns," in *Proc. Symp. IEEE/LEOS Benelux Chapter*, Ghent, Belgium, 2004, pp. 211–214.
- [12] C. P. Tsekrekos, R. W. Smink, B. P. de Hon, A. G. Tijhuis, and A. M. J. Koonen, "Near-field intensity pattern at the output of silica-based graded-index multimode fibers under selective excitation with a single-mode fiber," *Opt. Express*, vol. 15, pp. 3656–3664, 2007.
- [13] C. P. Tsekrekos and A. M. J. Koonen, "Mode-selective spatial filtering for increased robustness in a mode group diversity multiplexing link," *Opt. Lett.*, vol. 32, pp. 1041–1043, 2007.
- [14] C. P. Tsekrekos, M. de Boer, A. Martinez, F. M. J. Willems, and A. M. J. Koonen, "Temporal stability of a transparent mode group diversity multiplexing link," *IEEE Photon. Technol. Lett.*, vol. 18, no. 23, pp. 2484–2486, Dec. 2006.
- [15] S. Schöllmann, S. Soneff, and W. Rosenkranz, "10.7 Gb/s over 300 m GI-MMF using a 2×2 MIMO system based on mode group diversity multiplexing," in *Proc. OFC/NFOEC 2007*, Anaheim, CA, USA, 2007, pp. 1–3.
- [16] C. Schöllmann, C. Xia, and W. Rosenkranz, "Experimental investigations of mode group diversity multiplexing on multimode fibre," in *Proc. Opt. Fiber Commun. Conf. Nat. Fiber Optic Eng. Conf.*, Anaheim, CA, USA, 2006, p. 3.
- [17] J. Siuzdak, L. Maksymiuk and G. Stepniak, "A 2 and 3 channel mode group diversity multiplexing transmission over graded and step index multimode fibers," in *Proc. 34th Eur. Conf. Opt. Commun.*, Brussels, Belgium, 2008, pp. 1–2.
- [18] C. Alexander Bunge *et al.*, "Experimental mode-coupling analysis of graded-index polymer optical fibers in mode domain," submitted for publication.
- [19] K. Ohdoko, T. Ishigure, and Y. Koike, "Propagating mode analysis and design of waveguide parameters of GI POF for very short-reach network use," *IEEE Photon. Technol. Lett.*, vol. 17, no. 1, pp. 79–81, Jan. 2005.
- [20] K. Kitayama, S. Seikai, and N. Uchida, "Impulse response prediction based on experimental mode coupling coefficient in a 10-km long graded-index fiber," *IEEE J. Quant. Electron.*, vol. 16, no. 3, pp. 356–362, Mar. 1980.
- [21] R. Olshansky, "Mode coupling effects in graded-index optical fibers," *Appl. Opt.*, vol. 14, pp. 935–945, 1975.
- [22] S. Savović and A. Djordjevich, "New method for calculating the coupling coefficient in graded index optical fibers," *Opt. Laser Technol.*, vol. 101, pp. 223–226, 2019.
- [23] A. Djordjevich and S. Savović, "Investigation of mode coupling in step index plastic optical fibers using the power flow equation," *IEEE Photon. Technol. Lett.*, vol. 12, no. 11, pp. 1489–1491, Nov. 2000.
- [24] K. Nagano and S. Kawakami, "Measurements of mode conversion coefficients in graded-index fibers," *Appl. Opt.*, vol. 19, pp. 2426–2434, 1980.
- [25] S. Savović and A. Djordjevich, "Mode coupling in strained and unstrained step-index plastic optical fibers," *Appl. Opt.*, vol. 45, pp. 6775–6780, 2006.
- [26] S. Savović, A. Djordjevich, A. Simovic, and B. Drljača, "Equilibrium mode distribution and steady-state distribution in 100–400 μm core step-index silica optical fibers," *Appl. Opt.*, vol. 50, pp. 4170–4173, 2011.



Full length article

Enhanced bandwidth of W type plastic optical fibers designed from singly clad step index plastic optical fibers

Ana Simović^a, Svetislav Savović^{a,b,*}, Branko Drljača^c, Alexandar Djordjevich^{b,*}

^a University of Kragujevac, Faculty of Science, R. Domanovića 12, 34000 Kragujevac, Serbia

^b City University of Hong Kong, 83 Tat Chee Avenue, Hong Kong, China

^c Faculty of Science, University of Kosovska Mitrovica, Lole Ribara 29, Kosovska Mitrovica, Serbia

HIGHLIGHTS

- We propose a multimode W type plastic optical fiber (POF).
- For different widths of the inner cladding and refractive index of the outer cladding, the bandwidth is determined.
- Bandwidth of W type POF is significantly higher than the bandwidth of the original singly clad POF.
- The bandwidth of W type plastic optical fiber is enhanced by reducing the width of its inner cladding.

ARTICLE INFO

Keywords:

W type plastic optical fiber
Step-index optical fiber
Power flow equation
Bandwidth
Steady-state loss

ABSTRACT

We propose a multimode W type (doubly clad) plastic optical fiber which takes the characteristic W-shaped index profile designed from a multimode singly clad step index plastic optical fiber upon modification of the cladding layer of the latter. For different widths of the inner cladding and refractive index of the outer cladding, the bandwidth and steady-state loss are determined for such W type plastic optical fiber. We have shown that bandwidth of W type plastic optical fiber is significantly higher than the bandwidth of the original singly clad step index plastic optical fiber. The bandwidth of W type plastic optical fiber is mostly enhanced by reducing the width of its inner cladding.

1. Introduction

Recently, the requirement for high-bandwidth that has been achieved with optical communications technology has rapidly expanded to datacoms applications in both office and home area networks. Furthermore, in view of the advances in both intelligent driving systems and multimedia services, this concept becomes a powerful approach for use in optical networking strategies for automobile communication systems. These systems are usually implemented using multimode plastic optical fibers (POFs), which have large cores and high numerical apertures (NAs) due to their ease of connection and robustness for tight bends.

Multimode optical fibers are usually singly clad (SC) in terms of the number of functional cladding layers. A various techniques have been proposed for improving bandwidth and attenuation properties of these fibers, such as special detection [1], modulation [2], equalization [3], and compensation of modal-dispersion [4]. The analysis and design of refractive index profile of multimode fiber with a view of advancing

fiber transmission characteristics have attracted a much attention in the last few decades. A variety of designs of step-index (SI), graded index (GI) and W type fibers (doubly clad fibers) has been proposed either for a long-distance communication links or high capacity local area networks [5–7]. It has been shown that waveguide dispersion is smaller in the W type fiber than it is in the singly-clad (SC) fiber [8]. W type fiber has a wider bandwidth and lower bending losses compared to a corresponding SC fiber. For glass optical fibers, the bandwidth-distance product is typically around 30 MHz·km for the SC variety and around 50 MHz·km for the W type. For POFs, these figures would typically be 15 MHz·km for the SC and 200 MHz·km for the W type fibers [5,7,9].

A W type fiber has an intermediate layer between its outer cladding and core. This layer lowers dispersion, widens bandwidth and reduces the number of guided modes. It achieves this by lowering the fiber's effective numerical aperture by reducing the number of guided modes – guided modes are thus held tighter to the core [10].

In general, due to mode coupling optical power is transferred between modes [11]. This reduces modal dispersion and improves fiber

* Corresponding authors at: University of Kragujevac, Faculty of Science, R. Domanovića 12, 34000 Kragujevac, Serbia.

E-mail address: savovic@kg.ac.rs (S. Savović).

<https://doi.org/10.1016/j.optlastec.2018.10.020>

Received 12 June 2018; Received in revised form 16 August 2018; Accepted 12 October 2018

0030-3992/ © 2018 Elsevier Ltd. All rights reserved.

bandwidth [12]. Methods are needed for calculating modal attenuation, dispersion, and coupling to lossy modes of W type fiber's intermediate layer, and for optimizing the fiber's refractive index profile in order to minimize the group delay difference between modes in the output field [9,13].

The bandwidth enhancement of W type POFs in respect to the GI POFs has been reported by Ishigure et al. [14]. In this work, we investigated how the bandwidth can be enhanced for variously configured W type POFs with SI distribution of the fiber core, in the terms of depth and width of the fiber's intermediate layer. The W type POFs proposed in this work has a simpler refractive index distribution of the fiber core if compared to the W type plastic optical fiber with GI distribution of the fiber core proposed by Ishigure et al. [14].

2. Time independent and time-dependent power flow equation

In multimode fibers, the guided modes with the same principal mode number can be treated as one mode group. Coupling was said to occur mainly between neighboring modes because the coupling strength decreases fast with the mode spacing [11]. For mode coupling between neighboring mode groups, the power flow can be represented by the Gloge's time independent coupled-power equation [11]:

$$\frac{\partial P(\theta, z)}{\partial z} = -\alpha(\theta)P(\theta, z) + \frac{1}{\theta} \frac{\partial}{\partial \theta} \left[\theta D(\theta) \frac{\partial P(\theta, z)}{\partial \theta} \right] \quad (1)$$

where $P(\theta, z)$ is the angular power distribution at distance z from the input end of the fiber, θ is the propagation angle with respect to the core axis, $D(\theta)$ is the coupling coefficient, and $\alpha(\theta) = \alpha_0 + \alpha_d(\theta)$ is the modal attenuation – where α_0 represents conventional losses (absorption and scattering) and is neglected as it features only as a multiplier $\exp(-\alpha_0 z)$ in the solution that is normalized. By solving Eq. (1) one can obtain an output angular power distribution at any fiber length and launch beam distribution. In practice Eq. (1) is solved up to the fiber length z_s at which a steady state distribution (SSD) is established in the fiber. SSD indicates the completion of the mode coupling process and the independence of the output light distribution from launch conditions.

In order to calculate the bandwidth of optical fiber, we solved the time-dependent power flow equation, which is in the form [12]:

$$\frac{\partial p(\theta, z, t)}{\partial z} + \tau(\theta) \frac{\partial p(\theta, z, t)}{\partial t} = -\alpha(\theta)P(\theta, z, t) + \frac{1}{\theta} \frac{\partial}{\partial \theta} \left[\theta D(\theta) \frac{\partial p(\theta, z, t)}{\partial \theta} \right] \quad (2)$$

where $p(\theta, z, t)$ is the angular power distribution at distance z and time t ; $\tau(\theta)$ is modal delay per unit length. The time dependent power flow Eq. (2) has been commonly employed for obtaining the bandwidth in SI and W type fibers [12,15–17]. The same form of equation, in which mode group number “ m ” replaces a variable θ , has been used for obtaining the bandwidth in GI optical fibers [18]. The finite element method and implicit finite difference method in frequency domain [19], as well as a multimode fiber link model [20] can also be employed in calculating the fiber bandwidth. We find that approach presented in this manuscript is one of the simplest and most effective in calculating the fiber bandwidth. In order to obtain the frequency response in the frequency domain, the Fourier transformation of Eq. (2) becomes:

$$\frac{\partial P(\theta, z, \omega)}{\partial z} + j\omega\tau(\theta)P(\theta, z, \omega) = -\alpha(\theta)P(\theta, z, \omega) + \frac{1}{\theta} \frac{\partial}{\partial \theta} \left[\theta D(\theta) \frac{\partial P(\theta, z, \omega)}{\partial \theta} \right] \quad (3)$$

where $\omega = 2\pi f$ is the angular frequency, and

$$P(\theta, z, \omega) = \int_{-\infty}^{+\infty} p(\theta, z, t) \exp(-j\omega t) dt \quad (4)$$

The boundary conditions are:

$$P(\theta_m, z, \omega) = 0, D(\theta) \frac{\partial P(\theta, z, \omega)}{\partial \theta} \Big|_{\theta=0} = 0 \quad (5)$$

It is apparent that $P(\theta, z, \omega)$ is complex. By separating $P(\theta, z, \omega)$ into the real part $P_r(\theta, z, \omega)$ and imaginary part $P_i(\theta, z, \omega)$ and assuming a constant coupling coefficient D [7,21,22], Eq. (2) can be rewritten as the following simultaneous partial differential equations:

$$\frac{\partial P_r(\theta, z, \omega)}{\partial z} = -\alpha(\theta)P_r(\theta, z, \omega) + \frac{D}{\theta} \frac{\partial P_r(\theta, z, \omega)}{\partial \theta} + D \frac{\partial^2 P_r(\theta, z, \omega)}{\partial \theta^2} + \omega\tau P_i(\theta, z, \omega) \quad (6a)$$

and

$$\frac{\partial P_i(\theta, z, \omega)}{\partial z} = -\alpha(\theta)P_i(\theta, z, \omega) + \frac{D}{\theta} \frac{\partial P_i(\theta, z, \omega)}{\partial \theta} + D \frac{\partial^2 P_i(\theta, z, \omega)}{\partial \theta^2} - \omega\tau P_r(\theta, z, \omega) \quad (6b)$$

where

$$P(\theta, z, \omega) = P_r(\theta, z, \omega) + jP_i(\theta, z, \omega) \quad (7)$$

We solved two simultaneous Eqs. (6) by the explicit finite difference method. It is worth noting that the simplifying assumption of constant coupling coefficient D , which is independent of the propagation angle, in SI POFs has been commonly used by many authors [12,23–25]. In our previous work [26] we have shown that modeling mode coupling in SI POFs assuming a constant coupling coefficient D can be used instead of the more complicated approach with angle-dependent coupling coefficient.

If $P_r(\theta, z, \omega)$ and $P_i(\theta, z, \omega)$ are obtained by solving Eq. (6), the transmission characteristics can be calculated. Thus the frequency response $H(z, \omega)$ at distance z from the input end of the fiber is:

$$H(z, \omega) = \frac{2\pi \int_{\theta_m}^{\theta_m} \theta [P_r(\theta, z, \omega) + jP_i(\theta, z, \omega)] d\theta}{2\pi \int_{\theta_m}^{\theta_m} \theta [P_r(\theta, 0, \omega) + jP_i(\theta, 0, \omega)] d\theta} \quad (8)$$

The modal power distribution $P_F(\theta, z, \omega)$ and the spatial transient of power $P_L(z, \omega)$ can be obtained by:

$$P_F(\theta, z, \omega) = [P_r(\theta, z, \omega)^2 + P_i(\theta, z, \omega)^2]^{1/2} \quad (9)$$

$$P_L(z, \omega) = 2\pi \int_{\theta_m}^{\theta_m} \theta P_F(\theta, z, \omega) d\theta \quad (10)$$

The doubly clad (W type) fiber transforms into a singly clad one by allowing the thickness of the intermediate layer (δa in Fig. 1) to either vanish or expand to fiber thickness. In the vanishing case, the core and the outer layer comprise the “SC_p” fiber. In the other case, the core and the intermediate layer as the only cladding form the “SC_q” fiber. A W type fiber with index profile shown in Fig. 1b can be viewed as the SC_q fiber and an additional cladding. Modes propagating along the SC_q fiber with subcritical angles $\theta < \theta_q$ ($\theta_q \cong (2\Delta_q)^{1/2}$), where $\Delta_q = (n_0 - n_q)/n_0$, are guided. The same is true for those propagating through the complete W-fiber with angles θ below the critical value θ_p for the SC_p fiber, that has only the outer cladding of the W type fiber (and lacks the intermediate layer), $\theta_p \cong (2\Delta_p)^{1/2}$, where $\Delta_p = (n_0 - n_p)/n_0$. However, modes with angles between θ_p and θ_q are transformed into leaky modes. Hence [27],

$$\alpha_L(\theta) = \frac{4(\theta^2 - \theta_p^2)^{1/2} \theta^2 (\theta_q^2 - \theta^2)}{a(1 - \theta^2)^{1/2} \theta_q^2 (\theta_q^2 - \theta_p^2)} \exp[-2\delta a n_0 k_0 (\theta_q^2 - \theta^2)^{1/2}] \quad (11)$$

where $k_0 = 2\pi/\lambda$ is the free-space wave number, a is core radius and δa intermediate layer (inner cladding) width. In an SC fiber, experimental results show that attenuation remains constant throughout the guided-mode region and rises quite steeply in the radiation-mode region [23].

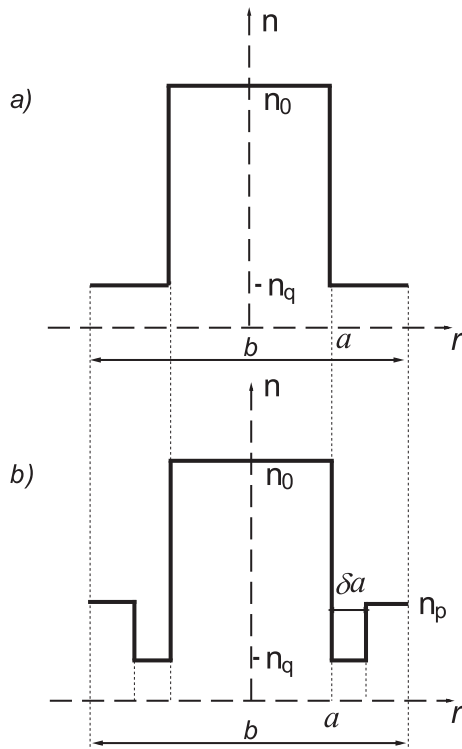


Fig. 1. Refractive index profile of (a) SC POF and (b) W POF.

Consequently, the modal attenuation in a W type fiber can be expressed as:

$$\alpha_d(\theta) = \begin{cases} 0 & \theta \leq \theta_p \\ \alpha_l(\theta) & \theta_p < \theta < \theta_q \\ \infty & \theta \geq \theta_q \end{cases} \quad (12)$$

Modal delay is expressed in terms of θ by:

$$\tau(\theta) = \frac{n_0}{c} \frac{1}{\cos \theta} \cong \frac{n_0}{c} \left(1 + \frac{\theta^2}{2} \right) = \tau_0 + \tau_d(\theta) \quad (13)$$

where c is the light velocity in free space. The first term τ_0 is common to all modes. It is the difference in group delay that determines the bandwidth. Therefore, only $\tau_d(\theta)$ is to be considered in the calculations. The bandwidth of a fiber determines the maximum transmission data rate and it is determined by the frequency response $H(z, \omega)$:

$$P_{L(out)}(z, \omega) = H(z, \omega) P_{L(in)}(z = 0, \omega) \quad (14)$$

The frequency response defines the bandwidth (–3 dB bandwidth) of the optical fiber as the frequency at which $H(z, \omega)$ is reduced to half the DC value, that is when it is reduced by 3 dB. In our knowledge for the first time, we determined the bandwidth of the W type POF by numerical solving the time-dependent power flow equation.

3. Numerical results

In this paper we investigate the transmission characteristics of W type POF which is designed from the SC POF (PGU-CD1001-22E) experimentally investigated by Mateo et al. [15]. A W-shape refractive index model is used for the structure shown in Fig. 1b. The characteristics of SC POF (Fig. 1a) were: core refractive index $n_0 = 1.492$, cladding refractive index $n_q = 1.4057$, critical angle (measured inside the fiber) $\theta_c = 19.6^\circ$, core diameter $d = 0.98$ mm, and fiber diameter $b = 1$ mm. The W type POF is designed from this SC POF in such a way that the W type POF's inner cladding retains the refractive index n_q of the SC POF's cladding while an outer cladding of the W type POF has a

refractive index n_p which is higher than refractive index n_q of the inner cladding (Fig. 1b). The three values of the refractive index of the outer cladding n_p were used in the modeling: $n_p = 1.4775, 1.4693, 1.4591$, corresponding to the critical angles $\theta_p = 8^\circ, 10^\circ, 12^\circ$, respectively. The normalized intermediate layer widths $\delta = 0.001, \delta = 0.002$ and $\delta = 0.003$ were employed (actual width is $\delta \cdot a$ mm). The coupling coefficient $D = 3.5 \times 10^{-4} \text{ rad}^2/\text{m}$ and wavelength $\lambda = 650$ nm were used in the calculations [28]. In the calculations, the launch beam distribution was in the Gaussian form with a FWHM = 7.5° .

Using the time-independent power flow equation, we calculated the length z_s , at which the SSD is achieved in W type POF and SC POF. The main difference between modeling the SC type and W POF is the existence of leaky modes in the latter, which propagate between angles θ_p and θ_q . Fig. 2 shows the output angular power distribution in SC POF and three different W type POFs with the widths of the intermediate layer $\delta = 0.001, \delta = 0.002$ and $\delta = 0.003$. One can see that at short fiber length (Fig. 2a), the output angular power distribution is almost the same in the SC POF and W type POFs. With increasing the fiber length, the SSD is first achieved in W type POF with $\delta = 0.001$ at fiber length $z_s = 15$ m, $\delta = 0.002$ at fiber length $z_s = 35$ m, then in W type POF with $\delta = 0.003$ at $z_s = 58$ m, and finally in SC POF at $z_s = 75$ m. In the case of W type POF fibers, appearance of leaky mode losses reduces the number of higher modes involved in the coupling process, thus reducing the length z_s . Leaky mode losses decrease with increasing the width of intermediate layer, which results in a longest length z_s in the case $\delta = 0.003$. With increasing the critical angle θ_p (decreasing the refractive index n_p) the length z_s slightly increases for three different widths of the inner cladding (Table 1). The change of the critical angle θ_p affects the lower leaky modes but not the highest leaky modes that have a larger impact on the length z_s . The influence of the width of the inner cladding δ on leaky mode losses is more pronounced than the influence of critical angle θ_p , which leads to a stronger influence of δ on the length z_s .

Our numerical solution of the time-dependent power flow equation is illustrated in Fig. 3 which shows the transmission length dependence of the bandwidth for W type POF for $\delta = 0.001, 0.002$ and 0.003 , and $n_p = 1.4775, 1.4693, 1.4591$, with corresponding critical angles $\theta_p = 8^\circ, 10^\circ$ and 12° , respectively, for Gaussian launch beam distribution with FWHM = 7.5° . From Fig. 3 one can also compare the bandwidth for two samples of the SC POF obtained experimentally by Mateo et al. [15] and our numerical results. A good agreement between experimental results [15] and our numerical results is seen. It can be seen that the bandwidth of W type POF is higher compared to the bandwidth of SC POF. This is explained by the leaky mode losses in the case of W type POF, which reduce the number of higher modes which remain guided along the fiber, thus decreasing the modal dispersion and increasing the bandwidth. The bandwidth is highest for the narrowest inner cladding ($\delta = 0.001$), because of larger leaky mode losses compared to the case of $\delta = 0.002$ and 0.003 . With increasing the refractive index of the outer cladding n_p (decreasing the critical angle θ_p), there is an increase in leaky mode losses, which results in the highest values of the bandwidth in the case of $\delta = 0.001$. The influence of n_p (critical angle θ_p) on the bandwidth is negligible in the case of $\delta = 0.003$, due to the low influence of critical angle θ_p on the leaky mode losses. It can be seen from Fig. 3 that the improvement of the bandwidth of W type POF is more pronounced at longer fiber lengths. Since a narrow launch beam distribution is assumed in the calculations, only guided modes are excited at the input fiber length. Therefore the role of leaky modes is of less significance at short fiber lengths. Due to mode coupling, more leaky modes are filtered out at longer fiber lengths, leading to the significant improving of the W type POF's bandwidth.

The trade-off relation between bandwidth and steady-state loss for W type POF and SC POF is shown in Fig. 4. With increasing the leaky mode losses the steady-state losses also increases. A trade-off relation between bandwidth and loss would have to be considered in designing the optimum W type POF by controlling parameters of the intermediate

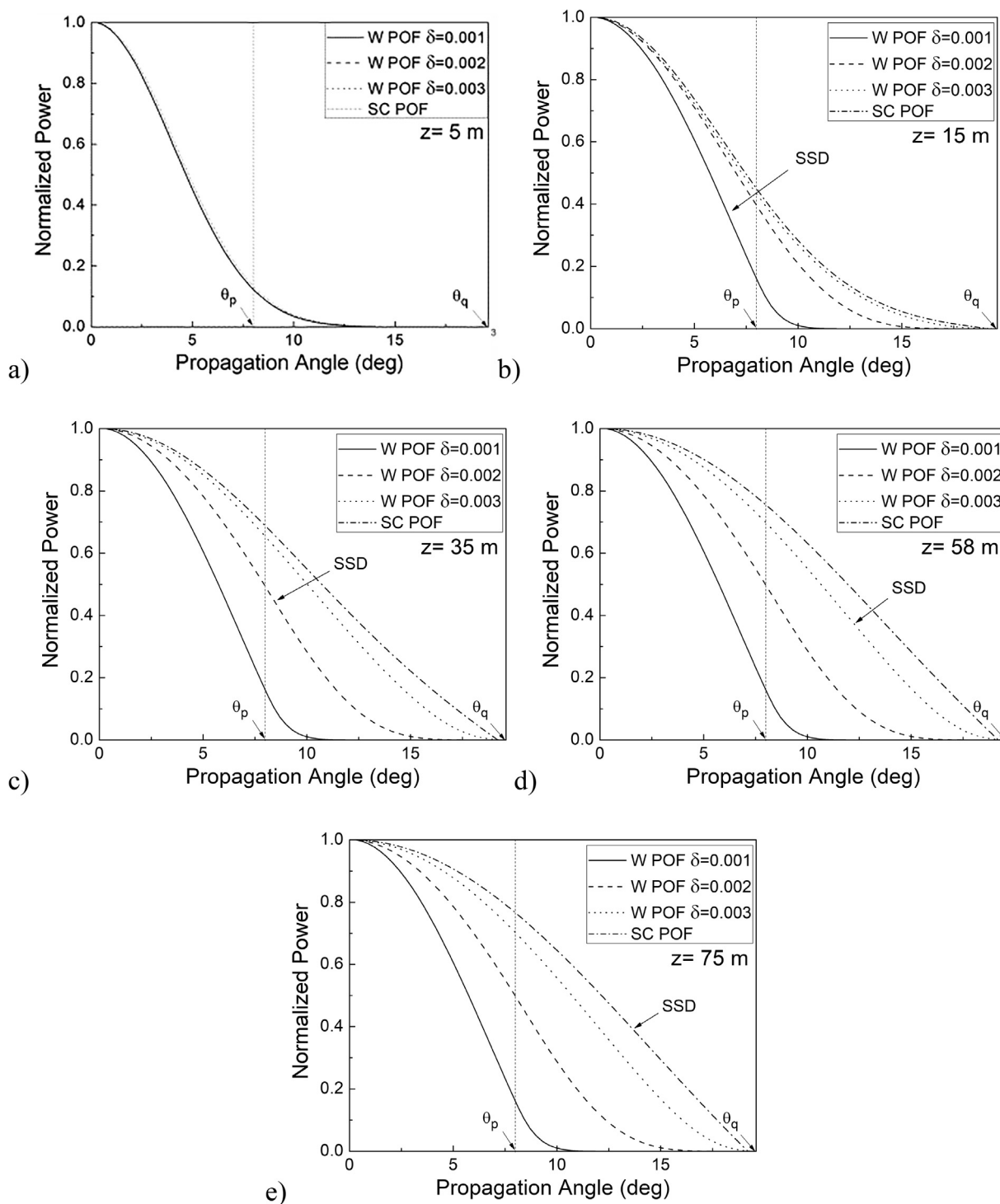


Fig. 2. Calculated output angular power distribution in W POF with $\delta = 0.002$ and $\delta = 0.003$, $n_p = 1.4775$ ($\theta_p = 8^\circ$), and SC POF at fiber lengths (a) 5 m, (b) 35 m (SSD for W POF with $\delta = 0.002$), (c) 58 m (SSD for W POF with $\delta = 0.003$) and (d) 75 m (SSD for SC POF), for Gaussian launch beam distribution with FWHM = 7.5° .

layer thickness and refractive index of the outer cladding. In practical fiber deployment conditions a macro-bends are expected to occur. It has been shown that the coupling coefficient D for the fibers with macro bands are higher than those found for straight ones [29]. This increase of mode coupling could be explained by microscopical material changes. As a consequence, substantially shorter coupling lengths L_c (where equilibrium mode distribution is achieved) are obtained for fibers with macrobands than for straight ones [29]. L_c is the fiber length after which the bandwidth becomes proportional to $1/z^{1/2}$ instead of $1/z$ (z is the fiber length). The shorter the length L_c , the

earlier the bandwidth would switch from the functional dependence of $1/z$ to $1/z^{1/2}$ (slower bandwidth decrease). On the other hand, mode coupling increases the amount of power radiated in fiber curves or bends and thus increases the fiber loss. In conclusion, in our best knowledge for the first time, by solving the time dependent power flow equation, we have shown that bandwidth in W type POFs with SI distribution of the fiber core is significantly higher than the bandwidth of the original singly clad SI POF. Although the W type POFs proposed in this work have a SI distribution of the fiber core, which is much simpler than the GI distribution of the

Table 1

Length z_s at which the SSD is achieved in W type POF with $\delta = 0.001$, $\delta = 0.002$ and $\delta = 0.003$, and critical angles of the outer cladding $\theta_p = 8^\circ$, 10° and 12° .

	z_s [m]		
	$\theta_p = 8^\circ$	$\theta_p = 10^\circ$	$\theta_p = 12^\circ$
$\delta = 0.001$	15	22	30
$\delta = 0.002$	35	38	40
$\delta = 0.003$	58	60	60

fiber core, a significant enhancement of the bandwidth of such W type POFs could be achieved with appropriate choice of the parameters of the intermediate layer.

4. Conclusion

A new design of POF which takes the characteristic W-shaped index profile is proposed. A W type POF is designed from a multimode SC POF upon modification of its cladding layer. By numerically solving the time-dependent power-flow equation under varied fiber design parameters, we have shown that the bandwidth of W type POF is higher than the bandwidth of the original SC POF. This enhancement of the bandwidth is due to the leaky mode losses in the W POF, which reduce the number of higher leaky modes which remain guided along the fiber,

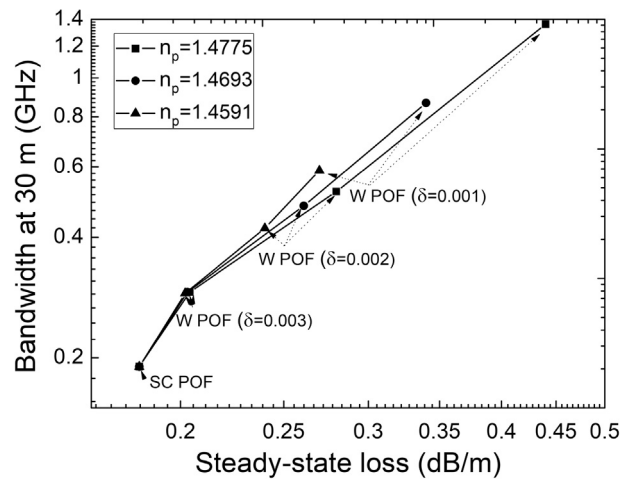


Fig. 4. Numerical results for trade-off relation between bandwidth and steady-state loss for W POF and SC POF.

thus decreasing the modal dispersion and increasing the bandwidth. The bandwidth of W type POF can be enhanced by reducing the width of its inner cladding. With increasing the leaky mode losses the steady-state losses also increases, thus a trade-off relation between bandwidth and loss would have to be considered in designing the optimum W type

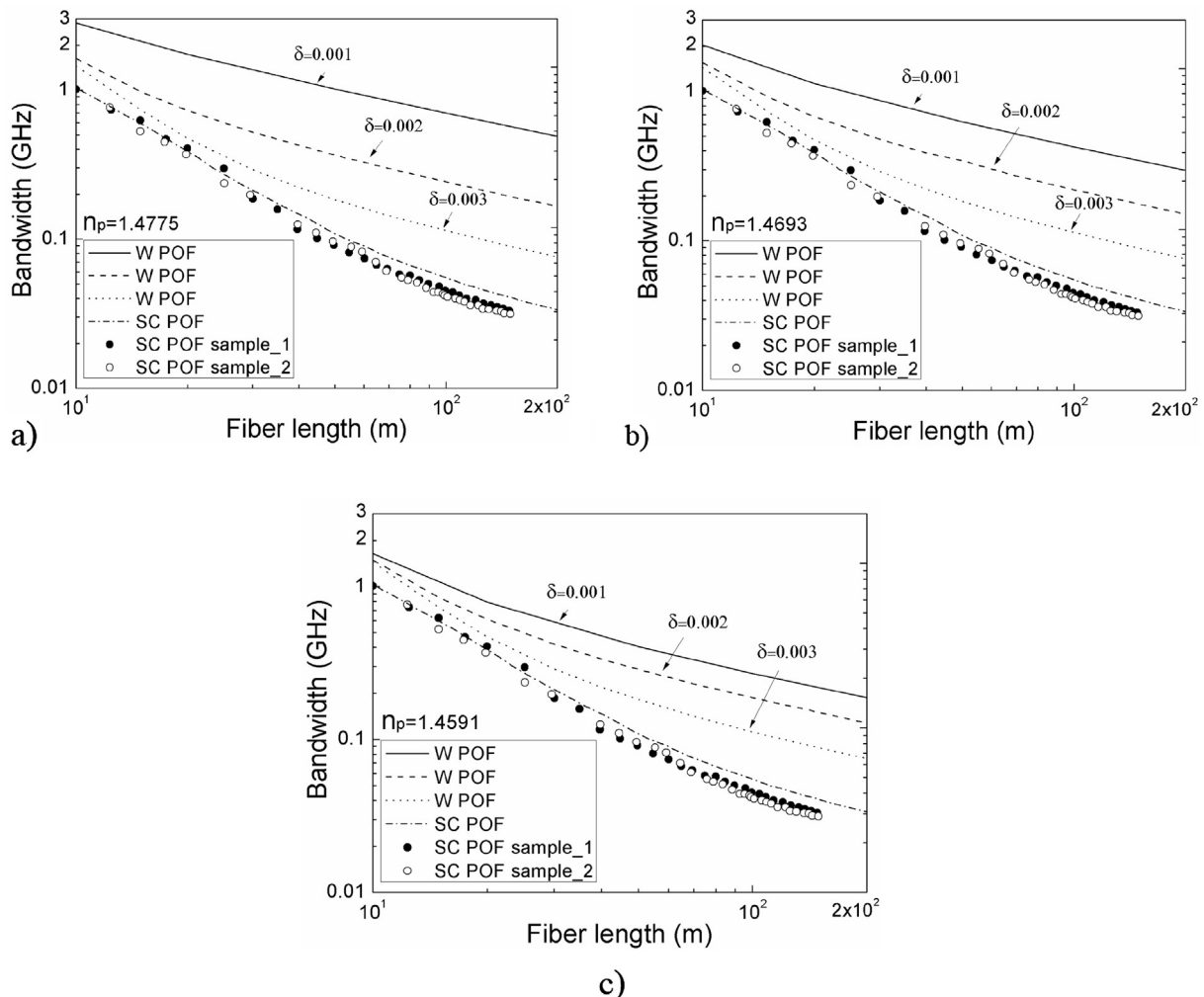


Fig. 3. Numerical results for transmission length dependence of bandwidth for W POF with $\delta = 0.002$ and 0.003 , for (a) $\theta_p = 8^\circ$, (b) 10° and (c) 12° and SC POF. Open and solid dots represent experimental results for SC POF obtained by Mateo et al. [15].

POF.

Acknowledgements

This work was supported in part by the grant from Serbian Ministry of Education, Science and Technological Development through the Project No. 171011 and by the Strategic Research Grant of City University of Hong Kong (Project No. CityU 7004600).

References

- [1] K.M. Patel, S.E. Ralph, Enhanced multimode fiber link performance using a spatially resolved receiver, *IEEE Photon. Technol. Lett.* 14 (2002) 393–395.
- [2] E.J. Tyler, M. Webster, R.V. Penty, I.H. White, S. Yu, J. Rorison, Subcarrier modulated transmission of 2.5 Gb/s over 300 m of 62.5- μm -core diameter multimode fiber, *IEEE Photon. Technol. Lett.* 14 (2002) 1743–1745.
- [3] X. Zhao, F.S. Choa, Demonstration of 10 Gb/s transmission over 1.5-km-long multimode fiber using equalization techniques, *IEEE Photon. Technol. Lett.* 14 (2002) 1187–1189.
- [4] J.S. Abbott, G.E. Smith, C.M. Truesdale, Multimode fiber link dispersion compensator, U.S. Patent 6 363 195, 2002.
- [5] T. Yamashita, M. Kagami, Fabrication of light-induced self-written waveguides with a W-shaped refractive index profile, *J. Lightwave Technol.* 23 (2005) 2542–2548.
- [6] M. Asai, Y. Inuzuka, K. Koike, S. Takahashi, Y. Koike, High-bandwidth graded-index plastic optical fiber with low-attenuation, high-bending ability, and high-thermal stability for home-networks, *J. Lightwave Technol.* 29 (2011) 1620–1626.
- [7] K. Mikoshiba, H. Kajioka, Transmission characteristics of multimode W-type optical fiber: experimental study of the effect of the intermediate layer, *Appl. Opt.* 17 (1978) 2836–2841.
- [8] K. Takahashi, T. Ishigure, Y. Koike, Index profile design for high-bandwidth W-shaped plastic optical fiber, *J. Lightwave Technol.* 24 (2006) 2867–2876.
- [9] T. Tanaka, S. Yamada, M. Sumi, K. Mikoshiba, Microbending losses of doubly clad (W-type) optical fibers, *Appl. Opt.* 18 (1977) 2391–2394.
- [10] Babita, V. Rastogi, A. Kumar, Design of large-mode-area three layered fiber structure for femtosecond laser pulse delivery, *Opt. Commun.* 293 (2013) 108–112.
- [11] D. Gloge, Optical power flow in multimode fibers, *Bell Syst. Tech. J.* 51 (1972) 1767–1783.
- [12] D. Gloge, Impulse response of clad optical multimode fibers, *Bell Syst. Tech. J.* 52 (1973) 801–816.
- [13] S. Savović, A. Simović, A. Djordjevich, Explicit finite difference solution of the power flow equation in W-type optical fibers, *Opt. Laser Technol.* 44 (2012) 1786–1790.
- [14] T. Ishigure, H. Endo, K. Ohdoko, K. Takahashi, Y. Koike, Modal bandwidth enhancement in a plastic optical fiber by W-refractive index profile, *J. Lightwave Technol.* 23 (2005) 1754–1762.
- [15] J. Mateo, M.A. Losada, J. Zubia, Frequency response in step index plastic optical fibers obtained from the generalized power flow equation, *Opt. Express* 17 (2009) 2850–2860.
- [16] S. Savović, B. Drljača, M.S. Kovačević, A. Djordjevich, J.S. Bajić, D.Z. Stupar, G. Stepniak, Frequency response and bandwidth in low NA step index plastic optical fibers, *Appl. Opt.* 53 (2014) 6999–7003.
- [17] A. Simović, S. Savović, B. Drljača, A. Djordjevich, Influence of the fiber design and launch beam on transmission characteristics of W-type optical fibers, *Opt. Laser Technol.* 68 (2015) 151–159.
- [18] K. Kitayama, S. Seikai, N. Uchida, Impulse response prediction based on experimental mode coupling coefficient in a 10-km long graded-index fiber, *IEEE J. Quant. Electron.* 16 (1980) 356–362.
- [19] F. Breyer, Multilevel Transmission and Equalization for Polymer Optical Fiber Systems, PhD Thesis TECHNISCHE UNIVERSITÄT MÜNCHEN, München, Germany, 2010.
- [20] P. Pepeljugoski, S.E. Golowich, P. Kolesar, A. John Ritger, A. Risteski, Modeling and simulation of next-generation multimode fiber links, *J. Lightwave Technol.* 21 (2003) 1242–1255.
- [21] A. Djordjevich, S. Savović, P.W. Tse, B. Drljača, A. Simović, Mode coupling in strained and unstrained step-index glass optical fibers, *Appl. Opt.* 49 (2010) 5076–5080.
- [22] A. Djordjevich, S. Savović, Investigation of mode coupling in step index plastic optical fibers using the power flow equation, *IEEE Photon. Technol. Lett.* 12 (2000) 1489–1491.
- [23] L. Jeunhomme, M. Fraise, J.P. Pocholle, Propagation model for long step-index optical fibers, *Appl. Opt.* 15 (1976) 3040–3046.
- [24] W.A. Gambling, D.N. Payne, H. Matsumura, Mode conversion coefficients in optical fibers, *Appl. Opt.* 14 (1975) 1538–1542.
- [25] M. Rousseau, L. Jeunhomme, Numerical solution of the coupled-power equation in step index optical fibers, *IEEE Trans. Microw. Theory Tech.* 25 (1977) 577–585.
- [26] S. Savović, A. Djordjevich, Influence of the angle-dependence of mode coupling on optical power distribution in step-index plastic optical fibers, *Opt. Laser Technol.* 44 (2012) 180–184.
- [27] T.P. Tanaka, S. Yamada, Numerical solution of power flow equation in multimode W-type optical fibers, *Appl. Opt.* 19 (1980) 1647–1652.
- [28] S. Savović, A. Djordjevich, Mode coupling in strained and unstrained step-index plastic optical fibers, *Appl. Opt.* 45 (2006) 6775–6780.
- [29] S. Savović, A. Djordjevich, Calculation of the coupling coefficient in strained step index plastic optical fibers, *Appl. Opt.* 47 (2008) 4935–4939.



Full length article

Influence of mode coupling on three, four and five spatially multiplexed channels in multimode step-index plastic optical fibers

Svetislav Savović^{a,b}, Alexandar Djordjevich^{b,*}, Ana Simović^a, Branko Drljača^c^aUniversity of Kragujevac, Faculty of Science, Kragujevac, Serbia^bCity University of Hong Kong, Department of Mechanical and Biomedical Engineering, Kowloon, Hong Kong, China^cUniversity of Priština, Faculty of Science, L. Ribara 29, Kosovska Mitrovica, Serbia

ARTICLE INFO

Article history:

Received 6 February 2018

Received in revised form 19 March 2018

Accepted 23 March 2018

Keywords:

Plastic optical fibers

Space division multiplexing

Mode coupling

ABSTRACT

We investigate the influence of mode coupling on space division multiplexing capability of three multimode step-index plastic optical fibers with different strengths of mode coupling. Results show that mode coupling significantly limits the fiber length at which the space division multiplexing can be realized with a minimal crosstalk between the neighbor optical channels. Three, four and five spatially multiplexed channels in the investigated multimode step-index plastic optical fibers can be employed with a minimal crosstalk up to the fiber lengths which are about 7%, 5% and 3% of the corresponding coupling lengths (fiber length where equilibrium mode distribution is achieved), respectively. Such characterization of optical fibers should be considered in designing an optical fiber transmission system for space division multiplexing.

© 2018 Elsevier Ltd. All rights reserved.

1. Introduction

The increasing demand for digital data bandwidth pushes the development of emerging technologies to increase network capacity, especially for optical fiber infrastructures. The increase capacity of optical fiber systems was caused by successive technology improvements: low losses single-mode fibers, fiber amplifiers, multiplexing, and high-efficiency spectral coding [1]. Multiplexing of optical data can be realized not only in wavelength [2], but also in polarization, in time, in phase and in space [1]. Space division multiplexing (SDM) including mode division multiplexing using multimode fibers or few-mode fibers and/or core multiplexing using multicore fibers, has attracted much attention in the last decade for the next multiplicative capacity growth for optical communication [1,3–8]. SDM may operate at the same wavelength or different wavelengths [9]. In the case of SDM at the same wavelength, radially distributed, dedicated spatial locations are assigned to every SDM channel inside the carrier fiber as these channels traverse the length of the carrier. The location of the each channel inside the fiber is a function of the launch angle and the strength of mode coupling. In practice the channel launched with input angle $\theta_0 = 0^\circ$ along the fiber axis appears as a far field in the form of disk, while all subsequent channels launched with

$\theta_0 > 0$ appear in the far field as concentric rings. The center disk and each ring represent a separate spatially modulated optical channel, thereby enhancing the bandwidth of optical fiber systems (see Fig. 1).

Plastic optical fibers (POFs) are a low-cost solution for short-distance applications in digital car networks, industrial networks, and home networks and appliances. Transmission characteristics of multimode step-index (SI) POFs depend upon the differential mode attenuation and rate of mode coupling [9,10]. The latter represents power transfer between neighbor modes caused by fiber impurities and inhomogeneities introduced during the fiber manufacturing process [11]. Mode coupling is very important for SDM because SDM involves tightly packing spatial channels into a fiber, thus making crosstalk between channels an obvious potential problem.

In this work, using the power flow equation, we examine the state of mode coupling in three multimode SI POFs with different strengths of mode coupling, investigated earlier [11,12]. This enables one to obtain the limits of the fiber lengths up to which a SDM can be realized with minimal crosstalk between the co-propagating optical channels.

2. Power flow equation

Assuming that mode coupling in multimode optical fibers occurs predominantly between neighbor modes, Gloge's power

* Corresponding author at: City University of Hong Kong, Department of Mechanical and Biomedical Engineering, Kowloon, Hong Kong, China.

E-mail address: mealex@cityu.edu.hk (A. Djordjevich).

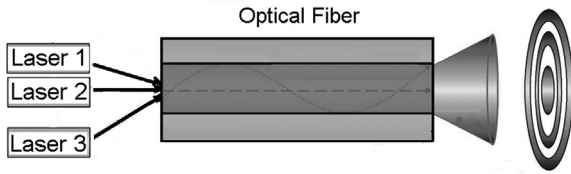


Fig. 1. Minimalistic system design of three channel SDM system.

flow equation for power distribution inside a multimode step-index fiber is [10]:

$$\frac{\partial P(\theta, z)}{\partial z} = -\alpha(\theta)P(\theta, z) + \frac{D}{\theta} \frac{\partial}{\partial \theta} \left(\theta \frac{\partial P(\theta, z)}{\partial \theta} \right) \quad (1)$$

where $P(\theta, z)$ is the angular power distribution, z is distance from the input end of the fiber, θ is the propagation angle with respect to the core axis, D is the coupling coefficient assumed constant [10,13–16] and $\alpha(\theta)$ is the modal attenuation. In our previous work [16] we have shown that modeling mode coupling in SI POFs assuming a constant coupling coefficient D can be used instead of the more complicated approach with angle-dependent coupling coefficient. Except near cutoff, the attenuation remains uniform $\alpha(\theta) = \alpha_0$ throughout the region of guided modes $0 \leq \theta \leq \theta_c$ [14] (it appears in the solution as the multiplication factor $\exp(-\alpha_0 z)$ that also does not depend on θ). Therefore, $\alpha(\theta)$ need not be accounted for when solving (1) for mode coupling and this equation reduces to [15]:

$$\frac{\partial P(\theta, z)}{\partial z} = \frac{D}{\theta} \frac{\partial P(\theta, z)}{\partial \theta} + D \frac{\partial^2 P(\theta, z)}{\partial \theta^2} \quad (2)$$

Numerical solution of the power flow Eq. (2) was obtained using the explicit finite-difference method [15], for Gaussian launch-beam distribution of the form:

$$P(\theta, z = 0) = \frac{1}{\sigma\sqrt{2\pi}} \exp \left[-\frac{(\theta - \theta_0)^2}{2\sigma^2} \right] \quad (3)$$

with $0 \leq \theta \leq \theta_c$, where θ_0 is the mean value of the incidence angle distribution, with the full width at half maximum $\text{FWHM} = 2\sigma\sqrt{2\ln 2} = 2.355\sigma$ (σ is standard deviation).

3. Results and discussion

In this paper, we analyze mode coupling in three multimode SI POFs used in the experiments reported earlier [11,12]. The three SI POFs had a 1-mm-diameter polymethylmetacrylate core. The fiber HFBR-RUS500 (HFBR fiber) from Hewlett-Packard has an NA = 0.47, the PGU-CD1001-22E (PGU fiber) fiber from Toray has an NA = 0.5 and the ESKA Premier GH 4001P (GH fiber) from Mitsubishi Rayon Co., Ltd. has an NA = 0.51. Critical angles are $\theta_c = 18.4, 20$ and 19.5° for the HFBR, GH and PGU fiber, respectively. It was found that $D = (8.7, 5.6$ and $3.3) \times 10^{-4} \text{ rad}^2/\text{m}$ for the HFBR, GH and PGU fiber, respectively [11,12] – which we have adopted in this work.

In Figs. 2–4, our numerical solution of the power flow equation is presented by showing the evolution of the normalized output power distribution with fiber length for HFBR fiber for five, four and three spatially multiplexed channels, respectively. The five co-propagating optical channels are launched at different input angles $\theta_0 = 0, 4, 8, 12$ and 16° thus maintaining a different spatial orientation. The four co-propagating optical channels are launched at different input angles $\theta_0 = 0, 5, 10$ and 15° , while the three co-propagating optical channels are launched at different input angles $\theta_0 = 0, 8$ and 16° . For multiple optical channels we selected Gaussian launch beam distribution with $(\text{FWHM})_0 = 0.127^\circ$ by setting $\sigma_0 = 0.054^\circ$ in Eq. (3). Ring radiation patterns in very short fibers in Figs. 2(a), 3(a) and 4(a) indicate that the mode coupling is so low thus leading to a minimal crosstalk observed between the neighbor co-propagating optical channels. With increasing a fiber length, a crosstalk between neighbor co-propagating optical channels continue to increase and significantly influence the quality of light signals which are transmitting through the channels (Figs. 2(b), (c), 3(b), (c) and 4(b), (c)). Finally, at fiber's coupling length L_c the mode-distributions of co-propagating optical channels which

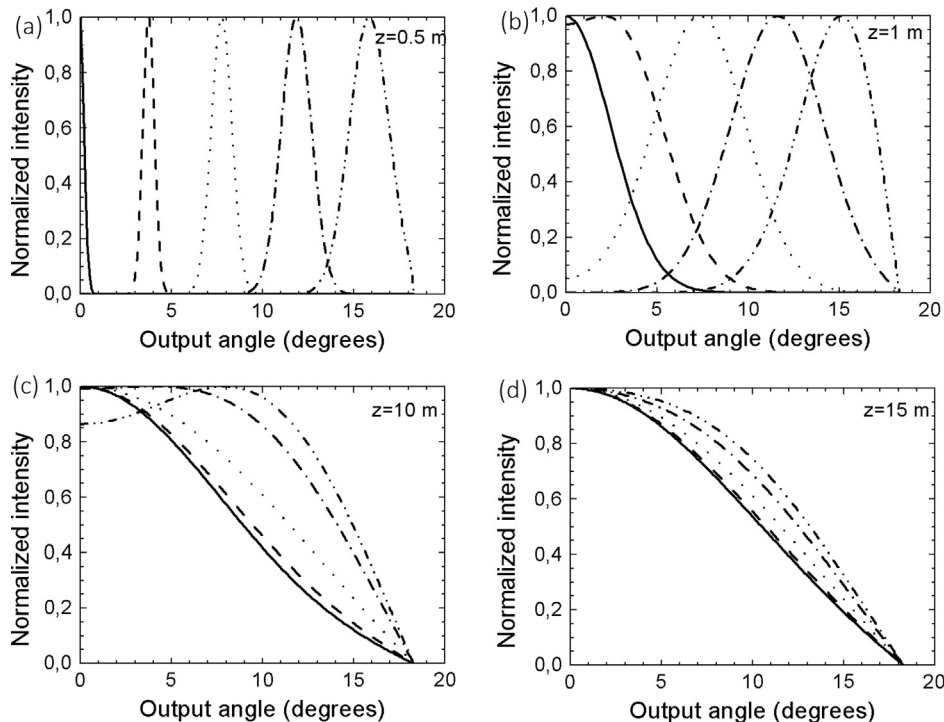


Fig. 2. Normalized output angular power distribution at different locations along the HFBR fiber calculated for five Gaussian input angles $\theta_0 = 0^\circ$ (solid line), 4° (dashed line), 8° (dotted line), 12° (dash-dotted line) and 16° (dash-dotted-dotted line) with $(\text{FWHM})_{z=0} = 0.127^\circ$ for: (a) $z = 0.5$ m; (b) $z = 1$ m; (c) $z = 10$ m and (d) $z = 15$ m.

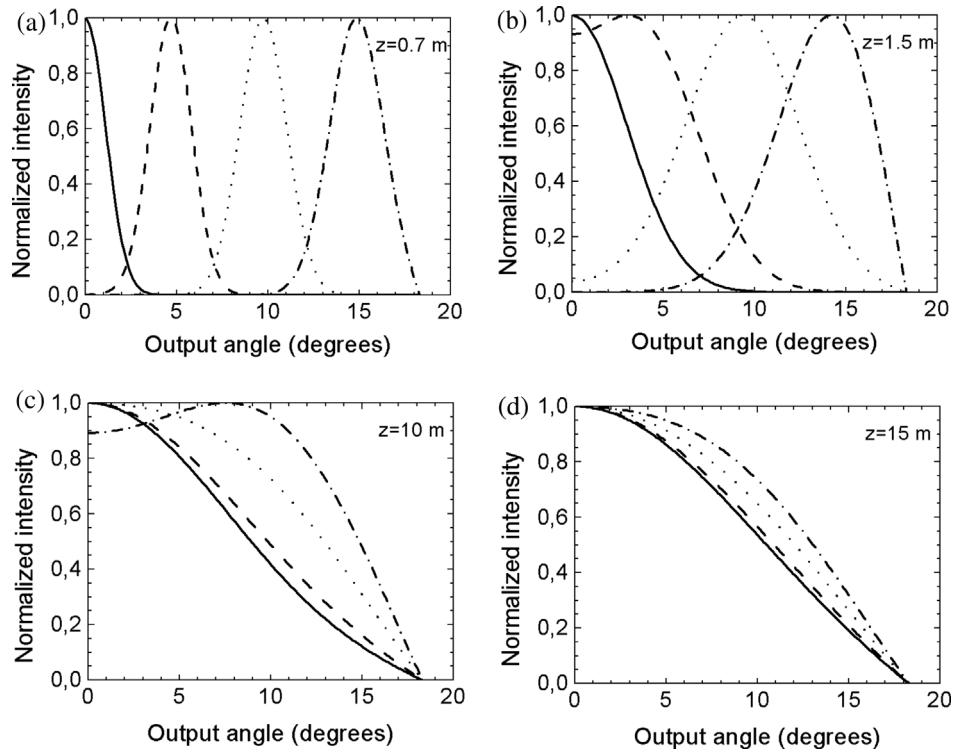


Fig. 3. Normalized output angular power distribution at different locations along the HFBR fiber calculated for four Gaussian input angles $\theta_0 = 0^\circ$ (solid line), 5° (dashed line), 10° (dotted line) and 15° (dash-dotted line) with $(FWHM)_{z=0} = 0.127^\circ$ for: (a) $z = 0.7$ m; (b) $z = 1.5$ m; (c) $z = 10$ m and (d) $z = 15$ m.

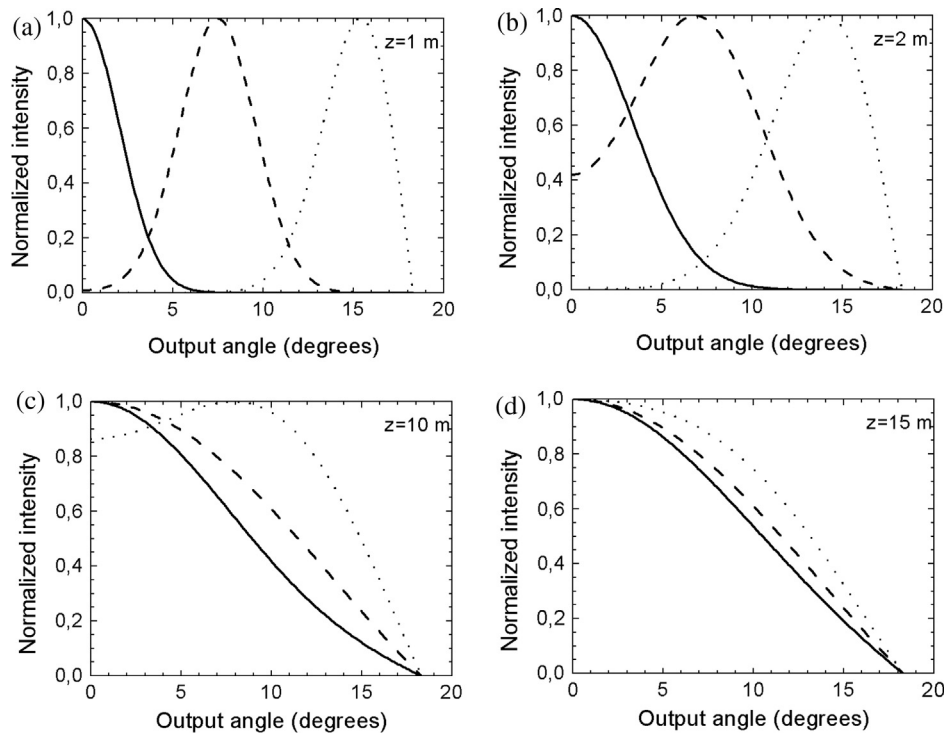


Fig. 4. Normalized output angular power distribution at different locations along the HFBR fiber calculated for three Gaussian input angles $\theta_0 = 0^\circ$ (solid line), 5° (dashed line) and 10° (dotted line) with $(FWHM)_{z=0} = 0.127^\circ$ for: (a) $z = 1$ m; (b) $z = 2$ m, (c) $z = 10$ m and (d) $z = 15$ m.

are in the ring form, shift their mid-points to zero degrees, producing the equilibrium mode distribution (EMD) in Figs. 2(d), 3(d) and 4(d): L_c is 15 m for HFBR. For GH and PGU fiber, the coupling length L_c is 20 and 35 m, respectively (Table 1). As a result, at fiber lengths $z \geq L_c$ the Gaussian distributions which corresponded to different

spatially multiplexed co-propagating optical channels are no more spatially separated since they form a disk-type circular far field outputs. One can see that mode coupling significantly limits the length of the POFs at which the space division multiplexing can be realized. This limitation is most pronounced in HFBR fiber which

Table 1

Length z_{SDM} for three-, four- and five-spatially multiplexed channels with minimal crosstalk in SI POFs with different mode coupling coefficient D . L_c is the coupling length at which the equilibrium mode distribution is achieved.

Fiber type	D (rad ² /m)	z_{SDM} (m) (3-channel)	z_{SDM} (m) (4-channel)	z_{SDM} (m) (5-channel)	L_c (m)
HFBR	8.7×10^{-4}	1.0	0.7	0.5	15
GH	5.62×10^{-4}	1.4	0.9	0.7	20
PGU	3.3×10^{-4}	2.4	1.6	1.2	35

showed the strongest mode coupling, with reducing the length for practical realization of five-, four- and three-channel space division multiplexing up to $z_{SDM} \approx 0.5, 0.7$ and 1.0 m, respectively. In GH fiber these lengths are $z_{SDM} \approx 0.7, 0.9$ and 1.4 m, respectively, while in PGU fiber these lengths are $z_{SDM} \approx 1.2, 1.6$ and 2.4 m, respectively. It is worth noting that the lengths z_{SDM} up to which a minimal crosstalk is observed between the neighbor co-propagating optical channels are much shorter than the corresponding coupling lengths L_c at which the EMD is achieved (Figs. 2(d), 3(d) and 4(d)). A three, four and five spatially multiplexed channels in the investigated multimode SI POFs can be realized with a minimal crosstalk up to the fiber lengths which are about 7%, 5% and 3% of the corresponding coupling lengths, respectively. In general, the larger number of co-propagating optical channels, the sooner crosstalk between the neighbor optical channels would appear. In practice, a tradeoff between a number of co-propagating optical channels and a length of fiber which one expect to transmit the spatially multiplexed signals with minimal crosstalk between the neighbor optical channels should be considered for a particular fiber use. Such characterization of optical fibers should be considered in designing an optical fiber transmission system with space division multiplexing. One should note that by calculating the normalized output power distribution at different fiber lengths in the case of five, four and three spatially multiplexed channels, it is difficult to exactly predict the level of the crosstalk which prohibits the system operation. In practice, for more accurate estimation of the SDM capacity of the particular POF, the transmission matrix should be used, with taking into account the noise terms which depend on the specific implementation of the receiver [19,20]. But, our numerical results can be used as a good approximation in the estimation of the fiber length at which SDM with five, four and three channels could be realized in the investigated SI POFs with a minimal crosstalk.

As comparison, the spatial multiplexing capabilities of the co-propagating optical channels in POFs analyzed in this work are poorer than in the silica optical fibers, due to weaker mode coupling and slower modal equilibration ($D \approx 10^{-6}$ rad²/m; $L_c \approx 10$ to 110 m) in the latter [17,18]. In conclusion, an optical fiber with weak mode coupling is desirable for future ultra-high capacity space-division multiplexing systems because mode coupling in an optical fiber results in crosstalk between guided optical modes.

4. Conclusion

The influence of mode coupling on three, four and five spatially multiplexed optical channels in three multimode SI POFs with different strengths of mode coupling is investigated by solving the power flow equation. We have shown that mode coupling significantly limits the length of SI POFs at which the space division multiplexing can be realized with minimal crosstalk between the neighbor optical channels. The larger number of co-propagating optical channels, the sooner crosstalk between the neighbor optical channels would appear. In practice, a tradeoff between a number of co-propagating optical channels and a length of fiber which one expect to transmit the spatially multiplexed signals with minimal crosstalk between the neighbor optical channels should be consid-

ered for a particular fiber use. Such characterization of optical fibers should be considered in designing an optical fiber transmission system with space division multiplexing.

Acknowledgement

The work described in this paper was supported by the Strategic Research Grant of City University of Hong Kong (Project No. CityU 7004600) and by a grant from Serbian Ministry of Education, Science and Technological Development (Project No. 171011).

References

- [1] D. Richardson, J. Fini, L. Nelson, Space-division multiplexing in optical fibres, *Nat. Photonics* 7 (2013) 354–362.
- [2] D.S. Montero, I.P. Garcilópez, C.V. García, P.C. Lallana, A.T. Moraleta, P.J.P. Castillo, "Recent Advances in Wavelength-Division-Multiplexing Plastic Optical Fiber Technologies" in *Advances in Optical Fiber Technology: Fundamental Optical Phenomena and Applications*, INTECH (2015).
- [3] P.J. Winzer, Optical networking beyond WDM, *IEEE Photon. J.* 4 (2012) 647–651.
- [4] G. Li, N. Bai, N. Zhao, C. Xia, Space-division multiplexing: the next frontier in optical communication, *Adv. Opt. Photonics* 6 (2014) 413–487.
- [5] C. Brunet, B. Ung, P.-A. Belanger, Y. Messaddeq, S. LaRochelle, L.A. Rusch, Vector mode analysis of ring-core fibers: design tools for spatial division multiplexing, *J. Lightwave Technol.* 32 (2014) 4046–4057.
- [6] S. Murshid, B. Grossman, P. Narakorn, Spatial domain multiplexing: a new dimension in fiber optic multiplexing, *Opt. Laser Technol.* 40 (2008) 1030–1036.
- [7] G. Labroille, B. Denolle, P. Jian, P. Genevieux, N. Treps, J.-F. Morizur, Efficient and mode selective spatial mode multiplexer based on multi-plane light conversion, *Opt. Exp.* 22 (2014) 15599–15607.
- [8] Y. Yan, J. Wang, L. Zhang, J.-Y. Yang, I. Fazal, N. Ahmed, B. Shamee, A. Willner, K. Birnbaum, J. Choi, B. Erkmen, and S. Dolinar, "New approach for generating and (de)multiplexing oam modes in a fiber coupler consisting of a central ring and four external cores," in *Optical Communication (ECOC) 2011, 37th European Conference and Exhibition, Sep. 2011*, pp. 1–3.
- [9] S.H. Murshid, A. Chakravarty, R. Biswas, Attenuation and modal dispersion models for spatially multiplexed co-propagating helical optical channels in step index fibers, *Opt. Laser Technol.* 43 (2011) 430–436.
- [10] D. Gloge, Optical power flow in multimode fibers, *Bell Syst. Tech. J.* 51 (1972) 1767–1783.
- [11] A.F. Garito, J. Wang, R. Gao, Effects of random perturbations in plastic optical fibers, *Science* 281 (1998) 962–967.
- [12] M.A. Losada, I. Garcés, J. Mateo, I. Salinas, J. Lou, J. Zubía, Mode coupling contribution to radiation losses in curvatures for high and low numerical aperture plastic optical fibers, *J. Lightwave Technol.* 20 (2002) 1160–1164.
- [13] W.A. Gambling, D.N. Payne, H. Matsumura, Mode conversion coefficients in optical fibers, *Appl. Opt.* 14 (1975) 1538–1542.
- [14] M. Rousseau, L. Jeunhomme, Numerical solution of the coupled-power equation in step index optical fibers, *IEEE Trans. Microwave Theory Tech.* 25 (1977) 577–585.
- [15] A. Djordjević, S. Savović, Investigation of mode coupling in step index plastic optical fibers using the power flow equation, *IEEE Photon. Technol. Lett.* 12 (2000) 1489–1491.
- [16] S. Savović, A. Djordjević, Influence of the angle-dependence of mode coupling on optical power distribution in step-index plastic optical fibers, *Opt. Laser Technol.* 44 (2012) 180–184.
- [17] K. Appaiah, R. Salas, S. Vishwanath, S.R. Bank, Offset coupling, feedback, and spatial multiplexing in 4×4 incoherent-MIMO multimode fiber links, *J. Lightwave Technol.* 31 (2013) 2926–2939.
- [18] S. Savović and A. Djordjević, "Influence of mode coupling on space division multiplexing in multimode step-index silica optical fibers" (submitted for publication).
- [19] C.P. Tsekrekos, A. Martinez, F.M. Huijskens, A.M.J. Koonen, "Design considerations for a transparent mode group diversity multiplexing link," *IEEE Photon. Technol. Lett.* 18 (2006) 2359–2361.
- [20] G. Stepniak, L. Maksymiuk, J. Siuzdak, Influence of mode coupling on mode group diversity multiplexing in multimode fibers, *Opt. Quantum Electron.* 41 (2009) 203–213.

Article

A Statistical Analysis of Long-Term Grid-Connected PV System Operation in Niš (Serbia) under Temperate Continental Climatic Conditions

Dragana D. Todorović^{1,*}, Marija Stojanović Krsić², Slavica Jovanović¹, Branko Drljača¹ and Tijana Kevkić¹

¹ Department of Physics, Faculty of Sciences and Mathematics, University of Priština in Kosovska Mitrovica, Lole Ribara 29, 38220 Kosovska Mitrovica, Serbia; slavica.jovanovic@pr.ac.rs (S.J.); branko.drljaca@pr.ac.rs (B.D.); tijana.kevkic@pr.ac.rs (T.K.)

² Faculty of Technology, University of Niš, Bulevar Oslobođenja 124, 16000 Leskovac, Serbia; marijastojanovickrsic@gmail.com

* Correspondence: dragana.todorovic@pr.ac.rs or dragana82nis@yahoo.com

Abstract: This study analyzes the grid-connected PV system performances over a 10-year period under temperate continental conditions in Niš. Based on the experimental results, we found the following: the 10-year yearly average values of PV system efficiency, Y_f , CF, and PR are 10.49%, 1178.51 kWh/kWp, 13.45%, and 0.87, respectively. The yearly average value of PV performances for a 10-year measurement indicates that the behavior of the given PV system over 10 years does not change significantly. Besides, a mathematical prediction model was obtained through regression analysis, and ANOVA was applied for testing the model's validity. It is shown that the obtained model is statistically significant and enables prediction better than a simple average, the mean values of PV electricity are not changed statistically significantly over the 10 observed years, and there is a statistically significant difference in POA mean radiation during the months over 10 years. Based on the obtained model and POA radiation values, a prediction of the PV system output can be made for similar PV installations. The analysis presented in this study significantly impacts energy prediction, PV energy modeling, and the economics and profitability of the grid-connected PV system utilization, as well as the PV systems' operation planning and maintenance.

Keywords: PV system; POA radiation; efficiency; performance ratio; statistical analysis; ANOVA; post hoc Tukey test



Citation: Todorović, D.D.; Stojanović Krsić, M.; Jovanović, S.; Drljača, B.; Kevkić, T. A Statistical Analysis of Long-Term Grid-Connected PV System Operation in Niš (Serbia) under Temperate Continental Climatic Conditions. *Appl. Sci.* **2023**, *13*, 6229. <https://doi.org/10.3390/app13106229>

Academic Editors: Manuela Sechilariu, Saleh Cheikh-Mohamad and Berk Celik

Received: 21 April 2023

Revised: 15 May 2023

Accepted: 16 May 2023

Published: 19 May 2023



Copyright: © 2023 by the authors. Licensee MDPI, Basel, Switzerland. This article is an open access article distributed under the terms and conditions of the Creative Commons Attribution (CC BY) license (<https://creativecommons.org/licenses/by/4.0/>).

1. Introduction

Energy shortage is a growing problem today. Climate changes have already been observed, on the one hand, while the use of fossil fuels is becoming more and more limited due to the high energy consumption and Earth's increasing population. Global fossil fuel resources are not yet exhausted; however, their use's negative environmental and social impacts are apparent [1].

The Sun is the largest energy source that has powered and sustained life on Earth for more than 4.5 billion years. Solar energy is more than enough to meet all energy needs worldwide. It is assessed that over one year, the solar energy that arrives at the Earth's surface is 10,000 times greater than the energy necessary for the entire population's needs worldwide. On the other hand, solar energy is an ecologically clean energy whose energy technologies do not pollute the environment. Besides, it represents an energy resource available to every country without import dependence. Photovoltaic (PV) technology is one of the best ways to utilize solar energy and represents one of the most competitive renewable sources for electricity production. The use of PV systems is recently on the rise in many countries, and PV systems are beginning to occupy a significant place in energetics worldwide. Recently, many studies have been conducted on the techno-economic effectiveness of PV systems applications and their benefits in different climatic conditions. These

studies are carried out in different countries worldwide, where the climatic specificities of these countries are taken into account. On the other hand, over the last decades, many life cycle assessments (LCAs) of PV systems have been carried out. LCA is an important tool to provide a comprehensive analysis of PV systems compared to conventional energy systems, especially with regard to the greenhouse gas (GHG) emissions assessment [1–7].

In practice, deploying PV technologies is the comprehension of the performance exhibited by each of them once installed outdoors and functions in real climatic conditions. Such investigations are necessary because the outdoor PV electrical characteristics differ from the reference STC characteristics in manufacturer data sheets [8].

Many studies provide PV systems' performance analysis in different periods and locations worldwide. Such studies provide experimental data on the PV systems' operation in real conditions, which are necessary for developing PV software and PV energy modeling and predicting PV system operations, as can be seen in [3,4,9–11]. Considering that many PV systems have been installed worldwide, there are numerous analyses about the performances of installed PV systems under different climatic conditions. On the other hand, some of them provide a comparison of experimental and simulated results of PV system performance parameters. The comprehensive review of the analysis of performance ratio (PR) and final yield (Y_f) for 3326 PV systems in Slovenia and a comparison with other countries' PV systems installed is given in [12]. A comparative performance analysis of two grid-connected PV systems with p-Si and CIS solar cells and power of 1 kWp and 1.36 kWp, respectively, in Southern India is presented in [13], while the prediction of performances, energy losses, and degradation of a 200 kWp grid-integrated PV system using the PVsyst simulation tool in Northern India is given in [14]. An analysis of the long-term performance of 594 PV systems from the power of less than 1 kW to the power of more than 2 MW from different countries (Australia, Germany, Italy, USA, The Netherlands, France, and Belgium) is provided in [15]. This study includes datasets of final yield, PR, and degradation rate of PV systems with different PV technologies, operation years, and installation types. The parameters of reference, array and final yields, system losses, PV and inverter efficiencies, and PR of a 13 kWp grid-connected PV system in Northern Ireland are analyzed on the hourly, daily, and monthly levels over three years of its operations, as can be seen in [16], and the results were compared with the simulation results obtained by TRNSYS simulation tool [17]. Experimental results and simulation results obtained by SAM and PVsyst simulation tools of PR, efficiency, and losses of a grid-connected 960 kW PV system in Italy are analyzed in [18]. Reference [19] provides the results of efficiencies, PR, and degradation rates by testing three PV systems with different PV technologies (c-Si, a-Si, and CdTe) under the same climatic conditions in Ankara (Anatolia) after 4 operation years. A comparison of the experimental and simulated performance of a grid-connected 49.92 kW PV system in the Irish climate over one year is presented in [20]. The energy efficiency analysis, specifically in terms of specific yield, of eight grid-connected and one hybrid PV system with various system configurations, tilt angles, and orientations, installed in southeastern Poland, is presented in [21]. A comprehensive review of PV system performances with a focus on comparative performance studies of different PV systems worldwide is analyzed in [22]. The outdoor performances (PR, system efficiency, and capacity utilization factor) of three grid-connected photovoltaic (PV) systems with c-Si, p-Si, and a-Si PV technologies and total installed power of 5.94 kWp in Morocco are analyzed in [23]. The analysis of PV-generated power in dependence on insolation, ambient, and module temperatures of PV systems with different PV technologies (c-Si, p-Si, and CIGS) in Poland is given in [24]. An experimental efficiency analysis of three PV systems with different PV technologies (p-Si, CdTe, and CIGS) under a temperate climate in Poland is given in [25]. The performance parameters of a 1.75 kW grid-connected PV system over the four years of its operation in Sydney (Australia) are determined and compared with simulation results obtained by PVsyst. This analysis is given in [26], while the performance indicators, such as performance index, solar fraction etc., are analyzed in [27]. The performance and I-U parameters of two 20-year-old PV systems installed on the west and east

side of the building at NREL (USA) are statistically analyzed in [28]. Special attention is focused on the degradation rate, which was found to be 0.8%/year, which is consistent with historical averages. The degradation rate of PV systems with different powers and PV technology and under different climate conditions is also analyzed in [29–37]. All those studies provide helpful insight into energy prediction, the economics and profitability of PV system utilization, and PV systems' operation planning and maintenance. However, there are not many experimental studies on long-term PV system operation in Serbia and surrounding countries with similar climates.

This study provides the original experimental results of PV system performances in Niš (Serbia) for 10 years of its operations. The collected results are statistically analyzed in order to obtain the PV system performances under real operating conditions for a specific region. Based on experimental measurements, the PV system performance parameters over the 10 years of its operations were determined, and a mathematical prediction model was created. Compared with other similar studies, the difference and originality of this study are reflected in terms of 10-year results obtained for a specific location as well as the application of statistical methods for the analysis of a large number of data obtained by experimental measurements of POA radiation and PV electricity. A regression analysis was performed to obtain a prediction model, and an Analysis of Variance (ANOVA) was applied for testing the model's validity. Considering that the variable "years" is a categorical variable and "PV electricity" and "POA radiation" are numerical ones, a one-way analysis was performed. In this regard, the conditions for applying ANOVA were tested, and the O'Brien test was used to check the equality of variances. Thus, the originality of this study compared to similar ones is particularly reflected in the statistical analysis of the results (PV electricity and POA radiation) and the determination of statistical significance in the prediction model. Related to this, this study aims to apply the obtained results in integrating PV systems into the country's electro-power system to increase commercial PV systems applications in Serbia. Besides, this study provides data necessary for increasing the PV modeling accuracy by analyzing the accurate data. On the other hand, the obtained data are useful as guidelines for predicting, planning, and applying PV systems in other locations with similar climates. Besides, the study findings are also useful for degradations analysis of long-term PV system operations, especially in moderate continental climate regions.

Background

The main meteorological parameter that impacts the PV system operation is solar irradiation. It is generally known that the PV module operating voltage is logarithmic-dependent while the current has linear dependence. The main problem is the assessment of solar irradiation effects, which stems from solar irradiation being related to other factors affecting PV performance, such as the clear sky or diffuse radiation due to cloudy sky, low radiation in the early morning or late afternoon (high AM), angle-of-incidence (AOI) radiation effects, spectral response, etc. On the other hand, global solar irradiation is generally measured on a horizontal surface, while the maximum amount of incident solar irradiation is measured on an inclined surface (POA radiation) [10]. Recently, many analytical models have been proposed to estimate the amount of solar irradiation on horizontal (GHI) and inclined surfaces (POA irradiation). These models have different ranges and applicability to specific surfaces and locations. To find the most suitable solar model for a given location, the hourly results predicted by the available models are usually compared with the experimental measurements for the given locations [10,37,38].

In general cases, solar irradiation is usually measured as long-term data on the horizontal surface worldwide, and based on these measurements, solar databases are created. These solar databases, containing solar resource data obtained from the ground and/or derived from satellite imagery, are widely available as open-source or paid datasets. Based on these solar datasets and analytical models for the estimates of solar irradiation on the inclined surface, new bases are formed. The availability of solar databases containing POA irradiation data is limited and very low [10].

In accordance with the reasons mentioned above, the special importance of this study is that it contains long-term measurements of POA solar irradiation and electrical parameters of a grid-connected PV system and provides a statistical analysis of the long-term PV system operation in real conditions.

2. Materials and Methods

For the performance analysis of PV system operation in the real climatic condition in Niš (Latitude: 43°19'28.99" N, Longitude: 21°54'11.99" E), 10 monocrystalline silicon solar modules (SST-200WM, Shenzhen Sunco Solar Technology Co., Shenzhen, China), with individual power of 200 W, were mounted right next to each other (in order to minimize cable losses) on the roof of Faculty of Sciences and Mathematics and serially interconnected in a string. The solar modules were set up on the fixed metal construction tilted at an optimal angle of 32° toward the south (Figure 1). The total PV array (solar modules surface) was 16.59 m² (or 1.659 m²/module). The minimum distance between the solar modules and the roof surface was 50 cm to ensure natural air circulation, i.e., a passive air-cooling method for the solar modules was used so that the system balance could take place naturally without any additional (mechanical) technique, as can be seen in Figure 1. It should also be noted that the solar modules were free from any shading.



Figure 1. PV array installed on the roof of the faculty [39].

By appropriate cables (conductors), the solar modules were connected to a DC junction box (DC-RO), then a 2 kW inverter (SunnyBoy 2000HF-30, SMA Solar Technology AG, Niestetal, Germany), then to an AC junction box (AC-RO), and finally to a city power grid. The used inverter was a single-phase inverter with a high-frequency (HF) transformer power of 2000 W and an efficiency of 96.3%, providing a single-phase AC voltage of 230 V, 50 Hz. This PV system was connected to the city power grid. However, its effects on the city grid, including the variation of power factor effect of load, PV penetration variation, anti-islanding effect, and introduction of harmonic into the system by the inverter, have not been investigated or considered. It should be noted that over the 10-year period of the PV system operation, there were no problems during the PV electricity transmission to the city network grid.

Global solar radiation on the surface of PV modules (POA radiation) was measured by a sensor unit (Sunny SensorBox), which was also placed next to solar modules at an optimal inclination angle of 32° toward the south. It should be noted that the solar sensor (Sunny

SensorBox) uses an a-Si solar cell and measures POA radiation with a resolution of 1 W/m^2 and measurement accuracy of $\pm 8\%$. A central communication interface (Sunny WEBBox) was interconnected to the inverter and SensorBox by Bluetooth. The POA radiation data and PV system electrical parameters continuously record every 5 min into the Sunny WEBBox internal memory [10,39]. The SunnyBoy inverter, Sunny WEBBOX, and DC and AC junction boxes were placed indoors in the faculty laboratory, where the optimum room temperature is maintained throughout the year.

A schematic of the grid-connected 2 kW_p PV system in Niš [28] is given in Figure 2.

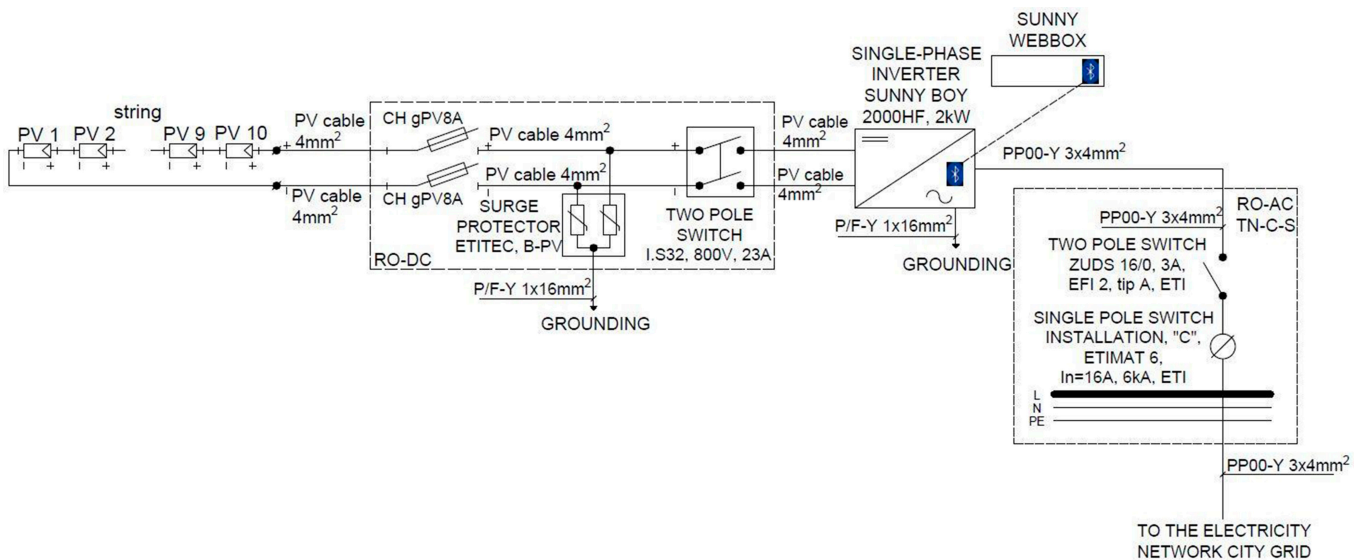


Figure 2. A schematic of grid-connected 2 kW_p PV system [39].

An approximate PV module efficiency at STC can be calculated using the Equation (1) [9]:

$$\eta_{STC} = (I_{SC} \cdot V_{OC} \cdot FF) / I_{STC} \quad (1)$$

where I_{STC} is the reference solar irradiance at STC of 1 kW/m^2 , FF is a fill factor of the solar module, I_{SC} is the short-circuit current of solar module, and V_{OC} is the open-circuit voltage of solar module [9]. If it is taken into account that $FF = 76\%$, $I_{SC} = 4.64 \text{ A}$, $V_{OC} = 57.12 \text{ V}$, and the inverter efficiency $\eta_{inv} = 96.3\%$, which is based on the specification of the modules and inverter given by the manufactory datasheet and presented in [10], the approximate PV system efficiency at STC (ideally, excluding cable losses) is around 19.4%.

Evaluation of the long-term grid-connected PV system operation in real conditions, based on the statistical processing of experimental data, was performed in two phases:

1. The main performance PV system parameters (PV system efficiency, PR, Y_r , Y_f , and CF), defined by IEC 61724:1998 standard and described in [8,10,39], were determined and are presented in this study.
2. The relationship between two numerical variables (PV system electricity output and total POA irradiation data), obtained by 10-year measurements, was statistically analyzed using JMP Pro software. For that purpose, a regression analysis, analysis of variance (ANOVA), and post hoc Tukey test were applied. ANOVA is a technique for statistical analysis where datasets are compared to provide and determine their significance. ANOVA also describes complex relationships between variables; in this case, they are POA radiation and PV electricity. As results in ANOVA do not identify which specific differences between pairs of means are significant, it is common to use post hoc tests to investigate differences between multiple groups' means. Based on obtained results, the conclusion of the grid-connected PV system application's degradation, efficiency, profitability, and stability during its 10-year operation for a specific climate region was presented.

3. Results and Discussion

As PV manufacturers give the electrical parameters of solar modules, such as open-circuit voltage, short-circuit current, MPP voltage, MPP current, max power, efficiency, and temperature coefficients at STC, and those parameters are not applicable to predict the PV system operation in actual conditions with increased accuracy, it is necessary to determine the main performance parameters of PV system, namely: energy yield (Ey), outdoor efficiency (η), and performance ratio (PR) for a more extended period.

In this section, the experimental results of 2 kWp grid-connected PV system operation in Niš for the period from 1 January 2013 to 31 December 2022 are presented. Since the measurements of all the mentioned parameters were performed every 5 minutes for 10 years, the statistical processing of the data calculated first the hourly, then the daily, and finally the monthly and annual values. Further on, the experimental results will be presented on a monthly level for 10 years.

3.1. Performance Parameters

The 10-year average values of energy yield (Ey) depending on the 10-year average values of total POA radiation reached on the total PV array area by month are given in Figure 3.

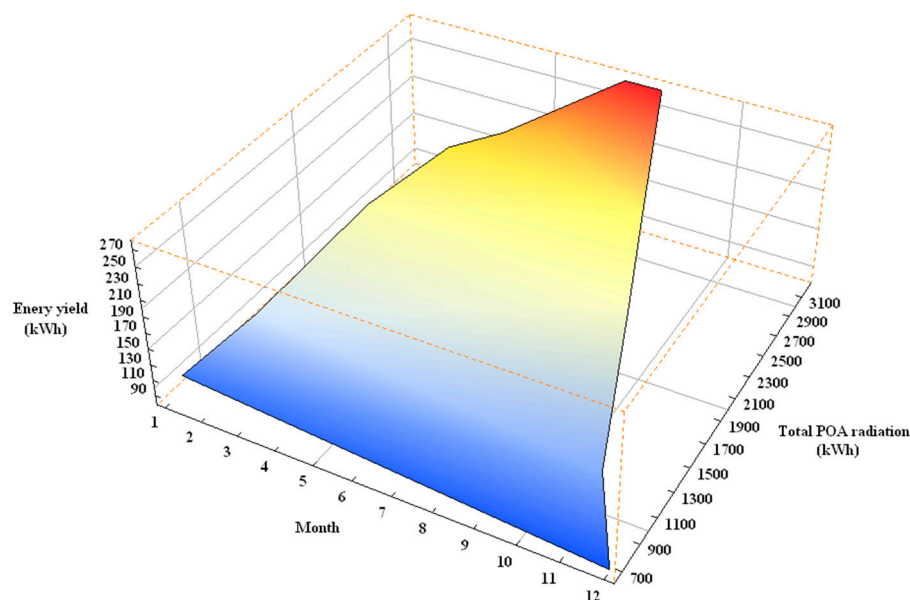


Figure 3. The 10-year average values of energy yield (Ey) depending on the 10-year average values of total POA radiation reached on the total PV array area by month.

The 10-year average values of total POA radiation on the total PV array by month range from 667.158 kWh (December) to 3204.684 kWh (July), while 10-year average values of energy yield by month range from 82.196 kWh (December) to 276.746 kWh (August), as can be seen in Figure 3.

One of the main parameters of PV system performance in real conditions is the efficiency of the given system (η_{sys}), which is determined as the ratio of the PV system output (AC output from the inverter and transmitted to the city grid) to the total POA radiation on the PV array [10,39]. The 10-year average values of PV system energy efficiency (η_{sys}) by month are given in Figure 4.

The 10-year average values of PV system energy efficiency (η_{sys}) by month range from 8.61% (July) to 12.61% (January), while the PV system efficiency at STC is 19%.

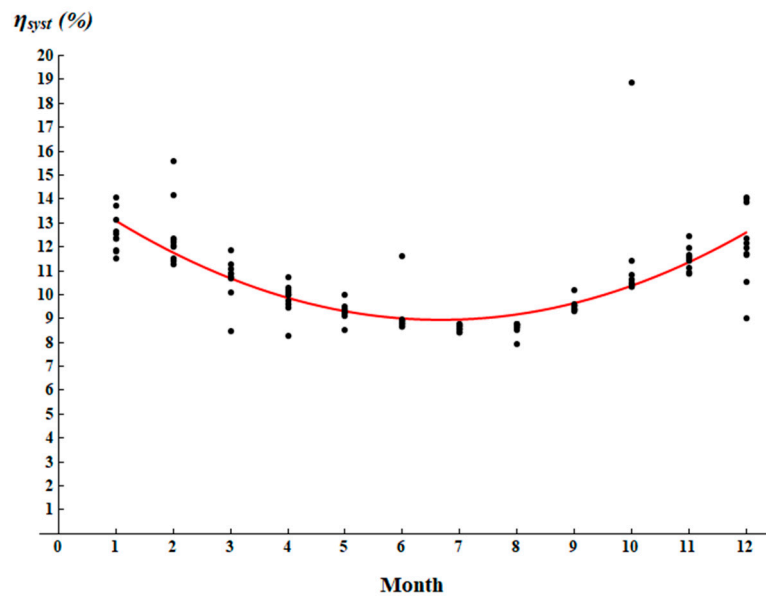


Figure 4. The 10-year average values of PV system energy efficiency (η_{sys}) by month.

The reference yield (Y_r) represents the ratio between the total POA radiation (in kWh/m²) and the reference solar radiation of 1 kW/m² (reference solar radiation is radiation at STC) and is a function of the geographical location and orientation of the PV array. On the other hand, the specific yield factor (Y_f) represents the ratio between the PV system output (in kWh) and the total installed power of the PV system (in kW_p). The specific yield factor (or final yield) is usually utilized to normalize the produced system energy relative to the PV system size. It could be said that Y_f is a good parameter for comparing the energy produced by different sized PV systems [10]. The ratio between the specific yield factor (Y_f) and the reference yield (Y_r) for 10-year measurements is given in Figure 5.

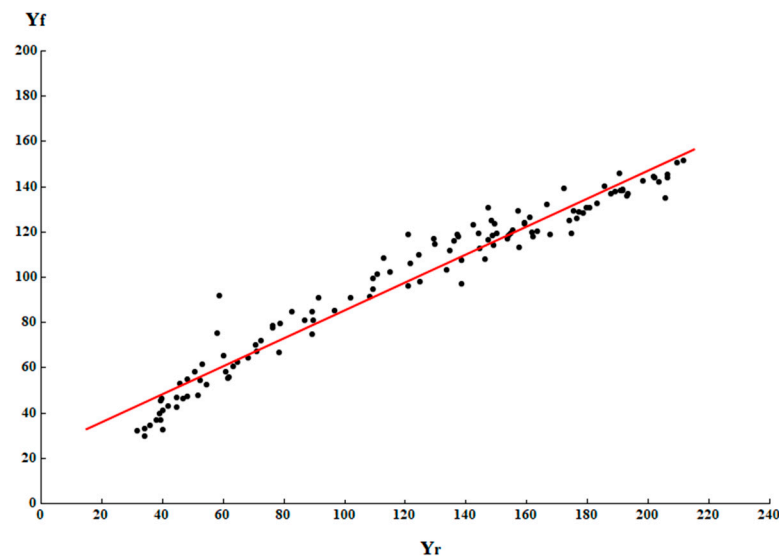


Figure 5. The ratio between the specific yield factor (Y_f) and the reference yield (Y_r) for 10-year measurements.

Figure 5 shows that there is a linear dependence between the specific yield factor and the reference yield. Plotting the regression line for each month during the 10 years (Figure 5) allows for the identification of the slope and, therefore, the average monthly performance ratio. In this case, the regression coefficient (slope in the regression model) amounts to 0.617536 and responds to the average change of the expected value of the dependent variable Y_f for the unit change of the independent variable Y_r . Thus, the ratio between the specific yield factor (Y_f) and the reference yield (Y_r) represents Performance

Ratio (PR). Hence, the PR defines the rate of effective produced energy with the energy the PV system would generate if it continually worked on its efficiency at standard test conditions. So, the PR comprises all PV optical and electric losses in a system without being directly dependent on input parameters such as meteorological data (temperature, solar radiation, wind speed, cloudiness, snow, precipitation, presence of aerosols, etc.), module efficiency, and orientation of the PV array [10,29–37].

Graphics of the change of yearly average values of the Performance Ratio (PR) for a 10-year period is given in Figure 6.

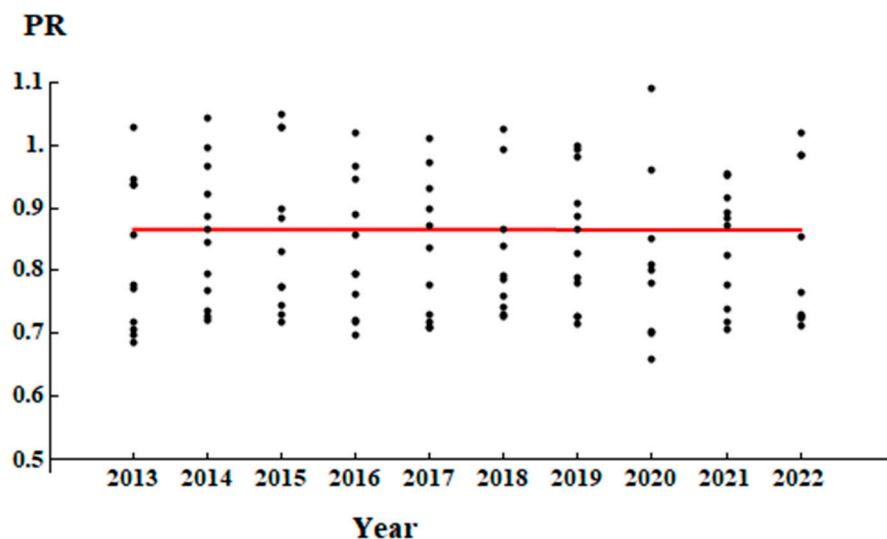


Figure 6. Graphics of the change of yearly average values of Performance Ratio (PR) for a 10-year period.

The yearly average values of PR for the 10 years, from 2013 to 2022, range from 0.849 to 0.93. On the other hand, the 10-year average values of PR by month range from 1.01 (December) to 0.713 (July). A PR higher than 1 is uncommon and can only be accomplished under particularly favorable weather conditions, such as high solar insolation values when cell temperatures are much below the temperatures at STC. In this case, deviations of PR values from the usual ones occurred in the winter months (December, January, and February) due to higher insolation, mild temperatures, and less precipitation and snow, which is unusual for that time of year. On the other hand, plotting the regression line of PR during the 10 years shows a very slight linear decrease over the years, with a regression coefficient of $|-0.0000583|$, representing the slope in a regression model. So, in this case, the PR, that is, the rate of effective produced energy with the energy the PV system would generate if it continually worked on its efficiency at STC, did not change statistically significantly over the 10 years of its operation. In other words, the losses in the PV system, which include soiling and aging of the system components, during its 10-year operation are insignificant (almost negligible) for the observed period. Thus, as PR is a quantitative characteristic of all PV system losses, including soiling and aging of the system’s components, the results show that the behavior of the given PV system over 10 years of its operation does not change significantly; that is, the PV system degradation over 10 years is minimal. Based on the specific yield factor, the capacity factor (CF) can be calculated, which presents the ratio of the yearly specific yield factor and yearly theoretical PV production capability. In this case, the yearly average of CF over the 10-year period range from 12.88% (2014) to 14.02% (2019).

On the other hand, the average value of total energy losses in the given PV system could be calculated as the difference between Y_r and Y_f , and for the 10-year measurement period, it is 22.3%.

Although solar radiation, to a great extent, affects the PV arrays’ electricity output, ambient temperature also affects electricity production and, therefore, other PV system performance parameters, such as PR. Ambient temperature can lead to heating of the

solar module surface, resulting in reduced PV system efficiency. Generally, an increase in temperature of 1 °C causes a decrease in relative PV efficiency between 0.14% and 0.47%, depending on the PV installation type [40]. Recently studies have shown that there are different PV cooling methods that noticeably increase the PV system efficiency but passive ventilation of the PV system, i.e., PV cooling under natural air convection, is the simplest and most inexpensive method for application [40,41]. With the natural air convection appearing behind the PV modules, the temperature of solar cells can decrease by about 15–20 K, as reported in [42]. In this case, as the ventilation of a given PV system unfolds naturally (passive air cooling), so solar modules' cooling is done only by the wind influence. The ratio between the average monthly values of PV system energy efficiency (η_{sys}) and the wind speed (v) for 10-year measurements is given in Figure 7.

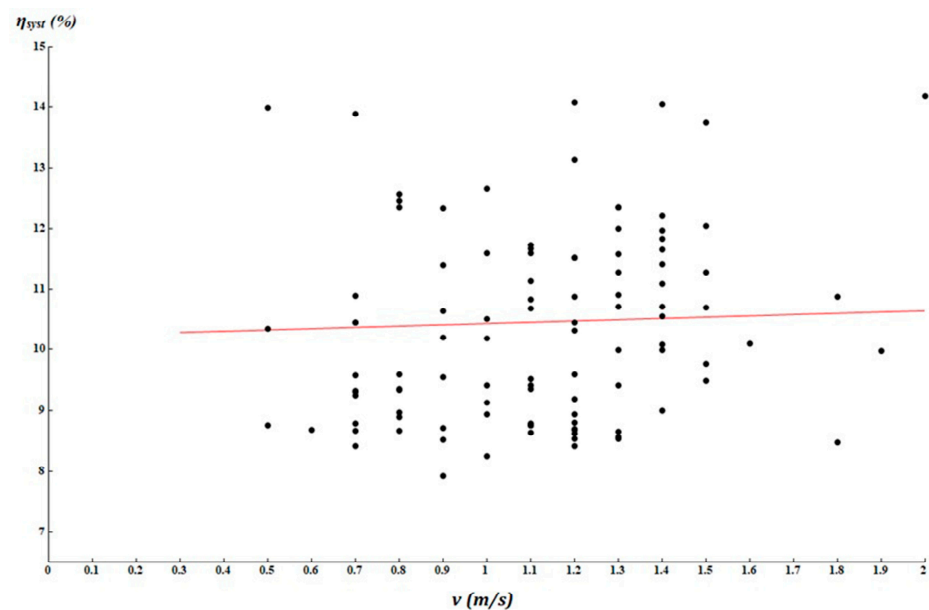


Figure 7. The ratio between the average monthly values of PV system energy efficiency (η_{sys}) and the wind speed (v) for 10-year measurements.

Based on simple linear regression, the plotted regression line for each month during the 10 years (Figure 7) allows for the identification of the slope so that, in this case, the regression coefficient (slope in the regression model) amounts to 0.214411 and responds to the average change of the expected value of the dependent variable η_{sys} for the unit change of the independent variable v . Figure 7 also shows that, with increasing wind speed, PV system efficiency linearly increases. However, this type of PV cooling does not significantly increase the system efficiency. It should be noted that wind speed values for Niš were taken from the website of the Hydrometeorological Institute of the Republic of Serbia (https://www.hidmet.gov.rs/ciril/meteorologija/klimatologija_godisnjaci.php, accessed on 8 May 2023.). It was also observed that the ratio between the average monthly values of PR and the wind speed (v) follows the same trend over the 10-year measurements, as is the case with PV system efficiency.

Performance comparison of grid-connected PV systems with similar installation, power (1–3 kW), and PV technology in the different climatic zone is given in Table 1 [13,22].

As the chosen PV systems, shown in Table 1, and PV system in Niš have similar power and PV configurations, it can be concluded that PV system efficiency and PR are lower in countries with a subtropical climate due to the negative impact of higher ambient temperatures and, therefore, higher solar module temperatures. PV systems with other PV technology and higher powers, installed worldwide and shown in [12–27,32], are not comparable to a given PV system in Niš.

Table 1. Performance comparison of grid-connected PV systems power of 1–3 kW with similar installation and crystalline-Si technology in different climatic zone [13,22].

Location	Power (kW)	PV Technology	Final Yield (h/d)	System Efficiency (%)	PR (%)	CF (%)	Climate	Year/Duration (Years)
Serbia—current study	2	c-Si	3.23	10.49	87	13.45	Temperate/continental	2022/10
Ireland	1.72	c-Si	2.4	12.6	81.5	10.1	Temperate/oceanic	/
Norway	2.1	p-Si	2.55	13–14	83.06	10.58	Temperate/subarctic	/
Brazil	2.2	p-Si	4.6	13.3	82.9	19.2	Tropical/subtropical	/
China	3	p-Si	2.86	10.73	80.6	/	Humid subtropical	2009/3
Morocco	2.4	c-Si, p-Si	4.34	11.67	76.7	18.16	Hot semi-arid subtropical	2018/4
Morocco	2.04	c-Si	4.34	11.7	76.7	/	Hot semi-arid subtropical	2015/2
India	2	p-Si	/	/	70	/	tropical	2019/1
Spain	2	/	/	7.11	64.5	/	Subtropical/Mediterranean	1997/1
Turkey	2.35	c-Si, p-Si	/	13.26	91	/	Humid subtropical	2014/1
Oman	1.4	p-Si	/	/	84.6	21	Hot desert	/
Korea	3	c-Si	/	7.9	63.3	11.5	Humid subtropical	2003/1

3.2. Statistical Analysis of PV System Electricity and Total POA Radiation Data during 10 Years of Measurements

For statistical analysis of the results, the JMP Pro software is used [43]. The regression analysis is used for building a mathematical model for the prediction of PV electricity at a given POA radiation on a PV array. The model enables a specific value of POA radiation (independent variable) to calculate PV electricity (dependent variable) simply. The criterion for estimating the regression coefficients is a least square method. In order to assess the adequacy of a linear regression model, the statistical hypotheses about the model parameters are tested by *T*-test. To test hypotheses about the slope and intercept of the regression model, the error component in the model has to be normally distributed and also independently distributed. The significance of the regression is tested via Analysis of Variance (ANOVA). The existing significance shows that the model gives more information about the system than the simple average. The one-way ANOVA is also used for comparing the groups of data (groups is a categorical variables). The significance of the ANOVA shows that at least two groups have different means. ANOVA also uses to describe complex relationships between variables, as can be seen in the [36,43–47]. As results in ANOVA do not identify which specific differences between pairs of means are significant, it is common to use post hoc tests to investigate differences between multiple groups' means while controlling for experimental error [47].

The PV and POA radiation are numerical variables. The relationship between numerical variables can be graphically shown via a scatter plot (Figure 8). A numerical representation that shows the strength of the relationship between numerical variables is the correlation coefficient. The resulting value of the correlation coefficient between two numerical variables, PV electricity and POA radiation on the PV array, is 0.90059, which shows that the relationship between these two variables is highly positive. The strong and positive relationship tendency between the two variables can also be seen in Figure 8. Such a high value of the correlation coefficient enables the formation of a regression model between the variables.

A linear regression model, developed by the least squares method with R square and R square adjusted at 0.811062 and 0.809344, respectively. The obtained model Equation (2) is:

$$y = 58.326117 + 0.0685116 * x, \quad (2)$$

where *y* is PV electricity in kWh, while *x* is the total POA radiation on PV array in kWh. This model, based on data obtained over 10 years of investigation, can be used for prediction PV electricity value for the known POA radiation value.

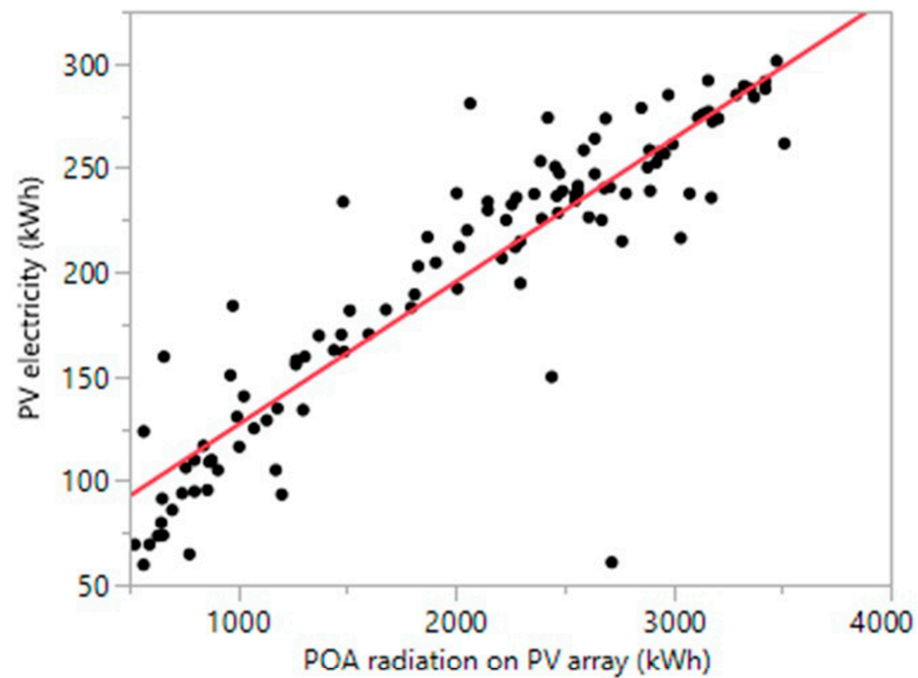


Figure 8. Scatter plot of two numerical variables, PV electricity and POA radiation on PV array with fitted line—red line.

In order to test validity of the model, an ANOVA was conducted. The analysis of variance of the regression model is given in Table 2, while the parameter estimates are given in Table 3.

Table 2. Analysis of variance of the regression model.

Source	DF	Sum of Squares	Mean Square	F Ratio
Model	1	421,038.40	421,038	472.2001
Error	110	98,081.77	892	Prob> F
C. Total	111	519,120.17		<0.0001

Table 3. Parameter estimates.

Term	Estimate	Std Error	t Ratio	Prob > t
Intercept	58.326117	7.002889	8.33	<0.0001
POA radiation on PV array (kWh)	0.0685116	0.003153	21.73	<0.0001

The ANOVA showed that the model is statistically significant $\alpha = 0.05$ with a p -value less than 0.001, which means that the model provides significantly more information than the simple average. The T test was used to test the significance of the intercept and x variable, and both are statistically significant with the p value less than 0.001.

Figure 9 considers POA radiation on PV array during the months measured over 10 years.

In Figure 9, the black line is the mean of the data. The top and bottom of green diamonds represent the confidence interval for each year. The middle line across the diamond represents the mean of the POA radiation for each group (month). The circles represent the results of Tukey–Kramer test, and circles with the same color are statistically significantly different.

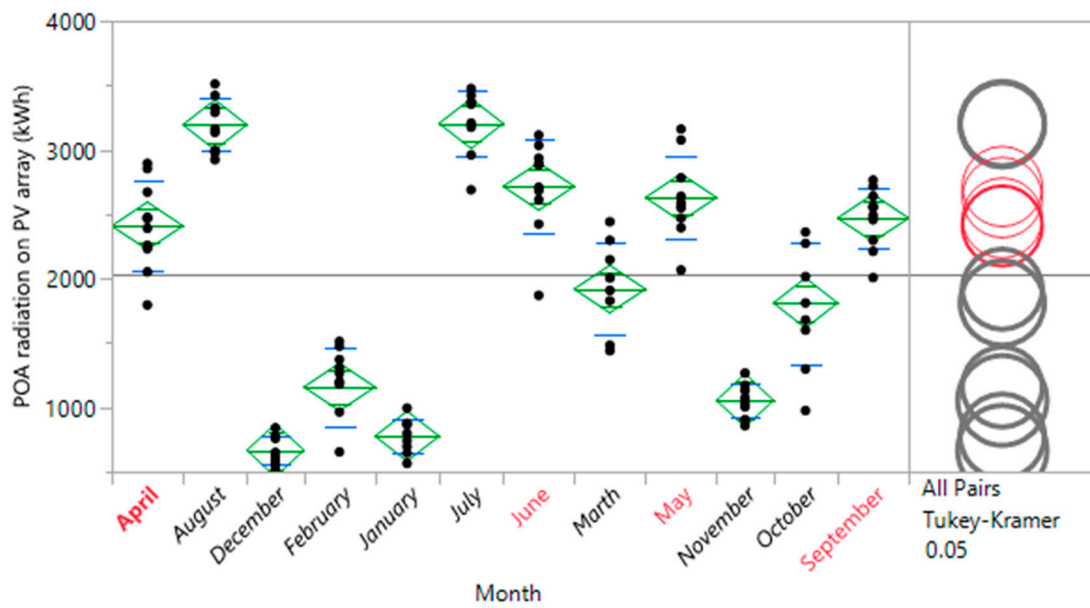


Figure 9. POA radiation on PV array during the months measured over the 10-year period.

The O’Brien test for checking equality of variances, with a p -value of 0.0692, shows that based on the data, there is no evidence that shows statistically unequal variances between the groups.

Results of the ANOVA, which are related to an analysis of variance of POA radiation on PV array by “months” groups, are shown in Table 4, and a p value less than 0.001 shows that at least the mean between two groups of data is statistically significantly different. However, with ANOVA it is not clear which of them are significantly different. For that reason, the post hoc Tukey test is performed (Table 5).

Table 4. Analysis of variance of POA radiation on PV array by “months” groups.

Source	DF	Sum of Squares	Mean Square	F Ratio	Prob > F
Month	11	81,047,311	7,367,937	85.1508	<0.0001
Error	100	8,652,807	86,528		
C. Total	111	89,700,118			

Table 5. The results of the Tukey test—connecting letters report.

Level	DF	Mean
July	A	3204.6841
August	A	3194.4330
June	B	2715.8129
May	B	2629.4805
September	B	2470.4103
April	B	2409.3351
Marth	C	1918.8154
October	C	1810.7883
February	D	1158.8864
November	D	1054.8455
January	D	776.5689
December	E	667.1575

As was expected, the mean of POA radiation has the highest values on July and August. Within the Table 5, the months which are not statistically significantly different are marked with the same letter, while those that are statistically significantly different have letters that are also different.

It should be noted that levels not connected by the same letter are significantly different. The values of PV electricity during the 10-year period are also analyzed and presented in Figure 10.

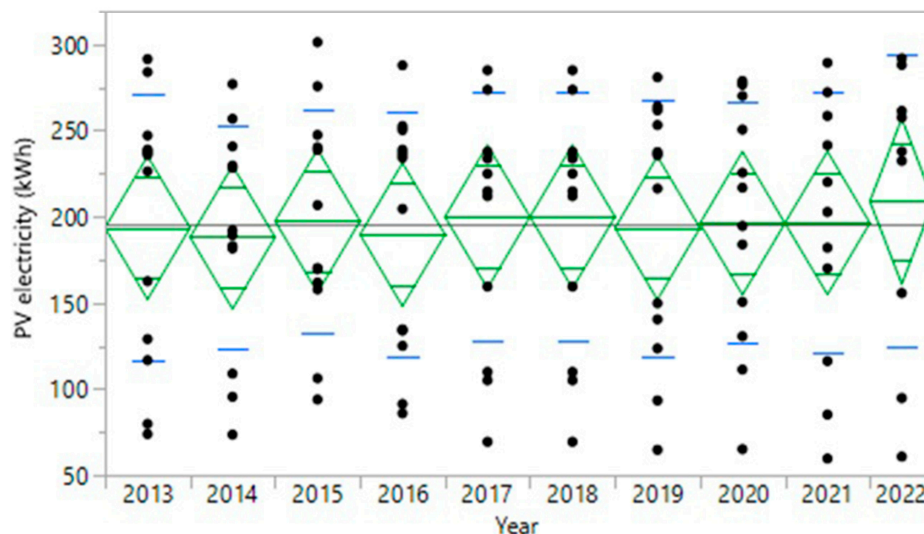


Figure 10. PV electricity during the 10-year period.

In Figure 10, the black line is the mean of the data. The top and bottom of the green diamonds represent the confidence interval $(1-\alpha) \times 100$ for each year (group). The middle line across the diamond represents the mean of the group (mean of the PV electricity within the specific year). The height of the diamonds is proportional to the reciprocal of the square root of the number of observations in the groups. The horizontal extent of each group along the horizontal axis is proportional to the sample size for each level of year variable. It means the narrower diamonds are usually taller. The mean line across the middle of each diamond represents the group mean (mean of PV electricity of the year).

Considering that the variable “years” is a categorical variable and “PV electricity” is numerical one, a one-way analysis needs to be performed. In this regard, it is necessary to test the conditions for applying ANOVA. The O’Brien test is used to check the equality of variances.

The obtained *p*-value of 0.9860 in the O’Brien test indicates that it cannot be said that the variance along the groups (the group is the PV electricity values for a specific year and it means that the sample consists of 10 groups/years) is not equal and ANOVA can be used. The analysis of variance of the PV electricity by years (groups) is given in Table 6.

Table 6. Analysis of variance of the PV electricity by “years”—groups.

Source	DF	Sum of Squares	Mean Square	F Ratio	Prob > F
Year	9	3305.57	367.29	0.0696	0.9999
Error	107	564,654.35	5277.14		
C. Total	116	567,959.92			

The ANOVA shows, with a *p*-value of 0.9999, that it cannot be stated that the mean values of PV electricity between the groups differ from each other. In other words, based on the data obtained over 10 years, it cannot be stated that the mean values of PV electricity change statistically significantly with the years. Because POA radiation and PV electricity are statistically speaking matched pairs data, it means that the same conclusion related to PV electricity could be applied on POA radiation in terms of mean difference over the 10 years.

Thus, the mathematical prediction model was obtained by regression analysis, and the model's validity was tested by ANOVA. As the obtained model is statistically significant and allows for a better prediction than the usual average, the mean values of PV electricity were found to not change statistically significantly during the 10 observed years, while there was a statistically significant difference in the mean POA radiation during the months over 10 years; by applying the obtained model, the PV system output for similar PV installations can be predicted with significant accuracy.

4. Conclusions

This study analyzes the performance and reliability parameters of a long-term grid-connected PV system operation that was exposed to moderately continental climatic conditions in Niš (Serbia).

Based on the experimental results, this study shows that:

- The yearly average values of POA radiation on a south-oriented and optimally inclined plane and total POA radiation on the PV array for a 10-year measurements level are 120.5931 kWh/m² and 1,999,512 kWh, respectively.
- The total electricity production of the PV system for 10 years of its operations is 22,934.65 kWh.
- The yearly average value of PV system efficiency, for the 10-year measurements level, is 10.49%, which is almost two times less than the given efficiency at STC, and the relative error of yearly average values of PV system efficiency, observed from year to year, range from 0.34% to 6.16%.
- The yearly average value of specific yield factor (Y_f) for the 10-year measurements level is 1178.51 kWh/kW_p.
- The yearly average value of CF over the 10-year period is 13.45%.
- The yearly average value of PR for the 10-year measurements level is 0.87, and the relative error of yearly average values of PR, observed from year to year, range from 0.97% to 6.83%. On the other hand, the PV system, which uses highly efficient components and is designed appropriately, shows a PR near 90% ("good" performances are >84%). Thus, the experimental results indicate that the behavior of the given PV system over 10 years of operation does not change significantly.

Based on a statistical analysis of PV system electricity and total POA radiation on PV array data over 10 years of measurements, it can be concluded that:

- A high correlation coefficient value allows for the formation of regression model between PV electricity and POA radiation of the PV array. The obtained model is statistically significant and enables prediction better than the simple average.
- ANOVA shows that the mean values of PV electricity are not statistically significant changed over the 10 observed years.
- ANOVA and post hoc Tukey test show that there is a statistically significant difference of POA mean radiation during the months over 10 years and that the highest values of POA radiation are in July and on August. The Tukey test enables the months to be separated within the groups based on difference of POA radiation on PV array. The months within the groups are without statistically significant differences of POA radiation, while the months in various groups differ statistically significantly in terms of POA radiation.
- Based on the POA radiation values and by applying the obtained model, a prediction of the PV system output can be made for similar PV installations.

It should be also noted that, by making the presented results publicly available, this research could benefit researchers in increasing the accuracy of modeling, prediction, and the cost-effectiveness of PV systems over a longer period of their operation.

Author Contributions: D.D.T. and M.S.K. wrote the manuscript. D.D.T. and B.D. performed conceptualization. D.D.T. and M.S.K. performed final analysis. M.S.K. and B.D. applied software. D.D.T. and M.S.K. provided validation of the results. D.D.T. and S.J. provided the methodology and conducted research. S.J. and T.K. reviewed the manuscript. All authors have read and agreed to the published version of the manuscript.

Funding: Ministry of Education, Science and Technological Development of the Republic of Serbia for support under Contract No. 451-03-47/2023-01/200123.

Institutional Review Board Statement: Not applicable.

Informed Consent Statement: Not applicable.

Data Availability Statement: The datasets generated during and/or analyzed during the current study are available from the corresponding author on reasonable request.

Acknowledgments: Authors thank the Ministry of Education, Science, and Technological Development of the Republic of Serbia for support under Contract No. 451-03-47/2023-01/200123. Additionally, corresponding author would like to thank all researchers (especially, academician Tomislav M. Pavlović) from the Faculty of Sciences and Mathematics in Niš (Department of Physics) for their long-term cooperation.

Conflicts of Interest: The authors declare no conflict of interest.

References

1. Milosavljević, D.D.; Pavlović, T.M.; Mirjanić, D.L.; Divnić, D.; Grozdanović, M.D. Climate changes and renewable sources of energy in Bosnia & Herzegovina. *Contemp. Mater.* **2018**, *IX*–1, 58–69.
2. Wilson, G.M.; Al-Jassim, M.; Metzger, W.K.; Glunz, S.W.; Verlinden, P.; Xiong, G.; Mansfield, L.M.; Stanbery, B.J.; Zhu, K.; Yan, Y.; et al. The 2020 photovoltaic technologies roadmap. *J. Phys. D Appl. Phys.* **2020**, *53*, 493001. [[CrossRef](#)]
3. Pavlović, T.; Milosavljević, D.; Radonjić, I.; Pantić, L.; Radivojević, A.; Pavlović, M. Possibility of electricity generation using PV solar plants in Serbia. *Renew. Sust. Energ. Rev.* **2013**, *20*, 201–218. [[CrossRef](#)]
4. Pavlović, T.; Milosavljević, D.; Mirjanić, D.; Pantić, L.; Radonjić, I.; Piršl, D. Assessments and perspectives of PV solar power engineering in the Republic of Srpska (Bosnia and Herzegovina). *Renew. Sust. Energ. Rev.* **2013**, *18*, 119–133. [[CrossRef](#)]
5. Choi, H.S. Kinetic Photovoltaic Facade System Based on a Parametric Design for Application in Signal Box Buildings in Switzerland. *Appl. Sci.* **2023**, *13*, 4633. [[CrossRef](#)]
6. Akpolat, A.N.; Dursun, E.; Yang, Y. Performance Analysis of a PEMFC-Based Grid-Connected Distributed Generation System. *Appl. Sci.* **2023**, *13*, 3521. [[CrossRef](#)]
7. Nguyen, N.-H.; Le, B.-C.; Bui, T.-T. Benefit Analysis of Grid-Connected Floating Photovoltaic System on the Hydropower Reservoir. *Appl. Sci.* **2023**, *13*, 2948. [[CrossRef](#)]
8. Makrides, G.; Zinsser, B.; Norton, M.; Georghiou, G.E. Performance of Photovoltaics under Actual Operating Conditions. In *Third Generation Photovoltaics*; Fthenakis, V., Ed.; IntechOpen: Nicosia, Cyprus, 2012. Available online: <https://www.intechopen.com/chapters/32596> (accessed on 1 February 2023).
9. Bouziane, K.; Chaouch, N.; Ouahrani, M.R.; Laouini, S.E.; Bouafia, A.; Ali, G.A.M.; Marwani, H.M.; Rahman, M.M.; Mena, F. Production of Photovoltaic Electricity at Different Sites in Algeria. *Appl. Sci.* **2022**, *12*, 10729. [[CrossRef](#)]
10. Milosavljević, D.; Kevkić, T.; Jovanović, S. Review and validation of photovoltaic solar simulation tools/software based on case study. *Open Phys.* **2022**, *20*, 431–451. [[CrossRef](#)]
11. Thar, H.A.; Ya, A.Z.; Win, Y.Y.; Phyu, A.M.K.; Myint, K.K.; Sein, M.T.W. Design and simulation of grid-connected photovoltaic-diesel hybrid system. In *International Conference on Sustainable Energy and Green Technology 2019 IOP Conf. Series: Earth and Environmental Science*; IOP Publishing: Bristol, UK, 2020; Volume 463, p. 012148. [[CrossRef](#)]
12. Seme, S.; Sredenšek, K.; Štumberger, B.; Hadžiselimović, M. Analysis of the performance of photovoltaic systems in Slovenia. *Solar Energy* **2019**, *180*, 550–558. [[CrossRef](#)]
13. Ramanan, P.; Kalidasa Murugavel, K.; Karthick, A. Performance analysis and energy metrics of grid-connected photovoltaic systems. *Energy Sustain. Dev.* **2019**, *52*, 104–115. [[CrossRef](#)]
14. Kumar, N.M.; Gupta, R.P.; Mathew, M.; Jayakumar, A.; Singh, N.K. Performance, energy loss, and degradation prediction of roof-integrated crystalline solar PV system installed in Northern India. *Case Stud. Therm. Eng.* **2019**, *13*, 100409. [[CrossRef](#)]
15. van Sark Wilfried, G.J.H.M.; Nordmann, T.; Luzzi, C.; Mike, G.; Analysis of Long-Term Performance of PV Systems-Different Data Resolution for Different Purposes. International Energy Agency Photovoltaic Power Systems Programme. *Report IEA-PVPS T13-05:2014*. Available online: https://dspace.library.uu.nl/bitstream/handle/1874/314901/IEA_PVPS_T13_ST1_Final_1.pdf?sequence=1&isAllowed=y (accessed on 1 February 2023).

16. Mondol, J.D.; Yohanis, Y.; Smyth, M.; Norton, B. Long term performance analysis of a grid connected photovoltaic system in Northern Ireland. *Energy Convers. Manag.* **2006**, *47*, 2925–2947. [[CrossRef](#)]
17. Mondol, J.D.; Yohanis, Y.G.; Norton, B. Comparison of measured and predicted long term performance of grid a connected photovoltaic system. *Energy Convers. Manag.* **2007**, *48*, 1065–1080. [[CrossRef](#)]
18. Malvoni, M.; Leggieri, A.; Maggiotto, G.; Congedo, P.M.; De Giorgi, M.G. Long term performance, losses and efficiency analysis of a 960 kW P photovoltaic system in the Mediterranean climate. *Energy Convers. Manag.* **2017**, *145*, 169–181. [[CrossRef](#)]
19. Ozden, T.; Akinoglu, B.G.; Turan, R. Long term outdoor performances of three different on-grid PV arrays in central Anatolia—An extended analysis. *Renew. Energy* **2017**, *101*, 182–195. [[CrossRef](#)]
20. Okorieimoh, C.C.; Norton, B.; Conlon, M. *Comparison of Predicted and Measured Annual Performance of a Roof-Top Grid-Connected PV System in the Irish Climate*; Technological University Dublin: Dublin, Ireland, 2021. [[CrossRef](#)]
21. Gulkowski, S. Specific Yield Analysis of the Rooftop PV Systems Located in South-Eastern Poland. *Energies* **2022**, *15*, 3666. [[CrossRef](#)]
22. Aslam, A.; Ahmed, N.; Qureshi, S.A.; Assadi, M.; Ahmed, N. Advances in Solar PV Systems; A Comprehensive Review of PV Performance, Influencing Factors, and Mitigation Techniques. *Energies* **2022**, *15*, 7595. [[CrossRef](#)]
23. Omar Nour-eddine, I.; Lahcen, B.; Fahd, O.H.; Amin, B.; Aziz, O. Outdoor performance analysis of different PV technologies under hot semi-arid climate. *Energy Rep.* **2020**, *6*, 36–48. [[CrossRef](#)]
24. Kaczorowska, D.; Leonowicz, Z.; Rezmer, J.; Janik, P. Long term performance of a PV system with monocrystalline PV cells—A case study. In Proceedings of the 2017 IEEE International Conference on Environment and Electrical Engineering and 2017 IEEE Industrial and Commercial Power Systems Europe (IEEEIC/ICEE/ICPS Europe), Milan, Italy, 6–9 June 2017; pp. 1–8. [[CrossRef](#)]
25. Gulkowski, S.; Zdyb, A.; Dragan, P. Experimental Efficiency Analysis of a Photovoltaic System with Different Module Technologies under Temperate Climate Conditions. *Appl. Sci.* **2019**, *9*, 141. [[CrossRef](#)]
26. Odeh, S. Long Term Assessment of a Grid Connected solar PV System in Sydney. *J. Energy Power Eng.* **2016**, *10*, 591–599.
27. Odeh, S. Analysis of the Performance Indicators of the PV Power System. *J. Power Energy Eng.* **2018**, *6*, 59–75. [[CrossRef](#)]
28. Jordan, D.C.; Sekulic, B.; Marion, B.; Kurtz, S.R. Performance and Aging of a 20-Year-Old Silicon PV System. *IEEE J. Photovolt.* **2015**, *5*, 744–751. [[CrossRef](#)]
29. Daher, D.H.; Gaillard, L.; Ménéz, C. Experimental assessment of long-term performance degradation for a PV power plant operating in a desert maritime climate. *Renew. Energy* **2022**, *187*, 44–55. [[CrossRef](#)]
30. Ishii, T.; Masuda, A. Annual degradation rates of recent crystalline silicon photovoltaic modules. *Prog. Photovolt. Res. Appl.* **2017**, *25*, 953–967. [[CrossRef](#)]
31. Carigiet, F.; Brabec, C.J.; Baumgartner, F.P. Long-term power degradation analysis of crystalline silicon PV modules using indoor and outdoor measurement techniques. *Renew. Sust. Energ. Rev.* **2021**, *144*, 111005. [[CrossRef](#)]
32. Pascual, J.; Martinez-Moreno, F.; García, M.; Marcos, J.; Marroyo, L.; Lorenzo, E. Long-term degradation rate of crystalline silicon PV modules at commercial PV plants: An 82-MWp assessment over 10 years. *Prog. Photovolt. Res. Appl.* **2021**, *29*, 1294–1302. [[CrossRef](#)]
33. Jordan, D.; Sarah, K. Photovoltaic Degradation Rates—An Analytical Review. *Prog. Photovolt. Res. Appl.* **2013**, *21*, 12–29. [[CrossRef](#)]
34. Reich, N.H.; Mueller, B.; Armbruster, A.; van Sark, W.G.J.H.M.; Kiefer, K.; Reise, C. Performance Ratio revisited: Are PR > 90% realistic? *Prog. Photovolt.* **2012**, *20*, 717–726. [[CrossRef](#)]
35. Romero-Fiances, I.; Livera, A.; Theristis, M.; Makrides, G.; Stein, J.S.; Nofuentes, G.; de la Casa, J.; Georghiou, G.E. Impact of duration and missing data on the long-term photovoltaic degradation rate estimation. *Renew. Energy* **2022**, *181*, 738–748. [[CrossRef](#)]
36. Kudelas, D.; Taušová, M.; Tauš, P.; Gabániová, L.; Koščo, J. Investigation of Operating Parameters and Degradation of Photovoltaic Panels in a Photovoltaic Power Plant. *Energies* **2019**, *12*, 3631. [[CrossRef](#)]
37. Mousavi Maleki, S.A.; Hizam, H.; Gomes, C. Estimation of Hourly, Daily and Monthly Global Solar Radiation on Inclined Surfaces: Models Re-Visited. *Energies* **2017**, *10*, 134. [[CrossRef](#)]
38. Govindasamy, T.; Chetty, N. Quantifying the global solar radiation received in Pietermaritzburg, KwaZulu-Natal to motivate the consumption of solar technologies. *Open Phys.* **2018**, *16*, 786–794. [[CrossRef](#)]
39. Milosavljević, D.D.; Pavlović, T.M.; Piršl, D.S. Performance analysis of a grid-connected solar PV plant in Niš, Republic of Serbia. *Renew. Sust. Energ. Rev.* **2015**, *44*, 423–435. [[CrossRef](#)]
40. Dwivedi, P.; Sudhakar, K.; Soni, A.; Solomin, E.; Kirpichnikova, I. Advanced cooling techniques of P.V. modules: A state of art. *Case Stud. Therm. Eng.* **2020**, *21*, 100674. [[CrossRef](#)]
41. Bayrak, F.; Oztop, H.F.; Selimefendigil, F. Experimental study for the application of different cooling techniques in photovoltaic (PV) panels. *Energy Convers. Manag.* **2020**, *212*, 112789. [[CrossRef](#)]
42. Mahdavi, A.; Farhadi, M.; Gorji-Bandpy, M.; Mahmoudi, A. A review of passive cooling of photovoltaic devices. *Cleaner Eng. Technol.* **2022**, *11*, 100579. [[CrossRef](#)]
43. Montgomery, D.C.; Runger, G.C. *Applied Statistics and Probability for Engineers*; John Wiley & Sons Inc.: Hoboken, NJ, USA, 2002; ISBN 0-471-20454-4.
44. Yan, B.; Wu, Q.; Chi, X.; Wu, C.; Luo, P.; Luo, Y.; Zeng, P. Numerical and Experimental Investigation of Photovoltaic/Thermal Systems: Parameter Analysis and Determination of Optimum Flow. *Sustainability* **2022**, *14*, 10156. [[CrossRef](#)]
45. Kim, S.; Aydin, B.; Kim, S. Simulation Modeling of a Photovoltaic-Green Roof System for Energy Cost Reduction of a Building: Texas Case Study. *Energies* **2021**, *14*, 5443. [[CrossRef](#)]

46. Lew, G.; Sadowska, B.; Chudy-Laskowska, K.; Zimon, G.; Wójcik-Jurkiewicz, M. Influence of Photovoltaic Development on Decarbonization of Power Generation—Example of Poland. *Energies* **2021**, *14*, 7819. [[CrossRef](#)]
47. Available online: <https://repository.unam.edu.na/handle/11070/2982> (accessed on 1 January 2023).

Disclaimer/Publisher’s Note: The statements, opinions and data contained in all publications are solely those of the individual author(s) and contributor(s) and not of MDPI and/or the editor(s). MDPI and/or the editor(s) disclaim responsibility for any injury to people or property resulting from any ideas, methods, instructions or products referred to in the content.



Contents lists available at ScienceDirect

Optik

journal homepage: www.elsevier.com/locate/ijleo

Investigation of bandwidth in multimode W-type microstructured plastic optical fibers

Branko Drljača^a, Svetislav Savović^{b,c}, Milan S. Kovačević^b, Ana Simović^b, Ljubica Kuzmanović^b, Aleksandar Djordjevich^c, Konstantinos Aidinis^{d,e}, Gulbakhar Yussupova^f, Rui Min^{g,*}

^a Faculty of Sciences and Mathematics, University of Pristina in Kosovska Mitrovica, L. Ribara 29, 38220 Kosovska Mitrovica, Serbia

^b Faculty of Science, University of Kragujevac, R. Domanovića 12, 34000 Kragujevac, Serbia

^c Department of Mechanical Engineering, City University of Hong Kong, Hong Kong, China

^d Department of Electrical Engineering, Ajman University, P.O. Box 346, Ajman, United Arab Emirates

^e Center of Medical and Bio-allied Health Sciences Research, Ajman University, P.O. Box 346, Ajman, United Arab Emirates

^f Department of Electronics, Telecommunications and Space Technologies, Satbayev University, 22 Satbaev St., Almaty, The Republic of Kazakhstan

^g Center for Cognition and Neuroergonomics, State Key Laboratory of Cognitive Neuroscience and Learning, Beijing Normal University, Zhuhai 519087, China

ARTICLE INFO

Keywords:

Plastic optical fiber
Microstructured optical fiber
Bandwidth
Power flow equation

ABSTRACT

By employing the time-dependent power flow equation (TD PFE), we examine the bandwidth in multimode W-type (double clad) microstructured plastic optical fibers (mPOFs) with a PMMA (polymethyl methacrylate) solid core for parametrically varying depth and width of the intermediate layer (IL) (inner cladding). The investigated W-type mPOF's bandwidth was calculated for various configurations of the air-holes in the inner cladding and varied launch excitations. We obtained that results for smaller inner cladding air-holes at longer fiber lengths exhibit greater bandwidth. On the other hand, for shorter fibers, the launch beam which only excites guided modes, has no effect on the bandwidth due to the air-hole size. The W-type mPOF with a narrower inner cladding has a greater bandwidth. The bandwidth is also larger for a narrow launch that only excites guided modes as opposed to a wider launch that excites both guided and leaky modes. Therefore, the bandwidth increases as the width of the IL is reduced, or by decreasing the diameter of air-holes in the IL, or by exciting only guided modes. W-type mPOFs can be more easily tailored for a specific use in optical fiber sensors and communications because to their programmable properties.

1. Introduction

Due to its ductility, light weight, and large core sizes (up to 1 mm), multimode POF technology are suited for short-range communication lines. POFs are also simple to treat. It is straightforward to integrate large-core POFs with VCSELs, LEDs, and lasers to create low-cost and reliable communication systems. They have also included illumination, sensing, and data processing in their applications. Traditional optical fibers cannot match the flexibility of the microstructured patterning of the optical fiber to affect the

* Corresponding author.

E-mail address: rumi@doctor.upv.es (R. Min).

<https://doi.org/10.1016/j.ijleo.2022.170207>

Received 14 August 2022; Received in revised form 2 November 2022; Accepted 7 November 2022

Available online 9 November 2022

0030-4026/© 2022 Elsevier GmbH. All rights reserved.

sectional profile [1–7]. We are aware that an "endlessly single-mode" mPOF that operates over a wide spectrum of wavelengths has been realized [2]. Photonic bandgap guidance additionally makes it possible to define the hollow core mPOF [8–13]. Applications for mPOFs include dispersion and birefringence for optical fiber communication [14–17], supercontinuum source generation [18–20], wavelength up-down conversion [21,22] and optical fluids sensing [23,24]. The mPOF typically has a numerical aperture (NA) of $NA \approx 0.5$ [25–27]. By using high NA mPOFs, lensless focusing with excellent resolution has been made possible [28].

With the goal of enhancing the transmission properties of multimode mPOFs, there has been a lot of attention in the design of the refractive index (RI) profile in recent years. This led to the development of numerous step-index, graded-index, and W-type mPOF designs [3–5,26,28,29]. When compared to a matched single-clad (SC) fiber, the IL of W-type fibers more tightly bonds the guided modes to the core, producing a wider bandwidth. Therefore, modal dispersion in W-type optical fibers is lower than that in SC fibers. In a typical mPOF design, the cladding layer can be modified by changing the air-hole pattern and/or size inside a concentric ring-like region, as shown in Fig. 1. Fig. 1 shows a mPOF with a changing pattern in the cladding that resembles a W-type optical fiber. When it comes to modifying the geometric properties, such as the air-hole sizes d_q , d_p , and pitch Λ , W-type mPOF is more adaptable.

The efficiency of light propagation through multimode optical fibers is influenced by mode coupling, modal attenuation, and modal dispersion. Mode coupling is primarily brought on by light scattering, which occurs naturally in multimode optical fibers due to the presence of vacancies, cracks, minute bends, and density variations. Because core modes travel at their own, mutually unequal group

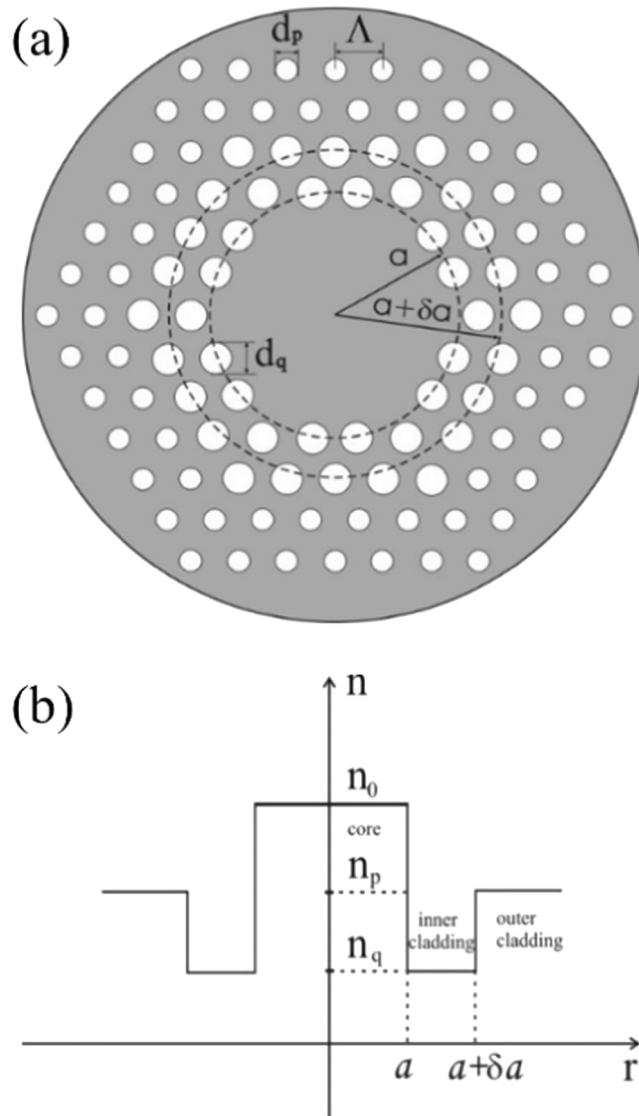


Fig. 1. (a) Cross section of multimode double clad W-type mPOF with a solid-core and rings of air-holes in the inner and outer cladding, where Λ is the hole-to-hole spacing (pitch), d_q and d_p are diameters of air-holes in the inner and outer cladding, respectively, (b) RI profile of the referent W-type mPOF.

velocities, which causes temporal pulse broadening with distance from the input fiber end, modal dispersion is a major limiting issue. It took some time for commercial simulation software programs to be developed in order to study the transmission characteristics of multimode mPOFs. The TD PFE for multimode double-clad W-type mPOF is numerically solved in this paper to address this flaw. Having triangular holes in the inner and outer cladding with a constant pitch (Λ in Fig. 1), enabled us to analyze the multimode W-type mPOF's bandwidth. Using the explicit finite difference method (EFDM) [30], we were able to solve the TD PFE for such a fiber. Results demonstrate the impact of different inner-cladding air-holes arrangements and launch excitations on bandwidth. To our knowledge, this article is the first to examine the bandwidth of a multimode mPOF with a W-type RI distribution.

2. A W-type mPOF design

The air-holes in the cladding of conventional mPOFs typically form a regular triangular lattice. The effective RI profile of the selected optical fiber layer can be changed by adjusting the geometric parameters d_q , d_p and Λ , as illustrated in Fig. 1-a. The outer cladding has smaller air-holes than the inner cladding (d_p vs d_q in Fig. 1-a). The core's RI is higher than that of the two claddings (Fig. 1-b). The inner cladding has the lowest effective RI n_q and the largest diameter d_q of the air-holes while the outer cladding has an effective RI n_p ($n_q < n_p < n_0$). The spacing and size of the air-holes as well as the width of the IL the modified holes are in, are also additional design parameters that are used to engineer dispersion and other fiber qualities. Such a system was simulated using the TD PFE.

3. Time-dependent power flow equation

Gloge's TD PFE [31] describes the power flow for light transmission in multimode optical fibers:

$$\frac{\partial p(\theta, z, t)}{\partial z} + \tau(\theta) \frac{\partial p(\theta, z, t)}{\partial t} = -\alpha(\theta)p(\theta, z, t) + \frac{1}{\theta} \frac{\partial}{\partial \theta} \left[\theta D(\theta) \frac{\partial p(\theta, z, t)}{\partial \theta} \right] \tag{1}$$

where $p(\theta, z, t)$ is power distribution; $\tau(\theta)$ is modal delay; $D(\theta)$ is coupling coefficient; and $\alpha(\theta) = \alpha_0 + \alpha_d(\theta)$ is the modal attenuation, where α_0 represents conventional losses (absorption and scattering). The term α_0 leads only to a multiplier $\exp(-\alpha_0 z)$ in the solution and is thus neglected. The boundary conditions are $p(\theta_m, z) = 0$ where θ_m is the maximum propagation angle, and $D(\theta)(\partial p/\partial \theta) = 0$ at $\theta = 0$.

In order to obtain the frequency response in the frequency domain, Eq. (1)'s Fourier transformation results in:

$$\frac{\partial P(\theta, z, \omega)}{\partial z} + j\omega\tau(\theta)P(\theta, z, \omega) = -\alpha(\theta)P(\theta, z, \omega) + \frac{1}{\theta} \frac{\partial}{\partial \theta} \left[\theta D(\theta) \frac{\partial P(\theta, z, \omega)}{\partial \theta} \right] \tag{2}$$

where $\omega = 2\pi f$ is the angular frequency, also:

$$P(\theta, z, \omega) = \int_{-\infty}^{+\infty} p(\theta, z, t) \exp(-j\omega t) dt \tag{3}$$

The boundary conditions become:

$$P(\theta_m, z, \omega) = 0, \quad D(\theta) \frac{\partial P(\theta, z, \omega)}{\partial \theta} \Big|_{\theta=0} = 0 \tag{4}$$

By splitting $P(\theta, z, \omega)$ into the real part $P_r(\theta, z, \omega)$ and imaginary part $P_i(\theta, z, \omega)$ and assuming a constant coupling coefficient D [32–34], Eq. (2) can be rewritten as the following simultaneous equations:

$$\frac{\partial P_r(\theta, z, \omega)}{\partial z} = -\alpha(\theta)P_r(\theta, z, \omega) + \frac{D}{\theta} \frac{\partial P_r(\theta, z, \omega)}{\partial \theta} + D \frac{\partial^2 P_r(\theta, z, \omega)}{\partial \theta^2} + \omega\tau P_i(\theta, z, \omega) \tag{5a}$$

and:

$$\frac{\partial P_i(\theta, z, \omega)}{\partial z} = -\alpha(\theta)P_i(\theta, z, \omega) + \frac{D}{\theta} \frac{\partial P_i(\theta, z, \omega)}{\partial \theta} + D \frac{\partial^2 P_i(\theta, z, \omega)}{\partial \theta^2} - \omega\tau P_r(\theta, z, \omega) \tag{5b}$$

where:

$$P(\theta, z, \omega) = P_r(\theta, z, \omega) + jP_i(\theta, z, \omega) \tag{6}$$

If $P_r(\theta, z, \omega)$ and $P_i(\theta, z, \omega)$ are obtained by solving Eq. (5), it is possible to obtain the transmission characteristics. The frequency response $H(z, \omega)$ at distance z along the optical fiber is:

$$H(z, \omega) = \frac{2\pi \int_0^{\theta_m} \theta [P_r(\theta, z, \omega) + jP_i(\theta, z, \omega)] d\theta}{2\pi \int_0^{\theta_m} \theta [P_r(\theta, 0, \omega) + jP_i(\theta, 0, \omega)] d\theta} \tag{7}$$

The modal power distribution $P_r(\theta, z, \omega)$ and the spatial transient of power $P_L(z, \omega)$ are given as:

$$P_F(\theta, z, \omega) = [P_r(\theta, z, \omega)^2 + P_i(\theta, z, \omega)^2]^{1/2} \tag{8}$$

$$P_L(z, \omega) = 2\pi \int_0^{\theta_m} \theta P_F(\theta, z, \omega) d\theta \tag{9}$$

A W-type mPOF with the RI distribution as Fig. 1-b shows can be thought of as a SC_q optical fiber and cladding system [32]. The angle $\theta_q \cong (2\Delta_q)^{1/2}$ is the critical angle for the guided modes in the SC_q optical fiber - where $\Delta_q = (n_0 - n_q)/n_0$. Similarly, the angle $\theta_p \cong (2\Delta_p)^{1/2}$ is the critical angle of a singly clad SC_p optical fiber with only the W-type mPOF outer cladding (and no IL), where $\Delta_p = (n_0 - n_p)/n_0$. The modes with propagation angles $\theta < \theta_p$ remain guided for the entire W-type mPOF. Lossy leaky modes are those with angles between θ_p and θ_q . As a result, the leaky mode attenuation is given as:

$$\alpha_L(\theta) = \frac{4(\theta^2 - \theta_p^2)^{1/2}}{a(1 - \theta^2)^{1/2}} \frac{\theta^2(\theta_q^2 - \theta^2)}{\theta_q^2(\theta_q^2 - \theta_p^2)} \exp\left[-2\delta a n_0 k_0 (\theta_q^2 - \theta^2)^{1/2}\right] \tag{10}$$

where $k_0 = 2\pi/\lambda$ is the free-space wave number, a is the core radius and δa is IL width. The modal attenuation in the W-type mPOF is given as:

$$\alpha_d(\theta) = \begin{cases} 0 & \theta \leq \theta_p \\ \alpha_L(\theta) & \theta_p < \theta < \theta_q \\ \infty & \theta \geq \theta_q \end{cases} \tag{11}$$

Modal delay is expressed in terms of θ by [33]:

$$\tau(\theta) = \frac{n_0}{c} \frac{1}{\cos \theta} \cong \frac{n_0}{c} \left(1 + \frac{\theta^2}{2}\right) = \tau_0 + \tau_d(\theta) \tag{12}$$

where c is the light propagation velocity in free space. The first term τ_0 is common to all modes, therefore only $\tau_d(\theta)$ is to be considered in the calculations. The maximum transmission data rate of a fiber is determined by its bandwidth, which is determined by the frequency response $H(z, \omega)$:

$$P_{L(out)}(z, \omega) = H(z, \omega) P_{L(in)}(z = 0, \omega) \tag{13}$$

The frequency response defines the bandwidth (−3 dB bandwidth) of the optical fiber as the frequency (at which output power is reduced to half of the input power (reduced by 3 dB) [35].

4. Numerical results and discussion

We investigated light transmission in a multimode W-type mPOF, as illustrated in Fig. 1. The effective V parameter for such a fiber is as follows:

$$V = \frac{2\pi}{\lambda} \sqrt{a_{eff}^2 n_0^2 - n_{fsm}^2} \tag{14}$$

where $a_{eff} = \sqrt{3}$ [36], and n_{fsm} is cladding’s effective RI, which is obtained from Eq. (4), using the following equation [36]:

$$V\left(\frac{\lambda}{\Lambda}, \frac{d}{\Lambda}\right) = A_1 + \frac{A_2}{1 + A_3 \exp(A_3 \exp(A_4 \lambda)/\Lambda)} \tag{15}$$

with the parameters A_i ($i = 1-4$), which are given in the following form:

$$A_i = a_{i0} + a_{i1} \left(\frac{d}{\Lambda}\right)^{b_{i1}} + a_{i2} \left(\frac{d}{\Lambda}\right)^{b_{i2}} + a_{i3} \left(\frac{d}{\Lambda}\right)^{b_{i3}} \tag{16}$$

Table 1
The coefficients in Eq. (16).

	a_{ij}				b_{ij}		
	$j = 0$	$j = 1$	$j = 2$	$j = 3$	$j = 1$	$j = 2$	$j = 3$
$i = 1$	0.54808	5.00401	-10.43248	8.22992	5	7	9
$i = 2$	0.71041	9.73491	47.41496	-437.50962	1.8	7.32	22.8
$i = 3$	0.16904	1.85765	18.96849	-42.4318	1.7	10	14
$i = 4$	-1.52736	1.06745	1.93229	3.89	-0.84	1.02	13.4

where the coefficients a_{i0} to a_{i3} and b_{i1} to b_{i3} ($i = 1-4$) are given in Table 1.

Table 2 displays significant values of the effective RI of the inner cladding n_q , relative RI difference Δ_q , and critical angles θ_q , for two inner cladding air-hole diameters $d_q = 1.5$ and $2 \mu\text{m}$, for a fixed diameter of the outer cladding air-holes $d_p = 1 \mu\text{m}$, and for $\Lambda = 3 \mu\text{m}$ and $\lambda = 645 \text{ nm}$. The critical angle θ_p for $d_p = 1 \mu\text{m}$ is $\theta_p = 5.8^\circ$, and the effective RI of the outer cladding is $n_p = 1.4844$. The following are the main multimode mPOF's parameters investigated in this paper: refractive index of PMMA solid core $n_0 = 1.492$ [29,36,37], optical fiber diameter $b = 1 \text{ mm}$, the core diameter $2a = 600 \mu\text{m}$ and coupling coefficient $D = 1.649 \times 10^{-4} \text{ rad}^2/\text{m}$ (typical value of D for conventional POFs and mPOFs) [29,36,37]. Because the mode coupling in both conventional POF and mPOF is affected by the polymer core material, the D values obtained for conventional POF can be used in the modeling process of W-type mPOF. In order to model a multimode silica W-type microstructured optical fiber, a similar assumption was used [38]. It should also be noted that because changing the depth of the outer cladding (i.e. the diameter of the air-holes in the outer cladding d_p) has a negligible effect on the bandwidth of the W-type mPOFs, it is not investigated in this work.

Figs. 2 and 3 show the bandwidth vs transmission length for two different diameters of the inner cladding air-holes $d_q = 1.5$ and $2 \mu\text{m}$, for a fixed diameter of the outer cladding air-holes $d_p = 1 \mu\text{m}$ - for three different widths of the Gaussian launch beam distribution FWHM = 1, 5, and 10° , respectively, for the case of a W-type mPOF with width of the inner cladding $\delta = 0.008$ and 0.024 . At longer fiber lengths, bandwidth increases with reducing diameter of the inner cladding air-holes d_q , as shown in Figs. 2 and 3. This is due to a decrease in leaky mode losses as d_q increases, thus power remains in higher leaky modes over longer transmission distances, which results in the increased modal dispersion and reduced bandwidth. At shorter fiber lengths, leaky modes are almost not guided along the fiber for narrower launch beam excitation (exciting only the guided modes), and the influence of d_q on bandwidth is negligible.

The bandwidth is larger in the case of narrower inner cladding ($\delta = 0.008$), as shown in Figs. 2 and 3. Because leaky mode losses are lower in optical fibers with wider inner cladding, power stays in leaky modes for longer optical fiber transmission lengths, resulting in increased modal dispersion and reduced bandwidth. When a narrow launch excites only guided modes, the bandwidth is larger than when a wider launch excites both leaky and guided modes. Modal dispersion rises as both leaky and guided modes are excited, thus reducing bandwidth. After reaching a steady-state distribution [29], the influence of launch excitation is negligible at longer fiber lengths. To summarize, we demonstrated that decreasing the width of the inner cladding, decreasing the diameter of the air-holes in inner cladding, or exciting only guiding modes can improve W-type mPOF's bandwidth.

Finally, one should mention that the theoretical model (time-dependent power flow equation) for calculation of bandwidth in multimode mPOF employed in this work has been successfully employed for calculation of bandwidth in multimode silica microstructured optical fiber [38].

5. Conclusions

The bandwidth of a multimode W-type mPOF with solid core is determined as a function of transmission length by numerically solving the TD PFE for various arrangements of the inner cladding's air-holes and different launch excitations. Longer lengths of optical fiber result in higher bandwidth for smaller diameter of inner cladding air-holes d_q . For shorter lengths, however, the effect of air-hole size d_q on bandwidth is negligible due to excitation that only launches guided modes (narrower launch beam). The bandwidth of W-type mPOF is greater when the inner cladding is narrower. The bandwidth is also larger in the case of a narrow launch that only excites guided modes, as opposed to a wider launch that excites both guided and leaky modes. As a result, as the width of the inner cladding is reduced, or the diameter of air-holes in the inner cladding is reduced, or only guided modes are excited, the bandwidth improves. Based on the results reported here, W-type mPOFs can be more easily tailored for a specific use in optical fiber sensors and communications.

Funding

Strategic Research Grant of City University of Hong Kong (CityU 7004600); Serbian Ministry of Education, Science and Technological Development grant (451-03-68/2022-14/200122); Science Fund of the Republic Serbia (CTPCF-6379382); Guangdong Basic and Applied Basic Research Foundation (2021A1515011997); Special project in key field of Guangdong Provincial Department of Education (2021ZDZX1050); The Innovation Team Project of Guangdong Provincial Department of Education (2021KCXTD014).

Declaration of Competing Interest

No conflict of interest exists in the submission of this manuscript, and manuscript is approved by all authors for publication. I would like to declare on behalf of my co-authors that the work described was original research that has not been published previously, and not

Table 2

For two air-hole diameters d_q in the inner cladding, the data show the effective RI n_q , relative RI difference Δ_q and critical angle θ_q - all for the inner cladding at $\lambda = 645 \text{ nm}$.

d_q (μm)	1.5	2.0
n_q	1.4757	1.4458
$\Delta_q = (n_0 - n_q)/n_0$	0.01092	0.03097
θ_q (deg)	8.5	14.3

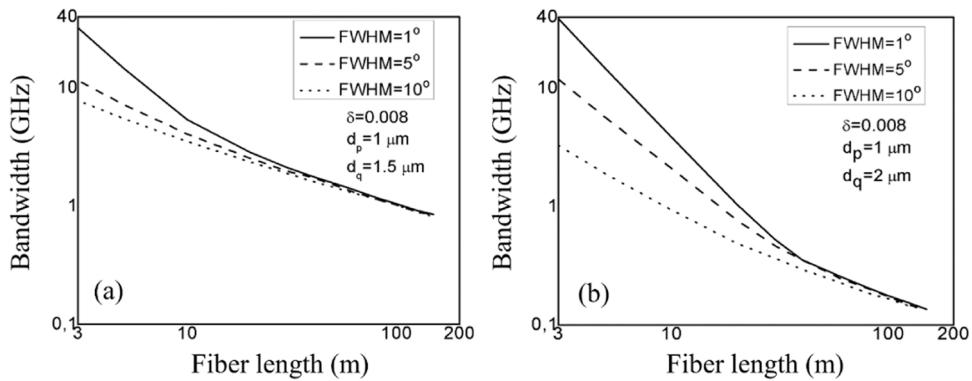


Fig. 2. Bandwidth as a function of transmission length for a fixed diameter of air-holes in the outer cladding $d_p = 1 \mu\text{m}$, width of the inner cladding $\delta = 0.008$, three different launch beam distributions with FWHM = 1, 5 and 10° and two different diameters of air-holes in the inner cladding (a) $d_q = 1.5$ and (b) $d_q = 2 \mu\text{m}$.

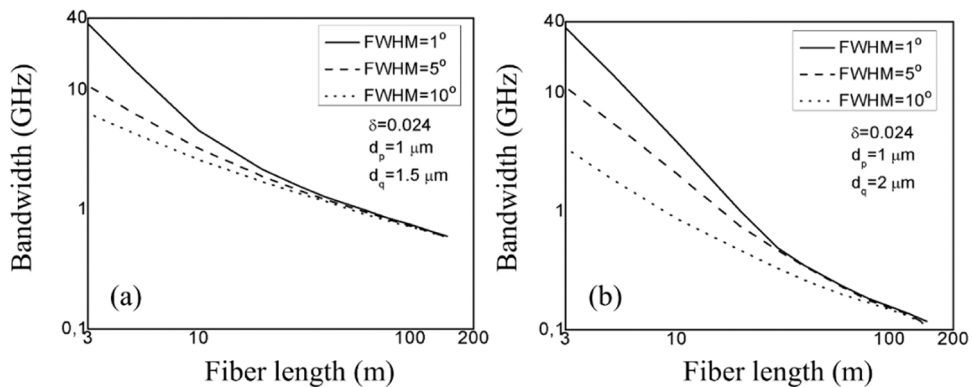


Fig. 3. Bandwidth as a function of transmission length for a fixed diameter of air-holes in the outer cladding $d_p = 1 \mu\text{m}$, width of the inner cladding $\delta = 0.024$, three different launch beam distributions with FWHM = 1, 5 and 10° and two different diameters of air-holes in the inner cladding (a) $d_q = 1.5$ and (b) $d_q = 2 \mu\text{m}$.

under consideration for publication elsewhere, in whole or in part. All the authors listed have approved the manuscript that is enclosed.

Data Availability

Data will be made available on request.

References

- [1] J.C. Knight, T.A. Birks, P.St.J. Russell, D.M. Atkin, All-silica single-mode optical fiber with photonic crystal cladding, *Opt. Lett.* 21 (1996) 1547–1549.
- [2] T.A. Birks, J.C. Knight, P.St.J. Russell, Endlessly single-mode photonic crystal fiber, *Opt. Lett.* 22 (1997) 961–963.
- [3] P.St.J. Russell, Photonic crystal fibers, *Science* 299 (2003) 358–362.
- [4] J.C. Knight, Photonic crystal fiber, *Nature* 424 (14) (2003) 847–851.
- [5] P.St.J. Russell, Photonic-crystal fibers, *J. Light. Technol.* 24 (2006) 4729–4749.
- [6] J.C. Knight, J. Broeng, T.A. Birks, P.S.J. Russell, Photonic band gap guidance in optical fibers, *Science* 282 (1998) 1476–1478.
- [7] J.C. Knight, P.S.J. Russell, Photonic crystal fibers: New way to guide light, *Science* 296 (2002) 276–277.
- [8] R.F. Cregan, B.J. Mangan, J.C. Knight, T.A. Birks, P.S.J. Russell, P.J. Roberts, D.C. Allan, Single-mode photonic band gap guidance of light in air, *Science* 285 (1999) 1537–1539.
- [9] R. Amezcua-Correa, F. Gerome, S.G. Leon-Saval, N.G.R. Broderick, T.A. Birks, J.C. Knight, Control of surface modes in low loss hollow core photonic bandgap fibers, *Opt. Express* 16 (2008) 1142–1149.
- [10] G. Bouwmans, L. Bigot, Y. Quiquempois, F. Lopez, L. Provino, M. Douay, Fabrication and characterization of an all-solid 2d photonic bandgap fiber with a low-loss region (<20 db/km) around 1550 nm, *Opt. Express* 13 (2005) 8452–8459.
- [11] F. Luan, A.K. George, T.D. Hedley, G.J. Pearce, D.M. Bird, J.C. Knight, P. St. J. Russell, All-solid photonic bandgap fiber, *Opt. Lett.* 29 (2004) 2369–2371.
- [12] F. Benabid, J.C. Knight, G. Antonopoulos, P.St.J. Russell, Stimulated Raman scattering in hydrogen-filled hollow-core photonic crystal fiber, *Science* 298 (2002) 399–402.
- [13] P.S. Light, F. Benabid, F. Couny, M. Maric, A.N. Luiten, Electromagnetically induced transparency in Rb-filled coated hollow-core photonic crystal fiber, *Opt. Lett.* 32 (2007) 1323–1325.
- [14] D. Mogilevsev, T.A. Birks, P.St.J. Russell, Group-velocity dispersion in photonic crystal fibers, *Opt. Lett.* 23 (1998) 1662–1664.

- [15] K. Saitoh, M. Koshiba, T. Hasegawa, E. Sasaoka, Chromatic dispersion control in photonic crystal fibers: application to ultra-flattened dispersion, *Opt. Express* 11 (2003) 843–852.
- [16] S. Lee, W. Ha, J. Park, S. Kim, K. Oh, A new design of low-loss and ultra-flat zero dispersion photonic crystal fiber using hollow ring defect, *Opt. Commun.* 285 (20) (2012) 4082–4087.
- [17] D. Chen, M.L.V. Tse, H.Y. Tam, Optical properties of photonic crystal fibers with a fiber core of arrays of sub-wavelength circular air holes: birefringence and dispersion, *Prog. Electromagn. Res.* 105 (2010) 193–212.
- [18] J.K. Ranka, R.S. Windeler, A.J. Stentz, “Visible continuum generation in air silica microstructured optical fibers with anomalous dispersion at 800 nm, *Opt. Lett.* 25 (2000) 25–27.
- [19] K.M. Hilligsøe, T.V. Andersen, H.N. Paulsen, C.K. Nielsen, K. Mølmer, S. Keiding, R. Kristiansen, K.P. Hansen, J.J. Larsen, Supercontinuum generation in a photonic crystal fiber with two zero dispersion wavelengths, *Opt. Express* 12 (2004) 1045–1054.
- [20] W.J. Wadsworth, N. Joly, J.C. Knight, T.A. Birks, F. Biancalana, P.St.J. Russell, Supercontinuum and four-wave mixing with Q-switched pulses in endlessly single-mode photonic crystal fibres, *Opt. Express* 12 (2004) 299–309.
- [21] J.H. Lee, W. Belardi, K. Furusawa, P. Petropoulos, Z. Yusoff, T.M. Monro, D.J. Richardson, Four-wave mixing based 10-Gb/s tunable wavelength conversion using a holey fiber with a high SBS threshold, *IEEE Photonics Technol. Lett.* 15 (2003) 440–442.
- [22] T.V. Andersen, K.M. Hilligsøe, C.K. Nielsen, J. Thøgersen, K.P. Hansen, S.R. Keiding, J.J. Larsen, Continuous-wave wavelength conversion in a photonic crystal fiber with two zero-dispersion wavelengths, *Opt. Express* 12 (2004) 4113–4122.
- [23] J. Park, D.E. Kang, B. Paulson, T. Nazari, K. Oh, Liquid core photonic crystal fiber with low-refractive-index liquids for optofluidic applications, *Opt. Express* 22 (14) (2014) 17320–17330.
- [24] S.H. Kassani, R. Khazaiezhad, Y. Jung, J. Kobelke, K. Oh, Suspended ring-core photonic crystal fiber gas sensor with high sensitivity and fast response, *IEEE Photon. J.* 7 (2015) 2700409.
- [25] W. Wadsworth, R. Percival, G. Bouwmans, J. Knight, T. Birks, T. Hedley, P.St.J. Russell, Very high numerical aperture fibers, *IEEE Photon. Technol. Lett.* 16 (2004) 843–845.
- [26] R. Lwin, G. Barton, L. Harvey, J. Harvey, D. Hirst, S. Manos, M.C.J. Large, L. Poladian, A. Bachmann, H. Poisel, K.-F. Klein, Beyond the bandwidth-length product: Graded index microstructured polymer optical fiber, *Appl. Phys. Lett.* 91 (2007), 191119.
- [27] K.P. Hansen, C.B. Olausson, J. Broeng, D. Noordegraaf, M.D. Maack, T.T. Alkeskjold, M. Laurila, T. Nikolajsen, P.M.W. Skovgaard, M.H. Sorensen, M. Denninger, C. Jakobsen, H.R. Simonsen, Aircad fiber laser technology, *Opt. Eng.* 50 (2011), 111609.
- [28] L.V. Amitonova, A. Descloux, J. Petschulat, M.H. Frosz, G. Ahmed, F. Babic, X. Jiang, A.P. Mosk, P.St.J. Russell, P.W.H. Pinkse, High-resolution wavefront shaping with a photonic crystal fiber for multimode fiber imaging, *Opt. Lett.* 41 (2016) 497–500.
- [29] B. Drljača, S. Savović, M.S. Kovačević, A. Simović, Lj. Kuzmanović, A. Djordjevič, R. Min, Transmission performance of multimode W-type plastic photonic crystal fibers, *Opt. Express* 29 (2022) 29589.
- [30] S. Savović, A. Simović, A. Djordjevič, Explicit finite difference solution of the power flow equation in W-type fibers, *Opt. Laser Technol.* 44 (2012) 1786–1790.
- [31] D. Gloge, Impulse response of clad optical multimode fibers, *Bell Syst. Tech. J.* 52 (1973) 801–816.
- [32] T.P. Tanaka, S. Yamada, Steady-state characteristics of multimode W-type fibers, *Appl. Opt.* 18 (1979) 3261–3264.
- [33] T.P. Tanaka, S. Yamada, Numerical solution of power flow equation in multimode W-type optical fibers, *Appl. Opt.* 19 (1980) 1647–1652.
- [34] A. Simović, A. Djordjevič, S. Savović, Influence of width of intermediate layer on power distribution in W-type optical fibers, *Appl. Opt.* 51 (2012) 4896–4901.
- [35] C.-A. Bunge, M. Beckers, B. Lustermann, Basic principles of optical fibres, in: Christian-Alexander Bunge, Thomas Gries, Markus Beckers (Eds.), In the Book: *Polymer Optical Fibres*, Elsevier Ltd, 2017, pp. 47–118.
- [36] S. Savović, M.S. Kovačević, B. Drljača, A. Simović, Lj. Kuzmanović, A. Djordjevič, Power flow in multimode step-index plastic photonic crystal fibers, *Optik* 247 (2021), 167868.
- [37] J. Mateo, M.A. Losada, I. Garcés, J. Zubia, Global characterization of optical power propagation in step-index plastic optical fibers, *Opt. Express* 14 (2006) 928–935.
- [38] B. Drljača, S. Savović, M.S. Kovačević, A. Simović, Lj. Kuzmanović, A. Djordjevič, R. Min, Theoretical investigation of bandwidth of multimode step-index silica photonic crystal fibers, *Photonics* 9 (2022) 214.

Theoretical Investigation of Bandwidth in Multimode Step-Index Silica Photonic Crystal Fibers

Branko Drljača ¹, Svetislav Savović ^{2,3}, Milan S. Kovačević ², Ana Simović ², Ljubica Kuzmanović ²,
Alexandar Djordjevich ³ and Rui Min ^{4,*}

¹ Faculty of Sciences and Mathematics, University of Priština in Kosovska Mitrovica, L. Ribara 29, 38220 Kosovska Mitrovica, Serbia; branko.drljaca@pr.ac.rs

² Faculty of Science, University of Kragujevac, R. Domanovića 12, 34000 Kragujevac, Serbia; savovic@kg.ac.rs (S.S.); kovac@kg.ac.rs (M.S.K.); asimovic@kg.ac.rs (A.S.); ljubica.kuzmanovic@pmf.kg.ac.rs (L.K.)

³ Department of Mechanical Engineering, City University of Hong Kong, Hong Kong, China; mealex@cityu.edu.hk

⁴ Center for Cognition and Neuroergonomics, State Key Laboratory of Cognitive Neuroscience and Learning, Beijing Normal University at Zhuhai, Zhuhai 519087, China

* Correspondence: ruimin@bnu.edu.cn

Abstract: Solving the time-dependent power flow equation (PFE) provides a useful method to study the transmission bandwidth of step-index silica photonic crystal fibers (SI SPCFs). The transmission bandwidth of these kinds of fibers is determined for different air-hole structures (different numerical apertures (NAs)) and different distribution widths of the Gaussian launch beam. The results indicate that the lower the NA of SI SPCFs, the higher the bandwidth (for example, for a lower NA of SI SPCFs, a bandwidth that is eight times larger is obtained at a fiber length of 3500 m). The narrower launch beam at short fiber lengths results in a wider bandwidth. The longer the fiber (>300 m), the much less the effect of the launch beam width on the bandwidth. The bandwidth becomes independent of the width of the launch beam distribution at the fiber length at which a steady-state distribution (SSD) is reached. These results are useful for some potential applications, such as high capacity transmission optical fiber systems.

Keywords: photonic crystal fiber; bandwidth; multimode optical fiber; step-index fiber; power flow equation

Citation: Drljača, B.; Savović, S.; Kovačević, M.S.; Simović, A.; Kuzmanović, Lj.; Djordjevich, A.; Min, R. Theoretical Investigation of Bandwidth of Multimode Step-Index Silica Photonic Crystal Fibers. *Photonics* **2022**, *9*, 214. <https://doi.org/10.3390/photonics9040214>

Received: 28 February 2022

Accepted: 22 March 2022

Published: 23 March 2022

Publisher's Note: MDPI stays neutral with regard to jurisdictional claims in published maps and institutional affiliations.



Copyright: © 2022 by the authors. Licensee MDPI, Basel, Switzerland. This article is an open access article distributed under the terms and conditions of the Creative Commons Attribution (CC BY) license (<https://creativecommons.org/licenses/by/4.0/>).

1. Introduction

The communication system based on optical fibers provides more reliability and flexibility than the wireless communication medium, which is the backbone of the modern telecommunication network [1]. The PCF first investigated by the Russell group is a specific optical fiber technology (optical fiber with micro-structure) for light guiding [2]. The light passing through PCFs follows two principles: the first one is light passing through a high refractive index (RI) medium surrounded by a lower RI medium, and the other one is light passing through a low RI medium surrounded by a higher RI medium. For some kinds of PCFs, a high RI material, such as silica material, is implemented as the background material, which is doped in a periodic manner with air holes. The hole pattern has lowered the effective RI of the fiber cladding and allows the optical fibers to guide light [2–7]. Choosing this cladding hole pattern allows one to adjust the RI profile of the optical fiber during the design process. PCFs exhibit excellent performance as the microstructure of the fibers provides additional flexibility to influence the cross-section during the design phase. The “end-less” PCF [2] has been shown to work only in fundamental mode over a wide range of wavelengths. On the other hand, a PCF may have an empty core. Photonic gap guidance [8–11] allows the “air center” of hollow fibers to have a lower RI than the RI

of the cladding material [12,13]. In practice, optical dispersion and birefringence of PCFs is often investigated [14–17]. Nowadays, PCFs are important since they can be implemented for many applications, such as supercontinuum light generation [18–20], light wavelength conversion [21,22], optical fluids [23], and different sensing area [24]. The width of the PCF material between the holes of the cladding determines the NA of the PCF, which is normally limited to $NA \approx 0.5\text{--}0.6$ [25–27]. Sometimes, PCFs considered include heavy metal oxide glass fibers [28] and liquid-filled hollow-core fibers for specific applications [29]. Additionally, high NA PCFs demonstrated excellent resolution in lensless focusing [30].

PCFs show high bandwidth performance and flexibility, making them useful for transmission and sensing technology. The propagation characteristics of PCFs are important parameters for their practical applications, which are affected by mode attenuation, mode coupling, and modal dispersion. The main cause of mode coupling lies in light scattering due to intrinsic perturbations in the fiber (micro-bend, changes in diameter, and changes in density and RI distribution). One of the most efficient approaches in modeling the transmission characteristics of multimode optical fibers is based on the employment of the PFE [31–36]. In this work, by solving the time-dependent PFE, we determine the bandwidth of a multimode SI SPCF with a solid core for two different launch beam distribution widths and two different air-hole sizes (two different NAs), which have a great potential for applications in optical fiber communication. The central part has the highest RI; holes with diameter d and pitch Λ in the cladding reduce the effective value of RI in the cladding.

2. The Design of the PCF

Here, we present a SI PCF design in which the air holes are uniform in size and form an equilateral triangular network in the cladding, as shown in Figure 1. Despite the fact that the material properties are uniform throughout the optical fiber, the hole-free central part has the highest RI; holes with diameter d and pitch Λ in the cladding reduce the effective value of RI in the cladding.

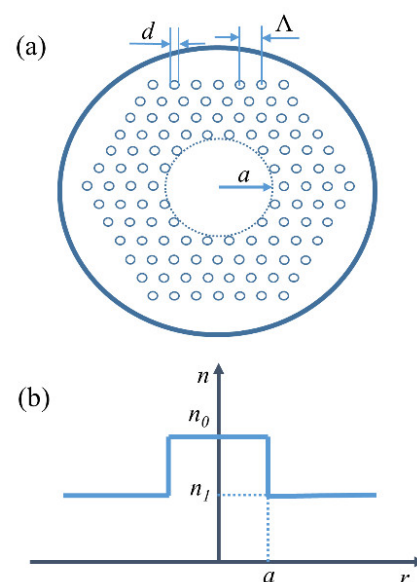


Figure 1. (a) Lateral end-face of a solid-core multimode SI PCF, where Λ is the pitch and d is the diameter of the air holes. (b) RI profile of a multimode SI PCF.

3. The Time-Dependent PFE

We used the time-dependent PFE for the bandwidth simulation, which is presented in the following form [31]:

$$\frac{\partial p(\theta, z, t)}{\partial z} + \tau(\theta) \frac{\partial p(\theta, z, t)}{\partial t} = -\alpha(\theta)P(\theta, z, t) + \frac{1}{\theta} \frac{\partial}{\partial \theta} \left[D(\theta) \frac{\partial p(\theta, z, t)}{\partial \theta} \right] \quad (1)$$

where t is the time, θ is the angle, z is the optical fiber length, $p(\theta, z, t)$ is the power distribution, $\tau(\theta)$ is the modal delay, $D(\theta)$ is the coupling coefficient (usually assumed constant [31,32]), and $\alpha(\theta) \approx \alpha_0$ (it does not have to be accounted when solving (1)) [32].

The Fourier transformation of Equation (1) is:

$$\frac{\partial P(\theta, z, \omega)}{\partial z} + j\omega\tau(\theta)P(\theta, z, \omega) = -\alpha(\theta)P(\theta, z, \omega) + \frac{1}{\theta} \frac{\partial}{\partial \theta} \left[\theta D(\theta) \frac{\partial P(\theta, z, \omega)}{\partial \theta} \right] \quad (2)$$

where $\omega = 2\pi f$ is the angular frequency, and we obtain:

$$P(\theta, z, \omega) = \int_{-\infty}^{+\infty} p(\theta, z, t) \exp(-j\omega t) dt \quad (3)$$

The boundary conditions are presented in the following form:

$$P(\theta_m, z, \omega) = 0, \quad D(\theta) \frac{\partial P(\theta, z, \omega)}{\partial \theta} \Big|_{\theta=0} = 0 \quad (4)$$

Since $P(\theta, z, \omega)$ has the real part $P_r(\theta, z, \omega)$ and imaginary part $P_i(\theta, z, \omega)$, Equation (2) can be rewritten as:

$$\frac{\partial P_r(\theta, z, \omega)}{\partial z} = -\alpha(\theta)P_r(\theta, z, \omega) + \frac{D}{\theta} \frac{\partial P_r(\theta, z, \omega)}{\partial \theta} + D \frac{\partial^2 P_r(\theta, z, \omega)}{\partial \theta^2} + \omega\tau P_i(\theta, z, \omega) \quad (5)$$

$$\frac{\partial P_i(\theta, z, \omega)}{\partial z} = -\alpha(\theta)P_i(\theta, z, \omega) + \frac{D}{\theta} \frac{\partial P_i(\theta, z, \omega)}{\partial \theta} + D \frac{\partial^2 P_i(\theta, z, \omega)}{\partial \theta^2} - \omega\tau P_r(\theta, z, \omega)$$

where

$$P(\theta, z, \omega) = P_r(\theta, z, \omega) + jP_i(\theta, z, \omega) \quad (6)$$

We obtained $P_r(\theta, z, \omega)$ and $P_i(\theta, z, \omega)$ by numerically solving Equation (5) using the explicit finite difference method (EFDM). The frequency response $H(z, \omega)$ is then obtained as:

$$H(z, \omega) = \frac{2\pi \int_{\theta_m}^{\theta_m} \theta [P_r(\theta, z, \omega) + jP_i(\theta, z, \omega)] d\theta}{2\pi \int_0^{\theta_m} \theta [P_r(\theta, 0, \omega) + jP_i(\theta, 0, \omega)] d\theta} \quad (7)$$

This equation can be used to determine the change of the transmission bandwidth with the transmission length.

4. Simulation Results

The bandwidth for various launch beam distribution widths in the multimode SI SPCF was investigated. For a PCF with triangular lattice air holes, the effective parameter V is presented as:

$$V = \frac{2\pi}{\lambda} a_{\text{eff}} \sqrt{n_0^2 - n_{\text{fsm}}^2} \quad (8)$$

where n_0 is the RI of the core, n_{fsm} is the effective RI of the cladding, and $a_{\text{eff}} = \Lambda/\sqrt{3}$ [33]. The effective RI of the cladding $n_1 \equiv n_{\text{fsm}}$, can be obtained from Equation (8), using the following equation [33]:

$$V\left(\frac{\lambda}{\Lambda}, \frac{d}{\Lambda}\right) = A_1 + \frac{A_2}{1 + A_3 \exp(A_4 \lambda / \Lambda)} \tag{9}$$

where the parameters for fitting A_i ($i = 1$ to 4) are presented as:

$$A_i = a_{i0} + a_{i1} \left(\frac{d}{\Lambda}\right)^{b_{i1}} + a_{i2} \left(\frac{d}{\Lambda}\right)^{b_{i2}} + a_{i3} \left(\frac{d}{\Lambda}\right)^{b_{i3}} \tag{10}$$

where the coefficients a_{i0} to a_{i3} and b_{i1} to b_{i3} ($i = 1$ to 4) are supplied in Table 1.

Table 1. Fitting coefficients in Equation (10) [33].

	$i = 1$	$i = 2$	$i = 3$	$i = 4$
a_{i0}	0.54808	0.71041	0.16904	-1.52736
a_{i1}	5.00401	9.73491	1.85765	1.06745
a_{i2}	-10.43248	47.41496	18.96849	1.93229
a_{i3}	8.22992	-43.750962	-42.4318	3.89
b_{i1}	5	1.8	1.7	-0.84
b_{i2}	7	7.32	10	1.02
b_{i3}	9	22.8	14	13.4

Figure 2 shows the cladding’s effective RI $n_1 \equiv n_{fsm}$ as a function of λ / Λ , for $\Lambda = 3 \mu\text{m}$ and for two values of the hole diameter d . The design parameters of the investigated SI SPCF are presented in Table 2.

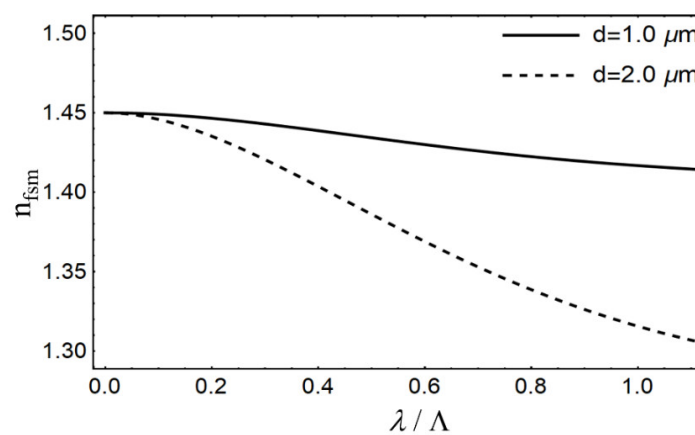


Figure 2. Effective RI of the inner cladding as a function of λ / Λ .

Table 2. Effective RI of the cladding n_1 , relative RI difference $\Delta = (n_0 - n_1)/n_0$, where $n_0 = 1.45$, and the critical angle θ_m for the varied air-hole diameter d at wavelength 850 nm.

d (μm)	1.0	2.0
n_1	1.443717	1.423679
$\Delta = (n_0 - n_1)/n_0$	0.00433	0.01815
θ_m (deg)	5.34	10.93

The Equation (5) are solved using the EFDM [34], where the coupling coefficient was $D = 2.3 \times 10^{-6} \text{ rad}^2/\text{m}$ (typical value of D for glass core fibers [35]). The cases with diameter of air holes $d = 1 \mu\text{m}$ ($n_1 = 1.443717$, $\Delta = 0.00433$) and $d = 2 \mu\text{m}$ ($n_1 = 1.423679$, $\Delta = 0.01815$) and launch beam distribution with $(\text{FWHM})_{z=0} = 1^\circ$ and 5° are analyzed.

For illustration purposes, Figure 3 shows the bandwidth expansion over the fiber length. This was calculated for the beam distributions with $(\text{FWHM})_{z=0} = 1^\circ$ and 5° , in the case of $\Delta = 0.00433$ and $\Delta = 0.01815$. From Figure 3, we can observe that a lower NA (smaller Δ) yields a higher bandwidth. For shorter fiber lengths, the smaller the Gaussian launch beam width, the wider the bandwidth. This is due to the narrow launch beam of $(\text{FWHM})_{z=0} = 1^\circ$, which reduces the modal dispersion. The effect of the $(\text{FWHM})_{z=0}$ of the launch beam distribution on the bandwidth vanishes with increasing the optical fiber length. Initial mode excitation has less effect on the bandwidth of longer fibers, because mode coupling affects the redistribution of energy between guide modes. Figure 3 shows a linear decrease in the bandwidth over short fiber lengths before switching to a $1/z^{1/2}$ functional dependence. For the larger widths of the Gaussian launch beams and lower NAs, this change, and therefore the equilibrium mode distribution, occurs at shorter fiber lengths. For $(\text{FWHM})_{z=0} = 1^\circ$, the length is $L_c \approx 500 \text{ m}$ for $n_1 = 1.443717$ and $L_c \approx 1650 \text{ m}$ for $n_1 = 1.423679$. For $(\text{FWHM})_{z=0} = 5^\circ$, the length is $L_c \approx 300 \text{ m}$ for $n_1 = 1.443717$ and $L_c \approx 1450 \text{ m}$ for $n_1 = 1.423679$ [36]. The shorter the length L_c , the slower the bandwidth decrease. The bandwidth tends to be length-independent for certain fiber lengths. This length marks the onset of an SSD. This length is $z_{SSD} \approx 1150 \text{ m}$ for $n_1 = 1.443717$ and $z_{SSD} \approx 3800 \text{ m}$ for $n_1 = 1.423679$ [36]. Finally, one can conclude that the examined PCFs seem to be suitable for short-haul rather than long-haul applications.

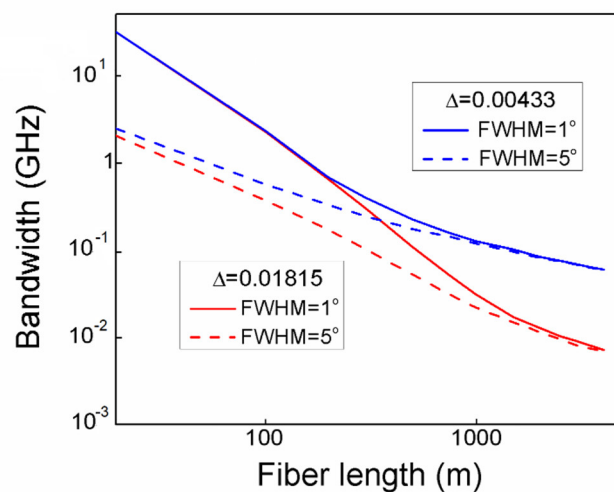


Figure 3. Bandwidth as a function of the optical fiber length for the Gaussian launch beams with $(\text{FWHM})_{z=0} = 1^\circ$ and 5° for $\Delta = 0.00433$ $\Delta = 0.01815$.

It is worth noting that the proposed method for the investigation of the bandwidth in SI SPCFs by employing the time-dependent power flow equation has already been proven as effective and accurate in several previously published works, including the theoretical and experimental investigation of bandwidths in graded-index plastic optical fibers and SI plastic optical fibers [34,37]. A block diagram that illustrates the procedure applied in this work for the calculation of the bandwidth in SI SPCFs is shown in Figure 4.

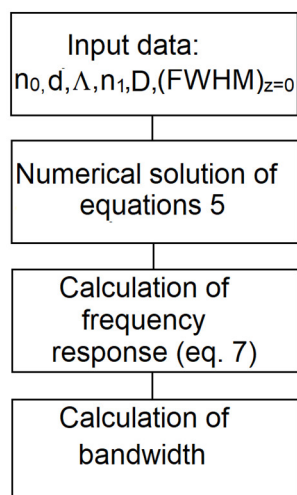


Figure 4. Block diagram for the calculation of the bandwidth in SI SPCFs.

5. Conclusions

To conclude, by solving the time-dependent PFE, an approach for estimating the bandwidth of multimode SI SPCFs is proposed. From the obtained results, we conclude that lower NA enables a higher fiber bandwidth (e.g., for lower NA of SI SPCFs, a bandwidth that is eight times larger is obtained at a fiber length of 3500 m). Additionally, a narrower Gaussian launch beam leads to a higher bandwidth at short fiber lengths. The bandwidth decreases with increasing the fiber length and tends to be launch-beam independent for a certain fiber length. This length marks the onset of the SSD. One can conclude that the examined PCFs seem to be suitable for short-haul rather than long-haul applications. Finally, we show that these tuning parameters provide additional flexibility in the construction of photonic crystal fibers for high bandwidth optical fiber transmission.

Author Contributions: Methodology, software, B.D., M.S.K.; writing—original draft preparation, S.S., L.K. and A.S.; writing—review and editing, A.D., S.S. and R.M.; funding acquisition, S.S. and R.M. All authors have read and agreed to the published version of the manuscript.

Funding: This research was funded by the NSFC (62003046, 6211101138); City University of Hong Kong (CityU 7004600); Serbian Ministry of Education, Science and Technological Development (451-03-68/2022-14/200122); Science Fund of the Republic of Serbia (CTPCF-6379382); Guangdong Provincial Department of Technology (2021A1515011997); Guangdong Provincial Department of Education (2021ZDZX1050,2021KCXTD014); and Guangdong Provincial Department of Science and Technology(2021A1313030055).

Institutional Review Board Statement: Not applicable.

Informed Consent Statement: Not applicable.

Data Availability Statement: The data presented in this study are available on request from the corresponding author.

Conflicts of Interest: The authors declare no conflicts of interest.

References

1. Knight, J.C.; Birks, T.A.; Russell, P.S.J.; Atkin, D.M. All-silica single-mode optical fiber with photonic crystal cladding. *Opt. Lett.* **1996**, *21*, 1547–1549, <https://doi.org/10.1364/OL.21.001547>.
2. Birks, T.A.; Knight, J.C.; Russell, P.S.J. Endlessly single-mode photonic crystal fiber. *Opt. Lett.* **1997**, *22*, 961–963, [doi:10.1364/ol.22.000961](https://doi.org/10.1364/ol.22.000961).
3. Russell, P.S.J. Photonic crystal fibers. *Science* **2003**, *299*, 358–362, <https://doi.org/10.1364/OE.11.002641>.
4. Knight, J.C. Photonic crystal fiber. *Nature* **2003**, *424*, 847–851, <https://doi.org/10.1126/science.1079280>.
5. Russell, P.S.J. Photonic-crystal fibers. *J. Lightwave Technol.* **2006**, *24*, 4729–4749, <https://doi.org/10.1364/PRJ.5.000088>.
6. Knight, J.C.; Broeng, J.; Birks, T.A.; Russell, P.S.J. Photonic Band Gap Guidance in Optical Fibers. *Science* **1998**, *282*, 1476–1478, <https://doi.org/10.1126/science.282.5393.1476>.
7. Knight, J.C.; Russell, P.S.J. Photonic crystal fibers: New way to guide light. *Science* **2002**, *296*, 276–277, <https://doi.org/10.1126/science.1070033>.
8. Cregan, R.F.; Mangan, B.J.; Knight, J.C.; Birks, T.A.; Russell, P.S.J.; Roberts, P.J.; Allan, D.C. Single-Mode Photonic Band Gap Guidance of Light in Air. *Science* **1999**, *285*, 1537–1539, <https://doi.org/10.1126/science.285.5433.1537>.
9. Amezcua-Correa, R.; Gèrôme, F.; Leon-Saval, S.; Broderick, N.G.R.; Birks, T.; Knight, J. Control of surface modes in low loss hollow-core photonic bandgap fibers. *Opt. Express* **2008**, *16*, 1142–1149, <https://doi.org/10.1364/oe.16.001142>.
10. Zhang, Z.; He, J.; Du, B.; Guo, K.; Wang, Y. Highly sensitive gas refractive index sensor based on hollow-core photonic bandgap fiber. *Opt. Express* **2009**, *27*, 29649–29658, <https://doi.org/10.1364/OE.27.029649>.
11. Zhang, X.; Gao, S.; Wang, Y.; Ding, W.; Wang, X.; Wang, P. 7-cell hollow-core photonic bandgap fiber with broad spectral bandwidth and low loss. *Opt. Express* **2019**, *27*, 11608–11616, <https://doi.org/10.1364/OE.27.011608>.
12. Benabid, F.; Knight, J.C.; Antonopoulos, G.; Russell, P.S.J. Stimulated Raman Scattering in Hydrogen-Filled Hollow-Core Photonic Crystal Fiber. *Science* **2002**, *298*, 399–402, <https://doi.org/10.1126/science.1076408>.
13. Light, P.; Benabid, F.; Couny, F.; Maric, M.; Luiten, A. Electromagnetically induced transparency in Rb-filled coated hollow-core photonic crystal fiber. *Opt. Lett.* **2007**, *32*, 1323–1325, <https://doi.org/10.1364/ol.32.001323>.
14. Mogilevtsev, D.; Birks, T.; Russell, P. Group-velocity dispersion in photonic crystal fibers. *Opt. Lett.* **1998**, *23*, 1662–1664, <https://doi.org/10.1364/ol.23.001662>.
15. Nair, A.A.; Amiri, I.S.; Boopathi, C.S.; Karthikumar, S.; Jayaraju, M.; Yupapin, P. Numerical investigation of co-doped microstructured fiber with two zero-dispersion wavelengths. *Results Phys.* **2018**, *10*, 766–771, <https://doi.org/10.1016/j.rinp.2018.07.032>.
16. Huang, Y.; Yang, H.; Zhao, S.; Mao, Y.; Chen, S. Design of photonic crystal fibers with flat dispersion and three zero dispersion wavelengths for coherent supercontinuum generation in both normal and anomalous regions. *Results Phys.* **2021**, *23*, 104033, <https://doi.org/10.1016/j.rinp.2021.104033>.
17. Anas, T.; Asaduzzaman, S.; Ahmed, K.; Bhuiyan, T. Investigation of highly birefringent and highly nonlinear Hexa Sected PCF with low confinement loss. *Results Phys.* **2018**, *11*, 1039–1043, <https://doi.org/10.1016/j.rinp.2018.11.013>.
18. Rajesh, A.; Chandru, S.; Robinson, S. Investigation of defective hybrid cladding with silicon nanocrystal PCF for super-continuum generation. *Laser Phys.* **2021**, *31*, 126206, <https://doi.org/10.1088/1555-6611/ac32da>.
19. Kuliesaitė, M.; Jarutis, V.; Pimpe, J.; Vengelis, J. Partially coherent UV–VIS light generation in photonic crystal fiber using femto-second pulses. *Results Phys.* **2021**, *31*, 104965, <https://doi.org/10.1016/j.rinp.2021.104965>.
20. Paul, B.K.; Moctader, M.G.; Ahmed, K.; Khalek, M.A. Nanoscale GaP strips based photonic crystal fiber with high non-linearity and high numerical aperture for laser applications. *Results Phys.* **2018**, *10*, 374–378, <https://doi.org/10.1016/j.rinp.2018.06.033>.
21. Wu, D.; Guo, Z.; Wu, Z.; Shum, P. 900 nm waveband four wave mixing generation in highly nonlinear photonic crystal fiber. *J. Opt.* **2018**, *20*, 035501, <https://doi.org/10.1088/2040-8986/aaa9ea>.
22. Yuan, J.; Kang, Z.; Li, F.; Zhou, G.; Sang, X.; Wu, Q.; Yan, B.; Zhou, X.; Zhong, K.; Wang, L.; et al. Polarization-dependent intermodal four-wave mixing in a birefringent multimode photonic crystal fiber. *Opt. Lett.* **2017**, *42*, 1644–1647, <https://doi.org/10.1364/OL.42.001644>.
23. Das, S.; De, M.; Singh, V.K. Single mode dispersion shifted photonic crystal fiber with liquid core for optofluidic applications. *Opt. Fiber Technol.* **2019**, *53*, 102012, <https://doi.org/10.1016/j.yofte.2019.102012>.
24. Monfared, Y.E.; Liang, C.; Khosravi, R.; Kacerovska, B.; Yang, S. Selectively toluene-filled photonic crystal fiber Sagnac interferometer with high sensitivity for temperature sensing applications. *Results Phys.* **2019**, *13*, 102297, <https://doi.org/10.1016/j.rinp.2019.102297>.
25. Wadsworth, W.; Percival, R.; Bouwmans, G.; Knight, J.; Birks, T.; Hedley, T.; Russell, P. Very High Numerical Aperture Fibers. *IEEE Photon. Technol. Lett.* **2004**, *16*, 843–845, <https://doi.org/10.1109/lpt.2004.823689>.
26. Hansen, K.P.; Broeng, J.; Petersson, A.; Nielsen, M.D.; Skovgaard, P.M.W.; Jakobsen, C.; Simonsen, H.R. High-power photonic crystal fibers. *Proc. SPIE* **2006**, *6102*, 61020B–61020B-11, <https://doi.org/10.1117/12.660174>.
27. Olausson, C.B.; Hansen, K.P.; Broeng, J.; Noordegraaf, D.; Maack, M.D.; Alkeskjold, T.T.; Laurila, M.; Nikolajsen, T.; Skovgaard, P.M.W.; Sørensen, M.H.; et al. Airclad fiber laser technology. *Opt. Eng.* **2011**, *50*, 111609, <https://doi.org/10.1117/1.3631872>.
28. Stepien, R.; Siwicki, B.; Pysz, D.; Stepniewski, G.; Kujawa, I.; Klimczak, M.; Buczynski, R. Characterization of a large core photonic crystal fiber made of lead–bismuth–gallium oxide glass for broadband infrared transmission. *Opt. Quantum Electron.* **2014**, *46*, 553–561, <https://doi.org/10.1007/s11082-013-9835-5>.

29. Tefelska, M.M.; Ertman, S.; Wolinski, T.R.; Mergo, P.; Dabrowski, R. Large Area Multimode Photonic Band-Gap Propagation in Photonic Liquid-Crystal Fiber. *IEEE Photon. Technol. Lett.* **2012**, *24*, 631–633, <https://doi.org/10.1109/lpt.2012.2184278>.
30. Amitonova, L.V.; Descloux, A.; Petschulat, J.; Frosz, M.H.; Ahmed, G.; Babic, F.; Jiang, X.; Mosk, A.P.; Russell, P.; Pinkse, P.W.H. High-resolution wavefront shaping with a photonic crystal fiber for multimode fiber imaging. *Opt. Lett.* **2016**, *41*, 497–500, <https://doi.org/10.1364/ol.41.000497>.
31. Gloge, D. Optical Power Flow in Multimode Fibers. *Bell Syst. Tech. J.* **1972**, *51*, 1767–1783, <https://doi.org/10.1002/j.1538-7305.1972.tb02682.x>.
32. Rousseau, M.; Jeunhomme, L. Numerical Solution of the Coupled-Power Equation in Step-Index Optical Fibers. *IEEE Trans. Microw. Theory Tech.* **1977**, *25*, 577–585, <https://doi.org/10.1109/tmtt.1977.1129162>.
33. Saitoh, K.; Koshiba, M. Empirical relations for simple design of photonic crystal fibers. *Opt. Express* **2005**, *13*, 267–274, <https://doi.org/10.1364/opex.13.000267>.
34. Simović, A.; Drljača, B.; Savović, S.; Djordjevich, A.; Min, R. Investigation of bandwidth in multimode graded-index plastic optical fibers. *Opt. Express* **2021**, *29*, 29587–29594, [HTTPS://DOI.ORG/10.1364/OE.433481](https://doi.org/10.1364/OE.433481).
35. Tanaka, T.P.; Yamada, S. Steady-state characteristics of multimode W-type fibers. *Appl. Opt.* **1979**, *18*, 3261–3264, <https://doi.org/10.1364/AO.18.003261>.
36. Savović, S.; Kovačević, M.S.; Simović, A.; Kuzmanović, L.; Drljača, B.; Djordjevich, A. Method for investigation of mode coupling in multimode step-index silica photonic crystal fibers. *Optik* **2021**, *246*, 167728, <https://doi.org/10.1016/j.ijleo.2021.167728>.
37. Savović, S.; Drljača, B.; Kovačević, M.S.; Djordjevich, A.; Bajić, J.S.; Stupar, D.Z.; Stepniak, G. Frequency response and bandwidth in low NA step index plastic optical fibers. *Appl. Opt.* **2014**, *53*, 6999–7003, <https://doi.org/10.1364/AO.53.006999>.

Communication

Theoretical Investigation of the Capacity of Space Division Multiplexing with Multimode Step-Index Air-Clad Silica Optical Fibers

Svetislav Savović^{1,2}, Alexandar Djordjevich³, Isidora Savović⁴, Branko Drljača⁵, Ana Simović² and Rui Min^{1,*}

¹ Center for Cognition and Neuroergonomics, State Key Laboratory of Cognitive Neuroscience and Learning, Beijing Normal University at Zhuhai, Zhuhai 519087, China; savovic@kg.ac.rs

² Faculty of Science, University of Kragujevac, R. Domanovića 12, 34000 Kragujevac, Serbia; asimovic@kg.ac.rs

³ Department of Mechanical Engineering, City University of Hong Kong, 83 Tat Chee Avenue, Kowloon, Hong Kong, China; mealex@cityu.edu.hk

⁴ Laboratory of Neurodegenerative Disease, School of Biomedical Sciences, LKS Faculty of Medicine, The University of Hong Kong, 21 Sassoon Road, Pokfulam, Hong Kong, China; u3008169@connect.hku.hk

⁵ Faculty of Sciences and Mathematics, University of Priština in Kosovska Mitrovica, L. Ribara 29, 38220 Kosovska Mitrovica, Serbia; branko.drljaca@pr.ac.rs

* Correspondence: rumi@doctor.upv.es

Abstract: We studied the effect of mode coupling on the space division multiplexing (SDM) capabilities of multimode step-index (SI) air-clad silica optical fibers by numerically solving the power flow equation. Mode coupling considerably reduces the length of these fibers at which space division multiplexing may be achieved with minimal crosstalk between neighboring optical channels, according to the findings. Up to 120 m and 30 m, respectively, the two and three spatially multiplexed channels in the investigated multimode step-index silica optical fibers can be used with low crosstalk. When building a space division multiplexing-based optical fiber transmission system, such characterization of optical fibers should be taken into account.

Keywords: air-clad silica optical fibers; microbends; mode coupling; space division multiplexing

Citation: Savović, S.; Djordjevich, A.; Savović, I.; Drljača, B.; Simović, A.; Min, R. Theoretical Investigation of the Capacity of Space Division Multiplexing with Multimode Step-Index Air-Clad Silica Optical Fibers. *Photonics* **2022**, *9*, 127. <https://doi.org/10.3390/photonics9030127>

Received: 25 January 2022

Accepted: 22 February 2022

Published: 23 February 2022

Publisher's Note: MDPI stays neutral with regard to jurisdictional claims in published maps and institutional affiliations.



Copyright: © 2022 by the authors. Licensee MDPI, Basel, Switzerland. This article is an open access article distributed under the terms and conditions of the Creative Commons Attribution (CC BY) license (<https://creativecommons.org/licenses/by/4.0/>).

1. Introduction

Global network traffic has expanded dramatically in recent decades, owing primarily to the rapid expansion of the Internet [1]. Optical fiber systems now support the majority of this data flow. Multiplexing, fiber amplifiers, and high-efficiency spectral coding have all contributed to this capacity gain [1]. Optical data multiplexing is possible not just in wavelength, but also in space, time, polarization, and phase. Optical fiber transmission systems can benefit from the multiplexing technique [1,2]. SDM, which includes mode division multiplexing using few-mode fibers or multimode and/or core multiplexing utilizing multicore fibers, has gotten a lot of attention as a way to increase optical communication's multiplicative capacity [1,3–8]. SDM can operate at the same or separate wavelengths [9]. If the SDM channels inside the carrier fiber are assigned radially distributed optical signals at the same wavelength, the central channel is launched along the fiber axis in the form of a disk, whereas all other channels are in the form of concentric rings. Thus, one increases the capacity of the optical fiber link (Figure 1).

Silica optical fibers (SOFs) are suited to long-distance signal communication [10], while plastic optical fibers (POFs) with a large core are extensively used in short-distance (less than 100 m) networks [11]. Optical measurements, telecommunications, and sensor

applications all use plastic-clad silica fibers (PCSFs) [12,13]. Currently, the only technology capable of reaching exceptionally high NAs is PCSFs and air-clad silica fibers. In commercially marketed PCSFs, NA is limited to ~ 0.46 . An all-silica fiber is promising for SDM because of the material durability and sufficient silica purity for strong transmission performance in the large wavelength range of 300 nm to 2.4 μm [14–16]. In contrast, air-clad fibers can have an extraordinarily high numerical aperture ($\text{NA}_{\text{meas}} > 0.9$) [17]. Figure 2 is a cross-sectional sketch of an all-silica air-clad fiber with an annulus made up of a single ring of holes, produced at the University of Sydney [15]. The ring, or rings, of air holes, whose surface roughness has been measured to be 0.5 nm [18], are solely responsible for the NA of air-clad fibers. The thin bridges are typically between 100 and 400 nm thick, with the ring of holes forming a corrugated surface at the core. To decrease light leakage, the thickness was chosen.

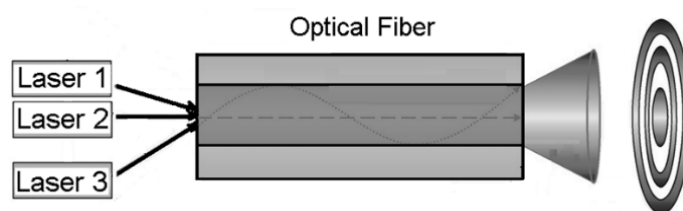


Figure 1. A schematic of a three-channel SDM system, consisting of a center disk and two concentric rings.

Fiber imperfections and inhomogeneities introduced during the optical fiber fabrication process cause power transfer between adjacent modes [9,19,20]. Because SDM entails densely packed spatial channels in a fiber, mode coupling is critical since it allows cross-talk between channels. As a result, the expected beam parameters are altered. The optical power distribution of an optical fiber determines its far-field pattern, which is influenced by launch conditions, fiber parameters, and fiber length. Only short fibers will produce a highly defined ring radiation pattern when light is launched at a given angle $\theta_0 > 0$ with respect to the fiber axis. The boundaries of such a ring grow fuzzy at the end of longer fibers due to mode coupling. At “coupling length” L_c , where the highest-order mode ring-pattern evolves into a disk, an equilibrium mode distribution (EMD) is established.

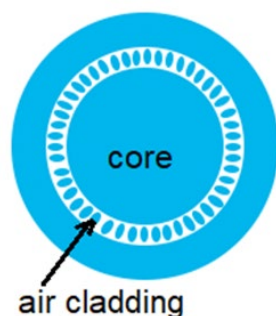


Figure 2. Sketch of cross section of air-clad silica fiber based on the design used in the experiments of [15].

Because information on SDM in multimode air-clad silica optical fibers is lacking in the literature, we investigated mode coupling in multimode SI air-clad silica optical fibers in this work by numerically solving the power flow equation. This fiber was previously investigated experimentally by Åslund et al. [15]. This allows one to determine the maximum fiber lengths for an SDM system that employs multimode SI air-clad silica optical fibers.

2. Power Flow Equation

Gloge’s power flow equation is [19]:

$$\frac{\partial P(\theta, z)}{\partial z} = -\alpha(\theta)P(\theta, z) + \frac{D}{\theta} \frac{\partial}{\partial \theta} \left(\theta \frac{\partial P(\theta, z)}{\partial \theta} \right), \quad (1)$$

where $P(\theta, z)$ is the angular power distribution, θ is the propagation angle in respect to the core axis, z is the distance from the input end of the optical fiber, D is the constant coupling coefficient [19,21–23], and $\alpha(\theta)$ is the modal attenuation. Since $\alpha(\theta)$ need not be accounted for in solving Equation (1) for mode coupling [22,23], Equation (1) reduces to [15]:

$$\frac{\partial P(\theta, z)}{\partial z} = \frac{D}{\theta} \frac{\partial P(\theta, z)}{\partial \theta} + D \frac{\partial^2 P(\theta, z)}{\partial \theta^2}. \quad (2)$$

The explicit finite-difference approach [24] was used to derive a numerical solution of the power flow Equation (2) for a Gaussian launch-beam distribution of the form:

$$P(\theta, z) = \frac{1}{\sigma\sqrt{2\pi}} \exp\left[-\frac{(\theta - \theta_0)^2}{2\sigma^2}\right], \quad (3)$$

with $0 \leq \theta \leq \theta_c$, where θ_0 is the mean value of the launch angular distribution, σ is the standard deviation, and $\text{FWHM} = 2\sigma\sqrt{2\ln 2} = 2.355\sigma$. We discretized Equation (2) using explicit finite difference method, so Equation (2) now reads [24]:

$$P_{i,j+1} = \left(\frac{\Delta z D}{\Delta \theta^2} - \frac{\Delta z D}{2\theta_{i,j}\Delta \theta}\right) P_{i-1,j} + \left(1 - \frac{2\Delta z D}{\Delta \theta^2}\right) P_{i,j} + \left(\frac{\Delta z D}{2\theta_{i,j}\Delta \theta} + \frac{\Delta z D}{\Delta \theta^2}\right) P_{i+1,j} \quad (4)$$

where indexes i and j refer to the discretization step lengths $\Delta\theta$ and Δz for the angle θ and length z , respectively. This is a simple formula for $P_{i,j+1}$ at the $(i, j + 1)$ th mesh point in terms of the known values along the j^{th} distance row. The truncation error for the difference in Equation (4) is $O(\Delta z, \Delta \theta^2)$. The grid dimension in the θ direction is $N = \theta_c/\Delta\theta$ and the grid dimension in the z direction is $M = L/\Delta z$, where θ_c is the critical angle and L is the fiber length.

3. Results and Discussion

In this study, we theoretically investigated the effect of mode coupling on SDM capabilities in a multimode SI air-clad silica optical fiber employed in a prior experiment by Åslund et al. [15]. The single-material air-clad fiber was made of low-grade natural silica and had material losses of less than 10 dB/km at 1550 nm. The fiber had $\text{NA} = 0.54$, a core diameter of $d_{\text{core}} = 180 \mu\text{m}$, and 59 bridges with a length of $l \sim 26 \mu\text{m}$ to sustain it. The maximum thickness of the bridge was 340 nm. The constant coupling coefficient for the fiber was $D = 3.5 \times 10^{-5} \text{ rad}^2/\text{m}$ at $\lambda = 1550 \text{ nm}$ [15,25], which we adopted in this work. The numerical solution to Equation (4) was obtained using discretization step lengths $\Delta\theta = 0.1^\circ$ and $\Delta z = 0.001 \text{ m}$.

Figure 3 illustrates the normalized output angular power distribution at two lengths of the multimode SI air-clad optical fiber obtained as a solution of Equation (2). The three launch beams in the Gaussian form with $(\text{FWHM})_{z=0} = 3.9^\circ$ and different input angles $\theta_0 = 0^\circ, 13^\circ$, and 26° represent three optical channels [15,25]. In the short SI air-clad optical fiber in Figure 3a, the mode coupling is minimal, and as a result there is no crosstalk between optical channels. Due to mode coupling, spatial power distributions broaden with increasing fiber length, so the three-channel SDM can be realized in this fiber up to a fiber length of $z_{\text{SDM}} = 30 \text{ m}$ (Figure 3b). In the case of two co-propagating optical channels, the two Gaussian launch distributions with input angles $\theta_0 = 0^\circ$ and 26° , and $(\text{FWHM})_{z=0} = 3.9^\circ$, are investigated. One can see from Figure 4b that practical realization of two-channel SDM

can be done up to a fiber length of $z_{SDM} = 120$ m. As can be seen, mode coupling severely restricts the length of multimode SI air-clad silica optical fibers that can be used for SDM (Table 1).

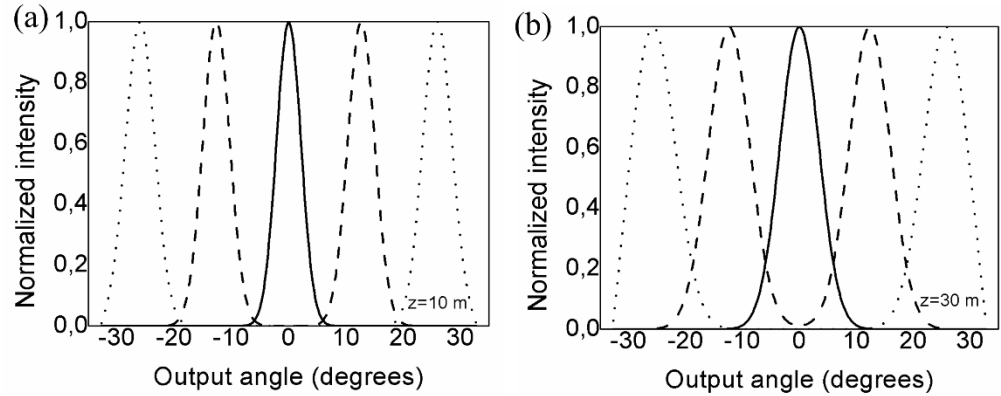


Figure 3. Normalized output intensity at different lengths of the multimode SI air-clad silica optical fiber obtained as solutions of Equation (2) for $D = 3.5 \times 10^{-5} \text{ rad}^2/\text{m}$, three launch beams in the Gaussian form, and input angles $\theta_0 = 0^\circ$ (solid line), 13° (dashed line) and 26° (dotted line), with $(\text{FWHM})_{z=0} = 3.9^\circ$ for: (a) $z = 10$ m and (b) $z = 30$ m.

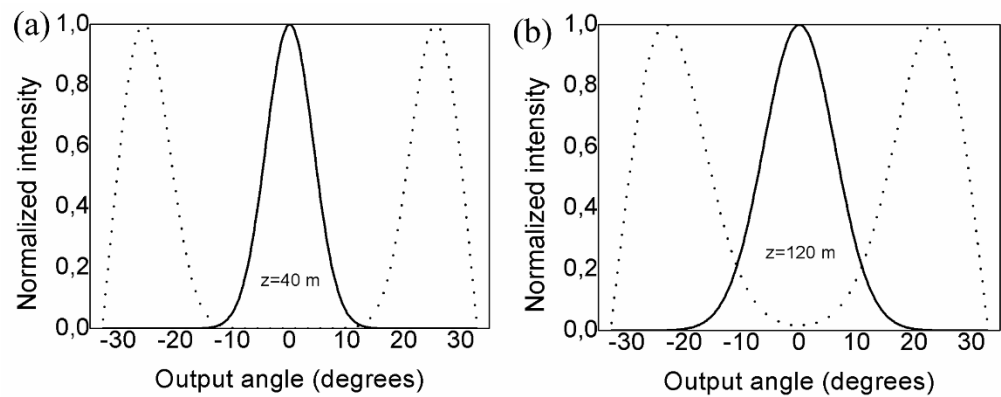


Figure 4. Normalized output intensity at different lengths of the multimode SI air-clad silica optical fiber obtained as solutions of Equation (2) for $D = 3.5 \times 10^{-5} \text{ rad}^2/\text{m}$, two launch beams in the Gaussian form, and input angles $\theta_0 = 0^\circ$ (solid line) and 26° (dotted line), with $(\text{FWHM})_{z=0} = 3.9^\circ$ for: (a) $z = 40$ m and (b) $z = 120$ m.

Table 1. Length z_{SDM} for two and three spatially multiplexed channels with minimal crosstalk in SI air-clad silica optical fibers and PCSFs, with different numerical apertures NA and coupling coefficients D .

Fiber type	NA	D (rad^2/m)	z_{SDM} (m) (2-channel)	z_{SDM} (m) (3-channel)
Air-clad silica fiber (this work)	0.54	3.5×10^{-5}	120	30
PCSF (1) [26]	0.4	1.28×10^{-5}	50	14
PCSF (2) [26]	0.37	4.5×10^{-5}	25	7

The coupling coefficient D of the multimode SI air-clad silica fiber investigated in this study is of the same order of magnitude as that of the previously investigated multimode SI PCSFs [26] (Table 1). SI PCSFs have a lesser capacity for SDM due to their lower NA of 0.37 to 0.4. For example, the capacity for three-channel SDM in the SI air-clad silica fiber investigated in this work, compared to PCSF (2) [26], is about four times greater, which is

mainly due to the much higher NA of the SI air-clad silica fiber (these two fibers have a similar coupling coefficient D). On the other hand, despite the higher coupling coefficient D (which restricts the capacity for SDM) of the SI air-clad silica fiber compared to that of PCSF (1) [26], the capacity for three-channel SDM in the SI air-clad silica fiber compared to PCSF (1) is about two times greater, due to the higher NA of the SI air-clad silica fiber. Therefore, in practical realization of SDM in PCSFs and air-clad silica fibers, the coupling coefficient is the dominant factor for lower NA PCSFs compared to high NA air-clad silica fibers. As a result, two- and three-channel SDM can be achieved in SI air-clad silica optical fibers with lengths longer than PCSFs (Table 1). Air-clad silica fibers are, hence, more suitable for SDM applications. It is worth noting that, in our previous works, we have shown that this kind of SDM can be employed in standard multimode SI plastic optical fibers at lengths of up to few meters [27–29] and multimode SI silica optical fibers at lengths of several hundreds of meters [30].

In order to investigate the influence of $(FWHM)_{z=0}$ of launch beam distribution on the capacity of SDM in the SI air-clad silica fiber, we solved Equation (1) for four different Gaussian beams with $(FWHM)_{z=0} = 0.5, 1, 2,$ and 3° . The numerical results are summarized in Table 2. One can see that, by increasing the width of the launch beam, the length of two- and three-channel SDM decreases. One can conclude that a narrower launch beam distribution is more desirable in practical realization of SDM in the investigated SI air-clad silica fiber.

To conclude, an optical fiber with weaker mode coupling and higher NA should be employed in order to achieve a higher capacity of SDM. A further improvement of the capacity of SDM can be achieved by choosing a narrower launch beam.

Table 2. Length z_{SDM} for two and three spatially multiplexed channels with minimal crosstalk in SI air-clad silica optical fibers for different widths $((FWHM)_{z=0})$ of the Gaussian launch beam distributions.

$(FWHM)_{z=0}$ (deg)	z_{SDM} (m) (2-channel)	z_{SDM} (m) (3-channel)
3.9	120	30
3	130	33
2	142	36
1	151	39
0.5	158	41

In general, for spatially multiplexed channels, it is difficult to precisely anticipate the amount of crosstalk that will prevent the system from operating by computing the normalized output power distribution for different fiber lengths. In practice, a transmission matrix should be employed for a more precise assessment of the SDM capacity of a specific fiber, taking into consideration the noise factors that are dependent on the receiver's individual implementation [27]. Our numerical results provide a good estimate of the optical fiber length, where SDM with three and two channels might be implemented with low crosstalk in the analyzed SI air-clad silica fibers.

4. Conclusions

The power flow equation was used to explore the effect of mode coupling on SDM in multimode SI air-clad silica optical fibers. We have shown that mode coupling limits the length at which the SDM can be realized in high-NA air-clad silica optical fiber. When compared to SI PCSFs with smaller NA, this constraint is less noticeable. For SDM, an optical fiber with a lower mode coupling and a higher NA is preferable. Furthermore, a narrower launch beam results in longer fiber lengths at which SDM can be realized. When building an optical fiber transmission system with space division multiplexing, such characterization of optical fibers should be taken into account.

Author Contributions: Methodology and software, S.S. and B.D.; conceptualization, S.S.; writing—original draft preparation, A.S. and B.D.; writing—review and editing, A.D., I.S., and R.M.; supervision, S.S.; funding acquisition, S.S. and R.M. All authors have read and agreed to the published version of the manuscript.

Funding: This research was funded by the National Natural Science Foundation of China (62003046, 6211101138); the Guangdong Provincial Department of Science and Technology (2021A1313030055); the Serbian Ministry of Education, Science, and Technological Development (Agreement No. 451-03-68/2020-14/200122); a Strategic Research Grant of the City University of Hong Kong (Project No. CityU 7004600); the Science Fund of the Republic of Serbia (Agreement No. CTPCF-6379382); the Innovation Team Project of Guangdong Provincial Department of Education (2021KCXTD014); a Special project in key field of the Guangdong Provincial Department of Education (2021ZDZX1050); and the Guangdong Basic and Applied Basic Research Foundation (2021A1515011997);

Institutional Review Board Statement: Not applicable

Informed Consent Statement: Not applicable

Data Availability Statement: The data presented in this study are available on request from the corresponding author.

Conflicts of Interest: The authors declare no conflict of interest.

References

- Richardson, D.; Fini, J.; Nelson, L. Space-division multiplexing in optical fibres. *Nat. Photonics* **2013**, *7*, 354–362.
- Savović, S.; Djordjevich, A.; Simović, A.; Drljača, B. Influence of mode coupling on angular division multiplexing in seven-core plastic optical fibers. *Laser Phys.* **2020**, *30*, 065103.
- Winzer, P.J. Optical networking beyond WDM. *IEEE Photonics J.* **2012**, *4*, 647–651.
- Li, G.; Bai, N.; Zhao, N.; Xia, C. Space-division multiplexing: The next frontier in optical communication. *Adv. Opt. Photonics* **2014**, *6*, 413–487.
- Brunet, C.; Ung, B.; Belanger, P.-A.; Messaddeq, Y.; LaRochelle, S.; Rusch, L.A. Vector mode analysis of ring-core fibers: Design tools for spatial division multiplexing. *J. Lightwave Technol.* **2014**, *32*, 4046–4057.
- Uden, R.G.H.; Huijskens, R.C.E.L.F.; Xia, C.; Li, G.; Schulzgen, A.; Waardt, H.; Koonen, A.; Okonkwo, C. Ultra-high-density spatial division multiplexing with a few-mode multicore fibre. *Nat. Photonics* **2014**, *8*, 865–870.
- Zhang, L.; Chen, J.; Agrell, E.; Lin, R.; Wosinska, L. Enabling Technologies for Optical Data Center Networks: Spatial Division Multiplexing. *J. Lightwave Technol.* **2020**, *38*, 18–30.
- Rommel, S.; Dodane, D.; Grivas, E.; Cimoli, B.; Bourderionnet, J.; Feugnet, G.; Morales, A.; Pikasis, E.; Roeloffzen, C.; Dijk, P.; et al. Towards a Scaleable 5G Fronthaul: Analog Radio-over-Fiber and Space Division Multiplexing. *J. Lightwave Technol.* **2020**, *38*, 5412–5422.
- Murshid, S.H.; Chakravarty, A.; Biswas, R. Attenuation and modal dispersion models for spatially multiplexed co-propagating helical optical channels in step index fibers. *Opt. Laser Technol.* **2011**, *43*, 430–436.
- Zhou, J.; Yang, C.; Sui, Q.; Wang, H.; Gao, S.; Feng, Y.; Liu, W.; Yan, Y.; Li, J.; Yu, C.; et al. Burst-Error-Propagation Suppression for Decision-Feedback Equalizer in Field-Trial Submarine Fiber-Optic Communications. *J. Lightwave Technol.* **2021**, *39*, 4601–4606.
- Apolo, J.; Ortega, B.; Almenar, V. Hybrid POF/VLC Links Based on a Single LED for Indoor Communications. *Photonics* **2021**, *8*, 254.
- Drljača, B.; Simović, A.; Djordjevich, A.; Savović, S. Wavelength dependence of equilibrium mode distribution and steady state distribution in W-type plastic-clad silica fibers. *Opt. Fiber. Technol.* **2020**, *54*, 102077.
- Savović, S.; Djordjevich, A. Mode coupling in multimode step-index plastic-clad silica fibers with corrugated surfaces. *Opt. Laser Technol.* **2017**, *97*, 400–404.
- Wang, W.; Wang, N.; Li, K.; Geng, Z.; Jia, H. A novel dual guided modes regions photonic crystal fiber with low crosstalk supporting 56 OAM modes and 4 LP modes. *Opt. Fiber. Technol.* **2020**, *57*, 102213.
- Åslund, M.L.; Canning, J. Air-clad fibres for astronomical instrumentation: Focal-ratio degradation. *Exp. Astron.* **2009**, *24*, 1–7.
- Corbett, J.C.W. A brief introduction to photonic crystal fibres for astronomical instrumentalists. *New Astron. Rev.* **2006**, *50*, 305–312.
- Wadsworth, W.J.; Percival, R.M.; Bouwmans, G.; Knight, J.C.; Birks, T.A.; Hedley, T.D.; Russel, P.S.J. Very high numerical aperture fibers. *IEEE Photonics Technol. Lett.* **2004**, *16*, 843–845.
- Canning, J.; Buckley, E.; Huntington, S.; Lyytikäinen, K. Using multi-micro channel capillaries for determination of the zeta potential of a microfluidic channel. *Electrochim. Acta* **2004**, *49*, 3581–3586.
- Gloge, D. Optical power flow in multimode fibers. *Bell Syst. Tech. J.* **1972**, *51*, 1767–1783.
- Garito, A.F.; Wang, J.; Gao, R. Effects of random perturbations in plastic optical fibers. *Science* **1998**, *281*, 962–967.

21. Djordjevich, A.; Savović, S. Numerical solution of the power flow equation in step index plastic optical fibers. *J. Opt. Soc. Am. B* **2004**, *21*, 1437–1442.
22. Gambling, W.A.; Payne, D.N.; Matsumura, H. Mode conversion coefficients in optical fibers. *Appl. Opt.* **1975**, *14*, 1538–1542.
23. Rousseau, M.; Jeunhomme, L. Numerical solution of the coupled-power equation in step index optical fibers. *IEEE Trans. Microwave Theory Tech.* **1977**, *25*, 577–585.
24. Djordjevich, A.; Savović, S. Investigation of mode coupling in step index plastic optical fibers using the power flow equation. *IEEE Photonics Technol. Lett.* **2000**, *12*, 1489–1491.
25. Savović, S.; Djordjevich, A.; Min, R. Investigation of mode coupling in step-index air-clad silica optical fibers. *Opt. Fiber Technol.* **2022**, submitted for publication.
26. Savović, S.; Djordjevich, A. Mode coupling and its influence on space division multiplexing in step-index plastic-clad silica fibers. *Opt. Fiber Technol.* **2018**, *46*, 192–197.
27. Tsekrekos, C.P.; Martinez, A.; Huijskens, F.M.; Koonen, A.M.J. Design considerations for a transparent mode group diversity multiplexing link. *IEEE Photonics Technol. Lett.* **2006**, *18*, 2359–2361.
28. Savović, S.; Djordjevich, A.; Simović, A.; Drljača, B. Influence of mode coupling on three spatially multiplexed channels in multimode graded index plastic optical fibers. *Laser Phys.* **2020**, *30*, 115102.
29. Savović, S.; Djordjevich, A.; Simović, A.; Drljača, B. Influence of mode coupling on three, four and five spatially multiplexed channels in multimode step-index plastic optical fibers. *Opt. Laser Technol.* **2018**, *106*, 18–21.
30. Savović, S.; Djordjevich, A.; Simović, A.; Drljača, B. A transmission length limit for space division multiplexing in step-index silica optical fibers. *J. Mod. Opt.* **2019**, *66*, 1695–1700.



A comparative study of two different finite difference methods for solving advection–diffusion reaction equation for modeling exponential traveling wave in heat and mass transfer processes

Svetislav Savović^{1,2} · Branko Drljača³ · Alexandar Djordjevič²

Received: 30 July 2021 / Revised: 1 October 2021 / Accepted: 12 October 2021 /
Published online: 26 October 2021
© Università degli Studi di Napoli "Federico II" 2021

Abstract

An unconditionally-positive finite difference (UPFD) and the standard explicit finite difference schemes are compared to the analytical solution of the advection–diffusion reaction equation which describes the exponential traveling wave in heat and mass transfer processes. It is found that although the unconditional positivity of the UPFD scheme, this scheme is less accurate than the standard explicit finite difference scheme. This is because the UPFD scheme contains additional truncation-error terms in the approximations of the first and second derivatives with respect to x , which are evaluated at different moments in time. While these terms tend to zero as the mesh is refined, the UPFD scheme nevertheless remains less accurate than its standard explicit finite difference counterpart. The presented results are important when modeling a heat and mass transfer processes using the investigated advection–diffusion reaction equation. Furthermore, current and future developers of coupled multi-species transport models may draw on the ideas of solutions methods employed in this study to further develop numerical models for various types of coupled multi-species transport problems.

Keywords Advection–diffusion reaction equation · Exponential traveling wave · Finite difference schemes · Heat and mass flow · Coupled multi-species transport problems

Mathematics Subject Classification 65M06 · 35K57 · 80A19 · 65L12

✉ Svetislav Savović
savovic@kg.ac.rs

¹ Faculty of Science, University of Kragujevac, R. Domanovića 12, Kragujevac, Serbia

² City University of Hong Kong, 83 Tat Chee Avenue, Kowloon, Hong Kong, China

³ University of Priština in Kosovska Mitrovica, Faculty of Sciences and Mathematics, Kosovska Mitrovica, Serbia

1 Introduction

Parabolic equations, with or without reaction terms, are used to model a wide variety of physical, chemical, biological, and engineering problems such as heat transfer, transmission of light through optical fibers, transport and reaction of chemical species, population dynamics, adsorption of pollutants in soil, and diffusion of radon and neutrons [1–8]. Solutions have often been obtained by the finite element method [9] or finite difference method [7]. Both methods have advantages and limitations. While the finite element method may be better suited for complex three-dimensional geometries, one-dimensional problems are more easily solved by the finite difference method. For neither does the standard finite discretization explicitly constrain the solutions to positive values. Due to truncation or other errors, the solutions may thus turn up negative and physically nonsensical, leading to numerical instabilities and oscillations.

In the 1970s and 1980s, implicit finite difference methods (IFDMs) were generally preferred over explicit finite difference methods (EFDMs). This trend has been changing with the advancement of computers, shifting the emphasis to EFDMs. Being often unconditionally stable, the IFDM allows larger step lengths. Nevertheless, this does not translate into IFDM's higher computational efficiency because extremely large matrices must be manipulated at each calculation step. We found that the EFDM is also simpler in addition to being computationally more efficient [2, 6, 10].

Chen-Charpentier and Kojouharov [11] proposed a numerical solution of the one dimensional advection–diffusion reaction equation that guarantees positivity of the solutions independent of the time step and mesh size. The method works with reaction terms that are the sum of a positive function and a negative function of the unknown—either or both may be zero. It is applicable to both, problems where either advection or diffusion dominates. In this work, a previously reported unconditionally positive finite difference scheme and a standard explicit finite difference scheme for solving parabolic differential equations with advection, diffusion and reaction terms which describes the exponential traveling wave in heat and mass transfer processes are compared to analytical solution reported in the literature.

2 The unconditionally positive finite difference method

Several authors (for example in [12, 13]) have developed schemes that preserve the positivity of solutions for parabolic equations. Chen-Charpentier and Kojouharov [11] previously proposed a numerical solution of the one dimensional advection–diffusion reaction equation with linear decay:

$$\frac{\partial c(x, t)}{\partial t} = D \frac{\partial^2 c(x, t)}{\partial x^2} - u \frac{\partial c(x, t)}{\partial x} - Kc(x, t), \quad x \in [0, x_{\max}], \quad t \in [0, T] \quad (1)$$

for the unknown $c(x, t)$, with appropriate boundary and initial conditions; whereby the parameters u , D , and K are positive constants. They used the following difference schemes for derivatives: $(\partial c(x, t)/\partial t) = (c_i^{n+1} - c_i^n)/\Delta t$, $(\partial c(x, t)/\partial x) = (c_i^{n+1} - c_{i-1}^n)/\Delta x$ and $(\partial^2 c(x, t)/\partial x^2) = (c_{i+1}^n - 2c_i^{n+1} + c_{i-1}^n)/\Delta x^2$. Then, the

unconditionally positive finite difference method they have proposed is:

$$\frac{c_i^{n+1} - c_i^n}{\Delta t} = D \frac{c_{i+1}^n - 2c_i^{n+1} + c_{i-1}^n}{\Delta x^2} - u \frac{c_i^{n+1} - c_{i-1}^n}{\Delta x} - K c_i^{n+1} \tag{2}$$

where c_i^n is the approximation of $c(x_i, n\Delta t)$. In the advection and diffusion terms in the above discretization, the spatial derivatives are approximated using values at different moments in time. Equation (2) is now rewritten in the following explicit form:

$$c_i^{n+1} = \frac{\hat{D}c_{i+1}^n + c_i^n/\Delta t + (\hat{u} + \hat{D})c_{i-1}^n}{1/\Delta t + \hat{u} + 2\hat{D} + K} \tag{3}$$

where $\hat{u} = u/\Delta x$ and $\hat{D} = D/\Delta x^2$. If the parameters u, K and D are all non-negative, and therefore \hat{u} and \hat{D} are both positive, then the numerical scheme represents a UPFD method for any $\Delta t > 0$ and $\Delta x > 0$. Thus, the solutions of the scheme are guaranteed to be positive independent of the choice of space and time steps [11]. If $u < 0$, Chen-Charpentier and Kojouharov [11] proposed that the advection term is discretized as $+ u \frac{c_i^n - c_{i-1}^{n+1}}{\Delta x}$ so that the UPFD solution would remain positive. This is not the case with standard finite differences.

The method (3) proposed by Chen-Charpentier and Kojouharov [11] is explicit and unconditionally positive. However, it is not unconditionally consistent. There are extra truncation error terms because the approximations of the first and second derivatives with respect to x are evaluated at different moments in time. One approach to addressing this problem is to choose the time step depending on the mesh size so that the inconsistent terms approach zero as the mesh is refined. Another approach is to incorporate these terms into the numerical scheme to achieve a consistent approximation of the original partial differential equation [11]. The main error term causing inconsistency is $\alpha(\partial c/\partial t)$, where $\alpha = \frac{\Delta t}{\Delta x^2}(2D + u\Delta x)$. This term imposes the largest restriction on Δt as a function of Δx . Adding it to (1), one gets:

$$\frac{\partial c(x, t)}{\partial t}(1 + \alpha) = D \frac{\partial^2 c(x, t)}{\partial x^2} - u \frac{\partial c(x, t)}{\partial x} - Kc(x, t), \quad x \in [0, x_{\max}], \quad t \in [0, T] \tag{4}$$

Defining a new time $\tilde{t} = t(1 + \alpha)$, we get the original equation but with a new time scale and without the inconsistent term. The scheme now has the truncation error $O(\Delta t, \Delta x)$ and x and t increments should be chosen such to keep this error small. It is of great interest to compare this unconditionally-positive finite difference scheme with standard explicit finite difference scheme.

3 Standard explicit finite difference method

Using the standard explicit finite difference method, where the forward difference scheme is used to represent the derivative terms $(\partial c(x, t)/\partial t) = (c_i^{n+1} - c_i^n)/\Delta t$ and $(\partial c(x, t)/\partial x) = (c_i^n - c_{i-1}^n)/\Delta x$, and central finite difference scheme is used to represent derivative term $(\partial^2 c(x, t)/\partial x^2) = (c_{i+1}^n - 2c_i^n + c_{i-1}^n)/\Delta x^2$ [14], Eq. (1) is written in the following form:

$$\frac{c_i^{n+1} - c_i^n}{\Delta t} = D \frac{c_{i+1}^n - 2c_i^n + c_{i-1}^n}{\Delta x^2} - u \frac{c_i^n - c_{i-1}^n}{\Delta x} - K c_i^n \tag{5a}$$

$$c_i^{n+1} = \left(\frac{u\Delta t}{\Delta x} + \frac{D\Delta t}{\Delta x^2} \right) c_{i-1}^n + \left(1 - \frac{u\Delta t}{\Delta x} - \frac{2D\Delta t}{\Delta x^2} - K\Delta t \right) c_i^n + \frac{D\Delta t}{\Delta x^2} c_{i+1}^n \tag{5b}$$

where $c_i^n \equiv c(x_i, t_n)$, indexes i and n refer to the discrete step lengths Δx and Δt for the coordinate x and time t , respectively, such that $x_i = i \Delta x$ and $t_j = n \Delta t$. Equation (8) represents a formula for c_i^{n+1} at the $(i, n + 1)$ th mesh point in terms of the known values along the n th time row. The truncation error for the difference Eq. (5) is $O(\Delta t, \Delta x)$. Using a small-enough value of Δt and Δx , the truncation error can be reduced until the accuracy achieved is within the error tolerance. Unlike the UPFD scheme, this one has no additional truncation error terms in the approximations of the first and second derivatives with respect to x that are evaluated at different moments in time; but one still has to choose a sufficiently small Δt to ensure stability of the scheme. The aim of this work is to compare the unconditionally-positive finite difference and the standard explicit finite difference schemes, especially in terms of their accuracy.

4 Numerical results and discussion

To compare the UPFD and EFD schemes, we consider the advection–diffusion reaction Eq. (1) for the same set of input data previously used by Chen-Charpentier and Kojouharov [11], $u = 1, D = 1$ and $K = 1$:

$$\frac{\partial c(x, t)}{\partial t} = \frac{\partial c^2(x, t)}{\partial x^2} - \frac{\partial c(x, t)}{\partial x} - c(x, t) \tag{6}$$

subject to the following initial and boundary conditions:

$$c(x, 0) = \exp(-x), \quad x \in [0, x_{\max}] \tag{7a}$$

$$c(0, t) = \exp(t), \quad t \in [0, T] \tag{7b}$$

$$\frac{\partial c(x_{\max}, t)}{\partial x} = -c(x_{\max}, t), \quad t \in [0, T] \tag{7c}$$

Equation (6) with initial and boundary conditions (7) describes the exponential traveling wave. It has an exact solution of the form $c(x, t) = \exp(t - x)$.

For $u = 1, D = 1$ and $K = 1$, stability of the EFD scheme (5) is given as [15]:

$$\left| 1 - \Delta t - \frac{2\Delta t}{\Delta x} - \frac{4\Delta t}{\Delta x^2} \right| \leq 1 \tag{8}$$

while the conditions for stability of the UPFD scheme (3) are given as [15]:

$$\left| \frac{1 - \frac{\Delta t}{\Delta x} - \frac{2\Delta t}{\Delta x^2}}{1 + \Delta t + \frac{\Delta t}{\Delta x} + \frac{2\Delta t}{\Delta x^2}} \right| \leq 1 \tag{9a}$$

$$\left| \frac{(1 + 210\Delta t)^2 + (4410\Delta t^2 - 210\Delta t)^2 \omega^2}{(1 + 210\Delta t)^2} \right| \leq 1 \tag{9b}$$

where $\omega \rightarrow 0$ is phase angle within the Von-Neumann stability analysis [15].

The initial and boundary conditions (7) in the EFD and UPFD schemes are given as:

$$c_i^0 = \exp(-x_i), \quad x \in [0, x_{\max}], \quad t = 0 \text{ (EFD and UPFD)} \tag{10a}$$

$$c_0^n = \exp(-t_j), \quad t > 0, \quad x = 0 \text{ (EFD and UPFD)} \tag{10b}$$

$$c_N^n = \frac{c_{N-1}^n}{(1 + \Delta x)}, \quad t > 0, \quad x = x_{\max} \text{ (EFD);}$$

$$c_N^{n+1} = \frac{c_{N-1}^n}{(1 + \Delta x)}, \quad t > 0, \quad x = x_{\max} \text{ (UPFD)} \tag{10c}$$

To facilitate the comparison of the UPFD scheme (3) and EFD scheme (5), we numerically solved (6) for $x_{\max} = 10$ and $T = 0.85$, using $\Delta x = 0.1$ and $\Delta t = 0.0047$. For $\Delta x = 0.1$, according to (8), EFD scheme becomes unstable for $\Delta t > 0.004750593824$. For $\Delta x = 0.1$, according to (9), UPFD scheme becomes unstable for $\Delta t > 0.04761904762$ [15]. As can be observed in Fig. 1, the EFD scheme produces a solution that is closer to the exact one than is the solution by the UPFD scheme. One can observe in Fig. 1 that results by the EFD scheme are more accurate than those by the UPFD scheme. This is attributed to the latter containing additional truncation error terms in the approximations to the first and second derivatives with respect to x , which are evaluated at different moments in time.

We modify numerical scheme (6) in order to minimize the extra truncation error terms of the UPFD scheme. Figure 2 shows solutions of (6) by the EFD, unmodified UPFD, and by our modified UPFD schemes. Modification of (6) leads to:

$$\frac{\partial c(x, t)}{\partial t} (1 + \alpha) = \frac{\partial c^2(x, t)}{\partial x^2} - \frac{\partial c(x, t)}{\partial x} - c(x, t) \tag{11}$$

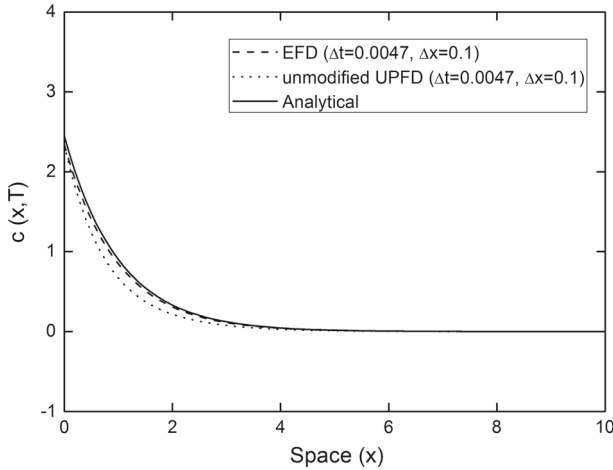


Fig. 1 Comparison of results by the EFD and unmodified UPFD numerical schemes to those by the analytical solution

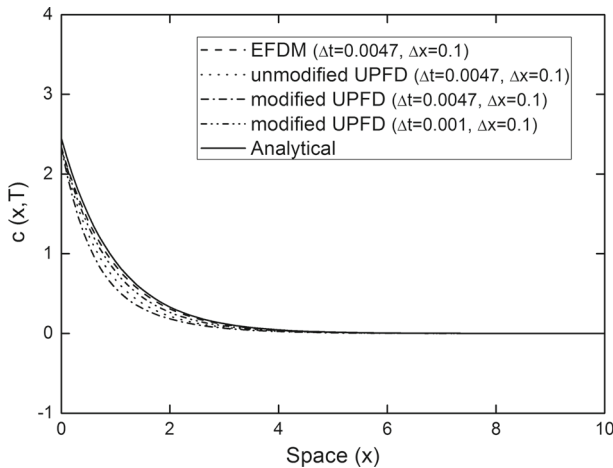


Fig. 2 Comparison of results by the EFD, unmodified UPFD, and modified UPFD numerical schemes to those by the analytical solution

where $\alpha = \frac{\Delta t}{\Delta x^2} (2D + u \Delta x)$. We have solved (11) for two values of time steps, $\Delta t = 0.0047$ and $\Delta t = 0.001$, where $\Delta x = 0.1$. One can observe in Fig. 2 that the solution by the modified UPFD scheme is less accurate than that by the unmodified UPFD scheme for step lengths $\Delta x = 0.1$ and $\Delta t = 0.0047$. This accuracy (of the former) improves as Δt is reduced from 0.0047 to 0.001, but remains below that by the EFD scheme with $\Delta t = 0.0047$. We tested further by refining the mesh size and decreasing the time step Δt from 0.001 to 0.0001, both for EFD and modified UPFD schemes, Fig. 3. One can observe in Fig. 3 that by decreasing the time step Δt , the accuracy improved for the modified UPFD scheme but remained unchanged for the EFD scheme (same as with step lengths $\Delta x = 0.1$ and $\Delta t = 0.0047$). We have obtained that by decreasing Δt

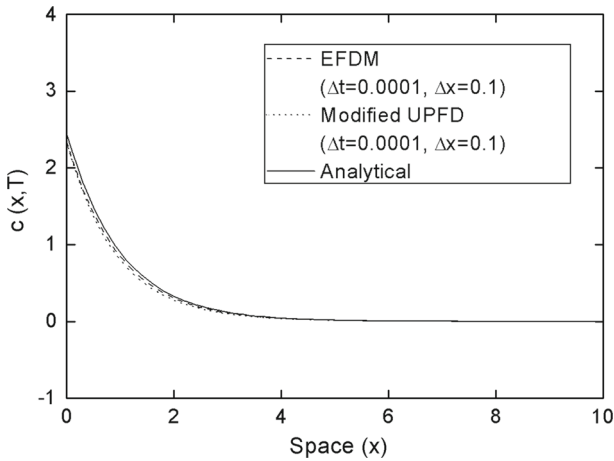


Fig. 3 On a refined mesh size, the comparison of results by the EFD scheme and modified UPFD scheme to those by the analytical solution

further does not translate into higher accuracy for either the EFD or modified UPFD schemes. Hence, we conclude that EFD scheme gives marginally better results than the modified UPFD scheme does for small values of the space coordinate x . With increasing x , results by both EFD and modified UPFD schemes agree well with the analytical solution. One should note here that the positivity and stability of the EFD scheme is easily achieved by choosing a small enough Δt .

In conclusion, in our best knowledge for the first time, we compare in this work the accuracy of the UPFD and standard EFD schemes. We obtained that in solving advection–diffusion reaction equation, EFD scheme is more accurate than either the unmodified or modified UPFD scheme. In our previous works we have shown that the standard explicit finite difference method is also effective and accurate for advection–diffusion equation with variable coefficients [16], which is especially important when arbitrary initial and boundary conditions are required. The presented results are important when modeling a heat and mass transfer processes using the investigated advection–diffusion reaction equation. Furthermore, current and future developers of coupled multi-species transport models may draw on the ideas of solutions methods employed in this study to further develop numerical models for various types of coupled multi-species transport problems.

5 Conclusion

A previously reported unconditionally positive finite difference (UPFD) scheme and standard explicit finite difference (EFD) scheme for solving parabolic differential equations with advection, diffusion and reaction terms are compared to analytical solution reported in the literature. We have shown that, although UPFD scheme guarantees the positivity of the solutions for arbitrary step sizes, this scheme is less accurate. The reason is that the UPFD scheme contains additional truncation error terms in the

approximations to the first and second derivatives with respect to x , which are evaluated at different moments in time. Although these inconsistent terms tend to zero as the mesh is refined, the UPFD scheme remains less accurate than the standard explicit finite difference scheme despite finer discretization. Current and future developers of coupled multi-species transport models may draw on the ideas of solutions methods employed in this study to further develop numerical models for various types of coupled multi-species transport problems.

Acknowledgements The work described in this paper was supported by the Strategic Research Grant of City University of Hong Kong (Project No. CityU 7004600) and by a grant from Serbian Ministry of Education, Science and Technological Development (Agreement No. 451-03-68/2020-14/200122).

Declarations

Conflict of interest All authors declare that they have no conflict of interest.

References

1. Shih, T.M.: Numerical Heat Transfer. Springer, Berlin (1984)
2. Savović, S., Caldwell, J.: Numerical solution of Stefan problem with time-dependent boundary conditions by variable space grid method. *Thermal Sci.* **13**, 165–174 (2009)
3. Savović, S., Simović, A., Djordjevich, A.: Explicit finite difference solution of the power flow equation in W-type optical fibers. *Opt. Laser Technol.* **44**, 1786–1790 (2012)
4. Murray, J.D.: Mathematical Biology I. Springer, Berlin (2002)
5. Bear, J.: Hydraulics of Groundwater. Dover, Minneola (2007)
6. Savović, S., Djordjevich, A., Ristić, G.: Numerical solution of the transport equation describing the radon transport from subsurface soil to buildings. *Rad. Prot. Dosim.* **150**, 213–216 (2012)
7. Savović, S., Djordjevich, A.: Numerical solution for temporally and spatially dependent solute dispersion of pulse type input concentration in semi-infinite media. *Int. J. Heat Mass Transf.* **60**, 291–295 (2013)
8. Hetrick, D.K.: Dynamics of Nuclear Reactors. University of Chicago, Chicago (1971)
9. Urošević, V., Nikezić, D.: Radon transport through concrete and determination of its diffusion coefficient. *Radiat. Prot. Dosim.* **104**, 65–70 (2003)
10. Djordjevich, A., Savović, S.: Numerical solution of the power flow equation in step index plastic optical fibers. *J. Opt. Soc. Am. B* **21**, 1437–1442 (2004)
11. Chen-Charpentier, B.M., Kojouharov, H.V.: An unconditionally positivity preserving scheme for advection–diffusion reaction equations. *Math. Comput. Model.* **57**, 2177–2185 (2013)
12. Quang, D.A., Ehrhardt, M.: Adequate numerical solution of air pollution problems by positive difference schemes on unbounded domains. *Math. Comput. Model.* **44**, 834–856 (2006)
13. Liu, L., Clemence, D.P., Mickens, R.E.: A nonstandard finite difference scheme for contaminant transport with kinetic Langmuir sorption. *Numer. Methods Part. D. E.* **27**, 767–785 (2011)
14. Anderson, J.D.: Computational Fluid Dynamics. McGraw-Hill, New York (1995)
15. Mphephu, N.: Numerical Solution of 1-D Convection-Diffusion-Reaction Equation. Master Thesis, University of Pretoria, South Africa, 25 October 2013.
16. Djordjevich, A., Savović, S.: Solute transport with longitudinal and transverse diffusion in temporally and spatially dependent flow from a pulse type source. *Int. J. Heat Mass Transf.* **65**, 321–326 (2013)

Publisher's Note Springer Nature remains neutral with regard to jurisdictional claims in published maps and institutional affiliations.



Contents lists available at ScienceDirect

Optik

journal homepage: www.elsevier.com/locate/ijleo

Original research article

Method for investigation of mode coupling in multimode step-index silica photonic crystal fibers

Svetislav Savović^{a,b,*}, Milan S. Kovačević^a, Ana Simović^a, Ljubica Kuzmanović^a,
Branko Drljača^c, Alexandar Djordjević^b

^a University of Kragujevac, Faculty of Science, Kragujevac, Serbia

^b City University of Hong Kong, Department of Mechanical Engineering, Hong Kong, China

^c University of Pristina in Kosovska Mitrovica, Faculty of Sciences and Mathematics, L. Ribara 29, Kosovska, Mitrovica, Serbia



ARTICLE INFO

Keywords:

Photonic crystal fiber
Step-index fiber
Power flow equation
Coupling lengths

ABSTRACT

We propose a new method for investigation the state of mode coupling in a multimode step-index silica photonic crystal fiber (SI SPCF) with a solid-core by solving the time-independent power flow equation. For various arrangements of air-holes (different numerical apertures (NAs)), as well as a different widths of launch beam distribution, the length L_c for achieving equilibrium mode distribution (EMD) and length z_s at which a steady state distribution (SSD) is established are determined for such fiber. We obtained that the larger the air holes in the cladding (higher NA), the longer length of the fiber it takes for the modal distribution-transients to reach their equilibrium and steady state. In the case of a wide launch that excites more guiding modes, these lengths shorten. Such information is of interest for application of multimode SI SPCFs in telecommunication and fiber optic sensors.

1. Introduction

Chemical doping or selective layering of materials have traditionally been used to achieve this refractive-index variation through an optical fiber. A micro-structured pattern of very small holes running the length of the “holey” or PCFs is another method. As shown in Fig. 1, a PCF may have a solid core and a holey cladding. The hole pattern reduces the cladding’s effective refractive index, allowing the fiber to direct light. The refractive index profile of the fiber can thus be adjusted during the design process by selecting this hole pattern in the cladding.

PCFs have demonstrated performance not matched by traditional fibers [1–7] because micro-structured patterning of the fiber provides additional versatility to affect its sectional profile during the design stage. A PCF, on the other hand, may have a hollow core. Thanks to photonic bandgap guidance [8–11] the hollow fiber’s “air center” can have a lower refractive index than the cladding material [12,13]. Dispersion [14–16], birefringence [17], supercontinuum generation [18–20], wavelength conversion [21,22], optofluidics [23], and sensing [24] are just a few of the many recorded applications of PCFs.

The numerical aperture, NA, of the PCF is determined by the width of the material between holes in the cladding. The impracticality of cleaving fibers with even larger NAs having big holes and little material remaining between [25–27] appears to limit it to $NA \approx 0.5$ – 0.6 . A heavy metal-oxide glass fiber [28] or a hollow core fiber filled with liquid [29] are two examples of PCFs to consider.

* Correspondence to: Faculty of Science, R. Domanovića 12, 34000 Kragujevac, Serbia.
E-mail address: savovic@kg.ac.rs (S. Savović).

<https://doi.org/10.1016/j.ijleo.2021.167728>

Received 21 May 2021; Received in revised form 23 July 2021; Accepted 27 July 2021

Available online 30 July 2021

0030-4026/© 2021 Elsevier GmbH. All rights reserved.

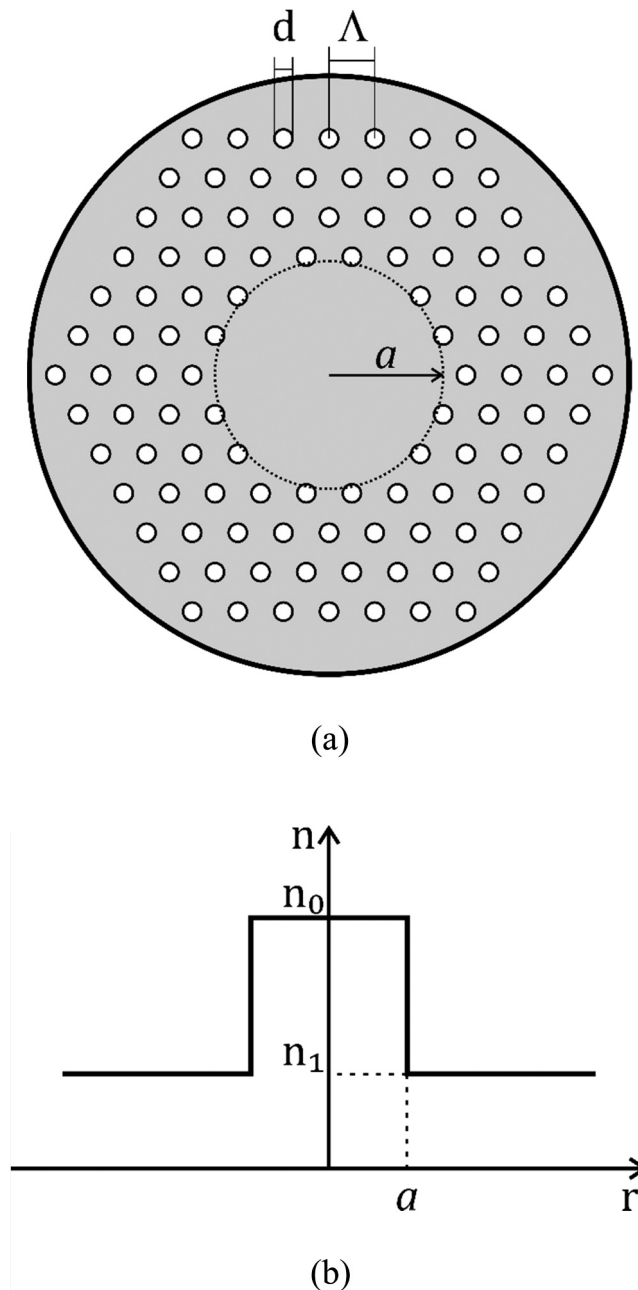


Fig. 1. (a) Cross section of multimode SI PCF with a solid-core and rings of air holes in the cladding, where Λ is the hole-to-hole spacing (pitch), d is diameter of air holes in the cladding. Gray background indicates pure silica and white area indicates air holes. (b) refractive-index profile of the referent multimode SI PCF.

Lensless focusing with excellent resolution has been registered with high NA PCFs [30].

Differential mode attenuation, mode coupling, and modal dispersion all affect PCF propagation characteristics. Mode coupling is primarily caused by light scattering that transfers power from one mode to another in multimode optical fibers due to intrinsic perturbations. Various irregularities, such as microscopic bends, voids and cracks, diameter variation, and density and refractive index variations, can cause these effects. The length-dependent variations of pulse dispersion and bandwidth are caused by mode coupling effects. We calculated spatial transients of power distribution and characteristic lengths at which EMD and SSD are achieved for different widths of launch beam distribution for multimode SI SPCF with solid core and three different diameters of air-holes in the cladding (three different NAs) for multimode SI SPCF with solid core. The cladding holes are set in a triangular pattern with a constant pitch (see Fig. 1).

Until recently, commercial simulation software packages were either designed specifically for single mode PCFs or they modeled

Table 1
Fitting coefficients in Eq. (4).

	$i = 1$	$i = 2$	$i = 3$	$i = 4$
a_{i0}	0.54808	0.71041	0.16904	-1.52736
a_{i1}	5.00401	9.73491	1.85765	1.06745
a_{i2}	-10.43248	47.41496	18.96849	1.93229
a_{i3}	8.22992	-43750962	-42.4318	3.89
b_{i1}	5	1.8	1.7	-0.84
b_{i2}	7	7.32	10	1.02
b_{i3}	9	22.8	14	13.4

individual guided modes in few mode PCFs in a considerable detail, which is not adequate for multimode PCFs having thousands of propagation modes, strong mode coupling and high variability. This inadequacy is resolved in this article, in our knowledge for the first time, by numerical solving the time-independent power flow equation. The parametric variance of the size of air-holes and the width of the launch beam distribution has an effect on mode coupling characteristics of SI SPCF, and thus on characteristic coupling lengths, as shown in the Numerical Results.

2. SI SPCF design

Air-holes are normally of uniform size and form a regular triangular lattice over the SI SPCF’s cladding. Where the size (d) or pitch (spacing density Λ) could be adjusted for desired effective refractive index in that cladding layer. Numerical aperture, dispersion and other fiber properties are thereby engineered by additional design parameters, namely spacing and size of air-holes (Fig. 1). Despite uniform material properties across the fiber, the central part without holes has the highest refractive index n_0 ; holes in the cladding reduce the effective value n_1 of such index; larger or more densely spaced holes in the cladding reduce it even more.

3. Time-independent power flow equation

The power flow in multimode SI optical fibers can be represented by the Gloge’s time independent power flow equation [31].

$$\frac{\partial P(\theta, z)}{\partial z} = -\alpha(\theta)P(\theta, z) + \frac{D}{\theta} \frac{\partial}{\partial \theta} \left(\theta \frac{\partial P(\theta, z)}{\partial \theta} \right) \tag{1}$$

where $P(\theta, z)$ is the angular power distribution at distance z from the input end of the fiber, θ is the propagation angle with respect to the core axis, D is the coupling coefficient assumed constant [31,32], and $\alpha(\theta) = \alpha_0 + \alpha_d(\theta)$ is the modal attenuation – where α_0 represents conventional losses (absorption and scattering) and is neglected as it features only as a multiplier $\exp(-\alpha_0 z)$ in the solution that is normalized [32]. The boundary conditions are $\partial P(\theta_m, z) = 0$ and $D(\partial P/\partial \theta)|_{\theta=0} = 0$, where θ_m is the maximum propagation angle (critical angle).

4. Numerical results

We investigated spatial transients of power distribution as well as an EMD and SSD for different widths of launch beam distribution in a multimode solid-core silica SI SPCF. For PCFs with air holes in a triangular lattice, the effective refractive index of cladding n_{fsm} can be obtained using the effective parameter V :

$$V = \frac{2\pi}{\lambda} a_{eff} \sqrt{n_0^2 - n_{fsm}^2} \tag{2}$$

where n_0 is the refractive index of the core. The effective refractive index of the cladding n_{fsm} is defined as the effective refractive index of so-called fundamental space-filling mode in the triangular hole lattice, and $a_{eff} = \Lambda/\sqrt{3}$ [33]. The effective refractive index of the cladding $n_1 \equiv n_{fsm}$, can be obtained from Eq. (2), using the effective V parameter [33]:

$$V \left(\frac{\lambda}{\Lambda}, \frac{d}{\Lambda} \right) = A_1 + \frac{A_2}{1 + A_3 \exp(A_4 \lambda/\Lambda)} \tag{3}$$

with the fitting parameters A_i ($i = 1$ to 4):

$$A_i = a_{i0} + a_{i1} \left(\frac{d}{\Lambda} \right)^{b_{i1}} + a_{i2} \left(\frac{d}{\Lambda} \right)^{b_{i2}} + a_{i3} \left(\frac{d}{\Lambda} \right)^{b_{i3}} \tag{4}$$

where the coefficients a_{i0} to a_{i3} and b_{i1} to b_{i3} ($i = 1$ to 4) are given in Table 1.

Fig. 2 shows the effective refractive index of the cladding $n_1 \equiv n_{fsm}$ as a function of λ/Λ , for $\Lambda = 3 \mu\text{m}$ and for two values of the hole

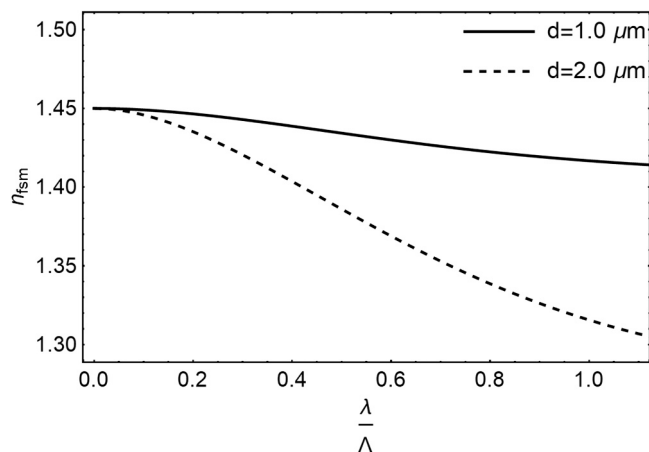


Fig. 2. Effective refractive index of the inner cladding as a function of λ/Λ .

Table 2

Effective refractive index of the cladding n_1 , relative refractive index difference $\Delta = (n_0 - n_1)/n_0$, where $n_0 = 1.45$, and the critical angle θ_m for varied air-hole diameter d (wavelength: 850 nm).

d (μm)	1.0	2.0
n_1	1.443717	1.423679
$\Delta = (n_0 - n_1)/n_0$	0.00433	0.01815
θ_m (deg)	5.34	10.93

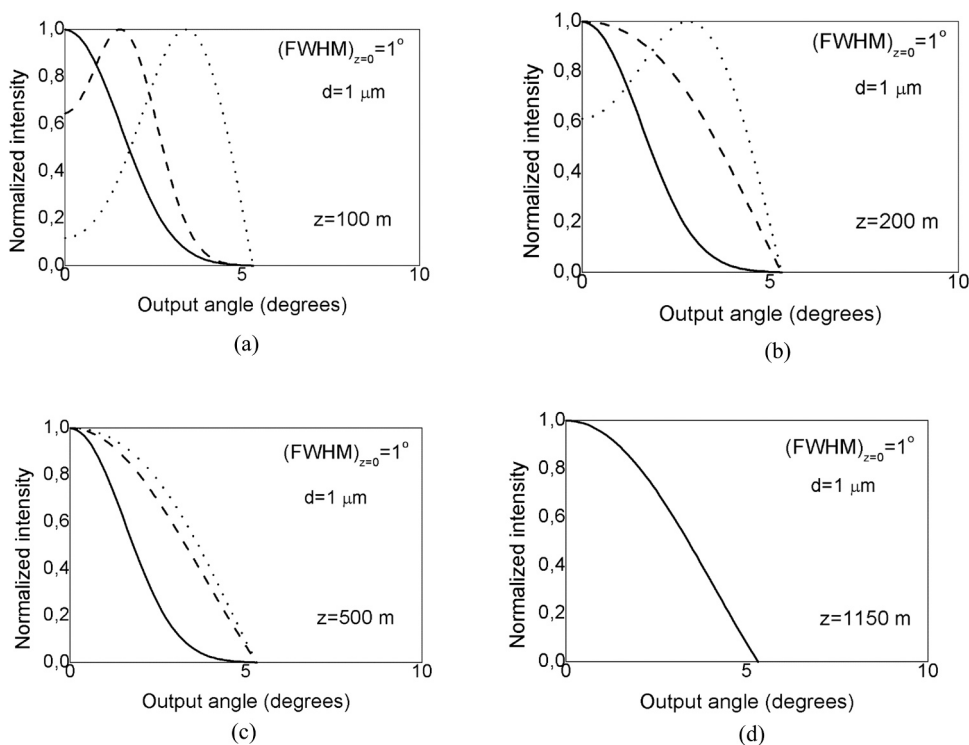


Fig. 3. The evolution of the normalized output angular power distribution with fiber length for the case with $d = 1 \mu\text{m}$ calculated for Gaussian input angles $\theta_0 = 0^\circ$ (solid line), 2° (dashed line) and 4° (dotted line), with $(\text{FWHM})_{z=0} = 1^\circ$ for: (a) $z = 100 \text{ m}$; (b) $z = 200 \text{ m}$; (c) $z \equiv L_c = 500 \text{ m}$ and (d) $z \equiv z_s = 1150 \text{ m}$.

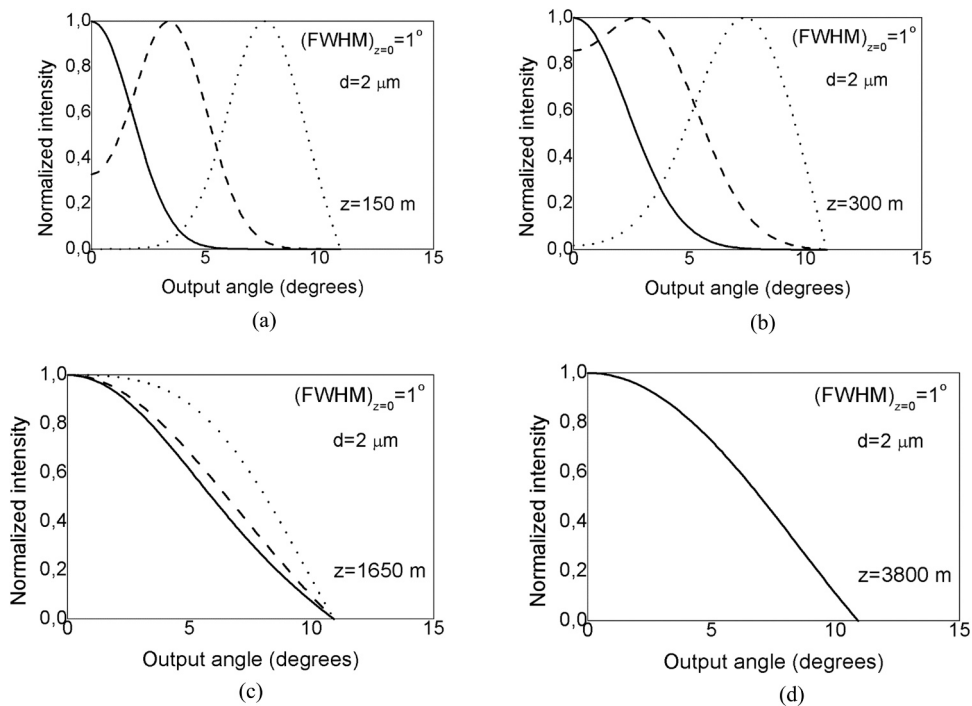


Fig. 4. The evolution of the normalized output angular power distribution with fiber length for the case with $d = 2 \mu\text{m}$ calculated for Gaussian input angles $\theta_0 = 0^\circ$ (solid line), 4° (dashed line) and 8° (dotted line), with $(\text{FWHM})_{z=0} = 1^\circ$ for: (a) $z = 150 \text{ m}$; (b) $z = 300 \text{ m}$; (c) $z = L_c = 1650 \text{ m}$ and (d) $z = z_s = 3800 \text{ m}$.

Table 3

Coupling length L_c (for EMD) and length z_s (for SSD) in SI PPCF with $d = 1 \mu\text{m}$ and $d = 2 \mu\text{m}$, for different $(\text{FWHM})_{z=0}$ of the incident beam.

	$(\text{FWHM})_{z=0} = 1^\circ$		$\text{FWHM} = 3^\circ$		$\text{FWHM} = 5^\circ$	
	L_c [m]	z_s [m]	L_c [m]	z_s [m]	L_c [m]	z_s [m]
$d = 1 \mu\text{m}$	500	1150	410	960	300	700
$d = 2 \mu\text{m}$	1650	3800	1520	3570	1450	3300

diameter d of the cladding. Relevant values of the effective refractive index n_1 , relative refractive index difference Δ , air-hole diameters of the cladding d , and critical angles θ_m , are summarized in Table 2 for the operating wavelength of light of 850 nm.

We solved the power flow Eq. (1) using the explicit finite difference method (EFDM) [34] for the multimode SI SPCF with pure silica core with $n_0 = 1.45$, $2a = 50 \mu\text{m}$, and coupling coefficient $D = 2.3 \times 10^{-6} \text{ rad}^2/\text{m}$ (typical value of D for glass core fibers [35]). In order to look at the impact of the diameter of the air holes in the cladding (i.e. the influence of NA of the fiber) on the power distribution, we analyzed cases with diameter of air holes in the cladding $d = 1 \mu\text{m}$ and $2 \mu\text{m}$ and launch beam distribution with full width of half maximum $(\text{FWHM})_{z=0} = 1^\circ, 3^\circ$ and 5° . As illustration, Figs. 3 and 4 show the evolution of the normalized output angular power distribution with fiber length for the case with $d = 1$ and $2 \mu\text{m}$ calculated for Gaussian launch beam distributions with $(\text{FWHM})_{z=0} = 1^\circ$. It can be seen from Figs. 3 and 4 that when the Gaussian launch beam distribution at the input end of the fiber is centered at $\theta_0 = 0^\circ$, the distribution of the power remains at the same angle as the distance from the input fiber end increases. However, due to mode coupling, its width increases. In short fibers, the radiation patterns of non-centrally launched beams are positioned at values similar to their initial values. With increasing the fiber length one can observe that coupling is stronger for the low-order modes: their distributions have shifted more towards $\theta = 0^\circ$. Coupling of higher-order modes can be observed only after longer fiber lengths. Coupling of higher-order modes can be observed only after longer fiber lengths. It is not until the fiber's coupling length L_c that all the mode-distributions shift their mid-points to zero degrees (from the initial value of θ_0 at the input fiber end), producing the EMD at fiber length $z = L_c = 500 \text{ m}$ for $d = 1 \mu\text{m}$ and $z = L_c = 1650 \text{ m}$ for $d = 2 \mu\text{m}$, and finally the SSD at length $z = z_s = 1150 \text{ m}$ for $d = 1 \mu\text{m}$ and $z = z_s = 3800 \text{ m}$ for $d = 2 \mu\text{m}$. Length z_s marks the fiber length at which the output angular power distribution becomes completely independent on the launch beam distribution. One can see from Figs. 3 and 4 that the lengths L_c and z_s increases with the air-hole size (diameter d), which corresponds to the increase of NA of the multimode SI SPCF. This is as a consequence of the greater participation rate of higher-order modes in higher-aperture photonic-crystal fibers. In contrary, the wider the launch beam, the shorter the length at which EMD and SSD are established (Table 3). This is due to the energy of a wide launch beam which is more uniformly distributed among guided modes in the fiber, that forces the EMD and SSD at shorter distances than for a narrow launch beam.

The mode coupling behavior determines the length dependence of the bandwidth of SI SPCF. Below coupling length L_c the pulse spreading is linear with length. However, beyond this equilibrium length, it has an $L^{1/2}$ dependence. Thus, the shorter the length L_c , the faster bandwidth improvement (slower bandwidth decrease).

5. Conclusion

We proposed a new method for investigation the state of mode coupling in a multimode step-index silica photonic crystal fiber with a solid-core by solving the time-independent power flow equation. For a multimode step-index silica photonic crystal fiber with a solid-core and triangular air-hole lattice in the cladding, spatial transients of the power distribution are presented in graph form. These transients are found to be highly dependent on the excitation conditions as well as the size of the air holes in the cladding (NA of the fiber). We obtained that the larger the air holes in the cladding (higher NA), the longer length of the fiber it takes for the modal distribution-transients to reach their equilibrium and steady state. In the case of a wide launch that excites more guiding modes, these lengths shorten. The photonic crystal fibers can be designed with more versatility thanks to these adjustable parameters. Such design flexibility of adjusting structural parameters of the fiber enables dispersion management by affecting the interplay between the material and geometrical dispersions. Dispersion and the resulting mode coupling affect the majority of fiber-based applications.

Declaration of Competing Interest

The authors declare that they have no known competing financial interests or personal relationships that could have appeared to influence the work reported in this paper.

Acknowledgments

This work was supported in part by the grant from Serbian Ministry of Education, Science and Technological Development (Agreement No. 451-03-68/2020-14/200122), Grant from Science Fund of Republic Serbia (Agreement No. CTPCF-6379382) and by the Strategic Research Grant of City University of Hong Kong (Project No. CityU 7004600).

References

- [1] J.C. Knight, T.A. Birks, P. St.J. Russell, D.M. Atkin, All-silica single-mode optical fiber with photonic crystal cladding, *Opt. Lett.* 21 (1996) 1547–1549.
- [2] T.A. Birks, J.C. Knight, P. St.J. Russell, Endlessly single-mode photonic crystal fiber, *Opt. Lett.* 22 (1997) 961–963.
- [3] P. St.J. Russell, Photonic crystal fibers, *Science* 299 (2003) 358–362.
- [4] J.C. Knight, Photonic crystal fiber, *Nature* 424 (14) (2003) 847–851.
- [5] P. St.J. Russell, Photonic-crystal fibers, *J. Light. Technol.* 24 (2006) 4729–4749.
- [6] J.C. Knight, J. Broeng, T.A. Birks, P.S.J. Russell, Photonic band gap guidance in optical fibers, *Science* 282 (1998) 1476–1478.
- [7] J.C. Knight, P.S.J. Russell, Photonic crystal fibers: new way to guide light, *Science* 296 (2002) 276–277.
- [8] R.F. Cregan, B.J. Mangan, J.C. Knight, T.A. Birks, P.S.J. Russell, P.J. Roberts, D.C. Allan, Single-mode photonic band gap guidance of light in air, *Science* 285 (1999) 1537–1539.
- [9] R. Amezcua-Correa, F. Gerome, S.G. Leon-Saval, N.G.R. Broderick, T.A. Birks, J.C. Knight, Control of surface modes in low loss hollow core photonic bandgap fibers, *Opt. Express* 16 (2008) 1142–1149.
- [10] G. Bouwmans, L. Bigot, Y. Quiquempois, F. Lopez, L. Provino, M. Douay, Fabrication and characterization of an all-solid 2d photonic bandgap fiber with a low-loss region (<20 db/km) around 1550 nm, *Opt. Express* 13 (2005) 8452–8459.
- [11] F. Luan, A.K. George, T.D. Hedley, G.J. Pearce, D.M. Bird, J.C. Knight, P. St.J. Russell, All-solid photonic bandgap fiber, *Opt. Lett.* 29 (2004) 2369–2371.
- [12] F. Benabid, J.C. Knight, G. Antonopoulos, P. St.J. Russell, Stimulated Raman scattering in hydrogen-filled hollow-core photonic crystal fiber, *Science* 298 (2002) 399–402.
- [13] P.S. Light, F. Benabid, F. Couny, M. Maric, A.N. Luiten, Electromagnetically induced transparency in Rb-filled coated hollow-core photonic crystal fiber, *Opt. Lett.* 32 (2007) 1323–1325.
- [14] D. Mogilevsev, T.A. Birks, P. St.J. Russell, Group-velocity dispersion in photonic crystal fibers, *Opt. Lett.* 23 (1998) 1662–1664.
- [15] K. Saitoh, M. Koshiba, T. Hasegawa, E. Sasaoka, Chromatic dispersion control in photonic crystal fibers: application to ultra-flattened dispersion, *Opt. Express* 11 (2003) 843–852.
- [16] S. Lee, W. Ha, J. Park, S. Kim, K. Oh, A new design of low-loss and ultra-flat zero dispersion photonic crystal fiber using hollow ring defect, *Opt. Commun.* 285 (20) (2012) 4082–4087.
- [17] D. Chen, M.L.V. Tse, H.Y. Tam, Optical properties of photonic crystal fibers with a fiber core of arrays of sub-wavelength circular air holes: birefringence and dispersion, *Prog. Electromagn. Res.* 105 (2010) 193–212.
- [18] J.K. Ranka, R.S. Windeler, A.J. Stentz, Visible continuum generation in air silica microstructure optical fibers with anomalous dispersion at 800 nm, *Opt. Lett.* 25 (2000) 25–27.
- [19] K.M. Hilligsøe, T.V. Andersen, H.N. Paulsen, C.K. Nielsen, K. Mølmer, S. Keiding, R. Kristiansen, K.P. Hansen, J.J. Larsen, Supercontinuum generation in a photonic crystal fiber with two zero dispersion wavelengths, *Opt. Express* 12 (2004) 1045–1054.
- [20] W.J. Wadsworth, N. Joly, J.C. Knight, T.A. Birks, F. Biancalana, P. St.J. Russell, Supercontinuum and four-wave mixing with Q-switched pulses in endlessly single-mode photonic crystal fibers, *Opt. Express* 12 (2004) 299–309.
- [21] J.H. Lee, W. Belardi, K. Furusawa, P. Petropoulos, Z. Yusoff, T.M. Monro, D.J. Richardson, Four-wave mixing based 10-Gb/s tunable wavelength conversion using a holey fiber with a high SBS threshold *IEEE Photonics Technol. Lett.* 15 (2003) 440–442.
- [22] T.V. Andersen, K.M. Hilligsøe, C.K. Nielsen, J. Thøgersen, K.P. Hansen, S.R. Keiding, J.J. Larsen, Continuous-wave wavelength conversion in a photonic crystal fiber with two zero-dispersion wavelengths, *Opt. Express* 12 (2004) 4113–4122.
- [23] J. Park, D.E. Kang, B. Paulson, T. Nazari, K. Oh, Liquid core photonic crystal fiber with low-refractive-index liquids for optofluidic applications, *Opt. Express* 22 (14) (2014) 17320–17330.
- [24] S.H. Kassani, R. Khazaeinezhad, Y. Jung, J. Kobelke, K. Oh, Suspended ring-core photonic crystal fiber gas sensor with high sensitivity and fast response, *IEEE Photonics J.* 7 (1) (2015) 1–9.
- [25] W. Wadsworth, R. Percival, G. Bouwmans, J. Knight, T. Birks, T. Hedley, P. St.J. Russell, Very high numerical aperture fibers, *IEEE Photon. Techn. Lett.* 16 (2004) 843–845.
- [26] K.P. Hansen, High-power photonic crystal fibers," in the Proceedings of SPIE, Vol. 6102, pp. 61020B–61020B–11 (SPIE 2006).

- [27] K.P. Hansen, C.B. Olausson, J. Broeng, D. Noordegraaf, M.D. Maack, T.T. Alkeskjold, M. Laurila, T. Nikolajsen, P.M.W. Skovgaard, M.H. Sorensen, M. Denninger, C. Jakobsen, H.R. Simonsen, Airclad fiber laser technology, *Opt. Eng.* 50 (2011), 111609.
- [28] R. Stepien, B. Siwicki, D. Pysz, G. Stepniewski, Characterization of a large core photonic crystal fiber made of lead–bismuth–gallium oxide glass for broadband infrared transmission, *Opt. Quant. Electron.* 46 (2014) 553–561.
- [29] M.M. Tefelska, S. Ertman, T.R. Wolinski, P. Mergo, R. Dabrowski, Large area multimode photonic band-gap propagation in photonic liquid-crystal fiber, *IEEE Photon. Technol. Lett.* 24 (2012) 631–633.
- [30] L.V. Amitonova, A. Descloux, J. Petschulat, M.H. Frosz, G. Ahmed, F. Babic, X. Jiang, A.P. Mosk, P. St.J. Russell, P.W.H. Pinkse1, High-resolution wavefront shaping with a photonic crystal fiber for multimode fiber imaging, *Opt. Lett.* 41 (2016) 497–500.
- [31] D. Gloge, Optical power flow in multimode fibers, *Bell Syst. Tech. J.* 51 (1972) 1767–1783.
- [32] M. Rousseau, L. Jeunhomme, Numerical solution of the coupled-power equation in step index optical fibers, *IEEE Trans. Microw. Theory Tech.* 25 (1977) 577–585.
- [33] K. Saitoh, M. Koshiba, Empirical relations for simple design of photonic crystal fibers, *Opt. Express* 13 (2005) 267–274.
- [34] A. Djordjevich, S. Savović, Investigation of mode coupling in step index plastic optical fibers using the power flow equation, *IEEE Photon. Technol. Lett.* 12 (2000) 1489–1491.
- [35] T.P. Tanaka, S. Yamada, Steady-state characteristics of multimode W-type fibers, *Appl. Opt.* 18 (1979) 3261–3264.



Contents lists available at ScienceDirect

Optik

journal homepage: www.elsevier.com/locate/ijleo

Power flow in multimode step-index plastic photonic crystal fibers

Svetislav Savović^{a,b,*}, Milan S. Kovačević^a, Branko Drljača^c, Ana Simović^a,
Ljubica Kuzmanović^a, Alexandar Djordjevich^b

^a University of Kragujevac, Faculty of Science, Kragujevac, Serbia

^b City University of Hong Kong, Department of Mechanical Engineering, Hong Kong, China

^c University of Pristina in Kosovska Mitrovica, Faculty of Sciences and Mathematics, L. Ribara 29, Kosovska Mitrovica, Serbia

ARTICLE INFO

Keywords:

photonic crystal fiber
step-index fiber
power flow equation
coupling lengths

ABSTRACT

We investigate the state of mode coupling in a multimode step-index plastic photonic crystal fiber (SI PPCF) with a solid-core by solving the time-independent power flow equation. For various arrangements of air-holes, and therefore a different numerical apertures (NAs), as well as a different widths of launch beam distribution, the length L_c for achieving equilibrium mode distribution (EMD) and length z_s at which a steady state distribution (SSD) is established are determined for such fiber. We show that the larger the air holes in the cladding (higher NA), the longer length of the fiber it takes for the modal distribution-transients to reach their equilibrium and steady state. This is as a consequence of the greater participation rate of higher-order modes in higher-aperture photonic-crystal fibers. In contrary, in the case of a wide launch that excites more guiding modes, these lengths shorten. This is because the energy of a wide launch beam is more uniformly distributed among guided modes in the fiber, thus the EMD and SSD are reached at shorter distances than for a narrow launch beam. Such information is of interest for application of multimode photonic crystal fibers in telecommunication and fiber optic sensors.

1. Introduction

Despite single-mode glass fibers' superior bandwidth, multimode plastic optical fibers (POFs) are often used for short-distance (less than 100 m) communication links such as high-bandwidth local area networks (LANs) and multi-node bus networks. Because of their ductility and light weight, POFs are easy to treat. Their main benefit is that they can be made with wide core diameters (up to 1 mm). Since systems can be made with low-precision plastic components instead of precision couplers, the tolerances needed for system interconnections are relaxed, and the total cost is reduced. Large-core POFs can easily be combined with lasers, LEDs, and VCSELs to build low-cost, high-reliability systems. Illumination, sensing, and data processing have also been used in their applications.

Chemical doping or selective layering of materials have traditionally been used to achieve this refractive-index variation through an optical fiber. A micro-structured pattern of very small holes running the length of the "holey" or photonic crystal fibers is another method (PCFs). As shown in Fig. 1, a PCF may have a solid core and a holey cladding. The hole pattern reduces the cladding's effective refractive index, allowing the fiber to direct light. The refractive index profile of the fiber can thus be adjusted during the design process by selecting this hole pattern in the cladding.

PCFs have demonstrated performance not matched by traditional fibers [1–7] because micro-structured patterning of the fiber

* Correspondence to: Faculty of Science, R. Domanovića 12, 34000 Kragujevac, Serbia.

E-mail address: savovic@kg.ac.rs (S. Savović).

<https://doi.org/10.1016/j.ijleo.2021.167868>

Received 30 June 2021; Received in revised form 18 August 2021; Accepted 20 August 2021

Available online 21 August 2021

0030-4026/© 2021 Elsevier GmbH. All rights reserved.

provides additional versatility to affect its sectional profile during the design stage. For example, “endlessly single-mode” PCFs that operate in only the fundamental mode across a broad wavelength range have been defined [2]. A PCF, on the other hand, may have a hollow core. The hollow fiber’s “air center” can have a lower refractive index than the cladding material [12,13] thanks to photonic bandgap guidance [8–11]. Dispersion [14–16], birefringence [17], supercontinuum generation [18–20], wavelength conversion [21, 22], optofluidics [23], and sensing [24] are just a few of the many recorded applications of PCFs.

The numerical aperture, NA, of the PCF is determined by the width of the material between holes in the cladding. The impracticality of cleaving fibers with even larger NAs having big holes and little material remaining between [25–27] appears to limit it to $NA \simeq 0.5\text{--}0.6$. A heavy metal-oxide glass fiber [28] or a hollow core fiber filled with liquid [29] are two examples of PCFs to consider. Lensless focusing with excellent resolution has been registered with high NA PCFs [30].

Differential mode attenuation, mode coupling, and modal dispersion all affect PCF propagation characteristics. Mode coupling is primarily caused by light scattering that transfers power from one mode to another in multimode optical fibers due to intrinsic perturbations. Various irregularities, such as microscopic bends, voids and cracks and density variations, can cause these effects. The length-dependent variations of pulse dispersion and bandwidth are caused by mode coupling effects. We calculated spatial transients of power distribution and characteristic lengths at which EMD and SSD are achieved for different widths of launch beam distribution for multimode SI PPCF with solid core and three different diameters of air-holes in the cladding (three different NAs) for multimode SI

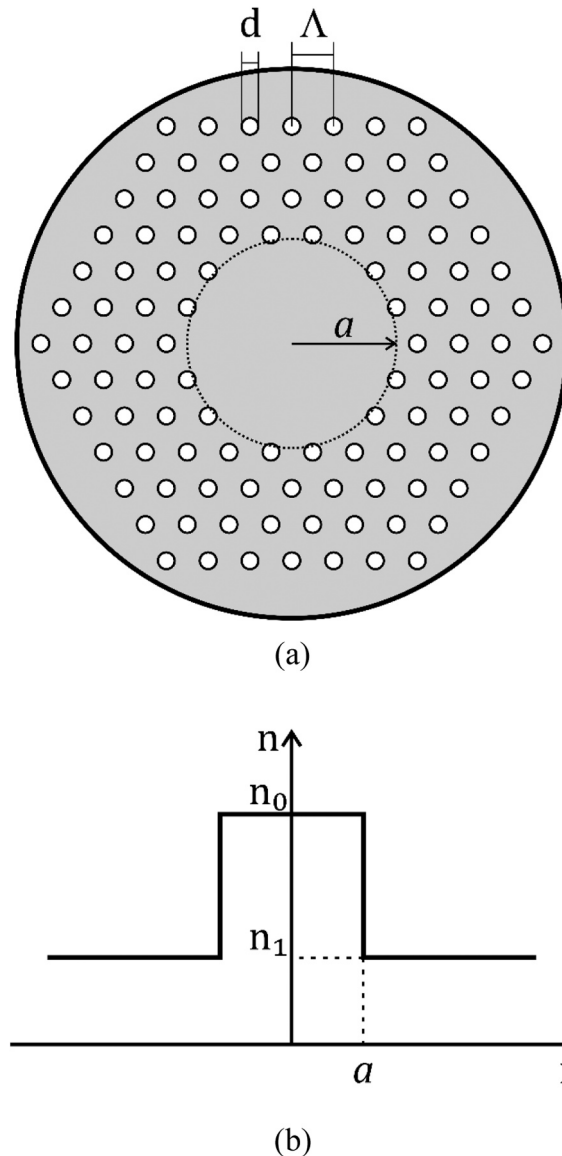


Fig. 1. (a) Cross section of multimode SI PCF with a solid-core and rings of air holes in the cladding, where Λ is the hole-to-hole spacing (pitch), d is diameter of air holes in the cladding, white area indicates air holes, (b) refractive-index profile of the referent multimode SI PPCF.

PPCF with solid core. The cladding holes are set in a triangular pattern with a constant pitch (see Fig. 1). We used the explicit finite differences method (EFDM) to solve the time-independent power flow equation for such a fiber. The parametric variance of the size of air-holes and the width of the launch beam distribution has an effect on characteristic coupling lengths, as shown in the Numerical Results.

2. SI PPCF design

Over the SI PPCF cladding, air-holes are usually uniform in size and form a regular triangular lattice. Where the size (d) or pitch (spacing density) (Λ) of the cladding layer could be changed to achieve the desired effective refractive index. Additional design parameters, such as air-hole spacing and size, are used to monitor numerical aperture, dispersion, and other fiber properties (Fig. 1). Despite uniform material properties in the fiber, the central part without holes has the highest refractive index n_0 ; holes in the cladding decrease the effective value n_1 of such index; larger or more densely spaced holes in the cladding further reduce it.

3. Time-independent power flow equation

The power flow in multimode SI optical fibers can be represented by the Gloge's time-independent power flow equation [31].

$$\frac{\partial P(\theta, z)}{\partial z} = -\alpha(\theta)P(\theta, z) + \frac{D}{\theta} \frac{\partial}{\partial \theta} \left(\theta \frac{\partial P(\theta, z)}{\partial \theta} \right) \tag{1}$$

where $P(\theta, z)$ is the angular power distribution at distance z from the input end of the fiber, θ is the propagation angle with respect to the core axis, D is the coupling coefficient assumed constant [31,32], and $\alpha(\theta)$ is the modal attenuation (except near cutoff, the attenuation remains uniform $\alpha(\theta) = \alpha_0$ throughout the region of guided modes $0 \leq \theta \leq \theta_m$) [33]. The boundary conditions are $\partial P(\theta_m, z) = 0$ and $D(\partial P/\partial \theta)|_{\theta=0} = 0$, where θ_m is the maximum propagation angle (critical angle).

In order to apply the EFDM, we express Eq. (1) in the following form:

$$\frac{\partial P(\theta, z)}{\partial z} = -\alpha_0 P(\theta, z) + \frac{D}{\theta} \frac{\partial P(\theta, z)}{\partial \theta} + D \frac{\partial^2 P(\theta, z)}{\partial \theta^2} \tag{2}$$

We used the central difference scheme to represent the $(\partial P(\theta, z))/\partial \theta$ and $(\partial^2 P(\theta, z))/\partial \theta^2$ terms, and the forward difference scheme for the derivative term $(\partial P(\theta, z))/\partial z$. Then, Eq. (2) reads:

$$P_{i,j+1} = \left(\frac{\Delta z D}{\Delta \theta^2} - \frac{\Delta z D}{2\theta_{ij}\Delta \theta} \right) P_{i-1,j} + \left(1 - \frac{2\Delta z D}{\Delta \theta^2} - \Delta z \alpha_0 \right) P_{i,j} + \left(\frac{\Delta z D}{2\theta_{ij}\Delta \theta} + \frac{\Delta z D}{\Delta \theta^2} \right) P_{i+1,j} \tag{3}$$

where indexes i and j refer to the discrete step lengths $\Delta \theta$ and Δz for the angle θ and length z , respectively. This is a simple formula for $P_{i,j+1}$ at the $(i, j + 1)^{\text{th}}$ mesh point in terms of the known values along the j^{th} distance row. The truncation error for the difference Eq. (3) is $O(\Delta z, \Delta \theta^2)$. In the difference form, the boundary conditions can be expressed as $P_{N,j} = 0$; $P_{0,j} = P_{1,j}$, where $N = (\theta_m/\Delta \theta)$ is grid dimension in the θ direction.

4. Numerical results

In a multimode solid-core SI PPCF, we investigated spatial transients of power distribution as well as an EMD and SSD for different widths of launch beam distribution. The effective refractive index of cladding n_{fsm} for SI PPCFs with air holes in a triangular lattice can be calculated using the effective parameter:

$$V = \frac{2\pi}{\lambda} a_{\text{eff}} \sqrt{n_0^2 - n_{fsm}^2} \tag{4}$$

where n_0 is the refractive index of the core. The cladding's effective refractive index n_{fsm} is defined as the effective refractive index of so-

Table 1
Fitting coefficients in Eq. (6).

	$i = 1$	$i = 2$	$i = 3$.
a_{i0}	0.54808	0.71041	0.16904	-1.52736
a_{i1}	5.00401	9.73491	1.85765	1.06745
a_{i2}	-10.43248	47.41496	18.96849	1.93229
a_{i3}	8.22992	-43750962	-42.4318	3.89
b_{i1}	5	1.8	1.7	-0.84
b_{i2}	7	7.32	10	1.02
b_{i3}	9	22.8	14	13.4

called fundamental space-filling mode in the triangular hole lattice, and $a_{eff} = \Lambda/\sqrt{3}$ [34]. The effective refractive index of the cladding $n_{1\equiv n_{fsm}}$ can be obtained from Eq. (4), using the effective V parameter [34]:

$$V\left(\frac{\lambda}{\Lambda}, \frac{d}{\Lambda}\right) = A_1 + \frac{A_2}{1 + A_3 \exp(A_4 \lambda/\Lambda)} \quad (5)$$

with the fitting parameters A_i ($i = 1$ to 4):

$$A_i = a_{i0} + a_{i1} \left(\frac{d}{\Lambda}\right)^{b_{i1}} + a_{i2} \left(\frac{d}{\Lambda}\right)^{b_{i2}} + a_{i3} \left(\frac{d}{\Lambda}\right)^{b_{i3}} \quad (6)$$

where the coefficients a_{i0} to a_{i3} and b_{i1} to b_{i3} ($i = 1$ to 4) are given in Table 1.

Fig. 2 depicts the effective refractive index of the cladding $n_{1\equiv n_{fsm}}$ as a function of λ/Λ , for $\Lambda = 3 \mu\text{m}$ and for three different values of the hole diameter of the cladding $d = 1 \mu\text{m}$, $1.5 \mu\text{m}$ and $2 \mu\text{m}$. Relevant values of the effective refractive index n_1 , relative refractive index difference Δ , air-hole diameters of the cladding d , and critical angles θ_m , are summarized in Table 2 for the operating wavelength of light of 645 nm.

The time-independent power flow Eq. (2) was solved using the EFDM for the multimode SI PPCF with solid core with $n_0 = 1.492$, core diameter $2a = 0.980$ mm, fiber diameter $b = 1$ mm, $D = 1.649 \times 10^{-4}$ rad²/m and $\alpha_0 = 0.22$ dB/m (typical value of D and α_0 for standard POFs [33]). One should note that in modeling the SI PPCF one can use the typical values of D which characterizes a standard SI POF, since a strength of mode coupling in both types of plastic optical fibers is related to the plastic core material. Namely, mode coupling in both types of optical fibers is mainly caused by light scattering that transfers power from one mode to another due to various irregularities in plastic core, such as microscopic bends, voids, cracks and density variations. A similar assumption has been made in modeling a silica W-type PCF [35]. One should note that for bent POFs mode coupling is much stronger [36], which is expected to happen in bent PPCFs too. In order to look at the impact of the diameter of the air holes in the cladding (i.e. the influence of NA of the fiber) on the power distribution, we analyzed cases with diameter of air holes in the cladding $d = 1 \mu\text{m}$, $1.5 \mu\text{m}$ and $2 \mu\text{m}$ and launch beam distribution with $(\text{FWHM})_{z=0} = 1^\circ$, 5° and 10° . As illustration, Fig. 3 shows the evolution of the normalized output angular power distribution with fiber length for the case with $d = 2 \mu\text{m}$ calculated for Gaussian launch beam distributions with $(\text{FWHM})_{z=0} = 5^\circ$. It can be seen from Fig. 3 that when the Gaussian launch beam distribution at the input end of the fiber is centered at $\theta_0 = 0^\circ$, the distribution of the power remains at the same angle as the distance from the input fiber end increases. However, due to mode coupling, its width increases. In short fibers, the radiation patterns of non-centrally launched beams are positioned at values similar to their initial values. With increasing the fiber length one can observe that coupling is stronger for the low-order modes: their distributions have shifted more towards $\theta = 0^\circ$. Coupling of higher-order modes can be observed only after longer fiber lengths. It is not until the fiber's coupling length L_c that all the mode-distributions shift their mid-points to zero degrees (from the initial value of θ_0 at the input fiber end), producing the EMD at fiber length $z = L_c = 39$ m and the SSD at length $z = z_s = 102$ m. Length z_s marks the fiber length where the output angular power distribution becomes completely independent on the launch beam distribution. The lengths L_c and z_s increase with the air-hole size (diameter d), that relates to the increase of NA of the multimode SI PPCF (Table 3). This is due to the higher participation rate of higher-order modes in photonic crystal fibers with larger numerical apertures. In contrary, the wider the launch beam, the shorter the length at which EMD and SSD are established (Figs. 4 and 5). This is due to the energy of a wide launch beam which is more uniformly distributed among guided modes in the fiber, that forces the EMD and SSD at shorter distances than for a narrow launch beam.

The results reported in this work can be used in employing the PPCFs as a part of various sensory systems [37] and compare their performance with standard POF sensors [38]. On the other hand, the mode coupling behavior determines the length dependence of the

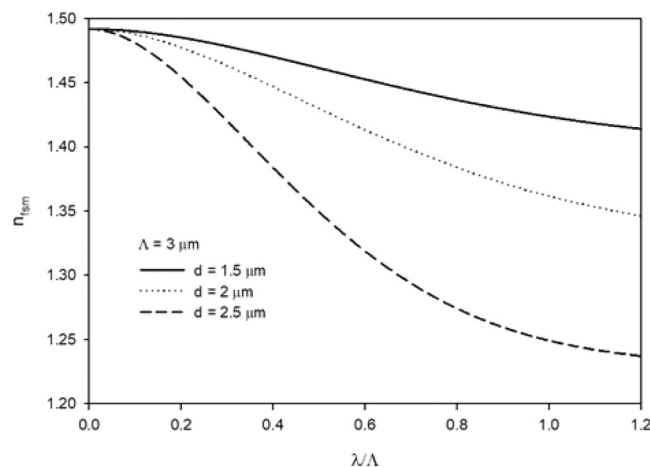


Fig. 2. Effective refractive index of the inner cladding as a function of λ/Λ .

Table 2

Effective refractive index of the cladding n_1 , relative refractive index difference $\Delta = (n_0 - n_1)/n_0$, where $n_0 = 1.492$, and the critical angle θ_m for varied air-hole diameter d (wavelength: 645 nm).

d (μm)	1.0	1.5	2.0
n_1	1.4844	1.4757	1.4458
$\Delta = (n_0 - n_1)/n_0$	0.673673	0.677645	0.691611
θ_m (deg.)	5.79	8.48	14.28

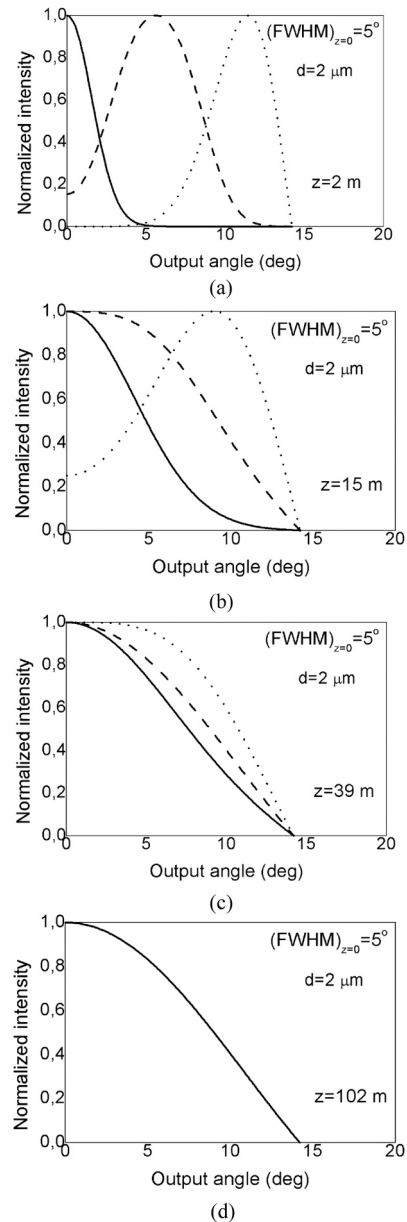


Fig. 3. The evolution of the normalized output angular power distribution with fiber length for the case with $d = 2 \mu\text{m}$ calculated for Gaussian input angles $\theta_0 = 0^\circ$ (solid line), 6° (dashed line), and 12° (dotted line) with $(\text{FWHM})_{z=0} = 5^\circ$ for: (a) $z = 2 \text{ m}$; (b) $z = 15 \text{ m}$; (c) $z = L_c = 39 \text{ m}$ and (d) $z = z_s = 102 \text{ m}$.

Table 3

Coupling length L_c (for EMD) and length z_s (for SSD) in SI PPCF with $d = 1 \mu\text{m}$, $d = 1.5 \mu\text{m}$ and $d = 3 \mu\text{m}$, for different $(\text{FWHM})_{z=0}$ of the incident beam.

	$(\text{FWHM}) = 1^\circ$		$(\text{FWHM}) = 5^\circ$		$(\text{FWHM}) = 10^\circ$	
	L_c [m]	z_s [m]	L_c [m]	z_s [m]	L_c [m]	z_s [m]
$d = 1 \mu\text{m}$	5	13	4.5	12	2.5	6
$d = 1.5 \mu\text{m}$	12.5	31	11	28	9	22
$d = 2 \mu\text{m}$	41	106	39	102	33	85

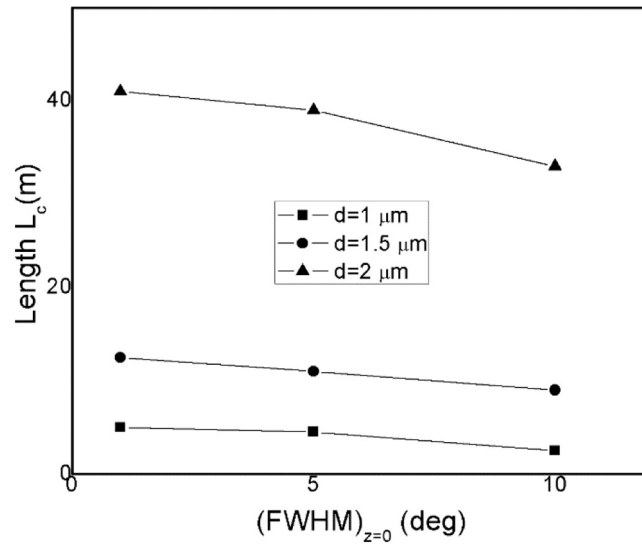


Fig. 4. Length L_c as a function of the launch beam's angular distribution that is Gaussian with $(\text{FWHM})_{z=0} = 1^\circ, 5^\circ$ and 10° , for $d = 1 \mu\text{m}$, $1.5 \mu\text{m}$ and $2 \mu\text{m}$.

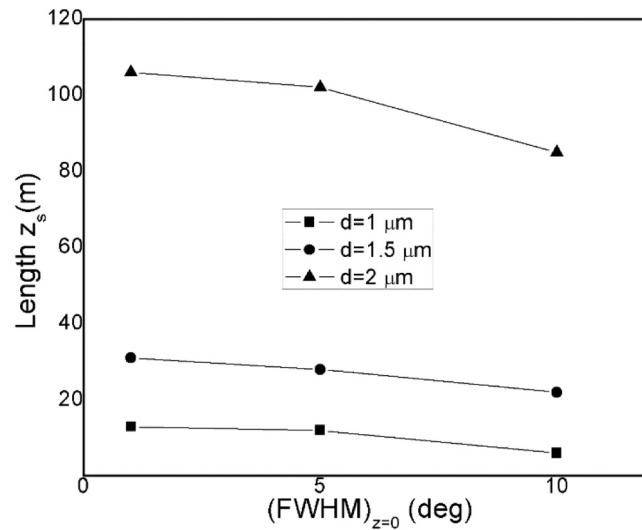


Fig. 5. Length z_s as a function of the launch beam's angular distribution that is Gaussian with $(\text{FWHM})_{z=0} = 1^\circ, 5^\circ$ and 10° , for $d = 1 \mu\text{m}$, $1.5 \mu\text{m}$ and $2 \mu\text{m}$.

bandwidth of SI PPCF. Below coupling length L_c the pulse spreading is linear with length. However, beyond this equilibrium length, it has an $L^{1/2}$ dependence. Thus, the shorter the length L_c , the faster bandwidth improvement (slower bandwidth decrease) [39–41].

5. Conclusion

For a multimode step-index plastic photonic crystal fiber with a solid-core and triangular air-hole lattice in the cladding, spatial transients of the power distribution are presented in graph form. These transients are found to be highly dependent on the excitation conditions as well as the size of the air holes in the cladding (NA of the fiber). We obtained that the larger the air holes in the cladding (higher NA), the longer length of the fiber it takes for the modal distribution-transients to reach their equilibrium and steady state. In the case of a wide launch that excites more guiding modes, these lengths shorten. The photonic crystal fibers can be designed with more versatility thanks to these adjustable parameters. Such design flexibility of adjusting structural parameters of the fiber enables dispersion management by affecting the interplay between the material and geometrical dispersions. Dispersion and the resulting mode coupling affect the majority of fiber-based applications.

Declaration of Competing Interest

No conflicts of interests.

Acknowledgements

This work was supported in part by the grant from Serbian Ministry of Education, Science and Technological Development (Agreement No. 451-03-68/2020-14/200122), grant from Science Fund of Republic Serbia (Agreement No. CTPCF-6379382) and by the Strategic Research Grant of City University of Hong Kong (Project No. CityU 7004600).

References

- [1] J.C. Knight, T.A. Birks, P. St.J. Russell, D.M. Atkin, All-silica single-mode optical fiber with photonic crystal cladding, *Opt. Lett.* 21 (1996) 1547–1549.
- [2] T.A. Birks, J.C. Knight, P. St. J. Russell, Endlessly single-mode photonic crystal fiber, *Opt. Lett.* 22 (1997) 961–963.
- [3] P. St.J. Russell, Photonic crystal fibers, *Science* 299 (2003) 358–362.
- [4] J.C. Knight, Photonic crystal fiber, *Nature* 424 (14) (2003) 847–851.
- [5] P. St.J. Russell, Photonic-crystal fibers, *J. Light. Technol.* 24 (2006) 4729–4749.
- [6] J.C. Knight, J. Broeng, T.A. Birks, P.S.J. Russell, Photonic band gap guidance in optical fibers, *Science* 282 (1998) 1476–1478.
- [7] J.C. Knight, P.S.J. Russell, Photonic crystal fibers: new way to guide light, *Science* 296 (2002) 276–277.
- [8] R.F. Cregan, B.J. Mangan, J.C. Knight, T.A. Birks, P.S.J. Russell, P.J. Roberts, D.C. Allan, Single-mode photonic band gap guidance of light in air, *Science* 285 (1999) 1537–1539.
- [9] R. Amezcua-Correa, F. Gerome, S.G. Leon-Saval, N.G.R. Broderick, T.A. Birks, J.C. Knight, Control of surface modes in low loss hollow core photonic bandgap fibers, *Opt. Express* 16 (2008) 1142–1149.
- [10] G. Bouwmans, L. Bigot, Y. Quiquempois, F. Lopez, L. Provino, M. Douay, Fabrication and characterization of an all-solid 2d photonic bandgap fiber with a low-loss region (<20 db/km) around 1550 nm, *Opt. Express* 13 (2005) 8452–8459.
- [11] F. Luan, A.K. George, T.D. Hedley, G.J. Pearce, D.M. Bird, J.C. Knight, P. St.J. Russell, All-solid photonic bandgap fiber, *Opt. Lett.* 29 (2004) 2369–2371.
- [12] F. Benabid, J.C. Knight, G. Antonopoulos, P. St.J. Russell, Stimulated Raman scattering in hydrogen-filled hollow-core photonic crystal fiber, *Science* 298 (2002) 399–402.
- [13] P.S. Light, F. Benabid, F. Couny, M. Maric, A.N. Luiten, Electromagnetically induced transparency in Rb-filled coated hollow-core photonic crystal fiber, *Opt. Lett.* 32 (2007) 1323–1325.
- [14] D. Mogilevtsev, T.A. Birks, P. St.J. Russell, Group-velocity dispersion in photonic crystal fibers, *Opt. Lett.* 23 (1998) 1662–1664.
- [15] K. Saitoh, M. Koshiba, T. Hasegawa, E. Sasaoka, Chromatic dispersion control in photonic crystal fibers: application to ultra-flattened dispersion, *Opt. Express* 11 (2003) 843–852.
- [16] S. Lee, W. Ha, J. Park, S. Kim, K. Oh, A new design of low-loss and ultra-flat zero dispersion photonic crystal fiber using hollow ring defect, *Opt. Commun.* 285 (20) (2012) 4082–4087.
- [17] D. Chen, M.L.V. Tse, H.Y. Tam, Optical properties of photonic crystal fibers with a fiber core of arrays of sub-wavelength circular air holes: birefringence and dispersion, *Prog. Electromagn. Res.* 105 (2010) 193–212.
- [18] J.K. Ranka, R.S. Windeler, A.J. Stentz, Visible continuum generation in air silica microstructure optical fibers with anomalous dispersion at 800 nm, *Opt. Lett.* 25 (2000) 25–27.
- [19] K.M. Hilligsøe, T.V. Andersen, H.N. Paulsen, C.K. Nielsen, K. Mølmer, S. Keiding, R. Kristiansen, K.P. Hansen, J.J. Larsen, Supercontinuum generation in a photonic crystal fiber with two zero dispersion wavelengths, *Opt. Express* 12 (2004) 1045–1054.
- [20] W.J. Wadsworth, N. Joly, J.C. Knight, T.A. Birks, F. Biancalana, P. St.J. Russell, Supercontinuum and four-wave mixing with Q-switched pulses in endlessly single-mode photonic crystal fibres, *Opt. Express* 12 (2004) 299–309.
- [21] J.H. Lee, W. Belardi, K. Furusawa, P. Petropoulos, Z. Yusoff, T.M. Monro, D.J. Richardson, Four-wave mixing based 10-Gb/s tunable wavelength conversion using a holey fiber with a high SBS threshold, *IEEE Photonics Technol. Lett.* 15 (2003) 440–442.
- [22] T.V. Andersen, K.M. Hilligsøe, C.K. Nielsen, J. Thøgersen, K.P. Hansen, S.R. Keiding, J.J. Larsen, Continuous-wave wavelength conversion in a photonic crystal fiber with two zero-dispersion wavelengths, *Opt. Express* 12 (2004) 4113–4122.
- [23] J. Park, D.E. Kang, B. Paulson, T. Nazari, K. Oh, Liquid core photonic crystal fiber with low-refractive-index liquids for optofluidic applications, *Opt. Express* 22 (14) (2014) 17320–17330.
- [24] S.H. Kassani, R. Khazaeinezhad, Y. Jung, J. Kobelke, K. Oh, Suspended ring-core photonic crystal fiber gas sensor with high sensitivity and fast response, *IEEE Photonics J.* 7 (2015) 1–9.
- [25] W. Wadsworth, R. Percival, G. Bouwmans, J. Knight, T. Birks, T. Hedley, P. St.J. Russell, Very high numerical aperture fibers, *IEEE Photon. Technol. Lett.* 16 (2004) 843–845.
- [26] K.P. Hansen, High-power photonic crystal fibers, in: *Proceedings of SPIE*, Vol. 6102, pp. 61020B–61020B–11 (SPIE 2006).
- [27] K.P. Hansen, C.B. Olausson, J. Broeng, D. Noordegraaf, M.D. Maack, T.T. Alkeskjold, M. Laurila, T. Nikolajsen, P.M.W. Skovgaard, M.H. Sorensen, M. Denninger, C. Jakobsen, H.R. Simonsen, Airclad fiber laser technology, *Opt. Eng.* 50 (2011), 111609.

- [28] R. Stepien, B. Siwicki, D. Pysz, G. Stepniewski, Characterization of a large core photonic crystal fiber made of lead–bismuth–gallium oxide glass for broadband infrared transmission, *Opt. Quant. Electron.* 46 (2014) 553–561.
- [29] M.M. Tefelska, S. Ertman, T.R. Wolinski, P. Mergo, R. Dabrowski, Large area multimode photonic band-gap propagation in photonic liquid-crystal fiber, *IEEE Photon. Technol. Lett.* 24 (2012) 631–633.
- [30] L.V. Amitonova, A. Descloux, J. Petschulat, M.H. Frosz, G. Ahmed, F. Babic, X. Jiang, A.P. Mosk, P. St.J. Russell, P.W.H. Pinkse, High-resolution wavefront shaping with a photonic crystal fiber for multimode fiber imaging, *Opt. Lett.* 41 (2016) 497–500.
- [31] D. Gloge, Optical power flow in multimode fibers, *Bell Syst. Tech. J.* 51 (1972) 1767–1783.
- [32] M. Rousseau, L. Jeunhomme, Numerical solution of the coupled-power equation in step index optical fibers, *IEEE Trans. Microw. Theory Tech.* 25 (1977) 577–585.
- [33] J. Mateo, M.A. Losada, I. Garcés, J. Zubia, Global characterization of optical power propagation in step-index plastic optical fibers, *Opt. Express* 14 (2006) 928–935.
- [34] K. Saitoh, M. Koshiba, Empirical relations for simple design of photonic crystal fibers, *Opt. Express* 13 (2005) 267–274.
- [35] M.S. Kovačević, Lj. Kuzmanović, A. Simović, S. Savović, A. Djordjević, Transients of modal-power distribution in multimode solid core W-type photonic crystal fibers, *J. Light. Technol.* 35 (2017) 4352–4357.
- [36] S. Savović, A. Djordjević, Calculation of the coupling coefficient in strained step index plastic optical fibers, *Appl. Opt.* 47 (2008) 4935–4939.
- [37] A.M.R. Pinto, M. Lopez-Amo, Photonic crystal fibers for sensing applications, *J. Sens.* 2012 (2012) 1–21.
- [38] L. Bilro, N. Alberto, J.L. Pinto, R. Nogueira, Optical sensors based on plastic fibers, *Sensors* 2012 (2012) 12184–12207.
- [39] R. Lwin, G. Barton, L. Harvey, J. Harvey, D. Hirst, S. Manos, M.C.J. Large, L. Poladian, A. Bachmann, H. Poisel, K.-F. Klein, Beyond the bandwidth-length product: graded index microstructured polymer optical fiber, *Appl. Phys. Lett.* 91 (2007), 191119.
- [40] A.F. Garito, J. Wang, R. Gao, Effects of random perturbations in plastic optical fibers, *Science* 281 (1998) 962–967.
- [41] D. Richards, A. Lopez, M.A. Losada, P.V. Mena, E. Ghillino, J. Mateo, N. Antoniadis, X. Jiang, Overcoming challenges in large-core SI-POF-based system-level modeling and simulation, *Photonics* 6 (2019) 88.



Contents lists available at ScienceDirect

Optik

journal homepage: www.elsevier.com/locate/ijleo

Original research article

Wavelength dependent transmission in W-type plastic optical fibers with graded index core distribution

Ana Simović^a, Svetislav Savović^{a,b,*}, Branko Drljača^c, Alexandar Djordjevich^{b,**}^a University of Kragujevac, Faculty of Science, R. Domanovića 12, Kragujevac, Serbia^b City University of Hong Kong, 83 Tat Chee Avenue, Kowloon, Hong Kong, China^c Faculty of Sciences and Mathematics, University of Pristina in Kosovska Mitrovica, Lole Ribara 29, Kosovska Mitrovica, Serbia

ARTICLE INFO

Keywords:

W-type plastic optical fiber
 Graded index optical fiber
 Power flow equation
 Equilibrium mode distribution
 Steady state distribution

ABSTRACT

This paper investigates the wavelength dependence of the equilibrium mode distribution (EMD) and steady state distribution (SSD) in W-type plastic optical fibers (POFs) with graded index (GI) core distribution for parametrically varied width of the fiber's intermediate optical layer and refractive index of the outer cladding. The numerical solution of the time-independent power flow equation is used to determine the transmission characteristics of the W-type GI POF. We demonstrated that the coupling length L_c required to achieve an EMD in W-type GI POF is shorter than the length determined experimentally for the original SC GI POF at 633 nm. We also demonstrated that as the wavelength increases, the EMD and steady-state distribution (SSD) are achieved at shorter W-type GI POF lengths. This is explained by the increase in leaky mode losses as wavelength increases. This makes it easier to tailor W-type GI POFs to a specific application at different wavelengths.

1. Introduction

In the last three decades the need for data traffic in access and backbone networks has increased dramatically. The increase has been hastened by streaming broadcast and cloud computing. Local networks and automotive systems normally work with multimode POFs because of their high numerical aperture, big core diameter and simplicity of usage of various light sources (LED, laser and VCSEL) [1]. Mode coupling affects the transmission qualities of POF. Mode couples is a consequence of random aberrations in multimode optical cables due to light scattering (various irregularities such as microscopic bends and refractive index fluctuations). They cause the power distribution to shift until an "equilibrium mode distribution" (EMD) is reached at a distance known as the "coupling length" L_c down the fiber. The L_c is the length at which the highest guiding mode's distribution has been shifted to an angle of zero. All alternative launch modal distributions take the same light-distribution across the fiber-section at distance z_s ($z_s > L_c$) from the input fiber end, and the steady state distribution (SSD) is attained. SSD denotes the end of the mode coupling process and the output light distribution's independence from launch conditions (e.g. width of the launch beam).

In terms of the number of functional cladding layers, multimode optical fibers are commonly classified as single cladding (SC). Special detection [1], modulation [2], equalization [3], and modal-dispersion correction [4] can improve the bandwidth and attenuation qualities of SC fibers. A variety of step-index (SI), graded index (GI), and W-type POFs (doubly clad fibers) have been developed

* Correspondence to: Faculty of Science, R. Domanovića 12, 34000 Kragujevac, Serbia.

** Corresponding author.

E-mail addresses: savovic@kg.ac.rs (S. Savović), mealex@cityu.edu.hk (A. Djordjevich).<https://doi.org/10.1016/j.ijleo.2021.167775>

Received 1 June 2021; Received in revised form 6 July 2021; Accepted 4 August 2021

Available online 8 August 2021

0030-4026/© 2021 Elsevier GmbH. All rights reserved.

[5–7] since the architecture of a fiber can considerably influence its transmission characteristics. Because the refractive index of the core decreases with radial distance from the fiber axis, GI POFs have significantly less modal dispersion than SI POFs [8]. When compared to an equivalent SC GI fiber, a W-type fiber with GI core distribution (Fig. 1) has a greater bandwidth [9]. This is due to the intermediate layer (inner cladding) of the W-type fiber, which minimizes the number of higher directed modes (due to existence of leaky modes), which are consequently held closer to the core, and therefore minimizes modal dispersion [10–15]. Thus, combining GI core with W-type cladding enables the most promising POF's bandwidth enhancement. The main purpose of this research for W-type GI POF is to look at the effect of wavelength on the length of fiber at which EMD is accomplished and the length of fiber z_s at which the SSD begins. The width of the intermediate layer of the fiber and the refractive index of the outer cladding were parametrically changed in this procedure to make it easier to find the best values for a given wavelength. The practical impact of the results presented in this work lies in the POF's feature that the shorter the POF's length at which EMD is achieved, the earlier the bandwidth would switch from the functional dependence of $1/z$ to $1/z^{1/2}$ (slower bandwidth decrease) [15].

2. Time-independent power flow equation

The time-independent power flow for multimode GI fibers (Fig. 1a) is described by the following coupled-power equation [16]:

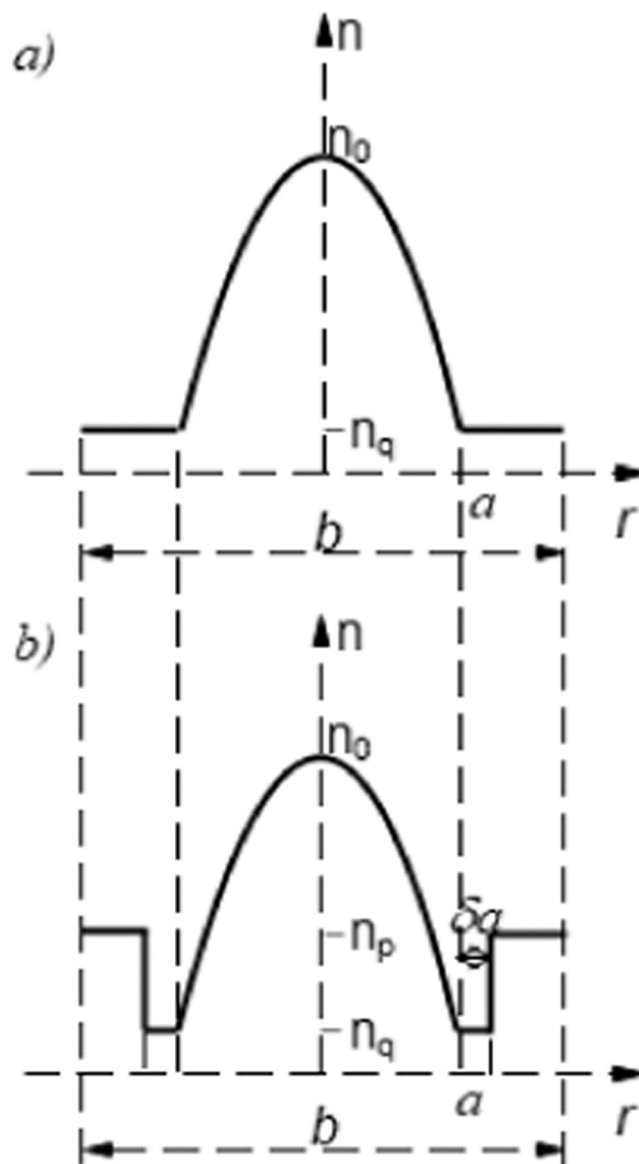


Fig. 1. Refractive index profile of (a) SC GI POF and (b) W-type GI POF.

$$\frac{\partial P(m, \lambda, z)}{\partial z} = -\alpha(m, \lambda)P(m, \lambda, z) + \frac{1}{m} \frac{\partial}{\partial m} \left(md(m, \lambda) \frac{\partial P(m, \lambda, z)}{\partial m} \right) \tag{1}$$

where $P(m, \lambda, z)$ is power in the m -th principal mode (modal group), z is the coordinate along the fiber axis from the input fiber end, $d(m, \lambda)$ mode coupling coefficient which can be assumed constant D [17], $\alpha(m, \lambda) = \alpha_0(\lambda) + \alpha_d(m, \lambda)$ is the modal attenuation, where α_0 represents conventional losses (absorption and scattering). The term α_0 leads only to a multiplier $\exp(-\alpha_0 z)$ in the solution and can be ignored.

Consider a W-type GI fiber with index profile shown in Fig. 1b. The index profile of W-type optical fibers with GI distribution of the core may be expressed as:

$$n \left(r, \lambda \right) = \begin{cases} n_0(\lambda) \left[1 - \Delta_q(\lambda) \left(\frac{r}{a} \right)^g \right]^{1/2} & (0 \leq r \leq a) \\ n_q & (a < r \leq a + \delta a) \\ n_p & \left(a + \delta a < r \leq \frac{b}{2} \right) \end{cases} \tag{2}$$

where g is the core index exponent, a is the core radius, δa is the intermediate layer width, b is the fiber diameter, $n_0(\lambda)$ is the maximum index of the core (measured at the fiber axis), n_q and n_p are refractive indices of the intermediate layer and outer cladding, respectively, $\Delta_q = (n_0 - n_q)/n_0$ is the relative index difference between core and intermediate layer. The maximum principal mode number $M(\lambda)$ can be obtained as [18]:

$$M(\lambda) = \sqrt{\frac{g \Delta_q(\lambda)}{g + 2}} a k n_0(\lambda) \tag{3}$$

where $k = 2\pi/\lambda$ is the free-space wave number. Gaussian launch-beam distribution $P_0(\theta, \lambda, z = 0)$ can be transformed into $P_0(m, \lambda, z = 0)$ (one needs $P_0(m, \lambda, z = 0)$ to numerically solve the power flow Eq. (1)), using the following relationship [19]:

$$\frac{m}{M(\lambda)} = \left[\left(\frac{r_0}{a} \right)^g + \frac{\theta^2}{2\Delta_q(\lambda)} \right]^{(g+2)/2g} \tag{4}$$

where r_0 is radial distance (radial offset) between the launch beam position and the core center and θ is the propagation angle with respect to the core axis.

The relative refractive index difference $\Delta_q = (n_0 - n_q)/n_0$ between the core and intermediate layer is larger than the difference $\Delta_p = (n_0 - n_p)/n_0$ between core and outer cladding. In this structure, the modes m between m_p and $m_q \equiv M$ are leaky modes [10]. Attenuation constants of leaky modes are given as:

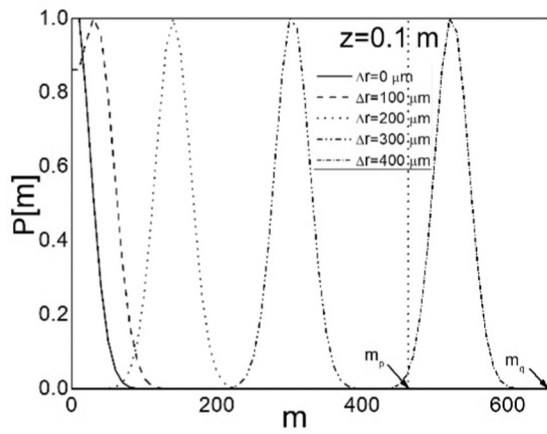
$$\alpha_L \left(m, \lambda \right) = \frac{4\sqrt{2\Delta_q} \left(\left(\frac{m}{m_q} \right)^{\frac{2g}{g+2}} - \left(\frac{m_p}{m_q} \right)^{\frac{2g}{g+2}} \right)^{1/2} \left(\frac{m}{m_q} \right)^{\frac{2g}{g+2}} \left(1 - \left(\frac{m}{m_q} \right)^{\frac{2g}{g+2}} \right)}{a \left(1 - 2\Delta_q \left(\frac{m}{m_q} \right)^{\frac{2g}{g+2}} \right)^{1/2} \left(1 - \frac{\Delta_p}{\Delta_q} \left(\frac{m_p}{m_q} \right)^{\frac{2g}{g+2}} \right)} \times \exp \left[-2\delta a n_0 k \left(2\Delta_q \left(1 - \left(\frac{m}{m_q} \right)^{\frac{2g}{g+2}} \right) \right)^{1/2} \right] \tag{5}$$

Experiments in a SC GI fiber demonstrate that attenuation remains constant in the guided-mode area ($m \leq m_p$) but rises dramatically in the radiation-mode area [20]. Consequently, the modal attenuation in a W-type GI POF can be expressed as

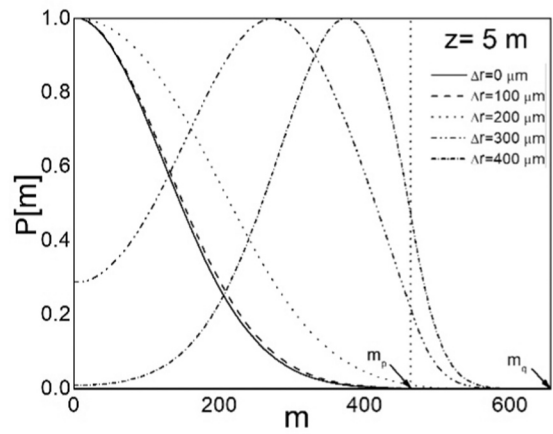
$$\alpha_d \left(m, \lambda \right) = \begin{cases} 0 & m \leq m_p \\ \alpha_L(m, \lambda) & m_p < m < m_q \\ \infty & m \geq m_q \end{cases} \tag{6}$$

A W-type fiber can be regarded as a system consisting of SC_q fiber and cladding. In the SC_q fiber, modes $m < m_q$ can be guided. When the SC_q fiber is coupled with surrounding medium of index n_p , the lower order modes $m < m_p$ remain guided, while the higher order modes m ($m_p < m < m_q$) are transformed into leaky modes. Because of the strong dependence of $\alpha_L(m)$ on the intermediate layer width δa (Eq. (5)), it is expected that characteristics of a W-type GI fiber also depend on δa and coincide with those of SC_p and SC_q GI fibers in the limits of $\delta \rightarrow 0$ and $\delta \rightarrow \infty$, respectively [10,21,22].

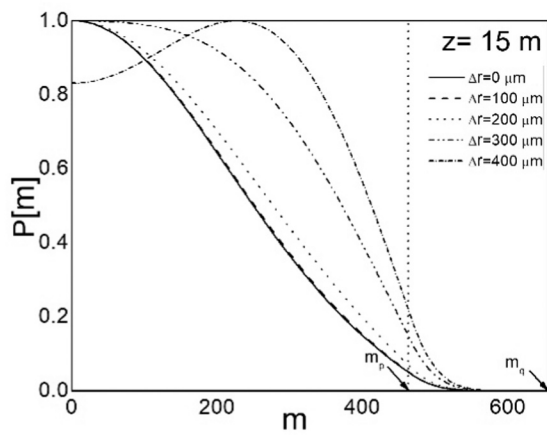
Using the explicit finite difference method, discretization of Eq. (1) leads to:



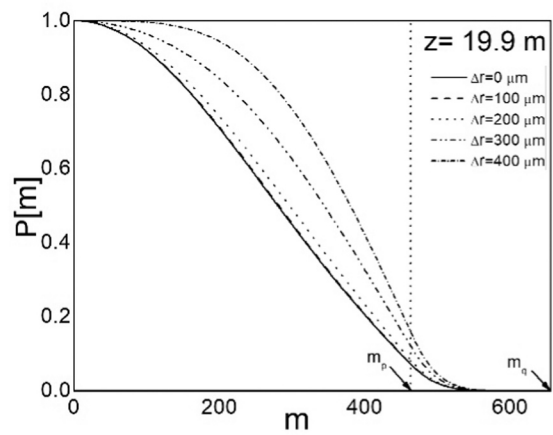
a)



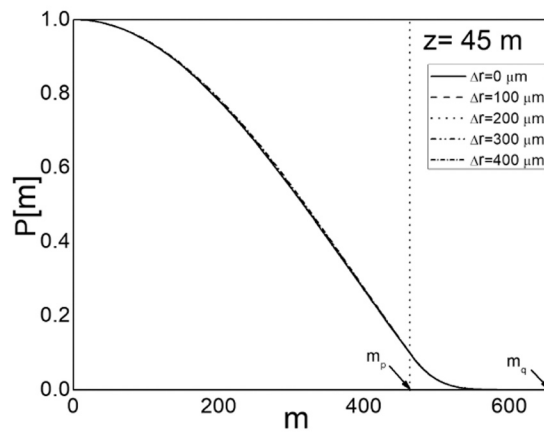
b)



c)



d)



e)

Fig. 2. Calculated output modal power distribution $P(m)$ in W-type GI POF with $\delta = 0.003$, $n_p = 1.50718$, and $\lambda = 633$ nm over a range of radial offsets Δr , at fiber lengths a) $z = 0.1$ m, b) $z = 5$ m, c) $z = 15$ m d) $z = 19.9$ m and e) $z = 45$ m for Gaussian launch beam distribution with $\langle \theta \rangle = 0^\circ$ and FWHM = 3.06° .

$$\begin{aligned}
 P_{i,j+1} = & \left(\frac{d(m_i, \lambda) \Delta z}{(\Delta m)^2} - \frac{d(m_i, \lambda) \Delta z}{2m_i \Delta m} - \frac{\partial d(m_i, \lambda)}{\partial m} \frac{\Delta z}{2 \Delta m} \right) P_{i-1,j} \\
 & + \left(1 - \frac{2d(m_i, \lambda) \Delta z}{(\Delta m)^2} - \alpha_d \left(m_i, \lambda \right) \Delta z \right) P_{i,j} \\
 & + \left(\frac{\partial d(m_i, \lambda)}{\partial m} \frac{\Delta z}{2 \Delta m} + \frac{d(m_i, \lambda) \Delta z}{2m_i \Delta m} + \frac{d(m_i, \lambda) \Delta z}{(\Delta m)^2} \right) P_{i+1,j}
 \end{aligned} \quad (7)$$

where i and j refer to the discretization step lengths Δm and Δz for the mode m and length z , respectively.

3. Numerical results and discussion

The effects of wavelength on transmission properties of W-type GI POF [23] designed from the SC GI POF (Fig. 1), which we experimentally studied in our recently published work [17], is explored in this research. The core diameter of the fiber was $2a = 0.9$ mm (fiber diameter was 1 mm), the refractive index of the core measured at the fiber axis was $n_0 = 1.522$, and the refractive index of the intermediate layer (inner cladding) cladding was $n_q = 1.492$, the maximum principal mode number was $M = 656$ (for $\lambda = 633$ nm), $g = 1.8$, and $\Delta_q = (n_0 - n_q)/n_0 = 0.019711$ were the characteristics of SC GI POF [17]. W-type GI POF's inner cladding maintains the distribution of the SC GI POF's cladding ($n_q = 1.492$). The outer cladding n_p refractive indices used in the modeling were as follows: $n_p = 1.51366$ ($m_p = 346$), $n_p = 1.51065$ ($m_p = 404$) and $n_p = 1.50718$ ($m_p = 461$). The normalized intermediate layer widths $\delta = 0.001$, $\delta = 0.002$ and $\delta = 0.003$ were employed (actual width is $\delta \cdot a$ mm). The constant coupling coefficient $d(m, \lambda) \equiv D = 1482$ 1/m was used in the calculations [17]. The length L_c required to reach EMD is defined as the length at which the highest guiding modes' modal power distributions shifted their maxima to $m = 0$. The length z_s for SSD is defined as the length at which the modal light distribution stops changing while the fiber length is increased (becomes steady).

We determined the length L_c at which the EMD is attained and the length z_s at which SSD is established in W-type GI POF at different wavelengths using the time-independent power flow equation. Fig. 2 illustrates the output angular power distribution in W-type GI POF with the width of the intermediate layer $\delta = 0.003$, $n_p = 1.50718$, and $\lambda = 633$ nm obtained by numerical solving the time-independent power flow Eq. (1). In the numerical calculations, a Gaussian beam $P(\theta, z)$ is assumed to be launched with $\langle \theta \rangle = 0^\circ$ and standard deviation $\sigma_\theta = 1.3^\circ$ (FWHM = 3.06°) (measured in our previous experiment [17]). Results are displayed for five different radial offsets $\Delta r = 0, 100, 200, 300$ and 400 μm . Fig. 3 illustrates the normalized experimental output modal power distributions $P(m, \lambda, z)$ obtained in SC GI POF at $\lambda = 633$ nm [17]. It can be observed from Figs. 2 and 3 that when the launch distribution at the input end of the fiber is centered at $\Delta r = 0$ μm , as the distance from the input fiber end grows, the modal power distribution remains in the same place, but its width grows owing to mode coupling. Radiation patterns in Figs. 2 and 3 of launched beams with $\Delta r > 0$ μm shift their distributions towards $m = 0$. At the fiber's coupling length L_c all the mode-distributions shift their mid-points to $m = 0$, producing the EMD in Fig. 2(d) of $L_c = 19.9$ m. Finally, the SSD is reached at length $z_s = 45$ m in Fig. 2(e). The coupling length $L_c = 19.9$ m of the W-type GI POF (Fig. 2d) is shorter than $L_c = 31$ m which we have experimentally determined for the original SC GI POF at wavelength of 633 nm (Fig. 3d) [17]. The number of higher directed modes is reduced as a result of leaky mode losses, resulting in a shorter L_c .

It can be observed in Figs. 4 and 5 that widening the intermediate layer width results in a wavelength-dependent decrease of lengths L_c and z_s . This is a direct consequence of wavelength-dependence of leaky mode losses in Eq. (5) (no other wavelength dependent effects have been considered), where this decrease is more pronounced at short wavelengths as leaky mode losses are then reduced, i.e. a smaller number of leaky modes remain guided at larger wavelengths at longer fiber lengths, resulting in decrease of fiber lengths L_c and z_s . The lengths L_c and z_s are larger in the case of wider intermediate layer widths. Because leaky modes are minimized at small transmission lengths in the case of a thinner intermediate layer, the beginning of SSD takes a shorter fiber length z_s than in the case of a broader intermediate layer. EMD and SSD occur at longer fiber lengths when the outer cladding refractive index n_p drops, which is attributable to the correspondingly growing number of guiding modes. The smaller the parameter n_p , the longer the fiber length is required for completion of the coupling process. Because leaky mode losses increase with increasing wavelength, the EMD and SSD are established at shorter fiber lengths - the shorter the length at which EMD is achieved, the earlier the bandwidth would switch from the functional dependence of $1/z$ to $1/z^{1/2}$ (slower bandwidth decrease) [15].

4. Conclusion

For a variable W-type GI POF's intermediate layer width and refractive index of the outer cladding, the EMD and SSD of power are explored. The coupling length of the W-type GI POF is shorter than that of the original SC GI POF, which we have measured experimentally at 633 nm. The length L_c is reduced as a result of leaky mode losses, which reduce the amount of higher directed modes involved in the coupling process. The length L_c at which EMD is achieved and length z_s marking the onset of the SSD decrease with increasing the wavelength. This is due to the fact that leaky mode losses increase with increasing wavelength, resulting in a smaller number of leaky modes being guided in longer fibers at longer wavelengths. When the intermediate layer widths are greater (bigger),

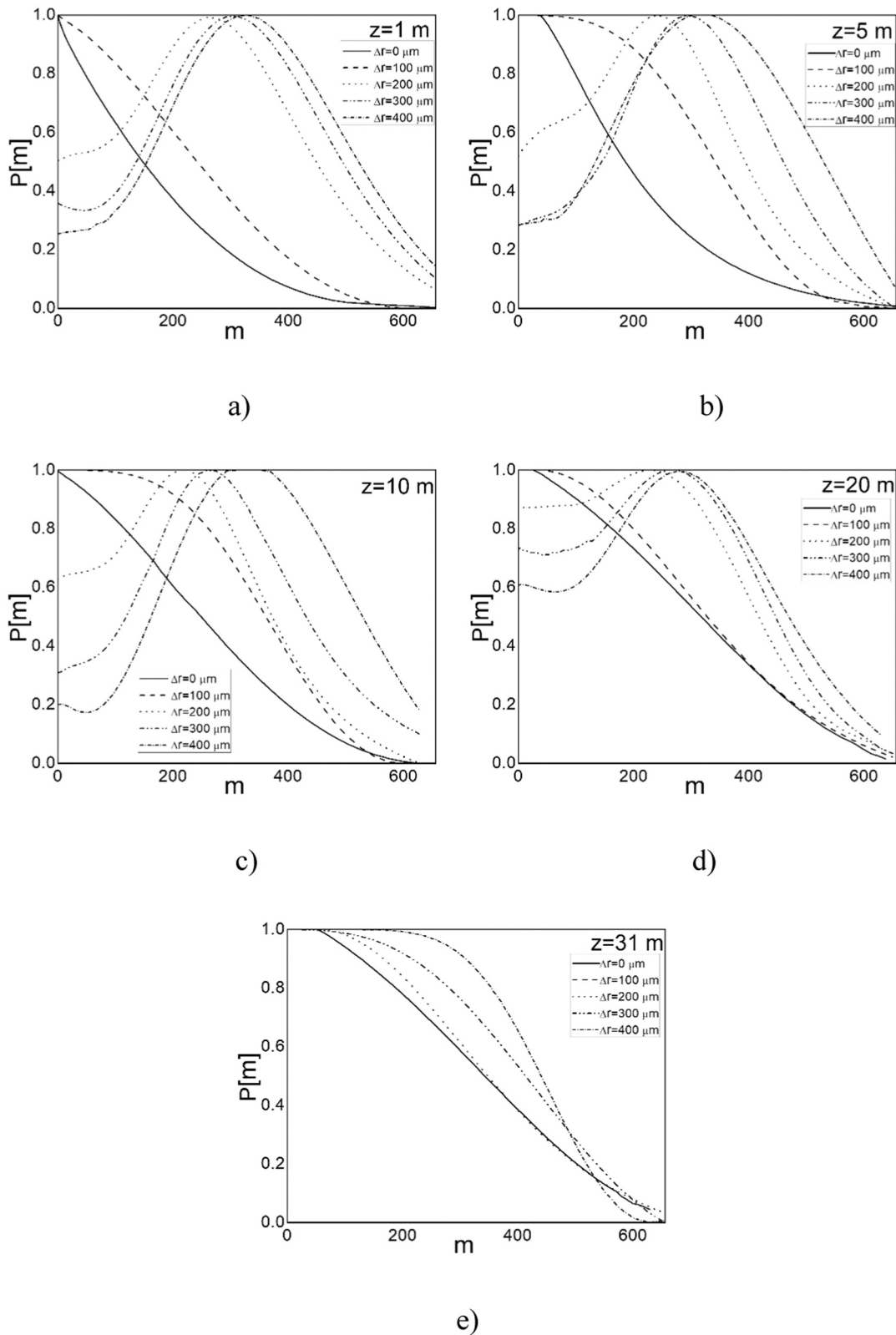


Fig. 3. Normalized output modal power distribution $P(m)$ in SC GI POF over a range of radial offsets Δr , obtained from the measured angular power distributions $P(\theta)$ at $\lambda = 633 \text{ nm}$, at different fiber lengths (a) $z = 1 \text{ m}$, (b) $z = 5 \text{ m}$, (c) $z = 10 \text{ m}$, (d) $z = 20 \text{ m}$ and (e) $z = 31 \text{ m}$ [17].

the lengths L_c and z_s are longer. Because leaky modes are minimized at small transmission lengths in the case of a narrower intermediate layer, the beginning of SSD takes a shorter fiber length z_s than in the case of a broader intermediate layer. The number of guiding modes rises as the outer cladding's refractive index n_p drops, and EMD and SSD are established at longer fiber lengths. The longer the fiber length is required to complete the coupling process, the smaller the parameter n_p is.

In summary, the narrower intermediate layer width, the larger outer cladding refractive index and the larger wavelength result in shorter length L_c and z_s . The presented results make easier to tailor W-type GI POFs to a specific application at different wavelengths, particularly for achieving a slower (at shorter lengths) bandwidth decrease. Finally, one should note that a similar behavior of the transmission in W-type plastic clad silica fiber (with SI distribution of the core) has been observed at different wavelengths which are employed for silica core fibers [24].

Declaration of Competing Interest

The authors declare that they have no known competing financial interests or personal relationships that could have appeared to influence the work reported in this paper.

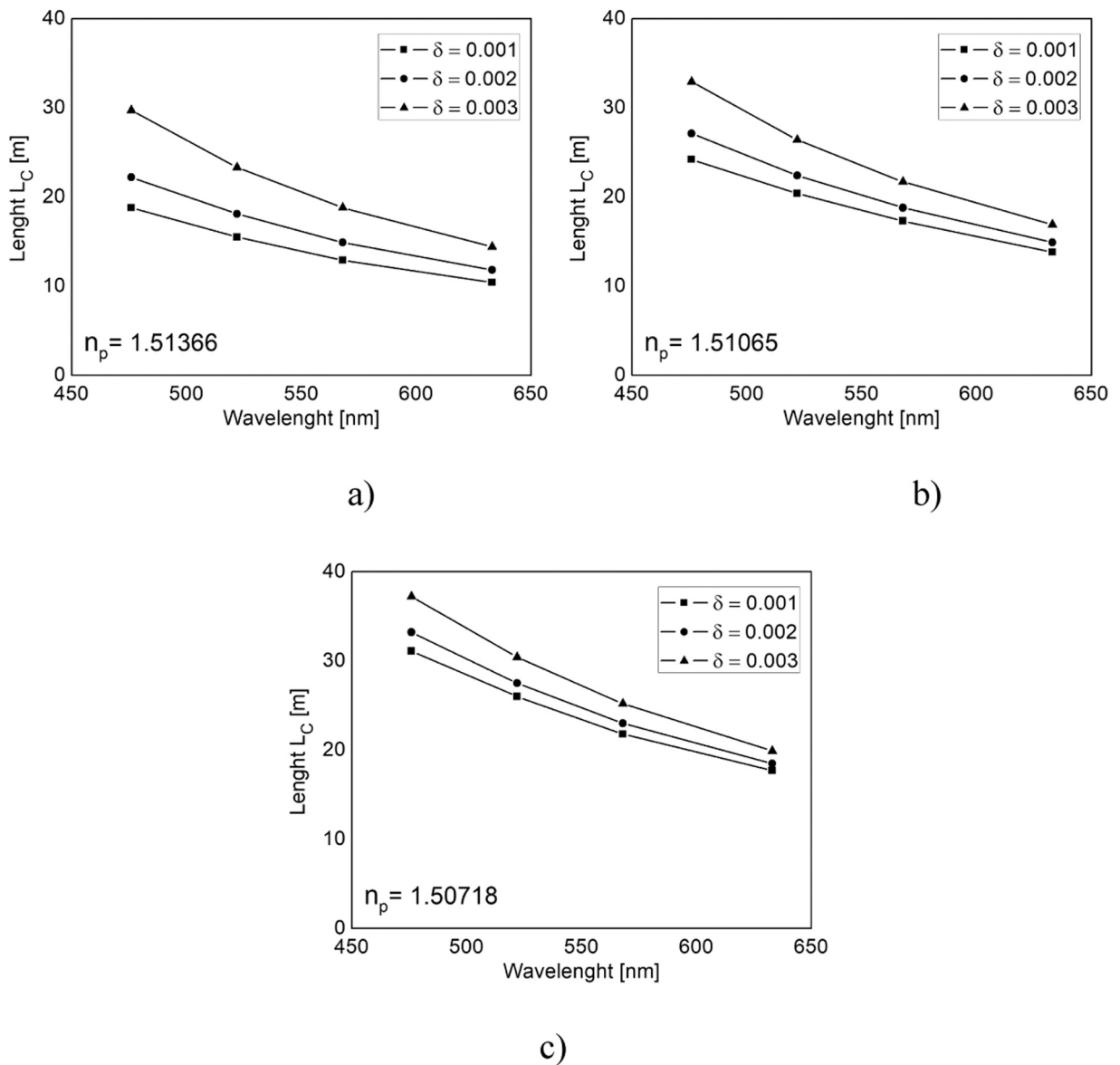


Fig. 4. Wavelength dependence of length L_c for Gaussian launch excitation with $\langle \theta \rangle = 0^\circ$ and FWHM = 3.06°, $\delta = 0.001, 0.002$ and 0.003 , and (a) $n_p = 1.51366$ ($m_p = 346$), (b) $n_p = 1.51065$ ($m_p = 404$) (c) $n_p = 1.50718$ ($m_p = 461$).

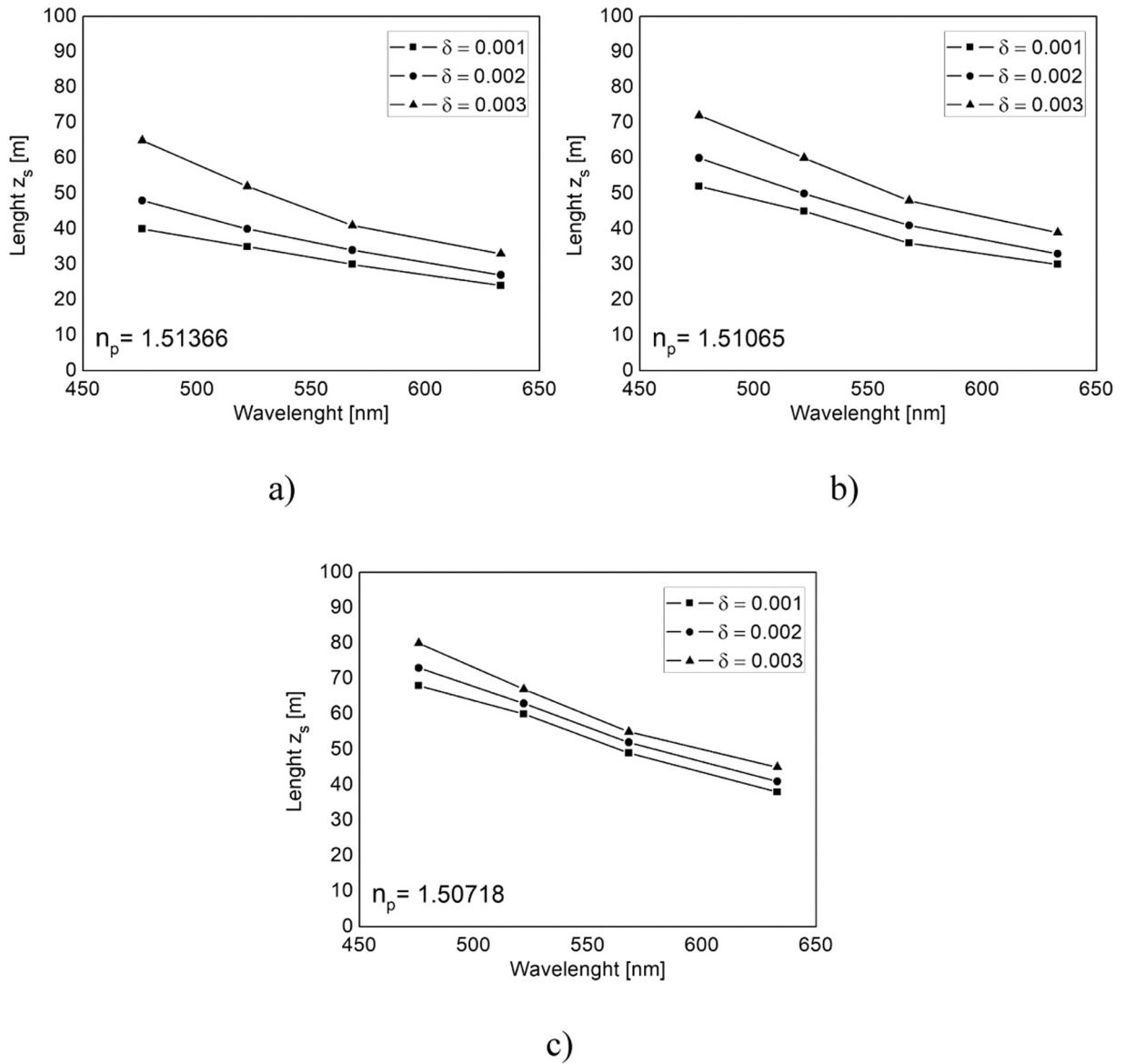


Fig. 5. Wavelength dependence of length z_s for Gaussian launch excitation with $\langle \theta \rangle = 0^\circ$ and FWHM = 3.06° , $\delta = 0.001, 0.002$ and 0.003 , and (a) $n_p = 1.51366$ ($m_p=346$), (b) $n_p = 1.51065$ ($m_p=404$) (c) $n_p = 1.50718$ ($m_p=461$).

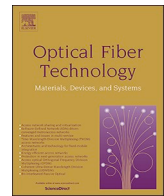
Acknowledgments

The work described in this paper was supported by the Strategic Research Grant of City University of Hong Kong (Project No. CityU 7004600), by the grant from Science Fund of Republic Serbia (Agreement No. CTPCF-6379382) and by a grant from Serbian Ministry of Education, Science and Technological Development (Agreement No. 451-03-68/2020-14/200122).

References

- [1] K.M. Patel, S.E. Ralph, Enhanced multimode fiber link performance using a spatially resolved receiver, *IEEE Photon. Technol. Lett.* 14 (2002) 393–395.
- [2] E.J. Tyler, M. Webster, R.V. Pentz, I.H. White, S. Yu, J. Rorison, Subcarrier modulated transmission of 2.5 Gb/s over 300 m of 62.5- μm -core diameter multimode fiber, *IEEE Photon. Technol. Lett.* 14 (2002) 1743–1745.
- [3] X. Zhao, F.S. Choa, Demonstration of 10 Gb/s transmission over 1.5-km-long multimode fiber using equalization techniques, *IEEE Photon. Technol. Lett.* 14 (2002) 1187–1189.
- [4] J.S. Abbott, G.E. Smith, and C.M. Truesdale, "Multimode fiber link dispersion compensator", U.S. Patent 6 363 195, 2002.
- [5] T. Yamashita, M. Kagami, Fabrication of light-induced self-written waveguides with a W-shaped refractive index profile, *J. Light. Technol.* 23 (2005) 2542–2548.

- [6] M. Asai, Y. Inuzuka, K. Koike, S. Takahashi, Y. Koike, High-bandwidth graded-index plastic optical fiber with low-attenuation, high-bending ability, and high-thermal stability for home-networks, *J. Light. Technol.* 29 (2011) 1620–1626.
- [7] K. Mikoshiba, H. Kajioka, Transmission characteristics of multimode W-type optical fiber: experimental study of the effect of the intermediate layer, *Appl. Opt.* 17 (1978) 2836–2841.
- [8] Y. Koike, K. Koike, Progress in low-loss and high-bandwidth plastic optical fibers, *J. Polym. Sci. B* 49 (2011) 2–17.
- [9] K. Takahashi, T. Ishigure, Y. Koike, Index profile design for high-bandwidth W-shaped plastic optical fiber, *J. Light. Technol.* 24 (2006) 2867–2876.
- [10] T. Tanaka, S. Yamada, M. Sumi, K. Mikoshiba, Microbending losses of doubly clad (W-type) optical fibers, *Appl. Opt.* 18 (1977) 2391–2394.
- [11] V. Babita, Rastogi, A. Kumar, Design of large-mode-area three layered fiber structure for femtosecond laser pulse delivery, *Opt. Commun.* 293 (2013) 108–112.
- [12] A. Simović, S. Savović, B. Drljača, A. Djordjevich, Influence of the fiber design and launch beam on transmission characteristics of W-type optical fibers, *Opt. Laser Technol.* 68 (2015) 151–159.
- [13] D. Gloge, Optical power flow in multimode fibers, *Bell Syst. Tech. J.* 51 (1972) 1767–1783.
- [14] D. Gloge, Impulse response of clad optical multimode fibers, *Bell Syst. Tech. J.* 52 (1973) 801–816.
- [15] S. Savović, A. Simović, A. Djordjevich, Explicit finite difference solution of the power flow equation in W-type optical fibers, *Opt. Laser Technol.* 44 (2012) 1786–1790.
- [16] K. Kitayama, S. Seikai, N. Uchida, Impulse response prediction based on experimental mode coupling coefficient in a 10-km long graded-index fiber, *IEEE J. Quant. Electron.* 16 (1980) 356–362.
- [17] S. Savović, A. Simović, B. Drljača, A. Djordjevich, G. Stepniak, C.A. Bunge, J. Bajić, Power flow in graded index plastic optical fibers, *J. Light. Technol.* 37 (2019) 4985–4990.
- [18] R. Olshansky, Mode coupling effects in graded-index optical fibers, *Appl. Opt.* 14 (1975) 935–945.
- [19] K. Nagano, S. Kawakami, Measurements of mode conversion coefficients in graded-index fibers, *Appl. Opt.* 19 (1980) 2426–2434.
- [20] G. Yabre, Comprehensive theory of dispersion in graded-index optical fibers, *J. Light. Technol.* 18 (2000) 166–177.
- [21] T. Ishigure, H. Endo, K. Ohdoko, K. Takahashi, Y. Koike, Modal bandwidth enhancement in a plastic optical fiber by W-refractive index profile, *J. Light. Technol.* 23 (2005) 1754–1762.
- [22] A. Simović, S. Savović, B. Drljača, A. Djordjevich, Enhanced bandwidth of W type plastic optical fibers designed from single clad step index plastic optical fibers, *Opt. Laser Technol.* 111 (2019) 629–634.
- [23] A. Simović, A. Djordjevich, B. Drljača, S. Savović, Power flow in multimode W-type plastic optical fibers with graded index core distribution, *Opt. Laser Technol.* 143 (2021), 107295 (6pp).
- [24] B. Drljača, A. Simović, S. Savović, A. Djordjevich, Influence of wavelength on the bandwidth of W-type plastic-clad silica optical fibers, *Laser Phys.* 30 (2020), 025103 (6pp).



Wavelength dependence of equilibrium mode distribution and steady state distribution in W-type plastic-clad silica fibers

Branko Drljača^a, Ana Simović^b, Alexandar Djordjevich^{c,*}, Svetislav Savović^{b,c,*}

^a University of Priština, Faculty of Science, Lole Ribara 29, Kosovska Mitrovica, Serbia

^b University of Kragujevac, Faculty of Science, R. Domanovića 12, Kragujevac, Serbia

^c City University of Hong Kong, Department of Mechanical Engineering, 83 Tat Chee Avenue, Hong Kong, China

ARTICLE INFO

Keywords:

W-fiber
Plastic-clad silica fiber
Equilibrium mode distribution
Steady state distribution
Power flow equation

ABSTRACT

Wavelength dependence of equilibrium mode distribution (EMD) and steady state distribution (SSD) in W-type plastic-clad silica fibers (PCSFs) is investigated in this paper for parametrically varied width of the fiber's intermediate optical layer and refractive index of the outer cladding. We have shown that the W-type PCSF has better transmission characteristics at longer infrared wavelengths. This is explained by the rise of the leaky mode losses with increasing wavelength. This facilitates tailoring W-fibers to a specific application at hand in the infrared wavelength region.

1. Introduction

Singly-clad (SC) optical fibers made of glass dominate in long-distance communication networks. Plastic optical fibers (POFs), with their higher attenuation and lower transmission bandwidth, are restricted to local area networks with short data links [1]. PCSFs have many applications in optical measurements, short-to-long distance communications, and sensors [2–4]. The ease of cladding removal makes PCSFs particularly useful for sensors when access to evanescent wave is desired.

The analysis and design of refractive index profile of multimode fiber with a view of advancing fiber transmission characteristics have attracted a much attention in the last few decades [5–8]. A variety of designs of step-index, graded index and W-type fibers (fiber with core and two claddings) has been proposed either for a long-distance communication links or high capacity local area networks [6–8]. It has been shown that waveguide dispersion is smaller in the W-type fiber than it is in the single-clad (SC) fiber [9]. W-type fiber with intermediate layer binds the guided modes firmer to the core and reduces the effective numerical aperture of the fiber. Consequently, W-type fiber has a wider transmission bandwidth and lower bending losses compared to a corresponding SC fiber.

Optical fibers inevitably incorporate irregularities in the form of a shape-variation or material inhomogeneity including voids and cracks. Such random irregularities in multimode optical fibers cause light

diffraction that couples power between the propagating modes. This mode coupling is an effect in addition to the reduction of the transmitted power by differential mode attenuation. Both influence fiber transmission characteristics strongly.

On the positive side, coupled modes may be less dispersed for multimodal launch. This translates into higher bandwidth. However, mode coupling also leads to higher losses, particularly in curved segments. Moreover, the output-field is altered and generally degraded as it contains modes of high order even if the launch was restricted to modes of only low order. W-fibers are more resilient to these effects. Their intermediate layer between the core and cladding retains some lossy leaky modes [9–14]. Yet, the more complex profile of the refractive index of the fiber opens the question of optimization of such profile.

Angular input optical power distribution that results from a specific launch gets modified gradually with distance from the input fiber-end by the effect of mode coupling [15]. The expected beam properties, including the far-field radiation pattern, are altered as a consequence. The far-field pattern of an optical fiber is determined by the optical power distribution that depends on the launch conditions, fiber properties and fiber length. Light launched at a specific angle $\theta_0 > 0$ with respect to the fiber axis will form a sharply defined ring radiation pattern at the output end of only short fibers. Because of mode coupling, the boundary (edges) of such a ring become fuzzy at the end of longer fibers. Up to a “coupling length” L_c from the input fiber end, the

* Corresponding authors at: University of Kragujevac, Faculty of Science, R. Domanovića 12, 34000 Kragujevac, Serbia (S. Savović) and City University of Hong Kong, Department of Mechanical Engineering, 83 Tat Chee Avenue, Hong Kong, China (A. Djordjevich).

E-mail addresses: mealex@cityu.edu.hk (A. Djordjevich), savovic@kg.ac.rs (S. Savović).

<https://doi.org/10.1016/j.yofte.2019.102077>

Received 7 September 2019; Received in revised form 25 October 2019; Accepted 15 November 2019

1068-5200/ © 2019 Elsevier Inc. All rights reserved.

extent of this fustiness increases further with fiber length and the ring-pattern evolves gradually into a disk extending across the entire fiber cross-section. An equilibrium mode distribution (EMD) exists beyond the coupling length L_c of the fiber. It is characterized by the absence of rings regardless of launch conditions, even though the resulting light distribution of the disk-pattern may vary with launch conditions. EMD indicates a substantially complete mode coupling. It is of critical importance when measuring characteristics of multimode optical fibers (linear attenuation, bandwidth, etc). At distance z_s ($z_s > L_c$) from the input fiber end, all individual disk patterns corresponding to different launch angles take the same light-distribution across the fiber-section and the SSD is achieved. SSD indicates the completion of the mode coupling process and the independence of the output light distribution from launch conditions.

“Coupling coefficient” D has been used widely [16–19] to describe how power is transferred between modes. This allowed modeling by the power flow equation of the angular power distributions in the far field fiber output as a function of the fiber length and conditions of launch. For W-type PCSF, the main goal of this work is to investigate the influence of infrared wavelength on the length of fiber at which EMD is achieved and on the length of fiber z_s that marks the onset of the SSD. In this process, the width of the fiber’s intermediate layer and refractive index of the outer cladding were varied parametrically to facilitate the selection of their optimal values for a particular infrared wavelength.

2. Power flow equation

The Gloge’s time-independent power flow equation is [16]:

$$\frac{\partial P(\theta, z)}{\partial z} = -\alpha(\theta)P(\theta, z) + \frac{D}{\theta} \frac{\partial P(\theta, z)}{\partial \theta} + D \frac{\partial^2 P(\theta, z)}{\partial \theta^2} \quad (1)$$

where θ is mode angle, $P(\theta, z)$ is power distribution over angle θ , $\alpha(\theta)$ is the modal attenuation and D is a constant “coupling coefficient”. It is assumed that mode coupling mainly occurs between neighboring modes due to the fact that coupling strength decreases sufficiently fast with the mode spacing [16]. This assumption is commonly used in modeling a mode coupling process both in SC and W-type fibers [16–20]. Describing the evolution of the modal power distribution along the fiber, (1) is the time-independent power flow equation with the mode angle θ taken as a continuous variable, where the next-neighbor mode coupling is assumed as a diffusion process in a continuum. Modal attenuation $\alpha(\theta)$ can be expanded into $\alpha(\theta) = \alpha_0 + \alpha_d(\theta)$. The term α_0 represents conventional losses by absorption and scattering. It can be neglected in the solution because it would feature as just a fixed multiplier $\exp(-\alpha_0 z)$. The term $\alpha_d(\theta)$ in the expansion of $\alpha(\theta)$ is dominant for higher order modes. Boundary conditions for (1) are $P(\theta_m, z) = 0$ and $D(\partial P/\partial \theta) = 0$ at $\theta = 0^\circ$, with θ_m denoting the largest propagation angle. The condition $P(\theta_m, z) = 0$ implies that modes with infinitely high loss do not carry power. Condition $(\partial P/\partial \theta) = 0$ at $\theta = 0$ indicates that the coupling is limited to modes propagating with $\theta > 0$.

Fig. 1 represents the index profile of a W-fiber with n_0 , n_p and n_q ($n_0 > n_p > n_q$) being indices of refraction of the core, cladding, and intermediate layer, respectively. Modes propagating at angles that are between $\theta_p \cong (2\Delta_p)^{1/2}$ and $\theta_q \cong (2\Delta_q)^{1/2}$ have been shown to be leaky modes [9,20]; here, $\Delta_p = (n_0 - n_p)/n_0$ or $\Delta_q = (n_0 - n_q)/n_0$ is the relative difference of the refraction index of the cladding, or (respectively) intermediate layer, to that of the core.

Denoting the free-space wave number as $k_0 = 2\pi/\lambda$ and expressing the thickness of the intermediate layer as $\delta \cdot a$ where a is the core-radius, constants of attenuation of leaky modes are given as [9]:

$$\alpha_d(\theta) = \frac{4(\theta^2 - \theta_p^2)^{1/2} \theta^2 (\theta_q^2 - \theta^2)}{a(1 - \theta^2)^{1/2} \theta_q^2 (\theta_q^2 - \theta_p^2)} \exp[-2\delta a n_0 k_0 (\theta_q^2 - \theta^2)^{1/2}] \quad (2)$$

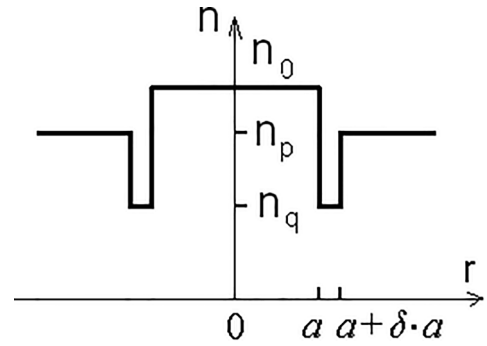


Fig. 1. Refractive index profile of a W-fiber.

All guided-modes in SC fibers regardless of their propagation angle θ are attenuated equally; the attenuation rises steeply for radiated-modes. For W-type fibers, this can be generalised in terms of $\alpha_d(\theta)$ in the already introduced expansion for attenuation $\alpha(\theta) = \alpha_0 + \alpha_d(\theta)$, in which $\alpha_0 = \text{const}$, and where:

$$\alpha_d(\theta) = \begin{cases} 0 & \theta \leq \theta_p \\ \alpha_L(\theta) & \theta_p < \theta < \theta_q \\ \infty & \theta \geq \theta_q \end{cases} \quad (3)$$

Equation (3) can also be explained if one would think of a W-fiber as having a vanishing, and then infinite, thickness of its intermediate layer $\delta \cdot a$ (a is the core radius). With $\delta \rightarrow 0$, and then $\delta \rightarrow \infty$, two distinct SC (SC_p and SC_q) fibers result with respective critical angles of θ_p and then θ_q , respectively. This results in three subdomains for the propagation angle evident in (3): less than one critical angle, greater than the other, and between the two of them. Modes propagating at angles between the two critical angles θ_p and θ_q are termed leaky modes. For that range, strong influence of the intermediate layers’ thickness $\delta \cdot a$ on $\alpha_L(\theta)$ in (3) has been noted [9].

W-fiber’s characteristics were reported to vary strongly with the intermediate layer’s width $\delta \cdot a$. As mentioned, they approach those of corresponding SC_p or SC_q fibers when, respectively, the thickness either vanishes or approaches infinity [9], under SSD conditions. Also of influence is the index of refraction n_p of the outer cladding (Fig. 1). The influence is investigated in this paper of the width of intermediate layer and index of refraction n_p on the length L_c for achieving the EMD and length z_s for reaching the SSD – across an infrared wavelength spectrum. This facilitates tailoring W-fibers to a specific application at hand.

3. Numerical results

The length at which EMD is achieved and the length z_s for establishing the SSD are analysed in this work at different wavelengths for the W-type PCSF. The fiber structural characteristics were: core refractive index $n_0 = 1.4535$, cladding refractive index $n_q = 1.405385$, critical angle (measured inside the fiber) $\theta_m = 14.75^\circ$, core diameter $d = 0.2$ mm, and fiber diameter $b = 0.23$ mm [21]. The W-type PCSF is designed from this singly-clad PCSF in such a way that the W-type PCSF’s inner cladding retains the refractive index n_q of the SC PCSF’s cladding, while an outer cladding of the W-type PCSF has a refractive index n_p , which is higher than the refractive index n_q of the inner cladding (Fig. 1). The three values of the refractive index of the outer cladding n_p were used in the modeling: $n_p = 1.4455385$, 1.4393461 , 1.4313855 , corresponding to the critical angles $\theta_p = 6^\circ$, 8° , 10° , respectively. The normalized intermediate layer widths $\delta = 0.01$, $\delta = 0.02$, $\delta = 0.03$ and $\delta = 0.05$ were employed (actual width is $\delta \cdot a$ mm). We solved the time-dependent power flow equation (1) using explicit finite difference method for the coupling coefficient $D = 6.4 \times 10^{-6} \text{ rad}^2 \text{ m}^{-1}$ [4]. In the calculations, the launch beam

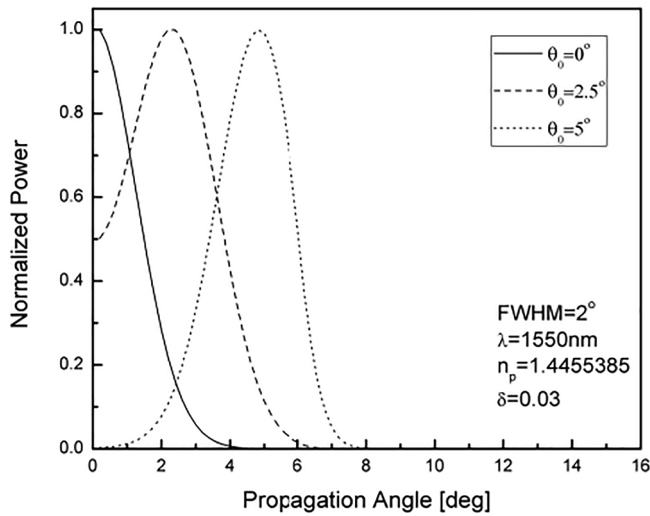


Fig. 2. Normalized angular power distribution for FWHM = 2°, λ = 1550 nm, n_p = 1.4455385, δ = 0.03 and D = 6.4 × 10⁻⁶ rad² m⁻¹ for four launch angles (θ₀ = 0°, 2.5°, and 5°) at lengths: a) 20 m, b) 70 m, c) 220 m and d) 450 m.

distribution was in the Gaussian form with an FWHM = 2°. One should mention here that the change of depth of the intermediate layer has a negligible influence on the lengths L_c and z_s of the W-type PCSFs, and therefore is not analyzed in this work. Length L_c for reaching EMD is determined as a length at which the angular power distribution of the highest guiding modes shifted their maxima to θ = 0°. Length z_s for achieving SSD is determined as a length at which the angular light distribution stops evolving with further increase of the fiber length (becomes steady).

In Fig. 2 our numerical solution of the power flow equation is presented by showing the evolution of the normalized output power distribution with fiber length for W-type PCSF with characteristics n_p = 1.4455385 (θ_p = 6°), δ = 0.03 and D = 6.4 × 10⁻⁶ rad² m⁻¹ at λ = 1550 nm, for Gaussian launch distribution with FWHM = 2°, for three different input angles θ₀ = 0°, 2.5° and 5° (measured inside the fiber). One can observe from Fig. 2 that when the launch distribution at the input end of the fiber is centered at θ₀ = 0°, the power distribution remains at the same angle as the distance from the input fiber end increases, but its width increases due to mode coupling. Radiation patterns in Fig. 2(a) of non-centrally launched beams in short fibers are centered at values which are close to their initial values. With increasing the fiber length one can observe from Fig. 2(b) that coupling is

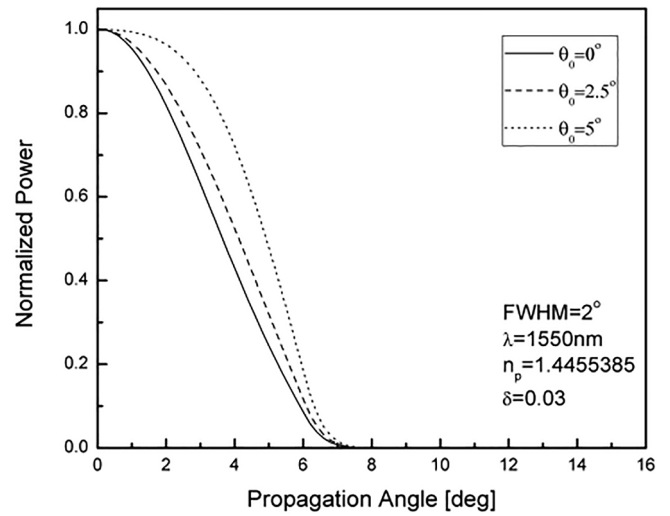


Fig. 2. (continued)

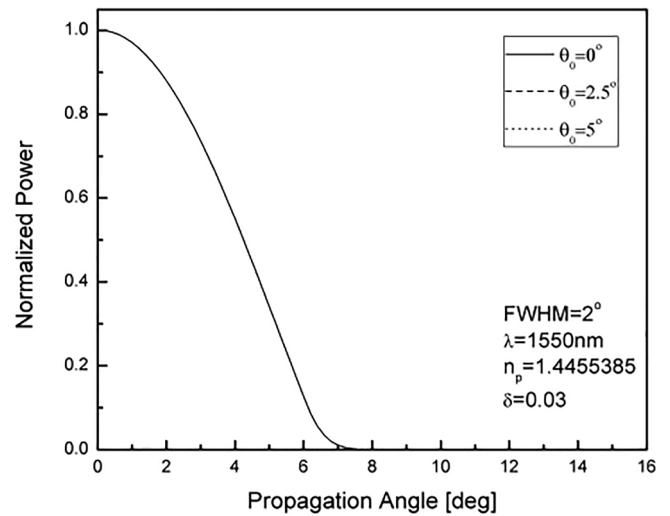


Fig. 2. (continued)

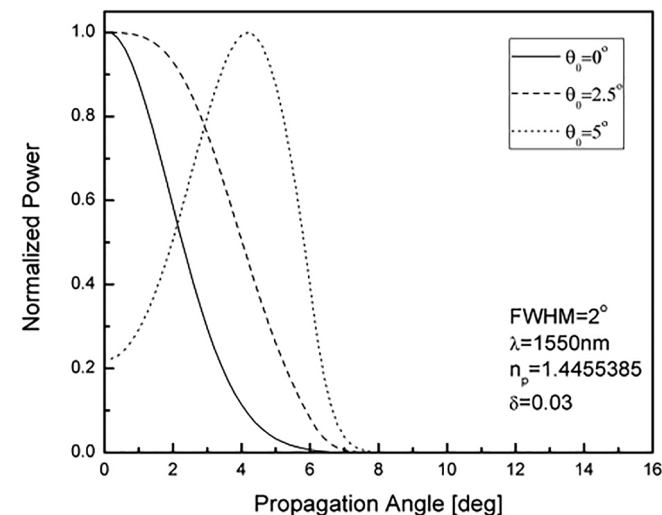


Fig. 2. (continued)

stronger for the low-order modes: their distributions have shifted more towards θ = 0°. Coupling of higher-order modes can be observed only after longer fiber lengths. It is not until the fiber's coupling length L_c that all the mode-distributions shift their mid-points to zero degrees (from the initial value of θ₀ at the input fiber end), producing the EMD in Fig. 2(c) of L_c = 220 m. Steady state distribution is achieved at length z_s = 450 m in Fig. 2(d).

One can observe in Figs. 3 and 4 that for the smallest width of intermediate layer (δ = 0.01), there is no influence of wavelength on lengths L_c and z_s. This is due to large leaky mode losses; as these modes are practically not guided along the fiber. With increasing width of the intermediate layer, there is a wavelength-dependent decrease of lengths L_c and z_s. This decrease is more pronounced at short wavelengths as leaky mode losses are then reduced, i.e. a smaller number of leaky modes remain guided at larger wavelengths at longer fiber lengths, resulting in drop of fiber lengths L_c and z_s. The lengths L_c and z_s are larger in the case of wider intermediate layer widths (larger δδ). Since the leaky modes are reduced at short transmission length in the case of thinner intermediate layer, consequently, it takes a shorter fiber length z_s for the onset of SSD – compared to the case with a wider intermediate layer. As refractive index of the outer cladding n_p decreases (θ_p increases), EMD and SSD occurs at longer fiber lengths – which is attributed to the correspondingly increasing number of guiding modes. The smaller the parameter n_p, the longer the fiber length is required for

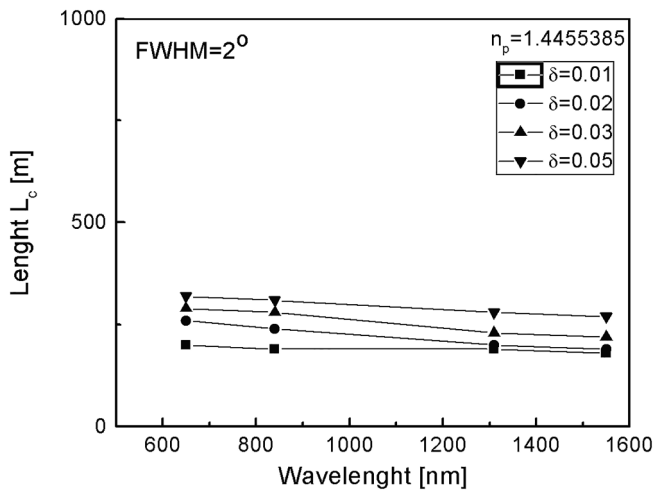


Fig. 3. Wavelength dependence of length L_c for Gaussian launch excitation with $\text{FWHM} = 2^\circ$, $\delta = 0.01, 0.02, 0.03$ and 0.05 , and (a) $n_p = 1.4455385$, (b) $n_p = 1.4393461$ and (c) $n_p = 1.4313855$.

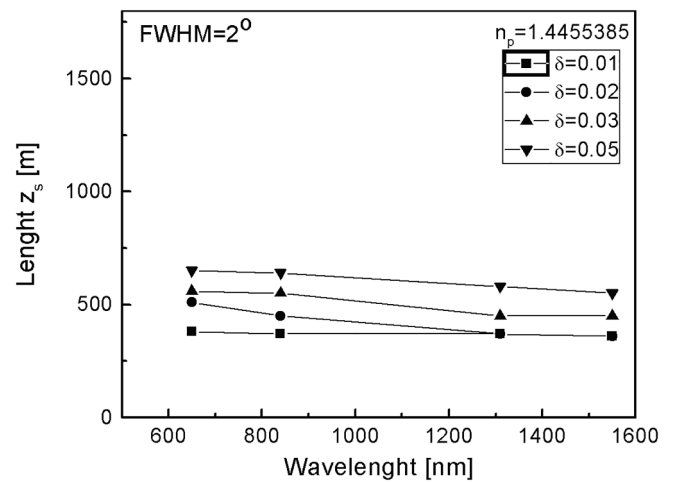


Fig. 4. Wavelength dependence of length z_s for Gaussian launch excitation with $\text{FWHM} = 2^\circ$, $\delta = 0.01, 0.02, 0.03$ and 0.05 , and (a) $n_p = 1.4455385$, (b) $n_p = 1.4393461$ and (c) $n_p = 1.4313855$.

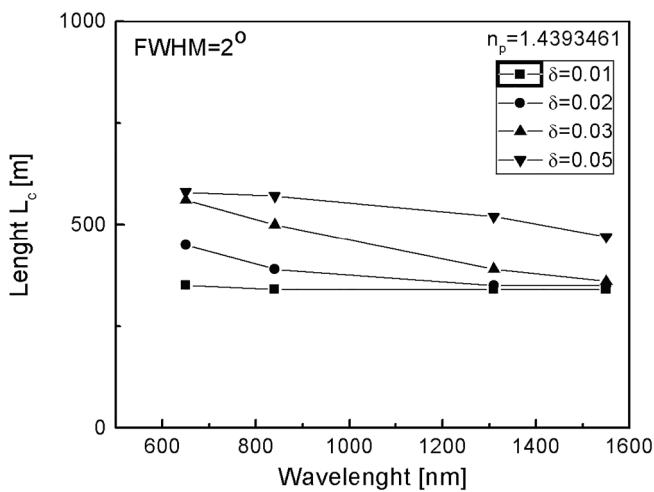


Fig. 3. (continued)

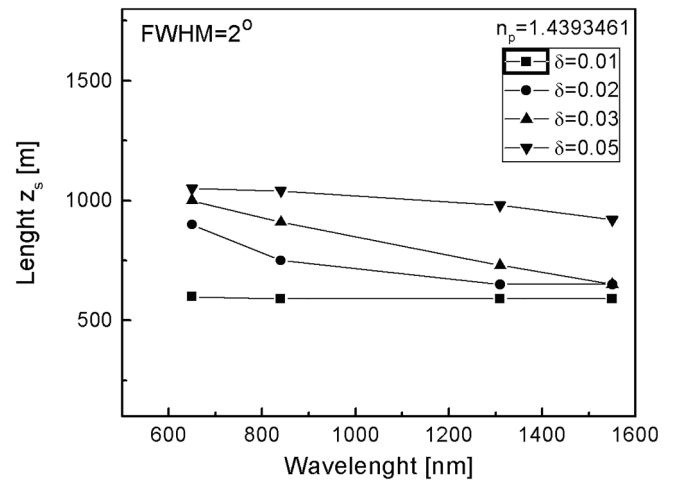


Fig. 4. (continued)

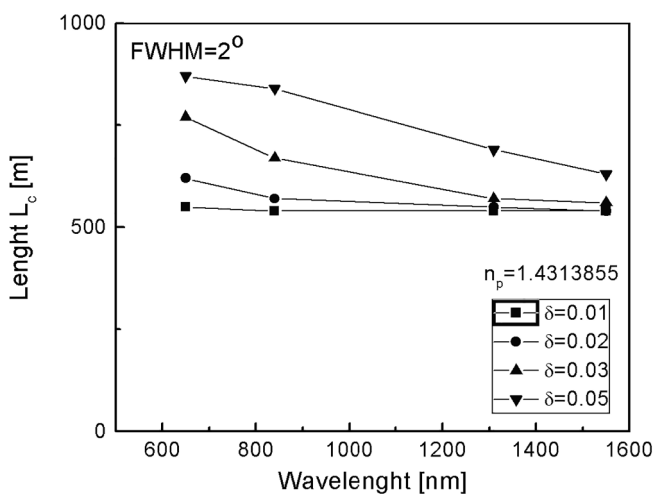


Fig. 3. (continued)

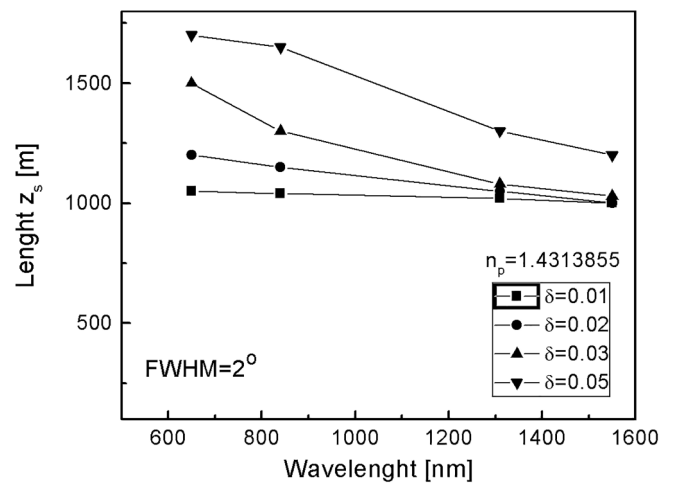


Fig. 4. (continued)

completion of the coupling process.

Since it is found that with increasing the infrared wavelength the leaky mode losses rise while EMD and SSD are established at shorter fiber lengths, the W-type PCSF has better transmission characteristics at

longer infrared wavelengths. This is explained by the rise of the leaky mode losses with increasing wavelength as fewer leaky modes remain guided along the fiber; which decreases modal dispersion and increases bandwidth. At longer wavelengths a higher rate of filtering of leaky modes results in establishing the SSD (and therefore the equilibrium

mode distribution) at shorter fiber lengths - the shorter the length at which equilibrium mode distribution is achieved, the earlier the bandwidth would switch from the functional dependence of $1/z$ to $1/z^{1/2}$ (faster bandwidth improvement) [15].

4. Conclusion

EMD (equilibrium mode distribution) and SSD (steady state distribution) of power are investigated for a varied W-type PCSF's width of intermediate layer and refractive index of the outer cladding. The length L_c at which EMD is achieved and length z_s marking the onset of the SSD decrease with increasing wavelength. This is a result of the rise of the leaky mode losses with rising wavelength, which is to say that a smaller number of leaky modes continue to be guided in longer fibers at larger wavelengths.

The lengths L_c and z_s are larger in the case of wider intermediate layer widths (larger δ). Since the leaky modes are reduced at short transmission length in the case of thinner intermediate layer, consequently, it takes a shorter fiber length z_s for the onset of SSD – compared to the case with a wider intermediate layer.

As refractive index of the outer cladding n_p decreases (θ_p increases), number of guiding modes increases, EMD and SSD is established at longer fiber lengths. The smaller the parameter n_p , the longer the fiber length is required for completion of the coupling process.

Finally, the investigated W-type PCSF has better transmission characteristics at longer infrared wavelengths. This is explained by the rise of the leaky mode losses with increasing wavelength as fewer leaky modes remain guided along the fiber; which decreases modal dispersion and increases bandwidth.

Declaration of Competing Interest

The authors declare that they have no known competing financial interests or personal relationships that could have appeared to influence the work reported in this paper.

Acknowledgment

The work described in this paper was supported by the Strategic Research Grant of City University of Hong Kong (Project No. CityU 7004600) and by a grant from Serbian Ministry of Education, Science and Technological Development (Project No. 171011).

References

- [1] W. Daum, J. Krauser, P.E. Zamzow, O. Ziemann, *Polymer Optical Fibers for Data Communication*, Springer, Berlin, 2002.
- [2] V. Ruddy, G. Shaw, Mode coupling in large-diameter polymer-clad silica fibers, *Appl. Opt.* 34 (1995) 1003–1006.
- [3] S. Savović, A. Djordjević, Mode coupling in multimode step-index plastic-clad silica fibers with corrugated surfaces, *Opt. Laser Technol.* 97 (2017) 400–404.
- [4] S. Savović, A. Djordjević, Mode coupling and its influence on space division multiplexing in step-index plastic-clad silica fibers, *Opt. Fiber Technol.* 46 (2018) 192–197.
- [5] Y. Daido, E. Miyauchi, T. Iwama, T. Otsuka, Determination of modal power distribution in graded-index optical waveguides from near-field patterns and its application to differential mode attenuation measurement, *Appl. Opt.* 18 (1979) 2207–2213.
- [6] T. Yamashita, M. Kagami, Fabrication of light-induced self-written waveguides with a W-shaped refractive index profile, *J. Lightwave Technol.* 23 (2005) 2542–2548.
- [7] M. Asai, Y. Inuzuka, K. Koike, S. Takahashi, Y. Koike, High-bandwidth graded-index plastic optical fiber with low-attenuation, high-bending ability, and high-thermal stability for home-networks, *J. Lightwave Technol.* 29 (2011) 1620–1626.
- [8] K. Mikoshiba, H. Kajioka, Transmission characteristics of multimode W-type optical fiber: experimental study of the effect of the intermediate layer, *Appl. Opt.* 17 (1978) 2836–2841.
- [9] T.P. Tanaka, S. Yamada, Numerical solution of power flow equation in multimode W-type optical fibers, *Appl. Opt.* 19 (1980) 1647–1652.
- [10] S. Onoda, T. Tanaka, M. Sumi, W fiber design considerations, *Appl. Opt.* 15 (1976) 1930–1935.
- [11] M. Maeda, S. Yamada, Leaky modes on W-fibers: mode structure and attenuation, *Appl. Opt.* 16 (1977) 2198–2203.
- [12] T. Tanaka, S. Yamada, M. Sumi, K. Mikoshiba, Microbending losses of doubly clad (W-type) optical fibers, *Appl. Opt.* 18 (1977) 2391–2394.
- [13] T.P. Tanaka, S. Yamada, Steady-state characteristics of multimode W-type fibers, *Appl. Opt.* 18 (1979) 3261–3264.
- [14] S. Yu. Otrokhov, Yu. K. Chamorovskiy, A.D. Shatrov, Leaking modes of guiding W fibers with a large difference in the refractive index profiles, *J. Commun. Technol. Electronics* 55 (1108–1114) (2010).
- [15] G. Jiang, R.F. Shi, A.F. Garito, Mode coupling and equilibrium mode distribution conditions in plastic optical fibers, *IEEE Photon. Technol. Lett.* 9 (1997) 1128–1130.
- [16] D. Gloge, Optical power flow in multimode fibers, *Bell Syst. Tech. J.* 51 (1767–1783) (1972).
- [17] L. Jeunhomme, M. Fraise, J.P. Pocholle, Propagation model for long step-index optical fibers, *Appl. Opt.* 15 (1976) 3040–3046.
- [18] M. Rousseau, L. Jeunhomme, Numerical solution of the coupled-power equation in step index optical fibers, *IEEE Trans. Microwave Theory Tech.* 25 (1977) 577–585.
- [19] A. Djordjević, S. Savović, Numerical solution of the power flow equation in step index plastic optical fibers, *J. Opt. Soc. Am. B* 21 (1437–1442) (2004).
- [20] S. Savović, A. Simović, A. Djordjević, Explicit finite difference solution of the power flow equation in W-type optical fibers, *Opt. Laser Technol.* 44 (2012) 1786–1790.
- [21] M. Kagami, A. Kawasaki, M. Yonemura, M. Nakai, P.V. Mena, D.R. Selviah, Encircled angular flux representation of the modal power distribution and its behavior in a step index multimode fiber, *J. Lightwave Technol.* 34 (2016) 943–951.

LETTER

Controlling the bandwidth of W-type plastic-clad silica optical fibers

To cite this article: A Simovi *et al* 2019 *Laser Phys. Lett.* **16** 085106

View the [article online](#) for updates and enhancements.



IOP | ebooks™

Bringing you innovative digital publishing with leading voices to create your essential collection of books in STEM research.

Start exploring the collection - download the first chapter of every title for free.

Letter

Controlling the bandwidth of W-type plastic-clad silica optical fibers

A Simović¹, S Savović^{1,2,4}, B Drljača³ and A Djordjevich²¹ University of Kragujevac, Faculty of Science, R. Domanovića 12, 34000 Kragujevac, Serbia² City University of Hong Kong, 83 Tat Chee Avenue, Hong Kong, People's Republic of China³ Faculty of Sciences, University of Priština, Lole Ribara 29, Kosovska Mitrovica, SerbiaE-mail: savovic@kg.ac.rs

Received 17 March 2019

Accepted for publication 3 June 2019

Published 27 June 2019

**Abstract**

A new design of a multimode plastic-clad silica optical fiber that takes the characteristic W-shaped index profile is proposed. The bandwidth and steady-state loss are determined for such a W-type plastic-clad silica optical fiber for the different structural parameters of the fiber. We have shown that the bandwidth of a W-type plastic-clad silica optical fiber is significantly higher (up to 15 times at a fiber length of 2 km) than the bandwidth of the singly clad step index plastic-clad silica optical fiber.

Keywords: W-type plastic-clad silica optical fiber, bandwidth, steady-state loss

1. Introduction

Glass optical fibers are often used for high-speed long-distance communication due to their low attenuation and high bandwidth [1]. Large core (~1 mm diameter) plastic optical fibers are most frequently employed for short-distance (<100 m) communication links [2]. Plastic-clad silica fibers (PCSFs) have many applications in optical measurements, short-to-long distance communications, and sensors [3–5]. The ease of the cladding removal makes PCSFs particularly useful for sensors when access to evanescent waves is desired.

Multimode optical fibers are usually singly clad (SC) in terms of the number of functional cladding layers. The analysis and design of the refractive index profile of a multimode fiber with a view to advancing the fiber transmission characteristics have attracted much attention in the last few decades. A variety of designs for step-index (SI), graded index (GI) and W-type fibers (doubly clad fibers) have been proposed either for long-distance communication links or high capacity local area networks [6–8]. There are also many reports on the effect of GI on evanescent wave (EW) parameters and the sensitivity of EW fiber optic sensors [9–11]. A W-type fiber has an

intermediate layer between its outer cladding and core. The reduced number of guided modes in W-type fibers and the lowered fiber's effective numerical aperture result in guided modes that are held tighter to the core [12].

In general, due to mode coupling, optical power is transferred between modes. This reduces the modal dispersion and improves the fiber bandwidth [13, 14]. Methods are needed for calculating the modal attenuation, dispersion, and coupling to the lossy modes of a W-type fiber's intermediate layer, and for optimizing the fiber's refractive index profile in order to minimize the group delay difference between modes in the output field [12, 13].

The far-field pattern of an optical fiber is determined by the optical power distribution that depends on the launch conditions, fiber properties and fiber length. If light-launched at a specific angle $\theta_0 > 0$ with respect to the fiber axis, it will form a sharply defined ring radiation pattern at the output end of only the short fibers. Because of mode coupling, the boundaries (edges) of such a ring become fuzzy at the end of the longer fibers. Up to a 'coupling length' L_c from the input fiber end, the extent of this fuzziness increases further with the fiber length and the ring-pattern evolves gradually into a disk extending across the entire fiber cross-section. An equilibrium mode distribution (EMD) exists beyond the coupling length

⁴ Author to whom any correspondence should be addressed.

L_c of the fiber. It is characterized by the absence of rings, regardless of launch conditions, even though the resulting light distribution of the disk-pattern may vary with the launch conditions. The EMD indicates a substantially complete mode coupling. It is of critical importance when measuring the characteristics of multimode optical fibers (linear attenuation, bandwidth, etc). At a distance z_s ($z_s > L_c$) from the input fiber end, all individual disk patterns corresponding to the different launch angles take the same light distribution across the fiber section, and the ‘steady state distribution’ (SSD) is achieved. The SSD indicates the full completion of the mode coupling process and the independence of the output light distribution from the launch conditions.

In this work, we investigated how the bandwidth can be enhanced for variously configured W-type PCSFs, in the terms of the width of the fiber’s intermediate layer, for different launch beams. One should mention that the change of depth of the intermediate layer has a negligible influence on the bandwidth of the W-type PCSFs.

2. Time-independent and time-dependent power flow equation

For mode coupling between the neighboring mode groups, the power flow in the multimode optical fiber can be represented by the Gloge’s time-independent coupled-power equation [15]:

$$\frac{\partial P(\theta, z)}{\partial z} = -\alpha(\theta)P(\theta, z) + \frac{1}{\theta} \frac{\partial}{\partial \theta} \left[\theta D(\theta) \frac{\partial P(\theta, z)}{\partial \theta} \right] \quad (1)$$

where $P(\theta, z)$ is the angular power distribution at distance z from the input end of the fiber, θ is the propagation angle with respect to the core axis ($0 \leq \theta \leq \theta_m$), θ_m is the critical angle of the fiber, $D(\theta)$ is the coupling coefficient, and $\alpha(\theta) = \alpha_0 + \alpha_d(\theta)$ is the modal attenuation—where α_0 represents the conventional losses (absorption and scattering) and is neglected as it features only as a multiplier $\exp(-\alpha_0 z)$ in the solution that is normalized. By solving equation (1) one can obtain an output angular power distribution at any fiber length and launch beam distribution. In practice, equation (1) is solved up to the fiber length z_s at which an SSD is established in the fiber. The SSD indicates the completion of the mode coupling process and the independence of the output light distribution from the launch conditions.

In order to calculate the bandwidth of the optical fiber, we solved the time-dependent power flow equation, which is in the form [13]:

$$\begin{aligned} \frac{\partial p(\theta, z, t)}{\partial z} + \tau(\theta) \frac{\partial p(\theta, z, t)}{\partial t} = -\alpha(\theta) p(\theta, z, t) \\ + \frac{1}{\theta} \frac{\partial}{\partial \theta} \left[D(\theta) \frac{\partial p(\theta, z, t)}{\partial \theta} \right] \end{aligned} \quad (2)$$

where $p(\theta, z, t)$ is the angular power distribution at distance z and time t ; $\tau(\theta)$ is the modal delay per unit length. In order to obtain the frequency response in the frequency domain, the Fourier transformation of equation (2) becomes:

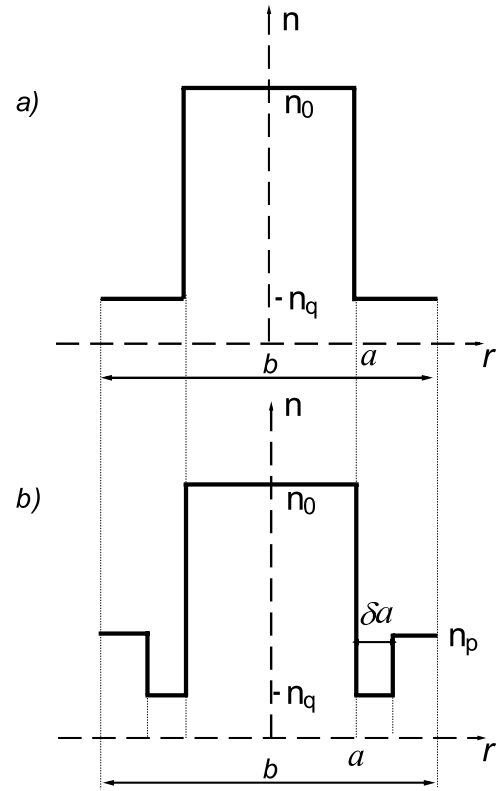


Figure 1. Refractive index profile of (a) SC PCSF and (b) W-type PCSF.

$$\begin{aligned} \frac{\partial P(\theta, z, \omega)}{\partial z} + j\omega\tau(\theta)P(\theta, z, \omega) = -\alpha(\theta)P(\theta, z, \omega) \\ + \frac{1}{\theta} \frac{\partial}{\partial \theta} \left[D(\theta) \frac{\partial P(\theta, z, \omega)}{\partial \theta} \right] \end{aligned} \quad (3)$$

where $\omega = 2\pi f$ is the angular frequency, and

$$P(\theta, z, \omega) = \int_{-\infty}^{+\infty} p(\theta, z, t) \exp(-j\omega t) dt. \quad (4)$$

It is worth noting that the simplifying assumption of the constant coupling coefficient D , which is independent of the propagation angle, has been commonly used by many authors [1, 13, 16–18]. The method of solving equation (1) and a calculation of the bandwidth of the W-type optical fibers has been described in more detail in our previously reported work [19].

The doubly clad (W-type) fiber transforms into a singly clad one by allowing the thickness of the intermediate layer (δa in figure 1) to either vanish or expand to the fiber thickness. In the vanishing case, the core and the outer layer comprise the ‘SC_p’ fiber. In the other case, the core and the intermediate layer as the only cladding form the ‘SC_q’ fiber. A W-type fiber with the index profile shown in figure 1(b) can be viewed as the SC_q fiber and an additional cladding. The modes propagating along the SC_q fiber with subcritical angles $\theta < \theta_q$ ($\theta_q \cong (2\Delta_q)^{1/2}$), where $\Delta_q = (n_0 - n_q)/n_0$, are guided. The same is true for those propagating through the complete W-fiber with angles θ below the critical value θ_p for the SC_p fiber, that has only the outer cladding of the W-type

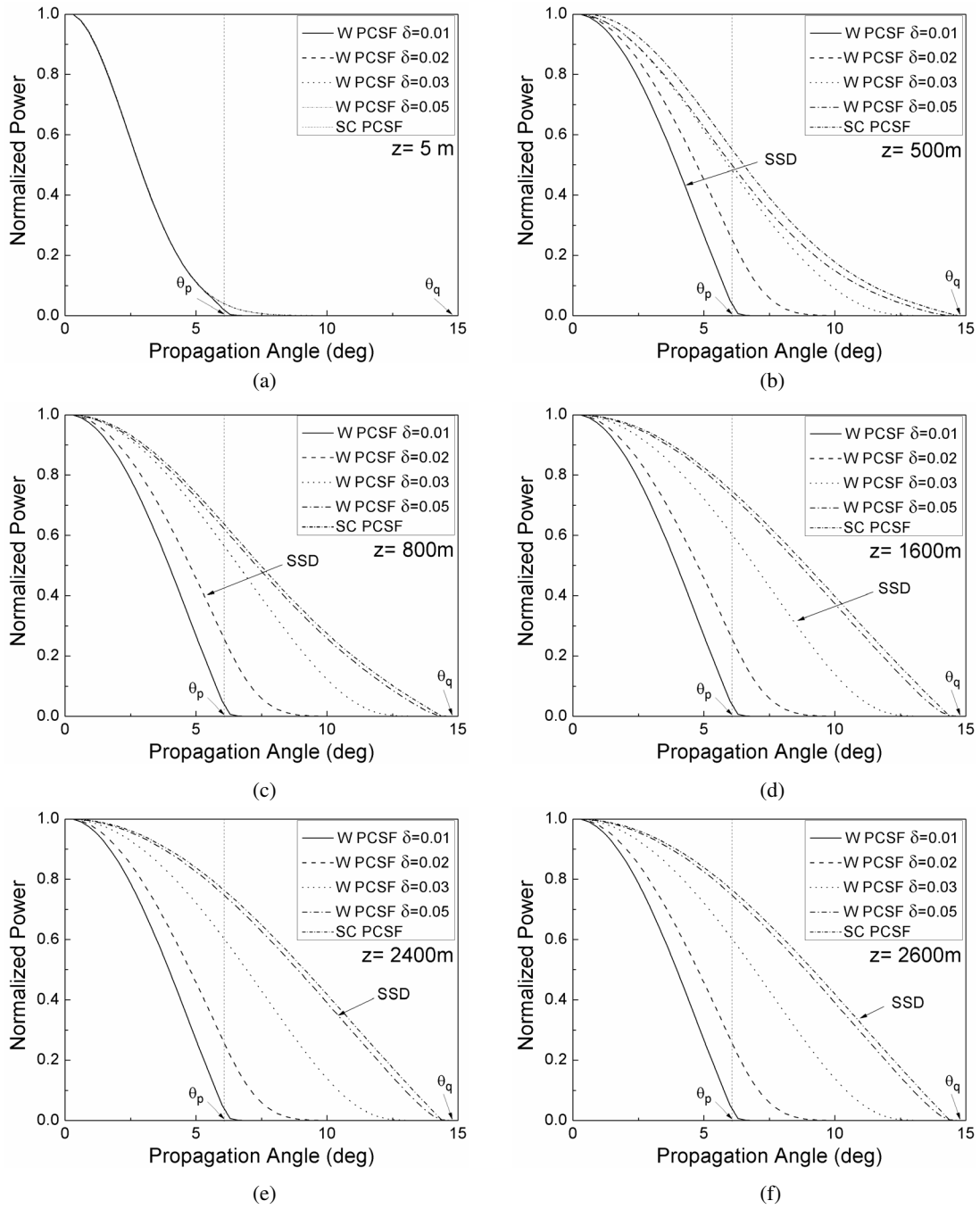


Figure 2. Calculated output angular power distribution in W-type PCSF with $\delta = 0.01$, $\delta = 0.02$, $\delta = 0.03$ and $\delta = 0.05$, $n_p = 1.4455385$ ($\theta_p = 6^\circ$), and SC PCSF at fiber lengths (a) 5 m, (b) 500 m (SSD for W-type PCSF with $\delta = 0.01$), (c) 800 m (SSD for W-type PCSF with $\delta = 0.02$) (d) 1600 m (SSD for W-type PCSF with $\delta = 0.03$), (e) 2400 m (SSD for W-type PCSF with $\delta = 0.05$) and (f) (SSD for SC PCSF) for Gaussian launch beam distribution with FWHM = 5.5° .

fiber (and lacks the intermediate layer), $\theta_p \cong (2\Delta_p)^{1/2}$, where $\Delta_p = (n_0 - n_p)/n_0$. However, modes with angles between θ_p and θ_q are transformed into leaky modes. Hence [16],

$$\alpha_L(\theta) = \frac{4(\theta^2 - \theta_p^2)^{1/2} \theta^2 (\theta_q^2 - \theta^2)}{a(1 - \theta^2)^{1/2} \theta_q^2 (\theta_q^2 - \theta_p^2)} \exp \left[-2\delta a n_0 k_0 (\theta_q^2 - \theta^2)^{1/2} \right] \quad (5)$$

where $k_0 = 2\pi/\lambda$ is the free-space wave number, a is core radius and δa is the intermediate layer (inner cladding) width.

In an SC fiber, the experimental results show that attenuation remains constant throughout the guided-mode region and rises quite steeply in the radiation-mode region [1]. Consequently, the modal attenuation in a W-type fiber can be expressed as:

$$\alpha_d(\theta) = \begin{cases} 0 & \theta \leq \theta_p \\ \alpha_L(\theta) & \theta_p < \theta < \theta_q \\ \infty & \theta \geq \theta_q \end{cases} \quad (6)$$

Table 1. Lengths L_c and z_s at which the EMD and SSD are achieved in W-type PCSF with $\delta = 0.01$, $\delta = 0.02$, $\delta = 0.02$ and $\delta = 0.05$, critical angles of the outer cladding $\theta_p = 6^\circ$, 8° and 10° and FWHM (a) 2° and (b) 5.5° .

(a)	$\theta_p = 6^\circ$		$\theta_p = 8^\circ$		$\theta_p = 10^\circ$	
	L_c (m)	z_s (m)	L_c (m)	z_s (m)	L_c (m)	z_s (m)
FWHM = 2°						
$\delta = 0.01$	220	550	370	850	580	1450
$\delta = 0.02$	360	850	450	1100	640	1500
$\delta = 0.03$	710	1750	730	1800	770	1900
$\delta = 0.05$	1060	2700	1060	2700	1600	2700
(b)	$\theta_p = 6^\circ$		$\theta_p = 8^\circ$		$\theta_p = 10^\circ$	
	L_c (m)	z_s (m)	L_c (m)	z_s (m)	L_c (m)	z_s (m)
FWHM = 5.5°						
$\delta = 0.01$	200	500	340	800	540	1400
$\delta = 0.02$	320	800	420	1050	570	1450
$\delta = 0.03$	650	1600	660	1650	700	1750
$\delta = 0.05$	970	2400	970	2400	970	2400

3. Numerical results

In this paper we investigate the transmission characteristics of a W-type PCSF, which is designed from the SC PCSF (HPCF-M0200T) investigated by Kagami *et al* [20]. A W-shaped refractive index model is used for the structure shown in figure 1(b). The characteristics of the SC PCSF (figure 1(a)) were: core refractive index $n_0 = 1.4535$, cladding refractive index $n_q = 1.405385$, critical angle (measured inside the fiber) $\theta_m = 14.75^\circ$, core diameter $d = 0.2$ mm, and fiber diameter $b = 0.23$ mm. The W-type PCSF is designed from this SC PCSF in such a way that the W-type PCSF's inner cladding retains the refractive index n_q of the SC PCSF's cladding, while an outer cladding of the W-type PCSF has a refractive index n_p , which is higher than the refractive index n_q of the inner cladding (figure 1(b)). The three values of the refractive index of the outer cladding n_p were used in the modeling: $n_p = 1.4455385$, 1.4393461 , 1.4313855 , corresponding to the critical angles $\theta_p = 6^\circ$, 8° , 10° , respectively. The normalized intermediate layer widths $\delta = 0.01$, $\delta = 0.02$, $\delta = 0.03$ and $\delta = 0.05$ were employed (actual width is $\delta \cdot a$ mm). The coupling coefficient $D = 6.4 \times 10^{-6}$ rad² m⁻¹ was used in the calculations [5]. In the calculations, the launch beam distributions were in the Gaussian form with an FWHM = 2° and FWHM = 5.5° . One should mention here that the change of depth of the intermediate layer has a negligible influence on the bandwidth of the W-type PCSFs, and therefore is not analyzed in this work.

Using the time-independent power flow equation, we calculated the lengths L_c and z_s , at which the EMD and SSD were achieved in the W-type PCSF and SC PCSF. The SC type and W-type PCSF mainly differ due to the existence of leaky modes in the latter, which propagate between angles θ_p and θ_q . Figure 2 shows the output angular power distribution in the SC PCSF and four different W-type PCSFs with the widths of the intermediate layer being $\delta = 0.001$, $\delta = 0.002$, $\delta = 0.003$

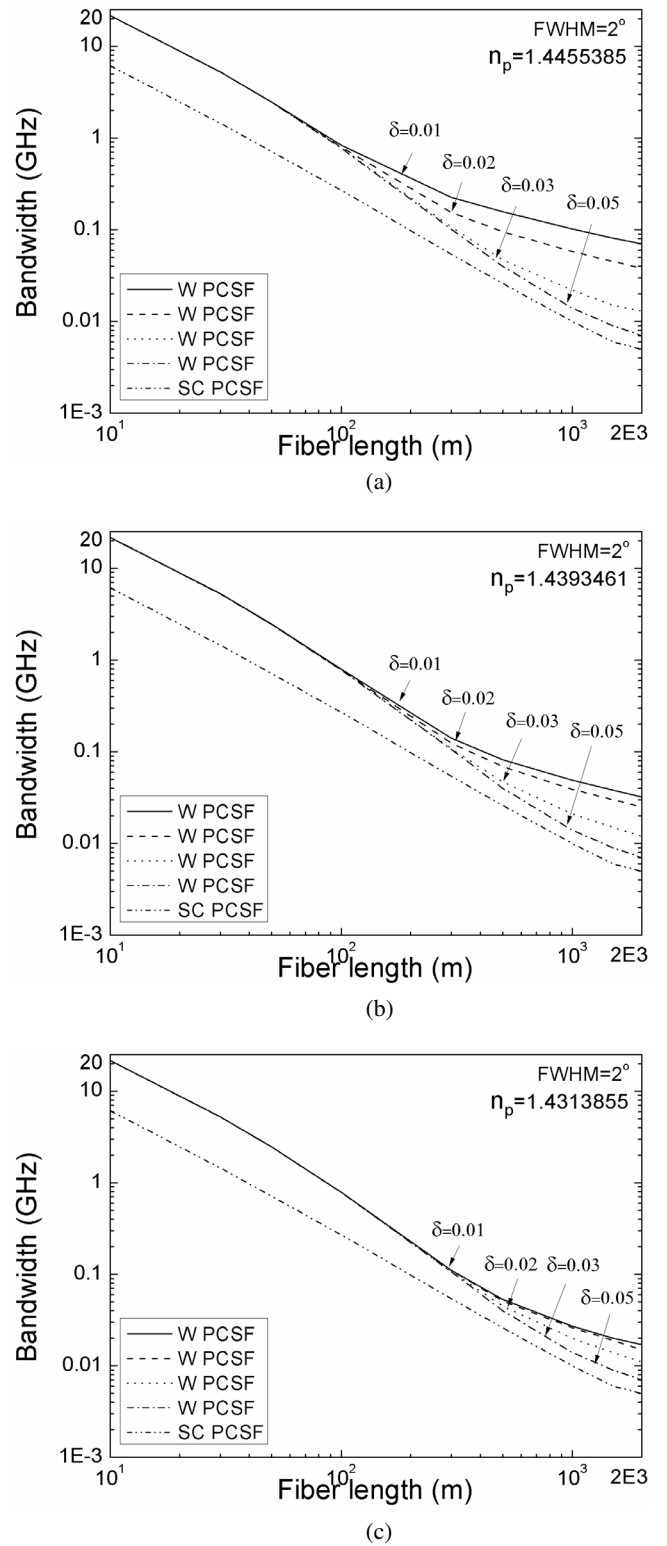


Figure 3. Numerical results for transmission length dependence of bandwidth for W-type PCSF with $\delta = 0.01$, $\delta = 0.02$, $\delta = 0.03$ and $\delta = 0.05$, for (a) $\theta_p = 6^\circ$, (b) 8° and (c) 10° and SC PCSF, for Gaussian launch beam distribution with FWHM = 2° .

and $\delta = 0.005$ in the case of the FWHM = 5.5° . The output angular power distribution at a short fiber length is almost the same in the SC PCSF and W-type PCSFs. By increasing the fiber length, the SSD is first achieved in the W-type PCSF

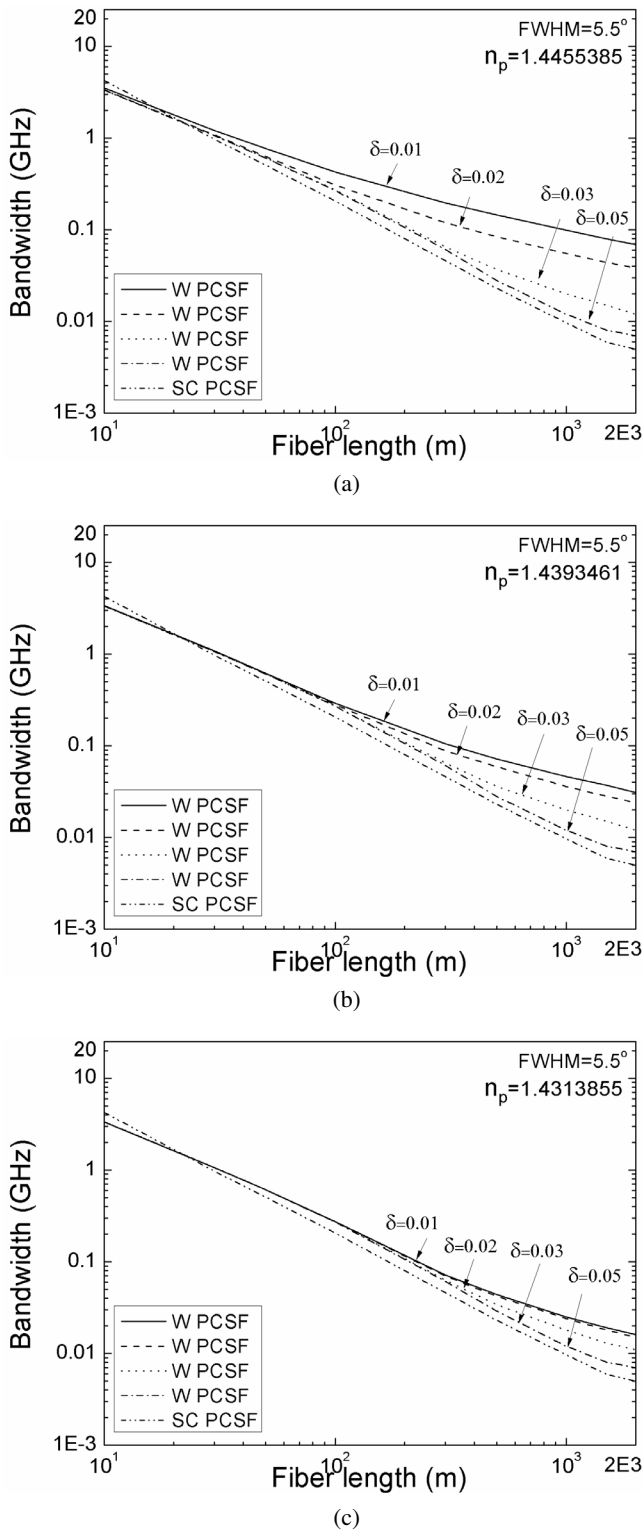


Figure 4. Numerical results for transmission length dependence of bandwidth for W-type PCSF with $\delta = 0.01$, $\delta = 0.02$, $\delta = 0.03$ and $\delta = 0.05$, for (a) $\theta_p = 6^\circ$, (b) 8° and (c) 10° and SC PCSF, for Gaussian launch beam distribution with FWHM = 5.5° .

with $\delta = 0.01$ at the fiber length $z_s = 500$ m, $\delta = 0.02$ at fiber length $z_s = 800$ m, $\delta = 0.03$ at fiber length $z_s = 1600$ m, then in the W-type PCSF with $\delta = 0.05$ at $z_s = 2400$ m, and finally in the SC PCSF at $z_s = 2600$ m. The number of higher modes involved in the coupling process in the W-type PCSF fibers is

reduced due to leaky mode losses, thus reducing the lengths L_c and z_s . Since leaky mode losses decrease with the increasing δ , the longest lengths L_c and z_s are obtained in the case of $\delta = 0.05$. By increasing the critical angle θ_p , the lengths L_c and z_s increase for all analyzed widths δ and two different widths of the launch beam (table 1). By increasing the critical angle θ_p , number of guided modes increases while the number of leaky modes decreases; increasing the lengths L_c and z_s . The lengths L_c and z_s are more influenced by the value of the critical angle θ_p in the case of smaller widths δ because of the higher leaky mode losses.

Figures 3 and 4 show the transmission length dependence of the bandwidth for the W-type PCSF for $\delta = 0.01$, 0.02 , 0.03 and 0.05 , and $n_p = 1.4455385$, 1.4393461 , 1.4313855 , with corresponding critical angles $\theta_p = 6^\circ$, 8° and 10° , respectively, for two different Gaussian launch beams, with the FWHM = 2° and 5.5° . One can see that the bandwidth of the W-type PCSF is higher than the bandwidth of the SC PCSF. Leaky mode losses in the W-type PCSF reduce the number of guided higher modes, decrease the modal dispersion and thus increase the bandwidth. The bandwidth is highest for the narrowest inner cladding ($\delta = 0.01$) because of the largest leaky mode losses compared to the case of $\delta = 0.02$, 0.03 and 0.05 . By increasing the refractive index of the outer cladding n_p , the leaky mode losses increase, which results in the highest values of the bandwidth in the case of $\delta = 0.01$. The influence of n_p on the bandwidth is negligible in the case of $\delta = 0.05$ due to the low influence of the critical angle θ_p on the leaky mode losses. It can be seen from figures 3 and 4 that the improvement of the bandwidth of the W-type PCSF, with δ change, is more pronounced at longer fiber lengths. Thus, at the achievable bandwidth in W-type PCSFs at a fiber length of 2 km, it is about 15 times higher than the bandwidth of the SI PCSF. Since narrow launch beam distributions are assumed in the calculations, only the guided modes are excited at the input fiber length. Therefore, the role of leaky modes is of less significance at short fiber lengths. Due to mode coupling, more leaky modes are filtered out at longer fiber lengths, leading to significant improvements in the W-type PCSF's bandwidth. The effect of the launch beam distributions on the bandwidth is more pronounced at a shorter fiber length. Using narrow launch beam distributions (FWHM = 2°), the improvement in the bandwidth is very pronounced; while, in the case of FWHM = 5.5° , the improvement in the bandwidth is negligible.

Figure 5 shows the trade-off relation between a bandwidth and a steady-state loss for the W-type PCSF and the SC PCSF. By increasing the leaky mode losses, the steady-state losses also increase. A trade-off relation between the bandwidth and steady-state loss would have to be considered in designing the optimum W-type PCSF by controlling the parameters of the intermediate layer thickness and the refractive index of the outer cladding.

To our best knowledge, for the first time, by solving the time-dependent power flow equation, we have shown that the bandwidth in W-type PCSFs is significantly higher (up to 15 times at fiber length of 2 km) than the bandwidth of the SI PCSF. It is an important conclusion since the PCSFs are

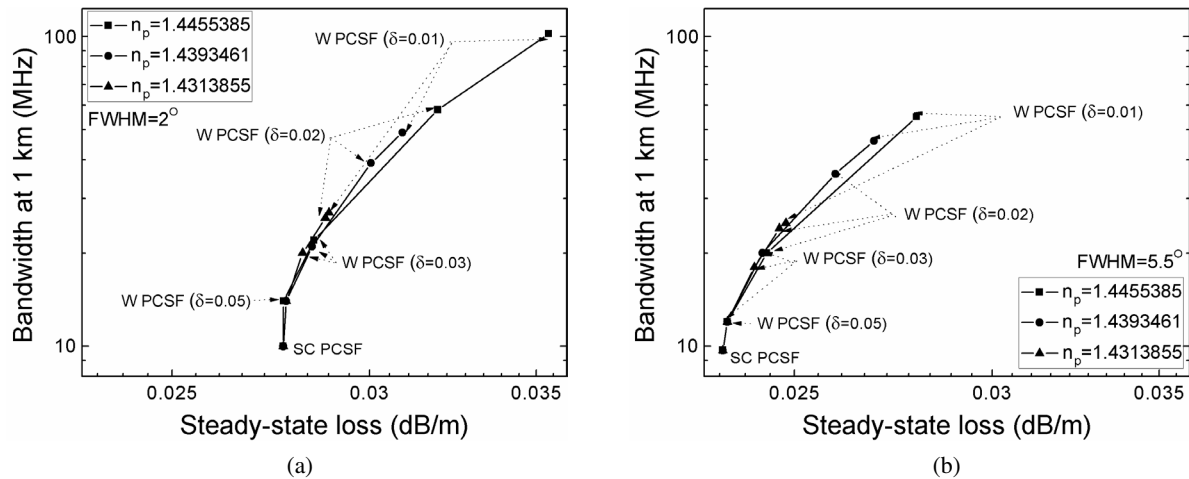


Figure 5. Numerical results for trade-off relation between bandwidth and steady-state loss for W-type PCSF and SC PCSF, for Gaussian launch beam distribution with (a) FWHM = 2° and (b) FWHM = 5.5°.

often used in a long-distance communication. A significant enhancement of the bandwidth of such W-type PCSFs could be achieved with an appropriate choice of the parameters of the intermediate layer and launch beam width. Similarly, in our previous work [21] we have shown that the bandwidth of a W-type plastic optical fiber is also higher than the bandwidth of the original SC plastic optical fiber.

4. Conclusion

A new design of a PCSF with a characteristic W-shaped index profile is proposed. It has been shown that the bandwidth of the W-type PCSF is significantly higher than the bandwidth of the SC PCSF. This enhancement of the bandwidth is due to the leaky mode losses in the W-type PCSF, which reduces the number of guided modes along the fiber, decreasing the modal dispersion and increasing the bandwidth. The bandwidth of the W-type PCSF can be enhanced by reducing the width of its inner cladding, increasing the refractive index of the outer cladding and using a narrow launch beam distribution. Since, with increasing leaky mode losses, the steady-state losses also increase, a trade-off relation between the bandwidth and loss would have to be considered in designing the optimum W-type PCSF.

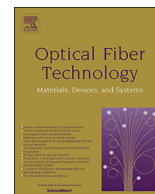
Acknowledgments

This work was supported in part by a grant from the Serbian Ministry of Education, Science and Technological Development through the Project No. 171011 and by the Strategic Research Grant of City University of Hong Kong (Project No. CityU 7004851).

References

- [1] Jeunhomme L, Fraise M and Pocholle J P 1976 Propagation model for long step-index optical fibers *Appl. Opt.* **15** 3040–6
- [2] Koeppen C, Shi W D, Chen R F and Garito A F 1998 Properties of plastic optical fibers *J. Opt. Soc. Am. B* **15** 727–39
- [3] Ruddy V and Shaw G 1995 Mode coupling in large-diameter polymer-clad silica fibers *Appl. Opt.* **34** 1003–6
- [4] Savović S and Djordjević A 2017 Mode coupling in multimode step-index plastic-clad silica fibers with corrugated surfaces *Opt. Laser Technol.* **97** 400–4
- [5] Savović S and Djordjević A 2018 Mode coupling and its influence on space division multiplexing in step-index plastic-clad silica fibers *Opt. Fiber Technol.* **46** 192–7
- [6] Yamashita T and Kagami M 2005 Fabrication of light-induced self-written waveguides with a W-shaped refractive index profile *J. Lightwave Technol.* **23** 2542–8
- [7] Asai M, Inuzuka Y, Koike K, Takahashi S and Koike Y 2011 High-bandwidth graded-index plastic optical fiber with low-attenuation, high-bending ability, and high-thermal stability for home-networks *J. Lightwave Technol.* **29** 1620–6
- [8] Mikoshihba K and Kajioka H 1978 Transmission characteristics of multimode W-type optical fiber: experimental study of the effect of the intermediate layer *Appl. Opt.* **17** 2836–41
- [9] Zhong N, Zhao M, Zhong L, Liao Q, Zhu X, Luo B and Li Y 2016 A high-sensitivity fibre-optic evanescent wave sensor with a three-layer structure composed of Canada balsam doped with GeO₂ *Biosens. Bioelectron.* **85** 876–82
- [10] Xin X, Zhong N, Liao Q, Cen Y, Wu R and Wang Z 2017 High-sensitivity four-layer polymer fibre-optic evanescent wave sensor *Biosens. Bioelectron.* **91** 623–8
- [11] Zhong N, Wang Z, Chen M, Xin X, Wu R, Cen Y and Li Y 2018 Three-layer-structure polymer optical fiber with a rough inter-layer surface as a highly sensitive evanescent wave sensor *Sens. Actuators B* **254** 133–42
- [12] Tanaka T, Yamada S, Sumi M and Mikoshihba K 1977 Micro-bending losses of doubly clad (W-type) optical fibers *Appl. Opt.* **18** 2391–4
- [13] Gloge D 1973 Impulse response of clad optical multimode fibers *Bell Syst. Tech. J.* **52** 801–16
- [14] Savović S, Simović A and Djordjević A 2012 Explicit finite difference solution of the power flow equation in W-type optical fibers *Opt. Laser Technol.* **44** 1786–90
- [15] Gloge D 1972 Optical power flow in multimode fibers *Bell Syst. Tech. J.* **51** 1767–83
- [16] Tanaka T P and Yamada S 1980 Numerical solution of power flow equation in multimode W-type optical fibers *Appl. Opt.* **19** 1647–52
- [17] Rousseau M and Jeunhomme L 1977 Numerical solution of the coupled-power equation in step index

- optical fibers *IEEE Trans. Microw. Theory Tech.* **25** 577–85
- [18] Gambling W A, Payne D N and Matsumura H 1975 Mode conversion coefficients in optical fibers *Appl. Opt.* **14** 1538–42
- [19] Simović A, Savović S, Drljača B and Djordjevich A 2015 Influence of the fiber design and launch beam on transmission characteristics of W-type optical fibers *Opt. Laser Technol.* **68** 151–9
- [20] Kagami M, Kawasaki A, Yonemura M, Nakai M, Mena P V and Selviah D R 2016 Encircled angular flux representation of the modal power distribution and its behavior in a step index multimode fiber *J. Lightwave Technol.* **34** 943–51
- [21] Simović A, Savović S, Drljača B and Djordjevich A 2019 Enhanced bandwidth of W type plastic optical fibers designed from single clad step index plastic optical fibers *Opt. Laser Technol.* **111** 629–34



Enhancement of the bandwidth of W-type glass optical fibers in the infrared wavelength region

Ana Simović^a, Svetislav Savović^{a,b,*}, Branko Drljača^c, Alexandar Djordjevich^{b,*}

^a University of Kragujevac, Faculty of Science, R. Domanovića 12, 34000 Kragujevac, Serbia

^b City University of Hong Kong, 83 Tat Chee Avenue, Hong Kong, China

^c Faculty of Science, University of Kosovska Mitrovica, Lole Ribara 29, Kosovska Mitrovica, Serbia

ARTICLE INFO

Keywords:

W-type glass optical fiber
Power flow equation
Bandwidth
Steady-state loss
Infrared wavelength region

ABSTRACT

Transmission characteristics (bandwidth and steady state loss) of multimode W-type glass optical fibers are investigated by solving the time-dependent power flow equation. Results show how the bandwidth in W-type glass optical fibers can be enhanced by shifting from the red to infrared wavelength region for different depths and widths of the intermediate layer as well as for different launch excitations. Such characterization of these fibers is consistent with their manifested effectiveness in reducing modal dispersion and bending loss.

1. Introduction

The analysis and design of refractive index profile of multimode fiber with a view of advancing fiber transmission characteristics have attracted a much attention in the last few decades [1–3]. A variety of designs of step-index, graded index and W-type fibers has been proposed either for a long-distance communication links or high capacity local area networks [1–7]. It has been shown that waveguide dispersion is smaller in the W-type fiber than it is in the single-clad (SC) fiber [5]. W-type fiber has a wide transmission bandwidth and lower bending losses compared to a corresponding SC fiber. For glass optical fibers, the bandwidth-distance product is typically around 30 MHz·km for the SC variety and around 50 MHz·km for the W-type. For plastic optical fibers, these figures would typically be 15 MHz·km for the SC and 200 MHz·km for the W-type fibers [3,7,8].

Differential mode-attenuation and mode coupling strongly affect the transmission characteristics of multimode optical fibers. Differential mode-attenuation is a consequence of absorption and scattering of light within the fiber material, which reduces the transmitted power. Mode coupling transfers power between individual modes which is caused by fiber's intrinsic random anomalies [9]. Mode coupling reduces modal dispersion thus increasing fiber bandwidth. On the other side, mode coupling increases fiber loss especially in a curved fiber [10] and degrades the beam quality. W-type fiber properties differ from the ones pertaining to SC fibers [5,8,11]. This is because of the lossy leaky modes that propagate within the W-type fiber's intermediate layer. Higher order modes which propagate along the W-type fiber reduce its

bandwidth and necessitate that the group delay difference between modes be minimized by optimizing the fiber's refractive index profile [11]. As modal attenuation, coupling and dispersion affect transmission characteristics of the W-type optical fiber, methods for calculating their contributions are needed.

Light launched at a specific angle $\theta_0 > 0$ with respect to the fiber axis can form a ring radiation pattern at the output end of only short fibers. Because of mode coupling, such a ring evolves into a disk at the end of longer fibers. "Coupling length" L_c marks a fiber length at which a ring-pattern of the highest guiding modes evolves into a disk. An equilibrium mode distribution (EMD) exists beyond the coupling length L_c of the fiber. It is characterized by the absence of rings regardless of launch conditions (launch angle and width of the launch distribution) [9]. At fiber lengths $z > L_c$ the bandwidth becomes proportional to $1/z^{1/2}$ instead of $1/z$ (z is the fiber length). The shorter the length L_c , the earlier the bandwidth switches from the functional dependence of $1/z$ to $1/z^{1/2}$ (slower bandwidth decrease) [12]. Mode coupling leads to the formation of a steady-state distribution (SSD) that is reached some distance $z_s > L_c$ from the input fiber end. The steady-state is characterized by the one and the same intensity distribution in the far field independently on the launch mode that produced it [9,13].

In this work, we investigated how the bandwidth can be enhanced in the infrared wavelength region for variously configured W-type optical fibers in the terms of depth and width of the fiber's intermediate layer. This was done for two different launch excitation conditions. One should mention that modal attenuation, coupling and dispersion are included in our calculations (material dispersion has not been taken into account [20]).

* Corresponding authors at: University of Kragujevac, Faculty of Science, R. Domanovića 12, 34000 Kragujevac, Serbia (S. Savović).

E-mail addresses: savovic@kg.ac.rs (S. Savović), mealex@cityu.edu.hk (A. Djordjevich).

2. Power flow equation

The time-dependent power flow for multimode W-type fibers is described by the following coupled-power equation [14]:

$$\frac{\partial p(\theta, z, t)}{\partial z} + \tau(\theta) \frac{\partial p(\theta, z, t)}{\partial t} = -\alpha(\theta)p(\theta, z, t) + \frac{1}{\theta} \frac{\partial}{\partial \theta} \left[\theta D(\theta) \frac{\partial p(\theta, z, t)}{\partial \theta} \right] \quad (1)$$

where t is time; $p(\theta, z, t)$ is power distribution over angle, space, and time; $\tau(\theta)$ is mode delay per unit length; $D(\theta)$ is the mode-dependent coupling coefficient; and $\alpha(\theta) = \alpha_0 + \alpha_d(\theta)$ is the modal attenuation, where α_0 represents conventional losses due to absorption and scattering. The term α_0 leads only to a multiplier $\exp(-\alpha_0 z)$ in the solution and is thus neglected. The second term in the expansion of $\alpha(\theta)$ is dominant for higher order modes. The coupling coefficient is usually assumed constant [12–20]. The method of solving Eq. (1) and calculation of the bandwidth of W-type optical fibers has been described in more detail in our previously reported work [19].

For W-type fiber shown in Fig. 1, the modes whose propagation angles are between $\theta_p \cong (2\Delta_p)^{1/2}$ and $\theta_q \cong (2\Delta_q)^{1/2}$, where $\Delta_q = (n_0 - n_q)/n_0$ and $\Delta_p = (n_0 - n_p)/n_0$, are leaky modes. Attenuation constants of leaky modes are given as [9,12,15]:

$$\alpha_L(\theta) = \frac{4(\theta^2 - \theta_p^2)^{1/2} \theta^2 (\theta_q^2 - \theta^2)}{a(1 - \theta^2)^{1/2} \theta_q^2 (\theta_q^2 - \theta_p^2)} \exp[-2\delta a n_0 k_0 (\theta_q^2 - \theta^2)^{1/2}] \quad (2)$$

where k_0 is the free-space wave number, a is core radius and δa intermediate layer (inner cladding) width. The modal attenuation in a W-type fiber can be expressed as [9,12,15]:

$$\alpha_L(\theta) = \begin{cases} 0; & \theta \leq \theta_p \\ \alpha_L(\theta); & \theta_p < \theta < \theta_q \\ \infty; & \theta \geq \theta_q \end{cases} \quad (3)$$

One can see that attenuation constants of leaky modes (2) are wavelength dependent through the free-space wave number k_0 .

A W-type fiber can be regarded as a system consisting of SC_q fiber and cladding. In the SC_q fiber, only modes with propagation angles smaller than the critical angle θ_q can be guided. When the SC_q fiber is surrounded with a medium of index n_p , the lower order modes, whose propagation angles are smaller than the critical angle of the SC_p fiber θ_p , remain guided. The higher order modes with angles between θ_p and θ_q are transformed into leaky modes. It is shown that because of the strong dependence of $\alpha_L(\theta)$ on the intermediate layer width δa , steady-state characteristics of a W-type fiber depend on δa and coincide with those of SC_p and SC_q fibers in the limits of $\delta \rightarrow 0$ and $\delta \rightarrow \infty$, respectively [15]. Another parameter which influences the power distribution in W-type optical fibers is depth of the intermediate layer (Fig. 1). One should mention that bandwidth enhancement of W-type plastic optical

fibers in respect to the graded index plastic optical fibers at a $\lambda = 650$ nm wavelength has been reported by Ishigure et al. [21]. In contrast to the W-type glass optical fibers investigated in this work, which have a step-index distribution of the fiber core (Fig. 1), the W-type plastic optical fiber with more complex graded index distribution of the fiber core is investigated by Ishigure et al. [21].

In this work, in our best knowledge for the first time, we investigated how the bandwidth in W-type glass optical fibers can be enhanced by shifting from the red to infrared wavelength region for different depths and widths of the intermediate layer as well as for different launch excitations. The results obtained could be applied when designing W-type glass optical fibers.

3. Numerical results

In this paper, we analyze bandwidth as well as steady-state loss at different wavelengths in a variously configured W-type glass optical fiber. The fiber structural characteristics were: $\Delta_p = 0.2\%$ ($\theta_p \cong 3.62^\circ$), $\Delta_q = 0.7\%$ ($\theta_q \cong 6.76^\circ$) and $2a = 60 \mu\text{m}$ [13,15,17–20]. Further, $n_0 = 1.46$ was used in the calculations. In order to investigate the influence of wavelength on the transmission characteristics of this fiber for different depths and widths of the intermediate layer as well as launch excitation, we consider the case when the core index n_0 and outer cladding index n_p are fixed. The depth of the intermediate layer is varied by changing the initial value of $\Delta_q = 0.7\%$ by $\pm 25\%$ – we thus analyzed the following three cases: $\Delta_q = 0.525\%$ ($\theta_q \cong 5.87^\circ$), $\Delta_q = 0.7\%$ ($\theta_q \cong 6.76^\circ$) and $\Delta_q = 0.875\%$ ($\theta_q \cong 7.58^\circ$). The change in θ_q for constant θ_p changes the number of leaky modes as well as their attenuation (6). We solved the time-dependent power flow equation (2) using explicit finite difference method for the coupling coefficient $D = 2.3 \times 10^{-7} \text{ rad}^2/\text{m}$ [8,13] for two different normalized intermediate layer widths δ ($\delta = 0.2$ and $\delta = 0.5$; actual widths δa are $0.2 \cdot 30 \mu\text{m}$ and $0.5 \cdot 30 \mu\text{m}$). The number of modes for different θ_p and θ_q excitations are given in Table 1.

Our numerical solution of the time-dependent power flow equation is illustrated in Fig. 2. It shows, in three inserts corresponding to three depths with respective $\Delta_q = 0.525, 0.7$ and 0.875% , and for the θ_q launch excitation, the evolution of the W-fiber's bandwidth at 1 km with wavelength for different widths of intermediate layer δ . It is apparent in Fig. 2 that the W-fiber bandwidth increases with increasing wavelength for all widths and depths of the intermediate layer. This is explained by the rise of the leaky mode losses with increasing wavelength as fewer leaky modes remain guided along the fiber; which decreases modal dispersion and increases bandwidth [20]. Also with increasing wavelength, SSD and EMD distributions develop at shorter fiber lengths, resulting in faster bandwidth improvement [20]. One can observe in Fig. 2(a) that, for the smallest width ($\delta = 0.2$) and depth of intermediate layer ($\Delta_q = 0.525\%$), the influence of wavelength on bandwidth is negligible. This is due to large leaky mode losses; as these modes are practically not guided along the fiber, modal dispersion (bandwidth) changes little. With increasing depth of the intermediate

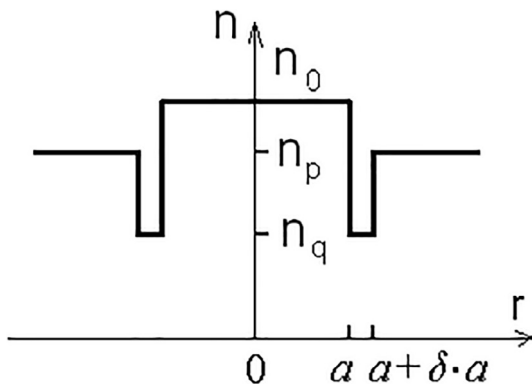
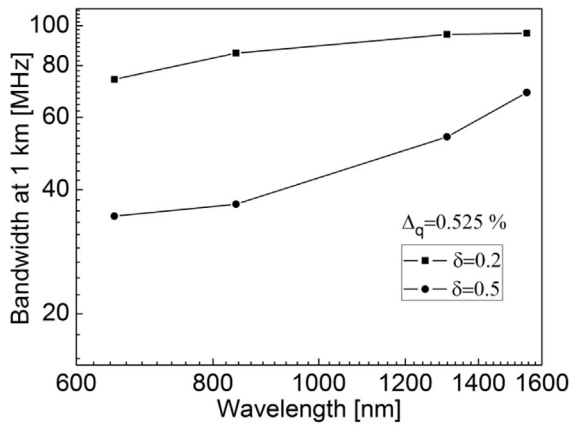


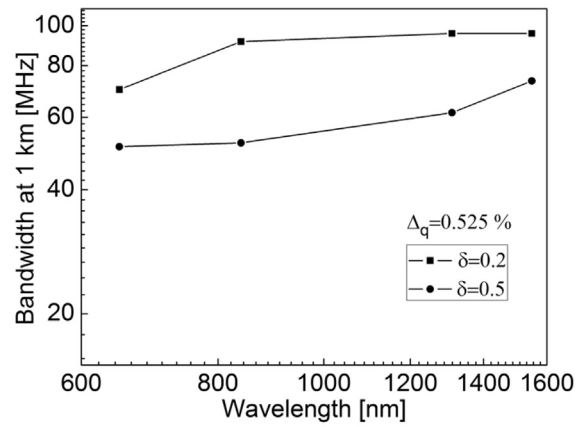
Fig. 1. Refractive index profile of a W-type fiber.

Table 1
Number of modes in W-type glass optical fiber for different θ_p and θ_q excitations at different wavelengths λ .

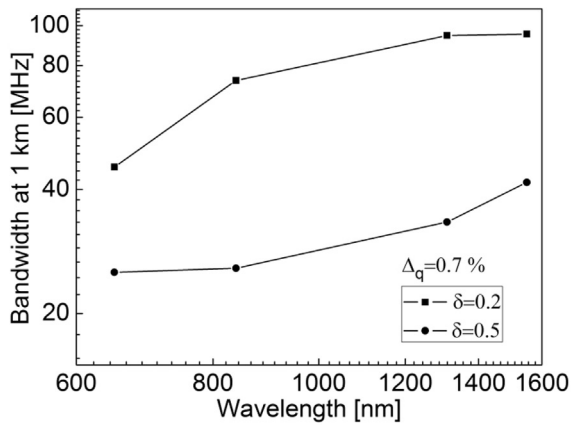
	Number of modes			
	Wavelength λ [nm]			
	650	840	1310	1550
θ_p excitation				
$\theta_p = 3.6^\circ$	338	214	88	62
$\theta_q = 5.87^\circ$	924	562	231	165
θ_q excitation				
$\theta_q = 6.76^\circ$	1200	744	306	218
$\theta_q = 7.58^\circ$	1512	934	384	274



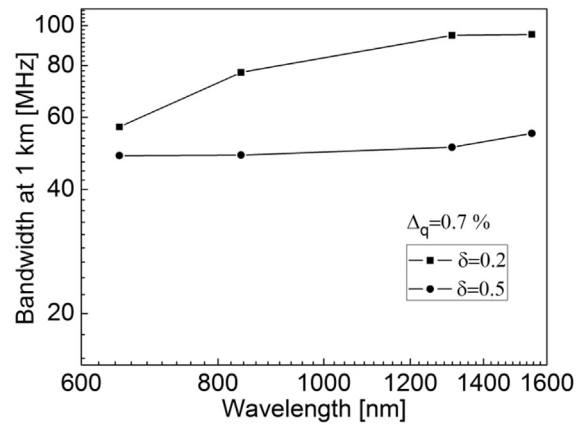
(a)



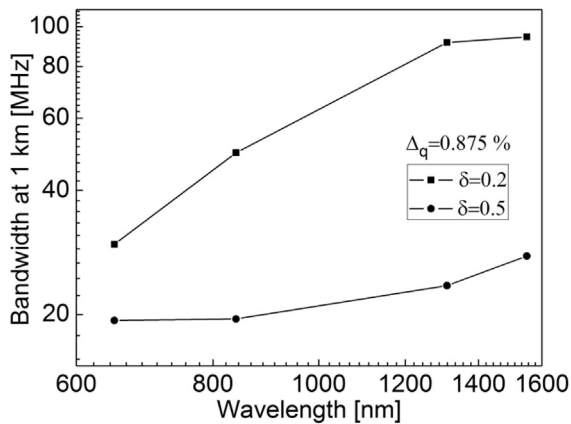
(a)



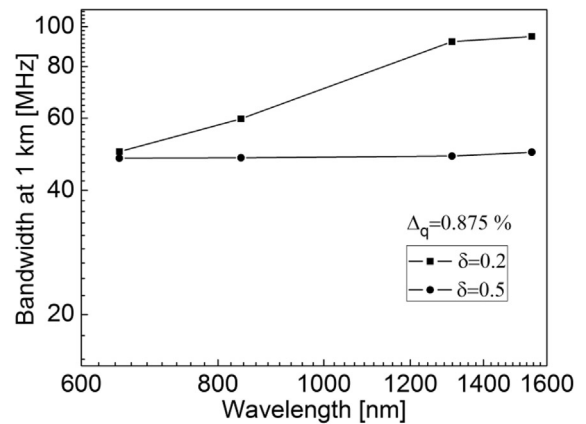
(b)



(b)



(c)



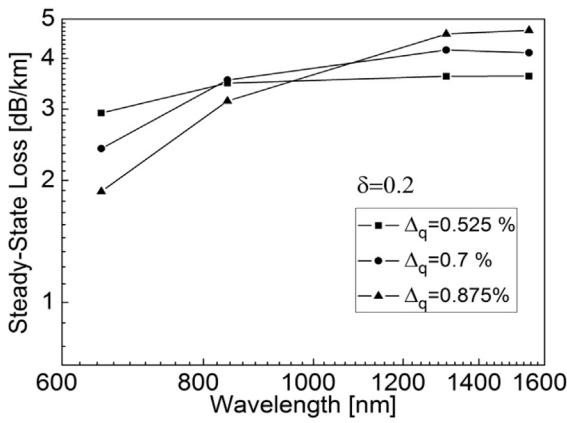
(c)

Fig. 2. Bandwidth at 1 km as a function of wavelength for θ_q launch excitation, $\delta = 0.2$ and 0.5 , and (a) $\Delta_q = 0.525\%$, (b) $\Delta_q = 0.7\%$ and (c) $\Delta_q = 0.875\%$.

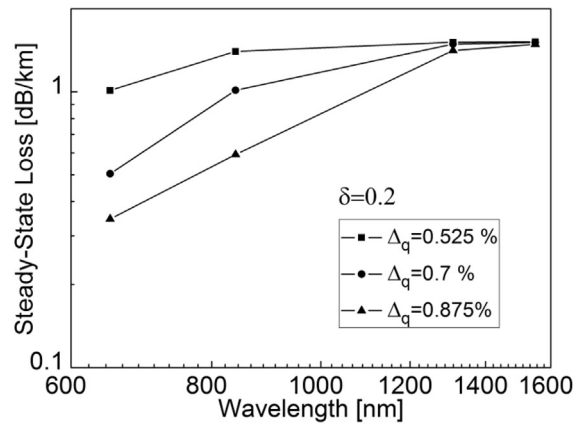
layer, there is a wavelength-dependent decrease of bandwidth. This decrease is more pronounced at short wavelengths as leaky mode losses are then reduced, resulting in the rise of modal dispersion and drop of fiber bandwidth. For the wider layer ($\delta = 0.5$), the rise in bandwidth with wavelength is most pronounced for the smallest depth of the intermediate layer ($\Delta_q = 0.525\%$). The bandwidth drop with increasing depth of the intermediate layer is more pronounced at longer wavelengths. For the wider and deeper layer (the case of $\delta = 0.5$ and $\Delta_q = 0.875\%$), bandwidth remains constant over the relevant wavelength range because the majority of leaky modes remain guided along the fiber.

Fig. 3. Bandwidth at 1 km as a function of wavelength for θ_p launch excitation, $\delta = 0.2$ and 0.5 , and (a) $\Delta_q = 0.525\%$, (b) $\Delta_q = 0.7\%$ and (c) $\Delta_q = 0.875\%$.

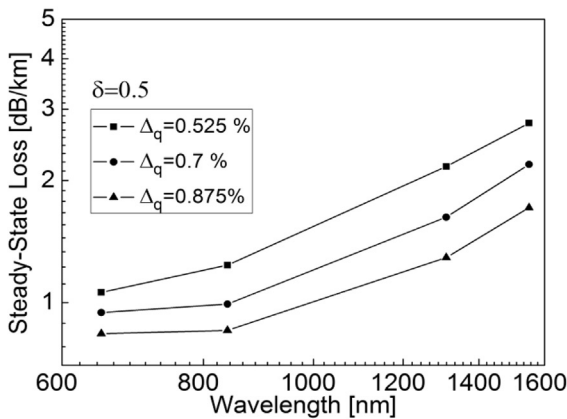
Similar considerations, but for the θ_p launch excitation, where only guiding modes are excited at the input fiber length, are shown in Fig. 3. For all depths of the intermediate layer, bandwidth at 1 km is generally higher in this figure with θ_p launch excitation relative to that with the launch excitation of both guiding and leaky modes (θ_q launch excitation), particularly for deeper intermediate layers ($\Delta_q = 0.7$ and 0.875%) and higher value of $\delta = 0.5$. Conversely for the thinner layer with $\delta = 0.2$, leaky modes are practically not guided due to their high losses; the θ_q launch excitation is then similar to θ_p launch excitation and so is the bandwidth. It can be seen from Figs. 2 and 3 that for $\delta = 0.2$, there is a maximum value of the bandwidth-distance product which is



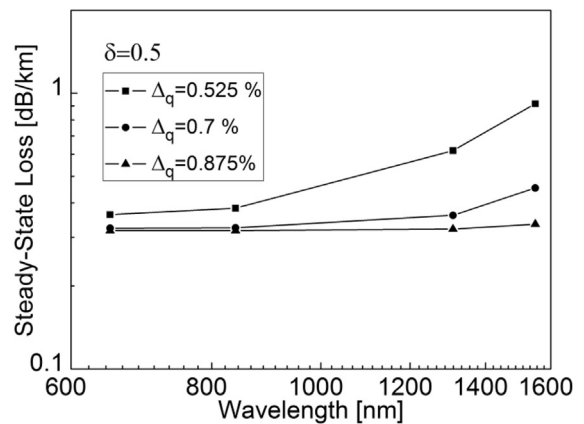
(a)



(a)



(b)



(b)

Fig. 4. Steady-state loss at 1 km as a function of wavelength for θ_q launch excitation, $\Delta_q = 0.525\%$, 0.7% and 0.875% , in case of (a) $\delta = 0.2$ and (b) $\delta = 0.5$.

Fig. 5. Steady-state loss at 1 km as a function of wavelength for θ_p launch excitation, $\Delta_q = 0.525\%$, 0.7% and 0.875% , in case of (a) $\delta = 0.2$ and (b) $\delta = 0.5$.

reached at wavelength $1.31 \mu\text{m}$ or $1.55 \mu\text{m}$. In the case of $\delta = 0.5$, the bandwidth-distance product monotonically increases with increasing the wavelength.

Figs. 4 and 5 show steady-state loss as a function of wavelength for θ_q and θ_p launch excitations, respectively. One can observe that the influence of wavelength on steady-state loss is negligible for longer wavelengths in the case of narrow layer with $\delta = 0.2$, and for shorter wavelengths in the case of the wider layer with $\delta = 0.5$. It is also apparent from Fig. 4a for $\delta = 0.2$ that steady-state losses increase at longer wavelengths with the increasing depth of the intermediate layer – because a greater number of leaky modes can be excited at the input end of the fiber. At longer wavelengths and for $\delta = 0.2$, leaky mode losses become significant already over short fiber lengths and these modes are mostly not guided further. Losses of leaky modes rise with deeper intermediate layer, contributing to steady state losses. For the width with $\delta = 0.5$, the power carried by leaky modes remains guided over longer fiber lengths.

Although the W-type glass optical fibers investigated in this work have a step-index distribution of the fiber core (Fig. 1), which is simpler than the graded index distribution of a fiber core, a significant enhancement of the bandwidth of such W-type glass optical fibers could be achieved by increasing the operating wavelength, with appropriate choice of the excitation type and parameters of the intermediate layer of the W-fiber.

Finally, one should mention here that a numerical modeling of the bandwidth of W-type glass optical fibers presented in this work can be employed in investigation of other W-type optical fibers, such as a W-

type plastic optical fibers and W-type plastic clad silica optical fibers, which have a step-index distribution of the core.

4. Conclusions

Bandwidth and steady-state loss are calculated by the time-dependent power flow equation over a range of light wavelengths and for two types of input into a W-type glass optical fiber with a varied depth and width of the intermediate layer. It is shown that bandwidth of W-fibers broadens for longer wavelengths for all widths and depths of the intermediate layer and for both kinds of launch excitation. This broadening of bandwidth results from higher leaky mode losses and from the consequent drop in modal dispersion. Moreover, SSD and EMD occur at shorter fiber lengths as wavelength is elongated; the bandwidth improvement therefore commences sooner along the fiber. However, this influence of wavelength on bandwidth is negligible for narrow and shallow intermediate layers. With deepening of the intermediate layer, bandwidth drops as a function of wavelength; more notably so for short wavelengths. For the width with $\delta = 0.5$, the wavelength-dependent bandwidth broadening is most pronounced for the shallowest intermediate layer ($\Delta_q = 0.525\%$); conversely for the deepest and widest intermediate layer ($\Delta_q = 0.875\%$ and $\delta = 0.5$), leaky mode losses rise only slightly with wavelength and, hence, modal dispersion and bandwidth then vary little.

At longer wavelengths, excitation of only guiding modes (θ_p launch excitation) leads to higher bandwidth relative to that with excitation of

both guiding and leaky modes (θ_q launch excitation). The difference is largely insignificant for a narrow ($\delta = 0.2$) and shallow intermediate layer ($\Delta_q = 0.525\%$). Because leaky mode losses are large for the θ_q launch excitation of the fiber with a narrow intermediate layer ($\delta = 0.2$), leaky modes are mostly not guided and the remaining modes resemble the θ_p launch excitation. While more of the leaky modes can be excited when the W-fiber's intermediate layer is deeper, they encounter significant losses in fibers with a narrow layer, at longer wavelengths.

It has been shown that the influence of wavelength on steady-state losses is negligible at longer wavelengths when the intermediate layer is narrow ($\delta = 0.2$), and at shorter wavelengths when this layer is wider ($\delta = 0.5$). Longer wavelengths boost bandwidth. The launch excitation type, wavelength, and parameters of the intermediate layer of the W-fiber all affect bandwidth and steady-state loss and have to be considered to match the application at hand.

Acknowledgments

The work described in this paper was supported by the Strategic Research Grant of City University of Hong Kong (Project No. CityU 7004600) and by a grant from Serbian Ministry of Education, Science and Technological Development (Project No. 171011).

References

- [1] L. Jeunhomme, M. Fraise, J.P. Pocholle, Propagation model for long step-index optical fibers, *Appl. Opt.* 15 (1976) 3040–3046.
- [2] Y. Daido, E. Miyauchi, T. Iwama, T. Otsuka, Determination of modal power distribution in graded-index optical waveguides from near-field patterns and its application to differential mode attenuation measurement, *Appl. Opt.* 18 (1979) 2207–2213.
- [3] T. Yamashita, M. Kagami, Fabrication of light-induced self-written waveguides with a W-shaped refractive index profile, *J. Lightwave Technol.* 23 (2005) 2542–2548.
- [4] M. Asai, Y. Inuzuka, K. Koike, S. Takahashi, Y. Koike, High-bandwidth graded-index plastic optical fiber with low-attenuation, high-bending ability, and high-thermal stability for home-networks, *J. Lightwave Technol.* 29 (2011) 1620–1626.
- [5] K. Mikoshiba, H. Kajioka, Transmission characteristics of multimode W-type optical fiber: experimental study of the effect of the intermediate layer, *Appl. Opt.* 17 (1978) 2836–2841.
- [6] J. Dugas, G. Maurel, Mode-coupling processes in polymethyl methacrylate-core optical fibers, *Appl. Opt.* 31 (1992) 5069–5079.
- [7] W. Daum, J. Krauser, P.E. Zamzow, O. Ziemann, *Polymer Optical Fibers for Data Communication*, Springer, Berlin, 2002.
- [8] T. Tanaka, S. Yamada, M. Sumi, K. Mikoshiba, Microbending losses of doubly clad (W-type) optical fibers, *Appl. Opt.* 18 (1977) 2391–2394.
- [9] S. Savović, A. Djordjević, A. Simović, B. Drljača, Equilibrium mode distribution and steady-state distribution in 100–400 μm core step-index silica optical fibers, *Appl. Opt.* 50 (2011) 4170–4173.
- [10] M.A. Losada, I. Garcés, J. Mateo, I. Salinas, J. Lou, J. Zubia, Mode coupling contribution to radiation losses in curvatures for high and low numerical aperture plastic optical fibers, *J. Lightwave Technol.* 20 (2002) 1160–1164.
- [11] K. Takahashi, T. Ishigure, Y. Koike, Index profile design for high-bandwidth W-shaped plastic optical fiber, *J. Lightwave Technol.* 24 (2006) 2867–2876.
- [12] A. Simović, S. Savović, B. Drljača, A. Djordjević, Influence of intermediate layer on transmission characteristics of W-type optical fibers, *Opt. Laser Technol.* 57 (2014) 565–569.
- [13] A. Simović, A. Djordjević, S. Savović, Influence of depth of intermediate layer on power distribution in W-type optical fibers, *Appl. Opt.* 51 (2012) 4896–4901.
- [14] D. Gloge, Optical power flow in multimode fibers, *Bell Syst. Tech. J.* 51 (1972) 1767–1783.
- [15] T.P. Tanaka, S. Yamada, Numerical solution of power flow equation in multimode W-type optical fibers, *Appl. Opt.* 19 (1980) 1647–1652.
- [16] T.P. Tanaka, S. Yamada, Steady-state characteristics of multimode W-type fibers, *Appl. Opt.* 18 (1979) 3261–3264.
- [17] S. Savović, A. Simović, A. Djordjević, Explicit finite difference solution of the power flow equation in W-type optical fibers, *Opt. Laser Technol.* 44 (2012) 1786–1790.
- [18] S. Savović, A. Simović, A. Djordjević, Influence of width of launch beam distribution on equilibrium mode distribution in W-type glass optical fibers, *Opt. Laser Technol.* 48 (2013) 565–569.
- [19] A. Simović, S. Savović, B. Drljača, A. Djordjević, Influence of the fiber design and launch beam on transmission characteristics of W-type optical fibers, *Opt. Laser Technol.* 68 (2015) 151–159.
- [20] A. Djordjević, A. Simović, S. Savović, B. Drljača, Wavelength dependence of leaky mode losses and steady state distribution in W-fibers, *Opt. Commun.* 419 (2018) 1–7.
- [21] T. Ishigure, H. Endo, K. Ohdoko, K. Takahashi, Y. Koike, Modal bandwidth enhancement in a plastic optical fiber by W-refractive index profile, *J. Lightwave Technol.* 23 (2005) 1754–1762.



Calculation of the bandwidth of W-type photonic crystal fibers by time-dependent power flow equation



Milan S. Kovačević^a, Ljubica Kuzmanović^a, Ana Simović^a, Svetislav Savović^{a,c},
Branko Drljača^b, Alexandar Djordjevich^{c,*}

^a University of Kragujevac, Faculty of Science, Department of Physics, Kragujevac, Serbia

^b University of Priština, Faculty of Science, L. Ribara 29, Kosovska Mitrovica, Serbia

^c City University of Hong Kong, Department of Mechanical and Biomedical Engineering, Kowloon, Hong Kong, China

ARTICLE INFO

Keywords:

Photonic crystal fiber
W-type fiber
Power flow equation
Bandwidth

ABSTRACT

A multimode photonic crystal fiber with a solid-core takes the characteristic W-shaped index profile upon forming an inner cladding layer with its own value of the effective refractive index corresponding to the distinct size and/or spacing of air holes in it. For various arrangements of air-holes, bandwidth is determined for such fiber by the time-dependent power flow equation. Fiber bandwidth is thus not only a function of transmission length but also of the spacing and size of air-holes as well of the number of bands with the distinct configuration of holes. These additional adjustable geometric parameters offer greater design flexibility. We have shown that bandwidth can be improved by reducing the number of rings of inner cladding air holes, decreasing the diameter of inner cladding air holes or exciting only guiding modes.

1. Introduction

This variation of refractive-index across an optical fiber has usually been achieved either by selective layering of materials or by chemical doping. Another method is by a micro-structured pattern of very small holes running the length of the “holey” or photonic crystal fibers (PCFs). A PCF may have a solid core and a hollow cladding as illustrated in Fig. 1. The pattern of holes lowers the effective refractive index of the cladding, enabling the fiber to guide light. The fiber’s refractive index profile can thus be tailored during the design process by the choice of this pattern of holes in the cladding. It can be seen from Fig. 1 that W-type PCF has two distinct cladding regions which have two different refractive indices. This is the reason for calling these two cladding regions as inner and outer cladding.

As micro-structured patterning of the fiber offers an additional flexibility to affect its sectional profile at the design stage, PCFs have demonstrated performance not matched by conventional fibers [1–7]. For example, “endlessly single-mode” PCFs have been described that operate in only the fundamental mode across a very wide spectrum of wavelengths [2]. Similarly, a PCF can have a hollow core. The photonic bandgap guidance [8–11] in such a hollow fiber permits the fiber’s “air core” to have a lower refractive index than the material of the cladding [12,13]. Among the many reported applications of

PCFs are those in connection to dispersion [14–16], birefringence [17], supercontinuum generation [18–20], wavelength conversion [21,22], optofluidics [23], and sensing [24].

Waveguide dispersion is smaller in the W-type fiber than it is in the single-clad fiber. The W-type fiber is also easier to splice. It has a wide transmission bandwidth and lower bending losses compared to a corresponding single-clad fiber because the number of guided modes in the W-type fiber is reduced. By analogy to W-type fibers that have double cladding (for the total of three optical layers), the second cladding in PCFs can be affected by altering the pattern of holes [25]. An intermediate layer is thus discernible in Fig. 1 as a ring-like band with larger holes than in the rest of the cladding (diameter d_q versus d_p). Hence, the effective index profile for the resulting fiber has three distinct values as illustrated at the bottom of Fig. 1 — which is characteristic of the W-type fiber profile.

The width of the material between holes in the cladding determines the PCF’s numerical aperture, NA. It tends to be limited to $NA \approx 0.55–0.60$ by the impracticality of cleaving fibers with even larger NAs having large holes and little material remaining between [26,27]. Notable examples of PCFs to mention are a heavy metal-oxide glass fiber [28] or a hollow core fiber that is filled with liquid [29]. With high NA PCFs, lensless focusing with excellent resolution was reported [30].

* Corresponding author.

E-mail addresses: savovic@kg.ac.rs (S. Savović), mealex@cityu.edu.hk (A. Djordjevich).

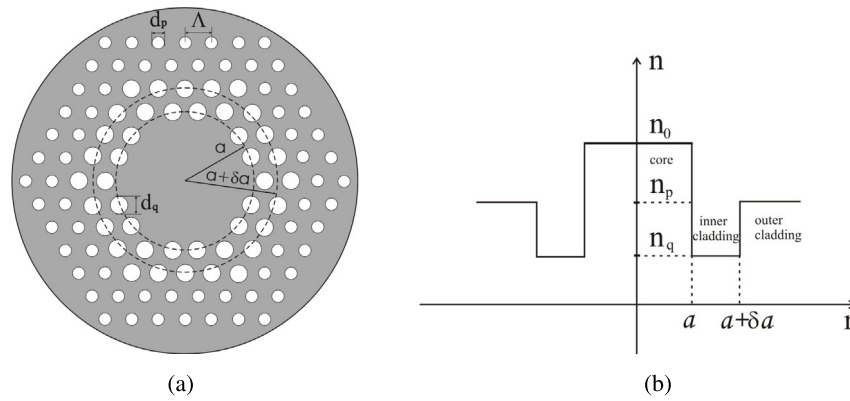


Fig. 1. (a) Cross section of double clad (W-type) multimode PCF with a solid-core and two rings of air holes in the inner cladding, where Λ is the hole-to-hole spacing (pitch), d_q and d_p are diameters of air holes in the inner and outer rings, respectively. Gray background indicates pure silica and white area indicates air holes, (b) refractive-index profile of the referent W-type PCF.

Air-holes in the inner cladding of the first-reported W-type PCF [31] were larger than in the outer cladding. For such multimode PCF with solid core and W-shaped index profile, we determined spatial transients of power distribution [32] for a variety of air-hole sizes, spacing between them and width (sometimes referred to as “depth”) of the intermediate layer containing holes. Such wealth of adjustable geometric parameters (d_q , d_p and Λ in Fig. 1) translates into a greater design flexibility over conventional W-type designs, leading to improved dispersion management.

Propagation characteristics of PCFs such as dispersion, loss, and particularly bandwidth have attracted much attention. The unit of measure of bandwidth is MHz km. It reveals the maximum rate of transmission by a 1 km long fiber. Intermodal dispersion is its principal limiting factor because core modes propagate at own – mutually unequal – group velocities, which leads to temporal pulse broadening with distance from the input fiber end. While PCFs are attractive for high-bandwidth communication, only designs with six holes [33] arranged hexagonally [34] have been considered thus far. Measurements of high bandwidth of graded-index PCFs are reported in [35]. It is evident that PCFs achieve high multimode performance while not needing complicated doping techniques typical of conventional fibers.

We investigate in this paper the bandwidth of a solid-core multimode W-type PCFs of pure silica having holes in the cladding arranged triangularly at constant pitch (Λ in Fig. 1). We solved the time-dependent power flow equation (1) for such fiber by the explicit finite differences method (EFDM) [36]. Results show the influence on bandwidth of the parametric variation of the size of air-holes and the width of the band containing them — for the excitation of only guided modes.

2. Design of a W-type PCF

Air-holes are normally of uniform size and form a regular triangular lattice over the PCF cladding. As already mentioned, this is altered in the W-type PCF by forming an intermediate layer in the cladding in which the size (d) or pitch (spacing density Λ) are adjusted for desired effective refractive index in that layer. Dispersion and other fiber properties are thereby engineered by additional design parameters, namely spacing and size of air-holes, as well as the width of the intermediate layer the modified holes are in (which is indicative of the number of modified air-holes such as one ring, two rings, etcetera). Since the holes in such inner cladding are larger than in other cladding, a W-type PCF is a result with the profile of its effective refractive index as in Fig. 1. Despite uniform material properties across the fiber, the central part without holes has the highest refractive index n_0 ; holes in the outer cladding reduce the effective value of such index; larger or more densely spaced holes in the inner cladding reduce it even more. In our model, the three layers are considered to be insulators and the outer cladding extends to infinity. Respectively, a and δa in Fig. 1 denote the core radius and width of the intermediate layer (inner cladding).

3. Time-dependent power flow equation

It is widely accepted to represent the discrete mode spectrum in multimode fibers by a continuous propagation angle θ relative to the fiber axis [37]. For multimode W-type fibers, the power flow is described by Gloge’s time-dependent coupled-power equation [37]:

$$\frac{\partial p(\theta, z, t)}{\partial z} + \tau(\theta) \frac{\partial p(\theta, z, t)}{\partial t} = -\alpha(\theta)p(\theta, z, t) + \frac{1}{\theta} \frac{\partial}{\partial \theta} \left[\theta D(\theta) \frac{\partial P(\theta, z, t)}{\partial \theta} \right] \quad (1)$$

where $p(\theta, z, t)$ is power distribution per unit solid angle at distance z and time t ; $\tau(\theta)$ is modal delay per unit length; $D(\theta)$ is the mode-dependent coupling coefficient; and $\alpha(\theta) = \alpha_0 + \alpha_d(\theta)$ is the modal attenuation, where α_0 represents conventional losses (absorption and scattering). The term α_0 leads only to a multiplier $\exp(-\alpha_0 z)$ in the solution and is thus neglected. The boundary conditions are $p(\theta_m, z) = 0$ where θ_m is the maximum propagation angle, and $D(\theta)(\partial p/\partial \theta) = 0$ at $\theta = 0$. The condition $P(\theta_m, z) = 0$ implies that modes with infinitely high loss do not carry power. Condition $D(\theta)(\partial p/\partial \theta) = 0$ at $\theta = 0$ indicates that the coupling is limited to modes propagating with $\theta > 0$.

It is convenient to discuss obtaining frequency response in the frequency domain rather than in the time domain. The Fourier transformation of Eq. (1) becomes:

$$\frac{\partial P(\theta, z, \omega)}{\partial z} + j\omega\tau(\theta)P(\theta, z, \omega) = -\alpha(\theta)P(\theta, z, \omega) + \frac{1}{\theta} \frac{\partial}{\partial \theta} \left[\theta D(\theta) \frac{\partial P(\theta, z, \omega)}{\partial \theta} \right] \quad (2)$$

where $\omega = 2\pi f$ is the angular frequency, and

$$P(\theta, z, \omega) = \int_{-\infty}^{+\infty} p(\theta, z, t) \exp(-j\omega t) dt \quad (3)$$

The boundary conditions are

$$P(\theta_m, z, \omega) = 0, \quad D(\theta) \frac{\partial P(\theta, z, \omega)}{\partial \theta} \Big|_{\theta=0} = 0 \quad (4)$$

Coupling was said to occur mainly between neighboring modes because the coupling strength decreases fast with the mode spacing [37–41]. It is apparent that $P(\theta, z, \omega)$ is complex. By separating $P(\theta, z, \omega)$ into the real part $P_r(\theta, z, \omega)$ and imaginary part $P_i(\theta, z, \omega)$ and assuming a constant coupling coefficient D [40–42], Eq. (2) can be rewritten as the following simultaneous partial differential equations:

$$\begin{aligned} \frac{\partial P_r(\theta, z, \omega)}{\partial z} &= -\alpha(\theta)P_r(\theta, z, \omega) + \frac{D}{\theta} \frac{\partial P_r(\theta, z, \omega)}{\partial \theta} \\ &+ D \frac{\partial^2 P_r(\theta, z, \omega)}{\partial \theta^2} + \omega\tau P_i(\theta, z, \omega) \end{aligned} \quad (5a)$$

and

$$\frac{\partial P_r(\theta, z, \omega)}{\partial z} = -\alpha(\theta)P_r(\theta, z, \omega) + \frac{D}{\theta} \frac{\partial P_i(\theta, z, \omega)}{\partial \theta} + D \frac{\partial^2 P_i(\theta, z, \omega)}{\partial \theta^2} - \omega \tau P_r(\theta, z, \omega) \quad (5b)$$

where

$$P(\theta, z, \omega) = P_r(\theta, z, \omega) + jP_i(\theta, z, \omega) \quad (6)$$

If $P_r(\theta, z, \omega)$ and $P_i(\theta, z, \omega)$ are obtained by solving Eq. (5), the transmission characteristics can be calculated. Thus the frequency response $H(z, \omega)$ at distance z from the input end of the fiber is:

$$H(z, \omega) = \frac{2\pi \int_0^{\theta_m} \theta [P_r(\theta, z, \omega) + jP_i(\theta, z, \omega)] d\theta}{2\pi \int_0^{\theta_m} \theta [P_r(\theta, 0, \omega) + jP_i(\theta, 0, \omega)] d\theta} \quad (7)$$

The modal power distribution $P_F(\theta, z, \omega)$ and the spatial transient of power $P_L(z, \omega)$ can be obtained by:

$$P_F(\theta, z, \omega) = [P_r(\theta, z, \omega)^2 + P_i(\theta, z, \omega)^2]^{1/2} \quad (8)$$

$$P_L(z, \omega) = 2\pi \int_0^{\theta_m} \theta P_F(\theta, z, \omega) d\theta \quad (9)$$

A W-type fiber with index profile shown in Fig. 1b can be regarded as a system of an SC_q fiber and cladding [40]. In the SC_q fiber, the angle $\theta_q \cong (2\Delta_q)^{1/2}$ is the critical angle for the guided modes — where $\Delta_q = (n_0 - n_q)/n_0$. Similarly, the angle $\theta_p \cong (2\Delta_p)^{1/2}$ is the critical angle of a singly clad SC_p fiber that has only the outer cladding of the W-type fiber (and lacks the intermediate layer), where $\Delta_p = (n_0 - n_p)/n_0$. For the complete W-type fiber, the modes with propagation angles less than the critical angle θ_p remain guided. Those with angles between θ_p and θ_q are lossy leaky modes. Hence,

$$\alpha_L(\theta) = \frac{4(\theta^2 - \theta_p^2)^{1/2} \theta^2 (\theta_q^2 - \theta^2)}{a(1 - \theta^2)^{1/2} \theta_q^2 (\theta_q^2 - \theta_p^2)} \exp \left[-2\delta a n_0 k_0 (\theta_q^2 - \theta^2)^{1/2} \right] \quad (10)$$

where $k_0 = 2\pi/\lambda$ is the free-space wave number, a is core radius and δa intermediate layer (inner cladding) width. In an SC fiber, experimental results show that attenuation remains constant throughout the guided-mode region and rises quite steeply in the radiation-mode region [43]. Consequently, the modal attenuation in a W-type fiber can be expressed as:

$$\alpha_d(\theta) = \begin{cases} 0 & \theta \leq \theta_p \\ \alpha_L(\theta) & \theta_p < \theta < \theta_q \\ \infty & \theta \geq \theta_q \end{cases} \quad (11)$$

Modal delay is expressed in terms of θ by [41,44]:

$$\tau(\theta) = \frac{n_0}{c} \frac{1}{\cos \theta} \cong \frac{n_0}{c} \left(1 + \frac{\theta^2}{2} \right) = \tau_0 + \tau_d(\theta) \quad (12)$$

where c is the light velocity in free space. The first term τ_0 is common to all modes. It is the difference in group delay that determines the transmission bandwidth. Therefore, only $\tau_d(\theta)$ is to be considered in the calculations.

The bandwidth of a fiber determines the maximum transmission data rate and it is determined by the frequency response $H(z, \omega)$:

$$P_{L(out)}(z, \omega) = H(z, \omega)P_{L(in)}(z = 0, \omega) \quad (13)$$

The frequency response defines the bandwidth (–3 dB bandwidth) of the optical fiber as the frequency at which $H(z, \omega)$ is reduced to half the DC value, that is when it is reduced by 3 dB.

This method for determining bandwidth is the simplest, most effective and accurate if compared to other alternative approaches (such as ray tracing and electromagnetic theory) in modeling the three major effects which occur during the light transmission in multimode optical fiber: modal attenuation, mode coupling and modal dispersion. The other two mentioned approaches do not take into account all three

Table 1

Effective refractive index n_q for varied air-hole diameter d_q (μm), relative refractive index difference $\Delta_q = (n_0 - n_q)/n_0$, and the critical angle θ_q (wavelength: 850 nm).

Inner cladding				
d_q (μm)	2.0	2.1	2.2	2.3
n_q	1.423679	1.418848	1.412813	1.405174
$\Delta_q = (n_0 - n_q)/n_0$	0.018	0.021	0.026	0.045
θ_q (deg)	10.87	11.74	13.07	17.19

effects and/or are less accurate due to the difficulties which arise in their practical implementation. In our best knowledge for the first time, we determined the bandwidth of such a novel PCF with W-shaped refractive index distribution by numerical solving the time-dependent power flow equation.

4. Numerical results

We investigated bandwidth in a multimode solid-core W-type glass PCF. A W-shape refractive index model is used for the structure shown in Fig. 1. For PCFs with air holes in a triangular lattice, the effective refractive index of cladding $n_{f,sm}$ was obtained using the effective parameter V [32,45]. For a range of air-hole diameters d_q , summarized in Table 1 are the effective refractive index n_q , relative refractive index difference $\Delta_q = (n_0 - n_q)/n_0$, and the corresponding critical angle θ_q — all for the inner cladding and at wavelength of 850 nm [32].

We solved the time-dependent power flow Eq. (1) using the explicit finite difference method for the W-type PCF fiber with pure silica core with $n_0 = 1.45$, $2a = 50 \mu\text{m}$, and coupling coefficient $D = 2.3 \times 10^{-6} \text{ rad}^2/\text{m}$ (typical value of D for glass core fibers [40]), for two and four rings of air holes in the inner cladding [36]; the two respective widths of the inner cladding used in the calculations are $\delta a = 6 \mu\text{m}$ ($\delta = 0.24$) and $\delta a = 12 \mu\text{m}$ ($\delta = 0.48$). In order to investigate the influence of diameter of air holes in the inner cladding on bandwidth and steady-state losses, we analyzed cases with $d_q = 2.0, 2.1, 2.2, 2.3 \mu\text{m}$, for a fixed diameter of air holes in the outer cladding $d_p = 1.0, 1.1, 1.2, 1.3 \mu\text{m}$.

Fig. 2 shows the dependence of bandwidth on transmission length for different diameters of air holes $d_q = 2.0, 2.1, 2.2, 2.3 \mu\text{m}$ and fixed $d_p = 1 \mu\text{m}$ — for the case of a W-type PCF with two ($\delta = 0.24$) and four rings ($\delta = 0.48$) of air holes in the inner cladding and for the θ_p excitation. One can observe that bandwidth increases with decreasing diameter of the inner cladding air holes d_q at longer fiber lengths. This is a result of a drop in leaky mode losses with increasing diameter of the inner cladding air holes d_q [32] as power remains in higher leaky modes over longer transmission length, boosting thus modal dispersion and reducing bandwidth. At shorter fiber lengths for θ_p excitation (exciting only the guided modes), leaky modes are almost not guided along the fiber and the influence of d_q on bandwidth is negligible. At longer fiber lengths, the influence of d_q on bandwidth is more pronounced because leaky modes appear due to mode coupling. The bandwidth of W-type PCF is larger for the fiber with two – rather than four – rings of air holes in the inner cladding (Figs. 2 and 3). Since leaky mode losses are smaller in the fiber with four inner rings [32], power remains in leaky modes for a longer transmission length, increasing modal dispersion and decreasing bandwidth.

For a number of air-hole diameters $d_q = 2.0, 2.1, 2.2, 2.3 \mu\text{m}$ and for a fixed $d_p = 1 \mu\text{m}$, Fig. 3 shows how transmission length influences bandwidth when there are two ($\delta = 0.24$) or four rings ($\delta = 0.48$) of inner-cladding air holes — with the θ_q excitation. The bandwidth is larger in the case of a narrow launch that excites only the guided modes (the θ_p excitation, Fig. 2), compared to a wide launch (θ_q excitation, that excites both guided and leaky modes). Modal dispersion increases by exciting both guided and leaky modes, decreasing bandwidth. At longer fiber lengths, after achieving SSD, influence of launch excitation is negligible [32].

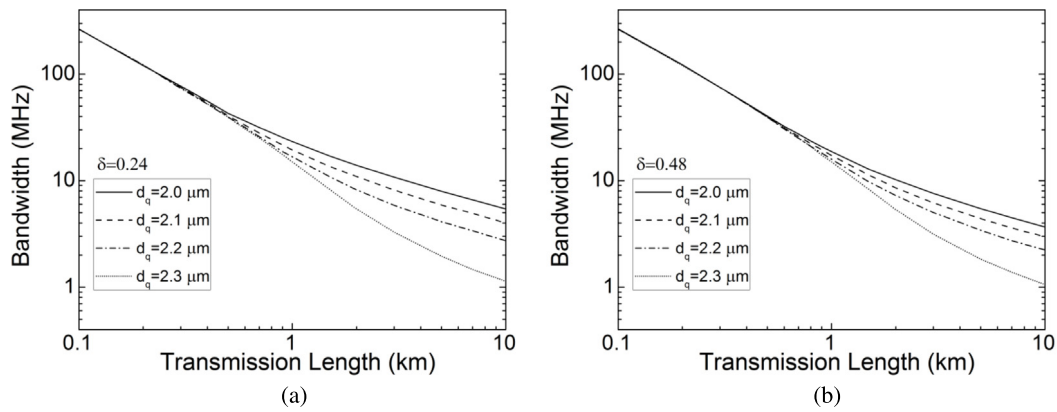


Fig. 2. For the θ_p excitation, bandwidth as a function of transmission length over a range of sizes (diameter d_q) of air holes in the inner cladding (a) with two rings ($\delta = 0.24$) and (b) with four rings ($\delta = 0.48$) of holes.

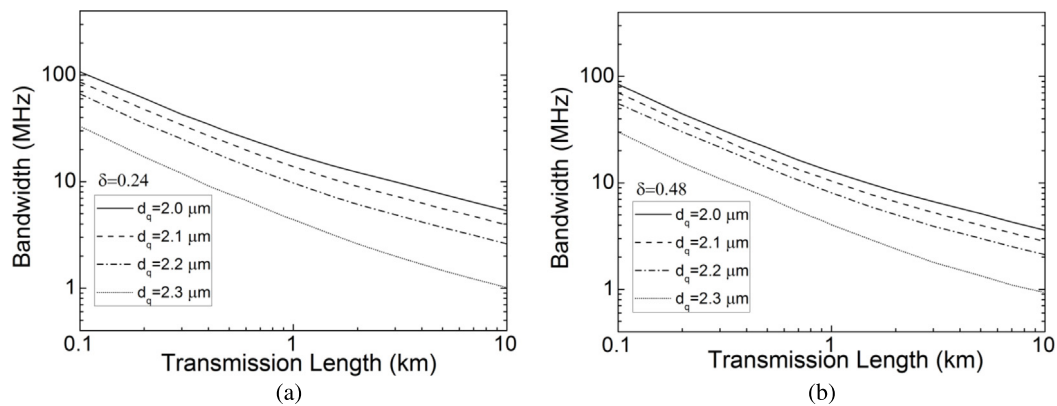


Fig. 3. For the θ_q excitation, bandwidth as a function of transmission length over a range of sizes (diameter d_q) of air holes in the inner cladding (a) with two rings ($\delta = 0.24$) and (b) with four rings ($\delta = 0.48$) of such air holes.

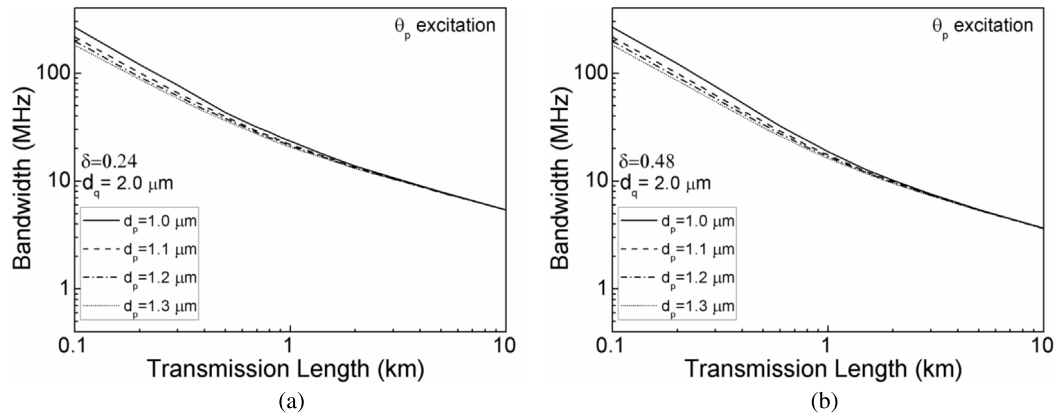


Fig. 4. For the θ_p excitation, bandwidth as a function of transmission length for a varied size (diameter d_p) of air holes in the outer cladding, with (a) two rings ($\delta = 0.24$) and (b) four rings ($\delta = 0.48$) of holes in the inner cladding.

Figs. 4 and 5 show how transmission length influences bandwidth for different diameters of air holes in the outer cladding $d_p = 1.0, 1.1, 1.2, 1.3 \mu\text{m}$; for fixed $d_q = 2.0 \mu\text{m}$ and with the W-type PCF fiber having two ($\delta = 0.24$) or four rings ($\delta = 0.48$) of air holes in the inner-cladding, and for the θ_p and θ_q excitations, respectively. With θ_p excitation and short fiber lengths, bandwidth decreases with increasing air hole diameters in the outer cladding d_p (i.e. with increasing the critical angle θ_p). This is because then the critical angle for guiding modes θ_p increases, giving rise to the number of guided modes, thus increasing modal dispersion and decreasing bandwidth. At longer fiber

lengths, this influence of air hole diameters in the outer cladding d_p is negligible. The corresponding graphs for θ_q excitation are shown in Fig. 5(a) and (b): the bandwidth is not affected by the air-hole diameter in the outer cladding d_p . This is because leaky modes are in this case excited at the input fiber end ($z = 0$) rather than generated by d_p -dependent processes along the fiber.

Fig. 6 shows the trade-off relation between bandwidth and steady-state loss for $\delta = 0.24$ and $\delta = 0.48$, for θ_p and θ_q excitations. One can observe that steady-state losses increase for smaller diameter of inner air holes d_q — because of larger leaky mode losses (for both widths δ and

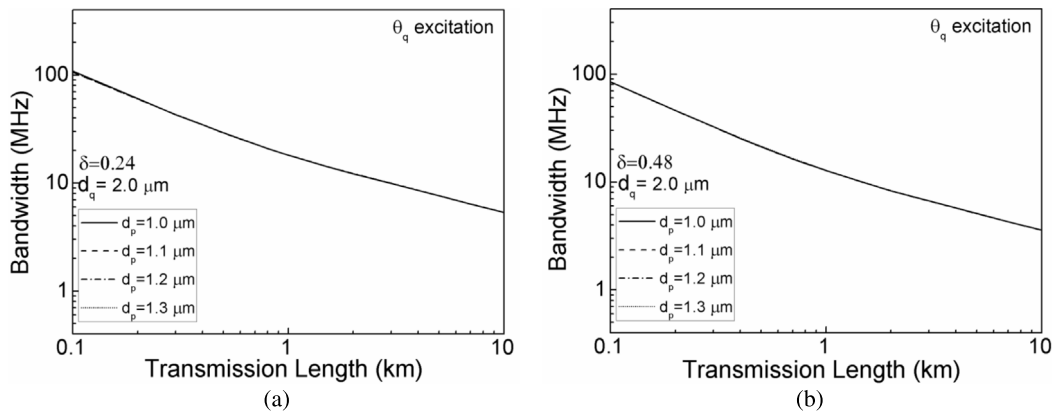


Fig. 5. For the θ_q excitation, bandwidth as a function of transmission length for a varied size (diameter d_p) of air holes in the outer cladding, with (a) two rings ($\delta = 0.24$) and (b) four rings ($\delta = 0.48$) of holes in the inner cladding.

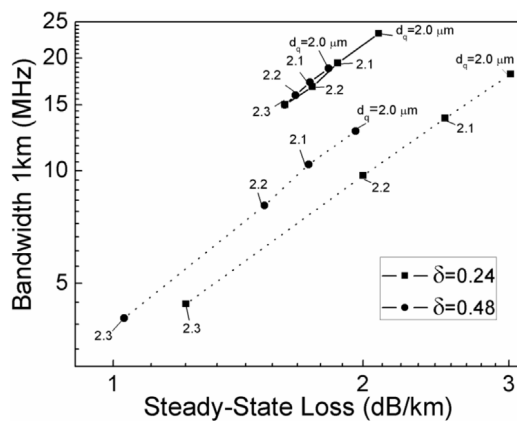


Fig. 6. Bandwidth versus steady-state loss, trade-off relation for $\delta = 0.24$ and $\delta = 0.48$ in the case of θ_p (solid lines) and θ_q (dotted lines) excitations.

both excitations θ). The influence of diameter d_q and width δ on steady-state losses is more pronounced for the θ_q than for θ_p excitation as larger number of leaky modes remain guided along the fiber. It can be observed that depending on the input excitation and structural fiber parameters, a higher value of bandwidth can be achieved for the same steady-state losses. An optimized value for transmission length can be estimated after considering a trade-off relation between the bandwidth and steady state loss for a particular fiber length (as it has been illustrated in Fig. 6 for 1 km fiber length).

We have shown that bandwidth can be improved by reducing the number of rings of inner cladding air holes, decreasing the diameter of inner air holes or exciting only guiding modes. In practice, a trade-off relation between bandwidth and steady-state loss would have to be considered in designing the optimum W-type PCF fiber. Finally, we have obtained that number of rings of air holes in the inner cladding has no influence on the bandwidth.

5. Conclusions

As a function of transmission length along a multimode W-type photonic crystal fiber with solid core, bandwidth is determined for a wide range of sizes and spacing of holes in the inner and outer cladding of the fiber by solving the time-dependent power flow equation numerically. At longer fiber lengths, results show higher bandwidth for smaller holes of the inner cladding (meaning for a smaller diameter of the holes, d_q). Conversely at shorter lengths, this influence of the hole size d_q on bandwidth is negligible with the θ_p excitation (that

launches only guided modes); bandwidth decreases as the holes in the outer cladding are increased in size (larger d_p) and with the broader θ_q excitation. At longer fiber lengths, the influence of hole diameter in the outer cladding d_p is negligible. The bandwidth of W-type PCF is larger for the fiber with two rings of holes in the inner cladding than for the one with four rings. We obtained that bandwidth is larger in the case of a narrow launch that excites only guided modes (θ_p excitation), compared to wider excitation where both guided and leaky modes are excited (θ_q excitation). Finally, we have obtained the trade-off relation between bandwidth and steady-state loss for $\delta = 0.24$ and $\delta = 0.48$, in the case of θ_p and θ_q excitations. The bandwidth improves as the number of rings with holes in the inner cladding is reduced, or by decreasing the size (diameter) of air holes in the inner cladding, or by exciting only guided modes.

Acknowledgments

This work was supported in part by the grants from Serbian Ministry of Education, Science and Technological Development through the Project Nos. 171011 and 171021 and by the Strategic Research Grant of City University of Hong Kong (Project No. CityU 7004069).

References

- [1] J.C. Knight, T.A. Birks, P.St.J. Russell, D.M. Atkin, All-silica single-mode optical fiber with photonic crystal cladding, *Opt. Lett.* 21 (1996) 1547–1549.
- [2] T.A. Birks, J.C. Knight, P.St.J. Russell, Endlessly single-mode photonic crystal fiber, *Opt. Lett.* 22 (1997) 961–963.
- [3] P.St.J. Russell, Photonic crystal fibers, *Science* 299 (2003) 358–362.
- [4] J.C. Knight, Photonic crystal fiber, *Nature* 424 (14) (2003) 847–851.
- [5] P.St.J. Russell, Photonic-crystal fibers, *J. Lightwave Technol.* 24 (2006) 4729–4749.
- [6] J.C. Knight, T. A. Birks, J. Broeng, P.S.J. Russell, Photonic band gap guidance in optical fibers, *Science* 282 (1998) 1476–1478.
- [7] J.C. Knight, P.S.J. Russell, Photonic crystal fibers: New way to guide light, *Science* 296 (2002) 276–277.
- [8] R.F. Cregan, B.J. Mangan, J.C. Knight, T.A. Birks, P.S.J. Russell, P.J. Roberts, D.C. Allan, Single-mode photonic band gap guidance of light in air, *Science* 285 (1999) 1537–1539.
- [9] R. Amezcua-Correa, F. Gerome, S.G. Leon-Saval, N.G.R. Broderick, T.A. Birks, J.C. Knight, Control of surface modes in low loss hollow core photonic bandgap fibers, *Opt. Express* 16 (2008) 1142–1149.
- [10] G. Bouwmans, L. Bigot, Y. Quiquempois, F. Lopez, L. Provino, M. Douay, Fabrication and characterization of an all-solid 2d photonic bandgap fiber with a low-loss region (<20 db/km) around 1550 nm, *Opt. Express* 13 (2005) 8452–8459.
- [11] F. Luan, A.K. George, T.D. Hedley, G.J. Pearce, D.M. Bird, J.C. Knight, P.St.J. Russell, All-solid photonic bandgap fiber, *Optim. Lett.* 29 (2004) 2369–2371.
- [12] F. Benabid, J.C. Knight, G. Antonopoulos, P.St.J. Russell, Stimulated raman scattering in hydrogen-filled hollow-core photonic crystal fiber, *Science* 298 (2002) 399–402.
- [13] P.S. Light, F. Benabid, F. Couny, M. Maric, A.N. Luiten, Electromagnetically induced transparency in Rb-filled coated hollow-core photonic crystal fiber, *Optim. Lett.* 32 (2007) 1323–1325.

- [14] D. Mogilevtsev, T.A. Birks, P.St.J. Russell, Group-velocity dispersion in photonic crystal fibers, *Optim. Lett.* 23 (1998) 1662–1664.
- [15] K. Saitoh, M. Koshiba, T. Hasegawa, E. Sasaoka, Chromatic dispersion control in photonic crystal fibers: application to ultra-flattened dispersion, *Opt. Express* 11 (2003) 843–852.
- [16] S. Lee, W. Ha, J. Park, S. Kim, K. Oh, A new design of low-loss and ultra-flat zero dispersion photonic crystal fiber using hollow ring defect, *Opt. Commun.* 285 (20) (2012) 4082–4087.
- [17] D. Chen, M.L.V. Tse, H.Y. Tam, Optical properties of photonic crystal fibers with a fiber core of arrays of sub-wavelength circular air holes: birefringence and dispersion, *Prog. Electromagn. Res.* 105 (2010) 193–212.
- [18] J.K. Ranka, R.S. Windeler, A.J. Stentz, Visible continuum generation in air silica microstructure optical fibers with anomalous dispersion at 800 nm, *Opt. Lett.* 25 (2000) 25.
- [19] K.M. Hilligsøe, T.V. Andersen, H.N. Paulsen, C.K. Nielsen, K. Mølmer, S. Keiding, R. Kristiansen, K.P. Hansen, J.J. Larsen, Supercontinuum generation in a photonic crystal fiber with two zero dispersion wavelengths, *Opt. Express* 12 (2004) 1045–1054.
- [20] W.J. Wadsworth, N. Joly, J.C. Knight, T.A. Birks, F. Biancalana, P. St. J. Russell, Supercontinuum and four-wave mixing with Q-switched pulses in endlessly single-mode photonic crystal fibres, *Opt. Express* 12 (2004) 299–309.
- [21] J.H. Lee, W. Belardi, K. Furusawa, P. Petropoulos, Z. Yusoff, T.M. Monro, D.J. Richardson, Four-wave mixing based 10-Gb/s tunable wavelength conversion using a holey fiber with a high SBS threshold, *IEEE Photonics Technol. Lett.* 15 (2003) 440–442.
- [22] T.V. Andersen, K.M. Hilligsøe, C.K. Nielsen, J. Thøgersen, K.P. Hansen, S.R. Keiding, J.J. Larsen, Continuous-wave wavelength conversion in a photonic crystal fiber with two zero-dispersion wavelengths, *Opt. Express* 12 (2004) 4113–4122.
- [23] J. Park, D.E. Kang, B. Paulson, T. Nazari, K. Oh, Liquid core photonic crystal fiber with low-refractive-index liquids for optofluidic applications, *Opt. Express* 22 (14) (2014) 17320–17330.
- [24] S.H. Kassani, R. Khazaeinezhad, Y. Jung, J. Kobelke, K. Oh, Suspended ring-core photonic crystal fiber gas sensor with high sensitivity and fast response, *IEEE Photon. J.*, *IEEE* 7 (1) (2015) 2700409.
- [25] W. Wadsworth, R. Percival, G. Bouwmans, J. Knight, T. Birks, T. Hedley, P.St.J. Russell, Very high numerical aperture fibers, *IEEE Photon. Technol. Lett.* 16 (2004) 843–845.
- [26] K.P. Hansen, High-power photonic crystal fibers, in: *Proceedings of SPIE*, vol. 6102, SPIE, 2006 61020B–61020B–11.
- [27] K.P. Hansen, C.B. Olausson, J. Broeng, D. Noordegraaf, M.D. Maack, T.T. Alkeskjold, M. Laurila, T. Nikolajsen, P.M.W. Skovgaard, M.H. Sorensen, M. Denninger, C. Jakobsen, H.R. Simonsen, Airclad fiber laser technology, *Opt. Eng.* 50 (2011) 111609.
- [28] R. Stepien, B. Siwicki, D. Pysz, G. Stepniowski, Characterization of a large core photonic crystal fiber made of lead–bismuth–gallium oxide glass for broadband infrared transmission, *Opt. Quant. Electron.* 46 (2014) 553–561.
- [29] M.M. Tefelska, S. Ertman, T.R. Wolinski, P. Mergo, R. Dabrowski, Large area multimode photonic band-gap propagation in photonic liquid-crystal fiber, *IEEE Photon. Technol. Lett.* 24 (2012) 631.
- [30] L.V. Amitonova, A. Descloux, J. Petschulat, M.H. Frosz, G. Ahmed, F. Babic, X. Jiang, A.P. Mosk, P. St.J. Russell, P.W.H. Pinkse, High-resolution wavefront shaping with a photonic crystal fiber for multimode fiber imaging, *Opt. Lett.* 41 (2016) 497–500.
- [31] H. Chen, S. Chen, J. Hou, Q. Lu, Photonic crystal fiber with W-type effective refractive index profile, *Optik* 124 (2013) 2309–2312.
- [32] M. Kovačević, Lj. Kuzmanović, A. Simović, S. Savović, A. Djordjević, Transients of modal-power distribution in multimode solid-core w-type photonic crystal fibers, *J. Lightwave Technol.* 35 (2017) 4352–4357.
- [33] N.A. Mortensen, et al., Multi-mode photonic crystal fibers for VCSEL based data transmission, *Opt. Express* 11 (2003) 1953–1959.
- [34] M. Nielsen, J. Folkner, N. Mortensen, A. Bjarklev, Bandwidth comparison of photonic crystal fibers and conventional single-mode fibers, *Opt. Express* 912 (3) (2004) 430–435.
- [35] M.A. van Eijkelenborg, A. Argyros, A. Bachmann, G. Barton, M.C.J. Large, G. Henry, N.A. Issa, K.F. Klein, H. Poisel, W. Pok, L. Poladian, S. Manos, J. Zagari, Bandwidth and loss measurements of graded-index microstructured polymer optical fibre, *Electron. Lett.* 40 (10) (2004) 592–593.
- [36] S. Savović, A. Simović, A. Djordjević, Explicit finite difference solution of the power flow equation in W-type fibers, *Opt. Laser Technol.* 44 (2012) 1786–1790.
- [37] D. Gloge, Optical power flow in multimode fibers, *Bell Syst. Technol. J.* 51 (1972) 1767–1783.
- [38] M. Rousseau, L. Jeunhomme, Numerical solution of the coupled-power equation in step index optical fibers, *IEEE Trans. Microwave Theory Technol.* 25 (1977) 577–585.
- [39] T. Tanaka, S. Yamada, M. Sumi, K. Mikoshiba, Microbending losses of doubly clad (W-type) optical fibers, *Appl. Opt.* 18 (1977) 2391–2394.
- [40] T.P. Tanaka, S. Yamada, Steady-state characteristics of multimode W-type fibers, *Appl. Opt.* 18 (1979) 3261–3264.
- [41] T.P. Tanaka, S. Yamada, Numerical solution of power flow equation in multimode W-type optical fibers, *Appl. Opt.* 19 (1980) 1647–1652.
- [42] A. Simović, A. Djordjević, S. Savović, Influence of width of intermediate layer on power distribution in W-type optical fibers, *Appl. Opt.* 51 (2012) 4896–4901.
- [43] L. Jeunhomme, M. Fraise, J.P. Pocholle, Propagation model for long step-index optical fibers, *Appl. Opt.* 15 (1976) 3040–3046.
- [44] S. Kawakami, S. Nishida, Perturbation theory of doubly clad optical fiber with a low index inner cladding, *IEEE J. Quantum Electron.* QE-11 (1975) 130–138.
- [45] K. Saitoh, M. Koshiba, Empirical relations for simple design of photonic crystal fibers, *Opt. Express* 13 (2005) 267–274.



Infrared wavelength dependence of leaky mode losses and steady state distribution in W-type glass optical fibers



Alexandar Djordjevich^a, Ana Simović^b, Svetislav Savović^{a,b,*}, Branko Drljača^c

^a City University of Hong Kong, 83 Tat Chee Avenue, Hong Kong, China

^b University of Kragujevac, Faculty of Science, R. Domanovića 12, Kragujevac, Serbia

^c Faculty of Science, University of Priština, Lole Ribara 29, Kosovska Mitrovica, Serbia

ARTICLE INFO

Keywords:

W-fiber
Steady state distribution
Power flow equation
Infrared wavelengths

ABSTRACT

Infrared wavelength dependence of leaky mode losses and steady state distribution (SSD) in W-type glass optical fibers (doubly clad fibers with three layers) is investigated in this paper for parametrically varied depths and widths of the fiber's intermediate optical layer. This enables a tailoring of configuration of the W-type fiber to suit an application at hand. We have shown that the proposed W-type fiber has better transmission characteristics at longer infrared wavelengths.

1. Introduction

Singly clad (SC) optical fibers made of glass dominate in long-distance communication networks. Plastic optical fibers (POFs), with their higher attenuation and lower transmission bandwidth, are restricted to local area networks with short data links. Much research has been devoted to overcoming these challenges such as by applying equalization [1], or spatial modulation [2] and detection [3]. A less investigated approach is how the transmission bandwidth could be improved through redesign of the fiber profile. POFs with an addition of a third optical layer have been shown experimentally to have bandwidths higher than POFs with graded index profile [4]. When the intermediate layer has a lower index of refraction than the neighboring layers, such fibers are said to be of W-type (because a symmetrical plot of their refractive index may resemble the letter W — as in Fig. 1). W-fibers are generally characterized by lower waveguide dispersion in comparison to similar SC fibers and are easier to splice.

In a W-fiber, its intermediate layer binds the guided modes firmer to the core and reduces the effective numerical aperture of the fiber [5]. Consequently, transmission bandwidth widens and bending losses drop. The bandwidth-distance product of such a fiber is around 50 MHz km, which is significantly higher than the typical 30 MHz km for their SC counterparts (also of glass). The relative improvement is even more dramatic for POFs [4,6–8].

Optical fibers inevitably incorporate irregularities in the form of a shape-variation or material inhomogeneity including voids and cracks. Such random irregularities in multimode optical fibers cause light

diffraction that couples power between the propagating modes. This mode coupling is an effect in addition to the reduction of the transmitted power by differential mode attenuation. Both influence fiber transmission characteristics strongly.

On the positive side, coupled modes may be less dispersed for multimodal launch. This translates into higher bandwidth. However, mode coupling also leads to higher losses, particularly in curved segments [9]. Moreover, the output-field is altered and generally degraded as it contains modes of high order even if the launch was restricted to modes of only low order. W-fibers are more resilient to these effects. Their intermediate layer between the core and cladding retains some lossy leaky modes [10–16]. Yet, the more complex profile of the refractive index of the fiber opens the question of optimization of such profile [17].

Angular input optical power distribution that results from a specific launch gets modified gradually with distance from the input fiber-end by the effect of mode coupling. The expected beam properties, including the far-field radiation pattern, are altered as a consequence [18,19]. Thus for example, if we arrange a centrally symmetric launch (along a cone) at a fixed angle $\theta = \theta_0$ to the fiber axis, a ring can be imaged behind the output-end of a short fiber — the ring diameter is related to that initial launch angle θ_0 . As the fiber is “lengthened” (replaced by longer and longer fibers), edges of this ring become blurred and the ring morphs gradually into a disk. This is due to effects of mode coupling accumulating with distance from the input-end and causing the angular power distribution, initially narrowly centered around $\theta = \theta_0$, to gradually widen and shift towards $\theta = 0^\circ$. By lengthening the fiber to

* Correspondence to: Faculty of Science, R. Domanovića 12, 34000 Kragujevac, Serbia.
E-mail address: savovic@kg.ac.rs (S. Savović).

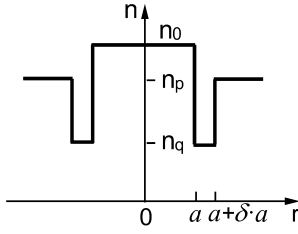


Fig. 1. Refractive index profile of a W-fiber.

beyond the value known as z_s , the angular light distribution becomes fixed and centered (the disk is brightest in its center). This is a “steady-state distribution” (SSD) that is independent of the launch conditions except for the overall brightness: normalized to its peak value, SSD is one and the same whatever the launch angle(s).

The above case is about narrow angular launch-beam distributions. They widen (and center) with distance along the fiber from the input end. The opposite is true as well: broad angular launch-beam distributions will narrow to produce the same SSD because each narrow component of a broad input distribution converges to the same SSD.

“Coupling coefficient” D has been used widely [19–26] to describe how power is transferred between modes. This allowed modeling by the power flow equation [e.g. [19]] of the angular power distributions in the far field fiber output as a function of the fiber length and conditions of launch. For W-type optical fibers made of glass, the main goal of this work is to investigate the influence of infrared wavelength on the attenuation of leaky modes and on the length of fiber z_s that marks the onset of the SSD. In this process, the width and depth of the fiber’s intermediate layer were varied parametrically to facilitate the selection of their optimal values for a particular infrared wavelength.

2. Modeling

Gloge’s equation for power distribution inside a multimode SC fiber is:

$$m \frac{\partial P_m(z)}{\partial z} = -m\alpha_m P_m(z) + md_m [P_{m+1}(z) - P_m(z)] + (m-1)d_{m-1} [P_{m-1}(z) - P_m(z)] \quad (1)$$

where m is the compound mode number (containing $2m$ modes due to two different states of polarization and taking integral values beginning at $m = 1$), P_m is the power of (each) mode m , z is the axial position along the fiber, α_m is the dissipation and loss (scattering) coefficient of mode m , and d_m is the coupling coefficient between (each) mode m and $m + 1$. The compound mode number is defined as $m = 2p + \nu$, where p is a radial mode number and ν is an azimuthal mode number. In this formulation, a mode propagates as a plane wave along the fiber (reflecting at the core/clad interface) at an angle $\theta_m(m\Delta\theta)$ with respect to the core axis, where $\Delta\theta = \lambda/4an$, a is a core radius and n is a core refractive index [19]. This equation is also often used in its continuous form in which it is assumed that θ_m is a continuous parameter θ :

$$\frac{\partial P(\theta, z)}{\partial z} = -\alpha(\theta)P(\theta, z) + \frac{D}{\theta} \frac{\partial}{\partial \theta} \left(\theta \frac{\partial P(\theta, z)}{\partial \theta} \right) \quad (2)$$

where $\alpha(\theta)$ is the modal attenuation and D is a constant “coupling coefficient”. It is assumed that mode coupling mainly occurs between neighboring modes due to the fact that coupling strength decreases sufficiently fast with the mode spacing [19]. This assumption is commonly used in modeling a mode coupling process both in SC and W-type fibers [6,18–27]. Describing the evolution of the modal power distribution along the fiber, (2) is the time-independent power flow equation with the mode angle θ taken as a continuous variable. The form of the last term in (2) identifies the next-neighbor mode coupling

as a diffusion process in a continuum. The time-independent power flow Eq. (2) is further expressed as:

$$\frac{\partial P(\theta, z)}{\partial z} = -\alpha(\theta)P(\theta, z) + \frac{D}{\theta} \frac{\partial P(\theta, z)}{\partial \theta} + D \frac{\partial^2 P(\theta, z)}{\partial \theta^2}. \quad (3)$$

Modal attenuation $\alpha(\theta)$ can be expanded into $\alpha(\theta) = \alpha_0 + \alpha_d(\theta)$. The term α_0 represents conventional losses by absorption and scattering. It can be neglected in the solution because it would feature as just a fixed multiplier $\exp(-\alpha_0 z)$. The term $\alpha_d(\theta)$ in the expansion of $\alpha(\theta)$ is dominant for higher order modes.

Boundary conditions for (3) are $P(\theta_m, z) = 0$ and $D \cdot (\partial P / \partial \theta) = 0$ at $\theta = 0$, with θ_m denoting the largest propagation angle. The condition $P(\theta_m, z) = 0$ implies that modes with infinitely high loss do not carry power. Condition $(\partial P / \partial \theta) = 0$ at $\theta = 0$ indicates that the coupling is limited to modes propagating with $\theta > 0$.

Fig. 1 represents the index profile of a W-fiber with n_0, n_p and $n_q (n_0 > n_p > n_q)$ being indices of refraction of the core, cladding, and intermediate layer, respectively. Modes propagating at angles that are between $\theta_p \cong (2\Delta_p)^{1/2}$ and $\theta_q \cong (2\Delta_q)^{1/2}$ have been shown to be leaky modes [22]; here, $\Delta_p = (n_0 - n_p)/n_0$ or $\Delta_q = (n_0 - n_q)/n_0$ is the relative difference of the refraction index of the cladding, or (respectively) intermediate layer, to that of the core.

Denoting the free-space wave number as $k_0 = 2\pi/\lambda$ and expressing the thickness of the intermediate layer as $\delta \cdot a$ where a is the core-radius, constants of attenuation of leaky modes are given as [23]:

$$\alpha_L(\theta) = \frac{4(\theta^2 - \theta_p^2)^{1/2}}{a(1 - \theta^2)^{1/2}} \frac{\theta^2(\theta_q^2 - \theta^2)}{\theta_q^2(\theta_q^2 - \theta_p^2)} \exp \left[-2\delta a n_0 k_0 (\theta_q^2 - \theta^2)^{1/2} \right]. \quad (4)$$

It has been shown experimentally [24] that all guided-modes in SC fibers regardless of their propagation angle θ are attenuated equally; the attenuation rises steeply for radiated-modes. For W-type fibers, this can be generalized in terms of $\alpha_d(\theta)$ in the already introduced expansion for attenuation $\alpha(\theta) = \alpha_0 + \alpha_d(\theta)$, in which $\alpha_0 = \text{const}$, and where:

$$\alpha_d(\theta) = \begin{cases} 0 & \theta \leq \theta_p \\ \alpha_L(\theta) & \theta_p < \theta < \theta_q \\ \infty & \theta \geq \theta_q \end{cases} \quad (5)$$

Eq. (5) can also be explained if one would think of a W-fiber as having a vanishing, and then infinite, thickness of its intermediate layer $\delta \cdot a$ (a is the core radius). With $\delta \rightarrow 0$, and then $\delta \rightarrow \infty$, two distinct SC (SC_p and SC_q) fibers result with respective critical angles of θ_p and then θ_q , respectively. This results in three subdomains for the propagation angle evident in (5): less than one critical angle, greater than the other, and between the two of them. Modes propagating at angles between the two critical angles θ_p and θ_q are termed leaky modes. For that range, strong influence of the intermediate layers’ thickness $\delta \cdot a$ on $\alpha_L(\theta)$ in (5) has been noted [23,26].

W-fiber’s characteristics were reported to vary strongly with the intermediate layer’s width $\delta \cdot a$. As mentioned, they approach those of corresponding SC_p or SC_q fibers when, respectively, the thickness either vanishes or approaches infinity [23,26], under SSD conditions. Also of influence is the index of refraction n_q of the intermediate layer, referred to as this layer’s “depth” (Fig. 1). The influence is investigated in this paper of both intermediate layer’s parameters, namely width and depth, on the length z_s for reaching the SSD and on the attenuation of leaky modes in glass W-fibers — across a infrared wavelength spectrum. This facilitates tailoring W-fibers to a specific application at hand.

3. Numerical implementation

With constants of attenuation for leaky modes as given by Eq. (4), the closed-form solution of Eq. (3) does not exist. Hence, the corresponding

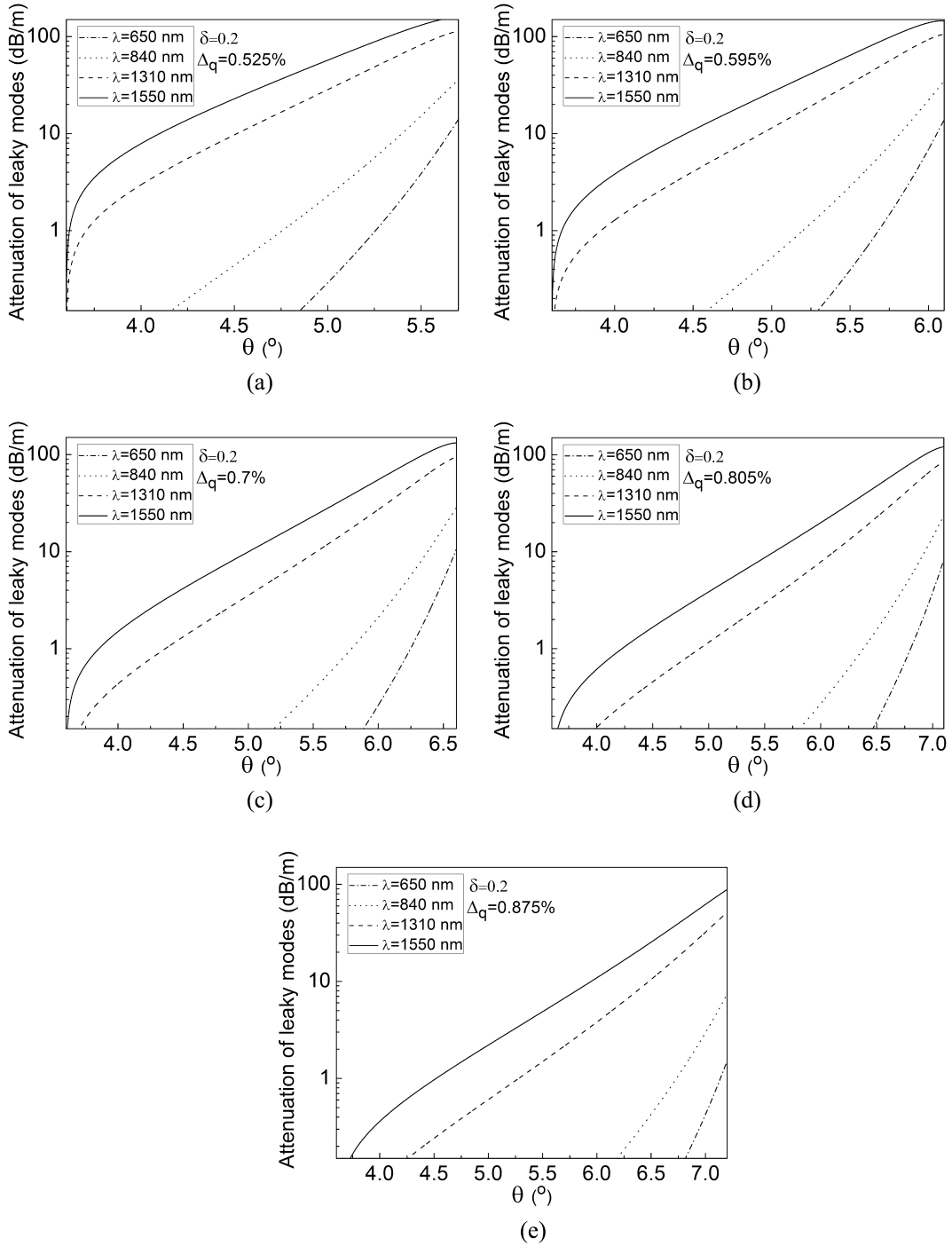


Fig. 2. Leaky mode losses α_L as a function of the propagation angle θ and parametric wavelength λ . Each plot is for a different value of the intermediate layer's depth Δ_q : (a) $\Delta_q = 0.525\%$, (b) $\Delta_q = 0.595\%$, (c) $\Delta_q = 0.7\%$, (d) $\Delta_q = 0.805\%$ and (e) $\Delta_q = 0.875\%$. The width of the intermediate layer is $\delta = 0.2$.

power flow equation for the W-fiber is solved by the explicit finite difference method (EFDM). To achieve this, the terms $(\partial^2 P(\theta, z))/\partial\theta^2$ and $(\partial P(\theta, z))/\partial\theta$ in (3) were modeled by the central difference scheme [28]. The derivative term $(\partial P(\theta, z))/\partial z$ was modeled by the forward difference scheme. This resulted in the following equation in which k and l denote $\Delta\theta$ and Δz as discretization steps for the respective angle θ and length z :

$$P_{k,l+1} = \left(\frac{\Delta z D}{\Delta\theta^2} - \frac{\Delta z D}{2\theta_k \Delta\theta} \right) P_{k-1,l} + \left(1 - \frac{2\Delta z D}{\Delta\theta^2} - (\alpha_d)_k \Delta z \right) P_{k,l} + \left(\frac{\Delta z D}{2\theta_k \Delta\theta} + \frac{\Delta z D}{\Delta\theta^2} \right) P_{k+1,l} \quad (6)$$

where:

$$(\alpha_d)_k = \begin{cases} 0 & ; \theta_k \leq \theta_p \\ \frac{4(\theta_k^2 - \theta_p^2)^{1/2} \theta_k^2 (\theta_q^2 - \theta_k^2)}{a(1 - \theta_k^2)^{1/2} \theta_q^2 (\theta_q^2 - \theta_p^2)} & ; \theta_p < \theta_k < \theta_q \\ \exp \left[-2\delta a n_0 k_0 (\theta_q^2 - \theta_k^2)^{1/2} \right] & ; \theta_k \geq \theta_q \\ \infty & \end{cases} \quad (7)$$

with $N = \theta_q/\Delta\theta$ denoting the grid dimension for the variable θ , boundary conditions can be expressed as:

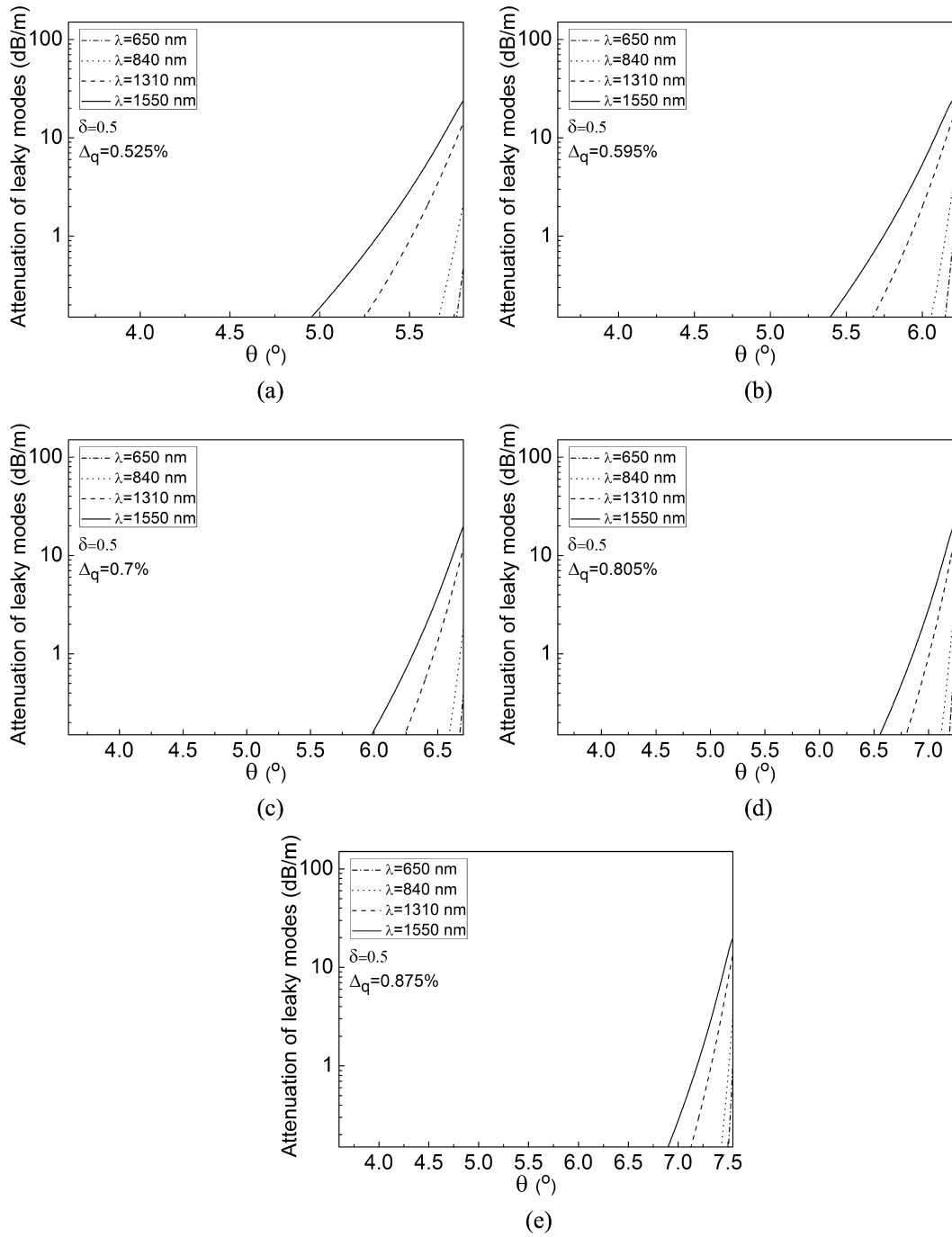


Fig. 3. Leaky mode losses α_L as in Fig. 2 but with the width of the intermediate layer $\delta = 0.5$.

$$\begin{aligned}
 P_{N,l} &= 0 \\
 P_{0,l} &= P_{1,l} \\
 \lim_{\theta \rightarrow 0} \frac{1}{\theta} \frac{\partial}{\partial \theta} \left(\theta \frac{\partial P}{\partial \theta} \right) &= 2 \frac{\partial^2 P}{\partial \theta^2} \Big|_{\theta=0}.
 \end{aligned} \tag{8}$$

The purpose of the last of expressions in (8) is to avoid singularity at $\theta = 0$. To complete the numerical implementation, the input $P(\theta, 0) = 1$ for $0 \leq \theta \leq \theta_q$ and $z = 0$ is written in the difference form $P_{k,0} = 0$. This input represents axial input of all modes including the leaky ones. With this implementation, angular distribution of power can be determined at different lengths of W-fibers.

4. Numerical results

Leaky mode losses and the length z_s for achieving the SSD are analyzed in this work at different wavelengths for the following W-fiber: $n_0 = 1.46$, $\Delta_p = 0.2\%$ ($\theta_p \cong 3.62^\circ$), $\Delta_q = 0.7\%$ ($\theta_q \cong 6.76^\circ$) and $2a = 60 \mu\text{m}$ [22,26]. This was done for fixed values of the refractive index of the core ($n_0 = 1.46$) and that of the outer cladding (n_p is expressed relative to n_0 by specifying $\Delta_p = 0.2\%$).

The intermediate layer's depth n_q was varied over five values corresponding to $\Delta_q = (n_0 - n_q)/n_0 = 0.525\%$, 0.595% , 0.7% , 0.805% , and 0.875% (these values are 0.7 and variations of 0.7 by $\pm 15\%$ and $\pm 25\%$ as

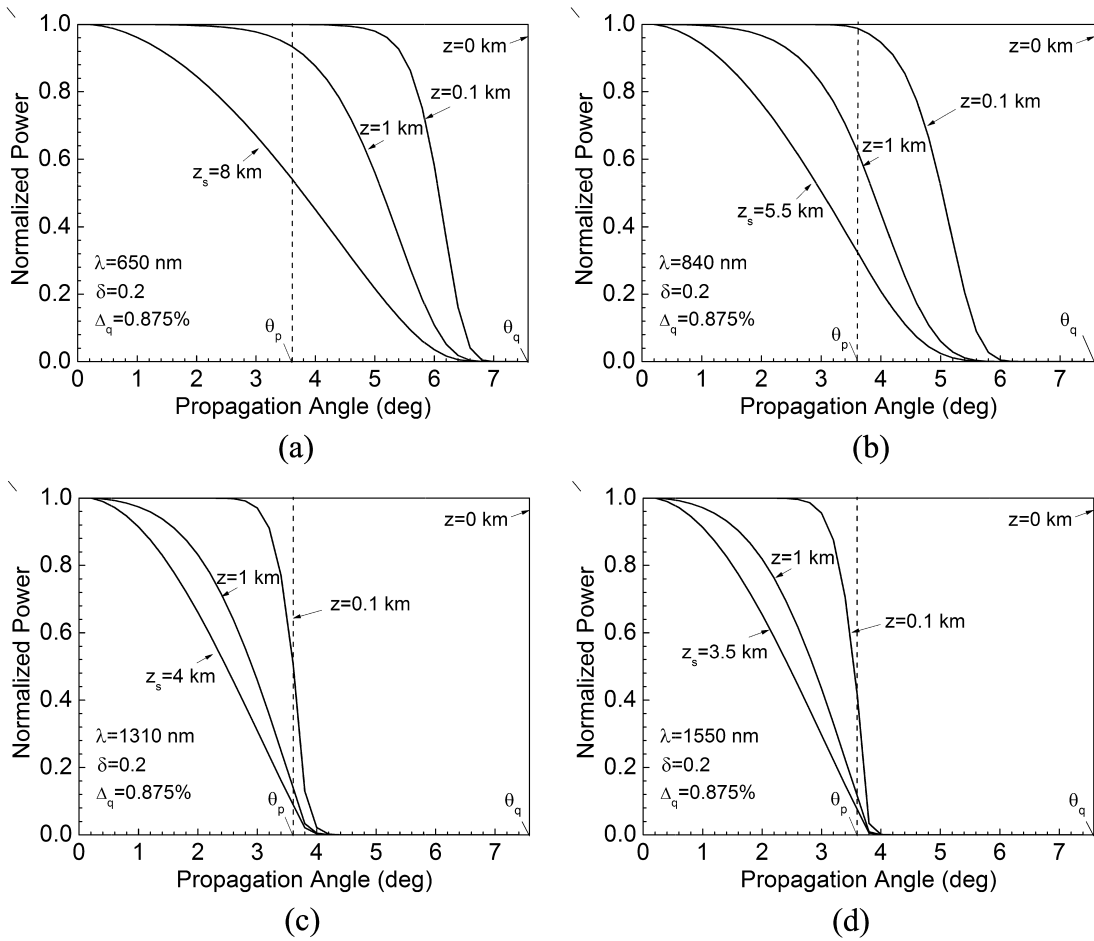


Fig. 4. Spatial transient of power distributions for $\Delta_q = 0.875\%$, $\delta = 0.2$ and for the coupling coefficient $D = 2.3 \times 10^{-7} \text{ rad}^2/\text{m}$ (centrally launched input) when guided and leaky modes are equally excited at the input fiber end (the θ_q excitation) for (a) $\lambda = 650 \text{ nm}$, (b) $\lambda = 840 \text{ nm}$, (c) $\lambda = 1310 \text{ nm}$ and (d) $\lambda = 1550 \text{ nm}$.

in [27]). Respective values for the critical angle are $\theta_q \cong \sqrt{2 \cdot \Delta_q} = 5.87^\circ$, 6.25° , 6.76° , 7.27° , and 7.58° . In other words, five different values for n_q (and thereby for critical angle θ_q) were applied. This varied the number and attenuation of leaky modes. Two normalized intermediate layer widths were considered, $\delta = 0.2$ and 0.5 (which values must be multiplied by the core radius for actual widths of 6 and $15 \mu\text{m}$). Respectively for these two widths, Figs. 2 and 3 show five sets of plots each, corresponding to the said five values for Δ_q . The wavelength was varied parametrically over four values in each plot.

One can observe in Figs. 2 and 3 that leaky mode losses increase with increasing wavelength. For the narrower intermediate layer (the smaller δ in Fig. 2), this increase is sharper. By moving from one plot to another, it is also apparent that the deeper the intermediate layer, the lower the leaky mode losses in all cases (in both, Figs. 2 or 3 and for any selected infrared wavelength). Leaky mode losses also increase with increasing the mode propagation angle θ (higher order leaky modes propagate with larger angles θ and attenuate faster in comparison to lower order ones).

In order to determine the length z_s for the onset of SSD, we solved the power flow equation by selecting θ_q excitation [26]. Fig. 4 shows angular power distributions in a W-type fiber for $\Delta_q = 0.875\%$, $\delta = 0.2$ and $D = 2.3 \times 10^{-7} \text{ rad}^2/\text{m}$, for centrally launched beam when guided and leaky modes are equally excited at the input fiber-end (the θ_q excitation) for different wavelengths. Length z_s for achieving SSD is determined as a length at which the angular light distribution stops evolving with further increase of the fiber length (becomes steady).

Respectively for $\delta = 0.2$ and 0.5 , Fig. 5a and b show how the length z_s varies with wavelength for parametric $\Delta_q = 0.525\%$, 0.595% , 0.7% , 0.805% and 0.875% . The value of $D = 2.3 \cdot 10^{-7} \text{ rad}^2/\text{m}$ was used for the coupling coefficient in the calculations [22,27]. One can observe

from Fig. 4 that the length z_s marking the onset of SSD decreases with increasing wavelength. This is a result of the increase of the leaky mode losses (with increasing wavelength), i.e. a smaller number of leaky modes remain guided at larger wavelengths at longer fiber lengths (Figs. 2 and 3).

As can be seen from Fig. 5, the length z_s is larger in the case of wider intermediate layer widths (larger δ). Since the leaky short transmission length in the case of thinner intermediate layer; consequently, it takes a shorter fiber length z_s for the onset of SSD — compared to the case with a wider intermediate layer. The reduction in length z_s with increasing wavelength is greater in the case of W-fiber with a narrower intermediate layer (smaller δ). This is a consequence of higher leaky mode losses at larger wavelengths for smaller δ — in comparison to the case of wider intermediate layer (larger δ). As depth of the intermediate layer (Δ_q) decreases, SSD occurs at shorter fiber lengths — which is attributed to the correspondingly decreasing number of leaky modes. The smaller the parameter Δ_q (consequently smaller θ_q), the shorter the fiber length is required for completion of the coupling process. For narrow intermediate layer $\delta = 0.2$, the influence of the depth of the intermediate layer Δ_q on the wavelength-dependence of length z_s weakens due to large losses of leaky modes at larger wavelengths (Fig. 5(a)). Thus, for the smallest depth analyzed ($\Delta_q = 0.525\%$), the influence of the wavelength on the length z_s becomes negligible. On the contrary for wider intermediate layer $\delta = 0.5$, the influence of the depth of the intermediate layer Δ_q on the wavelength-dependence of length z_s is not negligible for the smallest depth ($\Delta_q = 0.525\%$) because of much smaller leaky mode losses in the case of the intermediate layer width of $\delta = 0.5$ (i.e. longer lengths at which leaky modes remained guided) in comparison to the case with the intermediate layer width of $\delta = 0.2$.

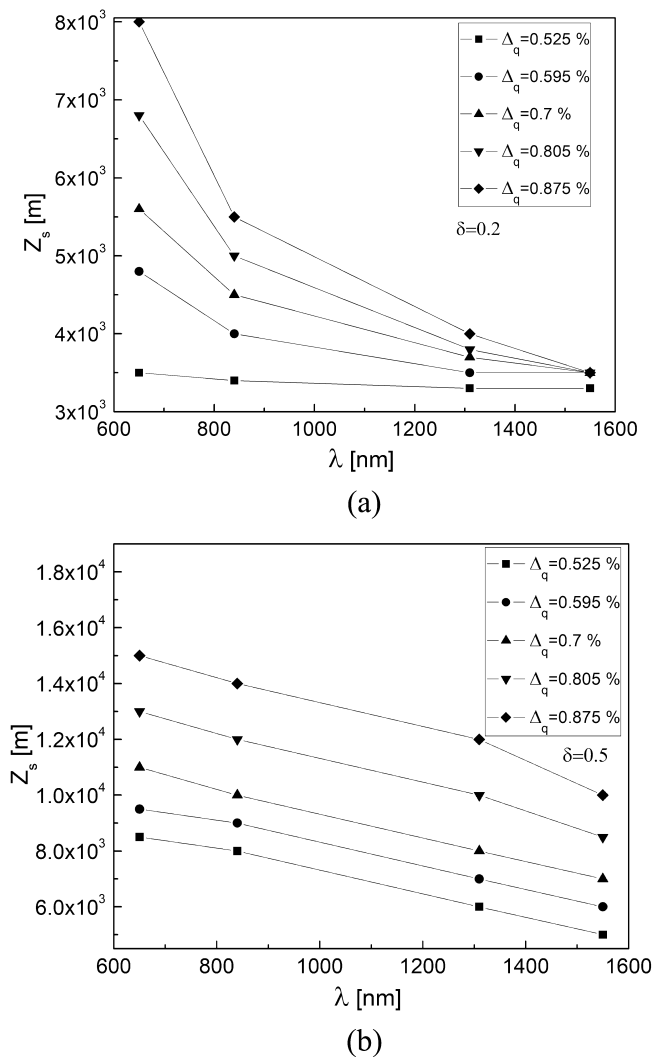


Fig. 5. Length z_s (marking the onset of SSD) as a function of wavelength, for (a) $\delta = 0.2$ and (b) $\delta = 0.5$ and for parametric Δ_q as in Figs. 2 and 3.

Since it is found that with increasing the infrared wavelength the leaky mode losses rise while SSD is established at shorter fiber lengths, the proposed W-type fiber has better transmission characteristics at longer infrared wavelengths. This is explained by the rise of the leaky mode losses with increasing wavelength as fewer leaky modes remain guided along the fiber; which decreases modal dispersion and increases bandwidth. At longer wavelengths a higher rate of filtering of leaky modes results in establishing the SSD (and therefore the equilibrium mode distribution) at shorter fiber lengths — the shorter the length at which equilibrium mode distribution is achieved, the earlier the bandwidth would switch from the functional dependence of $1/z$ to $1/z^{1/2}$ (faster bandwidth improvement) [20].

Needless to say, the strength of mode coupling also effects SSD [27]. SSD develops at shorter z_s when mode coupling is stronger.

5. Conclusion

Leaky mode losses and SSD (steady state distribution of power) are investigated for a varied glass W-fiber's intermediate layer in terms of its width and depth. It is found that leaky mode losses rise with wavelength. The rise is sharper for narrower intermediate layer widths (smaller δ). In contrast, the length z_s marking the onset of the SSD decreases with increasing wavelength. This is a result of the rise of the

leaky mode losses with rising wavelength, which is to say that a smaller number of leaky modes continue to be guided in longer fibers at larger wavelengths. For shorter intermediate layer's depths (Δ_q), SSD onsets at shorter fiber lengths due to fewer leaky modes. The smaller the Δ_q (implying smaller critical angle θ_q), the shorter the fiber length that is needed for completion of the coupling process.

For narrow intermediate layer $\delta = 0.2$, the wavelength dependence of length z_s is less affected by the intermediate layer's depth Δ_q due to large losses of leaky modes at larger infrared wavelengths (Fig. 5(a)). Thus for the smallest depth analyzed ($\Delta_q = 0.525\%$), the influence of infrared wavelength on the length z_s becomes negligible. In contrast, for wider intermediate layer $\delta = 0.5$, the depth of the intermediate layer Δ_q does affect the wavelength dependence of length z_s for the smallest depth ($\Delta_q = 0.525\%$) because of much smaller leaky mode losses. Because a wider intermediate layer ($\delta = 0.5$) reduces losses for leaky modes, these modes retain power over longer distances than in the case with the narrower layer ($\delta = 0.2$). This reflects accordingly in the length z_s that marks the onset of SSD — z_s is longer for ($\delta = 0.5$). It is similarly noted that the deeper the intermediate layer, the longer the length z_s — due to the rise in the number of leaky modes.

Finally, the proposed W-type fiber has better transmission characteristics at longer infrared wavelengths. This is explained by the rise of the leaky mode losses with increasing wavelength as fewer leaky modes remain guided along the fiber; which decreases modal dispersion and increases bandwidth.

Acknowledgments

The work described in this paper was supported by the Strategic Research Grant of City University of Hong Kong (Project No. CityU 7004600) and by a grant from Serbian Ministry of Education, Science and Technological Development (Project No. 171011).

References

- [1] E.J. Tyler, M. Webster, R.V. Penty, I.H. White, S. Yu, J. Rorison, Subcarrier modulated transmission of 2.5 Gb/s over 300 m of 62.5- μ m-diameter multimode fiber, *IEEE Photonics Technol. Lett.* 14 (2002) 1743–1745.
- [2] K.M. Patel, S.E. Ralph, Enhanced multimode fiber link performance using a spatially resolved receiver, *IEEE Photonics Technol. Lett.* 14 (2002) 393–395.
- [3] X. Zhao, F.S. Choa, Demonstration of 10 Gb/s transmission over 1.5-km-long multimode fiber using equalization techniques, *IEEE Photonics Technol. Lett.* 14 (2002) 1187–1189.
- [4] T. Ishigure, M. Kano, Y. Koike, Which is more serious factor to the bandwidth of GI POF: differential mode attenuation or mode coupling? *J. Lightwave Technol.* 18 (2000) 959–965.
- [5] K. Mikoshiba, H. Kajioka, Transmission characteristics of multimode W-type optical fiber: experimental study of the effect of the intermediate layer, *Appl. Opt.* 17 (1978) 2836–2841.
- [6] T. Tanaka, S. Yamada, M. Sumi, K. Mikoshiba, Microbending losses of doubly clad (W-type) optical fibers, *Appl. Opt.* 18 (1977) 2391–2394.
- [7] W. Daum, J. Krauser, P.E. Zamzow, O. Ziemann, *Polymer Optical Fibers for Data Communication*, Springer, Berlin, 2002.
- [8] T. Yamashita, M. Kagami, Fabrication of light-induced self-written waveguides with a W-shaped refractive index profile, *J. Lightwave Technol.* 23 (2005) 2542–2548.
- [9] M.A. Losada, I. Garcés, J. Mateo, I. Salinas, J. Lou, J. Zubía, Mode coupling contribution to radiation losses in curvatures for high and low numerical aperture plastic optical fibers, *J. Lightwave Technol.* 20 (2002) 1160–1164.
- [10] L.G. Cohen, D. Marcuse, W.L. Mammel, Radiating leak-mode losses in single mode light guides with depressed-index claddings, *IEEE J. Quantum Electron.* QE-18 (1982) 1467–1472.
- [11] M. Maeda, S. Yamada, Leaky modes on W-fibers: Mode structure and attenuation, *Appl. Opt.* 16 (1977) 2198–2203.
- [12] B.P. Pal, R.L. Gallawa, I.C. Goyal, LP11-mode leakage loss in coated depressed clad fibers, *IEEE Photonics Technol. Lett.* 4 (1992) 376–378.
- [13] C.-C. Chou, N.-H. Sun, Analysis of leaky-mode losses for optical fibers, *J. Opt. Soc. Amer. B* 25 (2008) 545–554.
- [14] S. Onoda, T. Tanaka, M. Sumi, W fiber design considerations, *Appl. Opt.* 15 (1976) 1930–1935.
- [15] I.V. Neves, A.S.C. Fernandes, Modal characteristics for W-type and M-type dielectric profile fibers, *Microwave Opt. Technol. Lett.* 22 (1999) 398–405.
- [16] S. Yu. Otrokho, Yu. K. Chamorovskiy, A.D. Shatrov, Leaking modes of guiding W fibers with a large difference in the refractive index profiles, *J. Commun. Technol. Electron.* 55 (2010) 1108–1114.

- [17] K. Takahashi, T. Ishigure, Y. Koike, Index profile design for high-bandwidth W-shaped plastic optical fiber, *J. Lightwave Technol.* 24 (2006) 2867–2876.
- [18] J. Dugas, G. Maurel, Mode-coupling processes in polymethyl methacrylate-core optical fibers, *Appl. Opt.* 31 (1992) 5069–5079.
- [19] D. Gloge, Optical power flow in multimode fibers, *Bell Syst. Tech. J.* 51 (1972) 1767–1783.
- [20] G. Jiang, R.F. Shi, A.F. Garito, Mode coupling and equilibrium mode distribution conditions in plastic optical fibers, *IEEE Photonics Technol. Lett.* 9 (1997) 1128–1130.
- [21] M. Rousseau, L. Jeunhomme, Numerical solution of the coupled-power equation in step index optical fibers, *IEEE Trans. Microw. Theory Tech.* 25 (1977) 577–585.
- [22] T.P. Tanaka, S. Yamada, Numerical solution of power flow equation in multimode W-type optical fibers, *Appl. Opt.* 19 (1980) 1647–1652.
- [23] T.P. Tanaka, S. Yamada, Steady-state characteristics of multimode W-type fibers, *Appl. Opt.* 18 (1979) 3261–3264.
- [24] L. Jeunhomme, M. Fraise, J.P. Pocholle, Propagation model for long step-index optical fibers, *Appl. Opt.* 15 (1976) 3040–3046.
- [25] A. Djordjevich, S. Savović, Numerical solution of the power flow equation in step index plastic optical fibers, *J. Opt. Soc. Amer. B* 21 (2004) 1437–1442.
- [26] S. Savović, A. Simović, A. Djordjevich, Explicit finite difference solution of the power flow equation in W-type optical fibers, *Opt. Laser Technol.* 44 (2012) 1786–1790.
- [27] A. Simović, A. Djordjevich, S. Savović, Influence of width of intermediate layer on power distribution in W-type optical fibers, *Appl. Opt.* 51 (2012) 4896–4901.
- [28] J.D. Anderson, *Computational Fluid Dynamics*, McGraw-Hill, New York, 1995.



Influence of the fiber design and launch beam on transmission characteristics of multimode glass W-type optical fibers



Ana Simović^a, Svetislav Savović^{a,b,*}, Branko Drljača^c, Alexandar Djordjevich^b

^a Faculty of Science, University of Kragujevac, R. Domanovića 12, 34000 Kragujevac, Serbia

^b City University of Hong Kong, 83 Tat Chee Avenue, Kowloon, Hong Kong, China

^c Faculty of Science, University of Kosovska Mitrovica, Lole Ribara 29, Kosovska Mitrovica, Serbia

ARTICLE INFO

Article history:

Received 25 September 2014

Received in revised form

18 November 2014

Accepted 26 November 2014

Keywords:

W-type multimode glass optical fiber

Power flow equation

Bandwidth

ABSTRACT

Bandwidth and steady-state loss of multimode glass W-type optical fibers (doubly clad fibers with three functional layers) are evaluated for the varied fiber design and launch beam parameters. These transmission characteristics are determined from the solution of the time-dependent power flow equation by the explicit finite difference method. Results are presented in a graph form as functions either of the fiber length or loss for the varied thickness and depth of the fiber's intermediate layer (inner cladding), fiber's coupling strength, and input beam (mean angle and width). The trade-off relation between the bandwidth and steady-state loss for designing multimode glass W-type optical fibers is shown in graphs and highlighted the text. We found that bandwidth improves with thinner and shallower intermediate layers, narrower and more central launch-beam, and stronger mode coupling.

© 2014 Elsevier Ltd. All rights reserved.

1. Introduction

Multimode optical fibers are usually singly clad (SC) in terms of the number of functional cladding layers. Techniques have been reported for improving bandwidth and attenuation properties of these fibers through special detection [1], modulation [2], equalization [3], and compensation of modal-dispersion [4]. For additional performance enhancement, fiber design is revisited in this paper with the aim of refining the fiber profile.

Our focus here is on doubly clad, “W-type” optical fibers. They have three distinct optical layers: core plus double cladding. In other words, a W-type fiber has an intermediate layer between its outer cladding and core. This layer is known to lower dispersion and bending losses, widen transmission bandwidth, and reduce the number of guided modes. It achieves this by lowering the fiber's effective numerical aperture by reducing the number of guided modes – guided modes are thus held tighter to the core [5]. As an illustration, while the bandwidth-distance product of an SC plastic fiber may be 15 MHz km that of a W-type plastic fiber may be 200 MHz km; these values are perhaps 30 MHz km and 50 MHz km for respective glass fibers [6–8]. Such improvement is attributed to the coupling of guided to lossy leaky modes in the W-type fiber's intermediate layer.

In general, mode coupling power is transferred between modes; this reduces modal dispersion because fractions of power do not keep to distinct propagation velocities of their launch modes, but tend to average them out through intermodal coupling. Bandwidth improves with less relative delay between modes. However, if mode coupling results in leaky mode condition, it increases fiber loss and changes beam properties. This is particularly notable after junctions and fiber bends [9] that promote coupling strongly.

The operational range of a multimode optical fiber as a data link is limited by the fiber bandwidth and mode-dependent attenuation. Much apparent performance improvement is offered by the W-type variant. Methods are needed for calculating modal attenuation, dispersion, and coupling to lossy modes of W-type fiber's intermediate layer, and for optimizing the fiber's refractive index profile including in order to minimize the group delay difference between modes in the output field. Our calculations in this work are based on the time-dependent power flow in glass W-type fibers.

2. Power flow in multimode singly clad fibers

Power flow in multimode singly clad fibers can be described by the following time-dependent equation [10]:

$$\frac{\partial p(\theta, z, t)}{\partial z} + \tau(\theta) \frac{\partial p(\theta, z, t)}{\partial t} = -\alpha(\theta) p(\theta, z, t) + \frac{1}{\theta} \frac{\partial}{\partial \theta} \left[\theta D(\theta) \frac{\partial p(\theta, z, t)}{\partial \theta} \right] \quad (1)$$

* Corresponding author at: Faculty of Science, R. Domanovića 12, 34000 Kragujevac, Serbia. Fax: +381 34 335040.

E-mail address: savovic@kg.ac.rs (S. Savović).

where $p(\theta, z, t)$ is power distribution over angle θ , position z , and time t ; $\tau(\theta)$ is modal delay per unit length; $D(\theta)$ is the mode-dependent coupling coefficient; and $\alpha(\theta) = \alpha_0 + \alpha_d(\theta)$ is the modal attenuation, with α_0 representing conventional losses (absorption and scattering) that feature in the solution only as a multiplier $\exp(-\alpha_0 z)$ that is therefore dropped. It should be noted here that the angle θ is subtended by the direction of propagation of each plane wave component of the guided mode and the fiber axis.

To obtain the frequency response, Fourier transformation is applied to Eq. (1)

$$\frac{\partial P(\theta, z, \omega)}{\partial z} + j\omega\tau(\theta)P(\theta, z, \omega) = -\alpha(\theta)P(\theta, z, \omega) + \frac{1}{\theta} \frac{\partial}{\partial \theta} \left[\theta D(\theta) \frac{\partial P(\theta, z, \omega)}{\partial \theta} \right] \quad (2)$$

where $\omega = 2\pi f$ is the angular frequency, and

$$P(\theta, z, \omega) = \int_{-\infty}^{+\infty} p(\theta, z, t) \exp(-j\omega t) dt \quad (3)$$

Two boundary conditions are formulated. They express that power is not transferred by modes with infinitely large loss, and that the coupling of modes is restricted to those propagating at angles $\theta > 0$

$$P(\theta_m, z, \omega) = 0, \quad D(\theta) \frac{\partial P(\theta = 0, z, \omega)}{\partial \theta} = 0 \quad (4)$$

where θ_m is the critical angle. Gaussian distribution for the launch-beam has been used

$$P(\theta, z = 0) = \exp \left[-\frac{(\theta - \theta_0)^2}{2\sigma^2} \right] \quad (5)$$

where θ_0 is the mean of the incidence angle distribution, and $0 \leq \theta \leq \theta_m$. The full width at half maximum was FWHM = $2\sigma\sqrt{2 \ln 2} \approx 2.355\sigma$ (σ is standard deviation).

By separating the complex $P(\theta, z, \omega)$ into its real $P_r(\theta, z, \omega)$ and imaginary $P_i(\theta, z, \omega)$ parts, Eq. (2) can for constant D (constant D is commonly assumed both for W-type [11–13,15,16] and step-index optical fibers [10,14]) be rewritten as the following simultaneous partial differential equations:

$$\frac{\partial P_r(\theta, z, \omega)}{\partial z} = -\alpha(\theta)P_r(\theta, z, \omega) + \frac{D}{\theta} \frac{\partial P_r(\theta, z, \omega)}{\partial \theta} + D \frac{\partial^2 P_r(\theta, z, \omega)}{\partial \theta^2} + \omega\tau P_i(\theta, z, \omega) \quad (6a)$$

$$\frac{\partial P_i(\theta, z, \omega)}{\partial z} = -\alpha(\theta)P_i(\theta, z, \omega) + \frac{D}{\theta} \frac{\partial P_i(\theta, z, \omega)}{\partial \theta} + D \frac{\partial^2 P_i(\theta, z, \omega)}{\partial \theta^2} - \omega\tau P_r(\theta, z, \omega) \quad (6b)$$

where

$$P(\theta, z, \omega) = P_r(\theta, z, \omega) + jP_i(\theta, z, \omega) \quad (7)$$

Frequency response $H(z, \omega)$ of the fiber of length z can be calculated once (6) is solved for $P_r(\theta, z, \omega)$ and $P_i(\theta, z, \omega)$

$$H(z, \omega) = \frac{2\pi \int_0^{\theta_m} \theta [P_r(\theta, z, \omega) + jP_i(\theta, z, \omega)] d\theta}{2\pi \int_0^{\theta_m} \theta [P_r(\theta, 0, \omega) + jP_i(\theta, 0, \omega)] d\theta} \quad (8)$$

Modal power distribution $P_F(\theta, z, \omega)$ and the spatial transient of power $P_L(z, \omega)$ can then also be calculated

$$P_F(\theta, z, \omega) = [P_r(\theta, z, \omega)^2 + P_i(\theta, z, \omega)^2]^{1/2} \quad (9)$$

$$P_L(z, \omega) = 2\pi \int_0^{\theta_m} \theta P_F(\theta, z, \omega) d\theta \quad (10)$$

3. Power flow in multimode W-type fibers

Fig. 1 illustrates a possible index profile of a W-type fiber whereby n_0 , n_q , and n_p are refractive indices of the core, intermediate

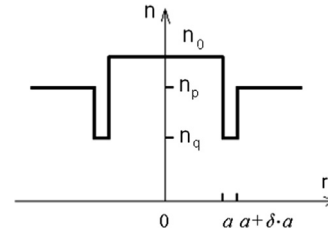


Fig. 1. Refractive index profile of a W-type fiber.

layer, and cladding, respectively. It is noted that the relative difference between refractive indexes of the core and intermediate layer $\Delta_q = (n_0 - n_q)/n_0$ is larger than that between the core and cladding $\Delta_p = (n_0 - n_p)/n_0$. Leaky modes are those propagating in the range of angles from $\theta_p \cong (2\Delta_p)^{1/2}$ to $\theta_q \cong (2\Delta_q)^{1/2}$ [12] and their attenuation constants are [13]

$$\alpha_L(\theta) = \frac{4(\theta^2 - \theta_p^2)^{1/2} \theta^2 (\theta_q^2 - \theta^2)}{a(1 - \theta^2)^{1/2} \theta_q^2 (\theta_q^2 - \theta_p^2)} \exp \left[-2\delta a n_0 k_0 (\theta_q^2 - \theta^2)^{1/2} \right] \quad (11)$$

where a and δa are the core radius and width of the intermediate layer, respectively, and k_0 is the wave number (free-space).

Similar to how the attenuation for SC fibers is constant for guided-modes but rises steeply for radiation-modes [14], the corresponding relationship for a W-type fiber can be expressed as

$$\alpha_d(\theta) = \begin{cases} 0 & \theta \leq \theta_p \\ \alpha_L(\theta) & \theta_p < \theta < \theta_q \\ \infty & \theta \geq \theta_q \end{cases} \quad (12)$$

Modal delay is [12]

$$\tau(\theta) = \frac{n_0}{c} \frac{1}{\cos \theta} \cong \frac{n_0}{c} \left(1 + \frac{\theta^2}{2} \right) = \tau_0 + \tau_d(\theta) \quad (13)$$

where c is the velocity of light in free space. In (13), the term τ_0 is the same for all modes. It therefore does not affect the group delay or transmission bandwidth and only $\tau_d(\theta)$ needs to be considered further in this respect.

The doubly clad (W-type) fiber transforms into a singly clad one by allowing the thickness of the intermediate layer (δa in Fig. 1) to either vanish or expand to fiber thickness. In the vanishing case, the core and the outer layer comprise the “SC_p” fiber. In the other case, the core and the intermediate layer as the only cladding form the “SC_q” fiber. A W-type fiber can be viewed as the SC_q fiber and an additional cladding.

Modes propagating along the SC_q fiber with subcritical angles $\theta < \theta_q$ ($\theta_q \cong (2\Delta_q)^{1/2}$) are guided. The same is true for those propagating through the complete W-fiber with angles θ below the critical value θ_p for the SC_p fiber, $\theta_p \cong (2\Delta_p)^{1/2}$. However, modes with angles between θ_p and θ_q are transformed into leaky modes. Because $\alpha_L(\theta)$ depends strongly on the intermediate-layer’s thickness δa , so do steady-state characteristics of W-type fibers: they approach those of SC_p or SC_q fibers at limits $\delta \rightarrow 0$ or $\delta \rightarrow \infty$, respectively [13,15]. Depth of the intermediate layer in the form of the refraction index differences (Fig. 1) also influences the power distribution in W-type optical fibers [15].

In an earlier work [16], bandwidth and steady-state loss of a glass W-type fiber were determined for a beam launched along the axis with distribution wider than that of the steady-state. With such launch, both guided and leaky modes were excited at the input end. In this work, the launch beam distribution is narrower than in the steady-state. Only guided modes are thus excited. Results show the influence that this width and mean input angle have on bandwidth and steady-state loss of glass W-type fibers for

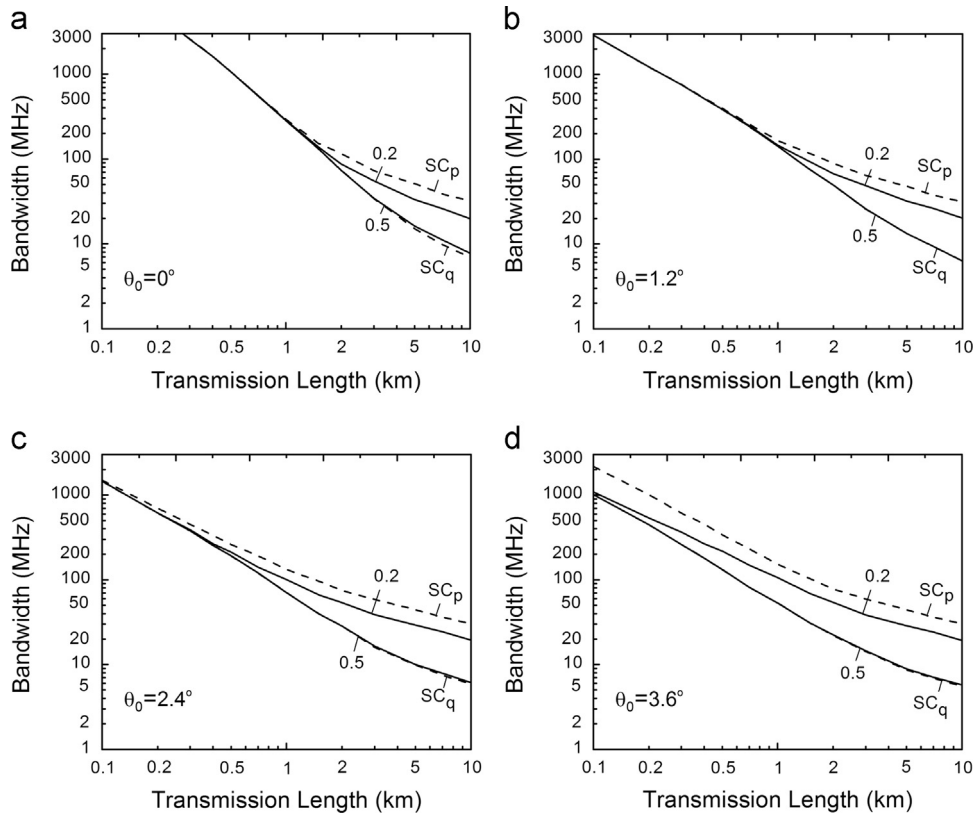


Fig. 2. Base case. Bandwidth versus transmission length for (a) $\theta_0=0^\circ$, (b) $\theta_0=1.2^\circ$, (c) $\theta_0=2.4^\circ$ and (d) $\theta_0=3.6^\circ$, where $\text{FWHM}_{z=0}=1^\circ$, $\delta=0.2$ and 0.5 , $\Delta_q=0.7\%$ and $D=2.3 \times 10^{-7} \text{ rad}^2/\text{m}$.

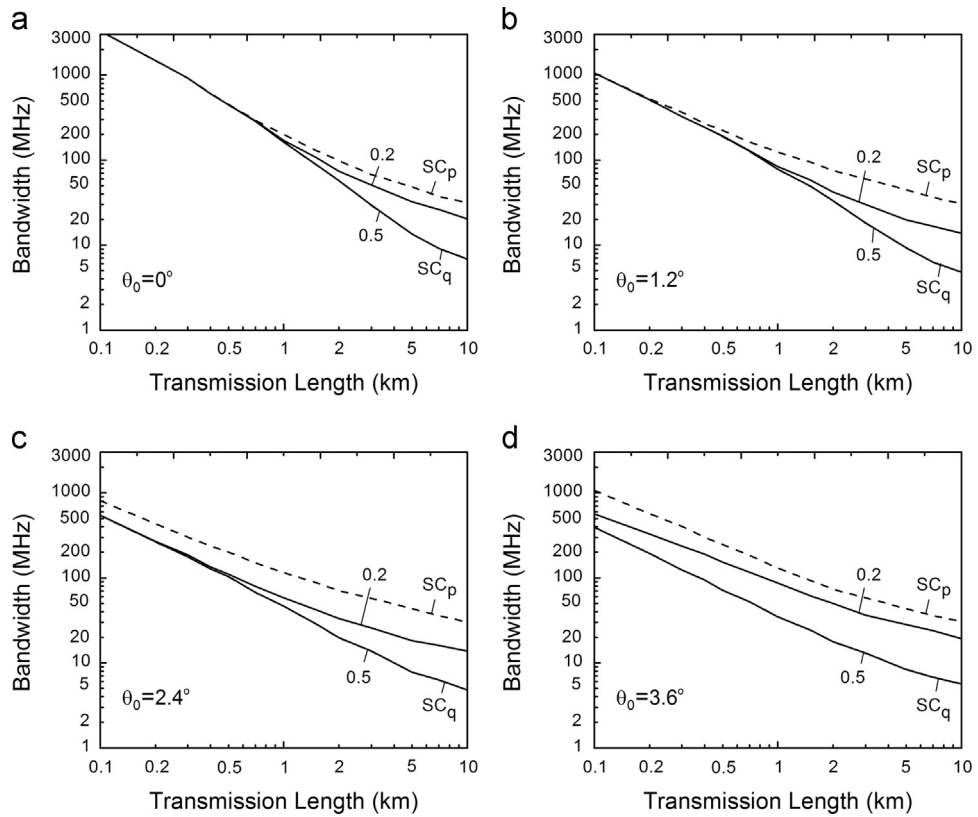


Fig. 3. Impact of larger FWHM. Bandwidth versus transmission length for (a) $\theta_0=0^\circ$, (b) $\theta_0=1.2^\circ$, (c) $\theta_0=2.4^\circ$ and (d) $\theta_0=3.6^\circ$, where $\text{FWHM}_{z=0}=3^\circ$, $\delta=0.2$ and 0.5 , $\Delta_q=0.7\%$ and $D=2.3 \times 10^{-7} \text{ rad}^2/\text{m}$.

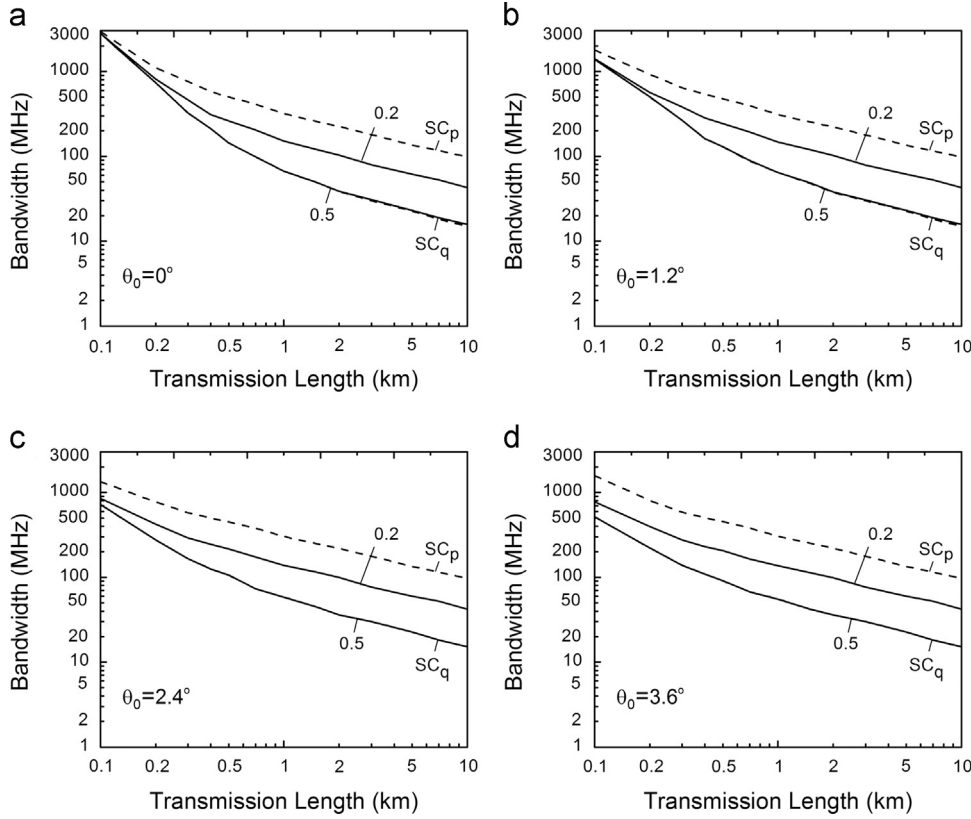


Fig. 4. Impact of larger mode coupling. Bandwidth versus transmission length for (a) $\theta_0=0^\circ$, (b) $\theta_0=1.2^\circ$, (c) $\theta_0=2.4^\circ$ and (d) $\theta_0=3.6^\circ$, where $\text{FWHM}_{z=0}=1^\circ$, $\delta=0.2$ and 0.5 , $\Delta_q=0.7\%$ and $D=2.3 \times 10^{-6}$ rad²/m.

different depths and widths of the intermediate layer and different coupling strengths.

4. Numerical method

Analytical solution of the simultaneous partial differential equations with the attenuation constants of leaky modes in the form of (11) is not available. Our numerical solution is by the explicit finite difference method (EFDM). With the central difference scheme applied to the terms $(\partial P(\theta, z, \omega))/\partial \theta$ and $(\partial^2 P(\theta, z, \omega))/\partial \theta^2$, and the forward difference scheme applied to the derivative term $(\partial P(\theta, z, \omega))/\partial z$ [17], Eqs. (6a) and (6b) becomes

$$P_{k,l+1}^r = \left(\frac{\Delta z D}{\Delta \theta^2} - \frac{\Delta z D}{2\theta_k \Delta \theta} \right) P_{k-1,l}^r + \left(1 - \frac{2\Delta z D}{\Delta \theta^2} - (\alpha_d)_k \Delta z \right) P_{k,l}^r + \left(\frac{\Delta z D}{2\theta_k \Delta \theta} + \frac{\Delta z D}{\Delta \theta^2} \right) P_{k+1,l}^r + \frac{\omega n_0 \Delta z}{2c} \theta_k^2 P_{k,l}^i \quad (14a)$$

$$P_{k,l+1}^i = \left(\frac{\Delta z D}{\Delta \theta^2} - \frac{\Delta z D}{2\theta_k \Delta \theta} \right) P_{k-1,l}^i + \left(1 - \frac{2\Delta z D}{\Delta \theta^2} - (\alpha_d)_k \Delta z \right) P_{k,l}^i + \left(\frac{\Delta z D}{2\theta_k \Delta \theta} + \frac{\Delta z D}{\Delta \theta^2} \right) P_{k+1,l}^i - \frac{\omega n_0 \Delta z}{2c} \theta_k^2 P_{k,l}^r \quad (14b)$$

where indexes k and l are the discretization step lengths $\Delta \theta$ and Δz for the angle θ and length z , respectively, and $P_{k,l}^r = P_r(\theta_k, z_l, \omega)$ and $P_{k,l}^i = P_i(\theta_k, z_l, \omega)$. In its finite difference form, modal attenuation is

$$(\alpha_d)_k = \begin{cases} 0 & \theta_k \leq \theta_p \\ \frac{4(\theta_k^2 - \theta_p^2)^{1/2} \theta_k^2 (\theta_q^2 - \theta_k^2)}{a(1 - \theta_k^2)^{1/2} \theta_k^2 (\theta_q^2 - \theta_p^2)} \exp \left[-2\delta a n_0 k_0 (\theta_q^2 - \theta_k^2)^{1/2} \right] & \theta_p < \theta_k < \theta_q \\ \infty & \theta_k \geq \theta_q \end{cases} \quad (15)$$

In the difference form, boundary conditions become $P_{N,l}^r = P_{N,l}^i = 0$ and $P_{0,l}^i = P_{1,l}^i$, $P_{0,l}^r = P_{1,l}^r$, where $N = \theta_q / \Delta \theta$ is the grid dimension in θ direction. To prevent the problem of singularity at grid points $\theta = 0$, we have used the following relationship [11]:

$$\lim_{\theta \rightarrow 0} \frac{1}{\theta} \frac{\partial}{\partial \theta} \left(\theta \frac{\partial P}{\partial \theta} \right) = 2 \frac{\partial^2 P}{\partial \theta^2} \Big|_{\theta=0} \quad (16)$$

The input condition (5) also has to be expressed in a finite difference form

$$p_{k,l=0}^r = \exp \left[-\frac{(\theta_k - \theta_0)^2}{2\sigma^2} \right]; \quad p_{k,l=0}^i = \exp \left[-\frac{(\theta_k - \theta_0)^2}{2\sigma^2} \right], \quad 0 \leq \theta_k < \theta_q \quad (17)$$

where $k=0, \dots, N-1$.

5. Numerical results

For a launch that is a Dirac input-impulse in time with Gaussian mode distribution, solutions of the time-dependent power flow equation (2) by EFDM shown, in Figs. 2 and 3, the bandwidth evolution with length of the reference fiber [11,12,15] for the mean input angles of (a) $\theta_0=0$, (b) 1.2° , (c) 2.4° and (d) 3.6° . Beam width (full width at half maximum) is $\text{FWHM}_{z=0}=1^\circ$ in Fig. 2 and $\text{FWHM}_{z=0}=3^\circ$ in Fig. 3. These solutions are given for two thicknesses of the normalized intermediate layer $\delta=0.2$ and $\delta=0.5$ (these should be multiplied by the fiber radius $a=30 \mu\text{m}$ for actual thicknesses). Values for the coupling coefficient $D=2.3 \times 10^{-7}$ rad²/m and for the intermediate layer's depth $\Delta_q=0.7$ percent ($\theta_q \cong 6.76^\circ$) are varied in subsequent figures while fiber parameter $\Delta_p=0.2\%$ ($\theta_p \cong 3.62^\circ$) is kept constant [11,12,15]. Further, $n_0=1.46$ and $\lambda=840$ nm.

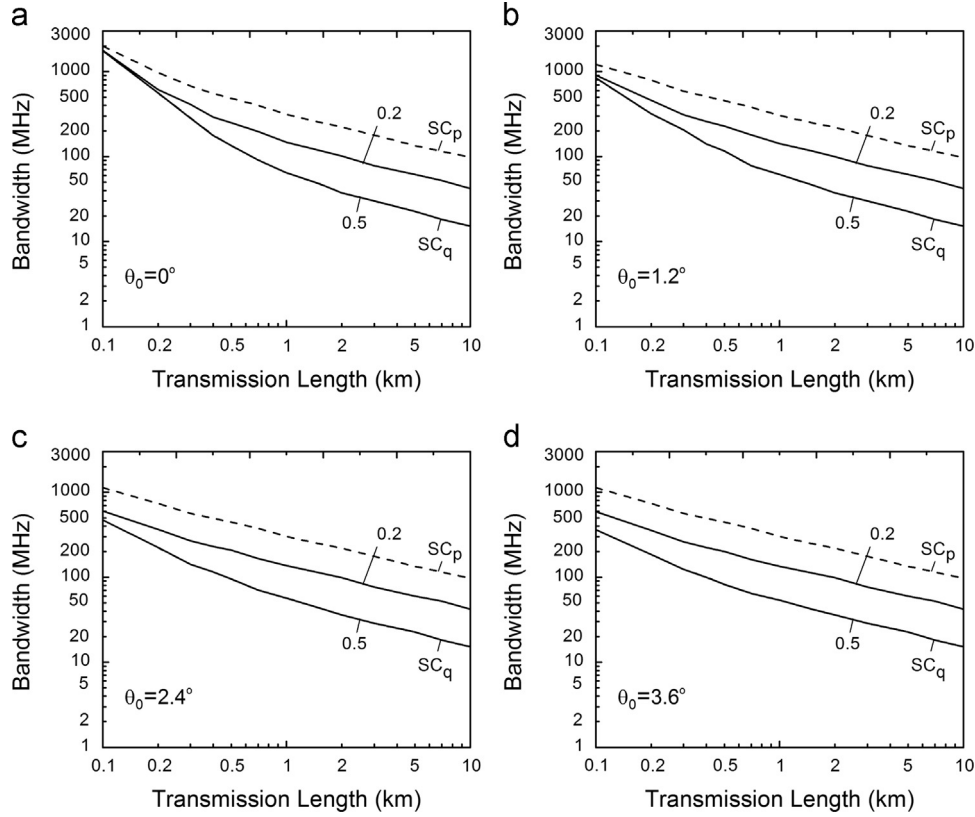


Fig. 5. Impact of larger FWHM and mode coupling. Bandwidth versus transmission length for (a) $\theta_0=0^\circ$, (b) $\theta_0=1.2^\circ$, (c) $\theta_0=2.4^\circ$ (d) $\theta_0=3.6^\circ$, where $\text{FWHM}_{z=0}=3^\circ$, $\delta=0.2$ and 0.5 , $\Delta_q=0.7\%$ and $D=2.3 \times 10^{-6} \text{ rad}^2/\text{m}$.

Moving from (a) to (d) in Figs. 2 and 3, it can be observed for short fiber lengths that the bandwidth decreases as the mean input angle θ_0 increases. This is attributed to higher dispersion of higher order modes for short fibers. Due to mode coupling, the effect diminishes with fiber length as the individual launch distributions approach the steady-state distribution for this fiber.

Relative to Fig. 2, it can be observed for short fiber lengths that bandwidth is lower in Fig. 3 where the launch-beam distribution is wider. This is because the energy of a wider launch beam is more uniformly distributed among guided modes at short fiber lengths, which increases modal dispersion and decreases bandwidth (for short fibers). Such influence of the width of the launch-beam distribution on bandwidth diminishes with fiber length.

It is also apparent in Figs. 2–5 that bandwidth of the W-type fiber is between those of the SC_p and SC_q fibers. Moreover, the bandwidth decreases linearly for short lengths and switches later to the $1/z^{1/2}$ functional dependence. This switch, and therefore equilibrium-mode distribution, occurs at shorter fiber lengths for the thinner intermediate-layer ($\delta=0.2$).

For a fiber with the intermediate layer's thickness $\delta=0.2$, a launch distribution with $\text{FWHM}=3^\circ$ at $\theta_0=3.6^\circ$ (Figs. 3d and 5d) generates input modes in the range wider than the steady-state distribution. Hence, mode coupling does not widen the input distribution further (which would otherwise be expected at short lengths) and stronger coupling (Fig. 5d vs. 3d) starts improving bandwidth from the beginning of the fiber.

With respect to the situation of Fig. 2, depth of the intermediate layer of $\Delta_q=0.7$ percent is scaled in Figs. 6 and 7 by a quarter of its value: $\Delta_q=0.525$ percent in Fig. 6 and $\Delta_q=0.875$ percent in Fig. 7 (this depth is a measure of refraction index differences). Bandwidth improves as this depth is reduced because fewer leaky modes then persist along the fiber and dispersion lessens. The

smaller the Δ_q and consequently θ_q , the shorter the fiber length for complete coupling. This decrease is more pronounced for thinner intermediate layers (smaller δ) due to their higher leaky mode loss that shortens the coupling length further.

With a narrow launch-beam of only guided modes, the role of leaky modes is insignificant at short fiber lengths. Hence, neither thickness nor depth of the intermediate layer influences bandwidth of short fibers (Figs. 6 and 7) until mode coupling gradually changes this along the fiber. Only for wide beams launched at steep mean input angles are leaky modes significant enough at short fiber lengths for the thickness and depth of the intermediate layer to influence the fiber bandwidth at both short and long fiber lengths.

With stronger mode coupling, the influence of the intermediate layer's thickness and depth on bandwidth intensifies for all fiber lengths. This is because a stronger mode coupling shifts the onset of leaky modes to shorter fiber lengths. Similarly for short fibers, thinner intermediate layers affect bandwidth stronger as then the leaky lossy modes appear earlier along the fiber. With the increasing launch-beam width, incidence angle, or fiber coupling strength, lossy leaky modes gain prominence at shorter lengths and so does the influence of the cladding that commences at shorter lengths for all depths.

Depth of the intermediate layer is given the value of $\Delta_q=0.525$ percent in Fig. 8, $\Delta_q=0.7$ percent in Fig. 9, and $\Delta_q=0.875$ percent in Fig. 10. In all three figures, the trade-off relationship between bandwidth and steady-state loss is shown for $\text{FWHM}_{z=0}=1$ and 3° , $\delta=0.2$ and 0.5 , $D=2.3 \times 10^{-7}$ and $2.3 \times 10^{-6} \text{ rad}^2/\text{m}$, and for (a) $\theta_0=0$, (b) 1.2 , (c) 2.4 and (d) 3.6° . It is evident from these figures that both steady-state loss and bandwidth are larger with a narrower launch-beam. Further, steady-state loss and, to a lesser extent, bandwidth decrease as the mean input angle increases.

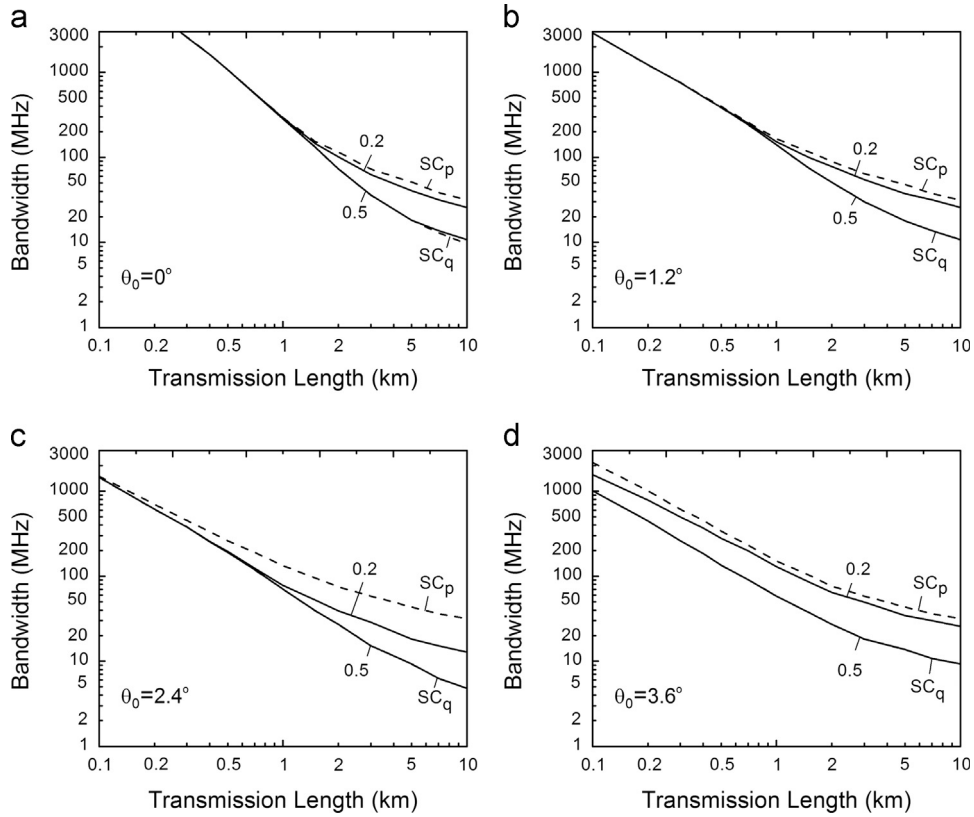


Fig. 6. Impact of smaller inner-cladding Δq . Bandwidth versus transmission length for (a) $\theta_0=0^\circ$, (b) $\theta_0=1.2^\circ$, (c) $\theta_0=2.4^\circ$ and (d) $\theta_0=3.6^\circ$, where $FWHM_{z=0}=1^\circ$, $\delta=0.2$ and 0.5 , $\Delta q=0.525\%$ and $D=2.3 \times 10^{-7} \text{ rad}^2/\text{m}$.

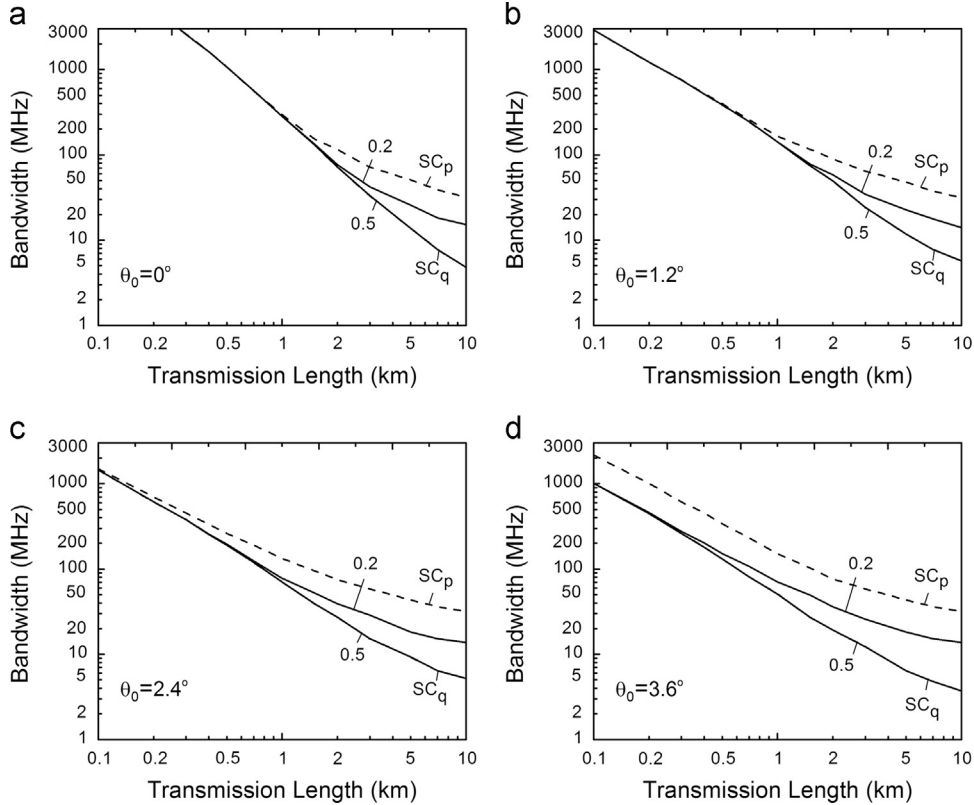


Fig. 7. Impact of larger inner-cladding Δq . Bandwidth versus transmission length for (a) $\theta_0=0^\circ$, (b) $\theta_0=1.2^\circ$, (c) $\theta_0=2.4^\circ$ (d) $\theta_0=3.6^\circ$, where $FWHM_{z=0}=1^\circ$, $\delta=0.2$ and 0.5 , $\Delta q=0.875\%$ and $D=2.3 \times 10^{-7} \text{ rad}^2/\text{m}$.

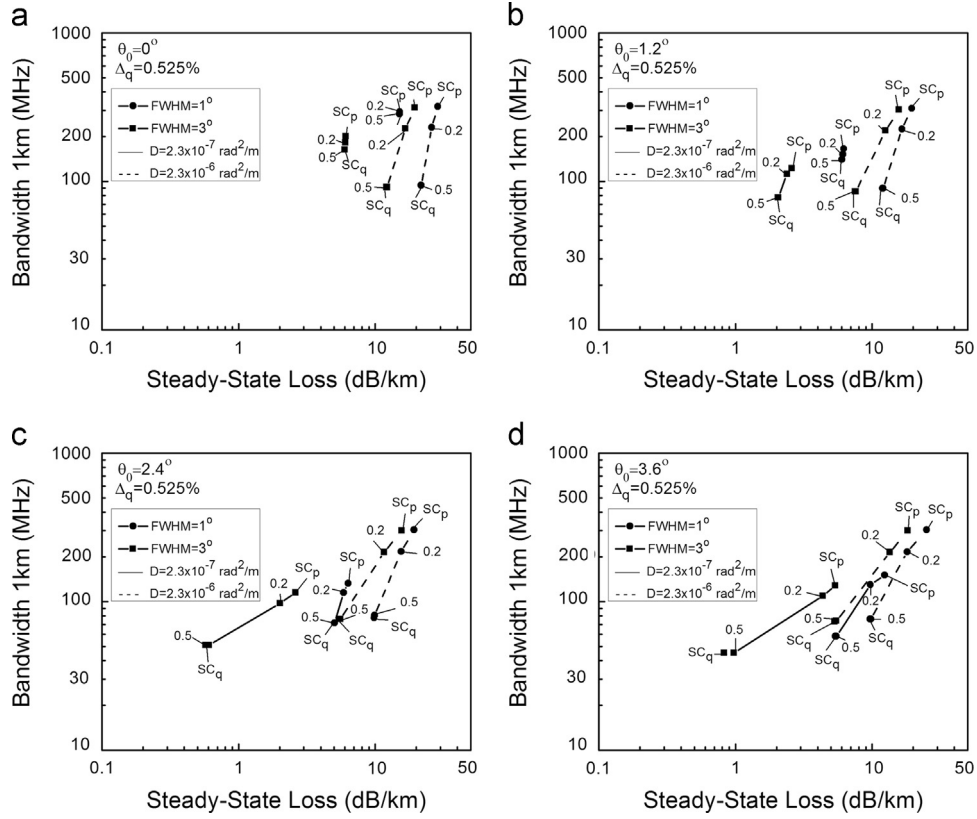


Fig. 8. Trade-off relation between bandwidth and steady-state loss for (a) $\theta_0 = 0^\circ$, (b) $\theta_0 = 1.2^\circ$, (c) $\theta_0 = 2.4^\circ$ and (d) $\theta_0 = 3.6^\circ$, where $\text{FWHM}_{z=0} = 1^\circ$ and 3° , $\delta = 0.2$ and 0.5 , $\Delta_q = 0.525\%$ and $D = 2.3 \times 10^{-7} \text{ rad}^2/\text{m}$.

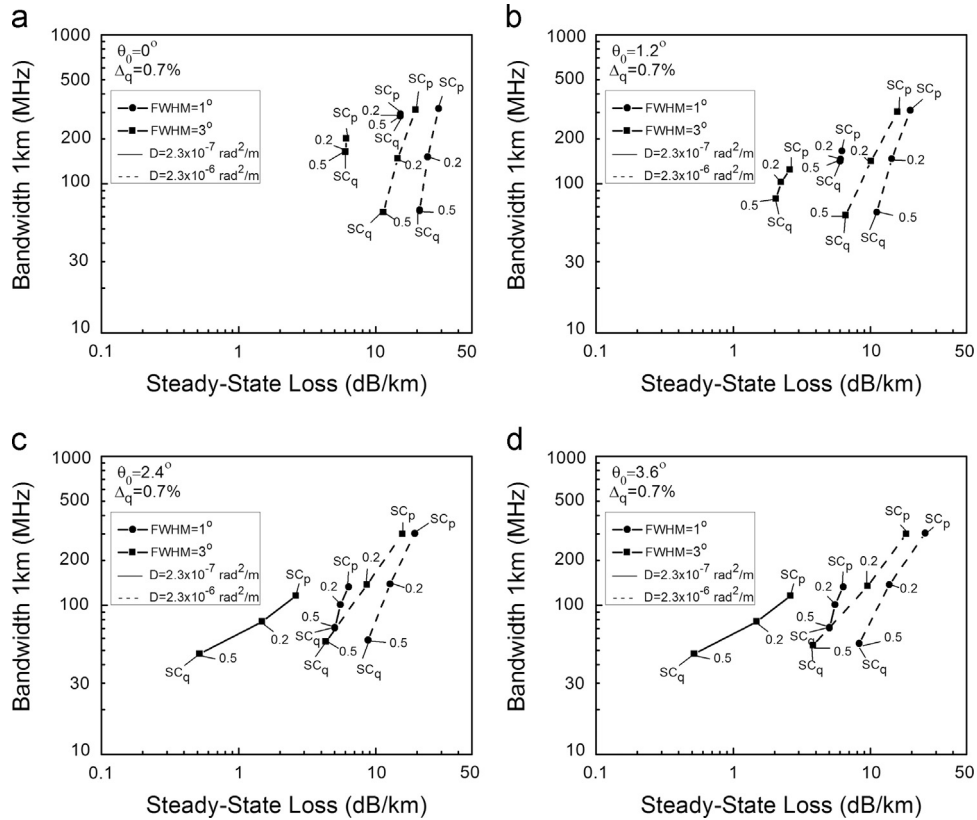


Fig. 9. Trade-off relation between bandwidth and steady-state loss for (a) $\theta_0 = 0^\circ$, (b) $\theta_0 = 1.2^\circ$, (c) $\theta_0 = 2.4^\circ$ and (d) $\theta_0 = 3.6^\circ$, where $\text{FWHM}_{z=0} = 1^\circ$ and 3° , $\delta = 0.2$ and 0.5 , $\Delta_q = 0.7\%$ and $D = 2.3 \times 10^{-7} \text{ rad}^2/\text{m}$.

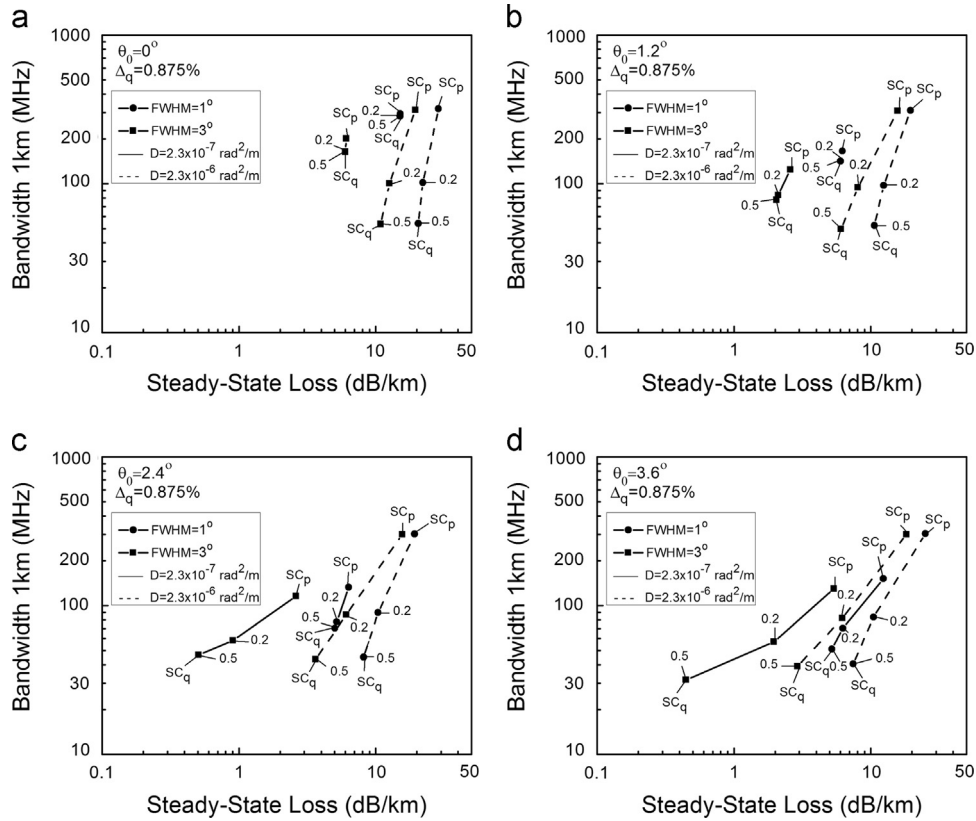


Fig. 10. Trade-off relation between bandwidth and steady-state loss for (a) $\theta_0=0^\circ$, (b) $\theta_0=1.2^\circ$, (c) $\theta_0=2.4^\circ$ and (d) $\theta_0=3.6^\circ$, where $\text{FWHM}_{z=0}=1^\circ$ and 3° , $\delta=0.2$ and 0.5 , $\Delta_q=0.875\%$ and $D=2.3 \times 10^{-7} \text{ rad}^2/\text{m}$.

Bandwidth can therefore be improved by reducing the intermediate layer's thickness or depth, by narrowing the launch-beam width, or opting for the central launch. Increasing the coupling strength, while beneficial in this respect, would be impractical due to its adverse effect on loss characteristics.

6. Conclusion

Bandwidth and steady-state loss of glass W-type optical fibers are evaluated by numerically solving the time-dependent power-flow equation under varied conditions of the launch beam and fiber design parameters. These transmission characteristics are calculated by the time-dependent power flow equation and presented in a graph form as functions either of fiber length or steady-state loss. Varied are the main input angle, width of the launch-beam distribution, thickness and depth of the fiber's intermediate layer, as well as the fiber length and its coupling strength. The coupling coefficients D are chosen to match the mode coupling strength seen in glass multimode optical fibers.

It is shown for the range of short glass W-type fiber lengths that bandwidth decreases as the mean input angle or width of the launch-beam distribution increase. This is attributed to larger modal dispersion of higher order modes that are present in both launches, whether steeper or wider. Due to mode coupling, the effect diminishes with fiber length as the individual launch distributions approach the steady-state distribution. Moreover for short fibers, it was shown that the stronger the coupling, the lower the bandwidth. The opposite is the case for longer fibers. Mode coupling has positive effects for bandwidth at fiber lengths beyond the coupling length L_c , which is when the bandwidth-drop switches from its $1/z$ to $1/z^{1/2}$ functional dependence, thus slowing

down the further bandwidth drop with length. This switch to decelerated drop occurs sooner with stronger coupling as the coupling length L_c is then reduced.

With a narrow launch exciting only guided modes, there would be few (if any) leaky modes in short fibers. Consequently, the intermediate layer and its influence on bandwidth are insignificant in short fibers (Figs. 6 and 7). Mode coupling changes this in longer fibers and the role of the fiber's intermediate layer gains in importance with the greater abundance of leaky modes. For wide launch-beams and steep mean input angles, the leaky modes are plentiful at both short and long fiber lengths and the design parameters of the intermediate layer influence bandwidth at all fiber lengths. Both steady-state loss and bandwidth are larger with narrower launch-beam.

The bandwidth-distance product of modern W-type multimode glass optical fibers is reported to be up to 50 MHz km [7,8]. In this work it is shown that bandwidth-distance product of about 250 MHz km could be achieved with thinner and shallower intermediate layers, narrower and more central launch-beam, and stronger mode coupling. Stronger mode coupling, however, increases steady-state loss and a trade-off relation between bandwidth and loss would have to be considered in designing the optimum W-type index profile by controlling parameters of the intermediate layer (thickness and depth) and input beam (width and angle).

Acknowledgment

The work described in this paper was supported by the Strategic Research Grant of City University of Hong Kong (Project no. CityU 7004069) and by a grant from Serbian

Ministry of Education, Science and Technological Development (Project no. 171011).

References

- [1] Patel KM, Ralph SE. Enhanced multimode fiber link performance using a spatially resolved receiver. *IEEE Photon Technol Lett* 2002;14:393–5.
- [2] Tyler EJ, Webster M, Penty RV, White IH, Yu S, Rorison J. Subcarrier modulated transmission of 2.5 Gb/s over 300 m of 62.5- μm -core diameter multimode fiber. *IEEE Photon Technol Lett* 2002;14:1743–5.
- [3] Zhao X, Choa FS. Demonstration of 10 Gb/s transmission over 1.5-km-long multimode fiber using equalization techniques. *IEEE Photon Technol Lett* 2002;14:1187–9.
- [4] Abbott JS, Smith GE, Truesdale CM. Multimode fiber link dispersion compensator. U.S Patent 6,363,195, 2002.
- [5] Babita V Rastogi, Kumar A. Design of large-mode-area three layered fiber structure for femtosecond laser pulse delivery. *Opt Commun* 2013;293:108–12.
- [6] Tanaka T, Yamada S, Sumi M, Mikoshiba K. Microbending losses of doubly clad (W-type) optical fibers. *Appl Opt* 1977;18:2391–4.
- [7] Daum W, Krauser J, Zamzow PE, Ziemann O. Polymer optical fibers for data communication. Berlin: Springer; 2002.
- [8] Yamashita T, Kagami M. Fabrication of light-induced self-written waveguides with a W-shaped refractive index profile. *J Lightw Technol* 2005;23:2542–8.
- [9] Losada MA, Garcés I, Mateo J, Salinas I, Lou J, Zubía J. Mode coupling contribution to radiation losses in curvatures for high and low numerical aperture plastic optical fibers. *J Lightw Technol* 2002;20:1160–4.
- [10] Gloge D. Impulse response of clad optical multimode fibers. *Bell Syst Tech J* 1973;52:801–16.
- [11] Simović A, Djordjević A, Savović S. Influence of depth of intermediate layer on power distribution in W-type optical fibers. *Appl Opt* 2012;51:4896–901.
- [12] Tanaka TP, Yamada S. Numerical solution of power flow equation in multimode W-type optical fibers. *Appl Opt* 1980;19:1647–52.
- [13] Tanaka TP, Yamada S. Steady-state characteristics of multimode W-type fibers. *Appl Opt* 1979;18:3261–4.
- [14] Jeunhomme L, Fraise M, Pocholle JP. Propagation model for long step-index optical fibers. *Appl Opt* 1976;15:3040–6.
- [15] Savović S, Simović A, Djordjević A. Explicit finite difference solution of the power flow equation in W-type optical fibers. *Opt Laser Technol* 2012;44:1786–90.
- [16] Simović A, Savović S, Drljača B, Djordjević A. Influence of intermediate layer on transmission characteristics of W-type optical fibers. *Opt Laser Technol* 2014;57:209–15.
- [17] Anderson JD. Computational fluid dynamics. New York: Mc Graw-Hill; 1995.

Frequency response and bandwidth in low-numerical-aperture step-index plastic optical fibers

Svetislav Savović,^{1,2,*} Branko Drljača,³ Milan S. Kovačević,^{1,2} Alexandar Djordjevich,² Jovan S. Bajić,⁴ Dragan Z. Stupar,⁴ and Grzegorz Stepniak⁵

¹University of Kragujevac, Faculty of Science, R. Domanovića 12, Kragujevac, Serbia

²City University of Hong Kong, Tat Chee Avenue, Kowloon, Hong Kong, China

³University of Kosovska Mitrovica, Faculty of Science, Lole Ribara 29, Kosovska Mitrovica, Serbia

⁴University of Novi Sad, Faculty of Technical Sciences, Novi Sad, Serbia

⁵Warsaw University of Technology, Institute of Telecommunications, Warsaw, Poland

*Corresponding author: savovic@kg.ac.rs

Received 6 August 2014; revised 12 September 2014; accepted 12 September 2014;
posted 15 September 2014 (Doc. ID 220428); published 14 October 2014

By experimental measurement and from a numerical solution to the time-dependent power flow equation, the frequency response, bandwidth, mode coupling, and mode-dependent attenuation are determined for a low-numerical-aperture (NA) plastic optical fiber. Frequency response and bandwidth are specified as a function of fiber length. Numerical results are verified against experimental measurements. Mode coupling and modal attenuation are found to differ substantially between two fiber varieties of the same type (both low-NA, step-index, and plastic), implying their preferential suitability that is application-specific. © 2014 Optical Society of America

OCIS codes: (060.2310) Fiber optics; (060.2400) Fiber properties.

<http://dx.doi.org/10.1364/AO.53.006999>

1. Introduction

Large core (0.5–1 mm or greater) step-index plastic optical fibers (SI-POFs) have some tempting features, such as low cost and easy handling, making them an attractive medium for high speed interconnects [1–4]. However, their large attenuation and modal dispersion influence severely the link length and the rate, respectively.

Transmission properties of SI multimode optical fibers, such as frequency response and bandwidth, depend strongly upon mode-dependent attenuation, modal dispersion, and the rate of mode coupling (power transfer from lower to higher order modes) caused by intrinsic perturbation effects (primarily due to microscopic bends, irregularity of the core–

cladding boundary, and refractive index distribution fluctuations). Different models have been used to simulate these three important effects for SI optical fibers. The ray tracing model can determine the output angular power distribution while accounting for the mode-dependent attenuation. The time delay between individual rays can also be calculated in the presence of modal dispersion. This model is computationally intensive because a large number of ray-trajectories must be simulated. In contrast, the time-independent power flow equation [5] is effective in modeling mode-dependent attenuation, mode coupling, and how these influence the output angular power distribution for different fiber lengths and launch conditions. However, the frequency response and bandwidth are not calculated by such time-independent analysis.

The center launch technique (with the incident spot in the center of the multimode optical fiber core)

is commonly used in local area networks to achieve bandwidth enhancement in support of multimedia applications [6]. In contrast, the offset launch (with the off-centered incident spot) allows for several services (voice, telephony, Internet) to be multiplexed by exploiting submodes or groups as independent communication channels [7].

In our previous works, using the time-dependent power flow equation, we have determined the POF bandwidth in addition to mode coupling and mode-dependent attenuation for the high numerical-index (NA) (~ 0.5) POFs [8–10]. In this work, using the time-dependent power flow equation, we calculate frequency response and bandwidth in addition to mode coupling and mode-dependent attenuation in low NA (0.3) SI-POFs. Frequency response and bandwidth are specified in the paper as a function of fiber length. Numerical results are compared with our measurements. We showed how the variation of bandwidth with fiber length is strongly affected by mode coupling, modal attenuation, and NA.

2. Time-Dependent Power Flow Equation

We use Gloge's time-dependent power flow equation to describe the evolution of the modal power distribution along a POF. Individual propagating modes are characterized by the respective inner propagation angle with respect to fiber axis (θ), which can be taken as a continuous variable [11]. Gloge's time-dependent power flow equation can be written as [11]:

$$\frac{\partial P(\theta, z, t)}{\partial z} + \frac{\partial t}{\partial z} \frac{\partial P(\theta, z, t)}{\partial t} = -\alpha(\theta)P(\theta, z, t) + \frac{1}{\theta} \frac{\partial}{\partial \theta} \left[\theta D(\theta) \frac{\partial P(\theta, z, t)}{\partial \theta} \right], \quad (1)$$

where t is time; $P(\theta, z, t)$ is power distribution over angle, space, and time; $\alpha(\theta)$ is mode-dependent attenuation; $\partial t/\partial z$ is mode delay per unit length; and $D(\theta)$ is the mode-dependent coupling coefficient. Mode-dependent attenuation can be written in the form $\alpha(\theta) = \alpha_0 + A\theta^2 + \dots$, where α_0 is the loss common to all modes. It can be accounted for by multiplying the end solution by $e^{-\alpha_0 z}$ [12,13]. Therefore, when solving Eq. (1), one needs only to consider the term $A\theta^2$ as the most dominant of the higher order modes [5]. Assuming that the coupling coefficient D is mode-independent, Eq. (1) can be written as [11]:

$$\frac{\partial P(\theta, z, t)}{\partial z} + \frac{\partial t}{\partial z} \frac{\partial P(\theta, z, t)}{\partial t} = -A\theta^2 P(\theta, z, t) + \frac{D}{\theta} \frac{\partial}{\partial \theta} \left[\theta \frac{\partial P(\theta, z, t)}{\partial \theta} \right]. \quad (2)$$

The derivative $\partial t/\partial z$ can be obtained using the group velocity of a mode with characteristic angle θ , which is

$$\frac{dz}{dt} = \frac{c}{n(1 + \theta^2/2)}. \quad (3)$$

Neglecting the delay n/c common to all modes, it follows that [11]:

$$\frac{\partial P(\theta, z, t)}{\partial z} = -A\theta^2 P(\theta, z, t) - \frac{n}{2c} \theta^2 \frac{\partial P(\theta, z, t)}{\partial t} + \frac{D}{\theta} \frac{\partial}{\partial \theta} \left(\theta \frac{\partial P(\theta, z, t)}{\partial \theta} \right). \quad (4)$$

By applying the Fourier transform,

$$p(\theta, z, \omega) = \int_{-\infty}^{\infty} P(\theta, z, t) e^{-j\omega t} dt, \quad (5)$$

the time-dependent Eq. (4) transforms into Eq. (6):

$$\frac{\partial p(\theta, z, \omega)}{\partial z} = -\left[A\theta^2 + j\omega \frac{n}{2c} \theta^2 \right] p(\theta, z, \omega) + \frac{D}{\theta} \frac{\partial p(\theta, z, \omega)}{\partial \theta} + D \left(\theta \frac{\partial^2 p(\theta, z, \omega)}{\partial \theta^2} \right), \quad (6)$$

where $\omega = 2\pi f$ is the angular frequency.

The boundary conditions are

$$p(\theta_c, z, \omega) = 0, \quad D \frac{\partial p(\theta, z, \omega)}{\partial \theta} \Big|_{\theta=\theta_0} = 0, \quad (7)$$

where θ_c is the critical angle. The first condition implies that modes with infinitely large loss do not transfer any power; the second condition implies that mode coupling is limited to modes travelling with the angle $\theta > 0$.

We used Gaussian launch-beam distribution of the form

$$P(\theta, z = 0) = \exp \left[-\frac{(\theta - \theta_0)^2}{2\sigma^2} \right], \quad (8)$$

with $0 \leq \theta \leq \theta_c$, where θ_0 is the mean value of the incidence angle distribution, and the full width at half-maximum FWHM $= 2\sigma\sqrt{2 \ln 2} = 2.355\sigma$ (σ is standard deviation). This distribution is suitable both for light-emitting diodes and laser beams.

It is apparent that $p(\theta, z, \omega)$ is complex. We can therefore separate $p(\theta, z, \omega)$ into its real and imaginary parts, $p = p^r + jp^i$. Equation (6) can now be rewritten as the following simultaneous differential equations:

$$\begin{aligned} \frac{\partial p^r}{\partial z} &= -A\theta^2 p^r + \frac{D}{\theta} \frac{\partial p^r}{\partial \theta} + D \frac{\partial^2 p^r}{\partial \theta^2} + \omega \frac{n}{2c} \theta^2 p^i, \\ \frac{\partial p^i}{\partial z} &= -A\theta^2 p^i + \frac{D}{\theta} \frac{\partial p^i}{\partial \theta} + D \frac{\partial^2 p^i}{\partial \theta^2} - \omega \frac{n}{2c} \theta^2 p^r. \end{aligned} \quad (9)$$

Once p^r and p^i are obtained by solving Eqs. (9), the frequency response at z can be calculated as

$$H(z, \omega) = \frac{2\pi \int_0^{\theta_c} \theta [p^r(\theta, z, \omega) + jp^i(\theta, z, \omega)] d\theta}{2\pi \int_0^{\theta_c} \theta [p^r(\theta, 0, \omega) + jp^i(\theta, 0, \omega)] d\theta}. \quad (10)$$

After separating the power flow Eq. (6) into two simultaneous Eqs. (9), we solved the latter by the explicit finite difference method [14].

3. Experimental Setup

We present in this section the experimental setup for measuring the mode-dependent attenuation coefficient $\alpha(\theta)$, frequency response, and bandwidth of the MH4001 ESKA Mitsubishi Rayon fiber (MH fiber). This fiber has typical dimensions, core diameter $d_{\text{core}} = 980 \mu\text{m}$ and clad diameter $d_{\text{clad}} = 1000 \mu\text{m}$, NA = 0.3, core refractive index $n = 1.49$, and critical angle $\theta_c = 11.7^\circ$ (measured inside the fiber) or $\theta_c = 17.6^\circ$ (measured in air). The number of modes in this SI multimode POF at $\lambda = 660 \text{ nm}$ is $N = 2\pi^2 a^2 (\text{NA})^2 / \lambda^2 \approx 1.02 \times 10^6$, where a is radius of the fiber core. This large number of modes may be represented by a continuum as required for application of Eq. (2). The ends of the sample fibers have been polished carefully for reduced imperfections and associated light diffraction.

Figure 1 shows schematics of the experimental setup for measuring the mode-dependent attenuation coefficient $\alpha(\theta)$. The input fiber end was mounted on a rotation stage (MRS/PRM1/M by Thorlabs, Inc.) to permit angled launches from a 660 nm laser diode (type HL6501MG). The output intensity from the other fiber end was measured by a power meter (PM300E by Thorlabs, Inc.).

The frequency responses have been measured directly by transmitting sinusoids of different frequencies and measuring their amplitudes. For this purpose, a harmonic signal from a tracking generator (Rohde & Schwarz FSH6) was used to modulate the laser diode. The diode output was first coupled to an OM1 patch cord of NA = 0.275, to which the fiber samples of different lengths were connected. Filtration in OM1 controlled the input power and ensured the consistent launch NA for all spans of POF. The receiver was a large-area photoreceiver (Graviton SPA-2) with bandwidth of 1 GHz connected to a spectrum analyzer and synchronized with the generator. Bandwidth (electrical) of 500 MHz of

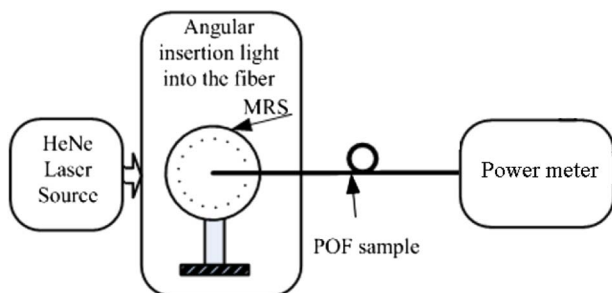


Fig. 1. Block diagram of the experimental setup for measuring the mode-dependent attenuation $\alpha(\theta)$ (MRS—manual rotation stage).

the generator, laser, and receiver, combined, was measured on a short OM1 cable and accounted for in the overall measurements.

4. Numerical and Experimental Results

The time-dependent power flow Eq. (1) is applied to calculate the frequency response and bandwidth of the MH fiber. In our recently published work [14], coupling coefficient D for this fiber was calculated as $D = 1.62 \times 10^{-3} \text{ rad}^2/\text{m}$. In order to obtain the value for constant A for the MH fiber, we used the graph for $\alpha(\theta)$ in Fig. 2. Since mode-dependent attenuation can be written in the form $\alpha(\theta) \approx \alpha_0 + A\theta^2$, one can determine A by fitting the experimental graph of Fig. 2 using this $\alpha(\theta)$ function. In doing so, we have obtained $\alpha_0 = 0.10793 \text{ 1/m}$ and $A = 0.29166 (\text{rad}^2 \text{ m})^{-1}$. The lengths of the MH fiber span utilized in measuring mode-dependent attenuation $\alpha(\theta)$ were 1 and 25 m. The maximum estimated relative error of determination of the mode-dependent attenuation $\Delta\alpha(\theta)/\alpha(\theta)$ is approximately 10%.

A Dirac impulse in time and a laser mode distribution with the $\theta_0 = 0^\circ$ (central launch) and FWHM = 7.5° in the parallel plane were used for the input. Equation (10) has been used to calculate the frequency response at fiber lengths $z = 3, 5, 10, 15, 25, 50,$ and 100 m . Numerical and experimental results for the frequency response for different fiber lengths of the MH fiber are shown in Fig. 3. Experimental and numerical results match well. A pronounced drop at low frequencies is apparent for long fiber lengths. A certain amount of noise is visible in the measured frequency responses. Furthermore, which at first may seem unusual, the responses of shorter fibers seem more affected by the noise. This behavior has two reasons. The first one is that to avoid the receiver saturation, the total received optical power was kept approximately the same for all measured fibers and there was not any signal-to-noise ratio gain for shorter fibers. The second reason

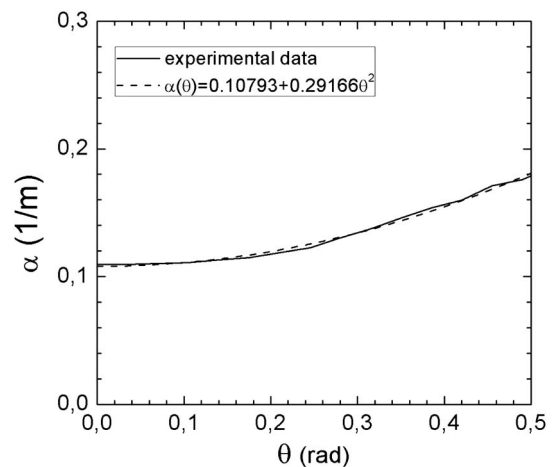


Fig. 2. Mode-dependent attenuation $\alpha(\theta)$ for the MH fiber: measured (solid line) and fit by the function $\alpha(\theta) \approx \alpha_0 + A\theta^2$, with $\alpha_0 = 0.10793 \text{ 1/m}$ and $A = 0.29166 (\text{rad}^2 \text{ m})^{-1}$ (dashed line).

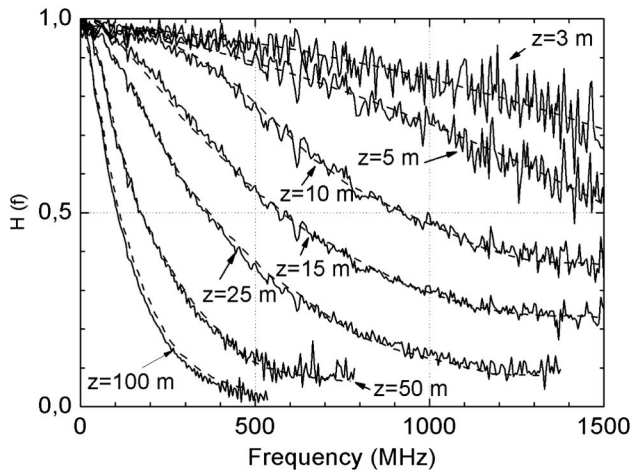


Fig. 3. Frequency response of the MH fiber: numerical results (dashed line) and measurements (solid line).

is the low-pass characteristics of the transmitter and receiver. The 3 dB bandwidth of this setup was about 500 MHz, and the frequency response plummeted below this value. Thus, despite the applied post-compensation for this drop, the sensitivity of the measurement decreased with frequency, and the fluctuation visible in Fig. 3 is increased accordingly. The latter effect is more affecting the responses of shorter fibers as their bandwidth is higher. Furthermore, the shown curves are in linear scale, and the relative error of the measurement scales with the magnitude response value.

Measured and calculated bandwidths for the MH fiber are compared in Fig. 4. A good match is apparent. In logarithmic coordinates, this graph can be approximated by a straight line or segments of straight lines. The line slope, known as the concatenation factor, is unity in the absence of mode coupling and differential mode attenuation; a slope other than unity is evidence of diffusive nonlinear effects [7] whereas the point of switch to the slowed drop is indicative of the equilibrium mode distribution. In Fig. 4, the line slope is steepest for short fiber

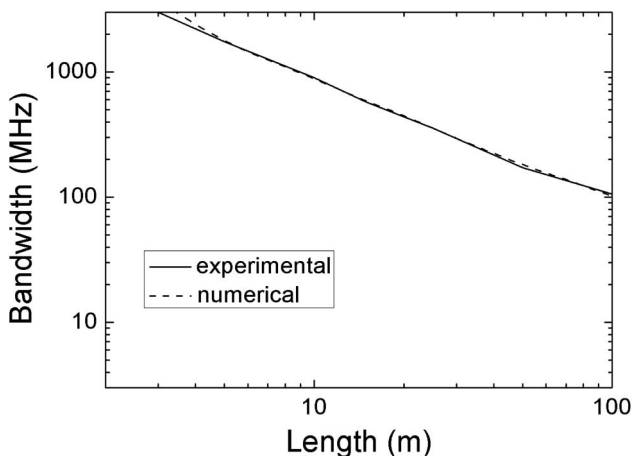


Fig. 4. Bandwidth of the MH fiber versus length of the fiber: numerical results (dashed line) and measurements (solid line).

lengths. Bandwidth then decreases with its length most rapidly. The switch to a less rapid drop occurs at $z \approx 5$ m. The further decrease in bandwidth with fiber length slows due to stronger modal diffusion that causes the weakly coupled regimes to become strongly coupled.

It was similarly observed [14] that equilibrium mode distribution in MH fibers occurs at the coupling length of around $z = L_c = 4$ m. The coupling coefficient of the fiber used in this work ($NA = 0.3$) is one order of magnitude greater than that for the previously investigated low-NA SI-POF ($NA = 0.32$; $D = 2.6 \times 10^{-4} \text{ rad}^2/\text{m}$) [13,15] when the coupling length L_c was much longer ($L_c = 18$ m) due to weaker intrinsic perturbation effects. One should note that the coupling length L_c increases with the NA because a greater number of guided modes are permitted—and they slow down the bandwidth decrease [8–10]. Furthermore, mode-dependent attenuation $\alpha(\theta) \approx \alpha_0 + A\theta^2 = 0.10793 (1/\text{m}) + 0.29166 (\text{rad}^2/\text{m})^{-1} \theta^2$ of the MH fiber is larger relative to the previously investigated SI-POFs (with $NA = 0.47$ and 0.5) [8–10], where $\alpha_0 = 0.0154 1/\text{m}$ and $A = 0.7539 (\text{rad}^2/\text{m})^{-1}$ for the Agilent HFBR-RUS100 fiber, $\alpha_0 = 0.0150 1/\text{m}$ and $A = 0.9953 (\text{rad}^2/\text{m})^{-1}$ for the PGU-FB1000 fiber from Toray, and $\alpha_0 = 0.0159 1/\text{m}$ and $A = 0.4025 (\text{rad}^2/\text{m})^{-1}$ for the Mitsubishi PREMIER GH4001 fiber.

In short, mode coupling and modal attenuation are larger in the MH fiber than in the previously investigated POFs [8–10,13,15]. As a consequence, mode-dependent attenuation and modal dispersion are more dominant effects upon bandwidth, shortening the coupling length. With increasing fiber length, mode coupling begins to influence strongly the bandwidth, enhancing the overall fiber performance and slowing the bandwidth drop; the switch to the slowed drop occurs sooner than in the case of the previously investigated low-NA (0.32) POF [13,15].

5. Conclusion

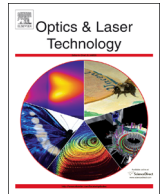
Frequency response, bandwidth, mode coupling, and mode-dependent attenuation were determined for a low-NA ($NA = 0.3$) SI-POF by experimental measurement and from a numerical solution to the time-dependent power flow equation. Frequency response and bandwidth are given as a function of fiber length. It was obtained that mode-dependent attenuation and modal dispersion were the dominant effects influencing the bandwidth of short fibers. “Short” for the fibers used in this work is below 5 m. Yet for a different fiber of the same basic type and similar NA (0.32), the corresponding length was reported earlier at up to 18 m, implying the fibers’ application-specific suitability. Furthermore, for longer fibers, mode coupling in the former fiber influences bandwidth more strongly and enhances the overall fiber performance more by slowing the bandwidth drop sooner.

The work described in this paper was supported by the Strategic Research Grant of City University of

Hong Kong (Project No. CityU 7004069) and by the Serbian Ministry of Education, Science and Technological Development (Project Nos. 171011, 171021, III43008, and III45003).

References

1. P. E. Green, Jr., "Optical networking update," *IEEE J. Sel. Areas Commun.* **14**, 764–779 (1996).
2. C. Koeppen, R. F. Shi, W. D. Chen, and A. F. Garito, "Properties of plastic optical fibers," *J. Opt. Soc. Am. B* **15**, 727–739 (1998).
3. S. E. Golowich, W. White, W. A. Reed, and E. Knudsen, "Quantitative estimates of mode coupling and differential modal attenuation in perfluorinated graded-index plastic optical fiber," *J. Lightwave Technol.* **21**, 111–121 (2003).
4. N. Raptis, E. Grivas, E. Pikasis, and D. Syvridis, "Space–time block code based MIMO encoding for large core step index plastic optical fiber transmission systems," *Opt. Express* **19**, 10336–10350 (2011).
5. D. Gloge, "Optical power flow in multimode fibers," *Bell Syst. Tech. J.* **51**, 1767–1783 (1972).
6. F. Breyer, N. Hanik, J. Lee, and S. Randel, "Getting impulse response of SI-POF by solving the time-dependent power-flow equation using Crank–Nicolson scheme," in *Proceedings of the POF Modelling Workshop*, Nurneberg, Germany, June 24–28, 2007, pp. 111–119.
7. J. Mateo, M. A. Losada, and J. Zubía, "Frequency response in step index plastic optical fibers obtained from the generalized power flow equation," *Opt. Express* **17**, 2850–2860 (2009).
8. S. Savović, B. Drljača, and A. Djordjevich, "Influence of launch beam distribution on bandwidth in step index plastic optical fibers," *Appl. Opt.* **52**, 1117–1121 (2013).
9. B. Drljača, S. Savović, and A. Djordjevich, "Calculation of the frequency response and bandwidth of step-index plastic optical fibres using the time-dependent power flow equation," *Physica Scripta* **T149**, 014028 (2012).
10. B. Drljača, A. Djordjevich, and S. Savović, "Frequency response in step-index plastic optical fibers obtained by numerical solution of the time-dependent power flow equation," *Opt. Laser Technol.* **44**, 1808–1812 (2012).
11. D. Gloge, "Impulse response of clad optical multimode fibers," *Bell Syst. Tech. J.* **52**, 801–816 (1973).
12. M. Rousseau and L. Jeunhomme, "Numerical solution of the coupled-power equation in step index optical fibers," *IEEE Trans. Microwave Theory Tech.* **25**, 577–585 (1977).
13. S. Savović and A. Djordjevich, "Influence of numerical aperture on mode coupling in step index plastic optical fibers," *Appl. Opt.* **43**, 5542–5546 (2004).
14. S. Savović, M. S. Kovačević, A. Djordjevich, J. S. Bajić, D. Z. Stupar, and G. Stepniak, "Mode coupling in low NA plastic optical fibers," *Opt. Laser Technol.* **60**, 85–89 (2014).
15. M. A. Losada, I. Garcés, J. Mateo, I. Salinas, J. Lou, and J. Zubía, "Mode coupling contribution to radiation losses in curvatures for high and low numerical aperture plastic optical fibers," *J. Lightwave Technol.* **20**, 1160–1164 (2002).



Influence of intermediate layer on transmission characteristics of W-type optical fibers



Ana Simović^a, Svetislav Savović^{a,*}, Branko Drljača^b, Alexandar Djordjevich^c

^a Faculty of Science, University of Kragujevac, R. Domanovića 12, 34000 Kragujevac, Serbia

^b Faculty of Science, University of Kosovska Mitrovica, Lole Ribara 29, Kosovska Mitrovica, Serbia

^c City University of Hong Kong, 83 Tat Chee Avenue, Kowloon, Hong Kong, China

ARTICLE INFO

Article history:

Received 29 August 2013

Received in revised form

14 October 2013

Accepted 19 October 2013

Available online 7 November 2013

Keywords:

W-type optical fiber

Power flow equation

Bandwidth

ABSTRACT

Transmission characteristics of multimode W-type optical fibers (doubly clad fibers with three layers) are investigated by solving the time-dependent power flow equation. A numerical solution has been obtained by the explicit finite difference method. Results show how the bandwidth in W-type optical fibers varies with depth and width of the intermediate layer for different coupling strengths and excitations. The trade-off between the bandwidth and steady-state loss is also specified. Such characterization of these fibers is consistent with their manifested effectiveness in reducing modal dispersion and bending loss.

© 2013 Elsevier Ltd. All rights reserved.

1. Introduction

Singly clad (SC) glass optical fibers are often used for signal transmission in long-distance communication and high-capacity networks. In contrast, plastic optical fibers (POFs) exhibit comparatively high attenuation and low bandwidth. This limits the achievable transmission rate of POF systems and restricts their application in the communications field to short data links and local area networks. To mitigate these performance boundaries, the application of spatial modulation [1] and detection techniques [2], equalization [3], modal dispersion compensation [4], and restricted modal launch have been reported. A potential for additional bandwidth enhancement seems to be achievable through improved design of the profile of the multimode fiber.

Doubly clad “W-type” optical fibers have three distinct optical layers. They exhibit reduced dispersion compared to their singly clad counterparts. They are also easier to splice, have a reduced number of guided modes, wider transmission bandwidth and lower bending losses. It is the W-type fiber's intermediate layer that reduces the number of guided modes, which lowers the fiber's effective numerical aperture by keeping the guided modes tighter to the core [5]. For reference, the bandwidth-distance product of SC and W-type glass fibers may be around 30 MHz km and 50 MHz km, respectively, and 15 MHz km and 200 MHz km for the corresponding POFs. [6–8].

Transmission of multimode optical fibers is affected strongly by coupling and differential mode-attenuation. The latter reduces the transmitted power by absorption and scattering within the fiber material. Mode coupling, on the other hand, is a form of light diffraction. It transfers power between propagating modes and is caused by fiber-anomalies of random nature (such as voids, cracks, microscopic bends, and variations in fiber density, diameter and shape). The positive effect of mode coupling is that it reduces modal dispersion because the transfer of energy between modes with different propagation velocities tends to average out the total propagation delays. This reduces the intermodal dispersion and increases bandwidth. On the negative side, mode coupling increases fiber loss, particularly in curved fibers [9], and alters the output-field properties or beam quality.

It is the lossy leaky modes in the intermediate layer (between the outer cladding and core) that distinguish properties of the W-type fiber from those of the corresponding SC fibers. Therefore, coupling of guided to lossy modes in the W-type fibers deserves a closer examination. The unavoidable fiber bends and inevitable junctions in the fiber network additionally couple low-order modes to higher-order ones. Higher order modes will therefore always be present in the fiber output even if only low-order modes had initially been launched by some selective input conditions. Because this affects fiber bandwidth, it is desirable to optimize the fiber's refractive index profile [10] with the objective of minimizing the group delay difference between modes. In addition to coupling, modal attenuation and dispersion also affect transmission of the W-type optical fiber; hence, methods for calculating their contributions are needed.

* Corresponding author. Tel.: +381 34 335039; fax: +381 34 335040.
E-mail address: savovic@kg.ac.rs (S. Savović).

Launch conditions, fiber properties and fiber length determine the output optical power distribution, and hence the far-field pattern, of an optical fiber [11]. A ring-pattern launch at an angle of $\theta_0 > 0$ to the axis can be reproduced in the output field pattern of only short fibers. Such ring becomes fuzzy at the end of longer fibers due to more extensive mode coupling. This fuzziness of the output pattern increases with fiber length up to some characteristic value referred to as the “coupling length” L_c where the pattern appears like a disk. The ensuing “equilibrium mode distribution” (EMD) for lengths in excess of L_c preserve no ring patterns regardless of the launch, although the resulting light distribution across the disk-pattern may still vary with the launch indicating a substantially (but not fully) complete mode coupling. Moreover, from length L_c onwards, the bandwidth is proportional to $1/z^{1/2}$ instead of $1/z$ (z being the length variable). In fibers with shorter lengths L_c , the bandwidth switches earlier from the functional dependence $1/z$ to $1/z^{1/2}$ (faster bandwidth improvement). Further mode coupling (beyond L_c) leads to the steady-state power distribution at some fiber length z_s . From there onwards, the same intensity distribution results in the far field regardless of the modes launched (the steady-state output light distribution becomes independent of the launch conditions). We investigate in this work how fiber bandwidth, steady-state loss, and mode coupling strength of W-type optical fibers are affected by the depth and width of its intermediate layer.

2. Power flow equation

The time-dependent power flow for multimode W-type fibers is described by the following coupled-power equation [12]:

$$\frac{\partial p(\theta, z, t)}{\partial z} + \tau(\theta) \frac{\partial p(\theta, z, t)}{\partial t} = -\alpha(\theta)p(\theta, z, t) + \frac{1}{\theta} \frac{\partial}{\partial \theta} \left[\theta D(\theta) \frac{\partial p(\theta, z, t)}{\partial \theta} \right] \quad (1)$$

where t is time; $p(\theta, z, t)$ is power distribution over angle, space, and time; $\tau(\theta)$ is modal delay per unit length; $D(\theta)$ is the mode-dependent coupling coefficient; and $\alpha(\theta) = \alpha_0 + \alpha_d(\theta)$ is the modal attenuation, where α_0 represents conventional losses (absorption and scattering). The term α_0 leads only to a multiplier $\exp(-\alpha_0 z)$ in the solution and is thus neglected. The boundary conditions are $p(\theta_m, z, t) = 0$, where θ_m is the maximum propagation angle, and $D(\theta) (\partial p(\theta, z, t) / \partial \theta) = 0$ at $\theta = 0$.

The frequency response is obtained more conveniently in the frequency, rather than time, domain. Fourier transformation is therefore applied to Eq. (1):

$$\frac{\partial P(\theta, z, \omega)}{\partial z} + j\omega\tau(\theta)P(\theta, z, \omega) = -\alpha(\theta)P(\theta, z, \omega) + \frac{1}{\theta} \frac{\partial}{\partial \theta} \left[\theta D(\theta) \frac{\partial P(\theta, z, \omega)}{\partial \theta} \right] \quad (2)$$

where $\omega = 2\pi f$ is the angular frequency, and

$$P(\theta, z, \omega) = \int_{-\infty}^{+\infty} p(\theta, z, t) \exp(-j\omega t) dt \quad (3)$$

The boundary conditions are

$$P(\theta_m, z, \omega) = 0, \quad D(\theta) \frac{\partial P(\theta = 0, z, \omega)}{\partial \theta} = 0 \quad (4)$$

It is apparent that $P(\theta, z, \omega)$ is complex. By separating $P(\theta, z, \omega)$ into the real $P_r(\theta, z, \omega)$ and imaginary part $P_i(\theta, z, \omega)$, and assuming a constant coupling coefficient D [13–15], Eq. (2) can be rewritten as the following simultaneous partial differential equations:

$$\begin{aligned} \frac{\partial P_r(\theta, z, \omega)}{\partial z} &= -\alpha(\theta)P_r(\theta, z, \omega) + \frac{D}{\theta} \frac{\partial P_r(\theta, z, \omega)}{\partial \theta} \\ &+ D \frac{\partial^2 P_r(\theta, z, \omega)}{\partial \theta^2} + \omega\tau P_i(\theta, z, \omega) \end{aligned} \quad (5a)$$

$$\begin{aligned} \frac{\partial P_i(\theta, z, \omega)}{\partial z} &= -\alpha(\theta)P_i(\theta, z, \omega) + \frac{D}{\theta} \frac{\partial P_i(\theta, z, \omega)}{\partial \theta} + D \frac{\partial^2 P_i(\theta, z, \omega)}{\partial \theta^2} \\ &- \omega\tau P_r(\theta, z, \omega) \end{aligned} \quad (5b)$$

where

$$P(\theta, z, \omega) = P_r(\theta, z, \omega) + jP_i(\theta, z, \omega) \quad (6)$$

If $P_r(\theta, z, \omega)$ and $P_i(\theta, z, \omega)$ are obtained by solving Eq. (5), the transmission characteristics can be calculated. Thus the frequency response $H(z, \omega)$ at fiber length z is

$$H(z, \omega) = \frac{2\pi \int_0^{\theta_m} \theta [P_r(\theta, z, \omega) + jP_i(\theta, z, \omega)] d\theta}{2\pi \int_0^{\theta_m} \theta [P_r(\theta, 0, \omega) + jP_i(\theta, 0, \omega)] d\theta} \quad (7)$$

The modal power distribution $P_F(\theta, z, \omega)$ and the spatial transient of power $P_L(z, \omega)$ can be obtained by

$$P_F(\theta, z, \omega) = [P_r(\theta, z, \omega)^2 + P_i(\theta, z, \omega)^2]^{1/2} \quad (8)$$

$$P_L(z, \omega) = 2\pi \int_0^{\theta_m} \theta P_F(\theta, z, \omega) d\theta \quad (9)$$

Consider a W-type fiber with index profile shown in Fig. 1. The relative refractive index difference $\Delta_q = (n_0 - n_q)/n_0$ between the core and intermediate layer is larger than the difference $\Delta_p = (n_0 - n_p)/n_0$ between the core and cladding, where n_0 , n_q and n_p are refractive indices of the core, intermediate layer and cladding, respectively. In this structure, the modes whose propagation angles are between $\theta_p \cong (2\Delta_p)^{1/2}$ and $\theta_q \cong (2\Delta_q)^{1/2}$ are leaky modes [14]. Attenuation constants of leaky modes are given as [15]

$$\alpha_L(\theta) = \frac{4(\theta^2 - \theta_p^2)^{1/2} \theta^2 (\theta_q^2 - \theta^2)}{a(1 - \theta^2)^{1/2} \theta_q^2 (\theta_q^2 - \theta^2)} \exp[-2\delta a n_0 k_0 (\theta_q^2 - \theta^2)^{1/2}] \quad (10)$$

where k_0 is the free-space wave number, a is the core radius and δa is the width of the intermediate layer (inner cladding). In an SC fiber, experimental results show that attenuation remains constant throughout the guided-mode region and rises steeply in the radiation-mode region [16]. Consequently, the modal attenuation in a W-type fiber can be expressed as

$$\alpha_d(\theta) = \begin{cases} 0 & \theta \leq \theta_p \\ \alpha_L(\theta) & \theta_p < \theta < \theta_q \\ \infty & \theta \geq \theta_q \end{cases} \quad (11)$$

Modal delay is expressed in terms of θ by [14]

$$\tau(\theta) = \frac{n_0}{c} \frac{1}{\cos \theta} \cong \frac{n_0}{c} \left(1 + \frac{\theta^2}{2} \right) = \tau_0 + \tau_d(\theta) \quad (12)$$

where c is the velocity of light in free space. The first term τ_0 is common to all modes. It is the difference in group delay that determines the transmission bandwidth. Therefore, only $\tau_d(\theta)$ is to be considered in the calculations.

A W-type fiber can be regarded as a system consisting of SC_q fiber and cladding. In the SC_q fiber, modes having propagation angles smaller than the critical angle θ_q can be guided. When the SC_q fiber is coupled with surrounding medium of index n_p , the

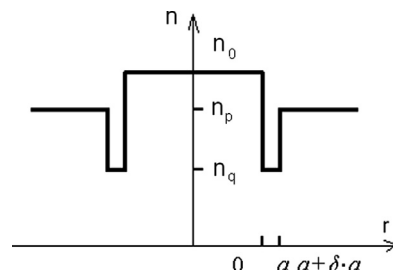


Fig. 1. Refractive index profile of a W-type fiber.

lower order modes, whose propagation angles are smaller than the critical angle of the SC_p fiber θ_p, remain guided. However, the higher order modes with angles between θ_p and θ_q are transformed into leaky modes. It is shown that because of the strong dependence of α_l(θ) on the intermediate layer width δa, steady-state characteristics of a W-type fiber depend on δa and coincide with those of SC_p and SC_q fibers at limits δ→0 and δ→∞, respectively [15,17]. Another parameter which influences the power distribution in W-type optical fibers is depth of the intermediate layer (Fig. 1). In this work, we investigate how depth and width of the intermediate layer influence the bandwidth and steady-state loss in W-type optical fibers for different strengths of mode coupling. The results obtained could be applied when designing W-type optical fibers.

3. Numerical method

Because analytical solution of the simultaneous partial differential Eq. (5) with the attenuation constants of leaky modes in the form of (10) is not available, one has to solve it numerically. We have done that using the explicit finite difference method (EFDM). In the 1970s and 1980s, implicit finite difference methods (IFDMs) were generally preferred over EFDMs [14]. This trend has been changing with the advancement of computers, shifting the emphasis to EFDMs. We now report, in our knowledge for the first time, the solution of the simultaneous partial differential Eq. (5) using EFDM. Being often unconditionally stable, IFDM allows larger step lengths than EFDM. Nevertheless, this does not translate into IFDM's higher computational efficiency because extremely large matrices must be manipulated at each calculation step. We find that the EFDM algorithm is also simpler in addition to being more efficient computationally. We used the central difference scheme to represent the (∂P(θ,z,ω))/∂θ and (∂²P(θ,z,ω))/∂θ² terms, and the forward difference scheme for the derivative term (∂P(θ,z,ω))/∂z [18]. Then, Eq. (5) reads

$$P_{k,l+1}^r = \left(\frac{\Delta z D}{\Delta \theta^2} - \frac{\Delta z D}{2\theta_k \Delta \theta} \right) P_{k-1,l}^r + \left(1 - \frac{2\Delta z D}{\Delta \theta^2} - (\alpha_d)_k \Delta z \right) P_{k,l}^r + \left(\frac{\Delta z D}{2\theta_k \Delta \theta} + \frac{\Delta z D}{\Delta \theta^2} \right) P_{k+1,l}^r + \frac{\omega n_0 \Delta z}{2c} \theta_k^2 P_{k,l}^i \quad (13a)$$

$$P_{k,l+1}^i = \left(\frac{\Delta z D}{\Delta \theta^2} - \frac{\Delta z D}{2\theta_k \Delta \theta} \right) P_{k-1,l}^i + \left(1 - \frac{2\Delta z D}{\Delta \theta^2} - (\alpha_d)_k \Delta z \right) P_{k,l}^i + \left(\frac{\Delta z D}{2\theta_k \Delta \theta} + \frac{\Delta z D}{\Delta \theta^2} \right) P_{k+1,l}^i - \frac{\omega n_0 \Delta z}{2c} \theta_k^2 P_{k,l}^r \quad (13b)$$

where indexes k and l refer to the discretization step lengths Δθ and Δz for angle θ and length z, respectively, and where P_{k,l}^r = P_r(θ_k, z_l, ω) and P_{k,l}ⁱ = P_i(θ_k, z_l, ω). Modal attenuation expressed in the finite difference form is

$$(\alpha_d)_k = \begin{cases} 0 & \theta_k \leq \theta_p \\ \frac{4(\theta_k^2 - \theta_p^2)^{1/2} \theta_k^2 (\theta_q^2 - \theta_k^2)}{a(1 - \theta_k^2)^{1/2} \theta_q^2 (\theta_q^2 - \theta_p^2)} \exp[-2\delta a n_0 k_0 (\theta_q^2 - \theta_k^2)^{1/2}] & \theta_p < \theta_k < \theta_q \\ \infty & \theta_k \geq \theta_q \end{cases} \quad (14)$$

In the difference form, boundary conditions become P_{N,l}^r = P_{N,l}ⁱ = 0 and P_{0,l}^r = P_{1,l}^r, P_{0,l}ⁱ = P_{1,l}ⁱ, where N = θ_q/Δθ is the grid dimension in θ direction. To prevent the problem of singularity at grid points θ = 0, we have used the following relation [13]:

$$\lim_{\theta \rightarrow 0} \frac{1}{\theta} \frac{\partial}{\partial \theta} \left(\theta \frac{\partial P}{\partial \theta} \right) = 2 \frac{\partial^2 P}{\partial \theta^2} \Big|_{\theta=0} \quad (15)$$

4. Numerical results

In this paper, we calculate bandwidth and steady-state loss in a W-type optical fiber. The fiber structural characteristics were: Δ_p = 0.2% (θ_p ≅ 3.62°), Δ_q = 0.7% (θ_q ≅ 6.76°) and 2a = 60 μm [13,14,17]. Further, n₀ = 1.46 and λ = 840 nm were used in the calculations. In order to investigate the influence of depth and width of the intermediate layer as well as coupling strength and excitation on the power distribution in this fiber, we consider the case when the core index n₀ and outer cladding index n_p are fixed. The depth of the intermediate layer is varied by changing the initial value of Δ_q = 0.7% by ±15% and ±25%; thus we analyzed cases with Δ_q = 0.525% (θ_q ≅ 5.87°), Δ_q = 0.595% (θ_q ≅ 6.25°), Δ_q = 0.7% (θ_q ≅ 6.76°), Δ_q = 0.805% (θ_q ≅ 7.27°) and Δ_q = 0.875% (θ_q ≅ 7.58°) [17]. The change in θ_q for constant θ_p changes the number of leaky modes as well as their attenuation (10). We solved the time-dependent power flow Eq. (2) using EFDM for the coupling coefficient D = 2.3 × 10⁻⁷ and 2.3 × 10⁻⁶ rad²/m, for five different normalized intermediate layer widths δ (δ = 0.15, 0.2, 0.3, 0.4 and 0.5; actual widths δa are 0.15 · 30 μm, 0.2 · 30 μm, 0.3 · 30 μm, 0.4 · 30 and 0.5 · 30 μm). As an illustration our numerical solution of the time-dependent power flow equation is presented in Fig. 2(a), (b) and (c) by showing the evolution of the bandwidth with fiber length with D = 2.3 × 10⁻⁷ rad²/m, for different widths of intermediate layer δ, for Δ_q = 0.525%, 0.7% and 0.875%, respectively, for θ_q excitation. One can observe in Fig. 2 that bandwidth of the W-type fiber varies between those of the reference SC_p and SC_q fibers. One can also observe in Fig. 2 that, for short fiber lengths, bandwidth decreases proportionally with fiber length. However, the bandwidth's decreasing tendency gradually switches to the 1/z^{1/2} functional characteristic at shorter fiber lengths for thinner intermediate layer widths (smaller δ). This is explained by EMD occurring at shorter fiber length in the case of thinner intermediate layer [17]. The shortest coupling lengths characterize SC_p fiber. This is because mode coupling occurs only between guided modes that propagate along the fiber with the propagating angles θ between 0 and 3.62°. Longer coupling lengths are associated with the SC_q rather than SC_p fiber because there is a larger number of modes in the SC_q fiber that propagate at angles θ between 0 and 6.76°.

Fiber bandwidth increases as depth of the intermediate layer decreases. This is consistent with our earlier observation [13] that as depth of the intermediate layer (Δ_q) decreases, EMD occurs at shorter fiber lengths (faster bandwidth improvement) – which is attributed to the correspondingly decreasing number of leaky modes. The smaller the number Δ_q (smaller Δ_q and consequently θ_q), the shorter fiber length it takes for the coupling process to complete. This decrease is more pronounced in the case of narrower intermediate layer widths (smaller δ). Since the leaky mode loss increases by decreasing the width of the intermediate layer, power remains in leaky modes for a rather short transmission length in the case of thicker intermediate layer; consequently, it takes a shorter fiber length for achieving the EMD compared to the case with thinner intermediate layer.

Fig. 3 shows the bandwidth change with fiber length for a W-type fiber with larger coupling coefficient D = 2.3 × 10⁻⁶ rad²/m and for the same fiber's structural parameters as shown in Fig. 2. One can observe an increase of fiber bandwidth with the increasing magnitude of mode coupling. Mode coupling improves fiber bandwidth, both at short and long fiber lengths. Larger mode coupling, associated with stronger intrinsic perturbation effects in the fiber, forces energy redistribution among guided modes to occur at shorter fiber lengths.

The evolution of bandwidth with fiber length for θ_p excitation is shown in Figs. 4 and 5. One can observe from Figs. 2–5 that θ_p excitation leads to the increase of fiber bandwidth compared to

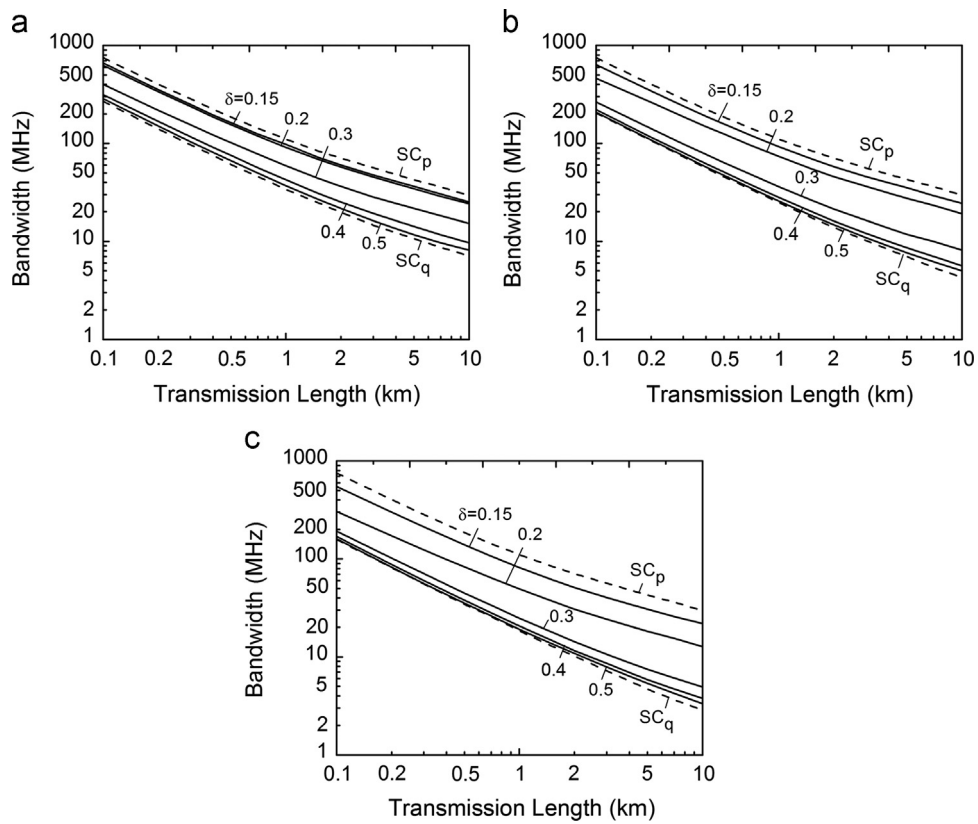


Fig. 2. Transmission length dependence of bandwidth for θ_q excitation, $D=2.3 \times 10^{-7} \text{ rad}^2/\text{m}$, and (a) $\Delta_q=0.525\%$, (b) $\Delta_q=0.7\%$ and (c) $\Delta_q=0.875\%$.

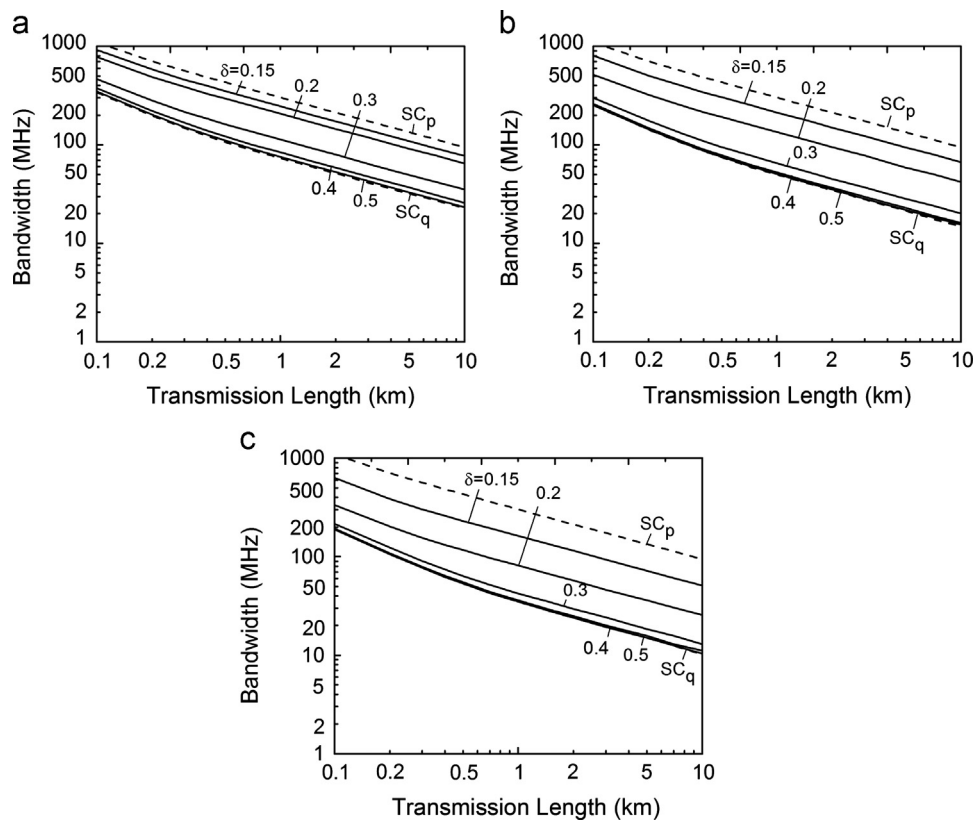


Fig. 3. Transmission length dependence of bandwidth for θ_q excitation, $D=2.3 \times 10^{-6} \text{ rad}^2/\text{m}$, and (a) $\Delta_q=0.525\%$, (b) $\Delta_q=0.7\%$ and (c) $\Delta_q=0.875\%$.

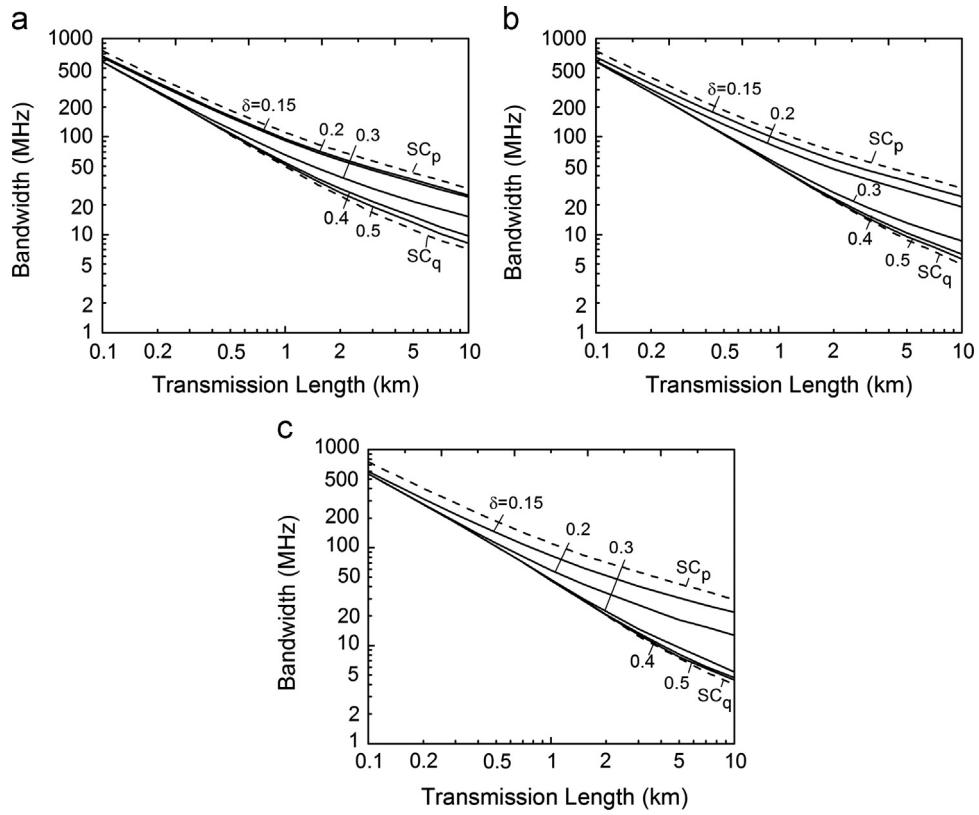


Fig. 4. Transmission length dependence of bandwidth for θ_p excitation, $D=2.3 \times 10^{-7}$ rad²/m, and (a) $\Delta_q=0.525\%$, (b) $\Delta_q=0.7\%$ and (c) $\Delta_q=0.875\%$.

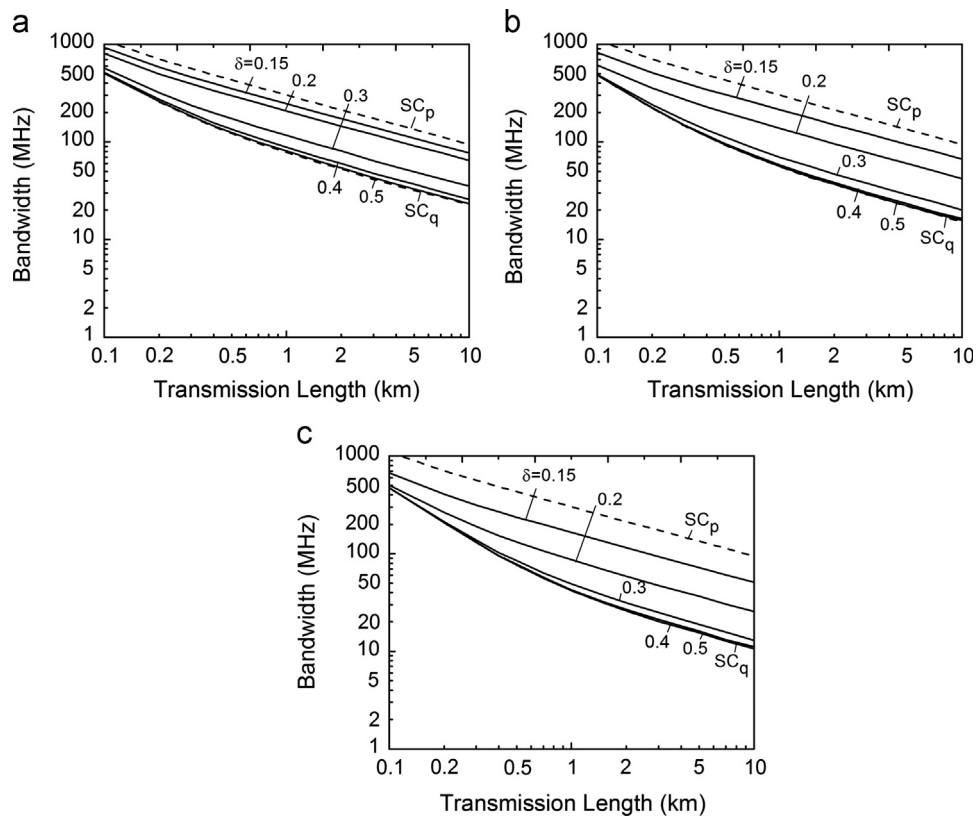


Fig. 5. Transmission length dependence of bandwidth for θ_p excitation, $D=2.3 \times 10^{-6}$ rad²/m, and (a) $\Delta_q=0.525\%$, (b) $\Delta_q=0.7\%$ and (c) $\Delta_q=0.875\%$.

the θ_q excitation. Excitation of only guiding modes (θ_p excitation) leads to higher bandwidth, both at small and intermediate fiber lengths compared to the excitation of both, guiding and leaky modes (θ_q excitation). Furthermore, the switch of the functional dependence of bandwidth from $1/z$ to $1/z^{1/2}$ shifts to shorter fiber lengths when only guiding modes are excited; improving bandwidth.

For θ_p excitation, the influence of width and depth of the intermediate layer is smaller at short fiber lengths. For this excitation, only guiding modes are excited so that there is only a small number of leaky modes at short fiber lengths. With increasing fiber length, the number of leaky modes increases due to mode coupling and, therefore, the influence of the width of the intermediate layer starts to occur at longer fiber lengths. In the case of θ_p excitation and stronger mode coupling (Fig. 5), the influence of the width of the intermediate layer δ on fiber bandwidth is more pronounced. This is because a stronger mode coupling shifts the onset of leaky modes to shorter fiber lengths.

Figs. 6 and 7 show the trade-off relation between bandwidth and steady-state loss for θ_q and θ_p excitations, respectively. We have shown that bandwidth can be improved by reducing the intermediate layer width, decreasing the intermediate layer depth, strengthening the mode coupling process or exciting only guiding modes. It is evident from Figs. 6 and 7 that the steady-state loss changes from that of SC_q to SC_p fiber as the intermediate layer width becomes thinner. Since stronger mode coupling results in an increased steady-state loss, in practice a trade-off relation between bandwidth and loss would have to be considered in designing the optimum W-type index profile. Controlling the intermediate layer width and depth entails a smaller sacrifice in loss than an increase in coupling strength. Furthermore, a choice between θ_q and θ_p excitation also influences trade-off relation between bandwidth and steady-state loss.

5. Conclusion

Bandwidth and steady-state loss are calculated by the time-dependent power flow equation for different intermediate layer depths and widths of multimode W-type optical fibers for different mode coupling strengths and excitations. It is shown for the first time that the shallower the intermediate layer, the higher the fiber bandwidth. With decreasing the depth of intermediate layer, EMD occurs at shorter fiber lengths resulting in faster bandwidth improvement. Bandwidth increases with decreasing the width of the intermediate layer. Since the leaky mode loss decreases with increasing the width of the intermediate layer, power remains in leaky modes for a rather long transmission length in the case of large intermediate layer width, necessitating longer fiber length for achieving the EMD than would be needed with a smaller intermediate layer width. Thus, the bandwidth can be improved by reducing the intermediate layer width that attenuates leaky modes faster.

Similarly it is shown that the stronger the mode coupling, the higher the fiber bandwidth. This is because stronger mode coupling (larger intrinsic perturbation effects in the fiber) forces energy redistribution among guided modes to occur within shorter fiber lengths, resulting in shorter fiber length for achieving EMD and resulting in faster bandwidth improvement.

Bandwidth can be improved by reducing the intermediate layer width, decreasing the intermediate layer depth, strengthening the mode coupling process or exciting only guiding modes. In practice, a trade-off relation between bandwidth and loss would have to be considered in designing the optimum W-type index profile. Controlling the intermediate layer width and depth entails a smaller sacrifice in loss than an increase in coupling strength. Excitation of only guiding modes leads to a higher bandwidth both at small and intermediate fiber lengths compared to the excitation of both guiding and leaky modes. With the excitation of only guided

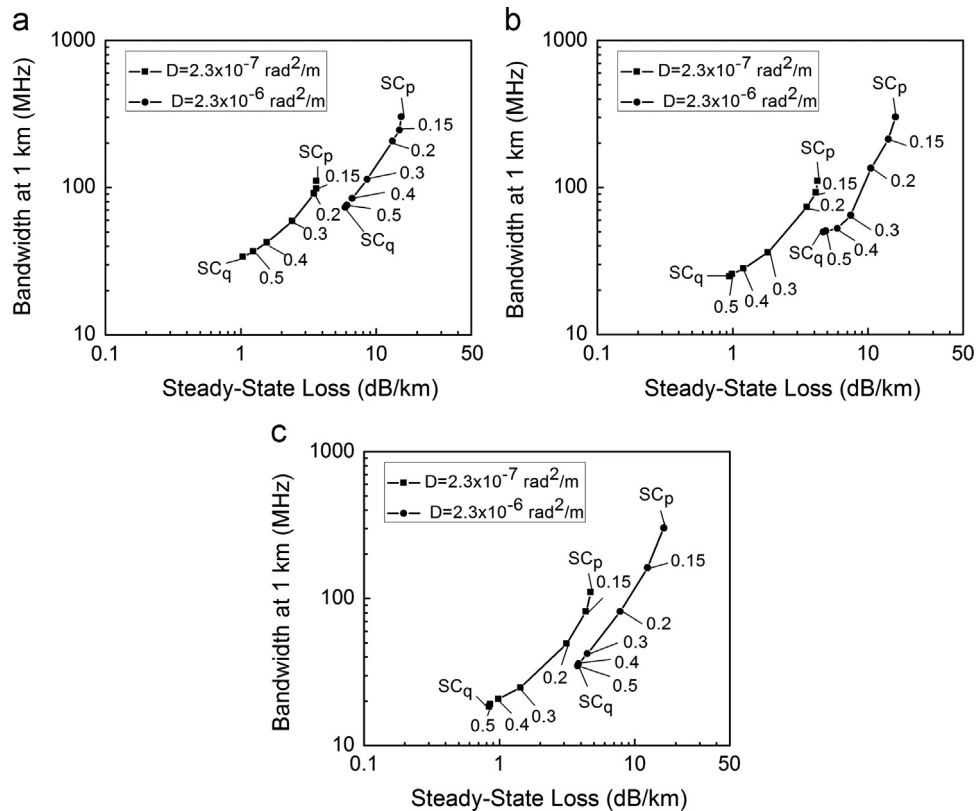


Fig. 6. Trade-off relation between bandwidth and steady-state loss for θ_q excitation, for different coupling strengths D and (a) $\Delta_q=0.525\%$, (b) $\Delta_q=0.7\%$ and (c) $\Delta_q=0.875\%$.

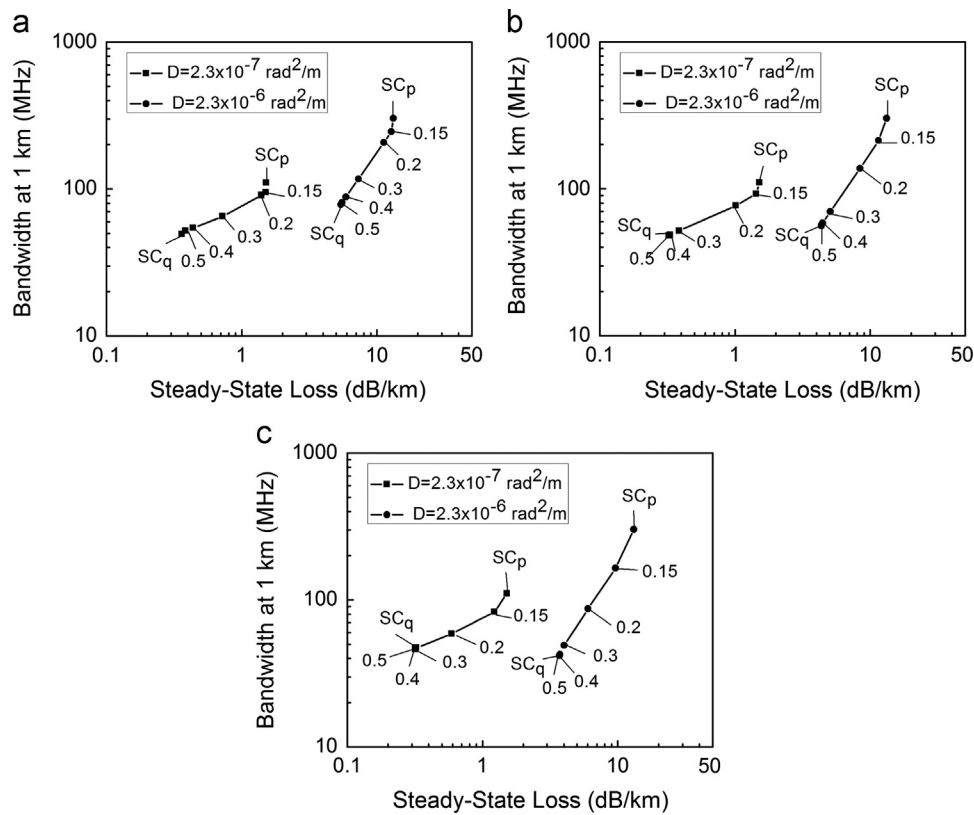


Fig. 7. Trade-off relation between bandwidth and steady-state loss for θ_p excitation, for different coupling strengths D and (a) $\Delta_q=0.525\%$, (b) $\Delta_q=0.7\%$ and (c) $\Delta_q=0.875\%$.

modes, the switch of the functional relations for bandwidth from $1/z$ to $1/z^{1/2}$ shifts to shorter fiber lengths, improving the bandwidth.

Acknowledgments

The work described in this paper was supported by the Strategic Research Grant of City University of Hong Kong (Project no. CityU 7004069) and by a Grant from Serbian Ministry of Education, Science and Technological Development (Project no. 171011).

References

- [1] Tyler EJ, Webster M, Penty RV, White IH, Yu S, Rorison J. Subcarrier modulated transmission of 2.5 Gb/s over 300 m of 62.5- μm -core diameter multimode fiber. *IEEE Photon Technol Lett* 2002;14:1743–5.
- [2] Patel KM, Ralph SE. Enhanced multimode fiber link performance using a spatially resolved receiver. *IEEE Photon Technol Lett* 2002;14:393–5.
- [3] Zhao X, Choa FS. Demonstration of 10 Gb/s transmission over 1.5-km-long multimode fiber using equalization techniques. *IEEE Photon Technol Lett* 2002;14:1187–9.
- [4] Abbott JS, Smith GE, Truesdale CM. Multimode fiber link dispersion compensator. U.S. Patent 6 363 195; 2002.
- [5] Mikoshiba K, Kajioka H. Transmission characteristics of multimode W-type optical fiber: experimental study of the effect of the intermediate layer. *Appl Opt* 1978;17:2836–41.
- [6] Tanaka T, Yamada S, Sumi M, Mikoshiba K. Microbending losses of doubly clad (W-type) optical fibers. *Appl Opt* 1977;18:2391–4.
- [7] Daum W, Krauser J, Zamzow PE, Ziemann O. *Polymer Optical Fibers for Data Communication*. Berlin: Springer; 2002.
- [8] Yamashita T, Kagami M. Fabrication of light-induced self-written waveguides with a W-shaped refractive index profile. *J Lightwave Technol* 2005;23:2542–8.
- [9] Losada MA, Garcés I, Mateo J, Salinas I, Lou J, Zubía J. Mode coupling contribution to radiation losses in curvatures for high and low numerical aperture plastic optical fibers. *J Lightwave Technol* 2002;20:1160–4.
- [10] Takahashi K, Ishigure T, Koike Y. Index profile design for high-bandwidth W-shaped plastic optical fiber. *J Lightwave Technol* 2006;24:2867–76.
- [11] Dugas J, Maurel G. Mode-coupling processes in polymethyl methacrylate-core optical fibers. *Appl Opt* 1992;31:5069–79.
- [12] Gloge D. Optical power flow in multimode fibers. *Bell Syst Tech J* 1972;51:1767–83.
- [13] Simović A, Djordjević A, Savović S. Influence of width of intermediate layer on power distribution in W-type optical fibers. *Appl Opt* 2012;51:4896–901.
- [14] Tanaka TP, Yamada S. Numerical solution of power flow equation in multimode W-type optical fibers. *Appl Opt* 1980;19:1647–52.
- [15] Tanaka TP, Yamada S. Steady-state characteristics of multimode W-type fibers. *Appl Opt* 1979;18:3261–4.
- [16] Jeunhomme L, Fraise M, Pocholle JP. Propagation model for long step-index optical fibers. *Appl Opt* 1976;15:3040–6.
- [17] Savović S, Simović A, Djordjević A. Explicit finite difference solution of the power flow equation in W-type optical fibers. *Opt Laser Technol* 2012;44:1786–90.
- [18] Anderson JD. *Computational Fluid Dynamics*. New York: Mc Graw-Hill; 1995.

Influence of width of launch beam distribution and mode coupling on transmission characteristics of W-type plastic optical fibers

B Drljača¹, A Simović², A Djordjević^{3,*}, R Min⁴, S Jovanović¹ and S Savović^{2,3,*}

¹ University of Priština, Faculty of Sciences and Mathematics, L. Ribara 29, Kosovska Mitrovica, Serbia

² University of Kragujevac, Faculty of Science, R. Domanovića 12, Kragujevac, Serbia

³ City University of Hong Kong, Department of Mechanical Engineering, Kowloon, Hong Kong, People's Republic of China

⁴ Center for Cognition and Neuroergonomics, State Key Laboratory of Cognitive Neuroscience and Learning, Beijing Normal University at Zhuhai, 519087 Guangdong, People's Republic of China

E-mail: mealex@cityu.edu.hk and savovic@kg.ac.rs

Received 4 February 2021

Accepted for publication 25 June 2021

Published 16 July 2021



Abstract

We show strong effects of width of the launch beam's angular distribution on bandwidth and mode coupling in W-type plastic optical fibers (POFs). In general, the broader this width, the stronger the coupling and the lower the bandwidth—but the bandwidth drop due to this effect tapers off with distance from the input end and ceases at lengths over 25 m as the steady state distribution is reached. With increasing the strength of mode coupling, the equilibrium mode distribution is reached at shorter fiber lengths, which results in slower bandwidth decrease and finally in higher bandwidth at longer fiber lengths for fibers with larger coupling coefficients D . These results are aimed at aiding designers and application integrators of W-type POFs, particularly in employing laser, LED or vertical cavity surface emitting laser (VCSEL) light source.

Keywords: plastic optical fibers, mode coupling, equilibrium mode distribution, bandwidth

(Some figures may appear in color only in the online journal)

1. Introduction

High bandwidth of plastic optical fibers (POFs) makes them attractive for optical communication in area networks for offices, homes, and vehicles that are enabled with autonomous driving and multimedia services. Such networks, while short in range, require ease of reconnection and typically feature tight bends to negotiate corners. This is where multimode POFs, with their relatively large cores, high numerical

apertures (NAs), and ease of connection, can provide the expected robustness cost-effectively.

Most multimode optical fibers have only one optically functional cladding—they are singly clad (SC). Methods for improving attenuation properties and bandwidth of SC fibers include modulation [1], spatial detection [2], equalization [3], and compensation of modal-dispersion [4]. Much effort has been devoted to designing a refractive index profile across a multimode fiber that advances characteristics of the fiber transmission. In addition to more conventional designs such as with a step-index (SI) or graded index profile (abrupt versus gradual index variation), doubly clad fibers with two optically

* Authors to whom any correspondence should be addressed.

functional cladding-layers have been proposed [5–7]. They are called W-type fibers. Each has an intermediate layer between its outer cladding and core.

W-type fibers exhibit lower waveguide dispersion, wider bandwidth, and lower bending losses compared to corresponding SC fibers [8]. For example, the bandwidth-distance product for a glass optical fiber of W-type may extend to 50 MHz km whereas it is typically 30 MHz km for a corresponding SC fiber. The difference is even more dramatic for POFs: 200 MHz km (W-type) versus 15 MHz km (SC) [5, 7, 9]. The addition of the intermediate layer brings such improvements by lowering the fiber's effective NA as the number of guided modes is reduced and they are held tighter to the core [10].

Optical fibers exhibit mode coupling. It alters the beam gradually along the fiber by transferring the optical power between modes [11]. In other words, the input beam's angular optical power distribution evolves with propagation. In the process, modal dispersion reduces, and fiber bandwidth improves [12]. We show in this paper how the choice of the width of the launch beam affects these outcomes.

The coupling-induced evolution of the launch beam for a chosen fiber length can be observed in the far-field radiation pattern emanating from the fiber's output end [13, 14]. For short fibers, a setup can be arranged with an input beam at a fixed angle $\theta = \theta_0$ to the fiber axis (forming a centrally symmetric input cone) that images into a ring behind the fiber's output end (the ring's diameter would be a function of the angle θ_0 of the launch). However, this image gets more and more blurred for longer and longer fibers until becoming a disk eventually. This is caused by mode coupling whose gradual effects along the fiber keep widening the initially narrow power distribution (that was around $\theta = \theta_0$ at start). Even the launch approaching the highest order takes the 'coupling length' L_c of the fiber for its midpoint to shift to zero degrees. The ring is unrecognizable as the disk-image is filled completely and equilibrium mode distribution (EMD) is reached. Further coupling along the fiber only changes light distribution across such a disk until it takes the form of a steady state distribution (SSD) at a characteristic length z_s ($z_s > L_c$). SSD (beyond z_s) is fully independent of the launch angles whereas EMD (beyond L_c) is practically independent for most purposes. In this work, we show by the power flow equation the influence of width of the launch beam distribution on z_s , L_c , and bandwidth in W-type POF.

2. Theoretical background

Modes propagating with the same principal mode number can be treated as one mode group in multimode fibers. Coupling occurs primarily between neighboring groups as the coupling strength drops with mode spacing [11]. Gloge's time independent coupled-power equation can be applied between neighboring mode groups [11]:

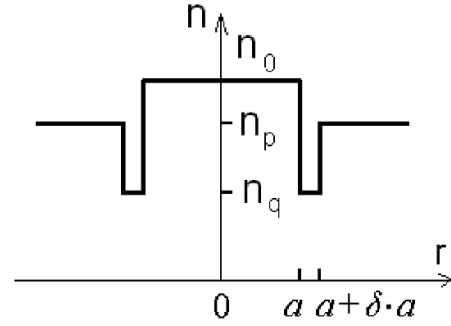


Figure 1. Refractive index profile of a W-type POF.

$$\frac{\partial P(\theta, z)}{\partial z} = -\alpha(\theta)P(\theta, z) + \frac{1}{\theta} \frac{\partial}{\partial \theta} \left[\theta D(\theta) \frac{\partial P(\theta, z)}{\partial \theta} \right] \quad (1)$$

here,

$P(\theta, z)$ is the angular power distribution at distance z from the input end of the fiber;

θ is the propagation angle with respect to the core axis;

$D(\theta)$ is the coupling coefficient (assumed constant [13–16]); and

$\alpha(\theta) = \alpha_0 + \alpha_d(\theta)$ is the modal attenuation.

In the expression for modal attenuation, α_0 accounts for absorption and scattering. It can be omitted because it appears in the solution as a multiplier $\exp(-\alpha_0 z)$ —and the solution will be normalized, thus eliminating it; $\alpha_d(\theta)$ is angle-dependent term in modal attenuation (equation (3)). For a specific beam distribution at launch, the solution of equation (1) provides the angular distribution of the output power for a fiber of a chosen length—that can be varied up to the length z_s , beyond which the same SSD would result.

For the fiber bandwidth, the time-dependent power flow equation is needed [12]:

$$\frac{\partial p(\theta, z, t)}{\partial z} + \tau(\theta) \frac{\partial p(\theta, z, t)}{\partial t} = -\alpha(\theta)p(\theta, z, t) + \frac{1}{\theta} \frac{\partial}{\partial \theta} \left[D(\theta) \frac{\partial p(\theta, z, t)}{\partial \theta} \right]. \quad (2)$$

In equation (2), $\tau(\theta)$ is the unit-length modal-delay and $p(\theta, z, t)$ angular distribution of power at distance z from the input fiber end.

Consider a W-type fiber with index profile shown in figure 1. The relative refractive index difference $\Delta_q = (n_0 - n_q)/n_0$ between the core and intermediate layer is larger than the difference $\Delta_p = (n_0 - n_p)/n_0$ between core and cladding, where n_0 , n_q and n_p are refractive indices of the core, intermediate layer and cladding, respectively. In this structure, the modes whose propagation angles are between $\theta_p \cong (2\Delta_p)^{1/2}$ and $\theta_q \cong (2\Delta_q)^{1/2}$ are leaky modes. For a W-type fiber, modal attenuation is [13]:

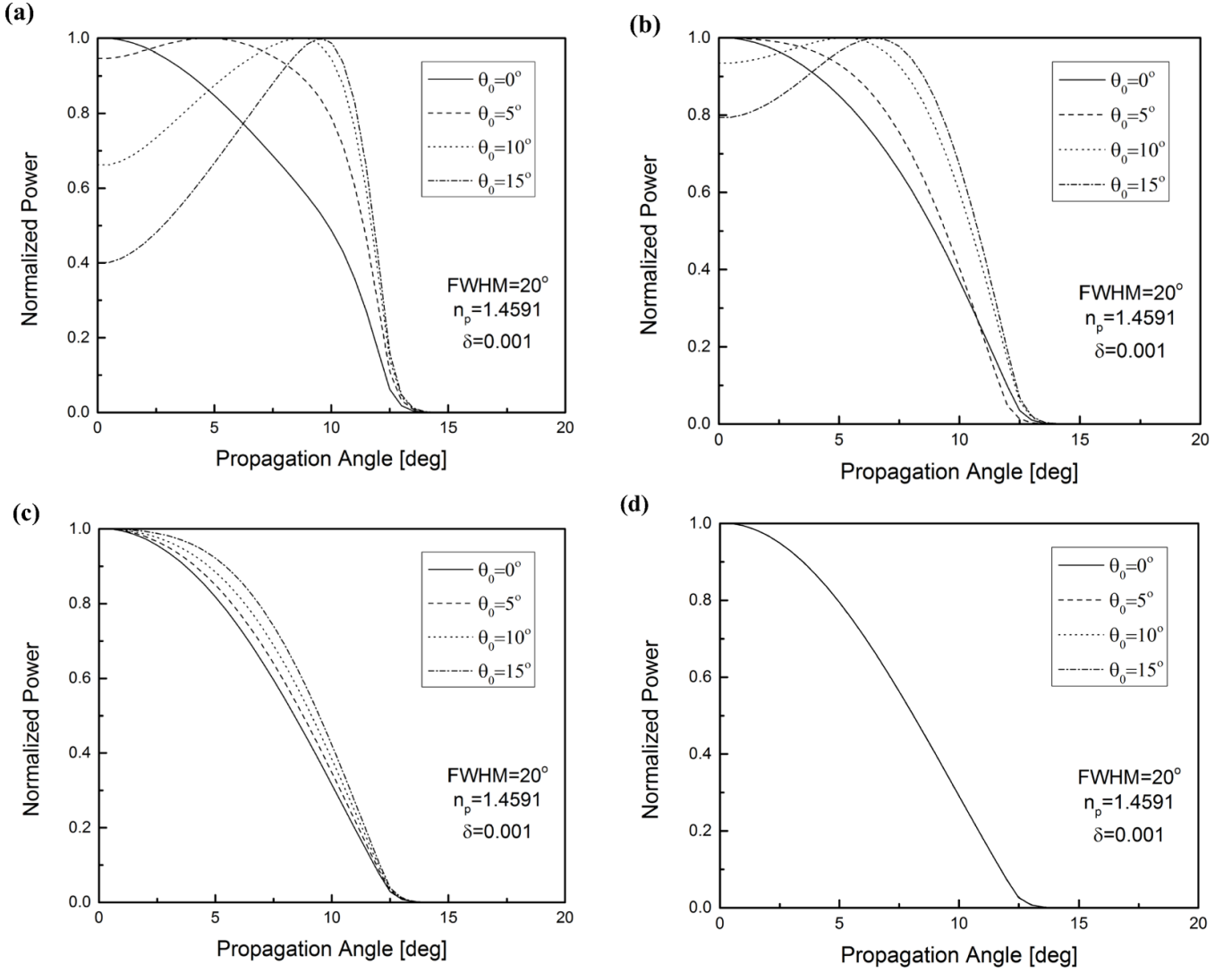


Figure 2. Normalized angular power distribution for FWHM = 20°, λ = 650 nm, n_p = 1.4591, δ = 0.001 and D = 3.5 × 10^{−4} rad² m^{−1}, for four launch angles θ₀ = 0°, 5°, 10° and 15°, at lengths: (a) 1 m, (b) 5 m, (c) 11 m and (d) 25 m.

$$\alpha_d(\theta) = \begin{cases} 0 & \theta \leq \theta_p \\ \alpha_L(\theta) & \theta_p < \theta < \theta_q \\ \infty & \theta \geq \theta_q \end{cases} \quad (3)$$

$$\Delta_p = (n_0 - n_p)/n_0; \Delta_q = (n_0 - n_q)/n_0; \theta_p \cong (2\Delta_p)^{1/2}; \theta_q \cong (2\Delta_q)^{1/2}.$$

How to solve equations (1) and (2) and calculate frequency response and bandwidth is detailed in our previous works [13, 17].

Modes between θ_p and θ_q become leaky modes [9, 13, 17]:

$$\alpha_L(\theta) = \frac{4(\theta^2 - \theta_p^2)^{1/2} \theta^2 (\theta_q^2 - \theta^2)}{a(1 - \theta^2)^{1/2} \theta_q^2 (\theta_q^2 - \theta_p^2)} \times \exp[-2\delta a n_0 k_0 (\theta_q^2 - \theta^2)^{1/2}] \quad (4)$$

where,

k₀ = 2π/λ is the free-space wave number;

a is core radius;

δa is width of the intermediate layer (inner cladding), figure 1;

n₀ is core refractive index;

n_q is intermediate layer (inner cladding) refractive index;

n_p is cladding refractive index;

3. Results and discussion

We investigate in this paper transmission characteristics of the W-type POF (figure 1) designed from the experimentally measured SC POF (PGU-CD1001-22E) by Mateo *et al* [18]. Its core and fiber diameters are d = 980 μm and b = 1000 μm, respectively, with NA = 0.50. The fiber’s inner critical angle, measured inside the fiber, is θ_c = 19.6°; the core refractive index is n₀ = 1.492; λ = 650 nm [18]. The W-type fiber’s refractive index of the inner cladding, n_q, is the same as that of the original cladding of its singly-clad counterpart, while the following three higher values of the refractive index were assumed in the modeling for the added outer

Table 1. Coupling length L_c (for EMD) and length z_s (for SSD) in W-type POF with $\delta = 0.001$, $\delta = 0.002$ and $\delta = 0.003$, $D = (3.5, 7.3, 9.8) \times 10^{-4} \text{ rad}^2 \text{ m}^{-1}$ for different FWHM of the incident beam.

			FWHM = 1°		FWHM = 7.5°		FWHM = 14°		FWHM = 20°	
			L_c (m)	z_s (m)	L_c (m)	z_s (m)	L_c (m)	z_s (m)	L_c (m)	z_s (m)
$D = 3.5 \times 10^{-4} \text{ rad}^2 \text{ m}^{-1}$	$\delta = 0.001$	$\theta_p = 8^\circ$	10	20	9	17	7	15	6	13
		$\theta_p = 10^\circ$	13	26	12	23	10	21	8	18
		$\theta_p = 12^\circ$	17	35	16	31	13	28	11	25
	$\delta = 0.002$	$\theta_p = 8^\circ$	20	40	18	35	14.5	32	12	27
		$\theta_p = 10^\circ$	21	43	19	36	15.5	34	13	29
		$\theta_p = 12^\circ$	23	48	21	40	17	38	15	33
	$\delta = 0.003$	$\theta_p = 8^\circ$	31	65	29	58	24	56	20.5	51
		$\theta_p = 10^\circ$	31	65	29	58	24	56	20.5	51
		$\theta_p = 12^\circ$	31.5	66	29	58	24	56	20.5	51
$D = 7.3 \times 10^{-4} \text{ rad}^2 \text{ m}^{-1}$	$\delta = 0.001$	$\theta_p = 8^\circ$	6.7	13.4	6.1	17	11.4	10.1	4.1	8.7
		$\theta_p = 10^\circ$	8.7	17.4	8.1	15.3	6.7	16.8	5.4	12
		$\theta_p = 12^\circ$	11.3	23.4	10.6	20.7	8.7	18.6	7.4	16.6
	$\delta = 0.002$	$\theta_p = 8^\circ$	13.4	26.7	12	23.3	9.7	21.3	8	18
		$\theta_p = 10^\circ$	14	28.7	12.6	24.1	10.2	22.7	8.6	19.3
		$\theta_p = 12^\circ$	15.3	32	14	26.8	11.3	25.3	10	22
	$\delta = 0.003$	$\theta_p = 8^\circ$	20.7	40.3	19.3	38.8	16	37.3	13.7	34
		$\theta_p = 10^\circ$	20.7	40.3	19.3	38.8	16	37.3	13.7	34
		$\theta_p = 12^\circ$	21	41.5	19.3	38.8	16	37.3	13.7	34
$D = 9.8 \times 10^{-4} \text{ rad}^2 \text{ m}^{-1}$	$\delta = 0.001$	$\theta_p = 8^\circ$	5	10	4.5	8.6	3.6	7.7	3.1	6.6
		$\theta_p = 10^\circ$	6.6	13.1	6.1	11.6	5	10.5	4.1	9.1
		$\theta_p = 12^\circ$	8.6	18	8.1	15.9	6.5	13.9	5.5	11.8
	$\delta = 0.002$	$\theta_p = 8^\circ$	10	20.1	9.1	17.7	7.3	16.1	6.1	13.7
		$\theta_p = 10^\circ$	10.5	21.6	9.5	18	7.8	17.1	6.6	14.5
		$\theta_p = 12^\circ$	11.6	24.1	10.6	20.1	8.6	19.1	7.6	16.6
	$\delta = 0.003$	$\theta_p = 8^\circ$	15.6	32.6	14.6	29.1	12.1	28	10.3	25.6
		$\theta_p = 10^\circ$	15.6	32.6	14.6	29.1	12.1	28	10.3	25.6
		$\theta_p = 12^\circ$	15.9	33.1	14.6	29.1	12.1	28	10.3	25.6

cladding: $n_p = 1.4775, 1.4693, 1.4591$ —with the corresponding critical angles $\theta_p = 8^\circ, 10^\circ, 12^\circ$, respectively. Three normalized widths of the intermediate layer were modeled: $\delta = 0.001, \delta = 0.002$, and $\delta = 0.003$, with the actual width being δa .

The resulting power flow equation (1) is time independent. We solved it by the method of explicit finite differences for different coupling coefficients $D = (3.5, 7.3, 9.8) \times 10^{-4} \text{ rad}^2 \text{ m}^{-1}$ [18, 19] and Gaussian launch beam with full width of half maximum (FWHM) = $1^\circ, 7.5^\circ, 14^\circ$ and 20° [13]. Because lengths L_c and z_s are practically unaffected by the intermediate layer's depth, the variation of this depth is not reported here. The onset of the EMD and the corresponding fiber length L_c are noted wherefrom the center points of the highest guided modes shift to $\theta = 0^\circ$. Similarly, the onset of the SSD and the corresponding fiber length z_s are noted wherefrom the angular distribution of power remains unchanged. Results show the evolution of the angular distribution of power in the normalized form and in the range of fiber length z up to z_s .

Figure 2 shows the outcomes for a Gaussian beam with $(\text{FWHM})_{z=0} = 20^\circ$ that is launched into the fiber with

$D = 3.5 \times 10^{-4} \text{ rad}^2 \text{ m}^{-1}$ at four angles (measured inside the fiber): $\theta_0 = 0^\circ, 5^\circ, 10^\circ$, and 15° . It is apparent in figure 2 that the centered launch ($\theta_0 = 0^\circ$) remains centered while the mode coupling broadens its width. For angled launches, centers of power distributions remain relatively unchanged only in short fibers, figure 2(a). For longer fiber lengths, figure 2(b), low-order modes experience stronger coupling effects as their distributions shift towards $\theta = 0^\circ$ more prominently. It takes more fiber length to observe similar coupling effects for higher-order modes. Eventually, all modes shift centers of their distributions from the initial θ_0 ($=5^\circ, 10^\circ, 15^\circ$) to zero degrees for the fiber length equal to the coupling length $L_c = 11$ m (the onset of EMD), figure 2(c). At $z_s = 25$ m, SSD is reached, figure 2(d).

As shown in table 1, the broader the width of the launch beam distribution, the shorter the coupling length L_c , figure 3, and the shorter the length z_s , figure 4. This is a consequence of the wide launch beams being more uniformly distributed across guided modes, promoting the onset of the EMD and SSD at shorter lengths.

We also obtain that the stronger mode coupling, the shorter the coupling length L_c , and length z_s (table 1). Leaky mode

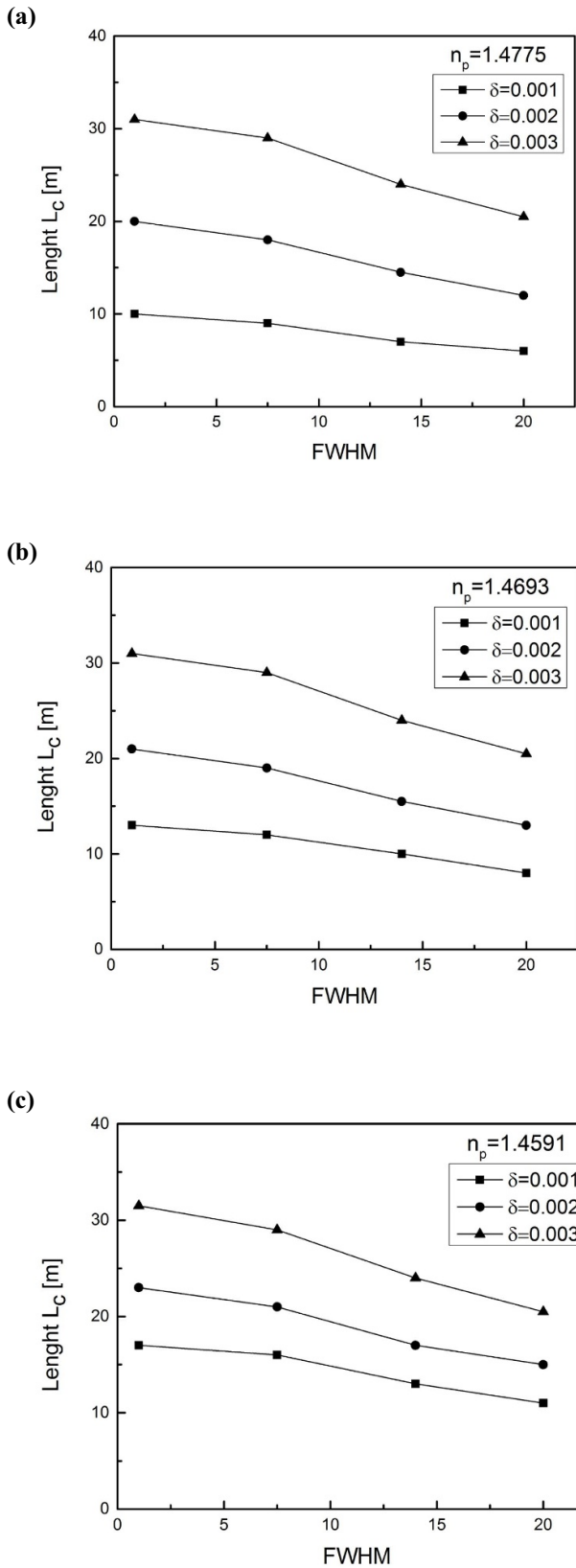


Figure 3. Length L_c as a function of the launch beam's angular distribution that is Gaussian with FWHM = 1°, 7.5°, 14° and 20°, for $\delta = 0.001, 0.002$ and 0.003 , $D = 3.5 \times 10^{-4} \text{ rad}^2 \text{ m}^{-1}$ and (a) $n_p = 1.4775$, (b) $n_p = 1.4693$ and (c) $n_p = 1.4591$.

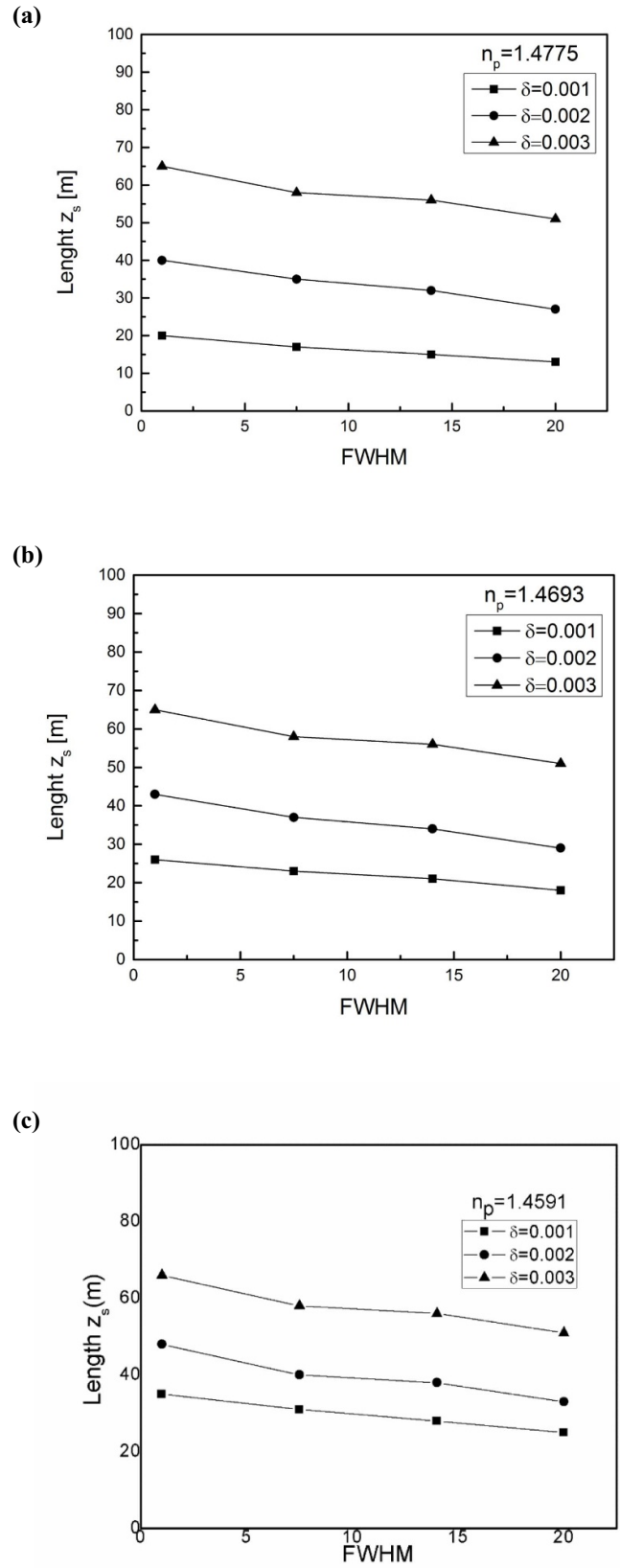


Figure 4. Length z_s as a function of the launch beam's angular distribution that is Gaussian with FWHM = 1°, 7.5°, 14° and 20°, for $\delta = 0.001, 0.002$ and 0.003 , $D = 3.5 \times 10^{-4} \text{ rad}^2 \text{ m}^{-1}$ and (a) $n_p = 1.4775$, (b) $n_p = 1.4693$ and (c) $n_p = 1.4591$.

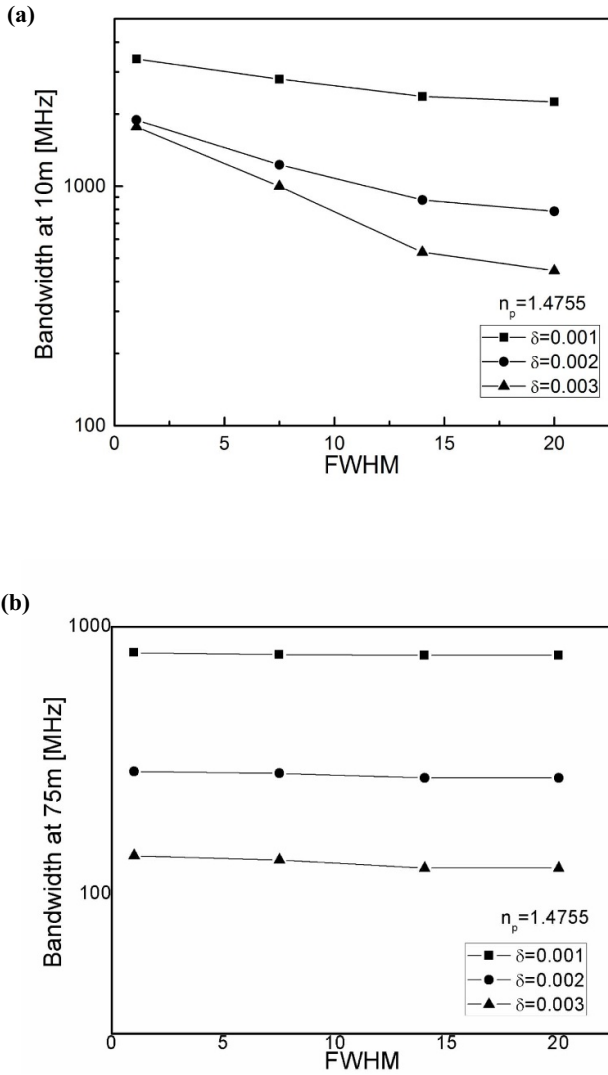


Figure 5. Bandwidth as a function of the launch beam’s angular distribution that is Gaussian, centered ($\theta_0 = 0^\circ$), with FWHM = 1° , 7.5° , 14° and 20° , for $\delta = 0.001, 0.002, 0.003$, $n_p = 1.4775$, and $D = 3.5 \times 10^{-4} \text{ rad}^2 \text{ m}^{-1}$ at fiber length of (a) 10 m and (b) 75 m.

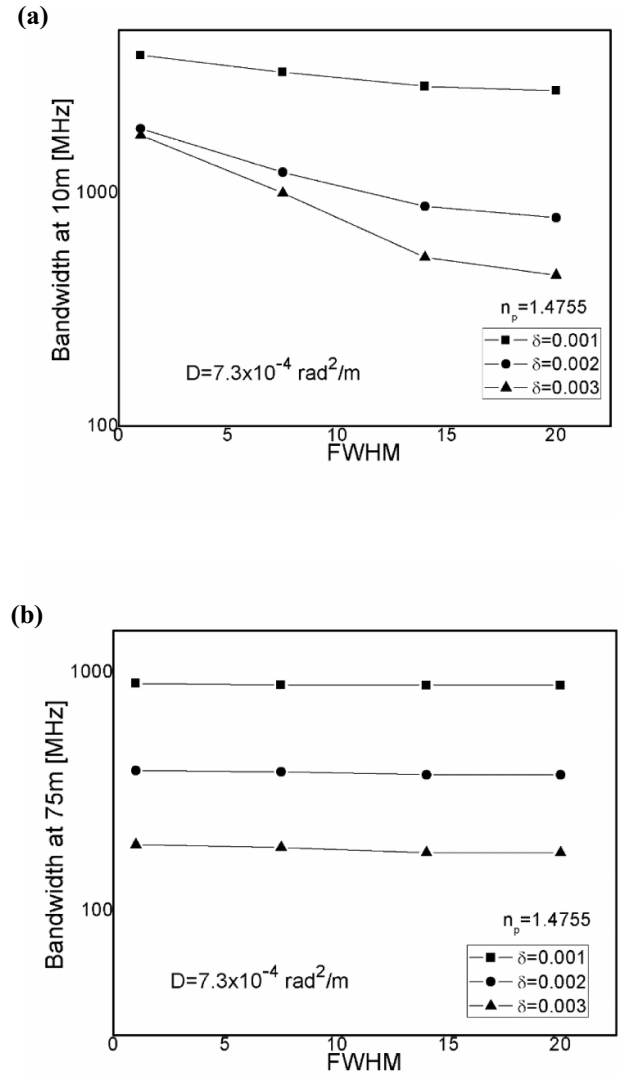


Figure 6. Bandwidth as a function of the launch beam’s angular distribution that is Gaussian, centered ($\theta_0 = 0^\circ$), with FWHM = 1° , 7.5° , 14° and 20° , for $\delta = 0.001, 0.002, 0.003$, and $n_p = 1.4775$, $D = 7.3 \times 10^{-4} \text{ rad}^2 \text{ m}^{-1}$, at fiber length of (a) 10 m and (b) 75 m.

losses drop as the intermediate layer widens, resulting in the longest lengths L_c and z_s for the case with $\delta = 0.003$. The length z_s increases also with the critical angle θ_p for all three widths of the inner cladding, table 1. However, such variability is less pronounced than for the width of the inner cladding δ .

Apparent from figure 5(a) is that for short fiber lengths the bandwidth drops as the launch beam widens (in terms of its FWHM). This is due to more dispersion for the higher order modes of the wider launch. Mode coupling reduces this effect further along the fiber length as the launch distributions approach that of the steady state. Eventually at length in

excess of z_s (SSD) in figure 5(b), bandwidth becomes independent of the launch. The highest bandwidth is for the case with the narrowest inner cladding with $\delta = 0.001$. This is to be expected as leaky mode losses are higher for this case than with $\delta = 0.002$ or 0.003 and with high such losses fewer higher modes continue to be guided—which decreases modal dispersion and boosts the bandwidth. Since with increasing the strength of mode coupling (D), the EMD is reached at shorter fiber lengths (table 1), thus the slower bandwidth decrease occurs, which results in higher bandwidth at 75 m for larger coupling coefficients D (figures 6 and 7).

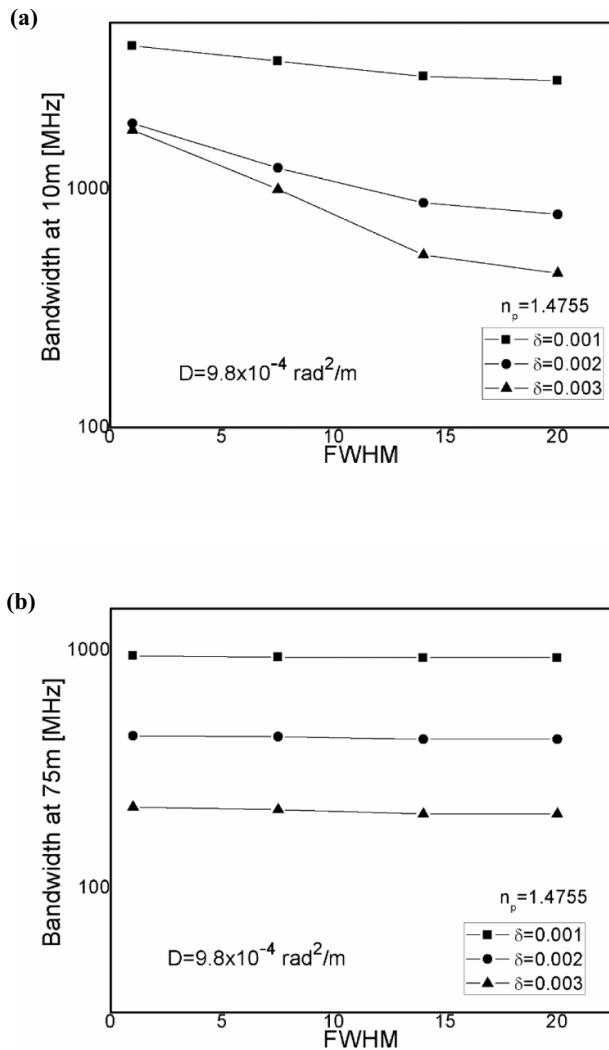


Figure 7. Bandwidth as a function of the launch beam's angular distribution that is Gaussian, centered ($\theta_0 = 0^\circ$), with FWHM = 1° , 7.5° , 14° and 20° , for $\delta = 0.001, 0.002, 0.003$, and $n_p = 1.4775$, $D = 9.8 \times 10^{-4} \text{ rad}^2 \text{ m}^{-1}$, at fiber length of (a) 10 m and (b) 75 m.

4. Conclusion

Results show how the width of the launch beam's angular distribution affects bandwidth and the equilibrium and steady state (EMD and SSD) angular power distributions of W-type POFs. The broader this width, the shorter the lengths L_c and z_s for the development of the respective two distributions. Being more uniformly distributed across guided modes, wide launch beams promote the onset of the EMD and SSD at shorter fiber lengths. In short fibers, the bandwidth drops as the angular distribution of the launch beam widens (as expressed by its FWHM). This is because of more dispersion for the higher order modes in the wider launch distribution. Such bandwidth drop tapers off with distance from the input end and ceases for fibers longer than $z_s = 25 \text{ m}$ when the bandwidth becomes independent of the launch conditions. With increasing the

strength of mode coupling, the EMD is reached at shorter fiber lengths, which results in slower bandwidth decrease and finally in higher bandwidth at longer fiber lengths for fibers with larger coupling coefficients D . These results are aimed at aiding designers and application integrators of W-type POFs, particularly in employing laser, LED or VCSEL light source.

Acknowledgments

This research was made possible in part by a grant from the Serbian Ministry of Education, Science, and Technological Development (Agreement No. 451-03-68/2020-14/200122), by the grant from Science Fund of Republic Serbia (Agreement No. CTPCF-6379382) and by the Strategic Research Grant of City University of Hong Kong (Project No. CityU 7004600).

References

- [1] Tyler E J, Webster M, Penty R V, White I H, Yu S and Rorison J 2002 Subcarrier modulated transmission of 2.5 Gb/s over 300 m of $62.5\text{-}\mu\text{m}$ -core diameter multimode fiber *IEEE Photon. Technol. Lett.* **14** 1743–5
- [2] Patel K M and Ralph S E 2002 Enhanced multimode fiber link performance using a spatially resolved receiver *IEEE Photon. Technol. Lett.* **14** 393–5
- [3] Zhao X and Choa F S 2002 Demonstration of 10 Gb/s transmission over 1.5-km-long multimode fiber using equalization techniques *IEEE Photon. Technol. Lett.* **14** 1187–9
- [4] Abbott J S, Smith G E and Truesdale C M 2002 Multimode fiber link dispersion compensator *U.S. Patent 6363 195*
- [5] Yamashita T and Kagami M 2005 Fabrication of light-induced self-written waveguides with a W-shaped refractive index profile *J. Lightwave Technol.* **23** 2542–8
- [6] Asai M, Inuzuka Y, Koike K, Takahashi S and Koike Y 2011 High-bandwidth graded-index plastic optical fiber with low-attenuation, high-bending ability, and high-thermal stability for home-networks *J. Lightwave Technol.* **29** 1620–6
- [7] Mikoshiba K and Kajioka H 1978 Transmission characteristics of multimode W-type optical fiber: experimental study of the effect of the intermediate layer *Appl. Opt.* **17** 2836–41
- [8] Takahashi K, Ishigure T and Koike Y 2006 Index profile design for high-bandwidth W-shaped plastic optical fiber *J. Lightwave Technol.* **24** 2867–76
- [9] Tanaka T, Yamada S, Sumi M and Mikoshiba K 1977 Microbending losses of doubly clad (W-type) optical fibers *Appl. Opt.* **18** 2391–4
- [10] Rastogi B V and Kumar A 2013 Design of large-mode-area three layered fiber structure for femtosecond laser pulse delivery *Opt. Commun.* **293** 108–12
- [11] Gloge D 1972 Optical power flow in multimode fibers *Bell Syst. Tech. J.* **51** 1767–83
- [12] Gloge D 1973 Impulse response of clad optical multimode fibers *Bell Syst. Tech. J.* **52** 801–16
- [13] Savović S, Simović A and Djordjević A 2012 Explicit finite difference solution of the power flow equation in W-type optical fibers *Opt. Laser Technol.* **44** 1786–90
- [14] Gambling W A, Payne D N and Matsumura H 1975 Mode conversion coefficients in optical fibers *Appl. Opt.* **14** 1538–42

- [15] Djordjevich A and Savović S 2000 Investigation of mode coupling in step index plastic optical fibers using the power flow equation *IEEE Photon. Technol. Lett.* **12** 1489–91
- [16] Rousseau M and Jeunhomme L 1977 Numerical solution of the coupled-power equation in step index optical fibers *IEEE Trans. Microw. Theory Tech.* **25** 577–85
- [17] Simović A, Savović S, Drljača B and Djordjevich A 2019 Enhanced bandwidth of W type plastic optical fibers designed from single clad step index plastic optical fibers *Opt. Laser Technol.* **111** 629–34
- [18] Mateo J, Losada M A and Zubia J 2009 Frequency response in step index plastic optical fibers obtained from the generalized power flow equation *Opt. Express* **17** 2850–60
- [19] Savović S and Djordjevich A 2006 Mode coupling in strained and unstrained step-index plastic optical fibers *Appl. Opt.* **45** 6775–80

INFLUENCE OF THE WAVELENGTH ON THE BANDWIDTH IN W-TYPE PLASTIC OPTICAL FIBERS

Branko Drljača,¹ Ana Simović,² Alexandar Djordjevich,³ and Svetislav Savović^{2,3*}

¹*Faculty of Sciences and Mathematics
University of Priština in Kosovska Mitrovica
Lole Ribara 29, Kosovska Mitrovica, Serbia*

²*Faculty of Science, University of Kragujevac
R. Domanovica 12, Kragujevac 34000, Serbia*

³*City University of Hong Kong
Tat Chee Avenue 83, Hong Kong, China*

*Corresponding author e-mail: savovic@kg.ac.rs

Abstract

We investigate the bandwidth and steady-state losses of multimode W-type plastic optical fibers solving the time-dependent power flow equation and show how the bandwidth in W-type plastic optical fibers can be enhanced by increasing the wavelength for different widths of the intermediate layer and refractive indices of the outer cladding. Such characterization of the fibers is consistent with their manifested efficiency in reducing modal dispersion and increasing bandwidth; this fact facilitates tailoring W-fibers to a specific application at hand at different wavelengths.

Keywords: W-type plastic optical fiber, laser launch beam, power flow equation, bandwidth, steady-state losses.

1. Introduction

Glass optical fibers are often used for high-speed long-distance communication due to their low attenuation and high bandwidth [1]. Large-core (with a diameter of ~ 1 mm) plastic optical fibers are most frequently employed for short-distance (< 100 m) communication links [2]. Plastic optical fibers (POFs) possess important advantages over their glass counterparts. Specifically, POFs may be manufactured with large-core diameters (0.5–1 mm or larger), allowing for interconnections with low-precision plastic components and reducing the overall cost of the system. POFs have excellent flexibility and are more easily handled than glass fibers. They impose less stringent constraints on the light source, and even luminescent diodes are suitable sources for multimode fibers. Hence, a variety of POF applications has been developed and commercialized, from simple light-transmission guides in displays to sensors and short-haul communication links [2–5].

The analysis and design of refractive-index profile of a multimode fiber with a view of advancing fiber transmission characteristics have attracted much attention in the last few decades [1, 6, 7]. A variety of designs of step-index, graded index, and W-type fibers has been proposed either for a long-distance communication links or high-capacity local area networks [1, 6–11]. It has been shown that waveguide dispersion is smaller in the W-type fiber than it is in the single-clad (SC) fiber [9]. A W-type fiber has a wide transmission bandwidth and lower bending losses compared to the corresponding SC fiber.

Differential mode attenuation and mode coupling strongly affect the transmission characteristics of multimode optical fibers. Differential mode attenuation is a consequence of absorption and scattering of light within the fiber material, which reduces the transmitted power. Mode coupling transfers the power between individual modes, which is caused by fiber intrinsic random anomalies. Mode coupling reduces modal dispersion, thus increasing the fiber bandwidth. On the other side, mode coupling increases fiber losses especially in a curved fiber and degrades the beam quality. The W-type fiber properties differ from the ones pertaining to the SC fibers [9, 12, 13]. This is because of the lossy leaky modes that propagate within the W-type fiber intermediate layer. Higher-order modes, which propagate along the W-type fiber, reduce its bandwidth and necessitate that the group delay difference between the modes be minimized by optimizing the fiber refractive index profile [13]. As modal attenuation, coupling, and dispersion affect transmission characteristics of the W-type optical fiber, methods for calculating their contributions are needed.

The main goal of this work is to investigate the influence of wavelength on the fiber bandwidth for variously configured W-type POFs in terms of width of the fiber intermediate layer and refractive indices of the outer cladding. One should mention that modal attenuation, coupling, and dispersion are included in our calculations.

2. Power Flow Equation

The time-dependent power flow for multimode W-type fibers is described by the following coupled power equation [14]:

$$\frac{\partial p(\theta, z, t)}{\partial z} + \tau(\theta) \frac{\partial p(\theta, z, t)}{\partial t} = -\alpha(\theta)p(\theta, z, t) + \frac{1}{\theta} \frac{\partial}{\partial \theta} \left[D(\theta) \frac{\partial p(\theta, z, t)}{\partial \theta} \right], \tag{1}$$

where t is time, $p(\theta, z, t)$ is the power distribution over angle, space, and time, $\tau(\theta)$ is mode delay per unit length, $D(\theta)$ is the mode-dependent coupling coefficient, and $\alpha(\theta) = \alpha_0 + \alpha_d(\theta)$ is the modal attenuation, with α_0 representing conventional losses due to absorption and scattering. The term α_0 leads only to a multiplier $\exp(-\alpha_0 z)$ in the solution and thus is neglected. The term α_d in the expansion of $\alpha(\theta)$ is dominant for higher-order modes. The coupling coefficient is usually assumed constant [12, 15–17]. The method of solving Eq. (1) and calculation of the bandwidth of W-type optical fibers has been described in more detail in our previous work [18].

For W-type fiber shown in Fig. 1, the modes whose propagation angles are between $\theta_p \cong (2\Delta_p)^{1/2}$ and $\theta_q \cong (2\Delta_q)^{1/2}$, where $\Delta_q = (n_0 - n_q)/n_0$ and $\Delta_p = (n_0 - n_p)/n_0$, are leaky modes. Attenuation constants of leaky modes are given as [12, 15]

$$\alpha_L(\theta) = \frac{4(\theta^2 - \theta_p^2)^{1/2} \theta^2 (\theta_q^2 - \theta^2)}{a(1 - \theta^2)^{1/2} \theta_q^2 (\theta_q^2 - \theta_p^2)} \exp \left[-2\delta a n_0 k_0 (\theta_q^2 - \theta^2)^{1/2} \right], \tag{2}$$

where k_0 is the free-space wave number, a is the core radius, and δa is the intermediate layer (inner

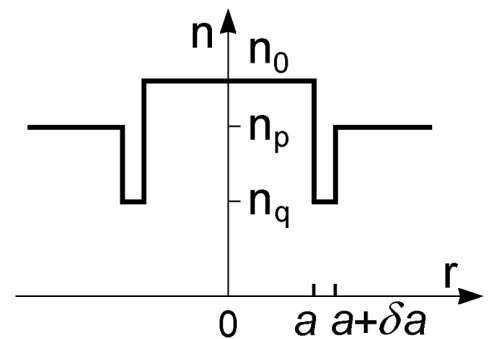


Fig. 1. Refractive index profile of a W-type fiber.

cladding) width. The modal attenuation in a W-type fiber can be expressed as [12, 15]

$$\alpha_d(\theta) = \begin{cases} 0; & \theta \leq \theta_p, \\ \alpha_L(\theta); & \theta_p < \theta < \theta_q, \\ \infty; & \theta \geq \theta_q. \end{cases} \quad (3)$$

One can see that attenuation constants of leaky modes (2) depend on the wavelength through the free-space wave number k_0 .

A W-type fiber can be regarded as a system consisting of SC_q fiber and cladding. In the SC_q fiber, only modes with propagation angles smaller than the critical angle θ_q can be guided. When the SC_q fiber is surrounded with a medium of the refractive index n_p , the lower-order modes, whose propagation angles are smaller than the critical angle θ_p of the SC_p fiber, remain guided. The higher-order modes with angles between θ_p and θ_q are transformed into leaky modes. It is shown in [12] that, because of the strong dependence of $\alpha_L(\theta)$ on the intermediate layer width δa , the steady-state characteristics of a W-type fiber depend on δa and coincide with those of SC_p and SC_q fibers in the limits of $\delta \rightarrow 0$ and $\delta \rightarrow \infty$, respectively.

To the best of our knowledge, in this work, we investigated for the first time how the bandwidth in W-type POFs can be enhanced by shifting from smaller to larger wavelengths for different widths of the intermediate layer and refractive indices of the outer cladding. The results obtained could be applied when designing W-type POFs.

3. Numerical Results and Discussion

We analyze the bandwidth as well as steady-state losses at different wavelengths in variously configured W-type POFs. The fiber structure characteristics are as follows: the core refractive index $n_0 = 1.492$, the cladding refractive index $n_q = 1.4057$, the critical angle $\theta_m = 19.6^\circ$ (measured inside the fiber), the core diameter $d = 0.98$ mm, and the fiber diameter $b = 1$ mm [19]. The W-type POF is designed from a singly-clad POF in such a way that the W-type POF inner cladding retains the refractive index n_q of the SC POF's cladding, while an outer cladding of the W-type POF has a refractive index n_p , which is higher than the refractive index n_q of the inner cladding; see Fig. 1. The three values of the refractive index of the outer cladding n_p are used in the modeling, namely, $n_p = 1.4775$, 1.4693 , and 1.4591 corresponding to the critical angles $\theta_p = 8^\circ$, 10° , and 12° , respectively. The normalized intermediate layer widths $\delta = 0.01$, 0.02 , 0.03 , and 0.05 were employed (actual width is δa in millimeters). We solved the time-dependent power flow equation (1) using the explicit finite difference method for the coupling coefficient $D = 3.5 \cdot 10^{-4} \text{ rad}^2 \cdot \text{m}^{-1}$ [4]. In the calculations, the laser launch beam distribution is taken in the Gaussian form with an FWHM of 7.5° . One should mention here that the change in the intermediate-layer depth has a negligible influence on the bandwidth of the W-type POFs, and therefore is not analyzed in this work.

Our numerical solution of the time-dependent power flow equation is illustrated in Fig. 2. In three inserts corresponding to three refractive indices of the outer cladding, $n_p = 1.4775$, 1.4693 , and 1.4591 and for the Gaussian launch excitation with FWHM = 7.5° , one sees the evolution of the W-type POF bandwidth at 75 m with the wavelength for different widths of the intermediate layer δ . One can observe in Fig. 2 that the bandwidth dependence on the wavelength is stronger for the intermediate-layer thickness $\delta = 0.02$ and 0.03 , and weaker for $\delta = 0.01$ and 0.05 . For the smallest width of the intermediate layer

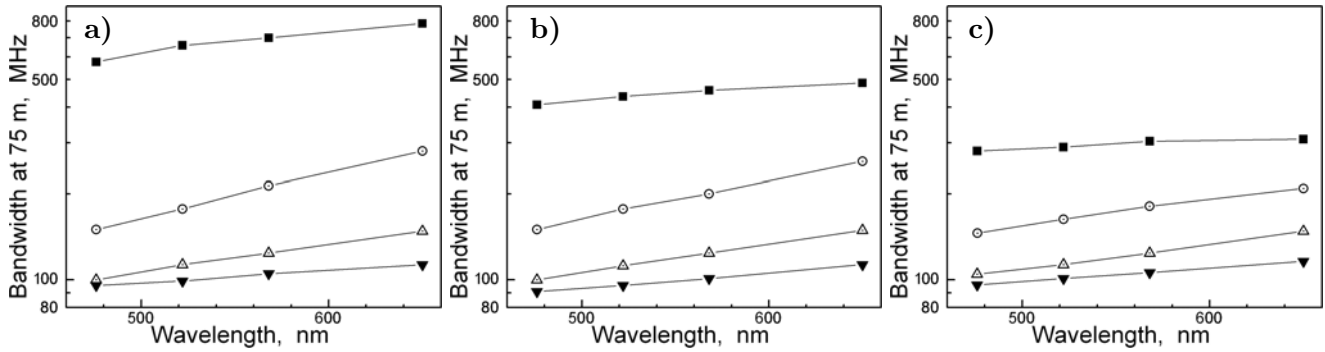


Fig. 2. Numerical results for the bandwidth at 75 m as a function of the wavelength for a W-type POF and the Gaussian launch excitation with FWHM = 7.5° , $\delta = 0.01$ (■), 0.02 (⊙), 0.03 (△), and 0.05 (▼), and $\theta_p = 8^\circ$, $n_p = 1.4775$ (a), $\theta_p = 10^\circ$, $n_p = 1.4693$ (b), and $\theta_p = 12^\circ$, $n_p = 1.4591$ (c).

$\delta = 0.01$, the wavelength influence on the bandwidth is negligible. This is due to large leaky mode losses; as these modes are practically not guided along the fiber, the modal dispersion (bandwidth) changes little. For $\delta = 0.05$, the leakage of modes is suppressed, and almost all modes remain guided. With increasing width of the intermediate layer, there is a wavelength-dependent decrease of the bandwidth. This decrease is more pronounced at short wavelengths as leaky mode losses are then reduced, resulting in the rise of modal dispersion and drop of the fiber bandwidth.

With increase in the refractive index of the outer cladding n_p (decrease of the critical angle θ_p), there is an increase in leaky mode losses, which results in highest values of the bandwidth in the case of $\delta = 0.01$. One can see in Fig. 2 that the improvement of the bandwidth of W-type POFs is more pronounced at longer fiber lengths. Since a narrow launch-beam distribution is assumed in the calculations, only guided modes are excited at the input fiber length. Therefore, the role of leaky modes is of less significance at short fiber lengths. Due to mode coupling, more leaky modes are filtered out at longer fiber lengths, leading to the significant improving of the W-type POF bandwidth.

In Fig. 3, we show the trade-off relation between the bandwidth and steady-state losses for the W-type POF. With increase in the leaky mode losses, the steady-state losses also increase. A trade-off relation between the bandwidth and losses would have to be considered in designing the optimum W-type POF by controlling the intermediate-layer thickness and refractive index of the outer cladding.

Finally, one should mention here that a numerical modeling of the bandwidth of W-type POFs presented in this work can be employed in investigations of other W-type optical fibers, such as a W-type plastic-clad silica optical fibers and W-type glass optical fibers, which have a step-index distribution of the core.

4. Conclusions

We calculated the bandwidth and steady-state losses by the time-dependent power flow equation over a range of light wavelengths for the W-type POF with a varied width of the intermediate layer and various refractive indices of the outer cladding. We showed that the bandwidth of W-type fibers broadens for longer wavelengths for all widths of the intermediate layer. This broadening of the bandwidth results from higher leaky mode losses and from the consequent drop in the modal dispersion. However, this influence of the wavelength on the bandwidth is negligible for narrow intermediate layers. With increase

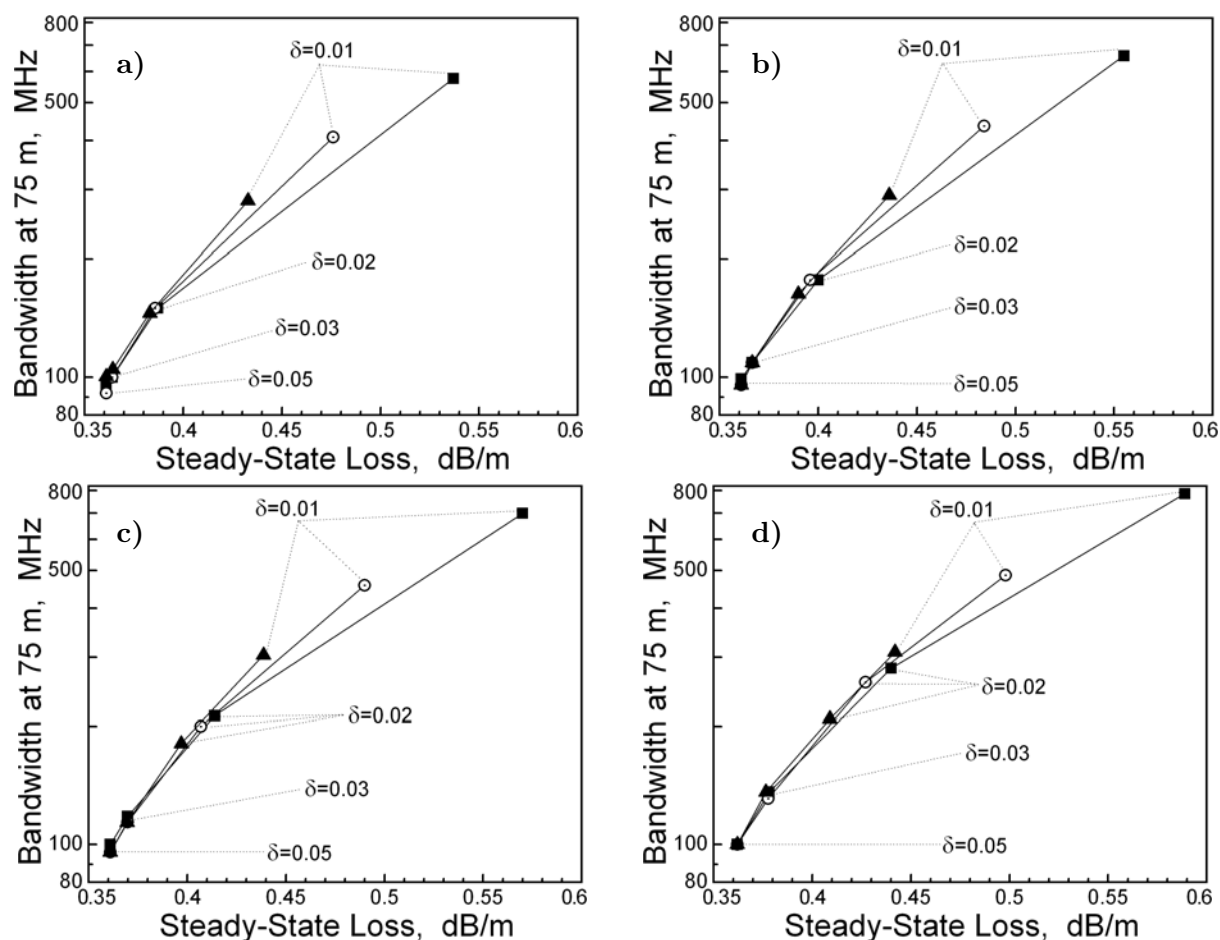


Fig. 3. Numerical results for the trade-off relation between the bandwidth at 75 m and the steady-state losses for the W-type POF with the Gaussian launch excitation of FWHM = 7.5° for four different wavelengths: $\lambda = 476$ nm (a), $\lambda = 522$ nm (b), $\lambda = 568$ nm (c), and $\lambda = 650$ nm (d). Here, $n_p = 1.4775$ is shown by \blacksquare , $n_p = 1.4775$ is shown by \circ , and $n_p = 1.4591$ is shown by \blacktriangle .

in the refractive index of the outer cladding, the bandwidth also increases due to increase of leaky mode losses.

Since, with increasing leaky mode losses, the steady-state losses also increase, a trade-off relation between the bandwidth and losses would have to be considered in designing the optimum W-type POF. This can be done by controlling the intermediate-layer width and the refractive index of the outer cladding at an appropriate infrared wavelength.

Acknowledgments

This work was supported in part by the Grant from Serbian Ministry of Education, Science, and Technological Development under Agreement No. 451-03-68/2020-14/200122, by the Grant from Science Fund of Republic Serbia under Agreement No. CTPCF-6379382, and by the Strategic Research Grant of City University of Hong Kong under Project No. City U 7004600.

References

1. L. Jeunhomme, M. Fraise, and J. P. Pocholle, *Appl. Opt.*, **15**, 3040 (1976).
2. C. Koepfen, R. F. Shi, W. D. Chen, and A. F. Garito, *J. Opt. Soc. Am. B*, **15**, 727 (1998).
3. P. E. Green, Jr., *IEEE J. Sel. Areas Commun.*, **14**, 764 (1996).
4. S. Savović and A. Djordjevich, *Appl. Opt.*, **45**, 6775 (2006).
5. S. Savović and A. Djordjevich, *Opt. Fiber Technol.*, **46**, 192 (2018).
6. Y. Daido, E. Miyauchi, T. Iwama, and T. Otsuka, *Appl. Opt.*, **18**, 2207 (1979).
7. T. Yamashita and M. Kagami, *J. Lightw. Technol.*, **23**, 2542 (2005).
8. M. Asai, Y. Inuzuka, K. Koike, et al., *J. Lightw. Technol.*, **29**, 1620 (2011).
9. K. Mikoshiba and H. Kajioka, *Appl. Opt.*, **17**, 2836 (1978).
10. J. Dugas and G. Maurel, *Appl. Opt.*, **31**, 5069 (1992).
11. W. Daum, J. Krauser, P. E. Zamzow, and O. Ziemann, *Polymer Optical Fibers for Data Communication*, Springer, Berlin (2002).
12. T. P. Tanaka and S. Yamada, *Appl. Opt.*, **19**, 1647 (1980).
13. K. Takahashi, T. Ishigure, and Y. Koike, *J. Lightw. Technol.*, **24**, 2867 (2006).
14. D. Gloge, *Bell Syst. Tech. J.*, **51**, 1767 (1972).
15. A. Simović, S. Savović, B. Drljača, and A. Djordjevich, *Opt. Laser Technol.*, **57**, 565 (2014).
16. A. Simović, A. Djordjevich, and S. Savović, *Appl. Opt.*, **51**, 4896 (2012).
17. S. Savović, A. Simović, and A. Djordjevich, *Opt. Laser Technol.*, **44**, 1786 (2012).
18. A. Simović, S. Savović, B. Drljača, and A. Djordjevich, *Opt. Laser Technol.*, **68**, 151 (2015).
19. J. Mateo, M. A. Losada, and J. Zubia, *Opt. Express*, **17**, 2850 (2009).

PAPER

Influence of mode coupling on three spatially multiplexed channels in multimode graded index plastic optical fibers

To cite this article: S Savovi *et al* 2020 *Laser Phys.* **30** 115102

View the [article online](#) for updates and enhancements.

Influence of mode coupling on three spatially multiplexed channels in multimode graded index plastic optical fibers

S Savović^{1,2}, A Djordjevich^{2,*}, A Simović¹ and B Drljača³

¹ Faculty of Science, University of Kragujevac, R. Domanovića 12, 34000, Kragujevac, Serbia

² Department of Mechanical Engineering, City University of Hong Kong, Kowloon, Hong Kong, People's Republic of China

³ Faculty of Science, University of Priština, L. Ribara 29, Kosovska Mitrovica, Serbia

E-mail: mealex@cityu.edu.hk

Received 4 July 2020

Accepted for publication 27 September 2020

Published 27 October 2020



CrossMark

Abstract

The influence of mode coupling on three-channel spatial division multiplexing capability in multimode graded index plastic optical fibers is investigated by solving the power flow equation. Our numerical results show that mode coupling significantly limits the fiber length at which the spatial division multiplexing can be realized with a minimal crosstalk between three neighbor spatial optical channels. Three spatial channels in the multimode graded index plastic optical fiber can be employed with a minimal crosstalk up to the fiber length of 3.5 m, which is about 12.5% of the coupling length (fiber length where equilibrium mode distribution is achieved). Such characterization of multimode graded index plastic optical fibers should be considered in designing an optical fiber transmission system for space division multiplexing, particularly for small office networking.

Keywords: plastic optical fibers, graded index optical fibers, space division multiplexing, mode coupling

(Some figures may appear in colour only in the online journal)

1. Introduction

The incessant demand of optical channels with increasing data rates continues to inspire new developments, as it has for many years. The increase capacity of optical fiber systems was caused by successive technology improvements: low losses single-mode fibers, fiber amplifiers, multiplexing, and high-efficiency spectral coding [1]. Multiplexing of optical data can be realized not only in wavelength [2], but also in polarization, in time, in phase and in space [1]. In spite of the fact that data traffic demand is easily covered by wavelength-division multiplexed (WDM) systems based on single-mode

fibers (SMFs), recent works show that the WDM systems are rapidly approaching their Shannon capacity limit [3]. Aimed to overcome the Shannon capacity limit of WDM networks using SMFs, space division multiplexing (SDM) including mode division multiplexing using multimode fibers or few-mode fibers and/or core multiplexing using multicore fibers [4], has attracted much attention in the last decade for the next multiplicative capacity growth for optical communication [1, 5–8]. SDM may operate at the same wavelength or different wavelengths [9]. In the case of SDM at the same wavelength, radially distributed, dedicated spatial locations are assigned to every SDM channel inside the carrier fiber as these channels traverse the length of the carrier [10]. The location of the each channel inside the optical fiber is a function of the launch angle and the strength of mode coupling. This technique

* Author to whom any correspondence should be addressed

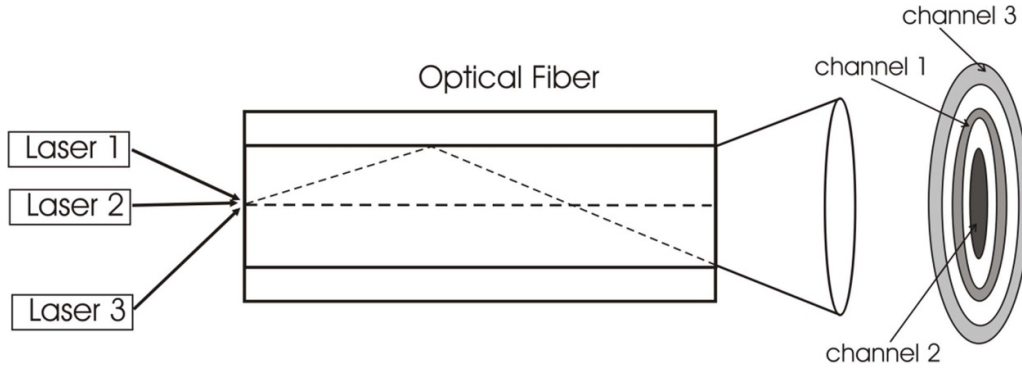


Figure 1. Minimalistic system design of three-channel SDM in GI POF.

requires a multicore and/or multimode fiber and utilizes the transverse spatial extent of the fiber to create parallel data channels.

Multimode plastic optical fibers (POFs) have been the preferred transmission medium in high-capacity communications networks and short-distance (few tens of meters) communications systems. These fibers have large numerical aperture which simplifies coupling of light. Compared to their glass counterparts, POFs offer a low-cost installation alternative with low-precision plastic components without precision couplers. POFs also tend to cost less to produce and are easier to handle. Their flexibility is especially useful when installing them in tight spaces such as in homes, offices or vehicles. Step-index (SI) POFs have large modal dispersion and low bandwidth-length product. Graded index (GI) POFs exhibit far less modal dispersion than SI POFs. This is due to their gradual, usually parabolic, decreasing of the refractive index of core with radial distance from the fiber axis.

Transmission characteristics of multimode POFs depend upon the differential mode attenuation and rate of mode coupling [9, 11]. The latter represents power transfer between neighbor modes caused by fiber impurities and inhomogeneities introduced during the fiber manufacturing process [11]. We have recently shown that SDM with three, four and five channels in the multimode SI POFs can be successfully employed with a minimal crosstalk only at very short fiber length, up to ≈ 2.4 , 1.6 and 1.4 m, respectively [10].

In this work, using the power flow equation, we examine the state of mode coupling in multimode GI POF investigated earlier [12]. This enables one to obtain the limits of the fiber lengths up to which a three-channel SDM can be realized with minimal crosstalk between the co-propagating optical channels.

Radially distributed, dedicated spatial locations are assigned to three SDM channels as these channels traverse the length of the carrier. The location of the each channel inside the GI POF is a function of the launch angle and the strength of mode coupling. In practice, the channel launched with input angle $\theta_0 = 0^\circ$ along fiber axis appears as a far field in the form of disk, while another channel launched with $\theta_0 > 0^\circ$ appear in the far field as concentric ring (figure 1). The center disk and two rings represent a three separated

SDM optical channels, thereby enhancing the bandwidth of optical fiber system. By solving the time-independent power flow equation, one can obtain the limits of the fiber lengths up to which a three-channel SDM can be realized with minimal crosstalk between the co-propagating optical channels in GI POF.

2. Time-independent power flow equation for GI optical fiber

The index profile of GI optical fibers may be expressed as:

$$n(r, \lambda) = \begin{cases} n_1(\lambda) \left[1 - 2\Delta(\lambda) \left(\frac{r}{a} \right)^g \right]^{1/2} & (0 \leq r \leq a) \\ n_1(\lambda) (1 - 2\Delta(\lambda))^{1/2} = n_2(\lambda) & (r > a), \end{cases} \quad (1)$$

where g is the core index exponent, a is the core radius, $n_1(\lambda)$ is the maximum index of the core (measured at the fiber axis), $n_2(\lambda)$ is the index of the cladding and $\Delta = [n_1(\lambda) - n_2(\lambda)]/n_1(\lambda)$ is the relative index difference. The optimum value of the core index exponent g to obtain maximum bandwidth depends on the wavelength λ (in free-space) of the source [13].

Time-independent power flow equation for GI optical fiber is [14–16]:

$$\frac{\partial P(m, \lambda, z)}{\partial z} = \frac{D}{m} \frac{\partial P(m, \lambda, z)}{\partial m} + D \frac{\partial P^2(m, \lambda, z)}{\partial m^2}, \quad (2)$$

where $P(m, \lambda, z)$ is power in the m th principal mode (modal group), z is the coordinate along the fiber axis from the input fiber end, D is a constant mode coupling coefficient [16] (assumption of constant coupling coefficient is valid for all values of m , except for $m \approx M$ [14, 16]). The maximum principal mode number $M(\lambda)$ can be obtained as [14, 15]:

$$M(\lambda) = \sqrt{\frac{g\Delta(\lambda)}{g+2}} akn_1(\lambda), \quad (3)$$

where $k = 2\pi/\lambda$. More details regarding the derivation of the power flow equation (2) can be found in [15].

Using the explicit finite difference method (EFDM), discretization of equation (2) leads to [17]:

$$P_{i,j+1} = \left(\frac{D\Delta z}{(\Delta m)^2} - \frac{D\Delta z}{2m_i\Delta m} \right) P_{i-1,j} + \left(1 - \frac{2D\Delta z}{(\Delta m)^2} \right) P_{i,j} + \left(\frac{D\Delta z}{2m_i\Delta m} + \frac{D\Delta z}{(\Delta m)^2} \right) P_{i+1,j}, \quad (4)$$

where i and j refer to the discretization step lengths Δm and Δz for the mode m and length z , respectively. This is a simple formula for $P_{i,j+1}$ at the $(i, j + 1)$ th mesh point in terms of the known values along the j th distance row. The power flow equation (2) for GI optical fiber is a parabolic partial differential equation, which is solved numerically (4) for Gaussian launch (excitation) distribution as an initial condition and the boundary conditions: $P(m, \lambda, z) = 0$, for $m > M(\lambda)$ and $d(m) \frac{\partial P(m, \lambda, z)}{\partial m} \Big|_{m=0} = 0$ for $m = 0$. The first condition implies that modes with infinitely high loss do not transmit power. The second one indicates that the coupling is limited to the modes $m > 0$. As first in the authors' best knowledge, numerical solution (4) of the time-independent power flow equation (2) is reported in this work for investigation of the state of mode coupling for three spatially multiplexed channels in GI POF in terms of mode variable (m). In our previous work [16] we proposed a new method for determination of the constant coupling coefficient D , using the following relation:

$$D = \frac{\sigma_{z_2}^2 - \sigma_{z_1}^2}{2(z_2 - z_1)}, \quad (5)$$

where $\sigma_{z_1}^2$ and $\sigma_{z_2}^2$ are variances of the output modal power distribution $P(m, \lambda, z_1)$ and $P(m, \lambda, z_2)$ measured at the fiber lengths $z_1 > 0$ and $z_2 > 0$, respectively ($z_2 > z_1$).

3. Results and discussion

In this paper we investigate the transmission characteristics of the GI POF (OM Giga, Fiber FinTM), we have recently experimentally investigated [12]. The characteristics of GI POF were: the core diameter of the fiber was 0.9 mm (fiber diameter was 1 mm), the refractive index of the core measured at the fiber axis was $n_1 = 1.522$ and the refractive index of the cladding was $n_2 = 1.492$. Using our recently proposed equation (5) [16], we have obtained the coupling coefficient for this fiber $D = 1482 \text{ l m}^{-1}$ [12], which is adopted in this work.

With increasing radial offset Δr or launch angle θ , higher-order mode groups can be excited. The relation between the radial offset Δr , angle θ and the principal mode m is [18]:

$$\frac{m}{M} = \left[\left(\frac{\Delta r}{a} \right)^g + \frac{\theta^2}{2\Delta} \right]^{(g+2)/2g}. \quad (6)$$

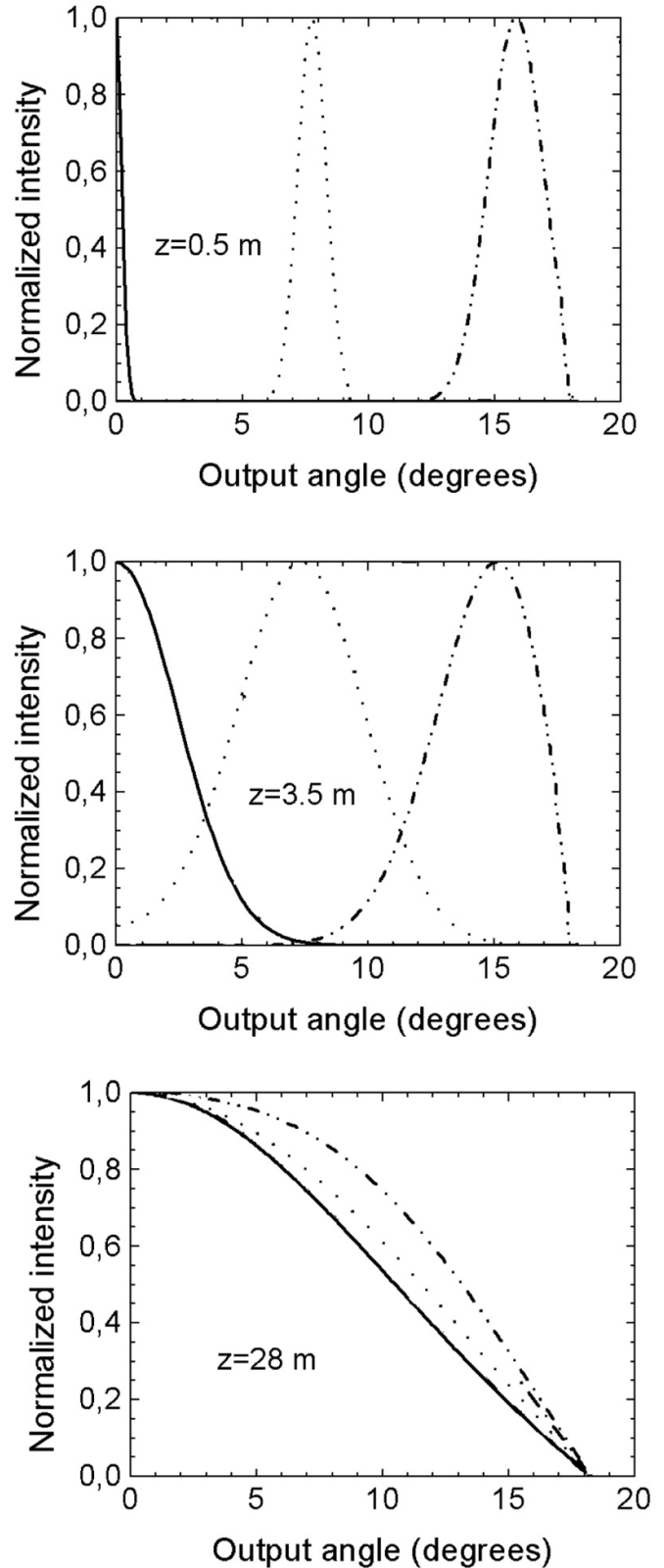


Figure 2. Normalized output power distribution at different locations along GI POF calculated for three Gaussian input angles $\theta_0 = 0^\circ$ (solid line), 8° (dotted line) and 16° (dashed-dotted line), with $(\text{FWHM})_{z=0} = 0.127^\circ$ for: (a) $z = 0.5 \text{ m}$; (b) $z = 3.5 \text{ m}$ and (c) $z = 28 \text{ m}$.

For the GI POF under investigation, the maximum principal mode number is $M = 656$ at $\lambda = 633$ nm, $g = 1.80101$ and $\Delta = (n_1 - n_2)/n_1 = 0.019711$.

Figure 2 shows the evolution of the normalized output modal power distribution with fiber length for three SDM channels launched at the input end of GI POF. The three co-propagating optical channels are launched at different input angles $\theta_0 = 0^\circ$, 8° and 16° thus maintaining a different angular orientation. In the numerical calculations, for three optical channels we selected Gaussian launch beam distribution $P(\theta, z)$ with $(\text{FWHM})_0 = 0.127^\circ$ by setting $\sigma_0 = 0.054^\circ$. A Gaussian beam is assumed to be launched with radial offset $< \Delta r \geq 0 \mu\text{m}$ and standard deviation $\sigma_{\Delta r} = 1.5 \mu\text{m}$ in equation (6). Results are shown for three different input angles $\theta_0 = 0^\circ$, 8° and 16° . As a result of redistribution of the optical power from lower to higher order modes during propagation, the coupling of higher-order modes can be observed only after longer fiber lengths (figure 2(b)). Power distributions of higher modes have shifted their mid-points to zero at the coupling length of $L_c = 28$ m (from their initial values at the input fiber end), resulting in the equilibrium mode distribution (EMD), figure 2(c).

Ring radiation pattern in very short fibers in figure 2 indicate that the mode coupling is so low thus leading to a minimal crosstalk observed between three co-propagating optical channels. With increasing a fiber length, a crosstalk between three co-propagating optical channels continue to increase and significantly influence the quality of light signals which are transmitting through three channels along carrier fiber. Finally, at fiber's coupling length L_c the mode-distribution of co-propagating optical channels which are in the ring form, shift their mid-point to zero degrees, producing the EMD at fiber length L_c (figure 2(c)). As a result, at fiber lengths $z \geq L_c$ the modal distributions which corresponded to different co-propagating optical channels are no more spatially separated since they form a disk-type circular far field outputs. One can see that mode coupling significantly limits the length of the GI POF at which the SDM can be realized. The maximum length for practical realization of three-channel SDM in this GI POF is $z_{\text{SDM}} \approx 3.5$ m. It is worth noting that the lengths z_{SDM} up to which a minimal crosstalk is observed between three neighbor co-propagating optical channels is much shorter than the coupling length $L_c = 28$ m at which the EMD is achieved. A three-channel SDM in the investigated multimode GI POF can be realized with a minimal crosstalk up to the fiber length which is about 12.5% of the coupling length. We have recently shown that the larger number of co-propagating optical channels (four and five) in SI POFs, the sooner crosstalk between the neighbor optical channels appeared [10]. One can conclude that in increasing capacity of optical fiber system, a SDM with three-channels can be realized with the GI POF at short fiber lengths up to ≈ 3.5 m. Such characterization of optical fibers should be considered in designing an optical fiber transmission system with multi-channel SDM in GI POFs.

One should note that by calculating the normalized output power distribution at different fiber lengths in the case of multi-channel SDM, it is difficult to exactly predict the level of

the crosstalk which prohibits the system operation. In practice, for more accurate estimation of the SDM capacity of the particular GI POF, the transmission matrix should be used, with taking into account the noise terms which depend on the specific implementation of the receiver. But, our numerical results can be used as a good approximation in the estimation of the fiber length at which SDM could be realized in GI POFs. SDM channels from different channels could be separated from each other by setting the proper positions of the individual photo-detectors [19].

4. Conclusion

The influence of mode coupling on three spatially multiplexed optical channels in multimode GI POF is investigated by solving the power flow equation. We have shown that mode coupling significantly limits the fiber length at which the SDM can be realized with a minimal crosstalk between three optical channels. Three optical channels with SDM in the GI POF can be employed with a minimal crosstalk up to the fiber length which is about 12.5% of the corresponding coupling length. Such characterization of optical fibers should be considered in designing an optical fiber transmission system for SDM, particularly for small office networking.

Acknowledgments

The work described in this paper was supported by the Strategic Research Grant of City University of Hong Kong (Project No. CityU 7004600) and by a grant from Serbian Ministry of Education, Science and Technological Development (Agreement No. 451-03-68/2020-14/200122).

References

- [1] Richardson D, Fini J and Nelson L 2013 Space-division multiplexing in optical fibres *Nat. Photon.* **7** 354–62
- [2] Montero D S, Garcilópez I P, García C V, Lallana P C, Moraleda A T and Castillo P J P 2015 Recent advances in wavelength-division-multiplexing plastic optical fiber technologies *Advances in Optical Fiber Technology: Fundamental Optical Phenomena and Applications* (Rijeka: InTech)
- [3] Ortiz A M and Sáez R L 2017 Multi-core optical fibers: theory, applications and opportunities *Selected Topics on Optical Fiber Technologies and Applications* (London: InTechOpen)
- [4] Saitoh K and Matsuo S 2013 Multicore fibers for large capacity transmission *Nanophotonics* **2** 441–54
- [5] Winzer P J 2012 Optical networking beyond WDM *IEEE Photon. J.* **4** 647–51
- [6] Li G, Bai N, Zhao N and Xia C 2014 Space-division multiplexing: the next frontier in optical communication *Adv. Opt. Photon.* **6** 413–87
- [7] Brunet C, Ung B, Belanger P-A, Messaddeq Y, LaRochelle S and Rusch L A 2014 Vector mode analysis of ring-core fibers: design tools for spatial division multiplexing *J. Lightwave Technol.* **32** 4046–57
- [8] Murshid S, Grossman B and Narakorn P 2008 Spatial domain multiplexing: a new dimension in fiber optic multiplexing *Opt. Laser Technol.* **40** 1030–6

- [9] Murshid S H, Chakravarty A and Biswas R 2011 Attenuation and modal dispersion models for spatially multiplexed co-propagating helical optical channels in step index fibers *Opt. Laser Technol.* **43** 430–6
- [10] Savović S, Djordjevich A, Simović A and Drljača B 2018 Influence of mode coupling on three, four and five spatially multiplexed channels in multimode step-index plastic optical fibers *Opt. Laser Technol.* **106** 18–21
- [11] Gloge D 1972 Optical power flow in multimode fibers *Bell Syst. Tech. J.* **51** 1767–83
- [12] Savović S, Simović A, Drljača B, Djordjevich A, Stepniak G, Bunge C A and Bajić J 2019 Power flow in graded index plastic optical fibers *J. Lightwave Technol.* **37** 4985–90
- [13] Ohdoko K, Ishigure T and Koike Y 2005 Propagating mode analysis and design of waveguide parameters of GI POF for very short-reach network use *IEEE Photon. Technol. Lett.* **17** 79–81
- [14] Kitayama K, Seikai S and Uchida N 1980 Impulse response prediction based on experimental mode coupling coefficient in a 10-km long graded-index fiber *IEEE J. Quant. Electron.* **16** 356–62
- [15] Olshansky R 1975 Mode coupling effects in graded-index optical fibers *Appl. Opt.* **14** 935–45
- [16] Savović S and Djordjevich A 2019 New method for calculating the coupling coefficient in graded index optical fibers *Opt. Laser Technol.* **101** 223–6
- [17] Djordjevich A and Savović S 2000 Investigation of mode coupling in step index plastic optical fibers using the power flow equation *IEEE Photon. Technol. Lett.* **12** 1489–91
- [18] Nagano K and Kawakami S 1980 Measurements of mode conversion coefficients in graded-index fibers *Appl. Opt.* **19** 2426–34
- [19] Puttnam B J, Luís R S, Rademacher G, Alfredsson A, Klaus W, Sakaguchi J, Awaji Y, Agrell E and Wada N 2019 Characteristics of homogeneous multi-core fibers for SDM transmission *APL Photon.* **4** 022804

PAPER

Influence of mode coupling on angular division multiplexing in seven-core plastic optical fibers

To cite this article: S Savovi *et al* 2020 *Laser Phys.* **30** 065103

View the [article online](#) for updates and enhancements.

Influence of mode coupling on angular division multiplexing in seven-core plastic optical fibers

S Savović^{1,2}, A Djordjevich², A Simović¹ and B Drljača³

¹ Faculty of Science, University of Kragujevac, Kragujevac, Serbia

² Department of Mechanical and Biomedical Engineering, City University of Hong Kong, Kowloon, Hong Kong, People's Republic of China

³ Faculty of Science, University of Priština, L. Ribara 29, Kosovska Mitrovica, Serbia

E-mail: savovic@kg.ac.rs

Received 16 December 2019

Accepted for publication 7 April 2020

Published 11 May 2020



CrossMark

Abstract

We propose an angular division multiplexing in new designed multicore plastic optical fiber with seven cores arranged in a hexagonal array. The influence of mode coupling on two-channel angular division multiplexing capability in each of seven cores is investigated by solving the power flow equation. Our numerical results show that mode coupling significantly limits the fiber length at which the angular division multiplexing can be realized in each of seven cores with a minimal crosstalk between two neighbor angular optical channels. Two angular channels in the proposed seven-core plastic optical fiber can be employed with a minimal crosstalk up to the fiber length which is about 20% of the coupling length (fiber length where equilibrium mode distribution is achieved). Such characterization of multicore optical fibers should be considered in designing a multicore optical fiber transmission system for space division multiplexing.

Keywords: multicore plastic optical fibers, angular division multiplexing, mode coupling

(Some figures may appear in colour only in the online journal)

1. Introduction

The increasing demand for digital data bandwidth in access and backbone networks pushes the development of emerging technologies to increase network capacity, especially for optical fiber infrastructures. The increase capacity of optical fiber systems was caused by successive technology improvements: low losses single-mode fibers, fiber amplifiers, multiplexing, and high-efficiency spectral coding [1]. Multiplexing of optical data can be realized not only in wavelength [2], but also in polarization, in time, in phase and in space [1]. In spite of the fact that data traffic demand is easily covered by wavelength-division multiplexed (WDM) systems based on single-mode single-core fibers (SM-SCFs), recent works show that the WDM systems are rapidly approaching their Shannon capacity limit [3]. Aimed to overcome the Shannon capacity limit of WDM networks using SM-SCFs, space division multiplexing (SDM) including mode division multiplexing using

multimode fibers or few-mode fibers and/or core multiplexing using multicore fibers [4], has attracted much attention in the last decade for the next multiplicative capacity growth for optical communication [1, 5–8]. SDM may operate at the same wavelength or different wavelengths [9]. In the case of SDM at the same wavelength, radially distributed, dedicated spatial locations are assigned to every SDM channel inside the carrier single-core fiber as these channels traverse the length of the carrier [10]. The location of the each channel inside the single-core fiber is a function of the launch angle and the strength of mode coupling.

Single-core plastic optical fibers (SC POFs) are a low-cost solution for short-distance applications in digital car networks, industrial networks, and home networks and appliances. Transmission characteristics of multimode step-index (SI) POFs depend upon the differential mode attenuation and rate of mode coupling [9, 11]. The latter represents power transfer between neighbor modes caused by fiber impurities

and inhomogeneities introduced during the fiber manufacturing process [11]. We have recently shown that angular division multiplexing (ADM) with three, four and five channels in the multimode single-core SI POFs can be successfully employed with a minimal crosstalk only at very short fiber length, up to ≈ 2.4 , 1.6 and 1.4 m, respectively [10]. In order to overcome the limited SC POF capability for SDM, we propose in this work a SDM based on multicore multiplexing using a novel multicore plastic optical fiber (MC POF) with seven cores arranged in a hexagonal array, which exhibits negligible inter-core crosstalk (figure 1). In addition, we explore a capability of the proposed seven-core MC POF for two-channel ADM (figure 2(a)). The refractive index profile of all homogeneous cores has a step between two constant values in the core and cladding interface. By using the power flow equation, we examine the state of mode coupling in each seven carrier cores of the proposed multimode MC POF. Radially distributed, dedicated spatial locations are assigned to two ADM channels inside the each carrier seven cores as these channels traverse the length of the carrier. The location of the each channel inside the each core of MC POF is a function of the launch angle and the strength of mode coupling. In practice the channel launched with input angle $\theta_0 = 0^\circ$ along axis of each carrier seven cores appears as a far field in the form of disk, while another channel launched with $\theta_0 > 0$ appear in the far field as concentric ring (figure 2(b)). The center disk and ring represent a two separated ADM optical channels, thereby enhancing the bandwidth of optical fiber system. This enables one to obtain the limits of the fiber lengths up to which a two-channel ADM can be realized with minimal crosstalk between the co-propagating optical channels in each carrier seven cores of MC POF.

2. Power flow equation

Assuming that mode coupling in multimode optical fibers occurs predominantly between neighbor modes, Gloge's power flow equation for power distribution inside a multimode step-index fiber is [11]:

$$\frac{\partial P(\theta, z)}{\partial z} = -\alpha(\theta)P(\theta, z) + \frac{D}{\theta} \frac{\partial}{\partial \theta} \left(\theta \frac{\partial P(\theta, z)}{\partial \theta} \right) \quad (1)$$

where $P(\theta, z)$ is the angular power distribution, z is distance from the input end of the fiber, θ is the propagation angle with respect to the core axis, D is the coupling coefficient assumed constant [11, 12] and $\alpha(\theta)$ is the modal attenuation. In our previous work [13] we have shown that modeling mode coupling in SI POFs assuming a constant coupling coefficient D can be used instead of the more complicated approach with angle-dependent coupling coefficient. Except near cutoff, the attenuation remains uniform $\alpha(\theta) = \alpha_0$ throughout the region of guided modes $0 \leq \theta \leq \theta_c$ [14] (it appears in the solution as the multiplication factor $\exp(-\alpha_0 z)$ that also does not depend on θ). Therefore, $\alpha(\theta)$ need not be accounted for when solving (1) for mode coupling and this equation reduces to [15]:

$$\frac{\partial P(\theta, z)}{\partial z} = \frac{D}{\theta} \frac{\partial P(\theta, z)}{\partial \theta} + D \frac{\partial^2 P(\theta, z)}{\partial \theta^2}. \quad (2)$$

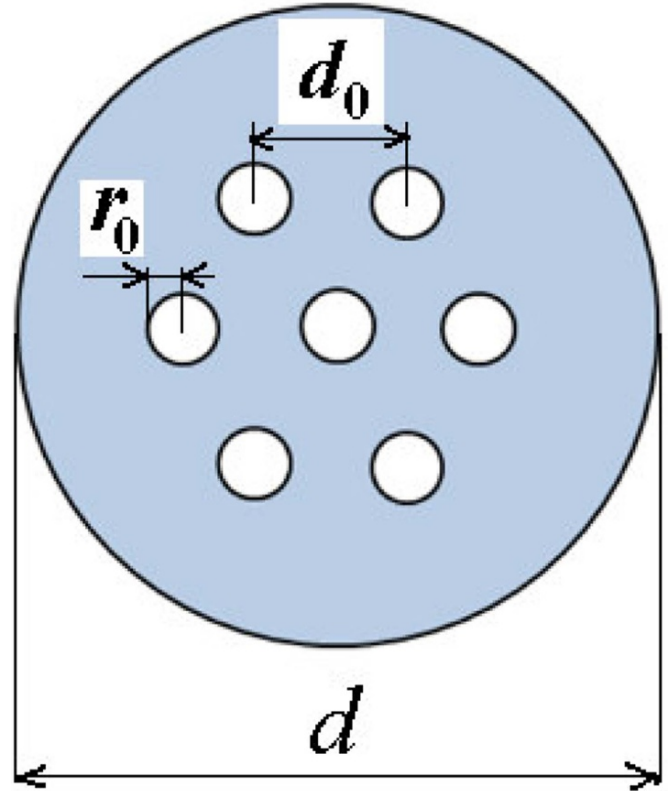


Figure 1. Multicore plastic optical fiber with seven cores arranged in a hexagonal array.

Numerical solution of the power flow equation (2) was obtained using the explicit finite-difference method [15], for Gaussian launch-beam distribution of the form:

$$P(\theta, z = 0) = \frac{1}{\sigma\sqrt{2\pi}} \exp \left[-\frac{(\theta - \theta_0)^2}{2\sigma^2} \right] \quad (3)$$

with $0 \leq \theta \leq \theta_c$, where θ_0 is the mean value of the incidence angle distribution, with the full width at half maximum FWHM = $2\sigma\sqrt{2\ln 2} = 2.355\sigma$ (σ is standard deviation).

3. Results and discussion

In this paper we investigate the transmission characteristics of the proposed MC POF with seven cores which is designed from the SC POF (PGU-CD1001-22E) experimentally investigated by Losada *et al* [16, 17]. The MC POF with seven cores arranged in a hexagonal array is shown in figure 1. The MC POF individual cores and cladding are assumed to be made of the same material as the SC POF core and cladding, respectively. The characteristics of SC POF were: core refractive index $n_0 = 1.492$, cladding refractive index $n_1 = 1.4057$, critical angle (measured inside the fiber) $\theta_c = 19.6^\circ$, core diameter $b = 0.98$ mm, and fiber diameter $d = 1$ mm. In order to avoid mode coupling between cores, the MC POF with fiber diameter $d = 1$ mm is designed from this SC POF in such a way that seven cores with radius $r_0 = 50$ μm , arranged in a hexagonal geometry, have inter-core distance $d_0 = 400$ μm

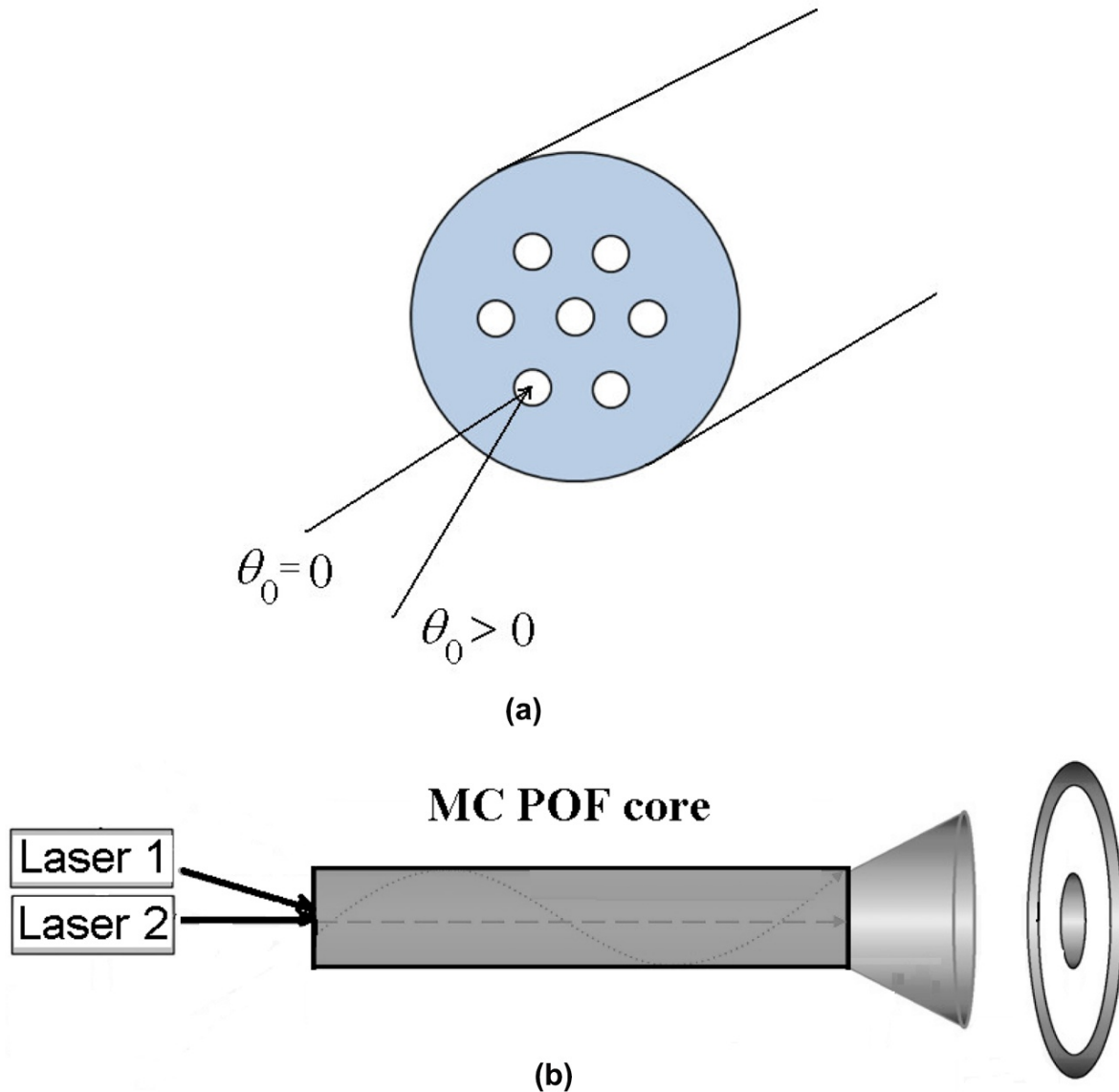


Figure 2. (a) Illustration of two angular channels launched with input angle $\theta_0 = 0^\circ$ along core axis and $\theta_0 > 0^\circ$ in respect to the core axis. These two angular channels are launched into each carrier seven cores for ADM in MC POF. (b) Minimalistic system design of two-channel ADM in MC POF.

(the cores are uncoupled for $d_0 \geq 7r_0$) [3]. The coupling coefficient $D = 3.3 \times 10^{-4} \text{ rad}^2 \text{ m}^{-1}$ for the PGU fiber is used in this work [10, 16, 17].

In this paper, we analyze the influence of mode coupling on two-channel ADM employed in each carrier seven cores of MC POF. In figure 3 our numerical solution of the power flow equation is presented by showing the evolution of the normalized output power distribution with fiber length for MC POF for two ADM channels launched at the input end of each carrier seven cores of MC POF. The two co-propagating optical channels are launched at different input angles $\theta_0 = 0$ and 18° thus maintaining a different angular orientation. For two angular optical channels we selected Gaussian launch beam distribution with $(\text{FWHM})_0 = 0.127^\circ$ by setting $\sigma_0 = 0.054^\circ$ in equation (3). Ring radiation pattern in very short fibers in figure 3 indicate that the mode coupling is so low thus leading to a minimal crosstalk observed between two co-propagating

optical channels. With increasing a fiber length, a crosstalk between two co-propagating optical channels continue to increase and significantly influence the quality of light signals which are transmitting through two angular channels along each carrier seven cores (figure 3(b)). Finally, at fiber's coupling length L_c the mode-distribution of co-propagating optical channels which is in the ring form, shift its mid-point to zero degrees, producing the equilibrium mode distribution (EMD) in figure 3(d): L_c is 35 m. As a result, at fiber lengths $z \geq L_c$ the Gaussian distributions which corresponded to different angular co-propagating optical channels are no more spatially separated since they form a disk-type circular far field outputs. One can see that mode coupling significantly limits the length of the MC POF with seven cores at which the ADM can be realized. The maximum length for practical realization of two-channel ADM in this seven-core MC POF is $z_{SDM} \approx 7$ m. It is worth noting that the lengths z_{SDM} up to

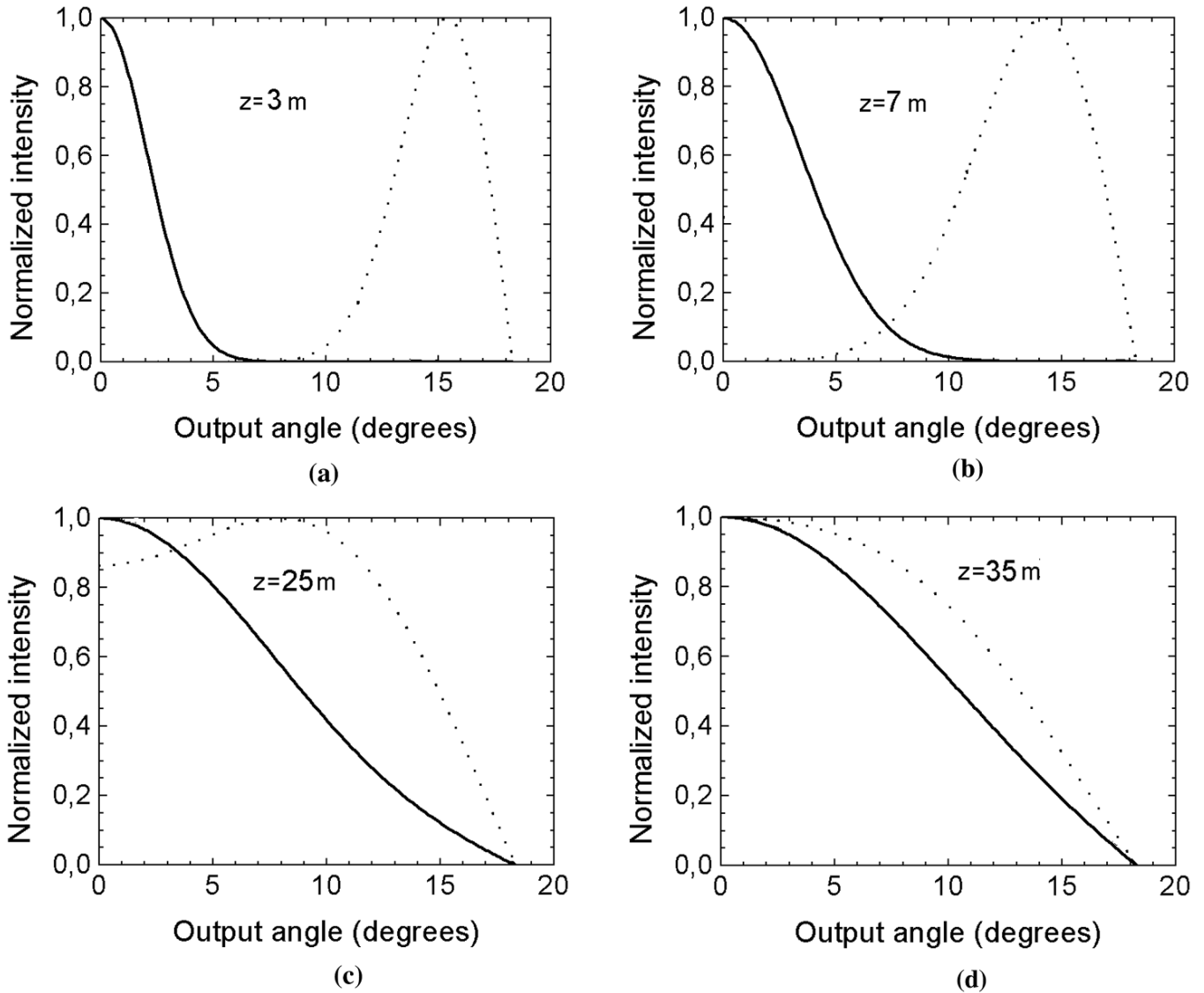


Figure 3. Normalized output angular power distribution at different locations along each carrier seven cores of MC POF calculated for two Gaussian input angles $\theta_0 = 0^\circ$ (solid line) and 18° (dashed line), with $(FWHM)_{z=0} = 0.127^\circ$ for: (a) $z = 3$ m; (b) $z = 7$ m; (c) $z = 25$ m and (d) $z = 35$ m.

which a minimal crosstalk is observed between two neighbor co-propagating optical channels is much shorter than the coupling length L_c at which the EMD is achieved (figure 3(d)). A two-channel ADM in the investigated multimode MC POFs can be realized with a minimal crosstalk up to the fiber length which is about 20% of the coupling length. We have recently shown that the larger number of co-propagating optical channels (three, four and five), the sooner crosstalk between the neighbor optical channels appeared [10]. One can conclude that in increasing capacity of optical fiber system, a SDM with two-channel ADM and multicore multiplexing can be realized with the proposed seven-core MC POF at short fiber lengths up to ≈ 7 m (2 ADM channels \times 7 cores). Such characterization of optical fibers should be considered in designing an optical fiber transmission system with multi-channel ADM in MC POFs.

One should note that by calculating the normalized output power distribution at different fiber lengths in the case of multi-channel ADM, it is difficult to exactly predict the level of the crosstalk which prohibits the system operation. In practice, for more accurate estimation of the ADM capacity of the particular MC POF, the transmission matrix should be used, with taking into account the noise terms which depend on the specific implementation of the receiver. But, our numerical results can be used as a good approximation in the estimation of the fiber length at which ADM could be realized in MC POFs. ADM channels from different cores could be separated from each other by setting the proper positions of the individual photo-detectors [18].

When single-core fiber is bent, a mode coupling becomes more intense, so mode coupling coefficient D increases. This leads to shortening the length L_c at which the equilibrium

mode distributions is achieved (faster shift from ring to disk pattern in a bent fiber than in a straight fiber) [19]. Similarly, a bent seven-core fiber should have a stronger mode coupling along the each of the seven cores and therefore a shorter length L_c at which the equilibrium mode distributions achieved. Thus, one can assume that ADM and multicore multiplexing in the bent seven-core POF could be realized at shorter fiber length than the length of straight seven-core POF. Since an inter-core cross talk is already prevented in straight seven-core POF by setting an appropriate inter-core distance, one can assume that it will remain preserved in a bent seven-core fiber.

4. Conclusion

A new design of MC POF with seven cores arranged in a hexagonal array, with negligible inter-core crosstalk, is proposed. The influence of mode coupling on ADM capability in each carrier seven cores is investigated by numerically solving the power flow equation. Our numerical results show that mode coupling significantly limits the fiber length at which the ADM can be realized with a minimal crosstalk between two optical channels. Two channels with ADM in the proposed seven-core plastic optical fiber can be employed with a minimal crosstalk up to the fiber length which is about 20% of the corresponding coupling length. Such characterization of multicore optical fibers should be considered in designing a multicore optical fiber transmission system for SDM.

Acknowledgments

The authors thank Dr V Cvjetkovic from the Faculty of Science, University of Kragujevac, for fruitful discussion. The work described in this paper was supported by the Strategic Research Grant of City University of Hong Kong (Project No. CityU 7004600) and by a grant from Serbian Ministry of Education, Science and Technological Development (Project No. 171011).

References

- [1] Richardson D, Fini J and Nelson L 2013 Space-division multiplexing in optical fibres *Nat. Photon.* **7** 354–62
- [2] Montero D S, Garcilópez I P, García C V, Lallana P C, Moraleda A T and Castillo P J P 2015 Recent advances in wavelength-division-multiplexing plastic optical fiber technologies *Advances in Optical Fiber Technology: Fundamental Optical Phenomena and Applications* (Rijeka: InTech)
- [3] Ortiz A M and Sáez R L 2017 Multi-core optical fibers: theory, applications and opportunities *Selected Topics on Optical Fiber Technologies and Applications* (Rijeka: InTech)
- [4] Saitoh K and Matsuo S 2013 Multicore fibers for large capacity transmission *Nanophotonics* **2** 441–54
- [5] Winzer P J 2012 Optical networking beyond WDM *IEEE Photonics J.* **4** 647–51
- [6] Li G, Bai N, Zhao N and Xia C 2014 Space-division multiplexing: the next frontier in optical communication *Adv. Opt. Photonics* **6** 413–87
- [7] Brunet C, Ung B, Belanger P-A, Messaddeq Y, LaRochelle S and Rusch L A 2014 Vector mode analysis of ring-core fibers: design tools for spatial division multiplexing *J. Lightwave Technol.* **32** 4046–57
- [8] Murshid S, Grossman B and Narakorn P 2008 Spatial domain multiplexing: a new dimension in fiber optic multiplexing *Opt. Laser Technol.* **40** 1030–6
- [9] Murshid S H, Chakravarty A and Biswas R 2011 Attenuation and modal dispersion models for spatially multiplexed co-propagating helical optical channels in step index fibers *Opt. Laser Technol.* **43** 430–6
- [10] Savović S, Djordjevich A, Simovic A and Drljača B 2018 Influence of mode coupling on three, four and five spatially multiplexed channels in multimode step-index plastic optical fibers *Opt. Laser Technol.* **106** 18–21
- [11] Gloge D 1972 Optical power flow in multimode fibers *Bell Syst. Tech. J.* **51** 1767–83
- [12] Gambling W A, Payne D N and Matsumura H 1975 Mode conversion coefficients in optical fibers *Appl. Opt.* **14** 1538–42
- [13] Savović S and Djordjevich A 2012 Influence of the angle-dependence of mode coupling on optical power distribution in step-index plastic optical fibers *Opt. Laser Technol.* **44** 180–4
- [14] Rousseau M and Jeunhomme L 1977 Numerical solution of the coupled-power equation in step index optical fibers *IEEE Trans. Microwave Theory Tech.* **25** 577–85
- [15] Djordjevich A and Savović S 2000 Investigation of mode coupling in step index plastic optical fibers using the power flow equation *IEEE Photonics Technol. Lett.* **12** 1489–91
- [16] Losada M A, Garcés I, Mateo J, Salinas I, Lou J and Zubía J 2002 Mode coupling contribution to radiation losses in curvatures for high and low numerical aperture plastic optical fibers *J. Lightwave Technol.* **20** 1160–4
- [17] Losada M A, Mateo J, Garcés I, Zubía J, Casao J A and Pérez-Vela P 2004 Analysis of strained plastic optical fibers *IEEE Photonics Technol. Lett.* **16** 1513–15
- [18] Puttnam B J, Luís R S, Rademacher G, Alfredsson A, Klaus W, Sakaguchi J, Awaji Y, Agrell E and Wada N 2019 Characteristics of homogeneous multi-core fibers for SDM transmission *APL Photonics* **4** 022804
- [19] Savović S and Djordjevich A 2008 Calculation of the coupling coefficient in strained step index plastic optical fibers *Appl. Opt.* **47** 4935–9

PAPER

Spatial division multiplexing in nine-core graded index plastic optical fibers

To cite this article: S Savovi *et al* 2020 *Laser Phys.* **30** 095103

View the [article online](#) for updates and enhancements.

Spatial division multiplexing in nine-core graded index plastic optical fibers

S Savović^{1,2}, A Djordjevich², A Simović¹ and B Drljača³

¹ Faculty of Science, University of Kragujevac, Kragujevac, Serbia

² Department of Mechanical Engineering, City University of Hong Kong, Kowloon, Hong Kong, People's Republic of China

³ Faculty of Science, University of Priština, L. Ribara 29, Kosovska Mitrovica, Serbia

E-mail: savovic@kg.ac.rs

Received 4 May 2020

Accepted for publication 29 June 2020

Published 28 July 2020



CrossMark

Abstract

We propose a spatial division multiplexing in a new designed multimode multicore graded index plastic optical fiber with nine cores arranged in an octagonal array. The influence of mode coupling on two-channel spatial division multiplexing capability in each of nine cores is investigated by solving the power flow equation. Our numerical results show that mode coupling significantly limits the fiber length at which the spatial division multiplexing can be realized in each of nine cores with a minimal crosstalk between two neighbor spatial optical channels. Two spatial channels in the proposed nine-core graded index plastic optical fiber can be employed with a minimal crosstalk up to the fiber length of 5 m, which is about 18% of the coupling length (fiber length where equilibrium mode distribution is achieved). Such characterization of multicore graded index plastic optical fibers should be considered in designing a multicore optical fiber transmission system for space division multiplexing.

Keywords: multicore plastic optical fibers, graded index optical fibers, space division multiplexing, mode coupling

(Some figures may appear in colour only in the online journal)

1. Introduction

The increasing demand for digital data bandwidth in access and backbone networks pushes the development of emerging technologies to increase network capacity, especially for optical fiber infrastructures. The increase capacity of optical fiber systems was caused by successive technology improvements: low losses single-mode fibers, fiber amplifiers, multiplexing, and high-efficiency spectral coding [1]. Multiplexing of optical data can be realized not only in wavelength [2], but also in polarization, in time, in phase and in space [1]. In spite of the fact that data traffic demand is easily covered by wavelength-division multiplexed (WDM) systems based on single-mode single-core fibers (SM-SCFs), recent works show that the WDM systems are rapidly approaching their Shannon capacity limit [3]. Aimed to overcome the Shannon

capacity limit of WDM networks using SM-SCFs, space division multiplexing (SDM) including mode division multiplexing using multimode fibers or few-mode fibers and/or core multiplexing using multicore fibers [4], has attracted much attention in the last decade for the next multiplicative capacity growth for optical communication [1, 5–8]. SDM may operate at the same wavelength or different wavelengths [9]. In the case of SDM at the same wavelength, radially distributed, dedicated spatial locations are assigned to every SDM channel inside the carrier single-core fiber as these channels traverse the length of the carrier [10]. The location of the each channel inside the single-core step index optical fiber is a function of the launch angle and the strength of mode coupling.

Multimode plastic optical fibers (POFs) have been the preferred transmission medium in high-capacity communications networks and short-distance (few tens of meters)

communications systems. These fibers have large numerical aperture which simplifies coupling of light. Compared to their glass counterparts, POFs offer a low-cost installation alternative with low-precision plastic components without precision couplers. POFs also tend to cost less to produce and are easier to handle. Their flexibility is especially useful when installing them in tight spaces such as in homes, offices or vehicles. Step-index (SI) POFs have large modal dispersion and low bandwidth-length product. Graded index (GI) POFs exhibit far less modal dispersion than SI POFs. This is due to their gradual, usually parabolic, decreasing of the refractive index of core with radial distance from the fiber axis.

Transmission characteristics of multimode POFs depend upon the differential mode attenuation and rate of mode coupling [9, 11]. The latter represents power transfer between neighbor modes caused by fiber impurities and inhomogeneities introduced during the fiber manufacturing process [11]. We have recently shown that space division multiplexing (SDM) with three, four and five channels in the multimode single-core SI POFs can be successfully employed with a minimal crosstalk only at very short fiber length, up to ≈ 2.4 , 1.6 and 1.4 m, respectively [10]. We propose in this work a SDM based on multicore multiplexing using a novel multicore graded index plastic optical fiber (MC GI POF) with nine cores arranged in an octagonal array, which exhibits negligible inter-core crosstalk (figure 1). In addition, we explore a capability of the proposed nine-core MC GI POF for two-channel SDM (figure 2(a)). The nine cores have the same graded index distribution, while cladding has a constant index distribution. By using the power flow equation, we examine the state of mode coupling in each of the nine carrier cores of the proposed multimode MC GI POF. Radially distributed, dedicated spatial locations are assigned to two SDM channels inside the each carrier nine cores as these channels traverse the length of the carrier. The location of the each channel inside the each core of MC GI POF is a function of the launch angle and the strength of mode coupling. In practice, the channel launched with input angle $\theta_0 = 0^\circ$ along axis of each carrier nine cores appears as a far field in the form of disk, while another channel launched with $\theta_0 > 0^\circ$ appear in the far field as concentric ring (figure 2(b)). The center disk and ring represent a two separated SDM optical channels, thereby enhancing the bandwidth of optical fiber system. This enables one to obtain the limits of the fiber lengths up to which a two-channel SDM can be realized with minimal crosstalk between the co-propagating optical channels in each carrier nine cores of MC GI POF.

2. Time-independent power flow equation for GI optical fiber

The index profile of GI optical fibers may be expressed as:

$$n(r, \lambda) = \begin{cases} n_1(\lambda) \left[1 - 2\Delta(\lambda) \left(\frac{r}{a} \right)^g \right]^{1/2} & (0 \leq r \leq a) \\ n_1(\lambda) (1 - 2\Delta(\lambda))^{1/2} = n_2(\lambda) & (r > a) \end{cases} \quad (1)$$

where g is the core index exponent, a is the core radius, $n_1(\lambda)$ is the maximum index of the core (measured at the

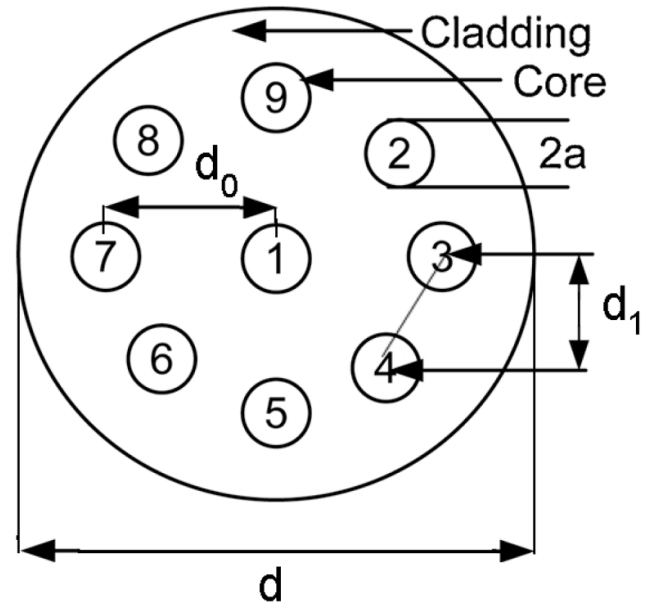


Figure 1. Multicore plastic optical fiber with nine cores arranged in an octagonal array.

fiber axis), $n_2(\lambda)$ is the index of the cladding and $\Delta = [n_1(\lambda) - n_2(\lambda)] / n_1(\lambda)$ is the relative index difference. The optimum value of the core index exponent g to obtain maximum bandwidth depends on the wavelength λ (in free-space) of the source [12].

Time-independent power flow equation for GI optical fiber is [13–15]:

$$\frac{\partial P(m, \lambda, z)}{\partial z} = \frac{D}{m} \frac{\partial P(m, \lambda, z)}{\partial m} + D \frac{\partial P^2(m, \lambda, z)}{\partial m^2} \quad (2)$$

where $P(m, \lambda, z)$ is power in the m -th principal mode (modal group), z is the coordinate along the fiber axis from the input fiber end, D is a constant mode coupling coefficient [15]. The maximum principal mode number $M(\lambda)$ can be obtained as [13, 14]:

$$M(\lambda) = \sqrt{\frac{g\Delta(\lambda)}{g+2}} akn_1(\lambda) \quad (3)$$

where $k = 2\pi/\lambda$.

Using the explicit finite difference method (EFDM), discretization of equation (2) leads to [16]:

$$P_{i,j+1} = \left(\frac{D\Delta z}{(\Delta m)^2} - \frac{D\Delta z}{2m_i\Delta m} \right) P_{i-1,j} + \left(1 - \frac{2D\Delta z}{(\Delta m)^2} \right) P_{i,j} + \left(\frac{D\Delta z}{2m_i\Delta m} + \frac{D\Delta z}{(\Delta m)^2} \right) P_{i+1,j} \quad (4)$$

where i and j refer to the discretization step lengths Δm and Δz for the mode m and length z , respectively. This is a simple formula for $P_{i,j+1}$ at the $(i, j + 1)$ th mesh point in terms of the known values along the j th distance row. As first in the

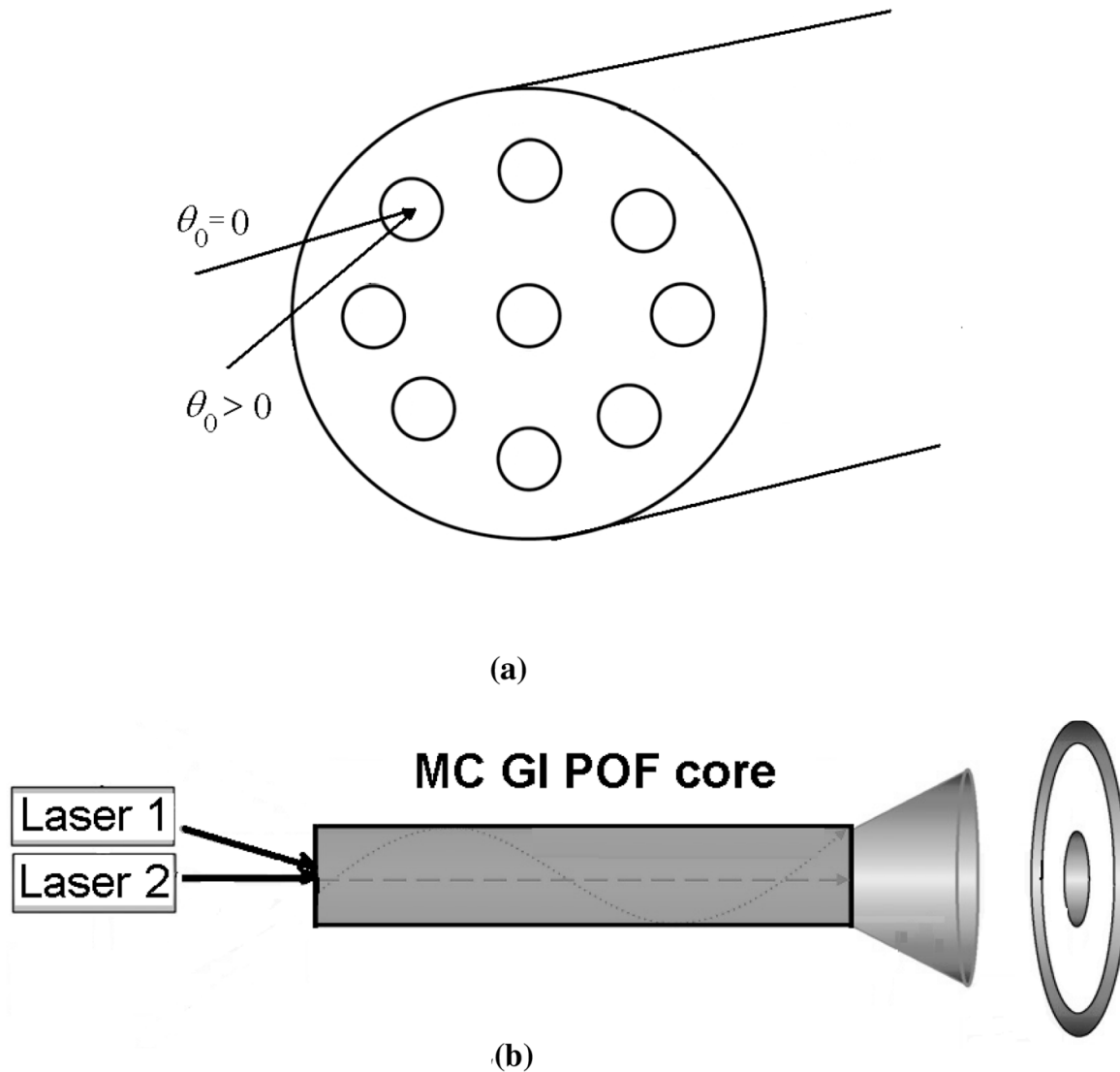


Figure 2. (a) Illustration of two optical channels launched with input angle $\theta_0 = 0^\circ$ along core axis and $\theta_0 > 0^\circ$ in respect to the core axis, and with radial offset $\Delta r = 0 \mu\text{m}$. These two optical channels are launched into each carrier nine cores for SDM in MC GI POF. (b) Minimalistic system design of two-channel SDM in MC GI POF.

authors' best knowledge, numerical solution (4) of the time-independent power flow equation (2) is reported in this work for investigation of the state of mode coupling along each core of multimode MC GI POF in terms of mode variable (m).

3. Results and discussion

In this paper we investigate the transmission characteristics of the proposed MC GI POF with nine cores which is designed from the single-core GI POF (OM Giga, Fiber FinTM), we have recently experimentally investigated [17]. The MC GI POF with nine cores arranged in an octagonal array is shown in figure 1. The MC GI POF individual cores and cladding are assumed to be made of the same material as the single-core POF core and cladding, respectively. The characteristics of single-core GI POF were: the core diameter of the fiber was 0.9 mm (fiber diameter was 1 mm), the refractive index of the core measured at the fiber axis was $n_1 = 1.522$

and the refractive index of the cladding was $n_2 = 1.492$. In order to avoid mode coupling between cores (inter-core crosstalk), the MC GI POF with fiber diameter $d = 1 \text{ mm}$ is designed from this single-core GI POF in such a way that nine cores with radius $a = 20 \mu\text{m}$, arranged in an octagonal geometry, have inter-core distances $d_0 = 400 \mu\text{m}$ and $d_1 = 306 \mu\text{m}$ (the cores are uncoupled for $d_0 \geq 7r_0$ and $d_1 \geq 7r_0$) [3]. We have obtained the coupling coefficient of $D = 1482 \text{ 1/m}$ [17].

With increasing radial offset Δr or launch angle θ , higher-order mode groups can be excited. The relation between the radial offset Δr , angle θ and the principal mode m is [18]:

$$\frac{m}{M} = \left[\left(\frac{\Delta r}{a} \right)^g + \frac{\theta^2}{2\Delta} \right]^{(g+2)/2g} \quad (5)$$

For the MC GI POF under investigation, the maximum principal mode number in each of nine cores is $M = 29$ at $\lambda = 633 \text{ nm}$, $g = 1.80101$ and $\Delta = (n_1 - n_2)/n_1 = 0.019711$.

Figure 3 shows the evolution of the normalized output modal power distribution $P(m, \lambda, z)$ with fiber length for two SDM channels launched at the input end of each carrier nine cores of MC GI POF. The two co-propagating optical channels are launched at different input angles $\theta_0 = 0^\circ$ and 15° thus maintaining a different angular orientation. In the numerical calculations, for two optical channels we selected Gaussian launch beam distribution $P(\theta, z)$ with $(\text{FWHM})_0 = 0.127^\circ$ by setting $\sigma_0 = 0.054^\circ$. A Gaussian beam is assumed to be launched with radial offset $< \Delta r \geq 0 \mu\text{m}$ and standard deviation $\sigma_{\Delta r} = 1.5 \mu\text{m}$ in equation (5). Results are shown for two different input angles $\theta_0 = 0^\circ$ and 15° . The angular power distributions in short fibers indicate that the coupling is stronger for low-order modes (their angular power distributions have already shifted towards $\theta_0 = 0^\circ$). As a result of redistribution of the optical power from lower to higher order modes during propagation, the coupling of higher-order modes can be observed only after longer fiber lengths. Power distributions of all modes have shifted their mid-points to zero at the coupling length of $L_c = 28 \text{ m}$ (from their initial values at the input fiber end), resulting in the equilibrium mode distribution (EMD), figure 3(d).

Ring radiation pattern in very short fibers in figure 3(a) indicate that the mode coupling is so low thus leading to a minimal crosstalk observed between two co-propagating optical channels. With increasing a fiber length, a crosstalk between two co-propagating optical channels continue to increase and significantly influence the quality of light signals which are transmitting through two channels along each carrier nine cores (figure 3(b)). Finally, at fiber's coupling length L_c the mode-distribution of co-propagating optical channels which is in the ring form, shift its mid-point to zero degrees, producing the EMD in figure 3(c): L_c is 28 m. As a result, at fiber lengths $z \geq L_c$ the modal distributions which corresponded to different co-propagating optical channels are no more spatially separated since they form a disk-type circular far field outputs. One can see that mode coupling significantly limits the length of the MC GI POF with nine cores at which the SDM can be realized. The maximum length for practical realization of two-channel SDM in this nine-core MC GI POF is $z_{SDM} \approx 5 \text{ m}$. It is worth noting that the lengths z_{SDM} up to which a minimal crosstalk is observed between two neighbor co-propagating optical channels is much shorter than the coupling length L_c at which the EMD is achieved (figure 3(d)). A two-channel SDM in the investigated multimode MC GI POF can be realized with a minimal crosstalk up to the fiber length which is about 18% of the coupling length. We have recently shown that the larger number of co-propagating optical channels (three, four and five) in SI POFs, the sooner crosstalk between the neighbor optical channels appeared [10]. One can conclude that in increasing capacity of optical fiber system, a SDM with two-channels and multicore multiplexing can be realized with the proposed nine-core MC GI POF at short fiber lengths up to $\approx 5 \text{ m}$ (2 channels \times 9 cores). Such characterization of optical fibers should be considered in designing an optical fiber transmission system with multi-channel SDM in MC GI POFs. One should mention here that a few-mode fibers with a quite limited number of modes

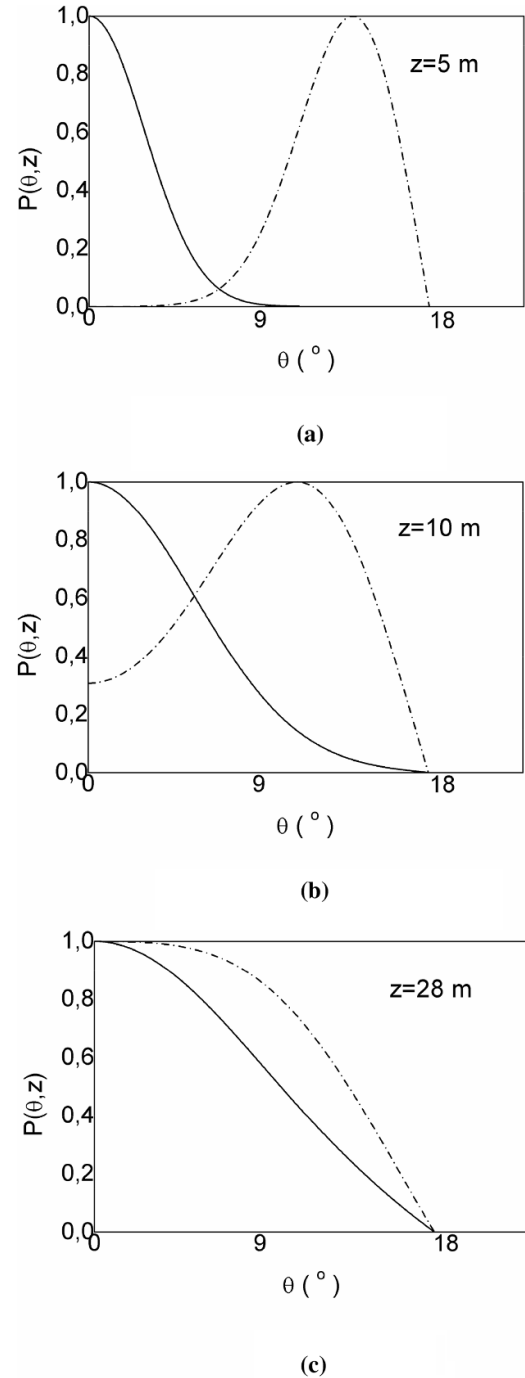


Figure 3. Normalized output power distribution at different locations along each carrier nine cores of MC GI POF calculated for two Gaussian input angles $\theta_0 = 0^\circ$ (solid line) and 15° (dashed-dotted line), with $(\text{FWHM})_{z=0} = 0.127^\circ$ for: (a) $z = 5 \text{ m}$; (b) $z = 10 \text{ m}$ and (c) $z = 28 \text{ m}$.

are also used for SDM in single-core and multicore fibers [19, 20].

One should note that by calculating the normalized output power distribution at different fiber lengths in the case of multi-channel SDM, it is difficult to exactly predict the level of the crosstalk which prohibits the system operation. In practice, for more accurate estimation of the SDM capacity of

the particular MC GI POF, the transmission matrix should be used, with taking into account the noise terms which depend on the specific implementation of the receiver. But, our numerical results can be used as a good approximation in the estimation of the fiber length at which SDM could be realized in MC GI POFs. SDM channels from different cores could be separated from each other by setting the proper positions of the individual photo-detectors [21].

Finally, it is well known that the analytical solution of the Helmholtz equation for graded (parabolic) fiber is given by the superposition of the Laguerre-Gaussian modes [22]. However, this analytical solution does not take into account all intrinsic perturbation effects such as microscopic bends, irregularity of the core-cladding boundary, and refractive-index distribution fluctuations of the fiber, which are the source of mode coupling in the fiber. In the power flow equation approach employed in this work, a mode coupling coefficient D takes into account all intrinsic perturbation effects in the fiber. This is the main advantage of the power flow equation approach if compared to the Helmholtz equation approach.

4. Conclusion

A new design of multimode MC GI POF with nine cores arranged in an octagonal array, with negligible inter-core crosstalk, is proposed. The influence of mode coupling on SDM capability in each carrier nine cores is investigated by numerically solving the power flow equation. Our numerical results show that mode coupling significantly limits the fiber length at which the SDM can be realized with a minimal crosstalk between two optical channels. Two optical channels with SDM in the proposed nine-core graded index plastic optical fiber can be employed with a minimal crosstalk up to the fiber length which is about 18% of the corresponding coupling length. Such characterization of multicore optical fibers should be considered in designing a multicore optical fiber transmission system for SDM.

Acknowledgments

The work described in this paper was supported by the Strategic Research Grant of City University of Hong Kong (Project No. CityU 7004600) and by a grant from Serbian Ministry of Education, Science and Technological Development (Agreement No. 451-03-68/2020-14/200122).

References

- [1] Richardson D, Fini J and Nelson L 2013 Space-division multiplexing in optical fibres *Nat. Photon.* **7** 354–62
- [2] Montero D S, Garcilópez I P, García C V, Lallana P C, Moraleda A T and Castillo P J P 2015 Recent advances in wavelength-division-multiplexing plastic optical fiber technologies *Advances in Optical Fiber Technology: Fundamental Optical Phenomena and Applications* (Rijeka: InTech)
- [3] Ortiz A M and Sáez R L 2017 Multi-core optical fibers: theory, applications and opportunities *Selected Topics on Optical Fiber Technologies and Applications* (London: InTechOpen)
- [4] Saitoh K and Matsuo S 2013 Multicore fibers for large capacity transmission *Nanophotonics* **2** 441–54
- [5] Winzer P J 2012 Optical networking beyond WDM *IEEE Photon. J.* **4** 647–51
- [6] Li G, Bai N, Zhao N and Xia C 2014 Space-division multiplexing: the next frontier in optical communication *Adv. Opt. Photon.* **6** 413–87
- [7] Brunet C, Ung B, Belanger P-A, Messaddeq Y, LaRochelle S and Rusch L A 2014 Vector mode analysis of ring-core fibers: design tools for spatial division multiplexing *J. Lightwave Technol.* **32** 4046–57
- [8] Murshid S, Grossman B and Narakorn P 2008 Spatial domain multiplexing: A new dimension in fiber optic multiplexing *Opt. Laser Technol.* **40** 1030–6
- [9] Murshid S H, Chakravarty A and Biswas R 2011 Attenuation and modal dispersion models for spatially multiplexed co-propagating helical optical channels in step index fibers *Opt. Laser Technol.* **43** 430–6
- [10] Savović S, Djordjevich A, Simović A and Drljača B 2018 Influence of mode coupling on three, four and five spatially multiplexed channels in multimode step-index plastic optical fibers *Opt. Laser Technol.* **106** 18–21
- [11] Gloge D 1972 Optical power flow in multimode fibers *Bell Syst. Tech. J.* **51** 1767–83
- [12] Ohdoko K, Ishigure T and Koike Y 2005 Propagating mode analysis and design of waveguide parameters of GI POF for very short-reach network use *IEEE Phot. Technol. Lett.* **17** 79–81
- [13] Kitayama K, Seikai S and Uchida N 1980 Impulse response prediction based on experimental mode coupling coefficient in a 10-km long graded-index fiber *IEEE J. Quant. Electron.* **16** 356–62
- [14] Olshansky R 1975 Mode coupling effects in graded-index optical fibers *Appl. Opt.* **14** 935–45
- [15] Savović S and Djordjevich A 2019 New method for calculating the coupling coefficient in graded index optical fibers *Opt. Laser Technol.* **101** 223–6
- [16] Djordjevich A and Savović S 2000 Investigation of mode coupling in step index plastic optical fibers using the power flow equation *IEEE Photon. Technol. Lett.* **12** 1489–91
- [17] Savović S, Simović A, Drljača B, Djordjevich A, Stepniak G, Bunge C A and Bajić J 2019 Power flow in graded index plastic optical fibers *J. Lightwave Technol.* **37** 4985–90
- [18] Nagano K and Kawakami S 1980 Measurements of mode conversion coefficients in graded-index fibers *Appl. Opt.* **19** 2426–34
- [19] Rademacher G et al 2018 Long-haul transmission over few-mode fibers with space-division multiplexing *J. Lightwave Technol.* **36** 1382–8
- [20] van Uden R G H, Correa R A, Lopez E A, Huijskens F M, Xia C, Li G, Schülzgen A, de Waardt H, Koonen A M J and Okonkwo C M 2014 Ultra-high-density spatial division multiplexing with a few-mode multicore fibre *Nat. Photon.* **8** 865–70
- [21] Puttnam B J, Luís R S, Rademacher G, Alfredsson A, Klaus W, Sakaguchi J, Awaji Y, Agrell E and Wada N 2019 Characteristics of homogeneous multi-core fibers for SDM transmission *APL Photon.* **4** 022804
- [22] Love J and Snyder A 2000 *Optical Waveguide Theory* (Dordrecht: Kluwer)

PAPER

Influence of wavelength on the bandwidth of W-type plastic-clad silica optical fibers

To cite this article: B Drljaa *et al* 2020 *Laser Phys.* **30** 025103

View the [article online](#) for updates and enhancements.

Influence of wavelength on the bandwidth of W-type plastic-clad silica optical fibers

B Drljača¹, A Simović², S Savović^{2,3,4,5} and A Djordjevich³

¹ Faculty of Sciences, University of Priština, Lole Ribara 29, Kosovska Mitrovica, Serbia

² Faculty of Science, University of Kragujevac, R. Domanovića 12, 34000 Kragujevac, Serbia

³ City University of Hong Kong, 83 Tat Chee Avenue, Hong Kong, People's Republic of China

E-mail: savovic@kg.ac.rs

Received 8 August 2019

Accepted for publication 27 November 2019

Published 7 January 2020



Abstract

The bandwidth and steady-state loss of multimode W-type plastic-clad silica optical fibers are investigated by solving the time-dependent power flow equation. The results show how the bandwidth of W-type plastic-clad silica optical fibers can be enhanced by shifting from the red to the infrared wavelength region for different intermediate layer widths and refractive indices of the outer cladding. Such characterization of these fibers is consistent with their manifest effectiveness in reducing modal dispersion and increasing bandwidth.

Keywords: W-type plastic clad silica optical fiber, power flow equation, bandwidth, steady-state loss, infrared wavelength region

1. Introduction

Glass optical fibers are often used for high-speed long-distance communication due to their low attenuation and high bandwidth [1]. Large-core (~1 mm diameter) plastic optical fibers are most frequently employed for short-distance (<100 m) communication links [2]. Plastic-clad silica fibers (PCSFs) have many applications in optical measurements, short-to-long distance communication and sensors [3–5]. The ease with which cladding can be removed makes PCSFs particularly useful for sensors when access to evanescent waves is desired.

The analysis and design of the refractive index profile of multimode fibers with the view of advancing fiber transmission characteristics have attracted much attention in the last few decades [1, 6, 7]. A variety of designs for step-index, graded-index and W-type fibers have been proposed either

for long-distance communication links or high-capacity local area networks [1, 6–11]. It has been shown that waveguide dispersion is smaller in W-type fibers than in single-clad (SC) fibers [9]. W-type fibers have a wide transmission bandwidth and lower bending losses than the corresponding SC fibers.

Differential mode attenuation and mode coupling strongly affect the transmission characteristics of multimode optical fibers. Differential mode attenuation is a consequence of absorption and scattering of light within the fiber material, which reduces the transmitted power. Mode coupling transfers power between individual modes and is caused by the fiber's intrinsic random anomalies. Mode coupling reduces modal dispersion, thus increasing fiber bandwidth. On the other hand, mode coupling increases fiber loss, especially in a curved fiber, and degrades beam quality. The properties of W-type fibers differ from those of SC fibers [9, 12, 13] because of the lossy leaky modes that propagate within the intermediate layer of W-type fibers. Higher-order modes which propagate along W-type fibers reduce their bandwidth and require that the group delay difference between modes be minimized by

⁴ Author to whom any correspondence should be addressed.

⁵ Faculty of Science, R. Domanovića 12, 34000 Kragujevac, Serbia.

optimizing the refractive index profile of such fibers [13]. As modal attenuation, coupling and dispersion affect the transmission characteristics of W-type optical fibers, methods for calculating their contributions are needed.

In this work, we investigate how the bandwidth can be enhanced in the infrared wavelength region for variously configured W-type PCSFs in terms of the width of the intermediate layers of the fiber and the refractive index of the outer cladding. One should mention that modal attenuation, coupling and dispersion are included in our calculations.

2. Power flow equation

The time-dependent power flow for multimode W-type fibers is described by the following coupled-power equation [14]:

$$\frac{\partial p(\theta, z, t)}{\partial z} + \tau(\theta) \frac{\partial p(\theta, z, t)}{\partial t} = -\alpha(\theta) P(\theta, z, t) + \frac{1}{\theta} \frac{\partial}{\partial \theta} \left[D(\theta) \frac{\partial p(\theta, z, t)}{\partial \theta} \right] \quad (1)$$

where t is time, θ is the propagation polar angle with respect to the core axis [14], $p(\theta, z, t)$ is power distribution over angle, space and time, $\tau(\theta)$ is mode delay per unit length, $D(\theta)$ is the mode-dependent coupling coefficient and $\alpha(\theta) = \alpha_0 + \alpha_d(\theta)$ is the modal attenuation, where α_0 represents conventional losses due to absorption and scattering. The term α_0 leads only to a multiplier $\exp(-\alpha_0 z)$ in the solution and is thus neglected. The term α_d in the expansion of $\alpha(\theta)$ is dominant for higher-order modes. The coupling coefficient is usually assumed constant [12, 15–17]. The method of solving equation (1) and calculation of the bandwidth of W-type optical fibers is described in more detail in our previous work [18]. For the W-type fiber shown in figure 1, the modes whose propagation angles are between $\theta_p \cong (2\Delta_p)^{1/2}$ and $\theta_q \cong (2\Delta_q)^{1/2}$, where $\Delta_q = (n_0 - n_q)/n_0$ and $\Delta_p = (n_0 - n_p)/n_0$, are leaky modes. The attenuation constants of leaky modes are given as [12, 15]

$$\alpha_L(\theta) = \frac{4(\theta^2 - \theta_p^2)^{1/2} \theta^2 (\theta_q^2 - \theta^2)}{a(1 - \theta^2)^{1/2} \theta_q^2 (\theta_q^2 - \theta_p^2)} \exp \left[-2\delta a n_0 k_0 (\theta_q^2 - \theta^2)^{1/2} \right] \quad (2)$$

where k_0 is the free-space wave number, a is the core radius and δa is the width of the intermediate layer (inner cladding). The modal attenuation in a W-type fiber can be expressed as [12, 15]

$$\alpha_d(\theta) = \begin{cases} 0; & \theta \leq \theta_p \\ \alpha_L(\theta); & \theta_p < \theta < \theta_q \\ \infty; & \theta \geq \theta_q. \end{cases} \quad (3)$$

One can see that the attenuation constants of leaky modes (2) are wavelength dependent through the free-space wave number k_0 .

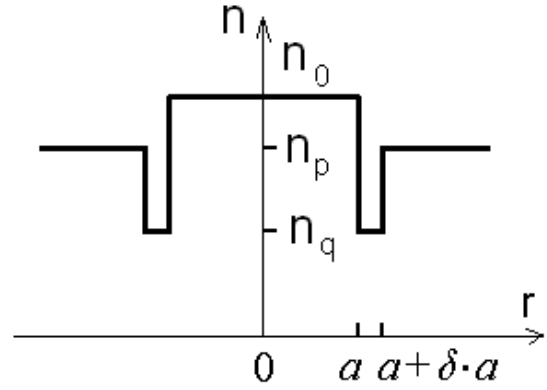


Figure 1. Refractive index profile of a W-type fiber.

A W-type fiber can be regarded as a system consisting of an SC_q fiber and cladding. In an SC_q fiber, only modes with propagation angles smaller than the critical angle θ_q can be guided. When an SC_q fiber is surrounded by a medium of index n_p , the lower-order modes, whose propagation angles are smaller than the critical angle of the SC_p fiber θ_p , remain guided. The higher-order modes with angles between θ_p and θ_q are transformed into leaky modes. It is shown that because of the strong dependence of $\alpha_L(\theta)$ on the intermediate layer width δa , steady-state characteristics of a W-type fiber depend on δa and coincide with those of SC_p and SC_q fibers in the limits of $\delta \rightarrow 0$ and $\delta \rightarrow \infty$, respectively [12].

In this work, to our best knowledge for the first time, we investigate how the bandwidth in W-type PCSFs can be enhanced by shifting from the red to the infrared wavelength region for different intermediate layer widths and refractive indices of the outer cladding. The results obtained could be applied when designing W-type PCSFs.

3. Numerical results

In this paper, we analyze bandwidth as well as steady-state loss at different wavelengths in a variously configured W-type PCSF. The structural characteristics of the fiber were as follows: core refractive index $n_0 = 1.4535$, cladding refractive index $n_q = 1.405385$, critical angle (measured inside the fiber) $\theta_m = 14.75^\circ$, core diameter $d = 0.2$ mm, fiber diameter $b = 0.23$ mm [19]. The W-type PCSF is designed from this singly clad PCSF in such a way that the inner cladding of the W-type PCSF retains the refractive index n_q of the SC PCSF's cladding, while the outer cladding of the W-type PCSF has a refractive index n_p , which is higher than the refractive index n_q of the inner cladding (figure 1). Three values were used in the modeling for the refractive index of the outer cladding, $n_p = 1.4455385$, 1.4393461 and 1.4313855 , corresponding to critical angles θ_p of 6° , 8° and 10° , respectively. The normalized intermediate layer widths $\delta = 0.01$, $\delta = 0.02$,

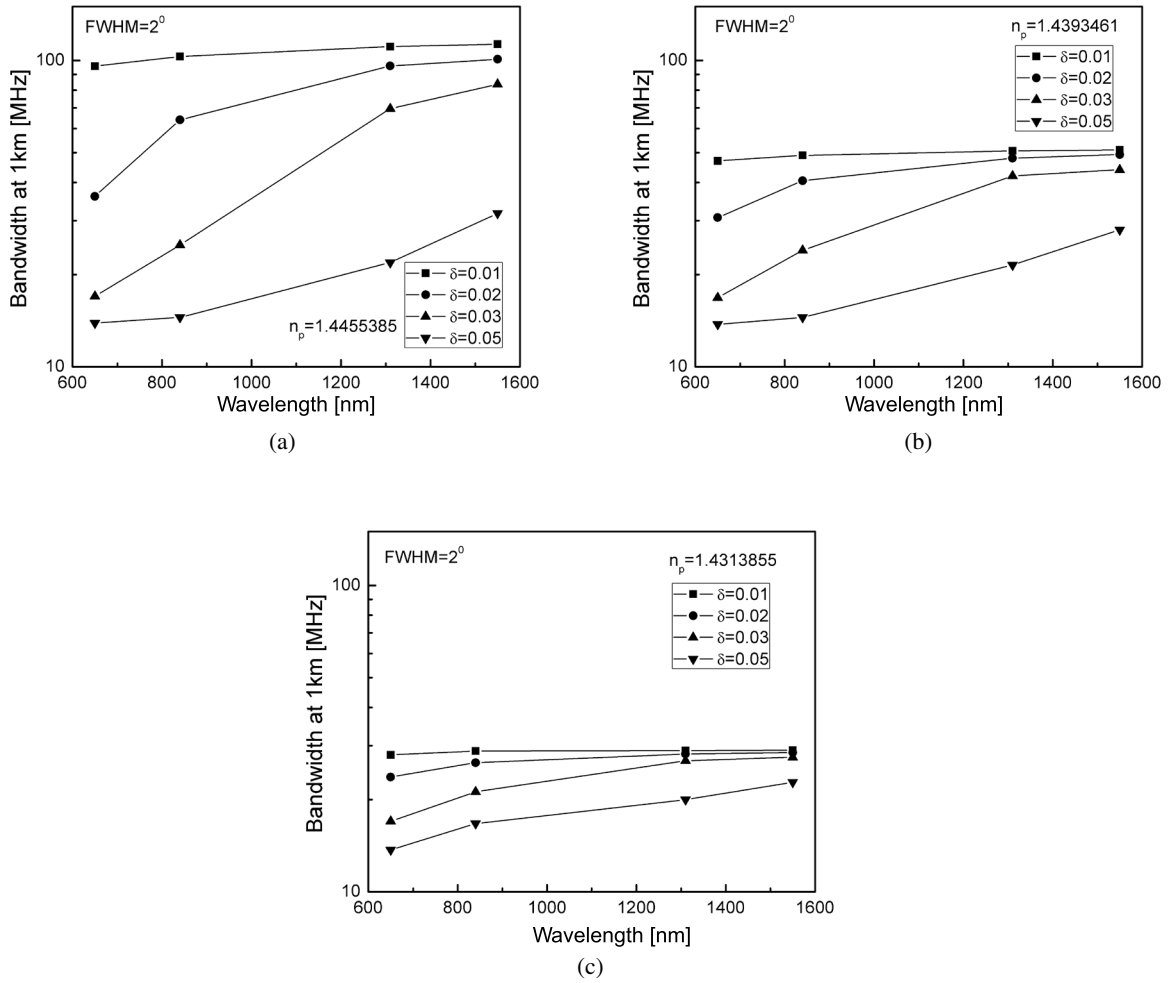


Figure 2. Numerical results for bandwidth at 1 km as a function of wavelength for Gaussian launch excitation with $\text{FWHM} = 2^\circ$, $\delta = 0.01$, 0.02 , 0.03 and 0.05 and (a) $\theta_p = 6^\circ$, (b) $\theta_p = 8^\circ$ and (c) $\theta_p = 10^\circ$.

$\delta = 0.03$ and $\delta = 0.05$ were employed (actual width is δa mm). The coupling coefficient $D = 6.4 \times 10^{-6} \text{ rad}^2 \text{ m}^{-1}$ was used in the calculations [5]. In the calculations, the launch beam distribution was in the Gaussian form with a FWHM of 2° . One should mention here that the change of depth of the intermediate layer has a negligible influence on the bandwidth of a W-type PCSF and is therefore not analyzed in this work.

We solved the time-dependent power flow equation (2) using the explicit finite difference method for the coupling coefficient $D = 6.4 \times 10^{-6} \text{ rad}^2 \text{ m}^{-1}$ for four different normalized intermediate layer widths δ (0.01, 0.02, 0.03 and 0.05). Our numerical solution of the time-dependent power flow equation is illustrated in figure 2. It shows, in three inserts corresponding to three refractive indices of the outer cladding $n_p = 1.4455385$, 1.4393461 and 1.4313855 , and for the Gaussian launch excitation with $\text{FWHM} = 2^\circ$, the evolution of the bandwidth of the W-type PCSF with wavelength at 1 km for different intermediate layer widths δ . One

can observe in figure 2 that for the smallest intermediate layer width ($\delta = 0.01$) the influence of wavelength on bandwidth is negligible. This is due to large leaky mode losses; as these modes are practically not guided along the fiber, modal dispersion (bandwidth) changes little. With increasing intermediate layer width there is a wavelength-dependent decrease of bandwidth. This decrease is more pronounced at short wavelengths as leaky mode losses are then reduced, resulting in an increase in modal dispersion and decrease of fiber bandwidth. For the wider layers ($\delta = 0.02$, 0.03 and 0.05), the rise in bandwidth with wavelength is more pronounced. It can be seen from figure 2 that for $\delta = 0.01$, 0.02 and 0.03 , there is a maximum value of the bandwidth–distance product which is reached at wavelengths of $1.31 \mu\text{m}$ or $1.55 \mu\text{m}$. For $\delta = 0.5$, the bandwidth–distance product increases monotonically with increasing wavelength.

With increasing refractive index of the outer cladding n_p (decreasing critical angle θ_p), there is an increase in leaky

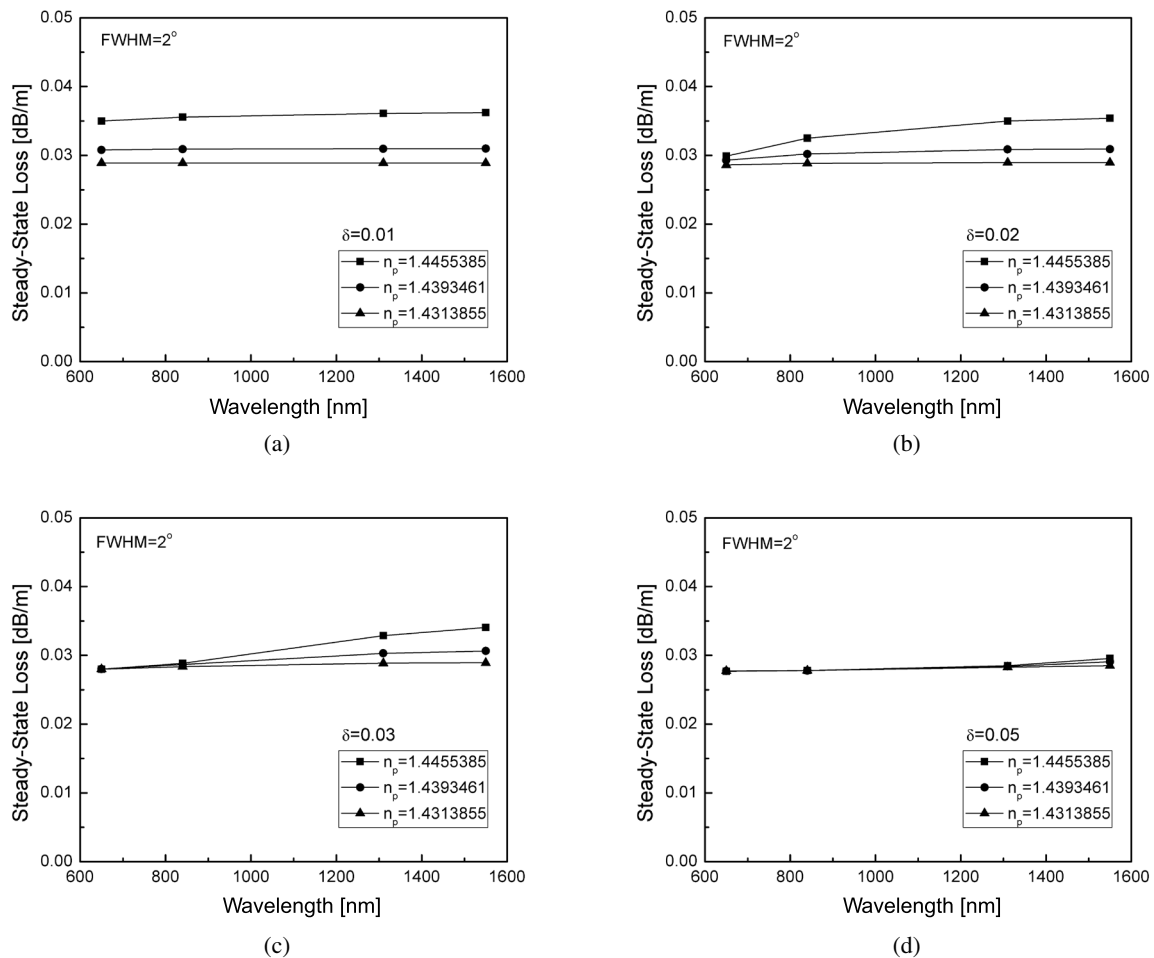


Figure 3. Steady-state loss at 1 km as a function of wavelength for Gaussian launch excitation with $\text{FWHM} = 2^\circ$, for three values of ($n_p = 1.445\ 5385$, $1.439\ 3461$, $1.431\ 3855$) in the case of (a) $\delta = 0.01$, (b) $\delta = 0.02$, (c) $\delta = 0.03$ and (d) $\delta = 0.05$.

mode losses, which results in the highest values of the bandwidth for the case of $\delta = 0.01$. It can be seen from figure 2 that the improvement of the bandwidth of the W-type PCSF is more pronounced at longer fiber lengths. Since a narrow launch beam distribution is assumed in the calculations, only guided modes are excited at the input fiber length. Therefore the role of leaky modes is of less significance for short fiber lengths. Due to mode coupling, more leaky modes are filtered out at longer fiber lengths, leading to a significant improvement in the bandwidth of the W-type PCSF.

Figure 3 shows steady-state loss as a function of wavelength for different intermediate layer widths δ and refractive indices n_p of the outer cladding. One can observe that the influence of wavelength on steady-state loss is negligible in the case of the narrowest intermediate layer with $\delta = 0.01$. At longer wavelengths, and for $\delta = 0.02$, 0.03 and 0.05 , leaky mode losses

already become significant over short fiber lengths and these modes are mostly not guided further.

Figure 4 shows the trade-off relation between bandwidth and steady-state loss for a W-type PCSF. With increasing leaky mode losses the steady-state losses also increase. A trade-off relation between bandwidth and loss would have to be considered in designing the optimum W type PCSF by controlling the intermediate layer thickness and refractive index of the outer cladding.

Finally, one should mention here that the numerical modeling of the bandwidth of a W-type PCSF presented in this work can be employed in the investigation of other W-type optical fibers, such as W-type plastic optical fibers and W-type glass optical fibers, which have a step-index distribution of their core.

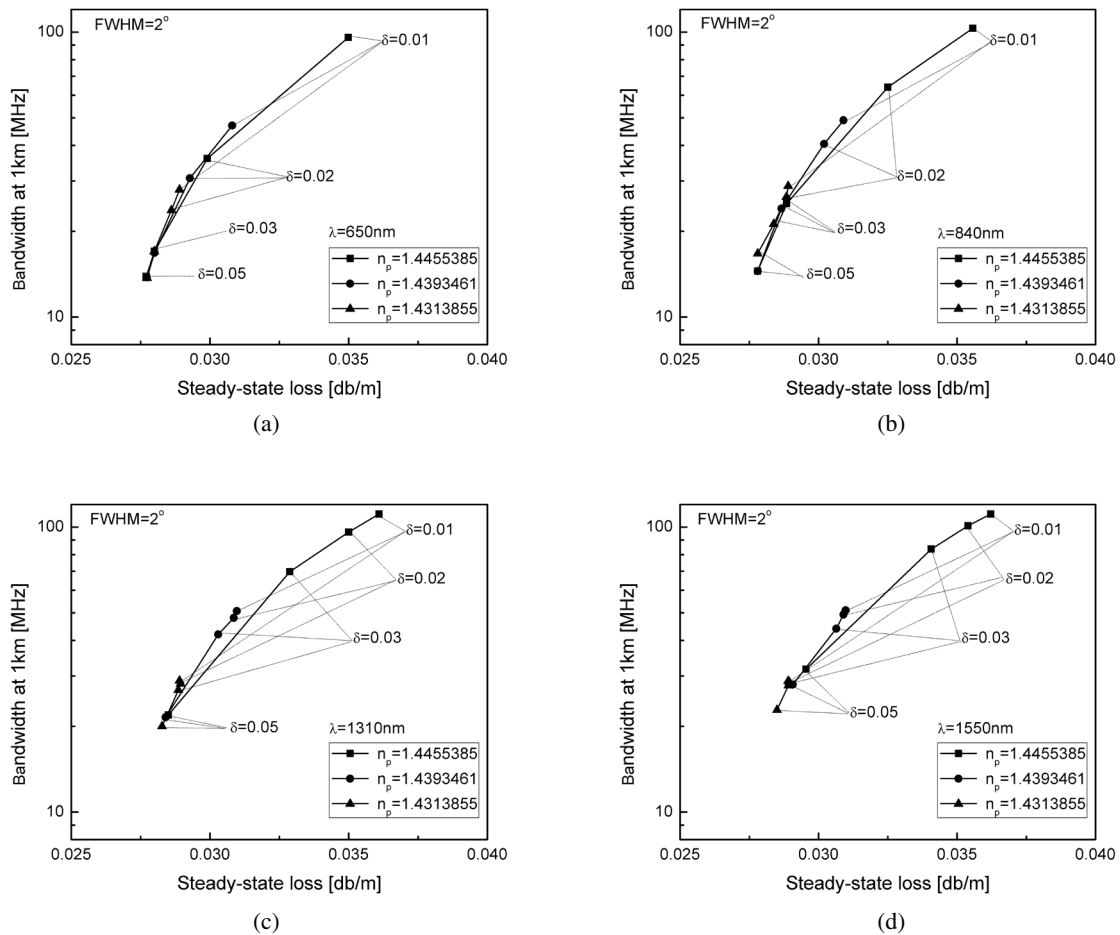


Figure 4. Numerical results for the trade-off relation between bandwidth and steady-state loss for a W-type PCSF for Gaussian launch excitation with $\text{FWHM} = 2^\circ$ and for four different wavelengths: (a) $\lambda = 650\text{ nm}$, (b) $\lambda = 840\text{ nm}$, (c) $\lambda = 1310\text{ nm}$ and (d) $\lambda = 1550\text{ nm}$.

4. Conclusions

Bandwidth and steady-state loss are calculated by the time-dependent power flow equation over a range of light wavelengths for a W-type PCSF with various intermediate layer widths and refractive indices of the outer cladding. It is shown that the bandwidth of a W-fiber broadens for longer wavelengths for all intermediate layer widths. This broadening of the bandwidth results from higher leaky mode losses and the consequent drop in modal dispersion. However, this influence of wavelength on bandwidth is negligible for narrow intermediate layers. With increasing refractive index of the outer cladding the bandwidth also increases due to increased leaky mode losses.

Because the steady-state loss also increases with increasing leaky mode loss, a trade-off relationship between bandwidth and loss would have to be considered in designing the optimum W-type PCSF. This can be done by controlling the width of the intermediate layer and the refractive index of the outer cladding at an appropriate infrared wavelength.

Acknowledgment

The work described in this paper was supported by the Strategic Research Grant of City University of Hong Kong (project

no. CityU 7004600) and by a grant from the Serbian Ministry of Education, Science and Technological Development (project no. 171011).

References

- [1] Jeunhomme L, Fraise M and Pocholle J P 1976 Propagation model for long step-index optical fibers *Appl. Opt.* **15** 3040–6
- [2] Koepfen C, Shi W D, Chen R F and Garito A F 1998 Properties of plastic optical fibers *J. Opt. Soc. Am. B* **15** 727–39
- [3] Ruddy V and Shaw G 1995 Mode coupling in large-diameter polymer-clad silica fibers *Appl. Opt.* **34** 1003–6
- [4] Savovic S and Djordjevic A 2017 Mode coupling in multi-mode step-index plastic-clad silica fibers with corrugated surfaces *Opt. Laser Technol.* **97** 400–4
- [5] Savovic S and Djordjevic A 2018 Mode coupling and its influence on space division multiplexing in step-index plastic-clad silica fibers *Opt. Fiber Technol.* **46** 192–7
- [6] Daido Y, Miyauchi E, Iwama T and Otsuka T 1979 Determination of modal power distribution in graded-index optical waveguides from near-field patterns and its application to differential mode attenuation measurement *Appl. Opt.* **18** 2207–13
- [7] Yamashita T and Kagami M 2005 Fabrication of light-induced self-written waveguides with a W-shaped refractive index profile *J. Lightwave Technol.* **23** 2542–8

- [8] Asai M, Inuzuka Y, Koike K, Takahashi S and Koike Y 2011 High-bandwidth graded-index plastic optical fiber with low-attenuation, high-bending ability, and high-thermal stability for home-networks *J. Lightwave Technol.* **29** 1620–6
- [9] Mikoshiba K and Kajioka H 1978 Transmission characteristics of multimode W-type optical fiber: experimental study of the effect of the intermediate layer *Appl. Opt.* **17** 2836–41
- [10] Dugas J and Maurel G 1992 Mode-coupling processes in polymethyl methacrylate-core optical fibers *Appl. Opt.* **31** 5069–79
- [11] Daum W, Krauser J, Zamzow P E and Ziemann O 2002 *Polymer Optical Fibers for Data Communication* (Berlin: Springer)
- [12] Tanaka T P and Yamada S 1980 Numerical solution of power flow equation in multimode W-type optical fibers *Appl. Opt.* **19** 1647–52
- [13] Takahashi K, Ishigure T and Koike Y 2006 Index profile design for high-bandwidth W-shaped plastic optical fiber *J. Lightwave Technol.* **24** 2867–76
- [14] Gloge D 1972 Optical power flow in multimode fibers *Bell Syst. Tech. J.* **51** 1767–83
- [15] Simovic A, Savovic S, Drljaca B and Djordjevich A 2014 Influence of intermediate layer on transmission characteristics of W-type optical fibers *Opt. Laser Technol.* **57** 565–9
- [16] Simovic A, Djordjevich A and Savovic S 2012 Influence of depth of intermediate layer on power distribution in W-type optical fibers *Appl. Opt.* **51** 4896–901
- [17] Savovic S, Simovic A and Djordjevich A 2012 Explicit finite difference solution of the power flow equation in W-type optical fibers *Opt. Laser Technol.* **44** 1786–90
- [18] Simovic A, Savovic S, Drljaca B and Djordjevich A 2015 Influence of the fiber design and launch beam on transmission characteristics of W-type optical fibers *Opt. Laser Technol.* **68** 151–9
- [19] Kagami M, Kawasaki A, Yonemura M, Nakai M, Mena P V and Selviah D R 2016 Encircled angular flux representation of the modal power distribution and its behavior in a step index multimode fiber *J. Lightwave Technol.* **34** 943–51

PAPER

Influence of wavelength on equilibrium mode distribution and steady state distribution in W-type plastic optical fibers

To cite this article: B Drljaa *et al* 2020 *Laser Phys.* **30** 075101

View the [article online](#) for updates and enhancements.

Influence of wavelength on equilibrium mode distribution and steady state distribution in W-type plastic optical fibers

B Drljača¹, A Simović², A Djordjević³ and S Savović^{2,3}

¹ University of Priština, Faculty of Science, Lole Ribara 29, Kosovska Mitrovica, Serbia

² University of Kragujevac, Faculty of Science, R. Domanovića 12, Kragujevac, Serbia

³ City University of Hong Kong, Department of Mechanical Engineering, 83 Tat Chee Avenue, Hong Kong, People's Republic of China

E-mail: savovic@kg.ac.rs

Received 20 January 2020

Accepted for publication 8 April 2020

Published 27 May 2020



CrossMark

Abstract

Wavelength dependence of equilibrium mode distribution (EMD) and steady state distribution (SSD) in W-type plastic optical fibers (POFs) is investigated in this paper for parametrically varied width of the fiber's intermediate optical layer and refractive index of the outer cladding. We have shown that with increasing the wavelength EMD and SSD are achieved at shorter W-type POF lengths. This is explained by the rise of the leaky mode losses with increasing wavelength. This facilitates tailoring W-fibers to a specific application at hand at different wavelengths.

Keywords: W-fiber, plastic optical fiber, equilibrium mode distribution, steady state distribution, power flow equation

1. Introduction

Optical fibers made of glass dominate in long-distance communication networks. Plastic optical fibers (POFs), with their higher attenuation and lower transmission bandwidth, are restricted to local area networks with short data links [1–3]. POFs possess important advantages over their glass counterparts. Specifically, POFs may be manufactured with large core diameters (0.5–1 mm or larger), allowing for interconnections with low-precision plastic components and reducing the overall cost of the system. POFs have excellent flexibility and are more easily handled than glass fibers. They impose less stringent constraints on the light source and even luminescent diodes are suitable sources for multimode fibers. Hence, a variety of POF applications have been developed and commercialized, from simple light-transmission guides in displays, to sensors and short-haul communication links [2–4].

The analysis and design of the refractive index profile of a multimode fiber, with a view to advancing fiber transmission

characteristics, have attracted significant attention in the last few decades [5–8]. A variety of designs of step-index, graded index and W-type fibers (fibers with core and two claddings) has been proposed for either long-distance communication links or high capacity local area networks [6–8]. It has been shown that waveguide dispersion is smaller in a W-type fiber than it is in a single-clad (SC) fiber [9]. A W-type fiber with an intermediate layer binds the guided modes more firmly to the core and reduces the effective numerical aperture of the fiber. Consequently, a W-type fiber has a wider transmission bandwidth and lower bending losses compared to a corresponding SC fiber.

Optical fibers inevitably incorporate irregularities in the form of shape-variation or material inhomogeneity including voids and cracks. Such random irregularities in multimode optical fibers cause light diffraction that couples power between the propagating modes. This mode coupling is an effect in addition to the reduction of the transmitted power by differential mode attenuation. Both strongly influence fiber transmission characteristics.

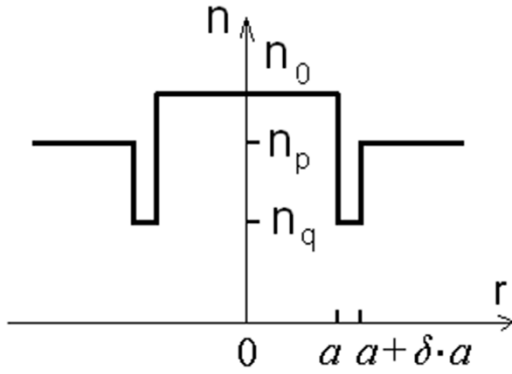


Figure 1. Refractive index profile of a W-fiber.

On the positive side, coupled modes may be less dispersed for a multimodal launch. This translates into higher bandwidth. However, mode coupling also leads to higher losses, particularly in curved segments. Moreover, the output field is altered and generally degraded as it contains modes of high order even if the launch was restricted to modes of only low order. W-fibers are more resilient to these effects. Their intermediate layer between the core and cladding retains some lossy leaky modes [9–14]. Yet, the more complex profile of the refractive index of the fiber opens the possibility of the optimization of such profile.

Angular input optical power distribution that results from a specific launch becomes gradually modified with distance from the input fiber end by the effect of mode coupling [15]. The expected beam properties, including the far-field radiation pattern, are altered as a consequence. The far-field pattern of an optical fiber is determined by the optical power distribution, which depends on the launch conditions, fiber properties and fiber length. Light launched at a specific angle $\theta_0 > 0$ with respect to the fiber axis will form a sharply defined ring radiation pattern at the output end of only short fibers. Because of mode coupling, the boundary (edges) of such a ring become fuzzy at the end of longer fibers. Up to a ‘coupling length’ L_c from the input fiber end, the extent of this fuzziness increases further with fiber length and the ring pattern evolves gradually into a disk extending across the entire fiber cross-section. An equilibrium mode distribution (EMD) exists beyond the coupling length L_c of the fiber. It is characterized by the absence of rings regardless of launch conditions, even though the resulting light distribution of the disk-pattern may vary with launch conditions. EMD indicates a substantially complete mode coupling. It is of critical importance when measuring characteristics of multimode optical fibers (linear attenuation, bandwidth, etc). At distance z_s ($z_s > L_c$) from the input fiber end, all individual disk patterns corresponding to different launch angles take the same light distribution across the fiber section and the steady state distribution (SSD) is achieved. SSD indicates the completion of the mode coupling process and the independence of the output light distribution from launch conditions.

The ‘coupling coefficient’ D has been used widely [16–19] to describe how power is transferred between modes. This allowed modeling by the power flow equation of the angular power distributions in the far field fiber output as a

function of the fiber length and conditions of launch. For a W-type POF, the main goal of this work is to investigate the influence of wavelength on the length of fiber at which EMD is achieved, and on the length of fiber z_s that marks the onset of the SSD. In this process, the width of the fiber’s intermediate layer and refractive index of the outer cladding were varied parametrically to facilitate the selection of their optimal values for a particular wavelength. The angular mode distribution model used in this work is valid only for step index W-type fibers and only for far field distribution.

2. Power flow equation

The Gloge’s time-independent power flow equation is [16]:

$$\frac{\partial P(\theta, z)}{\partial z} = -\alpha(\theta)P(\theta, z) + \frac{D}{\theta} \frac{\partial P(\theta, z)}{\partial \theta} + D \frac{\partial^2 P(\theta, z)}{\partial \theta^2} \quad (1)$$

where θ is the mode angle, $P(\theta, z)$ is the power distribution over angle θ , $\alpha(\theta)$ is the modal attenuation and D is a constant ‘coupling coefficient’. It is assumed that mode coupling mainly occurs between neighboring modes due to the fact that coupling strength decreases sufficiently fast with the mode spacing [16]. This assumption is commonly used in modeling a mode coupling process both in SC and W-type fibers [16–20]. Describing the evolution of the modal power distribution along the fiber, equation (1) is the time-independent power flow equation with the mode angle θ taken as a continuous variable, where the next-neighbor mode coupling is assumed as a diffusion process in a continuum. Modal attenuation $\alpha(\theta)$ can be expanded into $\alpha(\theta) = \alpha_0 + \alpha_d(\theta)$. The term α_0 represents conventional losses by absorption and scattering. It can be neglected in the solution because it would feature as just a fixed multiplier $\exp(-\alpha_0 z)$. The term $\alpha_d(\theta)$ in the expansion of $\alpha(\theta)$ is dominant for higher order modes. Boundary conditions for (1) are $P(\theta_m, z) = 0^\circ$ and $D \cdot (\partial P / \partial \theta) = 0$ at $\theta = 0^\circ$, with θ_m denoting the largest propagation angle. The condition $P(\theta_m, z) = 0$ implies that modes with infinitely high loss do not carry power. Condition $(\partial P / \partial \theta) = 0$ at $\theta = 0$ indicates that the coupling is limited to modes propagating with $\theta > 0$.

Figure 1 represents the index profile of a W-fiber with n_0 , n_p and n_q ($n_0 > n_p > n_q$) being indices of refraction of the core, cladding, and intermediate layer, respectively. Modes propagating at angles that are between $\theta_p \cong (2\Delta_p)^{1/2}$ and $\theta_q \cong (2\Delta_q)^{1/2}$ have been shown to be leaky modes [9, 20]; here, $\Delta_p = (n_0 - n_p)/n_0$ or $\Delta_q = (n_0 - n_q)/n_0$ is the relative difference of the refraction index of the cladding, or (respectively) intermediate layer, to that of the core.

Denoting the free-space wave number as $k_0 = 2\pi/\lambda$ and expressing the thickness of the intermediate layer as $\delta \cdot a$ where a is the core-radius, the constants of attenuation of leaky modes are given as [9]:

$$\alpha_L(\theta) = \frac{4(\theta^2 - \theta_p^2)^{1/2} \theta^2 (\theta_q^2 - \theta^2)}{a(1 - \theta^2)^{1/2} \theta_q^2 (\theta_q^2 - \theta_p^2)} \exp \left[-2\delta a n_0 k_0 (\theta_q^2 - \theta^2)^{1/2} \right]. \quad (2)$$

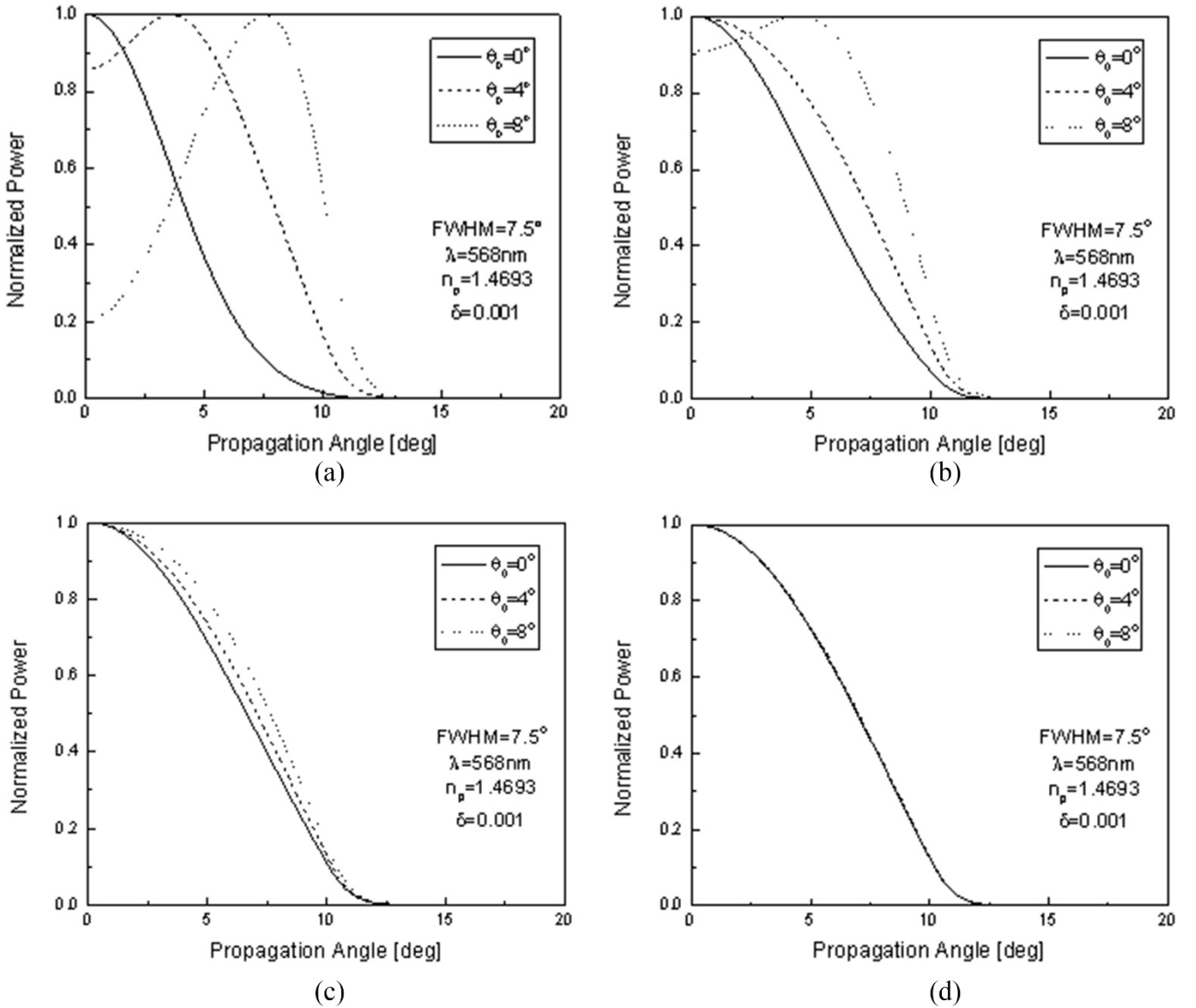


Figure 2. Normalized angular power distribution for $\text{FWHM} = 7.5^\circ$, $\lambda = 568 \text{ nm}$, $n_p = 1.4693$, $\delta = 0.001$ and $D = 3.5 \times 10^{-4} \text{ rad}^2 \text{ m}^{-1}$, for four launch angles $\theta_0 = 0^\circ, 4^\circ$, and 8° , at lengths: (a) 1 m, (b) 6 m, (c) 12 m and (d) 24 m.

All guided modes in SC fibers, regardless of their propagation angle θ , are attenuated equally; the attenuation rises steeply for radiated modes. For W-type fibers, this can be generalised in terms of $\alpha_d(\theta)$ in the already introduced expansion for attenuation $\alpha(\theta) = \alpha_0 + \alpha_d(\theta)$, in which $\alpha_0 = \text{const}$, and where:

$$\alpha_d(\theta) = \begin{cases} 0 & \theta \leq \theta_p \\ \alpha_L(\theta) & \theta_p < \theta < \theta_q \\ \infty & \theta \geq \theta_q \end{cases} . \quad (3)$$

Equation (3) can also be explained in the following way: if one thinks of a W-fiber as having a vanishing, and then infinite, thickness of its intermediate layer $\delta \cdot a$ (a is the core radius), with $\delta \rightarrow 0$, and then $\delta \rightarrow \infty$, two distinct SC (SC_p and SC_q) fibers result with respective critical angles of θ_p and then θ_q , respectively. This results in three subdomains for the

propagation angle, evident in equation (3): less than one critical angle, greater than the other, and between the two of them. Modes propagating at angles between the two critical angles θ_p and θ_q are termed leaky modes. For that range, strong influence of the intermediate layers' thickness $\delta \cdot a$ on $\alpha_L(\theta)$ in (3) has been noted [9].

The characteristics of W-fibers were reported to vary strongly with the intermediate layer's width $\delta \cdot a$. As mentioned, they approach those of corresponding SC_p or SC_q fibers when, respectively, the thickness either vanishes or approaches infinity [9], under SSD conditions. Also of influence is the index of refraction n_p of the outer cladding (figure 1). The influence is investigated in this paper of the width of intermediate layer and index of refraction n_p on the length L_c for achieving the EMD and length z_s for reaching the SSD—at different wavelengths. This facilitates tailoring W-fibers to a specific application at hand.

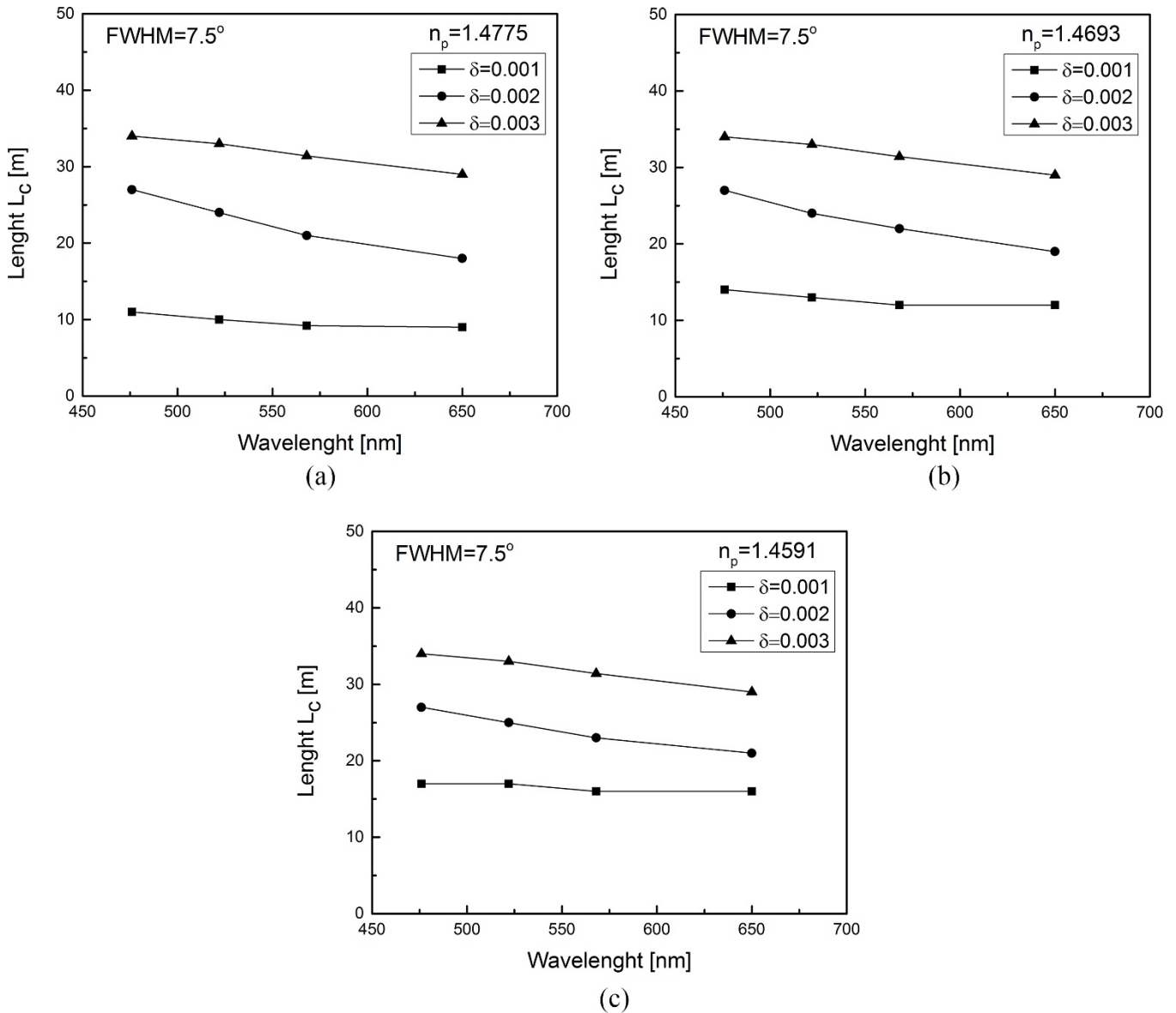


Figure 3. Wavelength dependence of length L_c for Gaussian launch excitation with FWHM = 7.5°, $\delta = 0.001, 0.002$ and 0.03 , and (a) $n_p = 1.4775$, (b) $n_p = 1.4693$ and (c) $n_p = 1.4591$.

3. Numerical results

The length L_c at which EMD is achieved and the length z_s for establishing the SSD are analysed in this work at different wavelengths for the W-type POF. The fiber structural characteristics were: core refractive index $n_0 = 1.492$, cladding refractive index $n_q = 1.4057$, critical angle (measured inside the fiber) $\theta_m = 19.6^\circ$, core diameter $d = 0.98$ mm, and fiber diameter $b = 1$ mm [21]. The W-type POF is designed from this singly-clad POF in such a way that the W-type POF's inner cladding retains the refractive index n_q of the SC POF's cladding, while an outer cladding of the W-type POF has a refractive index n_p , which is higher than the refractive index n_q of the inner cladding (figure 1). The three values

of the refractive index of the outer cladding n_p were used in the modeling: $n_p = 1.4775, 1.4693, 1.4591$, corresponding to the critical angles $\theta_p = 8^\circ, 10^\circ, 12^\circ$, respectively. The normalized intermediate layer widths $\delta = 0.01, \delta = 0.02$ and $\delta = 0.03$ were employed (actual width is $\delta \cdot a$ mm). We solved the time-independent power flow equation (1) using explicit finite difference method for the coupling coefficient $D = 3.5 \times 10^{-4} \text{ rad}^2 \text{ m}^{-1}$ [4]. In the calculations, the launch beam distribution was in the Gaussian form with an FWHM = 7.5°. One should mention here that the change of depth of the intermediate layer has a negligible influence on the lengths L_c and z_s of the W-type POFs, and therefore is not analyzed in this work. Length L_c for reaching EMD is determined as a length at which the angular power distribution of the highest guiding

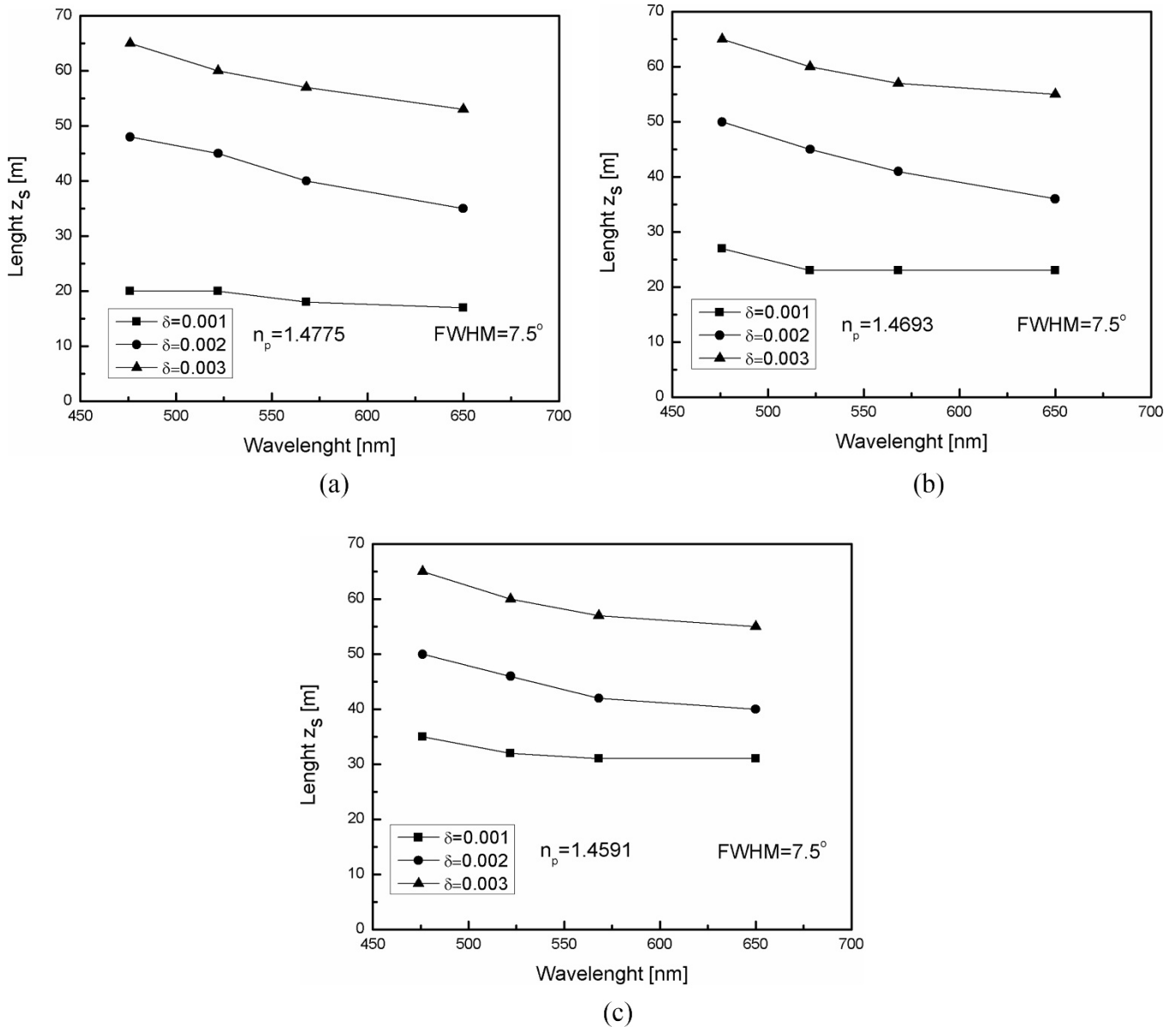


Figure 4. Wavelength dependence of length z_s for Gaussian launch excitation with FWHM = 7.5° , $\delta = 0.001, 0.002$ and 0.03 , and (a) $n_p = 1.4775$, (b) $n_p = 1.4693$ and (c) $n_p = 1.4591$.

modes shifted their maxima to $\theta = 0^\circ$. Length z_s for achieving SSD is determined as a length at which the angular light distribution stops evolving with further increase of the fiber length (becomes steady).

In figure 2 our numerical solution of the power flow equation is presented by showing the evolution of the normalized output power distribution with fiber length for a W-type POF with characteristics $n_p = 1.4693$ ($\theta_p = 10^\circ$), $\delta = 0.001$ and $D = 3.5 \times 10^{-4} \text{ rad}^2 \text{ m}^{-1}$ at $\lambda = 568 \text{ nm}$, for Gaussian launch distribution with FWHM = 7.5° , for three different input angles $\theta_0 = 0^\circ, 4^\circ$ and 8° (measured inside the fiber). One can observe from figure 2 that when the launch distribution at the input end of the fiber is centered at $\theta_0 = 0^\circ$, the power distribution remains at the same angle as the distance from the input fiber end increases, but its width increases due

to mode coupling. The radiation patterns in figure 2(a) of non-centrally launched beams in short fibers are centered at values which are close to their initial values. With increasing the fiber length one can observe from figure 2(b) that coupling is stronger for the low-order modes: their distributions have shifted more towards $\theta = 0^\circ$. Coupling of higher-order modes can be observed only after longer fiber lengths. It is not until the fiber's coupling length L_c that all the mode-distributions shift their mid-points to zero degrees (from the initial value of θ_0 at the input fiber end), producing the EMD in figure 2(c) of $L_c = 12 \text{ m}$. Steady state distribution is achieved at length $z_s = 24 \text{ m}$ in figure 2(d).

One can observe in figures 3 and 4 that for the smallest width of intermediate layer ($\delta = 0.001$), the influence of wavelength on lengths L_c and z_s is negligible. This is

due to large leaky mode losses; as these modes are practically not guided along the fiber. With increasing width of the intermediate layer, there is a wavelength-dependent decrease of lengths L_c and z_s . This decrease is more pronounced at short wavelengths as leaky mode losses are then reduced, i.e. a smaller number of leaky modes remain guided at larger wavelengths at longer fiber lengths, resulting in a drop of fiber lengths L_c and z_s . The lengths L_c and z_s are larger in the case of wider intermediate layer widths (larger δ). Since the leaky modes are reduced at short transmission length in the case of a thinner intermediate layer, it consequently takes a shorter fiber length z_s for the onset of SSD—compared to the case with a wider intermediate layer. As the refractive index of the outer cladding n_p decreases (θ_p increases), EMD and SSD occur at longer fiber lengths, which is attributed to the correspondingly increasing number of guiding modes. The smaller the parameter n_p , the longer the fiber length required for completion of the coupling process.

Since it is found that with increasing the wavelength the leaky mode losses rise, the EMD and SSD are established at shorter fiber lengths—the shorter the length at which equilibrium mode distribution is achieved, the earlier the bandwidth switches from the functional dependence of $1/z-1/z^{1/2}$ (faster bandwidth improvement) [15].

4. Conclusion

Equilibrium mode distribution (EMD) and steady state distribution (SSD) of power are investigated for a varied W-type POF's width of intermediate layer and refractive index of the outer cladding. The length L_c at which EMD is achieved and length z_s marking the onset of the SSD decrease with increase of the wavelength. This is a result of the rise of the leaky mode losses with rising wavelength, which is to say that a smaller number of leaky modes continue to be guided in longer fibers at larger wavelengths.

The lengths L_c and z_s are larger in the case of wider intermediate layer widths (larger δ). Since the leaky modes are reduced at short transmission length in the case of a thinner intermediate layer, it consequently takes a shorter fiber length z_s for the onset of SSD, compared to the case with a wider intermediate layer.

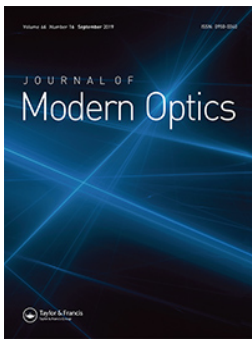
As refractive index of the outer cladding n_p decreases (θ_p increases), the number of guiding modes increases, and EMD and SSD are established at longer fiber lengths. The smaller the parameter n_p , the longer the fiber length required for completion of the coupling process.

Acknowledgments

The work described in this paper was supported by the Strategic Research Grant of City University of Hong Kong (Project No. CityU 7004600) and by a grant from Serbian Ministry of Education, Science and Technological Development (Project No. 171011).

References

- [1] Daum W, Krauser J, Zamzow P E and Ziemann O 2002 *Polymer Optical Fibers for Data Communication* (Berlin: Springer)
- [2] Green P E Jr. 1996 Optical networking update *IEEE J. Sel. Areas Commun.* **14** 764–79
- [3] Koeppen C, Shi R F, Chen W D and Garito A F 1998 Properties of plastic optical fibers *J. Opt. Soc. Am. B* **15** 727–39
- [4] Savović S and Djordjevich A 2006 Mode coupling in strained and unstrained step-index plastic optical fibers *Appl. Opt.* **45** 6775–80
- [5] Daido Y, Miyauchi E, Iwama T and Otsuka T 1979 Determination of modal power distribution in graded-index optical waveguides from near-field patterns and its application to differential mode attenuation measurement *Appl. Opt.* **18** 2207–13
- [6] Yamashita T and Kagami M 2005 Fabrication of light-induced self-written waveguides with a W-shaped refractive index profile *J. Lightwave Technol.* **23** 2542–8
- [7] Asai M, Inuzuka Y, Koike K, Takahashi S and Koike Y 2011 High-bandwidth graded-index plastic optical fiber with low-attenuation, high-bending ability, and high-thermal stability for home-networks *J. Lightwave Technol.* **29** 1620–6
- [8] Mikoshiha K and Kajioka H 1978 Transmission characteristics of multimode W-type optical fiber: experimental study of the effect of the intermediate layer *Appl. Opt.* **17** 2836–41
- [9] Tanaka T P and Yamada S 1980 Numerical solution of power flow equation in multimode W-type optical fibers *Appl. Opt.* **19** 1647–52
- [10] Onoda S, Tanaka T and Sumi M 1976 W fiber design considerations *Appl. Opt.* **15** 1930–5
- [11] Maeda M and Yamada S 1977 Leaky modes on W-fibers: mode structure and attenuation *Appl. Opt.* **16** 2198–203
- [12] Tanaka T, Yamada S, Sumi M and Mikoshiha K 1977 Microbending losses of doubly clad (W-type) optical fibers *Appl. Opt.* **18** 2391–4
- [13] Tanaka T P and Yamada S 1979 Steady-state characteristics of multimode W-type fibers *Appl. Opt.* **18** 3261–4
- [14] Otrokhov S Y, Chamorovskiy Y K and Shatrov A D 2010 Leaking modes of guiding W fibers with a large difference in the refractive index profiles *J. Commun. Technol. Electron.* **55** 1108–14
- [15] Jiang G, Shi R F and Garito A F 1997 Mode coupling and equilibrium mode distribution conditions in plastic optical fibers *IEEE Photon. Technol. Lett.* **9** 1128–30
- [16] Gloge D 1972 Optical power flow in multimode fibers *Bell Syst. Tech. J.* **51** 1767–83
- [17] Jeunhomme L, Fraise M and Pocholle J P 1976 Propagation model for long step-index optical fibers *Appl. Opt.* **15** 3040–6
- [18] Rousseau M and Jeunhomme L 1977 Numerical solution of the coupled-power equation in step index optical fibers *IEEE Trans. Microwave Theory Tech.* **25** 577–85
- [19] Djordjevich A and Savović S 2004 Numerical solution of the power flow equation in step index plastic optical fibers *J. Opt. Soc. Am. B* **21** 1437–42
- [20] Savović S, Simović A and Djordjevich A 2012 Explicit finite difference solution of the power flow equation in W-type optical fibers *Opt. Laser Technol.* **44** 1786–90
- [21] Mateo J, Losada M A and Zubia J 2009 Frequency response in step index plastic optical fibers obtained from the generalized power flow equation *Opt. Express.* **17** 2850–60



A transmission length limit for space division multiplexing in step-index silica optical fibres

Svetislav Savović, Alexandar Djordjevich, Ana Simović & Branko Drljača

To cite this article: Svetislav Savović, Alexandar Djordjevich, Ana Simović & Branko Drljača (2019) A transmission length limit for space division multiplexing in step-index silica optical fibres, Journal of Modern Optics, 66:16, 1695-1700, DOI: [10.1080/09500340.2019.1660006](https://doi.org/10.1080/09500340.2019.1660006)

To link to this article: <https://doi.org/10.1080/09500340.2019.1660006>



Published online: 28 Aug 2019.



Submit your article to this journal [↗](#)



Article views: 6



View related articles [↗](#)



View Crossmark data [↗](#)



A transmission length limit for space division multiplexing in step-index silica optical fibres

Svetislav Savović^{a,b}, Alexandar Djordjevich^b, Ana Simović^a and Branko Drljača^c

^aFaculty of Science, University of Kragujevac, Kragujevac, Serbia; ^bDepartment of Mechanical Engineering, City University of Hong Kong, Kowloon Tong, Hong Kong, People's Republic of China; ^cFaculty of Science, University of Priština, Kosovska Mitrovica, Serbia

ABSTRACT

By solving the power flow equation, we investigate the influence of mode coupling on space division multiplexing capability of three multimode step-index silica optical fibres with a different strengths of mode coupling. Results show that mode coupling significantly limits the length of these fibres at which the space division multiplexing can be realized with a minimal crosstalk between the neighbour optical channels. This is most pronounced in silica optical fibres with the strongest mode coupling. The two and three spatially multiplexed channels in the investigated step-index silica optical fibres can be employed with a minimal crosstalk up to the fibre lengths of few hundred of meters and few tens of meters, respectively. These lengths are much shorter than kilometer lengths at which these fibres are usually employed without space division multiplexing. Such characterization of optical fibres should be considered in designing an optical fibre transmission system for space division multiplexing.

ARTICLE HISTORY

Received 21 January 2019
Accepted 19 August 2019

KEYWORDS

Silica optical fibres; mode coupling; space division multiplexing

1. Introduction

During the last decades, global network traffic increased exponentially, mainly due to the rapid Internet evolution (1). With the increasingly use of video on demand, cloud storage and computing, and the emerging Internet of things, the trends show no sign of decline. Most of this data traffic is now supported by optical fibre systems. This capacity increase was caused by successive technology improvements: low losses single-mode fibres, fibre amplifiers, multiplexing, and high-efficiency spectral coding (1). Multiplexing of optical data can be realized not only in wavelength, but also in polarization, in time, in phase and in space. Multiplexing technique can be employed both in low-power and high-power optical fibre transmission systems (1,2). Space division multiplexing (SDM) including mode division multiplexing using multimode fibres or few-mode fibres and/or core multiplexing using multicore fibres, has attracted much attention in the last decade for the next multiplicative capacity growth for optical communication (1,3–8). SDM may operate at the same wavelength or different wavelengths (9). In the case of SDM at the same wavelength, radially distributed, dedicated spatial locations are assigned to every SDM channel inside the carrier

fibre as these channels traverse the length of the carrier. The location of the each channel inside the fibre is a function of the launch angle and the strength of mode coupling. In practice the channel launched with input angle $\theta_0 = 0^\circ$ along the fibre axis appears in the form of disk, while all subsequent channels launched with $\theta_0 > 0$ appear as concentric rings. The centre disk and each ring represent a separate spatially modulated optical channel, thereby enhancing the bandwidth of optical fibre system (Figure 1).

Transmission characteristics of multimode step-index optical fibres depend upon the differential mode attenuation and rate of mode coupling (9,10). The latter represents power transfer from adjacent modes caused by fibre impurities and inhomogeneities introduced during the fibre manufacturing process (such as microscopic bends, irregularity of the core-cladding boundary, and refractive index distribution fluctuations) (11). Mode coupling is very important for SDM because SDM involves tightly packing spatial channels into a fibre, thus making crosstalk between channels an obvious potential problem.

Angular input optical power distribution that results from a specific launch gets modified gradually with

CONTACT Svetislav Savović ✉ savovic@kg.ac.rs Faculty of Science, University of Kragujevac, R. Domanovića 12, Kragujevac 34000, Serbia; City University of Hong Kong, 83 Tat Chee Avenue, Kowloon Tong, Hong Kong, People's Republic of China; Alexandar Djordjevich ✉ mealex@cityu.edu.hk
City University of Hong Kong, 83 Tat Chee Avenue, Kowloon, Hong Kong, People's Republic of China

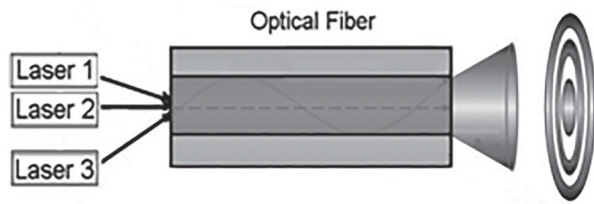


Figure 1. Minimalistic system design of three-channel SDM system. One channel is with input angle along the fibre axis and two channels launched with $\theta_0 > 0$, which appear in the far field as a centre disk and two concentric rings, respectively. The centre disk and two concentric rings represent a three separate spatially modulated optical channels.

distance from the input fibre-end by the effect of mode coupling. The expected beam properties, including the far-field radiation pattern, are altered as a consequence. The far-field pattern of an optical fibre is determined by the optical power distribution that depends on the launch conditions, fibre properties and fibre length. Light launched at a specific angle $\theta_0 > 0$ with respect to the fibre axis will form a sharply defined ring radiation pattern at the output end of only short fibres. Because of mode coupling, the boundary (edges) of such a ring become fuzzy at the end of longer fibres. Up to a ‘coupling length’ L_c from the input fibre end, the extent of this fuzziness increases further with fibre length and the ring-pattern evolves gradually into a disk extending across the entire fibre cross-section. An equilibrium mode distribution (EMD) exists beyond the coupling length L_c of the fibre. It is characterized by the absence of rings regardless of launch conditions, even though the resulting light distribution of the disk-pattern may vary with launch conditions. EMD indicates a substantially complete mode coupling.

Since the information regarding the SDM in silica optical fibres (SOFs) is missed in the literature, in this work, by numerical solving the power flow equation, we examine the state of mode coupling in three multi-mode SI SOFs with $NA = 0.22$ and different strengths of mode coupling, investigated earlier by Hurand et al. (12). This enables one to obtain the limits of the fibre lengths up to which a SDM can be realized with minimal crosstalk between the two and three co-propagating optical channels.

2. Power flow equation

Gloge’s power flow equation is (10):

$$\frac{\partial P(\theta, z)}{\partial z} = -\alpha(\theta)P(\theta, z) + \frac{D}{\theta} \frac{\partial}{\partial \theta} \left(\theta \frac{\partial P(\theta, z)}{\partial \theta} \right) \quad (1)$$

where $P(\theta, z)$ is the angular power distribution, z is the distance from the input end of the fibre, θ is the propagation angle with respect to the core axis, D is the coupling coefficient assumed constant (10,13–15) and $\alpha(\theta)$ is the modal attenuation. Except near cutoff, the attenuation remains uniform $\alpha(\theta) = \alpha_0$ throughout the region of guided modes $0 \leq \theta \leq \theta_c$ (14) (it appears in the solution as the multiplication factor $\exp(-\alpha_0 z)$ that also does not depend on θ). Therefore, $\alpha(\theta)$ need not be accounted for when solving (1) for mode coupling and this equation reduces to (15):

$$\frac{\partial P(\theta, z)}{\partial z} = \frac{D}{\theta} \frac{\partial P(\theta, z)}{\partial \theta} + D \frac{\partial^2 P(\theta, z)}{\partial \theta^2} \quad (2)$$

Numerical solution of the power flow Equation (2) was obtained using the explicit finite-difference method (15,16), for Gaussian launch-beam distribution of the form:

$$P(\theta, z) = \frac{1}{\sigma \sqrt{2\pi}} \exp \left[-\frac{(\theta - \theta_0)^2}{2\sigma^2} \right] \quad (3)$$

with $0 \leq \theta \leq \theta_c$, where θ_0 is the mean value of the incidence angle distribution, with the full width at half maximum $FWHM = 2\sigma \sqrt{2 \ln 2} = 2.355\sigma$ (σ is standard deviation).

3. Results and discussion

In this paper, by numerical solving the power flow equation, we analyse mode coupling in three multi-mode SI SOFs used in the previously reported experiment (12). The first fibre has core diameter $d_{core} = 100 \mu\text{m}$ and clad diameter $d_{clad} = 660 \mu\text{m}$ (100/660 fibre), the second fibre has $d_{core} = 200 \mu\text{m}$ and clad diameter $d_{clad} = 745 \mu\text{m}$ (200/745 fibre), while the third fibre has core diameter $d_{core} = 400 \mu\text{m}$ and clad diameter $d_{clad} = 720 \mu\text{m}$ (400/720 fibre). All fibres have $NA = 0.22$, core refractive index $n = 1.4570$ at $\lambda = 633 \text{ nm}$ and critical angle $\theta_c = 8.8^\circ$ (measured inside the core). Hurand et al. (12) obtained $D = 4.9 \times 10^{-7} \text{ rad}^2/\text{m}$ for 100/600 fibre, $D = 1.9 \times 10^{-6} \text{ rad}^2/\text{m}$ for 200/745 fibre and $D = 6.4 \times 10^{-6} \text{ rad}^2/\text{m}$ for 400/720 fibre at $\lambda = 633 \text{ nm}$ – which we have adopted in this work. One should mention here that the advantage of our method for calculating the coupling coefficient D , which was employed by Hurand et al. (12) for SI SOFs investigated in their work as well as we investigate in this work, is that one can determine D on the basis of the measurement of the evolution of the angular power distribution at two arbitrary chosen fibre lengths. These two lengths could be very short, as it was the case in the Hurand et al.’s measurements ($z = 0$ and 2 m). The coupling coefficient is assumed constant (independent on θ and z) (10,13–15)

and it can be used in the calculations of output angular power distributions at any fibre length.

In Figures 2–4, our numerical solution of the power flow equation is presented by showing the evolution of the normalized output power distribution with fibre length for 100/660, 200/745 and 400/720 fibre at $\lambda = 633$ nm. The three co-propagating optical channels are launched at different input angles $\theta_0 = 0^\circ$, 3° and 6° thus maintaining a different spatial orientation. For three optical channels we selected Gaussian launch beam distribution with $(\text{FWHM})_0 = 0.127^\circ$ by setting $\sigma_0 = 0.054^\circ$ in Equation (3) (12,16). In the case of three optical channels, ring radiation patterns in very short fibres in Figures 2(a), 3(a) and 4(a) indicate that the mode coupling is so low that their distributions still are positioned at their initial angular values. With increasing fibre length the Gaussian distributions broaden due to mode coupling leading to a minimal crosstalk observed between the neighbour co-propagating optical channels shown in Figures 2(b), 3(b) and 4(b) (a minimal crosstalk is assumed to occur at fibre length at which a tails of the neighbour Gaussian distributions (channels) overlap with intensity of $\approx 15\%$). The fibre lengths in Figures 2(b), 3(b) and 4(b) actually mark the lengths z_{SDM}

up to which a practical realization of three-channels space division multiplexing can be done in three investigated SOFs with a minimal crosstalk. With further increasing a fibre length, a crosstalk between neighbour co-propagating optical channels continue to increase and significantly influence the quality of light signals which are transmitting through the channels (Figures 2(c), 3(c) and 4(c)). Finally, at fibre's coupling length L_c the mode-distributions of two co-propagating optical channels which are in the ring form, shift their mid-points to zero degrees, producing the EMD in Figures 2(d), 3(d) and 4(d): L_c is 5400, 1380 and 430 m, for 100/660, 200/745 and 400/720 fibre, respectively. As a result, at fibre lengths $z \geq L_c$ the three Gaussian distributions which corresponded to three spatially multiplexed co-propagating optical channels are no more spatially separated since they form a disk-type circular outputs. One can see that mode coupling significantly limits the length of the SOFs at which the space division multiplexing can be realized. This limitation is most pronounced in 400/720 SOF which showed the strongest mode coupling, with reducing the length for practical realization of three-channels space division multiplexing up to $z_{SDM} \approx 11$ m. In 100/660 fibre and 200/745 fibre these lengths

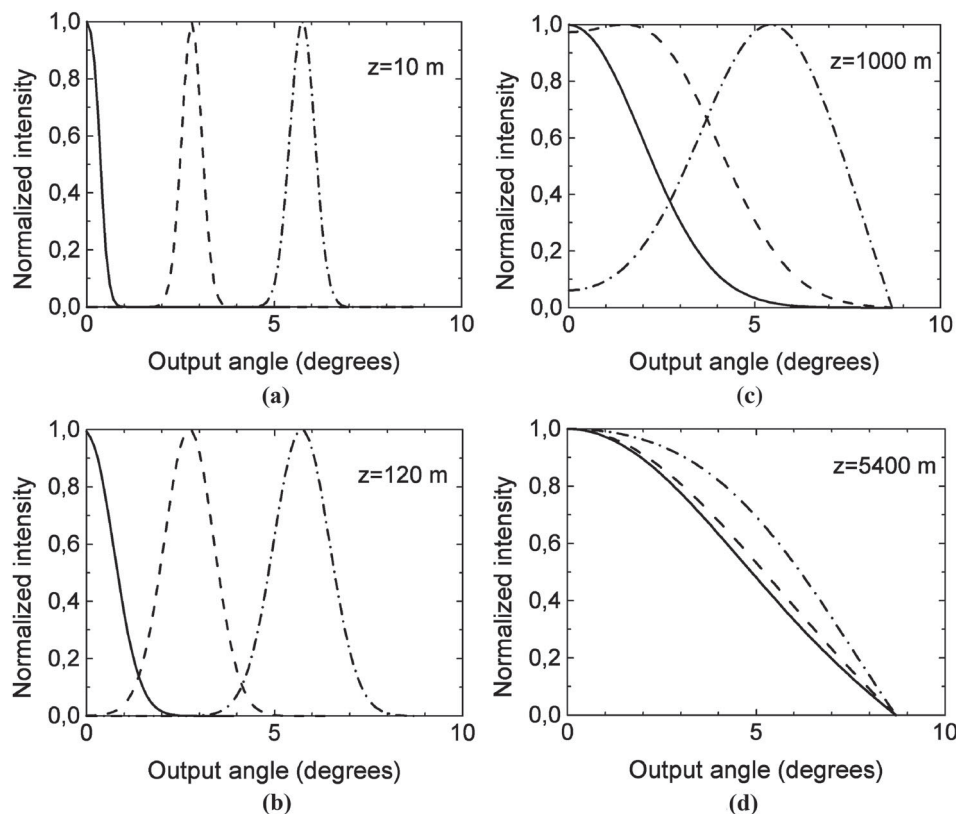


Figure 2. Normalized output angular power distribution at different locations along the 100/600 silica fibre with coupling coefficient $D = 4.9 \times 10^{-7}$ rad²/m calculated by numerical solving the power flow equation for three Gaussian input angles $\theta_0 = 0^\circ$ (solid line), 3° (dashed line) and 6° (dash-dotted line) with $(\text{FWHM})_{z=0} = 0.127^\circ$ for: (a) $z = 10$ m; (b) $z = 120$ m; (c) $z = 1000$ m and (d) $z = 5400$ m.

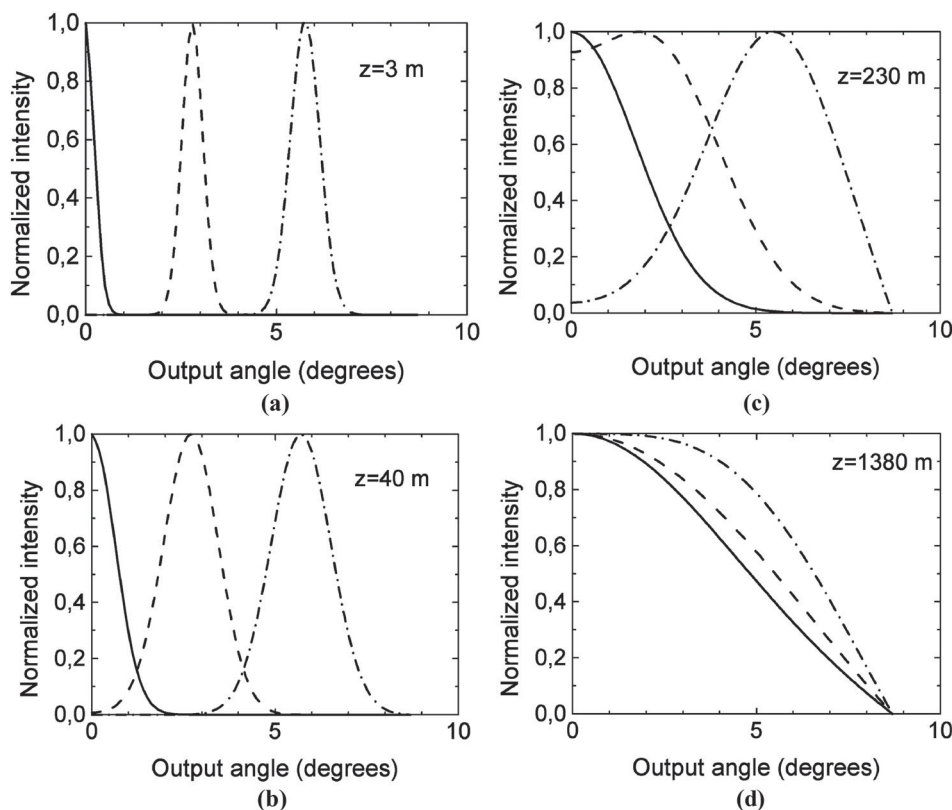


Figure 3. Normalized output angular power distribution at different locations along the 200/745 silica fibre with coupling coefficient $D = 1.9 \times 10^{-6} \text{ rad}^2/\text{m}$ calculated by numerical solving the power flow equation for three Gaussian input angles $\theta_0 = 0^\circ$ (solid line), 3° (dashed line) and 6° (dash-dotted line) with $(\text{FWHM})_{z=0} = 0.127^\circ$ for: (a) $z = 3 \text{ m}$; (b) $z = 40 \text{ m}$; (c) $z = 230 \text{ m}$ and (d) $z = 1380 \text{ m}$.

are $z_{SDM} \approx 120 \text{ m}$ and $\approx 40 \text{ m}$, respectively. It is worth noting that the lengths z_{SDM} up to which a minimal crosstalk is observed between the three neighbour co-propagating optical channels are much shorter than the corresponding coupling lengths L_c at which the EMD is achieved (Figures 2(d), 3(d) and 4(d)); the length z_{SDM} is 2.2%, 2.6% and 2.8% of the coupling length for 100/600 fibre, 200/745 fibre and 400/720 fibre, respectively. In the case of two propagating channels, which are launched at different input angles $\theta_0 = 0$ and 7° , the length z_{SDM} is 10.0%, 10.9% and 10.4% of the coupling length for 100/600 fibre, 200/745 fibre and 400/720 fibre, respectively (Table 1). It is interesting to note that z_{SDM} significantly decreases up to $D \approx 2 \times 10^{-6} \text{ rad}^2/\text{m}$, and thereafter this decrease is much slower (Figure 5). In general, a larger number of co-propagating optical channels, a sooner crosstalk between the neighbour optical channels would appear. In practice, a tradeoff between a number of co-propagating optical channels and a length of fibre which one expect to transmit the spatially multiplexed signals with minimal crosstalk between the neighbour optical channels should be considered for a particular fibre use.

Finally, one should mention that Hurand et al. reported the coupling coefficient D at three different wavelengths only for 200/745 fibre: $D = 2.4 \times 10^{-6}$, 1.8×10^{-6} and $1.5 \times 10^{-6} \text{ rad}^2/\text{m}$ at $\lambda = 403$, 633 and 1064 nm , respectively. By numerical extrapolation, using Hurand et al.'s dependence $D \approx \lambda^{-1/2}$ we obtained $D \approx 1.2 \times 10^{-6} \text{ rad}^2/\text{m}$ at $\lambda = 1550 \text{ nm}$. By solving the Equation (2), we obtained that the lengths z_{SDM} for two- and three-channel SDM for 200/745 fibre at $\lambda = 1550 \text{ nm}$ are 153 and 41 m, respectively. One can see that difference between the length z_{SDM} which we calculated at $\lambda = 633 \text{ nm}$ (Table 1) and z_{SDM} at 1550 nm is negligible (it is about 2.5%). Thus for other two investigated silica fibres, 100/660 fibre and 400/720 fibre, the lengths z_{SDM} at $\lambda = 633 \text{ nm}$ (shown in Table 1) can be used as a good approximation of the lengths at which SDM can be realized at $\lambda = 1550 \text{ nm}$ too.

In our previous work (17), we have shown that step-index glass optical fibre with a critical angle $\theta_c = 7.26^\circ$ (measured inside the core) and coupling coefficient $D = 7.9 \times 10^{-7} \text{ rad}^2/\text{m}$ at $\lambda = 633 \text{ nm}$ has a coupling length $L_c = 1800 \text{ m}$. We obtain in this work that two- and three-channels space division multiplexing in this fibre

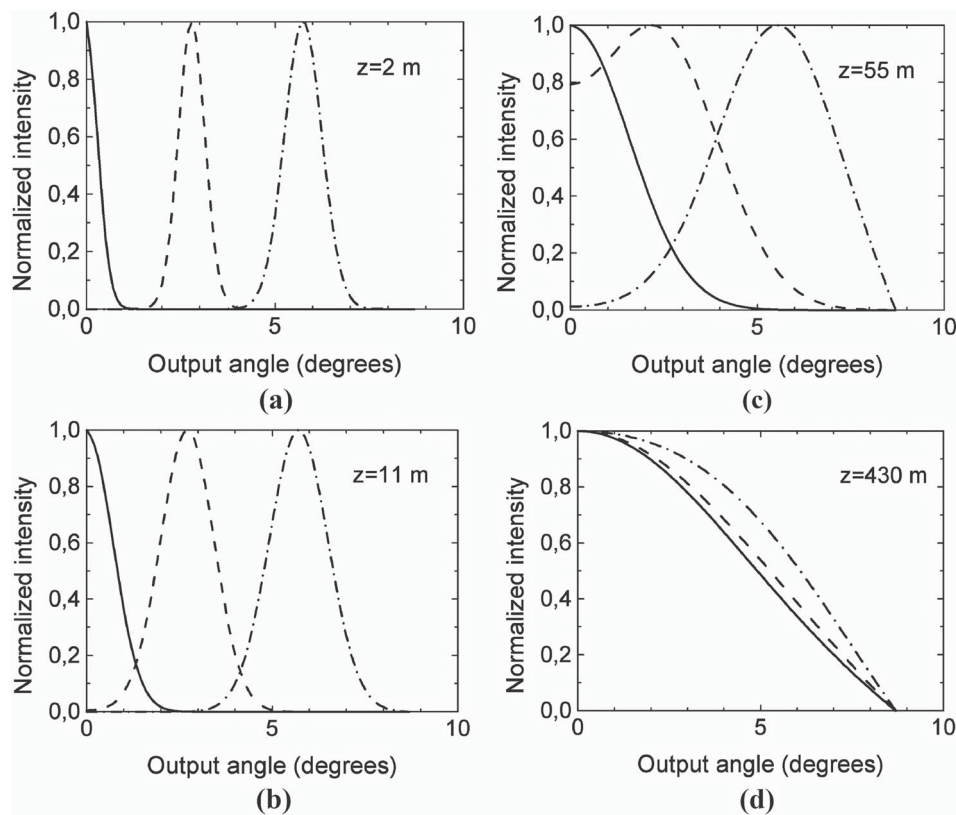


Figure 4. Normalized output angular power distribution at different locations along the 400/720 silica fibre with coupling coefficient $D = 6.4 \times 10^{-6} \text{ rad}^2/\text{m}$ calculated by numerical solving the power flow equation for three Gaussian input angles $\theta_0 = 0^\circ$ (solid line), 3° (dashed line) and 6° (dash-dotted line) with $(\text{FWHM})_{z=0} = 0.127^\circ$ for: (a) $z = 2 \text{ m}$; (b) $z = 11 \text{ m}$; (c) $z = 55 \text{ m}$ and (d) $z = 430 \text{ m}$.

Table 1. Length z_{SDM} for two and three spatially multiplexed channels with minimal crosstalk in SI SOFs with different mode coupling coefficient D measured at $\lambda = 633 \text{ nm}$. L_c is the coupling length at which the equilibrium mode distribution is achieved.

Fibre type	$D \text{ (rad}^2/\text{m)}$	$z_{SDM} \text{ (m) (2-channel)}$	$z_{SDM} \text{ (m) (3-channel)}$	$L_c \text{ (m)}$
100/660	4.9×10^{-7}	540	120	5400
200/745	1.9×10^{-6}	150	40	1380
400/720	6.4×10^{-6}	45	11	430

can be realized up to $z_{SDM} \approx 45$ and 12 m , respectively, which is consistent with results for 100/660, 200/745 and 400/720 fibre at $\lambda = 633 \text{ nm}$.

To conclude, for the current case study, decreasing the core/clad diameter ratio has resulted in the decrease of the measured mode coupling strength D , and the increase of the calculated z_{SDM} , indicating the efficient length for spatial multiplexing, which is useful for long distance communication. An optical fibre with weaker mode coupling is better choice for SDM. Such characterization of optical fibres should be considered in designing an optical fibre transmission system with space division multiplexing. A number of co-propagating optical channels in optical fibres can be increased by choosing an optical fibre with larger NA and keeping a reasonable large input

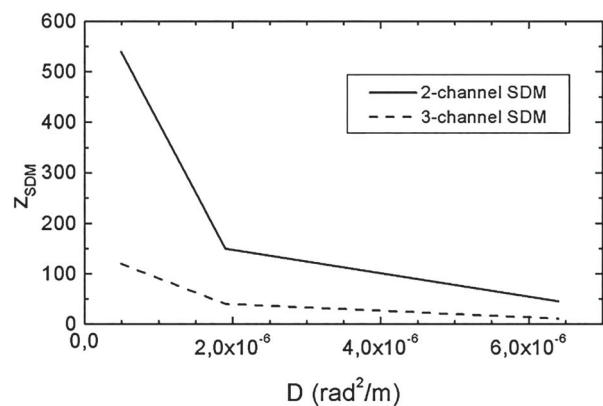


Figure 5. Length z_{SDM} for two and three spatially multiplexed channels with minimal crosstalk in SI SOFs as a function of mode coupling coefficient D measured at $\lambda = 633 \text{ nm}$.

angular separation between the channels (the angular separation between the optical channels should be at least 3° for typical laser launching beam [6]). As comparison, the spatial multiplexing capabilities of the co-propagating optical channels in SOFs for long distance applications analysed in this work are richer than in the plastic optical fibres, due to higher mode coupling and faster modal equilibration ($D \approx 10^{-4} \text{ rad}^2/\text{m}$; $L_c \approx 20\text{--}50 \text{ m}$) in the

latter (18,19). In contrast, the spatial multiplexing capability of POFs is larger than that of SOFs at short distances due to larger NA of POFs than that of SOFs (19).

4. Conclusion

The influence of mode coupling on space division multiplexing in three multimode step-index silica optical fibres with numerical aperture $NA = 0.22$ and different strengths of mode coupling is investigated by solving the power flow equation. We have shown that mode coupling significantly limits the length of silica optical fibres at which the space division multiplexing with two and three co-propagating optical channels can be realized with minimal crosstalk between the neighbour optical channels. This limitation is most pronounced in silica optical fibre with the strongest mode coupling. An optical fibre with weaker mode coupling is better choice for SDM. Such characterization of optical fibres should be considered in designing an optical fibre transmission system with space division multiplexing.

Disclosure statement

No potential conflict of interest was reported by the authors.

Funding

The work described in this paper was supported by the Strategic Research Grant of City University of Hong Kong [Project No. CityU 7004600] and by a grant from Ministry of Education, Science and Technological Development of the Republic of Serbia [Project No. 171011].

ORCID

Svetislav Savović  <http://orcid.org/0000-0002-9038-2393>

References

- (1) Richardson, D.; Fini, J.; Nelson, L. Space-division Multiplexing in Optical Fibres. *Nat. Photonics* **2013**, *7*, 354–362.
- (2) Ding, Y.; Zou, Y.; Jin, L.; Chen, H.; Ma, X. Fiber-coupled High Power Laser Diode by Wavelength Multiplexing. *Proceedings of the Photoelectronic Technology Committee Conferences: Optical Imaging, Remote Sensing, and Laser-Matter Interaction*, SuZhou, July–December 2013, 91420G, 2014.
- (3) Winzer, P.J. Optical Networking Beyond WDM. *IEEE Photon. J.* **2012**, *4*, 647–651.
- (4) Li, G.; Bai, N.; Zhao, N.; Xia, C. Space-division Multiplexing: The Next Frontier in Optical Communication. *Adv. Opt. Photonics* **2014**, *6*, 413–487.
- (5) Brunet, C.; Ung, B.; Belanger, P.-A.; Messaddeq, Y.; LaRochelle, S.; Rusch, L.A. Vector Mode Analysis of Ring-core Fibers: Design Tools for Spatial Division Multiplexing. *J. Lightwave Technol.* **2014**, *32*, 4046–4057.
- (6) Murshid, S.; Grossman, B.; Narakorn, P. Spatial Domain Multiplexing: A New Dimension in Fiber Optic Multiplexing. *Opt. Laser Technol.* **2008**, *40*, 1030–1036.
- (7) Labroille, G.; Denolle, B.; Jian, P.; Genevaux, P.; Treps, N.; Morizur, J.-F. Efficient and Mode Selective Spatial Mode Multiplexer Based on Multi-plane Light Conversion. *Opt Express* **2014**, *22*, 15599–15607.
- (8) Yan, Y.; Wang, J.; Zhang, L.; Yang, J.-Y.; Fazal, I.; Ahmed, N.; Shamee, B.; Willner, A.; Birnbaum, K.; Choi, J.; Erkmen, B.; Dolinar, S. New Approach for Generating and (De)multiplexing Oam Modes in a Fiber Coupler Consisting of a Central Ring and Four External Cores. *37th European Conference and Exhibition Optical Communication (ECOC) 2011*, Sep. 2011, pp. 1–3.
- (9) Murshid, S.H.; Chakravarty, A.; Biswas, R. Attenuation and Modal Dispersion Models for Spatially Multiplexed Co-propagating Helical Optical Channels in Step Index Fibers. *Opt. Laser Technol.* **2011**, *43*, 430–436.
- (10) Gloge, D. Optical Power Flow in Multimode Fibers. *Bell Syst. Tech. J.* **1972**, *51*, 1767–1783.
- (11) Garito, A.F.; Wang, J.; Gao, R. Effects of Random Perturbations in Plastic Optical Fibers. *Science* **1998**, *281*, 962–967.
- (12) Hurand, S.; Chauny, L.-A.; El-Rabii, H.; Joshi, S.; Yalin, A. Mode Coupling and Output Beam Quality of 100–400 μm Core Silica Fibers. *Appl. Opt.* **2011**, *50*, 492–499.
- (13) Gambling, W.A.; Payne, D.N.; Matsumura, H. Mode Conversion Coefficients in Optical Fibers. *Appl. Opt.* **1975**, *14*, 1538–1542.
- (14) Rousseau, M.; Jeunhomme, L. Numerical Solution of the Coupled-power Equation in Step Index Optical Fibers. *IEEE Trans. Microwave Theory Tech.* **1977**, *25*, 577–585.
- (15) Djordjevich, A.; Savović, S. Investigation of Mode Coupling in Step Index Plastic Optical Fibers Using the Power Flow Equation. *IEEE Photon. Technol. Lett.* **2000**, *12*, 1489–1491.
- (16) Savović, S.; Djordjevich, A.; Simović, A.; Drljača, B. Equilibrium Mode Distribution and Steady-state Distribution in 100–400 μm Core Step-index Silica Optical Fibers. *Appl. Opt.* **2011**, *50*, 4170–4173.
- (17) Savović, S.; Djordjevich, A.; Drljača, B.; Simović, A. Equilibrium Mode Distribution and Steady State Distribution in Step Index Glass Optical Fibers. *Acta Phys. Polonica A* **2009**, *116*, 655–657.
- (18) Appaiah, K.; Salas, R.; Vishwanath, S.; Bank, S.R. Offset Coupling, Feedback, and Spatial Multiplexing in 4×4 Incoherent-MIMO Multimode Fiber Links. *J. Lightwave Technol.* **2013**, *31*, 2926–2939.
- (19) Savović, S.; Djordjevich, A.; Simović, A.; Drljača, B. Influence of Mode Coupling on Spatially Multiplexed Channels in Multimode Step-index Plastic Optical Fibers. *Opt. Laser Technol.* **2018**, *106*, 18–21.

РАНИЈИ ПЕРИОД

Equilibrium mode distribution and steady-state distribution in 100–400 μm core step-index silica optical fibers

Svetislav Savović,^{1,2,*} Alexandar Djordjevich,¹ Ana Simović,² and Branko Drljača²

¹City University of Hong Kong, 83 Tat Chee Avenue, Kowloon, Hong Kong, China

²University of Kragujevac, Faculty of Science, R. Domanovića 12, 34000 Kragujevac, Serbia

*Corresponding author: savovic@kg.ac.rs

Received 4 April 2011; accepted 20 June 2011;
posted 22 June 2011 (Doc. ID 145334); published 19 July 2011

Using the power flow equation, the state of mode coupling in 100–400 μm core step-index silica optical fibers is investigated in this article. Results show the coupling length L_c at which the equilibrium mode distribution is achieved and the length z_s of the fiber required for achieving the steady-state mode distribution. Functional dependences of these lengths on the core radius and wavelength are also given. Results agree well with those obtained using a long-established calculation method. Since large core silica optical fibers are used at short distances (usually at lengths of up to 10 m), the light they transmit is at the stage of coupling that is far from the equilibrium and steady-state mode distributions. © 2011 Optical Society of America

OCIS codes: 060.2310, 060.2400.

1. Introduction

For decades, glass optical fibers (GOFs) have been the preferred transmission medium in high-capacity communications networks and long-distance communications systems [1]. Graded index multimode GOFs are used for 0–300 m 10 Gb Ethernet links or 0–100 m 40–100 Gb Ethernet links. Step-index (SI) multimode GOFs are often used for laser beam delivery, sensing systems, as part of lane control signal equipment, etc. For laser delivery, it is desirable to use relatively large core (200–500 μm core radius) silica optical fibers for transmission of high-power laser pulses with high beam quality [2]. On the other hand, multimode plastic optical fibers are usually considered for short data links (<100 m). Local networking with plastic optical fibers benefits from the rapid (less laborious) interconnectivity with low-precision and low-cost components as plastic optical fibers couple light efficiently due to their large

diameter ($\sim 1\text{ mm}$) and high numerical aperture. However, plastic optical fiber performance is clearly attenuation limited. A typical attenuation level for SI plastic optical fibers is $\sim 100\text{ dB/km}$ —compared with $\sim 0.5\text{ dB/km}$ for SI GOFs [3]. This limits plastic optical fiber data links to lengths shorter than 100 m.

Transmission characteristics of SI optical fibers depend heavily upon the differential mode attenuation and rate of mode coupling. The latter represents power transfer from lower- to higher-order modes caused by fiber impurities and inhomogeneities introduced during the fiber manufacturing process (such as microscopic bends, irregularity of the core-cladding boundary, and refractive index distribution fluctuations). When installing an optical-fiber-based link, the cable has to be bent repeatedly, thus increasing radiation losses [4,5].

Output angular power distribution in the near and far fields of an optical fiber end has been studied extensively. Work has been reported using geometric optics (ray approximation) to investigate mode coupling and predict output-field patterns [6,7]. By employing the power flow equation [8–12] as well as the

Fokker–Planck and Langevin equations [13], these patterns have been predicted as a function of the launch conditions and fiber length. A key prerequisite for achieving this is the knowledge of the rate of mode coupling expressed in the form of the coupling coefficient D [8–10], which has been shown to correctly predict coupling effects observed in practice (e.g., [14]).

The method of determining the coupling coefficient D proposed by Gambling *et al.* [8] required that the far-field output pattern be observed for various fiber lengths and at different launch angles. Only one fiber length and two launch angles must be considered in the method by Zubía *et al.* [15]. It determines the coupling coefficient D from the intersection point between two far-field output patterns that correspond to the two launch angles. A further alternative is Savović–Djordjević method [16], which determines the mode coupling coefficient D from just one far-field output pattern. This single pattern is for the input Gaussian beam launched along the fiber axis. The variance of the launch-beam distribution has to be known, which is usually the case. Should it not be known, variances of the far-field output patterns at two fiber lengths have to be measured.

Hurand *et al.* [2] have employed Savović–Djordjević method of determining the coupling coefficient D [16] in their investigation of mode coupling in SI silica optical fibers with core diameters of 100–400 μm and lengths of 2 m for central launch beam $\theta_0 = 0$. In this work, using the power flow equation, we extend their work and examine the state of mode coupling in SI silica optical fibers with core diameters of 100 μm , 200 μm , and 400 μm and lengths of kilometers, both for central launch beam $\theta_0 = 0$ as well as for a launch beam with $\theta_0 > 0$. Furthermore, for 200 μm core SI silica optical fiber, a dependence of the output angular power distribution on fiber length is investigated for three wavelengths. As a result, the coupling length L_c at which the equilibrium mode distribution (EMD) is achieved and the length z_s of fiber required for achieving the steady-state mode distribution (SSD) are obtained. We compare our results with those obtained using a long-established calculation method [2,9].

2. Power Flow Equation

Gloge’s power flow equation is [9]

$$\frac{\partial P(\theta, z)}{\partial z} = -\alpha(\theta)P(\theta, z) + \frac{D}{\theta} \frac{\partial}{\partial \theta} \left(\theta \frac{\partial P(\theta, z)}{\partial \theta} \right), \quad (1)$$

where $P(\theta, z)$ is the angular power distribution, z is the distance from the input end of the fiber, θ is the propagation angle with respect to the core axis, D is the coupling coefficient assumed constant [8,9,12], and $\alpha(\theta)$ is the modal attenuation. The boundary conditions are $P(\theta_c, z) = 0$, where θ_c is the critical angle of the fiber and $D(\partial P/\partial \theta) = 0$ at $\theta = 0$. Condition $P(\theta_c, z) = 0$ implies that modes with infinitely high loss do not carry power. Condition $D(\partial P/\partial \theta) = 0$ at

$\theta = 0$ indicates that the coupling is limited to the modes propagating with $\theta > 0$. Except near cutoff, the attenuation remains uniform $\alpha(\theta) = \alpha_0$ throughout the region of guided modes $0 \leq \theta \leq \theta_c$ [10,11] [it appears in the solution as the multiplication factor $\exp(-\alpha_0 z)$ that also does not depend on θ]. Therefore, $\alpha(\theta)$ need not be accounted for when solving Eq. (1) for mode coupling, and this equation reduces to [12]

$$\frac{\partial P(\theta, z)}{\partial z} = \frac{D}{\theta} \frac{\partial P(\theta, z)}{\partial \theta} + D \frac{\partial^2 P(\theta, z)}{\partial \theta^2}. \quad (2)$$

The solution of Eq. (2) for the steady-state power distribution is given by [10]

$$P(\theta, z) = J_0 \left(2.405 \frac{\theta}{\theta_c} \right) \exp(-\gamma_0 z), \quad (3)$$

where J_0 is the Bessel function of the first kind and zero order and $\gamma_0 [\text{m}^{-1}] = 2.405^2 D/\theta_c^2$ is the attenuation coefficient. We used this solution to test our numerical results for the case of the fiber length at which the power distribution becomes independent of the launch conditions. This length at which a steady-state distribution is achieved can be obtained using Eq. (4) [2,9]:

$$z_s = \frac{0.2}{D} \left(\frac{\text{NA}}{n} \right)^2, \quad (4)$$

where n is the refractive index of the core and NA is numerical aperture of the fiber.

In order to obtain numerical solution of the power flow Eq. (2) we have used the explicit finite-difference method (EFDM) employed in our earlier works [12,17]. To start the calculations, we used Gaussian launch-beam distribution of the form

$$P(\theta, z) = \exp \left[-\frac{(\theta - \theta_0)^2}{2\sigma^2} \right], \quad (5)$$

with $0 \leq \theta \leq \theta_c$, where θ_0 is the mean value of the incidence angle distribution, with the full width at half-maximum $\text{FWHM} = 2\sigma\sqrt{2\ln 2} = 2.355\sigma$ (σ is standard deviation). This distribution is suitable both for LED and laser beams (LED distribution can also be described by a Lambertian source).

3. Results and Discussion

In this paper, we analyze mode coupling in relatively large core SI silica optical fibers used in the experiment reported recently [2]. The first fiber has core diameter $d_{\text{core}} = 100 \mu\text{m}$ and clad diameter $d_{\text{clad}} = 660 \mu\text{m}$ (100/660 fiber), the second fiber has $d_{\text{core}} = 200 \mu\text{m}$ and clad diameter $d_{\text{clad}} = 745 \mu\text{m}$ (200/745 fiber), while the third fiber has core diameter $d_{\text{core}} = 400 \mu\text{m}$ and clad diameter $d_{\text{clad}} = 720 \mu\text{m}$ (400/720 fiber). All fibers have $\text{NA} = 0.22$, core refractive index $n = 1.4570$ at $\lambda = 633 \text{ nm}$, and critical angle $\theta_c = 8.8^\circ$. Fiber samples with a length of 2 m were tested

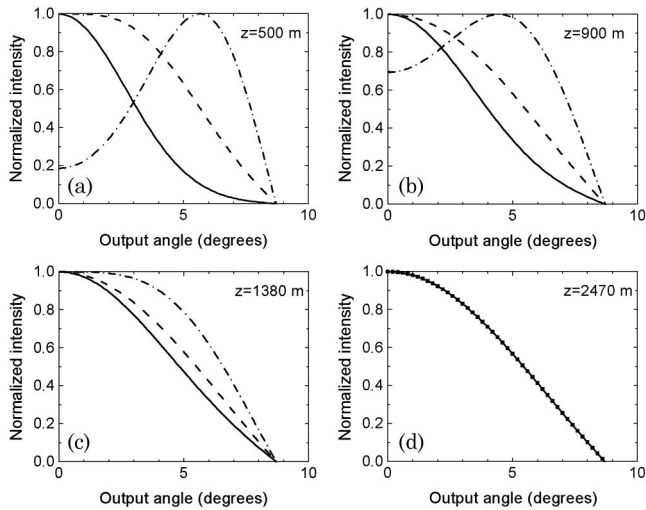


Fig. 1. Normalized output angular power distribution at different locations along the 200/745 silica fiber calculated for three Gaussian input angles $\theta_0 = 0^\circ$ (solid curve), 4° (dashed curve), and 8° (dotted–dashed curve) with $(\text{FWHM})_{z=0} = 0.127^\circ$ for (a) $z = 500$ m, (b) $z = 900$ m, (c) $z = 1380$ m, and (d) $z = 2470$ m (solid squares represent the analytical steady-state solution).

to obtain their mode coupling properties under the excitation of only a small number of modes, which is realized by a narrow (with standard deviation $\sigma_0 = 0.054^\circ$) centrally launched beam [2]. By measuring the standard deviation of the output angular power distribution at the end of the fiber and using the relation for mode coupling coefficient $D = (\sigma_z^2 - \sigma_0^2)/2z$ [16], Hurand *et al.* [2] obtained $D = 4.9 \times 10^{-7} \text{ rad}^2/\text{m}$ for 100/600 fiber, $D = 1.9 \times 10^{-6} \text{ rad}^2/\text{m}$ for 200/745 fiber, and $D = 6.4 \times 10^{-6} \text{ rad}^2/\text{m}$ for 400/720 fiber at $\lambda = 633 \text{ nm}$ —which we have adopted in this work.

In Fig. 1, our numerical solution of the power flow equation is presented by showing the evolution of the normalized output power distribution with fiber length for 200/745 fiber at $\lambda = 633 \text{ nm}$. We show results for three different input angles $\theta_0 = 0^\circ$, 4° , and 8° . We selected Gaussian launch-beam distribution with $(\text{FWHM}_0) = 0.127^\circ$ by setting $\sigma_0 = 0.054^\circ$ in Eq. (5). Using the step lengths of $\Delta\theta = 0.1^\circ$ and $\Delta z = 0.02 \text{ m}$, we have achieved the stability of our finite-difference scheme. Since a truncation error for our explicit finite-difference scheme is $O(\Delta z, \Delta\theta^2)$ [18], using a small enough value of Δz , the truncation errors were reduced until the accuracy achieved was within the error tolerance.

Radiation patterns in the short fiber ($z = 500$ m) in Fig. 1(a) indicate that the coupling is stronger for the low-order modes: their distributions have shifted toward $\theta = 0^\circ$. Coupling of higher-order modes can be observed better only after longer fiber lengths [Fig. 1(b)]. It is not until the fiber's coupling length L_c that all the mode distributions shift their mid-points to 0° (from the initial value of θ_0 at the input fiber end), producing the EMD in Fig. 1(c): L_c is 1380 m. The coupling continues further along the fiber beyond the L_c mark until all distributions' widths equalize and SSD is reached at length z_s in Fig. 1(d): $z_s = 2470$ m. For the 200/745 fiber, Fig. 1(d) shows normalized curves of the output angular distribution obtained by solving the power flow equation using the EFDM (solid curve) as well as the steady-state analytical solution of Eq. (2) (solid squares), where $\gamma_0 = 0.00047 \text{ m}^{-1}$. The two are in good agreement, with the relative error below 0.8%. In the same manner, we obtained $L_c = 5400$ m and $z_s = 9600$ m for the 100/600 fiber and $L_c = 430$ m and $z_s = 730$ m for the 400/720 fiber. In order to test the accuracy of results, we compared z_s with theoretical values determined by function (4), which are $z_s = 9306$ m for the 100/600 fiber, $z_s = 2400$ m for the 200/745 fiber, and $z_s = 712$ m for the 400/720 fiber. The relevant values are summarized in Table 1 to facilitate easier comparisons. Good agreement is apparent between our numerically obtained values for z_s and theoretical predictions by Gloge's function. One can observe that mode coupling coefficients varied as $\sim d_{\text{core}}^{1.85}$. The increase of mode coupling coefficient (rate of mode coupling) with core diameter is due to a simultaneous decrease of angular separation between adjacent modes $\Delta\theta = \lambda/(2d_{\text{core}}n)$. As a consequence, the coupling length L_c where the equilibrium mode distribution is achieved and length z_s where steady-state distribution is established decrease with increasing core diameter.

Hurand *et al.* [2] studied 200/745 fiber for two other wavelengths ($\lambda = 403$ and 1064 nm). The measured coupling coefficients are $D = 2.4 \times 10^{-6}$ and $1.5 \times 10^{-6} \text{ rad}^2/\text{m}$ at $\lambda = 403$ and 1064 nm , respectively. By adopting these two values for D , we solved the power flow equation numerically in order to investigate how wavelength influences characteristic fiber lengths, L_c and z_s . We obtained that $L_c = 1090$ m, $z_s = 1910$ m at $\lambda = 403 \text{ nm}$ and $L_c = 1800$ m, $z_s = 3170$ m at $\lambda = 1064 \text{ nm}$. Using Gloge's function, we obtain $z_s = 1866$ m at $\lambda = 403 \text{ nm}$ and $z_s = 3069$ m at $\lambda = 1064 \text{ nm}$ (core refractive index

Table 1. Core Diameter, Clad Diameter, Coupling Coefficient D , Coupling Length L_c , and Length z_s for Silica Fibers at $\lambda = 633 \text{ nm}$ ^a

Core Diameter (μm)	Clad Diameter (μm)	D (rad^2/m)	L_c (m) (Numerical Results)	z_s (m) (Numerical Results)	z_s (m) [Analytical Results, Eq. (4)]
100	600	4.9×10^{-7}	5400	9600	9306
200	745	1.9×10^{-6}	1380	2470	2400
400	720	6.4×10^{-6}	430	730	712

^aValues for D are those determined by Hurand *et al.* [2].

Table 2. Coupling Coefficient D , Coupling Length L_c , and Length z_s at Different Wavelengths λ for 200/745 Silica Fiber^a

λ (nm)	D (rad ² /m)	L_c (m) (Numerical Results)	z_s (m) (Numerical Results)	z_s (m) [Analytical Results, Eq. (4)]
403	2.4×10^{-6}	1090	1910	1866
633	1.9×10^{-6}	1380	2470	2400
1064	1.5×10^{-6}	1800	3170	3069

^aValues for D are those determined by Hurand *et al.* [2].

$n = 1.4703$ at $\lambda = 403$ nm and $n = 1.4502$ at $\lambda = 1064$ nm are assumed in the calculations). For three wavelengths mentioned, the relevant numerical values are summarized in Table 2 to facilitate easier comparisons. A good agreement is again apparent between our numerically obtained values for z_s and theoretical predictions obtained using Gloge's function [4]. One can observe that mode coupling coefficients varied as $\sim \lambda^{-1/2}$. The decrease of the mode coupling coefficient with increasing wavelength is due to the simultaneous increase of angular separation between adjacent modes $\Delta\theta = \lambda/(2d_{\text{core}}n)$. As a consequence, the coupling length L_c where the equilibrium mode distribution is achieved and length z_s where steady-state distribution is established increase with increasing wavelength. Similar wavelength dependence $\sim \lambda^{-1/3}$ is obtained for chalcogenide-glass SI optical fiber, for which coupling length is even larger ($L_c \approx 13$ to 20 km) [19]. The coupling coefficients of the SI silica optical fibers that were analyzed are 2 orders of magnitude lower than for SI plastic optical fibers (typically $\approx 10^{-4}$ rad²/m). Consequently, the coupling length L_c and length z_s are much shorter ($L_c \approx 15$ to 35 m, $z_s = 45$ to 100 m) [20]. This is attributed to strong intrinsic perturbation effects in plastic optical fibers.

Finally, we conclude that, since large core silica optical fibers are used at short distances (usually at lengths of up to ten meters), the light they transmit is at the stage of coupling that is far from the equilibrium and steady-state mode distributions.

4. Conclusion

A solution is reported of the power flow equation employed to investigate the state of mode coupling along large core SI silica optical fibers. Results have been verified against the analytical solution for the steady-state coupling condition. Coupling lengths and lengths for achieving the steady-state distribution are shown to decrease with increasing the core radius. On the other hand, they increase with increasing the wavelength. Since these fibers are used at short distances (usually at lengths of up to ten meters), the light they transmit is at a stage of coupling that is far from the equilibrium or steady-state mode distributions. These results are of interest in predicting the transmission properties of large core SI silica optical fibers used for power delivery and sensing systems.

The work described in this paper was supported by a grant from the Serbian Ministry of Science and Technological Development (project 171011).

References

1. L. Jeunhomme and J. P. Pocholle, "Experimental determination of the radiation pattern of optical fibres," *Opt. Commun.* **12**, 89–92 (1974).
2. S. Hurand, L.-A. Chauny, H. El-Rabii, S. Joshi, and A. Yalin, "Mode coupling and output beam quality of 100–400 μm core silica fibers," *Appl. Opt.* **50**, 492–499 (2011).
3. W. Daum, J. Krauser, P. E. Zamzow, and O. Ziemann, *POF—Polymer Optical Fibers for Data Communications* (Springer, 2002).
4. J. Arrúe, J. Zubía, G. Fuster, and D. Kalymnios, "Light power behaviour when bending plastic optical fibres," *IEE Proc. Optoelectron.* **145**, 313–318 (1998).
5. M. A. Losada, J. Mateo, I. Garcés, J. Zubía, J. A. Casao, and P. Pérez-Vela, "Analysis of strained plastic optical fibers," *IEEE Photon. Technol. Lett.* **16**, 1513–1515 (2004).
6. M. Eve and J. H. Hannay, "Ray theory and random mode coupling in an optical fibre waveguide, I," *Opt. Quantum Electron.* **8**, 503–508 (1976).
7. J. Arrue, G. Aldabaldetrekú, G. Durana, J. Zubía, I. Garcés, and F. Jiménez, "Design of mode scramblers for step-index and graded-index plastic optical fibers," *J. Lightwave Technol.* **23**, 1253–1260 (2005).
8. W. A. Gambling, D. N. Payne, and H. Matsumura, "Mode conversion coefficients in optical fibers," *Appl. Opt.* **14**, 1538–1542 (1975).
9. D. Gloge, "Optical power flow in multimode fibers," *Bell Syst. Tech. J.* **51**, 1767–1783 (1972).
10. M. Rousseau and L. Jeunhomme, "Numerical solution of the coupled-power equation in step index optical fibers," *IEEE Trans. Microwave Theor. Tech.* **25**, 577–585 (1977).
11. L. Jeunhomme, M. Fraise, and J. P. Pocholle, "Propagation model for long step-index optical fibers," *Appl. Opt.* **15**, 3040–3046 (1976).
12. A. Djordjevich and S. Savović, "Investigation of mode coupling in step index plastic optical fibers using the power flow equation," *IEEE Photon. Technol. Lett.* **12**, 1489–1491 (2000).
13. S. Savović and A. Djordjevich, "Solution of mode coupling in step-index optical fibers by the Fokker–Planck equation and the Langevin equation," *Appl. Opt.* **41**, 2826–2830 (2002).
14. A. F. Garito, J. Wang, and R. Gao, "Effects of random perturbations in plastic optical fibers," *Science* **281**, 962–967 (1998).
15. J. Zubía, G. Durana, G. Aldabaldetrekú, J. Arrúe, M. A. Losada, and M. López-Higuera, "New method to calculate mode conversion coefficients in SI multimode optical fibers," *J. Lightwave Technol.* **21**, 776–781 (2003).
16. S. Savović and A. Djordjevich, "Method for calculating the coupling coefficient in step index optical fibers," *Appl. Opt.* **46**, 1477–1481 (2007).
17. S. Savović and A. Djordjevich, "Influence of numerical aperture on mode coupling in step-index plastic optical fibers," *Appl. Opt.* **43**, 5542–5546 (2004).
18. J. D. Anderson, *Computational Fluid Dynamics* (McGraw-Hill, 1995).
19. S. Savović and A. Djordjevich, "Mode coupling in chalcogenide-glass optical fibers," *Opt. Lasers Eng.* **49**, 855–858 (2011).
20. S. Savović and A. Djordjevich, "Mode coupling in strained and unstrained step-index plastic optical fibers," *Appl. Opt.* **45**, 6775–6780 (2006).

Mode coupling in strained and unstrained step-index glass optical fibers

Alexandar Djordjevich,¹ Svetislav Savović,^{1,2,*} Peter W. Tse,¹
Branko Drijača,² and Ana Simović²

¹City University of Hong Kong, 83 Tat Chee Avenue, Kowloon, Hong Kong, China

²Faculty of Science, R. Domanovića 12, 34000 Kragujevac, Serbia

*Corresponding author: savovic@kg.ac.rs

Received 26 April 2010; revised 9 August 2010; accepted 13 August 2010;
posted 17 August 2010 (Doc. ID 127589); published 14 September 2010

By using the power flow equation, we have examined the state of mode coupling in strained and unstrained step-index glass optical fibers. Strained fibers show stronger mode coupling than their unstrained counterparts of the same type. As a result, the coupling length where equilibrium mode distribution is achieved and the length of fiber required for achieving the steady-state mode distribution are shorter for strained than for unstrained fibers. © 2010 Optical Society of America
OCIS codes: 060.2310, 060.2400.

1. Introduction

For decades, glass optical fibers (GOFs) have been the preferred transmission medium in high-capacity communications networks and long-distance communications systems. Graded-index multimode GOFs are used for 0–300 m 10 GB Ethernet links or 0–100 m 40–100 GB Ethernet links. Step-index (SI) multimode GOFs are often used for laser beam delivery, sensory systems, as a part of lane control signal equipment, etc. On the other hand, multimode plastic optical fibers (POFs) are usually considered for short data links (<100 m). Local networking with POFs benefits from the rapid (less laborious) interconnectivity with low precision and cost components, as POFs couple light efficiently due to their large diameter (~1 mm) and high numerical aperture. However, POF performance is clearly attenuation limited. A typical attenuation level for SI POFs is ~100 dB/km, compared with ~0.5 dB/km for SI GOFs [1]. This limits POF data links to lengths shorter than 100 m.

The transmission characteristics of SI optical fibers depend heavily upon the differential mode

attenuation and rate of mode coupling. The latter represents power transfer from lower- to higher-order modes caused by fiber impurities and inhomogeneities introduced during the fiber manufacturing process (such as microscopic bends, irregularity of the core-cladding boundary, and refractive index distribution fluctuations). When installing an optical-fiber-based link, the cable has to be bent repeatedly, thus increasing radiation losses [2]. An increase in mode coupling induced by bending strain has been observed, and can become permanent if the fibers are subjected to repeated bending or are bent for a long time [3,4]. Such increase could be explained by microscopic changes in the fiber. In this work, the fibers altered by bending we call “strained fibers” and compare their properties to those of unstrained fibers.

The output angular power distribution in the near and far fields of an optical fiber end has been studied extensively. Work has been reported using geometric optics (ray approximation) to investigate mode coupling and predict output-field patterns [5,6]. By employing the power flow equation [7–11], as well as the Fokker–Planck and Langevin equations [12], these patterns have been predicted as a function of the launch conditions and fiber length. A key

prerequisite for achieving this is the knowledge of the rate of mode coupling expressed in the form of the coupling coefficient D [7,8], which has been shown to correctly predict coupling effects observed in practice [13].

The method of determining the coupling coefficient D proposed by Gambling *et al.* [7] required that the far-field output pattern be observed for various fiber lengths and at different launch angles. Only one fiber length and two launch angles must be considered in the method proposed by Zubía *et al.* [14]. It determines the coupling coefficient D from the intersection point between two far-field output patterns that correspond to the two launch angles. A further alternative is our recent method [15], which determines the mode coupling coefficient D from just one far-field output pattern. This single pattern is for the input beam launched along the fiber axis. The variance of the launch-beam distribution has to be known, which is usually the case. Should it not be known, variances of the far-field output patterns at two fiber lengths have to be measured.

Our recently proposed method of determining the coupling coefficient D [15] has been employed for unstrained and strained plastic optical fibers (POFs) [15,16] and for unstrained GOF [17]. In this work, we apply this method for the first time to strained SI GOF. The coupling coefficient D (hence the rate of mode coupling) is orders of magnitude smaller in glass than in plastic fibers (typically $D \approx 10^{-7} - 10^{-6} \text{ rad}^2/\text{m}$ versus $D \approx 10^{-4} \text{ rad}^2/\text{m}$, respectively [10,17,18]), leading to vastly longer coupling lengths (a few kilometers versus tens of meters). Because the distances for numerical integration are of different orders of magnitude, we believe it would be necessary to test the validity of the method both for strained and unstrained glass fibers. We verified this by reference to published experimental results [4]. To do so, we had to solve the power flow equation to determine the coupling characteristic of strained and unstrained glass fibers.

2. Power Flow Equation

Gloge's power flow equation is [8]

$$\frac{\partial P(\theta, z)}{\partial z} = -\alpha(\theta)P(\theta, z) + \frac{D}{\theta} \frac{\partial}{\partial \theta} \left(\theta \frac{\partial P(\theta, z)}{\partial \theta} \right), \quad (1)$$

where $P(\theta, z)$ is the angular power distribution, z is the distance from the input end of the fiber, θ is the propagation angle with respect to the core axis, D is the coupling coefficient assumed constant [7,8,11], and $\alpha(\theta)$ is the modal attenuation. The boundary conditions are $P(\theta, z) = 0$, where θ_c is the critical angle of the fiber, and $D(\partial P/\partial \theta) = 0$ at $\theta = 0$. Condition $P(\theta_c, z) = 0$ implies that modes with infinitely high loss do not carry power. Condition $D(\partial P/\partial \theta) = 0$ at $\theta = 0$ indicates that the coupling is limited to the modes propagating with $\theta > 0$. Except near cutoff, the attenuation remains uniform $\alpha(\theta) = \alpha_0$ throughout the region of guided modes $0 \leq \theta \leq \theta_c$ [9,10] (it

appears in the solution as the multiplication factor $\exp(-\alpha_0 z)$ that also does not depend on θ). Therefore, $\alpha(\theta)$ need not be accounted for when solving Eq. (1) for mode coupling, and this equation reduces to [11]

$$\frac{\partial P(\theta, z)}{\partial z} = \frac{D}{\theta} \frac{\partial P(\theta, z)}{\partial \theta} + D \frac{\partial^2 P(\theta, z)}{\partial \theta^2}. \quad (2)$$

The solution of Eq. (2) for the steady-state power distribution is given by [9]

$$P(\theta, z) = J_0 \left(2.405 \frac{\theta}{\theta_c} \right) \exp(-\gamma_0 z), \quad (3)$$

where J_0 is the Bessel function of the first kind and zero order, and $\gamma_0 [\text{m}^{-1}] = 2.405^2 D/\theta_c^2$ is the attenuation coefficient. We used this solution to test our numerical results for the case of the fiber length at which the power distribution becomes independent of the launch conditions.

To obtain a numerical solution of the power flow equation [Eq. (2)], we have used the explicit finite-difference method (EFDm) employed in our earlier works [11,18]. To start the calculations, we used Gaussian launch-beam distribution of the form

$$P(\theta, z) = \exp \left[-\frac{(\theta - \theta_0)^2}{2\sigma^2} \right], \quad (4)$$

with $0 \leq \theta \leq \theta_c$, where θ_0 is the mean value of the incidence angle distribution, with the full width at half-maximum $\text{FWHM} = 2\sigma\sqrt{2 \ln 2} = 2.355\sigma$ (σ is standard deviation). This distribution is suitable both for LEDs and laser beams.

3. Method for Calculating the Coupling Coefficient in SI Optical Fibers

A simple method has been proposed recently [15] for calculating the coupling coefficient for SI fibers. It calls for the variance σ_z^2 of the output angular power distribution for light launched centrally along the fiber axis:

$$\sigma_z^2 = \sigma_0^2 + 2Dz, \quad (5)$$

where σ_0^2 is the variance of the launch-beam distribution and z is the coordinate along the fiber axis. From Eq. (5), the coupling coefficient D is

$$D = \frac{\sigma_z^2 - \sigma_0^2}{2z}. \quad (6)$$

In order to determine D from Eq. (6), one needs to determine the variance σ_z^2 of the output angular power distribution at an arbitrary length z along the fiber (the variance of the launch-beam distribution σ_0^2 has to be known).

If the variance of the launch-beam distribution σ_0^2 is not known, coupling coefficient D can be determined using the following relation:

$$D = \frac{\sigma_{z_2}^2 - \sigma_{z_1}^2}{2(z_2 - z_1)}, \quad (7)$$

where $\sigma_{z_1}^2$ and $\sigma_{z_2}^2$ are variances of the output angular power distribution measured at the fiber lengths $z_1 > 0$ and $z_2 > 0$, respectively.

4. Results and Discussion

In this paper, we analyze mode coupling in the SI GOF used in the experiment reported earlier [4]. This fiber's core diameter is $d = 90 \mu\text{m}$, core refractive index $n_1 = 1.46$, critical angle measured in air $\theta_c = 9^\circ$ (corresponding to inner critical angle of $\theta_c = 6^\circ$), with 12 dB/km of attenuation at $0.633 \mu\text{m}$. Fiber samples with homogenous bending strain (induced by winding) were tested to obtain their mode coupling properties. These were then compared to those of reference (unaltered) samples [4]. Jeunhomme and Pocholle [4] reported the measurements shown in Fig. 1 in experiments with the launch-beam standard deviation of the angular power distribution of $\sigma_0 = 0.36^\circ$ (e^{-1} divergence angle $W = 1^\circ$, $W = 1.18 \cdot \text{FWHM}$) and $\sigma_z = 5^\circ$ and 6° for the unstrained and strained fibers, respectively, for the beam at a fiber length of $z = 980 \text{ m}$. From Eq. (7), we have obtained the coupling coefficients of $D = 3.86 \times 10^{-6} \text{ rad}^2/\text{m}$ and $D = 5.57 \times 10^{-6} \text{ rad}^2/\text{m}$ for unstrained and strained fibers, respectively.

In Figs. 2 and 3, our numerical solution of the power flow equation is presented by showing the

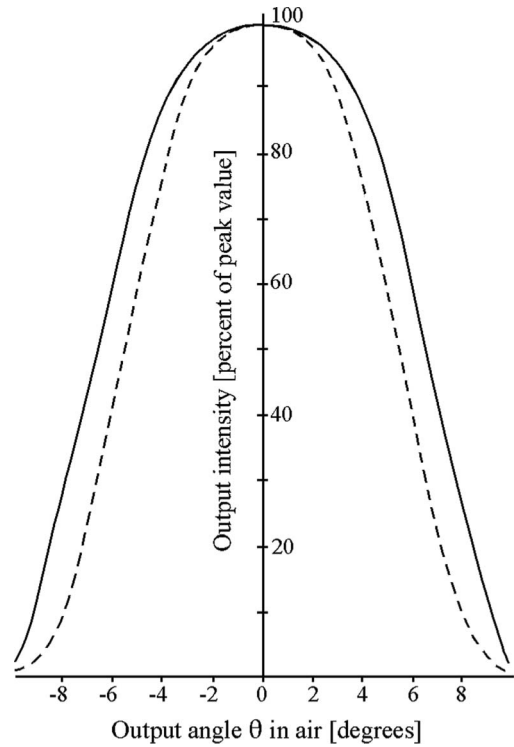


Fig. 1. Experimental output angular power distribution at fiber length $z = 980 \text{ m}$ for strained (solid curve) and unstrained (dashed curve) SI GOFs illuminated with a laser beam $(\text{FWHM})_{z=0} = 0.85^\circ$ parallel to the fiber axis, obtained by Jeunhomme and Pocholle [4].

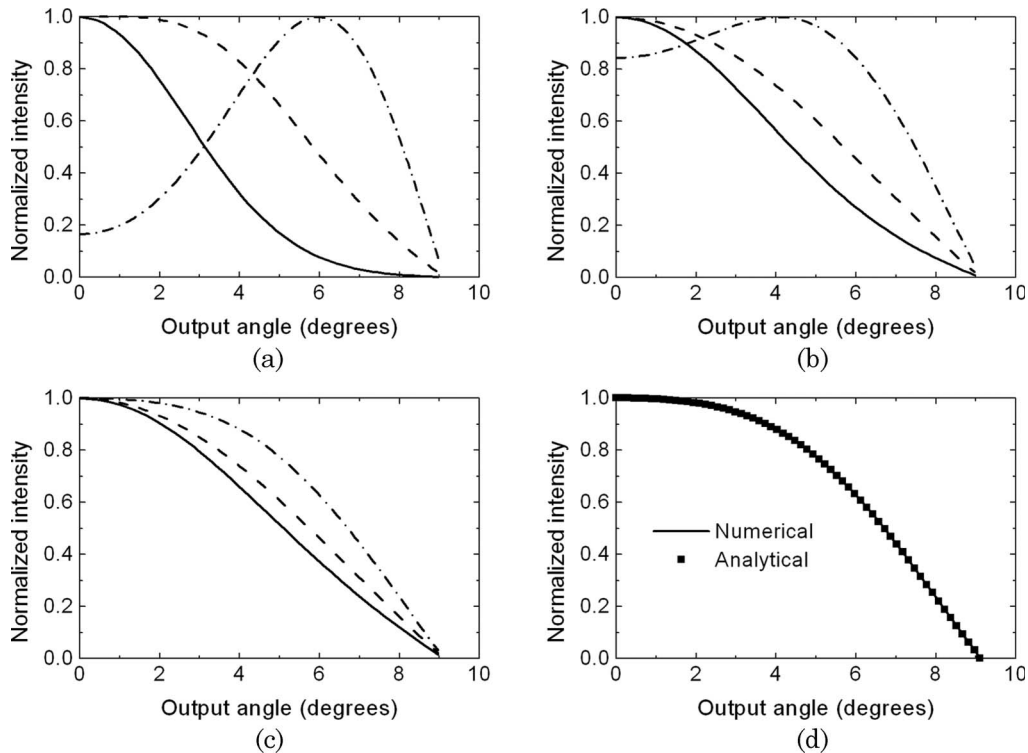


Fig. 2. Normalized output angular power distribution at different locations along the unstrained SI GOF calculated for three Gaussian input angles $\theta_0 = 0^\circ$ (solid curve), 4° (dashed curve), and 8° (dashed-dotted curve) with $(\text{FWHM})_{z=0} = 0.85^\circ$ for (a) $z = 120 \text{ m}$, (b) $z = 240 \text{ m}$, (c) $z = 340 \text{ m}$, and (d) $z = 1040 \text{ m}$ (filled squares represent the analytical steady-state solution).

evolution of the normalized output power distribution with fiber length for unstrained (Fig. 2) and strained (Fig. 3) SI GOF. We show results for three different input angles, $\theta_0 = 0^\circ$, 4° , and 8° measured in air (corresponding to input angles measured in fiber $\theta_0 = 0^\circ$, 2.7° , and 5.4°). We selected Gaussian launch-beam distribution with $(\text{FWHM})_0 = 0.85^\circ$ by setting $\sigma_0 = 0.36^\circ$ in Eq. (4). Using step lengths of $\Delta\theta = 0.1^\circ$ and $\Delta z = 0.01$ m, we have achieved the stability of our finite-difference scheme [19] for both unstrained and strained fibers. Since a truncation error for our explicit finite-difference scheme is $o(\Delta z, \Delta\theta^2)$, [19], by using a small enough value of Δz , the truncation errors were reduced until the accuracy achieved was within the error tolerance.

Radiation patterns in the short fiber ($z = 120$ m for unstrained and $z = 80$ m for strained fiber) in Figs. 2(a) and 3(a) indicate that the coupling is stronger for the low-order modes: their distributions have shifted toward $\theta = 0^\circ$. Coupling of higher-order modes can be observed better only after longer fiber lengths [Figs. 2(b) and 3(b)]. It is not until the fiber's coupling length L_c that all the mode-distributions shift their midpoints to 0° (from the initial value of θ_0 at the input fiber end), producing the equilibrium mode distribution (EMD) in Figs. 2(c) and 3(c): L_c is 340 and 300 m for the unstrained and strained fibers, respectively. The coupling continues farther along the fiber, beyond the L_c mark, until all distributions' widths equalize and steady state distribution (SSD) is reached at length z_s in Figs. 2(d) and

3(d): $z_s \approx 1040$ and 950 m for the unstrained and strained fibers, respectively.

The value of $z_s = 1040$ m [Fig. 3(d)] for the unstrained fiber is consistent with the observation by Jeunhomme and Pocholle [4] that the length of 980 m is slightly smaller than the length necessary to reach the steady-state distribution. Because of the more intense mode coupling caused by fiber bending, a steady-state mode distribution in strained fiber is achieved at a shorter fiber length of $z_s = 950$ m.

For the unstrained and strained SI GOF, Figs. 2(d) and 3(d) show normalized curves of the output angular distribution obtained by solving the power flow equation using the EFDM (solid curve), as well as the steady-state analytical solution of Eq. (2) (filled squares), where $\gamma_0 = 0.00204$ and 0.00294 m^{-1} for the unstrained and strained fibers, respectively. The two are in good agreement, with the relative error below 0.9%. This leads us to conclude that EFDM and the method for calculating the coupling coefficient [15] are accurate for solving the power flow equation, not only for short plastic, but also for very long GOFs. It is interesting to note that strain of the SI GOF induced by bending causes a small relative decrease of the coupling length L_c and the length z_s (where SSD is achieved) in comparison to those of SI POFs that exhibit a more significant change ($L_c \approx 0.5$ to 3 m for strained and $L_c \approx 14$ to 34 m for unstrained POFs, respectively; $z_s \approx 1.5$ to 8.2 m for strained and $z_s \approx 42$ to 98 m for unstrained POFs, respectively [20]). This is because POFs are more

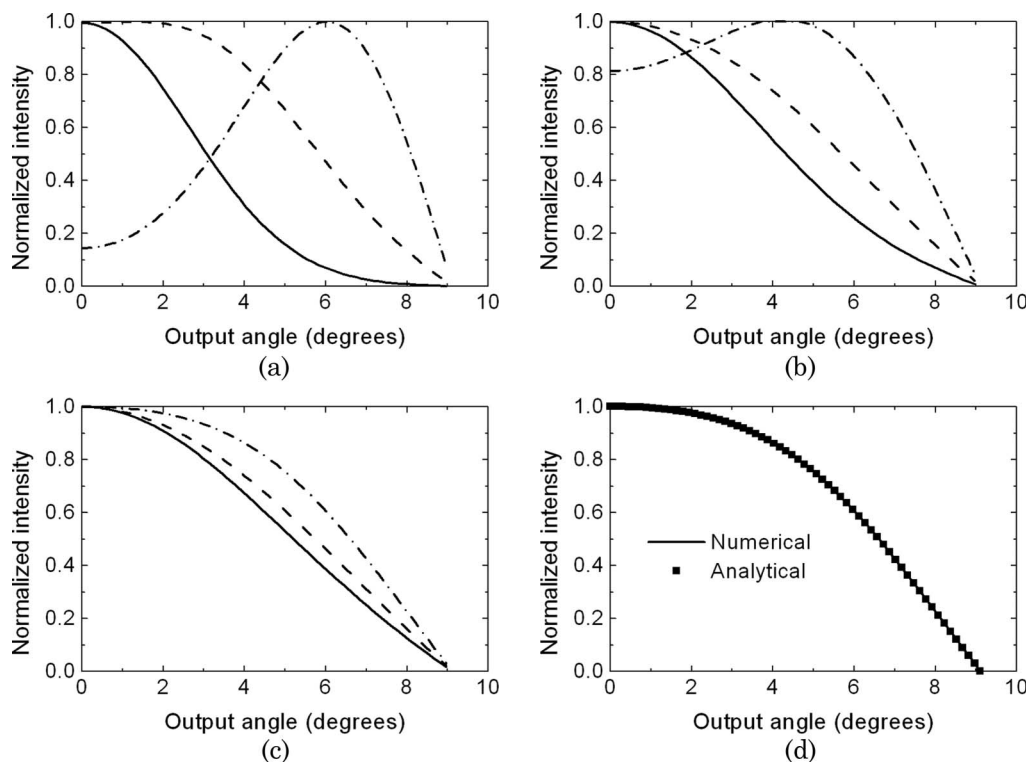


Fig. 3. Normalized output angular power distribution at different locations along the strained SI GOF calculated for three Gaussian input angles $\theta_0 = 0^\circ$ (solid curve), 4° (dashed curve), and 8° (dashed-dotted curve) with $(\text{FWHM})_{z=0} = 0.85^\circ$ for (a) $z = 80$ m, (b) $z = 160$ m, (c) $z = 300$ m, and (d) $z = 950$ m (filled squares represent the analytical steady-state solution).

sensitive to strain induced by bending, which significantly changes POF mode coupling characteristics.

A permanent increase of mode coupling for fibers under bending strain can be explained by an increase of power transfer caused by fiber microdeformations. Such deformations cause the equilibrium mode distribution and steady-state distribution to develop within shorter distances than is the case with straight fibers.

5. Conclusion

We report on the solution of the power flow equation employed to investigate the state of mode coupling along strained and unstrained SI GOFs. Our results have been verified against the analytical solution for the steady-state coupling condition. They are also consistent with experimental observations reported in the literature.

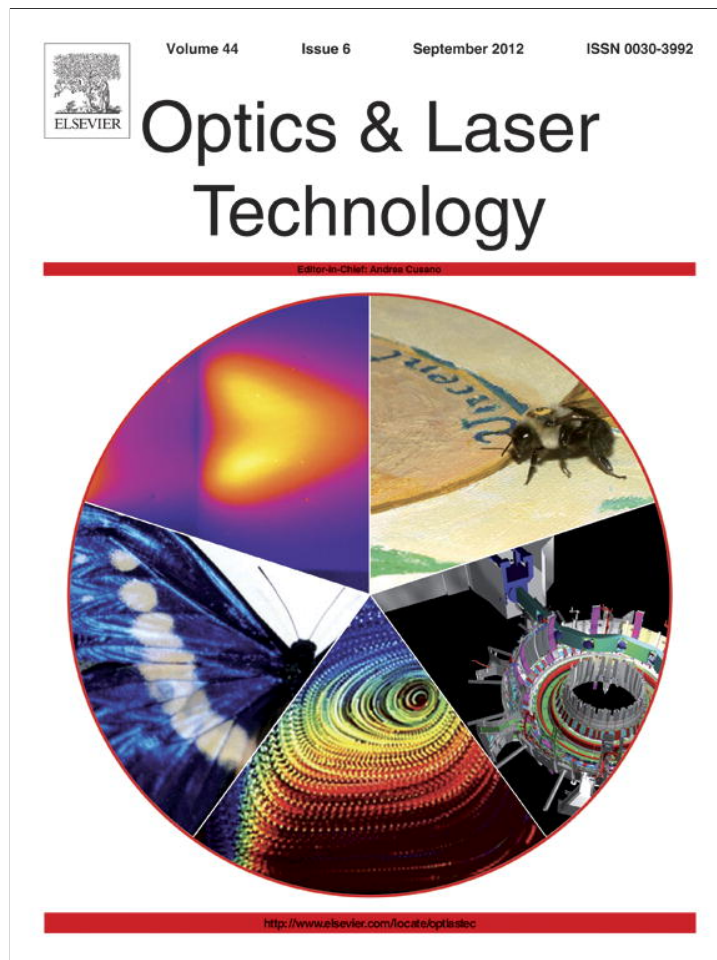
We show that coupling lengths and lengths for achieving the SSD in strained SI GOF are shorter than lengths in unstrained fiber. Bending strain increases mode coupling, which can be explained by an increase of power transfer between modes caused by microscopic changes in the fiber. As a consequence, the equilibrium mode distribution and steady-state distribution are achieved at shorter distances than for straight fibers.

The work described in this paper was supported by a grant from the Serbian Ministry of Science (project 141037).

References

1. W. Daum, J. Krauser, P. E. Zamzow, and O. Ziemann, *POF-Polymer Optical Fibers for Data Communications* (Springer, 2002).
2. J. Arrúe, J. Zubía, G. Fuster, and D. Kalymnios, "Light power behavior when bending plastic optical fibers," *IEE Proc. Optoelectron.* **145**, 313–318 (1998).
3. M. A. Losada, J. Mateo, I. Garcés, J. Zubía, J. A. Casao, and P. Pérez-Vela, "Analysis of strained plastic optical fibers," *IEEE Photonics Technol. Lett.* **16**, 1513–1515 (2004).
4. L. Jeunhomme and J. P. Pocholle, "Experimental determination of the radiation pattern of optical fibres," *Opt. Commun.* **12**, 89–92 (1974).
5. M. Eve and J. H. Hannay, "Ray theory and random mode coupling in an optical fibre waveguide, I," *Opt. Quantum Electron.* **8**, 503–508 (1976).
6. J. Arrue, G. Aldabaldetrekú, G. Durana, J. Zubía, I. Garcés, and F. Jiménez, "Design of mode scramblers for step-index and graded-index plastic optical fibers," *J. Lightwave Technol.* **23**, 1253–1260 (2005).
7. W. A. Gambling, D. N. Payne, and H. Matsumura, "Mode conversion coefficients in optical fibers," *Appl. Opt.* **14**, 1538–1542 (1975).
8. J. Arrúe, J. Zubía, G. Fuster, and D. Kalymnios, "Light power behavior when bending plastic optical fibers," *IEEE Proc. Optoelectron.* **145**, 313–318 (1998).
9. M. Rousseau and L. Jeunhomme, "Numerical solution of the coupled-power equation in step index optical fibers," *IEEE Trans. Microwave Theory Tech.* **25**, 577–585 (1977).
10. L. Jeunhomme, M. Fraise, and J. P. Pocholle, "Propagation model for long step-index optical fibers," *Appl. Opt.* **15**, 3040–3046 (1976).
11. A. Djordjevich and S. Savović, "Investigation of mode coupling in step index plastic optical fibers using the power flow equation," *IEEE Photonics Technol. Lett.* **12**, 1489–1491 (2000).
12. S. Savović and A. Djordjevich, "Solution of mode coupling in step-index optical fibers by the Fokker-Planck equation and the Langevin equation," *Appl. Opt.* **41**, 2826–2830 (2002).
13. A. F. Garito, J. Wang, and R. Gao, "Effects of random perturbations in plastic optical fibers," *Science* **281**, 962–967 (1998).
14. J. Zubía, G. Durana, G. Aldabaldetrekú, J. Arrúe, M. A. Losada, and M. López-Higuera, "New method to calculate mode conversion coefficients in SI multimode optical fibers," *J. Lightwave Technol.* **21**, 776–781 (2003).
15. S. Savović and A. Djordjevich, "Method for calculating the coupling coefficient in step index optical fibers," *Appl. Opt.* **46**, 1477–1481 (2007).
16. S. Savović and A. Djordjevich, "Calculation of the coupling coefficient in strained step index plastic optical fibers," *Appl. Opt.* **47**, 4935–4939 (2008).
17. S. Savović and A. Djordjevich, "Calculation of the coupling coefficient in step-index glass optical fibers," *Appl. Opt.* **48**, 4496–4500 (2009).
18. S. Savović and A. Djordjevich, "Influence of numerical aperture on mode coupling in step-index plastic optical fibers," *Appl. Opt.* **43**, 5542–5546 (2004).
19. J. D. Anderson, *Computational Fluid Dynamics* (McGraw-Hill, 1995).
20. S. Savović and A. Djordjevich, "Mode coupling in strained and unstrained step-index plastic optical fibers," *Appl. Opt.* **45**, 6775–6780 (2006).

Provided for non-commercial research and education use.
Not for reproduction, distribution or commercial use.



This article appeared in a journal published by Elsevier. The attached copy is furnished to the author for internal non-commercial research and education use, including for instruction at the authors institution and sharing with colleagues.

Other uses, including reproduction and distribution, or selling or licensing copies, or posting to personal, institutional or third party websites are prohibited.

In most cases authors are permitted to post their version of the article (e.g. in Word or Tex form) to their personal website or institutional repository. Authors requiring further information regarding Elsevier's archiving and manuscript policies are encouraged to visit:

<http://www.elsevier.com/copyright>

Contents lists available at [SciVerse ScienceDirect](#)

Optics & Laser Technology

journal homepage: www.elsevier.com/locate/optlastec

Frequency response in step-index plastic optical fibers obtained by numerical solution of the time-dependent power flow equation

Branko Drljača^{a,c}, Alexandar Djordjevich^b, Svetislav Savović^{a,*}

^a Faculty of Science, R. Domanovića 12, 34000 Kragujevac, Serbia

^b City University of Hong Kong, 83 Tat Chee Avenue, Kowloon, Hong Kong, China

^c Faculty of Science, Lole Ribara 29, Kosovska Mitrovica, Serbia

ARTICLE INFO

Article history:

Received 14 January 2012

Received in revised form

17 February 2012

Accepted 20 February 2012

Available online 8 March 2012

Keywords:

Plastic optical fiber

Frequency response

Bandwidth

ABSTRACT

The time-dependent power flow equation is employed to calculate frequency response and bandwidth in addition to mode coupling and mode-dependent attenuation in step-index plastic optical fibers. Frequency response is specified in the paper as a function of fiber length. Results are found to match reported measurements better than the existing analytical solution does. Mode-dependent attenuation and mode dispersion and coupling are known to be strong in plastic optical fibers, leading to major implications for their frequency response.

© 2012 Elsevier Ltd. All rights reserved.

1. Introduction

Plastic optical fibers (POFs) are often considered for high-performance short-distance data transmission systems including high-bandwidth local-area networks and multi-node bus networks [1–4]. In addition to being a more affordable, flexible and rugged alternative to glass fibers, POFs are also easier to handle. Their large core-diameter (0.5–1 mm or greater) allows pairing with LED sources using low-precision plastic components. This results in inexpensive but robust systems that are easy to interconnect. A variety of POF applications have been commercialized ranging from simple light-transmission guides in displays and power delivery systems to sensors and short-haul communication links [4]. Installations within buildings or vehicles where sharp corners and branches are many, or the network is repeatedly reconfigured, represent a domain with growth potential for POF applications.

Transmission properties of step-index (SI) multimode optical fibers, such as frequency response and bandwidth, depend strongly upon mode-dependent attenuation, modal dispersion and the rate of mode coupling (power transfer from lower to higher order modes) caused by intrinsic perturbation effects (primarily due to microscopic bends, irregularity of the core-cladding boundary and refractive index distribution fluctuations). Different models have been used to simulate these three important effects for SI optical fibers. The ray tracing model can

determine the output angular power distribution while accounting for the mode-dependent attenuation. The time delay between individual rays can also be calculated in presence of modal dispersion. This model is computationally intensive because large number of ray-trajectories must be simulated. In contrast, the time-independent power flow equation [5] is effective in modeling mode-dependent attenuation, mode coupling, and how these influence the output angular power distribution for different fiber lengths and launch conditions. However, the frequency response and bandwidth are not calculated by such time-independent analysis.

In our recent works [6,7], we have overcome this limitation by using Gloge's analytical solution of the time-dependent power flow equation [8] and have determined the POF frequency response and bandwidth in addition to mode coupling and mode-dependent attenuation. Unfortunately, one is bound to use in the analytical approach a specific value of the width of the launch beam distribution [8] that is unrelated to its actual value. Thus, Gloge's analytical solution will not necessarily accommodate the actual launch beam-width used in a related experiment, which may result in inaccurate calculation of POF's frequency response and bandwidth.

In addition to Gloge's analytical solution for the time-dependent power flow equation [8], two numerical approaches have also been reported. They are the implicit finite-difference method (IFDM) by Breyer et al. [9] and explicit finite-difference method (EFDM) in the matrix form by Mateo et al. [10]. Although IFDM is unconditionally stable, we have opted for EFDM in this work albeit not in the matrix form as used by Mateo et al. [10]. This method of solving the time-dependent power flow equation is

* Corresponding author. Fax: +381 34 335040.

E-mail address: savovic@kg.ac.rs (S. Savović).

easier to work with in comparison to extremely large matrices that must be manipulated at each calculation step when using IFDM. We compared our numerical results to those obtained experimentally by Mateo et al. [10] and also to the recent analytical solution [6,7].

2. Numerical solution of the time-dependent power flow equation

We use Gloge's time-dependent power flow equation to describe the evolution of the modal power distribution along a POF. Individual propagating modes are characterized by the respective inner propagation angle with respect to fiber axis (θ), which can be taken as a continuous variable [8]. Gloge's time-dependent power flow equation can be written as [8]

$$\frac{\partial P(\theta, z, t)}{\partial z} + \frac{\partial t}{\partial z} \frac{\partial P(\theta, z, t)}{\partial t} = -\alpha(\theta)P(\theta, z, t) + \frac{1}{\theta} \frac{\partial}{\partial \theta} \left[\theta D(\theta) \frac{\partial P(\theta, z, t)}{\partial \theta} \right] \quad (1)$$

where t is the time; $P(\theta, z, t)$ is the power distribution over angle, space, and time respectively; $\alpha(\theta)$ is the mode-dependent attenuation; $\partial t/\partial z$ is the mode delay per unit length and $D(\theta)$ is the mode-dependent coupling coefficient. Mode-dependent attenuation can be written in the form: $\alpha(\theta) = \alpha_0 + A\theta^2 + \dots$, where α_0 is the loss common to all modes. It can be accounted for by multiplying the end-solution by $e^{-\alpha_0 z}$ [11,12]. Therefore, when solving (1), one needs to consider only the term $A\theta^2$ as the most dominant of the higher order modes [5]. Assuming that the coupling coefficient D is mode-independent, Eq. (1) can be written as [8]

$$\frac{\partial P(\theta, z, t)}{\partial z} + \frac{\partial t}{\partial z} \frac{\partial P(\theta, z, t)}{\partial t} = -A\theta^2 P(\theta, z, t) + \frac{D}{\theta} \frac{\partial}{\partial \theta} \left[\theta \frac{\partial P(\theta, z, t)}{\partial \theta} \right] \quad (2)$$

The derivative $\partial t/\partial z$ can be obtained using the group velocity of a mode with characteristic angle θ , which is

$$\frac{dz}{dt} = \frac{c}{n(1+\theta^2/2)} \quad (3)$$

Neglecting the delay n/c common to all modes, it follows [8]

$$\frac{\partial P(\theta, z, t)}{\partial z} = -A\theta^2 P(\theta, z, t) - \frac{n}{2c} \theta^2 \frac{\partial P(\theta, z, t)}{\partial t} + \frac{D}{\theta} \frac{\partial}{\partial \theta} \left(\theta \frac{\partial P(\theta, z, t)}{\partial \theta} \right) \quad (4)$$

By applying the Fourier transform:

$$p(\theta, z, \omega) = \int_{-\infty}^{\infty} P(\theta, z, t) e^{-j\omega t} dt \quad (5)$$

the time-dependent Eq. (4) transforms into the following equation:

$$\frac{\partial p(\theta, z, \omega)}{\partial z} = -\left[A\theta^2 + j\omega \frac{n}{2c} \theta^2 \right] p(\theta, z, \omega) + \left(\frac{D}{\theta} \frac{\partial p(\theta, z, \omega)}{\partial \theta} \right) + D \left(\theta \frac{\partial^2 p(\theta, z, \omega)}{\partial \theta^2} \right) \quad (6)$$

where $\omega = 2\pi f$ is the angular frequency.

The boundary conditions are

$$p(\theta_c, z, \omega) = 0, \quad D \frac{\partial p(\theta, z, \omega)}{\partial \theta} \Big|_{\theta=0} = 0, \quad (7)$$

where θ_c is the critical angle. The first condition implies that modes with infinitely large loss do not transfer any power; the second condition implies that mode coupling is limited to modes traveling with the angle $\theta > 0$.

It is apparent that $p(\theta, z, \omega)$ is complex. We can therefore separate $p(\theta, z, \omega)$ into its real and imaginary parts, $p = p^r + jp^i$. Eq. (6) can now be rewritten as the following simultaneous

differential equations:

$$\begin{aligned} \frac{\partial p^r}{\partial z} &= -A\theta^2 p^r + \frac{D}{\theta} \frac{\partial p^r}{\partial \theta} + D \frac{\partial^2 p^r}{\partial \theta^2} + \omega \frac{n}{2c} \theta^2 p^i \\ \frac{\partial p^i}{\partial z} &= -A\theta^2 p^i + \frac{D}{\theta} \frac{\partial p^i}{\partial \theta} + D \frac{\partial^2 p^i}{\partial \theta^2} - \omega \frac{n}{2c} \theta^2 p^r \end{aligned} \quad (8)$$

Once p^r and p^i are obtained by solving Eq. (8), frequency response at z can be calculated as

$$H(z, \omega) = \frac{2\pi \int_0^{\theta_c} \theta [p^r(\theta, z, \omega) + jp^i(\theta, z, \omega)] d\theta}{2\pi \int_0^{\theta_c} \theta [p^r(\theta, 0, \omega) + jp^i(\theta, 0, \omega)] d\theta} \quad (9)$$

After separating the power flow Eq. (6) into two simultaneous Eq. (8), we solved the latter (8) by EFDM, which is the first in our knowledge.

In the 1970s and 1980s, implicit finite difference methods (IFDMs) were generally preferred over EFDMs. This trend has been changing with the advancement of computers, shifting the emphasis to EFDMs. Being often unconditionally stable, the IFDM allows larger step lengths. Nevertheless, this does not translate into IFDM's higher computational efficiency because extremely large matrices must be manipulated at each calculation step. We find that the EFDM is also simpler in addition to being computationally more efficient [13,14]. Using central difference scheme for derivatives $\partial p(\theta, z, \omega)/\partial \theta$ and $\partial^2 p(\theta, z, \omega)/\partial \theta^2$ [12–14]:

$$\begin{aligned} \left(\frac{\partial p(\theta, z, \omega)}{\partial \theta} \right)_{k,l} &= \frac{p_{k+1,l} - p_{k-1,l}}{2\Delta\theta} + O(\Delta\theta)^2 \\ \left(\frac{\partial^2 p(\theta, z, \omega)}{\partial \theta^2} \right)_{k,l} &= \frac{p_{k+1,l} - 2p_{k,l} + p_{k-1,l}}{(\Delta\theta)^2} + O(\Delta\theta)^2 \end{aligned} \quad (10)$$

and using the forward difference scheme for the derivative $\partial p(\theta, z, \omega)/\partial z$:

$$\left(\frac{\partial p(\theta, z, \omega)}{\partial z} \right)_{k,l} = \frac{p_{k,l+1} - p_{k,l}}{\Delta z} + O(\Delta z) \quad (11)$$

Eq. (8) can be written in the form:

$$\begin{aligned} p_{k,l+1}^r &= \left(\frac{\Delta z D}{\Delta\theta^2} - \frac{\Delta z D}{2\theta_k \Delta\theta} \right) p_{k-1,l}^r + \left(1 - \frac{2\Delta z D}{\Delta\theta^2} - \Delta z A \theta_k^2 \right) p_{k,l}^r \\ &+ \left(\frac{\Delta z D}{2\theta_k \Delta\theta} + \frac{\Delta z D}{\Delta\theta^2} \right) p_{k+1,l}^r + \frac{\omega n \Delta z}{2c} \theta_k^2 p_{k,l}^i \end{aligned} \quad (12)$$

and

$$\begin{aligned} p_{k,l+1}^i &= \left(\frac{\Delta z D}{\Delta\theta^2} - \frac{\Delta z D}{2\theta_k \Delta\theta} \right) p_{k-1,l}^i + \left(1 - \frac{2\Delta z D}{\Delta\theta^2} - \Delta z A \theta_k^2 \right) p_{k,l}^i \\ &+ \left(\frac{\Delta z D}{2\theta_k \Delta\theta} + \frac{\Delta z D}{\Delta\theta^2} \right) p_{k+1,l}^i - \frac{\omega n \Delta z}{2c} \theta_k^2 p_{k,l}^r \end{aligned} \quad (13)$$

Boundary conditions (7) now become

$$p_{N,l}^r = 0, \quad p_{N,l}^i = 0 \quad \text{and} \quad p_{0,l}^r = p_{1,l}^r, \quad p_{0,l}^i = p_{1,l}^i \quad (14)$$

where $N = \theta_c/\Delta\theta$ is the grid size in the θ direction. In order to prevent the problem of singularity at grid points $\theta=0$, the following relation is used [14]:

$$\lim_{\theta \rightarrow 0} \frac{1}{\theta} \frac{\partial}{\partial \theta} \left(\theta \frac{\partial p}{\partial \theta} \right) = 2 \frac{\partial^2 p}{\partial \theta^2} \Big|_{\theta=0} \quad (15)$$

A typical solution of Eqs. (12) and (13) run takes up to 4 s on the Intel (R) Core (TM) i3 CPU 540 @ 3.07 GHz personal computer for the longest fiber analyzed (of 150 m in length).

3. Numerical results

It was shown in the preceding Section that the time-dependent analysis is reduced to its time-independent equivalent. This is applied to calculate the frequency response and bandwidth of

the same SI POFs that were investigated by Mateo et al. [10]. The relevant POFs are the PGU-FB1000 (PGU) from Toray with numerical aperture $NA=0.5$ (corresponding to the inner critical angle of $\theta_c=19.5^\circ$) and 0.15 dB/m of nominal attenuation; then the PREMIER GH4001 (GH) from Mitsubishi with numerical aperture $NA=0.5$ (corresponding to the inner critical angle of $\theta_c=19.5^\circ$) and 0.15 dB/m of nominal attenuation; and HFBR-RUS100 (HFBR) from Agilent, with numerical aperture $NA=0.47$ (corresponding to the inner critical angle of $\theta_c=18.5^\circ$) and 0.22 dB/m of nominal attenuation.

Mateo et al. [10] measured frequency responses at different fiber lengths by feeding pure sinusoidal waveforms of different frequencies to an AlGaInP laser diode (LD Sanyo DL-3147-021). The laser source emits a maximum power of 5 mW at 645 nm and has a typical divergence of 30° in the perpendicular and 7.5° in the parallel plane. The detailed procedure to measure the frequency response is described in [10] and references within. In calculating the impulse response and frequency response of PGU, GH and HFBR fibers, Mateo et al. [10] have assumed mode-dependent attenuation $\alpha(\theta)$ and mode-dependent coupling coefficient $D(\theta)$. In contrast, Gloge's time-dependent power flow Eq. (2) assumes a constant coupling coefficient D and constant A (A is the second order multiplicative factor in the series expansion of the mode-dependent attenuation $\alpha(\theta)$). In order to obtain the value for A for the HFBR fiber, we used the graph for $\alpha(\theta)$ in Fig. 1 that was proposed for HFBR fiber by Mateo et al. [15]. Since mode-dependent attenuation can be written in the form $\alpha(\theta) \approx \alpha_0 + A\theta^2$, one can determine A by fitting the graph of Fig. 1 using this $\alpha(\theta)$ function. In doing so, we have obtained $\alpha_0=0.0154 \text{ m}^{-1}$ and $A=0.7539 \text{ rad}^{-2} \text{ m}^{-1}$ for the HFBR fiber [7]. In the same manner, we have obtained $\alpha_0=0.0150 \text{ m}^{-1}$ and $A=0.9953 \text{ rad}^{-2} \text{ m}^{-1}$ for the PGU fiber [6] and $\alpha_0=0.0159 \text{ m}^{-1}$ and $A=0.4025 \text{ rad}^{-2} \text{ m}^{-1}$ for the GH fiber [7].

On the basis of the distribution of mode-dependent coupling coefficient $D(\theta)$ proposed earlier for the HFBR, PGU and GH fibers by Mateo et al. [15] (Fig. 2), we have obtained that the coupling coefficient $D \approx 4.31 \times 10^{-4} \text{ rad}^2/\text{m}$ characterizes mode coupling in the HFBR fiber in the angular range of interest, namely $\theta \approx 0^\circ - 7.5^\circ$. In the same manner, the values obtained for the coupling coefficients for the PGU and GH fibers are $D \approx 5.02 \times 10^{-4} \text{ rad}^2/\text{m}$ and $D \approx 1.91 \times 10^{-4} \text{ rad}^2/\text{m}$, respectively. One should mention here that modeling the mode coupling process with a constant D is routine [5,11,16–19].

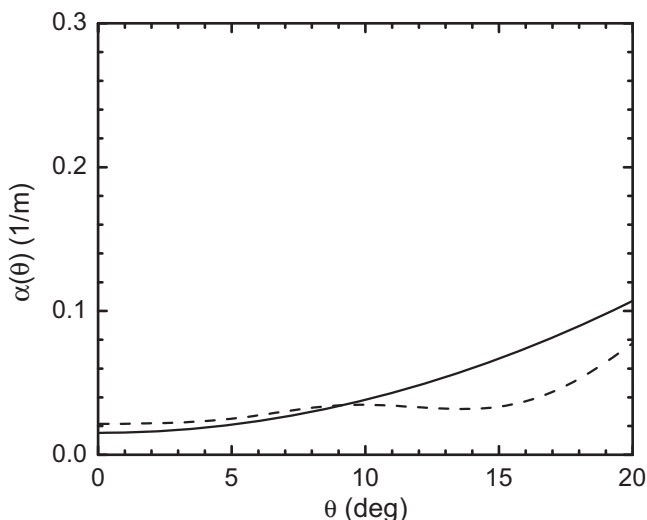


Fig. 1. Mode-dependent attenuation $\alpha(\theta)$ for the HFBR fiber proposed by Mateo et al. [15] (dashed line) and our fit obtained using the function $\alpha(\theta) \approx \alpha_0 + A\theta^2$, with $\alpha_0=0.0154 \text{ m}^{-1}$ and $A=0.7539 \text{ rad}^{-2} \text{ m}^{-1}$ (solid line).

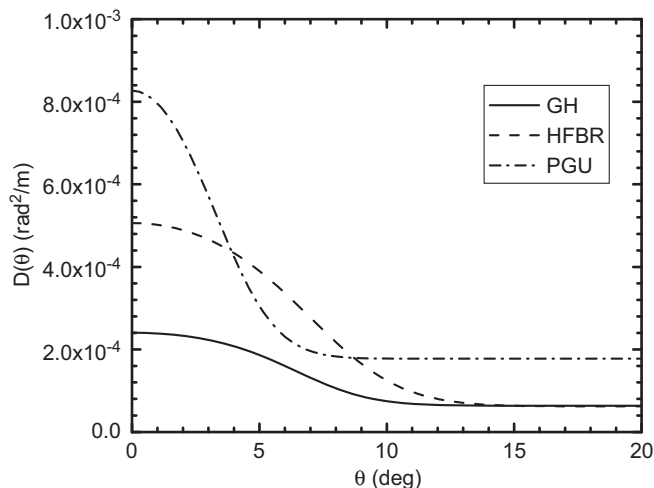


Fig. 2. Mode-dependent coupling coefficient $D(\theta)$ for the GH, HFBR and PGU fibers proposed by Mateo et al. [15].

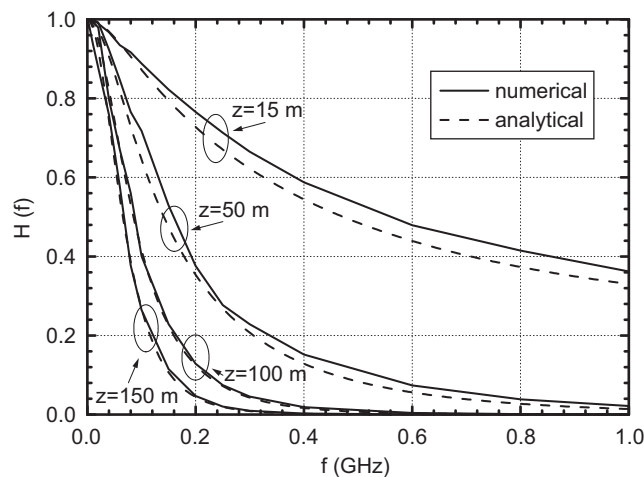


Fig. 3. Comparison of numerical results and analytical solution [6] for frequency response of the PGU fiber at different fiber lengths.

For consistency with [10], a Dirac impulse in time and a laser diode mode distribution with the $FWHM=7.5^\circ$ in the parallel plane were used for the input. Eq. (9) has been used to calculate the frequency response at fiber lengths $z=15, 50, 100$ and 150 m . Numerical results for the frequency response for different fiber lengths of the PGU and GH fibers are shown in Figs. 3 and 4, respectively, and are compared to the recent analytical solution [6,7]. As shown in Fig. 5, frequency response of the HFBR fiber is shown for the fiber lengths of 15, 50 and 100 m, and are compared with experimental results obtained by Mateo et al. [10] as well as with the analytical solution [7]. A more pronounced drop at lower frequencies is apparent for longer fiber length. One can observe that differences between the numerical and analytical results are more evident for smaller and intermediate fiber lengths. The issue is of less relevance for longer lengths when the two solutions match better. For short fiber lengths, experimental results by Mateo et al. [10] match our numerical results better than they do with the analytical solution [6,7]. All the three match well for longer fiber lengths.

As shown in Figs. 6–8, our numerical results for the bandwidth for the PGU, GH and HFBR fibers are compared to Mateo et al.'s [10] experimental measurements and to our recent analytical solution [6,7]. Measurements match the numerical results better

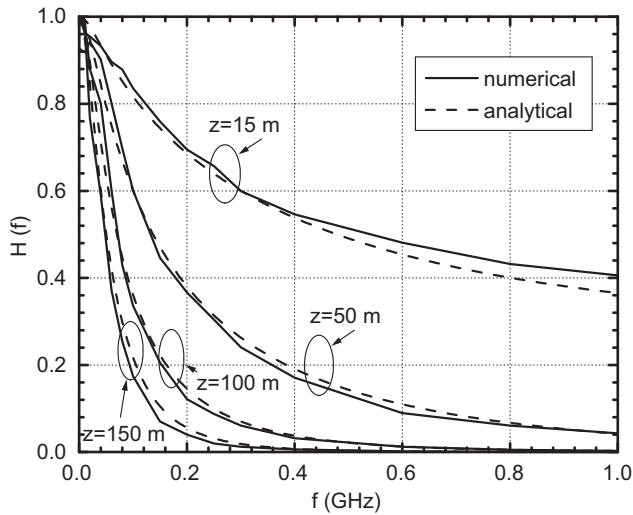


Fig. 4. Comparison of numerical results and analytical solution [7] for frequency response of the GH fiber at different fiber lengths.

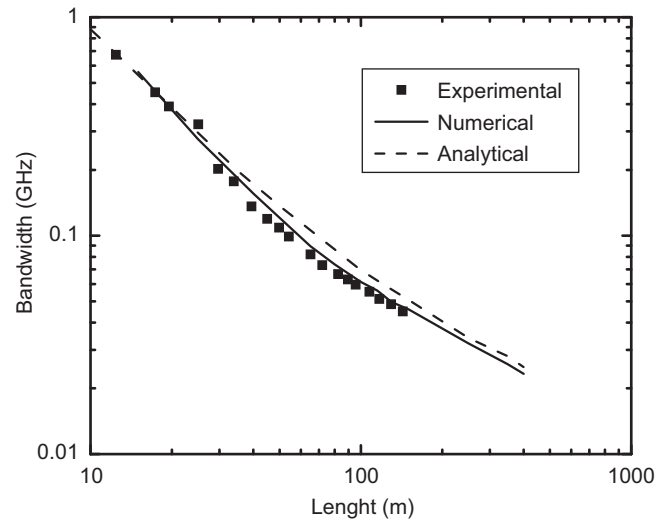


Fig. 7. Comparison of numerical results, measurements by Mateo et al. [10] and analytical solution [7] for the functional dependence of the GH fiber bandwidth on its length.

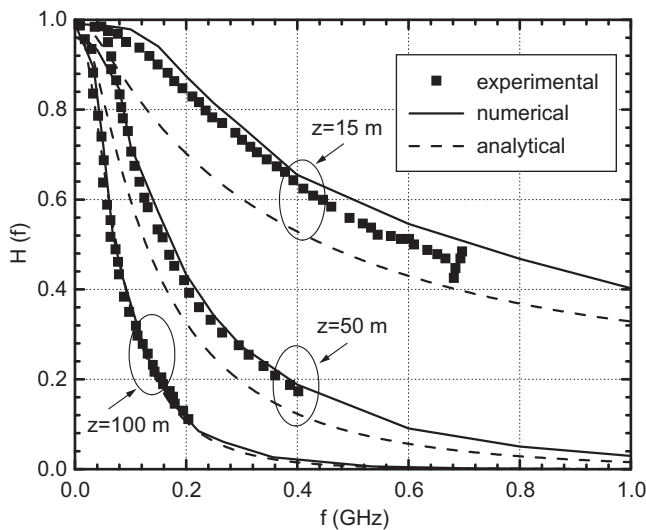


Fig. 5. Comparison of numerical results, measurements by Mateo et al. [10] and analytical solution [7] for frequency response of the HFBR fiber.

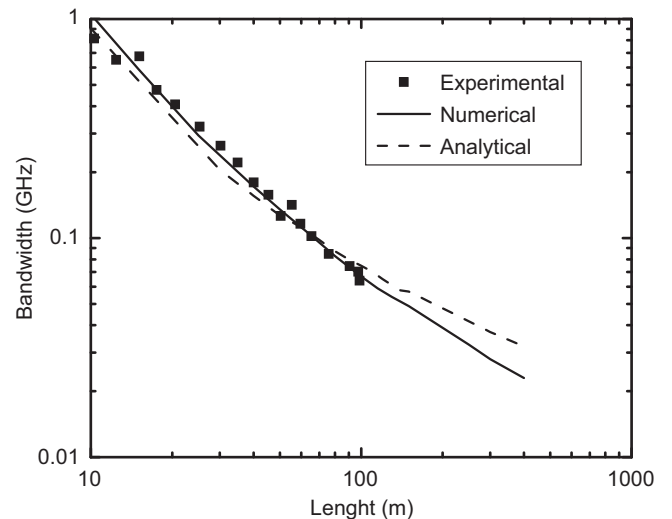


Fig. 8. Comparison of numerical results, measurements by Mateo et al. [10] and analytical solution [7] for the functional dependence of the HFBR fiber bandwidth on its length.

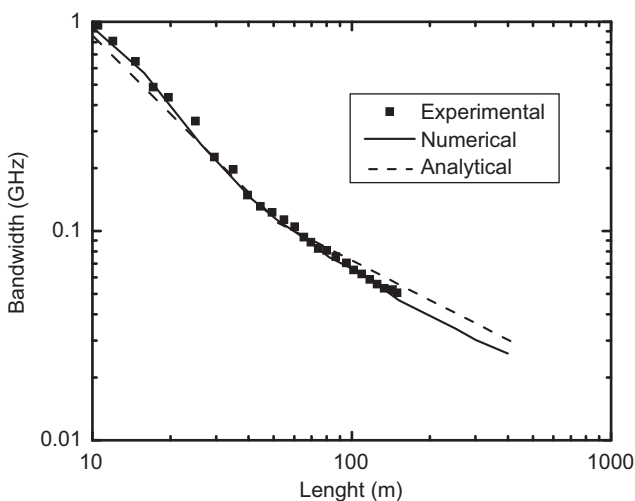


Fig. 6. Comparison of numerical results, measurements by Mateo et al. [10] and analytical solution [6] for the functional dependence of the PGU fiber bandwidth on its length.

than they do with the analytical solution. This is explained by the fact that to obtain the analytical solution of the time-dependent power flow equation, the launch mode distribution with FWHM=10.2°, 8.35° and 10.6° had to be used for the PGU, GH and HFBR fibers respectively [6,7], whereas the actual FWHM of the laser diode Mateo et al. used in their experiment was 7.5° [10]. In other words, one cannot use Gloge's analytical solution the actual launch beam width but, rather, a value that depends on the attenuation parameter A and on mode coupling coefficient D for the particular fiber [6]; leading thus to a reduced calculation accuracy (an underestimate) of bandwidth at short fiber lengths [20]. Alternatively, one can change the FWHM of the source to match the behavior of each fiber which in practice is not justified.

One should mention here that differences between our numerical results obtained assuming the simplified attenuation and diffusion coefficients, and numerical results obtained by Mateo et al. [10], who used more complex form of the attenuation and diffusion coefficients, are negligible. This is in agreement with our recent findings that modeling mode coupling in SI POFs assuming a constant coupling coefficient D can be used

instead of the more complicated approach with angle-dependent coupling coefficient [21].

POF bandwidth as a function of fiber length (in logarithmic coordinates) has usually been approximated by straight lines. The slope of these lines is known as the concatenation factor and is related to mode coupling. In the absence of mode coupling and differential mode attenuation, the concatenation factor is unity. A slope other than unity is the evidence of diffusive non-linear effects [10]. Mateo et al. [10] showed that bandwidth of PGU fiber decreases with length more steeply for shorter fiber lengths. Namely, the bandwidth data for the PGU fiber can be fitted with two lines intercepting at about 60 m, with a slope of 1.3 for the first and 0.8 for the second line. Slope above unity is caused by underfilled launch. Combined with modal diffusion, it degrades the overall fiber performance by causing faster drop in bandwidth. The segment with a slope of 0.8 (slower decrease in bandwidth) is due to stronger modal diffusion that leads to the equilibrium mode distribution faster. Thus, one can conclude that at the PGU fiber length of about 60 m, weakly coupled regimes become strongly coupled ones. Based on numerical results that we have obtained for bandwidth for the GH and HFBR fibers, Figs. 7 and 8, one can observe the same behavior as for the PGU fiber but with a change in slope appearing at a longer fiber length of about 100 m. Similar numerical results have been obtained by Mateo et al. [10], with transition lengths of about 120 m. None of Mateo et al.'s experiments, however, revealed slope below 0.8 even though they measured up to fiber lengths where the steady state power distribution is achieved. In fact, they showed that their experimental data for the GH and HFBR fibers can be fitted by single straight lines of slopes 1.2 and 1.1, respectively. Larger slope in bandwidth graph observed for the GH fiber relative to that of the HFBR fiber can be attributed to stronger modal diffusion in the latter fiber, which enhances its bandwidth.

4. Conclusion

The numerical solution of the time-dependent power flow equation is employed to calculate the frequency response and bandwidth in the same step-index plastic optical fibers that had been investigated experimentally by Mateo et al. [10]. Frequency response calculations for a range of fiber lengths enabled us to derive the functional dependence of bandwidth with distance. For short fiber lengths, measurements by Mateo et al. [10] match our numerical results better than they do with the analytical solution [6,7]. All three match well for longer fiber lengths. The underestimate of bandwidth resulting from the analytical solution at short fiber lengths is attributed to the necessity of using a specific (fixed) value of the width of the launch beam distribution in Gloge's analytical approach with the time-dependent power flow equation [8]. This fixed value is determined by the attenuation parameter A and mode coupling coefficient D [6] for the fiber in question and may differ from the actual launch-beam width.

It is apparent that the switch from weakly to strongly coupled regimes in the PGU fiber results in the slower drop of bandwidth for fibers longer than the transition length, implying that mode coupling enhances fiber bandwidth. Steeper slope in the bandwidth-graph for GH fiber relative to that of the HFBR fiber is

attributed to stronger modal diffusion in the latter, which enhances its bandwidth.

Finally, we have shown that the explicit finite difference method is effective and accurate for solving the power flow Eq. (8) for step-index optical fibers.

Acknowledgments

The work described in this paper was supported by the grant from the Serbian Ministry of Education and Science (Project no. 171011).

References

- [1] Ishigure T, Kano M, Koike Y. Which is a more serious factor to the bandwidth of GI POF: differential mode attenuation or mode coupling? *Journal of Lightwave Technology* 2000;18:959–65.
- [2] Golowich SE, White W, Reed WA, Knudsen E. Quantitative estimates of mode coupling and differential modal attenuation in perfluorinated graded-index plastic optical fiber. *Journal of Lightwave Technology* 2003;21:111–21.
- [3] Green Jr PE. Optical networking update. *IEEE Journal on Selected Areas in Communications* 1996;14:764–79.
- [4] Koeppen C, Shi RF, Chen WD, Garito AF. Properties of plastic optical fibers. *Journal of the Optical Society of America B: Optical Physics* 1998;15:727–39.
- [5] Gloge D. Optical power flow in multimode fibers. *Bell System Technical Journal* 1972;51:1767–83.
- [6] Drljača B, Savović S, Djordjević A. Calculation of the frequency response of step-index plastic optical fibers using the time-dependent power flow equation. *Optics and Lasers in Engineering* 2011;49:618–22.
- [7] Drljača B, Savović S, Djordjević A. Calculation of the frequency response and bandwidth of step-index plastic optical fibers using the time-dependent power flow equation. *Physica Scripta*, submitted for publication.
- [8] Gloge D. Impulse response of clad optical multimode fibers. *Bell System Technical Journal* 1973;52:801–16.
- [9] Breyer F, Hanik N, Lee J, Randel S. Getting impulse response of SI-POF by solving the time-dependent power-flow equation using Crank-Nicholson scheme. In: Bunge C-A, Poisel H, editors. *Proceedings of the POF Modelling Workshop*. p. 111–119.
- [10] Mateo J, Losada MA, Zubía J. Frequency response in step index plastic optical fibers obtained from the generalized power flow equation. *Optics Express* 2009;17:2850–60.
- [11] Rousseau M, Jeunhomme L. Numerical solution of the coupled-power equation in step index optical fibers. *IEEE Transactions on Microwave Theory and Techniques* 1977;25:577–85.
- [12] Savović S, Djordjević A. Influence of numerical aperture on mode coupling in step index plastic optical fibers. *Applied Optics* 2004;43:5542–6.
- [13] Anderson JD. *Computational Fluid Dynamics*. New York: McGraw-Hill; 1995.
- [14] Djordjević A, Savović S. Investigation of mode coupling in step index plastic optical fibers using the power flow equation. *IEEE Photonics Technology Letters* 2000;12:1489–91.
- [15] Mateo J, Losada MA, Garcés I, Zubía J. Global characterization of optical power propagation in step-index plastic optical fibers. *Optics Express* 2006;14:9028–35.
- [16] Gambling WA, Payne DN, Matsumura H. Mode conversion coefficients in optical fibers. *Applied Optics* 1975;14:1538–42.
- [17] Dugas J, Maurel G. Mode-coupling processes in polymethyl methacrylate-core optical fibers. *Applied Optics* 1992;31:5069–79.
- [18] Jeunhomme L, Fraise M, Pocholle JP. Propagation model for long step-index optical fibers. *Applied Optics* 1976;15:3040–6.
- [19] Garito AF, Wang J, Gao R. Effects of random perturbations in plastic optical fibers. *Science* 1998;281:962–7.
- [20] Savović S, Djordjević A, Tse PW, Zubia J, Mateo J, Losada MA. Determination of the width of the output angular power distribution in step index multimode optical fibers. *Journal of Optics-Nouvelle Revue D Optique* 2010;12: 115405 (5 pp.).
- [21] Savović S, Djordjević A. Influence of the angle-dependence of mode coupling on optical power distribution in step-index plastic optical fibers. *Optics and Laser Technology* 2012;44:180–4.

Calculation of the frequency response and bandwidth in step-index plastic optical fibres using the time-dependent power flow equation

This content has been downloaded from IOPscience. Please scroll down to see the full text.

2012 Phys. Scr. 2012 014028

(<http://iopscience.iop.org/1402-4896/2012/T149/014028>)

View [the table of contents for this issue](#), or go to the [journal homepage](#) for more

Download details:

IP Address: 128.104.46.196

This content was downloaded on 08/09/2014 at 11:45

Please note that [terms and conditions apply](#).

Calculation of the frequency response and bandwidth in step-index plastic optical fibres using the time-dependent power flow equation

B Drljača^{1,2}, S Savović¹ and A Djordjevich³

¹ Faculty of Science, R Domanovića 12, 34000 Kragujevac, Serbia

² Faculty of Science, Lole Ribara 29, Kosovska Mitrovica, Serbia

³ City University of Hong Kong, 83 Tat Chee Avenue, Kowloon, Hong Kong, People's Republic of China

E-mail: brdrjljaca@gmail.com

Received 4 August 2011

Accepted for publication 5 October 2011

Published 27 April 2012

Online at stacks.iop.org/PhysScr/T149/014028

Abstract

The power flow equation is used to calculate the frequency response and bandwidth in step-index plastic optical fibres (POFs). The frequency response is specified as a function of distance from the input fibre end. Good agreement is seen between our analytical results and the experimental results from the literature. Mode-dependent attenuation and mode dispersion and coupling are known to be strong in POFs, leading to major implications for their frequency response in data transmission systems.

PACS numbers: 42.81.-i, 42.81.Qb, 42.81.Uv

1. Introduction

Plastic optical fibres (POFs) are often considered for high-performance short-distance data transmission systems including high-bandwidth local-area networks and multi-node bus networks [1–4]. In addition to being a more affordable, flexible and rugged alternative to glass fibres, POFs are also easier to handle. Their large core diameter (0.5–1 mm or larger) allows for pairing with LED sources using low-precision plastic components. This results in inexpensive but robust systems that are easy to interconnect. Various POF applications have been reported ranging from simple light-transmission guides in displays and power delivery systems to sensors and short-haul communication links [4].

Transmission properties of step index (SI) multimode optical fibres, such as frequency response and bandwidth, depend strongly on mode-dependent attenuation, modal dispersion and the rate of mode coupling (power transfer from lower to higher order modes) caused by intrinsic perturbation effects (primarily due to microscopic bends, irregularity of the core-cladding boundary and refractive index distribution fluctuations) [5–7]. Using the time-dependent power flow equation [7], we have determined the POF

frequency response and bandwidth in addition to mode coupling and mode-dependent attenuation. Verified against measurements by Mateo *et al* [6], we showed how the resulting change in bandwidth with fibre length is strongly affected by mode coupling and attenuation typical of POFs.

2. The time-dependent power flow equation

Gloge's time-dependent power flow equation can be written as [7]

$$\frac{\partial P(\theta, z, t)}{\partial z} + \frac{\partial t}{\partial z} \frac{\partial P(\theta, z, t)}{\partial t} = -\alpha(\theta)P(\theta, z, t) + \frac{1}{\theta} \frac{\partial}{\partial \theta} \left[\theta D(\theta) \frac{\partial P(\theta, z, t)}{\partial \theta} \right], \quad (1)$$

where $P(\theta, z, t)$ is the power distribution over angle θ measured with respect to the fibre axis, space z and time t ; $\alpha(\theta)$ is mode-dependent attenuation; $\partial t / \partial z$ is mode delay per unit length; and $D(\theta)$ is the mode-dependent coupling coefficient. Mode-dependent attenuation can be written in the form $\alpha(\theta) = \alpha_0 + A\theta^2 + \dots$, where α_0 is the loss common to all modes. It can be accounted for by multiplying the

end solution by $e^{-\alpha_0 z}$ [8]. Therefore, in solving (1), one only needs to consider the term $A\theta^2$ as the most dominant of the higher-order modes [5]. Assuming that the coupling coefficient D is mode independent, equation (1) can be written as [7]

$$\frac{\partial P}{\partial z} = -A\theta^2 P - \frac{n}{2c}\theta^2 \frac{\partial P}{\partial t} + \frac{D}{\theta} \frac{\partial}{\partial \theta} \left(\theta \frac{\partial P}{\partial \theta} \right). \quad (2)$$

The time-dependent equation (2) can be transformed into the time-independent equation [7]

$$\frac{\partial p}{\partial z} = -A\sigma^2 \theta^2 p + \frac{D}{\theta} \frac{\partial}{\partial \theta} \left(\theta \frac{\partial p}{\partial \theta} \right). \quad (3)$$

Using the time-independent power flow equation (3), the analytical solution for impulse response can be obtained [7]. For short fibres ($z \ll 1/(2(AD)^{1/2})$), the impulse response is

$$Q(z, t) = \frac{2c\pi}{nz(1+\gamma_\infty z)} \exp(-2ct/n\Theta_0^2 z), \quad (4)$$

whereas in the case of long fibres ($z \gg 1/(2(AD)^{1/2})$), it is

$$Q(z, t) = \Theta_0^2 \sqrt{\frac{\pi}{Tt}} \left(\frac{t}{\gamma_\infty z T} + \frac{1}{2} \right)^{-1} \exp\left(-\frac{\gamma_\infty^2 z^2 T}{4t} - \frac{t}{T} \right). \quad (5)$$

After obtaining the impulse response, the frequency response can be obtained easily by applying Fourier transform to the impulse response:

$$H(f) = \int_{-\infty}^{\infty} Q(t) \exp(2\pi i f t) dt. \quad (6)$$

In our previous work [9], we determined the impulse response, frequency response and bandwidth of the SI POF only for long fibre lengths ($z \gg 1/(2(AD)^{1/2})$). In this work, using Gloge's analytical solution to (2), we calculated the impulse response, frequency response and bandwidth of two different SI POFs investigated earlier by Mateo *et al* [6], both for short ($z \ll 1/(2(AD)^{1/2})$) and long ($z \gg 1/(2(AD)^{1/2})$) fibre lengths, and compared our analytical results to their experimental results.

3. Results

To facilitate the comparison of results, we calculated the impulse response, frequency response and bandwidth of the SI POFs investigated by Mateo *et al* [6]. These fibres were PREMIER GH4001 (GH) obtained from Mitsubishi with numerical aperture $NA = 0.5$ (corresponding to the inner critical angle of $\theta_c = 19.5^\circ$) and 0.15 dB m^{-1} nominal attenuation, and HFBR-RUS100 (HFBR) from Agilent, with numerical aperture $NA = 0.47$ (corresponding to the inner critical angle of $\theta_c = 18.5^\circ$) and 0.22 dB m^{-1} of nominal attenuation. In calculating the impulse response and frequency response of those fibres, Mateo *et al* [6] have assumed mode-dependent attenuation $\alpha(\theta)$ and a mode-dependent coupling coefficient $D(\theta)$. In contrast, Gloge's analytical solution to the time-dependent power flow equation (2) is obtained assuming a constant coupling coefficient D and constant A . In order to obtain the value of A for the fibres in

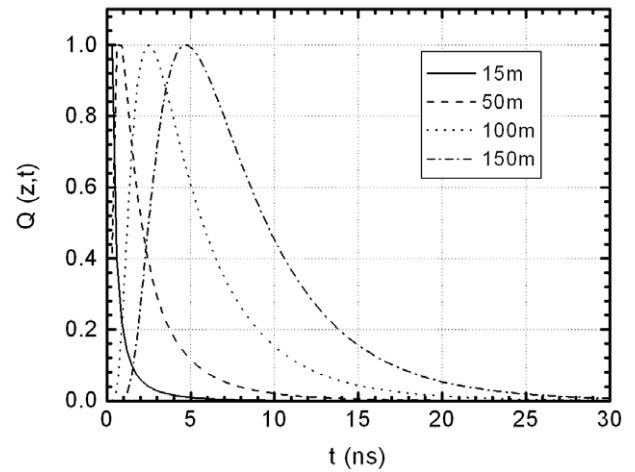


Figure 1. Analytical results for the impulse response for GH fibre.

question, we used the procedure used in our previous work [9]. In doing so, we have obtained $\alpha_0 = 0.01591 \text{ m}^{-1}$ and $A = 0.4025 (\text{rad}^2 \text{ m})^{-1}$ for GH fibre and $\alpha_0 = 0.01541 \text{ m}^{-1}$ and $A = 0.7539 (\text{rad}^2 \text{ m})^{-1}$ for HFBR fibre. On the basis of the distribution of mode-dependent coupling coefficient $D(\theta)$ proposed earlier for GH and HFBR fibres by Mateo *et al* [10], we have obtained that the values of the coupling coefficient are $D \approx 1.91 \times 10^{-4} \text{ rad}^2 \text{ m}^{-1}$ for GH and $D \approx 4.31 \times 10^{-4} \text{ rad}^2 \text{ m}^{-1}$ for HFBR fibre (in the calculations we assumed that the light beam is launched centrally along the fibre axis with full-width at half-maximum, $\text{FWHM} = 8.35^\circ$ for GH and $\text{FWHM} = 10.6^\circ$ for HFBR fibre). One should mention here that modelling the mode coupling process with a constant D has been done by many other authors [5, 11–15].

A Dirac impulse in time and a mode distribution with the width at $1/e$ of $\Theta_0 = \Theta_\infty = 9.85^\circ$ and $\Theta_0 = \Theta_\infty = 12.45^\circ$ ($\text{FWHM} = 8.35^\circ$ and $\text{FWHM} = 10.6^\circ$), for GH and HFBR fibres, respectively, at the beginning of the fibre are used (Mateo *et al* [6] used a laser diode with $\text{FWHM} = 7.5^\circ$ in the parallel plane). Equation (4), valid for short fibre lengths $z \ll 1/\gamma_\infty = 57 \text{ m}$ for the GH fibre and $z \ll 1/\gamma_\infty = 27.7 \text{ m}$ for the HFBR fibre, has been applied to calculate the impulse responses at $z = 15 \text{ m}$. Equation (5), valid for long fibre lengths $z \gg 1/\gamma_\infty$, has been used to calculate the impulse responses at fibre lengths $z = 50, 100$ and 150 m . Our analytical results for the impulse response for different fibre lengths of the GH and HFBR fibres are shown in figures 1 and 2, respectively.

One can observe from figures 1 and 2 that at short fibre lengths ($z = 15 \text{ m}$), the mode-dependent attenuation and modal dispersion are the dominant effects. With increasing fibre length, mode coupling begins to influence strongly the impulse shape, changing it to a more or less Gaussian shape. The power exiting the fibres at the highest angles (the tails of the Gaussian launch beam) is delayed the most. This suggests an efficient means of improving the fibre performance by spatially filtering out the tail ends at higher angles [6]. As most power is confined within the range of lower angles, such a filtering of the power at highest angles would cause only minor power loss while producing a narrower overall impulse response. Figures 3 and 4 show the frequency response of the GH and HFBR fibres obtained using equation (6).

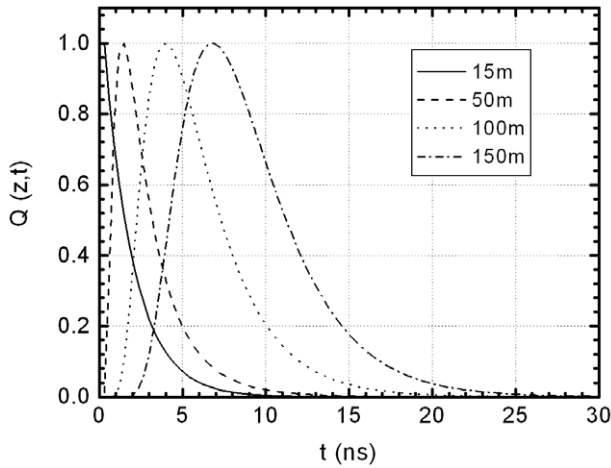


Figure 2. Analytical results for the impulse response for HFBR fibre.

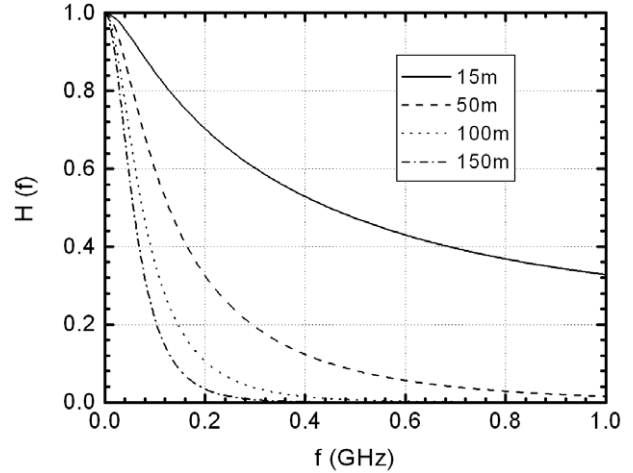


Figure 4. Analytical results for the frequency response for HFBR fibre.

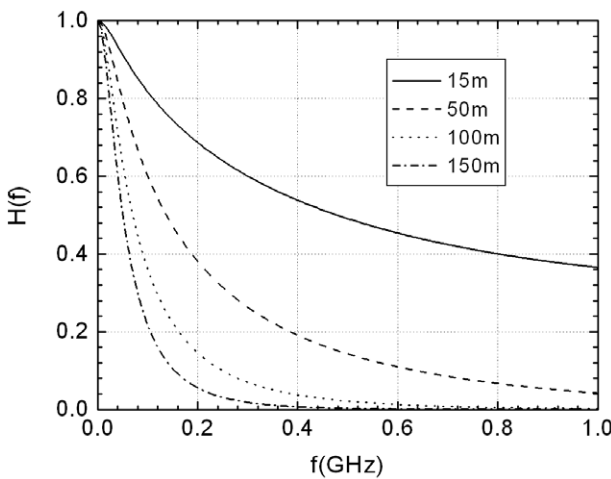


Figure 3. Analytical results for the frequency response for GH fibre.

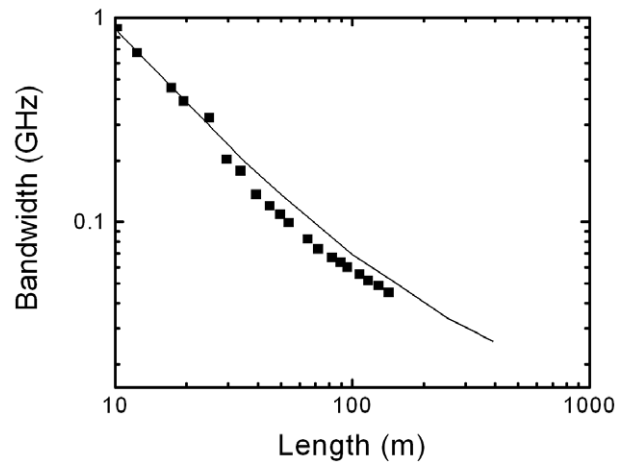


Figure 5. Analytical results for the bandwidth versus fibre length for GH fibre (line) compared to experimental results (filled squares) obtained by Mateo *et al* [6].

The low-frequency performance differs from that at high frequencies. Moreover, a more pronounced drop at lower frequencies is apparent for longer fibre length. In figures 5 and 6, Mateo’s and our results for bandwidth in a two-axis logarithmic scale are compared for GH and HFBR fibres, and show a good match. Bandwidth decreases with length more steeply for shorter fibre lengths. Mateo *et al* [6] showed that the bandwidth data for both GH and HFBR fibres can be fitted with a single straight line, with a slope of 1.2 and 1.1, respectively. The larger slope observed for GH fibre as compared to HFBR fibre can be attributed to a stronger modal diffusion in HFBR fibre, which enhances the overall fibre performance by causing a slower drop in bandwidth.

4. Conclusion

The analytical solution of the time-dependent power flow equation is used to calculate the impulse response, frequency response and bandwidth in SI POFs investigated experimentally by Mateo *et al* [6]. It has been observed that at short fibre lengths the mode-dependent attenuation is dominant. With increasing fibre length, mode coupling begins to significantly influence the impulse shape, changing it to a

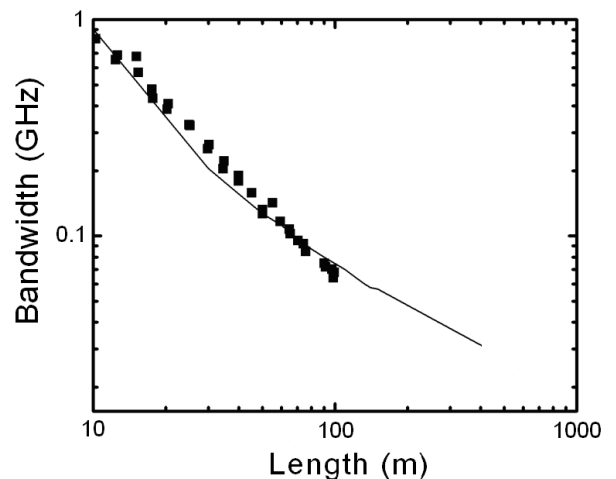


Figure 6. Analytical results for the bandwidth versus fibre length for HFBR fibre (line) compared to experimental results (filled squares) obtained by Mateo *et al* [6].

Gaussian-like shape. Frequency response at a range of lengths enabled us to derive the bandwidth dependence on distance. Good agreement was obtained between our results and the experimental results from the literature [6]. The larger slope in the bandwidth graph observed for GH fibre as compared to

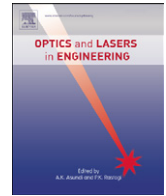
HFBR fibre can be attributed to stronger modal diffusion in the latter, which enhances its bandwidth.

Acknowledgment

The work described in this paper was supported by a grant from the Serbian Ministry of Science and Technological Development (project no. 171011).

References

- [1] Ishigure T, Kano M and Koike Y 2000 *J. Lightwave Technol.* **18** 959–65
- [2] Golowich S E, White W, Reed W A and Knudsen E 2003 *J. Lightwave Technol.* **21** 111–21
- [3] Green P E Jr 1996 *IEEE J. Sel. Areas Commun.* **14** 764–79
- [4] Koeppen C, Shi R F, Chen W D and Garito A F 1998 *J. Opt. Soc. Am. B* **15** 727–39
- [5] Gloge D 1972 *Bell Syst. Tech. J.* **51** 1767–83
- [6] Mateo J, Losada M A and Zubía J 2009 *Opt. Express* **17** 2850–60
- [7] Gloge D 1973 *Bell Syst. Tech. J.* **52** 801–16
- [8] Savović S and Djordjevich A 2004 *Appl. Opt.* **43** 5542–6
- [9] Drljača B, Savović S and Djordjevich A 2011 *Opt. Lasers Eng.* **49** 618–22
- [10] Mateo J, Losada M A, Garcés I and Zubía J 2006 *Opt. Express* **14** 9028–35
- [11] Gambling W A, Payne D N and Matsumura H 1975 *Appl. Opt.* **14** 1538–42
- [12] Dugas J and Maurel G 1992 *Appl. Opt.* **31** 5069–79
- [13] Rousseau M and Jeunhomme L 1977 *IEEE Trans. Microw. Theory Tech.* **25** 577–85
- [14] Jeunhomme L, Fraise M and Pocholle J P 1976 *Appl. Opt.* **15** 3040–6
- [15] Garito A F, Wang J and Gao R 1998 *Science* **281** 962–7



Calculation of the frequency response in step-index plastic optical fibers using the time-dependent power flow equation

Branko Drljača^a, Svetislav Savović^{a,*}, Alexandar Djordjevich^b

^a Faculty of Science, R. Domanovića 12, 34000 Kragujevac, Serbia

^b City University of Hong Kong, 83 Tat Chee Avenue, Kowloon, Hong Kong, China

ARTICLE INFO

Article history:

Received 25 October 2010

Received in revised form

17 January 2011

Accepted 18 January 2011

Available online 5 February 2011

Keywords:

Plastic optical fiber

Frequency response

Bandwidth

ABSTRACT

The time-dependent power flow equation, which is reduced to its time-independent counterpart is employed to calculate frequency response and bandwidth in addition to mode coupling and mode-dependent attenuation in a step-index plastic optical fiber. The frequency response is specified as a function of distance from the input fiber end. This is compared to reported measurements. Mode-dependent attenuation and mode dispersion and coupling are known to be strong in plastic optical fibers, leading to major implications for their frequency response in data transmission systems.

© 2011 Elsevier Ltd. All rights reserved.

1. Introduction

Plastic optical fibers (POFs) are often considered for high-performance short-distance data transmission systems including high-bandwidth local-area networks and multi-node bus networks [1–4]. In addition to being a more affordable, flexible and rugged alternative to glass fibers, POFs are also easier to handle. Their large-core diameter (0.5–1 mm or larger) allows pairing with LED sources using low-precision plastic components. This results in inexpensive but robust systems that are easy to interconnect. Variety of POF applications have been commercialized ranging from simple light-transmission guides in displays and power delivery systems to sensors and short-haul communication links [4]. Installations within buildings or vehicles, where sharp corners and branches are many or the network is repeatedly reconfigured, represent a domain with growth potential for POF applications.

Transmission properties of step-index (SI) multimode optical fibers, such as frequency response and bandwidth, depend strongly upon mode-dependent attenuation, modal dispersion and the rate of mode coupling (power transfer from lower to higher order modes) caused by intrinsic perturbation effects (primarily due to microscopic bends, irregularity of the core-cladding boundary and refractive index distribution fluctuations). Different models have been used to simulate these three important effects for SI optical fibers. The ray tracing model can determine the output angular power distribution while accounting for the mode-dependent attenuation. The time delay between

individual rays can also be calculated in presence of modal dispersion. This model is computationally intensive because large number of ray-trajectories must be simulated. In contrast, the time-independent power flow equation [5] is effective in modeling mode-dependent attenuation, mode coupling, and how these influence the output angular power distribution with fiber length for different launch conditions. However, the frequency response and bandwidth are not calculated.

We have overcome this limitation using the time-dependent power flow equation and have determined the POF frequency response and bandwidth in addition to mode coupling and mode-dependent attenuation. Verified against measurements by Mateo et al. [6], we showed how the resulting change in bandwidth with fiber length is strongly affected by mode coupling typical of POFs.

2. Time-dependent power flow equation

We use Gloge's time-dependent power flow equation to describe the evolution of the modal power distribution along the axis of the SI POF (as the z -coordinate). Individual modes are characterized by their inner propagation angle θ measured with respect to fiber axis. Gloge's time-dependent power flow equation can be written as [7]:

$$\frac{\partial P(\theta, z, t)}{\partial z} + \frac{\partial t}{\partial z} \frac{\partial P(\theta, z, t)}{\partial t} = -\alpha(\theta)P(\theta, z, t) + \frac{1}{\theta} \times \frac{\partial}{\partial \theta} \left[\theta D(\theta) \frac{\partial P(\theta, z, t)}{\partial \theta} \right] \quad (1)$$

where t is the time, $P(\theta, z, t)$ is the power distribution over angle, space and time, respectively, $\alpha(\theta)$ is the mode-dependent attenuation,

* Corresponding author. Fax: +381 34 335040.

E-mail address: savovic@kg.ac.rs (S. Savović).

$\partial t/\partial z$ is the mode delay per unit length and $D(\theta)$ is the mode-dependent coupling coefficient. Mode-dependent attenuation can be written in the form $\alpha(\theta) = \alpha_0 + A\theta^2 + \dots$, where α_0 is loss common to all modes. It can be accounted for by multiplying the end-solution by $e^{-\alpha_0 z}$ [8]. Therefore, in solving Eq. (1), one needs only to consider the term $A\theta^2$ as the most dominant of the higher order modes [5]. Assuming that the coupling coefficient D is mode-independent, Eq. (1) can be written as [7]:

$$\frac{\partial P(\theta, z, t)}{\partial z} + \frac{\partial t}{\partial z} \frac{\partial P(\theta, z, t)}{\partial t} = -A\theta^2 P(\theta, z, t) + \frac{D}{\theta} \times \frac{\partial}{\partial \theta} \left[\theta \frac{\partial P(\theta, z, t)}{\partial \theta} \right] \quad (2)$$

The derivative $\partial t/\partial z$ can be obtained using the group velocity of a mode with characteristic angle θ , which is:

$$\frac{dz}{dt} = \frac{c}{n(1 + \theta^2/2)} \quad (3)$$

Neglecting the delay n/c common to all modes, it follows [7]:

$$\frac{\partial P}{\partial z} = -A\theta^2 P - \frac{n}{2c} \theta^2 \frac{\partial P}{\partial t} + \frac{D}{\theta} \times \frac{\partial}{\partial \theta} \left(\theta \frac{\partial P}{\partial \theta} \right) \quad (4)$$

By applying the Laplace transform:

$$p(\theta, z, s) = \int_0^\infty e^{-st} P(\theta, z, t) dt \quad (5)$$

the time-dependent Eq. (4) transforms into an expression that differs from the following Gloge's [5] time-independent power flow Eq. (6) only in the multiplier A that is $A\sigma^2$ in Eq. (6):

$$\frac{\partial p}{\partial z} = -A\sigma^2 \theta^2 p + \frac{D}{\theta} \times \frac{\partial}{\partial \theta} \left(\theta \frac{\partial p}{\partial \theta} \right) \quad (6)$$

where $\sigma = (1 + ns/2cA)^{1/2}$. Therefore, by substituting A in Eq. (4) with $A\sigma^2$, the solution of the time-dependent power flow Eq. (4) is obtained from the solution of the time-independent power flow Eq. (6).

For the Gaussian input distribution:

$$p_{in} = f(0, s) \exp[-\theta^2/\theta_0^2] \quad (7)$$

one obtains [5]:

$$p(\theta, z, s) = f(z, s) \exp[-\theta^2/\theta^2(z, s)] \quad (8)$$

where $\theta^2(z, s)$ and $f(z, s)$ are described by [5]:

$$\theta^2(z, s) = \frac{\theta_\infty^2 \sigma \theta_0^2 + \theta_\infty^2 \tan h \sigma \gamma_\infty z}{\sigma \theta_\infty^2 + \sigma \theta_0^2 \tan h \sigma \gamma_\infty z} \quad (9)$$

and

$$f(z, s) = \frac{f(0, s) \sigma \theta_0^2}{\theta_\infty^2 \sin h \sigma \gamma_\infty z + \sigma \theta_0^2 \cosh \sigma \gamma_\infty z} \quad (10)$$

with

$$\theta_\infty = (4D/A)^{1/4} \quad (11)$$

and

$$\gamma_\infty = 2(AD)^{1/2} \quad (12)$$

For continuous wave excitation ($s=0$), the angular width $\theta(z, 0)$ changes monotonically from θ_0 to θ_∞ as z increases. Since the width θ_∞ characterizes a distribution, which propagates unchanged (at steady state) and with the minimum overall loss coefficient γ_∞ , it seems practical to excite this distribution right from the beginning ($\theta_0 = \theta_\infty$) [7]. The closed-form Laplace transform of Eq. (8) exists only for the approximation given in the limits $z \ll 1/\gamma_\infty$ (short fiber) and $z \gg 1/\gamma_\infty$ (long fibers) [7].

For short fibers, Eq. (8) becomes [7]:

$$p(\theta, z, s) = \frac{f(0, s)}{1 + \gamma_\infty z} \exp \left[-\theta^2 \left(\frac{1}{\theta_0^2} + \frac{nz}{2c} s \right) \right] \quad (13)$$

The total output is obtained from the integration $p(\theta, z, s)$ over all angles [7]. With reference to Eq. (13) and for $z \ll 1/\gamma_\infty$, one obtains:

$$q = \frac{\pi f(0, s) \theta_0^2}{(1 + \gamma_\infty z)(1 + n\theta_0^2 z/2c)} \quad (14)$$

If one sets $f(0, s) = 1$, which corresponds to an infinitesimally short input pulse of energy 1, the Laplace transformation of Eq. (14) yields the impulse response of the fiber [7]:

$$Q(z, t) = \frac{2c\pi}{nz(1 + \gamma_\infty z)} \exp(-2ct/n\theta_0^2 z) \quad (15)$$

where $Q(t)$ is limited in practice to a time interval narrower than $n\theta_c^2 z/(2c)$, which is the delay between the fastest and the slowest modes (θ_c is the fiber's critical angle).

In the case of a long fiber, Eq. (8) assumes the form [7]:

$$p = \frac{2\sigma}{1 + \sigma} \exp[-\sigma(\theta^2/\theta_0^2 + \gamma_\infty z)] \quad (16)$$

which leads to:

$$q = \frac{2\pi\theta_0^2}{1 + \sigma} \exp(-\sigma\gamma_\infty z) \quad (17)$$

where p is integrated over all angles θ . Introducing $\sigma = (1 + ns/2cA)^{1/2}$ into Eq. (17), one can form the Laplace transform of $q(s)$. By using the condition $\gamma_\infty z > 1$, the impulse response of the fiber is:

$$Q(z, t) = \theta_0^2 \sqrt{\frac{\pi}{Tt}} \left(\frac{t}{\gamma_\infty z T} + \frac{1}{2} \right)^{-1} \exp \left(-\frac{\gamma_\infty^2 z^2 T}{4t} - \frac{t}{T} \right) \quad (18)$$

where

$$T = \frac{n}{2cA} = \frac{n}{2c} \times \frac{\theta_0^2}{\gamma_\infty} \quad (19)$$

After obtaining impulse response, frequency response can be obtained easily by applying Fourier transform to the impulse response:

$$H(f) = \int_{-\infty}^{+\infty} Q(t) \exp(-2\pi i f t) dt \quad (20)$$

In addition to Gloge's analytical solution for the time-dependent power flow Eq. (2) [7], two numerical approaches for solving the time-dependent power flow Eq. (1) have also been reported. They are the implicit finite-difference method (Crank-Nicholson scheme) by Breyer et al. [9] and explicit finite-difference method in the matrix form by Mateo et al. [6]. In this work, to our knowledge for the first time, using Gloge's analytical solution of Eq. (2), we calculate the impulse response, frequency response and bandwidth of the SI POF investigated earlier by Mateo et al. [6] and compare our analytical to their experimental results. One should mention here that numerical approaches in solving Eq. (2) [6,9] are often very complex and computationally more difficult to perform, so application of the analytical solution of the problem is always more convenient if such solution exists.

3. Results

It was shown in the preceding Section how the time-dependent analysis is reduced to its time-independent equivalent. This is applied to calculate the impulse response, frequency response and bandwidth of the SI POF that was investigated by Mateo et al. [6]. This fiber is the PGU-FB1000 (PGU) from Toray with numerical aperture NA=0.5 (corresponding to the inner critical angle of $\theta_c=19.5^\circ$) and 0.15 dB/m of nominal attenuation. Mateo et al. [6] measured frequency responses at different fiber lengths by feeding pure sinusoidal waveforms of different frequencies to an AlGaInP laser diode (LD Sanyo DL-3147-021). The laser source

emits a maximum power of 5 mW at 645 nm and has a typical divergence of 30° in the perpendicular plane, and 7.5° in the parallel plane. Power was launched directly into the fiber using a connector, which limits the NA to near 0.19 (under-filled launch) but is close to the conditions achieved in real links. The receptor is based on a 1 mm diameter photodiode (FDS010) with a 50Ω load resistance and whose bandwidth is 200 MHz. The fiber-output is free-space coupled to the receptor using another connector. Most of the power is captured due to the large area of the detector, avoiding spatial filtering that could modify measured frequency responses. The receptor output is amplified using a 40 dB amplifier (Mini-Circuits ZKL-1R5) with a band-pass from 10 MHz to 1.5 GHz. A wideband Infinium DCA 86100A oscilloscope from Agilent is connected to the output of the amplifier and captures the received signal whose amplitude is directly related with the frequency response of the system at that frequency. Device control and data acquisition are performed by the computer. The detailed procedure to obtain the frequency response is described in [6] and references within. In calculating the impulse response and frequency response of PGU fiber, Mateo et al. [6] have assumed mode-dependent attenuation $\alpha(\theta)$ and mode-dependent coupling coefficient $D(\theta)$. In contrast, Gloge's analytical solution of the time-dependent power flow Eq. (2) is obtained assuming a constant coupling coefficient D and constant A (A is the second order multiplicative factor in the series expansion of the mode-dependent attenuation $\alpha(\theta)$). In order to obtain the value for A for the fiber in question, we used the graph for $\alpha(\theta)$ in Fig. 1 proposed earlier for PGU fiber by Mateo et al. [10]. Since mode-dependent attenuation can be written in the form $\alpha(\theta) \approx \alpha_0 + A\theta^2$, one can determine A by fitting the graph of Fig. 1 using this $\alpha(\theta)$ function. In doing so, we have obtained $\alpha_0 = 0.015 \text{ m}^{-1}$ and $A = 0.9953 \text{ (rad}^2 \text{ m)}^{-1}$. On the basis of the distribution of mode-dependent coupling coefficient $D(\theta)$ proposed earlier for PGU fiber by Mateo et al. [10] (Fig. 2), we have obtained that the value of the coupling coefficient $D \approx 5.02 \times 10^{-4} \text{ rad}^2/\text{m}$ characterizes mode coupling in the angular range of interest $\theta \approx 0$ to 7° (in the calculations we assumed that the light beam is launched centrally along the fiber axis with FWHM = 10.2°). One should mention here that modeling the mode coupling process with a constant D is commonly done by many other authors [5, 11–15].

A Dirac impulse in time and a mode distribution with the width at $1/e$ of $\theta_0 = \theta_\infty = 12^\circ$ (FWHM = 10.2°) at the beginning of the fiber are used (Mateo et al. [6] used a laser diode with

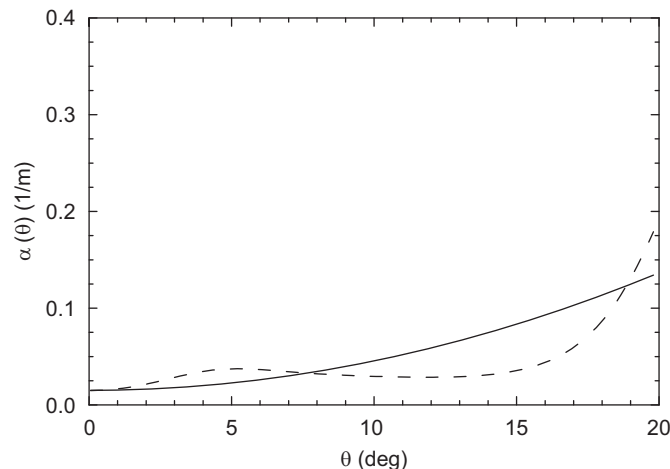


Fig. 1. Mode-dependent attenuation $\alpha(\theta)$ for PGU fiber proposed by Mateo et al. [10] (dashed line) and our fit obtained using the function $\alpha(\theta) \approx \alpha_0 + A\theta^2$, with $\alpha_0 = 0.015 \text{ m}^{-1}$ and $A = 0.9953 \text{ (rad}^2 \text{ m)}^{-1}$ (solid line).

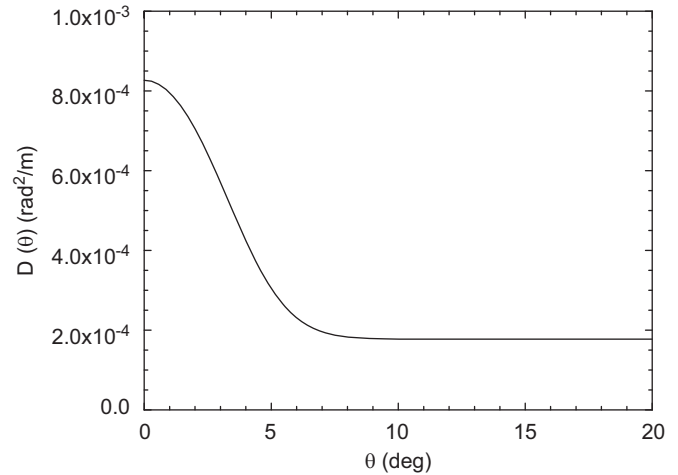


Fig. 2. Mode-dependent coupling coefficient $D(\theta)$ for PGU fiber proposed by Mateo et al. [10].

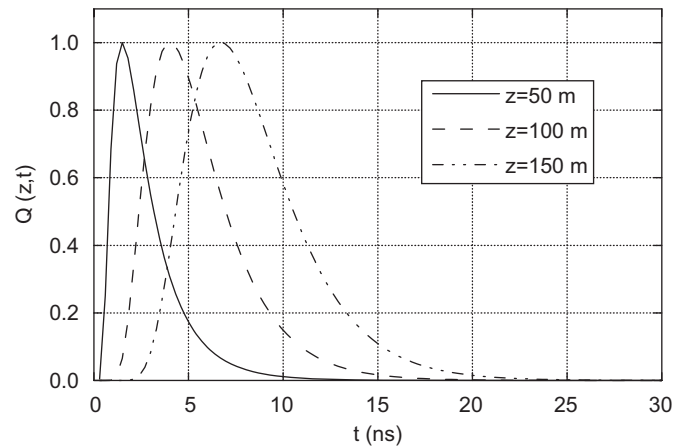


Fig. 3. Analytical results for the impulse response for different fiber lengths for PGU fiber.

FWHM = 7.5° in the parallel plane). Eq. (8), valid for long fiber lengths $z \gg 1/\gamma_\infty = 22.4 \text{ m}$, has been used to calculate the impulse response at fiber lengths $z = 50, 100$ and 150 m . Our analytical results for the impulse response for different fiber lengths of the PGU fiber are shown in Fig. 3. In Fig. 4, experimental results obtained by Mateo et al. [6] for impulse response are shown for the fiber length of 150 m . A good agreement between these results is apparent. The tail beyond 20 ns of the experimentally obtained impulse response [6] at the end of 150 m PGU fiber length seems longer than our analytical results and possibly is due to the noticeable difference in the attenuation functions as shown in Fig. 1. One can observe from Fig. 3 that at short fiber lengths, the mode-dependent attenuation and modal dispersion are the dominant effects. With increasing fiber length, mode coupling begins to influence significantly the impulse shape, changing it to a more or less Gaussian shape. The power exiting the fiber at the highest angles (the tails of the Gaussian launch beam) is delayed the most. This suggests an efficient means of improving the fiber performance by spatially filtering-out of the tail-ends at higher angles [6]. As most power is confined within the range of lower angles, such filtering of the power at highest angles would cause only minor power loss while producing a narrower overall impulse response.

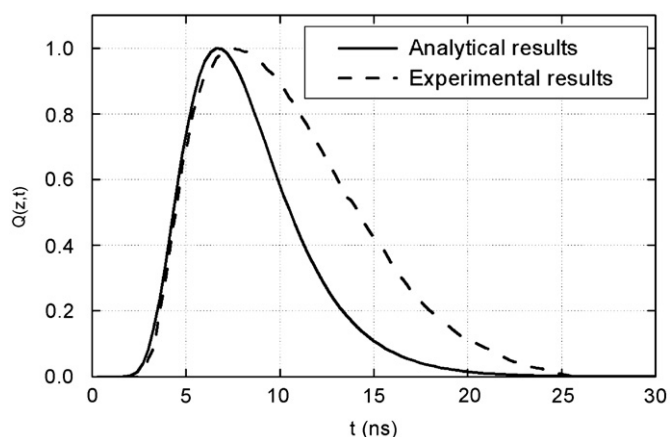


Fig. 4. Experimental results for the impulse response at the end of 150 m PGU fiber length obtained by Mateo et al. [6] compared with our analytical results.

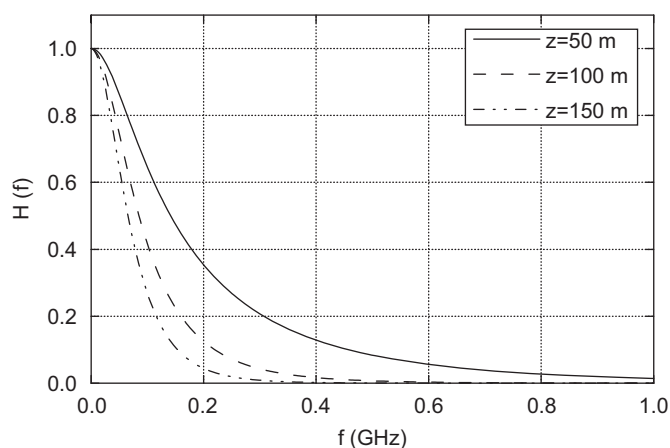


Fig. 5. Analytical results for the frequency response for different fiber lengths for PGU fiber.

Fig. 5 shows frequency response of the PGU fiber obtained using Eq. (9). The low frequency performance differs from that at high frequencies. Moreover, a more pronounced drop at lower frequencies is apparent for longer fiber length. A similar frequency response has been observed for HFB POF investigated by Mateo et al. [6].

In Fig. 6, Mateo's and our results are compared and show a good match for the bandwidth. The differences between these results at short fiber lengths can be explained by the fact that in our calculations the launch mode distribution with $\text{FWHM}=10.2^\circ$ is used while Mateo et al. [6] in the experiment used a laser diode with $\text{FWHM}=7.5^\circ$. Namely, influence of the width of the launched beam on the evolution of the width of the output angular power distribution, and consequently on the fiber bandwidth, is more pronounced at short fiber lengths [16], leading to the underestimated analytically obtained bandwidth. With increasing fiber length this influence becomes negligible. One can also see that bandwidth decreases with length more steeply for shorter fiber lengths. POF bandwidth as a function of fiber length (in logarithmic coordinates) has usually been approximated by straight lines. The slope of these lines is known as the concatenation factor and is related to mode coupling. In the absence of mode coupling and differential mode attenuation, the concatenation factor is unity. Therefore, a slope higher or lower than this is evidence of diffusive non-linear effects [6]. Mateo et al. [6] showed that the bandwidth data for the PGU fiber

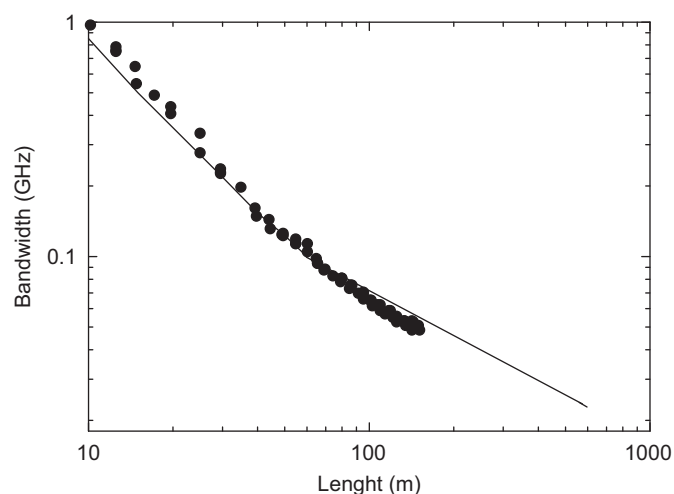


Fig. 6. Analytical results for the bandwidth versus fiber length for PGU fiber (line) compared to experimental results (symbols) obtained by Mateo et al. [6]. Line shows model predictions extended up to 600 m.

can be fitted with two lines intercepting at about 60 m, with a slope of 1.3 for the first and 0.8 for the second line. Slope above unity is caused by under-filled launch. Combined with modal diffusion, it degrades the overall fiber performance by causing faster drop in bandwidth. The segment with a slope of 0.8 is indicative of stronger modal diffusion that leads to the equilibrium distribution faster. Thus, one can conclude that at the fiber length of about 60 m, weakly coupled regimes become strongly coupled beyond the coupling length L_c (the fiber length where equilibrium mode distribution is achieved) [15].

4. Conclusion

The analytical solution of the time-dependent power flow equation is employed for the first time to calculate the impulse response, frequency response and bandwidth in a step-index plastic optical fiber that was investigated experimentally by Mateo et al. [6]. Our results for the impulse response agree well with experiments [6]. It has been observed that at short fiber lengths the mode-dependent attenuation is dominant. With increasing fiber length, mode coupling begins to influence the impulse response of the fiber, which begins to take the Gaussian-like shape. Frequency response at a range of lengths enabled us to derive the bandwidth dependence on distance. A good agreement between our results and experimental results from the literature [6] is obtained. One could observe that the switch from weakly to strongly coupled regimes results in the slower drop of bandwidth for fibers longer than the coupling length L_c , which means that mode coupling enhances the fiber bandwidth.

Acknowledgement

The work described in this paper was supported by the grant from the Serbian Ministry of Science and Technological Development (Project no. 171011).

References

- [1] Ishigure T, Kano M, Koike Y. Which is a more serious factor to the bandwidth of GI POF: differential mode attenuation or mode coupling? *J Lightwave Technol* 2000;18:959–65.

- [2] Golowich SE, White W, Reed WA, Knudsen E. Quantitative estimates of mode coupling and differential modal attenuation in perfluorinated graded-index plastic optical fiber. *J Lightwave Technol* 2003;21:111–21.
- [3] Green Jr. PE. Optical networking update. *IEEE J Sel Areas Commun* 1996;14:764–79.
- [4] Koepfen C, Shi RF, Chen WD, Garito AF. Properties of plastic optical fibers. *J Opt Soc Am B* 1998;15:727–39.
- [5] Gloge D. Optical power flow in multimode fibers. *Bell Syst Tech J* 1972;51:1767–83.
- [6] Mateo J, Losada MA, Zubía J. Frequency response in step index plastic optical fibers obtained from the generalized power flow equation. *Opt Express* 2009;17:2850–60.
- [7] Gloge D. Impulse response of clad optical multimode fibers. *Bell Syst Tech J* 1973;52:801–16.
- [8] Savović S, Djordjevich A. Influence of numerical aperture on mode coupling in step index plastic optical fibers. *Appl Opt* 2004;43:5542–6.
- [9] Breyer F, Hanik N, Lee J, Randel S. Getting impulse response of SI-POF by solving the time-dependent power-flow equation using Cranck-Nicholson scheme. In: Bunge C-A, Poisel H, editors. *Proceedings of the POF Modelling Workshop*, 24–28 June, Nurnberg, Germany, 2007, p. 111–9.
- [10] Mateo J, Losada MA, Garcés I, Zubía J. Global characterization of optical power propagation in step-index plastic optical fibers. *Opt Express* 2006;14:9028–35.
- [11] Gambling WA, Payne DN, Matsumura H. Mode conversion coefficients in optical fibers. *Appl Opt* 1975;14:1538–42.
- [12] Dugas J, Maurel G. Mode-coupling processes in polymethyl methacrylate-core optical fibers. *Appl Opt* 1992;31:5069–79.
- [13] Rousseau M, Jeunhomme L. Numerical solution of the coupled-power equation in step index optical fibers. *IEEE Trans Microwave Theory Tech* 1977;25:577–85.
- [14] Jeunhomme L, Fraise M, Pocholle JP. Propagation model for long step-index optical fibers. *Appl Opt* 1976;15:3040–6.
- [15] Garito AF, Wang J, Gao R. Effects of random perturbations in plastic optical fibers. *Science* 1998;281:962–7.
- [16] Savović S, Djordjevich A, Tse PW, Zubia J, Mateo J, Losada MA. Determination of the width of the output angular power distribution in step index multimode optical fibers. *J Opt* 2010;12(115405):5.

Comparison of Methods for Calculating Coupling Length in Step-Index Optical Fibers

S. SAVOVIĆ^{a,b,*}, A. DJORDJEVIĆ^b, B. DRLJAČA^a AND M.S. KOVAČEVIĆ^a

^aFaculty of Science, R. Domanovica 12, 34000 Kragujevac, Serbia

^bCity University of Hong Kong, 83 Tat Chee Avenue, Hong Kong, China

A recently reported function for calculation of the coupling length at which the equilibrium mode distribution is achieved in step-index plastic optical fibers is compared to a long established calculation method and to experimental findings. The recent function, while simpler to apply as it eliminates the need to numerically solve the power flow equation repeatedly for every case, is also more accurate for high numerical aperture (0.45 to 0.5) plastic optical fibers.

PACS numbers: 42.81.-i, 42.81.Qb, 42.81.Uv

1. Introduction

Mode coupling in a step-index (SI) plastic optical fiber transfers power between neighboring modes. It thus progressively alters the input power distribution along the fiber length. Consequently, it has been described as strongly affecting transmission characteristics of the fiber [1–5]. Mode coupling is caused by fiber impurities and inhomogeneities introduced during the fiber manufacturing process. Examples of such imperfections are microscopic bends, diameter variations, irregularity of the core-cladding boundary, and refractive index distribution fluctuations [6].

Due to mode coupling, the optical power distribution at the output end of the fiber depends not only on the launch conditions, but also on fiber properties and length. For example, light launched along a cone with a specific angle relative to the fiber axis will form a sharply defined ring radiation pattern at the output end of only short fibers. Because of mode coupling, the boundary (edges) of such a ring become blurred or fuzzy at the end of longer fibers. The extent of this fogginess increases with fiber length and the ring-pattern evolves gradually into a disk. The disk extends across the entire fiber core when the “coupling length” L_c of the fiber is reached.

An equilibrium mode distribution (EMD) exists beyond the coupling length L_c of the fiber. It is characterized by the absence of rings regardless of launch conditions (i.e. angle of launch). While extending fully across the fiber core, the resulting disk pattern is not yet uniform throughout as light distribution across it still varies with launch conditions. Nevertheless, EMD indicates a substantially complete mode coupling. It is of critical importance when measuring characteristics of multimode

optical fibers (linear attenuation, band width, etc.). Measurement of these characteristics is considered meaningful only if performed at or beyond the EMD condition when it is possible to assign to a fiber a unique value of loss per unit length [1]. At distance z_s ($z_s > L_c$) from the input fiber end, all individual disk patterns corresponding to different launch angles take the same light-distribution across the fiber core. The “steady state distribution” (SSD) is then said to have been achieved as the output light distribution becomes independent of launch conditions. SSD indicates the full completion of (the effects of) the mode coupling process (actually the coupling process continues but with no further apparent effects).

To experimentally determine the fiber length L_c where the EMD is achieved, pulse broadening measurements can be performed for different fiber lengths z while trying to identify the length $z = L_c$ beyond which the band width becomes proportional to $1/z^{1/2}$ instead of $1/z$ [2, 7]. An alternative method of determining L_c is to identify the fiber length after which all output angular power distributions take the disk form regardless of the incidence angle (within the numerical aperture (NA) of the fiber).

As for analytical methods, most reported calculations make use of the coupling constant D in Gloge’s power flow equation [8], which is a partial differential equation. In this paper, the coupling length L_c for achieving EMD in SI plastic optical fiber (POF) is calculated also using a recently reported function [9]. This allowed the comparison of the two methods with respect to reported experimental findings.

2. Calculation of the coupling length L_c

Assuming that mode coupling in multimode optical fibers occurs predominantly between adjacent modes,

* corresponding author; e-mail: savovic@kg.ac.rs

Gloge has derived his time-dependent power flow equation (1) [7]. It determines the power distribution in the core $P(\theta, z, t)$ as a function of the propagation angle θ (measured relative to the core axis), coordinate along the fiber axis z (measured from the input fiber end), and time t . This power distribution $P(\theta, z, t)$ is related to the modal attenuation, modal dispersion, and mode coupling, which are represented by three respective terms on the right side of (1):

$$\frac{\partial P(\theta, z, t)}{\partial z} = -A\theta^2 P(\theta, z, t) - \frac{n}{2c}\theta^2 \frac{\partial P(\theta, z, t)}{\partial t} + \frac{D}{\theta} \frac{\partial}{\partial \theta} \left(\theta \frac{\partial P(\theta, z, t)}{\partial \theta} \right), \quad (1)$$

where A is the second-order multiplicative factor in the series expansion of the power loss coefficient $\alpha(\theta)$ due to absorption and scattering: $\alpha(\theta) = \alpha_0 + A\theta^2 + \dots$; c is the velocity of light in vacuum; and $D = d_0(\lambda/4an)^2$ in which λ , a and n are the free-space wavelength of light, core radius and refractive index of the core, respectively, while d_0 is the zero-order term in the series expansion of the expression for the coupling coefficient $d(\theta) = d_0 + \alpha(\theta)\theta^2 + \dots$. The tacit assumption that the coupling coefficient $d(\theta)$ is constant (equal to d_0) has been used routinely for SI POF in the absence of reliable estimates of other terms in the expansion series of $d(\theta)$ [6, 8–14].

Using the power-flow Eq. (1), Gloge obtained that the broadening of the transmitted (relative to the input) pulse width in step-index optical fibers progresses slower with, than without, mode coupling [7]. This broadening in the presence of coupling effects is proportional to $z^{1/2}$ (rather than z without coupling):

$$\tau = \frac{n^2 \sin^2(\Theta_\infty)}{2nc} \left(\frac{z}{4\gamma_\infty} \right)^{1/2}, \quad (2)$$

where $\Theta_\infty = (4D/A)^{1/4}$ is the angular width of the steady state mode distribution and $\gamma_\infty = (4DA)^{1/2}$ is the overall loss coefficient.

Expression (2) reveals the improvement and penalty resulting from mode coupling. On the one hand, uncoupled and uniformly attenuated modes cause the impulse response to broaden to a higher effective width of $z(n \sin \Theta_\infty)^2/2nc$ in z km of fiber. Mode coupling reduces this undesirable effect by a factor of $(4\gamma_\infty z)^{1/2}$. On the other hand, the overall attenuation increases by $4.35\gamma_\infty$ dB/km in the presence of coupling. For trade-off analysis, “coupling length” L_c is defined as:

$$L_c = \frac{1}{4\gamma_\infty} = \frac{1}{8(DA)^{1/2}}. \quad (3)$$

This coupling length marks the point at which the width of the impulse response changes from linear to a square-root dependence of length.

In our previous works we have shown that coupling length of SI POFs depends both on NA of the fiber [13] as well as on the width of the launch beam distribution [9]. One can calculate the coupling length in SI POFs with high NA (0.45 to 0.5) using equation [9]:

$$\log L_c = a + b \log D \quad (4)$$

i.e.

$$L_c = 10^a D^b, \quad (5)$$

where $a = -1.9700 \pm 0.0448$ and $b = -1.0243 \pm 0.0168$ for laser launch beam distributions (full width at half maximum (FWHM) of 2.5° was assumed); and $a = -2.2908 \pm 0.0069$ and $b = -0.9986 \pm 0.0026$ for LED launch beam distributions (FWHM of 33° was assumed).

The expression (4) takes two different sets of coefficients for different launch-beam widths. This contrasts Gloge’s result (3) in which the coupling length is independent of the width of the launch beam distribution. We will verify the accuracy of the proposed function (4) for calculating the coupling length L_c .

3. Results

In order to test and compare the Gloge function (3) and our recently proposed function (4), we used them to evaluate the coupling length L_c for high-NA SI POF investigated experimentally by Zubia et al. [11]. This fiber’s core diameter is $d = 0.98$ mm. Its refractive index of the core is $n = 1.492$, theoretical numerical aperture $NA = 0.5$, and critical angle $\theta_c = 19.6^\circ$ (measured inside the fiber), i.e. $\theta_c = 30^\circ$ (measured in air). Values of $D = 7.5 \times 10^{-4}$ rad²/m and $A = 1.37$ (rad² m)⁻¹ have been reported for this fiber [11]. Using Gloge’s Eq. (3), we obtain coupling length $L_c = 3.9$ m. Using Eq. (4), we obtain $L_c = 17$ m, where $a = -1.9700 \pm 0.0448$ and $b = -1.0243 \pm 0.0168$ for laser launch beam distributions with FWHM of 2.5° , since Zubia et al. have used laser source in their experiment. In our previous work [14], by solving the time-independent power flow equation (Eq. (1) without the second term on the right-hand side), we have obtained that $L_c = 17.6$ m. Zubia et al.’s experimental results [11] showed for 3 m long optical fiber that the coupling of only lower order modes occurs at such short fiber length while higher order modes have apparently still not started to couple. This is experimental evidence that the coupling length $L_c = 3.9$ m obtained using Gloge’s function is not accurate and that a longer fiber length ($L_c = 17.6$ m) is needed for achieving EMD.

A similar value for $L_c = 15$ – 20 m has been obtained experimentally by Garito et al. [6] for high NA (0.51) SI POF. Short coupling lengths of 0.5 to 4 m for laser launch beam input were reported only for SI POF’s strained by many small-radius bends [15, 16]. In strained fibers due to their tight bends introduced an additional coupling effect (by curvature) occurs that is reflected in a more than one order of magnitude higher coupling coefficient D for the overall fiber configuration (of $D \approx 10^{-3}$ to 10^{-2} rad²/m depending on the number, frequency and severity of bends in the configuration; whereas for unstrained fibers $D \approx 10^{-4}$ rad²/m and $D = 5.62 \times 10^{-4}$ rad²/m in Garito’s case [6]). As a consequence, equilibrium mode distribution in strained fibers is achieved at shorter distances than for straight fibers.

It follows that our recently proposed function (4) for calculating the coupling length in SI POFs with high NA (0.45 to 0.5) is more accurate than Gloge's function (3) which substantially underestimates the coupling length. The reason for this is that Gloge's function (3) takes into account neither the influence of NA on the coupling length, nor the width of the launch beam distribution. Finally, using our recently proposed method of calculating L_c , one does not need to know the coefficient A in (1). This is not the case when using Gloge's function.

4. Conclusion

We have tested the recently reported function (4) [9] for calculation of the coupling length (fiber length where the equilibrium mode distribution is achieved) in the case of SI POF. This function simplifies the determination of the coupling length by eliminating the need to numerically solve the power flow equation (or equivalent) repeatedly for every new case including every new geometric configuration (i.e. bending arrangement) of the fiber if strained fibers are considered as well [16]. We found that this function is more accurate for high-NA (0.45 to 0.5) SI POFs than Gloge's function (3) [7] that then substantially underestimates the coupling length. The reason for this is that Gloge's function (3) takes into account neither the dependence of the coupling length on fiber's NA, nor the width of the launch beam distribution, which factors play more prominent role in high-NA fibers than in lower-NA fibers.

Acknowledgments

The work described in this paper was supported by a grant from City University of Hong Kong (Project

No. 7002313) and by a grant from Serbian Ministry of Science (Project No. 141037).

References

- [1] J. Dugas, G. Maurel, *Appl. Opt.* **31**, 5069 (1992).
- [2] G. Jiang, R.F. Shi, F. Garito, *IEEE Photon. Technol. Lett.* **9**, 1128 (1997).
- [3] S. Zheng, X. Jin, X. Zhang, *Microwave Opt. Technol. Lett.* **48**, 432 (2006).
- [4] J. Mateo, M.A. Losada, I. Garcés, J. Zubía, *Opt. Express* **14**, 9028 (2006).
- [5] F. Breyer, M. Moerz, N. Hanik, L. Li, S. Randel, B. Spinnler, *Eur. Trans. Telecomm.* **18**, 881 (2007).
- [6] A.F. Garito, J. Wang, R. Gao, *Science* **281**, 962 (1998).
- [7] D. Gloge, *Bell Syst. Tech. J.* **52**, 801 (1973).
- [8] D. Gloge, *Bell Syst. Tech. J.* **51**, 1767 (1972).
- [9] A. Djordjevich, S. Savović, *Opt. Eng.* **47**, 125001 (2008).
- [10] W.A. Gambling, D.P. Payne, H. Matsumura, *Appl. Opt.* **14**, 1538 (1975).
- [11] J. Zubía, G. Durana, G. Aldabaldetrekú, J. Arrue, M.A. Losada, M. Lopez-Higuera, *J. Lightwave Technol.* **21**, 776 (2003).
- [12] S. Savović, A. Djordjevich, *Appl. Opt.* **46**, 1477 (2007).
- [13] S. Savović, A. Djordjevich, *Appl. Opt.* **43**, 5542 (2004).
- [14] A. Djordjevich, S. Savović, *J. Opt. Soc. Am. B* **21**, 1437 (2004).
- [15] S. Savović, A. Djordjevich, *Appl. Opt.* **45**, 6775 (2006).
- [16] M.A. Losada, I. Garcés, J. Mateo, I. Salinas, J. Lou, J. Zubía, *J. Lightwave Technol.* **20**, 1160 (2002).

Equilibrium Mode Distribution and Steady State Distribution in Step-Index Glass Optical Fibers

S. SAVOVIĆ^{a,b,*}, A. DJORDJEVIĆ^a, B. DRLJAČA^b AND A. SIMOVIĆ^b

^aCity University of Hong Kong, 83 Tat Chee Avenue, Hong Kong, China

^bFaculty of Science, R. Domanovica 12, 34000 Kragujevac, Serbia

Using the power flow equation, we have examined mode coupling in a step-index multimode glass optical fiber. As a result, the coupling length at which the equilibrium mode distribution is achieved and the length of fiber required for achieving the steady-state mode distribution are obtained. These lengths are much longer for glass fiber than they are for plastic optical fibers. Our results are in good agreement with experimental results reported earlier.

PACS numbers: 42.81.-i, 42.81.Qb, 42.81.Uv

1. Introduction

For decades, glass optical fibers (GOFs) have been the preferred transmission medium in high-capacity communications networks and long-distance communications systems. In contrast, plastic optical fibers (POFs) are usually considered for short data links. Local networking with POFs benefits from the rapid (less laborious) interconnectivity with low precision and cost components as POFs couple light efficiently due to their large diameter (≈ 1 mm) and high numerical aperture. However, POF performance is clearly attenuation limited. A typical attenuation level for step-index (SI) POFs is ≈ 100 dB/km — compared with ≈ 0.5 dB/km for SI GOFs [1]. This limits POF data links to lengths shorter than 100 m. Typically, optical implementations of long-distance communications systems (greater than 1 km) employ GOF.

Transmission characteristics of step-index optical fibers depend strongly upon the differential mode attenuation and the rate of mode coupling. The latter represents power transfer from lower to higher order modes caused by fiber impurities and inhomogeneities introduced during the fiber manufacturing process (such as microscopic bends, irregularity of the core-cladding boundary and refractive index distribution fluctuations). In the absence of these intrinsic perturbation effects, light launched at a specific angle with respect to the fiber axis forms a sharply defined ring radiation-pattern at the output fiber end. Due to mode coupling, the boundaries of the ring become blurred at the end of longer fibers. This fuzziness increases with fiber length. As the ring-pattern evolves gradually, it eventually takes the form of a disk covering the entire fiber cross-section in fibers longer than the “coupling length” L_c . The “equilibrium mode distribution” (EMD) exists beyond the coupling length L_c of the fiber. It is characterized by the absence of rings re-

gardless of the launch conditions, even though the disk pattern may have different light distributions across it depending on the launch conditions. EMD indicates a substantially complete mode coupling and is of critical importance when measuring characteristics of multimode optical fibers (linear attenuation, bandwidth, etc.). Indeed, measurement of these characteristics would only be considered as meaningful if performed at the EMD condition when it is possible to assign to a fiber a unique value of loss per unit length [2]. At distance z_s ($z_s > L_c$) from the input fiber end, all individual disk patterns corresponding to different launch angles take the same light-distribution across the fiber-section and the “steady state distribution” (SSD) is achieved. SSD indicates the completion of the mode coupling process and the independence of the output light distribution from launch conditions.

Output angular power distribution in the near and far fields of an optical fiber end has been studied extensively. Work has been reported using geometric optics (ray approximation) to investigate mode coupling and predict output-field patterns [3, 4]. By employing the power flow equation [5–9] as well as the Fokker–Planck and Langevin equations [10], these patterns have been predicted as a function of the launch conditions and fiber length. In this paper, our solution of the power flow equation determines the coupling length L_c for achieving the EMD, the transition states along L_c , as well as the length z_s for achieving the SSD. To allow comparisons, results are illustrated on the case of the SI GOF investigated earlier by Jeunhomme et al. [11].

2. Power flow equation

Gloge’s power flow equation is [6]:

$$\frac{\partial P(\theta, z)}{\partial z} = -\alpha(\theta)P(\theta, z) + \frac{D}{\theta} \frac{\partial}{\partial \theta} \left(\theta \frac{\partial P(\theta, z)}{\partial \theta} \right), \quad (1)$$

where $P(\theta, z)$ is the angular power distribution, z is distance from the input end of the fiber, θ is the prop-

* corresponding author; e-mail: savovic@kg.ac.rs

agation angle with respect to the core axis, D is the coupling coefficient assumed constant [5, 7] and $\alpha(\theta)$ is the modal attenuation. The boundary conditions are $P(\theta_c, z) = 0$, where θ_c is the critical angle of the fiber, and $D(\partial P/\partial\theta) = 0$ at $\theta = 0$. Condition $P(\theta_c, z) = 0$ implies that modes with infinitely high loss do not carry power. Condition $D(\partial P/\partial\theta) = 0$ at $\theta = 0$ indicates that the coupling is limited to the modes propagating with $\theta > 0$. Except near cutoff, the attenuation remains uniform $\alpha(\theta) = \alpha_0$ throughout the region of guided modes $0 \leq \theta \leq \theta_c$ [7] (it appears in the solution as the multiplication factor $\exp(-\alpha_0 z)$ that also does not depend on θ). Therefore, $\alpha(\theta)$ need not be accounted for when solving (1) for mode coupling, and this equation reduces to [8]:

$$\frac{\partial P(\theta, z)}{\partial z} = \frac{D}{\theta} \frac{\partial P(\theta, z)}{\partial \theta} + D \frac{\partial^2 P(\theta, z)}{\partial \theta^2}. \quad (2)$$

The solution of Eq. (2) for the steady-state power distribution is given by [7]:

$$P(\theta, z) = J_0 \left(2.405 \frac{\theta}{\theta_c} \right) \exp(-\gamma_0 z), \quad (3)$$

where J_0 is the Bessel function of the first kind and zero order and $\gamma_0 [\text{m}^{-1}] = 2.405^2 D/\theta_c^2$ is the attenuation coefficient. We used this solution to test our numerical results for the case of the fiber length at which the power distribution becomes independent of the launch conditions.

In order to obtain numerical solution of the power flow Eq. (2) we have used the explicit finite-difference method (EFDM) to investigate mode coupling in short step-index plastic optical fibers (length up to hundred meters) [8, 12, 13]. We now employ EFDM, in our knowledge for the first time, for solving the power flow equation in much longer (kilometers in length) step-index glass optical fiber. This should also be a test of accuracy and efficiency of the EFDM for such a long fiber.

To start the calculations, we used Gaussian launch-beam distribution of the form

$$P(\theta, z) = \exp \left(-\frac{(\theta - \theta_0)^2}{2\sigma^2} \right), \quad (4)$$

with $0 \leq \theta \leq \theta_c$, where θ_0 is the mean value of the incidence angle distribution, with the full width at half maximum FWHM = 2.355σ (σ is standard deviation). This distribution is suitable both for LED and laser beams.

3. Numerical results

In this paper, we analyze mode coupling in the CGW-CGE-68 step-index multimode glass optical fiber used in the experiment reported earlier [11]. This fiber's critical angle is $\theta_c = 7.26^\circ$ (measured inside the fiber), i.e. $\theta_c = 10.6^\circ$ (measured in air). Value of coupling coefficient of $D = 7.9 \times 10^{-7} \text{ rad}^2/\text{m}$ has been reported for this fiber [11] (it is required in Eq. (1)) — which we have adopted in this work.

Our numerical solution of the power flow equation gives the evolution of the normalized output power distribution with fiber length z as z is incremented from zero until achieving the SSD. The situation is shown in Fig. 1 for

selected four such z values, each for three different input angles $\theta_0 = 0, 3$ and 6° (measured inside the fiber). We selected Gaussian launch beam distribution with FWHM = 1.2° by setting $\sigma = 0.5095^\circ$ in Eq. (4). We used the step lengths of $\Delta\theta = 0.05^\circ$ and $\Delta z = 0.0005 \text{ m}$ in order to achieve stability of our finite difference scheme [8, 14].

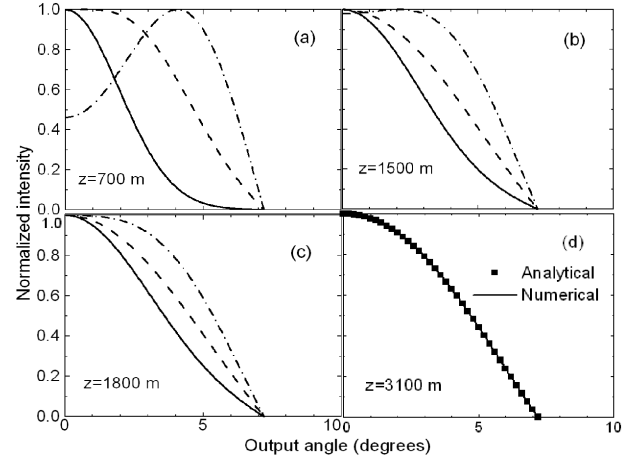


Fig. 1. Normalized output angular power distribution at different locations along the SI GOF calculated for three Gaussian input angles $\theta_0 = 0^\circ$ (solid line), 3° (dashed line) and 6° (dash-dotted line) with FWHM = 1.2° for: (a) $z = 700 \text{ m}$, (b) $z = 1500 \text{ m}$, (c) $z = 1800 \text{ m}$, and (d) $z = 3100 \text{ m}$ (filled squares represent the analytical steady-state solution).

One can observe from radiation patterns in the fiber of shorter length $z = 700 \text{ m}$ in Fig. 1a that the coupling is stronger for the low-order modes: the Gaussian beam launched at 3° has already shifted to $\theta = 0^\circ$. Coupling of higher order modes can be observed better only after more substantial fiber lengths (Fig. 1b). It is not until the fiber's coupling length $L_c = 1800 \text{ m}$ that all the mode-distributions shift their mid-points to zero degrees (from their respective initial values at the input fiber end), producing the EMD in Fig. 1c. The coupling continues further along the fiber beyond the L_c mark until all distributions' widths equalize and SSD is reached at the length of $z_s = 3100 \text{ m}$, Fig. 1d. Figure 1d shows normalized curves of the output angular power distribution obtained by the power flow equation by the EFDM (solid curve) as well as the steady state analytical solution of Eq. (2) (squares), where $\gamma_0 = 2.86 \times 10^{-4} \text{ m}^{-1}$. The two solutions are in good agreement with the relative error below the 0.95%. It is important to note here that although the total integration fiber length (length for achieving SSD) in this case is of the order of kilometers, which is much longer than the length for achieving SSD in plastic optical fibers (typically up to hundred meters), the accumulated truncation errors of the applied numerical procedure is not too much larger if compared to the case of short plastic optical fibers where relative error is usually up to 0.2% [8, 12, 13]. Thus, we conclude that EFDM is efficient and accurate for solving the

power flow equation, both in the case of short (plastic) and very long (glass) optical fibers. Our numerical result for z_s is in good agreement with the experimental result by Jeunhomme et al. [11]. who obtained, by varying the launch beam angle, that SSD is achieved in 3000 m long SI GOF (Jeunhomme's experimental steady state output-field pattern is shown in Fig. 2).

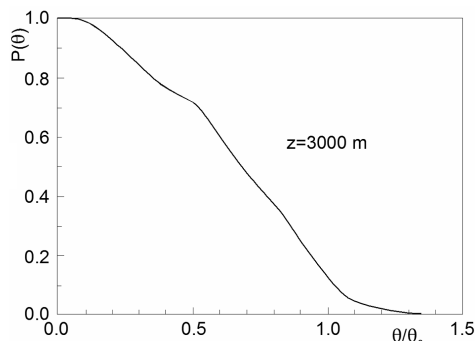


Fig. 2. Experimentally determined [11] normalized steady state output angular power distribution for He-Ne laser launch beam at fiber length of 3000 m (reconstructed).

In summary, our numerical results show a much longer coupling length ($L_c = 1800$ m) in SI GOF than in SI POFs (typically $L_c \cong 15$ to 35 m [13, 14]). Similarly, the length for achieving the SSD is also much longer in the SI GOF ($z_s = 3100$ m) than in SI POFs (usually up to one hundred meters). This is attributed to the weaker intrinsic perturbation effects in SI GOFs.

4. Conclusions

Using the power flow equation, we have examined the state of mode coupling in a long step-index glass optical fiber by observing, for different launch angles, the output angular power distribution as it varied with the fiber length. For the CGW-CGE-68 fiber, we have obtained that the coupling length for achieving the equilibrium mode distribution is 1800 m and the length for achieving the steady state power distribution is 3100 m. This is much longer than for plastic optical fibers with typi-

cal coupling lengths from 15 to 35 m [13]. On a separate note, the explicit finite difference method applied in our knowledge for the first time to solve the power flow equation in a kilometers long fiber has turned out to be efficient and accurate.

Acknowledgments

The work described in this paper was supported by a grant from City University of Hong Kong (project No. 7002313) and by a grant from Serbian Ministry of Science (project No. 141023).

References

- [1] W. Daum, J. Krauser, P.E. Zamzow, O. Ziemann, *POF-Polymer Optical Fibers for Data Communications*, Springer, Berlin 2002.
- [2] J. Dugas, G. Maurel, *Appl. Opt.* **31**, 5069 (1992).
- [3] M. Eve, J.H. Hannay, *Opt. Quantum Electron.* **8**, 503 (1976).
- [4] J. Arrue, G. Aldabaldetrekue, G. Durana, J. Zubia, I. Garcés, F. Jiménez, *J. Lightwave Technol.* **23**, 1253 (2005).
- [5] W.A. Gambling, D.N. Payne, H. Matsumura, *Appl. Opt.* **14**, 1538 (1975).
- [6] D. Gloge, *Bell Syst. Tech. J.* **51**, 1767 (1972).
- [7] M. Rousseau, L. Jeunhomme, *IEEE Trans. Microwave Theory Tech.* **25**, 577 (1977).
- [8] A. Djordjevich, S. Savović, *IEEE Photon. Technol. Lett.* **12**, 1489 (2000).
- [9] S. Savović, A. Djordjevich, *Appl. Opt.* **41**, 7588 (2002).
- [10] S. Savović, A. Djordjevich, *Appl. Opt.* **41**, 2826 (2002).
- [11] L. Jeunhomme, M. Fraise, J.P. Pocholle, *Appl. Opt.* **15**, 3040 (1976).
- [12] S. Savović, A. Djordjevich, *Appl. Opt.* **43**, 5542 (2004).
- [13] S. Savović, A. Djordjevich, *Appl. Opt.* **45**, 6775 (2006).
- [14] G. Jiang, R.F. Shi, A.F. Garito, *IEEE Photon. Technol. Lett.* **9**, 1128 (1997).

Calculation of the Impulse Response of Step-Index Plastic Optical Fibers Using the Time-Dependent Power Flow Equation

B. DRLJAČA^a, S. SAVOVIĆ^{a,b,*} AND A. DJORDJEVIĆ^b

^aFaculty of Science, R. Domanovica 12, 34000 Kragujevac, Serbia

^bCity University of Hong Kong, 83 Tat Chee Avenue, Hong Kong, China

The analytical solution of the time-dependent power flow equation is employed to calculate impulse response in a step-index plastic optical fiber. Results are given at different fiber lengths and are shown to agree with those reported in the literature. Mode-dependent attenuation, modal dispersion and mode coupling in plastic optical fibers are known to affect fiber-optic power delivery, data transmission, and sensing systems.

PACS numbers: 42.81.-i, 42.81.Qb, 42.81.Uv

1. Introduction

Transmission properties of step-index (SI) multimode optical fibers depend strongly upon mode-dependent attenuation, modal dispersion and the rate of mode coupling (power transfer from lower to higher order modes) caused by intrinsic perturbation effects (primarily due to microscopic bends, irregularity of the core-cladding boundary and refractive index distribution fluctuations). Different simulation models are usually required for these three important effects in SI optical fibers. The ray tracing model calculates the trajectory for each ray through the fiber. It enables the calculation of the impulse response including the process of mode-dependent attenuation and modal dispersion. This model is computationally intensive as a large number of ray-trajectories must be generated. In contrast, using the time-independent power flow equation [1], mode-dependent attenuation and mode coupling can be modeled effectively to reveal their influence on transmission characteristics of the fiber. Furthermore, using the time-dependent power flow equation, one can model all three major fiber effects [2]. Using the time-dependent power flow equation, we report in this work on the impulse response in SI plastic optical fiber (POF) that has been investigated by Breyer et al. [3].

2. Time-dependent power flow equation

We use Gloge's time-dependent power flow equation to describe the evolution of the modal power distribution

along the axis of the SI POF (as coordinate z). Individual modes are characterized by their inner propagation angle θ measured with respect to fiber axis. Gloge's time-dependent power flow equation can be written as [2]:

$$\frac{\partial P(\theta, z, t)}{\partial z} + \frac{\partial t}{\partial z} \frac{\partial P(\theta, z, t)}{\partial t} = -\alpha(\theta)P(\theta, z, t) + \frac{1}{\theta} \frac{\partial}{\partial \theta} \left[\theta D(\theta) \frac{\partial P(\theta, z, t)}{\partial \theta} \right], \quad (1)$$

where t is time, $P(\theta, z, t)$ is power distribution over angle, space and time, $\alpha(\theta)$ is mode-dependent attenuation, $\partial t/\partial z$ is mode delay per unit length and $D(\theta)$ is mode-dependent coupling coefficient. Mode-dependent attenuation can be written in the form $\alpha(\theta) = \alpha_0 + A\theta^2 + \dots$, where α_0 describes the loss common to all modes. It can be accounted for later by multiplying the end-solution by the term $e^{-\alpha_0 z}$ [4]. Therefore, in solving (1) one should consider only the term $A\theta^2$, which is most important among the higher order modes [1]. Assuming also that coupling coefficient D is mode-independent, Eq. (1) can be written as follows [2]:

$$\frac{\partial P(\theta, z, t)}{\partial z} + \frac{\partial t}{\partial z} \frac{\partial P(\theta, z, t)}{\partial t} = -A\theta^2 P(\theta, z, t) + \frac{D}{\theta} \frac{\partial}{\partial \theta} \left[\theta \frac{\partial P(\theta, z, t)}{\partial \theta} \right]. \quad (2)$$

The derivative $\partial t/\partial z$ can be obtained using the group velocity of a mode with characteristic angle θ , which is

$$\frac{dz}{dt} = \frac{c}{n(1 + \theta^2/2)}. \quad (3)$$

Neglecting the delay n/c common to all modes, Eq. (2) could be rewritten [2], and after applying the Laplace transform

* corresponding author; e-mail: savovic@kg.ac.rs

$$p(\theta, z, s) = \int_0^\infty e^{-st} P(\theta, z, t) dt, \quad (4)$$

Eq. (2) agrees with the time-independent power flow equation

$$\frac{\partial p}{\partial z} = -A\sigma^2\theta^2 p + \frac{D}{\theta} \frac{\partial}{\partial \theta} \left(\theta \frac{\partial p}{\partial \theta} \right), \quad (5)$$

except for the factor σ^2 [1]. One can therefore use the solution of the time-independent power flow equation, if A is replaced by $A\sigma^2$. For the Gaussian input distribution one obtains [1]:

$$p(\theta, z, s) = f(z, s) \exp(-\theta^2/\Theta^2(z, s)), \quad (6)$$

where $\Theta^2(z, s)$ and $f(z, s)$ are described by Gloge [1].

For continuous wave excitation ($s = 0$), the angular width $\Theta(z, 0)$ changes monotonically from Θ_0 to Θ_∞ as z increases. Since the width Θ_∞ characterizes a distribution which propagates unchanged (at steady state) and with the minimum overall loss coefficient γ_∞ , it seems practical to excite this distribution right from the beginning ($\Theta_0 = \Theta_\infty$) [2]. The closed-form Laplace transform of (6) exists only for the approximation given in the limits $z \ll 1/\gamma_\infty$ (short fiber) and $z \gg 1/\gamma_\infty$ (long fiber) [2].

In the case of short fiber, Eq. (6) becomes [2]:

$$p(\theta, z, s) = \frac{f(0, s)}{1 + \gamma_\infty z} \exp\left(-\theta^2 \left(\frac{1}{\Theta_0^2} + \frac{nz}{2c}s\right)\right). \quad (7)$$

The total output is obtained from the integration $p(\theta, z, s)$ over all angles [2]. With reference to (7) and for $z \ll 1/\gamma_\infty$, one obtains [2]:

$$q = \frac{\pi f(0, s) \Theta_0^2}{(1 + \gamma_\infty z)(1 + n\Theta_0^2 z s / 2c)}. \quad (8)$$

If one sets $f(0, s) = 1$, which corresponds to an infinitesimally short input pulse of energy 1, the Laplace transformation of (8) yields the impulse response of the fiber [2]:

$$Q(z, t) = \frac{2c\pi}{nz(1 + \gamma_\infty z)} \exp(-2ct/n\Theta_0^2 z), \quad (9)$$

where $Q(t)$ is limited practically to a time interval narrower than $n\theta_c^2 z / (2c)$, which is the delay between the fastest and the slowest mode (θ_c is the fiber's critical angle).

In case of a long fiber, Eq. (6) assumes the form [2]:

$$p = \frac{2\sigma}{1 + \sigma} \exp(-\sigma(\theta^2/\Theta_0^2 + \gamma_\infty z)), \quad (10)$$

which leads to

$$q = \frac{2\pi\Theta_0^2}{1 + \sigma} \exp(-\sigma\gamma_\infty z), \quad (11)$$

where p is integrated over all angles θ , as before. Introducing $\sigma = \sqrt{1 + ns/2cA}$ into (12), one can form the Laplace transform of $q(s)$. By using the condition $\gamma_\infty z > 1$, the impulse response of the fiber is

$$Q(z, t) = \Theta_0^2 \sqrt{\frac{\pi}{Tt}} \left(\frac{t}{\gamma_\infty z T} + \frac{1}{2} \right)^{-1} \times \exp\left(-\frac{\gamma_\infty^2 z^2 T}{4t} - \frac{t}{T}\right), \quad (12)$$

where

$$T = \frac{n}{2cA} = \frac{n}{2c} \frac{\Theta_0^2}{\gamma_\infty}. \quad (13)$$

Besides the analytical solution of the time-dependent power flow Eq. (2) which is obtained by Gloge [2], two numerical approaches for solving the time-dependent power flow Eq. (1) have been reported recently: implicit finite-difference method (Crank-Nicholson scheme) by Breyer et al. [3] and explicit finite-difference method in the matrix form by Mateo et al. [5]. In this work using Gloge's analytical solution of (2), we calculate the impulse response of the SI POF investigated earlier by Breyer et al. [3] and compare our analytical results with their numerical results.

3. Results

Using Gloge's analytical solution of the time-dependent power flow Eq. (2) we have calculated impulse response of SI POF investigated earlier by Breyer et al. [3]. The fiber analyzed is the PREMIER GH4001 (GH fiber) from Mitsubishi with the diameter of 1 mm and numerical aperture $NA = 0.5$ (corresponding to inner critical angle of $\theta_c = 19.5^\circ$) and 0.15 dB/m of nominal attenuation. In obtaining the impulse response of GH fiber, Breyer et al. [3] have assumed mode-dependent attenuation $\alpha(\theta)$ and mode-dependent coupling coefficient $D(\theta)$. In contrast, Gloge's analytical solution of the time-dependent power flow Eq. (2) is obtained assuming a constant coupling coefficient D and constant A (A is the second order multiplicative factor in the series expansion of the mode-dependent attenuation $\alpha(\theta)$). In order to obtain the value for A for the fiber analyzed, we used the graph for $\alpha(\theta)$ in Fig. 1 proposed earlier by Mateo

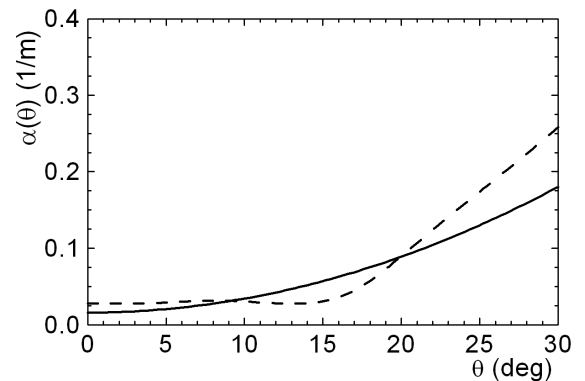


Fig. 1. Mode-dependent attenuation $\alpha(\theta)$ for GH fiber proposed by Mateo et al. [6] (dashed line) and our fit obtained using the function $\alpha(\theta) \approx \alpha_0 + A\theta^2$, with $\alpha_0 = 0.0159$ 1/m and $A = 0.4025$ (rad² m)⁻¹ (solid line).

et al. [6] and used in numerical calculations by Breyer et al. [3]. Since mode-dependent attenuation can be written in the form $\alpha(\theta) \approx \alpha_0 + A\theta^2$, one can determine A by fitting the graph shown in Fig. 1 using this function. In this way, we have obtained $\alpha_0 = 0.0159$ 1/m and $A = 0.4025$ (rad² m)⁻¹. The value of the constant

coupling coefficient $D = 1.171 \times 10^{-4}$ rad²/m has been used in the first approach to the modeling of mode coupling in the analyzed fiber by Mateo et al. [6], which we have adopted in this work. One should mention here that modeling the mode coupling process with a constant D is commonly done by many other authors [1, 4, 7, 8].

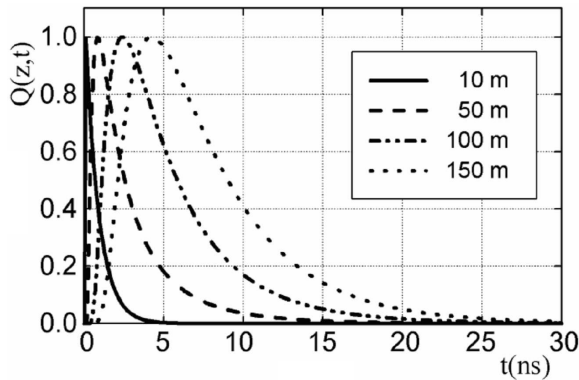


Fig. 2. Analytical results for the impulse response for different fiber lengths for GH fiber (this work).

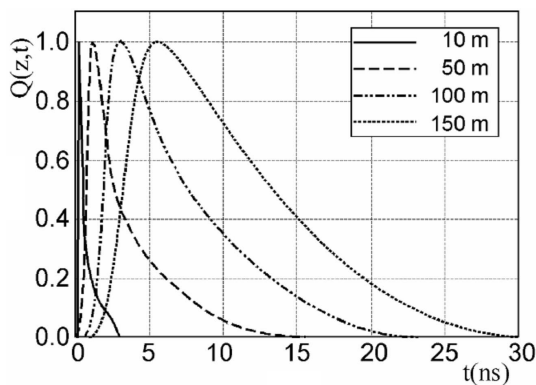


Fig. 3. Numerical results for the impulse response for different fiber lengths for GH fiber obtained by Breyer et al. [3] (retraced).

A Dirac impulse in time and a mode distribution with the width at $1/e$ of $\Theta_0 = \Theta_\infty = 9.85^\circ$ (FWHM = 8.35°) at the beginning of the fiber is used. Equation (9), valid for short fiber lengths $z \ll 1/\gamma_\infty = 41.3$ m, has been used for calculating impulse response at $z = 10$ m. Equation (12), valid in a case of long fiber lengths $z \gg 1/\gamma_\infty$, has been used for calculating impulse response at fiber lengths $z = 50, 100$ and 150 m. Our analytical results for the impulse response of the fiber analyzed are shown in Fig. 2. In Fig. 3, numerical results obtained by Breyer et al. [3] for impulse response are shown for the same fiber lengths. A good agreement between these results is apparent. One can observe that, at short fiber lengths ($z = 10$ m), the mode-dependent attenuation is

the dominant effect. With increasing fiber length, mode coupling begins to influence the impulse shape changing it to Gaussian.

Finally, the power exiting the fiber at the highest angles (tails of the Gaussian launch beam) has the longest delays. This suggests an efficient means of improving the fiber capability by spatial filtering-out of the tail at higher angles [5]. As most power is confined within the range of lower angles, such filtering-out of the power at the highest angles will cause only a small power loss while producing a narrower overall impulse response.

4. Conclusion

The analytical solution of the time-dependent power flow equation is employed to calculate the impulse response in a step-index plastic optical fiber that was investigated earlier by Breyer et al. [3]. Our results for the impulse response at different fiber lengths agree well with the earlier reported numerical results [3]. It has been observed that at short fiber lengths mode-dependent attenuation is the dominant effect. With the increasing fiber length, mode coupling begins to influence impulse response of the fiber, resulting in the impulse shape changing to a Gaussian-like shape. In general, using the information provided by the space-time power distribution, fiber transmission characteristics can be enhanced using an appropriate spatial filter. In doing so, a good fiber characterization can be applied to optimize the fiber performance in POF links.

Acknowledgments

The work described in this paper was supported by a grant from City University of Hong Kong (project No. 7002313) and by a grant from Serbian Ministry of Science (project No. 141037).

References

- [1] D. Gloge, *Bell Syst. Tech. J.* **51**, 1767 (1972).
- [2] D. Gloge, *Bell Syst. Tech. J.* **52**, 801 (1973).
- [3] F. Breyer, N. Hanik, J. Lee, S. Randel, *Proc. POF Modelling Workshop, Nuremberg (Germany), 2007*, Eds. C.-A. Bunge, H. Poisel, 2007, p. 111.
- [4] A. Djordjevich, S. Savović, *J. Opt. Soc. Am. B* **21**, 1437 (2004).
- [5] J. Mateo, M.A. Losada, J. Zubía, *Opt. Express* **17**, 2850 (2009).
- [6] J. Mateo, M.A. Losada, I. Garcés, J. Zubía, *Opt. Express* **14**, 9028 (2006).
- [7] W.A. Gambling, D.P. Payne, H. Matsumura, *Appl. Opt.* **14**, 1538 (1975).
- [8] G. Jiang, R.F. Shi, A.F. Garito, *IEEE Photon. Technol. Lett.* **9**, 1128 (1997).

M30

**МИНИСТЕРСТВО НАУКИ И ВЫСШЕГО ОБРАЗОВАНИЯ
РОССИЙСКОЙ ФЕДЕРАЦИИ**

**Некоммерческое акционерное общество
«Алматинский университет энергетики и связи имени
Гумарбека Даукеева»**

**Федеральное государственное бюджетное образовательное учреждение
высшего образования
«Казанский государственный энергетический университет»**

**ЭНЕРГЕТИКА, ИНФОКОММУНИКАЦИОННЫЕ
ТЕХНОЛОГИИ И ВЫСШЕЕ ОБРАЗОВАНИЕ**

**Международная научно-техническая конференция
(Алматы, Казань, 20-21 октября 2022 г.)**

Электронный сборник научных статей по материалам конференции

В трех томах

Том 2

Алматы, Казань

2023

УДК 620+004+378
ББК 31.1+32.81+74.48
М43

Рецензенты:

д-р техн. наук, профессор кафедры «Гидроэнергетика и возобновляемые источники энергии»
Национального исследовательского университета «МЭИ» К.В. Суслов

д-р экон. наук, зав. сектором «Экономика энергетики» Института энергетики Национальной
академии наук Беларуси Зорина Т.Г.

Редакционная коллегия:

Э.Ю. Абдуллазянов, С.С. Сагинтаева, И.Г. Ахметова, А.А. Саухимов, Ю.С. Валеева,
Р.С. Зарипова, Ж.Б. Суйменбаева

М43 Международная научно-техническая конференция «Энергетика, инфокоммуникационные технологии и высшее образование»: электронный сборник научных статей по материалам конференции: [в 3 томах] / ред.кол. Э.Ю. Абдуллазянов, С.С. Сагинтаева, И.Г. Ахметова, А.А. Саухимов, Ю.С. Валеева, Р.С. Зарипова, Ж.Б. Суйменбаева. – Казань: КГЭУ, 2023. – Т. 2. – 637 с.

ISBN 978-5-89873-616-3 (т. 2)

ISBN 978-5-89873-618-7

В электронном сборнике представлены научные статьи по материалам Международной научно-технической конференции «Энергетика, инфокоммуникационные технологии и высшее образование» по следующим научным направлениям:

1. Теплоэнергетика и теплотехнологии;
2. Электроэнергетика;
3. Радиотехника, электроника и телекоммуникации;
4. Энергообеспечение сельского хозяйства;
5. Промышленная и экологическая безопасность;
6. Математическое моделирование и системы управления;
7. Информационные технологии и кибербезопасность;
8. Космическая инженерия и робототехника;
9. Социально-политическое и культурное развитие Евразии;
10. Экономика знаний как фактор инновационного развития высшего образования.

Предназначены для научных работников, аспирантов и специалистов, работающих в области энергетики, а также для обучающихся образовательных учреждений энергетического профиля.

Статьи публикуются в авторской редакции. Ответственность за содержание статей возлагается на авторов.

УДК 620+004+378
ББК 31.1+32.81+74.48

ISBN 978-5-89873-616-3 (т. 2)
ISBN 978-5-89873-618-7

© КГЭУ, 2023

[10] *Веровкин А.А., Циркунов Ю.М.* Течение дисперсной примеси в сопле Лавалья и рабочей секции двухфазной гиперзвуковой ударной трубы // ПМТФ. 2008. Т. 49. № 5. С. 102.

[12] *Леонтьев А.И., Луцкич В.Г., Реимин А.И.* Теплообмен в конических расширяющихся каналах // ТВТ. 2016. Т. 54. № 2. С. 287.

МРНТИ 49.03.05

УДК 535.24

MODELING OF POWER FLOW IN MULTIMODE W-TYPE PHOTONIC CRYSTAL FIBERS

Branko Drljača¹, Svetislav Savović², Milan S. Kovačević², Ana Simović², Ljubica Kuzmanović², Alexandar Djordjevich³, Gulbakhar Yussupova⁴

¹ University of Priština in Kosovska Mitrovica, Faculty of Sciences and Mathematics, L. Ribara 29, 38220 Kosovska Mitrovica, Serbia

² University of Kragujevac, Faculty of Science, R. Domanovića 12, 34000 Kragujevac, Serbia

³ City University of Hong Kong, Department of Mechanical Engineering, Hong Kong, China

⁴ Satbayev University, 22 Satbaev St., Almaty, The Republic of Kazakhstan

***Abstract:** In this paper recent advances in application of power flow equation to W-type photonic crystal fibers (PCF) is presented. As known for many years power flow equation has been proven to be best solution when transmission characteristics of multimode optical fibers are to be modeled. Transmission properties of multimode optical fibers depend strongly upon modal dispersion, mode-dependent attenuation and the rate of mode coupling. Throughout years different simulation models have been developed to model light transmission in optical fibers. Electromagnetic wave model is usually used in modeling of single mode and few mode fibers and it is not applicable to multimode fibers. The ray tracing model, which calculates the trajectory for each ray through the fiber, enables the calculation of the impulse response (and therefore frequency response and bandwidth) including the process of mode-dependent attenuation and modal dispersion. Beside this model is computationally intensive since it requires a large number of ray trajectories it can't account for mode coupling. In contrast, using the time-independent power flow equation, mode-dependent attenuation and mode coupling can be modeled effectively in order to calculate their influence on transmission characteristics of an optical fiber. Furthermore, using the time-dependent power flow equation, all three major fiber effects can be modeled. In this work we describe application of time-independent power flow equation (TI PFE) on different types of multimode optical fibers.*

Introduction:

Gloge suggested that instead of determining distribution of individual modes in an multimode optical fiber continuum of modes should be introduced [1]. This can be done if two conditions are satisfied: 1) number of modes is large enough and 2) mode coupling occurs only between adjacent modes. Introducing these assumptions, Gloge proposed a partial differential equation which describes the power distribution as a function of fiber length and continuous modal parameter θ , which represents the mode's propagation angle along fibers measured relative to the fiber axis [1]:

$$\frac{\partial P(\theta, z)}{\partial z} = -\alpha(\theta)P(\theta, z) + \frac{1}{\theta} \frac{\partial}{\partial \theta} \left(\theta D(\theta) \frac{\partial P(\theta, z)}{\partial \theta} \right) \quad (1)$$

where $P(\theta, z)$ is the angular power distribution, z is distance from the input end of the fiber and $D(\theta)$ is the mode-dependent coupling coefficient. Modal attenuation $\alpha(\theta)$ can be written in the form $\alpha(\theta) = \alpha_0 + \alpha_d(\theta)$. The term α_0 represents conventional losses by absorption and scattering. It can be neglected in the solution because it would feature as just a fixed multiplier $\exp(-\alpha_0 z)$. The term $\alpha_d(\theta)$ in the expansion of $\alpha(\theta)$ becomes dominant for higher order modes. Boundary conditions for eq. 1 are:

$$P(\theta_c, z) = 0; \quad D \frac{\partial P}{\partial \theta} \Big|_{\theta=0} = 0, \quad (2)$$

where θ_c is critical angle of the fiber.

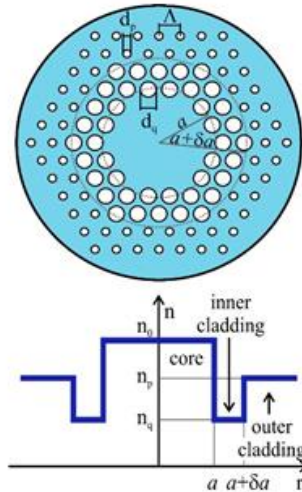


Fig. 1. The cross section and the refractive-index profile of the multimode doubly clad W-type MOF. Λ is the pitch, d_q and d_p are the diameters of inner outer cladding air-holes, respectively.

Considering that in real applications more diverse initial conditions of light injection are required numerical solution is usually often employed in order to model different input conditions that correspond to real application. In recent years explicit finite difference method has been used more often due to its simplicity and ease of use [3,6]. The central difference scheme is used to represent the $(\partial P(\theta, z))/\partial \theta$ and $(\partial^2 P(\theta, z))/\partial \theta^2$ terms, and the forward difference scheme for the term $(\partial P(\theta, z))/\partial z$. We present application of TI PFE for W-type PCF.

W-type PCF

Figure 1 represents the index profile of a W-type PCF with n_0 , n_p and n_q ($n_0 > n_p > n_q$) being indices of refraction of the core, cladding, and intermediate layer, respectively. Modes propagating at angles that are between $\theta_p \cong (2\Delta_p)^{1/2}$ and $\theta_q \cong (2\Delta_q)^{1/2}$ are called the leaky modes [7]; here, $\Delta_p = (n_0 - n_p)/n_0$ or $\Delta_q = (n_0 - n_q)/n_0$ is the relative difference of the refraction index of the cladding, or intermediate layer (respectively).

Using the free-space wave number $k_0 = 2\pi/\lambda$ and expressing the thickness of the intermediate layer as $\delta \cdot a$ where a is the core-radius, constants of attenuation of leaky modes are given as [7]:

$$\alpha_L(\theta) = \frac{4(\theta^2 - \theta_p^2)^{1/2}}{a(1 - \theta^2)^{1/2}} \frac{\theta^2(\theta_q^2 - \theta^2)}{\theta_q^2(\theta_q^2 - \theta_p^2)} \exp\left[-2\delta n_0 k_0 (\theta_q^2 - \theta^2)^{1/2}\right] \quad (3)$$

All guided-modes in singly clad (SC) fibers regardless of their propagation angle θ are attenuated equally; the attenuation rises steeply for radiated-modes. For W-type fibers, this can be generalized in terms of $\alpha_d(\theta)$ in the previously introduced expansion for attenuation $\alpha(\theta) = \alpha_0 + \alpha_d(\theta)$, where:

$$\alpha_d(\theta) = \begin{cases} 0 & \theta \leq \theta_p \\ \alpha_L(\theta) & \theta_p < \theta < \theta_q \\ \infty & \theta \geq \theta_q \end{cases} \quad (4)$$

Equation (4) can also be explained if one would think of a W-fiber as having a vanishing, and then infinite, thickness of its intermediate layer $\delta \cdot a$ (a is the core radius). With $\delta \rightarrow 0$, and then $\delta \rightarrow \infty$, two distinct SC (SC_p and SC_q) fibers result with respective critical angles of θ_p and then θ_q , respectively. This results in three region for the propagation angle evident in (4): less than a critical angle, between the two of them and greater than the other. Modes propagating at angles between the two critical angles θ_p and θ_q are termed leaky modes. For

that range, strong influence of the intermediate layers' thickness $\delta \cdot a$ on $\alpha_L(\theta)$ in (4) has been noted [7].

Fig 1 also represents cross section and refractive-index profile of named multimode W-type PCF with a solid-core and rings of air holes in the cladding, where Λ is the hole-to-hole spacing (pitch), d is diameter of air holes in the cladding. Numerical aperture, dispersion and other fiber properties are thereby engineered by additional design parameters, namely pitch and air-holes size. Despite uniform material properties across the fiber, the central part without holes has the highest refractive index n_0 ; holes in the cladding reduce the effective value n_1 of such index. Larger or more densely spaced holes in the cladding reduce it even more. For PCFs with air holes in a triangular lattice, the effective refractive index of cladding n_{fsm} can be obtained using the effective parameter V :

$$V = \frac{2\pi}{\lambda} a_{eff} \sqrt{n_0^2 - n_{fsm}^2} \quad (5)$$

where n_0 is the refractive index of the core. The effective refractive index of the cladding n_{fsm} is defined as the effective refractive index of so-called fundamental space-filling mode in the triangular hole lattice, and $a_{eff} = \Lambda / \sqrt{3}$ [8]. The effective refractive index of the cladding $n_1 \equiv n_f$, can be obtained from equation (5), using the effective v parameter [8]:

$$V\left(\frac{\lambda}{\Lambda}, \frac{d}{\Lambda}\right) = A_1 + \frac{A_2}{1 + A_3 \exp(A_4 \lambda / \Lambda)} \quad (6)$$

with the fitting parameters A_i ($i=1$ to 4):

$$A_i = a_{i0} + a_{i1} \left(\frac{d}{\Lambda}\right)^{b_{i1}} + a_{i2} \left(\frac{d}{\Lambda}\right)^{b_{i2}} + a_{i3} \left(\frac{d}{\Lambda}\right)^{b_{i3}} \quad (7)$$

where the coefficients a_{i0} to a_{i3} and b_{i1} to b_{i3} ($i=1$ to 4) are given in [11,12]. For this type of fiber, except near cutoff the attenuation remains uniform $\alpha(\theta) = \alpha_0$ throughout the region of guided modes $0 \leq \theta \leq \theta_m$ [10]. Therefore, $\alpha(\theta)$ need not be accounted when solving 1.

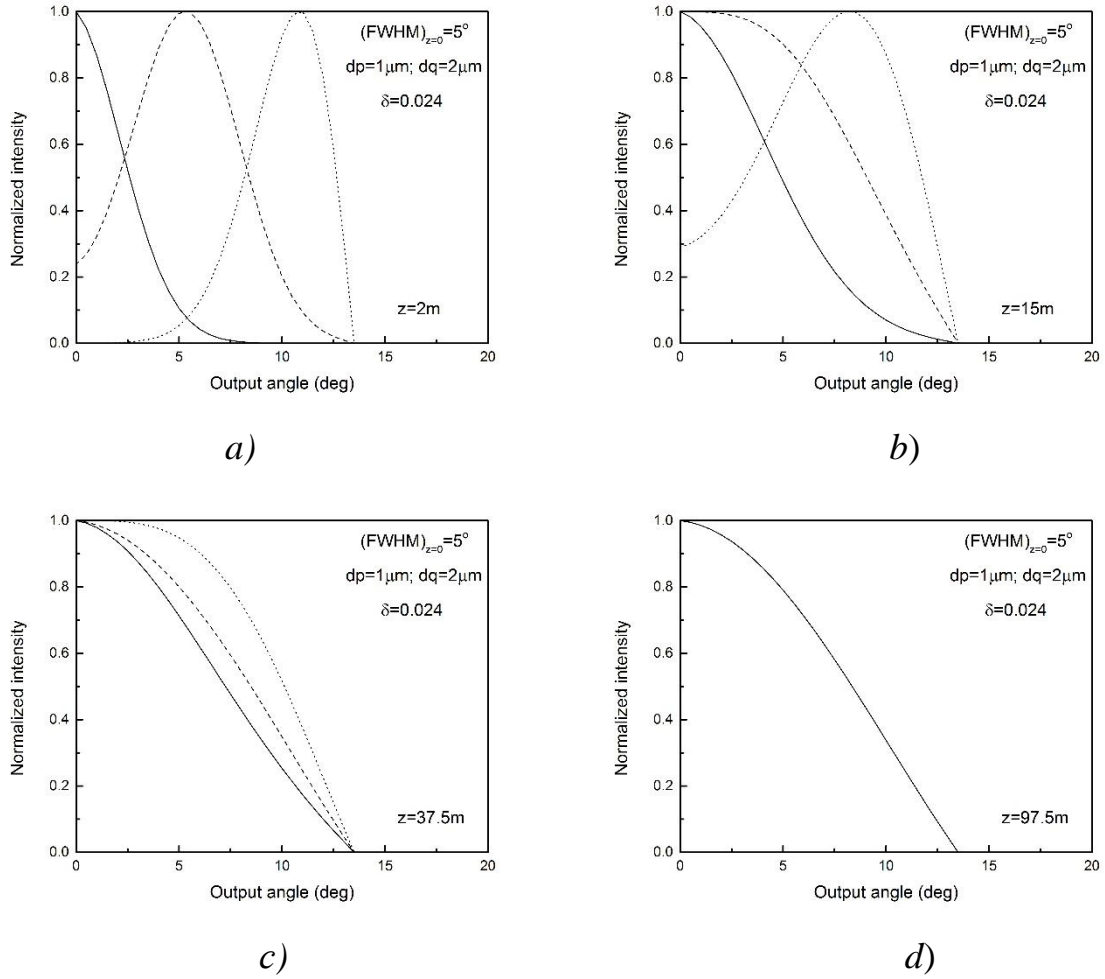


Fig. 2. The evolution of the normalized output angular power distribution obtained with TI PFE for W-type PCF fiber with fiber length for the case with $d_p = 1 \mu\text{m}$ ($n_p = 1.4844$), $d_q = 2 \mu\text{m}$ ($n_q = 1.4458$), $\delta = 0.024$, calculated for Gaussian launch distribution with input angles $\theta_0 = 0^\circ$ (solid line), 6° (dashed line), and 12° (dotted line) with $(\text{FWHM})_{z=0} = 5^\circ$ for: (a) $z = 2 \text{ m}$; (b) $z = 15 \text{ m}$; (c) $z = L_c = 37.5 \text{ m}$ and (d) $z = z_s = 97.5 \text{ m}$.

For W-type PCF the air-holes in the outer cladding are smaller than those in the inner cladding, Fig. 1. The refractive index of the core n_0 is higher than those in two claddings. The lowest effective refractive index n_q is found in the inner cladding, and the outer cladding's effective RI is n_p ($n_q < n_p < n_0$). Attenuation in W-type PCF is calculated using eq. (4) where the attenuation of leaky modes is given by eq. (3). As an illustration of the application of the TI PFE to W-type PCF fibers, we show the results in Fig. 2.

Conclusion:

Mechanism for application of time-independent power flow equation in modeling optical power flow in W-type PCF is presented. In this way equilibrium mode distribution (EMD) and steady state distribution (SSD) of power can be investigated in various types of fibers, out of which one is W-type plastic photonic crystal fiber. For plastic photonic crystal fibers method for determination of effective refractive index of the cladding n_{fsm} are detailed design of holes for obtaining W-type refractive index distribution are presented. This allowed us application of time-independent power flow equation for determining SSD and EMD. Procedure for application of time-independent power flow equation for other types of optical fibers, such as step-index plastic optical fiber or graded-index plastic optical fiber, isn't presented in this paper since it can be found in some of our previous research [13,14].

Funding:

National Natural Science Foundation of China (62003046, 6211101138); Strategic Research Grant of City University of Hong Kong (CityU 7004600); Serbian Ministry of Education, Science and Technological Development grant (451-03-68/2020-14/200122); Science Fund of the Republic Serbia (CTPCF-6379382).

SOURCES

- [1] D. Gloge, Bell Syst. Tech. J., vol. 51, 1767 (1972).
- [2] W. A. Gambling, D. N. Payne and H. Matsumura, "Mode conversion coefficients in optical fibers", Appl. Opt. vol. 14, 1538–1542 (1975).
- [3] A.F. Garito, J. Wang, R. Gao, Science, vol. 281, 962 (1998).
- [4] A. Djordjevich, S. Savović, Opt. Eng., vol. 47, 125001 (2008).
- [5] J. Zubía, G. Durana, G. Aldabaldetrekú, J. Arrue, M.A. Losada, M. Lopez-Higuera, J. Lightwave Technol. vol. 21, 776 (2003).
- [6] A. Djordjevich and S. Savović, "Investigation of mode coupling in step index plastic optical fibers using the power flow equation", IEEE Photon. Technol. Lett. 12, 1489–1491 (2000).
- [7] T.P.Tanaka and S.Yamada, "Numerical solution of power flow equation in multimode W-type optical fibers", Appl. Opt. 19, 1647–1652 (1980).
- [8] K. Saitoh, M. Koshiba, "Empirical relations for simple design of photonic crystal fibers," Opt. Express 13, 267 – 274 (2005).
- [9] Drljača, Branko, Svetislav Savović, Milan S. Kovačević, Ana Simović, Ljubica Kuzmanović, Alexandar Djordjevich, and Rui Min, "Calculation of Bandwidth of Multimode Step-Index Polymer Photonic Crystal Fibers" Polymers 13, no. 23: 4218 (2021).

[10] M. Rousseau and L. Jeunhomme, "Numerical solution of the coupled-power equation in step index optical fibers," IEEE Trans. Microwave Theory Tech. 25, 577–585 (1977).

[11] Branko Drljača, Svetislav Savović, Milan S. Kovačević, Ana Simović, Ljubica Kuzmanović, Alexandar Djordjevich, And Rui Min, „Transmission performance of multimode W- type microstructured polymer optical fibers“, Optics Express Vol. 30, No. 14 (2022).

[12] B Drljača, A Simović, A Djordjevich, S Savović, „Influence of wavelength on equilibrium mode distribution and steady state distribution in W-type plastic optical fibers”, Laser Physics, Vol. 30, No. 7 - 075101, 6 p. (2020).

[13] A. Djordjevich, S. Savovic, “Numerical solution of the power flow equation in step index plastic optical fibers,” Journal of the Optical Society of America B 21, 1437–1442 (2004).

[14] Svetislav Savović, Ana Simović, Branko Drljača, Alexandar Djordjevich, Grzegorz Stepniak, Christian Alexander Bunge, and Jovan Bajić, „Power Flow in Graded-Index Plastic Optical Fibers“, Journal of Lightwave Technology, Vol. 37, no. 19, pp. 4985-4990, (2019).

УДК 681.513:004.31

МОДЕРНИЗАЦИЯ ПЕРВИЧНЫХ ОТСТОЙНИКОВ НА БАЗЕ КАНАЛИЗАЦИОННОГО ОЧИСТНОГО СООРУЖЕНИЯ "АСТАНА СУ АРНАСЫ" Г. НУР-СУЛТАН

Г.А.Омарова „С.Н.Аблямитов

НАО АУЭС им.Гумарбека Даукеева, г.Алматы, Казахстан

ТОО «BEI Electro», г.Алматы, Казахстан

E-mail: omargulnar@mail.ru ,seiran.ablyamitov@beielectro.kz

***Аннотация.** В данной работе представлены результаты, полученные в ходе модернизации системы автоматического управления и контроля насосов для откачки сырого осадка в первичных отстойниках станции механической очистки на городских канализационных очистных сооружениях г.Нур-Султан.*

Управление и контроль данной системы заключается в регулировании работы насосов откачки сырого осадка по уровню осадка и по концентрации взвешенных веществ в первичных отстойниках. Рассмотрены современные методы очистки сточных вод и типовые решения автоматизации таких процессов, чтобы лучше понимать какие процессы происходят до первичных отстойников и после. Изучена подробно механическая очистка – первичные отстойники и связанная с ними система насосов для откачки сырого осадка, а также другие применяемые технические

ОГЛАВЛЕНИЕ

СЕКЦИЯ «ПРОМЫШЛЕННАЯ И ЭКОЛОГИЧЕСКАЯ БЕЗОПАСНОСТЬ»	3
ОЧИСТКА СТОЧНЫХ ВОД ПРОМЫШЛЕННЫХ ПРЕДПРИЯТИЙ ОТ ИОНОВ МЕДИ ЗОЛОЙ ОТХОДОВ ПОТРЕБЛЕНИЯ Николаева Лариса Андреевна, Аджигитова Айгуль Айдаровна	3
ОЦЕНКА НЕГАТИВНОГО ВОЗДЕЙСТВИЯ ОБЪЕКТА РАЗМЕЩЕНИЯ ОТХОДОВ ВОДОПОДГОТОВКИ ПРЕДПРИЯТИЙ ТЭК Королев Владислав Игоревич, Зверева Эльвира Рафиковна	8
КАРТОГРАФИЧЕСКИЙ МОНИТОРИНГ РАДОНА НА ТЕРРИТОРИИ ГОРОДА КАЗАНЬ Апкин Ренат Нуриханович	13
ПРОБЛЕМА ПЕРЕНАСЕЛЕНИЯ ПЛАНЕТЫ И СПОСОБЫ ЕЁ РЕШЕНИЯ Пигилова Роза Наилевна, Осипова Виктория Павловна	17
ОЦЕНКА ПОЖАРНОЙ БЕЗОПАСНОСТИ ВЫСОТНЫХ ЗДАНИЙ Серик Алина Бериккызы, Абикенова Асель Амангельдиевна	22
ЭКОЛОГИЧЕСКИЕ ПРОБЛЕМЫ РАЗЛИЧНЫХ ОТРАСЛЕЙ ПРОМЫШЛЕННОСТИ Новиков Максим Витальевич, Зверева Эльвира Рафиковна	30
ПРОМЫШЛЕННАЯ БЕЗОПАСНОСТЬ ТЕХНОЛОГИЧЕСКИХ ПРОЦЕССОВ Пигилова Роза Наилевна, Филиппова Фарида Мизхатовна	36
ПРОБЛЕМАТИКА КЛАССИФИЦИРОВАНИЯ ОЗЕРНЫХ ЭКОСИСТЕМ Галеева Асия Ильдаровна, Мингазова Нафиса Мансуровна, Гильманшин Искандер Рафаилевич	41
ПРОМЫШЛЕННАЯ БЕЗОПАСНОСТЬ НА ОПАСНЫХ ПРОИЗВОДСТВЕННЫХ ОБЪЕКТАХ Р.Э. Хамидуллин, Филиппова Фарида Мизхатовна, Пигилова Роза Наилевна	46
БЕЗОПАСНОСТЬ НА АЭС С ВВЭР РАЗЛИЧНЫХ КЛАССИФИКАЦИЙ Крылов Марсель Эдуардович, Низамова Адиля Шамилевна	51
ТАБИҒИ СИПАТТАҒЫ ТӨТЕНШЕ ЖАҒДАЙЛАРДЫҢ АЛДЫН АЛУ ҮШІН ҚАР КӨШКІНІ МОНИТОРИНГІНІҢ АҚПАРАТТЫҚТЕЛЕКОММУНИКАЦИЯЛЫҚ ЖҮЙЕСІН ЗЕРТТЕУ Жойқынбекова Әсел Төлегенқызы, Бегимбетова Айнур Серикбаевна	55
СУТЕКТІ ӨНДІРУ ӘДІСТЕРІН САЛЫСТЫРМАЛЫ ТАЛДАУ. ӨНЕРКӘСІПТІК МАҚСАТТА СУТЕКТІ ӨНДІРУДІҢ НЕГІЗГІ ӘДІСТЕРІНІҢ БІРІ РЕТІНДЕ - БУ РИФОРМИНГІ Шабхатов Ақылжан Болатұлы, Санатова Тоты Сабиловна	66
ОЧИСТКА СТОЧНЫХ ВОД ОТ БИОГЕННЫХ ЭЛЕМЕНТОВ В СИСТЕМЕ ГОРОДСКИХ ОЧИСТНЫХ СООРУЖЕНИЙ	77

Шайнурова Альбина Зульфатовна, Николаева Лариса Андреевна ИССЛЕДОВАНИЕ СПОСОБОВ ЭВАКУАЦИИ ДЛЯ НЕСКОЛЬКИХ ПОМЕЩЕНИЙ К ОДНОМУ ПУТИ ЭВАКУАЦИИ	84
Тулеген Еркебулан Саятұлы, Санатова Тоты Сабировна, Айтбаева Жанаргуль Матжановна P ЛАСТАНУ ДЕНГЕЙІН БОЛЖАУ ПАРАМЕТРІН АНЫҚТАУ	97
АРҚЫЛЫ АЛМАТЫ ҚАЛАСЫНЫҢ МЕДЕУ АУДАНЫНЫҢ АТМОСФЕРАЛЫҚ АУАСЫНЫҢ ЛАСТАНУ ЖАҒДАЙЫНА БАҒАЛАУ ЖҮРГІЗУ	
Санатова Тоты Сабировна, Абжал Дана Қанатқызы, Абикенова Асель Амангельдиевна, Бейсекова Тулеужан Иманмуханмедовна СИСТЕМА ПОДДЕРЖКИ ПРИНЯТИЯ РЕШЕНИЙ	109
АВАРИЙНОСПАСАТЕЛЬНОЙ СЛУЖБЫ	
Умбетов Умирбек Умбетович, Яворский Владимир Викторович, Чванова Анастасия Олеговна МОНИТОРИНГ КАЧЕСТВА ВОДЫ ХОЗЯЙСТВЕННОПИТЬЕВОГО	115
НАЗНАЧЕНИЯ В Г. КАЗАНЬ ЗА 2021 ГОД	
Медведева Софья Николаевна АНАЛИЗ И СТАТИСТИКА ПРИЧИН ПОЖАРОВ В ГОРОДЕ	119
АЛМАТЫ ЗА 2020-2021 ГГ.	
Курма Жаксылык Кайратулы, Бейсекова Тулеужан Иманмуханмедовна, Куралов Жандос Егенкулович ИССЛЕДОВАНИЕ МЕТОДОВ ОН-ЛАЙН МОНИТОРИНГА	128
ПАРАМЕТРОВ УСЛОВИЙ ТРУДА В АО «АЛАТАУ ЖАРЫҚ КОМПАНИЯСЫ»	
Абикенова Асель Амангельдиевна, Жандаулетова Фарида Рустембековна, Санатова Тоты Сабировна, Остемир Гаухар Сериккызы НАНОЧАСТИЦЫ В ОКРУЖАЮЩЕЙ СРЕДЕ, ИСТОЧНИКИ ИХ	141
ПОСТУПЛЕНИЯ И СТЕПЕНЬ ОПАСНОСТИ	
Тасмагамбетова Диляра Ардаккызы, Приходько Николай Георгиевич, Сагытаева Куралай Асеткызы ПОВЫШЕНИЕ ЭФФЕКТИВНОСТИ ОЧИСТКИ МАСЛО- И	149
НЕФТЕСОДЕРЖАЩИХ СТОЧНЫХ ВОД	
Исхакова Регина Яновна, Нургалиев Артур Ильесович ЭКОЛОГО-ЭКОНОМИЧЕСКОЕ ОБОСНОВАНИЕ ПРИМЕНЕНИЯ	154
СИСТЕМЫ ОЧИСТКИ ГОРОДСКОГО АТМОСФЕРНОГО ВОЗДУХА ДЛЯ УЛАВЛИВАНИЯ РМ 2.5 (Г. АСТАНА)	
Жандаулетова Фарида Рустембековна, Абикенова Асель Амангельдиевна, Бекмуратова Нуржамал Сарсенбаевна, Тыщенко Елена Михайловна ОБОСНОВАНИЕ ПАРАМЕТРОВ УПРОЧНЕНИЯ НЕУСТОЙЧИВОЙ	168
КРОВЛИ В ОЧИСТНЫХ ЗАБОЯХ УГОЛЬНЫХ ШАХТ	
Демин Владимир Федорович, Яворский Владимир Викторович, Демина Татьяна Владимировна, Киселев Михаил Сергеевич	

СОВРЕМЕННЫЕ ЭКОЛОГИЧЕСКИЕ ПРОБЛЕМЫ ОТЕЧЕСТВЕННОЙ ТЕПЛОЭНЕРГЕТИКИ	175
Бариева Зухруша Ф., Габдрахманова Диляра Рашитовна, К.А.Каримова	
ИССЛЕДОВАНИЕ ВОЗМОЖНОСТИ ОБРАЗОВАНИЯ ГИПСА ПРИ ОЧИСТКИ ДЫМОВЫХ ГАЗОВ ОТ ОКСИДОВ СЕРЫ ПУТЕМ УТИЛИЗАЦИИ СОБСТВЕННЫХ СТОЧНЫХ ВОД	182
Ж.А.Айдымбаева, А.Т.Аршабекова, Г.К.Смагулова, Э.А.Нурмадиева	
ЭКОЛОГИЧЕСКИЕ АСПЕКТЫ ПРИМЕНЕНИЯ ТЕПЛОВЫХ НАСОСОВ В ИНДИВИДУАЛЬНОМ ОТОПЛЕНИИ	192
Даутов Руслан Радикович, Кондратьев Александр Евгеньевич	
СОВРЕМЕННЫЕ ФИЛЬТРУЮЩИЕ МАТЕРИАЛЫ, ПРИМЕНЯЕМЫЕ ДЛЯ ПОДГОТОВКИ ВОДЫ	195
Галлямова Ильнара Рабисовна, Власова Алёна Юрьевна	
СОВРЕМЕННЫЕ МЕТОДЫ ОЧИСТКИ СТОЧНЫХ ВОД НА ТЕПЛОВЫХ ЭЛЕКТРОСТАНЦИЯХ	201
Иксанова Ольга Евгеньевна, Власова Алёна Юрьевна	
НАХОЖДЕНИЕ И ЛИКВИДАЦИЯ АВАРИИ НА ТРУБОПРОВОДЕ	205
Коньжов Кирилл Вадимович, Политова Татьяна Олеговна	
СЕКЦИЯ «МАТЕМАТИЧЕСКОЕ МОДЕЛИРОВАНИЕ И СИСТЕМЫ УПРАВЛЕНИЯ»	209
ОРГАНИЗАЦИОННАЯ СТРУКТУРА АВТОМАТИЗИРОВАННОЙ СИСТЕМЫ УПРАВЛЕНИЯ ПРОИЗВОДСТВЕННЫМИ ПРОЦЕССАМИ	209
Е.С. Ким, А.А. Копесбаева	
РЕШЕНИЕ ЗАДАЧИ ДИРИХЛЕ ДЛЯ ЦИЛИНДРИЧЕСКОЙ ОБЛАСТИ ДЛЯ МНОГОМЕРНЫХ ГИПЕРБОЛОПАРАБОЛИЧЕСКИХ УРАВНЕНИЙ С ВЫРОЖДЕНИЕМ ТИПА И ПОРЯДКА	218
М.Н.Майкотов, Ж.Ж.Кожамкулова	
СТОХАСТИЧЕСКИЕ ДИФФЕРЕНЦИАЛЬНЫЕ УРАВНЕНИЯ В ОПИСАНИИ СИГМА ЧАСТОТНО – ИМПУЛЬСНОЙ СИСТЕМЫ УПРАВЛЕНИЯ ТЕМПЕРАТУРНЫМ РЕЖИМОМ ПРОЦЕССА ВЫТЯЖКИ ОПТИЧЕСКОГО ВОЛОКНА	226
Б.Х. Айтчанов, В.Вуйцик, А.С.Тергеусизова	
ЦИФРОВОЕ СТАТИСТИЧЕСКОЕ МОДЕЛИРОВАНИЕ СИГМА ЧАСТОТНО – ИМПУЛЬСНОЙ СИСТЕМЫ УПРАВЛЕНИЯ ТЕМПЕРАТУРНЫМ РЕЖИМОМ ПРОЦЕССА ВЫТЯЖКИ ОПТИЧЕСКОГО ВОЛОКНА	235
Б.Х. Айтчанов, В.Вуйцик, А.С.Тергеусизова	
ӨЛШЕУ БЕЛГІСІЗДІГІН БАҒАЛАУ ЕҢ КІШІ КВАДРАТТАР ӨДІСІ	243
С.Г.Хан, Ж.С.Тлеубаева	
ЕКІ КОНТУРЛЫ АҒЫН ҮШІН ЖЫЛУ АЛМАСУ ПРОЦЕСІН МОДЕЛЬДЕУ	250
Г.Д. Бэзіл, Г. Искакова, Қ. Алдоңғар, А. Шерхан	

СИСТЕМА АВТОМАТИЧЕСКОГО УПРАВЛЕНИЯ РЕЖИМАМИ РАБОТЫ ТОКАРНОГО СТАНКА А.П. Муслимов, Е.О. Елеукулов	256
МЕТОД КОНТРОЛЯ ДИСБАЛАНСА МАЛЫХ ТЕЛ ВРАЩЕНИЯ И УСТРОЙСТВО ДЛЯ ЕГО КОНТРОЛЯ А.П. Муслимов, А.К. Аталыкова	260
СОЗДАНИЕ ВИРТУАЛЬНЫХ ИЗМЕРИТЕЛЬНЫХ ПРИБОРОВ НА БАЗЕ ПЛАТ СБОРА ДАННЫХ NI ELVIS И DAQ С. А. Кульмамиров, Ә. Т. Қуанышбаева	265
ПРОЕКТИРОВАНИЕ ЦИФРОВЫХ БИЗНЕС-ПРОЦЕССОВ А.К.Болшибаева, К.Д.Рахым	273
МЕТОДОЛОГИЯ АВТОМАТИЗИРОВАННОГО МЕНЕДЖМЕНТА КАЧЕСТВА Ш.Д. Тойбаева, И.Т. Утепбергенов, Л.К. Бобров, А.Н. Нургулжанова	281
ВОЗМОЖНЫЕ ПЕРСПЕКТИВЫ ГЕОТЕРМАЛЬНОЙ ЭНЕРГЕТИКИ В КАЗАХСТАНЕ Г. Д. Базил, Р. Тохтиев	289
РАЗРАБОТКА СИСТЕМЫ АВТОМАТИЗАЦИИ ПРОЦЕССА УЛФ Г. Д. Базил, Р. Мелисов	295
ҚОЛДАНЫСТАҒЫ БАР МАТЕМАТИКАЛЫҚ МОДЕЛЬДЕР МЕН ТОПЫРАҚ БЕРІКТІГІН АНЫҚТАЙТЫН КОМПЬТЕРЛІК ТЕХНОЛОГИЯЛАРҒА АНАЛИТИКАЛЫҚ ТАЛДАУ Бодесова А.Е., Тойбаева Ш.Д.	306
МОДЕЛИРОВАНИЕ И ИССЛЕДОВАНИЕ МНОГОСВЯЗНЫХ ОБЪЕКТОВ УПРАВЛЕНИЯ Жусупбеков Сарсенбек Сейтбекович, Сабырова Аружан	316
Бағытжанқызы, Мухтарова Аружан Казыбекқызы, Агатаев Бекдаулет Айжарыкулы	
СИНТЕЗ СТРУКТУРЫ СИСТЕМЫ УПРАВЛЕНИЯ ТЕХНОЛОГИЧЕСКИМ ПРОЦЕССОМ СЕПАРАЦИИ НЕФТИ Жусупбеков С.С., Сабырова А., Мухтарова А.	325
ПРОСТАЯ МОДЕЛЬ ПРОЦЕССА ДОБЫЧИ УРАНА Муханов Бахыт, Дучио Фанели, Адилова Шинар	333
МАТЕМАТИЧЕСКОЕ МОДЕЛИРОВАНИЕ ТЕЧЕНИЙ ДВУХФАЗНОЙ ПАРОКАПЕЛЬНОЙ СМЕСИ В КАНАЛЕ ПЕРЕМЕННОГО СЕЧЕНИЯ ПРИ НАЛИЧИИ ФАЗОВЫХ ПЕРЕХОДОВ Т.Р. Аманбаев, Г.Е. Тилеуов	339
MODELING OF POWER FLOW IN MULTIMODE W-TYPE PHOTONIC CRYSTAL FIBERS Branko Drljača, Svetislav Savović, Milan S. Kovačević, Ana Simović, Ljubica Kuzmanović, Alexandar Djordjevich, Gulbakhar Yussupova	349
МОДЕРНИЗАЦИЯ ПЕРВИЧНЫХ ОТСТОЙНИКОВ НА БАЗЕ КАНАЛИЗАЦИОННОГО ОЧИСТНОГО СООРУЖЕНИЯ "АСТАНА СУ АРНАСЫ" Г. НУР-СУЛТАН	355

Г.А.Омарова, С.Н.Аблямитов	
СЕКЦИЯ «ИНФОРМАЦИОННЫЕ ТЕХНОЛОГИИ И КИБЕРБЕЗОПАСНОСТЬ»	367
ЖҮРЕК-ТАМЫР ЖҮЙЕСІНІҢ ПАТОЛОГИЯСЫН БОЛЖАУ ҮШІН МАШИНАЛЫҚ ОҚЫТУДЫҢ ӘДІСТЕРІ МЕН АЛГОРИТМДЕРІН ЗЕРТТЕУ	367
С.Б. Рахметуллаева, Д.М. Мұхаммеджанова, А.К. Мукашева ӘДІСТЕРДІҢ ТИІМДІЛІГІН БАҒАЛАУДА АҚПАРАТТЫҚ ҚАУІПСІЗДІК ТӘУЕКЕЛДЕРІН ТАЛДАУДЫ ЗЕРТТЕУ	378
А.А.Зиро, Ш.Д.Тойбаева, С.А.Гнатюк, А.Ж.Иманбаев VISUAL TESTING INSTRUMENTS AND APPROACHES	387
A.N. Myrzakulova СОЗДАНИЕ JAVA-ПРИЛОЖЕНИЙ: ПЛЮСЫ И МИНУСЫ ЯЗЫКА	393
Пырнова О. А., Зарипова Р.С. РАЗРАБОТКА И ВНЕДРЕНИЕ ВИРТУАЛЬНОЙ ЛАБОРАТОРИИ ДЛЯ ИЗУЧЕНИЯ ЕСТЕСТВЕННО-ТЕХНИЧЕСКИХ ДИСЦИПЛИН	397
Ф.Е. Темірбекова, Б.О.Тастанбекова, М.Т.Байжанова, А.Б.Сейтханова ИСПОЛЬЗОВАНИЕ ЧАТ-БОТА В ГОСТИНИЧНО-РЕСТОРАННОМ БИЗНЕСЕ	402
Мустафин Р.Ф., Зарипова Р.С. МОДЕЛИРОВАНИЕ РЕЖИМОВ АЛГОРИТМА AES В СРЕДЕ CRYPTOOL 2	405
О.А.Мананкова, М.З.Якубова, М.А.Рахматуллаев АЛГОРИТМЫ ПРИКЛАДНОЙ ПРОГРАММЫ «LAYER-BY-LAYER 3D» РЕКОНСТРУКЦИИ ТРЕХМЕРНЫХ ДАННЫХ РЕНТГЕНОВСКИХ ИССЛЕДОВАНИЙ	412
Саутбекова З.С., Трубицын А.А. СРАВНИТЕЛЬНЫЙ АНАЛИЗ КЛАССИЧЕСКОЙ И КВАНТОВОЙ КРИПТОГРАФИИ	421
А. Б. Кусаинов БЫСТРОДЕЙСТВУЮЩИЕ УСТРОЙСТВА МОДУЛЬНОГО ВОЗВЕДЕНИЯ ЧИСЕЛ В КВАДРАТ ДЛЯ КРИПТОСИСТЕМ С ОТКРЫТЫМ КЛЮЧОМ	429
Тынымбаев С.Т., Бердибаев Р.Ш., Мукашева А.К. ИНФОРМАЦИОННАЯ БЕЗОПАСНОСТЬ В ЭПОХУ КВАНТОВЫХ ТЕХНОЛОГИЙ	439
Пырнова О.А. SMART-GRID МОДЕЛЬДЕУ ӘДІСТЕРІ МЕН ҚҰРАЛДАРЫН ЗЕРТТЕУ ЖӘНЕ ӘЗІРЛЕУ	443
Е.Б.Берік, У.Н.Иманбекова МОБИЛЬДІ ҚОСЫМШАЛАРДЫ ТАЛДАУ ЖӘНЕ АЛДАҒЫ УАҚЫТТА КҮТЕЛІН ЖАҢАРТУЛАРДЫ ЗЕРТТЕУ	456
Е.Қ. Есенғазыев, У.Н. Иманбекова	

МОБИЛЬНОЕ ПРИЛОЖЕНИЕ ДЛЯ ИНФОРМИРОВАНИЯ НАСЕЛЕНИЯ РЕСПУБЛИКИ ТАТАРСТАН ОБ ЭКОЛОГИЧЕСКОЙ СИТУАЦИИ	470
Замалиева А.М., Зарипова Р.С	
BIG DATA КӨМЕГІМЕН ҚАНТ ДИАБЕТІН ДИАГНОСТИКАЛАУ ЖҮЙЕСІН ӨЗІРЛЕУ	475
Е.Ж. Суйнуллаев, Мукашева А.К.	
КРИТИКАЛЫҚ МАҢЫЗДЫ ҚОЛДАНБАЛАР ҮШІН БҮЛТТІК ЕСЕПТЕУЛЕРДІҢ ҚАУІПСІЗ АҚПАРАТТЫҚ ЖҮЙЕСІ	490
Бердібаев Р.Ш., Гнатюк С.А., Альмуратова К.Б.	
VPN ТЕХНОЛОГИЯСЫН ҚОЛДАНА ОТЫРЫП NETCRACKER БАҒДАРЛАМАСЫНДА ЖЕЛЛІК МОДЕЛЬ ӨЗІРЛЕУ	498
М.З.Якубова, Д.А.Наубетов, М.Б.Амреев	
ЖАСАНДЫ ИНТЕЛЛЕКТІҢ ДАМУЫ: «АҚЫЛДЫ ҮЙ» ТЕХНОЛОГИЯСЫНЫҢ ҚОЛДАНУ ТЕНДЕНЦИЯЛАРЫ	509
Т.Ф. Маратова, Д.Б.Наурызбаев, А.Т.Сакатай	
ПЕРСПЕКТИВЫ РАЗВИТИЯ ИСКУССТВЕННОГО ИНТЕЛЛЕКТА В КОДИНГЕ	519
Никоноров Д.П.	
СОВРЕМЕННОЕ СОСТОЯНИЕ ВОПРОСА ОРГАНИЗАЦИИ ПРОЦЕССА CONTINUOUS DELIVERY	524
Валяев Д.Е., Тусупова Б.Б.	
ПРОГРАММА «MIRROR-TOF-CRM» ДЛЯ МОДЕЛИРОВАНИЯ ЭЛЕКТРОСТАТИЧЕСКИХ ЗЕРКАЛ ВРАЩАТЕЛЬНОЙ СИММЕТРИИ	529
С.Б. Бимурзаев, З.С. Саутбекова	
ИСПОЛЬЗОВАНИЕ ИСКУССТВЕННОГО ИНТЕЛЛЕКТА В ОБЛАСТИ ОНЛАЙН-ПЕРЕВОДА	536
Силкина О.Ю., Зарипова Р.С	
EXPLORING MODELS FOR MANAGING REGULATIONS AND STANDARDS FOR CIVIL-MILITARY INTEGRATION IN THE FIELD OF IT	540
A.U. Utegenova, O.A. Vaimuratov, A.E. Aden, Zh. B. Suimenbayeva, A.M. Varyshev	
ОНТОЛОГИЯЛЫҚ ИНЖИНИРИНГ ӘДІСТЕРІМЕН НОРМАТИВТІК ҚҰЖАТТАРДАН ТЕХНИКАЛЫҚ АҚПАРАТТЫ АЛУ	546
А.У. Утегенова, О.А. Баймуратов, Ә.Е. Әден, Ж.Б. Суйменбаева, А.М.Бапышев	
ПРИМЕНЕНИЕ ИСКУССТВЕННОГО ИНТЕЛЛЕКТА В СФЕРЕ ЭНЕРГЕТИКИ	551
Пырнова О.А., Зарипова Р.С.	
ҚАЗІРГІ ЗАМАНҒЫ АҚПАРАТТЫҚ-КОММУНИКАЦИЯЛЫҚ ЖҮЙЕЛЕР МЕН ЖЕЛЛІЛЕРДЕГІ КРИПТОГРАФИЯЛЫҚ АҚПАРАТТЫ ҚОРҒАУДЫҢ ЖЕТІЛДІРІЛГЕН МОДЕЛІ	554
Р.Ш.Бердибаев, С.О.Гнатюк, Г.С.Бекетова	

КРАУДФАНДИНГОВЫЕ ПЛАТФОРМЫ КАК СПОСОБ РЕАЛИЗАЦИИ СВОИХ ПРОЕКТОВ В ВИРТУАЛЬНОЙ СРЕДЕ Ю.А.Мустахитдинова, Р.С.Зарипова	563
ОПТИМИЗАЦИЯ УПРАВЛЕНИЯ ТРАНСПОРТНЫМИ СИСТЕМАМИ С ИСПОЛЬЗОВАНИЕМ ИМИТАЦИОННОГО МОДЕЛИРОВАНИЯ О.Ю. Силкина, Р.С. Зарипова	571
INTRUSION DETECTION USING MACHINE LEARNING ON KDDCUP-99 DATASET: ANALYSIS OF FEATURE SELECTION S.M. Vozorov	578
ВИЗУАЛИЗАЦИЯ И КОМПЬЮТЕРНОЕ МОДЕЛИРОВАНИЕ ЭНЕРГЕТИЧЕСКИХ СИСТЕМ Никоноров Д.П., Зарипова Р.С.	584
FACE SKETCH RECOGNITION L.U. Davronova	587
МЕТОДЫ МНОГОФАКТОРНОЙ АУТЕНТИФИКАЦИИ И СВЯЗАННЫЕ С НИМИ ПРОБЛЕМЫ БЕЗОПАСНОСТИ З.Т. Худойкулов, А.Т. Имамалиев	595
ANALYSIS OF ENCRYPTION ALGORITHMS FOR CLOUD SECURITY Z.T. Khudoykulov, A.A.Karimov, I.S.Olimov	603
ПРИМЕНЕНИЕ ИСКУССТВЕННОГО ИНТЕЛЛЕКТА ДЛЯ ФИЛЬТРАЦИИ СПАМ-СООБЩЕНИЙ В ЭЛЕКТРОННОЙ ПОЧТЕ Хамидов Ш.Ж	611
ПРОБЛЕМЫ АУТЕНТИФИКАЦИИ ПРИ ЭЛЕКТРОННОМ ГОЛОСОВАНИИ З.Т.Худойкулов, О.Т.Имомалиев, У.У.Тожиакбарова	620
ОГЛАВЛЕНИЕ	630

Научное издание

**ЭНЕРГЕТИКА, ИНФОКОММУНИКАЦИОННЫЕ
ТЕХНОЛОГИИ И ВЫСШЕЕ ОБРАЗОВАНИЕ**

Международная научно-техническая конференция
(Алматы, Казань, 20-21 октября 2022 г.)

Электронный сборник научных статей по материалам конференции

В трех томах

Том 2

Корректор Р.С. Зарипова
Компьютерная верстка Р.С. Зарипова

Центр публикационной активности КГЭУ
420066, г. Казань, ул. Красносельская, 51

ISBN 978-5-89873-616-3





**ТРЕТА МЕЃУНАРОДНА КОНФЕРЕНЦИЈА
ЗА ОБРАЗОВАНИЕ
ПО МАТЕМАТИКА, ФИЗИКА И СРОДНИ НАУКИ**

ЗБОРНИК НА ТРУДОВИ

Природно-математички факултет

Скопје 6-8 мај, 2022



Зборник на трудови

**Трета меѓународна конференција за
образованието по математика,
физика и сродни науки**

Природно-математички факултет, Скопје

6 – 8 мај, 2022

Зборник на трудови
Трета меѓународна конференција за образованието по математика,
физика и сродни науки

Издавачи:

Сојуз на математичари на Македонија
Природно-математички факултет, Скопје

Уредници:

Ѓорѓи Маркоски
Ламбе Барандовски
Анета Гацовска – Барандовска

Редакциски одбор:

Александар Скепаровски
Ѓорѓи Маркоски
Ламбе Барандовски
Даница Крстовска
Ирена Стојковска
Анета Гацовска – Барандовска
Оливер Зајков
Боце Митревски
Марина Стојановска
Јасмина Марковска
Валентина Гоговска
Валентина Миовска

CIP - Каталогизација во публикација
Национална и универзитетска библиотека "Св. Климент Охридски", Скопје

37.012/.013:5(062)

МЕЃУНАРОДНА конференција за образованието по математика, физика и сродни науки
(3 ; 2023 ; Скопје)

Зборник на трудови : трета меѓународна конференција за образованието по математика,
физика и сродни науки, Скопје, 6 – 8 мај, 2022 /
[уредници Ѓорѓи Маркоски, Ламбе Барандовски, Анета Гацовска – Барандовска]. - Скопје :
Сојуз на математичари на Македонија, 2023. - 376 стр. : илустр. ; 25 см

Дел од трудовите и на други јазици. - Фусноти кон текстот. - Библиографија кон трудовите

ISBN 978-608-4929-04-8

а) Образование -- Настава -- Природни науки -- Математика -- Собири

COBISS.MK-ID 59184901

© 2023 CMM

Сите права се задржани. Ниту еден дел од оваа книга не смее да се препечатува или пренесуван во каква било форма или со какви било средства, електронски или механички, вклучувајќи и фотокопирање, документирање или да биде зачуван во систем за повторно пронаоѓање без писмена согласност од издавачот.

Печати: Печатница MAP-CAЖ, Скопје

Тираж: 220

Зборник на трудови

Трета меѓународна конференција за образованието по математика, физика и сродни науки

во организација на

Природно – математички факултет во Скопје (ПМФ)
Сојуз на математичарите на Македонија (СММ)
Друштво на физичарите на Република Македонија (ДФРМ)

Организациски одбор

Ѓорѓи Маркоски
Ламбе Барандовски
Александар Скепаровски
Ирена Стојковска
Даница Крстовска
Анета Гацовска-Барандовска
Валентина Миовска
Милена Мицковска
Фадил Ајредини
Весна Манчевска
Ерблина Зеќири
Катерина Русевска

Поканети предавачи

Петар Кендеров, Бугарија
Дончо Димовски, Македонија
Александар Липковски, Србија
Мира Вучељиќ, Црна Гора
Саша Ивковиќ, Србија
Бенјамин Фетиќ, Босна и Херцеговина
Оливер Зајков, Македонија
Евгенија Сендова, Бугарија
Љубиша Нешиќ, Србија
Јасмина Милинковиќ, Србија
Зоран Михајловски, Македонија
Тони Чехларова, Бугарија

Програмски одбор

Дончо Димовски, Македонија
Петар Кендеров, Бугарија
Мичо Митровиќ, Србија
Јасмина Милинковиќ, Србија
Боце Митревски, Македонија
Ристо Атанасов, САД
Крешо Задро, Хрватска
Бенјамин Фетиќ, Босна и Херцеговина
Слаѓана Јакимовиќ, Македонија
Небојша Икодиновиќ, Србија
Тони Чехларова, Бугарија
Валентина Гоговска, Македонија
Евгенија Сендова, Бугарија
Барбара Ровшек, Словенија
Весна Целакоска - Јорданова, Македонија
Мира Вучељиќ, Црна Гора
Драгица Д. Тривиќ, Србија
Марина Стојановска, Македонија

Благодарност

Сојузот на математичарите на Македонија и Друштвото на физичарите на Република Македонија, ја изразуваат својата благодарност на Институтот за математика и Институтот за физика при Природно – математичкиот факултет во Скопје за успешната коорганизација на Третата меѓународна конференција за образованието по математика, физика и сродни науки.

Посебна благодарност изразуваме до Министерството за образование и наука кои го потпомогнаа издавањето на вој Зборник на трудови.

Организаторите на КОМФСН 2022 најискрено се заблагодаруваат на Генералниот поддржувач на конференцијата, проектот „Разновидноста во природните науки низ социјална инклузија – неформално образование по природни науки и ученичка разноликост“ и неговиот раководител проф. д-р Марина Стојановска, вонреден професор на Институтот за хемија, при Природно-математичкиот факултет во Скопје. Благодарение на проектот учесниците на конференцијата имаа можност да учествуваат во специјализирани работилници од областа на природните науки.



СОДРЖИНА

1.	Benjamin Fetic , <i>Quantum tunneling and ultrafast phenomena</i>	11
2.	Jasmina Milinković , <i>Visualization as a Primary Means or a Backup Teaching Aid</i>	17
3.	Дончо Димовски, Јасмина Маркоска, Анета Гацовска-Барандовска, Ѓорѓи Маркоски , <i>Математички јазик</i>	24
4.	Toni Chehlarova , <i>Redefining in-service teacher education for work in a STEM center</i>	32
5.	Евгенија Сендова , <i>Истражувачи-наставници-ученици: (една вечна STEAM плетенка во програмска средина)</i>	38
6.	Љубиша Нешиќ, Дарко Радованчевиќ , <i>Општа и Специјална теорија релативности у школи</i>	48
7.	Оливер Зајков, Соња Геговска-Зајкова , <i>Сто и една приказна</i>	54
8.	Erblina Zeqiri, Stevo Gjorgiev, Irena Stojkovska , <i>Statistical Literacy of Undergraduate Students Before Taking the Introductory Statistics Course</i>	62
9.	Dragana Valjarević, Bojana Stojčetović, Milena Petrović, Novica Zlatanović and Milica Ivanović , <i>Pupil's perspective of distance learning during the COVID-19 pandemic in primary school</i>	71
10.	Filip Nikolovski, Irena Stojkovska , <i>Teaching probability using computer-based simulations</i>	79
11.	Делчо Лешковски, Анета Гацовска-Барандовска , <i>Потребата од изучување веројатност и статистика во средното гимназиско образование, како подготовка за универзитетските предмети</i>	87
12.	Josip Slisko , <i>Water-filled balloon that jumps in free fall: A Predict – Observe - Explain learning sequence on weightlessness</i>	93
13.	Бобан Ђокиќ, Миљана Милентијевиќ, Бранко Дрљача , <i>Софтверски пакет као интерактивни алат у настави физике</i>	101
14.	Љубчо Јованов, Драган Радивојевиќ, Катерина Дрогрешка , <i>CD и DVD дискови – подостапна замена за дифракциона решетка во демонстрациите од физичка оптика</i>	109
15.	Ирена Златановска, Илија Јованов, Гоце Гегоски, Ламбе Барандовски , <i>Изучување на распаѓањето на пената кај пивото</i>	115
16.	Мирослав Петроски, Ѓоко Атанасовски , <i>Определување дијаметар на тенка жица со помош на ласер</i>	124
17.	Стојан Манолев , <i>Термоелектричните ефекти, физички основи и нивната примена во наставата по физика</i>	132
18.	Никола Делевски , <i>Учење физика преку практична активност – Интерференција на тенок слој од сапун</i>	136

19.	Делчо Лешковски, Валентина Миовска, <i>Геометриски докази на адисионите теореми и на идентитетите за трансформирање на збир на тригонометриски функции</i>	141
20.	Eugen Ljajko, <i>Do we find at schools what we were prepared for at universities?</i>	153
21.	Петар Соколоски, <i>Искусства од наставата по предметот Геометрија во МИГ – Скопје</i>	158
22.	Зоран Трифунов, <i>Примена на интерактивни аплети во решавање на задачи со определен интеграл</i>	168
23.	Абдула Букла, Бесник Исмаили, <i>Примена на Геогебра во апроксимативно решавање на проблеми од планиметрија</i>	176
24.	Бети Ламева, Јасмина Маркоска, <i>Улогата на меѓународните тестирања во македонското математичко образование-предизвици и заклучоци</i>	183
25.	Бети Ламева, Јасмина Маркоска, Елизабета Наумовска, <i>Улогата на меѓународните тестирања во македонското образование по природни науки-предизвици и заклучоци</i>	195
26.	Виктор Урумов, <i>Македонски публикации во областа на образованието</i>	204
27.	Марина Стојановска, Катерина Русевска, Ламбе Барандовски, Владимир М. Петрушевски, <i>Природните науки низ игра: Escape room како дел од DiSSI активностите</i>	210
28.	Владимир Петрушевски, Катерина Русевска, Ламбе Барандовски, Марина Стојановска, <i>Примена на 5E методот во наставата по природни науки: DiSSI активности за гасови</i>	217
29.	Катерина Русевска, Ламбе Барандовски, Владимир Петрушевски, Славица Тофиловска, Марина Стојановска, <i>Примена на 5E методот во наставата по природни науки: DiSSI активности за екологија</i>	224
30.	Ламбе Барандовски, Катерина Русевска, Владимир Петрушевски, Марина Стојановска, <i>Примена на 5E методот во наставата по природни науки: DiSSI активности за струјни кола</i>	229
31.	Катерина Дрогрешка, Љубчо Јованов, Драган Радивојевиќ, <i>Земјотресот во процесот на образовната технологија</i>	234
32.	Јасмина Најдовска, Моника Андрееска, Ивана Молеровиќ, <i>Сеизмолошката опсерваторија како дел од образованието</i>	238
33.	Боце Митревски, Гордана Станојевиќ, Вера Зороска, <i>Споредба на знаењето и концептуалното разбирање меѓу основци од Македонија и Србија</i>	244
34.	Валентина Миовска, Анета Гацовска-Барандовска, Делчо Лешковски, Стефан Мирчевски, <i>Најчести грешки и математички заблуди кај студентите од прва година на техничките факултети во средношколски задачи</i>	252
35.	Снежана Ристовска, Лидија Кондинска, Даниела Тачевска Николов, <i>Влијанието на наставната стратегија превртена училница на постигнувањата на ученици во време на пандемијата од COVID – 19</i>	260
36.	Петар Соколоски, Слаѓан Станковиќ, <i>Математичко-информатичка гимназија - ново средно училиште и нова надеж за математичкото образование во Македонија</i>	270

37. **Јасмина Ангелевска Костадиноска, Соња Геговска-Зајкова, Катерина Хаџи-Велкова Санева**, *Влијанието на онлајн наставата и начинот на полагање на испитите врз успешноста на студентите* 280
38. **Југослав Ачкоски, Невена Серафимова, Кристијан Илиевски, Анер Бехлиќ**, *Управувач на фази логика за предвидување на резултатите во онлајн наставата* 287
39. **Методија Јанчески, Анкица Спасова, Викторија Илиеска**, *Интеракција и комуникација во образованието на далечина во македонските училишта* 295
40. **Аида Петровска**, *Придобивките од STEM во развојот на интелектуалните компетенции на учениците од основните училишта* 303
41. **Силвана Јакимовска Бинова**, *Атрактивност на STEM професији – зошто и како преку примери од наставата по математика* 310
42. **Славица Карбева Стојковиќ**, *Визуелизирање на податоци во наставата по математика во основно образование* 319
43. **Кети Иваноска, Марина Стојановска**, *Претставите на учениците од деветто одделение во врска со граббените единици на супстанциите* 326
44. **Цветанка Трајковски, Емилија Накова, Катерина Русевска**, *Изработка на дихотомен клуч за одредување на жаби присутни во македонија и негова примена во образовниот процес по предметите природни науки и биологија* 334
45. **Маре Жежовска - Трајковски, Марина Јанеска, Јулијана Трајковска**, *Влијанието на загадувањето на животната средина врз квалитетот на водата* 346
46. **Вангелина Мојаноска**, *Студија на наставен час по математика: Примена на инструменти за самооценување на учениците на часовите по математика* 351
47. **Фроска Смилкова**, *Улога и значење на воннаставните активности во основното образование* 358
48. **Маре Миленковска**, *Значењето на играта во формирањето на математичките поими* 367

Софтверски пакет као интерактивни алат у настави физике

Бобан Ђокић¹, Миљана Милентијевић¹, Бранко Дрљача¹

¹Универзитет у Приштини са привременим седиштем у Косовској Митровици, Природно-математички факултет, Ул. Лоле Рибара 29, 38220 Косовска Митровица, Србија

Апстракт. Развој савремених технологија утиче на промену живота људи све већом брзином. Напредак технологије омогућава примену великог броја мултимедијалних уређаја помоћу којих се ученицима могу приближити и поједноставити појаве које је тешко дочарати помоћу стандардних метода предавања табла, креда и презентација. У овом раду је кроз неколико примера из физике, у оквиру једне наставне теме, предложено могуће решење за извођење наставе у школама које немају адекватно опремљене кабинете за наставу физике.

Клучни зборови: настава физике, софтверски пакет, огледи

УВОД

Настава физике у Србији из године у годину постаје све изазовнија. Једном дуг процес, са довољним бројем школских часова, често се скраћује, посебно у средњим стручним школама. Овај процес би требало да се састоји из три дела: теоријског предавања, рачунских задатака и демонстрација – лабораторијских вежби (уколико је могуће). Уобичајени метод који се користи у настави физике у Србији је предавање. Утврђено је да овај метод није ефикасан за наставу у науци, јер се показало да су резултати ниски [1]. Начин на који свет функционише није одговор који ће се добити традиционалним начином подучавања, пошто постоји мала или никаква промена у разумевању физичких феномена код већине ученика када се користи овај метод. [2]. Показано је да овај метод функционише за око десет процената ученика за које се претпоставља да су самомотивисани ученици који би у суштини сами научили предвиђено градиво [3].

Ако се у наставни процес уврсте нумерички промемблеми и задаци, резултат је бољи. Ипак, ова наставна техника је корисна само за мали број тематских целина за које је утврђено да су теоријско предавање и нумерички задаци довољни да ученици стекну знања о обрађеној теми и стекну потпуно разумевање проблема. Са друге стране, већи број наставних тема захтева одговарајуће демонстрације, како би ученици јасније разумели оно што уче. Штавише, те демонстрације су се показале као кључне за разумевање физике на нивоу основног и средњег образовања. Демонстрације из физике помажу ученицима да постигну дубље разумевање физичких процеса и нашироко су коришћени у свету, како у предуниверзитетском али и универзитетском периоду на светски познатим универзитетима. Као резултат тога, ученици су више заинтересовани за истраживање света физике што доводи до побољшаних компетенција на крају наставног процеса.

Демонстрације се могу поделити у две групе. Прву групу чине класични демонстрациони експерименти који се изводе испред ученика, или заједно са ученицима,

са потребном опремом. Као што је раније поменуто, постоји велики број тих експериментата које су спровели и еминентни универзитетски професори на еминентним универзитетима [4]. Ова врста демонстрационих експериментата помаже ученицима да стекну бољи увид у физичке феномене. Показало се да када су ученици активно укључени у демонстрације постижу боље резултате у поређењу са случајем када само посматрају нивно извођење [5].

Друга група је наставни процес заснован на информационо-комунакационим технологијама. Ова врста наставног процеса подразумева активно и практично учешће ученика и на тај начин им омогућава да стекну неопходну пажњу наставника. Према мишљењу познатих истраживача квалитет дизајна и развоја директно утиче на квалитет наставног процеса и један је од најважнијих фактора квалитетног садржаја наставног процеса [6,7]. Често смо сведоци да ученици основних, средњих школа и гимназија, који имају одговарајућу опрему, кроз квалитетне и садржајем богате информационо-комуникационе системе постижу велике успехе на републичким и меѓународним такмичењима и олимпијадама знања.

Напредак технологије намеће неопходност промене начина реализације наставног процеса у савременом образовању у смислу потребе за брзим и ефикасним трансфером знања [8].

Савремена настава физике мора бити тако организована да се ученицима створе околности у чијим оквирима они самостално откривају већ откривена знања у науци.

Овом приликом смо извршили прилагођавање кодова писаних у софтверском пакету *Mathematica*[®] тако да одговарају наставној теми *Хармонијске осцилације* за ученике трећег разреда гимназије који раде по плану и програму Министарства просвете, науке и технолошког развоја Републике Србије.

ПРОГРАМСКИ ПАКЕТ MATHEMATICA[®]

Програмски пакет *Mathematica*[®] развијен је у софтверској компанији *Wolfram Research* и користи се за математичке и друге примене. Посебно је погодан за обраду нумеричких података, за симболичка процесирања, као и за графичко приказивање података и функција.

За рад у програмском пакету *Mathematica*[®] користе се документа која се зову бележнице (*notebooks*). Бележнице се састоје од ћелија које могу садржати текст, израчунавања или графиконе. Ћелија се препознаје по угластој загради са десне стране ({}).

МОДЕЛИ ОСЦИЛАТОРНОГ КРЕТАЊА

Периодично кретање представља посебан облик кретања које се после одређеног временског интервала понавља на истоветан начин. На пример равномерно кружно кретање, кретање тела обешеног о опругу, осциловање клатна, вибрирање жице, ваздушног стуба итд.

Посебан вид периодичног кретања јесте осцилаторно кретање или осциловање.

Осцилаторно кретање или осциловање је неравномерно праволинијско или криволинијско кретање тела око равнотежног положаја између две тачке у којима се тело зауставља и мења смер кретања.

Тело врши хармонијско осциловање под дејством силе која тежи да га врати у равнотежни положај и чији је интензитет пропорционалан удаљењу од тог положаја. Ово својство имају еластичне силе које се називају повратне или реституционе силе.

Величине које карактеришу хармонијско осциловање:

- Амплитуда осциловања је максимално удаљење тела од равнотежног положаја. Означаваче се са x_0 или са A .
- Елонгација је удаљење тела од равнотежног положаја у произвољном тренутку времена. Може имати вредности од $-x_0$ до x_0 .
- Период осциловања (T) је време потребно да тело изврши једну осцилацију.
- Учестаност (фреквенција) представља број осцилација које осцилатор изврши у јединици времена, тј. $\nu = n/t$. Једнака је реципрочној вредности периода осциловања: $\nu = 1/T$. Јединица за учестаност је Херц (Hz).
- Кружна учестаност (ω) је број осцилација у 2π секунди: $\omega = 2\pi\nu = 2\pi/T$. Јединица за учестаност је радијан у секунди (rad/s).

На Слици 1. приказано је осциловање тела у вертикалном правцу.

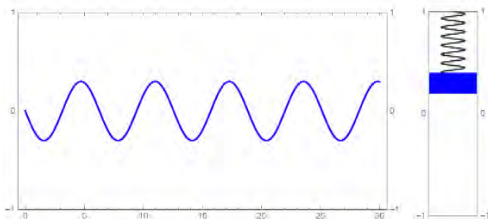
С обзиром да се кретање тела врши под дејством реституционе (повратне) силе облика $F = -kx$, једначина кретања тела по Другом Њутновом закону облика је: $ma = -kx$.

Функција која описује елонгацију осциловања је косинусна функција од ωt и може се написати у облику:

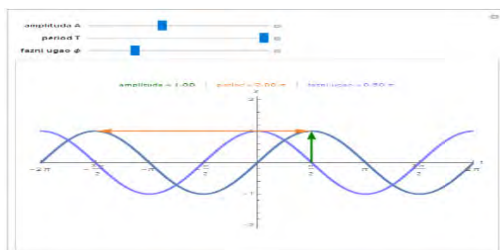
$$x = A \cos(\omega t + \varphi_0) \quad (1)$$

Овде је са A – означена амплитуда осциловања. Величина ω представља кружну учестаност осциловања, израз у загради ($\omega t + \varphi$) је фаза осциловања или фазни угао φ , док је φ_0 почетна фаза (слика 2).

Хармонијско осцилаторно кретање је осцилаторно кретање које се може представити хармонијском кривом линијом (синусоидом или косинусоидом).



СЛИКА 1. Зависност положаја тела од времена



СЛИКА 2. Функција положаја

ЛИНЕАРНИ ХАРМОНИЈСКИ ОСЦИЛАТОР

Хармонијски осцилатор представља један од најважнијих модела у физици. С обзиром да се ученици по први пут срећу са представом хармонијског осцилатора потребно је приказати им то на прихватљив и разумљив начин, путем визуелизације одговарајућих примера. Користимо демонстрацију која нам омогућава да посматрамо кретање које описује материјална тачка масе m закачена на опругу константе еластичности k дуж једног правца осциловања линеарног хармонијског осцилатора (слика 3).

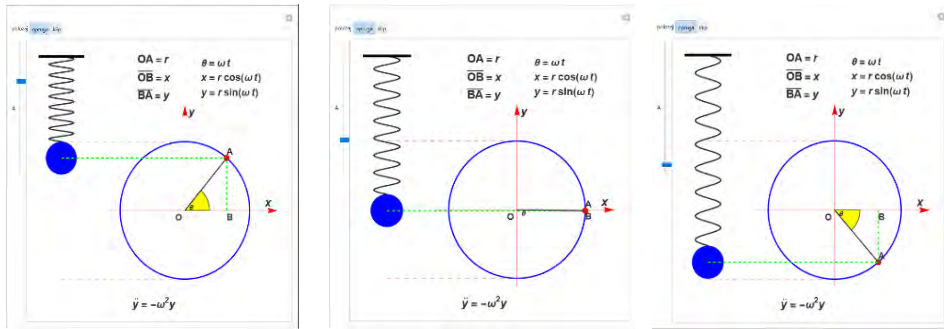
Демонстрација омогућава промену положаја материјалне тачке (команда означена са A на контролном панелу): вредности параметра $A = 0$ одговара положај $x = x_0$, а максималној удаљености положај $x = -x_0$. Једначине којима се описује ово кретање јесу:

$$x(t) = x_0 \cos(\omega t + \varphi_0), \quad v(t) = -v_0 \sin(\omega t + \varphi_0), \quad a(t) = -a_0 \cos(\omega t + \varphi_0) \quad (1)$$

при чему у сва три случаја важи: $\omega = \sqrt{\frac{k}{m}}$, $v_0 = \omega x_0$ и $a_0 = \omega^2 x_0$.

Такође се и Њутнов закон за хармонијски осцилатор може написати у облику:

$$a = -\omega^2 x. \quad (2)$$



СЛИКА 3. Шематски приказ помоћу честице на опрузи

Први панел на Сlici 3. приказује тренутак у којем је материјална тачка у близини тачке $y = y_0$, други панел приказује положај у близини равнотежног, а последњи панел приказује положај у близини тачке $x = x_0$. На Сlici 4. приказан је код за генерисање модела осциловања честице на опрузи.

b = 1/2;
f[x_] := 4 Sin[8 x];

```
Manipulate[
Graphics[
Switch[gv,
"opruzg", {ParametricPlot[{f[x], -x}, {x, 0, 2 Pi/a}], PlotStyle->Directive[Thick, GrayLevel[.2]], PlotRange->{{-1, 7}, {-2.5 Pi, 0.1}}, Axes->None, AspectRatio->1, ImageSize->{400, 400}}][[1]],
Thickness[.01], Line[{{-7, 0}, {7, 0}}], Blue, Disk[{0, -2 Pi/a}, b], PointSize[.006], Black, Point[{0, -2 Pi/a}], Blue, Thick, Circle[{4, -4 Pi/3-b}, 2 Pi/3], Red,
Thickness[.001], Arrow[{{4, -7}, {4, -1.5}}], Arrow[{{1.5, -4 Pi/3-b}, {7, -4 Pi/3-b}}], Dashed, Line[{{0, -2 Pi/a}, {4, -2 Pi/a-b}}], Line[{{0, -2 Pi-a}, {4, -2 Pi-b}}],
PointSize[.023], Point[{4+Re0*sqrt((2 Pi/3)^2 - (2 Pi/a + 4 Pi/3)^2), -2 Pi/a-b}], Green, Thick, Line[{{0, -2 Pi/a}, {4+Re0*sqrt((2 Pi/3)^2 - (2 Pi/a + 4 Pi/3)^2), -2 Pi/a-b}}],
Line[{{4+Re0*sqrt((2 Pi/3)^2 - (2 Pi/a + 4 Pi/3)^2), -4 Pi/3-b}, {4+Re0*sqrt((2 Pi/3)^2 - (2 Pi/a + 4 Pi/3)^2), -2 Pi/a-b}}], Yellow, EdgeForm[Thickness[.002]],
Disk[{4, -4 Pi/3-b}, .8, Which[{4 Pi/3 - 2 Pi/a >= 0} && Re0*sqrt((2 Pi/3)^2 - (2 Pi/a + 4 Pi/3)^2) > 0, {0, ArcTan[{4 Pi/3 - 2 Pi/a}/Re0*sqrt((2 Pi/3)^2 - (2 Pi/a + 4 Pi/3)^2)}, {4 Pi/3 - 2 Pi/a < 0} && Re0*sqrt((2 Pi/3)^2 - (2 Pi/a + 4 Pi/3)^2) > 0,
{ArcTan[{4 Pi/3 - 2 Pi/a}/Re0*sqrt((2 Pi/3)^2 - (2 Pi/a + 4 Pi/3)^2)}, 0}, {4 Pi/3 - 2 Pi/a < 0} && Re0*sqrt((2 Pi/3)^2 - (2 Pi/a + 4 Pi/3)^2) = 0, {0, Pi/2}, {4 Pi/3 - 2 Pi/a < 0} && Re0*sqrt((2 Pi/3)^2 - (2 Pi/a + 4 Pi/3)^2) = 0, {-2 Pi/3, 0}}],
Dashing[1], GrayLevel[.2], Thickness[.004], Line[{{4, -4 Pi/3-b}, {4+Re0*sqrt((2 Pi/3)^2 - (2 Pi/a + 4 Pi/3)^2), -2 Pi/a-b}}],
Text[Style["0", 12, Bold], Which[{4 Pi/3 - 2 Pi/a >= 0}, {4.2, -4.6}, {4 Pi/3 - 2 Pi/a < 0}, {4.2, -4.8}],
Text[Style[Column@{HoldForm[0 = omega t], TraditionalForm@HoldForm[x = v Cos[omega t]], TraditionalForm@HoldForm[y = v Sin[omega t]], 16, Bold}, {5.5, -.67}],
Text[Style[Column@{TraditionalForm@HoldForm[OB = x], TraditionalForm@HoldForm[BA = y]}, 17, Bold], {3, -.67}],
Text[Style["a", 18, Bold, Italic], {6.7, -4.45}], Text[Style["y", 17, Bold, Italic], {4.22, -1.7}], Text[Style["O", 14, Bold], {3.8, -4.9}],
Text[Style["A", 14, Bold], {4.1+Re0*sqrt((2 Pi/3)^2 - (2 Pi/a + 4 Pi/3)^2), -2 Pi/a-b-2}], "kkip",
{Thickness[.01], Line[{{-7, 0}, {7, 0}}], EdgeForm[Thick], White, Rectangle[{-5, -2 Pi/3-b+2}, {5, -2 Pi-b}], Blend[{LightGreen, Yellow}], Rectangle[{-5, -2 Pi-b}, {5, -2 Pi/a-b}],
GrayLevel[.8], Rectangle[{-2, 0}, {2, -2 Pi/a-b}], Brown, Rectangle[{-5, -2 Pi/a-b+2}, {5, -2 Pi/a-b}], PointSize[.006], Black, Point[{0, -2 Pi/a}], Blue, Thick,
Circle[{4, -4 Pi/3-b}, 2 Pi/3], Red, Thickness[.001], Arrow[{{4, -7}, {4, -1.5}}], Arrow[{{1.5, -4 Pi/3-b}, {7, -4 Pi/3-b}}], Dashed, Line[{{0.5, -2 Pi/3-b}, {4, -2 Pi/3-b}}],
Line[{{0.5, -2 Pi-a}, {4, -2 Pi-b}], PointSize[.023], Point[{4+Re0*sqrt((2 Pi/3)^2 - (2 Pi/a + 4 Pi/3)^2), -2 Pi/a-b}], Green, Thick, Line[{{0.5, -2 Pi/a-b}, {4+Re0*sqrt((2 Pi/3)^2 - (2 Pi/a + 4 Pi/3)^2), -2 Pi/a-b}}].
```

СЛИКА 4. Код за генерисање модела зависности положаја тела од времена
Енергија хармонијског осцилатора

Осцилатор је тело које врши хармонијско осциловање, при кретању непрекидно мења положај и брзину, што значи да располага одређеном потенцијалном и кинетичком енергијом. Како осцилатор представља изолован систем, његова механичка енергија се током времена не мења, ако занемаримо силе отпора средине (Слика 5).

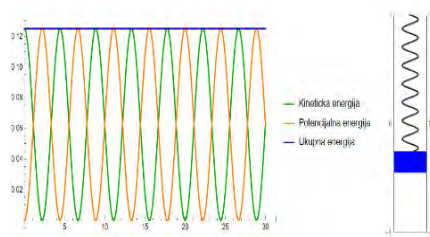
Укупна механичка енергија осцилатора једнака је збиру његове кинетичке и потенцијалне енергије. Укупна енергија хармонијског осцилатора износи:

$$E = E_k + E_p = \frac{m\omega^2 A^2}{2} \quad (3)$$

Укупна механичка енергија осцилатора има сталну вредност и сразмерна је његовој маси, квадрату амплитуде и квадрату кружне учестаности (Слика 6).



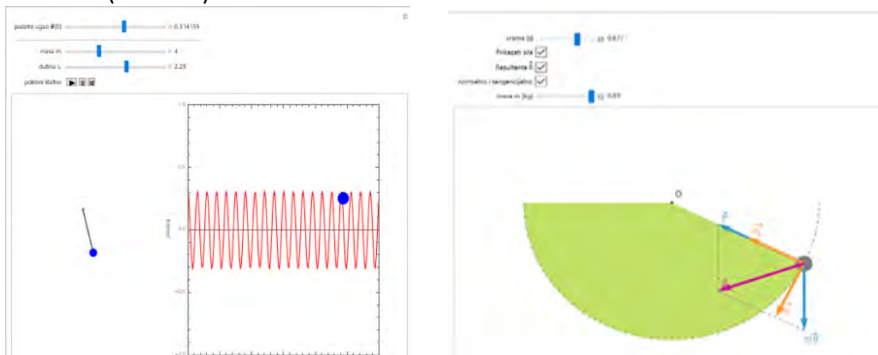
СЛИКА 5. Контролни панел



СЛИКА 6. Зависност енергије осцилатора од времена

МАТЕМАТИЧКО КЛАТНО

Математичко клатно је систем који се состоји из куглице занемарљивих димензија, која је окачена о неистегљиву нит занемарљиве масе. Клатно изводи слободне осцилације, ако се занемари отпор ваздуха и трење у тачки вешања. За описивање кретања математичког клатна користимо демонстрацију која нам омогућава исцртавање путање осциловања клатна и приказ сила које делују на клатно при кретању. Обзиром да се ради о осцилаторном кретању под дејством силе Земљине теже, са демонстрације се јасно види да је узрок осциловања клатна сила која је директно сразмерна елонгацији, на слици означена са R (Слика 7).



СЛИКА 7. Приказ амплитуде осциловања и сила које делују на математичко клатно

Такође постоји могућност одабира приказивања нормалне и тангенцијалне компоненте силе, резултантне силе и амплитуде осциловања. На Сlici 8. приказан је код за генерисање демонстрације модела математичког клатна.

```
Manipulate[Module[{sol, \theta, t}, sol = NDSolve[{ \theta''[t] = -9.81 * Sin[\theta[t]], \theta'[0] = 0, \theta[0] = -Pi/2}, \theta, {t, 0, tmax}];
With[{ \varphi = \theta[tmax] /. First[sol], \omega = \theta'[tmax] /. First[sol], g = 9.81},
Pane[Graphics[{{Point[{0, 0}], Text["O", {0, 0}, {-2, -2}], Gray, {ColorData["WebSafe"]["#99CC00"], Opacity[0.6], Disk[{0, 0], 1, {-Pi, \varphi - Pi/2}}},
(PointSize[Sqrt[m/20]], Point[{Sin[\varphi], -Cos[\varphi]}], {Dashing[{.01, .01}], Circle[{0, 0], 1, {-Pi, 0}}},
If[F = True, {Thickness[.008], ColorData["WebSafe"]["#3399CC"], Arrow[{{Sin[\varphi], -Cos[\varphi]}, {-1 + m \omega^2 + g m Cos[\varphi]} {-Sin[\varphi], Cos[\varphi]}]},
Text["\vec{T}", {-1 + m \omega^2 + g m Cos[\varphi]} {-Sin[\varphi], Cos[\varphi]}, {-2, -1}],
Arrow[{{Sin[\varphi], -Cos[\varphi]}, {Sin[\varphi], -g m - Cos[\varphi]}]},
Text["\vec{g}", {Sin[\varphi], -g m - Cos[\varphi]}, {-1, 1}], Line[{{0, 0}, {Sin[\varphi], -Cos[\varphi]}]},
If[comp = True, {Thickness[.008], ColorData["WebSafe"]["#FF9933"], Arrow[{{Sin[\varphi], -Cos[\varphi]}, {1 - m \omega^2} {Sin[\varphi], -Cos[\varphi]}]},
Text["\vec{R}", {1 - m \omega^2} {Sin[\varphi], -Cos[\varphi]}, {-2, -1}],
Arrow[{{Sin[\varphi], -Cos[\varphi]}, {(1 - g m Cos[\varphi]) Sin[\varphi], -Cos[\varphi] - g m Sin[\varphi]^2}}]},
Text["\vec{R}/m", {(1 - g m Cos[\varphi]) Sin[\varphi], -Cos[\varphi] - g m Sin[\varphi]^2}, {-2, -1}], Point[{0, 0}],
If[R = True, {{Thickness[.008], ColorData["WebSafe"]["#CC0099"], Arrow[{{Sin[\varphi], -Cos[\varphi]}, {(1 - m \omega^2 - g m Cos[\varphi]) Sin[\varphi], -g m + Cos[\varphi]} {-1 + m \omega^2 + g m Cos[\varphi]}]},
Text["\vec{R}^n", {(1 - m \omega^2 - g m Cos[\varphi]) Sin[\varphi], -g m + Cos[\varphi]} {-1 + m \omega^2 + g m Cos[\varphi]}, {-2, -1}],
If[F = True, {Dashing[{.01, .008}], Line[{{Sin[\varphi], -g m - Cos[\varphi]}, {(1 - m \omega^2 - g m Cos[\varphi]) Sin[\varphi], -g m + Cos[\varphi]} {-1 + m \omega^2 + g m Cos[\varphi]}]},
Line[{{(1 - m \omega^2 - g m Cos[\varphi]) Sin[\varphi], -g m + Cos[\varphi]} {-1 + m \omega^2 + g m Cos[\varphi]}, {(1 - m \omega^2 - g m Cos[\varphi]) Sin[\varphi], Cos[\varphi]} {-1 + m \omega^2 + g m Cos[\varphi]}]},
}], PointSize[.01], Point[{0, 0}],
}], {PointSize[.01], Point[{0, 0}]}
}], PlotRange -> {{-1.1, 1.2}, {-1.7, .6}}, ImageSize -> {500, 400}], {500, 400}
]
],
{tmax, 0, "vreme [s]", 0, 4 * .296, .001, Appearance -> "Labeled", ImageSize -> Tiny},
{{F, False, "Prikazati sile"}, {False, True}},
{{R, False, "Rezultanta \vec{R}"}, {False, True}},
{{comp, False, "normalno i tangencijalno"}, {False, True}},
{{m, .05, "masa m [kg]", .02, .05, .001, Appearance -> "Labeled", ImageSize -> Tiny},
ControlPlacement -> Top, AutorunSequencing -> {2, 3, 4, 5}
]
]
```

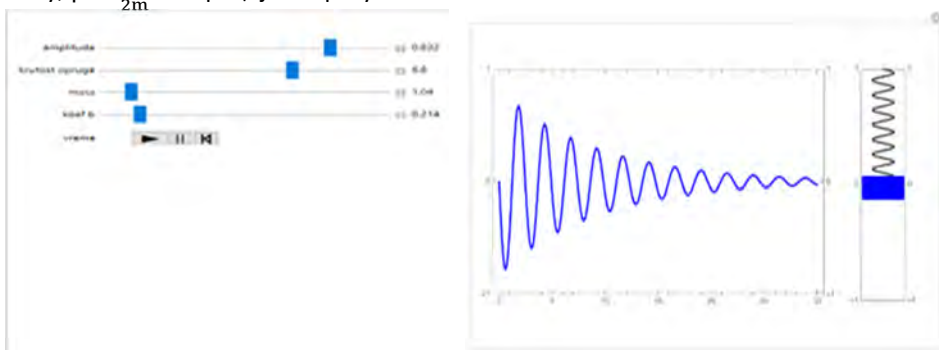
СЛИКА 8. Код за генерисање демонстрације модела математичког клатна

ПРИГУШЕНЕ ОСЦИЛАЦИЈЕ

Осцилације чија се амплитуда смањује с временом називају се пригушене или амортизоване осцилације. На Слици 9. представљена је демонстрација која исцртава пригушене осцилације. Демонстрација омогућава подешавање одговарајућих вредности амплитуде осцилаатора, коефицијента еластичности опруге, коефицијента пригушења и масе тега. Једначина кретања осцилатора је облика:

$$x = A(t)\sin(\omega t + \varphi_0) \quad (3)$$

где је: $A(t) = A_0 e^{-\beta t}$ амплитуда осциловања која се смањује по експоненцијалном закону у времену, $\beta = \frac{\mu}{2m}$ коефицијент пригушења.



СЛИКА 9. Демонстрација пригушених осцилација

ПРИНУДНЕ ОСЦИЛАЦИЈЕ

У физичким уређајима су потребни осцилатори који могу да одржавају осциловање дужи време. Да би се то остварило потребно је реалном осцилатору доводити у току сваке осцилације онолико енергије колико губи тако да му се не би смањивала амплитуда осциловања.

Принудне механичке осцилације настају када на осцилатор делује спољашња сила која се периодично мења у времену. У општем случају на осцилатор делују три силе: спољашња сила F , сила еластичности опруге $F = -kx$ и сила отпора средине $F = -\mu v$.

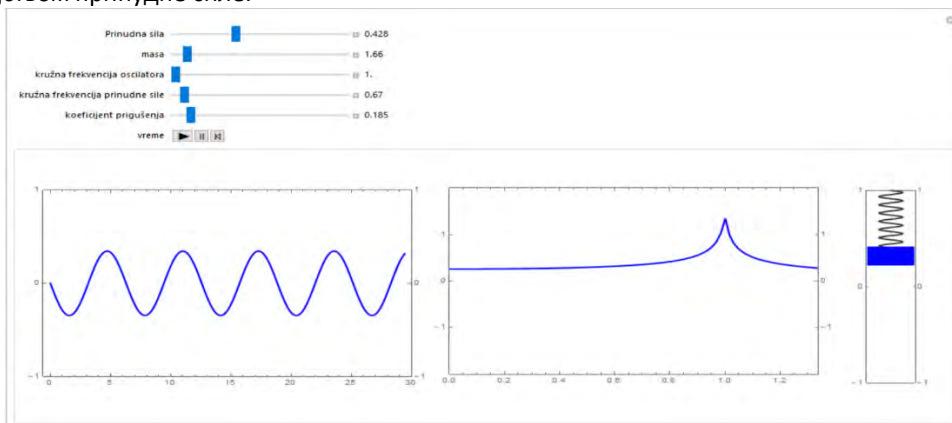
Амплитуда принудних осцилација зависи од принудне силе, њене фреквенције и сопствене фреквенције осцилатора.

Резонанција је појава при којој је амплитуда принудних осцилација максимална.

Фреквенција којом тада осцилује осцилатор назива се резонантна фреквенција ν_r па разликујемо два случаја:

- када нема отпора средине и трења једнака је сопственој фреквенцији осцилатора ($\nu_r = \nu_0$),
- када постоји отпор средине или трења (пригушења) мања од сопствене фреквенције осцилатора ($\nu_r < \nu_0$) – при малим пригушењима је мало мања од ње.

На слици 10. приказан је контролни панел који нам омогућава подешавање одговарајућих услова за настанак резонанције. Такође, дат је и приказ резонанције под дејством принудне силе.



СЛИКА 10. Демонстрација принудних осцилација

ЗАКЉУЧАК

Напредак савремених технологија нуди потенцијалне могућности за развој наставе у смислу потребе за брзим и ефикасним трансфером знања и потребно их је искористити. С обзиром да су демонстрације које смо користили модларне, омогућавају прилагођавање наставнику, као и афинитетима ученика. Посебно добијају на значају уз паметну таблу. На овај начин се може постићи боље разумевање наставне теме Хармонијске осцилације у ситуацијама извођења наставе у школама које нису довољно опремљене лабораторијама у којима би се појаве могле практично показати.

ЛИТЕРАТУРА

1. Toplis R. & Allen M., 'I do and I understand?' Practical work and laboratory use in United Kingdom schools, *Eurasia Journal of Mathematics, Science & Tehnology Educations*, 8 (1), (2012), pp. 3-9.
2. Capanis N., Chabalengula V.M., Mumba F., Mbewe S., How Pre-Service Teachers' Understand and Perform Science Process Skills, *Eurasia Journal od Mathematics, Sceince and Tehnology Education*, 7 (2), (2010), pp. 196-214.
3. Gekelman W., Pribyul P., Wise J., Lee A., Hwang R., Eghtebas C., Shin J., & Baker B., Using plasma experiments to illustrate a complex index of refraction, *American Journal of Physics*, 79 (9), (2011), pp. 894-902.
4. <https://ocw.mit.edu/courses/8-13-14-experimental-physics-i-ii-junior-lab-fall-2016-spring-2017/>
5. Amadallo M. M., Alphayo A.O., Thomas W. S., Physics Practical Work and Its Influence on Students' Academic Achievement, *Journal of Education and Practice*, Vol. 7, No.28, 2016.
6. Chau, P.Y., An empirial investigation on factors affecting the acceptance of CASE by systems developers, *Information & Management*, 30 (6), (1996), pp.269-280.
7. Davis, F.D., Perceived usefulness, perceived ease of use, and user acceptance of information technology, *MIS Quarterly*, 13 (3), (1989), pp. 319-340.
8. Drljača B., Đokić B., Šiljić I., Kevkić T., Gulan Lj., Primena softverskih paketa za demonstraciju oglada iz fizike, *Zbornik radova sa međunarodne konferencije o nastavi fizike i srodnih nauka*, br. 7, (2018), str. 181-186.
9. Физика уџбеник за трећи разред гимназије природно-математичког и општег смера, Klett, Београд 2016.
10. Физика уџбеник за трећи разред гимназије општег и природно-математичког смера, Завод за уџбенике, Београд 2015.
11. Физика уџбеник за трећи разред гимназије, Круг, Београд 2010.
12. Kenny F. Stephens II "Simple Harmonic Motion of a Spring"
<http://demonstrations.wolfram.com/SimpleHarmonicMotionOfASpring/>
Wolfram Demonstrations Project
13. Paul Rosemond "Simple Harmonic Motion"
<http://demonstrations.wolfram.com/SimpleHarmonicMotion/>
Wolfram Demonstrations Project
14. Stephen Wilkerson "An Oscillating Pendulum"
<http://demonstrations.wolfram.com/AnOscillatingPendulum/>
Wolfram Demonstrations Project
15. Bernard Vuilleumier "Forces on a Pendulum"
<http://demonstrations.wolfram.com/ForcesOnAPendulum/>
Wolfram Demonstrations Project

Poređenje komercijalnih softverskih paketa u nastavi fizike sa tradicionalnim metodama u osnovnom obrazovanju u ruralnim područjima Srbije

Branko Drljača, Boban Đokić, Dušica Spasić

Prirodno-matematički fakultet, Univerzitet u Prištini, Lole Ribara 29, Kosovska Mitrovica, Srbija

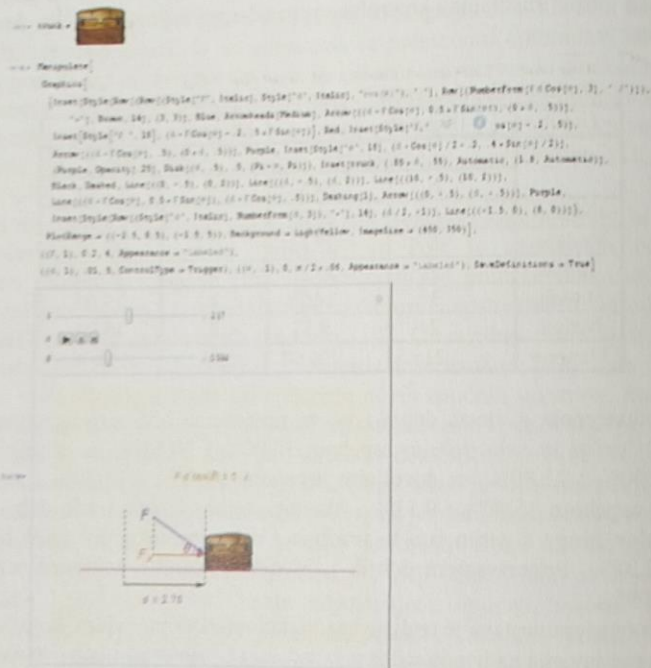
Apstrakt. Na osnovu pregleda savremene literature nastavni proces fizike u osnovnim školama svake godine postaje sve izazovniji. Osnovno pitanje je kako pronaći prikladna sredstva za približavanje fizike učenicima. U fizici na ovom nivou je često teško objasniti fizičke procese zbog potrebe za visokim nivoom apstrakcije. Škole koje se nalaze u gradovima su uglavnom opremljene nastavnim sredstvima koja se uspešno mogu koristiti u nastavi fizike. S druge strane, škole u seoskim oblastima Srbije slabo su ili nisu opremljene nastavnim sredstvima. Na ovaj način su nastavnici u ovim oblastima postavljeni u neravnotežan položaj u poređenju sa nastavnicima u urbanim sredinama. U ovom radu ćemo uporediti standardni način nastave u Srbiji sa efikasnim i jednostavnim metodom za poboljšanje razumevanja fizike za osnovno obrazovanje. Koristili smo komercijalno dostupne softverske pakete tokom nastave fizike koje su držali nastavnici u osnovnim školama, da bismo poboljšali razumevanje funkcionalnih zavisnosti u fizici. Uvođenje takvog nastavnog sredstva u nastavni proces povećalo je interesovanje učenika za fiziku i poboljšalo njihove kompetencije iz fizike.

Ključne reči: nastava fizike, softverski paket, ogledi.

UVOD

Nastava fizike u Srbiji postaje izazovnija iz godine u godinu. Dugi proces koji je nekada imao dovoljan broj školskih časova često se skraćuje, posebno u srednjim stručnim školama. Nastavni proces bi trebalo da se sastoji od tri komponente, i to teorijskog predavanja, problema iz radne sveske i demonstracija (ako je moguće) [1]. Predavanje je najčešće korišćena metoda u nastavi fizike u srpskim školama. Za ovu metodu se pokazalo da je najmanje efikasna za naučnu nastavu jer nakon nastavnog procesa učenici imaju slabe kompetencije iz fizike. Kako fizički svet funkcioniše, koje su suštinske veze između fizičkih veličina, su pitanja na koje ova tradicionalna metoda najčešće ne može dati dobre odgovore, jer se razumevanje fizičkih pojava, kod većine učenika malo ili nimalo ne menja primenom ove metode [2-3] Ispitivanja pokazuju da ih ovaj metod delotvoran kod oko deset procenata učenika [4] za koje se pretpostavlja da ih predstavljaju motivisani učenici, koji bi, u suštini i sami savladali nastavno gradivo. Ako su računski i problemi u radnim sveskama uključeni u nastavni proces, rezultat je donekle

je sila vektorska veličina učenici slikovito mogu da vide koje tri veličine su neophodne za potpuno određivanje vektorske fizičke veličine. Kao rezultat prikazuje se pređeni put tela pod dejstvom ovako definisane sile kao i izvršeni rad. U zavisnosti od ugla kao što se i vidi rad može biti pozitivan, negativan ili jednak nuli. Na osnovu demonstracije lako se zaključuje da: sila koja deluje u smeru kretanja tela vrši pozitivan rad, sila koja se suprotstavlja kretanju i deluje u suprotnom smeru, vrši negativan rad i sila koja deluje normalno na pravac kretanja tela ne vrši rad. Ovaj model moguće je vrlo lako korigovati i za više razrede uvođenjem težine tela, kao i sile trenja, čime se prikazuje modularnost demonstracije. Na slici 1 prikazan je kod za generisanje demonstracije modela mehaničkog rada.



Slika 1. Kod za generisanje demonstracije modela mehaničkog rada

REZULTATI ISTRAŽIVANJA

Kako bi se proverila efikasnost metode zasnovane na primeni komercijalnih softverskih paketa izvršeno je uporedno testiranje kontrolne i eksperimentalne grupe vezano za obrađenu nastavnu jedinicu, sa dodatkom pitanja koja su obrađena u dotadašnjem radu ali se eksplicitno ne pominju u udžbeniku u vezi te nastavne jedinice.

Provera je izvršena pomoću standardizovanog testa kojeg je činilo 10 pitanja, pri čemu je učenik mogao osvojiti maksimalno 20 bodova. Ocenjivanje je izvršeno na sledeći način: 18-20 bodova – ocena 5; 15-17 bodova – ocena 4; 12-15 bodova – ocena 3; 10-11 bodova – ocena 2; manje od 10 bodova – ocena 1.

Na osnovu dobijenih podataka sa testa došlo se do rezultata, pri čemu je eksperimentalna grupa imala bolji rezultat. Srednja ocena kontrolne grupe je 3,42, dok je srednja ocena eksperimentalne grupe 3,55.

Rezultati testa za kontrolnu i eksperimentalnu grupu prikazani su u Tabeli 2.

Tabela 2. Uspeh učenika na testu

Uspeh	Kontrolna grupa		Eksperimentalna grupa	
	Opšti uspeh		Opšti uspeh	
7.razred	N	N(%)	N	N(%)
Odlični	5	23,80	5	25,00
Vr.dobr.	5	23,80	6	30,00
Dobar	6	28,60	5	25,00
Dovolj.	4	19,04	3	15,00
Nedov.	1	4,76	1	5,00
Ukupno	21	100,00	20	100,00

ZAKLJUČAK

U radu su pokazane mogućnosti primene programskog paketa *Mathematica*® u modeliranju konkretnih fizičkih procesa sa ciljem povećanja aktivnosti učenika na času i boljem razumevanju fizičkih procesa u uslovima u kojima ne postoji potrebna oprema. Ispitivanje je izvršeno na dve grupe učenika približno istih rezultata, kroz obradu nastavne jedinice: Mehanički rad. Kontrolna grupa imala je tradicionalni oblik nastave, dok je eksperimentalna grupa metodom efikasnog učenja, upotrebom programskog paketa *Mathematica*® sa demonstracijom. Iz priložene tabele vidi se da je primena komercijalnog softverskog paketa *Mathematica*® doprinela boljem razumevanju nastavnog gradiva.

LITERATURA

1. T. Petrović, (1994). „Didaktika fizike – teorija nastave fizike“, Fizički fakultet, Beograd
2. Capanis N., Chabalengula V. M., Mumba F. & Mbewe S., (2010), How Pre-Service Teachers' Understand and Perform Science Process Skills, Eurasia Journal of Mathematics, Science and Technology Education 7(2), 106-214.
3. Garwin, M.R. & Ramsier, R.D., (2003). Experiential learning at the university level: a US case study, Education and Training, 45(5), 280-285.
4. Gekelman W., Pribyl, P., Wise J., Lee A., Hwang R., Eghtebas C., Shin J., & Baker B., (2011), Using plasma experiments to illustrate a complex index of refraction, American Journal of Physics, 79 (9), 894-902.
5. https://en.wikipedia.org/wiki/Walter_Lewin_Lectures_on_Physics
6. Gunther Roland, Janet Conrad, Sean Robinson, and Physics Department Faculty, Lecturers, and Technical Staff. 8.13-14 Experimental Physics I & II "Junior Lab". Fall, (2016). - Spring (2017). Massachusetts Institute of Technology: MIT OpenCourseWare
7. Basheer Ahmad. (2017), The Effectiveness of Teachers' Use of Demonstrations for Enhancing Students' Understanding of and Attitudes to Learning the Oxidation-Reduction Concept. EURASIA Journal of Mathematics, Science and Technology Education. 13.
8. Amadalo M. Musasia, Alphayo A.Ocholla, Thomas W.Sakwa, (2016), Physics Practical Work and Its Influence on Students' Academic Achievement, Journal of Education and Practice, Vol.7, No.28.

9. Lee Mei Chi, Sulaiman Fauziah, (2018), The Effectiveness Of Practical Work In Physics To Improve Students' Academic Performances, International Journal of Social Sciences, Vol 3.
10. Trends in International Mathematics and Science Study (TIMSS), (1995). International Reports in Mathematics and Science. (1995,1999). <http://timss.bc.edu/timss1999.html>
11. Stanley H. E., (2000). Exotic statistical physics: Applications to biology, medicine, and economics, *Physica A*, 285, 1-17.
12. Daramola S.O., (1987). Restructuring Science Education Programmes in Nigerian Higher Institutions, *Journal of Curriculum and Instruction*, 2(1 & 2), 235-240.
13. Nashon, S. M. (1989). Practical work in science: A critical look at practical work in Kenyan secondary schools. Unpublished MEd Thesis, School of Education, The University of Leeds, UK.
14. Hirschfeld, D. Interest in science careers wanes in Latin America, *Science and developmentnetwork*, 2012.
15. Yen-Jie Lee. *8.03SC Physics III: Vibrations and Waves*. Fall 2016. Massachusetts Institute of Technology: MIT OpenCourseWare, <https://ocw.mit.edu>. License: Creative Commons BY-NC-SA.
16. Violeta Šlekienė, Loretta Ragulienė, (2010), The Learning Physics impact of interactive lecture demonstrations, problems of education in the 21st century Vol. 24.
17. Davis, F. D., Bagozzi, R. P., & Warshaw, P. R. (1989), User acceptance of computer technology: A comparison of two theoretical models. *Management Science*, 35(8), 982-1003.
18. Chau, P.K.Y. (1996) An Empirical Assessment of a Modified Technology Acceptance Model. *Journal of Management Information Systems*, 13, 185-204.
19. Earl Babbie, *The Practice of Social Research*, Wadsworth Publishing Company, 1998.

Comparison of Commercial Software Packages in Physics Teaching With Traditional Methods in Primary Education in Rural Serbia

Branko Drljača, Boban Đokić, Dušica Spasić

Abstract: Based on the review of up to date literature physics teaching process in primary schools every year becomes more challenging. Major issue is how to find suitable means for bringing physics closer to pupils. On the primary level physics it is often difficult to explain physical processes due to relatively high level of imaginarity needed. Schools located in cities are mostly well equipped with teaching tools that can be used in physics teaching process. On the other hand schools located in rural areas of Serbia are poorly or nowise equipped with teaching tools. In this way, teachers in these areas are placed in an unequal position compared to teachers in urban areas. In this work we compare standard teaching method in Serbia with efficient and simple method for improving understanding of physics for primary education. We used commercially available software packages, during lectures of general physics given by primary school teachers, to improve understanding of functional dependences of physics phenomenon. Introduction of such teaching tool in teaching process increased pupils interest in physics and improved their competences in physics.

Fizika obojena muzikom

Gordana Stanojević, Marija Stojanović

OŠ "Učitelj Tasa", Niš

Apstrakt. U svakodnevnom školskom životu, kod velikog broja đaka, fizika često predstavlja bauk! Fizika je teška za učenje jer zahteva kontinuitet i konceptualno razumevanje. Da bi "fizika bila u modi" potrebno je primeniti vizuelne metode, IKT i omogućiti vršnjačku podršku (rad u grupi). Učite fiziku – proširite granice!

Ključne reči: fizika, muzika, integrativna nastava, zvuk, ton.

UVOD

„Znanje nije dovoljno, potrebna je primena. Želja nije dovoljna, potreban je rad.“
Johann Wolfgang von Goethe

Integrativni pristup podrazumeva aktivnog učenika ali i nastavnika. Znanje se ne svodi samo na prenošenje činjenica, već na smisljeno rešavanje problema, postavljanje pitanja i aktivnog traženja odgovora iz okoline i okruženja. U ovom slučaju, jača se horizontalno i vertikalno povezivanje fizike i muzičke kulture i omogućava sagledavanje različitih dimenzija jednog problema iz različitih uglova.

FIZIKA OBOJENA MUZIKOM

Nauka o zvuku je akustika. Učenici osnovne škole se susreću sa zvučnim pojavama još u ranom detinjstvu. Razlikuju govor, viku, pevanje, sviranje na instrumentu, itd. Znaju da naprave razliku o izvoru zvuka, ali sve do osmog razreda ne dobijaju odgovor zašto se tako prepoznaje zvuk klavira i gitare, muški i ženski vokal. Tek u osmom razredu, učenici spoznaju karakteristike zvuka, šta je zvuk, kako nastaje, kako i gde se zvuk prostire, zatim nauče kojim parametrima se opisuje zvuk. Otkriju kakva je veza između parametara t.j. nauče fizičke zakone kojima se opisuju zvučne pojave.

Zvuk je longitudinalni mehanički talas koji registruje čoveče uho sa frekvencom u intervalu 16 Hz – 20 kHz. Mehanički talas sa frekvencom manjom od 16Hz zove se infrazvuk; mehanički talas sa frekvencom većom od 20 kHz zove se ultrazvuk.

Za prostiranje zvuka potrebna je materijalna sredina; u zavisnosti od osobine sredine i temperature, menja se intenzitet brzine prostiranja zvuka - najbrže se svuk prostire kroz čvrstu sredinu, sporije kroz tečnu a najsporije kroz gasnu sredinu [1]. Kroz vakuum se zvuk ne prostire!

bolji. Ipak, ova metoda poučavanja je funkcionalna samo za mali broj tematskih jedinica za koje je utvrđeno da su teorijska predavanja i problemi u radnim sveskama dovoljni da bi učenici stekli znanje o obrađivanoj nastavnoj temi kao i potpuno razumevanje problema. S druge strane, najveći broj tema zahteva odgovarajuće praktično demonstriranje kako bi se učenicima približile fizičke pojave. Štaviše, ove demonstracije su se pokazale kao ključne u razumevanju fizike u osnovnom obrazovnom nivou i srednjem obrazovnom nivou. Demonstracije u fizici pomažu učenicima da postignu dublje razumevanje fizičkih procesa i široko se koriste širom sveta, čak i za pred diplomatske i diplomatske studije na svetski poznatim univerzitetima [5]. Kao rezultat, učenici su više zainteresovani za istraživanje sveta fizike što dovodi do poboljšanih kompetencija na kraju procesa.

Demonstracije se mogu podeliti u dve grupe. Prvu grupu čine klasični demonstrativni eksperimenti, izvedeni ispred ili sa učenicima sa potrebnom opremom. Kao što je već spomenuto, postoji niz eksperimenata koje su ugledni univerzitetski profesori sprovedi na svojim univerzitetima [6]. Ova vrsta demonstrativnih eksperimenata pomaže učenicima da steknu bolji uvid u fizičke pojave [7]. Pokazano je da kad su studenti aktivno uključeni u demonstracije, oni postižu bolje rezultate u poređenju sa slučajevima kada ih samo posmatraju [8-9].

Praktični rad uključuje učenje putem odabranih koncepta koje promovišu motivaciju i aktivnost učenika i kao rezultat imaju učenje koje je zasnovano na poređenju svakodnevnih iskustava i pojava [10-11]. Praktični rad pomaže otkrivanje učenicima mogućnosti za razumevanje i manipulisanje složenom i apstraktnom prirodom nauke u izazivanju efektivnih konceptualnih promena [12]. On ujedno pomaže u otkrivanju i uklanjanju zablude učenika, motiviše ih i intrigira čak naukom [13]. Kao rezultat toga, praktični rad vodi učenike ka potvrdi i sticanju novih naučnih saznanja. Samim tim oni preuzimaju odgovornost za sopstvenu sposobnost istraživanja i ispitivanja prirode [14-16].

Drugu grupu demonstracija čine tzv. virtualne demonstracije koje su zasnovane na informaciono-komunikacijskim tehnologijama. Ovaj metod je sveobuhvatniji, zanimljiviji i kvalitetniji od tradicionalnog modela zasnovanog na predavačkoj nastavi. Kroz ovu vrstu nastavnog procesa učešće učenika postaje praktično čime se omogućava bolje razumevanje fundamentalnih fizičkih procesa [17-18]. Često smo svedoci da učenici osnovnih škola i gimnazija, koji imaju odgovarajuću opremu, visoko kvalitetnim i sadržajno zasnovanim informacionim i komunikacionim sistemima postižu veliki uspeh na republičkim i međunarodnim takmičenjima i olimpijadi znanja. Uopredno govoreći, razlika u nivou obrazovanja, u ovim slučajevima je neprimetna [19].

ANALIZA I INTERPRETACIJA ISTRAŽIVANJA

Da bi se uporedio ukupan obrazovno-vaspitni učinak problemske nastave i naučne metode u odnosu na tradicionalnu nastavu u istraživanju je primenjen model eksperimenta u jednom razredu sa dva odeljenja kojima predaje isti nastavnik.

Ispitivanje je rađeno u OŠ „Veljko Dugošević“ koja se nalazi u Ranilugu, opština Kosovska Kamenica, koju pohađja 347 učenika. S obzirom da se škola nalazi u Kosovskom Pomoravlju koje je u velikoj meri pogođeno ratnim dešavanjima i da se suštinski nalazi u enklavi, opremljenost škole nastavnim sredstvima za fiziku je na

poređenje komercijalnih softverskih paketa u nastavi fizike sa tradicionalnim metodama u osnovnom obrazovanju u ruralnim područjima Srbije

niskom nivou. U najvećoj meri nastavnici fizike su ograničeni na primenu tradicionalnih metoda bez izglednih mogućnosti za uvođenje nastavnih sredstava u nastavi fizike.

S obzirom na nemogućnost primene nastavnih sredstava u nastavi fizike, odlučili smo se da nastavnicima OŠ „Veljko Dugošević“ predstavimo mogućnost primene komercijalnih softverskih paketa u nastavi fizike. Cilj je da primenom ovih softverskih paketa približimo fizičke procese koji se obrađuju u tematskim jedinicama u određenim razredima. Očekivani ishod je poboljšanje kompetencije đaka iz fizike.

Kako bi mogli da izvršimo poređenje efikasnosti predložene metode sa tradicionalnom metodom odabrali smo dve grupe učenika koje su imale prosečno slične rezultate (srednja ocena kontrolne grupe je 3,43 a srednja ocena eksperimentalne grupe je 3,2)

Namernim izborom uzorka pokušalo se na početku ujednačiti obe grupe. Pregled uspeha učenika eksperimentalne i kontrolne grupe učenika sedmog razreda škole „Veljko Dugošević“ dat je u Tabeli 1.

Tabela 1. Uspeh učenika 7. razreda OŠ „Veljko Dugošević“

Uspeh	Kontrolna grupa		Eksperimentalna grupa	
	Opšti uspeh		Opšti uspeh	
	N	N(%)	N	N(%)
Odlični	5	23,80	4	20,00
Vr.dobr.	6	28,58	6	30,00
Dobar	5	23,80	4	20,00
Dovolj.	3	14,29	3	15,00
Nedov.	2	9,53	3	15,00
Ukupno	21	100,00	20	100,00

Opšta ujednačenost je dosta dobra i to: za učenike sa odličnim uspehom 20,00% : 23,80%; za učenike sa vrlo dobrim uspehom 30,00% : 38,58%; za učenike sa dobrim uspehom 20,00% : 23,80%; sa dovoljnim uspehom 15,00% : 14,29% i za učenike sa nedovoljnim uspehom 15,00% : 9,53%. Ako povežemo odlične i vrlo dobre učenike iz eksperimentalne grupe a zatim isto to uradimo i u kontrolnoj grupi onda bi odnos bio 50,00% : 52,38%. Povezivanjem dobrih i dovoljnih učenika dobijamo sledeći odnos 35,00% : 38,09%.

U kontrolnoj grupi nastava je realizovana tradicionalnom metodom, koja podrazumeva tradicionalna predavanja uz izradu računskih zadataka i primenu radnih svesaka.

U odeljenju koje je činilo eksperimentalnu grupu, čas je realizovan metodom efikasnog učenja, upotrebom programskog paketa *Mathematica*® sa demonstracijom. U ovom softverskom paketu moguće je simulirati veliki broj mehaničkih, optičkih, električnih, itd. procesa iz fizike na jednostavan način. U sklopu pripreme nastavnika za električnih, itd. procesa iz fizike na jednostavan način. U sklopu pripreme nastavnika za izvođenje nastave nastavnik je obučen da koristi softverski paket *Mathematica*®, pri čemu su mu data detaljna uputstva. Tokom časa nastavnikova aktivnost je orijentisana na podsticanje učenika da sami dođu do rešenja, diskutuju sa učenicima, održavanje misaonog toka učenika sa intervencijama izraženim kroz sugestije u trenutku kada primeti da se učenici udaljavaju od bitnog ili kad njihova razmišljanja ne vode u pravcu rešavanja problema.

Za realizaciju demonstracionih oglada potreban je samo računar i (ali ne i neophodan projektor. U radu je obrađena nastavna jedinica Mehanički rad. Po definiciji : rad vrši sila koja pokreće neko telo ili mu menja oblik i takav rad se naziva mehanički. U demonstraciji je moguće lako podesiti intenzitet, pravac i smer dejstva sile. S obzirom da

Primena softverskih paketa za demonstraciju oglada iz fizike

Branko Drljača¹, Boban Đokić¹, Ivan Šiljić², Tijana Kevkić¹, Ljiljana Gulan¹

¹Univerzitet u Prištini, Prirodno-matematički fakultet, Priština – Kosovska Mitrovica, Srbija, branko.drljacapr.ac.rs

²OŠ "Despot Stefan", Kruševac

Apstrakt. Veliki broj osnovnih i srednjih škola u Republici Srbiji nije adekvatno opremljen za izvođenje nastave fizike. Tu se pre svega misli na nedovoljnu opremljenost kabineta za nastavu fizike, kojima često nedostaje oprema za izvođenje oglada. Ovaj problem je naročito izražen u ruralnim sredinama. U ovom radu smo ponudili jedno od mogućih rešenja kako bi se ovaj problem mogao prevazići i kako bi daci bar na neki način mogli da učestvuju u izvođenju oglada.

Ključnereči: nastava fizike, softverski paket, ogladi

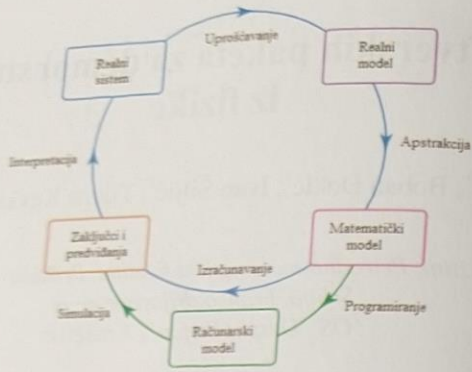
UVOD

Napredak tehnologije nameće neophodnost promene načina realizacije nastavnog procesa u savremenom obrazovanju u smislu potrebe za brzim i efikasnim transferom znanja. Zbog toga je u prirodnim naukama neophodna upotreba odgovarajućeg računarskog softvera koji omogućava da nastavni sadržaj bude pristupačniji i pregledniji. U ovom radu su predložena neka rešenja problema izvođenja praktične nastave, naročito u školama koje se nalaze u ruralnoj sredini.

POJAM MODELIRANJA

U prirodnim naukama pod modelom u širem smislu podrazumeva se misaono (ili praktično) stvorena struktura kojom se predstavlja neki deo idealizovane, često uprošćene realnosti. Model, kao element naučne slike sveta, po pravilu predstavlja neku uprošćenu idealizaciju realnosti, pri čemu je njen stepen a i karakter pojednostavljenjatokom vremena sasvim promenljiv.

Modeliranje je postupak proučavanja procesa ili neke pojave posrednim putem, pomoću modela. Kao dovoljno efikasan način proučavanja, modeliranje se primenjuje u gotovo svim nauka, zbog čega predstavlja generator razvoja nauke. Zadatak modeliranja je da osvetli glavne osobine i fenomene realnog procesa i da ih prevedu na neki apstraktan jezik, kao što je jezik matematike. Proces modeliranja odvija se u nekoliko faza kao što je prikazano na slici 1.



Slika 1. Uprošćeni prikaz procesa modeliranja

Proces modeliranja obično počinje posmatranjem realnog sistema, ponekad u relativno kontrolisanim uslovima u laboratoriji, sa ciljem razumevanja procesa ili pojava od interesa. Ukoliko je dobijeni matematički model jednostavniji, problem možemo da rešimo analitičkim putem. U slučaju složenih matematičkih modela, neretko je nemoguće sisteme jednačina rešiti analitičkim putem, zbog čega se pristupa procesu numeričkog rešavanja problema korišćenjem odgovarajućeg računarskog softvera, poput programskog paketa *Mathematica*®. Na osnovu dobijenih rezultata vrši se analiziranje i predviđanje ponašanja realnog sistema u različitim uslovima.

Finalni deo procesa modeliranja predstavlja upoređivanje izvedenih zaključaka i predviđenog ponašanja sa realnim sistemom koju model opisuje. Ukoliko je predviđeno ponašanje u saglasnosti sa realnim sistemom, formirali smo odgovarajući model. U protivnom, pristupamo ponovnoj formulaciji modela.

Važnu stavku prilikom formiranja modela predstavlja izbor ograničenja kojima je podvrgnut sistem. Ukoliko su granice sistema suviše široke može se dogoditi da je takav model sistema praktično nemoguće analizirati, pošto su mnoge važne osobine prikrivene nevažnim detaljima. S druge strane, ukoliko su izabrane granice sistema suviše uske, sve relevantne karakteristike realnog procesa neće biti obuhvaćene njegovim modelom, što će rezultovati neadekvatnom analizom sistema na bazi takvog modela.

PROGRAMSKI PAKET MATHEMATICA®

Programski paket *Mathematica*® razvijen je u softverskoj kompaniji *Wolfram Research* i koristi se za matematičke i druge primene. Posebno je pogodan za obradu numeričkih podataka, za simbolička procesiranja, kao i za grafičko prikazivanje podataka i funkcija.

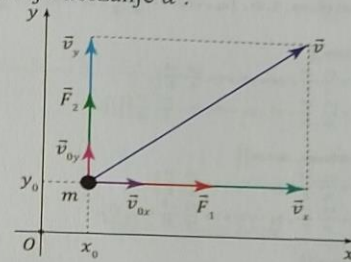
Za rad u programskom paketu *Mathematica*® koriste se dokumenta koja se zovu beležnice (*notebooks*). Beležnice se sastoje od ćelija koje mogu sadržati tekst, izračunavanja ili grafikone. Ćelija se prepoznaje po uglastoj zagradi sa desne strane (`]`). Ulazni podaci na osnovu kojih se vrši izračunavanje u programskom paketu *Mathematica*® se unose u ulaznim ćelijama.

MODELI MEHANIČKOG KRETANJA

U radu su obrađeni neki karakteristični primeri mehaničkog kretanja. Svaki primer je obrađen teorijski, nakon čega imamo praktičnu realizaciju modela u programskom paketu *Mathematica*® i kreirane demonstracije sa izvornim kodom.

Kretanje tela u ravni

Na slici 2. u ravni xOy je prikazano telo mase m , čiji je početni položaj definisan koordinatama x_0 i y_0 . Telo je saopštena početna brzina čije su komponente v_{0x} u pravcu x - ose i v_{0y} u pravcu y -ose. U pravcu x - ose na telo deluje sila \vec{F}_1 , a u pravcu y -ose sila \vec{F}_2 , koje posmatranom telu saopštavaju ubrzanje \vec{a} .



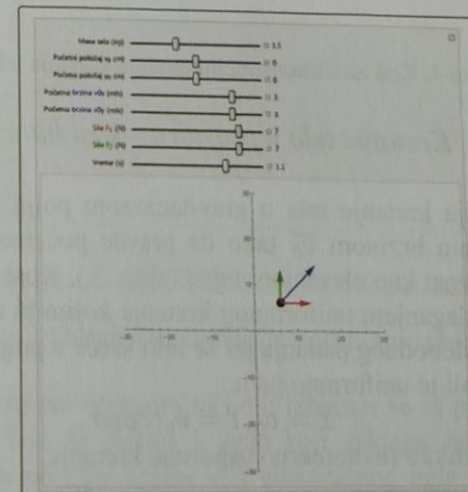
Slika 2. Kretanje tela u ravni

Položaj tela u odnosu na koordinatni početak posle vremena t određen je parametarskim jednačinama:

$$x = x_0 + v_{0x}t + \frac{F_1}{2m}t^2, \text{ i } y = y_0 + v_{0y}t + \frac{F_2}{2m}t^2 \quad (1)$$

Demonstracija modela kretanja tela u ravni

Demonstracija modela kretanja tela u ravni prikazana je na slici 3.



Telo promenljive mase m predstavljeno je pomoću kruga čiji je centar određen koordinatama početnog položaja tela x_0 i y_0 , koje možemo da biramo u demonstraciji. Početne brzine po odgovarajućim osama takođe možemo da menjamo. Sile koje deluju na posmatrano telo u pravcu x- ose i y- ose predstavljene su strelicama, čije se dužine menjaju u skladu sa odabranim intenzitetom sile. Intenzitet, pravac i smer trenutne brzine tela prikazani su strelicom odgovarajuće dužine i položaja u odnosu na koordinatne ose. Položaj tela u odnosu na koordinatni početak i njegova promena tokom vremena definisani su jednačinama (1). Kod koji generiše model i demonstraciju kretanja tela u ravni dat je na slici 4.

$$y_{max} = y_0 + \frac{v_0^2 \sin^2 \alpha}{2g}, \quad x_{max} = \frac{v_0^2 \sin 2\alpha}{2g} \left(1 + \sqrt{1 + \frac{2gy_0}{v_0^2 \sin^2 \alpha}} \right) \quad (4)$$

Vreme leta tela od njegovog izbacivanja do pada na površinu dato je u obliku:

$$\tau = \frac{v_0 \sin \alpha}{g} \left(1 + \sqrt{1 + \frac{2gy_0}{v_0^2 \sin^2 \alpha}} \right). \quad (5)$$

```
Manipulate[Graphics[
  (* Telo *)
  {Translate[Disk[{0, 0}, 1.0], {x0 + v0x*t + (v1^2)/2, y0 + v0y*t + (v2^2)/2}],
  (* Sila F1 *)
  {Thick, Red, Arrow[
    {x0 + v0x*t + (v1^2)/2, y0 + v0y*t + (v1^2)/2},
    {x0 + v0x*t + (v1^2)/2 + F1, y0 + v0y*t + (v1^2)/2}],
  (* Sila F2 *)
  {Thick, Darker@Green, Arrow[
    {x0 + v0x*t + (v1^2)/2, y0 + v0y*t + (v1^2)/2},
    {x0 + v0x*t + (v1^2)/2 + F2, y0 + v0y*t + (v1^2)/2}],
  (* Trenutna brzina *)
  {Thick, Blue, Arrow[
    {x0 + v0x*t + (v1^2)/2, y0 + v0y*t + (v1^2)/2},
    {x0 + v0x*t + (v1^2)/2 + v0x, y0 + v0y*t + (v1^2)/2 + v0y}],
  PlotRange -> {{-30.0, 30.0}, {-30.0, 30.0}}, ImageSize -> {600, 400},
  Axes -> True
],
  {{m, 1.5, "Masa tela (kg)"}, 1, 2.5, 0.5, Appearance -> "Labeled"},
  {{x0, 0, "Početni položaj x0 (m)"}, -1, 1, Appearance -> "Labeled"},
  {{y0, 0, "Početni položaj y0 (m)"}, -1, 1, Appearance -> "Labeled"},
  {{v0x, 3.0, Row[{"Početna ", Style["brzina v0x", Blue], " (m/s)"}]}, -5, 5,
  Appearance -> "Labeled"},
  {{v0y, 3.5, Row[{"Početna ", Style["brzina v0y", Blue], " (m/s)"}]}, -5, 5,
  Appearance -> "Labeled"},
  {{F1, 7, Row[{"Sila F1", Red, " (N)"}]}, -10, 10, Appearance -> "Labeled"},
  {{F2, 7, Row[{"Sila F2", Darker@Green, " (N)"}]}, -10, 10,
  Appearance -> "Labeled"},
  {{t, 0, "Vreme (s)"}, 0, 1.5, 0.1, Appearance -> "Labeled"}, ControlPlacement -> Top
]
```

Slika 4. Kod za demonstraciju modela kretanja tela u ravni

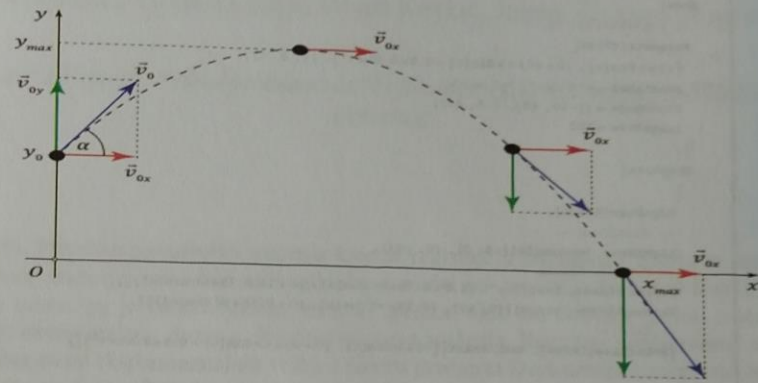
Kretanje tela u prostoru – kosi hitac

Kosi hitac predstavlja kretanje tela u gravitacionom polju Zemlje, koje je sa neke visine izbačeno početnom brzinom \vec{v}_0 tako da pravac početne brzine sa horizontalom zaklapa neki ugao α , poznat kao elevacioni ugao (slika 5.). Kosi hitac predstavlja složeno kretanje koje se dobija slaganjem uniformnog kretanja kojim bi telo trebalo da se kreće u pravcu početne brzine i slobodnog padanja jer se telo kreće u polju sile zemljine teže. Kretanje po horizontali je uniformno pa je:

$$x = v_{0x}t = v_0 t \cos \alpha, \quad (2)$$

$$y = y_0 + v_0 t \sin \alpha - \frac{gt^2}{2} \quad (3)$$

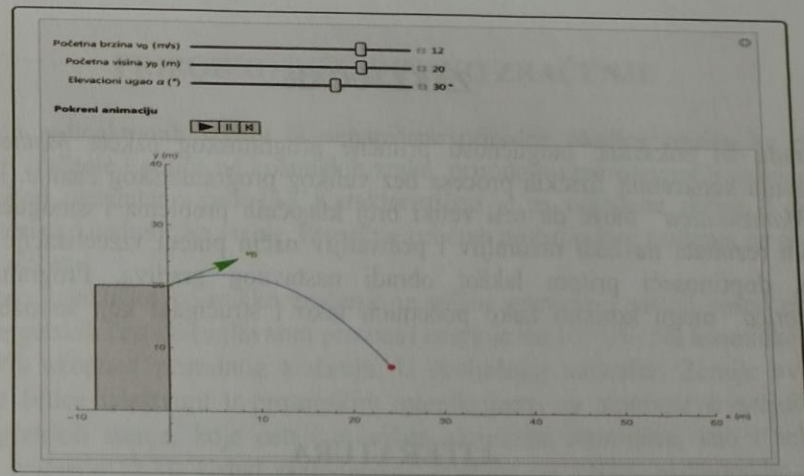
Maksimalna visina i maksimalni domet dati su u obliku:



Slika 5. Kosi hitac

Demonstracija modela kosog hica

Prikazan je model kosog hica izbačenog sa platforme promenljive visine y_0 , koje se u polju sile zemljine teže kreće bez otpora vazduha (slika 6.).



Slika 6. Demonstracija modela kosog hica

Telo koje je predstavljeno crvenom tačkom izbacuje se sa početnom brzinom \vec{v}_0 koja je prikazana strelicom čija se dužina i ugao koji zaklapa sa horizontalom menjaju u zavisnosti od intenziteta početne brzine v_0 i elevacionog ugla α , redom. Kretanje tela u koordinatnom sistemu xOy opisano je parametarskim jednačinama (2) i (3). Korišćenjem naredbe $Plot$ u programu Mathematica, dobijene su krive prikazane na slici 6. i trajektorija po kojoj se telo kreće.

kreće. Modelom kosog hica možemo da demonstriramo: vertikalni hitac naviše ($\alpha = 90^\circ$), vertikalni hitac naniže ($\alpha = -90^\circ$) i horizontalni hitac ($\alpha = 0^\circ$).
Na slici 7. prikazan je kod za generisanje demonstracije modela kosog hica.

```
Manipulate[
Show[
(* Projekcija *)
ParametricPlot[
{v0*t*Cos[a], y0+v0*t*Sin[a]-0.5*9.81*t^2}, {t, 0, t1},
AxesLabel -> {"x (m)", "y (m)"},
PlotRange -> {{-10, 60}, {-5, 40}},
ImageSize -> 600
],
Graphics[
{
EdgeForm[Black],
(* Platforma *)
LightGray, Rectangle[{-8, 0}, {0, y0}],
(* Početna brzina *)
DarkGreen, Text["v₀", {1.5*0.75*v0*Cos[a], y0+1*0.75*v0*Sin[a]}],
DarkGreen, Arrow[{{0, y0}, {0.75*v0*Cos[a], y0+0.75*v0*Sin[a]}],
(* Točak *)
{PointSize[Large], Red, Point[{v0*t*Cos[a], y0+v0*t*Sin[a]-0.5*9.81*t^2}]}
}
],
{{v0, 12, "Početna brzina v₀ (m/s)", 0.001, 15, Appearance -> "Labeled"},
{{y0, 20, "Početna visina y₀ (m)", 0, 25, Appearance -> "Labeled"},
{{a, 30, "Elevacioni ugao α (°)", -90, 90, 1, Appearance -> "Labeled"},
Style["Pokreni animaciju", Bold],
{{t, 0.001, ""}, 0.001, 5,
Trigger, AnimationRate -> 1, Appearance -> "Labeled"}
],
]
```

Slika 7. Kod za generisanje demonstracije modela kosog hica

ZAKLJUČAK

U radu su pokazane mogućnosti primene programskog paketa *Mathematica*[®] u modeliranju konkretnih fizičkih procesa bez velikog programerskog znanja. Programski paket *Mathematica*[®] može da reši veliki broj klasičnih problema i omogućava prikaz dobijenih rezultata na lako razumljiv i prihvatljiv način putem vizuelizacije obrađenih primera, doprinoseći pritom lakšoj obradi nastavnog gradiva. Programski paket *Mathematica*[®] mogu koristiti kako početnici, tako i stručnjaci koji se ozbiljno bave naukom.

LITERATURA

- [1] B. Jakupi, T. Kevkić, "Mehanika i termodinamika", Univerzitetu Prištini, Prirodno-matematički fakultet, Kosovska Mitrovica, 2009.
- [2] K. Surla, Đ. Hureg, S. Rapajić, "Mathematica za fizičare i hemičare", Univerzitet u Novom Sadu, Prirodno-matematički fakultet, Novi Sad, 1998.
- [3] M. M. Božinović, V. Stojanović, "Matematičke metode i modeli u ekonomiji preduzeća", Viša ekonomska škola, Leposavić, 2005.
- [4] R. L. Zimmerman, F. I. Olness, "Mathematica for Physics – Second Edition", Addison Wesley, 2002.

Raspodela ambijentalnog doznog ekvivalenta gama zračenja u ruralnim sredinama

Biljana Vučković, Ljiljana Gulan, Tijana Kevkić, Jelena Živković-Radovanović

Univerzitet u Prištini, Prirodno-matematički fakultet, Lole Ribara 29, 38220 Kosovska Mitrovica

Apstrakt. Prirodno pozadinsko zračenje koje se registuje u normalnim uslovima potiče od kosmičkog zračenja prirodnih radionuklida, a zavisi od geologije tla i nadmorske visine mernog mesta, pa je karakteristično za neki prostor. Ono što definiše jačinu zračenja je vrednost ambijentalnog doznog ekvivalenta gama zračenja. Rezultati predstavljeni u ovom radu jedna su od eksperimentalnih vežbi u okviru predmeta Dozimetrija i zaštita od zračenja na odseku za fiziku Prirodno-matematičkog fakulteta. Istraživanja su, uz aktivno učešće studenata, obavljena u ruralnim sredinama tri opštine jugoistočne Srbije na ukupno 27 lokacija: 14 na teritoriji opštine Kruševac, 6 na teritoriji opštine Blace i 7 na teritoriji opštine Kuršumlija. Vrednost ambijentalnog doznog ekvivalenta merena je digitalnim Gajgerovim brojačem RADEX RD1503⁺, i bila je u rasponu od 70 nSv/h do 240 nSv/h.

Ključne reči: ambijentalni dozni ekvivalent zračenja, RADEX RD1503⁺, varijacija.

PRIRODNO POZADINSKO ZRAČENJE

Zračenje radioaktivnih izvora iz nenarušene prirodne okoline naziva se prirodno pozadinsko zračenje i potiče od kosmičkih zraka, prirodnih i antropogenih radionuklida u zemljinoj kori, vazduhu i vodi [1]. Karakteristično je za određenu oblast, i zavisi od geologije terena i nadmorske visine. Prosečna veličina pozadinskog zračenja na godišnjem nivou je 2 mSv/y.

Primarno galaktičko kosmičko zračenje je solane energije i sastoji se od ekstremno visoko energetskih čestica (uglavnom protona) energije do 10^{18} eV. Na kosmičko zračenje otpada 13% ukupnog prirodnog zračenja. U spoljašnjoj atmosferi Zemlje ove visoko energetske čestice učestvuju u protonskim interakcijama sa atomima stvarajući čestice nižih energetske stanja, koje ostaju u višim slojevima atmosfere, kao i sekundarno kosmičko zračenje [2,3]. Usled razrednosti vazduha na većim nadmorskim visinama kosmičko zračenje daje veći doprinos ukupnoj dozi eksternog zračenja, čak i do 25% više nego na nižim visinama [4], a na istoj geografskoj širini. Sa druge strane, promenljivost geografskih širina nema tako izražen uticaj - oko 10% je ukupna doza zračenja niža na geomagnetnom ekvatoru nego na visokim geografskim širinama usled promenljivosti solarnih ciklusa na ovim područjima [1].

Najznačajniji izvori jonizujućeg zračenja su primoradijalni terestrički radionuklidi, čiji se poluživot može uprediti sa starošću Zemlje (10^5 - 10^{16} godina). Prisutni su u svim

Edukacija u korak sa savremenim istraživanjima radona

Ljiljana Gulan¹, Biljana Vučković¹, Tijana Kevkić¹, Branko Drljača¹

¹Univerzitet u Prištini, Prirodno-matematički fakultet, Kosovska Mitrovica

Apstrakt. Sistematska merenja koncentracije radona se najčešće izvode na slučajnim uzorcima stambenih objekata. Međutim, škole se mogu pokazati kao pogodniji izbor, jer su uniformno raspoređene po celoj teritoriji područja ili naselja, na način da se njihova prostorna raspodela može dovesti u vezu sa gustinom naseljenosti, tako da manji broj merenja može dati relevantne podatke. U cilju kontrole i zaštite dece i odraslih sprovedena istraživanja izlaganja populacije radonu u školama u većini evropskih zemalja, i u Srbiji, predstavljaju važnu komponentu nacionalnih programa za radon. U ovom radu merenje radona je sprovedeno krajem maja i početkom juna 2018. godine, uz učešće učenika osnovnih škola u Orahovcu i Velikoj Hoći, u području Metohije, s ciljem da informiše učenike o radonu, njegovoj štetnosti po zdravlje, i da ih motiviše na diskusiju i zaključke.

Ključne reči: radon, merenje, škole.

RADON

Radon je radiaktivni gas koji dospeva u zatvorene prostorije direktno iz zemlje kroz pore i šupljine u zemljištu i građevinskom materijalu korišćenom u izgradnji objekata. Radon može dospeti u zatvorene prostorije putem vode. Na mestu ulaska, koncentracija radona se povećava u odnosu na ostale delove prostorije. U njima je stalno prisutan niži pritisak, pa na akumulaciju i povećanje koncentracije radona utiču: njegova emanacija iz zemljišta i građevinskog materijala (zidova i podova), poroznost sredine kroz koju difunduje i ventilacija prostorija, kao i meteorološki parametri: atmosferski pritisak, temperatura, strujanje vazduha, itd.

Na osnovu sistematskih istraživanja sprovedenih u svetu došlo se do sledećih zaključaka: najveća koncentracija radona je u podzemnim spratovima zgrada, podrumima i garažama zbog direktne veze sa zemljom, i slabe ventilacije. U prizemlju je manja koncentracija nego u podrumu, a na prvom spratu je još manja. Raspodela koncentracije radona je uniformna po zapremini i približno ujednačena u prostorijama na istom spratu objekta. Intenzivna ventilacija je efikasan način da se eliminiše radon iz zatvorenih prostorija, npr. otvaranjem prozora i vrata.

Radon je najznačajniji radijacioni kontaminant u prirodi. Prema oceni Naučnog komiteta Ujedinjenih Nacija za efekte atomskog zračenja više od $\frac{1}{2}$ ukupne doze od prirodnih izvora zračenja potiče od inhalacije radona i njegovih potomaka [1]. Kada se nekontrolisano nakuplja u boravišnim prostorijama može predstavljati značajan zdravstveni rizik, jer udisanjem radona, i njegovim raspadom nastaju radioaktivni potomci – metalni atomi polonijuma, olova i bizmuta, koji se talože u plućima.

Promene na ćelijskom i molekularnom nivou koje su izazvane jonizujućim zračenjem znatno su izražene u ranom životnom dobu zbog formiranja i rasta tkiva i organa. Zato je potrebno obratiti posebnu pažnju na predškolske i školske ustanove. Efektivna ekvivalentna doza je veća kod dece nego kod odraslih, kod šestogodišnjeg deteta je oko 2,5 puta veća nego kod odraslog tridesetogodišnjeg čoveka. U proseku starosna grupa do deset godina prima efektivnu ekvivalentnu dozu 1,5 - 2 puta veću nego odrasli. S tim u vezi u našoj zemlji su izvršena sistematska merenja radona u školama i vrtićima [2].

MERENJA RADONA U ŠKOLAMA

U periodu od 2008. do 2012. godine sprovedeno je merenje radona čvrstim detektorima u školama u nekoliko okruga Južne Srbije (Jablanički okrug, Pčinjski okrug i Zaječarski okrug). Za 320 vrednosti godišnjih koncentracija radona u prizemnim prostorijama osnovnih škola aritmetička sredina je iznosila 121 Bq/m³ [3].

Laboratorija za ispitivanje radioaktivnosti Instituta za medicinu rada Srbije „Dr Dragomir Karajović“ izvršila je merenja koncentracije radona (2010. godine) u 112 škola i 78 vrtića na teritoriji Beograda (oko 50% od ukupnog broja škola i vrtića sa šireg područja glavnog grada). Prosečna koncentracija radona u školama i vrtićima je bila 171 Bq/m³, minimalna vrednost je 8 Bq/m³ (škola u opštini Rakovica), a maksimalna vrednost je 3382 Bq/m³ (škola u opštini Zvezdara - mala podrumaska prostorija bez ventilacije) [4].

U Kragujevcu je sprovedeno merenje koncentracije radona u 22 osnovne škole i 9 srednjih škola od novembra 2013. do februara 2014. godine. Odabrane su prostorije najniže spratnosti u kojima boravi nastavno osoblje. Izmerene koncentracije radona su se kretale u opsegu od 25-86 Bq/m³ [5].

Nacionalna kampanja merenja koncentracije radona bila je aktuelna od oktobra 2015. do aprila 2016. godine, kada je širom Srbije u različitim objektima raspoređeno 6000 detektora za merenje radona, u cilju kreiranja mape rizika od radona za našu zemlju [6].

Cilj ovog rada je bio da se merenjem utvrde nivoi koncentracije radona u školama u Orahovcu i Velikoj Hoči. Na taj način se može proceniti rizik i izvršiti kontrola izlaganja najmlađe i najosetljivije populacije. S druge strane, u okviru nastavnog časa fizike učenici su bili informisani o radioaktivnom gasu radonu i njegovoj štetnosti po zdravlje. Takođe, učenicima je omogućeno učešće u merenju na veoma jednostavan način, što ih je dodatno motivisalo na izvođenje samostalnih zaključaka.

Metod merenja

Za preliminarna merenja koncentracije radona u osnovnim školama Orahovca i Velike Hoče korišćen je detektor Airthings Corentium Home, trenutno najsavremeniji na tržištu i najprikladniji za merenja, koji u kraćem vremenskom intervalu (od jednog dana pa do nedelju i mesec dana) može dati veoma precizne podatke o prosečnoj koncentraciji radona u boravišnim prostorijama. To je digitalna verzija detektora zasnovana na alfa spektrometrijskom metodu. Tačnost merenja je u okviru ±5% od rezultata referentnih monitora, a preciznost u okviru intervala od ±20% od srednje vrednosti.

Detektori radona su ostavljeni po 7 dana u po dve prostorije svake škole; merenje je započeto u petak, a očitavanja radona su vršena od ponedeljka do petka sledeće sedmice, kada su preuzimani uređaji i stavljeni u drugu školu. Detektori su postavljeni na ormarima

(1,5-2 m visine) na udaljenosti od zidova oko 20 cm ili više, i na udaljenosti od najmanje 1,5 m od najbližeg prozora ili vrata u prostoriji. Učenici su aktivno učestvovali u očitavanju detektora: prve vrednosti merenja koncentracije radona beležene su nakon 72 časa, od ponedeljka do petka, svakog dana u isto vreme.

Rezultati merenja i diskusija

Rezultati merenja koncentracije radona u dve osnovne škole u Orahovcu i Velikoj Hoči dati su u tabelama 1 i 2. Merenja koncentracije radona imaju dve vrednosti koje pokazuje detektor: *long term* merenje je rezultat dugoročnog merenja u kome detektor usrednjuje vrednost svakog dana za trajanje merenja od 7 dana. *Short term* merenje je rezultat kratkoročnog merenja u kome detektor svakodnevno (svakih 24 časa) usrednjuje vrednost radona.

Tabela 1. Merenje koncentracije radona - Osnovna škola Orahovac

	Koncentracija radona (Bq/m ³)			
	Prva prostorija-učionica		Druga prostorija-kancelarija	
	Long term	Short term	Long term	Short term
1.	-	-	-	-
2.	-	-	-	-
3.	8	7	44	49
4.	7	10	43	14
5.	8	9	37	25
6.	9	11	31	13
7.	9	16	31	29

U osnovnoj školi u Orahovcu (Tabela 1) merenja su vršena u dve prostorije od kojih se ispod jedne nalazi dosta visoka podrumaska prostorija, a druga je prizemna. U prvoj prostoriji borave deca, a druga prostorija (bez podruma) je kancelarija. Izmerene srednje koncentracije radona za sedam dana su bile: 9 Bq/m³ u prvoj prostoriji i 31 Bq/m³ u drugoj prostoriji.

Tabela 2. Merenje koncentracije radona - Osnovna škola Velika Hoča

	Koncentracija radona (Bq/m ³)			
	Prva prostorija-hodnik		Druga prostorija-učionica	
	Long term	Short term	Long term	Short term
1.	-	-	-	-
2.	-	-	-	-
3.	55	52	287	246
4.	56	39	299	225
5.	54	59	298	315
6.	58	22	315	27
7.	44	7	235	8

U osnovnoj školi u Velikoj Hoči merenja su vršena u hodniku i u učionici, u kojoj se pre postavljanja detektora nije duže boravilo i nije bila provetravana. Takođe u prvim danima merenja prostorija je slabo provetravana. Objekat je starije gradnje, građen je od

cigle, ima betonsku ploču. Srednje sedmodnevne koncentracije radona su bile: 44 Bq/m^3 u prvoj prostoriji (hodnik) i 235 Bq/m^3 u drugoj prostoriji. Ovo je očekivano, jer položaj prve prostorije ne dozvoljava znatno akumuliranje radona.

Prvi dan merenja izmerena je najveća koncentracija radona (Tabela 2). Kada su prozori delimično otvoreni i tako ostavljeni i preko noći, posle toga, tj. poslednja dva dana merenja koncentracija radona se veoma smanjila.

Ovaj slučaj ukazuje na veliki značaj čestog provetranja boravišnih prostorija i veliku razliku u koncentraciji radona u slučajevima kada prostorije nisu provetravane i kada se provetravaju. Preporučena je obavezna mera ventilacije prostorija u školi pre ulaska učenika kao i često provetranje učionica.

ZAKLJUČAK

U ovom radu predstavljena su savremena istraživanja koncentracije radona koja se sprovede u svetu, a lako se mogu primeniti u edukaciji učenika osnovnih škola, demonstriranjem jednostavnog procesa merenja radona. Ovde je iskazana potreba da se kvalitetnoj nastavi doprinosi kontinuiranim radom, informisanjem i motivacijom. Ako se na adekvatan i pristupačan način predstave savremena istraživanja u različitim oblastima fizike učenici se mogu značajno stimulisati na dodatna saznanja.

ZAHVALNICA

Ovaj rad je urađen u okviru projekta III41028 Ministarstva prosvete, nauke i tehnološkog razvoja Republike Srbije i projekta IJ01-17 Prirodno-matematičkog fakulteta Univerziteta u Prištini. Autori su zahvalni Tatjani Šarić, master fizičaru za obavljena merenja.

LITERATURA

- [1] UNSCEAR, United Nations Scientific Committee on the Effects of Atomic Radiation, Sources and effects of ionizing radiation. Annex B: Exposure of the public and workers from various sources of radiation. UNSCEAR, 2008. United Nations, New York, 2010.
- [2] Lj. Gulan, "Radon i toron u vazduhu zatvorenih prostorija Kosova i Metohije," Akademska misao, Beograd, 2015.
- [3] Z.S. Žunić, P. Bosew, F. Bochicchio, N. Veselinović, "The relation between radon in schools and in dwellings: A case study in a rural region of Southern Serbia," Journal of Environmental Radioactivity vol. 167 pp.188-200, 2017.
- [4] V. Arsić, J. Ilić, S. Bogojević i I. Tanasković, "Pregled merenja koncentracije radona Instituta za medicinu rada Srbije "Dr Dragomir Karajović", XXVIII Simpozijum DZZSCG, Zbornik radova pp.186-192, Vršac 30.09.-02.10.2015.
- [5] J.M. Stajic, B. Milenkovic, D. Nikezic, "Radon concentrations in schools and kindergartens in Kragujevac city, Central Serbia," CLEAN – Soil, Air, Water vol. 43, pp.1361-1365, 2015.
- [6] V. Udovičić, D. Maletić, M. Eremitić Savković, G. Pantelić, P. Ujčić, I. Čeliković, S. Forkapić, D. Nikezić, V. Marković, V. Arsić, J. Ilić, P. Nilsson, "Preliminary results of the first national indoor radon survey in Serbia," In: Book of Abstracts of 8th Conference of Protection against Radon at Home and at Work, September 12-14, Prague, Czech Republic, 2016.

Education in step with contemporary radon research

Ljiljana Gulan, Biljana Vučković, Tijana Kevkić, Branko Drljača

Abstract: The systematic measurements of radon concentrations are most often performed on random samples of residential buildings. However, schools may prove a more convenient choice because they are uniformly distributed throughout the territory of the area or settlement, in such a way that their spatial distribution can be linked to the density of population. So, a smaller number of measurements can provide relevant data. For the purpose of controlling and protecting children and adults, the investigations of population exposure to radon in schools carried out in most European countries, and in Serbia, are an important component of national radon programs. In this paper, measurements of radon were carried out in late May and early June 2018, with the participation of primary school pupils in Orahovac and Velika Hoča, in the Metohija area, with the goal of informing pupils about radon, its harmfulness to health, and motivating them for discussion and conclusions.

Distribution of Ambient Dose Equivalent of Gamma Rate in Rural Areas

Biljana Vučković, Ljiljana Gulan, Tijana Kevkić, Jelena Živković-Radovanović

Abstract: Natural background radiation that can register in regular conditions comes from cosmic radiation, and natural radionuclides, and it depends on the geology of soil and altitude measuring point. Based on that we can say that it is typical for the measuring location. Level of radiation defines the value of the ambient dose equivalent of gamma radiation. The results presented in this paper are one of the experimental exercises within the subject of Dosimetry and Radiation Protection at the Department of Physics at the Faculty of Science and Mathematics. In addition to the active participation of students, the research carried out in rural areas of the three municipalities of southeastern Serbia on 27 locations: 14 in the territory of the municipality of Kruševac, 6 in the territory of the municipality of Blace and 7 in the territory of the municipality of Kuršumljija. The value of ambient dosage equivalent was measured by digital Gaigerian counter RADEX RD1503⁺, ranging from 70 nSv/h to 240 nSv/h.

Research of UV radiation intensity in relation with outdoor measurement conditions

Tijana Kevkić, Biljana Vučković, Ljiljana Gulan, Branko Drljača

*Faculty of Sciences and Mathematics, Lole Ribara 29, 38220, University of
Kosovska Mitrovica, Serbia*

Abstract. This paper presents the results of measurements of ultraviolet radiation in Kuršumljija - Blace on July the 15th 2018, and in Kruševac - Trstenik on July the 16th 2018. The measurements were carried out by using a professional high-quality instrument YK-35UV, from 9 AM to 15:30 PM. The obtained results are grouped in two series, labeled as series A and B, and their statistical analysis have been made by introducing some corresponding statistical tests. From the results, it has become clear that the main part of UVR reaching the Earth's surface were related to UVA band. Moreover, as the intensity of the UVR during summer day increases along with temperature of the air, a method of UV health risk reduction should be devised.

Keywords: UV radiation, temperature, light meter model YK-35UV, measurement, statistical analysis.

INTRODUCTION

Excessive exposure to solar ultraviolet radiation (UVR) can cause painful sunburns, premature ageing of the skin as well as the increased risk of developing skin cancers and cataracts [1]. In addition to the effects on human beings, the UVR also may bring various biological effects on ecosystems, plants and animals. Moreover, the absorption of UVR radiation is the main reason for the increase of air temperature in the stratosphere. On the other hand, moderate exposure to solar UVR has significant psychological and physical benefits, mainly related to vitamin D synthesis and prevention of certain diseases [2].

Within the spectrum of solar radiation, UVR is a form of electromagnetic wave with wavelength ranging from 100 nm to 400 nm and can be classified into three bands: UV-A (315 – 400 nm), UV-B (280 – 315 nm) and UV-C (100 – 280 nm). As sunlight passes through the atmosphere, all UV-C is absorbed by ozone, oxygen and water vapor in the high stratosphere, so this potentially the most dangerous UVR band, does not reach the Earth's surface. Unlike that, the UV-B reaching the Earth's surface in very small quantities, making about 5% of UV component of terrestrial radiation from the sun. The main part of UV-B is disappearing in the ozone layer, i.e. the region of stratosphere which is located at around 30 km in altitude. Finally, UV-A absorption by the gases present in the atmosphere is negligible, hence UV-A presents about 95% of UVR which reach to the Earth's surface. Beside the absorption and scattering UVR by air molecules, aerosol and

dust particles, climate change also influence surface UVR through changes induced mainly to clouds and the ability of the Earth's surface to reflect light [3].

To study the effects of solar URV there is a need to quantify variations of solar energy received on the Earth's surface at different intervals. We have used a professional high-quality instrument YK-35UV for measuring the UVR on some different locations in Serbia. This accurate device is designed to measure UV-A and UV-B radiation, and operates on wavelength of 290 to 390 nm. Simultaneously, we have measured temperature and recorded altitudes and latitudes of the chosen locations. In addition, we have followed the presence of the clouds in the sky in the moments of measuring. As a consequence of the fact that amount of absorber of UVR is reducing with increasing altitude, it has been observed the increasing intensity of UVR for 6 – 8% in every 1000 m of altitude. Since the measurements of UVR and temperature were made in different moments of time and different spatial locations, it has become clear that application of various statistical techniques and methods are need for comparative analysis of the obtained results.

UVR MEASUREMENT WITH YK-35UV LIGHT METER

The YK-35UV light meter is UV-A and UV-B radiation meter with external, exclusive UV photo sensor with the cosine correction filter (Fig. 1). It works in two ranges: 2 mW/cm^2 or 20 mW/cm^2 , and has microprocessor circuit which provides high reliability and durability. Its operating temperature is from 0 to 50°C while operating humidity is less than 85% R.H. Separate UV LIGHT probe allows user to measure the UV light at an optimum position. The results of measurement can be easily read for approximately 1 second, on LCD display.



Figure 1, Instrument YK-35UV

Calibration is executed under the UVA and compare with the standard UVA light meter. It is special tested under the environment RF field and shows strength less than 3 V/m and frequency less than 30 MHz only. The device has five buttons: power, hold, REC, range and zero, respectively. After power on by pushing the power button follows the range selection by pushing 2 mW/cm^2 or 20 mW/cm^2 button. After that is need use the hand to hold the UV probe handle and face the UV sensor to measuring UV light opposite. Then the display will show the light values exactly.

The measurements are more effective if the intensity of the sun's radiation is higher, and are affected by: sun position in the sky, altitude, cloudiness, the presence of aerosols and gases in the atmosphere which can absorb solar radiation on the same wavelengths [4].

METHODS AND RESEARCH PROCEDURES FOR THE MEASUREMENT RESULTS

This part is dedicated to researching the correlation structure between results of measurements of UVR, as well as temperature. For that purpose, observed data are grouped in two series:

- **Series A:** Measurements were carried out in locations of Kuršumljia and Blace, on July 15th 2018, in period from 9:10h until 15:30h.
- **Series B:** Measurements were carried out in locations of Kruševac and Trstenik, on July 16th 2018, in period from 9:40h until 15:00h.

Figure 2 shows the diagrams power UV radiation changes depending on the time, for both of these series. Since measurements were made in different time periods during the day, as well as at different locations, it is clear that a comparative analysis of the obtained results requires the application of various statistical techniques and methods.

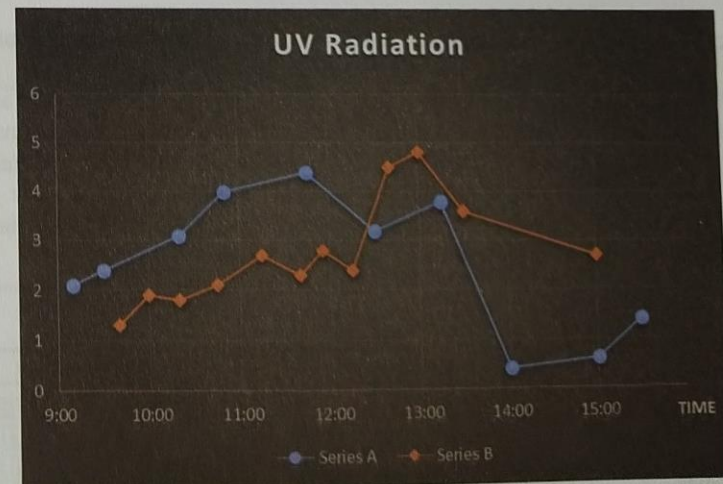


Figure 2. Comparison of the dynamics of changes for the UV radiation intensity.

In the moments of UVR measuring, simultaneously have been recorded the values of the temperature of the air. Figure 3 shows the diagram of temperature change over time for both considered series. At first glance, the different dynamics can be seen in increasing the temperature values. This is obvious consequence of the fact that the measurements were made in two different days, as well as in different, remote spatial locations. In addition, we point out that the altitudes of individual locations of measurement significantly differ from each other. In the case of Series A, the altitude ranges from 350 m to 532 m, while in Series B it is significantly lower (135 m – 230 m above sea level).

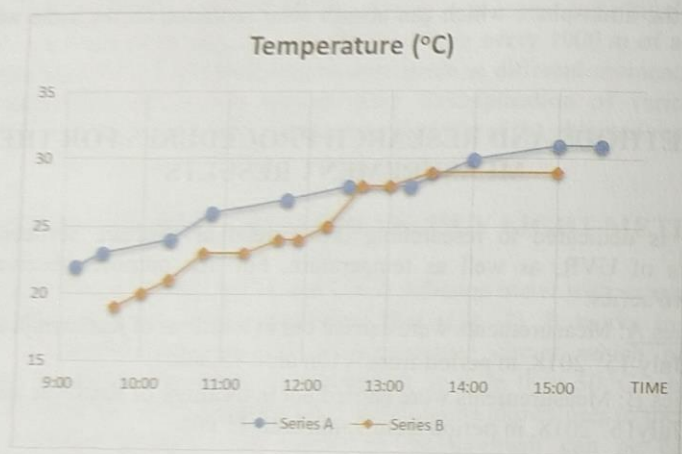


Figure 3. Comparison of the dynamics of temperature changes.

STATISTICAL ANALYSIS OF THE MEASUREMENT RESULTS

Statistical analysis of the obtained measurement results has been presented in following. The main purpose of this analysis, as already was mentioned, is formal verification of the (potential) similarity or difference in changes in the UVR at different locations, as well as in different weather, climate and geographical conditions. Table 1 shows the summary descriptive statistics of the UV measurements, and temperature values, for both Series A and B. In further analysis, a particular emphasis is put on comparing the two basic measures of central tendency: mean values and median, as well as variance, as a measure of the variability (dispersion) of the observed data.

Table 1. Summary descriptive statistics of observed measurement results.

Statistics	UV Radiation		Temperature	
	Series A	Series B	Series A	Series B
Mean	2.54	2.7417	27	24.4167
Stand. Error (SE)	0.4445	0.3073	1.0220	1.0035
Median	2.75	2.55	27.5	24
Stand. Deviation	1.4057	1.0647	3.2318	3.4761
Variance	1.9760	1.1336	10.444	12.0833
Rang	4	3.5	9	10

Further, in Table 2 are presented the results of testing equality of variance and mean values in series A and B, at the same significantly level which is equals 0.05. The presented results are obtained by introducing three statistical testing of different kind:

(i). Fisher's (F) test is a statistical test based on the initial (i.e. „null“) hypothesis which assumes that two normal populations have the same variance. In the other words, test statistics is the ratio of two sample variances [5]. As it is well-known, variance represents the measure of dispersion, or how far the data are scattered from the mean. That is why the larger values of variance indicates to greater dispersion of observed data. In our research, the results obtained by using F -test indicates that there is no significant difference between the variances of the Series A and B, both for UVR and for temperature values. Therefore, the variability of these series can be regarded as equal.

(ii). Student's (t) test compares the mean values of two data series, and shows to significance of their differences. This test is usually use on “small” samples, as is the case here, and gives a decision of accepting or rejecting the hypothesis of the mean values equality[6]. According to the results obtained by the previous F -test, the t -test which assumes the equality of the variances of both series was used. For the UVR, results obtained by using t -test, indicate no significant difference between the means of the Series A and B. Thus, the intensity of UVR of both samples can be considered as statistically identical. On the other hand, there is statistically significant means difference in temperatures (p -value is 0.0442, i.e. it is less than significantly level of 0.05).

(iii). Almost identical conclusions can be drawn from the results obtained by Mann-Whitney (U) test, which represents the non-parametric alternative to the aforementioned Student's t -test. The null hypothesis assumes that the medians of two data series (A and B) are equal, and computation of the test statistic is based on the ranks of the data [7]. In the case of UVR intensity it is confirmed again that there is no statistically significant difference in the distributions of observed Series A and B, i.e. they are equal in statistical sense. On the other hand, at the significance level of 0.05, there is a statistically significant difference in the temperature values of Series A and B.

Table 2. Test statistics and p -values of observed data.

Tests	UV Radiation	Temperature
Fisher F-test (p -values)	1.7432 (0.1904)	0.8644 (0.4201)
Student t-test (p -values)	-0.3829 (0.7058)	1.7912 (0.0442)*
Man-Whitney test (p -values)	-0.1000 (0.4602)	1.6800 (0.0465)*

CONCLUSION

The results of UVR measurements in different locations in Serbia by using YK-35UV light meter are presented in this paper. Simultaneously, the temperatures of the air, altitudes and latitudes of chosen locations have been recorded because they are the parameters which can affect the results significantly. The results of measurement were grouped in two series and subjected to statistical analysis. The usage of three appropriate

statistical tests show that the intensities of UVR in both series are not statistically different despite the differences in the measurement conditions, first of all the significant differences between the temperature values of these two series.

ACKNOWLEDGEMENTS

This work was done within the project IJ01-17 of the Faculty of Natural Sciences and Mathematics, University of Priština.

REFERENCES

- [1] Diffey, B.L. Solar ultraviolet radiation effects on biological systems. *Phys. Med. Biol.* **1991**, 36, pp. 299–328.
- [2] S. Seo Park, Y. Gon Lee, and J. Hyun Kim, „Impact of UV-A Radiation on Erythral UV and UV-index Estimation over Korea,” *Advances in atmospheric sciences*, vol. 32, pp.1639–1646, December **2015**.
- [3] International Commission on Non-Ionizing Radiation Protection. Guidelines on limits of exposure to ultraviolet radiation of wavelengths between 180 nm and 400 nm. *Health Phys.* **2004**, 87, 171–186.
- [4] World Health Organization, Global Solar UV index. A Practical Guide. World Health Organization, WHO/SDE/OEH/02.2, Geneva, Switzerland, **2002**, 28 pp.
- [5] Markowski, C. A. & Markowski, E. P. Conditions for the Effectiveness of a Preliminary Test of Variance. *The American Statistician.* **1990**, 44:4, pp.322–326.
- [6] B. Hazewinkel, M., ed. *Student test*, in: Encyclopedia of Mathematics. Springer, **2001**.
- [7] Lehmann, E. L. *Nonparametrics: Statistical methods based on ranks*. New York: Springer, **2006**.

Istraživanje zavisnosti intenziteta UV zračenja od spoljašnjih uslova merenja

Tijana Kevkić, Biljana Vučković, Ljiljana Gulan, Branko Drljača

Apstrakt. U radu su prikazani rezultati merenja intenziteta ultraljubičastog zračenja u Kuršumlji i Blacu 15. 07. 2018. godine i Kruševcu - Trsteniku 16. 07. 2018. godine. Merenja su vršena profesionalnim visokokvalitetnim YK-35UV instrumentom u periodu od 9h do 15:30h. Dobijeni rezultati su svrstani u dve serije, označene kao serija A i B, a njihova statistička analiza je sprovedena uvođenjem odgovarajućih statističkih testova. Rezultati merenja jasno pokazuju da glavni deo UV zračenja koji dostiže do površine Zemlje čini UV-A komponenta. Pored toga, uočeni porast intenziteta UV zračenja i temperature vazduha tokom letnjeg dana ukazuju na neophodnost primena metoda za smanjenje rizika od UV zračenja.



**ТРЕТА МЕЃУНАРОДНА КОНФЕРЕНЦИЈА
ЗА ОБРАЗОВАНИЕ
ПО МАТЕМАТИКА, ФИЗИКА И СРОДНИ НАУКИ**

ЗБОРНИК НА ТРУДОВИ

Природно-математички факултет

Скопје 6-8 мај, 2022



Зборник на трудови

**Трета меѓународна конференција за
образованието по математика,
физика и сродни науки**

Природно-математички факултет, Скопје

6 – 8 мај, 2022

Зборник на трудови
Трета меѓународна конференција за образованието по математика,
физика и сродни науки

Издавачи:

Сојуз на математичари на Македонија
Природно-математички факултет, Скопје

Уредници:

Ѓорѓи Маркоски
Ламбе Барандовски
Анета Гацовска – Барандовска

Редакциски одбор:

Александар Скепаровски
Ѓорѓи Маркоски
Ламбе Барандовски
Даница Крстовска
Ирена Стојковска
Анета Гацовска – Барандовска
Оливер Зајков
Боце Митревски
Марина Стојановска
Јасмина Марковска
Валентина Гоговска
Валентина Миовска

CIP - Каталогизација во публикација
Национална и универзитетска библиотека "Св. Климент Охридски", Скопје

37.012/.013:5(062)

МЕЃУНАРОДНА конференција за образованието по математика, физика и сродни науки
(3 ; 2023 ; Скопје)

Зборник на трудови : трета меѓународна конференција за образованието по математика,
физика и сродни науки, Скопје, 6 – 8 мај, 2022 /
[уредници Ѓорѓи Маркоски, Ламбе Барандовски, Анета Гацовска – Барандовска]. - Скопје :
Сојуз на математичари на Македонија, 2023. - 376 стр. : илустр. ; 25 см

Дел од трудовите и на други јазици. - Фусноти кон текстот. - Библиографија кон трудовите

ISBN 978-608-4929-04-8

а) Образование -- Настава -- Природни науки -- Математика -- Собири

COBISS.MK-ID 59184901

© 2023 CMM

Сите права се задржани. Ниту еден дел од оваа книга не смее да се препечатува или пренесуван во
каква било форма или со какви било средства, електронски или механички, вклучувајќи и
фотокопирање, документирање или да биде зачуван во систем за повторно пронаоѓање без
писмена согласност од издавачот.

Печати: Печатница MAP-CAЖ, Скопје

Тираж: 220

Зборник на трудови

Трета меѓународна конференција за образованието по математика, физика и сродни науки

во организација на

Природно – математички факултет во Скопје (ПМФ)
Сојуз на математичарите на Македонија (СММ)
Друштво на физичарите на Република Македонија (ДФРМ)

Организациски одбор

Ѓорѓи Маркоски
Ламбе Барандовски
Александар Скепаровски
Ирена Стојковска
Даница Крстовска
Анета Гацовска-Барандовска
Валентина Миовска
Милена Мицковска
Фадил Ајредини
Весна Манчевска
Ерблина Зеќири
Катерина Русевска

Поканети предавачи

Петар Кендеров, Бугарија
Дончо Димовски, Македонија
Александар Липковски, Србија
Мира Вучељиќ, Црна Гора
Саша Ивковиќ, Србија
Бенјамин Фетиќ, Босна и Херцеговина
Оливер Зајков, Македонија
Евгенија Сендова, Бугарија
Љубиша Нешиќ, Србија
Јасмина Милинковиќ, Србија
Зоран Михајловски, Македонија
Тони Чехларова, Бугарија

Програмски одбор

Дончо Димовски, Македонија
Петар Кендеров, Бугарија
Мичо Митровиќ, Србија
Јасмина Милинковиќ, Србија
Боце Митревски, Македонија
Ристо Атанасов, САД
Крешо Задро, Хрватска
Бенјамин Фетиќ, Босна и Херцеговина
Слаѓана Јакимовиќ, Македонија
Небојша Икодиновиќ, Србија
Тони Чехларова, Бугарија
Валентина Гоговска, Македонија
Евгенија Сендова, Бугарија
Барбара Ровшек, Словенија
Весна Целакоска - Јорданова, Македонија
Мира Вучељиќ, Црна Гора
Драгица Д. Тривиќ, Србија
Марина Стојановска, Македонија

Благодарност

Сојузот на математичарите на Македонија и Друштвото на физичарите на Република Македонија, ја изразуваат својата благодарност на Институтот за математика и Институтот за физика при Природно – математичкиот факултет во Скопје за успешната коорганизација на Третата меѓународна конференција за образованието по математика, физика и сродни науки.

Посебна благодарност изразуваме до Министерството за образование и наука кои го потпомогнаа издавањето на вој Зборник на трудови.

Организаторите на КОМФСН 2022 најискрено се заблагодаруваат на Генералниот поддржувач на конференцијата, проектот „Разновидноста во природните науки низ социјална инклузија – неформално образование по природни науки и ученичка разноликост“ и неговиот раководител проф. д-р Марина Стојановска, вонреден професор на Институтот за хемија, при Природно-математичкиот факултет во Скопје. Благодарение на проектот учесниците на конференцијата имаа можност да учествуваат во специјализирани работилници од областа на природните науки.



СОДРЖИНА

1.	Benjamin Fetic , <i>Quantum tunneling and ultrafast phenomena</i>	11
2.	Jasmina Milinković , <i>Visualization as a Primary Means or a Backup Teaching Aid</i>	17
3.	Дончо Димовски, Јасмина Маркоска, Анета Гацовска-Барандовска, Ѓорѓи Маркоски , <i>Математички јазик</i>	24
4.	Toni Chehlarova , <i>Redefining in-service teacher education for work in a STEM center</i>	32
5.	Евгенија Сендова , <i>Истражувачи-наставници-ученици: (една вечна STEAM плетенка во програмска средина)</i>	38
6.	Љубиша Нешић, Дарко Радованчевић , <i>Општа и Специјална теорија релативности у школи</i>	48
7.	Оливер Зајков, Соња Геговска-Зајкова , <i>Сто и една приказна</i>	54
8.	Erblina Zeqiri, Stevo Gjorgiev, Irena Stojkovska , <i>Statistical Literacy of Undergraduate Students Before Taking the Introductory Statistics Course</i>	62
9.	Dragana Valjarević, Bojana Stojčetović, Milena Petrović, Novica Zlatanović and Milica Ivanović , <i>Pupil's perspective of distance learning during the COVID-19 pandemic in primary school</i>	71
10.	Filip Nikolovski, Irena Stojkovska , <i>Teaching probability using computer-based simulations</i>	79
11.	Делчо Лешковски, Анета Гацовска-Барандовска , <i>Потребата од изучување веројатност и статистика во средното гимназиско образование, како подготовка за универзитетските предмети</i>	87
12.	Josip Slisko , <i>Water-filled balloon that jumps in free fall: A Predict – Observe - Explain learning sequence on weightlessness</i>	93
13.	Бобан Ђокић, Миљана Милентијевић, Бранко Дрљача , <i>Софтверски пакет као интерактивни алат у настави физике</i>	101
14.	Љубчо Јованов, Драган Радивојевић, Катерина Дрогрешка , <i>CD и DVD дискови – подостапна замена за дифракциона решетка во демонстрациите од физичка оптика</i>	109
15.	Ирена Златановска, Илија Јованов, Гоце Гегоски, Ламбе Барандовски , <i>Изучување на распаѓањето на пената кај пивото</i>	115
16.	Мирослав Петроски, Ѓоко Атанасовски , <i>Определување дијаметар на тенка жица со помош на ласер</i>	124
17.	Стојан Манолев , <i>Термоелектричните ефекти, физички основи и нивната примена во наставата по физика</i>	132
18.	Никола Делевски , <i>Учење физика преку практична активност – Интерференција на тенок слој од сапун</i>	136

19.	Делчо Лешковски, Валентина Миовска , <i>Геометриски докази на адиционите теореми и на идентитетите за трансформирање на збир на тригонометриски функции</i>	141
20.	Eugen Ljajko , <i>Do we find at schools what we were prepared for at universities?</i>	153
21.	Петар Соколки , <i>Искусства од наставата по предметот Геометрија во МИГ – Скопје</i>	158
22.	Зоран Трифунов , <i>Примена на интерактивни аплети во решавање на задачи со определен интеграл</i>	168
23.	Абдула Букла, Бесник Исмаили , <i>Примена на Геогебра во апроксимативно решавање на проблеми од планиметрија</i>	176
24.	Бети Ламева, Јасмина Маркоска , <i>Улогата на меѓународните тестирања во македонското математичко образование-предизвици и заклучоци</i>	183
25.	Бети Ламева, Јасмина Маркоска, Елизабета Наумовска , <i>Улогата на меѓународните тестирања во македонското образование по природни науки-предизвици и заклучоци</i>	195
26.	Виктор Урумов , <i>Македонски публикации во областа на образованието</i>	204
27.	Марина Стојановска, Катерина Русевска, Ламбе Барандовски, Владимир М. Петрушевски , <i>Природните науки низ игра: Escape room како дел од DiSSI активностите</i>	210
28.	Владимир Петрушевски, Катерина Русевска, Ламбе Барандовски, Марина Стојановска , <i>Примена на 5E методот во наставата по природни науки: DiSSI активности за гасови</i>	217
29.	Катерина Русевска, Ламбе Барандовски, Владимир Петрушевски, Славица Тофиловска, Марина Стојановска , <i>Примена на 5E методот во наставата по природни науки: DiSSI активности за екологија</i>	224
30.	Ламбе Барандовски, Катерина Русевска, Владимир Петрушевски, Марина Стојановска , <i>Примена на 5E методот во наставата по природни науки: DiSSI активности за струјни кола</i>	229
31.	Катерина Дрогрешка, Љубчо Јованов, Драган Радивојевиќ , <i>Земјотресот во процесот на образовната технологија</i>	234
32.	Јасмина Најдовска, Моника Андрееска, Ивана Молеровиќ , <i>Сеизмолошката опсерваторија како дел од образованието</i>	238
33.	Боце Митревски, Гордана Станојевиќ, Вера Зороска , <i>Споредба на знаењето и концептуалното разбирање меѓу основци од Македонија и Србија</i>	244
34.	Валентина Миовска, Анета Гацовска-Барандовска, Делчо Лешковски, Стефан Мирчевски , <i>Најчести грешки и математички заблуди кај студентите од прва година на техничките факултети во средношколски задачи</i>	252
35.	Снежана Ристовска, Лидија Кондинска, Даниела Тачевска Николов , <i>Влијанието на наставната стратегија превртена училница на постигнувањата на ученици во време на пандемијата од COVID – 19</i>	260
36.	Петар Соколки, Слаѓан Станковиќ , <i>Математичко-информатичка гимназија - ново средно училиште и нова надеж за математичкото образование во Македонија</i>	270

37. **Јасмина Ангелевска Костадиноска, Соња Геговска-Зајкова, Катерина Хаџи-Велкова Санева**, *Влијанието на онлајн наставата и начинот на полагање на испитите врз успешноста на студентите* 280
38. **Југослав Ачкоски, Невена Серафимова, Кристијан Илиевски, Анер Бехлиќ**, *Управувач на фази логика за предвидување на резултатите во онлајн наставата* 287
39. **Методија Јанчески, Анкица Спасова, Викторија Илиеска**, *Интеракција и комуникација во образованието на далечина во македонските училишта* 295
40. **Аида Петровска**, *Придобивките од STEM во развојот на интелектуалните компетенции на учениците од основните училишта* 303
41. **Силвана Јакимовска Бинова**, *Атрактивност на STEM професији – зошто и како преку примери од наставата по математика* 310
42. **Славица Карбева Стојковиќ**, *Визуелизирање на податоци во наставата по математика во основно образование* 319
43. **Кети Иваноска, Марина Стојановска**, *Претставите на учениците од деветто одделение во врска со граббените единици на супстанциите* 326
44. **Цветанка Трајковски, Емилија Накова, Катерина Русевска**, *Изработка на дихотомен клуч за одредување на жаби присутни во македонија и негова примена во образовниот процес по предметите природни науки и биологија* 334
45. **Маре Жежовска - Трајковски, Марина Јанеска, Јулијана Трајковска**, *Влијанието на загадувањето на животната средина врз квалитетот на водата* 346
46. **Вангелина Мојаноска**, *Студија на наставен час по математика: Примена на инструменти за самооценување на учениците на часовите по математика* 351
47. **Фроска Смилкова**, *Улога и значење на воннаставните активности во основното образование* 358
48. **Маре Миленковска**, *Значењето на играта во формирањето на математичките поими* 367

Софтверски пакет као интерактивни алат у настави физике

Бобан Ђокић¹, Миљана Милентијевић¹, Бранко Дрљача¹

¹Универзитет у Приштини са привременим седиштем у Косовској Митровици, Природно-математички факултет, Ул. Лоле Рибара 29, 38220 Косовска Митровица, Србија

Апстракт. Развој савремених технологија утиче на промену живота људи све већом брзином. Напредак технологије омогућава примену великог броја мултимедијалних уређаја помоћу којих се ученицима могу приближити и поједноставити појаве које је тешко дочарати помоћу стандардних метода предавања табла, креда и презентација. У овом раду је кроз неколико примера из физике, у оквиру једне наставне теме, предложено могуће решење за извођење наставе у школама које немају адекватно опремљене кабинете за наставу физике.

Клучни зборови: настава физике, софтверски пакет, огледи

УВОД

Настава физике у Србији из године у годину постаје све изазовнија. Једном дуг процес, са довољним бројем школских часова, често се скраћује, посебно у средњим стручним школама. Овај процес би требало да се састоји из три дела: теоријског предавања, рачунских задатака и демонстрација – лабораторијских вежби (уколико је могуће). Уобичајени метод који се користи у настави физике у Србији је предавање. Утврђено је да овај метод није ефикасан за наставу у науци, јер се показало да су резултати ниски [1]. Начин на који свет функционише није одговор који ће се добити традиционалним начином подучавања, пошто постоји мала или никаква промена у разумевању физичких феномена код већине ученика када се користи овај метод. [2]. Показано је да овај метод функционише за око десет процената ученика за које се претпоставља да су самомотивисани ученици који би у суштини сами научили предвиђено градиво [3].

Ако се у наставни процес уврсте нумерички промемлеми и задаци, резултат је бољи. Ипак, ова наставна техника је корисна само за мали број тематских целина за које је утврђено да су теоријско предавање и нумерички задаци довољни да ученици стекну знања о обрађеној теми и стекну потпуно разумевање проблема. Са друге стране, већи број наставних тема захтева одговарајуће демонстрације, како би ученици јасније разумели оно што уче. Штавише, те демонстрације су се показале као кључне за разумевање физике на нивоу основног и средњег образовања. Демонстрације из физике помажу ученицима да постигну дубље разумевање физичких процеса и нашироко су коришћени у свету, како у предуниверзитетском али и универзитетском периоду на светски познатим универзитетима. Као резултат тога, ученици су више заинтересовани за истраживање света физике што доводи до побољшаних компетенција на крају наставног процеса.

Демонстрације се могу поделити у две групе. Прву групу чине класични демонстрациони експерименти који се изводе испред ученика, или заједно са ученицима,

са потребном опремом. Као што је раније поменуто, постоји велики број тих експериментата које су спровели и еминентни универзитетски професори на еминентним универзитетима [4]. Ова врста демонстрационих експериментата помаже ученицима да стекну бољи увид у физичке феномене. Показало се да када су ученици активно укључени у демонстрације постижу боље резултате у поређењу са случајем када само посматрају нихово извођење [5].

Друга група је наставни процес заснован на информационо-комунакационим технологијама. Ова врста наставног процеса подразумева активно и практично учешће ученика и на тај начин им омогућава да стекну неопходну пажњу наставника. Према мишљењу познатих истраживача квалитет дизајна и развоја директно утиче на квалитет наставног процеса и један је од најважнијих фактора квалитетног садржаја наставног процеса [6,7]. Често смо сведоци да ученици основних, средњих школа и гимназија, који имају одговарајућу опрему, кроз квалитетне и садржајем богате информационо-комуникационе системе постижу велике успехе на републичким и меѓународним такмичењима и олимпијадама знања.

Напредак технологије намеће неопходност промене начина реализације наставног процеса у савременом образовању у смислу потребе за брзим и ефикасним трансфером знања [8].

Савремена настава физике мора бити тако организована да се ученицима створе околности у чијим оквирима они самостално откривају већ откривена знања у науци.

Овом приликом смо извршили прилагођавање кодова писаних у софтверском пакету *Mathematica*[®] тако да одговарају наставној теми *Хармонијске осцилације* за ученике трећег разреда гимназије који раде по плану и програму Министарства просвете, науке и технолошког развоја Републике Србије.

ПРОГРАМСКИ ПАКЕТ MATHEMATICA[®]

Програмски пакет *Mathematica*[®] развијен је у софтверској компанији *Wolfram Research* и користи се за математичке и друге примене. Посебно је погодан за обраду нумеричких података, за симболичка процесирања, као и за графичко приказивање података и функција.

За рад у програмском пакету *Mathematica*[®] користе се документа која се зову бележнице (*notebooks*). Бележнице се састоје од ћелија које могу садржати текст, израчунавања или графиконе. Ћелија се препознаје по угластој загради са десне стране ({}).

МОДЕЛИ ОСЦИЛАТОРНОГ КРЕТАЊА

Периодично кретање представља посебан облик кретања које се после одређеног временског интервала понавља на истоветан начин. На пример равномерно кружно кретање, кретање тела обешеног о опругу, осциловање клатна, вибрирање жице, ваздушног стуба итд.

Посебан вид периодичног кретања јесте осцилаторно кретање или осциловање.

Осцилаторно кретање или осциловање је неравномерно праволинијско или криволинијско кретање тела око равнотежног положаја између две тачке у којима се тело зауставља и мења смер кретања.

Тело врши хармонијско осциловање под дејством силе која тежи да га врати у равнотежни положај и чији је интензитет пропорционалан удаљењу од тог положаја. Ово својство имају еластичне силе које се називају повратне или реституционе силе.

Величине које карактеришу хармонијско осциловање:

- Амплитуда осциловања је максимално удаљење тела од рамнотежног положаја. Означаваче се са x_0 или са A .
- Елонгација је удаљење тела од рамнотежног положаја у произвољном тренутку времена. Може имати вредности од $-x_0$ до x_0 .
- Период осциловања (T) је време потребно да тело изврши једну осцилацију.
- Учестаност (фреквенција) представља број осцилација које осцилатор изврши у јединици времена, тј. $\nu = n/t$. Једнака је реципрочној вредности периода осциловања: $\nu = 1/T$. Јединица за учестаност је Херц (Hz).
- Кружна учестаност (ω) је број осцилација у 2π секунди: $\omega = 2\pi\nu = 2\pi/T$. Јединица за учестаност је радијан у секунди (rad/s).

На Слици 1. приказано је осциловање тела у вертикалном правцу.

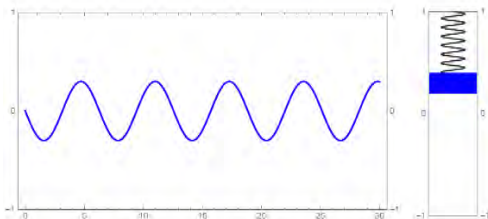
С обзиром да се кретање тела врши под дејством реституционе (повратне) силе облика $F = -kx$, једначина кретања тела по Другом Њутновом закону облика је: $ma = -kx$.

Функција која описује елонгацију осциловања је косинусна функција од ωt и може се написати у облику:

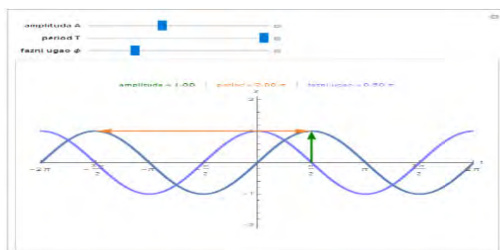
$$x = A \cos(\omega t + \varphi_0) \quad (1)$$

Овде је са A – означена амплитуда осциловања. Величина ω представља кружну учестаност осциловања, израз у загради ($\omega t + \varphi$) је фаза осциловања или фазни угао φ , док је φ_0 почетна фаза (слика 2).

Хармонијско осцилаторно кретање је осцилаторно кретање које се може представити хармонијском кривом линијом (синусоидом или косинусоидом).



СЛИКА 1. Зависност положаја тела од времена



СЛИКА 2. Функција положаја

ЛИНЕАРНИ ХАРМОНИЈСКИ ОСЦИЛАТОР

Хармонијски осцилатор представља један од најважнијих модела у физици. С обзиром да се ученици по први пут срећу са представом хармонијског осцилатора потребно је приказати им то на прихватљив и разумљив начин, путем визуелизације одговарајућих примера. Користимо демонстрацију која нам омогућава да посматрамо кретање које описује материјална тачка масе m закачена на опругу константе еластичности k дуж једног правца осциловања линеарног хармонијског осцилатора (слика 3).

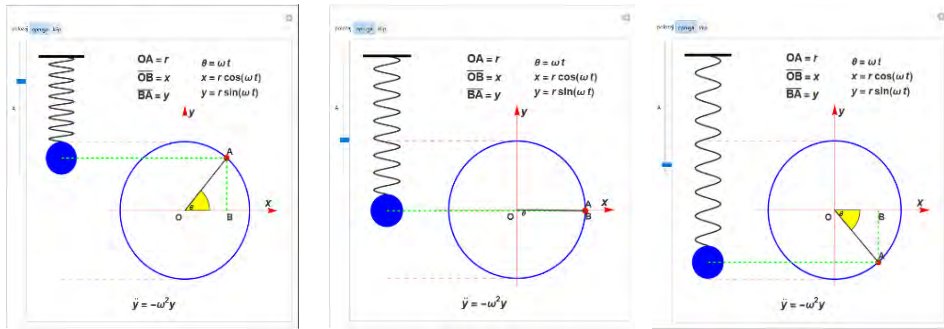
Демонстрација омогућава промену положаја материјалне тачке (команда означена са A на контролном панелу): вредности параметра $A = 0$ одговара положај $x = x_0$, а максималној удаљености положај $x = -x_0$. Једначине којима се описује ово кретање јесу:

$$x(t) = x_0 \cos(\omega t + \varphi_0), \quad v(t) = -v_0 \sin(\omega t + \varphi_0), \quad a(t) = -a_0 \cos(\omega t + \varphi_0) \quad (1)$$

при чему у сва три случаја важи: $\omega = \sqrt{\frac{k}{m}}$, $v_0 = \omega x_0$ и $a_0 = \omega^2 x_0$.

Такође се и Њутнов закон за хармонијски осцилатор може написати у облику:

$$a = -\omega^2 x. \quad (2)$$



СЛИКА 3. Шематски приказ помоћу честице на опрузи

Први панел на Сlici 3. приказује тренутак у којем је материјална тачка у близини тачке $y = y_0$, други панел приказује положај у близини равнотежног, а последњи панел приказује положај у близини тачке $x = x_0$. На Сlici 4. приказан је код за генерисање модела осциловања честице на опрузи.

b = 1/2;
f[x_] := 4 Sin[8 x];

```
Manipulate[
Graphics[
Switch[gv,
"opruzg", {ParametricPlot[{f[x], -x}, {x, 0, 2 Pi/a}], PlotStyle->Directive[Thick, GrayLevel[.2]], PlotRange->{{-1, 7}, {-2.5 Pi, 0.1}}, Axes->None, AspectRatio->1, ImageSize->{400, 400}}][[1]],
Thickness[.01], Line[{{-7, 0}, {7, 0}}], Blue, Disk[{0, -2 Pi/a}, b], PointSize[.006], Black, Point[{0, -2 Pi/a}], Blue, Thick, Circle[{4, -4 Pi/3 - b}, 2 Pi/3], Red,
Thickness[.001], Arrow[{{4, -7}, {4, -1.5}}], Arrow[{{1.5, -4 Pi/3 - b}, {7, -4 Pi/3 - b}}], Dashed, Line[{{0, -2 Pi/a}, {4, -2 Pi/a}], Line[{{0, -2 Pi - b}, {4, -2 Pi - b}}],
PointSize[.023], Point[{4 + Re@Sqrt[(2 Pi/3)^2 - (-2 Pi/a + 4 Pi/3)^2], -2 Pi/a - b}], Green, Thick, Line[{{0, -2 Pi/a}, {4 + Re@Sqrt[(2 Pi/3)^2 - (-2 Pi/a + 4 Pi/3)^2], -2 Pi/a - b}],
Line[{{4 + Re@Sqrt[(2 Pi/3)^2 - (-2 Pi/a + 4 Pi/3)^2], -4 Pi/3 - b}, {4 + Re@Sqrt[(2 Pi/3)^2 - (-2 Pi/a + 4 Pi/3)^2], -2 Pi/a - b}], Yellow, EdgeForm[Thickness[.002]],
Disk[{4, -4 Pi/3 - b}, .8, Which[{4 Pi/3 - 2 Pi/a > 0} && Re@Sqrt[(2 Pi/3)^2 - (-2 Pi/a + 4 Pi/3)^2] > 0, {0, ArcTan[{4 Pi/3 - 2 Pi/a}/Re@Sqrt[(2 Pi/3)^2 - (-2 Pi/a + 4 Pi/3)^2]}, {4 Pi/3 - 2 Pi/a < 0} && Re@Sqrt[(2 Pi/3)^2 - (-2 Pi/a + 4 Pi/3)^2] > 0,
{ArcTan[{4 Pi/3 - 2 Pi/a}/Re@Sqrt[(2 Pi/3)^2 - (-2 Pi/a + 4 Pi/3)^2]}, 0}, {4 Pi/3 - 2 Pi/a > 0} && Re@Sqrt[(2 Pi/3)^2 - (-2 Pi/a + 4 Pi/3)^2] = 0, {0, Pi/2}, {4 Pi/3 - 2 Pi/a < 0} && Re@Sqrt[(2 Pi/3)^2 - (-2 Pi/a + 4 Pi/3)^2] = 0, {-2 Pi/3, 0}],
Dashing[1], GrayLevel[.2], Thickness[.004], Line[{{4, -4 Pi/3 - b}, {4 + Re@Sqrt[(2 Pi/3)^2 - (-2 Pi/a + 4 Pi/3)^2], -2 Pi/a - b}],
Text[Style["0", 12, Bold], Which[{4 Pi/3 - 2 Pi/a > 0}, {4.2, -4.6}, {4 Pi/3 - 2 Pi/a < 0}, {4.2, -4.8}],
Text[Style[Column@{HoldForm[0 = omega t], TraditionalForm@HoldForm[x = r Cos[omega t]], TraditionalForm@HoldForm[y = r Sin[omega t]], 16, Bold}, {5.5, -.67}],
Text[Style[Column@{TraditionalForm@HoldForm[OB = x], TraditionalForm@HoldForm[BA = y]}, 17, Bold], {3, -.67}],
Text[Style["a", 18, Bold, Italic], {6.7, -4.45}], Text[Style["y", 17, Bold, Italic], {4.22, -1.7}], Text[Style["O", 14, Bold], {3.8, -4.9}],
Text[Style["A", 14, Bold], {4.1 + Re@Sqrt[(2 Pi/3)^2 - (-2 Pi/a + 4 Pi/3)^2], -2 Pi/a - b - 2}], "k1ip",
{Thickness[.01], Line[{{-7, 0}, {7, 0}}], EdgeForm[Thick], White, Rectangle[{-5, -2 Pi/3 - b + 2}, {5, -2 Pi - b}], Blend[{LightGreen, Yellow}], Rectangle[{-5, -2 Pi - b}, {5, -2 Pi/a - b}],
GrayLevel[.8], Rectangle[{-2, 0}, {2, -2 Pi/a - b}], Brown, Rectangle[{-5, -2 Pi/a - b + 2}, {5, -2 Pi/a - b}], PointSize[.006], Black, Point[{0, -2 Pi/a}], Blue, Thick,
Circle[{4, -4 Pi/3 - b}, 2 Pi/3], Red, Thickness[.001], Arrow[{{4, -7}, {4, -1.5}}], Arrow[{{1.5, -4 Pi/3 - b}, {7, -4 Pi/3 - b}}], Dashed, Line[{{0.5, -2 Pi/a - b}, {4, -2 Pi/a - b}],
Line[{{0.5, -2 Pi - b}, {4, -2 Pi - b}], PointSize[.023], Point[{4 + Re@Sqrt[(2 Pi/3)^2 - (-2 Pi/a + 4 Pi/3)^2], -2 Pi/a - b}], Green, Thick, Line[{{0.5, -2 Pi/a - b}, {4 + Re@Sqrt[(2 Pi/3)^2 - (-2 Pi/a + 4 Pi/3)^2], -2 Pi/a - b}].
```

СЛИКА 4. Код за генерисање модела зависности положаја тела од времена
Енергија хармонијског осцилатора

Осцилатор је тело које врши хармонијско осциловање, при кретању непрекидно мења положај и брзину, што значи да располага одређеном потенцијалном и кинетичком енергијом. Како осцилатор представља изолован систем, његова механичка енергија се током времена не мења, ако занемаримо силе отпора средине (Слика 5).

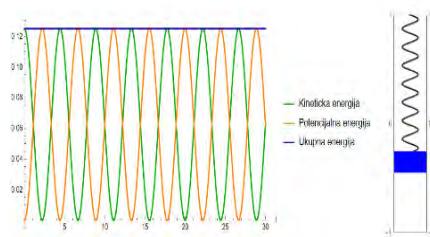
Укупна механичка енергија осцилатора једнака је збиру његове кинетичке и потенцијалне енергије. Укупна енергија хармонијског осцилатора износи:

$$E = E_k + E_p = \frac{m\omega^2 A^2}{2} \quad (3)$$

Укупна механичка енергија осцилатора има сталну вредност и сразмерна је његовој маси, квадрату амплитуде и квадрату кружне учестаности (Слика 6).



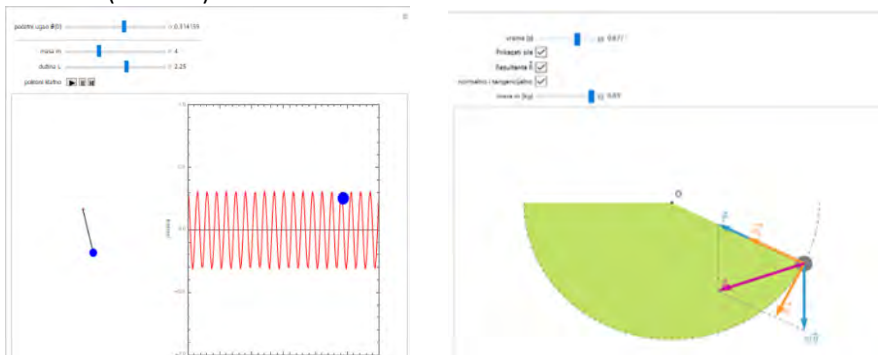
СЛИКА 5. Контролни панел



СЛИКА 6. Зависност енергије осцилатора од времена

МАТЕМАТИЧКО КЛАТНО

Математичко клатно је систем који се состоји из куглице занемарљивих димензија, која је окачена о неистегљиву нит занемарљиве масе. Клатно изводи слободне осцилације, ако се занемари отпор ваздуха и трење у тачки вешања. За описивање кретања математичког клатна користимо демонстрацију која нам омогућава исцртавање путање осциловања клатна и приказ сила које делују на клатно при кретању. Обзиром да се ради о осцилаторном кретању под дејством силе Земљине теже, са демонстрације се јасно види да је узрок осциловања клатна сила која је директно сразмерна елонгацији, на слици означена са R (Слика 7).



СЛИКА 7. Приказ амплитуде осциловања и сила које делују на математичко клатно

Такође постоји могућност одабира приказивања нормалне и тангенцијалне компоненте силе, резултантне силе и амплитуде осциловања. На Сlici 8. приказан је код за генерисање демонстрације модела математичког клатна.

```

Manipulate[Module[{sol, \theta, t}, sol = NDSolve[{ \theta''[t] = -9.81 * Sin[\theta[t]], \theta'[0] = 0, \theta[0] = -Pi/2}, \theta, {t, 0, tmax}];
With[{ \varphi = \theta[tmax] /. First[sol], \omega = \theta'[tmax] /. First[sol], g = 9.81},
Pane[Graphics[{{Point[{0, 0}], Text["O", {0, 0}, {-2, -2}], Gray, {ColorData["WebSafe"]["#99CC00"], Opacity[0.6], Disk[{0, 0], 1, {-Pi, \varphi - Pi/2}}},
(PointSize[Sqrt[m/20]], Point[{Sin[\varphi], -Cos[\varphi]}], {Dashing[{.01, .01}], Circle[{0, 0], 1, {-Pi, 0}}},
If[F = True, {Thickness[.008], ColorData["WebSafe"]["#3399CC"], Arrow[{{Sin[\varphi], -Cos[\varphi]}, {-1 + m \omega^2 + g m Cos[\varphi]} {-Sin[\varphi], Cos[\varphi]}]},
Text["\vec{T}^+", {-1 + m \omega^2 + g m Cos[\varphi]} {-Sin[\varphi], Cos[\varphi]}, {-2, -1}],
Arrow[{{Sin[\varphi], -Cos[\varphi]}, {Sin[\varphi], -g m - Cos[\varphi]}]},
Text["\vec{m}\vec{g}^+", {Sin[\varphi], -g m - Cos[\varphi]}, {-1, 1}], Line[{{0, 0}, {Sin[\varphi], -Cos[\varphi]}]},
If[comp = True, {Thickness[.008], ColorData["WebSafe"]["#FF9933"], Arrow[{{Sin[\varphi], -Cos[\varphi]}, {1 - m \omega^2} {Sin[\varphi], -Cos[\varphi]}]},
Text["\vec{R}^+", {1 - m \omega^2} {Sin[\varphi], -Cos[\varphi]}, {-2, -1}],
Arrow[{{Sin[\varphi], -Cos[\varphi]}, {(1 - g m Cos[\varphi]) Sin[\varphi], -Cos[\varphi] - g m Sin[\varphi]^2}}]},
Text["\vec{R}_T^+", {(1 - g m Cos[\varphi]) Sin[\varphi], -Cos[\varphi] - g m Sin[\varphi]^2}, {-2, -1}], Point[{0, 0}],
If[R = True, {{Thickness[.008], ColorData["WebSafe"]["#CC0099"], Arrow[{{Sin[\varphi], -Cos[\varphi]}, {(1 - m \omega^2 - g m Cos[\varphi]) Sin[\varphi], -g m + Cos[\varphi]} {-1 + m \omega^2 + g m Cos[\varphi]}]},
Text["\vec{R}^+", {(1 - m \omega^2 - g m Cos[\varphi]) Sin[\varphi], -g m + Cos[\varphi]} {-1 + m \omega^2 + g m Cos[\varphi]}, {-2, -1}],
If[F = True, {Dashing[{.01, .008}], Line[{{Sin[\varphi], -g m - Cos[\varphi]}, {(1 - m \omega^2 - g m Cos[\varphi]) Sin[\varphi], -g m + Cos[\varphi]} {-1 + m \omega^2 + g m Cos[\varphi]}]},
Line[{{(1 - m \omega^2 - g m Cos[\varphi]) Sin[\varphi], -g m + Cos[\varphi]} {-1 + m \omega^2 + g m Cos[\varphi]}, {(1 - m \omega^2 - g m Cos[\varphi]) Sin[\varphi], Cos[\varphi]} {-1 + m \omega^2 + g m Cos[\varphi]}]},
}], PointSize[.01], Point[{0, 0}]
}], {PointSize[.01], Point[{0, 0}]
}], PlotRange -> {{-1.1, 1.2}, {-1.7, .6}}, ImageSize -> {500, 400}],
]
],
{tmax, 0, "vreme [s]", 0, 4 * .296, .001, Appearance -> "Labeled", ImageSize -> Tiny},
{{F, False, "Prikazati sile"}, {False, True}},
{{R, False, "Rezultanta \vec{R}"}, {False, True}},
{{comp, False, "normalno i tangencijalno"}, {False, True}},
{{m, .05, "masa m [kg]", .02, .05, .001, Appearance -> "Labeled", ImageSize -> Tiny},
ControlPlacement -> Top, AutorunSequencing -> {2, 3, 4, 5}
]
    
```

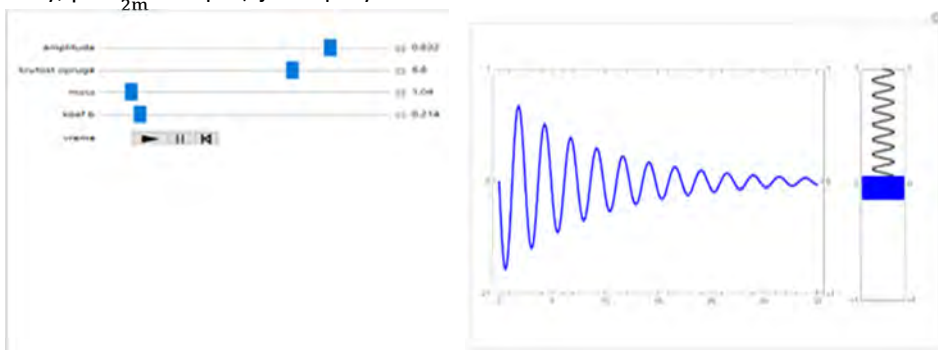
СЛИКА 8. Код за генерисање демонстрације модела математичког клатна

ПРИГУШЕНЕ ОСЦИЛАЦИЈЕ

Осцилације чија се амплитуда смањује с временом називају се пригушене или амортизоване осцилације. На Слици 9. представљена је демонстрација која исцртава пригушене осцилације. Демонстрација омогућава подешавање одговарајућих вредности амплитуде осцилатора, коефицијента еластичности опруге, коефицијента пригушења и масе тега. Једначина кретања осцилатора је облика:

$$x = A(t)\sin(\omega t + \varphi_0) \quad (3)$$

где је: $A(t) = A_0 e^{-\beta t}$ амплитуда осциловања која се смањује по експоненцијалном закону у времену, $\beta = \frac{\mu}{2m}$ коефицијент пригушења.



СЛИКА 9. Демонстрација пригушених осцилација

ПРИНУДНЕ ОСЦИЛАЦИЈЕ

У физичким уређајима су потребни осцилатори који могу да одржавају осциловање дужи време. Да би се то остварило потребно је реалном осцилатору доводити у току сваке осцилације онолико енергије колико губи тако да му се не би смањивала амплитуда осциловања.

Принудне механичке осцилације настају када на осцилатор делује спољашња сила која се периодично мења у времену. У општем случају на осцилатор делују три силе: спољашња сила F , сила еластичности опруге $F = -kx$ и сила отпора средине $F = -\mu v$.

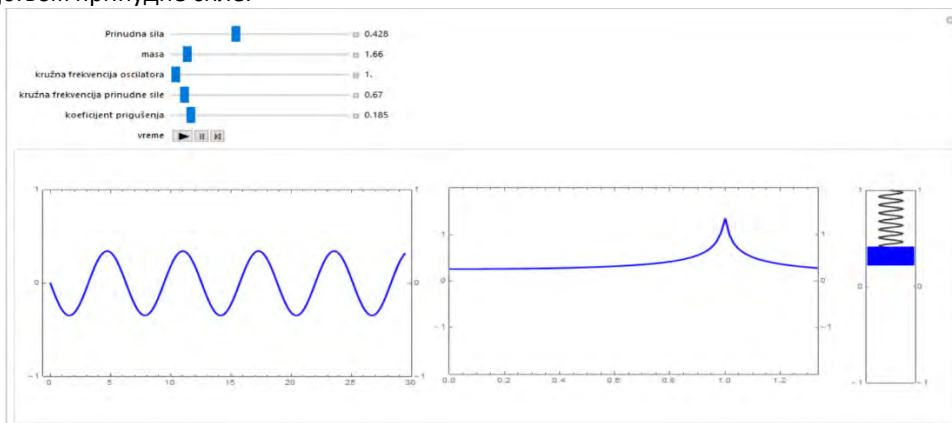
Амплитуда принудних осцилација зависи од принудне силе, њене фреквенције и сопствене фреквенције осцилатора.

Резонанција је појава при којој је амплитуда принудних осцилација максимална.

Фреквенција којом тада осцилује осцилатор назива се резонантна фреквенција ν_r па разликујемо два случаја:

- када нема отпора средине и трења једнака је сопственој фреквенцији осцилатора ($\nu_r = \nu_0$),
- када постоји отпор средине или трења (пригушења) мања од сопствене фреквенције осцилатора ($\nu_r < \nu_0$) – при малим пригушењима је мало мања од ње.

На слици 10. приказан је контролни панел који нам омогућава подешавање одговарајућих услова за настанак резонанције. Такође, дат је и приказ резонанције под дејством принудне силе.



СЛИКА 10. Демонстрација принудних осцилација

ЗАКЉУЧАК

Напредак савремених технологија нуди потенцијалне могућности за развој наставе у смислу потребе за брзим и ефикасним трансфером знања и потребно их је искористити. С обзиром да су демонстрације које смо користили модларне, омогућавају прилагођавање наставнику, као и афинитетима ученика. Посебно добијају на значају уз паметну таблу. На овај начин се може постићи боље разумевање наставне теме Хармонијске осцилације у ситуацијама извођења наставе у школама које нису довољно опремљене лабораторијама у којима би се појаве могле практично показати.

ЛИТЕРАТУРА

1. Toplis R. & Allen M., 'I do and I understand?' Practical work and laboratory use in United Kingdom schools, *Eurasia Journal of Mathematics, Science & Tehnology Educations*, 8 (1), (2012), pp. 3-9.
2. Capanis N., Chabalengula V.M., Mumba F., Mbewe S., How Pre-Service Teachers' Understand and Perform Science Process Skills, *Eurasia Journal od Mathematics, Sceince and Tehnology Education*, 7 (2), (2010), pp. 196-214.
3. Gekelman W., Pribyul P., Wise J., Lee A., Hwang R., Eghtebas C., Shin J., & Baker B., Using plasma experiments to illustrate a complex index of refraction, *American Journal of Physics*, 79 (9), (2011), pp. 894-902.
4. <https://ocw.mit.edu/courses/8-13-14-experimental-physics-i-ii-junior-lab-fall-2016-spring-2017/>
5. Amadallo M. M., Alphayo A.O., Thomas W. S., Physics Practical Work and Its Influence on Students' Academic Achievement, *Journal of Education and Practice*, Vol. 7, No.28, 2016.
6. Chau, P.Y., An empirial investigation on factors affecting the acceptance of CASE by systems developers, *Information & Management*, 30 (6), (1996), pp.269-280.
7. Davis, F.D., Perceived usefulness, perceived ease of use, and user acceptance of information technology, *MIS Quarterly*, 13 (3), (1989), pp. 319-340.
8. Drljača B., Đokić B., Šiljić I., Kevkić T., Gulan Lj., Primena softverskih paketa za demonstraciju oglada iz fizike, *Zbornik radova sa međunarodne konferencije o nastavi fizike i srodnih nauka*, br. 7, (2018), str. 181-186.
9. Физика уџбеник за трећи разред гимназије природно-математичког и општег смера, Klett, Београд 2016.
10. Физика уџбеник за трећи разред гимназије општег и природно-математичког смера, Завод за уџбенике, Београд 2015.
11. Физика уџбеник за трећи разред гимназије, Круг, Београд 2010.
12. Kenny F. Stephens II "Simple Harmonic Motion of a Spring"
<http://demonstrations.wolfram.com/SimpleHarmonicMotionOfASpring/>
Wolfram Demonstrations Project
13. Paul Rosemond "Simple Harmonic Motion"
<http://demonstrations.wolfram.com/SimpleHarmonicMotion/>
Wolfram Demonstrations Project
14. Stephen Wilkerson "An Oscillating Pendulum"
<http://demonstrations.wolfram.com/AnOscillatingPendulum/>
Wolfram Demonstrations Project
15. Bernard Vuilleumier "Forces on a Pendulum"
<http://demonstrations.wolfram.com/ForcesOnAPendulum/>
Wolfram Demonstrations Project

АКАДЕМИЈА НАУКА И УМЈЕТНОСТИ РЕПУБЛИКЕ СРПСКЕ

НАУЧНИ СКУПОВИ

Књига ХЛП

ОДЈЕЉЕЊЕ ПРИРОДНО-МАТЕМАТИЧКИХ И ТЕХНИЧКИХ НАУКА

Књига 35

САВРЕМЕНИ МАТЕРИЈАЛИ



Бања Лука 2018

Научни скуп
САВРЕМЕНИ МАТЕРИЈАЛИ
Зборник радова

ACADEMY OF SCIENCES AND ARTS OF THE REPUBLIC OF SRPSKA

SCIENTIFIC CONFERENCES

Book XLII

DEPARTMENT OF NATURAL-MATHEMATICAL AND TECHNICAL SCIENCES

Book 35

CONTEMPORARY MATERIALS

EDITORIAL BOARD

Academician Rajko Kuzmanović, academician Ljubomir Zuković,
academician Vaskrsija Janjić, academician Dragoljub Mirjanić,
academician Branko Škundrić

EDITOR IN CHIEF

Academician Rajko Kuzmanović

EDITOR

Academician Dragoljub Mirjanić



Banja Luka 2018

АКАДЕМИЈА НАУКА И УМЈЕТНОСТИ РЕПУБЛИКЕ СРПСКЕ

НАУЧНИ СКУПОВИ

Књига ХЛП

ОДЈЕЉЕЊЕ ПРИРОДНО-МАТЕМАТИЧКИХ И ТЕХНИЧКИХ НАУКА

Књига 35

САВРЕМЕНИ МАТЕРИЈАЛИ

РЕДАКЦИОНИ ОДБОР

Академик Рајко Кузмановић, академик Љубомир Зуковић,
академик Васкрсија Јањић, академик Драгољуб Мирјанић,
академик Бранко Шкундрић

ГЛАВНИ УРЕДНИК

Академик Рајко Кузмановић

ОДГОВОРНИ УРЕДНИК

Академик Драгољуб Мирјанић



Бања Лука 2018.

ОРГАНИЗАЦИОНИ ОДБОР
НАУЧНОГ СКУПА

Академик Драгољуб Мирјанић, председник
Академик Васкрсија Јањић, потпредседник
Академик Рајко Кузмановић
Академик Бранко Шкундрић
Проф. др Неђо Ђурић, дописни члан АНУРС-а
Проф. др Лудвик Топлак
Проф. др Владо Ђајић
Проф. др Небојша Јованић
Проф. др Зоран Рајилић

НАУЧНИ ОДБОР
НАУЧНОГ СКУПА

Академик Драгољуб Мирјанић
Академик Бранко Шкундрић
Академик Јован Шетрајчић
Академик Стане Пејовник (Словенија)
Проф. др Неђо Ђурић, дописни члан АНУРС-а
Академик Томислав Павловић
Академик Ростислав Андриевски (Русија)
Академик Филип Говоров (Украјина)
Академик Џералд Полак (САД)
Проф. др Роумиана Тсенкова (Јапан)
Проф. др Мај Ван Хо (Велика Британија)
Проф. др Ифа Говен (Ирска)
Проф. др Јукио Косуги (Јапан)
Др Мајрон Д. Еванс (Канада)
Проф. др Мартин Чаплин (Велика Британија)
Проф. др Ђуро Коруга (Србија)
Проф. др Драгица Лазич
Проф. др Перо Дугић
Проф. др Слободан Чупић

САДРЖАЈ

УМЈЕСТО ПРЕДГОВОРА.....	15
-------------------------	----

ОТВАРАЊЕ СКУПА

УВОДНА БЕСЈЕДА ПРЕДСЈЕДНИКА АНУРС-а Академика Рајка Кузмановића	19
--	----

РЕФЕРАТИ ПОДНЕСЕНИ НА СКУПУ

<i>Славица Малетић, Драгана Церовић, Иван Петронијевић, Милорад Шилегиновић, Јаблан Дојчиловић</i> КАРАКТЕРИЗАЦИЈА ЈОНСКИМ СНОПОВИМА МОДИФИКОВАНЕ ПОЛИЕТИЛЕН ТЕРЕФТАЛАТ МЕМБРАНЕ	23
Characterization ION-BEAM modified polyethyleneterephthalate membrane	

<i>Слађана Пантелић, Милеса Срећковић, Ацо Јанићијевић, Милорад Давидовић, Сања Јевтић, Зоран Карастојковић Вишеслава Рајковић</i> УТИЦАЈ Nd ³⁺ : YAG ЛАСЕРА НА ОПТИЧКЕ КОМПОНЕНТЕ ОД СТАКЛЕНИХ, КЕРАМИЧКИХ И ПЛАСТИЧНИХ МАТЕРИЈАЛА	33
Effects of Nd ³⁺ :Yag laser on optical components made from glass, ceramic and plastic materials	

<i>Svetislav Savović , Alexandar Djordjevich, Асо Јанићијевић, Dragoljub Mirjanić</i> MODE COUPLING IN STEP-INDEX PLASTIC-CLAD SILICA OPTICAL FIBERS WITH CHEMICALLY ETCHED FIBER SECTION	49
Спрезање модова у стакленим оптичким влакнима са пластичним омотачем и степенастим индексом преламања са хемијски нагриженим делом влакна	

Vladan Mičić, Stefan Pavlović, Jelena Pavličević, Olga Govedarica, Milovan Janković, Snežana Sinadinović Fišer, Jaroslava Budinski Simendić
MODELOVANJE POLUŠARŽNIH PROCESA PROIZVODNJE
POLIETERA ZA DOBIJANJE POLIURETANA 61
Modeling of semibatch processes of polyethers
production for polyurethane fabrication

Жељко Алексић, Душан Јешић
ИСПИТИВАЊЕ УПОРЕДНИХ КАРАКТЕРИСТИКА
ОРИГИНАЛНОГ МАТЕРИЈАЛА И ЗАМЕНСКИХ МАТЕРИЈАЛА 71
Testing of comparative characteristics of original
material and replacement

Selma Osmić, Sabina Begić, Vladan Mičić, Zoran Petrović
UTICAJ KONCENTRACIJE ETANOLA KAO EKSTRAKCIJONOG
SREDSTVA NA ANTIOKSIDATIVNO DEJSTVO EKSTRAKTA
ŽALFIJE (*SALVIA OFFICINALIS L.*)..... 81
The influence of ethanol concentration as an extraction agent on the
antioxidative effect of the sage extract (*SALVIA OFFICINALIS L.*)

Nikolay Angelov, Dimcho Pulov, Tsanko Karadzhov
INFLUENCE OF STEP ONTO LASER MARKING
OF SAMPLES OF STEEL 1CS60 91
Утицај поступног ласерског обележавања
узорака од челика 1CS60

*Олга Говедарица, Милован Јанковић,
Снежана Синадиновић-Фишер, Јарослава Будински-Симендић,
Јелена Павличевић, Весна Теофиловић*
МОДЕЛОВАЊЕ И ОПТИМИЗАЦИЈА ЕПОКСИДОВАЊА
БИЉНОГ УЉА ОРГАНСКОМ ПЕРКИСЕЛИНОМ 99
Modeling and optimization of the epoxidation
of vegetable oils with organic peracid

*Марица Дугић, Бранко Деспотовић, Мирко Петковић,
Перо Дугић, Новак Дамјановић*
РАЗВОЈ ФОРМУЛАЦИЈА ЦИРКУЛАЦИОНИХ УЉА
У СКЛАДУ СА ЗАХТЈЕВИМА НОВИХ СПЕЦИФИКАЦИЈА 111
Circulating oil formulations development
in accordance with the requirements of the new specifications

- Милеса Срећковић, Драган Дружијанић, Ацо Јанићијевић,
Милован Јанићијевић, Александар Бугариновић,
Слађана Пантелић, Сузана Полић*
АНАЛИТИЧКИ И ЕКСПЕРИМЕНТАЛНИ ПРИЛАЗИ
ИНТЕРАКЦИЈИ ЛАСЕРА СА РАЗНИМ МАТЕРИЈАЛИМА 123
Analytical and experimental approaches to laser
interaction with various materials
- Ivan Hegediš, Neđo Đurić, Arpad Čeh, Golub Karaman, Edita Tenji*
МЕШАВИНА ГЛИНЕ И ЈЕЛОВИХ ИГЛИЦА КАО МИКРОАРМАТУРЕ 149
Mixture of clay and fir needles as micro armature
- Ivan Hegediš, Neđo Đurić, Arpad Čeh, Golub Karaman, Edita Tenji*
ДОДАТАК БОРОВИХ ИГЛИЦА КАО ПРИРОДНЕ АРМАТУРЕ
У МЕШАВИНИ ГЛИНЕ И ЈЕЛОВИХ ИГЛИЦА 157
Addition of pine needles as natural armature in
a mixture of clay and fir needles
- Iva Despotović, Ksenija Janković*
ИНФЛУЕНЦА ТАЈЛИНГА И ПЛИНЕ АШЕ НА ЧВРСТОЋУ
САМОГРАЂУЈУЋЕГ БЕТОНА 163
Утицај јаловине и летећег пепела на чврстоћу
самоуграђујућег бетона
- Kristina O. Čajko, Svetlana R. Lukić Petrović, Mirjana V. Šiljegović,
Goran R. Štrbac, Dragoslav M. Petrović*
СПЕЦИФИЧНОСТИ ТЕРМИЧКИ ИНДУКОВАНЕ КРИСТАЛИЗАЦИЈЕ
У СТАКЛИМА ИЗ СИСТЕМА АГ-АС-С-СЕ 171
Специфичности термички индуковане кристализације
у стаклима из система Ag-As-S-Se
- Jelena N. Janevski, Branislav V. Stojanović, Mladen M. Stojiljković,
Predrag Živković, Mirko Dobrnjac, Mića Vukić*
АПЛИКАЦИЈА ЗЕОЛИТА У ИНДУСТРИЈИ 183
Примена зеолита у индустрији
- Горана Мрђан, Борко Матијевић,
Бенђи Ваштаг, Сузана Апостолов*
СОЛВАТОХРОМИЗАМ ОДАБРАНИХ НОВОСИНТЕТИСНИХ
ДЕРИВАТА КАРБОХИДРАЗОНА КАО ПОТЕНЦИЈАЛНО
БИОЛОШКИ АКТИВНИХ ЈЕДИЊЕЊА 193

Solvatochromism of newly synthesized potentially
biologically active derivatives carbohydrazones

Драгана Милисавић, Тања Околић, Савка Јанковић
СИНТЕЗА КАДМИЈУМ СУЛФИДА КАО МАТЕРИЈАЛА
ЗА СОЛАРНЕ ЋЕЛИЈЕ И ЊЕГОВА КАРАКТЕРИЗАЦИЈА..... 207
Synthesis of cadmium sulfide as a material
for solar cells and its characterization

*Dragana Dimitrijević Jovanović, Predrag Živković,
Jelena Janevski, Gordana Stefanović, Mirko Dobrnjac*
INFLUENCE OF GREEN ROOFS
ON RUNOFF WATER QUALITY 215
Утицај зеленог крова на квалитет воде у површинском отицају

*Dejan Kojić, Gordana Marković, Jelena Pavličević,
Nada Lazić, Pero Dugić, Vojislav Aleksić,
Ljiljana Tanasić, Jaroslava Budinski Simendić*
STRUKTURIRANJE ELASTOMERNIH МАТЕРИЈАЛА
ЗА ЕКОЛОШКИ ПРИХВАТЛЈИВЕ ПНЕУМАТИКЕ 229
Structuring of elastomeric materials for eco-friendly tyres

Боривоје Милошевић, Слободан Обрадовић, Никола Давидовић
НАНОТЕХНОЛОШКА РЕВОЛУЦИЈА ШАЉБЕ
БИНАРНО РАЧУНАЊЕ У ЛЕГЕНДУ 239
Nanotechnology revolution sent binary calculation to the legend

*Борислав Симендић, Весна Петровић, Татјана Божовић,
Невена Вукић, Весна Теофиловић, Тамара Ерџег*
УТИЦАЈ СТРУКТУРЕ ПОЛИМЕРНИХ МАТЕРИЈАЛА
НА МОГУЋНОСТ УСПОРАВАЊА ГОРЕЊА 257
The influence of polymer materials structure
on the possibility of flame inhibition

*Branko Drljača, Svetislav Savović, Aco Janićijević,
Slavica Jovanović, Dragoljub Mirjanić*
FREQUENCY RESPONSE AND BANDWIDTH
OF LOW-NUMERICAL APERTURE STEP-INDEX PLASTIC
OPTICAL FIBER OBTAINED BY SOLVING
THE TIME-DEPENDENT POWER FLOW EQUATION 269
Фреквентни одзив и пропусни опсег пластичног
оптичког влакна са степенастим индексом преламања

и малом нумеричком апертуром добијен решавањем
временски-зависне једначине протока снаге

Адриана Арбутина, Ребека Рудолф,

Валентина Веселиновић, Мирјана Умићевић Давидовић,

Маријана Араповић Савић, Владан Мирјанић

ПОБОЉШАЊЕ ОСОБИНА ОРТОДОНТСКИХ БРАВИЦА
ПРИМЈЕНОМ НАНОТЕХНОЛОГИЈЕ И НАНОЧЕСТИЦА 277

Improving the properties of orthodontic brackets
by the application of nanotechnology and nanoparticles

Branislava Petronijević, Aleksandra Maletin, Ivan Šarčev

TABLE TOP CERAMIC RESTAURATION – a case report..... 289

Табле топ керамичке реставрације – приказ случаја

Ирена Кузмановић Радман, Александра Ђери,

Рената Јосиповић, Наташа Кнежевић, Адријана Арбутина,

Владан Мирјанић, Ђорђе Мирјанић

УПОТРЕБА КОМПОЗИТНИХ МАТЕРИЈАЛА CHARISMA-e
I TETRIC EVOCERAM-a КОД РЕКОНСТРУКЦИЈЕ ЗУБА 299

Use of the composite material charisma
and tetric evoceram in reconstruction of the teeth

Ирена Кузмановић Радман, Александра Ђери,

Рената Јосиповић, Адриана Арбутина,

Љиљана Амиџић, Владан Мирјанић

ДЕЈСТВО ПРЕПАРАТА НА БАЗИ $\text{Ca}(\text{OH})_2$ НА ПУЛПУ 307

The effect of $\text{Ca}(\text{OH})_2$ -based preparations on the pulp

Мирослав Малиновић

МОГУЋНОСТИ ДОКУМЕНТОВАЊА АРХИТЕКТУРЕ

ИСТОРИЈСКИХ ГРАЂЕВИНА КОРИШЋЕЊЕМ

ЗД СКЕНЕРА И ЗД ШТАМПАЧА 319

The possibilities of documenting architecture of historical buildings
using 3D scanners and 3D printers

Милош Марковић, Мирко Добрњац, Сања Добрњац

СОЛАРНА МЈЕРНА СТАНИЦА ЗА ИСПИТИВАЊЕ

ТЕРМАЛНИХ ПРИЈЕМНИКА СОЛАРНЕ ЕНЕРГИЈЕ..... 331

The solar measurement station for examination
of the thermal receiver for solar energy

*Мирјана Умићевић Давидовић, Адриана Арбутина,
Маријана Араповић Савић, Валентина Веселиновић, Ребека Рудолф*
ПРИМЈЕНА НАНОТЕХНОЛОГИЈЕ И НАНОМАТЕРИЈАЛА
У УНАПРЕЂЕЊУ КАРАКТЕРИСТИКА ОРТОДОНТСКИХ ЖИЦА 343
Application of nanotechnology and nanomaterials in improving
characteristics of orthodontic wires

*Наташа Тртић, Тијана Адамовић, Радмила Арбутина,
Валентина Веселиновић, Жељка Којић*
АНТИМИКРОБНА СРЕДСТВА
У ТЕРАПИЈИ ОБОЉЕЊА УСНЕ ДУПЉЕ..... 355
Antimicrobial agents in the treatment of oral cavity disease

*Наташа Тртић, Валентина Веселиновић, Ребека Рудолф,
Радмила Арбутина, Саша Марин, Жељка Којић*
АНТИМИКРОБНА И ДИЈАГНОСТИЧКА ПРИМЈЕНА
НАНОЧЕСТИЦА ЗЛАТА У СТОМАТОЛОГИЈИ 365
Antimicrobial and diagnostic application
of gold nanoparticles in dentistry

Наташа Бубић Пајић, Биљана Гатарић, Анђелка Рачић
THE ROLE OF SURFACTANT ADDITION ON DISSOLUTION
PROPERTIES OF CARBAMAZEPINE TABLETS 377
Утицај присуства сурфактанта на брзину растварања
карбамазепина из таблета

Огњенка Јанковић, Радмила Арбутина, Рената Јосиповић, Игор Ђукић
KALCIJUM ALUMINATNI CEMENTI,
SVOJSTVA I BIOMEDICINSKA PRIMJENA 387
Calcium aluminate cements, properties
and biomedical applications

*Радмила Арбутина, Наташа Тртић,
Огњенка Јанковић, Валентина Веселиновић*
DENTALNE EROZIJE 405
Dental erosions

Саша Мићин
ПРИМЈЕНА ЕЛЕКТРОХЕМИЈСКИХ МЕТОДА
У ФОРЕНЗИЧКЕ СВРХЕ 411
Application electrochemistry methods in forensic

Тијана Адамовић, Наташа Тртић, Верица Павлић, Јована Ловрић
ПРОБИОТИЦИ У СТОМАТОЛОГИЈИ 427
Probiotics in dentistry

*Валентина Веселиновић, Ребека Рудолф,
Наташа Тртић, Верица Павлић*
МОДИФИКАЦИЈА МЕКИХ МАТЕРИЈАЛА ЗА ПОДЛАГАЊЕ
БАЗЕ ПРОТЕЗЕ НАНОЧЕСТИЦАМА
У САВРЕМЕНОЈ ТЕРАПИЈИ ПРОТЕЗНОГ СТОМАТИТИСА 435
Modification of soft-lining denture materials with nanoparticles
in contemporary therapy of denture stomatitis

*Валентина Веселиновић, Ребека Рудолф, Наташа Тртић,
Верица Павлић, Александра Чауровић*
НАНОМОДИФИКОВАНИ АКРИЛАТНИ МАТЕРИЈАЛИ
ЗА БАЗУ ПРОТЕЗЕ СА АНТИМИКРОБНИМ ДЈЕЛОВАЊЕМ -
- МОГУЋНОСТИ И ОГРАНИЧЕЊА 447
Nano-modified denture base acrylic materials with antimicrobial
properties – possibilities and limitation

Вељко Ђукић, Љиљана Вујаковић
ИНДИКАТОРИ КВАЛИТЕТА ВОДЕ РИЈЕКЕ НЕРЕТВЕ
У ФУНКЦИЈИ ОЧУВАЊА ФЛОРЕ И ФАУНЕ 461
Quality indicators of neretva river in the purpose
of conservation of flora and fauna

Vesna Matić, Mirjana Dragoljić, Ljiljana Simurdić
VALIDACIЈА METODE ZA IDENTIFIKACIЈU KANABISA
TEHNIKOM TANKOSLOЈNE HROMATOGRAFIЈE 479
Validation of method for kanabis identification
using thin layer chromatography technique

*Војкан Зорић, Весна Петровић, Борислав Симендић,
Томислав Јовановић, Милосав Стојановић*
ФИЗИЧКО-ХЕМИЈСКИ МЕТОДИ ИСПИТИВАЊА
МАТЕРИЈАЛА ПРИ ЕКСПЕРТИЗИ ПОЖАРА 489
Physical and chemical methods
for materials testing in fire expertise

Зорислава Бајић, Тања Шобот, Ђорђе Бајић, Никола Шобот
НАНОМАТЕРИЈАЛИ И ОКСИДАТИВНИ СТРЕС 499
Nanomaterials and oxidative stress

- Барбара Станимировић, Дејан Пејућ,
Јелена Мрђа, Драги Станимировић*
СЕРУМСКИ КАЛПРОТЕКТИН-НОВИ МАРКЕР
ИНФЛАМАЦИЈЕ КОД ДЈЕЦЕ СА ЈУВЕНИЛНИМ
ИДИОПАТСКИМ АРТРИТИСОМ..... 511
Serum calprotectin-a novel marker of inflammation
in children with juvenile idiopathic arthritis
- Milan Šljivić, Dejan Đurđević, Nataša Šljivić, Jovica Ilić*
POSSIBILITIES OF ADDITIVE MANUFACTURING
FOR 3D PRINTING IN MEDICINE: A CASE STUDY IN
MAXILLOFACIAL SURGICAL PLANNING 519
Могућности адитивне производње за 3Д штампање у медицини:
случај планирања операције у максилофационалној хирургији
- Драгана Грујић, Александар Савић, Љиљана Топалић Тривуновић,
Маја Чича, Младен Станчић, Бранко Нерал*
УТИЦАЈ АНТИМИКРОБНЕ ШТАМПЕ
НА СОРПЦИЈСКА СВОЈСТВА ПЛЕТЕНИНА 531
The influence of antimicrobial printing
on sorption properties of knitted fabrics
- Matavulj Milan, Karaman Maja, Lolić Svyetlana,
Matavulj Filip, Gassner Friedrich, Molitoris Hans Peter*
SUSTAINABLE, ENVIRONMENTALLY FRIENDLY PACKAGING
BASED ON BIOSYNTHETIC POLY-HYDROXYALKANOATES..... 543
Одржива, еколошка пластична амбалажа
на бази биосинтетичких поли-хидроксиалканоата
- Predrag Dašić, Dragoljub Lj. Mirjanić*
OSNOVNA SVOJSTVA I PRIMENE GRAFENA 557
Basic properties and applications of graphene

FREQUENCY RESPONSE AND BANDWIDTH OF LOW-NUMERICAL APERTURE STEP-INDEX PLASTIC OPTICAL FIBER OBTAINED BY SOLVING THE TIME-DEPENDENT POWER FLOW EQUATION

Branko Drljača¹, Svetislav Savović², Aco Janićijević³, Slavica Jovanović¹, Dragoljub Mirjanić⁴

¹Univerzitet u Prištini, Prirodno-matematički fakultet, Kosovska Mitrovica, Srbija

²Univerzitet u Kragujevcu, Prirodno-matematički fakultet, Beograd, Srbija

³Univerzitet u Beogradu, Tehnološko-metalurški fakultet, Beograd, Srbija

⁴Akademija nauka i umjetnosti Republike Srpske

Abstract: Analytical and numerical solution of the time-dependent power flow equation was used to calculate the frequency response and bandwidth of low numerical aperture step-index plastic optical fiber – Mitsubishi MH4001 in addition to mode coupling and mode-dependent attenuation. This optical fiber was excited with Gaussian-like light source with large angular width. The frequency response and bandwidth were calculated for different fiber lengths and good agreement was obtained between analytical and numerical solutions.

Key words: Plastic optical fiber, transfer characteristics, power flow equation.

1. INTRODUCTION

Past few decades brought significant growth in the amount of transferred data in overseas, long-distance and short-distance communication. For the last ten years there was special interest for high-performance short-distance communication, such as local-area networks (LANs), multi-node bus networks plastic or digital car and airplane networks. For this purpose plastic optical fibers (POFs) are often considered as best choice [1-4]. This is based upon their low cost, ease of manipulation due to their large core and high bandwidth over short distances.

When compared to systems based upon glass optical fiber or copper wire, systems based upon POFs are much more affordable in total. With a fiber diameter of 1 millimeter, and a core diameter of 980 μm (for most applications) cutting and treating of POF's ends is done with ease. Furthermore large core diameter allows plastic optical fibers to be paired with light sources of higher numerical aperture (LED sources, for example) using low-precision plastic couplers. This, in total, results in inexpensive but robust systems that are easy to interconnect. Bandwidth of typical step-index optical fiber (SI POF) is higher than with copper wire systems and approximately is 100 MHz over 100 m [5]. Over the last years bit rates over 1000 Mbit/s over 50 m have been realized with special transmission schemes

(equalizing, OFDM) and bit rates of about 200 Mbit/s over 50 m can be achieved without any additional measures.

From everything stated it is clear that most important transmission characteristics of SI POF, such as frequency response and bandwidth, have most significant role in their further development. Frequency response (and consequently) bandwidth of multimode SI POFs depend strongly on the mode-dependent attenuation, modal dispersion and the rate of mode coupling. In order to examine influence of the width of the input beam to frequency response and bandwidth we calculated frequency response and bandwidth using time-dependent power flow equation and compared obtained results with available results for the same fiber [6].

This paper is organized as follows. After introduction, chapter 2 deals with mathematical model based upon time-dependent power flow equation, developed by Gloge [7]. Using the time-dependent power flow equation we have obtained frequency response and bandwidth of SI POF with low numerical aperture in addition to mode coupling and mode-dependent attenuation. Further, comparison of results obtained by analytical and numerical solution is presented in chapter 3. At the end conclusion is presented in chapter 4.

2. TIME-DEPENDENT POWER FLOW EQUATION

2.1. Analytical solution

Time-dependent power flow equation, derived by Gloge, can be written as [7]:

$$\frac{\partial P(\theta, z, t)}{\partial z} + \frac{\partial t}{\partial z} \frac{\partial P(\theta, z, t)}{\partial t} = -\alpha(\theta)P(\theta, z, t) + \frac{1}{\theta} \frac{\partial}{\partial \theta} \left[\theta D(\theta) \frac{\partial P(\theta, z, t)}{\partial \theta} \right] \quad (1)$$

where $P(\theta, z, t)$ is power distribution over angle θ measured with respect to fiber axis, space z and time t ; $\alpha(\theta)$ is mode-dependent attenuation; $\partial t/\partial z$ is mode delay per unit length; and $D(\theta)$ is the mode-dependent coupling coefficient. Mode-dependent attenuation can be written in the form $\alpha(\theta) = \alpha_0 + A\theta^2 + \dots$ where term α_0 represents loss common to all modes and it can be accounted for by multiplying the end-solution by $e^{-\alpha_0 z}$ [7]. The term $A\theta^2$ is more important since it describes the losses at core-cladding boundary. For that reason, when solving (1), only the term $A\theta^2$ is to be considered as the most dominant of the higher order modes [8]. Coupling coefficient $D(\theta)$ is, as it is stated, also mode-dependent [9], but mode-independent coupling constant D has also been used frequently by other authors [7,10-11]. If coupling constant D is used instead of coupling coefficient $D(\theta)$ equation (1) can be written in the following form [7]:

$$\frac{\partial P(\theta, z, t)}{\partial z} = -A\theta^2 P(\theta, z, t) - \frac{n}{2c} \theta^2 \frac{\partial P(\theta, z, t)}{\partial t} + \frac{D}{\theta} \frac{\partial}{\partial \theta} \left(\theta \frac{\partial P(\theta, z, t)}{\partial \theta} \right). \quad (2)$$

With the help of Laplace transformation time-dependent equation (2) is transformed into time-independent equation [7]:

$$\frac{\partial p}{\partial z} = -A\sigma^2\theta^2 p + \frac{D}{\theta} \frac{\partial}{\partial \theta} (\theta \frac{\partial p}{\partial \theta}). \quad (3)$$

Using time-independent power flow equation (3) analytical solution for impulse response can be obtained [7]. Two cases are differed – for short and for long fibers. For short fibers ($z \ll 1/(2(AD)^{1/2})$), solution for impulse response is:

$$Q(z,t) = \frac{2c\pi}{nz(1+\gamma_\infty z)} \exp(-2ct/n\Theta_0^2 z), \quad (4)$$

while in case of long fibers ($z \gg 1/(2(AD)^{1/2})$), solution has the following form:

$$Q(z,t) = \Theta_0^2 \sqrt{\frac{\pi}{Tt}} \left(\frac{t}{\gamma_\infty z T} + \frac{1}{2} \right)^{-1} \exp\left(-\frac{\gamma_\infty^2 z^2 T}{4t} - \frac{t}{T} \right). \quad (5)$$

After obtaining impulse response, frequency response is obtained by applying Fourier transform to the impulse response:

$$H(f) = \int_{-\infty}^{\infty} Q(t) \exp(2\pi ift) dt. \quad (6)$$

After obtaining frequency response, -3dB bandwidth, for different lengths, is easily obtained by selecting frequencies for which frequency response has 50% drop for given length.

2.2. Numerical solution

In order to solve time-dependent power flow equation numerically we start from equation (1). Same as with analytical solution, coupling coefficient is assumed to be constant – D and for mode-dependent attenuation term $A\theta^2$ is used. When so, equation (1) can be rewritten as (2) and after applying the Fourier transform:

$$p(\theta, z, \omega) = \int_{-\infty}^{\infty} P(\theta, z, t) e^{-j\omega t} dt \quad (7)$$

the time-dependent equation (2) transforms into (8):

$$\frac{\partial p(\theta, z, \omega)}{\partial z} = -\left[A\theta^2 + j\omega \frac{n}{2c} \theta^2 \right] p(\theta, z, \omega) + \frac{D}{\theta} \frac{\partial p(\theta, z, \omega)}{\partial \theta} + D(\theta \frac{\partial^2 p(\theta, z, \omega)}{\partial \theta^2}) \quad (8)$$

where $\omega = 2\pi f$ is the angular frequency.

The boundary conditions are:

$$p(\theta_c, z, \omega) = 0, \quad D \frac{\partial p(\theta, z, \omega)}{\partial \theta} \Big|_{\theta=0} = 0, \quad (9)$$

where θ_c is the critical angle. The first condition implies that modes with infinitely large loss do not transfer any power; the second condition implies that mode coupling is limited to modes travelling with the angle $\theta > 0$.

Since $p(\theta, z, \omega)$ is complex we therefore separate $p(\theta, z, \omega)$ into its real and imaginary parts, $p = p^r + jp^i$ and we rewrite equation (8) as the system of simultaneous differential equations:

$$\frac{\partial p^r}{\partial z} = -A\theta^2 p^r + \frac{D}{\theta} \frac{\partial p^r}{\partial \theta} + D \frac{\partial^2 p^r}{\partial \theta^2} + \omega \frac{n}{2c} \theta^2 p^i \quad (10)$$

$$\frac{\partial p^i}{\partial z} = -A\theta^2 p^i + \frac{D}{\theta} \frac{\partial p^i}{\partial \theta} + D \frac{\partial^2 p^i}{\partial \theta^2} - \omega \frac{n}{2c} \theta^2 p^r$$

Simultaneous solving of equations (10) gives us p^r and p^i , and frequency response at distance z from input end of the fiber is calculated as:

$$H(z, \omega) = \frac{2\pi \int_0^{\theta_c} \theta [p^r(\theta, z, \omega) + jp^i(\theta, z, \omega)] d\theta}{2\pi \int_0^{\theta_c} \theta [p^r(\theta, 0, \omega) + jp^i(\theta, 0, \omega)] d\theta} \quad (11)$$

After separating the power flow equation (8) into two simultaneous equations (10), we solved the latter (10) by explicit finite difference method (EFDM). Using central difference scheme for derivatives $\partial p(\theta, z, \omega) / \partial \theta$ and $\partial^2 p(\theta, z, \omega) / \partial \theta^2$ [12-14]:

$$\left(\frac{\partial p(\theta, z, \omega)}{\partial \theta} \right)_{k,l} = \frac{p_{k+1,l} - p_{k-1,l}}{2\Delta\theta} + O(\Delta\theta)^2 \quad (12)$$

$$\left(\frac{\partial^2 p(\theta, z, \omega)}{\partial \theta^2} \right)_{k,l} = \frac{p_{k+1,l} - 2p_{k,l} + p_{k-1,l}}{(\Delta\theta)^2} + O(\Delta\theta)^2$$

and using the forward difference scheme for the derivative $\partial p(\theta, z, \omega) / \partial z$:

$$\left(\frac{\partial p(\theta, z, \omega)}{\partial z} \right)_{k,l} = \frac{p_{k,l+1} - p_{k,l}}{\Delta z} + O(\Delta z) \quad (13)$$

equations (10) can be written in the form:

$$p_{k,l+1}^r = \left(\frac{\Delta z D}{\Delta \theta^2} - \frac{\Delta z D}{2\theta_k \Delta \theta} \right) p_{k-1,l}^r + \left(1 - \frac{2\Delta z D}{\Delta \theta^2} - \Delta z A \theta_k^2 \right) p_{k,l}^r + \left(\frac{\Delta z D}{2\theta_k \Delta \theta} + \frac{\Delta z D}{\Delta \theta^2} \right) p_{k+1,l}^r + \frac{\omega n \Delta z}{2c} \theta_k^2 p_{k,l}^i \quad (14)$$

and

$$p_{k,l+1}^i = \left(\frac{\Delta z D}{\Delta \theta^2} - \frac{\Delta z D}{2\theta_k \Delta \theta} \right) p_{k-1,l}^i + \left(1 - \frac{2\Delta z D}{\Delta \theta^2} - \Delta z A \theta_k^2 \right) p_{k,l}^i + \left(\frac{\Delta z D}{2\theta_k \Delta \theta} + \frac{\Delta z D}{\Delta \theta^2} \right) p_{k+1,l}^i - \frac{cn\Delta z}{2c} \theta_k^2 p_{k,l}^r \quad (15)$$

Boundary conditions (9) now become:

$$\begin{aligned} p_{N,l}^r &= 0, \quad p_{N,l}^i = 0 \quad \text{and} \\ p_{0,l}^r &= p_{1,l}^r, \quad p_{0,l}^i = p_{1,l}^i \end{aligned} \quad (16)$$

where $N = \theta_c / \Delta \theta$ is the grid size in the θ direction. In order to prevent the problem of singularity at grid points $\theta = 0$, the following relation is used [14]:

$$\lim_{\theta \rightarrow 0} \frac{1}{\theta} \frac{\partial}{\partial \theta} \left(\theta \frac{\partial p}{\partial \theta} \right) = 2 \frac{\partial^2 p}{\partial \theta^2} \Big|_{\theta=0} \quad (17)$$

In our previous work [6], we have determined frequency response and bandwidth of the low numerical aperture (NA=0.3) SI POF for a Dirac impulse in time and a laser mode distribution with the $\theta_0 = 0^\circ$ (central launch) and FWHM = 7.5° in the parallel plane. In this work, using Gloge's analytical solution of (2) and our numerical results for (2) we calculate the frequency response and bandwidth of same SI POFs for a Dirac impulse in time and a laser mode distribution with the $\theta_0 = 0^\circ$ and FWHM = 16° in the parallel plane and compare obtained analytical to numerical results.

3. ANALYTICAL AND NUMERICAL RESULTS

In this section we present results for frequency response and bandwidth of the tested MH4001 ESKA Mitsubishi Rayon fiber (MH fiber). The fiber's dimensions have following values. Core and clad diameters are $d_{core} = 980 \mu\text{m}$ and $d_{clad} = 1000 \mu\text{m}$, respectively. Numerical aperture is NA=0.3, core refractive index is $n = 1.49$, and critical angle is $\theta_c = 11.7^\circ$ (measured inside the fiber) or $\theta_c = 17.6^\circ$ (measured in air). The number of modes in this step-index multimode plastic optical fiber at $\lambda = 660 \text{ nm}$ is $N = 2\pi^2 a^2 (\text{NA})^2 / \lambda^2 \approx 1.02 \times 10^6$, where a is radius of the fiber core. Since number of modes is large modes may be represented by a continuum as required for application of equation (2).

In recently published works [6, 15], coupling coefficient D and loss coefficient $\alpha(\theta)$ ($\alpha(\theta) \approx \alpha_0 + A\theta^2$) for this fiber were calculated as $D = 1.62 \times 10^{-3} \text{ rad}^2/\text{m}$ and $\alpha_0 = 0.10793 \text{ 1/m}$ and $A = 0.29166 \text{ (rad}^2 \text{ m)}^{-1}$. We used following lengths of the MH4001 fiber in our calculations: 3 m, 5 m, 10 m, 15 m, 25 m, 50 m and 100 m. Centrally launched beam ($\theta_0 = 0^\circ$) with Gaussian like distribution with FWHM = 16° in the parallel plane were used for the input. In Figure 1 analytical and numerical

results for the frequency response for different fiber lengths of the MH fiber are shown and good match is obtained.

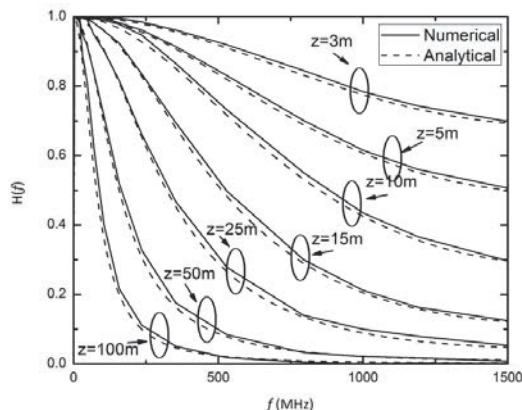


Figure 1. Analytical (dashed line) and numerical (solid line) results for the frequency response for MH fiber, for different fiber lengths.

A pronounced drop at low frequencies is apparent for long fiber lengths. Fig. 2 shows analytically and numerically obtained bandwidth for MH4001 fiber. Bandwidth is shown in log-log scale versus length of the fiber. Slightly lower values of bandwidth are observed than in the case of the narrower beam with $\text{FWHM}=7.5^\circ$ previously investigated by [6]. This is more pronounced for shorter fiber lengths and it is due to the excitation of higher order modes when fiber is excited with wider input light beam. This happens since higher modes experience higher loss at shorter fiber lengths and it is known that dominant process at shorter fiber lengths is mode-dependent attenuation. With increasing fiber length mode coupling begins to significantly influence fibers frequency response and bandwidth and becomes dominant process since it tends to equalize speeds of different modes. In that case influence of the width of the launched beam on the fiber bandwidth becomes negligible since process of mode coupling at those lengths is either finished or came near end.

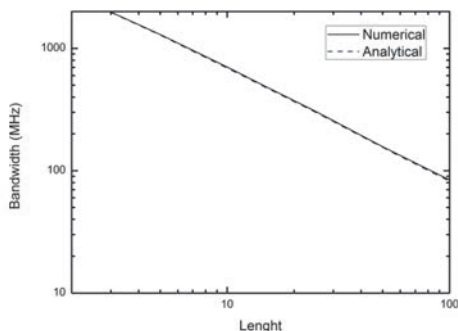


Figure 2. Analytical (dashed line) and numerical (solid line) results for the bandwidth for MH fiber, for different fiber lengths.

4. CONCLUSION

Analytical and numerical solution of time-dependent power flow equation were employed to calculate frequency response and bandwidth of MH4001 step-index optical fiber excited with wide Gaussian like input beam with FWHM=16°. Results obtained by analytical and numerical solutions show good match. Moreover if our results are compared to previously obtained results for the same fiber, but narrower input beam (FWHM=7.5°) [6], expected results are obtained. Namely, frequency response (and consequently bandwidth) obtained for the input light beam with FWHM=16° show slightly lower values than in the case of the narrower beam with FWHM=7.5° previously investigated by [6]. This is more pronounced for shorter fiber lengths where mode-dependent attenuation is dominant process. When fiber length is increased mode coupling begins to significantly influence fibers transfer characteristics that is frequency response and bandwidth by tending to equalize speed of different modes. That is why influence of the width of the launched beam on the fiber's frequency response and bandwidth, is more pronounced at shorter fiber lengths [16], which leads to lower values of frequency response and bandwidth and becomes negligible at longer fiber lengths leading to approximately same values of frequency response and bandwidth.

Acknowledgment

The work described in this paper was supported by the grant from Serbian Ministry of Education, Science and Technological Development (Project No. 171011).

5. LITERATURE

[1] Golowich S E, White W, Reed W A & Knudsen E J. *Lightwave Technol. Volume 21*, (2003), 111-121.

[2] Koeppen C, Shi R F, Chen W D & Garito A F J. „Properties of plastic optical fibers,” *Opt. Soc. Am. B, Volume 15*, (1998), 727-739

[3] Ishigure T, Kano M & Koike Y, „Which is a more serious factor to the bandwidth of GI POF: differential mode attenuation or mode coupling?”, *J. Lightwave Technol. Volume 18*, (2000), 959-965.

[4] Green P E Jr. „Optical networking update”, *IEEE J. Sel. Areas Commun. Volume 14*, (1996), 764-779.

[5] Koike Y, *Fundamentals of Plastic Optical Fibers*, Wiley-VCH, Weinheim, Germany, (2015).

[6] Svetislav Savović, Branko Drljača, Milan S. Kovačević, Alexandar Djordjević, Jovan S. Bajić, Dragan Z. Stupar & Grzegorz Stepniak, „Frequency response and bandwidth in low-numerical-aperture step-index plastic optical fibers”, *Applied Optics, Volume 53*, No. 28, (2014), 6999–7003.

[7] Gloge D, „Impulse Response of Clad Optical Multimode Fibers”, *Bell Syst.*

Tech. J. Volume 52, (1973), 801-816.

[8] Gloge D, „Optical power flow in multimode fibers”, *Bell Syst. Tech. J. Volume 51*, (1972), 1767-1783.

[9] Olshansky R., „Mode coupling effects in graded-index optical fibers”, *Appl. Opt. Volume 14*, (1975), 935–945.

[10] Drljača B, Djordjevich A & Savović S, „Frequency response in step-index plastic optical fibers obtained by numerical solution of the time-dependent power flow equation”, *Optics and Laser Technology, Volume 44 no. 6*, (2012), 1808-1812.

[11] Drljača B, Savović S & Djordjevich A, “Calculation of the Impulse Response of Step-Index Plastic Optical Fibers Using the Time-Dependent Power Flow Equation”, *Acta Phys. Pol. A 116*, (2009), 658–660.

[12] Savović S & Djordjevich A, „Influence of numerical aperture on mode coupling in step index plastic optical fibers” *Appl. Opt. Volume 43*, (2004), 5542–5546.

[13] Djordjevich A & Savović S, „Investigation of mode coupling in step index plastic optical fibers using the power flow equation”, *IEEE Photon. Technol. Lett. 12*, (2000), 1489–1491.

[14] Anderson J. D, *Computational Fluid Dynamics*, McGraw-Hill, New York, USA, (1995).

[15] Savović S, Kovačević M. S, Djordjevich A, Bajić J. S, Stupar D. Z & Stepniak G, “Mode coupling in low NA plastic optical fibers,” *Opt. Laser Technol. Volume 60*, (2014), 85-89.

[16] Savović S, Djordjevich A, Tse P. W, Zubia J, Mateo J & Losada M. A, „Determination of the width of the output angular power distribution in step index multimode optical fibers,” *J. Opt. 12*, 115405, (2010), 5pp.

Б. Дрљача, С. Савовић, А. Јанићјевић, С. Јовановић, Д. Мирјанић

ФРЕКВЕНТНИ ОДЗИВ И ПРОПУСНИ ОПСЕГ ПЛАСТИЧНОГ ОПТИЧКОГ ВЛАКНА СА СТЕПЕНАСТИМ ИНДЕКСОМ ПРЕЛАМАЊА И МАЛОМ НУМЕРИЧКОМ АПЕРТУРОМ ДОБИЈЕН РЕШАВАЊЕМ ВРЕМЕНСКИ ЗАВИСНЕ ЈЕДНАЧИНЕ ПРОТОКА СНАГЕ

Апстракт: Коришћењем аналитичког и нумеричког решења временски-зависне једначине протока снаге израчунати су фреквентни одзив и пропусни опсег за пластично оптичко влакно са степенастим индексом преламања које има малу нумеричку апертуру – Mitsubishi МН4001 влакно, узимајући у обзир спрезање модова и модално слабење. На улазу у влакно убациван је светлосни сноп велике угаоне ширине, који има Гаусову расподелу. У раду је приказана зависност фреквентног одзива и пропусног опсега од дужине влакна и добијено је добро слагање између аналитичких и нумеричких резултата.

Кључне ријечи: пластична оптичка влакна, преносне карактеристике, једначина протока снаге.

Contents

I. Introduction	3
Some introductory remarks from the Editors	5
II. Light propagation in POF	7
Molecular structure of optical polymers	9
Modal dispersion in the frequency domain	23
Temperature dependence of mode coupling	35
Coupling losses	47
Back scattering	57
III. Special types of POF	69
Tubular fibres	71
Active fibres	79
IV. Sensor applications	93
Gamma Radiation Induced Effects in Perfluorinated POFs	95
POF sensors in energy, oil and biotechnology areas	105
Optical power monitor with SI-POFs	123
V. Author biographies	133

© 2015 C.-A. Bunge, R. Kruglov

Herstellung und Verlag:

BoD – Books on Demand, Norderstedt

ISBN 978-3-7392-1499-3

Bibliografische Information der Deutschen Nationalbibliothek:

Die Deutsche Nationalbibliothek verzeichnet diese Publikation in der Deutschen Nationalbibliografie; detaillierte bibliografische Daten sind im Internet über <http://dnb.d-nb.de> abrufbar.

Temperature Dependence of Mode Coupling in Low-NA Plastic Optical Fibers

S. Savović,^{1,2,*} M. S. Kovačević,^{1,3} J. S. Bajić,⁴ D. Z. Stupar,⁴
A. Djordjevich,² M. Živanov,⁴ B. Drljača,⁵ A. Simović,¹ K. Oh³

¹*Faculty of Science, University of Kragujevac, R. Domanovića 12, Kragujevac, Serbia.*

²*City University of Hong Kong, 83 Tat Chee Avenue, Kowloon, Hong Kong, China.*

³*Institute of Physics and Applied Physics, Department of Physics, Yonsei University 134
Sinchon-dong, Seodaemun-gu, Seoul, South Korea.*

⁴*University of Novi Sad, Faculty of Technical Sciences, Serbia.*

⁵*Faculty of Science, University of Kosovska Mitrovica, Lale Ribara 29, Kosovska Mitrovica,
Serbia.*

* *Corresponding author: savovic@kg.ac.rs*

Using the power flow equation and experimental measurements, investigated in this article is the state of mode coupling in low NA (0.3) step-index (SI) plastic optical fibers under varied temperature. Numerical results obtained using the power flow equation agrees well with experimental measurements. It is found that elevated temperatures of low-NA SI plastic optical fibers strengthened mode coupling. These properties remained after a year, with the fiber being subjected to environmental temperature variations of more than 35 K. These thermally induced changes of the fiber properties are attributed to the increased intrinsic perturbation effects in the PMMA material at higher temperatures.

1. Introduction

The importance of plastic optical fibers (POFs) has grown tremendously over past decades. POFs are highly promising transmission media for short-range applications including in LANs, multi-node bus networks, sensors, power delivery systems, and light guides (as in toys, entertainment and medical devices). The attractiveness of POFs is chiefly due to their low cost, flexibility and ease of handling and interconnecting. However, their relatively large attenuation and modal dispersion limit the link length and transmission rate. The main types of POFs, their manufacturing and possible present and expected future applications have been reported

[1]. Much effort has been made in recent decades to mitigate the effect of limited bandwidth of SI-POFs [1,2]. Temperature variation as an avenue for additional improvements has been indicated by simulation [3] by showing that modal dispersion decreases as temperature is increased, leading to a bandwidth improvement. One should mention here that in reference [3] the simulations that concerned POFs were based on measurements for bulk PMMA and this is only a coarse approximation.

Ambient temperature can often affect structure of the POF material [4,5]. Intrinsic perturbation effects may also change with temperature [3,5] (these perturbations are by irregularities introduced predominantly during the fiber manufacturing process that resulted in microscopic bends, irregularity of the core-cladding boundary [6], and inconsistency of the refractive index). In spite of all fibers undergoing some degradation of optical transmission when exposed to heating, fiber-optic systems are nevertheless implemented in warm environments particularly as optical fiber sensors [5,7] and the influence of temperature may be considerable. Changes optical fibers undergo with temperature fluctuation have been investigated [3,5,8,9].

Transmission characteristics of multimode SI optical fibers depend heavily upon the differential mode attenuation and rate of mode coupling. The latter represents power transfer from lower to higher-order modes caused by the above-mentioned intrinsic perturbation effects. Mode coupling reduces modal dispersion, leading to a bandwidth improvement in local area networks (LANs) [10]. On the other hand, it increases the amount of power radiated in fiber curves or bends [11–13], significantly changing the output-field properties and degrading the beam quality. These consequences are difficult to predict intuitively and have a particular importance for power delivery and sensory systems [10,14].

In order to determine the fiber length L_c where an equilibrium mode distribution (EMD) is achieved, one can analyze the change of the output angular power distribution as a function of fiber length for different launch angles [14]. Coupling length L_c is the fiber length after which all output angular power distributions take the disk-form regardless of the incidence angle. The shorter the length L_c , the earlier the bandwidth would switch from the functional dependence of z^{-1} to $z^{-1/2}$ (slower bandwidth decrease).

Output angular power distribution in the near and far fields of an optical fiber end has been studied extensively. Work has been reported using geometric optics (ray approximation) to investigate mode coupling and predict output-field patterns [16,17]. By employing the power flow equation [15, 18–21], these patterns have been predicted as a function of the launch conditions and fiber length. A key prerequisite for achieving this is the knowledge of the rate of mode coupling expressed in the form of the coupling coefficient D [18–20], which has been shown to correctly predict coupling effects observed in practice (e. g. [15]).

In this work, we use the Savović-Djordjević method [22] for determining the mode coupling coefficient D in a low-NA POF at temperatures ranging from 293.15 K to 353.15 K. This enabled us to solve the power flow equation numerically in order to examine the state of mode coupling in the fiber being analyzed at different temperatures. As a result, the coupling length L_c at which the EMD is achieved and the fiber length z_0 required for achieving the

steady-state mode distribution (SSD) are obtained for different fiber temperatures. These numerical results are verified experimentally.

2. Power flow equation

Gloge's power flow equation is [18]:

$$\frac{\partial P(\theta, z)}{\partial z} = -\alpha'(\theta)P(\theta, z) + \frac{D}{\theta} \frac{\partial}{\partial \theta} \left(\theta \frac{\partial P(\theta, z)}{\partial \theta} \right), \quad (1)$$

where $P(\theta, z)$ is the angular power distribution, z is distance from the input end of the fiber, θ is the propagation angle with respect to the core axis, D is the coupling coefficient assumed constant [10,13–15,19,20,23] and $\alpha'(\theta)$ is the modal attenuation. The boundary conditions are $P(\theta_c, z) = 0$, where θ_c is the critical angle of the fiber, and $D \left(\frac{\partial P}{\partial \theta} \right) = 0$ at $\theta = 0$. Condition $P(\theta_c, z) = 0$ implies that modes with infinitely high loss do not carry power. Condition $D \left(\frac{\partial P}{\partial \theta} \right) = 0$ at $\theta = 0$ indicates that the coupling is limited to the modes propagating with $\theta = 0$. Except near cutoff, the attenuation remains uniform $\alpha'(\theta) = \alpha'_0$ throughout the region of guided modes $0 \leq \theta \leq \theta_c$ [20,21] (it appears in the solution as the multiplication factor $\exp(-\alpha'_0 z)$ that also does not depend on θ). Therefore, $\alpha'(\theta)$ need not be accounted for when solving Eq. (1) for mode coupling and this equation reduces to [15]:

$$\frac{\partial P(\theta, z)}{\partial z} = \frac{D}{\theta} \frac{\partial P(\theta, z)}{\partial \theta} + D \frac{\partial^2 P(\theta, z)}{\partial \theta^2} \quad (2)$$

In order to obtain numerical solution of the power flow equation (2) we have used the explicit finite-difference method (EFDM) employed in our earlier works [13,15].

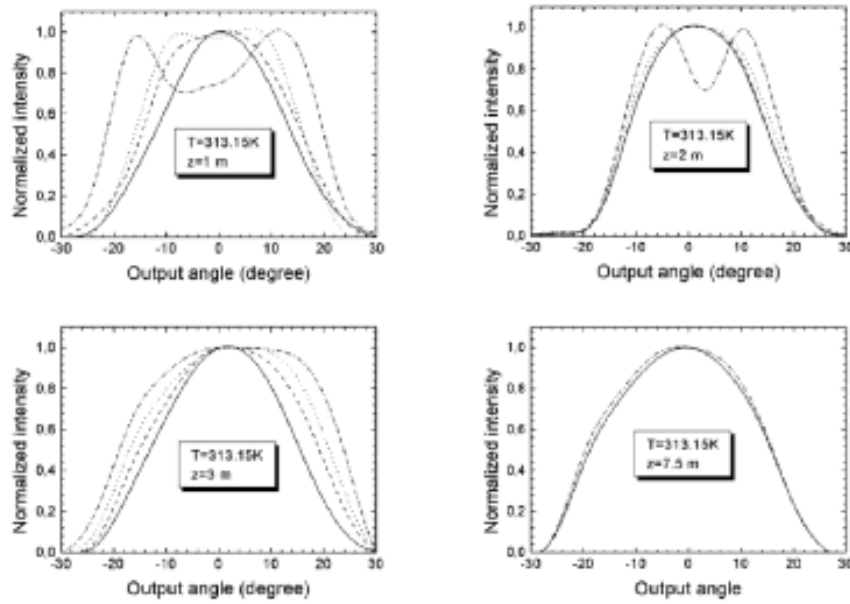


Fig. 3: Normalized **experimental** output angular power distribution at different locations along the MH4001 plastic optical fiber at $T = 313.15\text{K}$ for four Gaussian input angles $\theta_0 = 0^\circ$ (solid line), 5° (dashed line), 10° (dotted line) and 15° (dash-dotted line) at: (a) $z = 1\text{ m}$ (solid line); (b) $z = 2\text{ m}$ (dashed line); (c) $z = 3\text{ m}$ (dotted line) and (d) $z = 7.5\text{ m}$ (dash-dotted line).

0 at the input fiber end), producing the EMD in Figs. 3(c) and 4(c). The coupling continues further along the fiber beyond the L_c mark until all distributions' widths equalize and SSD is reached at length z_s in Figs. 3(d) and 4(d): $z_s = 7.5\text{ m}$. The maximum estimated relative error of determining the coupling coefficient $\Delta D/D$, coupling length $\Delta L_c/L_c$ and length at which a SSD is achieved $\Delta z_s/z_s$ is approximately 10%.

It can be seen from Table 1 that with increasing fiber temperature there is an increase of the coupling coefficient D , meaning that intrinsic perturbation effects in the fiber are stronger. With increasing fiber temperature the width of the output angular power distribution measured at a fixed fiber length increases too (Fig. 5). Consequently, the lengths L_c and z_s (Fig. 6) shorten.

We have obtained that with increasing temperature, there is a very small change of numerical aperture of the fiber (Fig. 7, left). Namely, measured numerical aperture of MH4001 fiber varies between $\text{NA} = 0.37$ and 0.38 , at temperatures between 293.15 K and 353.15 K , respectively. Thus, the influence of the change of the numerical aperture on temperature dependence of the coupling constant D can be excluded. One should mention here that measured numeri-

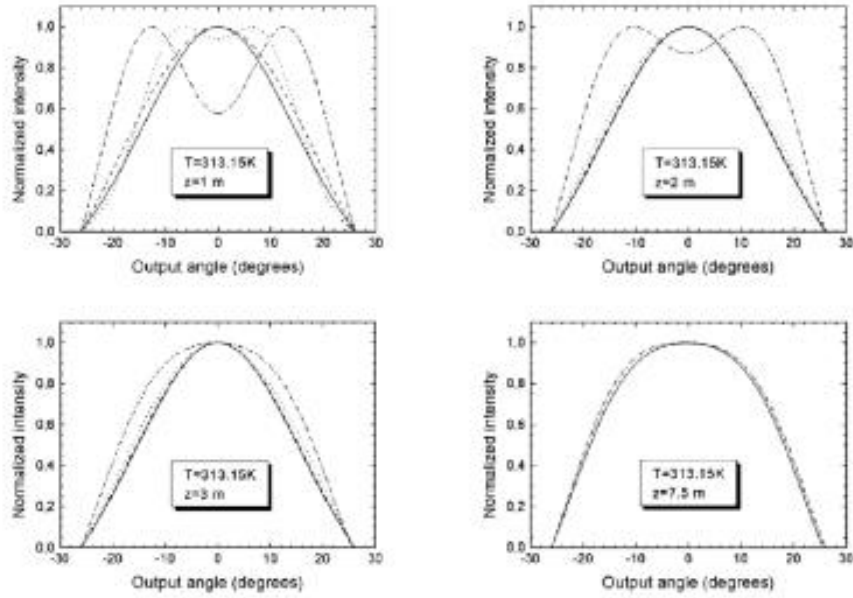


Fig. 4: Normalized **simulated** output angular power distribution at different locations along the MH4001 plastic optical fiber at $T = 313.15$ K for four Gaussian input angles $\theta_0 = 0^\circ$ (solid line), 5° (dashed line), 10° (dotted line) and 15° (dash-dotted line) at: (a) $z = 1$ m (solid line); (b) $z = 2$ m (dashed line); (c) $z = 3$ m (dotted line) and (d) $z = 7.5$ m (dash-dotted line).

Table 1: Fiber temperature T , coupling coefficient D , coupling length L_c for achieving the EMD and length z_s for achieving the SSD.

Temperature T [K]	D [rad ² /m]	L_c [m]	z_s [m]
293.15	1.62×10^{-3}	4.0	10.0
313.15	3.41×10^{-3}	3.0	7.5
333.15	4.53×10^{-3}	2.25	5.5
353.15	5.82×10^{-3}	1.5	4.0

cal aperture of $NA = 0.37$ at 293.15 K for MH4001 fiber differs from its theoretical numerical aperture of $NA=0.3$, due to the fact that this fiber is a double cladding fiber and not typical SI-POF [1].

We have also obtained that with increasing fiber temperature, there is a slight increase

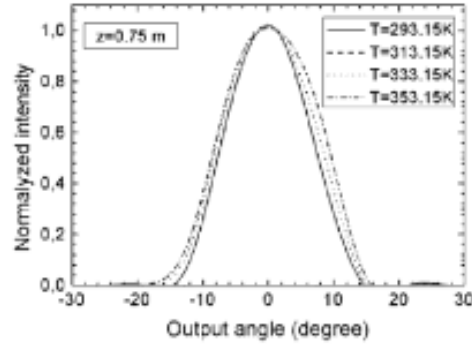


Fig. 5: Normalized experimental output angular power distribution along the MH4001 plastic optical fiber of length $z = 0.75$ m at different temperatures for centrally ($\theta = 0^\circ$) launched Gaussian beam.

of mode dependent attenuation coefficient (Fig. 7, right). This is in contrast with results reported by Chen et al. [8] for the MH4001 plastic optical fiber with higher numerical aperture of $NA=0.5$. They have obtained that there is a decrease of power loss with increasing fiber temperature.

One can see from Fig. 8 that the modal attenuation at a given temperature could be considered approximately constant with the propagation angle in the range $\theta = 0^\circ$ to $\theta \approx 18^\circ$, which enabled us to numerically solve the power flow equation in its simpler form (2) instead of solving the power flow equation (1).

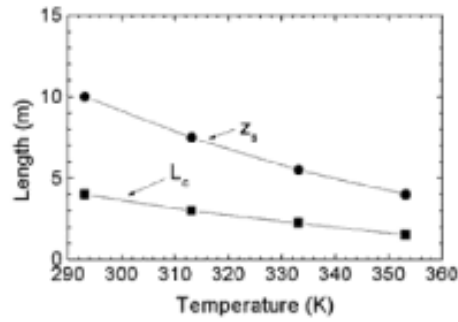


Fig. 6: Variation of the fiber's coupling length L_c for achieving the EMD and length z_0 for achieving the SSD with temperature for MH4001 plastic optical fiber.

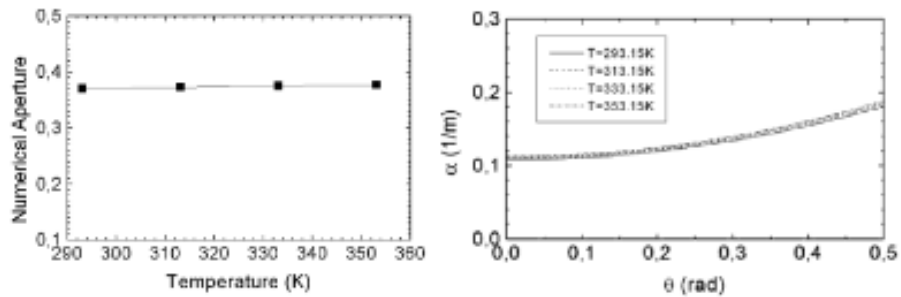


Fig. 7: Variation of the numerical aperture with temperature for MH4001 plastic optical fiber (left). Mode-dependent attenuation ($\alpha'(\theta)$) for MH4001 plastic optical fiber measured at different temperatures (right).

5. Conclusion

Using the power flow equation and experimental measurements, investigated in this article is the state of mode coupling in low-NA (0.3) step-index plastic optical fibers under varied temperature. Results are verified experimentally. It is found that elevated temperatures of low NA SI plastic optical fiber strengthened mode coupling. These properties remained after a year, with the fiber being subjected to environmental temperature variations of more than 35 K. The thermally induced changes of the fiber properties are attributed to the increased intrinsic perturbation effects in the fiber material. Stronger coupling shortens lengths L_c (for achieving the EMD) and z_p (for achieving the SSD). This also results in an increase of the measured bandwidth with increasing fiber temperature. Therefore, bandwidth can be altered by controlling fiber temperature and the results presented in this paper can be used to predict such change.

Acknowledgements

The work described in this paper was supported by the Strategic Research Grant of City University of Hong Kong (Project No. CityU 7004069) and by a grant from Serbian Ministry of Education, Science and Technological Development (Projects No. 171011 and III43008).

References

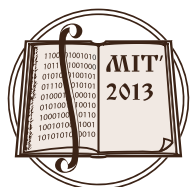
1. W. Daum, J. Krauser, P. E. Zamzow, O. Ziemann, POF-polymer optical fibers for data communications. Berlin: Springer; 2002.
2. N. Raptis, E. Grivas, E. Pikasis, and D. Syvridis, "Space-time block code based MIMO encoding for large core step index plastic optical fiber transmission systems," *Opt. Express* 19, 10336–10350 (2011).
3. M. Kovačević and A. Djordjević, "Variation of modal dispersion and bandwidth with temperature in PMMA based step-index polymer optical fibers," *J. Optoelectronics Advan. Mater.* 11, 1821–1825(2010).
4. L. Hoffmann, M. S. Müller, S. Krämer, M. Giebel, G. Schwotzer, T. Wieduwilt, "Applications of fibre optic temperature measurement," *Proc. Estonian Acad. Sci. Eng.* 13, 363–378 (2007).
5. T. Reinsch and J. Henniges, "Temperature dependent characterization of optical fibres for distributed temperature sensing in hot geothermal wells," arXiv:1206.1853v1 [physics.geo-ph] 8 Jun 2012.
6. C.-A. Bunge, R. Kruglov, H. Poisel, "Rayleigh and Mie Scattering in Polymer Optical Fibers," *J. of Lightwave Technol.*, Vol. 24, No. 8, pp. 3137-3146, 2006.
7. A. T. Moraleda, C. V. García, J. Zubia Zaballa and J. Arrue, "A "Temperature Sensor Based on a Polymer Optical Fiber Macro-Bend," *Sensors* 13, 13076-13089 (2013).

MIT 2013

Matematičke i informacione tehnologije

ZBORNİK RADOVA
KONFERENCIJE MIT 2013





**ZBORNIK RADOVA
KONFERENCIJE MIT 2013**

Zbornik radova konferencije MIT 2013

ISBN 978-86-80795-20-1 (PMF)

Urednik:

Dragan Aćimović

Radovi su prezentovani na konferenciji MIT 2013 u Vrnjačkoj Banji od 5. do 9. septembra i u Bečićima od 10. do 14. septembra 2013. godine.

Redakcija:

Jurij Ivanovič Šokin

Leonid Čubarov

Sofja Bejzelj

Hranislav Milošević

Dojčin Petković

Nataša Radenković

Aleksandar Valjarević

Dragan Aćimović

Grafička obrada:

Dragan Aćimović

Štampa:

Štamparija Ofsetpres, Kraljevo

Tiraž:

100 primeraka

Izdavači:



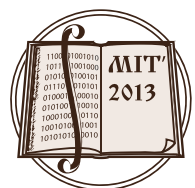
Prirodno matematički fakultet
Uiverziteta u Prištini
(Kosovska Mitrovica, Serbia)



Institute of Computational Technologies,
Siberian Branch of the Russian Academy of Sciences
(Novosibirsk, Russia)

Predsednik Organizacionog odbora:
prof. dr Hranislav Milošević

Beograd, 2014.



P R E D G O V O R

ZBORNIKU RADOVA KONFERENCIJE MIT 2013

Međunarodna konferencija MIT 2013 iz oblasti matematičkih, informacionih i telekomunikacionih nauka koja je održana u periodu od 5.09 - 14.09.2013. godine pokazala je da nauka i prava prijateljstva nemaju granice.

Po treći put u Srbiji je održana konferencija MIT, koja je istovremeno i 9 Konferencija za naše suorganizatore iz Rusije.

Kroz usmene, plenarne i sekcione prezentacije, te kroz poster prezentacije, pokazali smo da uspesno pratimo svetske naučne tokove iz matematičkih nauka, primenjene matematike i informatike.

Potvrdili su Srbi, Rusi i Kazahstanci, zajedno sa naucnicima iz 14 zemalja sveta da u nauci ne postoje granice i da je znanje osnov za sve dalje naučne saradnje i ostvarenja, koja imaju za cilj dobrobit čovečanstva.

Programski komitet MIT 2013
Organizacioni komitet MIT 2013

Dr Hranislav Milošević

Beograd, april 2014. godine

TABLE OF CONTENTS

- 15 *E. V. Amelina, S. K. Golushko*
MODELING AND CALCULATION OF STRESS-STRAIN STATE OF CIRCULAR PLATES, CIRCULAR AND ECCENTRIC RINGS
- 23 *E. V. Amelina, K. S. Voronkova, S. K. Golushko, A. V. Yurchenko, S. V. Nikolaev*
SIMULATION OF SHAPING OF THE EMBRYO PLANT CELLS AS ANISOTROPIC NONHOMOGENEOUS SHELL
- 28 *N. M. Andreeva*
THE AUTOMATION OF THE ANALYSIS OF THE TEST RESULTS WITH THE HELP OF THE CALCULATED SCRIPT OF MS EXCEL
- 37 *V. I. Anikina, S. V. Kapustina, A. Sh. Lyubanova*
ALGORITHMS OF RECOGNITION AND DETERMINATION OF PERCENTAGE PHASE CONSTITUTION IN ALLOYS
- 43 *K. K. Argunova, E. A. Bondarev, I. I. Rozhin*
MATHEMATICAL MODELLING OF HYDRATE FORMATION DURING NATURAL GAS PRODUCTION
- 51 *M. Artonovic, D. Nedic*
HOW TO LEARN A LINEAR FUNCTION USING GEOGEBRA MATHEMATICAL SOFTWARE
- 58 *E. A. Barakhtenko, D. V. Sokolov, V. A. Stennikov*
NEW RESULTS IN DEVELOPING OF ALGORITHMS INTENDED FOR PARAMETERS OPTIMIZATION OF HEAT SUPPLY SYSTEMS
- 67 *E. A. Barakhtenko, D. V. Sokolov, V. A. Stennikov*
AUTOMATING THE PROCESS OF SOFTWARE DEVELOPMENT FOR DESIGN AND RECONSTRUCTION OF HEAT SUPPLY SYSTEMS ON THE BASIS OF MODEL-DRIVEN DEVELOPMENT
- 75 *S. A. Beisel, H. Milosevic, A. D. Rychkov*
NUMERICAL MODELING OF TSUNAMI RUNUP USING METHOD OF LARGE PARTICLES
- 82 *E. F. Belyaev, P. N. Tsylev, I. N. Shchapova*
MATHEMATICAL MODELING FOR ELECTROMAGNETIC PROCESSES OF ELECTROMECHANICAL ENERGY CONVERTERS
- 89 *M. Bradic*
CONSTRUCTION OF FINITE CYCLIC GROUPS WITH FUZZY EQUALITIES
- 95 *S. Brsakoska*
ABOUT THE ACCORDANCE BETWEEN THE VEKUA DIFFERENTIAL EQUATION AND THE GENERALIZED LINEAR DIFFERENTIAL EQUATION
- 99 *F. Carbone, D. Dutykh, M. J. Dudley, F. Dias*
EXTREME WAVE RUN-UP ON A VERTICAL CLIFF
- 104 *A. A. Dekterev, A. V. Minakov, D. V. Platonov*
NUMERICAL INVESTIGATION OF SPATIAL UNSTEADY FLOWS IN HYDRAULIC TURBINES OF HIGH-HEAD POWER DEVELOPMENT
- 111 *D. Dimovski*
[n, ρ, m]-METRIC SPACES

- 116 *T. Djekic, I. Filipovic*
APPLICATION OF GEOGRAPHIC INFORMATION SYSTEM FOR CONTROLLING THE SOIL POLLUTION IN THE MUNICIPALITY VRBAS
- 123 *S. Djenic, A. Miletic, J. Mitic, V. Petkovic, V. Vasiljevic*
USE OF BLOGS IN E-LEARNING COURSE
- 128 *D. Djosic, R. Krneta, H. Milosevic, N. Kontrec, V. Petrovic*
THE RESULTS OF MOODLE PLATFORM APPLICATION IN REALIZATION OF TECHNICAL FUNDAMENTS OF INFORMATICS COURSE OF STUDY
- 134 *D. Djosic, C. Stefanovic, N. Kontrec, D. Stefanovic, S. Veljkovic, S. Maricic*
PERFORMANCE ANALYSIS OF DUAL MRC DIVERSITY SYSTEM OVER η - μ MULTIPATH FADING CHANNEL
- 140 *N. N. Dobretsov, V. A. Kikhtenko, V. V. Smirnov, D. L. Chubarov, L. B. Chubarov, Y. I. Shokin*
ON THE STATUS OF THE GROUND INFRASTRUCTURE FOR SATELLITE REMOTE SENSING FOR THE REGIONS OF SIBERIA AND THE FAR EAST OF RUSSIA
- 150 *B. Drljaca, S. Kuzmanovic, S. Savovic*
EXPLICIT FINITE DIFFERENCE METHOD FOR SOLVING POWER FLOW EQUATION WITH APPLICATIONS IN FIBER OPTICS MODELING
- 156 *I. Dundjerski, D. Matijevic, V. Dundjerski, V. Matijevic, D. Vukic*
COMPUTER OPTIMIZATION IN CHOOSING INTERNAL COMBUSTION ENGINE AND GEARBOX FOR GIVEN VEHICLE PERFORMANCE BY TRACTION DIAGRAM
- 164 *V. P. Fedotov*
PHYSICAL MODELS AND THE MATHEMATICAL MODELING OF THE COUPLED PROCESSES IN ENGINEERING SYSTEMS
- 174 *O. A. Fedotova*
REQUIREMENTS FOR AN INFORMATIONAL MODEL OF A SCIENTIFIC HERITAGE DIGITAL LIBRARY
- 183 *Z. I. Fedotova, G. S. Khakimzyanov*
NONLINEAR DISPERSION MODELS OF WAVE HYDRODYNAMICS ON A SPHERE AND CONSERVATIVE LAWS
- 191 *J. Gavrilovic, A. Savic, S. Strbac-Savic, I. Kovacevic*
TEACHING OF MATHEMATICS THROUGH DIFFERENT MEDIUMS CHANNELS OF KNOWLEDGE TRANSFER
- 195 *P. Gavrilovic, A. Miletic, V. Petkovic, V. Petrovic*
POSSIBILITIES OF USE OF MOBILE COMPUTING IN DISTANCE LEARNING
- 201 *A.V. Gerasimov*
NUMERICAL MODELING OF SOLIDS FRACTURE UNDER INTENSIVE DYNAMIC LOADING
- 208 *B. M. Glinskiy, D. A. Karavaev, I. M. Kulikov, N. V. Kuchin, N. V. Snytnikov*
HIGH SCALABLE COMPUTING USING HYBRID ARCHITECTURE SUPERCOMPUTER
- 216 *E. N. Golubeva, E. G. Klimova, V. I. Kuzin, V. V. Malakhova, G. A. Platov, V. A. Shlychkov*
INTEGRATED MODELING OF THE ARCTIC EAST-SIBERIAN SHELF HYDRODYNAMICS
- 227 *D. O. Glushkov, G. V. Kuznetsov, P. A. Strizhak*
MATHEMATICAL MODELLING OF PROCESSES OF THE HEAT AND MASS TRANSFER IN THE CONDITIONS OF PHASE TRANSITIONS AND CHEMICAL REACTION AT IGNITION OF CONDENSED SUBSTANCES BY A LOCAL POWER SOURCES

- 236 *S. K. Golushko, S. V. Idimeshev*
APPLICATION OF COLLOCATIONS AND LEAST RESIDUALS METHOD TO PROBLEMS OF MECHANICS OF ISOTROPIC AND ANISOTROPIC PLATES
- 243 *S. K. Golushko, B. V. Semisalov*
ON THE VARIOUS APPROACHES TO MODELING AND ANALYSIS OF DEFORMATION OF ANISOGRID STRUCTURES
- 251 *M. M. Gourary, S. G. Rusakov, A. L. Stempkovsky, S. L. Ulyanov, M. M. Zharov*
THE ELIMINATION TECHNIQUES TO SOLVE COMPUTATIONAL PROBLEMS OF MODEL ORDER REDUCTION FOR LARGE MULTITERMINAL CIRCUITS
- 260 *M. M. Gourary, S. G. Rusakov, S. L. Ulyanov, M. M. Zharov*
THE CONCEPT OF REDUNDANCY FOR TECHNIQUES OF MODEL ORDER REDUCTION IN CIRCUIT SIMULATION
- 267 *E. E. Gummel, H. Milosevic, V.V. Ragulin, Y.N. Zaharov, A.I. Zimin*
MOTION OF VISCOUS INHOMOGENEOUS INCOMPRESSIBLE FLUID OF VARIABLE VISCOSITY
- 275 *O. I. Gusev, V. A. Kutergin, G. S. Khakimzyanov, N. Yu. Shokina*
SIMULATION OF DISPERSIVE WAVES GENERATED BY UNDERWATER LANDSLIDE IN A LIMITED RESERVOIR
- 285 *A. Jainakov, Z.K. Imanaliev, B.Y. Ashirbaev*
ON A DISCRETE OPTIMAL CONTROL PROBLEMS WITH A SMALL STEP
- 290 *A. Jainakov, G. Kabaeva, N. Amankulova*
THE MATHEMATICAL MODELING OF NEAR-SURFACE PROCESSES ON THE ANODE AT THE PLASMA CUTTING OF METALS
- 301 *A. Jainakov, J. O. Usenkanov*
THE BALANCE TO THE POWER OF PLAZMATRONS OF DIRECT ACTION
- 305 *B. Jaksic, B. Gara, R. Ivkovic, M. Petrovic, M. Milosevic*
ANALISYS OF BRIGHTNESS EFFECT ON THE QUALITY OF PICTURES AFTER COMPRESSION WITH JPEG AND SPIHT COMPRESSION METHOD
- 312 *V. N. Kasyanov*
INFORMATION VISUALIZATION ON THE BASE OF GRAPH MODELS
- 322 *V. N. Kasyanov, S. N. Kasyanova*
SUPPORT TOOLS FOR APPLICATION OF GRAPHS AND GRAPH ALGORITHMS
- 329 *E. A. Kisic, S. M. Draskovic, Z. M. Djurovic*
APPLIED STATISTICS IN PROCESS CONTROL AND MONITORING
- 335 *N. Kontrec, H. Milosevic, D. Djosic*
ANALYSIS AND IMPLEMENTATION OF TREE-TYPE STORAGE MODEL FOR AIRCRAFT INVENTORY CONTROL
- 343 *A. N. Kopaygorodsky*
INFORMATION AND SOFTWARE TOOLS SUPPORT OF JOINT EXPERT ACTIVITY IN THE ENERGY SECTOR
- 348 *A. V. Koshkarev, I. N. Rotanova*
PROJECTS ON IMPLEMENTATION OF SPATIAL DATA INFRASTRUCTURE IN THE RUSSIAN FEDERATION: A REVIEW BASED ON AVAILABLE SOURCES

- 359 *O. A. Kovyrkina, V. V. Ostapenko*
ON MODELING OF WAVE FLOWS IN THE NON-PRISMATIC CHANNEL
- 366 *A. V. Laktyunkin, A. A. Potapov*
FRACTAL MODELS IN THE MICROWAVES FREQUENCY DIFFRACTION THEORY
- 376 *Lj. Lazic, I. Djokic, S. Milinkovic*
THE SOFTWARE DEFECTS FIXING PROBLEM OPTIMIZATION USING TAGUCHI METHOD
- 386 *V. A. Leontiev, I. S. Nudner, K. K. Semenov*
MARINE WAVES INTERACTION WITH SHIP MOORED NEAR BERTH
- 397 *A. Sh. Lyubanova*
ON INITIAL BOUNDARY VALUE PROBLEMS FOR SYSTEMS OF PARABOLIC EQUATIONS
- 405 *A. Mandak*
A CONSTRUCTION WEIGHTED PROJECTIVE PLANE OF ORDER 7 AND $(2, 7 - 1)$ -QUASIGROUP
- 410 *S. N. Martyushov*
NUMERICAL SIMULATION OF FLOWS IN ROTATION DETONATION ENGINE
- 418 *S. N. Martyushov*
NUMERICAL SIMULATION OF VISCOUS DIFFRACTION ON FREE MOVING BODY
- 423 *L. V. Massel*
DEVELOPMENT AND INTEGRATION OF INTELLIGENT, AGENT-BASED AND CLOUD COMPUTING IN SMART GRID
- 431 *M. M. Matijevic, M. D. Matijevic*
ICT MARKET ANALYSIS DATA CONCERN INTEROPERABILITY WITH FOCUS ON CONCEPTUAL BARRIERS
- 438 *V. V. Maximov, I. S. Nudner, K. K. Semenov, N. D. Titova*
RESTORATION OF THE WAVE EVALUATION THROUGH GIVEN PRESSURE INSIDE THE LIQUID IN FRAME OF THIRD-ORDER SURFACE WAVE THEORY
- 443 *Z. Mijajlovic, A. Valjarevic*
MULTILAYER DIGITAL MAP OF TOPLICA REGION
- 450 *G. V. Milovanovic*
INTEGRAL EQUATIONS OF LOVE'S TYPE AND APPLICATIONS
- 458 *S. G. Minic*
THE PROGRAMMING LANGUAGE MATLAB AS A FUNCTION OF DIGITAL STEGANOGRAPHY TECHNOLOGY
- 464 *A. D. Mizhidon, S. G. Barguev*
RESEARCH OF OWN VIBRATIONS FOR ONE HYBRID SYSTEM OF THE DIFFERENTIAL EQUATIONS
- 471 *V. V. Nicheporchuk, N. A. Chernyakova*
USE GEOINFORMATION TECHNOLOGIES FOR EMERGENCY RISK ESTIMATION ON WATER OBJECTS OF SIBERIA
- 479 *E. A. Novikov*
THE ADDITIVE SECOND ORDER METHOD FOR SOLVING STIFF PROBLEMS
- 488 *E. A. Novikov, A. E. Novikov*
ALGORITHMS INTEGRATING STIFF PROBLEMS ON HETEROGENEOUS NUMERICAL SCHEMES

- 497 *S. Panic, P. Spalevic, A. Markovic, M. Stefanovic*
PERFORMANCE ANALYSIS OF WIRELESS COMMUNICATION SYSTEM IN ALPHA-KAPPA-MU ENVIRONMENT SUBJECTED TO SHADOWING
- 502 *Lj. Paunovic*
THEOREMS HARDY-ROGERS-TYPE IN K-METRIC SPACES
- 507 *G. Pavlovic, M. Gasic, M. Rajovic, M. Savkovic*
OPTIMIZATION OF THE BOX SECTION OF THE MAIN GIRDERS OF THE BRIDGE CRANE BY USING THE METHOD OF LAGRANGE MULTIPLIERS
- 515 *Lj. Pecic*
METHODOLOGY FOR EVALUATING CORPORATIVE WEB PRESENTATIONS PROPOSAL
- 520 *S. I. Peregudin, S. E. Kholodova*
REDUCTION IN MODELING OF DYNAMICS OF A ROTATING LAYER OF AN IDEAL ELECTRICALLY CONDUCTING INCOMPRESSIBLE FLUID WITH ALLOWANCE EFFECTS OF DIFFUSIONS OF MAGNETIC FIELD
- 530 *A. A. Potapov*
SCALING, INTEGRAL OPERATORS AND FRACTALS IN LOW-CONTRAST AND FUZZY IMAGES PROCESSING
- 539 *A. A. Potapov*
THE GLOBAL FRACTAL METHOD, FRACTAL PARADIGM AND THE FRACTIONAL DERIVATIVES METHOD IN FUNDAMENTAL RADAR PROBLEMS AND DESIGNING OF REVOLUTIONARY RADIO SIGNALS DETECTORS
- 553 *A. A. Potapov, D. V. Slezkin*
FRACTAL LABYRINTHS AS SMALL ANTENNAS DEVELOPMENT BASE
- 560 *A. Raicevic, G. Prica*
TRANSFER FUNCTION OPTIMIZATION FOR PLL LOOP WITH REALISTIC OPERATIONAL AMPLIFIER
- 564 *A. A. Redyuk, A.S. Skidin, D. A. Tazba*
MATHEMATICAL MODELLING OF ONE-PUMP FIBER OPTICAL PARAMETRIC AMPLIFIERS
- 573 *G. V. Romanenko, I. V. Frolenkov*
ON EXISTENCE OF CAUCHY PROBLEMS SOLUTIONS FOR LOADED PARABOLIC EQUATIONS AND SYSTEMS OF SPECIAL FORM
- 580 *A. N. Ruchay*
CENTRALIZED MANAGING PERMISSIONS SYSTEM BASED ON THE ELECTION MULTIBIOMETRIC AUTHENTICATION
- 586 *V. V. Shaidurov, G. I. Shchepanovskaya*
THE PROBLEM OF NUMERICAL MODELING OF FLOW IN THE EXPANSIBLE CHANNEL
- 595 *V. A. Shchapov, A. G. Masich, G. F. Masich*
EXPERIMENTAL EVALUATION QUEUE MODEL AND ALGORITHMS OF PARALLEL DATA TRANSMISSION PERFORMANCE IN DATA INTENSIVE TASKS IN DISTRIBUTED SYSTEMS
- 602 *N. Shekutkovski*
TOPOLOGICAL STRUCTURE OF ATTRACTORS AND MORSE DECOMPOSITION
- 607 *Yu. I. Shokin, S. A. Beisel, A. D. Rychkov, G. S. Khakimzyanov, L. B. Chubarov*
THE STUDY OF TSUNAMI RUNUP ON THE EAST COAST OF JAPAN BY NUMERICAL SIMULATION

- 618 *Yu. I. Shokin, A. E. Guskov, D. V. Kosyakov*
ON INFORMATIZATION OF THE SIBERIAN BRANCH OF THE RUSSIAN ACADEMY OF SCIENCES
- 629 *Yu. I. Shokin, A. Yu. Vesnin, A. A. Dobrynin, O. A. Klimenko, E. V. Konstantinova, E. V. Rychkova, M. Yu. Savin*
STUDYING OF SCIENTIFIC WEB Space BY WEBOMETRICS AND GRAPH THEORY METHODS
- 640 *Yu. I. Shokin, A. Yu. Vesnin, A. A. Dobrynin, O. A. Klimenko, I. S. Petrov, E. V. Rychkova*
INVESTIGATION OF THE ACADEMIC WEB SPACE OF THE REPUBLIC OF SERBIA
- 647 *N. Yu. Shokina*
ON SOME PROBLEMS OF CONSTRUCTION OF DIFFERENCE SCHEMES ON MOVING GRIDS
- 656 *O. Y. Shvets*
INFORMATION-MODEL REPRESENTATION OF ECOLOGICAL MONITORING CENTER
FUNCTIONING FOR EMERGENCY SITUATIONS' PREVENTION
- 661 *E. G. Skripnyak, N. V. Skripnyak, V. A. Skripnyak, V. V. Skripnyak, I. K. Vaganova*
MULTISCALE COMPUTATIONAL MODEL FOR SIMULATION OF MECHANICAL BEHAVIOUR
OF HETEROGENEOUS BRITTLE CERAMICS UNDER DYNAMIC LOADING
- 671 *N. Stamenkovic, D. Zivaljevic, V. Stojanovic*
DIMINISHED-ONE MODULO ($2^n + 1$) MULTIPLIER DESIGN
- 677 *C. Stefanovic, D. Djosic, P. Spalevic, S. Maricic, A. Matovic, M. Matovic*
LEVEL CROSSING RATE OF THE RATIO OF PRODUCT OF TWO α - μ RANDOM VARIABLES AND α - μ
RANDOM VARIABLE
- 683 *H. Stefanovic, A. Savic, S. Veljkovic, D. Milic*
SOME SIMULATION METHODS FOR RECEIVE SATELLITE ANTENNA INSTALLING ANGLES
EVALUATION
- 689 *S. Stevovic, G. Ivanovic, H. Milosevic*
MATHEMATICAL MODEL FOR RELIABILITY CALCULATION ON MODEL EXAMPLE
- 698 *V. Stojanovic, M. Bozinovic, N. Petkovic*
SOFTWARE IMPLEMENTATION OF THE MODEL OF GAME THEORY IN MARKETING DECISIONS
- 706 *I. L. Trofimov*
USING METADATA TO QUERY THE DATABASE ON THERMAL ECONOMY OF RUSSIA
THROUGH THE INTERNET
- 715 *I. Vojinovic, A. Vukmirovic, M. Despotovic-Zratic, M. Milutinovic, K. Simic*
LEVERAGING INTERNET MARKETING CAMPAIGNS THROUGH SOCIAL NETWORK ANALYSIS
- 722 *J. Vujakovic, M. Rajovic*
PERIODIC SOLUTION OF SECOND ORDER DIFFERENTIAL EQUATION
- 727 *J. Vujakovic, P. Salimi*
APPLICATION OF TRIPLE COINCIDENT POINT RESULTS IN G METRIC SPACES TO INTEGRAL
EQUATIONS
- 734 *D. Vukic, I. Dundjerski, V. Matijevic*
APPLICATION OF EXPERT SYSTEMS IN TECHNICAL DIAGNOSTICS OF MOTOR VEHICLES
- 739 *A. V. Vyatkin, V. V. Shaydurov*
INTEGRAL SEMI-LAGRANGIAN APPROACH FOR TWO-DIMENSIONAL CONTINUITY EQUATION

- 746 *Z. Kh. Yuldashev, A. A. Ibragimov, P. J. Kalkhanov*
PROBLEM OF CREATION OF THE SOFTWARE FOR REALIZATION OF INTERVAL ALGORITHMS
- 751 *Y. N. Zakharov, K. S. Ivanov*
ON NUMERICAL SOLUTION OF NAVIER-STOCKS EQUATIONS WITH INFINITE BOUNDARY
CONDITIONS

EXPLICIT FINITE DIFFERENCE METHOD FOR SOLVING POWER FLOW EQUATION WITH APPLICATIONS IN FIBER OPTICS MODELING

Numerical method for solving time-dependent and time-independent power flow equation has been developed and tested. Explicit finite difference method was used in order to obtain angular power distribution solving time-independent power flow equation. Same method was used in solving time-dependent power flow equation which has resulted with solution for frequency response and bandwidth of the system.

INTRODUCTION

Need for fast data transmission grew steeply over last decade. In that light optical fibers became one of the best alternatives. Beside the possibility of transmitting large amounts of data fast, optical fibers have many others advantages. The most important are insensitivity to electromagnetic fields, smaller dimensions, smaller mass/length ratio and simple installation. Taking all of these advantages into account makes optical fibers excellent choice for data transmission.

Constant growth of data transmitted through data networks requires improvement of transfer characteristics of optical fibers. In order to examine and improve fiber characteristics several methods has been developed. Commonly used methods are ray tracing model, electromagnetic approach and solving power-flow equation. Ray tracing method calculates individual path for every ray that travels through fiber. Using this method impulse response, that includes modal induced loss and modal dispersion, can be determined. This method is computationally very demanding since it requires generation of large number of individual ray paths. Electromagnetic approach, beside it's very complicated, is very limited since only time delay of individual modes can be calculated using this method. On the other side usage of power flow equation [1] lets us efficiently model modal dispersion and modal loss in order to determine their influence on fibers transfer characteristics. Moreover, by using time-dependent power flow equation we can model all three important transfer characteristics of optical fibers; that is impulse response, frequency response and bandwidth.

Analytical solution of power flow equation exists only for some particular cases, with limitations in width and incidence angle of incidence light beam [1-3]. If we want to calculate transfer characteristics in generalized way, that is to include modal dependence of diffusion, choose incidence angle of light as well as width of light beam, we have to use some numerical approach. Several numerical approaches can be used for solving either time-independent or time-dependent power flow equation, such as finite elements method, nodal integral method, finite difference method and others [4-6]. When light propagation is modeled in two dimensions, like it is case with power flow equation, finite difference method is best choice.

At first implicit finite difference method prevailed over the explicit finite difference method, mainly because of the unconditioned stability which provided larger integration steps compared to explicit method [7]. Nevertheless this doesn't affect better computational efficiency of implicit finite difference method because there's necessity of manipulation with large matrices in every computational step. When we take this into account we can say that, although explicit finite difference method is more sensitive in the aspect of scheme stability, it's simpler and more efficient than implicit finite difference method. That is why we have chosen to use explicit finite difference method for solving power flow equation.

¹ Faculty of natural science, Kosovska Mitrovica, Serbia

² Faculty of natural science, Kragujevac, Serbia

EXPLICIT FINITE DIFFERENCE METHOD

First we will show how we employed explicit finite difference method in order to solve time-independent power flow equation. Later same method will be employed in solving time-dependent power flow equation. Examples for both equations are also shown.

Time-independent power flow equation can be written as [1]:

$$\frac{\partial P(\theta, z)}{\partial z} = -\alpha(\theta)P(\theta, z) + \frac{D(\theta)}{\theta} \frac{\partial}{\partial \theta} \left(\theta \frac{\partial P(\theta, z)}{\partial \theta} \right) \quad (1)$$

where $P(\theta, z)$ is power distribution over angle and space; $\alpha(\theta)$ is mode-dependent attenuation; and $D(\theta)$ is the mode-dependent coupling coefficient. Mode-dependent attenuation can be written in the form $\alpha(\theta) = \alpha_0 + A\theta^2 + \dots$, where α_0 is loss common to all modes. It can be accounted for by multiplying the end-solution by $e^{-\alpha_0 z}$ [7, 8], so equation (1) can be rewritten in form:

$$\frac{\partial P(\theta, z)}{\partial z} = -A\theta^2 P(\theta, z) + \frac{D}{\theta} \frac{\partial P(\theta, z)}{\partial \theta} + D \frac{\partial^2 P(\theta, z)}{\partial \theta^2} \quad (2)$$

The tacit assumption that coupling coefficient $D(\theta)$ is constant has been routinely made when mode coupling by the power flow equation has been investigated in the absence of reliable estimates of other terms in the expansion series of $D(\theta)$. Boundary conditions for equation (1) are:

$$P(\theta_c, z) = 0; \quad D \frac{\partial P}{\partial \theta} \Big|_{\theta=0} = 0 \quad (3)$$

where θ_c is critical angle of the fiber. First condition means that modes that propagate at angles $\theta > \theta_c$ don't transfer power. Second condition implies that mode coupling is limited only to modes that propagate at angles $\theta > 0$.

Using central difference scheme for derivatives $(\partial P(\theta, z))/\partial \theta$ and $(\partial^2 P(\theta, z))/\partial \theta^2$ [4, 9]:

$$\left(\frac{\partial P(\theta, z)}{\partial \theta} \right)_{i,j} = \frac{P_{i+1,j} - P_{i-1,j}}{2\Delta\theta} + O(\Delta\theta)^2 \quad (4)$$

$$\left(\frac{\partial^2 P(\theta, z)}{\partial \theta^2} \right)_{i,j} = \frac{P_{i+1,j} - 2P_{i,j} + P_{i-1,j}}{(\Delta\theta)^2} + O(\Delta\theta)^2 \quad (5)$$

and forward difference scheme for derivative $(\partial P(\theta, z))/\partial z$:

$$\left(\frac{\partial P(\theta, z)}{\partial z} \right)_{i,j} = \frac{P_{i,j+1} - P_{i,j}}{\Delta z} + O(\Delta z) \quad (6)$$

equation (2) can be written in form [10]:

$$P_{i,j+1} = \left(\frac{\Delta z D}{\Delta\theta^2} - \frac{\Delta z D}{2\theta_i \Delta\theta} \right) P_{i-1,j} + \left(1 - \frac{2\Delta z D}{\Delta\theta^2} - \Delta z A\theta_i^2 \right) P_{i,j} + \left(\frac{\Delta z D}{2\theta_i \Delta\theta} + \frac{\Delta z D}{\Delta\theta^2} \right) P_{i+1,j} \quad (7)$$

where subscripts i and j refer to discrete steps $\Delta\theta$ i Δz for angle θ and length z , respectively.

Boundary conditions (3) now become:

$$P_{N,j} = 0, P_{0,j} = P_{1,j} \quad (8)$$

where $N = \theta_c/\Delta\theta$ is grid dimension in direction θ . In order to overcome singularity problem in points $\theta = 0$ we use relation [6]:

$$\lim_{\theta \rightarrow 0} \frac{1}{\theta} \frac{\partial}{\partial \theta} \left(\theta \frac{\partial P}{\partial \theta} \right) = 2 \frac{\partial^2 P}{\partial \theta^2} \Big|_{\theta=0} \quad (9)$$

The input condition must also be expressed in difference form. For example, the plane-wave launch distribution, which is in the form of a Dirac delta function, can be expressed as:

$$\begin{aligned}
 P(\theta, 0) &= 1, \quad \text{za } \theta = \theta_0 \\
 P(\theta, 0) &= 0, \quad \text{za } \theta \neq \theta_0
 \end{aligned}
 \tag{10}$$

with $0 < \theta < \theta_c$, where θ_0 is the angle of the launch to the fiber axis.

To facilitate the comparison of results, we applied our method to (Mitsubishi Rayon) Eska Premier SI POF fiber, because this fiber was used in the experiment of Zubia *et al.* [11]. This fiber has a core diameter of $d = 0.98$ mm, a refractive index of the core of $n_1 = 1.492$, a theoretical numerical aperture (N.A.) of 0.5, and a critical angle $\theta_c = 19.6^\circ$ (measured inside the fiber; i.e., $\theta_c = 30^\circ$ measured in air). Values of $D = 7.5 \times 10^{-4}$ rad²/m and $A = 1.37$ (rad²m)⁻¹ have been reported for this fiber [11, 12].

Our numerical solution of the power flow equation gives the evolution of the normalized output power distribution with fiber length z as z is increased incrementally from zero until the steady state distribution is achieved. At each step a new distribution curve is obtained with a decreased maximum and increased width. The situation is shown in Fig. 1 for four such selected z values, each with four different input angles $\theta_0 = 0, 5.5, 16, 29^\circ$ (measured in air). In keeping with what has become a customary way of presenting such distributions [12], they are shown in Fig. 1 with their maxima normalized. Attention is drawn to the shift that occurs in the corresponding distribution curves while z is moved throughout the parts of Fig. 1. In the calculations we used step lengths $\Delta\theta = 0.05^\circ$ and $\Delta z = 0.0002$ m to achieve stability in our finite-difference scheme [4, 6].

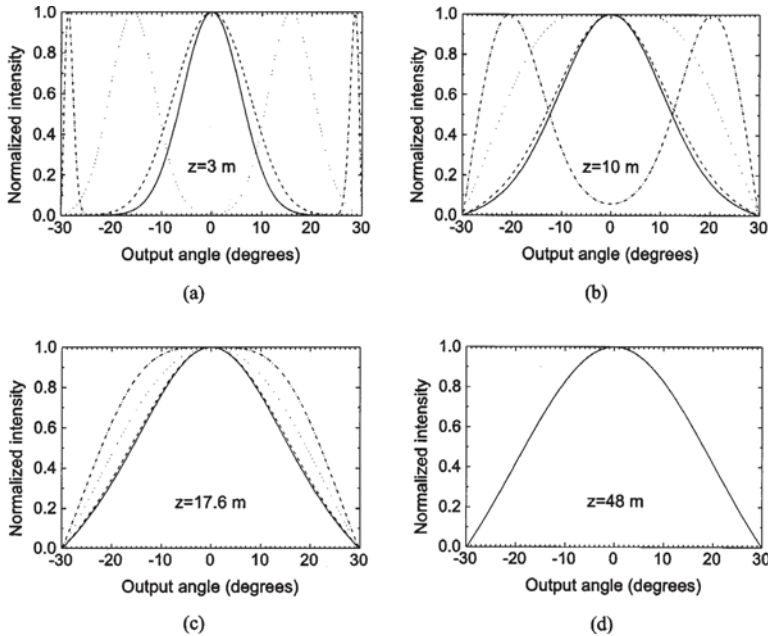


Fig. 1. Numerically determined normalized output angular power distribution for a plane wave launched with input angles $\theta_0 = 0^\circ$ (solid curves), 5.5° (dashed curves), 16° (dotted curves), and 29° (dashed-dotted curves) at various locations along the SI POF: $z = 3$ m, $z = 10$ m, $z = 17.6$ m, and $z = 48$ m.

Since our method can accommodate any initial condition we were able to test it with known analytical solution for same fiber. Without going into limitations of analytical method we will present obtained results for fiber mentioned above [10] and compare it with our numerical results. Results obtained by numerical solution are presented in Fig. 1, while analytical solutions are presented in Fig. 2.

Differences appear primarily for the highest modes and in the tails of the distribution curves. In our view, the tails in the analytical solution of Fig. 2 incorrectly imply that power is transmitted even at angles above the critical angle of 30° in air, as indicated by the nonzero intensity at $+30^\circ$ and -30° in Fig. 2. This difference between Figs. 1 and 2 is more pronounced for larger launch angles and is attributed to

the influence of the boundary condition at $\theta = \theta_c$ [$P(\theta_c, z) = 0$], which the analytical solution ignores.

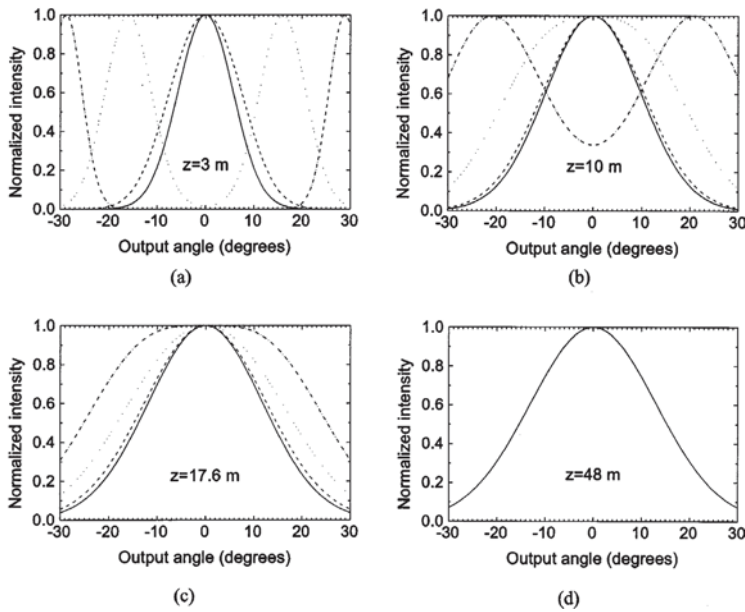


Fig. 2. Analytically determined normalized output angular power distribution for a plane wave launched with input angles $\theta_0 = 0^\circ$ (solid curves), 5.5° (dashed curves), 16° (dotted curves), and 29° (dashed-dotted curves) at several locations along the SI POF: $z = 3$ m, $z = 10$ m, $z = 11.6$ m, and $z = 48$ m.

Thus our numerical solution of the power flow equation, which takes into account the boundary conditions at both $\theta = 0$ and $\theta = \theta_c$, is more accurate.

By solving time-independent power flow equation we can determine coupling length of optical fibers. If we want to calculate transfer characteristics of optical fibers we have to employ Gloge's time-dependent power flow equation, which can be written in form [2]:

$$\frac{\partial P(\theta, z, t)}{\partial z} + \frac{\partial t}{\partial z} \frac{\partial P(\theta, z, t)}{\partial t} = -A\theta^2 P(\theta, z, t) + \frac{D}{\theta} \frac{\partial}{\partial \theta} \left[\theta \frac{\partial P(\theta, z, t)}{\partial \theta} \right] \quad (11)$$

The derivative $\partial t / \partial z$ can be obtained using the group velocity of a mode with characteristic angle θ , which is $\frac{dz}{dt} = \frac{c}{n(1 + \theta^2/2)}$ [2]. Neglecting the delay n/c common to all modes, it follows [8]:

$$\frac{\partial P(\theta, z, t)}{\partial z} = -A\theta^2 P(\theta, z, t) - \frac{n}{2c} \theta^2 \frac{\partial P(\theta, z, t)}{\partial t} + \frac{D}{\theta} \frac{\partial}{\partial \theta} \left(\theta \frac{\partial P(\theta, z, t)}{\partial \theta} \right) \quad (12)$$

By applying the Fourier transform, $p(\theta, z, \omega) = \int_{-\infty}^{\infty} P(\theta, z, t) e^{-j\omega t} dt$, the time-dependent equation (12) transforms into (13):

$$\frac{\partial p(\theta, z, \omega)}{\partial z} = - \left[A\theta^2 + j\omega \frac{n}{2c} \theta^2 \right] p(\theta, z, \omega) + \frac{D}{\theta} \frac{\partial p(\theta, z, \omega)}{\partial \theta} + D \left(\theta \frac{\partial^2 p(\theta, z, \omega)}{\partial \theta^2} \right) \quad (13)$$

where $\omega = 2\pi f$ is the angular frequency. The boundary conditions are same as for the time-independent power flow equation (3).

It is apparent that $p(\theta, z, \omega)$ is complex. We can therefore separate $p(\theta, z, \omega)$ into its real and imaginary parts, $p = p' + jp''$. Equation (13) can now be rewritten as the following simultaneous differential equations:

$$\begin{aligned}\frac{\partial p^r}{\partial z} &= -A\theta^2 p^r + \frac{D}{\theta} \frac{\partial p^r}{\partial \theta} + D \frac{\partial^2 p^r}{\partial \theta^2} + \omega \frac{n}{2c} \theta^2 p^i \\ \frac{\partial p^i}{\partial z} &= -A\theta^2 p^i + \frac{D}{\theta} \frac{\partial p^i}{\partial \theta} + D \frac{\partial^2 p^i}{\partial \theta^2} - \omega \frac{n}{2c} \theta^2 p^r\end{aligned}\quad (14)$$

Once p^r and p^i are obtained by solving equations (14), frequency response at z can be easily calculated [13]. After separating the power flow equation (13) into two simultaneous equations (14), we solved the latter (14) by explicit finite difference method. Using central difference scheme (4) and (5) for derivatives $\partial p(\theta, z, \omega) / \partial \theta$ and $\partial^2 p(\theta, z, \omega) / \partial \theta^2$ and forward difference scheme (6) for derivative $(\partial P(\theta, z, \omega) / \partial z)$ equations (14) can be written in the form [4, 6, 8]:

$$\begin{aligned}p_{k,l+1}^r &= \left(\frac{\Delta z D}{\Delta \theta^2} - \frac{\Delta z D}{2\theta_k \Delta \theta} \right) p_{k-1,l}^r + \left(1 - \frac{2\Delta z D}{\Delta \theta^2} - \Delta z A \theta_k^2 \right) p_{k,l}^r + \\ &+ \left(\frac{\Delta z D}{2\theta_k \Delta \theta} + \frac{\Delta z D}{\Delta \theta^2} \right) p_{k+1,l}^r + \frac{\omega n \Delta z}{2c} \theta_k^2 p_{k,l}^i\end{aligned}\quad (15)$$

and

$$\begin{aligned}p_{k,l+1}^i &= \left(\frac{\Delta z D}{\Delta \theta^2} - \frac{\Delta z D}{2\theta_k \Delta \theta} \right) p_{k-1,l}^i + \left(1 - \frac{2\Delta z D}{\Delta \theta^2} - \Delta z A \theta_k^2 \right) p_{k,l}^i + \\ &+ \left(\frac{\Delta z D}{2\theta_k \Delta \theta} + \frac{\Delta z D}{\Delta \theta^2} \right) p_{k+1,l}^i - \frac{\omega n \Delta z}{2c} \theta_k^2 p_{k,l}^r\end{aligned}\quad (16)$$

Boundary conditions (3) now become:

$$p_{N,l}^r = 0, \quad p_{N,l}^i = 0 \quad \text{and} \quad p_{0,l}^r = p_{1,l}^r, \quad p_{0,l}^i = p_{1,l}^i \quad (17)$$

where $N = \vartheta / \Delta \vartheta$ is the grid size in the θ direction. In order to prevent the problem of singularity at grid points $\theta = 0$, the relation (9) is used [6].

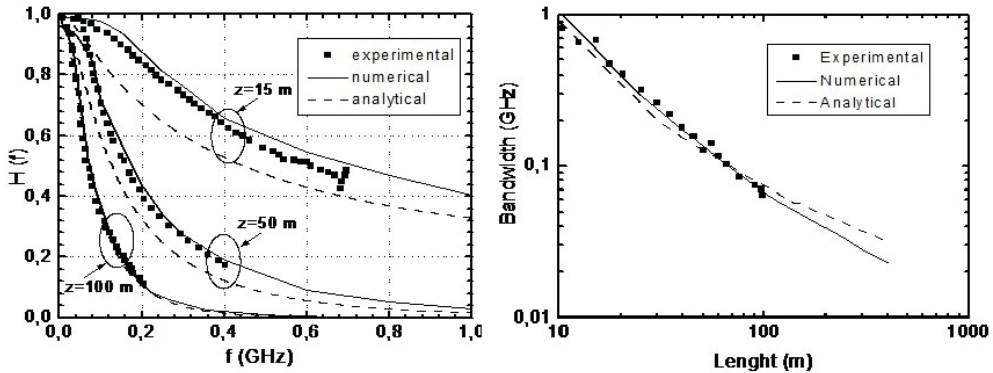


Fig. 3. Left - Comparison of numerical results, measurements by Mateo et al. [13] and analytical solution [15] for frequency response of the HFBR fiber. Right - Comparison of numerical results, measurements by Mateo et al. [13] and analytical solution [15] for the functional dependence of the HFBR fiber bandwidth on its length.

In order to test our results we have used our method and obtained frequency response and bandwidth of the same SI POF that was investigated by Mateo et al. [13]. The fiber is HFBR-RUS100 (HFBR) from Agilent, with numerical aperture $NA=0.47$ (corresponding to the inner critical angle of $\theta_c = 18.5^\circ$) and 0.22 dB/m of nominal attenuation. Values for A and D that we have used are $A=0.7539$ ($\text{rad}^2 \text{m}^{-1}$) and $D \approx 4.31 \times 10^{-4}$ rad^2/m [14].

In Fig. 3 (left), frequency response of the HFBR fiber is shown for the fiber lengths of 15, 50 and 100 m, and are compared with experimental results obtained by Mateo et al. [13] as well as with the analytical solution [15]. In figure 3 (right) our numerical results for the bandwidth for the HFBR fiber is compared to Mateo et. al's [13] experimental measurements and to our recent analytical solution [15, 16].

CONCLUSION

We have shown full numerical solution of power flow equation obtained by explicit finite difference method. Our method overcomes problems that are present in analytical solution of power flow equation. We were able to model, both, modal coupling process and modal loss. Firstly we solved time-independent power flow equation for one fiber and compared it to analytical solution, where we can clearly see advantage of our method. Later we have solved time-dependent power flow equation, whose solving is necessary if transfer characteristics of fiber are to be known. Solution has been compared to, both, experimental and analytical solution for sampled fiber. From the results above, we can conclude that our solution is stable, general and more accurate than analytical solution.

ACKNOWLEDGEMENTS

The work described in this paper was supported by grant from Serbian Ministry of Education and Science [Project No. 171011].

REFERENCES

- [1] Gloge D. Optical power flow in multimode fibers. *Bell Syst. Tech. J.* Vol. 51. 1972. P. 1767-1783.
- [2] Gloge D. Impulse Response of Clad Optical Multimode Fibers. *AT&T Tech. J.* Vol. 52. 1973. P. 801-816.
- [3] Drljaca B, Savovic S, Djordjevich A. Calculation of frequency response in step-index plastic optical fibers using the time-dependent power flow equation. *Opt. Laser Eng.* Vol. 49. 2011. P. 618-622.
- [4] Anderson J. D. *Computational Fluid Dynamics.* McGraw-Hill. New York. 1995.
- [5] Caldwell J, Savović S, Kwan Y. Y. Nodal integral and finite difference solution of one-dimensional Stefan problem. *J. Heat Transf.-Trans. ASME* 125, 2003. P. 523-527.
- [6] Djordjevich A, Savović S. Investigation of mode coupling in step index plastic optical fibers using the power flow equation. *IEEE Photon. Technol. Lett.* 12, 2000. P. 1489-1491.
- [7] Rousseau M, J eunhomme L. Numerical solution of the coupled-power equation in step index optical fibers. *IEEE Trans. Microwave Theory Tech.* 25, 1977. P. 577-585.
- [8] Savović S, Djordjevich A. Influence of numerical aperture on mode coupling in step index plastic optical fibers. *Appl. Opt.* Vol. 43. 2004. P. 5542-5546.
- [9] Savović S, Djordjevich A. Influence of initial dopant distribution in fiber core on refractive index distribution of thermally expanded core fibers. *Opt. Mat.* Vol. 30. 2008. P. 1427-1431.
- [10] Djordjevich A, Savović S. Numerical solution of the power flow equation in step index plastic optical fibers. *J. Opt. Soc. Am. B* Vol. 21, 2004. P. 1437-1442.
- [11] Toshiki P. T. Shoji Y. Numerical solution of power flow in multimode W-type optical fibers. *App. Opt.* Vol. 19. No. 10. 1980. P. 1647-1652.
- [12] Zubia J, Durana G, Aldabaldetrekú G, Arrue J, Losada M. A, Lopez-Higuera M. New method to calculate mode conversion coefficients in SI multimode optical fibers. *J. Lightwave Technol.* Vol. 21, 2003. P. 116-181.
- [13] Dugas J, Maurel G. Mode-coupling processes in poly-(methyl methacrylate) -core optical fibers. *Appl. Opt.* Vol. 31. 1992. P. 5069-5019.
- [14] Mateo J, Losada M.A, Zubía J. Frequency response in step index plastic optical fibers obtained from the generalized power flow equation. *Opt. Express* Vol. 17. 2009. P. 2850-2860.
- [15] Drljaca B, Djordjevich A, Savović S. Frequency response in step-index plastic optical fibers obtained by numerical solution of the time-dependent power flow equation. *Opt. Las. Tec.* Vol. 44. 2012. P. 1808-1812.
- [16] Drljaca B, Savović S, Djordjevich A. Calculation of the frequency response and bandwidth in step-index plastic optical fibres using the time-dependent power flow equation. *Phy. Scr. T.* 149. 2012.
- [17] Drljaca B, Savović S, Djordjevich A. Calculation of the frequency response of step-index plastic optical fibers using the time-dependent power flow equation. *Opt. Lasers Engg.* Vol. 49, 2011. P. 855-858.

CIP - Каталогизација у публикацији
Народна библиотека Србије, Београд

004(082)

КОНФЕРЕНЦИЈА Математичке и информационе технологије (2013 ; Врњачка Бања, Бечићи)

Zbornik radova Konferencije MIT [Matematičke i informacione tehnologije] 2013 : [[održane] u Vrnjačkoj Banji od 5. do 9. septembra i u Bečićima od 10. do 14. septembra 2013. godine] / [urednik Dragan Aćimović]. - Kosovska Mitrovica : Prirodno-matematički fakultet ; Novosibirsk : Institute of Computational Technologies, Siberian Branch of the Russian Academy of Sciences, 2014 (Kraljevo : Ofsetpres). - 756 str. : ilustr. ; 25 cm

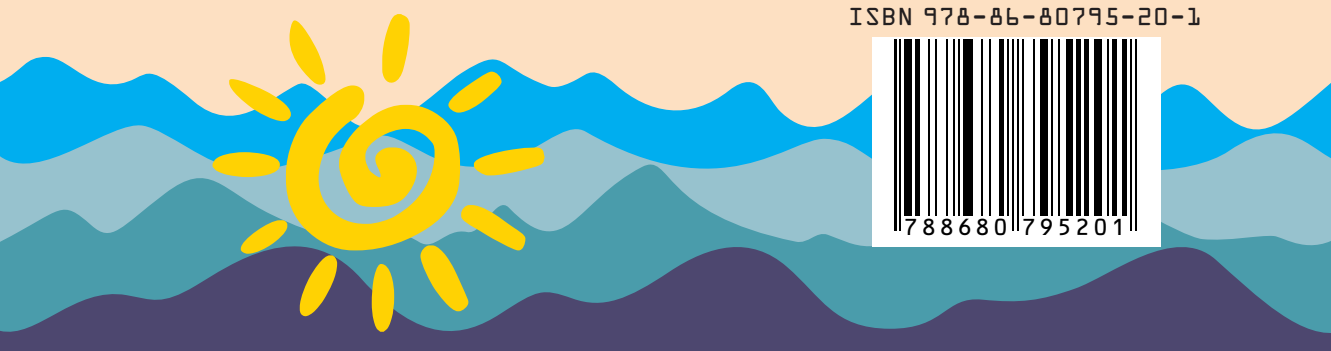
Radovi na srp., engl. i rus. jeziku. - Tekst ćir. i lat. - Tiraž 100. - Str. 6: Predgovor / Hranislav Milošević.
- Napomene uz tekst. - Bibliografija uz svaki rad. - Summaries.

ISBN 978-86-80795-20-1 (PMF)

1. Аћимовић, Драган [уредник], 1969-

а) Информациона технологија - Зборници

COBISS.SR-ID 206790412



ISBN 978-86-80795-20-1





УНИВЕРЗИТЕТ У БАЊОЈ ЛУЦИ
UNIVERSITY OF BANJA LUKA
ТЕХНОЛОШКИ ФАКУЛТЕТ
FACULTY OF TECHNOLOGY



BOOK OF ABSTRACTS

OCTOBER 21-22, 2022

ACADEMY OF SCIENCES AND ARTS
OF THE REPUBLIC OF SRPSKA,
BANJA LUKA, REPUBLIC OF SRPSKA, B&H

INTERNATIONAL SCIENTIFIC CONFERENCE

**XIV
CONFERENCE** OF CHEMISTS,
TECHNOLOGISTS AND
ENVIRONMENTALISTS
OF REPUBLIC OF SRPSKA

XIV CONFERENCE OF CHEMISTS, TECHNOLOGISTS AND
ENVIRONMENTALISTS OF REPUBLIC OF SRPSKA

BOOK OF ABSTRACTS

Publisher:

University in Banjaluka, Faculty of Technology

Editorial board:

Borislav Malinovic, PhD, dean

Design and computer processing

Pero Sailovic, PhD

Msc Branka Ruzicic

CIP - Каталогизacija u publikaciji
Народна и универзитетска библиотека
Републике Српске, Бања Лука

66(048.3)(0.034.2)
661:663/664(048.3)(0.034.2)
677(048.3)(0.034.2)
655(048.3)(0.034.2)
502(048.3)(0.034.2)

CONFERENCE of Chemists, Technologists and Environmentalists of
Republic of Srpska (14 ; Banja Luka ; 2022)

Book of Abstracts [Електронски извор] / XIV Conference of
Chemists, Technologists and Environmentalists of Republic of Srpska,
Banja Luka, October 21-22, 2022 ; [editorial board Borislav Malinović]. -
Onlajn izd. - El. zbornik. - Banja Luka : University in Banjaluka, Faculty of
Technology = Tehnološki fakultet, 2022

Sistemski zahtjevi: Nisu navedeni. - Način pristupa (URL):
<https://savjetovanje.tf.unibl.org/>. - El. publikacija u PDF formatu opsega
207 str. - Nasl. sa naslovnog ekrana. - Opis izvora dana 20.10.2022.

ISBN 978-99938-54-96-8

COBISS.RS-ID 137004033

Organizing Committee:

PhD Pero Sailovic, president, PhD Darko Bodroza, general secretary, M.Sc Maja Milijaš secretary, M.Sc Dajana Dragić, M.Sc Branka Ružičić, M.Sc Marina Rakanovic, M.Sc Maja Katic, Sanda Pilipović, M.Sc Nebojsa Gorgi, Biljana Vasić, Sanja Novakovic, M.Sc Jovanka Kotur

Students: Vladimir Ivković, Jovan Savić, Nevena Janjić, Bojana Milinković, Danijela Lazić

Scientific Committee:

Dr Božana Odžaković, president, University of Banja Luka, **B&H**, Dr Nada Štrbac, co-president, University of Belgrade, **Serbia**, Dr Borislav Malinović, University of Banja Luka, **B&H**, Dr Vlada Veljković, University of Nis, **Serbia**, Dr Todor Vasiljević, Victoria University Melbourne, **Australia**, Dr Sanja Mahović-Poljačak, University of Zagreb, **Croatia**, Dr Csaba Horvath, University Obuda, Budapest, **Hungary**, Dr Mihail Kochubovski, University of Skopje, **Macedonia**, Dr Massimiliano Fenice, Universityt Della Tuscia, **Italy**, Dr Georgij Petriaszwili, Warshav University of Technology, **Poland**, Dr Mira Vukcevic, University of Monte Negro, **Monte Negro**, Dr Ondrej Panák, University of Pardubice, **Czech Republic**, , Dr Pospiech Matej, University of Veterinary and Pharmaceutical Sciences, Brno, **Czech Republic**, , Dr Dani Dordevic, University of Veterinary and Pharmaceutical Sciences, Brno, **Czech Republic**, Dr Iskren Spiridonov, University of Chemical Technology and Metallurgy, **Bulgaria**, Dr Laura Benea, West University of Timisoara, **Romania**, Dr Savvas G. Vassiliadis, University of Piraeus, **Greece**, Dr Helena Prosen, University of Ljubljana, **Slovenia**, Dr Srečko Stopic, RWTH University Aachen, **Germany**, Dr Maria Iosune Cantalejo, UPNA, **Spain**, Dr Jurislav Babić, University of Osijek, **Croatia**, Dr Svetozar Milosavić, University of Kosovska Mitrovica, **Serbia**, Dr Petar Uskoković, University of Belgrade, **Serbia**, Dr Mitja Kolar, University of Ljubljana, **Slovenia**, Dr Dragiša Savić, , University of Nis, **Serbia**, Dr Dragan Vujadinović, University of East Sarajevo, **B&H**, Dr Biljana Pajin, University of Novi Sad, **Serbia**, Dr Sead Čatić, University of Tuzla, **B&H**, Dr Husein Vilić, University of Bihac, **B&H**, Dr Sanjin Gutić, University of Sarajevo, **B&H**, Dr Goran Trbić, University of Banja Luka, **B&H**, Dr Milica Balaban, University of Banja Luka, **B&H**, Dr Ljiljana Vukić, University of Banja Luka, **B&H**, Dr Ljiljana Topalić-Trivunović, University of Banja Luka, **B&H**, Dr Slavica Sladojević, University of Banja Luka, **B&H**, Dr Pero Dugić, University of Banja Luka, **B&H**, Dr Zoran Kukrić, University of Banja Luka, **B&H**, Dr Slavica Grujić, University of Banja Luka, **B&H**, Dr Milorad Maksimović, University of Banja Luka, **B&H**, Dr Branka Rodić-Grabovac, University of Banja Luka, **B&H**, Dr Rada Petrović, University of Banja Luka, **B&H**, Dr Dragana Grujić, University of Banja Luka, **B&H**, Dr Svjetlana Janjić, University of Banja Luka, **B&H**, Dr Zora Levi, University of Banja Luka, **B&H**, Dr Ladislav Vasilišin, University of Banja Luka, **B&H**

NOTE:

The authors have full responsibility for the originality and content of thier own papers



УНИВЕРЗИТЕТ У БАЊОЈ ЛУЦИ
UNIVERSITY OF BANJA LUKA
ТЕХНОЛОШКИ ФАКУЛТЕТ
FACULTY OF TECHNOLOGY



International scientific conference

"XIV CONFERENCE OF CHEMISTS, TECHNOLOGISTS AND ENVIRONMENTALISTS OF REPUBLIC OF SRPSKA"

under the auspices of



MINISTRY OF SCIENTIFIC AND TECHNOLOGICAL DEVELOPMENT, HIGHER
EDUCATION AND INFORMATION SOCIETY

MINISTRY OF AGRICULTURE, FORESTRY AND WATER MANAGEMENT



ACADEMY OF SCIENCES AND ARTS OF THE REPUBLIC OF SRPSKA

SPONSORS

OPTIMA GROUP and OIL RAFINERY MODRIČA

HOFSTETTER ENVIRONMENTAL SRL

SINEX LABORATORY

PREHTEH d.o.o.

DESTILACIJA ad

EAST CODE d.o.o.

MUNICIPALITY OF ČELINAC

J.P. DEP-OT

ASSOCIATION OF TECHNOLOGY ENGINEERS OF REPUBLIC OF
SRPSKA

EM PLUS d.o.o.

KESO GRADNJA d.o.o.

MARKWAY d.o.o.

EURO-LAB V d.o.o.

EKO-EURO TIM d.o.o.

MB-IMPEX d.o.o.

TRGO FORTUNA PLUS d.o.o.

EURO-INSPEKT d.o.o.

ABC PROJEKT d.o.o.

ŠTAMPARIJA PETROGRAF

CSK PRINT

CONTENTS

PLENARY LECTURES.....	13
THE MOST RELEVANT ROUTES OF BISPHENOL A EMISSION INTO FOOD AND THE ENVIRONMENT.....	14
Vesna Antić	
HYBRIDISATION OF OZONE-BASED ADVANCED OXIDATION PROCESSES WITH HYDRODYNAMIC CAVITATION: PROBLEMS AND BENEFITS IN WATER TREATMENT APPLICATIONS.....	15
Andreja Žgajnar Gotvajn	
ECO FRIENDLY PRODUCTION OF EDIBLE/BIODEGRADABLE PACKAGING.....	16
Dani Dordevic, Simona Dordevic, Bohuslava Tremlova	
GENERAL AND APPLIED CHEMISTRY.....	17
LUMINESCENT LIQUID CRYSTALLINE MATERIALS BASED ON LOW-MELTING PALLADIUM(II) AND PLATINUM(II) COMPLEXES.....	18
Viorel Cîrcu, Monica Iliş, Doina Manaila-Maximean	
SYNTHESIS AND ANTIPROLIFERATIVE ACTIVITY OF NITRO AND AMINO SUBSTITUTED BENZIMIDAZOLES AND BENZOTHAZOLES.....	19
Marijana Hranjec, Livio Racané, Ida Boček, Leentje Persoons, Dirk Daelmans	
THEORETICAL PREDICTION OF MAGNETIC AMINOFUNCTIONALIZED POLYMER SORBENT PERFORMANCE USING MOLECULAR MODELING METHODS.....	20
Ljiljana Suručić, Aleksandra Nastasović, Bojana Marković, Tamara Tadić, Antonije Onjia, Goran Janjić	
PHOTOLYSIS OF NADOLOL IN THE AQUATIC ENVIRONMENT: INSIGHTS INTO THE EFFECT OF BICARBONATES.....	21
Andrijana Vukojević, Maria M. Savanović, Stevan Armačević, Svetlana Peleliš, Sanja J. Armačević	
SYNTHESIS, CHARACTERIZATION AND CRYSTAL STRUCTURE OF THE 2-QUINOLONE DERIVATIVE ..	22
Lidija Radovanović, Jelena Lađarević, Bojan Božić, Marijana Kasalović, Nebojša Pantelić, Dušan Mijin, Jelena Rogan	
CAN E-CIGARETTES BE A THREAT TO ENVIRONMENT: HEAVY METALS ANALYSIS IN E-CIGARETTES FILTERS	23
Dijana Mihajlović, Nemanja Lončar, Ana Đurić, Bojana Đekanović, Dijana Jelić	
COMPARISON OF THREE EXTRACTION PROCEDURES FOR QUANTIFICATION OF Cu, Mn, Ni, Pb AND Zn IN THE PLANTS	24
Dijana Mihajlović, Vesna Antunović	
THERMAL STABILITY OF NEW COPPER(II) CYCLAM COMPLEX WITH AMINOCARBOXYLATE CO-LIGAND.....	25
Branka Dražić, Mirjana Antonijević-Nikolić, Milena Martinović-Cincović, Slađana Tanasković	
INFLUENCE OF COMPOSITIONAL VARIATION ON PHYSICO-CHEMICAL AND THERMAL PROPERTIES OF SAMPLES IN THE As ₂ Se ₃ -GeTe-CdTe AMORPHOUS SYSTEM	26
Ina Karadashka, Veronika Karadjova, Valeri Jordanov	
CORRELATION OF THE GLASS TRANSITION TEMPERATURE AND MEAN BOND ENERGY IN NETWORK OF CHALCOGENIDE GLASSES.....	27
Ina Karadashka, Veronika Karadjova, Valeri Jordanov	
ANTIPROLIFERATIVE AND ANTIBACTERIAL ACTIVITY <i>IN VITRO</i> OF AMIDINO SUBSTITUTED 2-NAPHTHYLBENZAZOLES	28
Livio Racané, Lucija Ptiček, Marijana Hranjec, Leentje Persoons, Dirk Daelmans, Mihailo Banjananc, Vedrana Radovanović	
EFFECT OF PHYSICAL AND CHEMICAL CHARACTERISTICS OF CERTAIN ZEOLITES ON ADSORPTION OF SYNTHETIC ORGANIC DYE RHODAMINE B.....	29
Marina Rakanović, Slavica Sladojević, Sanja Armačević	

BIOSYNTHESIS OF AgNPs USING ELDERBERRY MACERATE (<i>SAMBUCUS NIGRA</i>) AND ANALYSIS OF THEIR ANTIBACTERIAL AND ANTIOXIDANT ACTIVITY <i>IN VITRO</i>	30
Emir Horozic, Erna Begic, Rijad Kovačević, Mensud Alić	
BIOSYNTHESIS OF SILVER NANOPARTICLES USING MACERATE <i>ACHILLEA MILLEFOLIUM</i> L.	31
Emir Horozic, Vanja Srebro, Šejla Mešanović, Maid Omerović, Dženana Mehmedović	
SOLVATOCHROMIC PROPERTIES OF NEWLY SYNTHESIZED ARYL AZO PYRIDONE DYES	32
Borko Matijević, Gorana Mrđan, Dušan Mijin, Jelena Lađarević, Suzana Apostolov, Đendi Vaštag	
ELECTROCHEMICAL POTENTIAL OF POLY(VINYL ALCOHOL) MODIFIED BACTERIAL NANOCELLULOSE AS PLATINUM NANOPARTICLES SUPPORT	33
Marijana Ponjavic, Sanja Stevanovic, Sanja Jeremic, Jasmina Nikodinovic-Runic, Vladan Cosovic, Vesna Maksimovic	
SIGNIFICANCE OF SELECTION REPRESENTATIVE PARTS OF THE CANNABIS PLANT FOR FORENSIC ANALYSIS	34
Vesna Matić, Ljiljana Simurdić, Mirjana Dragoljić	
ASSESSMENT OF THE PRESENCE SOME ORGANIC POLLUTANTS IN AGRICULTURAL SOIL BY CHROMATOGRAPHIC ANALYSIS	35
Aleksandra Mikić, Adriana Modrušan, Nina Savić, Dejana Savić, Sanja Pržulj, Milica Balaban	
DETERMINATION OF DISSOCIATION CONSTANTS AND QSAR STUDY OF SOME AROMATIC BENZOYLHYDRAZONES.....	36
Mirjana S. Jankulovska, Vesna Dimova, Milena Jankulovska-Petkovska	
CHEMICAL DEFENSE AGAINST PREDATION IN THE GEOPHILOMORPH CENTIPEDES (CHILOPODA: GEOPHILOMORPHA).....	37
Bojan Mitić, Ljubodrag Vujisić, Ljubica Vasiljević, Vele Tešević	
DESIGN OF NANOPLATFORMS FOR ELECTROCHEMICAL SENSING OF BIOMOLECULES	38
Miloš Ognjanović, Biljana Dojčinović, Željko Jaćimović, Dalibor Stanković, Bratislav Antić	
ADSORPTION OF MALACHITE GREEN FROM AQUEOUS SOLUTION BY ACTIVATED CARBON	39
Rada Petrović, Jovana Tenić, Darko Bodroža	
SPECTROPHOTOMETRIC OBSERVATION OF ADSORPTION OF METHYL VIOLET FROM AQUEOUS ENVIRONMENT ON MORDENITE.....	40
Slavica Sladojević, Marina Rakanović, Sanja Armaković, Darko Bodroža	
CHEMICAL ENGINEERING	41
BIOBASED UNSATURATED POLYESTER RESINS REINFORCED WITH NATURAL FILLERS	42
Olga Pantić, Vesna Panić, Sanja Savić, Maja Marković, Melina Kalagasidis Krušić, Pavle Spasojević	
EFFECT OF NEUTRALIZATION DEGREE OF METHACRYLIC ACID ON HYDROGEL SWELLING AND DRUG RELEASE	43
Olga J. Pantic, Rada V. Pjanovic, Vesna V. Panic, Sanja I. Savic, Pavle M. Spasojevic, Maja D. Markovic	
POSSIBILITIES OF CROSSLINKING SILICONE MATERIALS IN EXCESS OF CROSSLINKER WITH TWO TYPES OF FILLERS	44
Darko Manjenčić, Marko Paić, Vesna Cvijetinović, Vladan Mičić, Anja Manjenčić, Duško Kostić, Pero Dugić	
PHOSPHATE GLASSY FERTILIZERS	45
Vladimir S. Topalović, Jelena D. Nikolić, Srdjan D. Matijašević, Veljko V. Savić, Marija S. Djošić, Ana M. Vujošević, Snežana R. Grujić	
PRODUCTION OF DISTILLATE – GRAPE BRANDY FROM THE MERLOT BRAND.....	46
Miljojka Mijailović, Miljana Krstić, Dejan Pilčević, Svetomir Milojević, Vladimir Pavičević	
BINARY MIXTURES OF SUBSTANCES WITH DOUBBLE AND SINGLE BONDS	47
Milana Zarić, Ivona Radović, Mirjana Kijevčanin	

INFLUENCE OF NATURAL ZEOLITES ON THE THERMAL DECOMPOSITION OF MULTI-LAYERED PLASTIC WASTE	48
Milica Durdevic, Sasa Papuga, Irma Kremer, Darko Bodroza	
ANALYSIS OF THE THERMAL BEHAVIOR OF A FIXED BED REACTOR DURING THE PYROLYSIS PROCESS.....	49
Milica Durdevic, Sasa Papuga, Aleksandra Kolundzija	
THERMODYNAMIC AND TRANSPORT PROPERTIES OF BINARY SYSTEM GUAIACOL+EUGENOL.....	50
Gorica Ivaniš, Ivona Radović, Mirjana Kijevčanin	
HETEROGENEOUSLY CATALYZED TRANSESTERIFICATION OF OIL BLENDS.....	51
Milica Z. Petković, Marija Miladinović, Ivana B. Banković-Ilić, Olivera S. Stamenković, Vlada B. Veljković	
THE INFLUENCE OF THE CONFIGURATION OF THE INERTIZATION SYSTEM ON PYROLYSIS IN A FIXED-BED REACTOR.....	52
Sasa Papuga, Milica Djurdjevic, Aleksandra Kolundzija	
CHEMICAL TECHNOLOGY	53
MINEROLOGICAL AND CHEMICAL CHARACTERIZATION OF CLAY FROM THE ZAGONI SITE MUNICIPALITY OF BRATUNAC	54
Dragana Kešelj, Dragica Lazić, Zoran Petrović, Nebojša Vasiljević	
STABILITY AND BIO-ACTIVITY OF HYDROGELS BASED ON SILVER NANOPARTICLES STABILIZED BY AQUEOUS EXTRACTS OF WILD BLACKBERRY (<i>RUBUS SPP.</i>) LEAVES	55
Marija Stevanović, Sanja Petrović, Bojana Danilović, Ljiljana Stanojević, Jelena Zvezdanović, Jelena Stanojević, Dragan Cvetković	
DETERMINATION OF THE MINERAL CONTENT OF <i>CENTAURIUM ERYTHRAEA</i> EXTRACTS BY ICP-OES.	56
Valentina G. Nikolić, Sanja M. Petrović, Saša R. Savić, Ivan M. Savić, Ivana M. Savić Gajić, Ina B. Konstantinović, Sandra S. Konstantinović	
UHPLC-DAD-ESI-MS ANALYSIS OF WASTE AS HERBAL TEA PRODUCTS FROM <i>Malus sylvestris</i> (WILD APPLE).....	57
Slađana V. Dončić, Jelena B. Zvezdanović, Dragan Troter, Ina B. Konstantinović Sandra S. Konstantinović	
THE PHOTOSTABILITY AND DYEING ABILITY OF SOME ANTHRAQUINONE REACTIVE DYES FOR COTTON AND PAPER.....	58
Polya Miladinova, Dimitrina Todorova	
SYNTHESIS AND INVESTIGATION OF 1,8-NAPHTHALIMIDE DERIVATIVE WITH SENSOR ACTIVITY	59
Polya Miladinova	
OXALINE AS "GREEN" SOLVENT AND CATALYST FOR SYNTHESIS OF 5-NITROISATIN-3-SEMICARBAZONE	60
Natalija T. Colić, Dragan Z. Troter, Bratislav Ž. Todorović, Zoran B. Todorović, Sandra S. Konstantinović	
INVESTIGATING INTO THE ADSORPTION MECHANISM OF HEAVY METALS ONTO GRAPHENE OXIDE	61
Jovana Pešić, Jasmina Nikić, Jasmina Agbaba, Marijana Kragulj Isakovski, Marko Šolić, Marija Ćurčić, Aleksandra Tubić, Malcolm Watson	
THE INFLUENCE OF CROSS-LINKER ON THE SWELLING PROCESS OF POLY(<i>N</i> -ISOPROPYLMETHACRYLAMIDE-CO- <i>N</i> -ISOPROPYLACRYLAMIDE)	62
Maja Urošević, Ljubiša Nikolić, Vesna Nikolić, Ivana Gajić, Ana Dinić, Snežana Ilić-Stojanović, Marijana Vladimirov, Natalija Tošić, Vojkan Miljković	
CHARACTERIZATION OF SYNTHESIZED THERMOSENSITIVE HYDROGELS	63
Maja Urošević, Ljubiša Nikolić, Vesna Nikolić, Ivana Gajić, Ana Dinić, Snežana Ilić-Stojanović, Marijana Vladimirov, Natalija Tošić, Vojkan Miljković	

ANTIOXIDANT ACTIVITY OF COMMERCIAL AND ISOLATED ESSENTIAL OIL OF INDIAN FRANKINCENSE (<i>Boswellia serrata</i>).....	64
Natalija Tošić, Ljubiša Nikolić, Vesna Nikolić, Ljiljana Stanojević, Ivana Gajić, Maja Urošević, Ana Dinić, Marijana Vladimirov	
COMPARATIVE GC/MS ANALYSIS OF COMMERCIAL AND ISOLATED ESSENTIAL OIL OF INDIAN FRANKINCENSE (<i>Boswellia serrata</i>).....	65
Natalija Tošić, Vesna Nikolić, Ljubiša Nikolić, Jelena Stanojević, Ljiljana Stanojević, Maja Urošević, Ana Dinić, Ivana Gajić	
CHARACTERISATION OF THE ELECTROSPUN POLY(LACTIDE) NANOFIBERS WITH BIOCHANIN A	66
Ivana Gajić, Ana Dinić, Maja Urošević, Vesna Nikolić, Ivan Ristić, Aleksandra Nešić, Branka Pilić, Stevo Najman	
IN VITRO RELEASE OF BIOCHANIN A FROM THE ELECTROSPUN POLY(VINYLPYRROLIDONE) NANOFIBERS	67
Ivana Gajić, Ana Dinić, Maja Urošević, Ljubiša Nikolić, Natalija Tošić, Marijana Vladimirov, Ivan Ristić, Ljiljana Stanojević	
ANTIOXIDANT ACTIVITY OF BETULIN, BETULINIC ACID AND WHITE BIRCH BARK EXTRACT (<i>Betula pendula</i>).....	68
Marijana Vladimirov, Vesna Nikolić, Ljiljana Stanojević, Ana Dinić, Maja Urošević, Ivana Gajić, Natalija Tošić, Ljubiša Nikolić	
GC-MS ANALYSIS OF THE WHITE BIRCH BARK EXTRACT (<i>Betula pendula</i>)	69
Marijana Vladimirov, Vesna Nikolić, Jelena Stanojević, Ana Dinić, Maja Urošević, Ivana Gajić, Ljubiša Nikolić	
EFFICIENCY OF "BRITA" HOME WATER FILTER FOR WATER PURIFICATION	70
Dijana Drljača, Dajana Dragić, Sanja Banjac	
THE INFLUENCE OF POLY(N-ISOPROPYLMETHACRYLAMIDE) HYDROGELS CROSSLINKING ON THEIR SWELLING CAPACITY.....	71
Snežana Ilić-Stojanović, Ljubiša Nikolić, Stevo Najman, Djordje Petrović, Maja Urošević, Vesna Nikolić, Suzana Cakić	
DECOMPOSITION OF POLY(N-ISOPROPYLMETHACRYLAMIDE) HOMOPOLYMER NETWORK	72
Snežana Ilić-Stojanović, Ljubiša Nikolić, Djordje Petrović, Jelena Stanojević, Maja Urošević, Vesna Nikolić, Suzana Cakić	
BRILLIANT GREEN DYE BIOSORPTION USING IMMOBILIZED SPENT BREWER'S YEAST.....	73
Tanja Ž. Krunic, Marica B. Rakin, Marko P. Rakin	
PRETREATMENT OF BIOMASS PELLETS BY ACID WASHING IN ORDER TO REDUCE ALKALINE COMPONENTS	74
Tatjana Botić, Dijana Drljača, Petar Gvero, Dajana Dragić, Aleksandra Borković, Slobodan Rakulj	
CONTEMPORARY STATE AND POSSIBILITIES OF FURTHER DEVELOPMENT OF COAL MINE PLJEVLJA	75
Biljana Zlatičanin, Sandra Kovačević	
ASH COMPOSITION OF MONTENEGRO COAL	76
Biljana Zlatičanin, Sandra Kovačević	
COMPARATIVE ANALYSIS OF BLEACHING OF SUNFLOWER OIL WITH COMMERCIAL BLEACHING EARTH AND BENTONITE POWDER ACTIVATED WITH SULFURIC ACID	77
Zoran Petrović, Jelena Mihajlović, Sabina Begić, Dragana Kešelj, Zorica Stojanović, Amir Fazlić	
MOUNTAIN GERMANDER (TEUCRIUM MONTANUM L.) - CHARACTERIZATION AND DETERMINATION OF TOTAL PHENOLS AND FLAVONOIDS IN THE EXTRACT OBTAINED BY THE CONVENTIONAL METHOD	78
Zoran Petrović, Nataša Stojanović, Tatjana Botić, Pero Dugić, Nebojša Vasiljević	

BIOTECHNOLOGY	79
ANTIMICROBIAL ACTIVITY OF SILVER NANOPARTICLES STABILIZED OF EXTRACT <i>Fumaria officinalis</i> L.	80
Slobodan Glišić	
CHARACTERIZATION OF CRUDE GLYCEROL FROM BIODIESEL INDUSTRY IN REPUBLIC OF SERBIA ..	81
Ida Zahović, Jelena Dodić, Ivana Pajčin, Jovana Grahovac, Zorana Trivunović	
XANTHAN BIOSYNTHESIS ON CRUDE GLYCEROL-BASED MEDIUM BY CULTIVATION OF <i>Xanthomonas</i> ISOLATE IN LABORATORY BIOREACTOR.....	82
Ida Zahović, Jelena Dodić, Damjan Vučurović, Siniša Dodić, Bojana Bajić, Zorana Trivunović	
THE CHARACTERISATION OF SILYMARIN AND SILIBININ LOADED LIPOSOMES	83
Aleksandra A. Jovanović, Svetlana Dinić, Aleksandra Uskoković, Jelena Arambašić Jovanović, Nevena Grdović, Melita Vidaković, Mirjana Mihailović	
THE IMPACT OF pH VALUE AND TEMPERATURE ON POLYPHENOL RECOVERY, ANTIOXIDANT CAPACITY AND PHYSICAL PROPERTIES OF SERPYLLI HERBA'S WASTE EXTRACTS.....	84
Aleksandra A. Jovanović, Predrag M. Petrović, Mina Volić, Nataša Obradović, Bojana Balanč, Radoslava Pravilović, Branko M. Bugarski	
THE POSSIBILITY OF ANTIBIOTIC AZALOMYCIN B PRODUCTION BY COMBINING BENZOYL HYDRAZONE DERIVATIVES AND WASTE RAPESEED OIL GLYCEROL	85
Jovan Ćirić, Slavica Ilić, Sandra Konstantinović, Đorđe Lazarević, Marko Živković, Nikola Stanković	
ANTIMICROBIAL ACTIVITY OF KOMBUHA BEVERAGE FROM BASIL WASTE MATERIAL	86
Dragoljub Cvetković, Aleksandra Ranitović, Ana Tomić, Olja Šovljanski, Siniša Markov, Milica Aćimović	
INHIBITION OF ALDO-KETO REDUCTASE 1C4 ACTIVITY BY A-RING FUSED PYRIDINE D-MODIFIED STEROIDS	87
Sofija Bekić, Marina Savić, Jovana Ajduković, Edward Petri, Anđelka Čelić	
BIOLOGICAL ACTIVITY EVALUATION OF STEROIDAL D-HOMO LACTONES	88
Sofija Bekić, Ivana Kuzminac, Andrea Nikolić, Marija Sakač, Edward Petri, Anđelka Čelić	
FOOD TECHNOLOGY	89
RESEARCH IN THE FIELD OF PACKAGING AND DISTRIBUTION OF PRODUCTS IN THE FOOD INDUSTRY	90
Slobodan Glišić	
THE ROLE OF NANOTECHNOLOGY IN PACKAGING AND MAINTENANCE OF FOOD PRODUCTS	91
Slobodan Glišić	
WASTEWATER IN THE FOOD INDUSTRY	92
Slobodan Glišić	
THE IMPORTANCE AND USE OF FOOD ADDITIVES AND THEIR EFFECT ON HEALTH	93
Slobodan Glišić	
APPLICATION OF BIODEGRADABLE POLYMERIC MATERIALS FOR FOOD PACKAGING.....	94
Slobodan Glišić	
COMPARATIVE ANALYSIS OF THE CHEMICAL COMPOSITION OF WILD CARROT (<i>Daucus carota</i> L.) ESSENTIAL OILS OBTAINED BY STEAM AND HYDRO-DISTILLATION	95
Ljiljana Stanojević, Aleksandra Milenković, Slobodan Glišić, Jelena Stanojević, Dragan Cvetković, Jovana Milutinović, Dragana Pavlović	
RED WINE COLOR AND STABILITY AS FUNCTION OF SIZE AND CONTENT OF SILICA GEL PARTICLES.....	96
Tanja Šaran, Dragan Vujadinović, Zoran Petković, Milan Vukić, Vesna Gojković, Vladimir Tomović	

ANTIOXIDANT ACTIVITY OF ESSENTIAL AND FATTY OIL ISOLATED FROM CORIANDER (<i>Coriandrum sativum</i> L.) SEEDS.....	97
Ljiljana Stanojević, Jelena Stanojević, Aleksandra Milenković, Slobodan Glišić	
AROMA PROFILE OF CIDER ENRICHED BY FOOD INDUSTRY BY - PRODUCTS - A GC/MS STUDY.....	98
Dragan Cvetković, Jelena Stanojević, Stojan Mančić, Sandra Stamenković Stojanović, Natalija Đorđević, Bojana Danilović, Ivana Karabegović	
THE SEASONAL VARIATIONS OF BIOCHEMICAL COMPOSITION OF COW'S MILK ON THE SOUTHERN SERBIA TERRITORY.....	99
Jovan Ćirić, Slavica Ilić, Aleksandar Veličković, Ivan Stojković, Dragana Stanisavljević, Nebojša Milosavljević	
BREAD WITH THE ADDITION OF FLAX SEED AS A FUNTIONAL FOOD	100
Gordana Jovanović, Ana Vasić, Ljubica Mijić, Ana Matić, Bojan Damjanović	
COMPARATIVE ANALYSIS OF OIL CONTENT IN ALTERNATIVE OIL SPECIES.....	101
Dajana Uletilović, Nada Grahovac, Snežana Kravić, Ana Đurović, Ana Marjanović-Jeromela, Žarko Kevrešan, Zorica Stojanović	
ICP-OES ANALYSIS OF REISHI AND CORDYCEPS ETHANOLIC EXTRACTS	102
Sandra Konstantinović, Dragan Stojiljković, Sanja Petrović, Saša Savić, Ina Konstantinović	
ISOLATION OF JUNIPER BERRY (<i>Juniperis communis</i> L.) ESSENTIAL OILS BY MODERN AND CONVENTIONA HYDRODISTILLATION.....	103
Milena Terzić, Jelena Bajac, Igor Antić, Gökhan Zengin, Branislava Nikolovski, Marija Radojković	
LEGUME AUTHENTICATION METHOD BASED ON FATTY ACID COMPOSITION: A CASE OF GREEN BEAN AND PEAS.....	104
Marko Ilić, Kristian Pastor, Mirjana Vasić, Đura Vujić, Marijana Ačanski	
ANTIOXIDANT ACTIVITY OF ESSENTIAL OIL AND HYDROLATE FROM ANISI FRUCTUS (<i>Pimpinella anisum</i> L.).....	105
Jelena Stanojević, Nataša Simonović, Ljiljana Stanojević, Aleksandra Milenković, Jelena Zvezdanović, Dragan Cvetković	
THE INFLUENCE OF <i>LACTOBACILLUS RHAMNOSUS</i> AND <i>LACTOBACILLUS HELVETICUS</i> ADMINISTRATION ON C57BL/6J MICE BODY WEIGHT.....	106
Gordana Zavišić, Slavica Ristić, Saša Petričević, Milena Rikalović	
EFFECT OF INCORPORATION OF THE PLANT EXTRACTS IN NATURAL CASING ON THE COLOR OF FERMENTED SAUSAGES.....	107
Ana Velemir, Snježana Mandić, Danica Savanović	
IMPACT OF FERMENTATION AND CARRIER COMPOSITION ON PROBIOTIC VIABILITY AND EFFICIENCY OF SPRAY DRY IMMOBILIZATION TECHNIQUE	108
Tanja Ž. Krunić, Marica B. Rakin	
THE EFFECT OF WILD THYME BY-PRODUCT EXTRACTS ON THE OXIDATIVE STABILITY OF COOKED HAMS WITH REDUCED LEVEL OF SODIUM NITRITE.....	109
Jovo Savanović, Branislav Šojić, Danica Savanović, Branimir Pavlić, Vladimir Tomović, Snežana Škaljac, Marija Jokanović	
CONTENT OF MACRO - AND MICROELEMENTS IN CHEESES PRODUCED WITH THE ADDITION OF DIFFERENT SPICES.....	111
Danica Savanović, Ana Velemir, Jovo Savanović, Jelena Sekulić	
POSSIBILITIES OF PRODUCTION OF FRESH CREAM CHEESE IN SEMI-INDUSTRIAL CONDITIONS	112
Danica Savanović, Jovo Savanović, Ana Velemir, Dijana Arsenić	
VALORIZATION OF FOOD INDUSTRY BY-PRODUCTS AS INGREDIENTS IN CIDER PRODUCTION.....	113
Bojana Danilović, Stojan Mančić, Sandra Stamenković Stojanović, Natalija Đorđević, Jelena Stanojević, Miodrag Lazić, Ivana Karabegović	
APPLICATION OF CHITOSAN COATING WITH THE ADDITION OF FREE AND NANOENCAPSULED <i>Satureja montana</i> L. ESSENTIAL OIL IN BEEF PRESERVATION.....	114

Bojana Danilović, Natalija Đorđević, Stojan Mančić, Jelena Stanojević, Dragan Cvetković, Ivana Karabegović, Dragiša Savić

INFLUENCE OF COLD MACERATION TREATMENT ON QUALITY AND AROMATIC PROFILE OF CHARDONNAY WINE 115

Ivana Karabegović, Marko Malićanin, Sandra Stamenković Stojanović, Stojan Mančić, Miodrag Lazić, Bojana Danilović

EFFECT OF NATIVE YEAST STRAINS ON THE VOLATILE CHEMICAL PROFILE OF TAMJANIKA WINES 116

Ivana Karabegović, Stojan Mančić, Sandra Stamenković Stojanović, Miodrag Lazić, Jelena Stanojević, Marko Malićanin, Bojana Danilović

HABITS OF FLUID INTAKE WITH STUDENTS..... 117

Dragana Ilić Udovičić, Ana Matić, Danijela Damnjanović, Aleksandra Vasić

EFFECT OF WHOLEGRAIN BUCKWHEAT FLOUR ADDITION ON CHEMICAL COMPOSITION AND SENSORY QUALITY OF NUTRITIVE ENRICHED WHEAT SCONES..... 118

Nataša Lakić-Karalić, Ladislav Vasilišin, Slavica Grujić, Božana Odžaković, Tanja Marić

QUALITY CONTROL AND FOOD SAFETY 119

EFFECT OF FORMULATION VARIABLES ON SENSORY QUALITY OF THERMO-REVERSIBLE FRUIT FILLING FOR FROZEN SEMI-FINISHED BAKERY PRODUCTS: MODELLING AND OPTIMIZATION 120

Slavica Grujić, Božana Odžaković, Goranka Atelj

ASSESSMENT OF ALIMENTARY INTAKE OF LEAD AND CADMIUM IN THE ADULT POPULATION IN THE REPUBLIC OF NORTH MACEDONIA..... 121

Ana Mitrova Rudovska, Gordana Ristovska

DETERMINATION OF THE TOTAL PHENOLIC CONTENT AND THE ANTIOXIDANT ACTIVITY OF PLUM KERNEL OIL..... 122

Biljana S. Đorđević, Milan D. Kostić, Olivera S. Stamenković, Zoran B. Todorović, Vlada B. Veljković

TESTING OF THE SENSORY QUALITY OF FRESH WHEAT BREAD ON THE TERRITORY OF THE TOWN OF ŠABAC..... 123

Gordana Jovanović, Ljubica Mijić, Ana Vasić, Aleksandra Krsmanović, Bojan Damnjanović

CONCENTRATIONS OF HEAVY METALS IN DOMESTIC HONEY FROM THE WIDER AREA OF BOSNIA AND HERZEGOVINA 124

H. Nanić, E. Pehlić, A. Džaferović, A. Šapčanin, A. Baltić, M. Halilović, M. Čejvan, M. Toromanović

ANTIMICROBIAL ACTIVITY OF COMMERCIAL CITRUS ESSENTIAL OILS..... 125

Nataša Simonović, Bojana Danilović, Ljiljana Stanojević, Dragan Cvetković, Jelena Zvezdanović, Jelena Stanojević

EVALUATION OF ANTIOXIDANT CAPACITY OF ONION EXTRACTS USING UV-VIS SPECTROSCOPY... 126

Mirjana S. Jankulovska, Lenche Velkoska-Markovska, Viktorija Sokolovska

THE CONTENT OF TOTAL IRON IN *Urtica dioica L.* FROM DIFFERENT LOCALITIES IN SERBIA..... 127

Jelena Đuričić Milanković, Kosana Popović, Mirjana Antonijević Nikolić, Bojana Milutinović, Danijela Damnjanović, Dragana Ilić Udovičić

THE PRESENCE OF PHOSPHATE IN MEAT PRODUCTS FROM THE MARKET OF REPUBLIC OF SRPSKA 128

Biljana Pećanac, Dragan Brenjo

CHEMICAL composition, BIOACTIVE COMPONENTS AND ANTIOXIDANT ACTIVITY OF WILD AND CULTIVATED BLACKBERRIES (*Rubus fruticosus L.*) 129

Zoran Kukrić, Ladislav Vasilišin, Goran Vučić, Božana Odžaković, Pero Sailović

TEXTILE ENGINEERING 130

DYNAMICAL MODEL OF YARN REWINDING 131

Nina Djapic

OPTIMIZATION OF THE CLASSICAL DYEING PROCESS OF PES KNITWEAR.....	132
Marija Kodrić, Suzana Đorđević, Nevena Tomić, Dragan Đorđević	
ANISOTROPY OF MECHANICAL PROPERTIES OF WOVEN TEXTILE MATERIALS IN PLAIN WEAVE	133
Jovana Stepanović, Tatjana Šarac, Dušan Trajković, Jovan Stepanović	
INFLUENCE OF KNIT PATTERN ON DIMENSIONAL STABILITY OF KNITTED FABRICS	134
Sandra Stojanović, Dušan Trajković, Jelka Geršak, Miodrag Đorđević	
DYEING OF POLYESTER FABRIC WITH SALICYLALDEHYDE-PHENYLHYDRAZONE.....	135
Milena Nikodijević, Milica Zlatković, Dragan Đorđević, Marija Kodrić, Sandra Konstantinović	
MECHANICAL CHARACTERISTICS ANALYSIS OF SEAMS IN KNITTED FABRICS.....	136
Nataša Stamenković, Nenad Ćirković, Dušan Trajković, Jovan Stepanović, Tatjana Šarac, Jovana Stepanović, Sandra Stojanović	
TESTING OF AIR AND WATER VAPOR PERMEABILITY IN FABRICS, NONWOVEN TEXTILES AND BLANKETS	137
Čedomir Dimić, Nenad Ćirković, Anita Sadiković, Ivana Petrović, Milena Nikodijević, Tatjana Šarac, Nataša Stamenković	
ANALYSIS OF DELAYS AND LOSS OF PRODUCTION TIME WHEN SEWING A WORKING BLOUSE	138
Nenad Ćirković, Ivana Petrović ¹ Tatjana Šarac, Nataša Stamenković, Anita Sadiković, Čedomir Dimić	
CALCULATION OF THE NUMBER OF LAYERS WHEN LAYING KNITWEAR FOR THE PURPOSE OF PRODUCTION RATIONALIZATION IN PRODUCTION OF CHILDREN'S SWEATSHIRT	139
Nenad Ćirković, Tatjana Šarac, Nataša Stamenković, Jovan Stepanović, Dušan Trajković, Jovana Stepanović	
ANALYSIS OF ELASTIC PROPERTIES OF RIGHT-LEFT KNITTED FABRICS	140
Ivana Petrović, Nenad Ćirković, Tatjana Šarac, Nataša Stamenković, Anita Sadiković, Čedomir Dimić	
EFFECT OF HYDROGEN-PEROXIDE TREATMENT ON THE PHYSICO-MECHANICAL PROPERTIES OF FLAX FIBERS	141
Biljana Lazic, Svjetlana Janjic, Vesna Ivanovic, Mirjana Kostic	
ANTIMICROBIAL TREATMENT OF LEATHER LINING FOR FOOTWEAR WITH THE EXTRACTS OF <i>Picea omorika</i> AND COPPER (I) OXIDE.....	142
Dragana Grujić, Aleksandar Savić, Ljiljana Topalić-Trivunović, Blanka Škipina, Branka Ružičić, Milica Jovanić, Mitja Kolar, Boštjan Novak	
TEXTILE INDUSTRY SUPPLY CHAIN: FINISHED GOODS INVENTORY MANAGEMENT.....	143
Miroslav Dragic	
SORPTION OF LIDOCAINE ON CHEMICALLY TREATED WOOL	144
Svjetlana Janjić, Milanka Kačar, Srđan Ristić, Pero Sailović	

GRAPHIC ENGINEERING AND DESIGN..... 145

A METHOD OF RANKING RESPONDENTS ACCORDING TO SENSE OF COLOR DIFFERENCES	146
Zoran Gazibarić, Predrag Živković, Vladimir Cviljušac, Miloš Ljubojević	
AN OVERVIEW OF VARIOUS POSSIBILITIES OF 3D PRINTING TECHNIQUES IN THE PRODUCTION OF FLEXOGRAPHIC PRINTING PLATES.....	147
Sandra Dedijer, Nemanja Kašiković, Magdolna Pal, Živko Pavlović, Gojko Vladić, Ivana Tomić, Bojan Banjanin	
CONTEMPORARY APPLICATIONS OF PULP MOULDED PACKAGING	148
Gojko Vladić, Nemanja Kašiković, Sandra Dedijer, Teodora Gvoka, Gordana Bošnjaković	
INFLUENCE OF THE SUBSTRATE ON THE PERMANENCE OF PRINTING INK.....	149
Branka Ružičić, Mladen Stančić, Đorđe Vujčić, Milijana Milić	
REMARKS ABOUT PRINTING AUTOMATION.....	150

Thomas Hoffmann Walbeck, Živko Pavlović

COMPARISON OF COLORIMETRIC RESULTS OBTAINED BY SPHERICAL AND SPECTROPHOTOMETER WITH DIRECTIONAL GEOMETRY ON SAMPLES WITH EXTREME UV VARNISH APPLICATION..... 151
Đorđe Vujčić, Sandra Dedijer, Mladen Stančić, Branka Ružičić, Igor Majnarić

ENVIRONMENTAL ENGINEERING AND ECOLOGY 152

ADSORPTION OF BEMACID RED DYE FROM AQUEOUS SOLUTIONS ON COAL FLY ASH MODIFIED WITH HCl 153
Dragana Raca, Ljiljana Vukić, Dijana Drljača, Dajana Dragić

ANALYSIS OF THE PHYSICO-CHEMICAL PARAMETERS OF VARDAR RIVER WATER FROM 2018 TO 2021 154
Tamara Jovanovska, Aleksandra Petrova, Donka Doneva-Sapceska, Mihail Kocubovski, Rejhan Muhamed Xumkar

DEPOSITION OF GOETHITE AND FERRIHYDRITE ONTO EXPANDED VERMICULITE SURFACE: CHEMICAL PROPERTIES AND POTENTIAL APPLICATION 155
Mladen Bugarčić, Aleksandar Jovanović, Aleksandar Marinković, Jovana Bošnjaković, Miroslav Sokić, Ana Radosavljević Mihajlović, Milan Milivojević

CARBOHYDRATE-COATED CERIUM OXIDE NANOPARTICLES AFFECT THE GERMINATION OF *Sinapis alba* AND *Chenopodium rubrum* SEEDS THROUGH THE GENERATIONS 156
Ivana Milenković, Slađana Z. Spasić, Ksenija Radotić

ANTIBACTERIAL AND ANTIFUNGAL EFFECT OF S- AND N- CDs@AgMOFs NANOCOMPOSITES..... 157
Ivana Milenković, Manuel Algarra, Kristina Joksimović, Vladimir Beškoski, Teresa J. Bandosz, Enrique Rodríguez-Castellón, Ksenija Radotić

CIRCADIAN ACTIVITY OF THE WELLS CATFISH (*SILURUS GLANIS*) IN THE DANUBE RIVER 158
Slađana Spasić, Marija Smederevac-Lalić, Mirjana Lenhardt, Stefan Hont, Marian Paraschiv, Ion Iani Marian, Iulian Nichersu, Cristian Trifanov, Miroslav Nikčević, Peter Klimley, Radu Suciú

REMOVAL OF XENOBIOTICS FROM WASTEWATERS USING PHOTOLYSIS UNDER SUN-LIGHT IRRADIATION: EXPERIMENTAL APPROACH AND PROCESS DESIGN 159
Aleksandar Jovanović, Mladen Bugarčić, Nataša Knežević, Jovana Bošnjaković, Jelena Lukić, Antonije Onjia, Aleksandar Marinković

PHYSICO-CHEMICAL TREATMENT OF HAZARDOUS COAL TAR WASTE BY THE SOLIDIFICATION PROCESS FOR THE PURPOSE OF ITS FINAL DISPOSAL 160
Siniša Cukut, Nebojša Knežević

GHG EMISSIONS IN THE CURRENT AND FUTURE MSW MANAGEMENT SYSTEM IN ZVORNIK, B&H... 161
Draženko Bjelić, Borislav Malinović, Dragana Nešković Markić, Brankica Gegić

SOLAR STABILITY OF COMMERCIAL PESTICIDES THAT CONTRIBUTE TO THE QUALITY OF GRAPES AND FRUITS..... 162
Maria M. Savanović, Aleksandra Jovanoski Kostić, Andrijana Vukojević, Stevan Armaković, Jelena Kalajdžić, Biserka Milić, Mladen Kalajdžić, Svetlana Pelemiš, Sanja J. Armaković

COMPARATIVE ASSESSMENT OF ZINC IONS SORPTION AND RETENTION BY PROSPECTIVE UNCONVENTIONAL SOIL ADDITIVES 163
Ivana Smičiklas, Marija Egerić, Mihajlo Jović

PERSPECTIVES OF CONSTRUCTION WASTE MANAGEMENT 164
Zorica Eraković, Ivana Mladenović-Ranisavljević, Stanko Žerajić

A TRIETHANOLAMINE-BASED DEEP EUTECTIC SOLVENT IN THE CALCIUM OXIDE CATALYZED ETHANOLYSIS OF *Brassica nigra* L. SEED OIL 165
Biljana S. Đorđević, Milan D. Kostić, Olivera S. Stamenković, Zoran B. Todorović, Ljiljana M. Veselinović, Vlada B. Veljković

DRY-WASHING PURIFICATION OF CRUDE BIODIESEL OBTAINED BY ALKALI-CATALYZED TRANSESTERIFICATION 166

Ivan J. Stojković, Vladimir P. Pavićević, Vlada B. Veljković	
REUSABLE Fe ₂ O ₃ /TiO ₂ /PVC PHOTOCATALYSTS SYNTHESIS AND APPLICATION FOR THE REMOVAL OF METHYLENE BLUE IN PRESENCE OF SIMULATED SOLAR RADIATION	167
Ivana Jagodić, Nemanja Banić	
A GREEN ADSORBENT BASED ON WHEAT STARCH FOR REMOVAL OF SELECTIVE ORGANIC POLLUTANTS FROM AQUEOUS SOLUTIONS	168
Nataša Karić, Marija Vukčević, Marina Maletić, Mirjana Ristić, Aleksandra Perić-Grujić, Katarina Trivunac	
EFFECT OF ALKALI MODIFICATION ON ADSORPTION EFFICIENCY OF FLY ASH	169
Nataša Karić, Sara Živojinović, Marija Vukčević, Marina Maletić, Aleksandra Perić-Grujić, Katarina Trivunac	
USE OF AGRICULTURAL WASTE AS RAW MATERIALS FOR OBTAINING GLASS AND GLASS-CERAMICS: A REVIEW	170
Vladimir S. Topalović, Jelena D. Nikolić, Veljko V. Savić, Srdjan D. Matijašević, Marija S. Djošić, Snežana N. Zildžović, Snežana R. Grujić	
PHOTOCATALYTIC DECOMPOSITION OF DIFENOCONAZOLE FROM WASTEWATERS	171
Jovana Bošnjaković, Nataša Knežević, Srećko Manasijević, Aleksandar Jovanović, Mladen Bugarčić, Aleksandar Marinković	
UTILIZATION OF CONSTRUCTION MATERIAL AND UNSATURATED RESIN FROM WASTE PET AS A STABILIZER FOR DESORBED METAL ION Pb ²⁺	172
Nataša Knežević, Jovana Bošnjaković, Aleksandar Jovanović, Mladen Bugarčić, Srećko Manasijević ² Aleksandar Marinković	
ANALYSIS OF ARSENIC MONITORING IN GROUNDWATER OF THE REPUBLIC OF SERBIA FOR THE PERIOD 2018-2020	173
Dunja Plavšić, Dimitrije Isoski, Ana Vidaković	
ECOLOGICAL RISKS FROM THE EMITTED HARMFUL GASES IN CASE OF FIRE ACTIONS ON STONE WOOL	174
Veronika Karadjova, Hristo Serbezov, Stefan Parvanov, Detelin Spasov	
GHG EMISSIONS FROM ROAD TRANSPORT IN THE REPUBLIC OF SRPSKA ACCORDING TO COPERT V MODEL	175
Ranka Radic, Svjetlana Borojevic, Ajda Seranic, Darko Sipka	
SLOW PYROLYSIS – TOOL FOR IMPROVEMENT OF FUEL PROPERTIES OF LIGNOCELLULOSIC WASTE. 176	
Zorica Lopičić, Anja Antanasković, Tatjana Šoštarić, Vladimir Adamović, Marina Orlić, Jelena Milojković, Milan Milivojević	
BIOCHAR AS EFFICIENT TOOL FOR SOIL AMMENDMENT	177
Zorica Lopičić, Anja Antanasković, Tatjana Šoštarić, Vladimir Adamović, Marina Orlić, Jelena Petrović, Jelena Avdalović	
ANTIBACTERIAL ACTIVITY OF SURFACE AMINE-FUNCTIONALIZED SILVER-ENRICHED ZEOLITE	178
Sanja Jevtić, Jelena Dimitrijević, Jelena Petrović, Jelena Dikić	
SYNTHESIS AND APPLICATION OF HYDROXYAPATITE/ZEOLITE COMPOSITE FOR ADSORPTION OF HEAVY METAL IONS FROM WATER MATRICES	179
Sanja Jevtić, Katarina Sokić, Jelena Dikić	
A STUDY OF PV SYSTEM APPLICATION ON THE SUSTAINABLE DEVELOPMENT IN SERBIA	180
Dragana Todorović, Slavica Jovanović, Tijana Kevkić, Marija Stojanović Krasić, Nenad Milojević, Branko Drljača	
FROM ELECTROOXIDATIONS TO MULTIANALYTICAL EVALUATION OF PHENOL DEGRADATION.....	181
Aleksander Kravos, Tijana Đuričić, Gabriela Kalčikova, Borislav N. Malinović, Helena Prosen	
THE ENVIRONMENTAL STATE OF THE DANUBE RIVER NEAR POWER PLANT "KOSTOLAC", SERBIA	182
Gordana Devic, Marija Pergal, Miodrag Pergal	
POLLUTION INDICES AS A USEFUL TOOL FOR MONITORING SEDIMENT CONTAMINATION IN THE LAST TWO DECADES IN BOKA KOTORSKA BAY, ADRIATIC SEA	183
Milena Radmirović, Bojan Tanaskovski, Nevenka Mijatović, Chiara Cantaluppi, Federica Ceccotto, Antonije Onjia, Slavka Stanković	

STATISTICAL ANALYSIS OF POLLUTION INDICES IN THE LAST TWO DECADES FOR THE BOKA KOTORSKA BAY, ADRIATIC SEA.....	184
Milena Radomirović, Bojan Tanaskovski, Nevenka Mijatović, Milica Vasić, Lato Pezo, Antonije Onjia, Slavka Stanković	
TIME AND SEASONAL VARIATIONS OF PARTICULATE MATTER (PM) AND GASEOUS POLLUTANTS CONCENTRATIONS IN AMBIENT AIR OF VALJEVO, SERBIA	185
Jelena Đuričić Milanković, Dragana Đorđević	
CONDITIONING OF WASTE SLUDGE FROM THE BIOLOGICAL WASTEWATER TREATMENT PLANT OF THE COKE INDUSTRY GIKIL.....	186
Mirnesa Zohorović, Abdel Đozić, Vedran Stuhli, Ljilja Bojanović, Adisa Halilčević Kovač, Edisa Papračanin, Emra Halilović, Jasmin Pandurović	
HISTOLOGY OF THE DIGESTIVE TRACT OF THE ENDEMIC AND ENDANGERED <i>SALMO OBTUSIROSTRIS</i> (TELEOSTEI: SALMONIDAE) FROM THE RIVER BUNA (NERETVA RIVER BASIN, BOSNIA AND HERZEGOVINA)	187
Ingrid Wolf Stefan, Ivana Markotić	
ORGANIC BIO-DEGRADABLE WASTE IN FRUIT PRODUCTION	188
Milica Đeković Šević, Zoranka Malešević, Milan Šević, Tamara Bartošek	
BIOFUELS AS A CHALLENGE OF SUSTAINABLE DEVELOPMENT	189
Saša Papuga, Aleksandra Kolundžija, Milica Đurđević	
ADSORPTION OF METHYLENE BLUE ON WASTE NEWSPAPER	190
Sanda Pilipović, Dijana Drljača, Tatjana Botić, Dajana Dragić, Aleksandra Borković	
MATERIAL SCIENCE AND METALLURGY	191
MANGANESE-PYROMELLITATE COMPLEX AS A PRECURSOR FOR PREPARATION OF SPINEL Mn_3O_4 ..	192
Lidija Radovanović, Željko Radovanović, Aleksandar Kremenović, Bojana Simović, Milica V. Vasić, Jelena Rogan	
DETERMINATION OF THE OPTIMAL THICKNESS FOR PROTECTION OF FIRE-RESISTANT AIR DUCTS ..	193
Veronika Karadjova, Nelly Simeonova, Stefan Parvanov	
OPTICAL LIGHT BEAM PROPAGATION CONTROL TROUGHT THE DEFECT IN ONE-DIMENSIONAL PHOTONIC LATTICE	194
Slavica Jovanović, Dragana Todorović, Marija Stojanović-Krasić, Tijana Kevkić, Nenad Milojević, Branko Drljača	
SURFACE CHARACTERISTICS OF POLYURETHANE/ORGANOCLAY NANOCOMPOSITES	195
Milena Rašljčić-Rafajilović, Dana Vasiljević-Radović, Milena Špírková, Gordana Gojgić-Cvijović, Marija V. Pergal	
CHARACTERIZATION OF POLY(DIMETHYLSILOXANE)/LASER-INDUCED GRAPHENE COMPOSITES...	196
Milena Rašljčić-Rafajilović, Dana Vasiljević-Radović, Teodora Vičentić, Marko Spasenović, Marko Bošković, Igor Pašti, Marija V. Pergal	
FLOWER-SHAPED MAGNETIC NANOPARTICLES FOR THERANOSTIC APPLICATIONS	197
Miloš Ognjanović, Marija Mirković, Željko Prijović, Sanja Vranješ-Đurić, Bratislav Antić	
THERMODYNAMIC PROPERTIES OF COMPOUND CRYSTALLINE NANOSTRUCTURES	198
Siniša M. Vučenović, Jovan P. Šetrajčić	
SIMULATION OF THE IMPACT OF PREHEATING TEMPERATURE ON RAILWAY ALUMINOTHERMIC WELDING	199
Gvozden Jovanović, Vaso Manojlović, Miroslav Sokić, Alen Delić, Milorad Gavrilovski	
THE INFLUENCE OF COMPOSITION ON THE PROPERTIES OF THERMOPLASTIC POLYURETHANE NANOCOMPOSITES.....	200
Gordana Dević, Milena Špírková, Miloš Steinhart, Sanja Ostojić, Dana Vasiljević-Radović, Ivan Stefanović, Marija V. Pergal	
OTHERS.....	201

STUDY OF ISOTHERMAL, KINETIC, AND THERMODYNAMIC PARAMETERS FOR SORPTION OF VANADIUM.....	202
Tamara T. Tadić, Bojana M. Marković, Aleksandra B. Nastasović, Ljiljana T. Suručić, Zvezdana P. Sandić , Antonije E. Onjia	
REMOVAL OF LINDANE FROM AQUEOUS SOLUTION BY GLYCIDYL METHACRYLATE BASED CHELATING MACROPOROUS COPOLYMER: KINETICS AND MECHANISM.....	203
Tamara T. Tadić, Bojana M. Marković, Mila V. Ilić, Aleksandra B. Nastasović, Antonije E. Onjia	
THE USE OF SOFT FOOD AS A VEHICLE FOR DRUG DELIVERY TO PEDIATRIC POPULATION – EFFECTS ON DISSOLUTION OF PROPRANOLOL	204
Maja Mirjanić, Aneta Stojmenovski, Biljana Gatarić, Nataša Bubić Pajić, Anđelka Račić	
BIOMONITORING ARSENIC SPECIES USING HONEY BEES	205
Nenad Zaric, Simone Braeuer, Walter Goessler	
EXPERIMENTAL DETERMINATION OF FIRE RESISTANCE OF STEEL ELEMENTS (X-BRACE) PROTECTED WITH INTUMESCENT PAINT	206
Neli Simeonova	
EXPERIMENTAL DETERMINATION OF FIRE RESISTANCE OF STEEL ELEMENTS (X-BRACE) PROTECTED WITH ROCK WOOL.....	207
Neli Simeonova	

A STUDY OF PV SYSTEM APPLICATION ON THE SUSTAINABLE DEVELOPMENT IN SERBIA

Dragana Todorović¹, Slavica Jovanović¹, Tijana Kevkić¹, Marija Stojanović Krasić², Nenad Milojević³, Branko Drljača¹

¹University of Priština, Faculty of Sciences and Mathematics, Kosovska Mitrovica, Serbia

²University of Niš, Faculty of Technology, Leskovac, Serbia

³University of Niš, Faculty of Sciences and Mathematics, Niš, Serbia

Corresponding author e-mail: slavica.jovanovic@pr.ac.rs

Abstract

Climate change is one of the most significant environmental problems and is affecting the entire global population. Renewable sources of energy (RES) are vital to deal with this problem. Solar energy, especially photovoltaic (PV) technologies, is one of the most promising renewable energy sources and is, therefore, one of the fastest-growing industries in this field. Thus, this paper focuses on the performance analyses of rooftop on-grid PV system in real climatic conditions in Niš (Serbia) in 2019 and its environmental benefits. Besides, the life cycle assessment (LCA) for the PV system, based on a case study in Niš, is also given in this paper. Based on this study, energy from PV systems could potentially be a part of the solution for Serbia's future energy demands, as well as for the preservation of the environment and the establishment of sustainable development in Serbia.

Keywords: PV system, PV system Efficiency, Performance Ratio, LCA, EPBT.

OPTICAL LIGHT BEAM PROPAGATION CONTROL THROUGH THE DEFECT IN ONE-DIMENSIONAL PHOTONIC LATTICE

Slavica Jovanović¹, Dragana Todorović¹, Marija Stojanović-Krasić², Tijana Kevkić¹, Nenad Milojević³, Branko Drljača¹

¹University of Priština, Faculty of Sciences and Mathematics, Kosovska Mitrovica, Serbia

²University of Niš, Faculty of Technology, Leskovac, Serbia

³University of Niš, Faculty of Sciences and Mathematics, Niš, Serbia

Corresponding author e-mail: slavica.jovanovic@pr.ac.rs

Abstract

Photonic lattices represent periodic structures, suitable for investigation of wave propagation and localization. Within these systems, different phenomena such as discrete diffraction, lattice solitons, Anderson localization and defect localizations can be analyzed. The lattice periodicity in one or more dimensions leads to the zonal structure in terms of existing permitted and forbidden zones which can allow or stop light beam propagation. Manipulation with the zonal structure can be done by introducing different types of defects into the lattice. As a consequence, the defects can stop, trap, reflect and also shape localized light beams. Defects which can be formed during the fabrication process change the zonal structure and allow the occurrence of different types of potentially stable localized defect modes. This gives additional opportunity for the light control in terms of suppressing waveguides, stopping light, trapping and shaping solitons and can be used for all-optical switching and routing. In this paper, we numerically analyzed the trapping effect in a one-dimensional lattice with a coupling defect as a function of wavelength and width of the input light beam. The input of 4 μm gives the best capturing effect at the 6 μm wide linear defect, while for 2 μm wide linear defect the narrower input beam 2 μm enables better capturing. The light propagation is modelled by the time-independent Helmholtz equation. The split-step Fourier method is used for the numerical simulations. These numerical findings may lead to interesting applications such as blocking, filtering and transporting light beams through the optical medium.

Keywords: photonic lattices, linear defect, light localization, trapping efficiency, control of light propagation.

Program and Organization Committees

Scientific Committee

Aleksandar Ivić	Faculty of Mining and Geology, Department of Mathematics, University of Belgrade, Serbia
Boško Jovanović	Faculty of Mathematics, University of Belgrade, Serbia
Francisco Marcellán	Charles III University of Madrid, Department of Mathematics Madrid, Spain
Giuseppe Mastroianni	University of Basilicata, Department of Mathematics and Computer Sciences, Viale dell'Ateneo Lucano, 10 85100 Potenza ITALY
Gradimir V. Milovanović, Chairman	Serbian Academy of Sciences and Arts, Kneza Mihaila 36, 11000 Beograd, Serbia
Giovanni Monegato	Institute of Geosciences and Earth Resources IGG, Rome, Italy
Sotirios E. Notaris	University of Athens, Department of Mathematics, Athens, Greece
Stevan Pilipović	Faculty of Sciences, Department of Mathematics and Informatics, University of Novi Sad, Serbia
Lothar Reichel	Kent State University, Department of Mathematical Sciences Kent, OH 44242, USA
Miodrag M. Spalević	Faculty of Mechanical Engineering, Department of Mathematics, University of Belgrade, Serbia
Endre Süli	Mathematical Institute, University of Oxford, UK
Walter Van Assche	University of Leuven, Department of Mathematics, Section of Analysis, Belgium

Organizing Committee

Nenad Cakić	School of Electrical Engineering, Department of mathematics, University of Belgrade, Serbia
Aleksandar Cvetković	Faculty of Mechanical Engineering, Department of Mathematics, University of Belgrade, Serbia
Dragan Djordjević	Faculty of Sciences and Mathematics, Department of Mathematics and Informatics, University of Niš
Davorka Jandrić	Faculty of Mechanical Engineering, Department of Mathematics, University of Belgrade, Serbia
Nataša Krejić	Faculty of Sciences, Department of Mathematics and Informatics, University of Novi Sad
Miodrag Mateljević	Faculty of Mathematics, University of Belgrade, Serbia
Zoran Ognjanović	Mathematical Institute SANU, Belgrade, Serbia

Note on right zero divisors in the ring of infinite upper triangular matrices over a field	48
<i>Zoran S. Pucanović</i>	
Unconditionally positive finite difference and standard finite difference schemes for advection—diffusion reaction equations	49
<i>Svetislav Savović, Branko Drljača and Alexandar Djordjevich</i>	
Numerical solution of one-dimensional advection—diffusion equation with constant and periodic boundary conditions	50
<i>Svetislav Savović, Branko Drljača and Alexandar Djordjevich</i>	
Approximation of generalized stochastic processes	51
<i>Dora Seleši</i>	
Generating functions for some special polynomials including Poisson-Charlier, Hermite type, Milne-Thomson type and the other polynomials	53
<i>Yilmaz Simsek</i>	
Finite difference method for the 2D heat equation with concentrated capacity	55
<i>Bratislav Sredojević and Dejan Bojović</i>	
RNN solution of linear matrix equation and its applications	56
<i>Predrag Stanimirović, Marko Petković and Miroslav Ćirić</i>	
Bayesian prediction of order statistics based on record values from Generalized exponential distribution	59
<i>Zoran Vidović</i>	
Application of machine learning algorithms to high frequency trading	60
<i>Ljubica Vujović and Željko Djurović</i>	

15:00-16:30 Session B3

CHAIR: [Katica R Stevanovic Hedrih](#)

LOCATION: 513 (Faculty of Mechanical Engineering)

15:00 [Irem Kucukoglu](#) and [Yilmaz Simsek](#)**Numerical evaluations on power series including the numbers of Lyndon words and interpolation functions for the Apostol-type polynomials**SPEAKER: [Irem Kucukoglu](#)

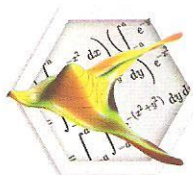
ABSTRACT. Recently, the Lyndon words and their numbers have been investigated by researchers using various methods. Contrary to other studies, in this paper, we use the methods associated with a family of zeta functions interpolating a family of higher-order Apostol-type numbers and polynomials. The main purpose of this paper is not only to define power series including the numbers of Lyndon words and binomial coefficients, but also to construct new computation algorithms in order to simulate these series with numerical analysis and plots. With these algorithms, we provide novel computational methods to the area of the combinatorics on words. Moreover, in order to reduce algorithmic complexity of these algorithms, our other aim is to present an approximation to these series by rational functions of the Apostol-type numbers. Finally, we give some remarks, observations and comments on these polynomials and the numbers of Lyndon words.

15:30 [Svetislav Savovic](#), [Branko Drjaca](#) and [Alexandar Djordjević](#)**Unconditionally positive finite difference and standard finite difference schemes for advection–diffusion reaction equations**SPEAKER: [Branko Drjaca](#)

ABSTRACT. A recently reported unconditionally-positive finite difference (UPFD) [1] and the standard explicit finite difference (EFD) schemes are compared to the analytical solution of the advection-diffusion reaction equation which describes the exponential traveling wave. It is found that although the unconditional positivity assures stability of the UPFD scheme regardless of the size of the discretization steps taken, this scheme is less accurate than the standard explicit finite difference scheme. This is because the UPFD scheme contains additional truncation-error terms in the approximations of the first and second derivatives with respect to x , which are evaluated at different moments in time. While these terms tend to zero as the mesh is refined, the UPFD scheme nevertheless remains less accurate than its standard explicit finite difference counterpart.

16:00 [Svetislav Savovic](#), [Branko Drjaca](#) and [Alexandar Djordjević](#)**Numerical solution of one-dimensional advection-diffusion equation with constant and periodic boundary conditions**SPEAKER: [Branko Drjaca](#)

ABSTRACT. For constant and periodic boundary conditions, the one-dimensional advection-diffusion equation with constant coefficients is solved by the explicit finite difference method in a semi-infinite medium. It is shown how far the periodicity of the oscillating boundary carries on until diminishing to below appreciable levels a specified distance away, which depends on the oscillation characteristics of the source. Results have been tested against an analytical solution reported for a special case [1]. The explicit finite difference method is shown to be effective for solving the advection-diffusion equation with constant coefficients in semi-infinite media with arbitrary initial and boundary conditions.



ACTA 2017

International Conference: ACTA 2017 - APPROXIMATION AND COMPUTATION – THEORY AND APPLICATIONS
(E-mail: acta2017@easychair.org)

Participant: Branko Drljača (Serbia)

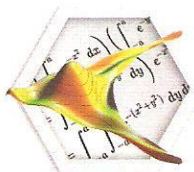
Talk: *Numerical solution of one-dimensional advection-diffusion equation with constant and periodic boundary conditions*

This is the certificate of your attending on the international conference ACTA 2017: APPROXIMATION AND COMPUTATION – THEORY AND APPLICATIONS that was held in Belgrade, Serbia, on November 30 - December 2, 2017.

Your participation and your contribution helped tremendously to make the conference a memorable event. Your involvement in the ACTA 2017 conference is very much appreciated and we hope to see you again in the near future.

In the name of Organizing committee
of the ACTA 2017 conference

Prof. Dr. Miodrag M. Spalević



ACTA 2017

**International Conference: ACTA 2017 - APPROXIMATION
AND COMPUTATION – THEORY AND APPLICATIONS**
(E-mail: acta2017@easychair.org)

Participant: Branko Drljača (Serbia)

Talk: *Unconditionally positive finite difference and standard finite difference schemes for advection–diffusion reaction equations*

This is the certificate of your attending on the international conference ACTA 2017: APPROXIMATION AND COMPUTATION – THEORY AND APPLICATIONS that was held in Belgrade, Serbia, on November 30 - December 2, 2017.

Your participation and your contribution helped tremendously to make the conference a memorable event. Your involvement in the ACTA 2017 conference is very much appreciated and we hope to see you again in the near future.

In the name of Organizing committee
of the ACTA 2017 conference

Prof. Dr. Miodrag M. Spalević

16:00–16:30	Zoran Vidović (Teacher Education Faculty, University of Belgrade, Serbia) <i>Bayesian prediction of order statistics based on record values from generalized exponential distribution</i>
15:00–16:30	Session B3
CHAIR	Katica R. (Stevanović) Hedrih
LOCATION	513 (Faculty of Mechanical Engineering)
15:00–15:30	Branko Drljača (University of Kosovska Mitrovica, Serbia) <i>Unconditionally positive finite difference and standard finite difference schemes for advection diffusion reaction equations</i>
15:30–16:00	Branko Drljača (University of Kosovska Mitrovica, Serbia) <i>Numerical solution of one-dimensional advection-diffusion equation with constant and periodic boundary conditions</i>
16:00–16:30	Dragan Pavlović (Faculty of Electrical Engineering, University of Belgrade, Serbia) <i>Calculation of the channel discharge function for the generalized lightning traveling current source return stroke model</i>
17:00–17:30	Coffee Break
17:00–19:00	Session A4
CHAIR	Donatella Occorsio
LOCATION	211 (Faculty of Mechanical Engineering)
17:00–17:30	Agnieszka Prusińska (Faculty of Science, Siedlce University, Poland) <i>P-regular nonlinear optimization – calculus and methods</i>
17:30–18:00	Predrag Stanimirović (Faculty of Sciences and Mathematics, University of Niš, Serbia) <i>RNN solution of linear matrix equation and its applications</i>
18:00–18:30	Tuğba Bostancı (Ankara University, Turkey) <i>An Extension of Stancu Operator</i>
18:30–19:00	Snežana S. Djordjević (Faculty of Technology Leskovac, University of Nis, Serbia) <i>Analysis of a class of conjugate gradient methods</i>
17:00–19:00	Session B4
CHAIR	Bilge Peker
LOCATION	513 (Faculty of Mechanical Engineering)
17:00–17:30	Zorica Milovanović Jeknić (Faculty of Construction Management, Serbia) <i>Parabolic-Hyperbolic Transmission Problem in Disjoint Domains</i>
17:30–18:00	Bratislav Sredojević (Faculty of Science, University of Kragujevac, Serbia) <i>Finite difference method for the 2D heat equation with concentrated capacity</i>
18:00–18:30	Katica R. (Stevanović) Hedrih (Mathematical institute SANU, Serbia) <i>Approximations in an investigation of the vibro-impact dynamics of rolling bodies in successive central collisions on curvilinear trace</i>
18:30–19:00	Haldun Alpaslan Peker (Selcuk University, Turkey) <i>A Semi-Analytical Approach to Solve a Flow Model</i>

Unconditionally positive finite difference and standard finite difference schemes for advection–diffusion reaction equations

Svetislav Savović^{1,2}, Branko Drljača³, and Alexandar Djordjevich²

¹ University of Kragujevac, Faculty of Science, R. Domanovića 12, Kragujevac, Serbia
savovic@kg.ac.rs

² City University of Hong Kong, 83 Tat Chee Avenue, Kowloon, Hong Kong, China
mealex@cityu.edu.hk

³ University of Kosovska Mitrovica, Faculty of Science,
Lole Ribara 29, Kosovska Mitrovica, Serbia
brdrljaca@gmail.com

Abstract

A recently reported unconditionally-positive finite difference (UPFD) [1] and the standard explicit finite difference (EFD) schemes are compared to the analytical solution of the advection-diffusion reaction equation which describes the exponential traveling wave. It is found that although the unconditional positivity assures stability of the UPFD scheme regardless of the size of the discretization steps taken, this scheme is less accurate than the standard explicit finite difference scheme. This is because the UPFD scheme contains additional truncation-error terms in the approximations of the first and second derivatives with respect to x , which are evaluated at different moments in time. While these terms tend to zero as the mesh is refined, the UPFD scheme nevertheless remains less accurate than its standard explicit finite difference counterpart.

Keywords: advection-diffusion reaction equation, exponential traveling wave, finite difference schemes

References

1. Chen-Charpentier, B. M., Kojouharov, H. V.: An unconditionally positivity preserving scheme for advection-diffusion reaction equations, *Math. Comput. Modelling* 57 (2013) 2177–2185.

Numerical solution of one-dimensional advection-diffusion equation with constant and periodic boundary conditions

Svetislav Savović^{1,2}, Branko Drljača³, and Alexandar Djordjevich²

¹ University of Kragujevac, Faculty of Science, R. Domanovića 12, Kragujevac, Serbia
savovic@kg.ac.rs

² City University of Hong Kong, 83 Tat Chee Avenue, Kowloon, Hong Kong, China
mealex@cityu.edu.hk

³ University of Kosovska Mitrovica, Faculty of Science,
Lole Ribara 29, Kosovska Mitrovica, Serbia
brdrljaca@gmail.com

Abstract

For constant and periodic boundary conditions, the one-dimensional advection-diffusion equation with constant coefficients is solved by the explicit finite difference method in a semiinfinite medium. It is shown how far the periodicity of the oscillating boundary carries on until diminishing to below appreciable levels a specified distance away, which depends on the oscillation characteristics of the source. Results have been tested against an analytical solution reported for a special case [1]. The explicit finite difference method is shown to be effective for solving the advection-diffusion equation with constant coefficients in semi-infinite media with arbitrary initial and boundary conditions.

Keywords: advection-diffusion equation, periodic boundary conditions, finite difference schemes

References

1. Wang, W., Dai, Z., Li, J., Zhou, L., A hybrid Laplace transform finite analytic method for solving transport problems with large Peclet and Courant numbers, *Comp. and Geosc.* 49 (2012) 182-189.

АКАДЕМИЈА НАУКА
И УМЈЕТНОСТИ
РЕПУБЛИКЕ СРПСКЕ



ACADEMY OF SCIENCES
AND ARTS OF THE
REPUBLIC OF SRSKA

**СЕДМИ МЕЂУНАРОДНИ НАУЧНИ СКУП
САВРЕМЕНИ МАТЕРИЈАЛИ 2014**

ПРОГРАМ РАДА

**SEVENTH INTERNATIONAL
SCIENTIFIC CONFERENCE
CONTEMPORARY MATERIALS 2014**

PROGRAMME

Бања Лука, 21–22. децембар 2014. године
Banja Luka, December 21 to 22, 2014

ОРГАНИЗАТОР НАУЧНОГ СКУПА

Академија наука и умјетности Републике Српске

ПОКРОВИТЕЉ НАУЧНОГ СКУПА

Министарство науке и технологије Републике Српске

ОДРЖАВАЊЕ СКУПА СУ ПОМОГЛИ

*Електропривреда Републике Српске
Универзитетска болница клинички центар Бања Лука
Комора доктора медицине РС*

ОРГАНИЗАЦИОНИ ОДБОР

Академик Рајко Кузмановић, предсједник
Академик Драгољуб Мирјанић, потпредсједник
Академик Васкрсија Јањић
Академик Бранко Шкундрић
Проф. др Симо Јокановић
Проф. др Зоран Рајилић
Проф. др Мирко Станетић
Проф. др Небојша Јованић
Мр Винко Богдан
Доц. др Синиша Вученовић

ORGANIZER OF THE CONFERENCE

Academy of Sciences and Arts of the Republic of Srpska

UNDER THE PATRONAGE OF

Ministry of Science and Technology of Republic of Srpska

THE CONFERENCE HAS BEEN SUPPORTED BY

*Power Utility of the Republic of Srpska
University Hospital Clinical Center Banja Luka
The Republic of Srpska Medical Association*

ORGANIZING COMMITTEE

Academician Rajko Kuzmanović, president
Academician Dragoljub Mirjanić, vice-president
Academician Vaskrsija Janjić
Academician Branko Škundrić
Prof. Simo Jokanović, Ph. D.
Prof. Zoran Rajilić, Ph. D.
Prof. Mirko Stanetić, Ph. D.
Prof. Nebojša Jovanić, Ph. D.
MSc Vinko Bogdan
Prof. Siniša Vučenović, Ph. D.

НАУЧНИ ОДБОР

Академик Драгољуб Мирјанић
Академик Бранко Шкундрић
Академик Јован Шетрајчић
Академик Стане Пејовник (Словенија)
Академик Пантелија Дакић
Проф. др Неђо Ђурић, дописни члан АНУРС-а
Академик Томислав Павловић
Академик Ростислав Андриевски (Русија)
Академик Филип Говоров (Украјина)
Академик Џералд Полак (САД)
Проф. др Румиана Тсенкова (Јапан)
Проф. др Мај Ван Хо (Велика Британија)
Проф. др Ифа Говен (Ирска)
Проф. др Јукио Косуги (Јапан)
Др Мајрон Д. Еванс (Канада)
Проф. др Мартин Чаплин (Велика Британија)
Проф. др Ђуро Коруга (Србија)
Проф. др Драгица Лазић
Проф. др Перо Дугић
Проф. др Слободан Чупић

Научни скуп одржаће се у Великој сали АНУРС-а.

SCIENTIFIC COMMITTEE

Academician Dragoljub Mirjanić
Academician Branko Škundrić
Academician Jovan Šetrajčić
Academician Stane Pejovnik (Slovenia)
Academician Pantelija Dakić
Prof. Neđo Đurić, Ph. D. corresponding member of ASARS
Academician Tomislav Pavlović
Academician Rostislav Andrievski (Russia)
Academician Filip Govorov (Ukraine)
Academician Gerald Pollak (USA)
Prof. Roumiana Tsenkova, Ph. D. (Japan)
Prof. Mae Wan Ho, Ph. D. (Great Britain)
Prof. Aoife Gowen (Ireland)
Prof. Yukio Kosugi, Ph. D. (Japan)
Mayron D. Evans, Ph. D. (Canada)
Prof. Martin Chaplin, Ph. D. (Great Britain)
Prof. Đuro Koruga, Ph. D. (Serbia)
Prof. Dragica Lazić, Ph. D.
Prof. Pero Dugić, Ph. D.
Prof. Slobodan Čupić, Ph. D.

The scientific conference will take place at the Big Hall of ASARS.

НЕДЈЕЉА, 21. ДЕЦЕМБАР 2014.

- Долазак и смјештај учесника научног скупа који живе изван Бање Луке у хотелу „Босна”.
- Регистрација учесника научног скупа у хотелу „Босна” од 17-20 часова.

ПОНЕДЈЕЉАК, 22. ДЕЦЕМБАР 2014.

- 8,30 Регистрација учесника научног скупа (АНУРС)
- 9,00 Свечано отварање скупа
- 9,30 Пленарна предавања
- 13,10 Постер презентације
- 14,10 Дискусија
- 15,00 Затварање конференције

SUNDAY, December 21, 2014

- Arrival of the participants and accommodation in the hotel „Bosna”.
- Registration of the participants at Hotel „Bosna” from 5 p.m. to 8 p.m.

MONDAY, DECEMBER 22, 2014

- 8,30 Registration of the participants in the ASARS
- 9,00 Opening ceremony
- 9,30 Plenary session
- 13,10 Poster presentations
- 14,10 Discussion
- 15,00 Closing ceremony

ПОНЕДЈЕЉАК, 22. ДЕЦЕМБАР 2014.
MONDAY, DECEMBER 22, 2014

СВЕЧАНО ОТВАРАЊЕ СКУПА
OPENING CEREMONY
(09,00 – 09,30)

- Скуп отвара и учеснике поздравља академик Рајко Кузмановић, председник АНУРС-а
Academician Rajko Kuzmanovic, president of ASARS, will give an opening speech
- Поздравни говор министра науке и технологије, проф. др Јасмина Комића
Welcome speech – Minister of Science and Technology
prof. Jasmin Komić, Ph. D.
- Поздравно обраћање гостију
Welcome speech of the guests

РАДНИ ДИО СКУПА
WORKING SESSION
(09,30 – 15,00)

ПЛЕНАРНА ПРЕДАВАЊА
PLENARY SESSIONS
(09,30–13,10)

- 9,30–9,50 Y. Tripanagnostopoulos, (Greece)
Solar energy materials and systems, for an aesthetic and sustainable future
Материјали и системи за соларну енергију – за естетску и одрживу будућност
- 9,50–10,10 S. Pejovnik, (Slovenia)
Contemporary Research in Battery Field
Савремено истраживање из области батерија
- 10,10–10,30 K. Žagar, S. Šturm, P. McGuinness, S. Kobe, (Slovenia)
Core-shell microstructure of RE-Fe-B grains to achieve maximum coercivity: HRTEM investigations
Микроструктура језгро-омотач RE-Fe-B зрна за постизање максималне коерсивности: HRTEM истраживања
- 10,30–10,50 M. Popović, K. Cionea, A. Bolind, P. Hozeman, (USA)
Liquid Lead-Bismuth Eutectic as a Coolant in Generation IV Nuclear Reactors and in High Temperature Solar Concentrator Applications: Characteristics, Challenges, Issues

Течни РВ-ВІ еутектик као материјал за пренос топлоте у нуклеарним реакторима 4. генерације, и високотемпературним соларним генераторима: карактеристике, захтеви, потешкоће

- 10,50–11,10 A. Senatore, M. Sarno, P. Ciambelli, (Italy)
Novel Nanosized Friction Modifiers for Engine, Gear-box and Rolling Bearings Lubricants
Иновативни лубриканти на основу модификатора фриkcије нано величине за моторе, редукторе и носаче
- 11,10–11,30 Kafe pauza
Coffee break
- 11,30–11,50 L. Matija, (Serbia)
Nanophysical approach to diagnosis of epithelial tissues using Opto-magnetic imaging spectroscopy
Нанофизички приступ дијагностици епителних ткива уз помоћ опто-магнетне спектроскопије
- 11,50 –12,10 E. C. Fuchs, (Netherland)
Electrohydrodynamic liquid bridging – from basics to application
Електрохидродинамско течно преоштавање – од основа до примјене
- 12,10 –12,30 V. Srebrenkoska (Macedonia)
Environmentally friendly technologies for new polymer composite materials: challenges and opportunities
Еколошки прихватљиве технологије за нове полимерне композитне материјале: изазови и шансе
- 12,30–12,50 T. Pavlović, (Serbia)
Energy Efficiency of Differently Oriented Solar Modules in Serbia and Republic of Srpska

Енергетска ефикасност различито позиционираних соларних модула у Србији и Републици Српској

12,50–13,10

Z. Ivić, G. Tsironis, N. Lazarides, (Serbia, Greece)

Self-Induced Transparency in Quantum Metamaterials

Самоиндукована прозачност у квантним метаматеријалима

POSTER PRESENTATIONS

ПОСТЕР ПРЕЗЕНТАЦИЈА

(13,10–14,10)

1. Z. Popović, M. Damnjanović, I. Milošević
Mobility of charge carriers with helical carbon nanotubes
Покретљивост носилаца наелектрисања код хеликалних угљеничних нанотуба
2. D. Kešelj, D. Lazić, B. Škundrić, J. Penavin Škundrić, M. Perušić
The Possibility of Hydrothermal Synthesis of NaY Zeolite Using Different Mineral Acids
Могућност хидротермалне синтезе NaY зеолита кориштењем различитих минералних киселина
3. D. Mirjanić, D. Divnić, S. Maksimović
Testing the Efficiency of Polycrystalline Solar Panels with Respect to Their Geographical Orientation and Tilt Angle
Испитивање ефикасности поликристалних соларних панела у односу на њихову географску оријентацију и угао нагиба
4. V. Aleksić, V. Mičić, Z. Petrović, D. Lukić, D. Manječić
Synthesis of Nonlinear Copolyesters Based on Lactide and Glycerol
Синтеза нелинеарних кополимера лактида и глицерола
5. M. Pavlović, M. Pavlović, M. Gligorić, V. Ćosović, V. Vojanić, M. Tomić
Electrical Conductivity of the Electrodeposited Copper Powder Filled Lignocellulose Composites
Електрична проводљивост лигноцелулозних композиата пуњених електролитичким бакарним прахом

6. P. Kovač, B. Savković, M. Gostimirović, D. Ješić
Adoption of Specific Boronising Technology of Steel Workpiece and Exemination of Borid Layer Wear
Усвајање специфичне технологије борирања челичног обрадка и испитивање добијеног боридног слоја на хабање
7. V. Mičić, B. Pejović, M. Tomić, I. Ristić, S. Begić
Recycling of Plastic Material and Products from Recycled Plastics Materials
Рециклажа пластичног материјала и производи од рециклираних пластичних материјала
8. D. Ješić, P. Kovač, B. Savković
Energetic and Economic Aspect of Tribological Properties of Austempered Nodular Casting
Енергетски и економски аспекти триболошких особина аустемперованог нодуларног лива
9. S. Pavlović, B. Pejović, V. Mičić, M. Perušić, G. Tadić
Graphical Determination of Polytropic Index in Characteristic Diagrams
Графичко одређивање експонента политропе у карактеристичним дијаграмима
10. S. Kirin, S. Trmčić, A. Sedmak, G. Dimić, B. Pejić
Economic and Energetic Aspects of Miscantus Use in Real Systems
Економски и енергетски показатељи коришћење мискантуса у реалном систему
11. B. Pejović, V. Mičić, G. Tadić, M. Perušić, S. Pavlović
New Model for Determining of Change Entropy of Semi Ideal Gas by Using Fractional Temperature Function
Нови модел за одређивање промене ентропије полуидеалног гаса применом разломљене температурне функције

12. D. Tošković, D. Rajić, S. Pavlović, N. Tošković
Determination of Corrosion Rate Austenitic Steels S 4571 and S 4580 in a Solution of Calcium Hypochlorite
Одређивање брзине корозије аустенитних челика Š 4571 и Š4580 у растворима калцијум хипохлорита
13. G. Tadić, V. Pejović, M. Radić, D. Petković, S. Pavlović
Optimization of Characteristic Temperature the Condenser Considering Techno-Economic Aspect
Оптимизација карактеристичне температуре код кондензатора с обзиром на техноекономски аспект
14. Lj. Vasiljević, B. Škundrić, D. Lazić, J. Penavin Škundrić, M. Gligorić, S. Sladojević, V. Mičić
The Oil Absorption and Morphological Properties in the Dependence of Crystallization Time of Zeolite
Зависност апсорпције уља и морфолошких особина од времена кристализације зеолита
15. B. Dugić Kojić, M. Dugić, P. Dugić, G. Dugić, T. Botić
Possibility of Application Nanomaterials in Industrial Lubricants
Могућности примјене наноматеријала у индустријским мазивима
16. M. Jotanović, V. Mičić, G. Tadić
Chemical Engineering and its Function in the Development of Science, Technology and Standards of the People
Хемијско инжењерство и његова улога у развоју науке, технике и стандарда људи
17. S. Papuga, P. Gvero, I. Musić
Influence of the Reaction Time on the Pyrolysis of Plastic Waste in the Fixed Bed Reactor
Утицај времена реакције на пиролизу отпадне пластике у реактору са фиксним слојем

18. D. Petković, M. Mandić
Application of Novel MCDM Method for Materials Selection
Примена новог метода вишекритеријумског одлучивања за избор материјала
19. M. Plavšić, S. Simić, D. Mihić, D. Talijan
Use of Mechanics of Fracture Materials on Stress Corrosion
Примјена механике лома на напонску корозију
20. M. Mandić, D. Petković
Application of MCDM Methods for Materials Selection
Примена метода вишекритеријумског одлучивања за избор материјала
21. M. Srećković, Z. Latinović, M. Dinulović, A. Janićijević, A. Bugarinović, N. Ratković Kovačević, M. Janićijević
Modern and Potential Laser Applications in Selected Branches of Medicine and Interactions Modeling
Савремене и потенцијалне примене ласера у изабраним гранама медицине и моделовање интеракције
22. A. Janićijević, S. Savović, A. Djordjevich, A. Simović, B. Drljača
Numerical Solution of the Diffusion Equation for Binary Gas Mixtures
Нумеричко решење дифузионе једначине за бинарне гасне смеше
23. S. Savović, A. Đorđević, A. Simović, B. Drljača, A. Janićijević
Numerical Solution of the Advection – Diffusion Equation with Constant and Periodic Boundary Conditions
Нумеричко решење адвекционо-дифузионе једначине са сталним и периодичним граничним условима

24. P. Mali, S. Radošević, M. Rutonjski, M. Pantić
Thermodynamic Properties of Frustrated $S=1/2$ Heisenberg $J1 - J2$ Antiferromagnet on a Complex Lattice
Термодинамичка својства фрустрираног $S=1/2$ Хајзенбергов $J1 - J2$ антиферомагнета на комплексној решеци
25. S. Pelemiš, M. Šljivić
Development of Sustainable Interrelations between Education, Research and Innovation at WBC Universities in Nanotechnologies and Advanced Materials where Innovation Means Business
Развој одрживих међусобних односа између образовања, истраживања и иновација на WBC Универзитетима код нанотехнологија и савремених материјалима код којих иновативност значи посао
26. V. Đukić, Lj. Vujaković, T. Baroš
Mechanical-Physical Treatment of Used Motor Oil with in a Sustainable Waste Management System
Механичко-физичка обрада истрошеног моторног уља у систему одрживог управљања отпадом
27. B. Šupić, P. Dakić, R. Ivanković, D. Jokanović
Energy Efficiency of Renewable Energy in the Republic of Srpska
Енергетска ефикасност код обновљивих извора енергије у Републици Српској
28. P. Dakić, B. Šupić
Impact of Contemporary Materials to Energy Efficiency in the Republic of Srpska
Утицај савремених материјала на енергетску вриједност у Републици Српској

29. P. Dakić, B. Grozdanić, B. Dakić
Effective, Efficient and Ecologically Friendly System of Heating Generated by Using the Advanced Methods and Materials
Ефективан, ефикасан и еколошки систем гријања генерисан коришћењем савремених метода и материјала
30. M. Balaban, V. Antić, J. Đonlagić
Rheological, Mechanical and Thermal Properties of Poly(Urethane-Urea) Copolymers Based on Poly(Dimethylsiloxane) Soft Segment
Реолошка, механичка и термичка својства поли(уретан-уреа) кополимера на бази поли(диметилсилоксанског) меког сегмента
31. N. Đurić
Geothermal Energy in Semberija Reality or Just Expecations???
Геотермална енергија у Семберији реалност или само очекивања???
32. Z. Petrović, P. Dugić, V. Aleksić, S. Begić, V. Mičić, N. Kljajić, B. Milovanović
Effect of Adsorption Processing of Solvent Base Oils by Activated Bentonite
Ефекти адсорпционе обраде солвентних базних улја активираним бентонитом
33. M. Stanković, U. Umićević
Daylight – the Oldest Contemporary Material in Architectural Accomplishments – Comfortable experience and healthy life in the century of knowledge stimulated by daylight
Дневна свјетлост – најстарији савремени материјал у архитектонском стваралаштву – Угодан доживљај и здрав живот у вијеку знања стимулисан дневном свјелошћу

34. D. Jevtić, G. Broćeta, A. Savić
Modification of Viscosity in Concrete Composite
Модификација вискозитета у бетонским композитима
35. M. Malešev, V. Radonjanin, G. Broćeta
Properties of Recycled Aggregate Concrete
Својства бетона на бази рециклираног агрегата
36. Ђ. Jovanović, D. Radaković, M. Matavulj
New Materials in Civil Engineering in the Concept of „Cleaner Production”
Нови материјали у грађевинарству у концепту „чистије производње”
37. N. Cekić
Impact of Contemporary Materials on Formation of Facades in Architecture
Утицај савремених материјала на израду фасада у архитектури
38. D. Grujić, A. Savić, Lj. Topalić Trivunović, S. Matoš, M. Čiča
Exploring the Effect of Knitted Fabrics Processing on the Degree of Coloration and Antimicrobial Properties
Истраживање утицаја начина обраде плетенина на степен обојења и антимикробна својства
39. D. Grujić, A. Savić, Lj. Topalić Trivunović, S. Matoš, D. Jokanović, M. Gorjanac
The Influence of Plasma Pretreatment and Processing with Herbal Extracts of Achillea Millefolium L. on Antimicrobial Properties of Knitted Fabrics
Утицај обраде плазмом и екстрактима биљке Achillea millefolium L. на антимикробна својства плетенина

40. M. Stančić, D. Grujić, D. Novaković, J. Geršak
Influence of Printing Parameters and Material Composition of Textile Materials on Warm or Cold Feeling
Утицај параметара штампе и сировинског састава текстилних материјала на топло-хладни осјећај
41. B. Rodić Grabovac, R. Đudić, P. Sailović
The Obtaining of Materials with Antibacterial Activity by Bonding of Cefazoline on Modified Cellulosic Bandage
Добијање материјала са антибактеријском активношћу везивањем цефазолина на модификовани целулозни завој
42. D. Manjenčić, G. Marković, M. Marinović Cincović, S. Samaržija Jovanović, V. Aleksić, V. Jovanović, J. Budinski Simendić
The Influence of Controlled Radiation on the Properties of Elastomers Based on Different Network Precursors
Утицај контролисане радијације на својства еластомера добијених од различитих прекурсора мрежа
43. V. Aleksić, Z. Bjelović, M. Jovičić, I. Ristić, N. Budinski, V. Teofilović, Z. Petrović, J. Budinski Simendić
The Influence of Isocyanate Type on the Reaction Kinetic of Polyurethanes Based on Castrol Oil
Утицај типа изоцијаната на реакциону кинетику полиуретана добијених од рицинусовог уља
44. Lj. Tanasić, M. Marinović Cincović, S. Cakić, I. Ristić, R. Radičević, J. Budinski Simendić
The Influence of the Method of Synthesis on the Properties of Environmentally-friendly poly (L-lactide)
Утицај метода синтезе на својства еколошки прихватљивог поли (L-лактида)

45. J. Budinski Simendić, J. Milić, Lj. Korugić-Karasz, N. Budinski, N. Vukić, T. Erceg, G. Marković, A. Aroguz
Dynamic-Mechanical Behaviour of Hybrid Materials Based on EPDM Rubber
Динамичко-механичко понашање хибридних материјала добијених од EPDM каучука
46. B. Malinović, J. Mandić, S. Bunić
Design Parameters of Electrochemical Reactor for Waste Water Treatment
Начела пројектовања електрохемијског реактора за третман отпадних вода
47. S. Sredić, M. Davidović, S. Zec, U. B. Mioč, Ž. Čupić, D. Jovanović, D. Lončarević
Structural Study of Composite Systems: Transition Metals Oxide (Co, Ni) / Montmorillonite
Структурна истраживања композитних система: Прелазни метали (Co, Ni) / минерал монтморилонит
48. S. Simić, B. Popović, M. Plavšić, D. Ganilović
Technological and Economic Aspects of Exploitation and Preparation Water Use for Production Processes in Refineries
Технолошки и економски аспекти експлоатације и припреме воде за потребе производног процеса у рафинеријама
49. S. Pelemiš, B. Škipina, D. Mirjanić, I. Hut
Biomedical Applications and Nanotoxicity some of Nanostructured Materials
Биомедицинске примјене и нанотоксичност неких наноструктурних материјала


50. J. Munćan, L. Matija, R. Tsenkova, Đ. Koruga
Spectroscopic Characterization of Aqueous Fullerol Solutions
Спектроскопска карактеризација водених раствора фулерола
51. I. Hut, B. Jeftić, S. Pelemiš, L. Matija
Comparative characterization of high purity diamagnetics (Ag & Cu) by the means of AFM, MFM and OMIS
Упоредна карактеризација дијамагнетика високе чистоће (Ag i Cu) AFM-ом, MFM-ом и OMIS-ом
52. A. Todorović, R. Rudolf, M. Čolić, I. Đorđević,
N. Milošević, B. Trifković, V. Veselinović, N. Romčević
Biocompatibility Evaluation of Cu-Al-Ni Shape Memory Alloys
Биокомпатибилност Cu-Al-Ni легура са меморисаним обликом
53. B. Trifković, A. B. Todorović, A. R. Todorović, T. Puškar,
R. Rudolf, V. Lazić, D. Jevremović, V. Veselinović
All – Ceramic Materials in Dental CAD/CAM Systems – Recent Trends in the Development
Керамички материјали у стоматолошким CAD/CAM технологијама – актуелни трендови у развоју
54. J. Vojinović, O. Dolić, M. Obradović, S. Sukara
Application of Polyol in the Prevention and Treatment of Caries
Примена полиола у превенцији и лечењу каријеса
55. O. Janković, T. Adamović, V. Veselinović
Vertise Flow Impact on the Quality of Composite Restorations
Утицај Vertise Flow на квалитет композитних рестаурација
56. V. Mirjanić, Đ. Mirjanić, J. Vojinović
Nanostructure analysis of Contec LC – Denaturum of orthodontic adhesive

*Наноструктурна анализа Contec LC – Dentaaurum
ортодонтског адхезива*

57. Đ. Mirjanić, V. Mirjanić, J. Vojinović
AFM Analysis of Enamel Nanostructure After the Action of Aggressive Beverage
АФМ анализа наноструктуре глеђи након дјеловања агресивног напитка
58. I. Kasagić Vujanović, D. Jelić, V. Antunović,
B. Jančić Stojanović, D. Ivanović
Stability Study of Amlodipine Besylate and Bisprolol Fumarate in Aqueous Solutions
Испитивање стабилности Амлодипин-Бесилата и Биспролол-Фумарата у воденим растворима
59. D. Jelić, V. Antunović, I. Kasagić Vujanović,
M. Đermanović, A. Đukić Drvar
The Use of Anhydrous Cobalt Chloride for Water Content Determination in Some Pharmaceutical Products by Means of Spectrophotometry
Употреба анхидрованог кобалт хлорида за одређивање садржаја воде у фармацеутским препаратима методом спектрофотометрије
60. S. Gotovac Atlagić, V. Pavlić
An Attempt to Obtain Medically Applicable Iron Nanoparticles from Iron Mine Waste Water
Покушај добијања медицински примјењивих жељезних наночестица из отпадне воде рудника жељеза
61. Lj. Marković Đurić, V. Pavlić
Effects of Solcoseryl® Dental Paste in Therapy of Oral Aphthous Ulcerations
Утицај Solcoseryl® денталне пасте у терапијском збрињавању афтозних улцерација

62. J. Ilić, J. Lovrić, T. Adamović
Mini Implants as an Anchorage in Orthodontic Therapy
Мини имплантати као упориште у ортодонтској терапији
63. J. Lovrić, J. Ilić, T. Adamović
Regenerative Endodontics
Регенеративна ендодонција
64. A. Figurek, V. Vlatković, D. Vojvodić
The Level of Serum Albumin According to Transport Characteristics of Peritoneal Membrane
Ниво серумских албумина у односу на транспортне карактеристике перитонеумске мембране
65. N. Knežević, A. Đeri
The Effect of Carbamid and Hydrogen Peroxide on the Colour Changing Degree in Endodontic Treated Teeth
Утицај карбамид и водоник пероксида на степен промјене боје ендодонтски третираног зуба
66. A. Đeri, N. Knežević
The Effect of Calcium Hydroxide on Rats Teeth Pulp Seven Days After Direct Pulp Capping
Ефекат калцијум-хидроксида на пулпу зуба пацова седам дана након директног прекривања пулпе
67. D. Jojić, S. Petrović Terpić, B. Čančarević Đajić, Lj. Solomun, M. Preradović, D. Jović
The Importance and Risk Factors of Screening for Retinopathy of Prematurity
Значај скрининга и фактори ризика код ретинопатије прематуритета

68. A. Maletin, B. Vujović, I. Nešković
Influence of the Preparation of Artificial Acrylic Teeth on the Bond Strength of the Denture base
Утицај припреме вештачког акрилатног зуба на јачину везе са базом протезе
69. R. Arbutina, N. Trtić, O. Janković, V. Veselinović, R. Knežević, A. Arbutina
The Erosive Potential of White Wine on Enamel Surface: An in Vitro Scanning Electron Microscopy Investigation
Ерозивни потенцијал бијелог вина на површину глеђи: In Vitro студија скенинг електронска микроскопија
70. S. Ilić, O. Janković
Materials for Filling Teeth in Patients with Mental Disabilities
Материјали за испуне зуба код особа ометених у менталном развоју
71. O. Janković, S. Ilić
Clinical Testing of Fluid Resin with Adhesive Characteristics in the Therapy of Non-carious Cervical Lesions
Клиничко испитивање течне смоле са адхезивним својствима у терапији некариозних цервикалних лезија



14,10 – 15,00 Дискусија
Discussion

15,00 ЗАТВАРАЊЕ НАУЧНОГ СКУПА
CLOSING CEREMONY

Ручак (Lunch)

ОДЛАЗАК УЧЕСНИКА НАУЧНОГ СКУПА
DEPARTURE OF THE PARTICIPANTS

РЕПУБЛИКА СРБИЈА
МИНИСТАРСТВО НАУКЕ,
ТЕХНОЛОШКОГ РАЗВОЈА И ИНОВАЦИЈА
Матични научни одбор за физику
Датум: 23. 06. 2023. године

**Природно-математички факултет Универзитета у Приштини
Проф. др Бранко Дрљача, редовни професор**

Лоле Рибара 29
38220 Косовска Митровица

Поштовани проф. др Дрљача,

Матични научни одбор за физику је на својој седници од 23. јуна 2023. године разматрао Ваш захтев за признавање и категорисање следеће публикације:

„Преносне карактеристике оптичких влакана са степенастим индексом преламања”, Природно-математички факултет Универзитета у Приштини (Косовска Митровица, 2016), стр. 1-284 (ISBN: 978-86-80795-27-0).

Узимајући у обзир критеријуме из Прилога 1 Правилника о стицању истраживачких и научних звања, Одбор је донео одлуку да се наведена публикација **категорисаће као истакнута монографија националног значаја (М41)** у смислу Правилника о стицању истраживачких и научних звања.


ОБРАЗЛОЖЕЊЕ

Ова монографска публикације је написана на српском језику и издата је 2016. године од стране Природно-математичког факултета Универзитета у Приштини, са привременим седиштем у Косовској Митровици. Она испуњава библиографске услове, јер од захтеваних 7 аутоцитата категорије М20 или М50 за националну монографију, у складу са Правилником о стицању истраживачких и научних звања, у списку референци постоји 10 аутоцитата аутора категорије М20. Што се тиче обима, публикација има 284 стране и једног аутора, па у потпуности задовољава тражени услов о минималном ауторском доприносу.

Наведена публикација се бави проучавањем оптичких влакана, а посебно њихових преносних карактеристика, метода за анализу, моделирања преносних карактеристика влакана са степенастим индексом преламања и садржи преглед оригиналних научних резултата аутора који су раније објављени у часописима категорије М20.

С поштовањем,

Председник Матичног научног одбора за физику


др Антун Балаж, научни саветник